AD-A272 957

An International Journal

IMPACT ENGINEERING

HYPERVELOCITY IMPACT

(2)

PROCEEDINGS OF THE 1992 SYMPOSIUM

Austin, Texas

17–19 November 1992

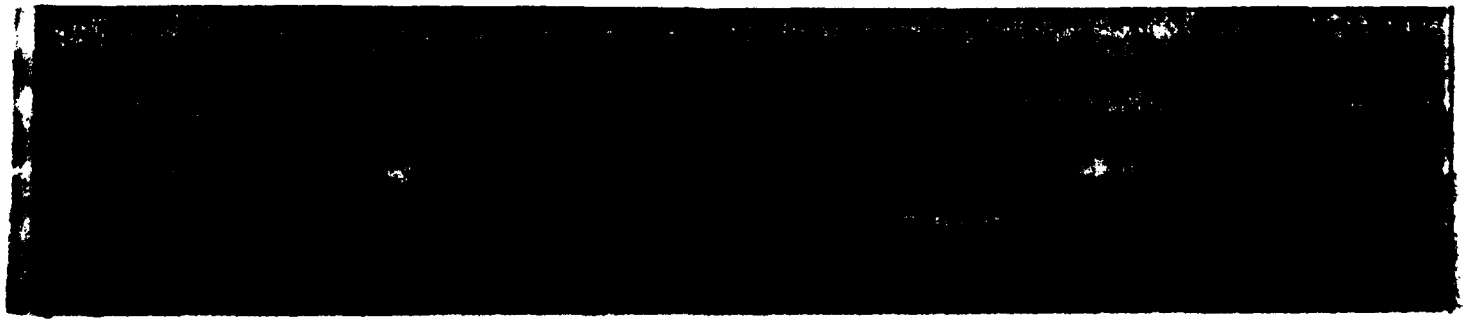
DISTRIBUTION STATEMENT A
Approved for public release;
Distribution Unlimited

ELECTE
NOV 18 1993
S B D

Guest Editor
CHARLES E. ANDERSON, JR.

Indexed/abstracted in *Current Contents (Engineering, Technology & Applied Science), Engng Ind Monthly & Author Index, Appl Mech Rev, Cam Sci Abstr, Int Civil Eng Abstr, Metals Abstr, Materials Science Citation Index*

ISSN 0734–743X
IJIEDA 14(1–4) 1–892 (1993)



Best
Available
Copy

REPORT DOCUMENTATION PAGE

Form Approvec
OMB No. 0704-0188

Public reporting burden for this collection of information is estimated to average 1 hour per response, including the time for reviewing instructions, searching existing data sources, gathering and maintaining the data needed, and completing and reviewing the collection of information. Send comments regarding this burden estimate or any other aspect of this collection of information, including suggestions for reducing this burden, to Washington Headquarters Services, Directorate for Information Operations and Reports, 1215 Jefferson Davis Highway, Suite 1204, Arlington, VA 22202-4302, and to the Office of Management and Budget, Paperwork Reduction Project (0704-0188), Washington, DC 20503.

1. AGENCY USE ONLY (Leave blank)	2. REPORT DATE	3. REPORT TYPE AND DATES COVERED
	October, 1993	Final—November 17 - November 20, 1992

4. TITLE AND SUBTITLE

1992 Hypervelocity Impact Symposium (U)
(three volumes: Classified, Unclassified NOFORN, and Unclassified)

5. FUNDING NUMBERS

DAAA21-90-D-0009

6. AUTHOR(S)

Dr. Harry D. Fair and Dr. Thomas M. Kiehne, editors

7. PERFORMING ORGANIZATION NAME(S) AND ADDRESS(ES)

Institute for Advanced Technology
The University of Texas at Austin
4030-2 West Braker Lane
Austin, TX 78759

8. PERFORMING ORGANIZATION REPORT NUMBER

IAT.R 0023

9. SPONSORING / MONITORING AGENCY NAME(S) AND ADDRESS(ES)

ARPA
3701 N. Fairfax Drive
Arlington, VA 22203-1714

10. SPONSORING / MONITORING AGENCY REPORT NUMBER

11. SUPPLEMENTARY NOTES

12a. DISTRIBUTION / AVAILABILITY STATEMENT

Classified and Unclassified NOFORN (S); Distribution authorized to U.S. Government agencies and their contractors; Critical Technology; Other requests for this document shall be referred to: Advanced Research Projects Agency, ORO/NC.

Unclassified (A): unlimited

DISTRIBUTION STATEMENT A
Approved for public release;
Distribution Unlimited

12b. DISTRIBUTION CODE

Classified, Unclassified NOFORN: C

Unclassified: A

13. ABSTRACT (Maximum 200 words)

(U) The 1992 Hypervelocity Impact Symposium was held in Austin, Texas on November 17-20, 1992. The proceedings are published in three volumes. Seventy-six papers were unclassified, and published together as Volume 14, Numbers 1-4 of the International Journal of Impact Engineering, which can be obtained from Pergamon Press, Maxwell House. Fairview Park, Elmsford, NY 10523. Nine papers were selected for presentation and publication in the Classified Proceedings, and eight papers were selected for presentation and publication in the NOFORN Proceedings.

14. SUBJECT TERMS

Anti-Armor	Experimental Techniques	Material Response
Cratering And Capture	Hypervelocity Impact	Penetration Mechanics
Debris Generation	Long Rod	Shield Design

15. NUMBER OF PAGES

1196

16. PRICE CODE

17. SECURITY CLASSIFICIATION OF REPORT	18. SECURITY CLASSIFICATION OF THIS PAGE	19. SECURITY CLASSIFICATION OF ABSTRACT	20. LIMITATION OF ABSTRACT
Secret	Unclassified	Unclassified	none

HYPERVELOCITY IMPACT

PROCEEDINGS OF THE 1992 SYMPOSIUM

Austin, Texas

17–19 November 1992

Guest Editor
CHARLES E. ANDERSON, JR

Accession For	
NTIS GRA&I	☑
DTIC TAB	☐
Unannounced	☐
Justification	
By	
Distribution/	
Availability Codes	
Dist	Avail and/or Special
A-1	



PERGAMON PRESS
OXFORD • NEW YORK • SEOUL • TOKYO

DTIC QUALITY INSPECTED

93-28088



93 11 16 027

Publishing, Subscription and Advertising Offices:
Headington Hill Hall, Oxford OX3 0BW, U.K. (*Phone* Oxford 794141, *telex* 83177)

Back Issues
Back issues of all previously published volumes are available direct from Pergamon Press offices.

Copyright © 1993 Pergamon Press Ltd. Published in two volumes: Volume 13 published quarterly in February, May, August and November, Volume 14 complete in May

Published as Volume 14 of the *International Journal of Impact Engineering* and supplied to subscribers as part of their subscription. Also available to non-subscribers. Papers reproduced by direct photographic process and authors remain fully responsible for the quality and content of the text.

It is a condition of publication that manuscripts submitted to this journal have not been published and will not be simultaneously submitted or published elsewhere. By submitting a manuscript, the authors agree that the copyright for their article is transferred to the publisher if and when the article is accepted for publication. However, assignment of copyright is not required from authors who work for organizations which do not permit such assignment. The copyright covers the exclusive rights to reproduce and distribute the article, including reprints, photographic reproductions, microform or any other reproductions of similar nature, and translations. No part of this publication may be reproduced, stored in a retrieval system or transmitted in any form or by any means, electronic, electrostatic, magnetic tape, mechanical, photocopying, recording or otherwise, without permission in writing from the copyright holder.
Whilst every effort is made by the publishers and editorial board to see that no inaccurate or misleading data, opinion or statement appear in this journal, they wish to make it clear that the data and opinions appearing in the articles and advertisements herein are the sole responsibility of the contributor or advertiser concerned. Accordingly, the publishers, the editorial board and editors and their respective employees, officers and agents accept no responsibility or liability whatsoever for the consequences of any such inaccurate or misleading data, opinion or statement.

Photocopying Information for Users in the U.S.A. The Item-fee Code for this publication indicates that authorization to photocopy items for internal or personal use is granted by the copyright holder for libraries and other users registered with the Copyright Clearance Center (CCC) Transactional Reporting Service provided the stated fee for copying, beyond that permitted by Section 107 or 108 of the United States Copyright Law, is paid. The appropriate remittance of $6.00 per copy per article is paid directly to the Copyright Clearance Center Inc., 27 Congress Street, Salem, MA 01970.
Permission for other use. The copyright owner's consent does not extend to copying for general distribution, for promotion, for creating new works, or for resale. Specific written permission must be obtained from the publisher for such copying.

The Item-fee code for this publication is: 0734–743X/93 $6.00 + 0.00

PROCEEDINGS OF THE 1992 HYPERVELOCITY IMPACT SYMPOSIUM

Contents

N. Jones	ix	Editorial
C. E. Anderson, Jr and S. J. Bless	xi	Preface
C. E. Anderson, Jr, D. L. Littlefield and J. D. Walker	1	Long-rod penetration, target resistance, and hypervelocity impact
J. A. Ang, B. D. Hansche, C. H. Konrad, W. C. Sweatt, S. M. Gosling and R. J. Hickman	13	Pulsed holography for hypervelocity impact diagnostics
Y.C. Angel and J. P. Smith	25	Critical response of shielded plates subjected to hypervelocity impact
N. Ari and J. S. Wilbeck	37	Debris fragment characterization in oblique hypervelocity impacts
D. Atkinson and A. Watts	49	Impact damage and optical scatter
S. Bahk, D. Chavez, B. Emery, B. Wilson and J. Stoltzfus	61	Protecting aluminum alloy from particle-impact ignition with an Al_2O_3 film
J. R. Baker and M. A. Persechino	73	An analytical model of hole size in finite plates for both normal and oblique hypervelocity impact for all target thicknesses up to the ballistic limit
S. J. Bless and C. E. Anderson, Jr	85	Penetration of hard layers by hypervelocity rod projectiles
M. B. Boslough, J. A. Ang, L. C. Chhabildas, W. D. Reinhart, C. A. Hall, B. G. Cour-Palais, E. L. Christiansen and J. L. Crews	95	Hypervelocity testing of advanced shielding concepts for spacecraft against impacts to 10 km/s
K. G. Budge and J. S. Peery	107	RHALE: a MMALE shock physics code written in C++
L. C. Chhabildas, J. E. Dunn, W. D. Reinhart and J. M. Miller	121	An impact technique to accelerate flier plates to velocities over 12 km/s
L. C. Chhabildas, E. S. Hertel and S. A. Hill	133	Hypervelocity impact tests and simulations of single Whipple bumper shield concepts at 10 km/s
E. L. Christiansen	145	Design and performance equations for advanced meteoroid and debris shields
E. L. Christiansen, E. Cykowski and J. Ortega	157	Highly oblique impacts into thick and thin targets

E. L. Christiansen and J. H. Kerr	169	Mesh double-bumper shield: a low-weight alternative for spacecraft meteoroid and orbital debris protection
T. Cooper	181	A novel method for launching flyer plates
B. G. Cour-Palais, A. J. Piekutowski, K. V. Dahl and K. L. Poormon	193	Analysis of the UDRI tests on Nextel multi-shock shields
D. A. Crawford and P. H. Schultz	205	The production and evolution of impact-generated magnetic fields
J. P. Curtis	217	The effects of a random off-axis velocity component on the penetration achieved by long rod kinetic energy penetrators and shaped charge jets
E. P. Fahrenthold	229	A Lagrangian model for debris cloud dynamics simulation
S. A. Finnegan, J. K. Pringle, J. C. Schulz, O. E. R. Heimdahl and A. J. Lindfors	241	Impact-induced delayed detonation in an energetic material debris bubble formed at an air gap
J. D. Frey, F. Janicot, X. Garaud, P. Groenenboom and M. Lambert	255	The validation of hydrocodes for orbital debris impact simulation
M. D. Furnish	267	Recent advances in methods for measuring the dynamic response of geological materials to 100 GPa
I. Gilath, S. Eliezer, T. Bar-Noy, R. Englman and Z. Jaeger	279	Material response at hypervelocity impact conditions using laser induced shock waves
J. J. Gilman	291	Metallization and insulization during impact
F. I. Grace	303	Nonsteady penetration of long rods into semi-infinite targets
D. J. Grosch and J. P. Riegel	315	Development and optimization of a "micro" two-stage light-gas gun
V. Hohler, H. Nahme, R. Tham, A. Stilp, K. Weber, Y.-K. Yeh, J.-P. Wang and T.-S. Lee	325	Experimental and numerical simulation of high velocity impact on steel targets
K. A. Holsapple	335	Hypervelocity impact experiments in surrogate materials
F. Hörz, M. J. Cintala, R. P. Bernhard and T. H. See	347	Dimensionally scaled penetration experiments to extract projectile sizes from space exposed surfaces

W. M. Isbell and W. J. Tedeschi	359	Hypervelocity research and the growing problem of space debris
G. R. Johnson and W. H. Cook	373	Lagrangian EPIC code computations for oblique, yawed-rod impacts onto thin-plate and spaced-plate targets at various velocities
G. R. Johnson, E. H. Petersen and R. A. Stryk	385	Incorporation of an SPH option into the EPIC code for a wide range of high velocity impact computations
W. H. Jolly and J. E. Williamsen	395	Statistical ballistic limit curve regression for Space Station *Freedom* meteoroid/orbital debris shielding
S. E. Jones, R. B. Marlow, J. W. House and L. L. Wilson	407	A one-dimensional analysis of the penetration of semi-infinite 1100-0 aluminum targets by rods
J. F. Kerrisk and J. K. Meier	417	Problems associated with launching hypervelocity projectiles from the fast shock tube
M. E. Kipp, D. E. Grady and J. W. Swegle	427	Numerical and experimental studies of high-velocity impact fragmentation
R. J. Lawrence and W. M. Trott	439	Theoretical analysis of a pulsed-laser-driven hypervelocity flyer launcher
R. Lee, J. Osher, H. Chau, M. Gerassimenko, G. Pomykal and R. Speer	451	The impact of flat, thin plates on aluminum targets in the 5–10 km/s velocity range
J. P. Leyrat, E. Charvet and H. C. Pujols	467	Creation and simulation of very fast jets
T. D. Maclay, R. D. Culp, L. Bareiss, T. G. Gillespie and F. M. Kustas	479	Topographically modified bumper concepts for spacecraft shielding
D. A. Mandell and R. Henninger	491	Ceramics models in the MESA codes
J. L. Mayes, S. L. Hatfield, P. P. Gillis and J. W. House	503	Void formation in OFE copper
R. A. McDonald, W. G. Tanner and W. M. Alexander	509	A comparison of hole size formation caused by a hypervelocity impact with a thin film using molecular dynamics and CTH
R. A. Mog, M. J. Helba and J. H. Robinson	519	Development and optimization of a multi-bumper design model for spacecraft protective structures
W. J. Nellis and A. J. Gratz	531	Recovery of materials impacted at high velocity

G. D. Olsen and A. M. Nolen	541	Advanced shield design for Space Station *Freedom*
D. L. Orphal, C. E. Anderson, Jr, R. R. Franzen, J. D. Walker, P. N. Schneidewind and M. E. Majerus	551	Impact and penetration by $L/D \leq 1$ projectiles
M. A. Persechino and A. E. Williams	561	Tumbling of hypervelocity rods induced by impact with oblique plate targets
A. J. Piekutowski	573	Characteristics of debris clouds produced by hypervelocity impact of aluminum spheres with thin aluminum plates
W. Reschauer and E. Igenbergs	587	Experiments on the hypervelocity penetration of thin aluminium sheets
M. Sanai and J. D. Colton	597	Explosive simulation to investigate enhanced ablator removal
I. Saravane and A. E. Williams	607	The size, velocity and trajectory of debris fragments produced by impact with plate targets
E. M. Schmidt, B. J. Held and D. S. Savick	619	Hypervelocity launch dynamics
E. Schneider, A. Stilp, M. Rott, F. Levadou and G. Schwehm	631	Hypervelocity impact simulation experiments on LDEF-foils
W. P. Schonberg	637	Effect of internal stress fields on the perforation response of dual-wall structures under hypervelocity impact
W. P. Schonberg and F. Yang	647	Response of space structures to orbital debris particle impact
P. H. Schultz	659	Impact crater growth in an atmosphere
G. L. Y. Shephard and S. A. Scheer	671	Secondary debris impact damage and environment study
C. G. Simon	683	Hypervelocity impact testing of micrometeorite capture cells in conjunction with a PVDF thin-film velocity/trajectory sensor and a simple plasma velocity detector
T. H. Sobota, S. M. Babcock and J. W. Humphrey	695	Development of a Scramaccelerator based hypervelocity launcher
R. F. Stellingwerf and C. A. Wingate	707	Impact modeling with smooth particle hydrodynamics

G. L. Stradling, G. C. Idzorek, B. P. Shafer, H. L. Curling, Jr, M. T. Collopy, A. A. Hopkins Blossom and S. Fuerstenau	719	Ultra-high velocity impacts: cratering studies of microscopic impacts from 3 km/s to 30 km/s
W. G. Tanner, Jr, R. A. McDonald, W. M. Alexander and C. R. Maag	729	An examination of hypervelocity particle penetration parameters for thin films flown in space
L. E. Thompson and M. S. Johnson	739	Response of woven ceramic bumpers to hypervelocity impacts
P. Tsou and D. J. Griffiths	751	Exploratory investigations of hypervelocity intact capture spectroscopy
J. D. Walker, D. J. Grosch and S. A. Mullin	763	A hypervelocity fragment launcher based on an inhibited shaped charge
J. M. Walsh, G. L. Stradling, G. C. Idzorek, B. P. Shafer and H. L. Curling, Jr	775	Microparticle impacts at ultra-high velocities: their relation to macroparticle impacts
J. A. Waschl and D. J. Hatt	785	Characterization of a small-scale exploding bridge foil flyer generator
K. Weber, V. Hohler and A. J. Stilp	797	Impact flash and debris cloud expansion of high-pure metal foils
C. A. Weickert and P. J. Gallagher	809	Penetration of explosively formed projectiles
C. A. Wingate, R. F. Stellingwerf, R. F. Davidson and M. W. Burkett	819	Models of high velocity impact phenomena
J. D. Yatteau and D. L. Dickinson	831	An engineering model to predict perforation damage to plates impacted by high velocity debris clouds
D. Yaziv and J. P. Riegel	843	The application of the integral theory of impact to model penetration of hypervelocity impact
C. H. Yew, D. E. Grady and R. J. Lawrence	851	A simple model for debris clouds produced by hypervelocity particle impact
L. Zernow and E. J. Chapyak	863	Experimental and analytical study of early time material processing, in a collapsing shaped-charge liner, using "softly-recovered" partially-collapsed copper liners
	877	List of Attendees
	883	Author Index
	885	Subject Index

EDITORIAL

This special issue of the *International Journal of Impact Engineering* contains the proceedings of the 1992 Hypervelocity Impact Symposium which was held in Austin, Texas, 17–19 November 1992.

I wish to take this opportunity of thanking Charles E. Anderson, Jr and Stephan J. Bless for their considerable assistance in preparing this special issue of the *International Journal of Impact Engineering*. Thanks are also due to the Organising Committee of the Hypervelocity Impact Symposium:

Charles E. Anderson Jr—Southwest Research Institute,
James R. Asay—Sandia National Laboratories,
Harry D. Fair—Institute for Advanced Technology,
William M. Isbell—General Research Corporation,
Gordon R. Johnson—Alliant Techsystems,
Dennis L. Orphal—California Research and Technology, Inc.

The proceedings of the 1986 and 1989 Hypervelocity Impact Symposia were also published as special issues of the *International Journal of Impact Engineering* (Volume 5, Nos 1–4, Volume 10, Nos 1–4). The next Hypervelocity Impact Symposium will be held in Santa Fe, New Mexico, 16–19 October 1994. Announcements will be published in this journal as they become available.

NORMAN JONES

PREFACE

This volume contains the papers presented at the 1992 *Hypervelocity Impact Symposium (HVIS)*, held in Austin, Texas, on 17–19 November 1992. This was the third symposium since the reinitiation of the symposia in 1986, and the proceedings for the 1986 *HVIS* and the 1989 *HVIS* were published as Volumes 5 and 10, respectively, of the *International Journal of Impact Engineering*. The 76 papers in this volume represent advancements in the basic understanding of hypervelocity impact physics and related phenomenology, and engineering applications focused on mitigating or enhancing specific aspects of hypervelocity impact.

In-depth review is a requirement for paper acceptance of the *HVIS*; this process distinguishes these proceedings from most conference proceedings. Each paper has undergone peer review by experts in their respective fields of research. The Organizing Committee is convinced that the overall technical content and presentation are enhanced by this review process. The authors are to be commended for keeping to the schedule for providing their draft manuscripts for review, making appropriate modifications and corrections, and preparing their final manuscript. As you look over the papers in this volume, we think you will agree that the authors have performed some very, very fine research. Indeed, we are certain that the articles in this volume will take their place alongside the 1986 and 1989 *HVIS* articles as often-referenced materials in hypervelocity impact phenomenology.

The Organizing Committee for the 1992 *HVIS* first met in late 1991 to begin planning for the Symposium. Assisting the Organizing Committee were session chairmen and chairmen of special committees. A listing of the various chairmen is given on the next page; their time and dedication greatly assisted in making the symposium a technical success.

We are indebted to Ms Julie Grosser who worked very diligently to assemble this volume. She was responsible for virtually all the details associated with putting this volume together, from abstract submissions to submission of the final manuscripts. She has very carefully gone over all the pages, checking correcting for consistency of format, cleaning up smudges, page numbering, etc. This volume is a reflection of and a tribute to Julie's dedication and attention to detail.

We are indebted to Professor Norman Jones, the Editor-in-Chief of the *International Journal of Impact Engineering*. We are grateful for his suggestions and assistance in bringing these proceedings to publication. Plans are to continue the Hypervelocity Impact Symposia, and we hope that future symposia can also become part of the archival literature.

Charles E. Anderson, Jr
Stephan J. Bless

San Antonio, TX
Austin, TX
March, 1993

Organizing Committee

Charles E. Anderson, Jr
Southwest Research Institute

James R. Asay
Sandia National Laboratories

Harry D. Fair
Institute for Advanced Technology

William M. Isbell
General Research Corporation

Gordon R. Johnson
Alliant Techsystems

Dennis L. Orphal
California Research and Technology, Inc.

Technical Program Chairman

Charles E. Anderson, Jr
Southwest Research Institute

Conference Co-Chairmen

Harry D. Fair
Institute for Advanced Technology

Thomas M. Kiehne
Institute for Advanced Technology

Publications Editor

Julie K. Grosser
Institute for Advanced Technology

Awards Committee Chairman

Dennis E. Grady
Sandia National Laboratories

Commercial Exhibits Chairman

James A. Ang
Sandia National Laboratories

Session Chairmen

Computational Techniques Numeric Modeling of Debris

J. Michael McGlaun
Sandia National Laboratory

Thomas F. Adams
Los Alamos National Laboratory

Cratering and Capture

Peter H. Schultz
Brown University

Debris Generation and Effects Shield Design and Analysis

Jeanne L. Crews
NASA-Johnson Space Center

Malcolm J. Kear
UK Culham Laboratory

Experimental Techniques: Launchers and Experimentation

William J. Nellis
Lawrence Livermore National Laboratory

Gustav-Adolf Schröder
Ernst-Mach-Institut

Penetration Mechanics

Hartmuth F. Lehr
Institute Saint Louis

Thomas Menna
General Research Corporation

Special Applications

William S. deRosset
U.S. Army Ballistic Research Laboratory

Thomas M. Kiehne
Institute for Advanced Technology

Int. J. Impact Engng Vol. 14, pp. 1 – 12, 1993
Printed in Great Britain

0734-743X/93 $6.00 + 0.00
1993 Pergamon Press Ltd

LONG-ROD PENETRATION, TARGET RESISTANCE, AND HYPERVELOCITY IMPACT

CHARLES E. ANDERSON, JR., DAVID L. LITTLEFIELD, and JAMES D. WALKER

Southwest Research Institute
San Antonio, TX 78228

ABSTRACT

Numerical simulations are used to examine long-rod penetration as a function of impact velocity. Similarities and differences between the penetration histories are analyzed, including penetration and tail velocities, penetration depths, crater radii, centerline interface pressures, and the extents of plastic flow in the projectile and target. The one-dimensional modified Bernoulli theory is often used to examine long-rod penetration into semi-infinite targets, and integral to the theory is a term that describes the resistance of the target to penetration. It is observed that the target resistance decreases with impact velocity, and it is shown that this is a consequence of both the residual phase of penetration and variations in the size of the plastic zone field.

NOTATION

c	elastic sound speed	s_{ij}	deviatoric stress tensor	$\dot{w}$	work rate
D	projectile diameter	S	surface	$\dot{W}_\sigma$	rate of work done by mean stress
D^e_{ij}	elastic deformation tensor	t	time	$\dot{W}_s$	rate of work done by deviatoric stress
D^p_{ij}	plastic deformation tensor	T^*	homologous temperature	x	axial coordinate
E	energy	u	penetration (interface) velocity	Y_p	projectile flow stress
l	instantaneous projectile length	v	projectile (tail) velocity	κ	bulk modulus
L	initial projectile length	v_o	impact velocity	ε^p	equivalent plastic strain
$\vec{n}$	unit normal vector	$\vec{v}$	velocity	$\dot{\varepsilon}^*$	normalized plastic strain rate
p	pressure	V	specific volume ($V = 1/\rho$)	η	compression ($1 - \rho_o/\rho$)
P	penetration depth	w	work done per unit volume	ρ	density
R_c	crater radius	$\dot{W}$	work rate per unit volume	σ	flow stress
R_t	target resistance	Ω	volume		

subscripts

p	projectile	P	depth-of-penetration averaged	int	internal energy
t	target	ss	steady state	KE	kinetic energy
o	initial condition	T	time averaged		

INTRODUCTION

Normalized depths of penetration P/L of tungsten-alloy, long-rod projectiles into hard steel targets as a function of impact velocity from two sources are shown in Fig. 1 (Hohler and Stilp, 1987; Sorensen, *et al.*, 1991). The solid line is for projectile length-to-diameter (L/D) ratios of 10, while the dash-dot line is for $L/D \geq 15$ projectiles. The curves represent least-squares curve fits through the experimental data. The steady-state hydrodynamic limit is given by $(\rho_p/\rho_t)^{1/2}$. The efficiency of shorter L/D projectiles, as measured by P/L, is higher than for the longer L/D projectiles. This is a well-known phenomenon; for example, see Hohler and Stilp (1987).

A one-dimensional model independently proposed by Tate (1967, 1969, 1986) and Alekseevskii (1966) has become the standard reference for modeling long-rod penetration of semi-infinite targets such as depicted in Fig. 1. The pressure at the interface of the projectile and the target is given by the modified Bernoulli equation (Tate, 1967, 1969):

$$\frac{1}{2}\rho_p(v-u)^2 + Y_p = \frac{1}{2}\rho_t u^2 + R_t. \tag{1}$$

Y_p is the flow stress of the projectile, and R_t is defined as the target resistance in the one-dimensional formulation. Within a one-dimensional context, some artificial means must be invoked to account for lateral confinement. The

constraint to radial flow in the target is modeled by increasing the target material strength by some factor. Thus, the value of R_t can be substantially higher than the flow stress of the target. Anderson and Walker (1991) show that R_t can be associated with radial gradient terms—in addition to the flow stress—in the axial momentum equation, but unfortunately, there exists no *a priori* means to compute these extra terms. A number of investigators have attempted to calculate the target resistance R_t in Eq. (1) from a variety of arguments; a summary of several of the formulae is given in Anderson and Walker (1991). The analytical procedures for estimating R_t are simply approximations for which there is no way to estimate the error. Thus, R_t is often determined by comparing the total depth of penetration predicted by the theory with experimental data and adjusting R_t until there is agreement. This procedure was used to compute the target resistances for the data of Fig. 1, and are shown in Fig. 2 as a function of impact velocity. A constant flow stress of 2.0 GPa was used for Y_p (Anderson and Walker, 1991). Although the influence of projectile *L/D* on target R_t is evident, the velocity dependence of R_t is certainly more striking. Note that as *P/L* approaches the hydrodynamic limit, R_t approaches Y_p; also, note that R_t must be less than Y_p for the penetration performance to exceed the hydrodynamic limit.

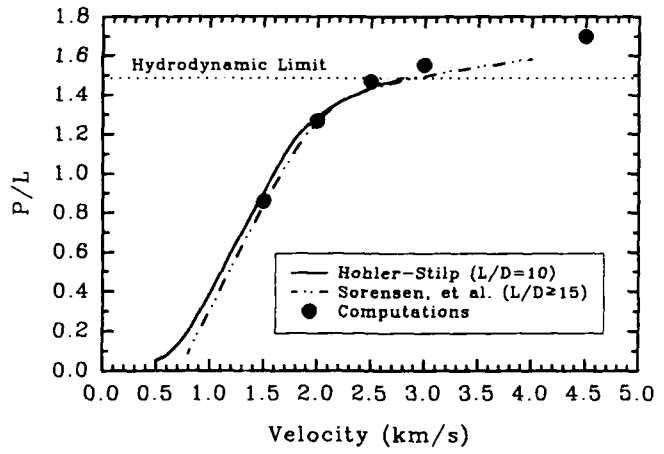


Figure 1: Normalized Depth of Penetration versus Impact Velocity

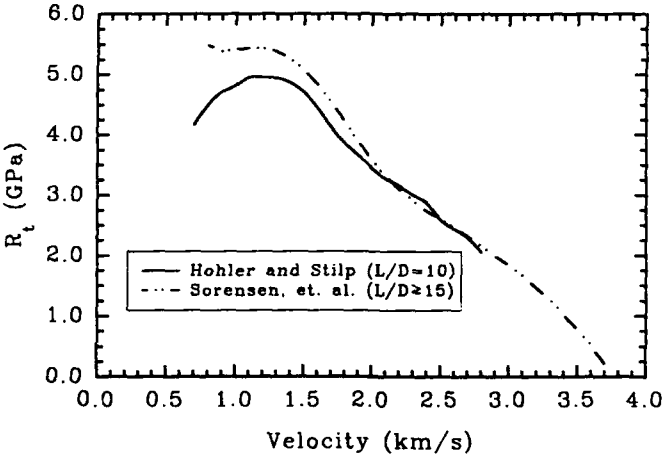


Figure 2: Target Resistance for Hardened Steel versus Impact Velocity

Even with the stated limitations and apparent problems, the Tate model has proven to be a very useful guide for long-rod penetration studies. Anderson and Walker (1991) provide a detailed comparison between numerical simulations of long-rod penetration and the predictions of the Tate model at typical ordnance velocities (1.2 - 1.7 km/s). They demonstrate that the Tate model provides an excellent first-order approximation to long-rod penetration of a semi-infinite target.

We have already seen in Fig. 2 that R_t is a strong function of velocity. Although R_t is generally considered constant during the penetration event, it in fact varies during penetration. This has been demonstrated in time-resolved depth-of-penetration experiments and numerical simulations (Anderson, Walker, and Hauver, 1992). One of the consequences of the Tate model is that the total depth of penetration is very sensitive to the assumed value of the target resistance R_t (Anderson, Walker, and Hauver, 1992). We chose to investigate the fundamental reason for the strong dependency of R_t on impact velocity because of the sensitivity of penetration performance on R_t, because R_t is used to rank the ballistic performance of advanced materials, and because of the uncertainties in the physical interpretation of R_t.

METHODOLOGY

The three-dimensional Eulerian wave propagation computer program, CTH (McGlaun, *et al.*, 1990), was used to perform the numerical experiments. The 2-D cylindrically symmetric option was used for the computations. CTH uses a van Leer algorithm for second-order accurate advection that has been generalized to account for a non-uniform and finite grid, and multiple materials. Further, CTH has an advanced material interface algorithm for the treatment of mixed cells (McGlaun, *et al.*, 1990). Also, CTH has been modified to account for more realistic constitutive treatment of material response by allowing the flow stress to be functions of strain and strain rate (Predebon, *et al.*, 1991; Silling, 1991).

Projectile and target materials typically used in armor penetration experiments were selected for the numerical simulations. The target was considered to be 4340 steel with a hardness of Rockwell C 30. The tungsten-alloy, long-rod projectile was modeled with a *L/D* of 10; the length was 8.17 cm. The impact velocity was varied for the study. Square zoning (with five zones across the radius of the projectile) was used in the interaction region. The constitutive response for 4340 steel was represented by the Johnson-Cook model (Johnson and Cook, 1985):

$$\sigma_t = 792[1 + 0.644(\varepsilon^p)^{0.26}][1 + 0.014 \ln \dot{\varepsilon}^*][1 - T^{*1.03}] \quad \text{MPa,} \qquad (2a)$$

where σ_f is the von Mises effective flow stress (in MPa), 792 MPa being the quasi-static yield stress, ε^p the equivalent plastic strain, $\dot{\varepsilon}^* = \dot{\varepsilon}^p/\dot{\varepsilon}_o^p$ the dimensionless plastic strain rate ($\dot{\varepsilon}_o^p = 1.0\,s^{-1}$), and T^* the homologous temperature. We have examined a number of tungsten (90-93% by weight) alloys, and the stress-strain response can be modeled using an expression of the form (Anderson and Walker, 1991):

$$\sigma_p = 1350\left[(1+\beta\varepsilon^p)^n + 0.06\ln\dot{\varepsilon}^*\right] \quad \text{MPa.} \qquad (2b)$$

In particular, the work hardening and strain rate effects are found to be "independent" in that the strain-rate effect does not alter the slope of the strain-hardening curve. For the particular tungsten alloy used in the numerical simulations, the initial yield stress is strain-rate dependent, but there is little work hardening, so β is set to zero.

COMPUTATIONAL RESULTS

The impact velocity was parametrically varied in a series of numerical simulations: 1.5, 2.0, 2.5, 3.0, and 4.5 km/s. The normalized depths of penetration are depicted in Fig. 1 by a solid circle at the respective impact velocities; agreement is generally within experimental scatter. The computational points are slightly above the experimental data at the higher velocities, but the computations are for L/D = 10 projectiles, while the experimental data are for $L/D \geq 15$ projectiles.

Phases of Penetration. The interface (penetration) and tail velocities, along the centerline, are shown in Fig. 3 for three of the computer runs. The primary phase of penetration is the steady-state phase in which the interface pressure and penetration velocities are approximately constant with time. The term v_o/L provides an estimate of the total penetration time; therefore, it is convenient to use a scaled time, given by tv_o/L, to display the results for different impact velocities. The phases of penetration, as conceptually devised by Eichelberger and Gehring (1962) and elaborated on by Christman and Gehring (1966), are readily apparent in the time history of the penetration velocity. These phases of penetration consist of an initial transient (shock) phase, a quasi-steady-state phase, a residual penetration phase, and an elastic recovery phase. The elastic recovery phase represents the elastic rebound of the crater at the end of penetration. A physical effect of elastic recovery is discussed in Anderson and Walker (1991), but is of little interest here. The relative length of time of each of these phases, in general, depends on the initial impact velocity (and the geometric dimensions of the projectile, which were kept constant for this investigation).

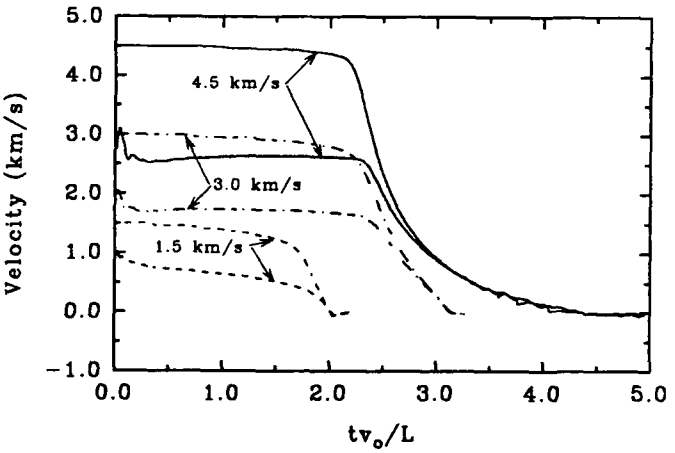


Figure 3: Penetration and Tail Velocities versus Scaled Time

Although the sets of curves in Fig. 3 are similar, there are also some distinct differences. During the shock phase of penetration, referred to as the transient phase in which wave effects dominate the physics and mechanics of penetration, there is an initial rapid increase in the penetration velocity as rarefaction waves from the free lateral surface of the projectile and the top surface of the target release the "geometric" confinement of impact. The stress release waves allow radial motion of target material, thus releasing confinement and allowing easier penetration; hence, the rapid increase in penetration velocity. However, the lateral motions fall to lower velocities as the high pressures from the shock are attenuated, and the penetration velocity subsequently decreases. At this point, the "mode" of penetration has changed from the transient wave phase to a steady-state material flow phase. For the projectile dimensions used in these calculations, it takes approximately 7 to 10 μs to achieve quasi-steady penetration. Although the shock pressures are dissipated in a time frame approximately given by D/c (= 1.80 μs for the specific dimensions and materials used for these computations), the high pressures from the shock sets the target material in motion, and it takes some time for this transient state to decay into a quasi-steady-state penetration. The penetration velocities versus normalized depth of penetration (on the centerline) are plotted in Fig. 4 for the five impact velocities. It is observed that the "duration" of the transient stage is approximately independent of impact velocity in that quasi-steady penetration is achieved after 1.2 - 1.5 D of penetration. [We note here that this conclusion is for a tungsten projectile into a steel target. Anderson, Walker, and Hauver (1992), showed that it takes approximately 2.5 D of penetration before quasi-steady penetration is achieved for tungsten impacting a titanium target. Therefore, density (inertial) effects are important in determining how long this phase lasts.] It is concluded that the duration of the transient phase, to first order, depends on geometric and material parameters, and not the impact velocity.

The quasi-steady phase of penetration persists until the projectile is essentially eroded. The penetration and tail positions of the projectile, as a function of scaled time, are shown in Fig. 5 for three of the impact velocities studied. The computations predict approximately 1.2 D of penetrator remaining at the end of penetration for an impact velocity of 1.5 km/s; only 0.3 D of the projectile remains at 2.0 km/s; and the projectile is completely eroded at impact velocities of 2.5 km/s and greater. Analysis of Figs. 3 through 5 indicates that the amount of residual penetration, that is, that

portion of penetration that occurs after the end of steady-state penetration, is velocity dependent; this is readily apparent in Fig. 4.

The penetration velocities, assuming hydrodynamic theory ($R_t = Y_p = 0$), are also plotted in Fig. 4. The steady-state hydrodynamic penetration depth is also shown. Even at an impact velocity of 4.5 km/s, it is seen that the penetration velocity falls below hydrodynamic theory. And the steady-state phase of penetration is completed before the depth of penetration reaches the hydrodynamic limit. From these observations, it is concluded that even though the interface stresses are substantially higher than the flow stress—such that the hydrodynamic approximation should be valid—strength effects result in a lower penetration velocity and an increased erosion rate compared to hydrodynamic theory. It is the residual penetration phase, resulting from the inertial effect of target material set in motion by the high stresses generated by projectile penetration, that allows penetration to continue towards the hydrodynamic limit and, if the velocity is sufficiently high, beyond. This is an important, if unexpected, conclusion.

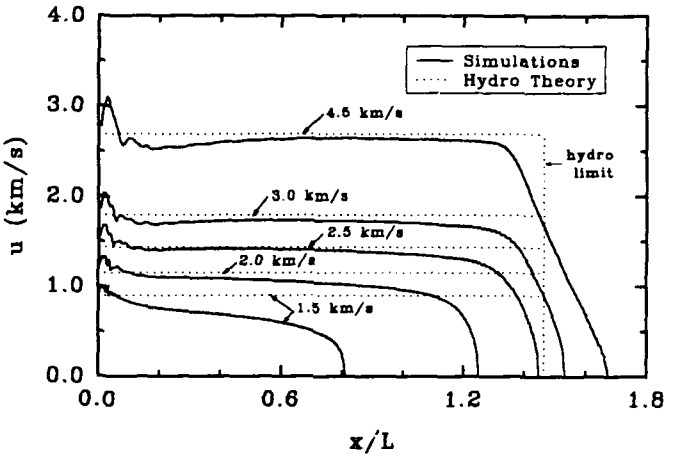


Figure 4: Penetration Velocities versus Normalized Depth of Penetration

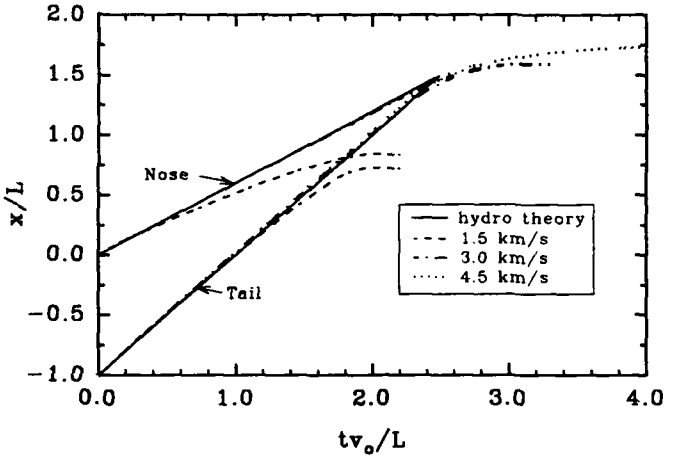


Figure 5: Penetration Depth and Tail Position versus Scaled Time

Eichelberger and Gehring (1962) and Christman and Gehring (1966) defined the residual penetration to be the penetration that occurs after the steady-state phase; they also refer to this phase of penetration as the cavitation phase. In Fig. 4, the residual penetration phase is seen to contribute substantially to the total penetration at the higher impact velocities. We make a slight distinction, however, between what is called residual penetration and what we will call secondary penetration, which requires a definition of the terms primary and secondary penetration. The primary phase of penetration is defined as that penetration resulting from the steady-state phase (and the transient phase). An estimate of when the projectile is fully eroded can be made, assuming steady-state penetration. From this, the primary phase of penetration ceases when the projectile is fully eroded.* Secondary penetration is then defined as any remaining penetration. [This definition of secondary penetration differs from that used by Allen and Rogers (1961) who defined it to be the penetration that results from forward flow of projectile erosion products for the case where the projectile has a higher density than the target. The criteria defined by Allen and Rogers for continued penetration by the erosion products are not met for the materials and impact velocities studied here.] The depths of penetration for the primary phase (open circles) are shown in Fig. 6. (At 1.5 km/s, one to two diameters of projectile remain at the end of penetration; full erosion of the projectile would give deeper penetration than observed, so an open circle is not shown.) Also shown are the penetrations at the end of the quasi-steady phase (open triangles) and total penetration (solid circles). The difference in penetration between total and the primary penetration is the secondary penetration; the difference between total penetration and the quasi-steady penetration is the residual penetration, per the definitions established above. Regardless of which nonsteady penetration is used, it is clear that the magnitude of the nonsteady portion of penetration increases with increasing velocity, and that it contributes significantly to the total penetration at the higher impact velocities.

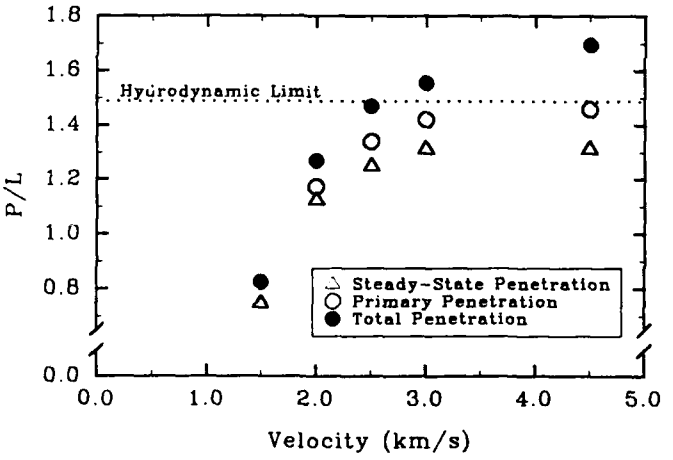


Figure 6. Primary, Secondary, and Residual Penetration

*This definition is motivated by experiments where flash radiography is used to determine the position of the nose and tail of the projectile at discrete instances of time. Typically, these data are used to estimate when the projectile is fully eroded by drawing linear curve fits, i.e., a steady-state approximation, through the position-time points.

Projectile Deceleration. The projectile is decelerated by elastic waves that reflect from the free surface at the tail of the projectile and the plastic interface near the projectile/target interface (Anderson and Walker, 1991; Walker and Anderson, 1992). At the slower impact velocity, penetration proceeds at a rate sufficiently slowly that a number of elastic wave transits occur, thereby decreasing both the tail and interface velocities (the step decrease in the tail velocity which results from the arrival of the stress wave at the rear surface of the projectile can be seen in the tail velocity histories depicted in Fig. 3). The decrement in velocity is given by $2Y_p/\rho_p c$, which is approximately 50 m/s; this number is independent of impact velocity over the range of interest here. This step deceleration occurs every (approximately) $2l/c$ time increment (notice that as the length of the projectile gets shorter, the step deceleration occurs more frequently). Thus, the relative percentage of this elastic wave deceleration goes from approximately 3% (6% on the penetration velocity) for the 1.5-km/s case to only 1% (2% on the penetration velocity) for the 4.5-km/s impact case. It is therefore concluded that although elastic deceleration is a second-order effect during penetration, it is more important at the lower impact velocities. This can also be seen from the fact that the elastic deceleration preserves a piece of the projectile for the lower velocity impacts, while it is unable to decelerate the projectile in the high velocity impacts quickly enough to prevent erosion at the interface from consuming the entire projectile.

Plastic Strain Contours and Crater Radii. Contours of equivalent plastic strain rate (left-hand side of each figure) and equivalent plastic strain (right-hand side of each figure) are shown in Fig. 7 for three of the cases studied. The figures are plotted when the projectile is approximately one-half of its original length. Several features are evident. The strain rate, as expected, increases with impact velocity. The impact craters are approximately cylindrical with a characteristic radius that is a function of the impact velocity. The minimum and maximum crater radii, along with the crater radius at the original target free surface, are tabulated in Table 1. Experimentally determined crater radii (Anderson, Morris and Littlefield, 1992) are also tabulated. The procedure for measuring the crater diameter varies between different investigators; further, although nominally the same type of material (armor steel), the flow stress does vary somewhat between various experiments. Therefore, a range in the experimentally measured crater radii is given.** Examination of Fig. 7 shows that the crater radius, as a function of penetration depth, becomes distinctly more variable as the impact velocity increases.

The plastic strain contours are similar at the three impact velocities shown, although the actual extents of the plastic zone fields increase with impact velocity. The velocity dependence of the crater radius and the extent of the plastic zone field is related to the higher stresses at the projectile/target interface. Figure 8 shows the centerline interface pressure for the five different impact cases; the peak values from the initial shock are listed in Table 2. It should be noted that the duration of the shock pressure is approximately a constant (since it is a function of the geometric and material parameters); therefore, when plotted as a function of scaled time in Fig. 8, the "duration" for the 4.5-km/s case is approximately 3 times longer than for the 1.5-km/s case.

Centerline Velocity. The velocity along the projectile/target centerline is plotted versus scaled distance in Fig. 9 for the same times represented in Fig. 7 (when the projectile is approximately 50% consumed). The dashed vertical line

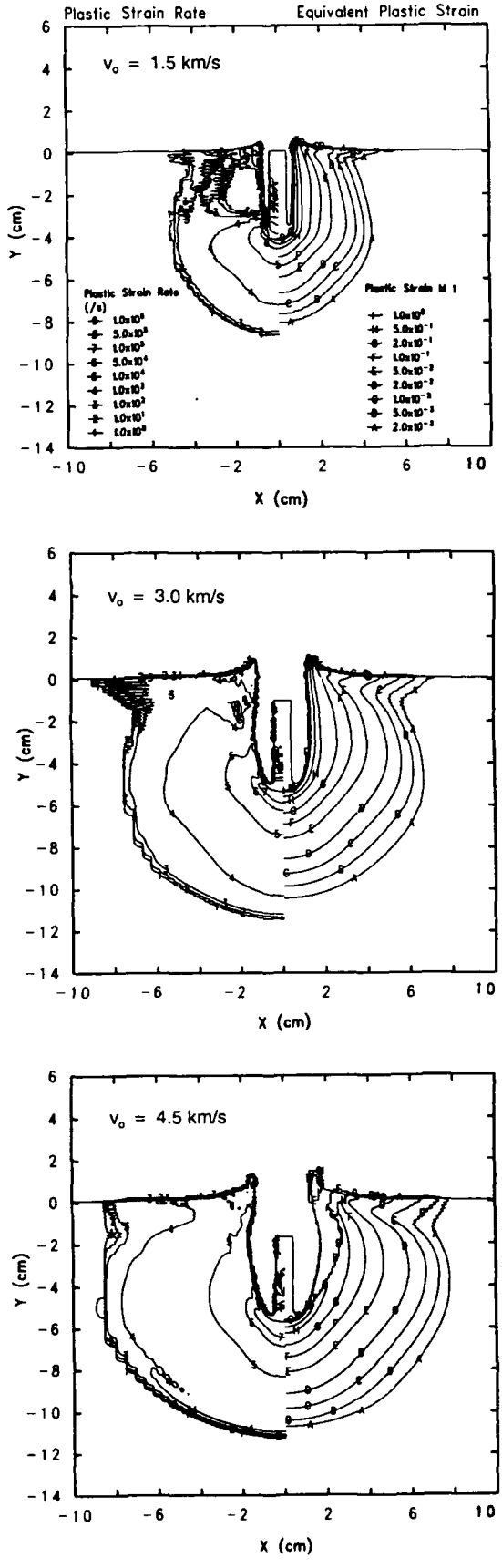


Figure 7: Plastic Strain Rate and Equivalent Plastic Strain Contours

**The values at 4.5 km/s come from only 3 data points; many data points exist at the other impact velocities.

Table 1. Crater Radii

Impact Velocity (km/s)	Radius at x = 0 R_c/D	Minimum Radius R_c/D	Maximum Radius R_c/D	Experimental Radii R_c/D
1.5	0.893	0.832	0.959	0.85-1.2
2.0	1.05	1.00	1.13	1.1-1.35
2.5	1.25	1.21	1.40	1.35-1.6
3.0	1.48	1.46	1.69	1.45-1.75
4.5	2.02	1.91	2.82	2.35-2.4

Table 2. Impact Shock Pressures

Impact Velocity (km/s)	Peak Pressure (GPa)
1.5	25.0
2.0	36.4
2.5	49.8
3.0	65.0
4.5	115.

represents the location of the projectile/target interface; the velocities to the left of the dashed line represent those of the projectile, and target velocities are represented to the right of the line. All results have been shifted so that the interfaces have a common coordinate of $x = 0$ to assist in comparing the results. At approximately $x/L = 0.5$, the velocity goes from zero (no material) to the material velocity of the projectile tail. The velocity in the projectile is then relatively constant until approximately 1.5 projectile diameters from the projectile/target interface. As observed earlier, elastic deceleration of the projectile has changed the tail velocity of the 1.5-km/s impact case by a larger percentage than for the higher velocity cases. A large velocity gradient exists at the projectile/target interface. Anderson and Walker (1991) demonstrated that this velocity gradient is coincident with the extent of plastic flow in both the projectile and the target. Rapid deceleration of projectile material occurs when the material enters the plastic zone, *i.e.*, when the material begins to "see" the large stresses at the projectile/target interface. The reason why the material does not see these stresses earlier is because the condition of uniaxial stress exists in most of the length of the projectile, which limits the magnitude of the stress to the flow stress of the material. It is observed that the extent of the plastic zone in the projectile is essentially independent of impact velocity. On the other hand, the amount of target material flowing plastically increases with penetration velocity, as inferred from the larger region of target material with a non-zero velocity (also see Fig. 7). Estimates for the extent of the plastic zone in the target (along the centerline), normalized by the crater diameter (at $x = 0$), were made from analysis of the computational results. These values correspond to the times in Fig. 7 when the projectiles are approximately one-half consumed. Two values were obtained: the 0.2% equivalent plastic strain contour, and the 1 s^{-1} plastic strain rate contour. Values are listed in Table 3.

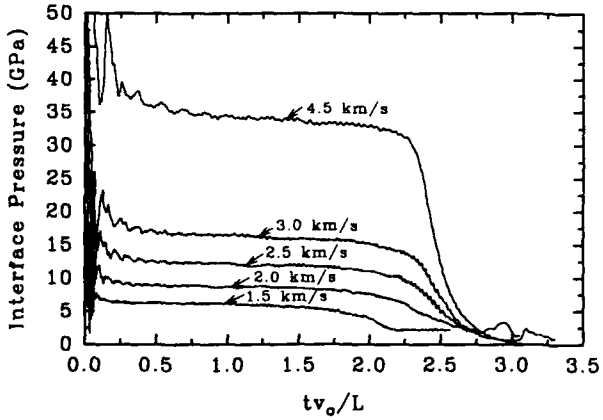


Figure 8: Centerline Interface Pressure versus Scale Time

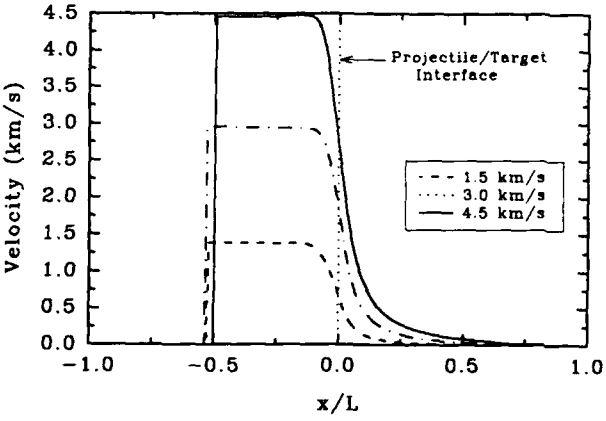


Figure 9: Velocity along Projectile/Target Centerline

The extent of the plastic zone is scaled by the crater radius, as opposed to the projectile diameter, because of the role the crater radius plays in analytical theories for nonsteady penetration (Ravid, *et al.* 1987; O'Donoghue, *et al.*, 1989; Walker and Anderson, 1992). There are several important items of note. As already mentioned, the extent of the plastic zone field in the projectile is approximately independent of penetration velocity. And although the actual physical extent of the flow field increases in the target with penetration velocity, the extent of the flow field decreases in terms of the crater radius. This appears to be a consequence of compressibility of the target (Walker and Anderson, 1992), discussed below.

ANALYSIS

Target Resistance. The deviation from idealized steady-state fluid flow behavior is given by the difference between R_t and Y_p in Eq. (1):

$$R_t - Y_p = \frac{1}{2}\rho_p(v-u)^2 - \frac{1}{2}\rho_t u^2. \tag{3}$$

The departure from idealized steady-state fluid response was calculated from the results of the numerical simulations using Eq. (3), and these are plotted in Fig. 10 as a function of scaled time tv_0/L. It is seen that R_t-Y_p varies considerably during penetration. If it is assumed that Y_p is approximately a constant during penetration, approximately 2.0±0.2 GPa for a tungsten alloy projectile (Anderson and Walker, 1991), then R_t is the quantity that varies appreciably during penetration. Even if Y_p increases at the very end of penetration (Frank and Zook, 1990), this is not sufficient to account for the large change in R_t.

The numerical results of Fig. 10 were integrated to provide "average" values over the total penetration event according to the following expressions:

$$\langle \bar{R}_t \rangle_T = \frac{1}{T}\int_0^T R_t(t)\,dt \qquad (4)$$

$$\langle \bar{R}_t \rangle_P = \frac{1}{P}\int_0^P R_t(x)\,dx \qquad (5)$$

where T and P are the total time interval of penetration and total depth of penetration, respectively. The time-averaged R_t can be slightly different than the space-averaged R_t because of the shock phase and final deceleration phases where the rates of penetration are different than in the steady-state phase. These values are listed in Table 4.

Table 4. Target Resistance Values

Impact Velocity (km/s)	$\langle \bar{R}_t \rangle_T$ (GPa)	$\langle \bar{R}_t \rangle_P$ (GPa)	$(R_t)_{ss}$ (GPa)	R_t (GPa) Model
1.5	4.27	4.31	4.92	5.21
2.0	3.10	3.24	3.88	3.54
2.5	2.29	2.46	3.22	2.18
3.0	1.71	1.91	2.83	0.87
4.5	0.922	1.21	2.52	-

As the impact velocity increases, there is a larger and larger negative contribution to R_t-Y_p from the residual penetration phase. This is a direct consequence that $u \approx v$ in Eq. (3), since the projectile is all or nearly all eroded. Thus, one of the explanations for the strong velocity dependence of R_t observed in Fig. 2 is the contribution of the residual stage of penetration to the total penetration depth. The last column in Table 4 lists the R_t's required for the Tate model to give the same depth of penetration as the computations. Considering that the Tate model neglects the shock phase, and the tail and penetration velocities are in error in the residual penetration phase (Anderson and Walker, 1992), there is reasonable agreement between the various columns. It is pointed out that R_t changes dramatically with almost no change in depth of penetration at impact velocities above 2.5 km/s (see Figs. 1 and 2). This makes the calculation of R_t very sensitive to the precision and numerical scheme used in the Tate model. No R_t value is listed at 4.5 km/s; the penetration depth is sufficiently above the hydrodynamic limit that R_t must be negative (for constant Y_p) for the model to match the depth of penetration.

An R_t can be calculated up to the time that the projectile tail begins its rapid deceleration, i.e., the end of the quasi-steady phase, thereby neglecting the residual penetration phase. These steady state values, $(R_t)_{ss}$, are also listed in Table 4. The R_t's listed in Table 4 are plotted in Fig. 11. Regardless of how R_t is calculated, it decreases with impact velocity. The underlying reason for this may be due to the incompressibility assumption central to the theory.

Table 3. Normalized Extent of Plastic Zone in the Projectile

Impact Velocity (km/s)	0.2% Plastic Strain Contour*	1 s^{-1} Strain Rate Contour*
1.5	2.7	3.2
2.0	2.6	3.1
2.5	2.5	3.0
3.0	2.2	2.6
4.5	1.8	2.0

*Normalized by the crater radius at $x = 0$.

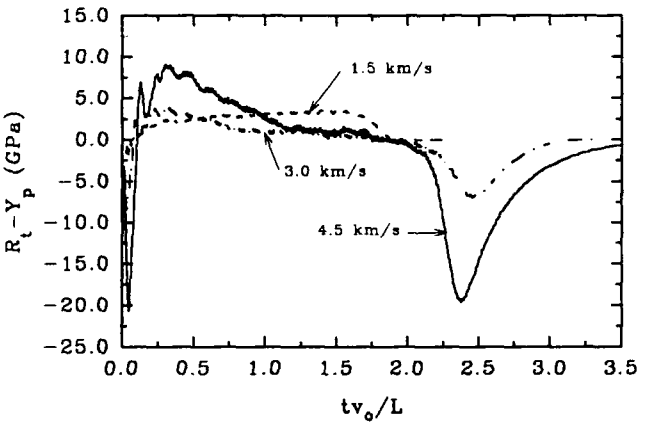


Figure 10: Deviation from Steady-State Hydrodynamic Theory

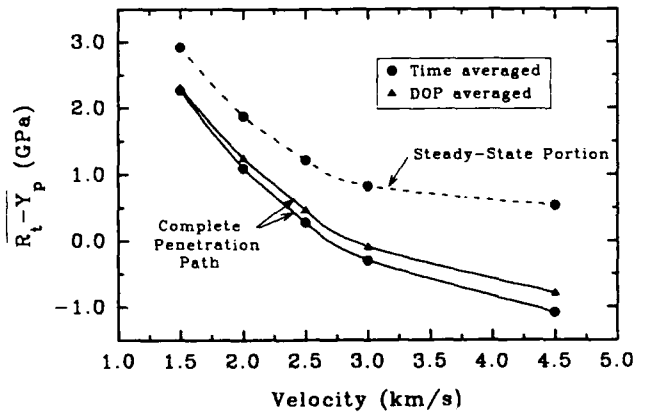


Figure 11: Computed R_t's as a Function of Impact Velocity

Compressibility Effects. The compression η is plotted on the right side in Fig. 12, and the equivalent plastic strain on the left. The density itself does not change appreciably, and in this sense, incompressibility is a reasonable approximation. However, in computing the resistance of the target to penetration, it is not obvious that compressibility effects can be ignored. Considerable elastic energy can be stored in a small amount of compression of the target (this is true also of the projectile, but the volume involved is small relative to that of the target). The effect of compressibility on target response is a function of impact velocity. At low impact velocities, e.g., 1.5 km/s, most of the plastic straining occurs within the vicinity (in front and to the side) of the projectile/target interface. After passage of the projectile, there is very little additional plastic strain accumulated in the target. At higher impact velocities, a significant amount of plastic straining occurs when the target unloads from a compressed state. This straining occurs in the target volume far "behind" the projectile, and hence does not directly affect penetration. This can be seen in Fig. 7; for the 3.0 and 4.5 km/s impact cases, plastic strain rates of 10^4 and 10^5 s^{-1} are evident in regions of the target well behind (above) the projectile/target interface plane. This attests to additional plastic strain due to release of compression. Thus, the radius of a constant strain contour increases as one moves from the vicinity of the projectile/target interface to the target volume behind the projectile.

It is the target volume in the vicinity of the projectile/target interface that mostly controls penetration. Because some of the energy transfer from the projectile to the target is temporarily stored in compression, the rate at which energy is dissipated by plastic work near the projectile/target interface is less than if there were no compression (as already discussed in the preceding paragraph, additional plastic work does occur in unloading, but this is away from the projectile/target interface and therefore does not directly influence penetration). Therefore, compressibility tends to decrease the extent of plastic dissipation in the vicinity of the projectile/target interface as compared to an incompressible case. Analytical models of penetration relate plastic dissipation to a plastic zone extent, and target resistance increases as the extent of the plastic zone, normalized by the crater radius, increases. Walker and Anderson (1992) demonstrated that the normalized extent of the plastic zone is velocity independent if compressibility effects are ignored, but that the normalized extent of the plastic zone decreases with impact velocity when compressibility is included. The analytical findings of Walker and Anderson are consistent with the results of the numerical simulations.

Estimates of the amount of energy per unit volume going into compression can be made from:

$$w = -\frac{1}{V_0}\int_{V_0}^{V} p\,dV \approx -\frac{1}{V_0}\int_{V_0}^{V} \kappa\left(1-\frac{V}{V_0}\right)dV$$

$$= -\kappa\left[\frac{V}{V_0} - \frac{1}{2} - \frac{1}{2}\left(\frac{V}{V_0}\right)^2\right] = \frac{\kappa\eta^2}{2}. \qquad (6)$$

Although only the first two terms of the equation of state have been retained, Eq. (6) will provide an adequate approximation for estimating energy densities. It is also useful for comparison purposes to calculate the plastic work equal to the work done in compression. The plastic work is approximately the area under the stress-strain curve, which is given by $\sigma\varepsilon^p$. Equating the plastic strain energy to the energy in compression, and solving for the plastic strain gives:

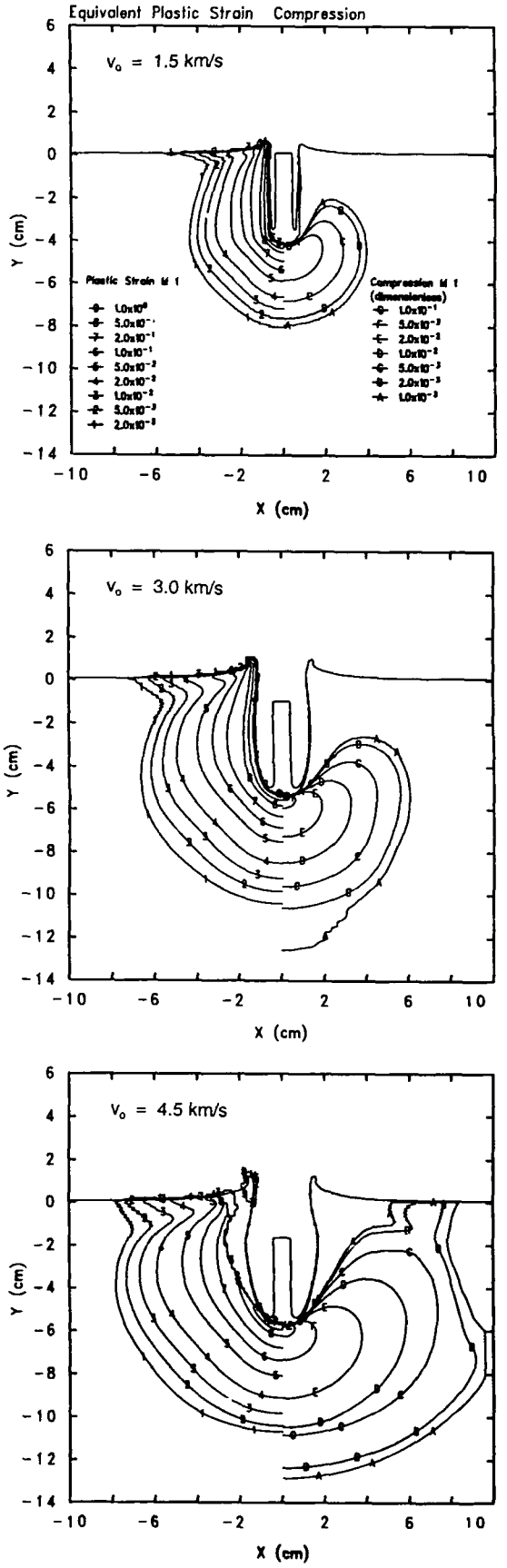


Figure 12: Plastic Strain and Compressibility Contours

$$\varepsilon^p = \frac{\kappa\eta^2}{2\sigma_t}. \quad (7)$$

The bulk modulus for steel is 152 GPa; an effective flow stress is approximately 1 GPa. Using these values, quantitative numbers can be calculated for Eqs. (6) and (7). Table 5 compares the energy density stored in compression with the energy density dissipated in plastic work for several different compressions.

Table 5. Comparison of Energy Densities

V/V_o	η (-)	Energy Density (J/cm^3)	ε^p (-)
0.990	0.010	7.60	0.0076
0.975	0.025	47.5	0.048
0.950	0.050	190.	0.19
0.925	0.075	428.	0.43
0.900	0.100	760.	0.76

Figure 12 can be used to make an estimate of the relative importance of the energy going into compression and into plastic work. The following estimates are made for a region approximately one projectile diameter into the target. At 1.5 km/s, ignoring the energy absorbed by compression is at most a 5% error. But as the impact velocity increases, the error increases disproportionately. At 3.0 km/s, the energy per unit volume going into compression is approximately 40% of the energy per unit volume dissipated by plastic work; at 4.5 km/s, the energy per unit volume in compression exceeds the energy per unit volume dissipated by plastic work by as much as a factor of two. This is an important observation since virtually all analytic models of penetration ignore compressibility.

The discussion in this subsection, along with the observation that R_t begins its precipitous decline in Fig. 2 at approximately 1.5 km/s, provides credence to our assessment that compressibility effects become increasingly important in the mechanics of penetration as the impact velocity increases above 1.5 km/s.*** Again, we make the distinction between the density of the target material remaining approximately constant versus the energy absorbed in compression. Even at 4.5 km/s, the target density in the vicinity of the projectile/target interface has changed only on the order of 10%, and significantly less elsewhere in the target.

Work Rates. It is possible to provide a quantitative analysis of the rate at which energy is absorbed by the target. The rate of work done per unit volume at any point in the target or projectile may be determined from the expression (e.g., see Anderson, 1987):

$$\dot{w} = \nabla \cdot (\vec{v} \cdot \sigma_{ij}) = -\nabla \cdot (\vec{v}p) + \nabla \cdot (\vec{v} \cdot s_{ij}). \quad (8)$$

On the right hand side of Eq. (8), stress tensor has been separated into pressure and deviatoric components. The first term is the rate of work done by the isotropic component of the stress, which includes work done due to pressure gradients in a velocity field as well as the work done by compression. The second term is the rate of work done by the deviatoric stress. Integration of Eq. (8) over the target volume yields the total rate of work done on the target at a particular time:

$$\dot{W} = \int_\Omega \nabla \cdot (\vec{v} \cdot \sigma_{ij}) d\Omega = \int_S (\vec{v} \cdot \sigma_{ij}) \cdot \vec{n} dS = -\int_S p\vec{v} \cdot \vec{n} dS + \int_S (\vec{v} \cdot s_{ij}) \cdot \vec{n} dS = \dot{W}_{\bar{\sigma}} + \dot{W}_s \quad (9)$$

where Ω is the target volume, S is the surface of the target, and $\vec{n}$ is the unit normal vector pointing out of the target. $\dot{W}_{\bar{\sigma}}$ is the rate of work done by pressure forces, and $\dot{W}_s$ is the rate of work done by deviatoric stress. The divergence theorem has been used to convert the volume integrals to surface integrals. The advantage in the conversion to surface integrals is the integrands now vanishes virtually everywhere except on the crater surface. Furthermore, the largest contributions within the crater occur near the crater base where the stresses are largest. The surface integrals were evaluated at a few different times for impact velocities of 1.5 and 3.0 km/s; the results are given in Table 6. Since the stresses are large in magnitude and negative in compression, and the velocity is in the opposite direction of $\vec{n}$, $\dot{W}$ is positive. Physically this is expected since the projectile is delivering energy to the target.

Table 6. Energy Rates

Time (μs)	$\dot{W}_{\bar{\sigma}}$	$\dot{W}_s$	$\dot{W}$ (kJ/μs)	Approx. Work Rate (kJ/μs)
Impact Velocity: 1.5 km/s				0.62
20	0.602	0.115	0.717	
40	0.586	0.101	0.687	
60	0.545	0.081	0.626	
Impact Velocity: 3.0 km/s				4.7
10	4.29	4.35	4.72	
20	4.41	5.22	4.93	
Impact Velocity: 4.5 km/s				16.

The relative magnitudes of the values in Table 6 are reasonably consistent with the results anticipated from scaling arguments. The time scale is given approximately by L/v_o, so the rate of change in the total energy for the

***It is convenient to use the impact velocity as the controlling measure, particularly since the impact velocity is the quantity measured experimentally. However, it is the penetration velocity—a function of the densities and strengths of the projectile and target materials, and the impact velocity—that is the controlling factor on the pressure.

target and projectile is proportional to v_o^3 since the length scales and materials remain constant. (The same scaling relationship can be determined from multiplying the energy density of the projectile by the velocity.) The total rates of work done on the target, given in Table 6, are reasonably consistent with this trend. Although the total work rate scales as v_o^3, the individual terms, in general, do not.

We can use the form of Eq. (9) to present an argument of why the normalized extent of the plastic zone decreases with impact velocity. The $\dot{W}_s$ term in Eq. (9) contains both elastic and plastic work rates, but the work done by the stress deviators is limited by the yield stress in the target, and thus tends to keep the work per unit volume due to plastic flow approximately constant, i.e., independent of velocity. (For a viscoplastic material, there is a slight velocity dependence.) Thus, the portion of the work done by the stress deviators s_{ij} in plastic flow scales approximately as v_o^0. $\bar{v}$, of course, scales as v_o^1. Therefore, the plastic work rate per unit volume scales approximately as $v_o^{1.0}$. The scaling for volume is somewhere between v_o^1 (momentum scaling) and v_o^2 (kinetic energy scaling). At lower impact velocities, the first power generally appears more applicable; at very high velocities (greater than 3.0 km/s), the exponent seems to be closer to 2. For the purposes here, we will take an exponent of 1.5. As a consequence, the plastic work rate per unit volume, when multiplied by the volume of the plastic zone, should scale approximately as $v_o^{2.5}$ (the data in Table 6 are also reasonably consistent with this assertion, suggesting the appropriate exponent for the velocity scaling of $\dot{W}_s$ is about 2.2). Since the *total* plastic work per unit volume is approximately velocity independent, the extent of plastic zone should scale as $v_o^{1.5/3}$, i.e., $v_o^{0.5}$, a relatively weak dependence on the velocity.

Many analytical models of penetration (e.g., Walker and Anderson, 1992) employ the extent of plastic zone normalized by the crater radius in their formulations. Therefore, it is also of interest to determine how this normalized extent of plastic zone scales with impact velocity. For purposes of determining this relationship we need to know how the crater radius varies with impact velocity. A function of the form $R_c/D = a v_o^n$ is used to describe the crater radius as a function of impact velocity (other functional forms for the curve fit, such as a parabolic fit in the velocity, provide better agreement with the data, but in order to estimate the velocity scaling we are restricted to the functional form listed above). Experimental data for the radii of craters from tungsten-alloy projectiles into hard steel targets (Anderson, Morris, and Littlefield, 1992) were used to obtain the exponent n; n was found to be 0.65 for impact velocities between 1.0 and 3.0 km/s. This is in excellent agreement with an exponent calculated from the numerically determined crater radii listed in Table 1. Therefore, since the extent of plastic zone scales approximately as $v_o^{0.5}$, the normalized extent of plastic zone should scale as $v_o^{-0.15}$. Results of the numerical simulations show that the normalized extent of the plastic zone scales as $v_o^{-0.27}$ (Table 3). The agreement is reasonably good considering the approximations to find the first-order dependence of the velocity. What is important is that the extent of the plastic zone does not grow as rapidly as the crater radius with impact velocity.

It was noted in Fig. 11 that R_t computed from the steady-state portion of penetration decreased with increasing impact velocity. The growth of the plastic zone in the target is a weaker function of velocity than the growth of the crater, thus, the normalized extent of the plastic zone decreases with velocity. The target resistance is directly proportional to the normalized extent of the plastic zone. This suggests another reason why R_t decreases with increasing impact velocity.

Energy Partitioning. Although Eq. (8) provides the rate at which energy is entering into the target, it does not address the question of how the energy is distributed between internal and kinetic energy within the target volume. Equation (8) can be rewritten using the momentum equation (e.g., see Anderson, 1987). This gives:

$$\dot{w} = \frac{1}{2}\rho\frac{\partial(v_i v_i)}{\partial t} - p\frac{\partial v_i}{\partial x_i} + s_{ij}D_{ij}^e + s_{ij}D_{ij}^p. \tag{10}$$

The rate of deformation tensor D_{ij}, $\frac{1}{2}(\partial v_i/\partial x_j + \partial v_j/\partial x_i)$, has also been separated in the elastic and plastic parts (superscript e and p, respectively). The first term is the time rate of change of kinetic energy per unit volume of the target. The second and third terms represent the rates of elastic compression and deformation, and the last term is the rate of dissipative (plastic) deformation. The last three terms together represent changes to the internal energy of the system.

Equation (10) has been integrated numerically over the volume and time to give the kinetic and internal energies as a function of time for the 1.5, 3.0 and 4.5 m/s impact cases. The results are shown in Fig. 13. Four curves are shown in each subfigure. One curve represents the kinetic energy of the projectile, and in all cases, the kinetic energy of the projectile decreases approximately linearly with time since the length of the projectile is decreasing linearly with time. The projectile kinetic energy is transferred to internal energy of the projectile, and internal and kinetic energy of the target. The initial kinetic energy and the final internal energies for the three impact cases are given in Table 7. (It might be noted that the third and fourth columns do not sum exactly to the initial kinetic energy. There is a small amount of residual kinetic energy in the target, which increases with impact velocity. There is also approximately 1.7% of the initial kinetic energy lost through the computational boundaries for each problem. These two quantities make up the difference between the original kinetic energy of the projectile and the sum of the internal energies of the projectile and target.) If the final internal energy from the projectile is subtracted from the initial kinetic energy of the projectile, the rate of energy transferred to the target can be estimated easily because of the linear decay in projectile energy. These values are listed in the last column of Table 6; these agree very well with the values calculated from Eq. (9). Exact agreement is not expected since Eq. (9) provides the instantaneous rate, while these last numbers represent average values.

The final internal energy within the projectile is approximately independent of the impact velocity, particularly in relation to the increase in internal energy of the target. The internal energy of the projectile represents 29% of the energy dissipated at 1.5 km/s, but only a little over 4% of the energy dissipated at 4.5 km/s. For the most part, the

Table 7. Energy Partitioning

Impact Velocity (km/s)	Initial Kinetic Energy (kJ)	Final Internal Energy Projectile (kJ)	Final Internal Energy Target (kJ)
1.5	82.4	23.6	57.3
3.0	330.	25.8	295.
4.5	742.	30.5	681.

increase in the kinetic energy of the projectile as the impact velocity goes from 1.5 km/s to 4.5 km/s is ultimately absorbed as internal energy of the target. However, as the velocity increases, more and more of the energy is temporarily stored as kinetic energy of the target.

The kinetic energy that the target achieves is very dependent upon the impact velocity. It is this observation that explains the large residual penetration at the higher impact velocities. At 1.5 km/s, the kinetic energy of the target is never very large, but at 4.5 km/s, the kinetic energy in the target is greater than that in the remaining projectile after approximately 33 μs. After approximately 45 μs, the projectile has essentially eroded, but considerable kinetic energy remains in the target. This kinetic energy is ultimately converted to internal energy of the target (and this occurs fairly linearly with time). Thus, the kinetic energy plot confirms that the deeper penetrations at higher velocities are due to the target material having been put in motion.

ACKNOWLEDGEMENT

The motivation and presentation of some of the results presented in this paper were strongly influenced by research findings of long-rod penetration into ceramics conduc' J by Dennis Orphal and Roland Franzen of CRT. The authors wish to express their appreciation for the professional and personal interactions with these very fine researchers. We thank Dr. Peter Kemmey and Dr. Joe Beno of the Defense Advanced Projects Research Agency for their support and encouragement during the course of this study; our thanks also to Mr. René Larriva of Interferometrics for his very helpful suggestions in the preparation of the manuscript. Lastly, we thank Ms. Janet Banda for her patience and diligence in the preparation of the final manuscript. This work was partially funded under contracts DAAL03-91-C-0021 and DAAL03-92-K-0001, administered by the U. S. Army Research Office.

REFERENCES

Alekseevskii, V. P. (1966). Penetration of a Rod into a Target at High Velocity. *Combustion, Explosion and Shock Waves*, Vol. 2, 63-66 (translation from the Russian) Faraday Press, New York.

Allen, W. A. and J. W. Rogers (1961). Penetration of a Rod into a Semi-Infinite Target. *J. Franklin Inst.*, 272, 275-284.

Anderson, C. E. Jr. (1987). An Overview of the Theory of Hydrocodes. *Int. J. Impact Engng.*, 5(1-4), 33-59.

Anderson, C. E. Jr., B. L. Morris and D. L. Littlefield (1992). A Penetration Mechanics Database. SwRI Report 3593/001, Southwest Research Institute, San Antonio, TX (AD# A246351).

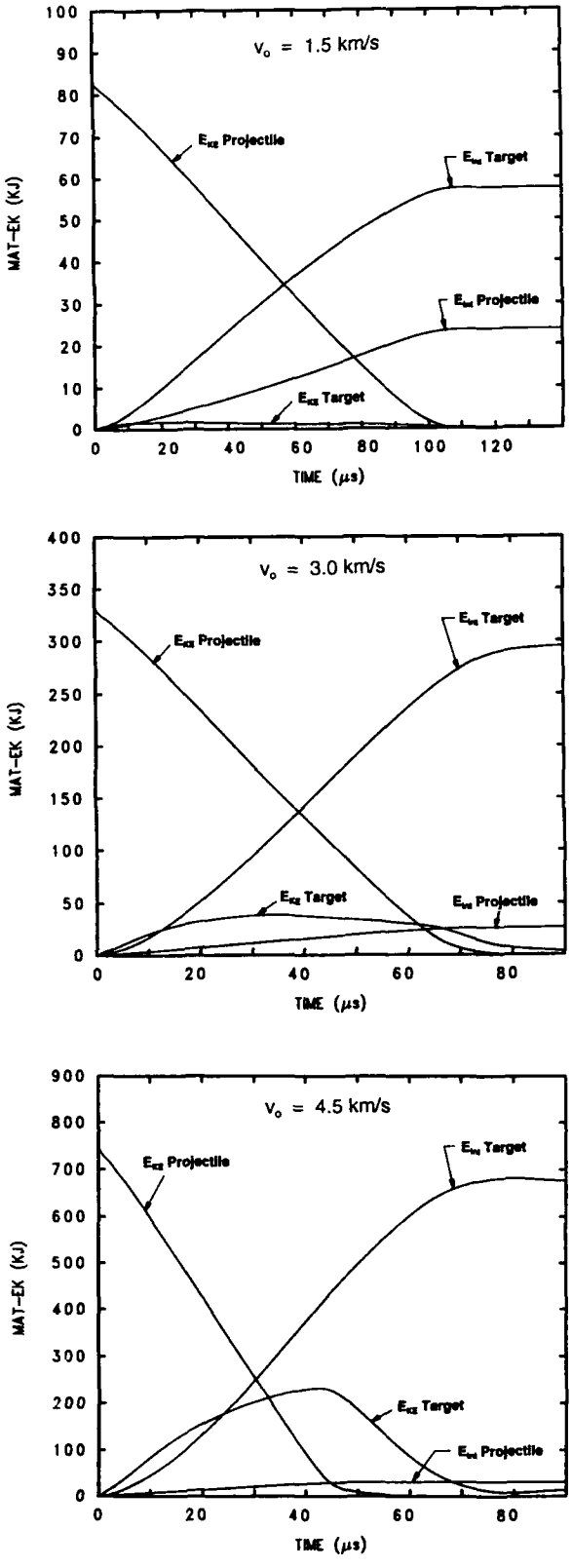


Figure 13: Energy Partitioning versus Time

Anderson, C. E. Jr. and J. D. Walker (1991). An Examination of Long-Rod Penetration. *Int. J. Impact Engng.*, **11**(4), 481-501.

Anderson, C. E. Jr, J. D. Walker and G. E. Hauver (1992). Target Resistance for Long-Rod Penetration into Semi-Infinite Targets. *Nuclear Engineering and Design*, in publication.

Christman, D. R. and J. W. Gehring (1966). Analysis of High-Velocity Projectile Penetration Mechanics. *J. Appl. Phys.*, **37**, 1579-1587.

Eichelberger, R. J. and J. W. Gehring (1962). Effects of Meteoroid Impacts on Space Vehicles. *ARS Journal*, **32**, 1583-1591.

Frank, K. and J. Zook (1990). Chunky Metal Penetrators Act like Constant Mass Penetrators. *Proc. of the 12th Int. Symp. on Ballistics*, Vol. 1, 441-449, Oct. 30 - Nov. 1, San Antonio, TX.

Hohler, V. and A. J. Stilp (1987). Hypervelocity Impact of Rod Projectiles with L/D from 1 to 32. *Int. J. Impact Engng.*, **5**(1-4), 323-331.

Johnson, G. R. and W. H. Cook (1985). Fracture Characteristics of Three Metals Subjected to Various Strains, Strain Rates, Temperatures and Pressures. *Engng. Fracture Mech.*, **21**(1), 31-48.

McGlaun, J. M., S. L. Thompson, and M. G. Elrick (1990). CTH: A Three-Dimensional Shock Wave Physics Code. *Int. J. Impact Engng*, **10**(1-4), 351-360.

O'Donoghue, P. E., S. R. Bodner, C. E. Anderson, Jr., and M. Ravid (1989). Comparison of a High Velocity Impact Model with Numerical Simulation. *Int. J. Impact Engng.*, **8**(4), 289-301.

Predebon, W. W., C. E. Anderson, Jr., and J. D. Walker (1991). Inclusion of Evolutionary Damage Measures in Eulerian Wavecodes. *Comput. Mech.*, **7**(4), 221-236.

Ravid, M., S. R. Bodner, and I. Holcman (1987). Analysis of Very High Speed Impact. *Int. J. Engng. Sci.*, **25**(4), 473-482.

Silling, S. A. (1991). Stability and Accuracy of Differencing Schemes for Viscoplastic Models in Wavecodes. SAND91-0141, Sandia National Laboratories, Albuquerque, NM.

Sorensen, B. R., K. D. Kimsey, G. F. Silsby, D. R. Scheffler, T. M. Sherrick, and W. S. deRosset (1991). High Velocity Penetration of Steel Targets. *Int. J. Impact Engng.*, **11**(1), 107-119.

Tate, A. (1967). A Theory for the Deceleration of Long Rods after Impact. *J. Mech. Phys. Solids*, **15**, 387-399.

Tate, A. (1969). Further Results in the Theory of Long Rod Penetration. *J. Mech. Phys. Solids*, **17**, 141-150.

Tate, A. (1986). Long Rod Penetration Models—Part II. Extensions to the Hydrodynamic Theory of Penetration. *Int. J. Engng. Sci.*, **28**(9), 599-612.

Walker, J. D. and C. E. Anderson, Jr. (1992). A Nonsteady-State Model for Penetration. *Proc. of the 13th Int. Symp. on Ballistics*, Vol. 3, TB-1/1-8, June 1-3, Stockholm, Sweden.

Int. J. Impact Engng Vol. 14, pp 13 - 24, 1993
Printed in Great Britain

0734-743X/93 $6.00 + 0.00
Pergamon Press Ltd

PULSED HOLOGRAPHY FOR HYPERVELOCITY IMPACT DIAGNOSTICS*

J. A. ANG, B. D. HANSCHE, C. H. KONRAD, and W. C. SWEATT

Sandia National Laboratories
Albuquerque, NM 87185

S. M. GOSLING and R. J. HICKMAN

Ktech Corporation
Albuquerque, NM 87110

ABSTRACT

The development of pulsed holography has two principal objectives. The first objective is to quantify the three dimensional characteristics of hypervelocity impact events, and the second is to provide a diagnostic with the ability to capture high fidelity information for the validation of sophisticated three-dimensional hydrocodes. The holographic image-capturing subsystem uses a Q-switched, seeded, frequency-doubled Nd-YAG laser which produces 5 ns, 750 mJ, coherent pulses at 532 nm. Holographic images have been captured of the back-surface debris bubble from 4 km/s perforating impacts and crater ejecta from 2 km/s non-perforating impacts. A prototype holographic reconstruction and image analysis subsystem has been assembled that provides the ability to measure both the spatial distribution of particles and the morphology of individual particles produced in a hypervelocity impact event. The demonstrated image resolution of this system is 20 μm; however, higher resolutions are possible with magnification optics.

INTRODUCTION

Pulsed holography is a significant advance in state-of-the-art hypervelocity impact diagnostics. Unlike conventional holography, which uses exposure times on the order of seconds, pulsed holography utilizes high-power pulsed lasers to provide exposure times on the order of nanoseconds. These short pulse durations are required to "freeze" the motion of impact-generated fragments and debris. Aside from these very short exposure times, pulsed holography is similar to conventional holography. This section describes the background for the development of pulsed holography, and following sections discuss how pulsed holographic images of hypervelocity impact events are formed and captured. The critical issue for the practical application of pulsed holography is the development of holographic image analysis techniques. This issue is addressed in the last sections on image reconstruction systems and image resolution limits.

Benefits of Pulsed Holography

The key technical advances of pulsed holography include the ability to collect three-dimensional information about the distribution, shape and orientation of hypervelocity impact-generated fragment clouds, and the ability to quantify the characteristics of very small fragments without the depth-of-focus restriction of conventional microscopy. The ability to capture the three-dimensional features of a hypervelocity impact event makes pulsed holography a powerful tool, especially for the validation of three-dimensional hydrocode simulations and fragmentation models. The development of these computational and analytical models is closely linked to the ability to compare model predictions to test results. With the advent of sophisticated three-dimensional hydrocodes, these computational tools are progressing beyond the ability of conventional imaging techniques to provide the necessary information for code validation. Pulsed holography has the potential to establish a diagnostic, and by extension, validation capability commensurate with the power of these three-dimensional hydrocodes.

*This work performed at Sandia National Laboratories and supported by the U. S. Department of Energy under contract DE-AC04-76DP00789.

Hypervelocity Impact Events of Interest

The two types of hypervelocity impact events that can be studied with pulsed holography are perforating and non-perforating impacts. Perforating impacts lead to debris cloud formation, where the debris cloud can consist of a mixture of solid fragments, liquid droplets, and/or vapor products. Non-perforating impact events produce crater ejecta and jet breakup. The study of these impact events has several applications, including understanding the formation and dispersal of back-armor debris for achieving survivability or lethality performance, studying strategic kinetic energy weapon lethality, and developing advanced debris shield designs to improve the survivability of aerospace systems. The solution to these problems requires the characterization of such factors as the extent, orientation and distribution of mass in a cloud of impact-generated fragments; the solid, liquid or vapor state of particles in an impact cloud; the shape, size, velocity and number of individual fragments; or the breakup of hypervelocity impact-formed jets into discrete fragments. For impact events with cylindrical symmetry, two-dimensional tools may be sufficient; however, for non-symmetric impacts, three-dimensional computational and experimental capabilities are generally required.

Present Imaging Techniques

Hypervelocity impact tests typically use conventional imaging tools such as flash X-rays, pulsed laser photography, and high speed photography with either rotating prism cameras or image-converter cameras. The use of these imaging diagnostics and their application to hypervelocity impact testing has been described in the literature (Swift, 1982 and Isbell, 1987). Unfortunately, with the exception of stereo photography, conventional imaging techniques are, by their nature, two dimensional. Therefore, they are unable to capture a significant portion of the information that is predicted by three-dimensional hydrocodes. Even stereo photography is subject to particle shadowing and masking that can limit impact event characterization. Conventional imaging techniques have practical resolution limits of about 200 μm either through a depth of focus constraint which restricts the practical image magnification, or the resolution capability of flash x-ray cassettes. As noted above, one of the primary motivations for the development of pulsed holography is to move beyond these limits and provide high fidelity information about the three-dimensional features of an impact event.

Conventional holograms typically image static objects and require vibration isolation tables to limit motion of the object and optical components to less than a fraction of the wavelength of the illuminating laser light source. This motion constraint is necessary for the formation of the constructive and destructive wave interaction that produces interference fringes on the holographic plate. If the object moves more than a fraction of a wavelength during the duration of the laser exposure these interference fringes are lost and with it the holographic image of the object. However there is an exception, whereby an object that moves many multiples of the laser wavelength during the pulse duration can form "shadowgraphic" hologram images. The topic of this paper is this exception and how it provides a key advance over conventional hypervelocity impact imaging techniques.

MEASUREMENT OBJECTIVES

There are several measurements that can characterize an impact event. For these different measurements a spectrum of resolution requirements may be defined. For example, an impact event can be characterized with macroscopic measurements to describe the overall spatial distribution of material resulting from an impact event. In the same event, microscopic measurements can focus on the impact-generated particles, their shape and volume; their state, solid, liquid or vapor; and for solid particles (fragments) their "roughness" or fractal dimension (Mandelbrot, 1983). There are a number of other measurements that can fall between these macroscopic and microscopic regimes, such as the total number of particles generated, their size distribution, and their velocities.

These measurements place different accuracy requirements on the hologram analysis and tolerances for the holographic layout. Accuracy requirements for a given property measurement may be obtained by examining the resolution limits for computational and analytical predictions of that property. Assuming a typical debris bubble cross-section of 100 mm, the accuracy requirement for macroscopic dimensions of impact-generated structures may be to within 1 mm. In the intermediate regime of holographic measurements, particle sizes and velocities may require resolution to within 100 μm. Finally in the microscopic measurement regime, to determine the particle shape, state or fractal dimensions may require resolutions of better than 10 μm. This spectrum of resolution requirements is illustrated in Table 1. Precise repositioning of the holographic plate and reference beam geometry is required to achieve these accuracies of better than 100 μm.

PULSED LASER HOLOGRAMS

The promise of pulsed holography for ballistic diagnostics was revealed by LTV Missiles and Electronics Group in a series of tests with a small powder gun (Hough, *et al.*, 1990). The key breakthrough by Hough and his colleagues was the demonstration of the ability to holographically capture information on fragments that move a distance that is

Table 1: Holographic Measurement Types and Estimated Resolution Requirements To Characterize a (100 mm)^3 Hypervelocity Impact Event

Macroscopic (~1000 μm resolution)	Intermediate Regime (~100 μm resolution)	Microscopic (~10 μm resolution)
Debris Bubble Envelope and Structure	Number of Particles Generated	Particle Shape & Volume
Crater Ejecta Envelope and Structure	Particle Size Distribution	Particle State: Solid, Liquid, or Vapor
Particle Position	Particle Velocity	Particle Roughness: Fractal Dimension

many times the wavelength of the laser light during a pulse duration. For example, 1 km/s particles move 30 μm along the velocity vector during a 30 ns laser pulse. While this distance is small with respect to macroscopic dimensions, it is more than one hundred times the wavelength of visible laser light. This motion prevents the formation of a direct hologram of the impact-generated particles, but the particles can still be characterized. The key is the use of a stationary backsheet, above which the outline of the particles appear as floating shadows.

The LTV system used a pulsed ruby laser to produce a 30 ns, 300 mJ pulse at 694 nm. A ruby laser offers several operational advantages including the ability to easily single-pulse the laser with an external trigger, the stability to provide reliable spatial and temporal beam coherence, and relatively low cost. However there are also a number of disadvantages to ruby lasers. The primary disadvantages are that it is not possible to operate a ruby laser in a continuous wave mode for the reconstruction system and the pulse duration is relatively long for freezing the motion of particles produced in a hypervelocity impact event. If a different wavelength laser such as a helium-neon is used for continuous wave reconstruction, the resulting image is useful for qualitative viewing, however it introduces a non-linear scale shift that complicates quantitative image analysis.

Another pulsed laser that is used for holography is a frequency-doubled Nd-YAG laser. There are a number of pulsed, seeded, doubled Nd-YAG lasers available that produce 5 ns, 750 mJ, coherent pulses at 532 nm. These lasers are more complex and expensive than a pulsed ruby laser, but diode-pumped, doubled Nd-YAG lasers are available that can provide a continuous wave monochromatic light source for use in a quantitative reconstruction system. Because these continuous wave lasers produce the same 532 nm wavelength as the pulsed lasers, no scale shifts are introduced that can complicate the quantitative image analysis. For pulsed, high coherence Nd-YAG systems, the seed laser is a small diode-pumped Nd-YAG laser that provides a reference oscillator cavity to increase coherence length of the main laser cavity. While ruby lasers are available with pulse energies of 2 to 3 J, holographic films are inherently more sensitive to the "green" doubled Nd-YAG at 532 nm than to the "red" ruby at 694 nm. A major disadvantage to the use of a doubled Nd-YAG laser is the complex triggering system that is required to obtain a reliably coherent, single pulse at the right time. This disadvantage is offset by the ability to use the same wavelength for a continuous wave quantitative image reconstruction system. Based on these considerations, the Sandia National Laboratories pulsed holography system utilizes a Q-switched, seeded, doubled Nd-YAG pulsed laser to capture "shadowgraphic" holograms, and a diode-pumped, doubled Nd-YAG laser for quantitative reconstruction.

TEST CONFIGURATION

This section summarizes the experimental setup that has been used for the development of a pulsed holography hypervelocity impact diagnostics system at Sandia National Laboratories. The integration of the laser triggering subsystem into a the gun control circuits for a small (12.7 mm diameter launch tube), two-stage light-gas gun was a key engineering accomplishment. Two different optical layouts that have been used to capture images on holographic plates. Optical layout design balances the need for high image resolution with protection of these glass plates from both impact-generated debris and potential fogging from impact flash. On all tests a pair of open shutter cameras equipped with line filters provide supplementary diagnostics.

Gun / Laser Synchronization and Triggering Subsystem

The main component of our pulsed holography system is a Continuum model NY-82 frequency-doubled Nd-YAG laser with a model SI-500 injection seed laser. As noted above, this type of laser was selected after considering a number of trade-offs with ruby lasers. The major disadvantage of using an Nd-YAG laser is the increased operational complexity of a subsystem to trigger and generate a coherent laser pulse at the correct time. For thermal stability, and to maintain closed-loop, frequency-locked coupling of the seed laser to the main Nd-YAG oscillator cavity, the laser requires continuous pulsing at a 10 Hz rate up to the desired shot time. Unfortunately the powder burn-time jitter of a two-stage light-gas gun prevents using the laser to trigger the gun.

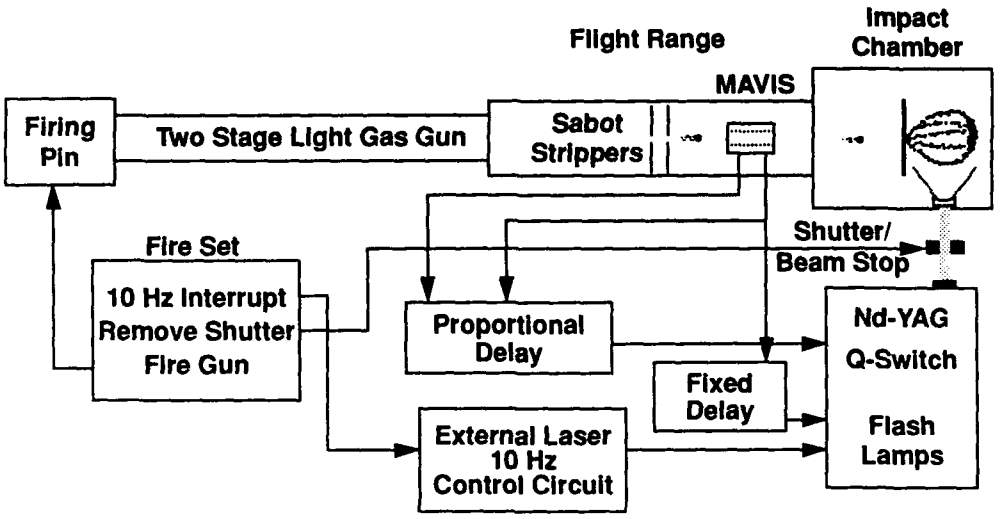


Figure 1. Schematic diagram of the gun-laser synchronization and triggering subsystem. The principal components include the MAVIS projectile sensing coils, the proportional delay, and the shutter/beam stop.

The following is a description of the subsystem for triggering the pulsed Nd-YAG laser after an impact event to within a micro-second of accuracy. An external circuit triggers the laser at a 10 Hz rate in order to maintain laser coherence length. This circuit provides a trigger to the flash lamps that optically pump the Nd-YAG laser cavity. Approximately 200 μs later a second trigger is sent to the Q-switch and seed laser to generate the laser pulse. These triggers are repeated at a 10 Hz rate until an interrupt signal is received just before the gun is fired. An aluminum shutter/beam stop blocks the stream of 750 mJ laser pulses to prevent fogging and over-exposure of the holographic plate.

When the gun fire button is pressed a number of actions occur prior to the actual firing pin release. First, an interrupt trigger is sent to the external 10 Hz pulsing circuit. Second, the shutter/beam-stop is moved out of the optical path into the impact chamber, and third, the laser flash lamp capacitors are charged and held. Then the gun firing pin is released, the projectile is launched, the sabots are stripped in the flight range, and the impactor to flies through a MAVIS coil station placed a known distance from the target (Moody and Konrad, 1984). The MAVIS provides a two-point measurement of the impactor velocity and is used with a proportional delay to trigger the Q-switch and pulse the laser at the desired time after impact. In addition, the MAVIS provides a timing point for triggering the flash lamps from 200 to 500 μs prior to the Q-switch trigger. A simple schematic diagram of this system is shown in Fig. 1.

Holographic Layouts

Two different optical layouts that use holographic plates have been used to capture holographic images of hypervelocity impact events. The first layout is a flat plate geometry that is analogous to the cylindrical geometry that was originally developed by LTV. Figure 2 illustrates our layout of this geometry. While the cylindrical geometry used by LTV produced dramatic images with the ability to examine the debris cloud from a full 180 degrees of view, this geometry is obtained with film-based holographic media. Because our effort has a primary objective of obtaining quantitative information from an analysis of the holographic images, better dimensional stability is required than can be provided with film. In order to achieve measurement accuracies that are better than 100 μm, flat, glass plate holograms are required to accurately reproduce initial reference beam geometries.

The use of flat plate holographic media led to the development of an improved layout shown in Fig. 3. This figure shows the layout of optical components in, and open shutter cameras above the impact chamber from a perspective looking back towards the gun. In contrast to the geometry in Fig. 2, this layout has the benefits of using the central and most intense portion of the beam, and eliminating the front surface mirror from the impact chamber that generates additional secondary debris which can damage the holographic plate. An additional benefit of this layout is the ability to capture holographic images of non-penetrating or cratering impact events. For these types of impacts, the thick target is positioned by the downstream edge of the translucent backsheet and holography plate in order to image the cratering ejecta that is thrown back from the target surface. Important supplementary diagnostics used for these tests are open-shutter stereo cameras equipped with 532 nm line filters. Both layouts provide a clear view from above for open shutter cameras. Figure 3 also illustrates a set of 3 datum pins (from this view one is

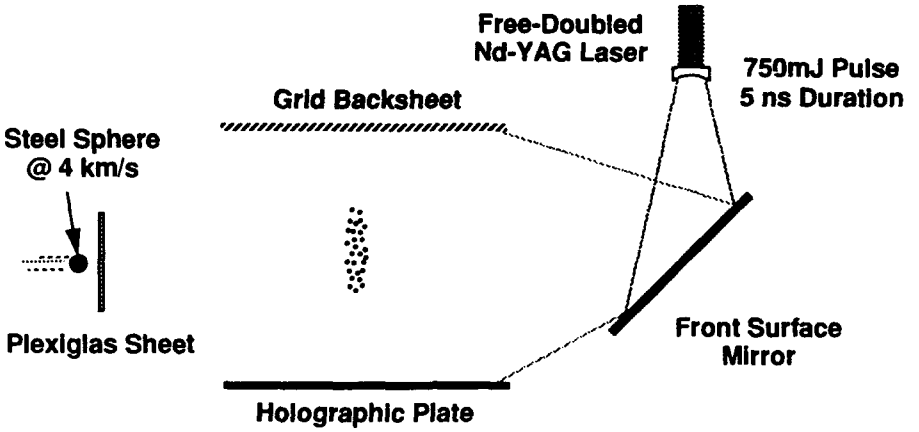


Figure 2. Schematic diagram of flat plate analog to LTV holography layout.

hidden), that are used as fiducials to establish the shot line direction and the horizontal plane perpendicular to the film and grid surfaces.

The holographic media used in these tests are Agfa 8E56-NAH or Ilford SP 695T (102 x 127 mm) glass plates. For dimensional precision glass plates are preferable to plastic film emulsion media; however unless steps are taken to protect the glass, they are subject to the risk of breakage from secondary impacts. A modest amount of protection is provided by placing the holographic plate in a liquid gate. A liquid gate is a flat-walled tank with high-quality optical windows that is used to reduce the sensitivity of the holographic imaging process to non-uniformities in the plate and thickness (Goodman, 1968). This tank is filled with an appropriate index of refraction matching fluid to reduce internal reflections. But this apparatus has the additional benefit of providing improved protection for the holographic plate and reducing potential fogging from impact flash.

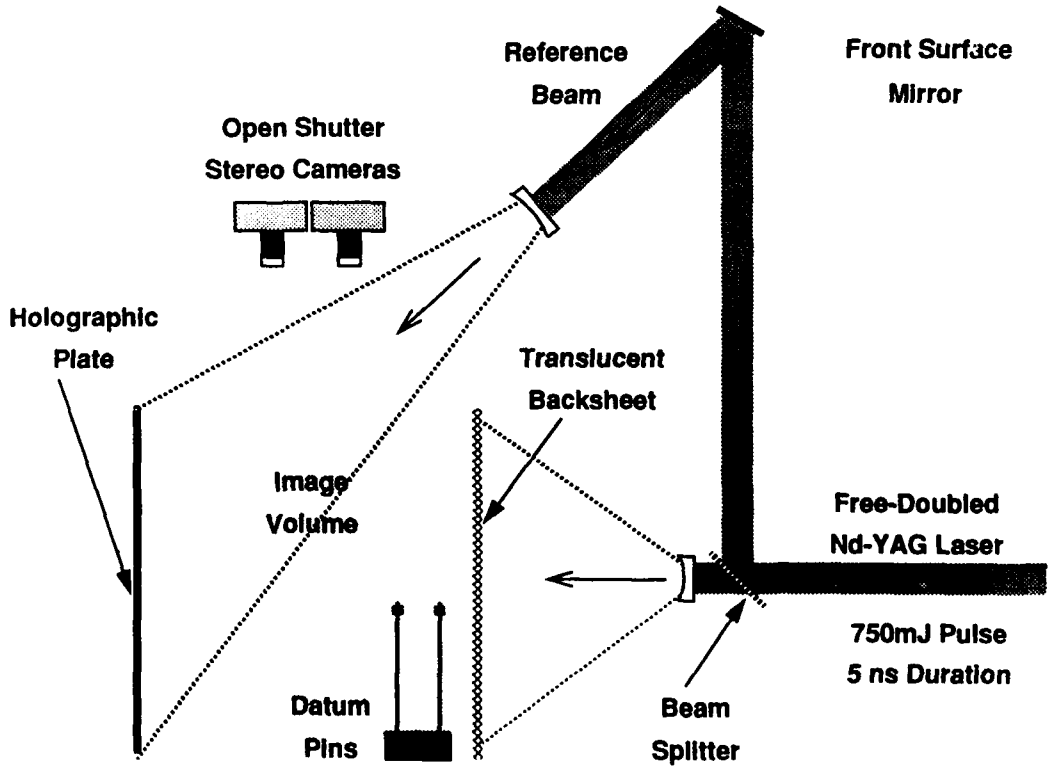


Figure 3. Schematic diagram of improved flat plate holography layout. Perspective is from the impact chamber looking towards the gun.

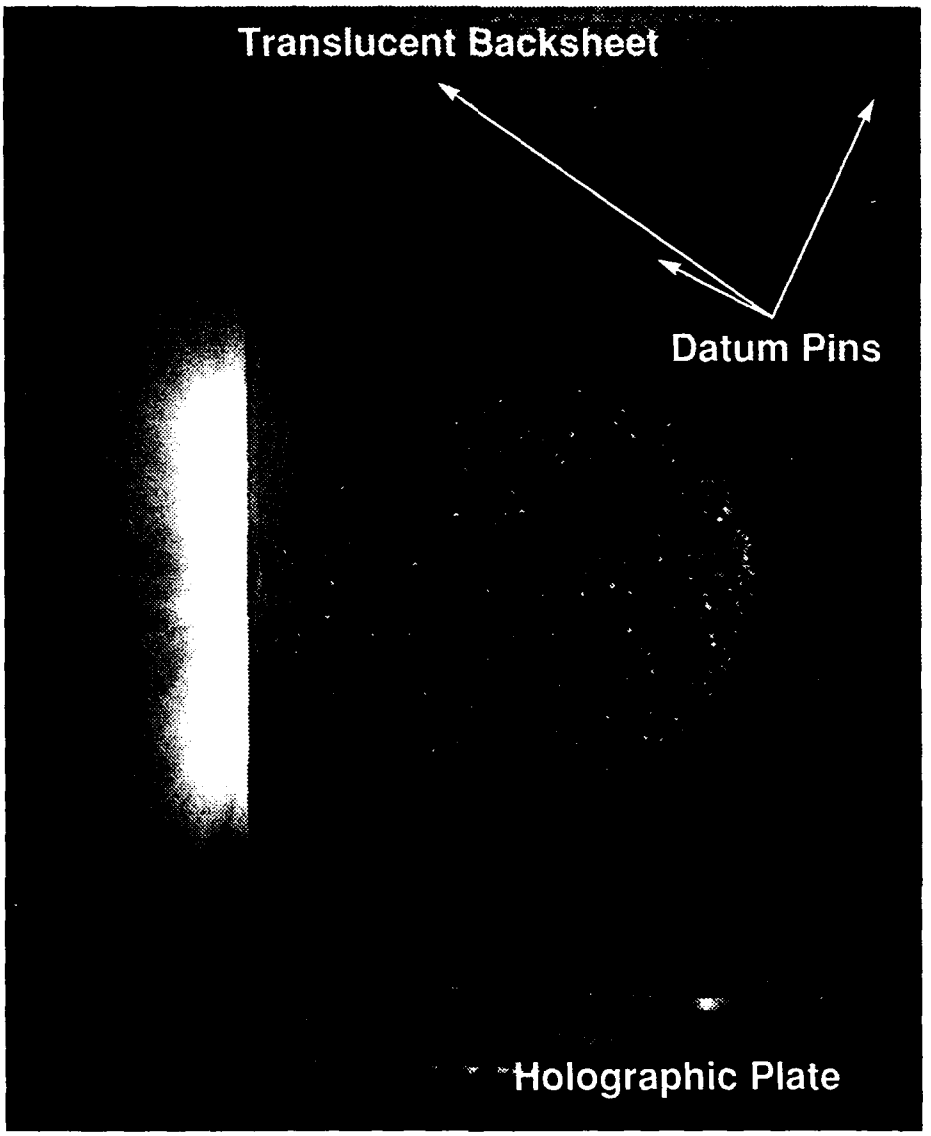


Figure 4. Open shutter photograph of the 4.22 km/s impact of a 6.35 mm steel ball through a 0.63 mm steel sheet 22 ms after impact with a time-integrated image of an impact flash. The holographic plate, translucent backsheet and datum pins are also clearly shown in this photograph.

Figure 4 shows an open-shutter camera photograph from the impact of a 6.35 mm steel sphere through a 0.63mm steel sheet at 4.22 km/s. In this test the laser was pulsed approximately 22 μs after impact of the sphere on the sheet to freeze the motion of hundreds of submillimeter-sized steel fragments. As indicated in Fig. 3, this open shutter camera has a view into the impact chamber from above. Shown at the top of the photograph is the translucent grid sheet and just below this sheet are the three datum pins. At the bottom of this image is the holographic plate. Also evident in this photo is an impact flash event. This test was not successful in capturing a holographic image because the light from the impact flash overexposed the holographic plate. Simple shielding techniques were used to minimize the effects of impact flash in a repeat of this impact test.

Several hypervelocity impact events have been holographically imaged. Table 2 summarizes these impact events. The impacts of steel and copper spheres through plexiglas sheets provide a clean breakup of the sphere. Similar impacts with flash x-ray diagnostics indicate that most of the metallic sphere remains in a tightly grouped cloud of fragments around the initial sphere trajectory. The impact of a steel sphere into a steel sheet results in a debris bubble of fine steel fragments as shown in Fig. 4. Figures 5 and 6 are open shutter photographs from the copper into plexiglas shot and the copper into copper block shot, respectively. The cratering impact shown in Fig. 6 clearly shows how the target block had a machined step cut into the impact face of the block. This step provided protection for the holographic plate by deflecting the crater ejecta that would have been thrown towards the plate.

Table 2: Impact Events Captured with Holographic Images

Impactor	Velocity (km/s)	Target
6.35 mm Steel Ball	4.32	1.3 mm Plexiglas Sheet
6.35 mm Steel Ball	4.22	3.0 mm Plexiglas Sheet
6.35 mm Cu Ball	4.32	1.3 mm Plexiglas Sheet
6.35 mm Steel Ball	4.22	0.63 mm Steel Sheet
6.35 mm Cu Ball	1.99	25.4 mm Cu Block @ 0°



Figure 5. Open shutter photograph of the 4.32 km/s impact of a 6.35 mm copper ball through a 1.3 mm Plexiglas sheet 144 μs after impact.

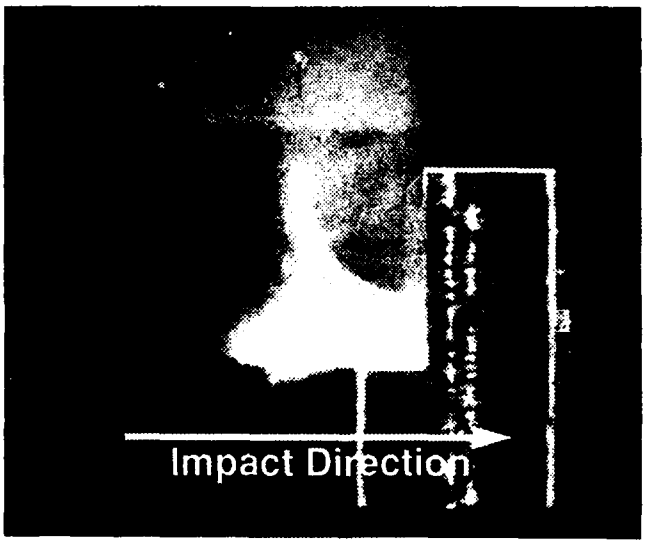


Figure 6. Open shutter photograph of the 1.99 km/s impact of a 6.35 mm copper ball into a 25.4 mm copper block 12 μs after impact.

HOLOGRAPHIC IMAGE RECONSTRUCTION SYSTEMS

The pulsed holograms produced in this study are transmission holograms that require a monochromatic light source to reconstruct the holographic image. For qualitative viewing, this source can be a laser with a different wavelength from the pulsed laser used for generating the hologram. It is also possible to use different optics and configurations for the reconstruction beam. Figure 7 is a photograph of our system for qualitative reconstruction of holographic images. This system uses a small continuous wave 25 mW diode-pumped Nd-YAG laser operating at 532 nm, but it departs from the original reference beam geometry in interests of packaging a portable system.

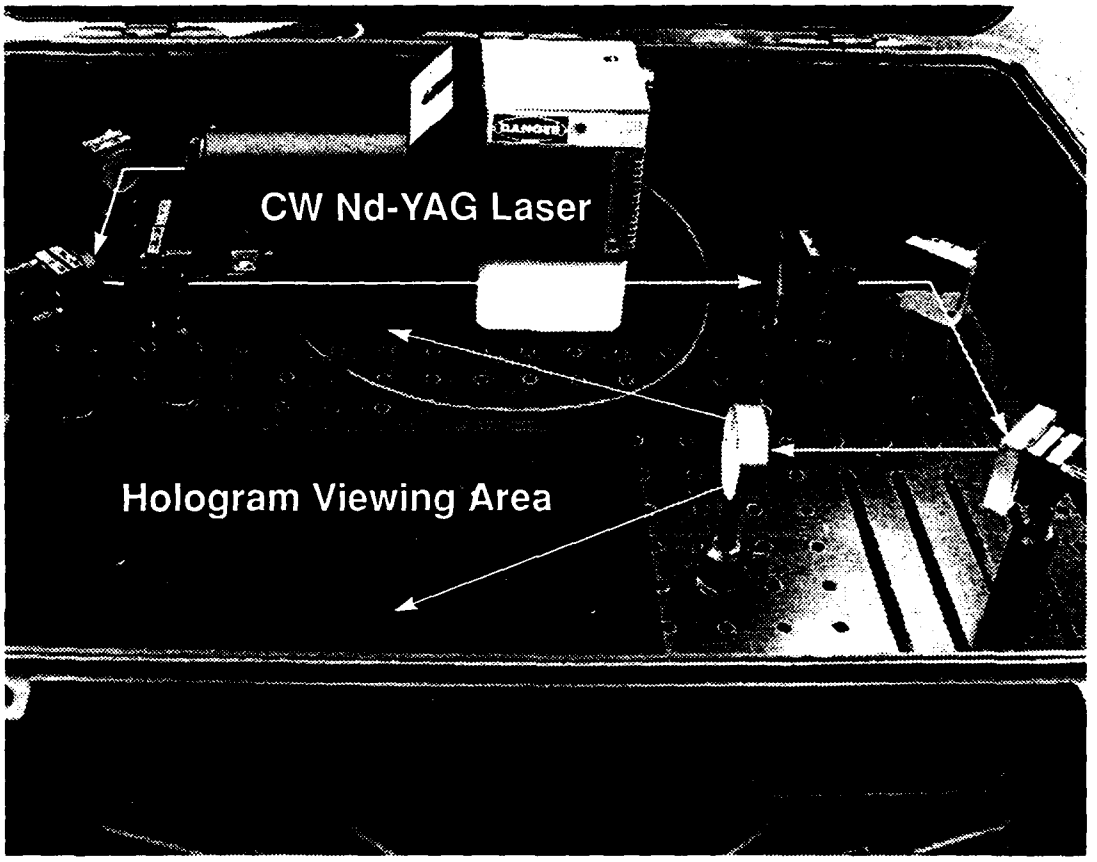


Figure 7. Portable, quantitative holographic image reconstruction system. Arrows indicate the beam path through the collimating and beam expanding optics. The reconstructed image is viewed above the black rectangular area.

As noted previously, if the same wavelength light is used for image reconstruction, it is possible to form a reconstructed image with no length scale shifts. To achieve the high levels of resolution given in Table 1, the original reference beam must be accurately reproduced. A prototype image analysis subsystem with a quantitative image reconstruction subsystem has been assembled. The same 532 nm laser from the portable qualitative reconstruction subsystem has been used; however, an identical reconstruction beam was used, including the impact chamber port. The reconstructed images were imaged with a CCD camera having 768 by 493 active pixels and either a zoom lens with a focal length range of 18 to 108 mm or a matched pair of achromat 1:1 image transfer lenses. This CCD camera has been mounted on a manual three axis stage. The RS-170 analog video signals from the CCD camera have been digitized with a commercial image processor board for a PC-compatible computer at a resolution of 640 by 480 pixels, with 8 bits intensity resolution. A photograph of this prototype image analysis subsystem is shown in Fig. 8.

Figure 9 is an example of the digitized images that can be obtained from the reconstructed holographic images with the image processing system. This set of images is from the same impact event captured with an open shutter camera photograph shown in Fig. 5. These images illustrate the ability to position the plane of focus of the CCD camera at fragments of interest, at a datum pin, or at the backsheet. The image in the lower right quadrant shows the high degree of detail that is revealed when the optics are focused on the upper edge of the large central copper fragment.

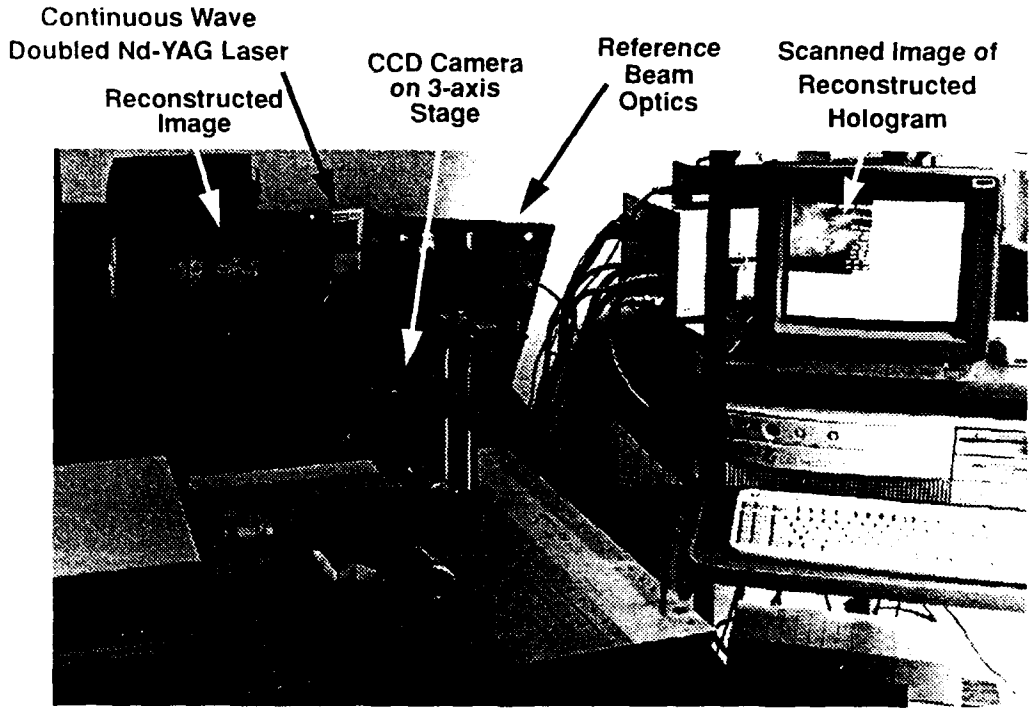


Figure 8. Photograph of the prototype quantitative holographic reconstruction and image processing system.

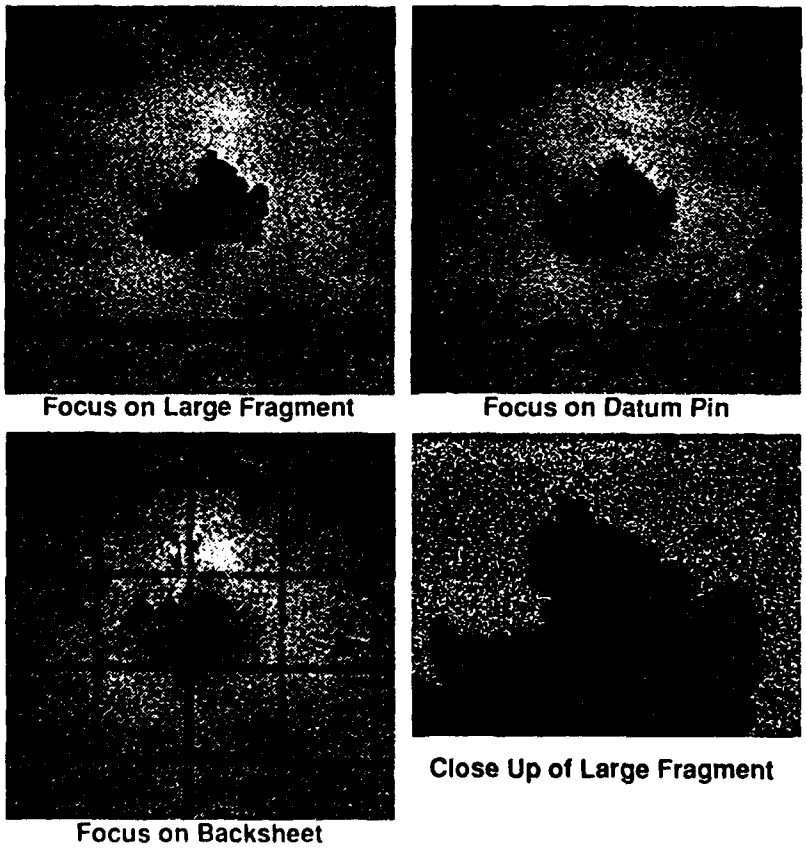


Figure 9. Digitized CCD camera images of the reconstructed hologram from the 4.32 km/s impact of a 6.35 mm diameter copper ball through a 1.3 mm Plexiglas sheet 144 μs after impact. This is the same impact event shown in Fig. 5.

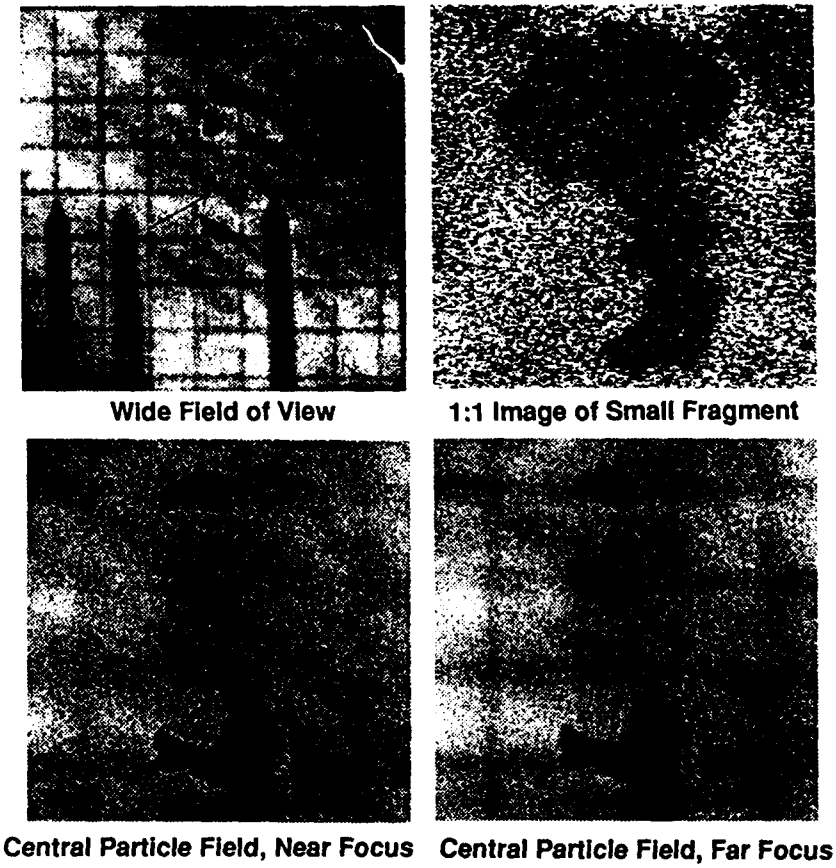


Figure 10. Digitized CCD camera images of the reconstructed hologram from the 4.22 km/s impact of a 6.35 mm diameter 1018 steel ball through a 3.0 mm Plexiglas sheet 134 μs after impact.

The images shown in Fig. 10 illustrate two capabilities that the analysis of pulsed holograms provide. The image in the upper left quadrant is a wide field of view that is focused on the impact-fragmented steel particles. Also shown are the out of focus datum pins and backsheet. The arrow points to a small particle below the center of the fragment field. The image in the upper right quadrant is the digitized image of this fragment using 1:1 image transfer optics. The waist of this fragment is approximately 350 μm in thickness. The two images in the lower quadrants demonstrate the ability to use depth of focus to throw particles into and out of focus. When coupled to a high precision three axis stage, a narrow depth of focus provides the ability to accurately determine the depth position for a particle. Particle in the plane of focus of the camera can then be located in the horizontal and vertical directions by reading positions from the corresponding axis of the stages.

HOLOGRAPHIC IMAGE RESOLUTION LIMITS

There are several factors that contribute to the resolution limit of these pulsed holographic images. These factors include the velocity of the particles, laser speckle and viewing optics resolution, the thickness of the particles, and the resolution of the CCD camera. Because the pulse duration is nominally 5 ns, there is a velocity blurring effect. The velocity blurring is roughly equal to the product of the pulse width of the laser and the particle velocity. Actually, it should be possible to estimate the particle size to about half of this number; so the axial blurring resolution limit is approximately 10 to 15 μm for 5 km/s particle velocities. There is an uncertainty in determination of the edge position of a particle. This is due to a coupling of laser speckle and the simple resolution limits of the viewing lens optics. The resolution of a simple lens viewing an incoherently illuminated object gives a blur size diameter of 1.3(f/no.)-(μm). The speckle phenomena will change the intensity in the blurred edge, so it may increase the over-all blurring by a factor of two, to about 2.5(f/no.)-(μm). For example, an f/6 viewing system will blur the edges by about 15 μm. Fortunately, the illumination is much broader in angle than the viewing system; in general, this factor does not limit the resolution. Thick particles, with significant depth parallel to the direction of viewing can increase the apparent cross-section of the fragments in some circumstances. This effect will be most noticeable when the viewing system is fast, e.g. f/2. There is a resolution limit imposed by the CCD camera due to the number

of pixels in the CCD array. Assuming a baseline high-resolution 1:1 image transfer optical system that is nominally a 500x500 CCD array with a 10 mm by 10 mm active area. Then in each dimension, a pixel represents a 20 μm by 20 μm area. Of course, to improve this resolution, it is possible to use a design with increased magnification in the image transfer optics. If a smaller image volume (e.g. $(25mm)^3$) is of interest, it is possible to use magnification optics such as microscope objectives or lithography lenses between the holographic plate and the impact event to achieve further increases in resolving power.

The image resolution of this pulsed holographic system was measured with a standard 1951 Air Force resolution test target capable of measuring resolutions from 2000 μm to 2 μm. The resolving power of the image analysis subsystem was measured by using the 1:1 image transfer optics to project the test target onto the focal plane of the CCD camera. With white-light illumination, a resolution of 12 μm was measured for the image analysis subsystem. To measure the resolution of the image-capturing subsystem, a hologram was made of the stationary resolution test target. By viewing this hologram with the image analysis subsystem, resolutions of 35 μm for the Agfa plates and 20 μm for the Ilford plates were measured. This resolution capability does not account for the velocity blurring effect or the uncertainties introduced by the thickness of particles, but it does account for the blur due to speckle and the resolution of the image capturing and image reconstruction processes. The velocity blur for hypervelocity particles is expected to further degrade image resolution. Note however, that velocity blur also degrades all conventional imaging techniques. These measurements demonstrate that the resolution capability of pulsed holograms can be approximately an order of magnitude greater than what is possible with conventional imaging techniques. When a 10x microscope objective was used as an optical magnifying optic, the resolution of the image analysis subsystem was measured to be over 1 μm. The corresponding measured resolution for the hologram was 3.5 μm. The trade-off for this technique is that it yields a field of view of about 19 mm and it complicates the ability to determine the depth location of a particle. Therefore, it is most applicable for tests where the spatial volume of interest is known *a priori*.

FUTURE EFFORTS

This pulsed holography development effort has achieved a number of key results. Holographic images have been captured of a number of hypervelocity impact events, including perforating and non-perforating impacts, and these holographic images have been digitized with a prototype image analysis system. While the open shutter cameras are a supplementary diagnostic, the analysis of these photographs with existing image analysis tools will provide a validation of the macroscopic holographic measurements.

There are several steps that can still be taken to improve image resolution. A spatial filter can be added to the reference beam to improve the beam quality and uniformity. The pulsed laser can be replaced with a similar frequency doubled Nd-YAG laser with 50 to 150 picosecond pulse duration to reduce the velocity blurring effect. Finally, higher quality imaging optics can be used to increase the resolving power of the image analysis subsystem.

The quantitative analysis of the information captured in these holograms can be achieved through different approaches. The next step in analyzing the digitized images will be to use existing image processing software to define particle edges, dimensions and areas. Sophisticated software packages are also capable of determining such factors as the image centroids. To accurately determine the location of impact-generated particles the CCD camera and image transfer optics will scan the image volume with a computer-controlled three-axis translation stage with at least one axis of rotation.

An interesting consideration is the information content potential of these holograms. Assuming the holographic image volume is $(250\ mm)^3$, the total potential image volume is $15.6x10^6\ mm^3$. If the depth of focus for the image transfer optics is 0.5 mm, then each 10 mm x 10 mm digitized image would cover a volume of $50\ mm^3$, therefore to completely record the entire image volume, more than 300,000 images would be required. Of course most of these images probably would not contain any useful information so sophisticated data handling and manipulating algorithms would be useful. This example indicates the need for applying high performance computing to handle the large volumes of data that will be generated in the analysis of holographic images.

Another option for analyzing the data in these holograms will be to take stereo photographs of the reconstructed holographic image. These stereo photograph pairs, like the initial open-shutter stereo camera photographs, can be analyzed with existing stereo image analysis tools (Franke, et al., 1991). This analysis will provide cross-correlation for the macroscopic measurements of an impact event.

ACKNOWLEDGEMENTS

We would like to acknowledge the support and interest of Drs. James R. Asay and Philip L. Stanton in the development of this advanced hypervelocity impact diagnostics capability. We also thank Scott Harland for his initiative in commissioning our pulsed, Nd-YAG laser and obtaining our first static holograms during his summer at our impact facility as a participant in the Sandia Outstanding Summer Student Program.

REFERENCES

Franke, E.A., D.J. Wenzel, and D.L. Davidson, (1991). Measurement of microdisplacements by machine vision photogrammetry (DISMAP). *Rev. Sci. Instrum.*, 62, No. 5, pp. 1270-1279.

Goodman, J.W., (1968). *Introduction to Fourier Optics*. McGraw-Hill Book Co., New York.

Hough, G.R., D.M. Gustafson, and W.R. Thursby, (1990). Enhanced holographic recording capabilities for dynamic applications. In: Proc. SPIE 34th Annual International Symposium.

Isbell, W.M., (1987). Historical overview of hypervelocity impact diagnostic technology. *Int. J. Impact Engng.*, 5, pp. 389-410.

Mandelbrot, B.B. (1983). *Fractal Geometry of Nature*. W.H. Freeman and Co., New York.

Moody, R.L. and C.H. Konrad, (1984). Magnetic induction system for two-stage gun projectile velocity measurements. Sandia Report, SAND84-0638, UC-13.

Swift, H.F., J.A. Zukas, T. Nicholas, L.B. Greszczuk and D.R. Curran (1982). Image forming instruments. In: *Impact Dynamics*. John Wiley and Sons, Inc., New York.

Int. J. Impact Engng Vol.14, pp.25–35, 1993
Printed in Great Britain

0734-743X/93 $6.00+0.00
1993 Pergamon Press Ltd

CRITICAL RESPONSE OF SHIELDED PLATES SUBJECTED TO HYPERVELOCITY IMPACT

Y.C. ANGEL and J.P. SMITH

Department of Mechanical Engineering and Materials Science
William Marsh Rice University
Houston, Texas 77251-1892, U.S.A.

ABSTRACT

A ballistic limit equation for hypervelocity impact on thin plates is derived analytically. This equation applies to cases of impulsive impact on a plate that is protected by a multi-shock shield, and is valid in the range of velocity above 6 km/s. Experimental tests were conducted at the NASA Johnson Space Center on square aluminum plates. Comparing the center deflections of these plates with the theoretical deflections of a rigid-plastic plate subjected to a blast load, one determines the dynamic yield strength of the plate material. The analysis is based on a theory for the expansion of the fragmented projectile and on a simple failure criterion. Curves are presented for the critical projectile radius versus the projectile velocity, and for the critical plate thickness versus the velocity. These curves are in good agreement with curves that have been generated empirically.

NOTATION

r	projectile radius	ν	Poisson's ratio of backwall
U_m	projectile velocity	σ_0	static yield strength of backwall
ρ_p	projectile mass density	σ	dynamic yield strength of backwall
m_p	projectile mass	λ	ratio of σ to σ_0
D	shield spacing	I_{bw}	impulse on the backwall
T	duration of rectangular load	$P(t)$	time-dependent load on backwall
T_L	load duration on backwall	P_m	maximum value of $P(t)$
R	load radius on backwall	μ	dimensionless load based on P_m
K	ratio of surface densities	μ^*	upper bound for μ
K^*	lower bound for K	W	permanent backwall deflection
$2h$	backwall thickness	δ	dimensionless backwall deflection
a	backwall half-width	δ^*	upper bound for δ
c	ratio of a to R	B	scaling factor
c^*	lower bound for c	Ω	backwall deformation
ρ	backwall mass density	Ω^*	upper bound for Ω

INTRODUCTION

Space debris and meteoroids of various sizes may impact space vehicles at relative velocities as high as 70 km/s, and the impacts may have catastrophic effects on the integrity of the vehicles. For protection, one uses dual-plate shields (Kinslow, 1970; Zukas *et al.*, 1982; Rajendran and Elfer, 1989) or multi-shock shields (Cour-Palais and Crews, 1990). These shields shatter the impacting objects into fragments, and spray the fragmented pieces (solid, molten, or vaporized – depending on the impact conditions) over an area much larger than that of the cross-section of the unshattered object.

In this paper, we derive a ballistic limit equation for hypervelocity impact on thin plates. This equation applies to cases of impulsive impact on a plate that is protected by a multi-shock shield; it is valid when the projectile velocity is in the range above 6 km/s, and when the area of the impact zone is much smaller than the area of the plate. The analysis that leads to the ballistic limit equation (Eqn (26) below) is discussed in detail in the following sections. For convenience, we reproduce here Eqn (26) in the form

$$\frac{\rho_p U_m^2}{\sigma_0}\frac{r^3}{Dh^2} = C, \qquad C = \frac{9\lambda\mu(1+K)\sqrt{K}}{2(1-K)}, \tag{1}$$

where the parameters K, λ, μ, and C take the values

$$K = 0.04, \qquad \lambda = 4.5, \qquad \mu = 50, \qquad C = 219.4. \tag{2}$$

The parameters ρ_p, r, and U_m denote the mass density, the radius, and the velocity of the projectile; h and σ_0 are the half-thickness and the static yield strength of the plate; D is the spacing between the outer sheet of the multi-shock shield and the plate; the dimensionless K measures the expansion of the fragmented projectile, λ is the ratio of the dynamic yield strength to the static yield strength of the plate material, and μ is the dimensionless load applied to the plate. In Eqn (1), the two groups $\rho_p U_m^2/\sigma_0$ and $r^3/(Dh^2)$ are dimensionless; the parameter C is also dimensionless.

Equation (1) represents a relation between the *critical* values of the parameters. If we let any two of the parameters ρ_p, U_m, σ_0, r, D, and h vary, while keeping all the other parameters fixed, we obtain from (1) a plane curve. The curve divides the plane in two regions: one of them is the safe region, and the other is the failure region.

It will be seen below that Eqn (1), together with (2), yields numerical results that are in good agreement with those obtained from the empirical equation of Christiansen (1990, 1991). Thus, Eqn (1) can be used to guide further experiments and shield design studies.

In a previous work, Angel and Whitney (1992) were able to obtain a ballistic limit equation by using a simple analytical solution for the permanent deflection of a rigid-plastic beam. In this work, we replace the beam solution by a plate solution. This yields Eqn (1), which is simpler than the previous ballistic limit equation.

To arrive at Eqn (1), we discuss first, in the next section, the plate solution of Hopkins and Prager (1954). This solution corresponds to a simply supported circular plate uniformly loaded over its entire area by a blast load. The plate is made of a rigid perfectly-plastic material. We give expressions for the permanent deflection of the plate at the center. Next, we compare the theoretical deflection with the experimental deflections of six aluminum square plates supplied by the Hypervelocity Impact Test Facility of NASA/JSC. In this process, we invoke the debris-expansion theory of Swift *et al.* (1982), and we determine the dynamic yield strength of the plate material. Then, we choose a failure criterion based on the maximum permissible deflection, and we establish that the critical values are related by Eqn (1). Finally, we present curves for the critical projectile radius r versus the projectile velocity U_m, and for the critical plate half-thickness h versus U_m.

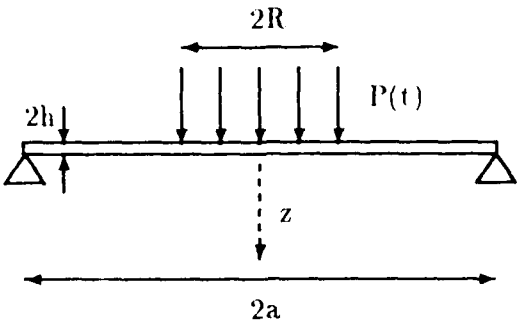


Fig. 1. Plate subjected to a uniformly distributed circular load.

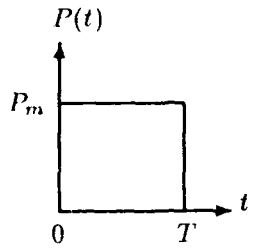


Fig. 2. Time dependence of the load.

PERMANENT DEFLECTION OF A CIRCULAR PLATE

Consider a simply supported circular plate of radius a and thickness $2h$ subjected to a circular load of radius R, as shown in Fig. 1. The plate is made of a rigid perfectly-plastic material, and the load $P(t)$, which is uniformly distributed, has a rectangular time-dependence as in Fig. 2. Let P_m be the maximum value of the load, and let T be the time at which the load returns instantaneously to zero.

When the deformations are small, the axisymmetric equation of dynamic equilibrium for the plate, which is given by Hopkins and Prager (1954, p. 318), can be written in cylindrical coordinates in the form

$$[rM_r(r,t)]' - M_\theta(r,t) = -\int_0^r [p(\alpha,t) - 2\rho h\ddot{w}(\alpha,t)]\alpha d\alpha, \tag{3}$$

where w is the deflection of the plate in the z direction of Fig. 1, M_r and M_θ are the bending moments per unit length caused by the radial and circumferential stresses, respectively, p is a force per unit area along the z direction, and ρ is the mass density of the plate. In (3), the prime superscript denotes differentiation with respect to the radial coordinate r, and the superimposed dots denote differentiation with respect to the time t.

Using the Tresca yield criterion, one can show (Jones, 1989, p. 31) that the moments M_r and M_θ take values in the (M_θ, M_r) plane inside, or on the boundary of, a hexagon containing the origin. The size of the hexagon is determined by the plastic collapse moment M_0 per unit length, which can be expressed in terms of the static yield strength σ_0 of the plate as

$$M_0 = \sigma_0 h^2. \tag{4}$$

When the circular load of Fig. 1 is applied over the entire area of the plate ($R = a$), the permanent deflection W_e at the center of the plate has been calculated by Hopkins and Prager (1954, Eqn

(22) p. 324 and Eqn (44) p. 329). The results of these authors can be written in the form

$$\delta_e = \begin{cases} 0 & ,0 < \mu < 1, \\ \mu(\mu - 1) & ,1 < \mu < 2, \\ \frac{\mu}{4}(3\mu - 2) & ,2 < \mu, \end{cases} \tag{5}$$

where the dimensionless deflection δ_e and the dimensionless load μ are defined by

$$\delta_e = \frac{\rho a^2}{3\sigma_0 h T^2} W_e, \qquad \text{and} \qquad \mu = \frac{P_m}{6\pi\sigma_0 h^2}. \tag{6}$$

Next, we recall that the *static* deflection W_s at the center of the plate of Fig. 1, when the total distributed load is equal to P_m, is given by (Timoshenko and Woinowsky-Krieger, 1959, pp. 64-67)

$$W_s = \frac{P_m}{16\pi F}\left[\frac{3+\nu}{1+\nu}a^2 - R^2 \ln\frac{a}{R} - \frac{7+3\nu}{4(1+\nu)}R^2\right], \tag{7}$$

where ν is Poisson's ratio and F is the flexural rigidity of the plate. The flexural rigidity can be expressed in terms of Young's modulus E as: $F = 2Eh^3/[3(1-\nu^2)]$.

Equation (7) can be used to evaluate the *static* deflection of a plate loaded over its entire area ($R = a$). The ratio $\overline{W}$ of the deflection (7) to the deflection that corresponds to $R = a$ is given by

$$\overline{W} = \frac{1}{5+\nu}\left[4(3+\nu)\frac{a^2}{R^2} - 4(1+\nu)\ln\left(\frac{a}{R}\right) - (7+3\nu)\right]\frac{R^2}{a^2}. \tag{8}$$

Next, let W be the permanent deflection at the center of the plate of Fig. 1 when the load $P(t)$ has the time-dependence of Fig. 2. In order to evaluate W, we assume that the ratio of W to the deflection W_e corresponding to (5) - (6) is equal to the ratio $\overline{W}$ of (8). Thus, one has

$$W = \overline{W} W_e. \tag{9}$$

We introduce now a dimensionless measure δ of the permanent deflection W, and a parameter c that is equal to the ratio of the plate radius to the load radius. These parameters are defined by

$$\delta = \frac{\rho R^2}{3\sigma_0 h T^2} W, \qquad \text{and} \qquad c = \frac{a}{R}. \tag{10}$$

Then, we infer from Eqns (9), (10), (8), $(5)_3$, and (6) that the expression of δ in terms of the parameter μ of (6) is

$$\delta = \frac{\mu}{4}(3\mu - 2)B(c,\nu), \tag{11}$$

where

$$B(c,\nu) = \frac{4(3+\nu)c^2 - 4(1+\nu)\ln c - (7+3\nu)}{(5+\nu)c^4}, \tag{12}$$

and $\mu > 2$, as indicated in $(5)_3$. Observe that the dimensionless δ in (10) is defined in terms of the load radius R, whereas the dimensionless δ_e of (6) is defined in terms of the plate radius a.

EXPERIMENTAL RESULTS

Six multi-shock shields and aluminum target plates were supplied by the Hypervelocity Impact Test Facility of NASA/JSC. The experimental tests are labeled A1229, A1230, A1233, A1235, A1237, and A1253. For each of the six experiments, the target consists of a backwall 15.24 cm (6 in.) square protected by a series of four evenly-spaced Nextel sheets, also 15.24 cm square.

Table 1. Experimental data.

Shot	U_m(km/s)	m_p(mg)	$2h$(mm)	D(cm)	W(mm)	R(cm)	K
A1229	6.49	47.04	0.508	10.16	4.018	2.08	0.0402
A1230	6.32	46.92	0.635	10.16	2.515	2.39	0.0522
A1233	6.26	46.84	0.813	10.16	1.102	2.12	0.0417
A1235	6.24	46.86	0.635	10.16	1.834	2.19	0.0442
A1237	6.20	46.84	0.813	7.620	2.118	2.16	0.0744
A1253	6.51	46.90	1.600	5.080	1.283	1.92	0.1250

Nextel is a lightweight ceramic fiber that is woven into a cloth fabric. The distance from the outer sheet to the target plate is D, as illustrated in Fig. 3.

In the experiments, aluminum spheres with a diameter of 3.175 mm (1/8 in.) and a mass density $\rho_p = 2796$ kg/m^3 are fired from a light-gas gun at velocities near 6.5 km/s. The projectile impacts the outer Nextel sheet normally, leaving a hole slightly larger than the projectile diameter, and shatters into fragments. Because the fragments move inside a cloud of expanding radius, the following sheets have increasingly larger holes. Finally, the fragments impact the backwall, causing a permanent plastic deformation.

Several parameters were varied in the experiments in order to see how each parameter affects the backwall deflection. The parameters (projectile velocity and mass, backwall thickness, shield spacing, permanent deflection, and load radius) of the six experiments are shown in Table 1. Four experiments were conducted with the shield spacing set at 10.16 cm, and two experiments have a reduced shield spacing. The yield strength of the backwall material is equal to 344.74 MPa (Al 2024-T3) and the mass density is $\rho = 2768$ kg/m^3 for all experiments, except for A1230, where the yield strength is 275.79 MPa (Al 6061-T6) and the mass density is $\rho = 2713$ kg/m^3. Also, the plate thickness takes four different values.

The permanent deflections of the backwalls, which are recorded in Table 1 as W, were measured using a precision lathe to a precision of three hundredths of a millimeter. The deflections W represent the *centerline* deflections of the backwalls.

The backwall in each experiment is tarnished and pitted by the impact. The tarnished area is nearly identical to the area of the backwall that is permanently deformed. Measurements of the load diameter were taken by carefully tracing the region of impact onto guideline tracing paper, where actual diameters could be more accurately determined and measured. Eight different diameters were measured and averaged for each of the six experiments to obtain the experimental values of the radius R listed in Table 1.

DEBRIS CLOUD DYNAMICS

In the range of projectile velocities above 6 km/s, which contains the six velocities of Table 1, the impact pressure applied by the Nextel sheets on the projectile is sufficiently high to melt the projectile completely before it impacts the backwall (Christiansen, 1990, 1991). Thus, the backwall is subjected to the impulse of a cloud of molten fragments. In the following, we consider only the case of impulsive loading caused by molten fragments.

The impulse on the backwall depends on two opposite effects. First, the rebounding effect discussed by Gehring (1970) tends to increase the impulse, and second the impacts on the successive

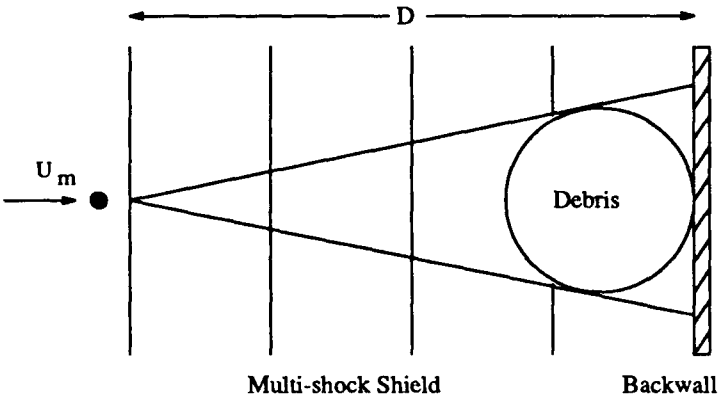


Fig. 3. Impact of a projectile on a multi-shock shield.

sheets tend to reduce it. Thus, we write as an approximation that the total impulse I_{bw} on the backwall is equal to the momentum of the incoming projectile. It follows that

$$I_{bw} = m_p U_m = \frac{4}{3}\pi \rho_p r^3 U_m, \tag{13}$$

where m_p, U_m, ρ_p, and r denote, respectively, the mass, the velocity, the mass density, and the radius of the projectile.

Next, we assume that the impulse I_{bw} is equivalent to that of a rectangular load $P(t)$ as in Fig. 2. It follows that the equivalent maximum load P_m is given by

$$P_m = \frac{I_{bw}}{T}. \tag{14}$$

We now recall that Swift *et al.* (1982) have proposed a theory for the debris expansion. This theory can be applied to our problem, provided that the four Nextel sheets are replaced by an equivalent shield. The equivalent shield is made of a single plate; it is located at the place of the outer Nextel sheet, and its material properties are such that the conical debris expansion is identical to that produced by the four sheets.

It follows from Swift *et al.* (1982) that the load duration T_L and the load radius R on the backwall can be written in the form

$$T_L = \frac{2D(1+K)\sqrt{K}}{U_m(1-K)}, \qquad R = D\left(\frac{K}{1-K}\right)^{1/2}, \tag{15}$$

where D is the distance between the equivalent shield and the backwall, and the parameter K is the ratio of the surface density of the equivalent shield to the surface density of the spherical projectile. The formulae (15) correspond to the case where the hole radius in the shield is equal to the projectile radius, and where the kinetic energy expended in the debris expansion is equal to the total available kinetic energy (Swift *et al.*, 1982, pp. 22-25).

Equation (15) shows that the values of K must satisfy the condition $0 < K < 1$. By using (15), together with the R and D values of Table 1, we have calculated the corresponding value of K for each of the six experiments. These values are recorded in the last column of Table 1. We observe here that the value of K increases when the shield spacing D decreases, as indicated by Shots A1229, A1237, and A1253. We now select from the list of values of K a lower bound K^* such that

$$K^* = 0.04. \tag{16}$$

The time T_L of (15) is the time necessary for the particle at the back of the spherical debris cloud to travel the length of the sphere diameter, starting at the instant when the first particle

touches the backwall. The time T of (14) is the duration of the rectangular load in the theoretical approach of Hopkins and Prager (1954). In order to determine a relation between T_L and T, we write that the impulse of an isosceles triangular load of duration T_L and height P_m is equal to the impulse of a rectangular load of duration T and height P_m. Then, one finds that

$$T = \frac{1}{2}T_L. \tag{17}$$

The argument that leads to (17) is consistent with the numerical results of Perzyna (1958); these results show that impact loads of equal impulses on rigid perfectly-plastic plates cause approximately the same permanent deflections.

BALLISTIC LIMIT EQUATION

Let σ be the dynamic yield strength of the backwall material. Then, using σ instead of the static yield strength σ_0, we can rewrite the dimensionless measure δ of the permanent deflection and the dimensionless measure μ of the maximum load in the form (see (10) and (6))

$$\delta = \frac{\rho R^2}{3\lambda\sigma_0 h T^2}W, \qquad \mu = \frac{P_m}{6\pi\lambda\sigma_0 h^2}, \tag{18}$$

where $\sigma = \lambda\sigma_0$, and λ is a multiplicative factor. The parameters δ and μ can be expressed in terms of ρ_p, r, U_m, D, K, ρ, h, W, σ_0, and λ. To see this, it suffices to substitute (13) - (15) and (17) into Eqns (18). The result is

$$\delta = \frac{1-K}{3\lambda(1+K)^2}\frac{\rho U_m^2}{\sigma_0}\frac{W}{h}, \qquad \mu = \frac{2(1-K)}{9\lambda(1+K)\sqrt{K}}\frac{\rho_p U_m^2}{\sigma_0}\frac{r^3}{Dh^2}. \tag{19}$$

We have determined the factor λ by substituting the experimental values of Table 1 into (19), and by plotting the corresponding points in a (μ, δ) system of axes. For each experiment in Table 1, and for varying values of λ, the points (μ, δ) describe a straight line through the origin. If, on the other hand, a fixed value of λ is chosen, then the six points corresponding to the six experiments of Table 1 are located on a parabola-like curve. Three such curves (for $\lambda = 1.8$, 4.5, and 7.0) are shown in dotted lines in Fig. 4. Also shown in Fig. 4 is a solid line. The solid line is obtained from Eqn (11) for $\mu > 2$, for a value of Poisson's ratio $\nu = 0.3$, and for a choice of the parameter c of (10) such that

$$c = c^* = 3.18. \tag{20}$$

The value c^* is a lower bound for the six experiments of Table 1; it is obtained by taking the values $a = 7.62$ cm and $R = 2.39$ cm of Shot A1230. For the other five experiments, the values of c are greater than c^*. Now, returning to equation (11), one can see that $B(c, \nu)$ takes the value 1.0 at $c = 1.0$ and decreases monotonically to zero as c approaches infinity (for fixed values of ν). Thus, the deflection δ of (11), for fixed values of ν and μ, decreases as c increases. It follows that the lower bound c^* yields a conservative upper bound for the deflection δ.

Figure 4 shows that the solid line, which represents the theoretical permanent deflection at the center of the plate, is very close to the dotted line representing the experimental deflection when $\lambda = \lambda^* = 4.5$. It is also shown in Fig. 4 that the experimental deflections for $\lambda = 1.8$ and $\lambda = 7.0$ are not near the theoretical curve. Consequently, in all our subsequent calculations, we choose

$$\sigma = 4.5\sigma_0 = \lambda^*\sigma_0. \tag{21}$$

The ballistic limit equation can now be obtained from Eqns (19). We begin by rewriting δ of (19) in the form

$$\delta = \frac{1-K}{3\lambda(1+K)^2}\frac{\rho U_m^2}{\sigma_0}\Omega, \tag{22}$$

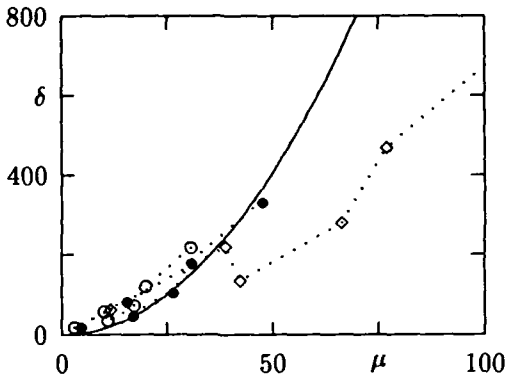


Fig. 4. Theoretical (solid line) and experimental backwall deflections for dynamic yield strengths of $1.8\sigma_0(\diamond)$, $4.5\sigma_0(\bullet)$, and $7\sigma_0(\circ)$.

where $\Omega = W/h$ is a measure of the deformation of the backwall. This measure is independent of the width $2a$ of the backwall. The values of Ω for the six experiments of Table 1 are: $\Omega = 15.82$, 7.921, 2.711, 5.776, 5.210, and 1.604. Based on these results, we choose an upper limit

$$\Omega^* = 15.82. \tag{23}$$

Equation (23) can be interpreted as a failure criterion: For values of Ω less than Ω^*, the backwall has sustained the impact; for values greater than Ω^*, the backwall has failed.

Substituting Ω^* into (22), using (21) and the values of Table 1, we find that the values of δ for the six experiments are: $\delta = 351.55$, 394.18, 325.62, 321.16, 290.02, and 275.69. We now select an upper bound δ^* for δ such that

$$\delta^* = 395. \tag{24}$$

Then, we use Eqn (11), together with $c = c^*$ as in (20), $\nu = 0.3$, and $\delta = \delta^*$ as in (24), to deduce an upper bound μ^* for μ. Assuming that μ^* is much greater than 2, one infers from (11) that

$$\mu^* = \left[\frac{4\delta^*}{3B(c^*, 0.3)}\right]^{1/2} = 50. \tag{25}$$

The ballistic limit equation follows now from (19), (21), (25), and (16). One has

$$\frac{\rho_p U_m^2}{\sigma_0}\frac{r^3}{Dh^2} = C, \qquad C = \frac{9\lambda\mu(1+K)\sqrt{K}}{2(1-K)}, \tag{26}$$

where the parameters K, λ, μ, and C take the values

$$K = 0.04, \qquad \lambda = 4.5, \qquad \mu = 50, \qquad C = 219.4. \tag{27}$$

BALLISTIC LIMIT CURVES

We now compare the ballistic limit curves corresponding to (26) to those developed by Christiansen (1991). The ballistic limit equation of Christiansen (1991) can be written in the form

$$r = 0.177\left(\frac{2h\rho D^2}{\rho_p U_m}\right)^{1/3}\left(\frac{\sigma_0}{275.79}\right)^{1/6}, \tag{28}$$

where r, D, and h are in centimeters, U_m is in km/sec, and σ_0 is in MPa.

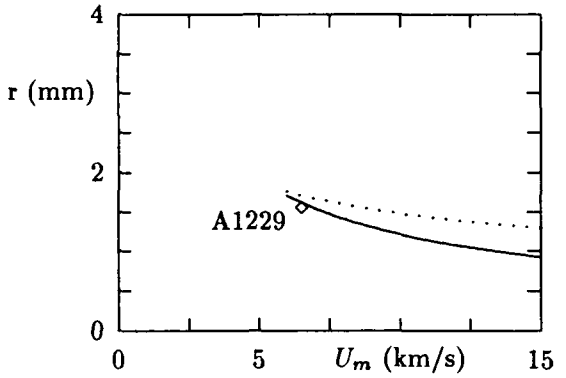


Fig. 5. Critical projectile radius for backwall thickness $2h = 0.508$ mm and shield spacing $D = 10.16$ cm (Christiansen: dotted line).

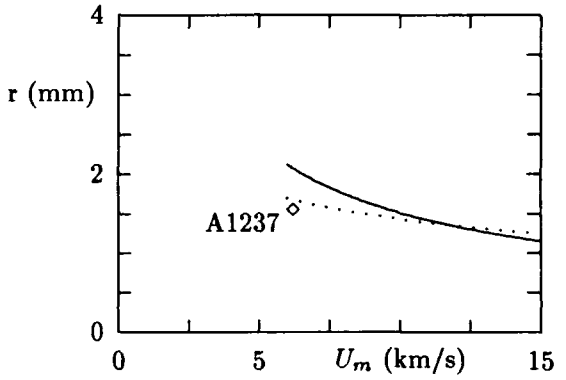


Fig. 6. Critical projectile radius for backwall thickness $2h = 0.813$ mm and shield spacing $D = 7.62$ cm (Christiansen: dotted line).

We first select the parameters r and U_m as variables. Using the experimental values for Shots A1229, A1237, and A1253, we obtain the ballistic limit curves shown in Figs 5-7. The dotted curves correspond to (28), while the solid curves correspond to (26). The actual experimental point is also shown in each of the three figures. The region below each curve is the safe region; the region above each curve is the failure region.

In Fig. 5, the ballistic limit curves are plotted for a backwall thickness $2h = 0.508$ mm (0.02 in.) and a shield spacing $D = 10.16$ cm. Notice that the two curves are very close and the solid line is more conservative than the dotted one. In Fig. 6, the backwall thickness is 0.813 mm (0.032 in.) and the shield spacing is 7.62 cm. The curves cross near $U_m = 12$ km/s. Thus, (28) is less conservative than (26) at the higher velocities, and it is more conservative than (26) at the lower velocities. In Fig. 7, the solid line is above the dotted one and predicts that Shot A1253 is not near failure, which is consistent with the experimental observation. For this case, the backwall thickness is 1.6 mm (0.063 in.) and the shield spacing is 5.08 cm.

Finally, we plot in Fig. 8 a ballistic limit curve for the backwall half-thickness h versus the projectile velocity U_m. The projectile radius is 1.588 mm (1/16 in.) and the shield spacing is 10.16 cm. The regions above the lines are the safe regions. The four experimental data points corresponding to the first four experiments in Table 1 are shown in Fig. 8. All four points lie above both curves. The solid line predicts that A1229 is very near failure, which is consistent

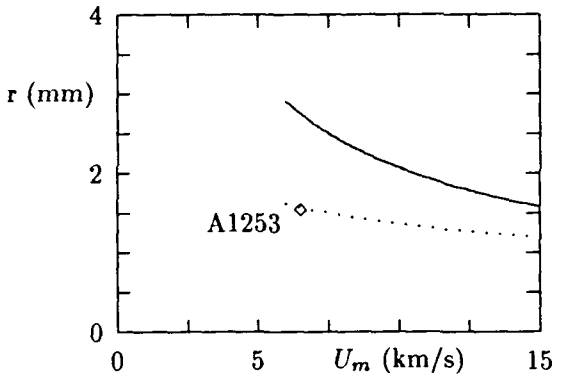


Fig. 7. Critical projectile radius for backwall thickness $2h = 1.6$ mm and shield spacing $D = 5.08$ cm (Christiansen: dotted line).

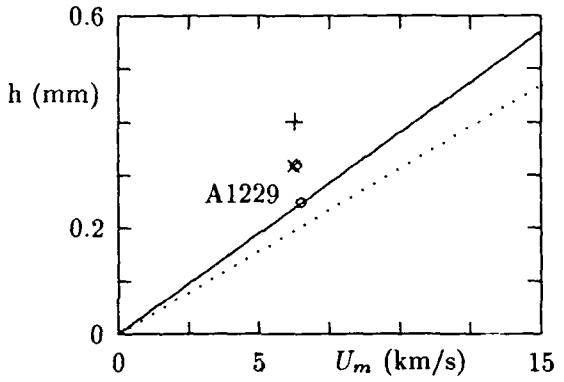


Fig. 8. Critical backwall half-thickness for projectile radius $r = 1.588$ mm and shield spacing $D = 10.16$ cm: ◇A1230, +A1233, ×A1235 (Christiansen: dotted line).

with the experimental observation. Figures 5-8 show that the solid lines corresponding to (26) are consistent with the six experiments of Table 1.

CONCLUSIONS

We have derived a new ballistic limit equation for a thin plate subjected to normal hypervelocity impact. This equation applies to cases of impulsive impact on a plate that is protected by a multi-shock shield; it is valid when the projectile velocity is in the range above 6 km/s, and when the area of the impact zone is much smaller than the area of the plate.

The ballistic equation contains two dimensionless groups ($\rho_p U_m^2/\sigma_0$ and $r^3/(Dh^2)$), and the product of these groups when the critical conditions of impact are reached must be equal to a constant C. We have found that the value $C = 219.4$ gives good agreement with the results of Christiansen (1991).

To arrive at this ballistic equation, it was necessary to determine the dynamic yield strength of the plate. This was achieved by comparing the experimental deflections of six aluminum square plates

supplied by the Hypervelocity Impact Test Facility of NASA/JSC with the theoretical deflections of a rigid perfectly-plastic plate subjected to a blast load.

In the course of this work, we have replaced the multi-shock shield by a single equivalent shield, and we have applied the debris-expansion theory of Swift *et al.* (1982) to the equivalent configuration. We have selected a failure criterion that places an upper bound on the ratio of the plate deflection to the plate thickness.

Taking into account the rebounding effect and the loss of energy as the projectile moves across the multi-shock shield, we have assumed that the impulse on the plate is equal to the momentum of the projectile. For simplicity, it was also assumed that the load transferred to the plate by the impacting cloud is uniformly distributed.

In future attempts to derive ballistic limit equations, particular attention should be given to the dynamics of the debris cloud expansion. This is a complicated issue, especially when the cloud moves across a multi-shock shield, but it must be examined carefully because recent experimental evidence (Piekutowski, 1990) has shown that debris-cloud fragments are not uniformly distributed on the surface of an expanding sphere. Further, the dynamics of debris-cloud expansion for oblique incidence should also be investigated, because impacts of space debris and meteoroids are expected to occur under all angles of incidence, not only under normal incidence.

ACKNOWLEDGEMENTS

The authors would like to express their gratitude for the support provided by the NASA Johnson Space Center under Grant NAG 9-457.

REFERENCES

Angel, Y.C. and J.P. Whitney (1992). Ballistic limit for shielded plates subjected to hypervelocity impact. *Int. J. Impact Engng*, 12, 573-583.

Christiansen, E.L. (1990). Advanced meteoroid and debris shielding concepts. Tech. Rep. 90-1336, AIAA/NASA/DOD Orbital Debris Conference, Baltimore, MD.

Christiansen, E.L. (1991). NASA Johnson Space Center Memorandum SN3-91-42.

Cour-Palais, B.G. and J.L. Crews (1990). A multi-shock concept for spacecraft shielding. *Int. J. Impact Engng*, 10, 135-146.

Gehring, J.W. (1970). Theory of impact on thin targets and shields and correlation with experiments. In: *High-Velocity Impact Phenomena* (R. Kinslow, ed.). Chap IV, pp. 105-156. Academic Press, New York.

Hopkins, H.G. and W. Prager (1954). On the dynamics of plastic circular plates. *J. Appl. Math. Phy. (ZAMP)*, 5, 317-330.

Jones, N. (1989). *Structural Impact.* Cambridge University Press, Cambridge.

Kinslow, R. (ed.) (1970). *High-Velocity Impact Phenomena.* Academic Press, New York.

Perzyna, P. (1958). Dynamic load carrying capacity of a circular plate. *Arch. Mech. Stos.*, 10, 635-647.

Piekutowski, A.J. (1990). A simple dynamic model for the formation of debris clouds. *Int. J. Impact Engng*, 10, 453-471.

Rajendran, A.M. and N. Elfer (1989). Debris impact protection of space structures. In: *Structural Failure* (T. Wierzbicki and N. Jones, eds). Chap II, pp. 41-78. Wiley, New York

Swift, H.F., R. Bamford and R. Chen (1982). Designing dual-plate meteoroid shields - a new analysis. Tech. Rep. 82-39. JPL Publications.

Timoshenko, S. and S. Woinowsky-Krieger (1959). *Theory of Plates and Shells.* McGraw-Hill, New York.

Zukas, J.A., T. Nicholas, H.F. Swift and D.R. Curran (1982). *Impact Dynamics.* Wiley, New York.

Int. J. Impact Engng Vol.14, pp.37–48, 1993
Printed in Great Britain

0734-743X/93 $6.00+0.00
Pergamon Press Ltd

DEBRIS FRAGMENT CHARACTERIZATION IN OBLIQUE HYPERVELOCITY IMPACTS

Nasit Ari* and J. S. Wilbeck**

Kaman Sciences Corporation
*1500 Garden of the Gods Road, Colorado Springs, Colorado 80907
**600 Boulevard South, Suite 208, Huntsville, Alabama 35802

ABSTRACT

A case history in debris characterization is presented for oblique impacts of chunky tungsten projectiles against thin plates. The integrated approach of scaled experiments and hydrocode simulations led to a semi-analytic model of behind the plate debris fragment distributions. This debris distribution model agreed quite well with the experimental fragment distributions derived from witness plate measurements. The 1/4 scale test program included three projectile masses, two target geometries (single and dual plates), a velocity range of 4-7 km/s and a strike angle range of 15-55 degrees. Close correlation of measured and predicted fragment distributions encouraged the extension of the model to higher velocities not currently obtainable in the laboratory.

The paper also includes discussions of critical features of debris in oblique hypervelocity impact, the scalability of fragment data, and the utilization of the derived fragment models in semi-analytic damage assessment codes.

I INTRODUCTION

Hypervelocity impacts of even very small projectiles on space structures generate energetic debris that can inflict serious damage on internal components. Lethality and survivability considerations as well as space debris concerns thus require a quantitative debris characterization. The present paper focuses on a subset of the parameter space of interest: Dense tungsten chunky projectiles (cylinders, L/d = 1) impacting thin (t/d<1) dual-plate aluminum targets at V=4-12 km/s and low strike angles (20°-55°) (An earlier paper reported related work on impacts on thin walled cylinders [1]).

Early debris models concentrated on normal impacts of like materials. The ensuing model of a spherical debris shell assumes that target and projectile fragments are distributed uniformly in this thin layer. For the impact configurations under study, however, the debris structure is complex and multiple fragmentation mechanisms coexist. Hence this idealized model is not appropriate.

The present debris characterization effort is not geared toward developing a theoretical debris model with some free parameters. Instead a more empirical but quantitative route was chosen to obtain a simple model quickly and to validate it by experiments. To this end a coordinated experimental/hydrocode-simulation study was initiated.

The paper first summarizes the experimental test program and the related data reduction effort, then the hydrocode simulation results, and finally the modeling process. The paper is significant because it addresses the following:

- The use of thin witness plates to characterize individual debris particle sizes down to a few tenths of a mm in diameter and their radial distribution.

- The variation of the debris size and radial distribution with projectile mass, impact velocity, and impact obliquity.
- The development of a cumulative mass distribution function based on the Grady formalism.
- The extension of the debris distribution model to higher impact velocities based on hydrocode analyses.
- Discussions on the determination of debris distribution for the full scale case based upon 1/4 scale test results.

II EXPERIMENTAL PROGRAM

Hypervelocity impact tests were conducted in the Impact Physics Laboratory at the University of Dayton Research Institute using the 50/20 mm, two stage, light-gas gun [2]. Quarter scale tungsten fragments, weighing 5/64, 10/64 and 20/64 gram, were launched against a simple, dual wall target backed by a thin witness plate. The fragments used in these tests were right-circular cylinders, L/d = 1, which were fabricated from Teledyne Firth Sterling tungsten alloy X-21C, which is a 93% tungsten alloy having a density of 17.5 g/cc. The dual target plates and the witness plate were fabricated from 5052-H32 aluminum.

A schematic of the target setup is presented in Fig. 1. The dual target plates were 4 inches by 6 inches in lateral dimensions. Each of the dual plates were 0.030 inches thick and the two plates were separated by a distance of 0.060 inches. The rear witness plate was also 0.030 inches thick. For the first three tests, the witness plate was set at the same angle as the target plate. For all subsequent tests, the witness plate was set at 90 degrees to the shotline to facilitate data reduction. For this series of tests, the impact velocities varied from 4 to 7 km/s, with 7 km/s being the highest obtainable in the gun facility. The strike angles varied from 15 to 55 degrees (which correspond to obliquity angles of 75 and 35 degrees, respectively.)

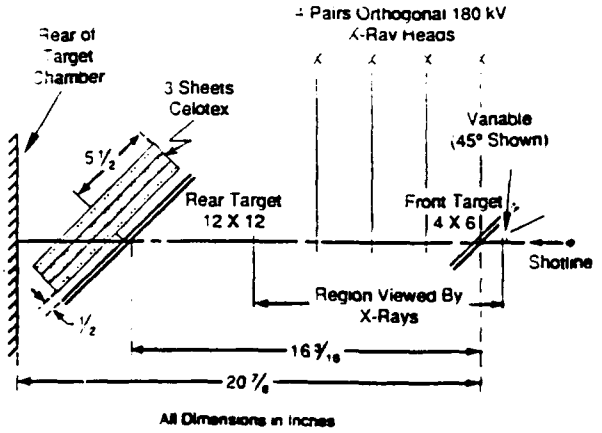


Fig. 1. Schematic of the target setup.



Fig. 2. Negative print of the hole pattern

As noted in Fig. 1, four pairs of orthogonal x-rays were used behind the dual plate target to obtain a good history of the debris velocity. Holes in the witness plate were used to obtain an estimate of the individual debris particle masses impacting the plate. Debris catchers, consisting of Armstrong ceiling panel material, were placed behind the witness plate. Catcher material was also employed to catch any fragment material which ricocheted off the front target plate.

The objective of these tests was to obtain sufficient data to allow the characterization of the residual

debris mass, velocity, and angular distribution as a function of initial fragment mass, impact velocity, and strike angle. A complete list of tests conducted is given in Table 1. All but two of the tests featured the double layer target plate. In the remaining two tests, a single plate of twice the thickness (0.060 inches) was used. These thicker plate tests were conducted to see if the debris from this type of target resembled that of the dual wall target. It should be noted that very few problems were encountered during the test program until efforts were made to obtain impact velocities of 7 km/s. Despite a number of difficulties, several good data tests were obtained at this velocity.

Table 1. Test matrix.

SHOT NO.	PROJ. MASS (g)	IMPACT VEL	STRIKE ANGLE (°)	FRONT TARGET		RESIDUAL VEL.		COMMENTS
				30 MIL DUAL LAYER	60 MIL SINGLE LAYER	MAX (km/s)	MIN (km/s)	
4-1198	5/64	6.06	45	X		5.20	4.60	
4-1199	10/64	6.02	45	X		5.61	5.01	
4-1200	20/64	6.06	45	X		5.74	5.29	
4-1201	10/64	6.02	50	X		5.64	5.25	
4-1202	10/64	6.07	30	X		5.37	4.16	
4-1203	10/64	6.05	20	X		4.78	3.42	
4-1204	5/64	6.05	20	X				LARGE DEVIATION FROM SHOTLINE
4-1205	10/64	5.95	15	X				EFFECTIVELY NO RESIDUAL DEBRIS
4-1206	10/64	6.01	45		X	5.52	4.52	
4-1207	10/64	6.01	20		X	4.99	4.41	
4-1208	10/64	--	45	X		--	--	HIGH VELOCITY - SABOT FAILED
4-1209	10/64	6.85	45	X		6.21	5.67	
4-1210	10/64	4.10	45	X		3.67	3.08	
4-1211	10/64	4.08	20	X		3.04	2.41	
4-1212	5/64	7.02	45	X		6.26	5.65	
4-1213	10/64	7.05	20	X		--	--	HIT SABOT STRIPPER
4-1214	10/64	6.99	20	X		--	--	HIT SABOT STRIPPER
4-1215	10/64	6.99	20	X		5.39	4.18	

An extensive effort was conducted to determine the mass of the residual particles for each test. After considering a number of other approaches, the approach chosen for this program was to calculate the mass of individual particles based upon the area of the holes created by each particle in the witness plate. Two other techniques which have been used previously include the use of a semi-infinite witness block and the use of debris catchers. With a witness block, the particles create craters upon impact. The volumes of these craters are then measured and correlated with the mass which caused the crater. It was felt that the crater formed by the very small particles would be so small as to greatly complicate the measurement of crater volume and that the measurement accuracies would not be sufficient. Likewise, the particles would be too small to be found in the debris catcher.

Because of the large number of holes in each witness plate (usually in excess of 200 holes were found), a special technique had to be developed for measuring the sizes of the holes. In this technique, photographic paper was placed behind the plate and a camera lamp was flashed. The resulting "photograph" was a negative print of the holes in the plate. The print corresponding to Test 4-1203 is presented in Figure 2. This negative photograph was scanned into a Macintosh computer and transferred into IMAGE version 1.22, written by the National Institute of Health, and scaled appropriately. By counting the number of pixels contained in each hole, the IMAGE program was able to calculate the hole area. Several corrections were made to the hole areas to account for pixel resolution errors and photographic blur.

In a parallel effort, an algorithm was developed which correlated the area of the hole in the plate with the mass of the debris particle which caused the hole. This algorithm development was necessitated because of the very small masses and hole sizes involved in this effort. The algorithm took the form:

$$\frac{D}{d} = 1 + \left(1.5v^{2/3} - 1\right)\left(1 - e^{-3t/d}\right) \tag{2.1}$$

where: D = Hole Diameter (cm), v = Impact Velocity of Fragment (km/s), d = Fragment Diameter (cm), t = Plate Thickness (cm)

and

$$M = \rho \frac{\pi}{6} d^3$$

where: M = Fragment Mass, ρ = Fragment Density

This algorithm was then applied to the tabulated hole data to determine the residual debris mass for each test. For each test in which sufficient hole data was available to obtain good residual mass distribution data, the masses were calculated and tabulated. Figures 3 and 4 display plots of typical residual debris mass distributions generated in this fashion. It should be noted that the data trends appear very much as expected, lending credibility to the data. The effort to use this data to develop analytical models of residual debris mass distribution is discussed in a later section.

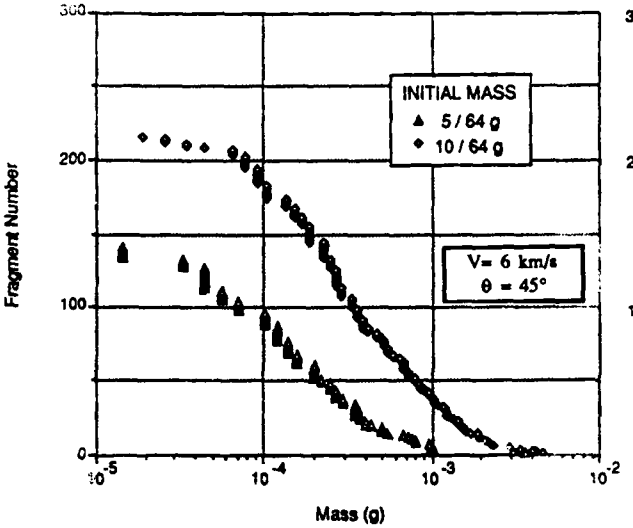


Fig. 3. Residual mass distribution for different size projectiles.

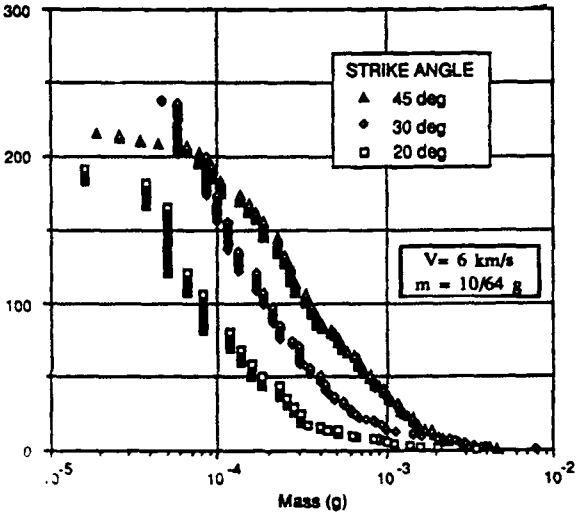


Fig. 4. Residual mass distribution for various strike angles.

Table 2. Measured residual mass and residual velocity data.

SHOT NO.	PROJ. MASS (g)	IMPACT VELOCITY (KM/S)	STRIKE ANGLE (°)	RESIDUAL VELOCITY		RESIDUAL MASS (M_R/M_O)
				MIN (km/s)	MAX (km/s)	
4-1198	5/64	6.06	45	4.60	5.20	0.48
4-1199	10/64	6.02	45	5.01	5.61	0.80
4-1201	10/64	6.02	50	5.25	5.64	0.67
4-1202	10/64	6.07	30	4.16	5.37	0.56
4-1203	10/64	6.05	20	3.42	4.78	0.23
4-1204	5/64	6.05	20	-	4.3	0.09
4-1205	10/64	5.95	15	-	-	0.00
4-1210	10/64	4.10	45	3.08	3.67	0.71
4-1211	10/64	4.08	20	2.41	3.04	0.18
4-1212	5/64	7.02	45	5.65	6.26	0.21
4-1215	10/64	6.89	20	4.18	5.39	0.23

For each test with good mass data, the masses of the all debris particles were summed and the resulting total residual debris mass, M_R, was obtained. This total residual mass data is presented in Table 2. Also included in this table is the range of residual velocity data obtained for each debris cloud as measured with the orthogonal x-ray.

III HYDROCODE SIMULATIONS

The primary objectives of hydrocode simulation were to extend experimental data to higher impact velocities and to complement experimental debris characterization with high resolution fragmentation maps. They were also utilized to provide pre-test predictions of test instrumentation and to quantify mass, momentum, kinetic energy and spread angle of residual projectile debris behind the target entry walls. 3-D HULL simulation results provided useful data for the development of an internal fragment distribution model which is a critical input to system level damage computations.

Utilization of hydrocodes to obtain fragmentation statistics is a formidable challenge. Uncertainties in fragmentation criteria and numerical difficulties with subgrid fragment advection prevent a direct hydrocode output of fragment distributions as discussed in Trucano and McGlaun [3]. In the current effort we utilize a hybrid approach (similar to that in [3]) to obtain the fragment distributions: First obtain continuum description of the early time debris (i.e. velocity, strain rate etc.) from hydrocodes, then post process to translate the debris fields into discrete fragment statistics with the help of continuum fragmentation formula as discussed in Section IV. In the current simulations a rather fine mesh is used to obtain high resolution maps of the debris initiation. There are five cells across the plate thickness (dx = 0.015 cm), allowing us to resolve tungsten fragments larger than 60 micrograms. Fragments with smaller mass thus are obtained only with the help of the continuum fragmentation formula.

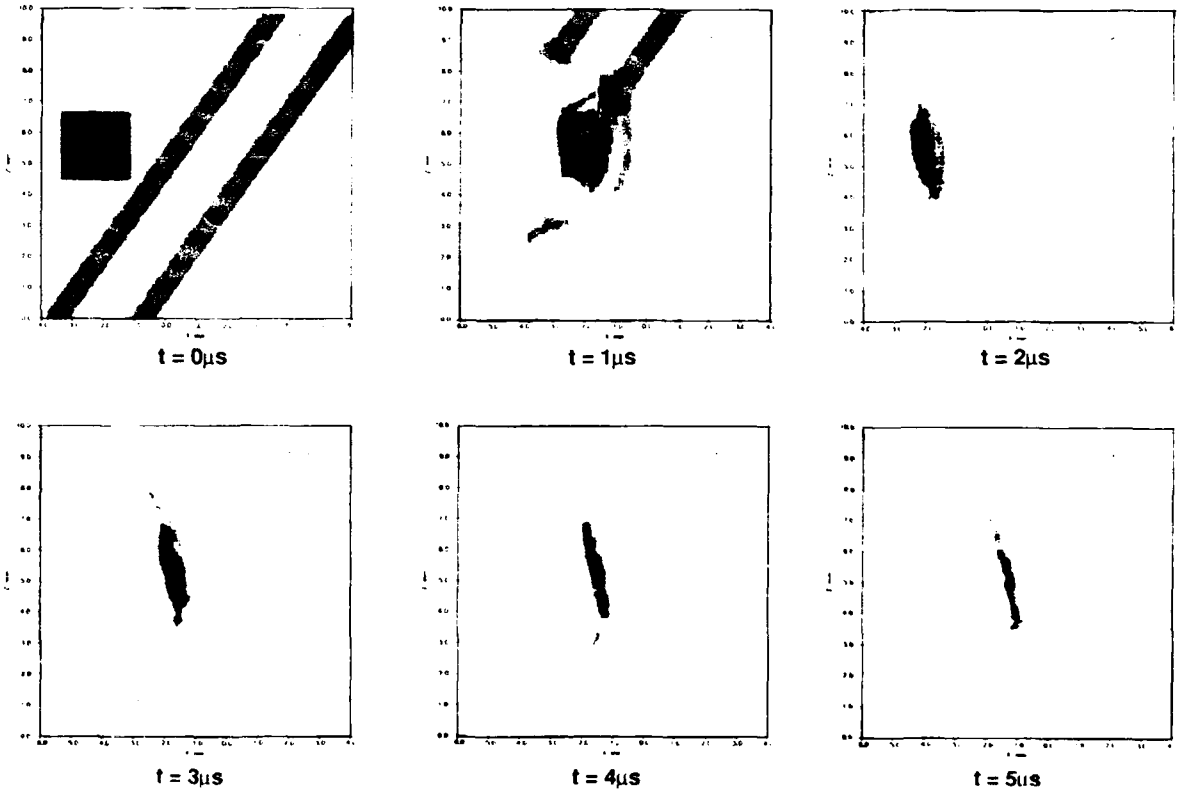


Fig. 5. 3-D HULL simulation of 6 km/s, 55° impact of a W10 (L/D = 1) cylinder impacting a double walled target: density maps of a slice on the impact symmetry.

Representative simulation maps for a 10/64g fragment impacting at 6 km/s, 55° are given in Figure 5. They illustrate the essential features of oblique impacts of dense projectiles against double layers of aluminum. At moderate obliquities, as shown in Figure 5, the tungsten projectile debris retains much of its initial momentum. At high obliquities (low strike angles) there is more extensive projectile fragmentation. Due to substantial erosion of the projectile the residual debris has lost most of its kinetic energy. At these large obliquity angles and high velocities the debris characteristics are relatively independent of the impact velocity. Further insights gained by hydrocode simulations could be listed as:

1. The projectile and the target debris have distinct spatial characteristics. They are not distributed uniformly in a thin surface layer of quasispherical bubble. Hence standard models based on these assumptions (such as the Swift, Bamford & Chen model [4]) are not applicable for this case.

2. For this projectile/target combination residual fragments subtend a rather small cone angle. This feature clearly enhances the debris damage potential.

3 Two main fragmentation mechanisms are observed; i) Multiple spalling near the edges and ii) Slow stretching fragmentation at the center. This might lead to two fragment distribution functions with different characteristics as anticipated by the Grady fragmentation formalism [5,6] as discussed in Section IV.

4. The axis of the debris cloud deviates from the original shotline toward the target surface normal. This deviation grows with increasing obliquity.

From x-ray observations it is difficult to define a unique debris spread angle and a unique representative residual velocity. This multi-valuedness demands extra caution in the interpretation of experimental results and in the comparison of data with hydrocode simulations. Quantitative results extracted from the hydrocode results are given in Table 3. The major conclusions one can draw are;

i. There is a drastic decrease in residual momentum below a strike angle of 20°. This is confirmed by the typical contact prints from experimental data for 6 km/s impacts.

ii. Effective debris half cone angles are small. This is likely due to large density differential between the projectile and target material and the high ductility of the projectile material.

Table. 3. 3-D HULL estimates of residual projectile mass, momentum, and kinetic energy behind the double entry wall.

Projectile			m/m_o	mU/m_oU_o	E/E_o	Half Cone Angle	Deflection Angle
m (g)	V (km/s)	θ					
Moderate Obliquity							
10	6	55	0.88	0.81	0.74	8.8	1.5
10	8	50	0.96	0.79	0.65	7.5	0.7
10	4	45	0.88	0.74	0.64	8.1	0.9
10	10	40	0.92	0.72	0.56	9.4	1.2
High Obliquity							
10	6	20	0.52	0.28	0.16	4.0	10.3
10	12	20	0.51	0.26	0.15	5.8	9.5
10	12	30	0.69	0.54	0.40	6.9	5.7
Smaller Mass							
5	6	45	0.72	0.57	0.46	8.5	3.4

Hydrocode results agreed well with experimental data when available. The residual velocities showed an excellent match. Other features of the debris are also well captured in hydrocode maps. Thus hydrocode results along with x-ray pictures and witness plate hole size data constituted a base for the development of an internal fragment model. Details of this model are given in the following section.

IV DEVELOPMENT OF THE BEHIND-THE-TARGET DEBRIS MODEL

The objective of the modeling effort was to develop models for use in the KNAPP code which were capable of predicting damage to internal components. The KNAPP code was originally developed by Kaman Sciences for the LTH-5 Space Based KEW community under contract to the Air Force Armament Laboratory. It is an empirically based code consisting of (a) the GIFT combinatorial geometry and ray tracing package, (b) models which describe the breakup of the original projectile upon impact of the outer target wall and the breakup of the resulting particles upon impact of succeeding layers. (c) a series or penetration algorithms, and (d) the bookkeeping required to keep track of all of the particles and the damage which they cause. The current version of the KNAPP code was developed for application to very

different target and projectile combinations from those in this study. Hence, new algorithms were required for residual mass debris distribution, residual debris velocity distribution, and residual debris spread angle.

Residual Mass Algorithm

Impact obliquity (at these high angles) is the dominant factor in determining the mass loss mechanisms of the projectile. In the tests, the residual projectile mass was determined indirectly from witness plate data subject to several uncertainties as explained in Section II. Nevertheless the data given in Table 1 provided a clear trend for the velocity range of 4-7 km/s and indeed it could be fitted by a regression form independent of impact velocity as shown in Figure 6.

$$\frac{m_R}{m_o} = 1 - \frac{0.16}{(\sin\theta)^{1.5}} \tag{4.1}$$

where:

m_R is the total residual debris mass

m_o is the original fragment mass prior to impact

θ is the strike angle

The hydrocode results obtained for a larger velocity range also supported the trend observed. Thus a decision was made to use Equation 4.1 to model residual debris mass in the KNAPP code for all impact velocities studied and not to investigate further refinements.

Residual Velocity Algorithm

Based on the hydrocode studies conducted for a wide range of cas. (see Table 3), an average residual velocity algorithm was developed. This model is given by the relationship

$$\frac{V_R}{V_O} = 1 - \frac{0.07}{(\sin\theta)^{1.5}} \tag{4.2}$$

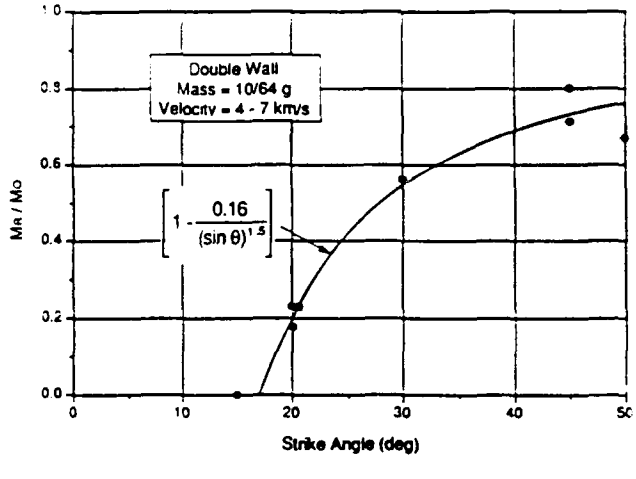


Fig. 6. Residual mass algorithm.

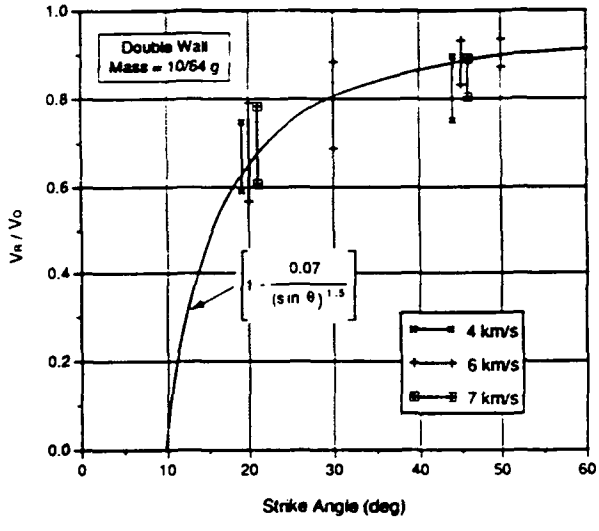


Fig. 7. Comparison of residual velocity algorithm with test data for 10/64 gram projectile.

Based only on a best fit to hydrocode results, this model is completely empirical in nature. An effort was made to check this model against the residual velocity data obtained during the tests. Figure 7 presents a plot of predictions based upon Equation (4.2) with the minimum and maximum residual velocity data given in Table 1 for 10/64 gram fragments impacting at velocities from 4 to 7 km/s. Again, the correlation of model with data is quite good. Note that neither model nor data show any significant dependence on initial impact velocity. Thus, it was decided to use this model for all impact velocities in this study.

Residual Debris Spray Angle

Results from the tests and the hydrocode studies were examined to determine the spray angle for the debris coming off the back of the double layer target. The measured spread angles were very small for all cases, with only a slight variation with impact velocity noted. For this modeling effort, it was decided to treat the spray angles as independent of impact velocity and strike angle. Errors caused by this assumption should be small. The values chosen are as follow:

Fragment Mass	Half Cone Angle
10/64 grams	4°
5/64 grams	2.5°

Figure 8 presents typical witness plate hole data and circles which represent various debris half cone angles. For this case (Test 1201), each of the twenty largest debris particles and 78% of all debris mass impacted within the 4° degree half cone angle. These values are smaller than the hydrocode results given in Table 3. However the hydrocode results did include the outlying fragments.

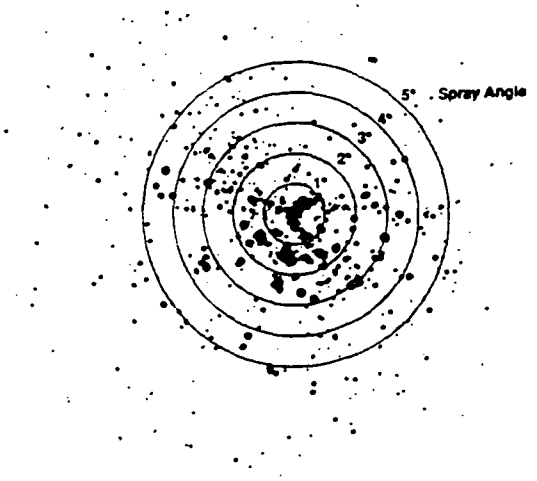


Fig. 8. Comparison of residual debris hole data from shot 4-1201 with various half cone angles.

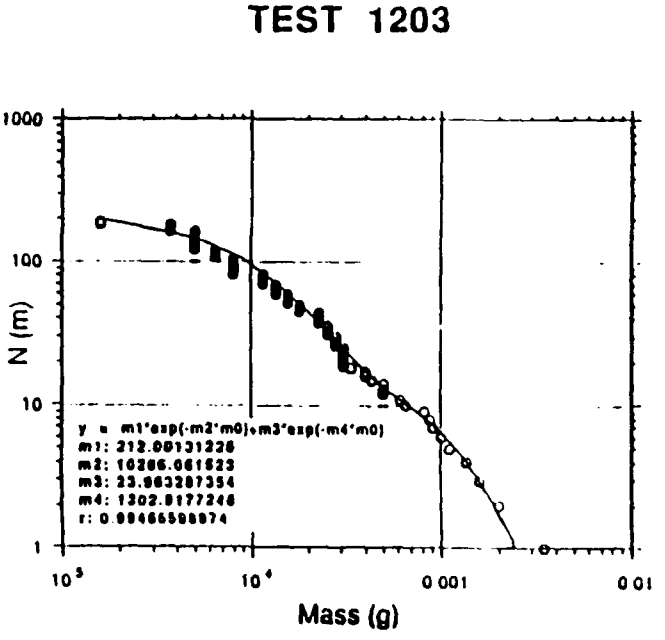


Fig. 9. A sample bi-exponential fit to fragment mass data.

Fragment Mass Distribution

The breakup of a fragment upon impact on a plate at velocities above 4 km/s is an area of intense interest today in the hypervelocity impact community. Modeling efforts based upon the mechanics of the impact event have only recently been started. Some of the most notable work today is being conducted by Grady of the Sandia Laboratory. His work, highlighted in [5], was used as the basis for much of the modeling effort discussed herein.

In Grady and Kipp's work [6], it was found that exponential cumulative mass distribution functions are efficient tools of debris characterization. A distribution due to a single uniform fragmentation mechanism can be given by

$$N(m) = N_o \exp(-m/m_a) \tag{4.3}$$

where N(m)) is the number of fragments with mass larger than m, m_a is the average fragment mass, N_0 is the total number of fragments and $N_0 \times m_a = m_0$ is the total fragmenting mass. In order to estimate the average mass, m_a, one can utilize a Grady type energy balance formula [5].

$$m_a = f\left(K_{Ic}/\rho C\dot{\varepsilon}_o\right)$$

where:
- K_{Ic} is the critical dynamic fracture toughness parameter
- ρ is the projectile density
- C is the speed of sound in the projectile material
- $\dot{\varepsilon}_0$ is the strain rate in the material at failure

For our case of a chunky tungsten fragment impacting a thin plate, the following functional form was assumed for this relationship.

$$d_a = \left(aK_{Ic}/\rho C\dot{\varepsilon}_o\right)^{2/3} \tag{4.4}$$

where: $\rho = 17 g/cm^3$ $\qquad a = (20)^{1/2}$

$C = 4$ km/s

The actual value of K_{Ic} is not easy to obtain. It is known to be a function of the strain rate but the relationship is not well characterized.

Grady and Kipp has also determined that for a given impact, the debris particles may fall into several size ranges, depending upon the dominant breakup mechanisms. In his model, each range of debris masses can be represented by an exponential distribution. For our case, all experimental data could be curve-fitted by bi-exponential distributions as shown in Figure 9. Hence it was assumed that the overall debris mass could be described by a double exponential distribution. The resulting model took the form

$$N(m) = N_\ell \exp(-m/m_\ell) + N_s \exp(-m/m_s) \tag{4.5}$$

where:
- $N(m)$ = Number of fragments with mass larger than m
- m_ℓ = Approximate average of larger fragments
- m_s = Approximate average of smaller fragments
- $N_\ell + N_s$ = Number of fragments in each category
- N_t = Total number of fragments = $N_\ell + N_s$
- m_ℓ = $3\ m_a$ (as indicated by data)
- $N_\ell m_\ell$ = $N_s m_s$ (as indicated by data)

In order to reduce the number of free parameters a specific partition of small and large particles needed to be assumed. The particular assumption given below was based on an examination of all data sets. A similar partition for tungsten fragments were also observed in [7]. Hence:

$$N_l = N_t/6 \qquad N_t = m_R/m_a$$
$$N_s = (5/6) \times N_t \qquad m_R = \text{residual mass}$$
$$m_s = 0.6\ m_a \qquad m_a = \text{average mass}$$

In the application of this model to the present case, a number of the values had to be obtained from the residual mass data discussed earlier in this section. Once these values were known, the exact models were formulated.

Average Fragment Mass

The average fragment mass needed to solve Equation (4.5) must be obtained by substituting proper values of the fracture toughness strength and the average strain rate during breakup into Equation (4.4). The first debris data analyzed in detail was that obtained for Shot 4-1199. This was the case of a 10/64 gram fragment impacting at a velocity of 6 km/s and a strike angle of 45 degrees. A hydrocode run for this case found an average value for strain rate of 1.52×10^5/s. For this case, the fracture toughness for the tungsten material was assigned to have the value

$$K_{Ic} = 20(MPa\ \ m^{1/2})$$

As stated earlier, this value is only approximate and considering the uncertainty due to strain rate effects, it is not too far from the reported value of (5-11) MPa $m^{1/2}$ in [7].

With these two values determined, Equation (4.4) was solved for the average diameter of a debris particle For the tungsten material used in this program this results in an average fragment mass, m_a, value for Shot 4-1199 of

$$m_a = 4x10^{-4}g$$

Based upon various strain rate trends obtained from empirical hydrocode runs of many of the other tests, a general relationship for average fragment mass was developed. This relationship is as follows:

$$m_a = \left[1.15 - \frac{0.075}{(\sin\theta)^2}\right] x \left[.07 - 0.3\left(\frac{6}{v}\right)^2\right] x \left[\frac{m_o}{10/64}\right] x 4x10^{-4}g \qquad (4.6)$$

It should be noted that this simple relationship reduces to the value given above for Shot 4-1199. Formula (4.6) reflects the expected trends: average mass decreases with higher impact velocities (larger $\dot{\varepsilon}$), higher obliquities (more erosion), and smaller mass (more shock wave effects).

Quarter Scale Fragment Mass Distribution

Equations (4.5) and (4.6) can now be substituted into Equation (4.7) to obtain the debris mass distribution for any of the cases tested. The data for most of the tests given in Table 1 were plotted on semi-log graphs to better display the mass distribution. These plots are presented in Figure 10

Full Scale Fragment Mass Distribution

Equations (4.4) thru (4.6) were developed for modeling the quarter scale fragment impact cases of interest

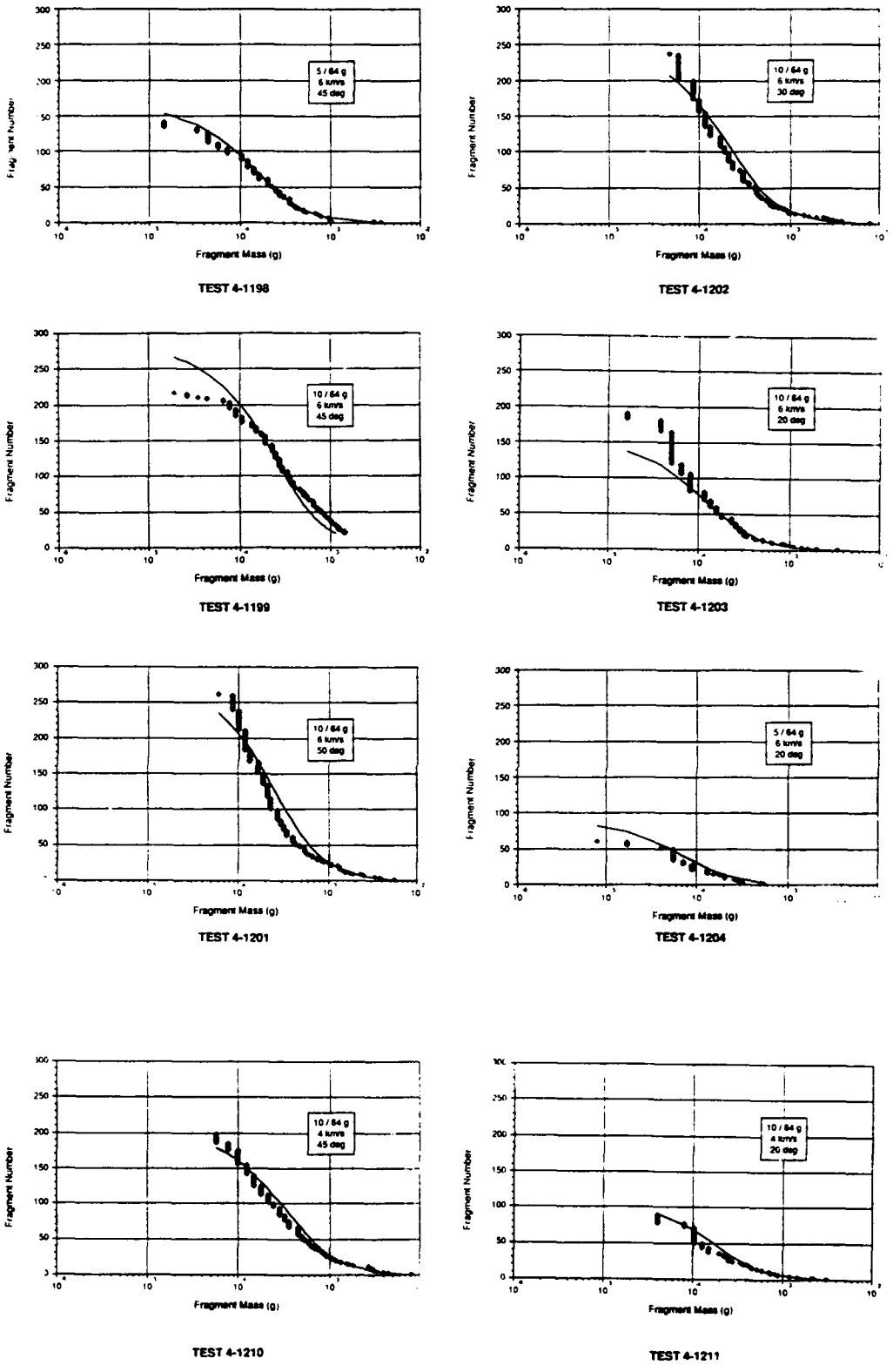


Fig. 10. Comparison of debris mass distribution model with data.

in this program. Since the models are somewhat empirical in nature, further thought was needed to determine how to use these relationships to predict full scale debris distributions. As stated earlier, all quarter scale projectiles and targets were replica scaled models of the full scale versions. Thus, the overall debris cloud characteristics would be expected to scale accordingly. However the strain rate effects preclude exact geometric scaling in full scale since the strain rate is only one fourth of that for the quarter scale ($\dot{\varepsilon}$ = dV/dx). Hence by the average mass formula (4.4)

$$m_a \sim d_a^3 \sim \left(K_{Ic} / \dot{\varepsilon}_o\right)^2 \tag{4.7}$$

The average mass in full-scale would be 16 times larger if K_{Ic} were to be independent of the strain rate. However, K_{Ic} increases strongly with strain rates, especially at high strain rates $\dot{\varepsilon}$ of 10^5 - 10^6. Thus an eight-fold increase in average mass could be a more realistic expectation for full scale impacts. With this assumption and noting also that the full scale projectile mass is 64 times larger, one can also deduce that there will be 8 times as many fragments in the full-scale case compared to the quarter scale.

CONCLUSIONS

The simple models given in Section IV leave out several second order effects. Nevertheless the model is validated by the agreement shown in Figure 10. It is valid for the intended parameter space and provides a very useful condensed representation of the data and supporting hydrocode results. The model coupled with KNAPP shotline analysis provides a first order design feedback. The simulations yielded extensive detail about the early debris evolution. We extrapolated a fragment model using an average projectile strain rate. Of course this methodology could be improved by incorporating local strain rate heterogeneities.

The current effort was able to coordinate experimental and hydrocode analysis tightly and hence illustrate the efficiency of a hybrid approach. As data from similar studies accumulate (e.g. [7]) they would serve as input to a more comprehensive theoretical debris analysis framework.

ACKNOWLEDGMENTS

The authors wish also to acknowledge the support of Mr. Andrew Piekutowski and Mr. Kevin Poorman of UDRI, for their excellent efforts in the conduct of the test program and for their help in the planning of these tests; Mr. Steve Diehl for help with hydrocode analysis; and Mr. Cary Mann for reducing the debris particle mass data. We would also like to thank Pam Harrell for typesetting.

REFERENCES

[1] Ari, N., and Diehl, S., 1991, "Debris Patterns Due to Hypervelocity Impacts on Thin Walled Cylinders." Proceedings of the Symposium on Structural Dynamics Produced by Extreme Loading Conditions, at the 1991 ASME Pressure Vessels and Piping Conference, San Diego, California.

[2] Piekutowski, A. J., "The University of Dayton Research Institute 50/20 mm, Two Stage, Light-Gas Gun, "Proceedings of the Aeroballistic Range Association, Southwest Research Institute, San Antonio, Texas. (Unpublished)

[3] Trucano, T.G., Grady, S.E., McGlaun, J.M., 1990, "Fragmentation Statistics from Eulerian Hydrocodes Calculations." (Int. J. Impact Engng., Vol. 10 pp. 587-600.

[4] Swift, H.F., Bamford, R., Chen, R., 1982, "Designing Dual-Plate Meteoroid Shields - A New Analysis," JPL Publication 62-39, Jet Propulsion Laboratory, Pasadena.

[5] Grady, D.E., 1982, "Local Intertial Effects in Dynamic Fragmentation," J. Appl. Phys., Vol. 53, pp 322-325.

[6] Grady, D.E., Kipp, M.E., 1985, "Geometric Statistics and Dynamic Fragmentation," J. Appl. Phys., Vol. 58 pp. 1210-1222.

[7] Chhabildas, L. C., Barker, L.M., Asay, J.R., Trucano, T.C., 1990, "Relationship of Fragment Size to Normalized Spall Strength for Materials," Int. J. Impact Engng., Vol.10, pp 107-124.

Int. J. Impact Engng Vol.14, pp.49–60, 1993
Printed in Great Britain

0734-743X/93 $6.00+0.00
© 1993 Pergamon Press Ltd

IMPACT DAMAGE AND OPTICAL SCATTER

Dale Atkinson & Alan Watts

POD Associates, Inc., 2309 Renard Place, NE,
Suite 201, Albuquerque, NM 87106

ABSTRACT

Much recent data from the Long Duration Exposure Facility (LDEF) have confirmed that for multiyear periods in LEO many satellite surfaces (especially the RAM) will be subjected to significant bombardment by small particles in the 1 to 100 micron size domain. These particles are both micrometeoroids and man-made debris. Of interest is the consequential effects on precision surfaces such as high-resolution optics. The damage produced does not necessarily seriously downgrade the reflectivity (for mirrors) or transmissivity (for lenses), but can significantly worsen optical scatter. Since many optics are not simple metal mirrors, for which the major response is near-hemispherical cratering, but frequently comprise brittle dielectrics (including multilayer coatings) which suffer conchoidal cratering, star cracking and interlayer differential delamination, the correlation between the induced mechanical damage and the resulting optical scatter is complex. An approach is given which attempts to analytically predict the material damage modes for various impact conditions, and also correlate this damage with optical scatter.

INTRODUCTION

With man's ever increasing activity in space an issue has arisen concerning the problem of impacts on space assets due to either the naturally occurring micrometeoroids or man-made debris. Both species of particles cover a large range of sizes, from sub-micron to many centimeters, and for each species the relative number of particles rapidly increases with decreasing particle size. The micrometeoroids approach the earth from all directions with a mean collision speed of about 20 km/s (ranging from a low of a few km/s to a high of about 79 km/s). These particles undergo a one-shot pass of the earth, since they are in orbit around the sun. The mean density of micrometeoroids is about 0.5 g/cm^3, although there is a small component of higher density asteroidal matter (8.0 g/cm^3). The man-made debris is assumed to be mostly in pseudo-circular orbits about the earth, with a mean collision speed of about 10 km/s (range from about zero for similar orbits to almost 16 km/s for counter orbits). The debris is primarily aluminum, but also comprises alumina (fuel pellets) and high density remnants of damaged satellites, rocket boosters, sundry bolts and lens caps, etc.. Full details of the micrometeoroid and debris models are given in Cour-Palais (1969) and Kessler (1988), respectively.

Historically much emphasis has been given to the problem of catastrophic collisions due to the larger particles (> 1.0 cm diameter) with satellites. However, these large particles constitute a relatively low flux (potential hits per m^2 per unit time), and much of the analysis is concentrated on the Poissonian

probability of impacts occurring on a given body. More recently attention is being devoted to the problems associated with the much higher flux of the small particles (especially in the 1 to 100 micron range). These latter can cause surface erosions of critical components such as optical surfaces.

This paper addresses the issue of surface erosion of optical components, and considers the nature of the impact damage and the first-order estimates of induced optical scatter. The studies are of interest to the hypervelocity impact community since they involve the problems of fragmentation, cratering and cracking logic, in addition to the estimates of optical scatter.

In order to assess impact damage we have incorporated the existing micrometeoroid and debris models into a computer program called SPENV. This code allows predictions of the expected impact fluences (hits per area) as functions of: satellite time on orbit, orbital inclination, altitude and the direction of a given surface of the satellite relative to the velocity vector (e.g. RAM, SPACE, EARTH, SIDES and TRAIL). The code has been benchmarked versus the recent LDEF data, giving agreement to better than a factor of three. LDEF was at an altitude of 475 km, with inclination of 28.5 degrees, and flew for 5.75 years. A large amount of impact data is steadily being gleaned from this experiment including cratering, perforations, and delaminations and star-cracking in brittle materials.

In order to more accurately determine the responses for altitudes near and above 1000 km, it is necessary to modify the Kessler model for orbital debris. This modification has been incorporated into the SPENV computer program using the ratio of US Space Command data versus the normal Kessler model. The underlying assumption for this modification is that the small debris distribution tends to follow that of the larger (> 10 cm), trackable, debris. This assumption has been borne out by the LDEF data at 500 km, and is assumed for the higher altitudes.

FRAGMENTATION

When bodies undergo hypervelocity impacts it is experimentally observed that the fragments usually display a power-law (i.e. fractal) distribution for the remnants of the form:

$$N(>m) = \alpha(M/m)^{\beta} \qquad (1)$$

where N is the cumulative number of fragments of mass m or greater, M is the original total mass, and α and β are constant coefficients. Typically, the experimental value of β is about 0.75. Assuming constant density and spherical particles the distribution becomes:

$$N(>d) = \alpha(D/d)^{3\beta} \qquad (2)$$

where D is the initial body diameter, and d is the fragment diameter. Thus $3\beta = 2.25$. This value is very close to the suggested index value of 2.5 used in the Kessler debris model to describe the small (<1 cm) particle distribution.

Assuming the power law applies from the largest remnant to very small ones, then in order to conserve total mass we require:

$$(1/\alpha) = (\beta/(1-\beta))^{\beta} \text{ which implies } m(1) = M\,(1/\alpha)^{-1/\beta} \qquad (3)$$

Thus for β= 0.75 we have α = 0.4387 and m(1) = 0.3334 M (or d(1) = 0.693 D) for the largest remaining fragment. To fit the Kessler model (i.e. $3\beta = 2.5$) we require α = 0.2615, and m(1) = 0.2 M (or d(1) = 0.585 D). It should be noted that the Kessler model is primarily based on an interpolation between small particle (< 10 micron) perforations observed on satellites (including Solar Max) and the radar-observable larger particles (> 5 cm), although the LDEF data is presently in agreement with the model to within the accuracies of interpretation. This fact suggests that a significant portion of the small particle population is itself caused by continual collisional fragmentation.

CRATERING DATA AND LOGIC

A large portion of the data from LDEF consists of impact craters, especially in the aluminum structure. The particle flux models describe numbers of particles, however. To relate the two it is necessary to invoke a scaling law for cratering. To date the SPENV code has invoked the simplest of the scaling laws, namely the "energy law", which predicts:

$$d_c = \text{const} \; (\rho_p/\rho_t)^{1/3} \; u^{2/3} d_p \qquad (4)$$

where d_c is the crater diameter, d_p is the particle diameter, ρ refers to the density of particle or target, and u is the impact speed normal to the target surface, while the constant is a normalizer based on experimental impact data of aluminum into aluminum. To date this simple law gives a reasonable fit to the LDEF data in collaboration with the existing micrometeoroid and debris models.

Most other scaling laws (e.g. those by Cour-Palais (1969), McDonnell and Sullivan (1984,1991), etc) are similar to the one above, but frequently differ in the values of the power indices. Changes in the latter will merely linearly shift the "crater count" versus the "particle count" when drawn in the form of cumulative hits per area against size of crater or particle. Since all the scaling laws invoke low indices (< 1) for sensitivities versus density and/or impact speed, the corresponding shifts in the predictions are within the uncertainties of the LDEF data. Supralinearity has been experimentally observed, such that the crater size increases more rapidly than the particle size, all other factors remaining constant. The most widely used superlinear term is in the form of $d_p^{1.056}$ in place of the simple d_p term. Use of this term will produce a "skew" to the data, but for such a small non-unity index the shift is well within the uncertainties of the LDEF interpretation.

Another uncertainty is the use of the "cosine rule", which is generally assumed, and which relates cratering only to the component of impact velocity normal to the target surface. For the lower impact speeds the material response is dependent on momentum and thus obeys the cosine rule, at least partially. For the higher impact speeds the response is dependent on energy, and it is by no means clear that the cosine rule applies (surface "explosions" do not depend on direction of arrival). Interestingly, although the particle flux models imply very infrequent normal impacts, the majority of LDEF craters are very close to hemispheres (likewise most of the craters on the moon are also closely hemispherical!). The effect of modifying the cosine rule will also produce a shift in the LDEF interpretation. However, we have not yet investigated this effect.

Fractional Area Damage

To estimate the degree of areal damage we need to know the impact fluences. Figures 1 through 4 give predictions of cumulative impacts per area of surface versus particle size and crater size, for an altitude of 1000 km, orbit inclination of 60 degrees and two satellite surface orientations of RAM and EARTH. The assumed period in orbit is 6 years starting in 1996. To estimate the fractional damage areas we first differentiate the cumulative impact-versus-size function, multiply the function by the corresponding areas of the damage regions (e.g. craters), and then reintegrate.

For example, if the cumulative number (CN) = A / D^n hits per area for particles greater than diameter D, with A a constant, and n the power index, then it can be shown that the corresponding fractional area damage is given by:

$$\text{Fractional area} = (\pi / 4) \times k^2 \times (n /(n-2)) \times A / D^{n-2} \qquad (5)$$

where k is the ratio of the crater diameter to the impactor diameter. For the case of small debris (less than 1 cm), n has the value of 2.5 for debris. The above equation can then be rewritten:

$$\text{Fractional area} = (\pi / 4) \times k^2 \times 5 \times CN_{(Dmin)} \times D_{min}^2 \qquad (6)$$

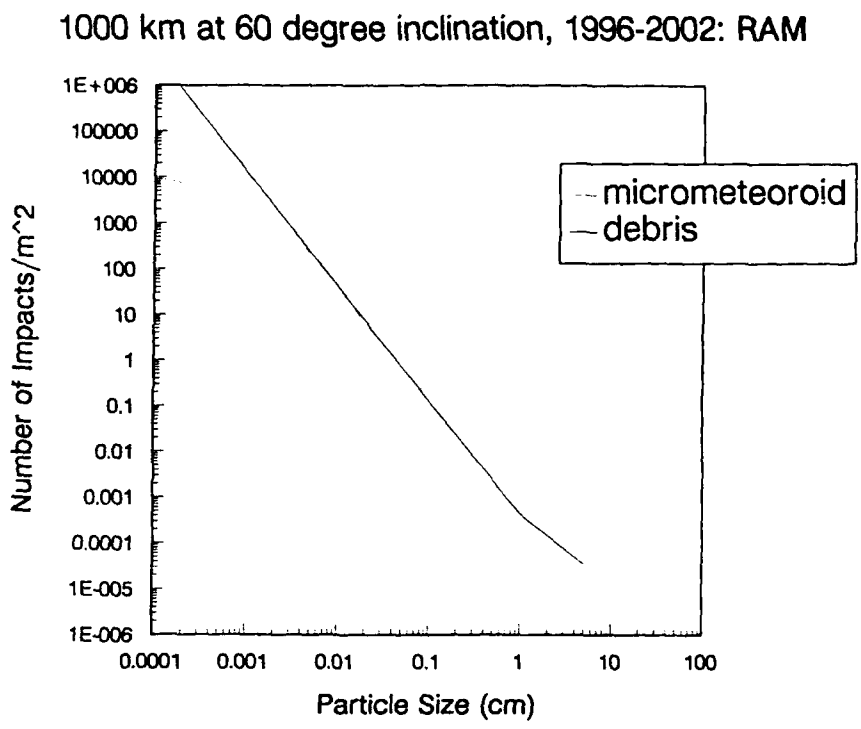


Fig. 1. Cumulative Impacts vs. Particle Size (RAM).

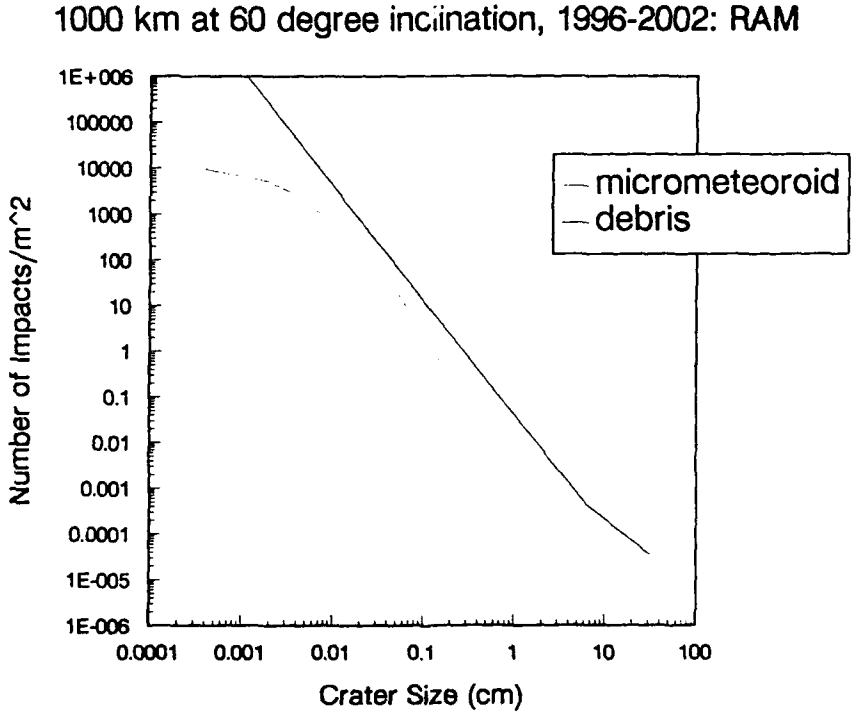


Fig. 2. Cumulative Impacts vs. Crater Size (RAM).

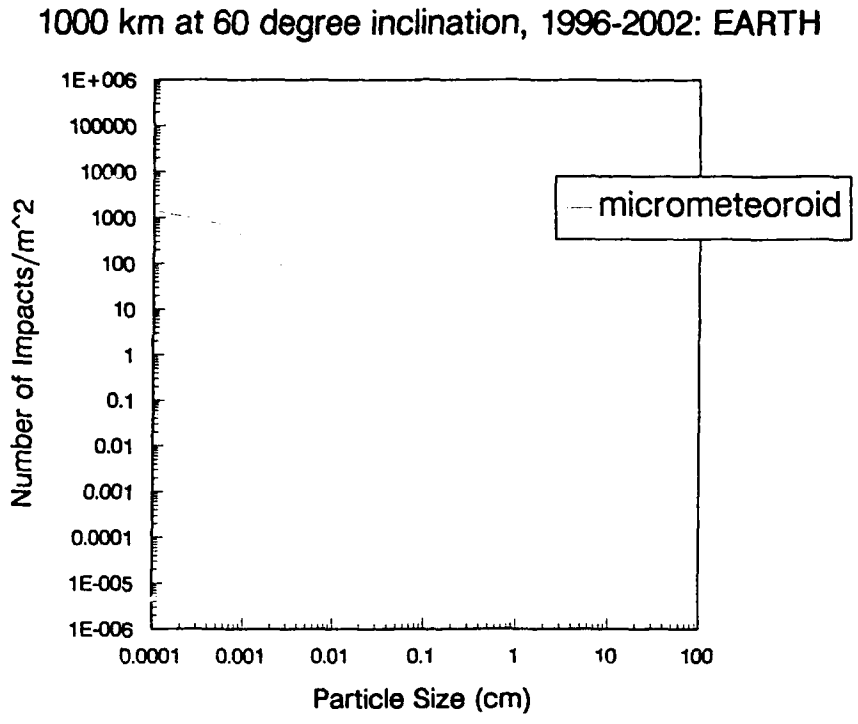


Fig. 3. Cumulative Impacts vs. Particle Size (EARTH).

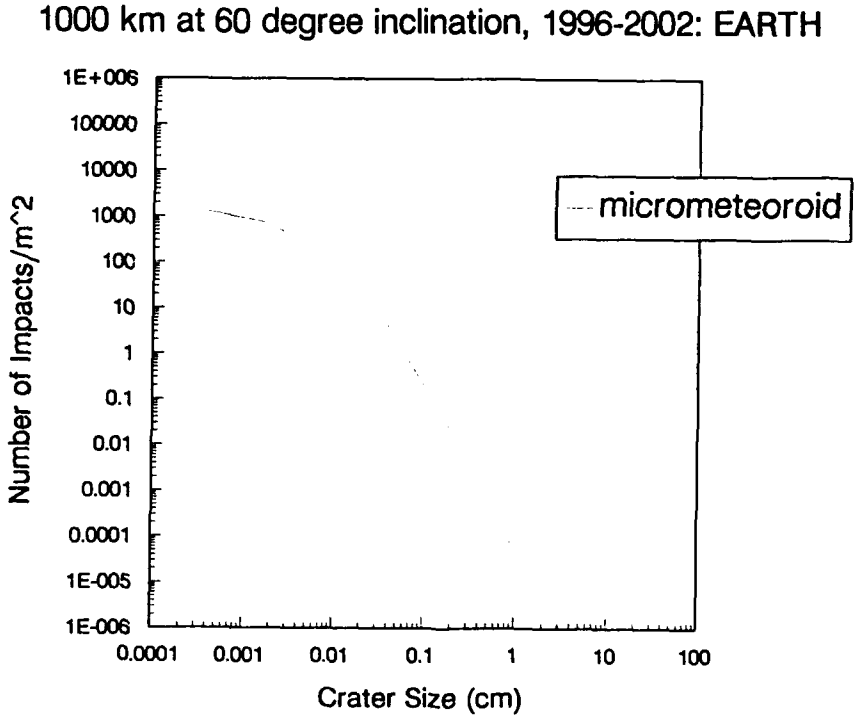


Fig. 4. Cumulative Impacts vs. Crater Size (EARTH).

The value depends on D_{min} since n is greater than 2. To consider a specific case, we calculate the fractional area of erosion for the RAM surface for the case of an altitude of 1000 km, and inclination of 60 degrees. For this case k = 7.0. Assuming that craters of size down to about 1 micron are important (this is comparable to operating wavelengths, and the thicknesses of quarter-wave dielectric optical layers), we obtain:

Fractional area = 7.3×10^{-4} , i.e. about 0.1 percent.

This is a significant amount of erosion, and can be expected to produce significant optical scatter, as discussed below. Note, however, that the LDEF data has indicated that the Kessler model is tending to over-predict the debris population at the smaller sizes. Consequently, the above estimate is probably too large, by perhaps a factor of three (the error would be much larger if an attempt was made to include sub-micron debris particles). However, the above calculation is only for man-made debris, and the micrometeoroids will also contribute, though to a smaller degree. LDEF itself indicated areal erosions of less than 1 percent for pure cratering, on the thermal control materials facing into the RAM. However, if the damage zone includes other related effects (spalling of paint coats, radial star cracking) then the fractional area affected increases rapidly since these effects increase the value of the k term.

OPTICAL SCATTER FOR CRATERS

The computations of the cumulative hit rate (per square meter) show the impact fluence versus impactor diameters for differing spacecraft surface orientations. These data are augmented with information versus crater sizes. From the latter it is possible to establish first-order estimates of increases in optical scatter. This is done by determining the equivalent "contamination level" as defined in MIL-STD 1246A. Young (1976) has already performed both experiments and computations (using Mie theory) to derive increases in the Bidirectional Reflection Distribution Function (BRDF, per steradian) as functions of contamination levels for small particles on mirror surfaces. Thus by finding the "equivalent" conditions (assuming craters scatter in a similar manner to spheres on a mirror) it is possible to derive the BRDF as functions of wavelength and cratering for any chosen spacecraft surface.

Figure 5 illustrates the MIL-STD 1246A data plotted on the same scales as used for the cumulative impacts (per area) versus crater sizes. Note that each "level" plot curves over as the size decreases (rather like the behavior for micrometeoroids), and that this tendency to asymptote is most obvious for the lower "levels". For reference, note that the meaning of "level" is that the distribution is one for which there is one particle per square foot of surface area (equal to 10.76 per m^2) of size "level" microns diameter (e.g. "200" means there is one particle/ft^2 of diameter 200 microns). The data from Fig. 5 is compared to each of the impact-versus-crater plots, and a mean estimate of equivalent contaminant level is obtained. Clearly, since the two groups of data do not have the same power index, there is no unique solution. However, optical scatter will be dominated by the larger craters, and so the "best" definition of equivalent "level" is found by matching the data at the larger sizes.

As an example, consider the data for the RAM with altitude 1000 km and inclination of 60 degrees. The predictions for debris give about 10.76 impacts/m^2 for craters of diameter about 0.100 cm (1000 microns), while for micrometeoroids the corresponding size is about 0.06 cm (600 microns). Thus the equivalent MIL-STD levels are about "1000" and "600" for the two particle species. However, the predictions for cratering "slew" across the MIL-STD plots, such that for craters of size 10 microns the corresponding "levels" are about "400" and "100" respectively. Reference to the work of Young, allows BRDF values (near zero degrees off specular) to be estimated. For a working wavelength of 5 microns these are:

For debris BRDF = 10.0 ("level" 1000) to 0.10 ("level" 400)
For meteoroids BRDF = 0.78 ("level" 600) to 1.0×10^{-4} ("level" 100)

For the EARTH direction, however, the corresponding crater size is about 250 microns (level "250") with

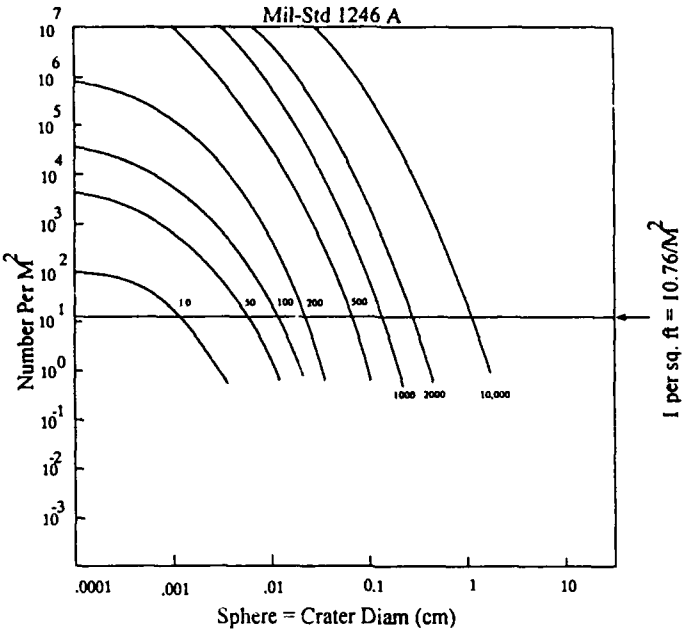


Fig. 5. Contamination Data Definition.

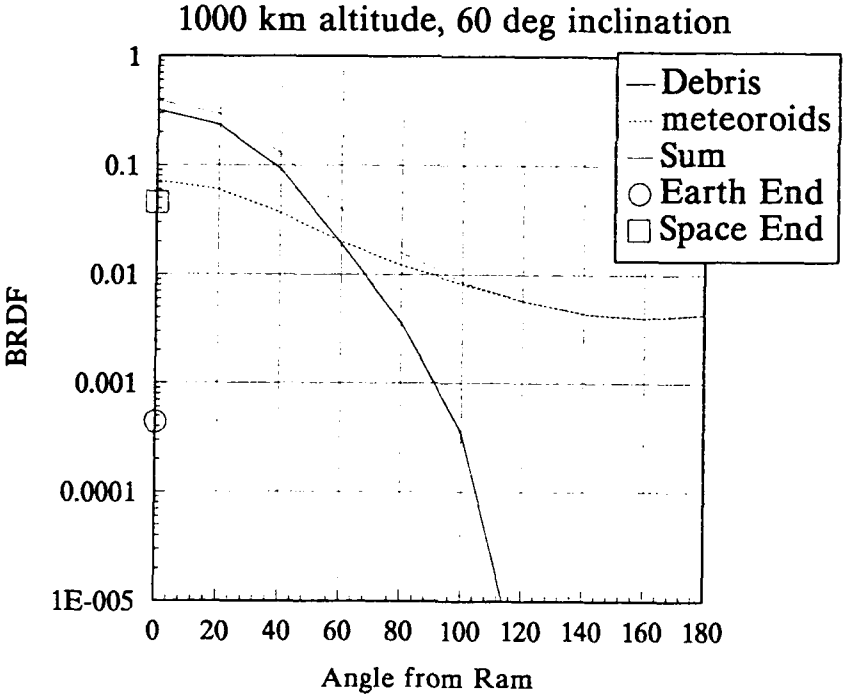


Fig. 6. Variation in BRDF with Angle from RAM.

a slew to level "50" for 10 micron craters, and applies only to micrometeoroids (since Kessler's model does not allow impacts on the Earth-facing surface). At 5 micron wavelength the corresponding scatter is:

For meteoroids BRDF = 9.8×10^{-3} ("level" 250) to 3.1×10^{-6} ("level" 50)

Clearly, the RAM surface suffers from far more scatter than does the EARTH surface.

Scrutiny of Young's data reveals that his results can be approximately fitted by:

$$BRDF = 2.5 \times 10^{-13} \times (level)^5 / \lambda^2 \quad (7)$$

for near-specular scatter, with the wavelength in microns. Note the rapid escalation in the scatter as the "level" increases.

An alternative approach to estimating the scatter is as follows. The fundamental relationship for scatter from craters (assumed the same as from spheres) is:

$$BRDF = \pi^2 \times D^4 \times N / 16 \lambda^2 \quad (8)$$

where D is the crater diameter, N is the number of craters per unit area, and λ is the operating wavelength. By first differentiating the function describing the cumulative impact rate (per area), multiplying by D^4, and re-integrating, we obtain the BRDF for the overall distribution.

Since both the micrometeoroid and debris cumulative impacts obey the form, cumulative number = D^{-n}, the result is:

$$BRDF = \pi^2 \times (n/(4-n)) \times k^4 \times CN_{Dmax} \times D_{max}^4 / 16 \lambda^2 \quad (9)$$

where n is the power index describing the cumulative number of impacts versus particle size (in the neighborhood of the value of D_{max}), k is the ratio of crater diameter to particle diameter (D), CN is the predicted cumulative hit rate, and λ is the wavelength.

The above equation involves the quantity D_{max}, which is the largest particle diameter to be used in the calculation. To determine the latter, we apply the following logic: if there is less than one (1) impact on the given optic, then there is no longer a meaningful definition of N, the areal impact density. Thus knowing the area of the optic, we compute the corresponding hits per meter. Referring to the predicted cumulative impact data versus particle size, we determine the value of D_{max}.

As an example, consider an optic of area 100 cm^2. For one crater, we have an areal density of 100 per m^2 (or 0.01 per cm^2), and thus this defines CN_{Dmax}. For debris, n = 2.5, and k = 7.0 (for the RAM surface). Reference to the particle plots of impacts on the RAM surface for the 1000 km, 60 degree orbit, gives the value D_{max} = 70 microns for debris. For micrometeoroids, n = 3.0, and k = 3.8, and D_{max} = 70 microns also.

Substituting into the equation for scatter (at 5 micron wavelength), we obtain:

For debris BRDF = 0.24 For meteoroids BRDF = 0.037

For the EARTH looking surface, we have n = 2.7, k = 3.25, and D_{max} = 25 microns, and only micrometeoroids apply. Thus we obtain (for 5 micron wavelength): BRDF = 2.2×10^{-4}

Thus, once more, the scatter for the RAM surface is much greater than for the EARTH surface. This effect is seen in Fig. 6, which shows computed scatter as a function of angle around the satellite (in the plane parallel to the Earth's surface) as well as the SPACE and EARTH-looking directions. Telescope

shroud shielding has not been included for these calculations, but will decrease all scatter values.

Although none of the above quotes for scatter can be considered precise, both approaches yield similar values (especially if the larger "level" quotes are used), suggesting the scatter for the RAM surface is enormous compared to that for the EARTH looking surface.

The data of Young gives BRDF as functions of off-specular angle. Inspection of these data reveal that the BRDF rapidly decreases over the range 0 to 10 degrees, and then follows a pseudo-exponential law for larger angles. To a reasonable approximation, the data for large angles (> 20 degrees) is given by:

$$\text{BRDF} = 5.4 \times 10^{-15} \times (\text{level})^5 \times \exp(-8.91 \times 10^{-2} \times \text{degrees}) / \lambda^2 \qquad (10)$$

By integrating Young's data for BRDF versus off-specular angle, the total integrated scatter (TIS) can be obtained. A simple graphical integration gives:

$$\text{TIS} = 2.2 \times 10^{-3} \times \text{BRDF}(0 \text{ degrees}), \qquad \text{or TIS} = 5.5 \times 10^{-17} \times (\text{level})^5 / \lambda^2 \qquad (11)$$

with λ in microns. Note that for BRDF (0 degrees) > 455, this implies scatter greater than the input, which is obviously nonsense. The conclusion is that for the larger degrees of scatter, the BRDF versus angle data must change its form, versus the lower cases (Young only presented data for contamination levels of 500 and below). Thus extrapolation of Young's data becomes suspect for large degrees of scatter. However, the estimates of scatter for the RAM surface, quoted above, are not within this uncertain region.

Brittle Material Response

All of the above pre-supposes that the optic behaves as if a metallic mirror with simple hemispherical craters. In reality, many mirrors (or lenses) are made of dielectrics and employ multiple thin layers (quarter-wave optical phasing logic). These materials are usually brittle. Upon hypervelocity impact, the damage consists of irregular craters with conchoidal surfaces, surrounded by star-cracks which can extend up to about 50 times the size of the impacting particle. To assess the optical scatter for these conditions it is necessary to invoke the theory of dielectric needles or cylinders as done by Van de Hulst (1957, 1981).

The evidence from LDEF indicates that impacts into brittle materials produce craters similar to those for ductile materials. However, the morphology is different, with the smooth-surface craters for ductile targets being replaced by a conchoidal, multi-crack surface for brittle targets, which is much rougher. Additionally, whereas ductile targets frequently display lips around the craters which stand proud of the initial surface, brittle targets frequently do not (presumably because the equivalent lip material was also brittle and cracked off). The other major difference is that brittle targets frequently display radial star cracking, with several (about 4 on average) cracks propagating away from the impact point over distances of up to 50 times the diameter of the impactor. Little systematic study has been done to date on these star cracks, though the work is ongoing by Jean-Claude Mandeville in France, a member of the LDEF Micrometeoroid and Debris Special Investigative Group (M&D SIG).

For the purpose of predicting cratering, the accepted meaning of a crater diameter is the value at the original target surface. However, the ductile target craters with lips can be about 50% larger if the diameter across the highest portion of the lips is measured, and up to 100% larger if the total diameter across the complete lip pattern is included. The previous methodology for computing fractional area damage did not account for these lips. If lips are included in the definition of areal damage, the values can clearly be up to 4 times as large, since area is proportional to the square of the size of the region considered. The inclusion of lips also has a large impact on the value of optical scatter owing to the k^4 term.

Although there are several existing scaling laws describing simple cratering there are none, to our knowledge, describing the behavior of star cracks in brittle materials. Accordingly, we have formulated a *possible* equation describing them. This equation is:

$$r_c/r_p = (\rho'\pi/K_{Ic})^{0.4} (c_t/c_p)^{0.4} u^{0.8} r_p^{0.2} \quad (12)$$

where r_c is the radial extent of the crack from the impact point, r_p is the impactor radius, ρ' is the effective density (defined below), K_{Ic} is the target fracture toughness, c_t and c_p are the bulk sound speeds for target and projectile respectively, and u is the impact speed. Note that this equation predicts supralinearity, with the crack length increasing faster than the impactor diameter. This equation is derived by assuming that immediately following the outward compressive wave in the target the material develops hoop tensions. If these tensions are greater than the stress necessary to propagate an unstable crack at distance r from the impact site, then crack growth is assumed. The definition of effective density is based on the assumption of a Bernoulli fluid flow pressure state, and is given by:

$$\rho' = \rho_p\rho_t/((\rho_p)^{0.5} + (\rho_t)^{0.5})^2 \quad (13)$$

where the ρ values are for impactor and target, respectively.

As examples of the consequential predictions, consider an impactor of aluminum (density of 2.8 g/cm^3) and a target of fused silica (density of 2.2 g/cm^3). Thus the effective density is 0.618 g/cm^3. For fused silica the fracture toughness is 6.4 x 10^{7}dynes/cm^2 x cm$^{0.5}$. These values are reasonably typical of the conditions for impacts on LDEF for glass. Using the average LEO collision speed of 10 km/s, we predict:

for r_p=	1.0 micron,	r_c/r_p = 8.80,	hence r_c = 8.80 microns,
for r_p=	10.0 micron,	r_c/r_p = 13.95,	hence r_c = 139.50 microns,
for r_p=	100.0 micron,	r_c/r_p = 22.11,	hence r_c = 0.22 cm,
for r_p=	0.1 cm,	r_c/r_p = 35.00,	hence r_c = 3.50 cm,
for r_p=	1.0 cm,	r_c/r_p = 55.53,	hence r_c = 55.53 cm.

Note that for particle radii in the range 1 - 1000 microns, the cracks are predicted to extend in the range of 9 to 35 times the impactor size, in approximate agreement with observations. At present, there is no simple method of predicting the widths of these cracks. Assuming the crack widths to be, say, one-tenth the impactor diameter (d_p), and taking an average crack to be 15 d_p long, with 4 cracks per impact, the cracks represent an area of 6 d_p^2, while the typical crater of about 5 d_p wide has an area of about 20 d_p^2. Thus, unless the cracks are much wider, or there are more cracks per impact, they will usually represent only a relatively small portion (e.g. 30%) of the total fractional area damage. However, for wider cracks, less-tough targets, higher impact speeds, or larger impactors, the fractional area due to the radial cracks could easily double that due to craters alone.

Optical Scatter for Brittle Materials

We have assessed the optical scattering for brittle, cracked targets. A typical package of interest is the multi-layered dielectric stack mirror. Frequently, such mirrors comprise a dielectric substrate (e.g. fused silica) with a thin (<2000 Å) metallic reflecting coating, overlaid by a stack of alternating dielectric layers, each of one-quarter wavelength. The stack may have anywhere from only one dielectric layer up to several tens of layers. Depending on the operating wavelength, this results in optical coatings with thicknesses in the range of from about 0.3 micron (single layer, visible) up to perhaps 50 micron (multiple layers, infrared). Since impactors can produce craters with depths of about 3.5 times the impactor diameter (e.g. for a RAM surface at 1000 km altitude and 60 degree inclination), even a 50 micron thick stack can be completely penetrated by a 14 micron particle, while the more typical 3 micron thick stack is penetrated by a particle of only 0.86 micron.

There is a fundamental difference between cratering in a ductile metal mirror and in a coated stack. For the metal mirror, the crater surface is still metallic, and thus still has high local reflectivity. However, penetration through the coating stack reveals the underlying substrate, and this usually has low reflectivity (e.g. 4% for silica). Thus, in essence cratering in coated optics is equivalent to punching holes in the mirror. While the holes will still give diffractive scattering (as with craters), the percentage loss of reflective area will also give a corresponding loss in overall reflectivity. Since these coating stacks are usually designed to maximize reflectivity (e.g. >98%), the loss due to the impactor cratering/"hole-punching" (with associated cracks) is significant.

An attempt to address the scattering caused by cracks can be done by treating them as equivalent to dielectric cylinders or needles, as done by van der Hulst (1981). Treating the cracks as cylinders with all dimensions large compared to the operating wavelength, the scatter is given by:

$$\text{BRDF} = (4a^2l/\pi r^2\lambda\theta)\, E^2(ka\theta) \quad \text{per cylinder,} \tag{14}$$

where a is the radius of the cylinder, l is the length, r is the distance from the cylinder, λ is the operational wavelength, θ is the scatter angle (zero being the initial light direction), k is $2\pi/\lambda$, and E is the angular scatter function. If the crack pattern becomes "dense", such that cracks intercept with length l, we have $1/l^2$ cracks per unit area. Then we obtain:

$$\text{BRDF} \Rightarrow (4a^2/\pi l\lambda\theta)\, E^2(ka\theta) \Rightarrow (8a^2/\lambda^2) \quad \text{for } \theta \Rightarrow 0. \tag{15}$$

Note that this implies the scatter depends only on the radius of the cylinders and the wavelength. The scatter from these cracks varies with the crack-width squared, whereas scatter from craters is proportional to the crater radius to the fourth power. Hence cracks are less efficient scatterers than are craters. Since it was shown above that the usual associated damage area of the cracks is also less than that of the craters, the result is that the craters are expected to dominate the overall scattering.

If the cracks are narrow compared to the operating wavelength, they behave as if dielectric "needles". For this case the scatter is given by:

$$\text{BRDF} = (2\pi^5a^4l)(m^2-1)^2/(\lambda^3) \quad \text{per needle,} \tag{16}$$

where a is the radius of the needle, l is the length, and m is the "effective" refractive index. This "effective" index is based on the mismatch between the crack region and the surrounding medium. For scatter measurements done at wavelengths which are different from the "tuned" wavelength of the quarter-wave stack, the value of this index is similar to that for the individual layer materials. However, at the "tuned" wavelength, the effective index may be much higher, since the optical stack behaves as if a single dielectric with high refractive index (giving high reflectivity).

Since cracks are not truly circular in cross section, for both "cylinders" and "needles", the value of the "radius" is the equivalent one, given by one half of the square-root of the product of the crack width and the crack depth.

If the crack pattern becomes dense and intersecting, then the areal density of cracks (number per area) is given by $N = 1/l^2$ where l is the mean length between interceptions. Thus the equation for BRDF moves the "l" term from the numerator into the denominator.

As a check, consider the case of the dense crack pattern often observed due to hysterectic stress cracking after a sudden surface heating (e.g. by a pulsed laser, pulsed electron beam or a pulsed x-ray beam). Typically, the crack may have a depth equal to the optical stack which may be 3 microns, while the crack width may be about 300Å, giving an equivalent crack radius of order 0.15 micron. For such intersecting dense crack patterns, the mean length of each crack may be about 20 microns. Assuming an interrogation wavelength of 0.5 micron (visible, not at the "tuned" wavelength), and an effective refractive index of 2.0, the predicted scatter is: BRDF = 1.12. This value is very large compared to the

initial virgin (undamaged) scatter value, which can be as low as BRDF = 10^{-5} to 10^{-7}. Even for widely spaced cracks with lengths of 1000 micron (1 mm), the predicted scatter is BRDF = 2.24 x 10^{-2}. Such scatter values have indeed been measured for such damaged samples. Detailed Mie scattering calculations are required to accurately determine the scatter for a cracked dielectric multilayered stack. This would be especially true for scatter at the tuned wavelength of the stack. For this case the anticipated scatter is even higher, since the effective refractive index is larger (put another way, crack perturbations are worse for the high-reflectivity tuned case).

Note, that for needles the scatter increases with the needle width to the fourth power (similar to craters), and inversely with the wavelength cubed. For both cylinders and craters, scatter varies inversely with wavelength squared. Thus the precise level of scatter will depend strongly on the crack widths and the operational wavelength.

SUMMARY

We have performed first-order estimates of the probable modes of particle impact damage and consequential increases in optical scatter for satellite optics in LEO. The methodology requires use of the existing near-earth particle environment. Both simple ductile metal cratering and brittle material cracking have been addressed. The analyses include estimates of fractional area affected. For an orbit of 1000 km, inclination of 60 degrees and period of 6 years, even the RAM surface suffers from less than 1 percent areal damage due to simple ductile cratering. However, if star cracking in brittle materials occurs the affected areas rapidly increase. Note that the orbit chosen for analysis is one of the worst cases, involving a local peak in the man-made debris population.

The models used presently give reasonable agreement with the LDEF experimental data in terms of impact fluences and directionality on the spacecraft body. However, the effects on optical surfaces is still under study. The analyses of increased optical scatter (BRDF) demonstrate strong dependencies on the details of crater sizes and crack lengths. For this reason there is a continuing need for better understanding of these impact responses.

Presently, our analyses indicate the potential for large increases in optical scatter for unshielded optics staring into the RAM, but only small increases for EARTH-looking cases.

We will perform future impact experiments on metallic and dielectric optics, and will directly measure the resulting optical scatter. These experiments will allow verification or modification of our estimates of damage modes and scatter.

REFERENCES

This work is done on behalf of the Air Force Phillips Laboratory, Kirtland AFB, NM, under contract F29601-91-C-0071, via a subcontract to SAIC, Albuquerque, NM.

Cour-Palais, B.G. et al. (1969). Micrometeoroid Environment Model - 1969 (Near Earth to Lunar Surface), *NASA SP-8013.*

Kessler, D.J. and Reynolds, R.C. (1988). Orbital Debris Environment for Spacecraft Designed to Operate in Low Earth Orbit, *NASA-TM-100471.*

McDonnell, J.A.M. et al (1984). An Empirical Penetration Equation for Thin Metallic Films used in Capture Cell Techniques, *Nature 309* 237-240. Updates with Sullivan, K. (1991) private communication.

Young, R.P. (1976). Low-Scatter Mirror Degradation by Particle Contamination, *Optical Engineering, Vol 15, No.6,* Nov-Dec.

Van de Hulst, H.C. (1957, 1981). *Light Scattering by Small Particles*, Dover Publications.

Int. J. Impact Engng Vol.14, pp.61–71, 1993
Printed in Great Britain

0734-743X/93 $6.00+0.00
Pergamon Press Ltd

PROTECTING ALUMINUM ALLOY FROM PARTICLE-IMPACT IGNITION WITH AN Al_2O_3 FILM

SAEMAHN BAHK, DAVID CHAVEZ, BRYAN EMERY, and BRUCE WILSON
LOCKHEED-ESC

JOEL STOLTZFUS, NASA

P. O. Drawer MM, NASA White Sands Test Facility
Las Cruces, NM 88004

ABSTRACT

Bare aluminum alloy is compared to soft-anodized aluminum alloy (oxide film thickness 5 μm, 10 μm, 20 μm, or 50 μm) for susceptibility to ignition by supersonic particle impact in pure oxygen. The particle diameter ranged from 1600 μm to 2000 μm, temperature ranged from 220 K to 672 K and oxygen pressure was 27.6 MPa. The event of ignition was recorded on video tape. The results of ignition frequency are reported as a Logistic Regression Model over the variable space. In addition, the impact process was simulated using the computer code ZEUS to identify ignition temperatures and ignition sites as well as to qualitatively describe the mechanism of protection offered by the soft-anodized oxide film. Significant improvement against particle-impact ignition was achieved through the use of the anodized oxide film.

INTRODUCTION

Ignition of metal structures in high pressure oxygen systems can be caused by the impact of metallic particles entrained in a fast flowing gas stream (Clark and Hurst, 1972; Wegener, 1964). Subsequent combustion can lead to serious damage or destruction of the system. Aluminum is especially susceptible to ignition in this manner (Benz et al., 1986).

Aluminum oxide films on aluminum structures have long been recognized as providing protection against corrosion and some erosion (Hunter and Fowle, 1956). The protection given by such a film against auto-ignition has been recognized in metal ignition theory in terms of a transition temperature, the temperature at which the oxide film is no longer protective (Mellor and Glassman, 1965).

This paper describes research that examines the protection provided by aluminum oxide films against particle-impact ignition. Aluminum oxide films were prepared by soft-anodization. Four different

film thicknesses, 5 μm, 10 μm, 20 μm, and 50 μm, were compared to bare aluminum alloy 6061-T6. The event of particle impact and subsequent hot-spot generation were modeled by computer simulation and compared to the experimental result.

CHEMISTRY OF ALUMINUM OXIDE FILMS

The natural aluminum oxide film formed on fresh aluminum, while extremely thin and thus easily damaged, has such remarkable self-healing properties, that when damaged, it immediately starts to reform. In dry oxygen at room temperature the natural film reaches an ultimate thickness of about 10 Å in a matter of minutes (Hunter and Fowle, 1956). A film formed in ordinary air is much thicker and takes weeks, months, and even years to reach its ultimate thickness. The thinner film is an impermeable barrier-type film; while the thick film has a compact barrier type of film adjacent to the metal and an outer layer of porous or more permeable oxide.

The effect of temperature on the aluminum oxide film is significant. Figure 1 shows the qualitative change in film growth and in film crystallography with temperature. Hunter and Fowle (1956) also report the Al_2O_3 barrier film thickness also changes with temperature. There is a constant increase in ultimate film thickness with increasing temperature. Two levels of film thickness were identified, with the jump between levels occurring above 575 K and below 725 K.

EXPERIMENT AND RESULTS

The experiments were conducted using the White Sands Test Facility (WSTF) supersonic particle-impact chamber (Bahk, et al., 1991). A single spherical, aluminum (2017-T4 type alloy) particle either 1600 or 2000 microns in diameter, was accelerated to a supersonic velocity of approximately 353 m/sec and impacted on the target (6061-T6 alloy). Pure oxygen, 99.9 percent, at 27.6 MPa was the carrier gas. Test temperatures varied over the range of 220 K to 672 K.

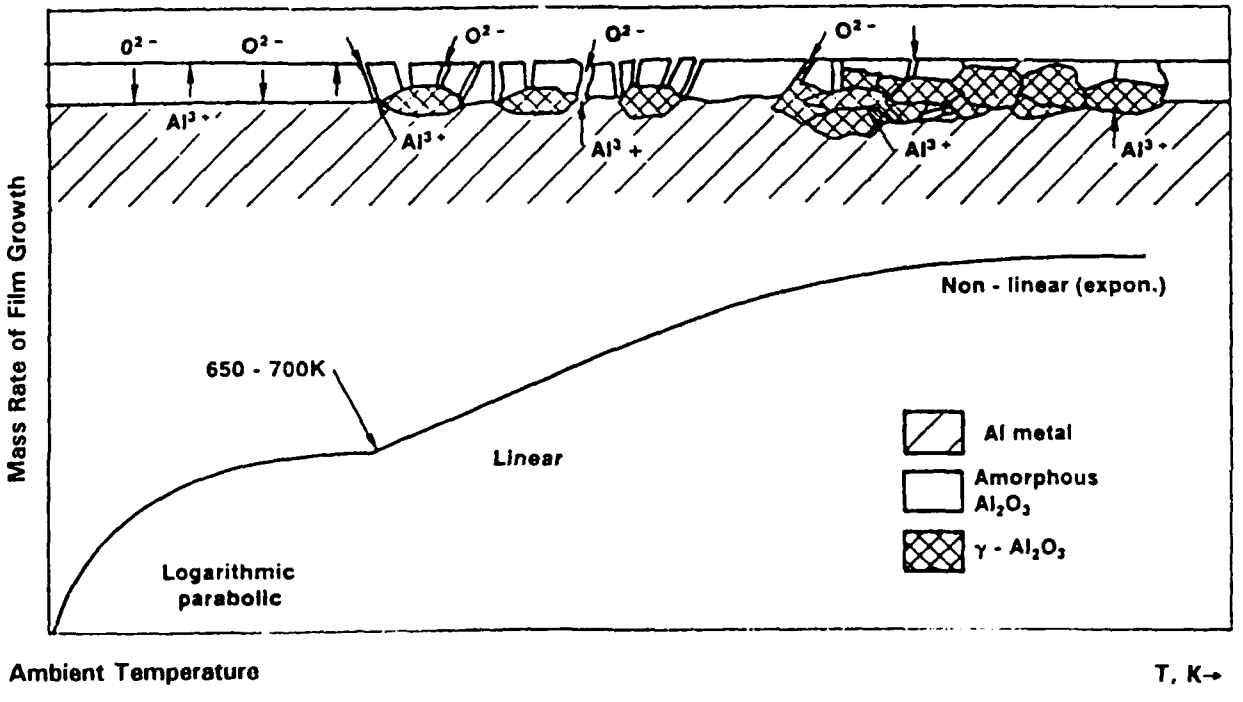


Fig. 1. Natural growth of aluminum oxide film

Experiments were replicated and test parameters were derived from standard formulas for binomial experiments, ie, experiments producing a yes/no result. For these experiments, the results were in terms of whether ignition occurred.[1] Details of the experimental equipment and procedure are given in the reference by Benz et al. (1986).

Figures 2 through 6 are photographs of impacted targets without ignition. All photographs are magnified approximately 35 times. In Fig. 2, a cross-sectional view of a bare aluminum target with an imbedded particle is shown. Figure 3 shows the same sample prior to cross-sectioning. In Figs. 4, 5, and 6, the fractured aluminum oxide film is seen; however, in each case all the oxide film is present (has not broken and separated). Experimental conditions are given for each figure. Although it is not evident from these photographs, the amorphous aluminum oxide coating must still be present, as dictated by the experimental conditions.

Figure 7 is the composite experimental data for the bare aluminum tests. The curve fit is a logistic regression model showing the 95 percent confidence limits as an envelope. The abrupt change in ignition occurrence at 550 K is an observed and reproducible phenomenon.

Figure 8 is a composite plot for the experiments with the bare aluminum and each of the four anodized films. The curves in the figure are plotted from a logistic regression model fitted using a standard SAS routine (LOGISTIC). Comparison of the experimental conditions of Figs. 2 through 6 with these curves shows that these experimental conditions may or may not lead to ignition.

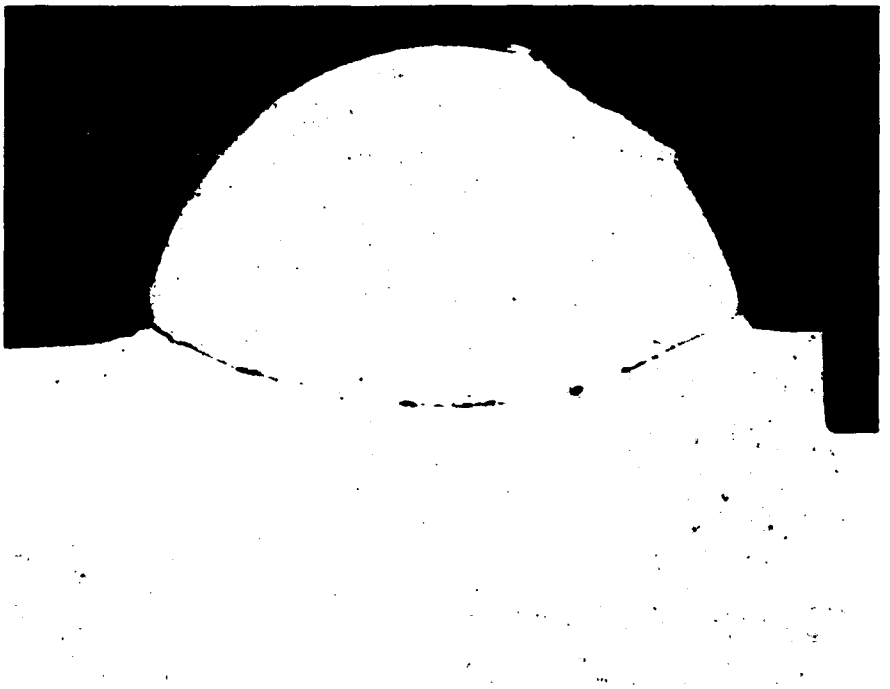


Fig. 2. Cross-section of bare aluminum target showing an imbedded particle; temperature 550 K: 27.6 MPa oxygen

[1]Emery, B. private communication, WSTF Memo dated Oct 1991.



Fig. 3. Bare aluminum target showing both an imbedded particle and an impact; temperature 550 K; 27.6 MPa oxygen

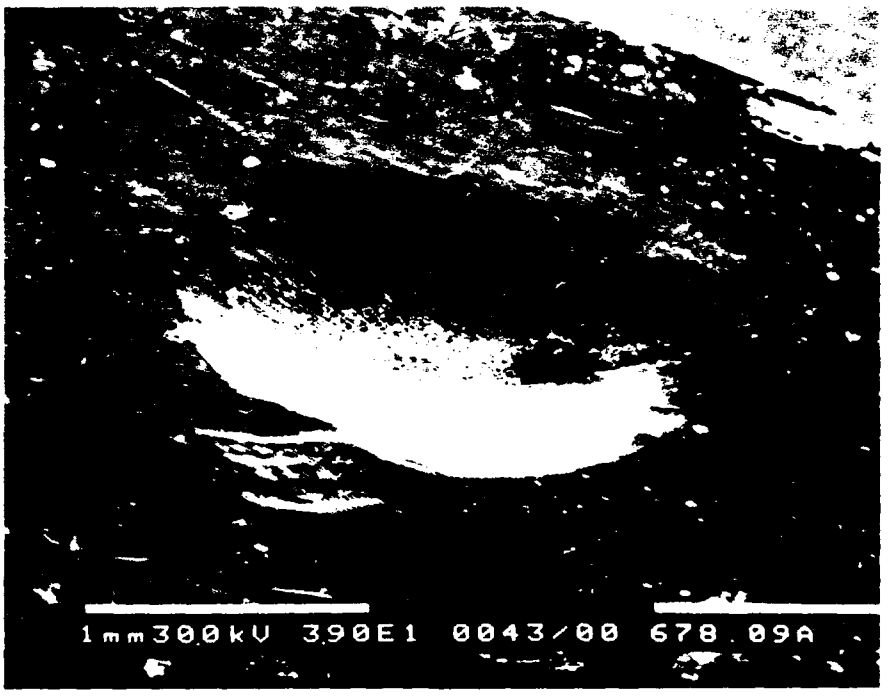


Fig. 4. 10 μ anodized coating; temperature 550 K; 27.6 MPa oxygen



Fig. 5. 20 μ anodized coating; temperature 550 K; 27.6 MPa oxygen



Fig. 6. 50 μ anodized coating; temperature 550 K; 27.6 MPa oxygen

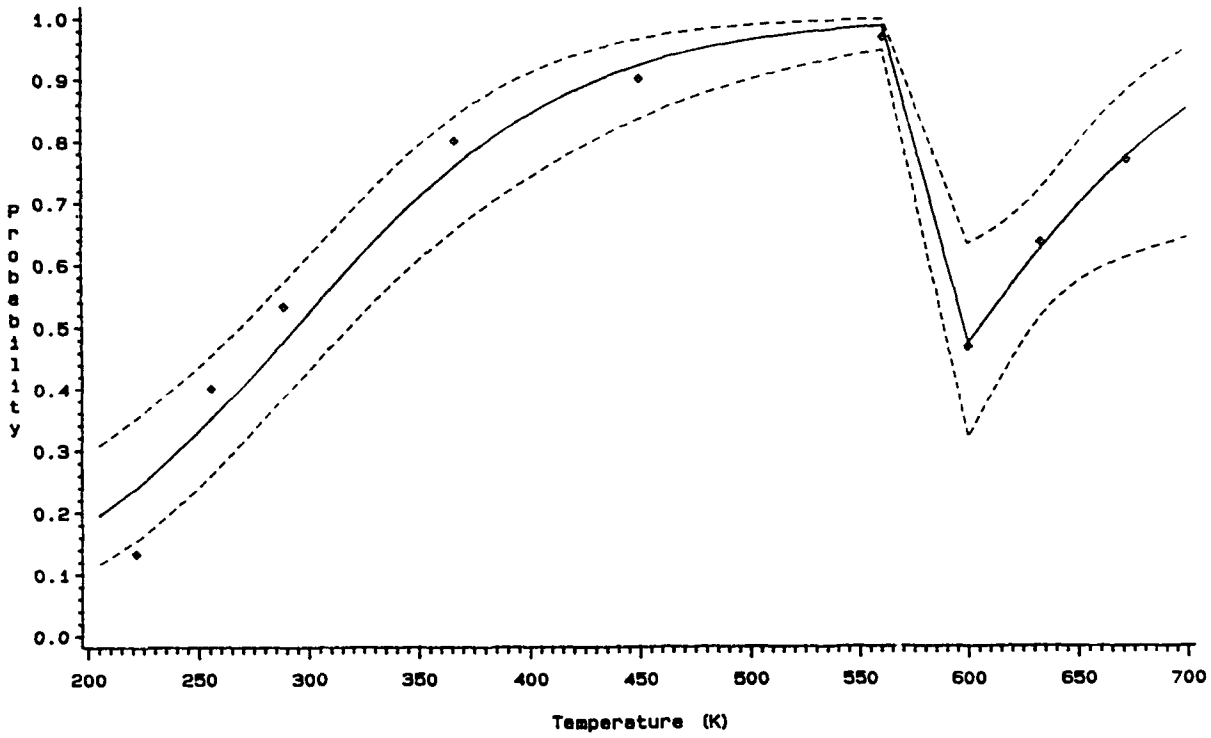


Fig. 7. Representative plot of observed and fitted probabilities of ignition; dashed lines are 95 percent confidence limits

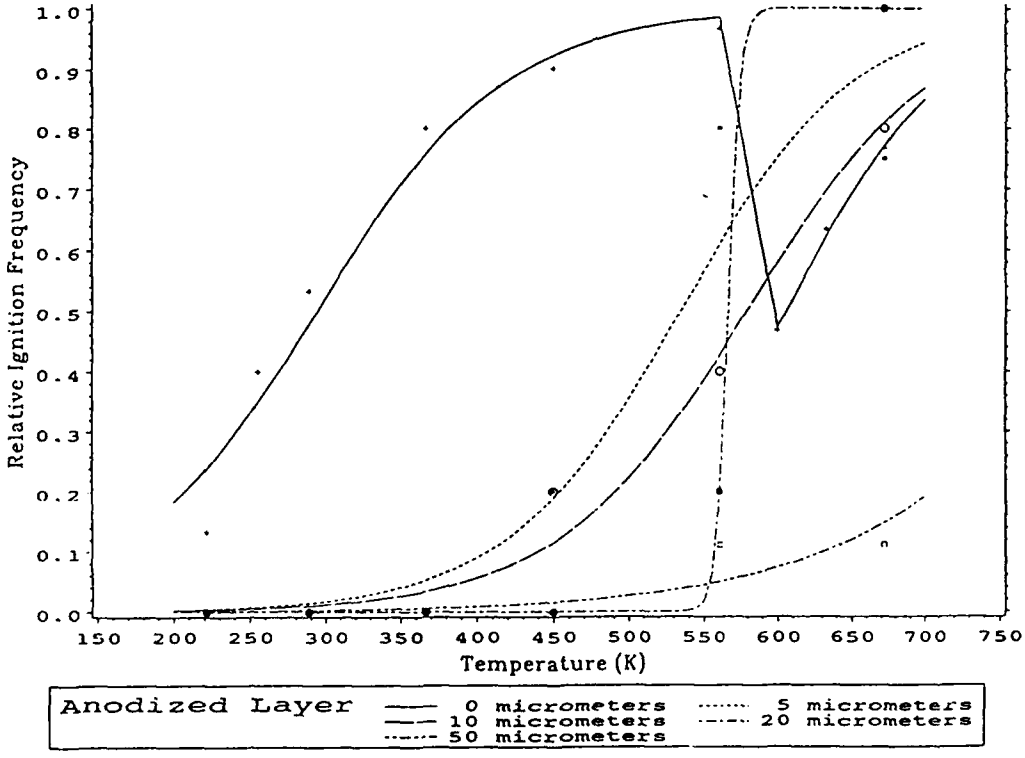


Fig. 8. Aluminum logistic distribution for different anodized layers

IMPACT SIMULATION

In addition to the experiments, the single particle impact was simulated using the ZEUS (Zukas, 1987). The ZEUS code is a two dimensional finite element code using the Mie-Gruneisen equation of state. The basic Hugoniot data was obtained from Los Alamos National Laboratories data (Marsh, 1980) and Air Force Weapons Laboratory data (Kohn, 1969). The Johnson-Cook (Johnson and Cook, 1983) strength model was used to determine the strength data at initial target temperature and high strain rates. The data needed for the Johnson-Cook model was obtained from Los Alamos National Laboratories (Johnson and Holmquist, 1988).

Figure 9 shows the results of a simulation corresponding to the experimental conditions represented in Figs. 2 and 3.

Figures 10 and 11 show the results of the simulation corresponding to the experimental conditions represented by Figs. 5 and 6.

A major parameter in the simulation is the velocity of the impacting particle. While the velocity was not measured experimentally for any of the tests, approximate velocities were established using two independent methods. The first method was a series of drop-weight impact penetration measurements,[2] and the second one was an in-house stream flow model.[3] The velocity of the oxygen stream was measured. Using the oxygen stream velocity, the velocity of the particle was determined.

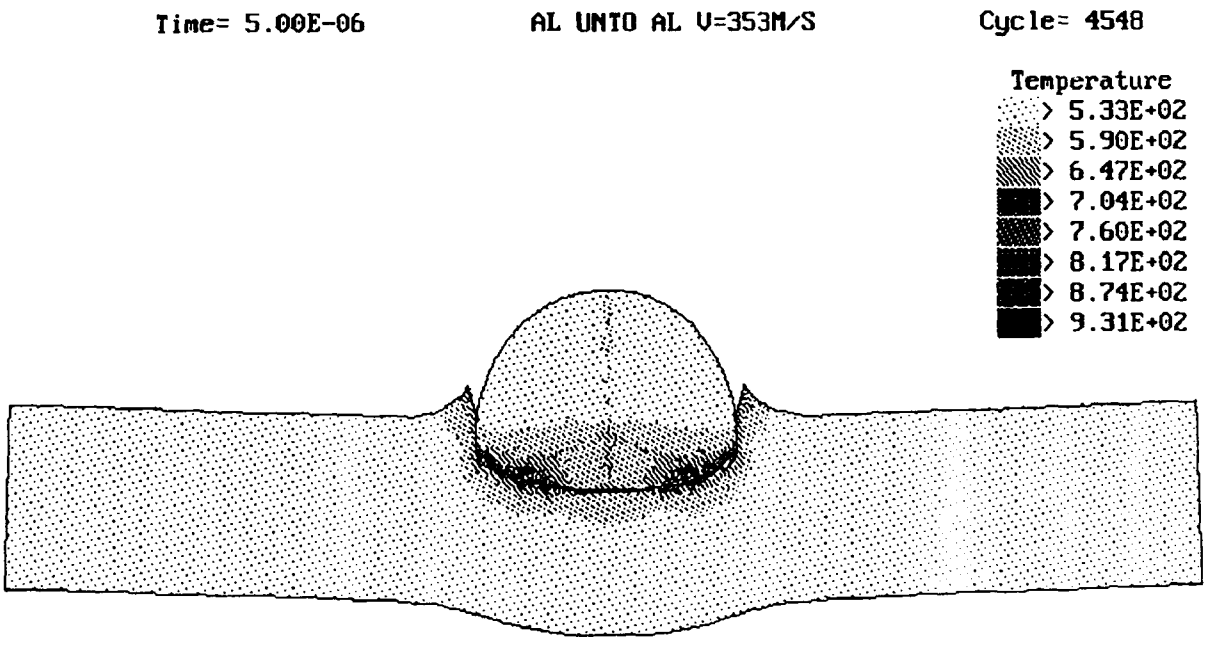


Fig. 9. Simulated impact on bare AL 6061-T6 target

[2]Stoltzfus, J. M. "Estimation of Minimum Particle Velocity by a Dent-Block Comparison Test." Private communication, pp. B-1, (1990).

[3]Bahk, S. "Estimation of Particle Velocity by Dry Flow Model." Private communication, (1990).

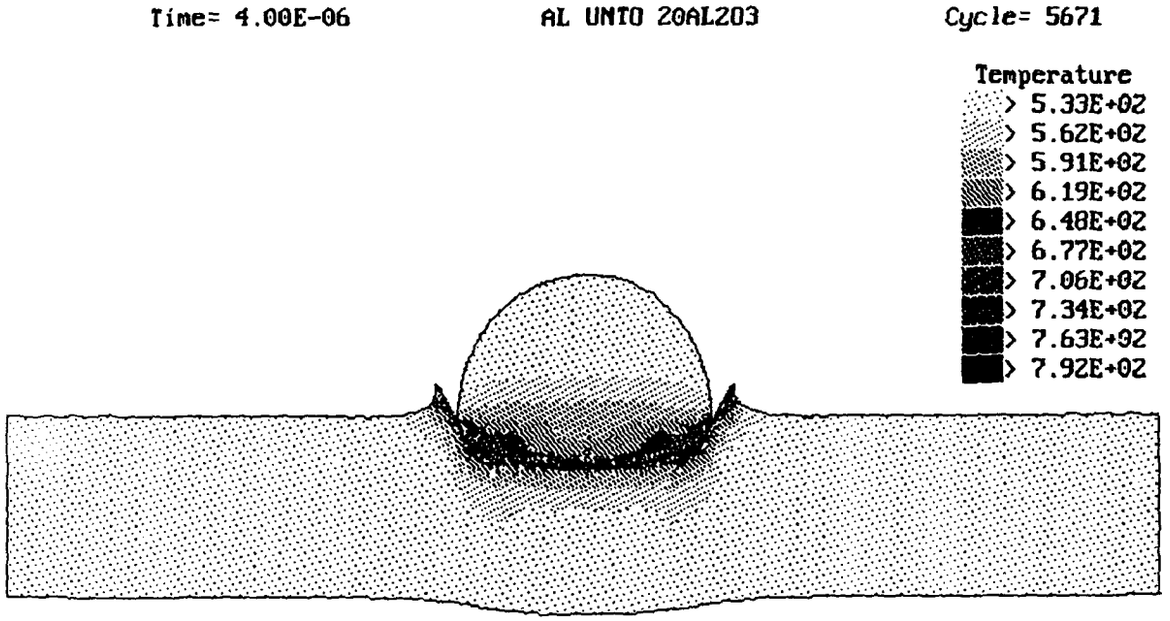


Fig. 10. Simulated impact on Al 6061-T6 target with 20μ anodized coating

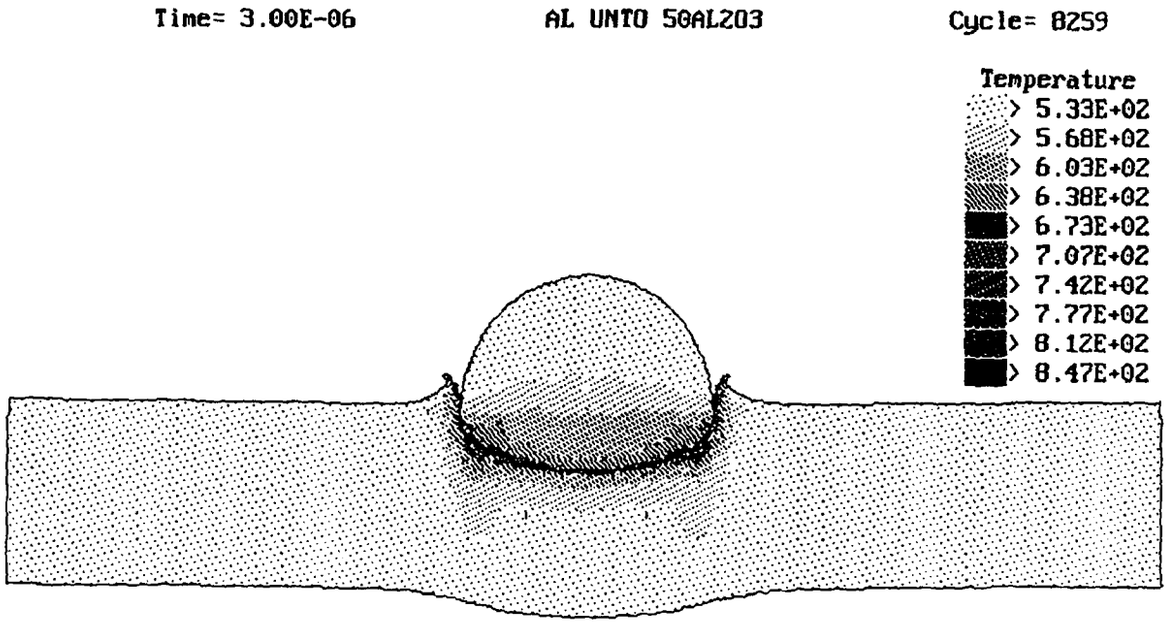


Fig. 11. Simulated impact on AL 6061-T6 target with 50μ anodized coating

The results of the two independent methods were within 5 percent. From these results a simulation velocity equal to 353 m/sec was established.

The variation in temperature, over the experimental range reported, changed the velocity of the particle (Benz et al., 1986). In addition, the temperature variation affected the reaction rates and thermal energy exchange. In the simulation runs, the impact velocity used (353 m/sec) corresponded to the 550 K experiments. The temperature will rise as the impact velocity increases.

At the selected temperature the simulation predicted temperature increases between 244 K and 388 K above ambient (777 K to 931 K absolute).

DISCUSSION

In an impact problem, a particle with radius a, velocity u and mass density ρ_p impacts a material target with mass density ρ_t and strength Y (assumed to have stress units). The particle parameters also determine the particle kinetic energy and its momentum (the non-zero component perpendicular to the target). The particle is spherical and the impact to the target surface is assumed to be normal.

There are a variety of phenomena of interest in the classical impact problem - depth of penetration, diameter of crater, pressure and temperature generated, stresses, etc. (Bjorkman and Holsapple, 1987; Vinogrador and Cherviakov, 1984). However, this analysis is concerned with ignition of the target. For those targets where ignition occurred, the target was consumed by burning. Hence these phenomena were not available for study. In experiments where ignition did not occur, as in Figs. 2 through 6, depth of penetration and width of crater provided visual evidence of consistency of the experimental conditions.

The classic definition for metal ignition is that ignition occurs when "...heat produced exceeds heat losses to such an extent that the temperature rise continues at an accelerating rate" (Reynolds, 1959).

On impact ignition, energy deposition into the target occurs over a very short time and hot spots must be created whose temperature exceeds the autoignition temperature of the metal. Aluminum's melting temperature, 933 K, is its autoignition temperature (Reynolds, 1959).

Not only must the aluminum's temperature exceed its melting point, it must also be exposed to ambient oxygen (the natural aluminum oxide film must be disrupted). Ignition studies at WSTF have shown that the entire aluminum core of a 3.2 mm-diameter rod may be molten and ignition will not occur if the natural amorphous aluminum oxide film remains intact (Bahk et al., 1992). The addition of anodized aluminum oxide further protects against ignition. Since the melting point of aluminum oxide is 2230 K, it is unlikely that a single particle impact, under the conditions of these experiments, would lead to a hot spot sufficient to melt the aluminum oxide. Therefore the exposure of aluminum metal will require mechanical disruption of the aluminum oxide film.

The experimental evidence of Figs. 4, 5, and 6, and the corresponding computer simulations of these same experiments show that the anodized aluminum oxide remained intact, and there were no hot spots sufficient to cause ignition. However Figs. 2 and 3, and the corresponding computer simulation (Fig. 9) describe a probable ignition event.

In Figs. 2 and 3 one particle which impacted this target remained imbedded. This photograph clearly shows that surrounding this particle there is a raised, irregular ridge of target material. The corresponding computer simulation Fig. 9 shows a similar raised ridge of target material. The computer simulation shows that there are regions in the target where a hot spot occurred, and its absolute (computed) temperature is near the melting point of aluminum (931 K as opposed to 933 K). Further, the natural aluminum oxide film was disrupted and while it reestablishes itself rapidly, the

time duration of impact and temperature rise predict that molten aluminum was exposed to the ambient oxygen atmosphere. This is substantiated by Fig. 7 which shows that at the target temperature before impact, 550 K, nine out of ten experimental impact events resulted in ignition. It is apparent that the computer simulation provides a realistic model for particle-impact ignition of the bare aluminum target. Further the computer simulation of the behavior of the three different thicknesses of the anodized aluminum oxide is consistent with the experimental observations.

Figure 7 shows that between 570 K and 600 K there is an abrupt change in the susceptibility of bare aluminum targets to ignition; the probability falls to 50 percent. In the early work of Hunter and Fowle (1956) and consistently since, there has been recognition of the strong temperature dependency of the growth and nature of the natural aluminum oxide film. Hunter and Fowle identify this temperature range as the region where there is a transition between a thin (less than 10 Å) oxide barrier and a thick barrier (extent undefined). Under the experimental conditions, 570 K, 27.6 MPa pure oxygen pressure and at least ten minutes for film growth, there may be appreciable oxide film thickness developed. In fact Fig. 8 shows a distinct similarity of the 'bare' aluminum target and the 5 micron/10 micron anodized oxide targets. This suggests that the bare aluminum natural oxide film may have grown to this thickness at these experimental conditions.

The 50 micron anodized film, Fig. 6, is the only oxide coating which is clearly distinguishable at the level of magnification of these photographs. Figure 8 also shows that it provides significant protection against particle-impact ignition. Although there was no observed spalling of any of the coatings in the impact region, the 50 micron coating photograph suggests that this may have occurred. Likewise the computer simulation, which includes mass conservations, predicts that no spalling will occur under these experimental conditions.

CONCLUSIONS

The computer simulation successfully predicted the development of hot spots sufficient to cause ignition of the aluminum target. These hot spots were predicted to form adjacent to the crater caused by the impacting particle. The material properties of both the aluminum and the aluminum oxide used in the computer simulation were satisfactory for handling the temperature rise.

The anodized aluminum oxide films do provide ignition protection from particle impact. Experiments confirm this behavior. The computer simulation also gives results consistent with the experiments. As expected the 50 micron thick film provides the best protection against ignition by particle impact.

Finally, what may have appeared as an anomaly in the ignition characteristics of bare aluminum at 570 K is explained by the accelerated oxide film growth predicted due to the experimental conditions. This natural oxide film gave the same results as a 5 micron/10 micron anodized oxide film.

REFERENCES

Bahk, S., M. Gunaji, D. B. Wilson and J. M. Stoltzfus (1992). Modeling of Promoted Combustion Ignition Using Polymer Promoters. *WSTF Technical Report* (In preparation).

Bahk, S., D. D. Reeves, M.V. Gunaji, and J. M. Stoltzfus (1991). *Particle Impact Test on Anodized Aluminum*. Special Test Data Report, WSTF #90-24545. NASA White Sands Test Facility. Las Cruces, New Mexico.

Benz, F. J., R. E. Williams, and D. Armstrong (1986). Ignition of Metals and Alloys by High-Velocity Particles. In *Flammability and Sensitivity of Materials in Oxygen-Enriched Atmospheres*, (M.A. Benning, ed.), pp. 16-37. ASTM STP 910, Philadelphia, PA.

Bjorkman, M. D. and K. A. Holsapple (1987). Velocity Scaling Impact Melt Volume. *Int J Impact Engr.*, 5, 155-163.

Clark, A. F. and T. G. Hurst (1974). A Review of the Computability of Structural Materials with Oxygen. *AIAA Journal*, 12, 441-454.

Hunter, M. S. and P. Fowle (1956). Natural and Thermally Formed Oxide Films on Aluminum. *J. of Electrochemical Soc.*, 103, 482-485.

Johnson, G. R. and W. H. Cook (1983). A Constitutive Model and Data for Metals Subjected to Large Strains, High Strain Rates, and High Temperatures. In *Proceedings of Seventh International Symposium on Ballistics*. pp. 541-548. The Hague, The Netherlands.

Johnson, G. R. and T. J. Holmquist (1988). *Test Data and Computational Strength and Fracture Model Constants for 23 Materials Subjected to Large Strains, High Strain Rates and High Temperatures*. LA-11463-MS.

Kohn, B. J. (1969). *Compilation of Hugoniot Equations of State*. AFWL-TR-69-38.

Marsh, S. P. (1980). *LASL Shock Hugoniot DATA*. University Press, University of Berkeley, California.

Mellor, A. W. and I. Glassman (1965). A Physical Criterion for Metal Ignition. *Pyrodynamics*, 3, 43-64.

Reynolds, W. C. (1959). Investigation of Ignition Temperatures of Solid Metals. *NASA TND-182*. Washington, D.C.

Vinogrador, V. N. and I. B. Cherviakov (1984). Physical Mathematical Model of Interaction betw en Hard Spherical Particles and Metal Surfaces at High Strain Rates. *Inst Phys Conf Ser # 70 3rd Conf Mech Prop. High Rates of Strain*. Oxford, England.

Wegener, W. (1964) Investigation on the Safe Flow Velocity to be Admitted for Oxygen in Steel Pipe Lines. *Stall and Eisen*, 84, 469-475.

Zukas, J. A. (1987) *ZEUS Technical Manual, Computational Mechanics*.

Int. J. Impact Engng Vol. 14, pp. 73–84, 1993
Printed in Great Britain

0734-743X/93 $6.00+0.00
1993 Pergamon Press Ltd

AN ANALYTICAL MODEL OF HOLE SIZE IN FINITE PLATES FOR BOTH NORMAL AND OBLIQUE HYPERVELOCITY IMPACT FOR ALL TARGET THICKNESSES UP TO THE BALLISTIC LIMIT

JAY R. BAKER and MARIO A. PERSECHINO

B & P Associates, 2400 Butler Road
Beaverdam, Virginia 23015, (804) 448-3605

ABSTRACT

This paper presents, for the first time, a single comprehensive analytical model for the hole size produced by hypervelocity impact into finite plates. This model is based on experimental data for 2017 aluminum spheres impacting 2014, 2024 and 6061 aluminum plates.

The significance of this model is that it spans the entire range of target thickness from very thin to very thick, which makes it possible to determine when the impact conditions are those of thin target behavior (where the hole size increases with increasing target thickness and debris formation and damage is important) and when the impact conditions are those of thick target behavior (where the hole size decreases with increasing target thickness and the debris formation is significantly decreased). The model makes it clear that the target thickness that divides the thin target regime from the thick target regime is a function of velocity. This means that an impact configuration which exhibits thick target behavior at common experimental velocities could actually exhibit thin target behavior at velocities in the tens of kilometers per second such as that of meteroid impacts. This hole size model also includes the effects of oblique impact and computes both the major and the minor diameters of the hole.

This paper also raises, for the first time, the possibility that the commonly accepted models for crater diameter (and by implication those for penetration depth as well), which are taken to be a power function of velocity, might be wrong. Only a linear dependence on velocity for the crater diameter is consistent with the linear velocity dependence of this and all other accepted models of hole diameter in finite plates. If this is correct, it would raise questions about the validity of using any target damage computer models, that are based on the old crater modeling equations, to extrapolate to higher velocities.

INTRODUCTION

The analytical equations of this hole size model were constructed using an ad hoc process that gave a reasonable fit to the data while avoiding functions that would produce runaway results at the extreme values of the independent variables. It should therefore be recognized that, while these equations were not obtained by pure deduction from fundamental first principles of physics, nevertheless the physics of the impact process is inherent in the data itself and is therefore contained in the analytical model.

The basic equations of the hole size model, for both the major and minor diameters of an elliptical hole, are given by the following:

$$D_{minor}/d = (\alpha + \sigma v)\beta_L \tag{1a}$$

$$D_{major}/d = \phi D_{minor}/d \tag{1b}$$

where d is the projectile diameter, v is the projectile impact velocity, and α and σ are functions of the target thickness t/d and impact angle θ. The ballistic limit factor β_L, which is a function of t/d, v and θ, goes to zero for impact conditions near the ballistic limit and otherwise has a value of one. The shape factor ϕ, which is the ratio D_{major}/D_{minor}, is a strong function of v and θ but also has some dependence on t/d. For normal impact, where the hole is round, $D_{major} = D_{minor}$ so that $\phi = 1$. Note that both the hole diameter and the target thickness are normalised by dividing by the projectile diameter. This is based on the assumption that the impact process scales linearly with the projectile size.

COMPARISON OF EXPERIMENTAL AND ANALYTICAL RESULTS

Figure 1 shows a comparison of the hole size model (solid lines) with the experimental data points for normal impact in the target thickness domain. It can be seen that for small values of t/d (thin target regime) the hole size increases with increasing target thickness. For large values of t/d (thick target regime), the hole size decreases with increasing target thickness. The point at which the thin target regime ends and the transition region begins, as well as where the thick target regime begins, have never been clearly defined quantitatively. In addition, empirically determined equations have not previously been available for treating perforations in either the transition or the thick target regimes.

It is important to observe in Fig. 1 that the locations of the maxima of the curves shift steadily to higher values of t/d as the velocity increases from 4 to 8 km/s. Because this shift is not very large at common experimental velocities below 10 km/s, it has sometimes been assumed that the target thickness which separates thin target behavior from thick target behavior has a constant value. That this dividing line between thin and thick target behavior is actually a function of the impact velocity can be seen in Fig. 2 where the analytical model has been used to extrapolate the hole size to much higher velocities.

Figure 2 shows, for example, that for aluminum into aluminum the maximum hole size at 30 km/s occurs at a value of $t/d = 4$ compared to a value of $t/d = 1.3$ at 6 km/s. Although scaling to such high velocities cannot now be verified, the validity of the point being made, that the value of t/d at which D/d is a maximum increases steadily with increasing velocity, does not depend on the quantitative correctness of the extrapolation and none is implied.

The important point is that when scaling hole size with target thickness using previous models, which were developed for (and therefore only valid in) the thin target regime, it is essential to be certain that the impact configuration remains within the same target thickness regime. This is illustrated in Fig. 3 where the hole size model of this paper (solid line) is compared to the GM model (dashed line, Maiden *et al.*, 1963) along with experimental data points. It can be seen that the GM model diverges significantly from the data for $t/d \geq 1.0$ while the hole size model presented here continues to follow the data. Since the model presented in this paper is valid over the entire range of target thickness, from the thin target to the thick target regime, the concern about staying in a particular target thickness regime is removed.

For oblique impact the model describes both the major and minor diameters of the hole over the full range of obliquity from normal impact to ricochet. Figure 4 shows a comparison between the model and the experimental data for the major diameter of the hole as a function of the impact angle. Note that the model describes both the increase in the major diameter with obliquity and the subsequent sharp decrease as the effects of ricochet dominate the process. The effect of impact

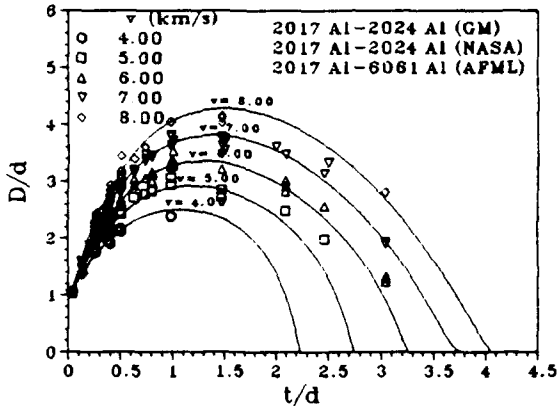


Fig. 1. Comparison of the hole size model and experimental data, in the target thickness domain, for the normal impact of 2017 Al into 2024 and 6061 Al at selected velocities.

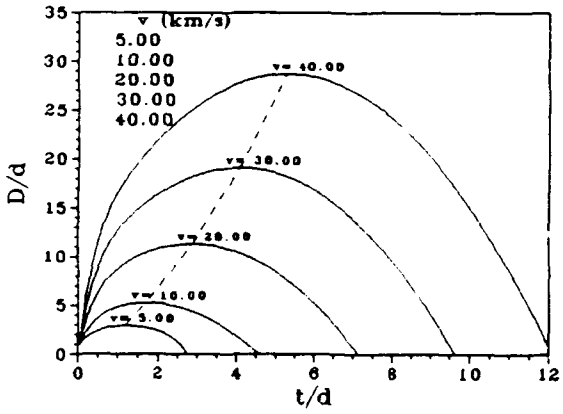


Fig. 2. Extrapolation of the hole size model, in the target thickness domain, for the normal impact of Al-Al at 5, 10, 20, 30 and 40 km/s.

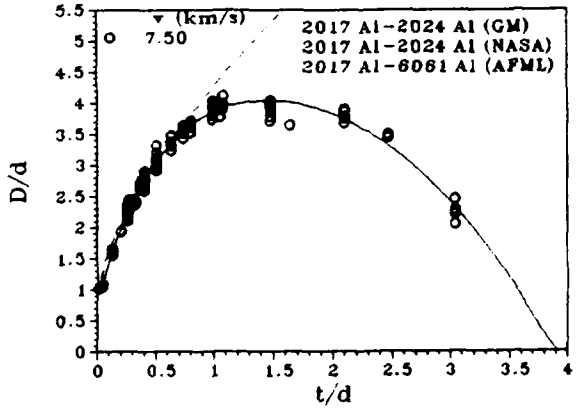


Fig. 3. Comparison of the hole size model (solid line), the GM model (dashed line), $D/d = 0.9 + 0.45v(t/d)^{2/3}$, and experimental data for normal impact at 7.5 km/s.

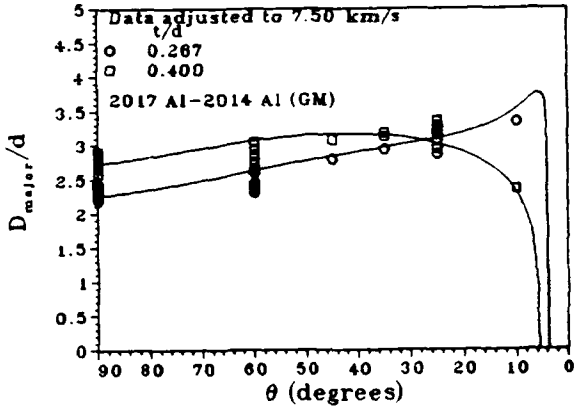


Fig. 4. The hole size model and experimental data for the major diameter, in the impact angle domain, for 2017 Al impacting 2024 Al at 7.5 km/s for $t/d = 0.267$ and 0.400.

angle on the minor diameter of the hole and a comparison of the model with the experimental data is shown in Fig. 5. Note that the minor diameter of the hole also increases somewhat with impact angle and has a maximum value for an impact angle of approximately 60 degrees. Although both Figs. 4 and 5 show good agreement between the model and the experimental data, it must be kept in mind that the equations for oblique impact were developed using data that had only two, relatively small values of target thickness. Consequently, more data is needed to properly validate the model over the full range of target thickness for oblique impact.

DEVELOPMENT OF THE HOLE SIZE MODEL

Normal Impact

Figures 6 and 7 show that the hole size data (Maiden *et al.*, 1963; Nysmith and Denardo, 1969, Carson and Swift, 1967; and Turpin and Carson, 1970), in the velocity domain, is a linear function of velocity and can therefore be fitted by an equation of the form

$$D/d = \alpha_n + \sigma_n v \tag{2}$$

The first step was therefore to find a straight line, least squares fit to the data for each value of t/d. Note that these straight line fits to the data are only intended to model the hole size in the high velocity regime and not in the low velocity regime where the effects of the ballistic limit become important (see the following section). The values for the slopes σ_n were then plotted as a function of t/d, as shown in Fig. 8. The model for the slopes (the solid line in Fig. 8) is given by the following function of target thickness:

$$\sigma_n = (\sigma_1 + \sigma_2 t/d)(1 - e^{-\sigma_3(t/d-\sigma_4)}) \tag{3}$$

where the constants, $\sigma_1 = 0.26$, $\sigma_2 = 0.15$, $\sigma_3 = 3.20$ and $\sigma_4 = 0.035$, were obtained using a trial and error process to find the best fit to the data. Note that since σ_n is zero for $t/d \leq 0.035$, it follows that the hole size is independent of velocity for very thin targets, i.e., for $t/d \leq 0.035$.

The least squares fitting process was then repeated for each value of t/d, using the corresponding slope σ_n from the slope model in Fig. 8, to find the values of the intercepts α_n. The resulting values of α_n are plotted as a function of t/d in Fig. 9. The intercept model (the solid line in Fig. 9) is given by the following functions of target thickness:

$$\alpha_n = 1 + \alpha_1(1 - e^{-\alpha_2 t/d}) \qquad \text{for } t/d \leq 0.70 \tag{4a}$$

$$\alpha_n = 1 + \alpha_1 - (\alpha_3 + \alpha_4(t/d - 0.07))(t/d - 0.07) \qquad \text{for } t/d > 0.70 \tag{4b}$$

where the constants $\alpha_1 = 0.085$, $\alpha_2 = 18.$, $\alpha_3 = 0.313$ and $\alpha_4 = 0.62$, were obtained using a trial and error process to find the best fit to the data. Because of the complex behavior of α_n it had to be fitted piecewise in two parts. A single function, if one could be found, would be preferrable.

Effects of the Ballistic Limit

Although there is virtually no hole size data in the regime where the impact velocity v approaches the ballistic limit, nevertheless it is logically necessary that the hole size must depart from its linear behavior and go to zero as the velocity decreases to the ballistic limit velocity v_L. This means that (2) must be multiplied by a ballistic limit function, β_L, which will go to zero as v approaches v_L and will rise gradually to a value of one as v rises above v_L. The following function for β_L has the desired properties:

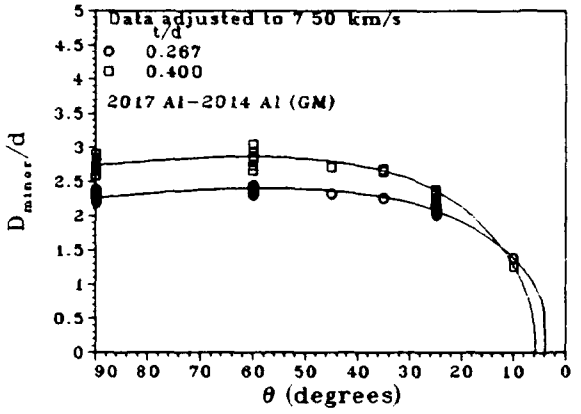


Fig. 5. The hole size model and experimental data for the minor diameter, in the impact angle domain, for 2017 Al impacting 2024 Al at 7.5 km/s for t/d 0.267 and 0.400.

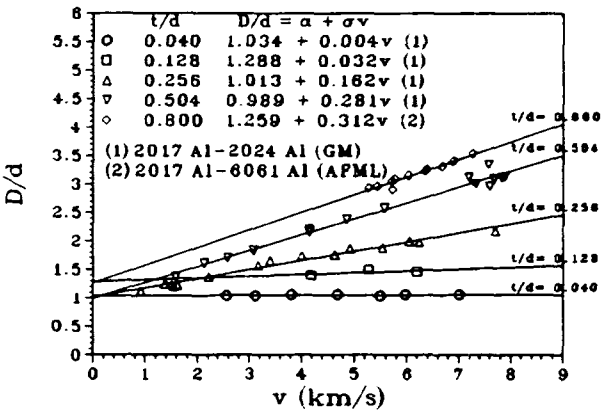


Fig. 6. Linear least squares fit to the experimental hole size data, in the velocity domain, for the normal impact of 2017 Al into 2024 and 6061 Al for target thicknesses of $t/d < 1$.

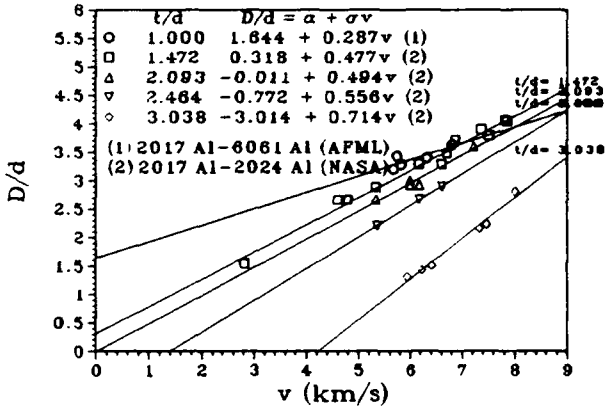


Fig. 7. Linear least squares fit to the experimental hole size data, in the velocity domain, for the normal impact of 2017 Al into 2024 and 6061 Al for target thicknesses of $t/d > 1$.

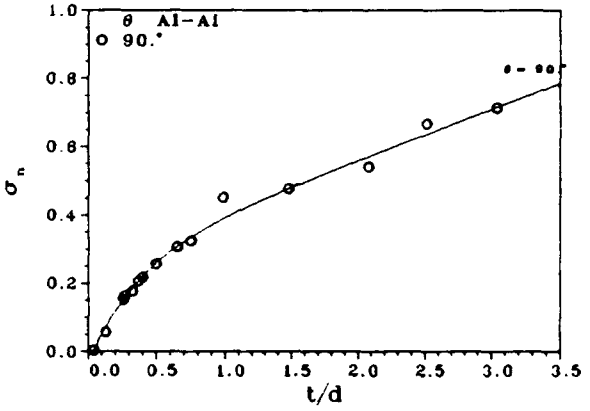


Fig. 8. Slope values σ_n *vs* t/d for normal impact of Al-Al from Figs. 6 and 7 and the analytical function (solid line) fitted to those values.

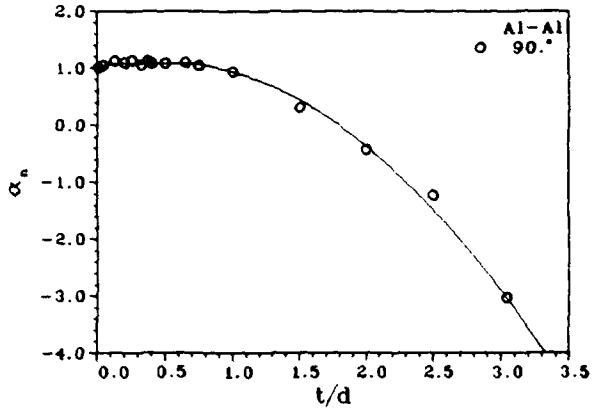


Fig. 9. Intercept values α_n *vs* t/d for normal impact of Al-Al and the analytical function(s) (solid line) fitted to those values.

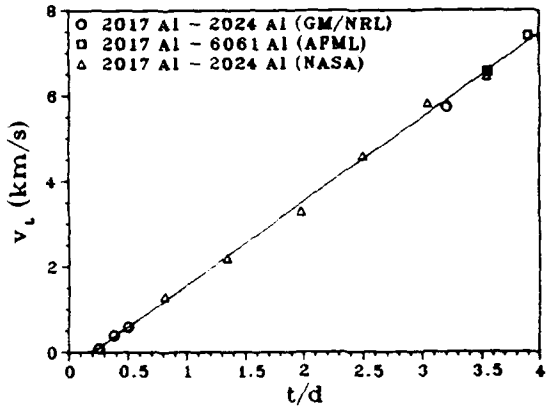


Fig. 10. Experimental values of the ballistic limit velocity v_L *vs* t/d for the normal impact of Al-Al and the equation(s) fitted to the data (solid line).

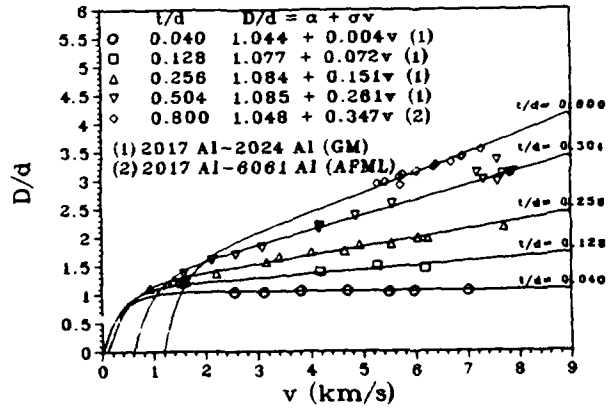


Fig. 11. Comparison of the hole size model, including the ballistic limit factor, and the experimental data for normal impact of 2017 Al into 2024 and 6061 Al for $t/d < 1$.

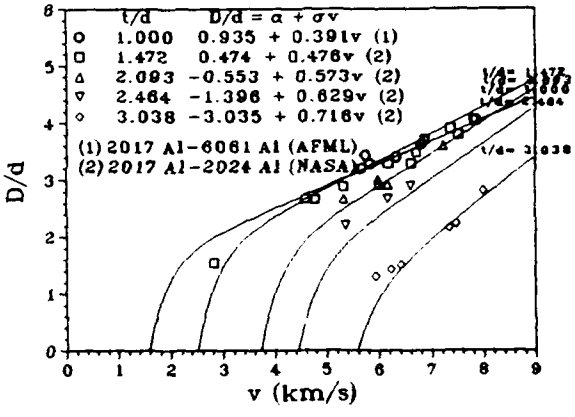


Fig. 12. Comparison of the hole size model, including the ballistic limit factor, and the experimental data for normal impact of 2017 Al into 2024 and 6061 Al for $t/d \geq 1$.

$$\beta_L = 1 - e^{-3(v - v_L)} \tag{5}$$

so that

$$D/d = (\alpha_n + \sigma_n v)\beta_L. \tag{6}$$

In the absence of data in the near ballistic limit region, the value of 3 for the coefficient in the exponential term was selected somewhat arbitrarily so that the function asymptotes neither too quickly nor too slowly to a value of one.

The available ballistic limit data (Maiden *et al.*, 1963; Fish and Summers, 1965; and Swift and Carson, 1967) shows that the ballistic limit velocity is a linear function of the target thickness (Fig. 10) which is given by

$$v_L = -0.393 + 1.964t/d \qquad \text{for } t/d \geq 0.25 \tag{7a}$$
$$v_L = (e^{19.49t/d} - 1)/1323.6 \qquad \text{for } t/d < 0.25. \tag{7b}$$

Note that (7*a*) gives negative values for the ballistic limit velocity when $t/d < 0.2$. Since this is physically unrealistic, the exponential function given by (7*b*) was introduced for $t/d < 0.25$ so that the ballistic limit velocity will go to zero as the target thickness goes to zero. The effect of β_L on the curves in Figs. 6 and 7 is shown in Figs. 11 and 12.

Oblique Impact

The effect of oblique impact on the hole size was obtained first for the minor diameter of the hole using the data of Warnica and Gehring (1964) for 2017 aluminum spheres impacting 2014 aluminum plates with t/d of 0.267 (Fig. 13) and t/d of 0.400.

Since the minor diameter is also a linear function of velocity, then (6) can also be used for D_{minor}/d, i.e.,

$$D_{minor}/d = (\alpha + \sigma v)\beta_L \tag{8}$$

The first step in building the oblique impact model was to find the straight line, least squares fit to the D_{minor}/d vs velocity data for impact angles of 60^o and 25^o. The values for the slopes σ were then compared, in Fig. 14, to the normal slope model σ_n from (3). From this it was determined that the effect of the impact angle on the slope σ could be obtained by multiplying the normal slope model σ_n by a function of impact angle given by the following equation:

$$\sigma = \sigma_n(1 - e^{-\sigma_5\theta/(\sigma_6 - \theta)}) \tag{9}$$

where the values of the constants, $\sigma_5 = 6.90$ and $\sigma_6 = 185^o$, were obtained using a trial and error process to find the best fit to the data points.

The process was then repeated using values of the slope from the oblique slope model to find the corresponding intercepts α from a linear, least squares fit of the minor diameter hole data. The resulting values of α were then compared in Fig. 15 to the normal intercept model, α_n from (4). From this it was determined that the effect of impact angle on the intercept could be obtained by adding a function α_θ to the normal intercept model as given by the following equations:

$$\alpha = \alpha_n + \alpha_\theta \tag{10a}$$
$$\alpha_\theta = \alpha_5(1 - e^{-\alpha_6(90^o - \theta)/\theta}) + (1 - 1/sin^n(90^o\theta/35^o)) \tag{10b}$$

where the values of the constants, $\alpha_5 = 0.258, \alpha_6 = 2.65$ and $n = e^{1.13t/d} - 1$, were obtained using a trial and error process to find the best fit to the data points. Note that the second term in (10*b*), which can be associated with the effect of ricochet, is only included when $\theta \leq 35^o$.

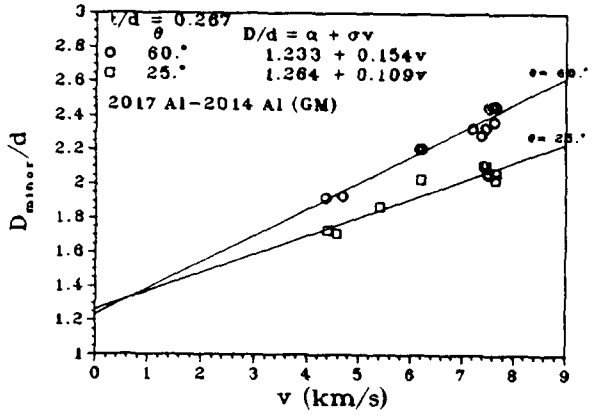


Fig. 13. Linear least squares fit to the experimental D_{minor}/d data, in the velocity domain, for the oblique impact of 2017 Al into 2014 Al for $t/d = 0.267$ and selected impact angles.

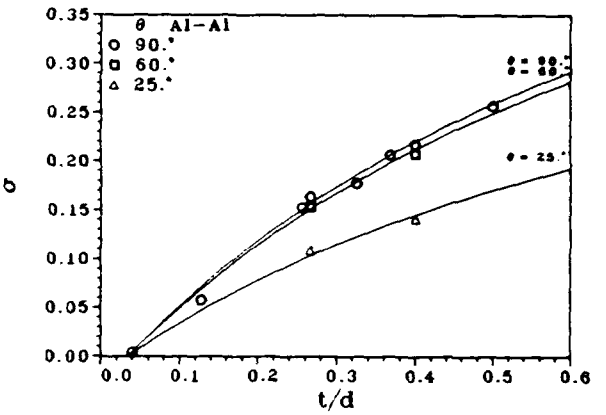


Fig. 14. The slope values σ for oblique Al-Al impact compared to the normal slope model.

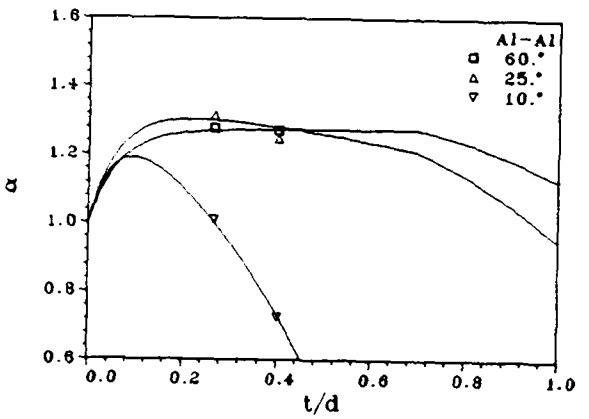


Fig. 15. The intercept values α for oblique Al-Al impact compared to the normal intercept model.

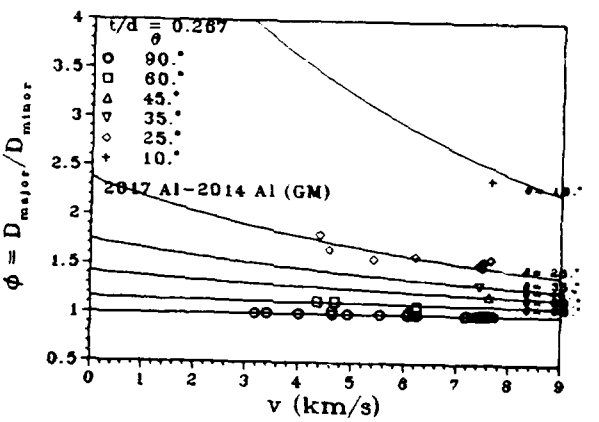


Fig. 16. Comparison of the shape factor, $\phi = D_{major}/D_{minor}$, and the experimental data for 2017 Al impacting 2014 Al for $t/d = 0.267$ and different values of impact angle.

One final detail of the oblique intercept model is that D_{minor}/d must logically go to a value of one as t/d goes to zero. In order for this to be true, the intercept α must go to one as t/d goes to zero. Since α_n already exhibits this behavior, then the required condition will be met if the α_θ term in (10a) goes to zero as t/d goes to zero. This is accomplished by multiplying α_θ by an appropriate exponential function such that (10a) becomes

$$\alpha = \alpha_n + \alpha_\theta(1 - e^{-15t/d}) \tag{11}$$

where the value of 15 for the coefficient in the exponential was selected so that (11) would reduce to (10b) for values of t/d in the range of the experimental data.

The model for the major diameter of the hole is obtained from that for the minor diameter by using the following equation:

$$D_{major}/d = \phi D_{minor}/d \tag{12}$$

where ϕ is the shape factor, the ratio D_{major}/D_{minor}. Figure 16 shows the experimental data for ϕ vs velocity for $t/d = 0.267$. The data suggests that ϕ starts out at some value greater than one at zero velocity and then asymptotically approaches a value of one as the velocity increases. Furthermore the initial value of ϕ at zero velocity seems to increase rapidly with decreasing impact angle, very much like the function $1/sin\theta$. The desired function for ϕ is therefore one that starts at $1/sin\theta$ and then decreases asymptotically to a value of one as the velocity goes to inifinity. Note that this behavior of asymptoting to a value of one with velocity means that the hole becomes more nearly round as the velocity increases.

The function for ϕ, having the desired fit to the data (solid lines in Fig. 16), is given by

$$\phi = 1 + (1/sin\theta - 1)e^{-\lambda v} \tag{13}$$

where λ (at least for the two target thicknesses for which there is data) is a linear function of t/d, with a slope s, given by

$$\lambda = s(t/d - 0.035) \tag{14a}$$

$$s = s_1(1 - \theta/90^o) - s_2(1 - sin(90^o\theta/35^o)) \tag{14b}$$

where $s_1 = 0.84$ and $s_2 = 0.18$. Note th t the second term in (14b) is added only for $\theta \leq 35^o$. The parameter λ is made to go to zero for $t/d = 0.035$ in order to be consistent with (3) in which σ_n goes to zero at that same target thickness so that the diameter of the hole does not depend on the impact velocity for $t/d \leq 0.035$.

Because the equations for λ were based on data for only two relatively thin targets, any calculation of the major diameter of the hole for thicker targets must be treated with caution until oblique impact data for thick targets becomes available with which to either confirm or revise the model.

Figure 17 shows a comparison of the model (solid line) and the experimental data for the major diameter in the velocity domain for $t/d = 0.267$. Figures 18 and 19 show the results of the model for both the major and minor diameters in the target thickness domain. The comparison between the model and the data in in the impact angle domain has already been shown in Figs. 4 and 5.

CONFLICT WITH CRATER MODELS

In the model for hole diameter presented in this paper (as well as other such models proposed in the past), the hole diameter is a linear function of the velocity. Empirical studies of hole size have determined that the hole diameter cannot be larger than the front surface diameter of a crater formed by the same projectile impacting a semi-infinite target of the same material at the same velocity (Hermann and Wilbeck, 1987). Furthermore past studies of the cratering process have concluded that the crater penetration depth is a power function of velocity with an exponent between 1/2 and 2/3 (Hermann and Wilbeck, 1987). Since, in the hypervelocity regime, the crater

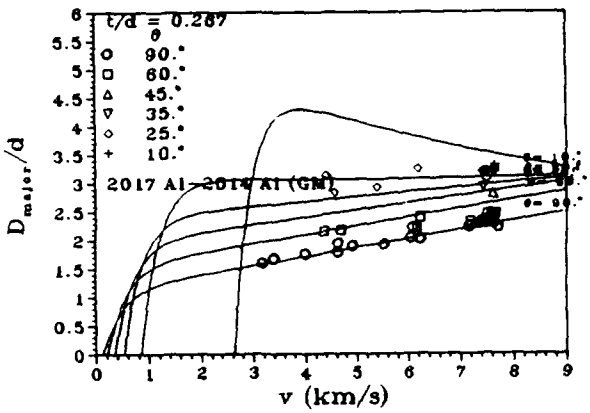


Fig. 17. Comparison of the hole size model for D_{major}/d and the experimental data for 2017 Al impacting 2014 Al for $t/d = 0.267$ and different values of impact angle.

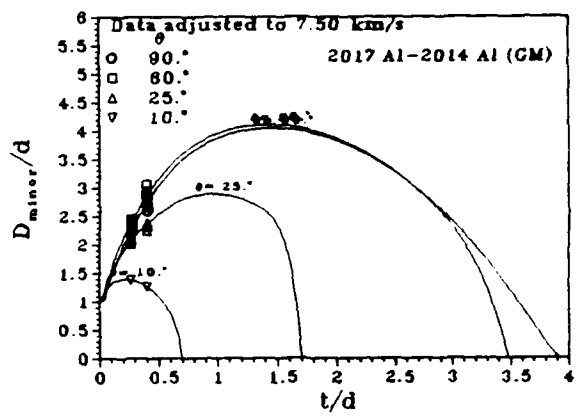


Fig. 18. Comparison of the hole size model for D_{minor}/d and the experimental data for 2017 Al impacting 2014 Al at 7.5 km/s for different values of impact angle.

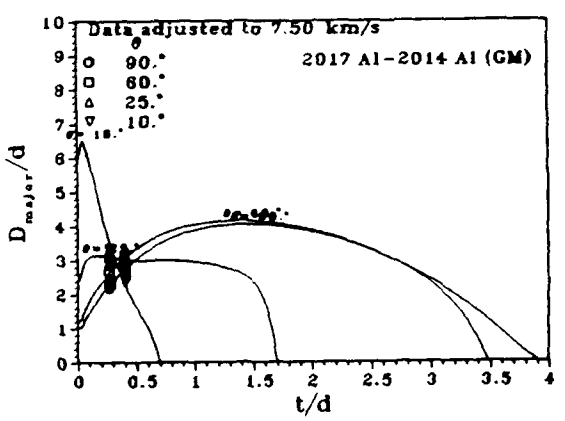


Fig. 19. Comparison of the hole size model for D_{major}/d and the experimental data for 2017 Al impacting 2014 Al at 7.5 km/s for different values of impact angle.

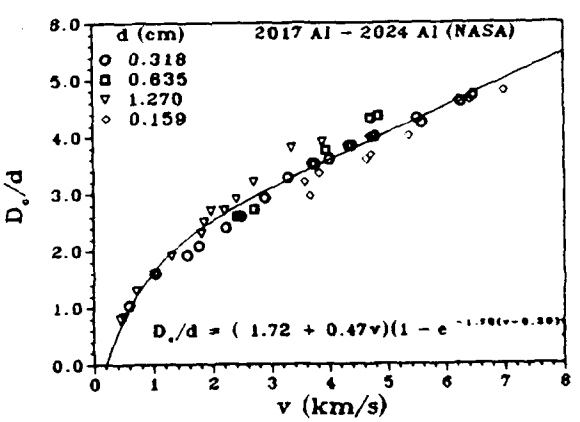


Fig. 20. Experimental data for crater diameter *vs* velocity for 2017 Al impacting 2024 Al and the proposed equation (solid line) fitted to the data.

is nearly hemispherical (particularly for like material impact) and that shape remains constant with velocity, it follows that the crater diameter must vary with velocity in the same manner as the penetration depth. Therefore the crater diameter should also be a power function of velocity with an exponent between 1/2 and 2/3.

Thus there is an unavoidable conflict between the hole diameter models and the crater diameter models at very high velocities. Although the hole diameter models start out with smaller values than those of the crater diameter models in the range of the experimental velocities, as the velocity continues to increase there must come a point, because of the difference in the velocity exponents, where the hole diameter will exceed the corresponding crater diameter.

An obvious resolution of this conflict would be for both the crater and the hole size models to have the same velocity dependence. A preliminary examination of the crater data from Denardo and Nysmith (1964) shows that it could be equally well fitted by a linear function of velocity of the same form as (6) (solid line in Fig. 20). Since it is really beyond the scope of this paper to pursue this issue, it is important to at least call attention here to the need to further investigate the possibility that both the crater diameter and the crater depth are a linear function of the impact velocity in the hypervelocity regime.

CONCLUSIONS

The analytical methods presented in this paper, which were used to develop the unified description of hypervelocity impact hole size in finite thickness plates, have produced the following results:

1. A single equation for the diameter of the hole that spans the entire range of target thickness from very thin, through the transition region between thin and thick targets and finally ending at the ballistic limit. This model makes it possible to determine when the impact conditions are those that produce thin target behavior (where the hole size increases with increasing target thickness and debris formation and damage is important) and when the impact conditions are those that produce thick target behavior (where the hole size decreases with increasing target thickness and the debris formation is significantly decreased).

2. The quantifying of the target thickness and impact velocity at which the hole diameter reaches a maximum value. The model makes it clear that the target thickness which divides the thin target regime from the thick target regime is a function of velocity which means that an impact configuration which exhibits thick target behavior at experimental velocities below 10 km/s could very well exhibit thin target behavior when the velocity is tens of kilometers per second.

3. An analytical hole diameter model for oblique impact (at least for very thin targets with $t/d \leq 0.400$) that includes the onset of ricochet and the cessation of perforation at the ballistic limit. Hole size data for $t/d > 0.400$ is needed to either validate or revise the oblique model for thick targets.

4. Since most of the available impact data was for 2017 Aluminum spheres impacting 2014, 2024 and 6061 Aluminum plates, the model presented here is specifically valid for that combination of materials, however it is important to recognize that the methodology and the form of the equations should be applicable to other combinations of projectile and target materials as well.

5. The recognition that the commonly accepted models of crater diameter, which are taken to be a power function of velocity, might be wrong. Only a linear dependence on velocity for the crater diameter (and by implication the penetration depth as well) is consistent with the linear velocity dependence of this and all other accepted models of hole diameter in finite plates. This possibility directly affects the validity of using any target damage models, which are based on the old crater modeling equations, to extrapolate to higher velocities, and therefore requires further investigation.

REFERENCES

Carson, J.M. and Swift, H.F. (1967). Hole Diameters in Thin Plates Perforated by Hypervelocity Projectiles. Air Force Materials Laboratory, *AFML/MAY-TM-67-9.*

Denardo, B.P. and Nysmith, C.R. (1964). Momentum Transfer and Cratering Phenomena Associated with the Impact of Aluminum Spheres into Thick Aluminum Targets at Velocities to 24,000 feet per second. NASA/ARC. *NASA TM X-54,046.*

Fish, Richard H. and Summers, James L. (1965). The Effects of Material Properties on Threshold Penetration. NASA/ARC. *Proceedings of the Seventh Hypervelocity Impact Symposium, Vol. VI.*

Halperson, S.M. (1963). Some Phenomena Associated with Impacts into Aluminum. Naval Research Laboratory. *Proceddings of the Sixth Hypervelocity Impact Symposium, Vol II Part 2,* p.525.

Hermann, W. and Wilbeck, J.S. (1987). Review of Hypervelocity Penetration Theories. Proceedings of the 1986 Hypervelocity Impact Symposium. *International Journal of Impact Engineering, Vol.5,* pp. 307-322.

Maiden, C.J., Gehring, J.W. and McMillan, A.R. (1963). Final Report on Investigation of Fundamental Mechanism of Damage to Thin Targets by Hypervelocity Projectiles. General Motors, *GM/DRL TR 63-225.*

Nysmith, C.R. and Denardo, B.P. (1969). Experimental Investigation of the Momentum Transfer Associated with Impact into Thin Aluminum Targets. National Aeronautics and Space Administration, *NASA TN-D-5492.*

Schonberg, W.P. (U. of Alabama) and Taylor, R.A. (NASA/MSFC) (1989a). Oblique Hypervelocity Impact Response of Dual-Sheet Structures. National Aeronautics and Space Administration, *NASA-TM-100358.*

Schonberg, W.P. (U. of Alabama) and Taylor, R.A. (NASA/MSFC) (1989b). Penetration and Ricochet Phenomena in Oblique Hypervelocity Impact. *AIAA Journal, Vol.27, No.5.*

Schonberg, W.P. (1990). Hypervelocity Impact Response of Spaced Composite Material Structures. U. of Alabama. Proceedings of the 1989 Hypervelocity Impact Symposium. *International Journal of Impact Engineering, Vol.10*

Swift, H.F. and Carson, J.M. (1967). Ballistic Limits of 6061-T6 Aluminum Bumper Systems. Air Force Materials Laboratory, *AFML-TR-67-324.*

Turpin, W.C. and Carson, J.M. (1970). Hole Growth in Thin Plates Perforated by Hypervelocity Pellets. Air Force Materials Laboratory, *AFML-TR-70-83.*

Warnica, R.L. and Gehring, J.W. (1964). Hypervelocity Impact Experiements. General Motors, *GM/DRL TR 64-41* (declassified from Secret after 12 years).

Int. J. Impact Engng Vol 14, pp.85–93, 1993
Printed in Great Britain

0734-743X/93 $6.00+0.00
Pergamon Press Ltd

PENETRATION OF HARD LAYERS BY HYPERVELOCITY ROD PROJECTILES

S. J. BLESS and C. E. ANDERSON, JR.

Institute for Advanced Technology,
The University of Texas at Austin, Austin, Texas 78759

Southwest Research Institute,
P. O. Drawer 28510, San Antonio, Texas 78228

ABSTRACT

The penetration resistance of hard layers, such as ceramics and hardened steels, struck by high velocity long rod projectiles can be characterized by the depth of penetration (DOP) test. The DOP test can be used to calculate average penetration resistance, which can be expressed as R_T. The tests can also be used to compute differential efficiency. For hard materials, these values differ markedly from those for conventional armor steel (RHA). Implications for the effectiveness of hypervelocity penetrators are that the optimum velocity for energy efficient penetration will be much higher for hard materials than for RHA. Furthermore, ceramics will continue to substantially outperform armor steels, while high hardness steels will lose their relative advantages against long rod projectiles above 3 km/s.

INTRODUCTION

Bless, et al., (1987) investigated the response of ceramic tiles to short hypervelocity projectiles and found that penetrator effectiveness increased with velocity. The case of long rod projectiles was treated by Frank and Zook (1987), who showed that the functional form of penetration by long rods into most materials implied that there was an optimum velocity at which penetration is maximized, assuming projectile shape and energy are held constant. Several cases were discussed for which the optimum velocity was near 2 km/s. This work has led several research teams working on high velocity penetrators to focus on alternatives to long rods, e.g., Orphal et al, 1992. The purpose of this paper is to point out that the optimum velocity identified by Frank and Zook (1987) was particular to rolled homogeneous armor (RHA) and similar hardness steels (neighborhood of BHN 270), and that much higher optimum velocities are expected from harder barriers.

We analyze penetration of materials by high velocity rods by using steady state theory, develop by Tate (1967) and others and discussed in detail by Anderson and Walker (1991). An important advantage of this analysis is that the resistance of a target to penetration is described by a single effective strength parameter, R_T.

Very high-velocity penetration of semi-infinite targets is only approximately described by the Tate theory, largely because nonsteady processes account for considerable penetration after completion of the steady-state process (Anderson, et al., 1993). For example, Fig. 1 illustrates the discrepancy between steady-state theory and penetration data for RHA, using the value of R_T derived from penetration rate measurements (Hauver, 1992a). It is noteworthy that since the difference between the steady-state model [based on Tate (1967)] and data does not increase with velocity, the discrepancy cannot be readily accounted for by terminal cratering effects, which normally have a velocity to the 2/3 power dependence, e.g., Christman and Gehring (1966). Nevertheless, the Tate model provides the correct trends even if the quantitative numbers do not agree exactly with experimental values.

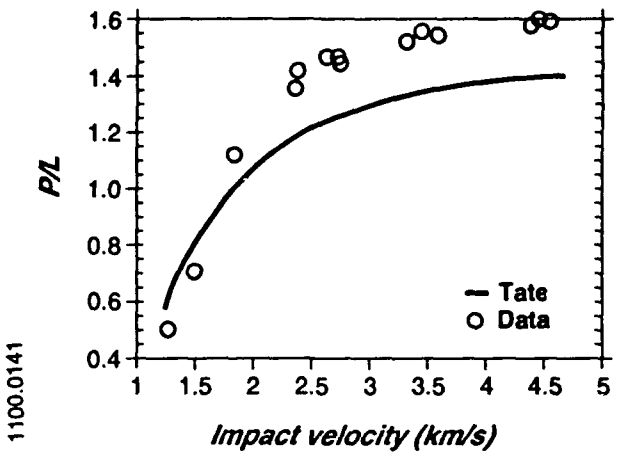


Fig. 1 Comparison of Tate (1967) analysis and data from Silsby [11] for tungsten rods into armor steel. P/L is penetration divided by length.

On the other hand, most proposed applications of hard materials are layered designs in which the hard material is sandwiched between RHA or structural materials. Thus, penetration of layers of hard materials is more relevant for armor design than penetration of semi-infinite materials. Tate theory is more accurate for layers because effects due to deceleration are relatively less important.

The depth of penetration (DOP) test is very useful for evaluating armor layers. An armor element or layer is placed on a substrate and struck with a projectile that penetrates through into the substrate. As is now well known, the differential efficiency of a layer relative to a substrate is given by the equation:

$$e_\Delta = \frac{W_{Ref} - W_R}{W_C}$$

where W_{Ref} is the penetration density (penetration times density) in the substrate with no armor layer, W_R is the penetration density below the armor test layer, and W_C is the arial density of the test layer. Thus, for example, when the differential efficiency is two, the test material is equivalent in penetrator stopping resistance to a layer of the substrate that is twice as heavy. The reference material for differential efficiency is usually RHA.

R_T can be computed by several different methodologies. These methodologies are summarized in the Appendix, along with limitations of their use. For the purposes of this paper, R_T is primarily calculated by two methods, both of which use DOP experiments.

DEFINITION OF PROBLEM

Our first interest is the optimum velocity for penetration by a constant-shape constant-energy projectile. The numerical values provided by Frank and Zook (e.g., length-to-diameter ratio) were for RHA. According to Hauver, the steady state value of R_T for RHA is 53 kbar. Cavity expansion analysis predicts that R_T is proportional to flow stress, which is in turn proportional to Brinell hardness. Mil-spec 46100 (high hard) steel is 1.9 times harder than RHA, so the value of R_T for this material should be about 100 kbar. Harder steels are also available that may have higher R_T values. Therefore, we want to extend the Frank and Zook analysis of penetration of steel to values of R_T over 100 kbar. We will use conventional steady state theory, which, as discussed above, is reasonably accurate for penetration of layers.

Ceramics have lower densities and similar R_T values to armor steels. In this analysis, we will use (ρ_t = 3.2 g/cm^3 (target density), which is in the mid-range of armor ceramics. Values of R_T for ceramics penetrated by rods vary from about 40 to 110 kbar.

Moreover, R_T values for ceramics may depend on impact conditions. The strength of some ceramics, like titanium diboride and aluminum nitride, is pressure dependent (Rosenberg, et al., 1992); strength, and hence R_T, may double over the pressure range 100 to 200 kbar, which loosely corresponds to impact velocities of 3 to 5 km/s. Likewise, the strength of these ceramics may be strongly affected by impact face confinement (Hauver, 1992a, Bless, et al.,1992). Other ceramics, such as B_4C, have been shown to pressure soften (Kipp and Grady, 1989). Kozhushko, et al., 1991 have postulated a dramatic change in R_T values when u transcends C_F, the maximum crack front speeds in ceramics. Values of C_F in ceramics are said to be 3 to 4 km/s. Values of R_T for $u > C_F$ may exceed 300 kbar.

Thus, as regards ceramics, it is worthwhile to extend Frank and Zook's analysis to case of R_T of over 300 kbar for target densities of about 3.2 g/cm^2, and for cases where R_T depends on dynamic pressure or penetration velocity.

Hauver (1992b) has observed that R_t decreases during penetration of very thick ceramic tiles. In this paper, which treats layers, we ignore this effect. We also limit our analysis to tungsten alloy rods, for which ρ_p (projectile density) = 17.4 g/cm^3, and Y_p (projectile strength) = 18 kbar (1.8 GPa).

OPTIMUM PENETRATION VELOCITIES

We first consider the case of a steel layer. We use conventional Tate theory (including projectile deceleration) to compute the scaled penetration, P/L. We convert this to the case of a constant-energy constant-shape rod by multiplying by $(v_o/v)^{2/3}$. The reference velocity, v_o, was taken as 1.6 km/s. Fig. 2 shows penetration as a function of v. As noted by Frank and Zook, there is an optimum velocity for each R_T value. However, the optimum becomes much broader for large R_T values. Fig. 3 shows the variation of the optimum velocity with R_T. It can be seen that for high hardness steels, the optimum velocity increases to over 3 km/s.

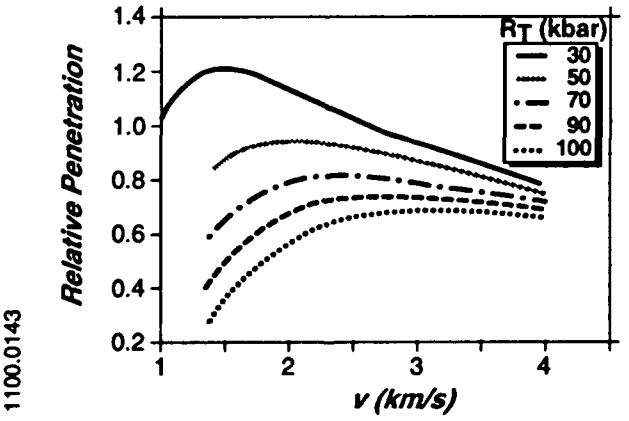


Fig. 2. **Penetration as a function of velocity for constant-shape constant-energy long rod striking steel.**

The same calculations were carried out for a generic 3.2 g/cm^2 ceramic. This calculation was only carried out to R_T = 200 kbar, because for higher values the maximum became so broad the concept of optimum penetration velocity had little meaning. The results are also shown in Fig. 3. For ceramics, the optimum velocity increases steadily with increasing target resistance. Over the range that is probably of greatest application, $60 < R_T < 90$ kbar, the optimum velocity increases from about 2.6 to 3.4 km/s.

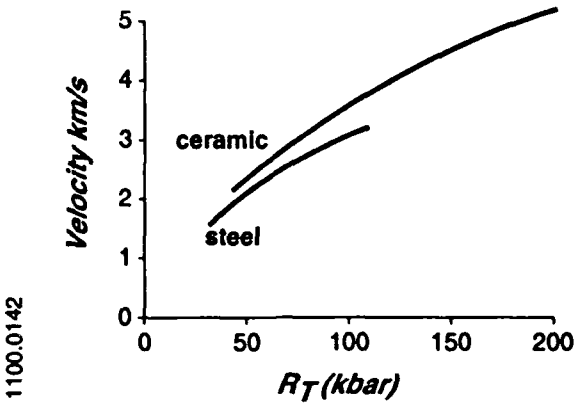


Fig. 3. **Velocity for maximum long rod penetration as a function of target strength parameter.**

These results are not substantially altered by step increases in R_T occurring when $u > C_F$, for which the maximum in the p/L vs. v curve is slightly drawn out. However, if materials of substantially lower C_F values were examined, the result would be to shift the optimum velocity to lower values. Increases in R_T due to higher dynamic pressure will have a similar effect in depressing optimum velocity values.

OPTIMUM ARMOR

Relative efficiency will also be a function of impact velocity. Fig. 4 is a graph of the variation of efficiency predicted for hypervelocity rods striking layers. The efficiency of RHA is unity by definition. The efficiency of high hardness steel (R_T = 90 kbar) decreases, so that by 3 km/s, there is little advantage to this material. Ceramics also decrease in efficiency. As velocity becomes very high and penetration approaches the hydrodynamic limit, the efficiency of ceramics will approach $(\rho_{RHA}/\rho_{ceramic})^{1/2} = 1.56$. Thus, ceramics will remain effective, but for hypervelocity they are less effective, and thus may not be worth their additional cost.

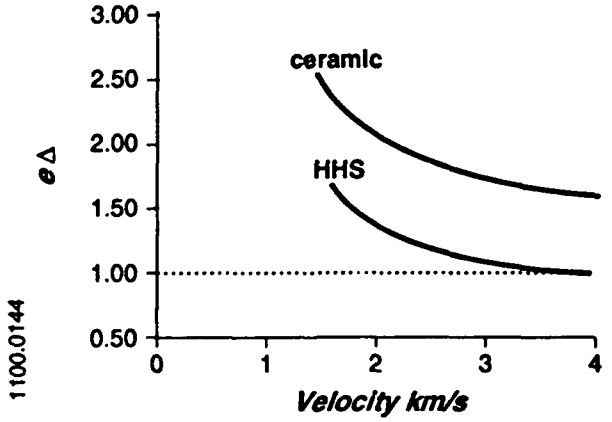


Fig. 4. **Efficiency of armors as a function of impact velocity for long tungsten-alloy rods. HHS is a steel with R_T = 90 kbar, the ceramic example is for R_T = 60 kbar.**

SUMMARY

We have shown how DOP tests can be combined with Tate theory to predict the response of layers of very hard materials to hypervelocity impact. The optimum velocity for penetration, which is about 2 km/s for armor steel, increases substantially for these materials. Selection of armor for hypervelocity projectiles should favor ceramic armor over high hardness steels.

REFERENCES

C. E. Anderson, Jr., and B. L. Morris, "The Ballistic Performance of Confined Al_2O_3 Ceramic Tiles," *Int'l J. Impact Eng.*, **12**, 167-188, 1992.

C. E. Anderson, D. L. Littlefield, J. D. Walker, "Long-Rod Penetration, Target Resistance, and Impact", *Proc. 1992 Hypervelocity Impact Symp.*, Nov. 17-19, 1992.

S. Bless, Z. Rosenberg, and B. Yoon, "Hypervelocity Penetration of Ceramics," *Int. J. Impact Eng.*, **5**, 165-171, 1987.

S. J. Bless, M. Benyami, L. S. Apgar, and D. Eylon, "Conditions for Impenetrability of Ceramic Impact SUSI 92, Portsmouth, UK, June 16 - 18, 1992. Targets Struck by High Velocity Tungsten Long Rods," *Proc. Conf. Structures Under Shock* and M. Burkett, private communication, 1992.

D. R. Christman and J. W. Gehring, "Analysis of High-Velocity Projectile Penetration Mechanics," *J. Apply Phys.*, **37**, 1579-1587, 1966.

K. Frank and J. Zook, "Energy-Efficient Penetration and Performation of Targets in the Hypervelocity Regime," *Int. J. Impact Engng.*, **5**, 277-284, 1987.

W. Gooch, private communication, 1992.

G. Hauver, private communication, 1992a.

G. Hauver, "Variation of Target Resistance During Long Rod Penetration into Ceramics," *13th Int'l Symp. Ballistics*, Stockholm, Sweden, June 1 - 3, 1992b.

M. E. Kipp, and D. E. Grady, "Shock Compression and Release in High Strength Ceramics," *Sandia Report SAND-89-1461*, July 1989.

A. H. Kozhushko, I. I. Rykova, and A. B. Sinani, "Resistance of Ceramics to Penetration at Impact Velocities above 5km/s," *J. de Physique IV*, **C3**, 117-122, 1991.

S. Mariano and P. Woolsey, "Alternative Test Method for Ballistic Performance Ranking of Armor Ceramics," *Fifth TACOM Armor Coordinating Conference*, Monterey, CA, March 7 - 9, 1989.

D. L. Orphal, C. E. Anderson, R. R. Franzen, J. D. Walker, P. N. Schneiderwind, M. E. Majerus, "Impact and Penetration by L/D $\leq$ 1 Projectiles", *Proc. 1992 Hypervelocity Impact Symp.*, Nov. 17-19, 1992.

Z. Rosenburg and J. Tsaliah, "Applying Tate's Model for the Interaction of Long Rod Projectiles with Ceramic Targets," *Int. J. Impact Eng.*, August 1989.

Z. Rosenburg, N.S. Brar, and S. J. Bless, "Shear Strength of Titanium Diboride under Shock Loading Measured by Transverse Manganin Gauges," *Shock Waves in Condensed Matter*, 1991, Elsevier, 1992.

G. Silsby, "Penetration of Semi-Infinite Steel Targets by Tungsten Long Rods at 1.3 to 4.5 km/s," *8th Int'l. Symp. Ballistics*, Orlando, FL, October 1984.

A. Tate, "A Theory for the Deceleration of Long Rods After Impact," *J. Mech. Phys. Solids*, **15**, 387-399, 1967.

P. Woolsey, "Ceramic Materials Screening by Residual Penetration Ballistic Testing," *13th Int'l Symp. Ballistics*, Stockhold, Sweden, 1-3 June, 1992.

Table A1
R_T Data for Two Alumina Ceramics

Proj. Mat'l	Tile Width (mm)	Tile Thick. (mm)	Alumina Grade	Substrate	R_T (kbar)	Method	Reference
DU	NR	NR	high dens. (AD995)	steel	60±5	eq. A-4	Goc ?
WA	NR	NR	high dens. (AD995)	steel	55	eq. A-1	Hau.., 1992b
WA	150	23-37	high dens. (AD995)	steel	65 (large scatter)	eq. A-4	Woolsey, 1992
					59	eq. A-6	
WA	75	25	high dens. (H.P.)	Al	70	eq. A-4	Bless, unpublished
WA	98 (round)	89	high dens. (AD995)	steel	65±9	eq. A-1	Burkett, 1992
WA	NR	NR	med. dens. (AD90)	steel	47±1	eq. A-1	Hauver, 1992b
WA	150	25-50	med dens. (AD90)	steel	55±1	eq. A-4	Mariano & Woolsey, 1989
					47±1	eq. A-6	
WA	100 (round)	28-42	med dens. (AD90)	steel	65±3	eq. A-4	Anderson & Morris, 1992
					58±2	eq. A-6	

Notes:

Projectile: All projectiles are long rods impacting at about 1.5 km/s; the material is either tungsten alloy (WA) or depleted uranium (DU).

Dimensions: NR means not reported.

Alumina grade: AD are Coors Porcelin designations, and hot processed is Ebon A, a Cercom designation.

R_T: There are a lot of scatter in R_T data; uncertainty estimates are based on data sets, including dividing the standard deviation by the root of the number of data points, where appropriate. Uncertainty where not given may be as much as 15%, which is a typical value of standard deviation in a test series. In calculating R_T, we used 18 or 20 kbar for WA strength and 12 kbar for DU strength.

Method: P_R means calculation based on residual penetration, and extrapolated means linear extrapolation to tile thickness where rod is fully consumed; u means calculated directly from measurements of penetration velocity.

APPENDIX: The Calculation of R_T

There are several ways to compute the target resistance R_T, with each having advantages and disadvantages. The various methods are summarized here.

Experimentally Measured Penetration Velocity Method. The most straightforward way of finding R_T is to experimentally measure the steady-state penetration velocity. Assuming that the projectile flow stress Y_p is known (20 ±2 Kbar), R_T is found from the modified Bernoulli equation:

$$R_T = Y_\rho + \frac{1}{2}\rho_p(v-u)^2 - \frac{1}{2}\rho_t u^2 \qquad \text{(A-1)}$$

where v is the tail velocity of the projectile, u is the penetration velocity, and ρ is the density. The subscripts ρ and T refer to the projectile and target, respectively. The penetration velocity is found by taking a sequence of flash X-rays of the penetration process and differentiating the position-time data. Unfortunately, this procedure must generally be performed in the reverse ballistics mode or with low density materials (and little confinement) in order for the X-rays to penetrate the target and expose the film. Further, R_T does change with depth of penetration (e.g., see Anderson, et al. (1992)], but in the quasi-steady region of penetration, R_T varies very slowly. Although there are X-ray systems with the energy capable of penetrating large targets, e.g., 1-2 MV systems or larger, usually only one data point per test can be obtained. Thus, a number of "duplicate" experiments must be performed with different time delays for the X-ray pictures. Although impact velocities may be approximately the same, they are never identical. Also, for very hard but brittle materials, experimental experience has shown there can be considerable variability in target performance from test to test under nominally identical conditions.

Critical Velocity Method. Rosenberg and Tsaliah (1990) used the concept of critical or threshold velocity, below which no penetration occurs. The critical velocity is given by the expression:

$$v_c = \sqrt{\frac{2(R_T - Y_p)}{\rho_p}} \qquad \text{(A-2)}$$

for the case of $R_T > Y_P$. A projectile is fired at successively lower velocities until it does not penetrate the target material; this gives v_c. Then Eq. (A-2) is used to find R_T. Several tests are required to determine v_c , but the procedure is straightforward. It would appear, however, that care must be taken with the nose shape of the projectile; a hemispherical nose would seem to be the most appropriate nose shape. The methodology gives a value for the target resistance near the critical velocity.

Layered Tate Model Method. Target resistance can change with impact velocity, which could indicate a potential weakness of the critical velocity technique. But Rosenberg and Tsaliah (1990) adapted the Tate model to compute penetration through a layered target. In their work, they performed depth-of-penetration (DOP) experiments where a relatively thin ceramic tile (12-20 mm thick) was bonded to a "semi-infinite" steel backup plate. The residual depth of penetration was measured in the steel substrate. The authors report good agreement between the results from the layered Tate model, using the R_T values obtained from the critical velocity experiments, and the measured depths of penetration.

The use of the layered Tate model has been extended to analyze DOP test data, i.e., critical velocity experiments were not performed to obtain an estimate of R_T. Instead, R_T is varied in the model until agreement is reached between the model results and the measured residual penetration (Rosenberg and Tsaliah, 1990; Yaziv, 1992). In application of a layered Tate model, assumptions must be made on the transition of penetration from the hard layer to the steel substrate. It is also assumed that the penetration process can be described as nominally steady state, in both the ceramic and the substrate, since the Tate model is a steady-state model.

Average Penetration Velocity Method from DOP Test Data. The depth of penetration into the substrate can be used to obtain an estimate of the penetration velocity in the hard layer assuming that penetration is steady state in both the hard layer and the substrate (the steady-state velocity, in general, is different in

the two layers). An estimate of the projectile eroded, ΔL, in going through the hard layer is needed. ΔL is found by assuming that penetration into the substrate is proportional to the residual rod length, i.e.,:

$$\frac{P_\infty}{L_o} = \frac{P_1}{L_o - \Delta L} \tag{A-3}$$

where P_∞ is the depth of penetration into the substrate material with no hard layer, L_0 is the original rod length and P_1 is the measured residual depth of penetration with the hard layer in place. With these assumptions, the penetration velocity in the hard layer if given by:

$$u = \frac{v}{\left(1 + \frac{\Delta L}{T}\right)} \tag{A-4}$$

Equation (A-3) is a reasonable approximation for impact velocities between 0.8 and 1.8 km/s for tungsten-alloy long rod projectiles into armor steel. In this velocity regime, penetration is linear with velocity. However, above 1.8 km/s the penetration curve begins to saturate with impact velocity, and the linear relationship is no longer valid. On the other hand, what is particularly nice about this methodology is its simplicity; there is no need to run the Tate model, as in the preceding and following methodologies.

Extrapolated Tile Thickness Method from DOP Test Data. This methodology uses the residual penetration and the tile thickness to estimate the depth of penetration T_C into a semi-infinite target made of the hard material. It is assumed that the residual penetration is linearly dependent on the thickness of the hard layer.

$$\frac{P_1}{P_\infty} = 1 - \frac{T}{T_c} \tag{A-5}$$

T_C is the thickness of the tile to give zero residual penetration. Equation (A-5) can be rearranged to give the following:

$$T_c = \frac{TP_\infty}{P_\infty - P_1} \tag{A-6}$$

Once T_C is known, R_T is adjusted in the Tate model until the depth of penetration predicted by the model gives T_C.

This methodology works over the entire velocity range of the preceding methodology, but it can also be extended to impact velocities above 1.8 km/s. Although the Tate model is used iteratively to find R_T similar to the layered Tate model methodology, no assumptions need be made concerning the transition of penetration from the hard layer into the substrate material. However, the larger the residual penetration, the more critical the assumption of linearity in Eq. (A-5). In general, linear extrapolations are reasonable, even for rather nonlinear responses, up to approximately 10% change. Clearly, the more linear the response, the further the extrapolation can be made. In practice, residual penetrations have often been over 50% of the semi-infinite penetration.

Summary. Each of the methodologies is based on application of steady-state theory, and in particular, application of the Tate model. But each of the methodologies, aside from the steady-state premise, invokes different assumptions. Three of the methods for determining R_T use the DOP test: the layered Tate model method, the penetration velocity method, and the extrapolated tile thickness method. As contrasted to the critical velocity method, where a series of tests must be performed to find the critical velocity, only one DOP test is required to estimate R_T. This is really academic, however, since the scatter in ceramic DOP test data generally mandates that a minimum of three DOP tests be conducted at

nominally the same impact conditions in order to obtain an averaged response. The DOP test measures the performance of the ceramic in an pseudo armor-like configuration (e.g., see Anderson and Morris, 1992), and at the nominal impact velocity of interest. Implicit in a DOP test is that there should be at least several rod diameters of penetration into the substrate to avoid the very rapid deceleration of the tail velocity (that occurs in the final stage of penetration) as the projectile transitions between the hard layer and the substrate. The linear extrapolation method is least affected by a very small residual penetration.

The value of Y_P assumed for the flow stress is not particularly critical in any of the methods. Armor steels have values of R_T that are 50 kbar or larger. The uncertainty in Y_P is approximately 2 kbar, i.e., $Y_P = 20 \pm 2$kbar. This uncertainty (some of which is due to various investigators using different tungsten alloys) has only a 4% variation or less on R_T. If the Tate model is used to find R_T, a variation of 2kbar makes only 1kbar difference in the value of R_T.

Table A-1 compares calculated R_T values for several sets of DOP experiments. Reasonably good agreement has been obtained for target resistances of ceramic tiles calculated using the various methodologies. This is encouraging, and suggests that the concept of a target resistance for hard materials is fairly robust and that it can be used to quantitatively rank the ballistic performance of a hard material.

Int. J. Impact Engng Vol.14, pp.95 - 106, 1993
Printed in Great Britain

0734-743X/93 $6.00+0.00
Pergamon Press Ltd

HYPERVELOCITY TESTING OF ADVANCED SHIELDING CONCEPTS FOR SPACECRAFT AGAINST IMPACTS TO 10 KM/S

M. B. BOSLOUGH*, J. A. ANG*, L. C. CHHABILDAS*, W. D. REINHART*, C. A. HALL*
B. G. COUR-PALAIS**, E. L. CHRISTIANSEN*** and J. L. CREWS***

*Sandia National Laboratories, Albuquerque, New Mexico 87185
**McDonnell Douglas Space Systems Division, Houston, Texas 77062
***NASA, Johnson Space Center, Houston, Texas 77058

ABSTRACT

Experiments have been performed on NASA state-of-the-art hypervelocity impact shields using the Sandia Hypervelocity Launcher (HVL) to obtain test velocities greater than those achievable using conventional two stage light-gas gun technology. The objective of the tests was to provide the first experimental data on the advanced shielding concepts for evaluation of the analytical equations (shield performance predictors) at velocities previously unattainable in the laboratory, and for comparison to single Whipple Bumper Shields (WBS) under similar loading conditions. The results indicate that significantly more mass is required on the back sheet of the WBS to stop an approximately flat-plate particle impacting at 7 km/sec and at 10 km/sec than the analytical equations (derived from spherical particle impact data) predicted. The Multi-Shock Shield (MSS) consists of four ceramic fabric bumpers, and is lighter in terms of areal density by up to 33%, but is as effective as the heavier WBS under similar impact conditions at about 10 km/s. The Mesh Double Bumper shield (MDB) consists of an aluminum wire mesh bumper, followed by a sheet of solid aluminum and a layer of Kevlar® fabric. It provides a weight savings in terms of areal density of up to 35% compared to the WBS for impacts of around 10 km/s.

1. INTRODUCTION

There is an increasing requirement to protect spacecraft from the serious threat posed by naturally occurring meteoroids and human-generated orbital debris in low earth orbit. The meteoroid threat is primarily dust size particles having an average relative impact velocity of 20 km/sec; for very large, long-duration spacecraft, the probability of an impact by a larger particle of human-generated debris becomes significant. The orbital debris size distribution of this "space junk" ranges from micron size flakes of paint to inactive satellites (Kessler *et al.*, 1989). The most probable size of impacting particles for spacecraft such as the Space Station Freedom is expected to be in the millimeter to centimeter range. The practicable passive shielding capability for such a spacecraft will defend against a particle up to a few centimeters in diameter with an average relative impact velocity of 10 km/sec. Other schemes such as avoidance maneuvering will need to be implemented for the larger debris that can be tracked by radar and other means (Interagency Group, 1989).

The need for low-weight passive hypervelocity impact shielding is obvious, and NASA has been instrumental in the area of spacecraft hypervelocity shielding research. Several innovative low-weight shielding concepts have been developed by NASA including the Multi-Shock Shield (Cour-Palais and Crews, 1990) and the Mesh Double Bumper (Christiansen, 1990). The velocity limitations of existing two stage light-gas guns resulted in a research project using the Sandia Hypervelocity Launcher (Chhabildas *et al.*, 1992a, b) to attain even higher impact test velocities to characterize these new shields. This paper will discuss the results of these experiments.

2. DEBRIS SHIELD DESIGNS

2.1 Whipple Bumper Shield (WBS)

The conventional shield that has been used to protect satellite systems from hypervelocity meteoroid impact is called the Whipple Bumper Shield (Whipple, 1947). The effectiveness of this shield comes from its ability to fragment the impacting object into a debris cloud which is solid, liquid, and/or vapor, depending on the impact velocity. The WBS typically consists of a single sheet of aluminum, called the bumper, which provides a surface away from the hull of the spacecraft on which an incoming particle of debris can impact. By the time the resulting debris cloud reaches the spacecraft, it will disperse and the kinetic energy density will decrease. In the present study, the Whipple shield design consists of two spaced aluminum sheets: an aluminum bumper sheet separated from an aluminum "back" sheet. For the

present investigation, the back sheet is intended to be an element of the shield rather than a hull plate bulkhead or a pressure vessel wall. Two thicknesses of bumpers were tested in this study: 1) 0.30 mm thick 2024-T3 aluminum, and 2) 1.27 mm thick 6061-T6 aluminum. In all cases, the bumper was placed 305 mm in front of the back sheet. The results of a few WBS tests have already been published (Ang *et al.*, 1992; Chhabildas *et al.*, 1992c; Hertel *et al.*, 1992). Some of these results are summarized here, providing a baseline for comparison to the more advanced shielding concepts.

2.2 Multi-Shock Shield (MSS)

The Multi-Shock Shield concept (Cour-Palais and Crews, 1990), is based on the use of a number of spaced bumpers placed in front of a back sheet element to excite the projectile impact debris to higher internal energy states (and temperatures) by repeated collisions. The final state of the projectile and shield material impacting the back sheet depends on the initial impact velocity, the mass density of the first bumper, the number of subsequent bumpers and their mass densities, and the spacing between the individual bumpers and the back sheet. An optimally designed MSS could result in a significant weight saving over the conventional WBS, primarily because the back sheet will be much lighter. The MSS used in these tests had four Nextel® BF54 or AF62 ceramic fabric bumpers (Fig. 1a) spaced 76.2 mm apart, with an aluminum alloy back sheet the same distance behind the last bumper. Nextel® is the trade name for the high-temperature, ceramic fabrics made by the 3M company. BF54 is woven from fibers composed of 70% aluminum oxide, 28% silicon dioxide and 2% boric oxide and has an areal density of 0.108 g/cm^2. AF62, on the other hand, has the same weave but the fiber composition is 62% aluminum oxide, 24% silicon dioxide and 14% boric oxide, which makes it lighter at 0.100 g/cm^2. The back sheet was 6061-T6 aluminum with a thickness of 2.03 mm.

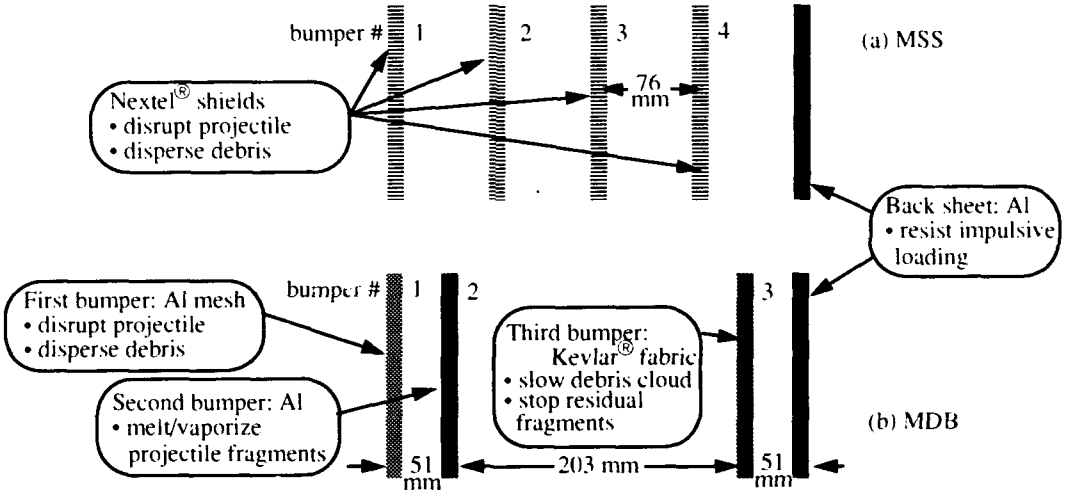


Fig. 1. Advanced Debris shielding concepts: (a) Multi-Shock Shield, (b) Mesh Double Bumper.

2.3 Mesh Double Bumper Shield (MDB)

The Mesh Double Bumper shield (Christiansen, 1990) provides weight savings of approximately 50% at two-stage light-gas gun velocities for a sphere compared with conventional dual-sheet aluminum WBS's. The MDB shield is based on the concept of a dual bumper system with an initial mesh bumper that disrupts the projectile, followed by a high strength fabric layer that slows the expansion of the debris cloud prior to contacting the back sheet (Fig. 1b). The mesh is composed of overlapping wires in a square pattern. Where the wires overlap, localized mesh areas with greater bumper thickness are created which contribute to the disruptive forces exerted on the projectile by increasing the shock duration in the projectile during the impact event. Generally, in two stage light-gas gun testing with projectile diameters of around 30 mm, the mesh is selected with wire-to-projectile diameter ratios from 0.07 to 0.10, so that 4 to 6 wires are "cut" by the diameter of the projectile. In these studies, an MDB was tested with a mesh that would be effective against a spherical projectile with the same mass as the thin HVL flyer plate.

The MDB shields were also subjected to HVL testing. The mesh consisted of 0.3 mm diameter aluminum wires in a ~12 by 12 per cm^2 square pattern (the first series of tests used 0.58 mm diameter wires in a ~9 by 9 per cm^2 square pattern--see Christiansen, 1990). The second bumper was a continuous 0.635 mm-thick aluminum 6061-T6 sheet 51 mm behind the mesh. A third bumper consisted of a number of sheets of Kevlar® 710 mounted 203 mm away from the second bumper and 51 mm in front of the back sheet. The MDB's that were tested had Kevlar® bumpers consisting of between 4 and 6 layers. The 6061-T6 aluminum back sheets that were tested were 1.6 to 2.0 mm thick.

3. HYPERVELOCITY IMPACT EXPERIMENTS

At the lower end of expected debris impact velocities, the degree of damage to various shield configurations can be generally predicted quite well both with analytic methods (Cour-Palais, 1969; Wilkinson, 1969) and hydrodynamics code simulations (Hertel *et al.*, 1992). At impact velocities below about 7 km/s, these calculations have been validated with experiments performed on two-stage light gas guns. With the recent development at Sandia National Laboratories of a hypervelocity launch capability (Chhabildas *et al.*, 1992a, b) it has become possible to perform experiments over the velocity range of 7 to 12 km/s. This higher velocity regime has previously been inaccessible for gram-sized plates but is necessary to evaluate various debris shield configurations in the mass and velocity regime associated with the bulk of orbital debris.

3.1 The HyperVelocity Launcher (HVL)

Though the hypervelocity launcher at Sandia has been described elsewhere (Chhabildas *et al.*, 1992a,b) it will be summarized briefly here. There are theoretical as well as practical limits on velocities that can be attained by two-stage light gas guns (Charters, 1987). To launch flyers to hypervelocities (in the range of 7 to 12 km/s), higher loading pressures are required. These higher velocities are attained by a scheme in which a fraction of the momentum of a projectile launched from a two stage light-gas gun is transferred to a lighter, stationary flyer plate. A multi-step "shockless" loading is required (to accelerate the plate without melting or fragmenting it). This is accomplished by means of a graded-density layer that is carried by a projectile and impacts the flyer.

The diameters of the flyer plate assemblies used in this set of experiments varied from 17 to 19 mm. The flyer deforms somewhat as it is accelerated, so at impact its diameter and effective areal density may be different (see Fig. 3 and section 5). There is also a later arrival of debris associated with the launch of the flyer. This "launch debris" is made up of remnants of the graded-density impactor and the rest of the projectile, as well as portions of a guard ring and debris generated by its impact on a stripper. Because of this ancillary debris from the launch, there is a limited time frame during which useful data can be collected. The estimated time of arrival of the launch debris at the shield assembly marks the end of the time window for useful "real-time" data collection.

3.2 Diagnostics

Two primary methods of instrumentation were used to record data from these experiments: flash x-rays and fast framing photography. The x-rays were principally used to determine the velocity of the flyer and its condition just prior to impact on the shield assembly. The framing cameras recorded the propagation and evolution of the debris clouds generated by the impact on the bumper shields, and monitored the condition of the back sheet. In a few cases, flash x-rays

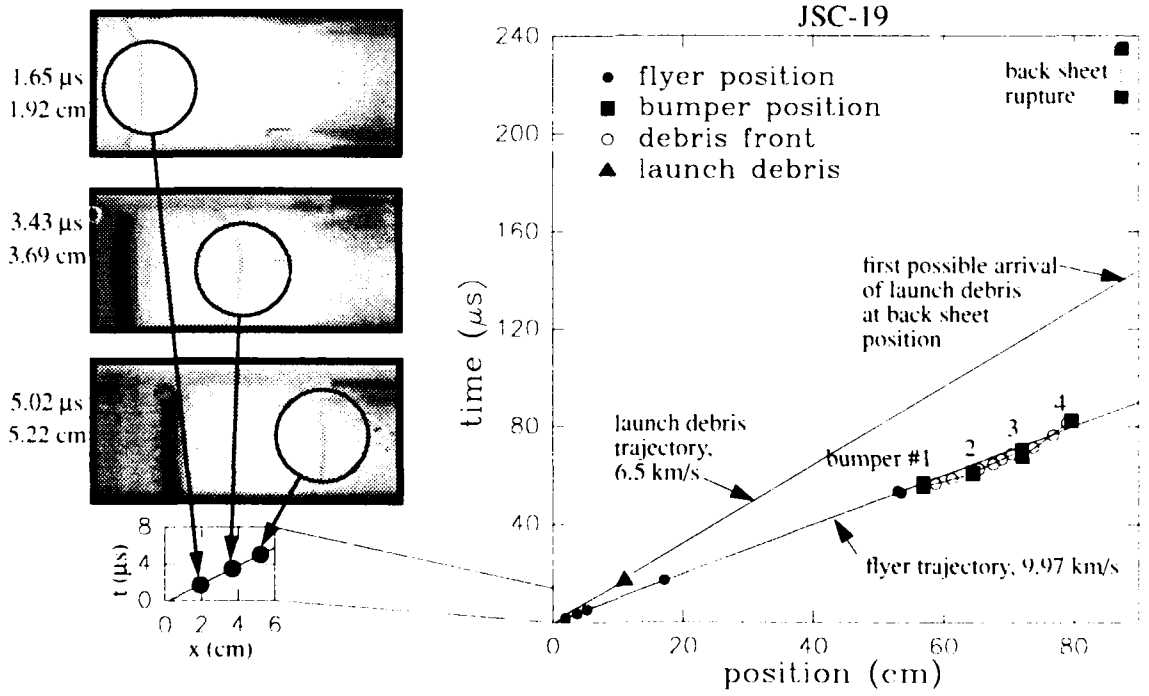


Fig. 2. X-ray images of flyer and x-t diagrams for JSC-19.

were also used to capture the shape and position of the debris cloud a few microseconds after impact of the flyer. Because of present space limitations, these images will be discussed in a subsequent report (Boslough *et al.*, 1993). Several flash x-rays were set to fire in sequence to capture the flyer at various positions along its flight path. The first three x-ray images of the launch sequence are depicted in Fig. 2 for experiment JSC-19. To determine the position of the flyer, the position of its x-ray image was measured relative to markers on a calibration rod that was placed along the boreline for calibration x-rays prior to the experiment. The flash time of each x-ray was recorded on a common time base with a LeCroy 8828 digitizer. To determine the flyer velocity, a data point corresponding to each x-ray image was plotted in the x-t plane, and a linear regression was performed. Such a plot is shown for experiment JSC-19 in Fig. 2. The origin of the plot is approximately at the time and position of projectile impact on the flyer. To determine the condition of the flyer at impact, it was imaged by means of flash x-ray radiography during its approach to the bumper. In Fig. 3(a), images of the flyer condition are reproduced for several selected experiments. In some experiments, the launch debris described in section 3.1 was imaged using flash x-rays, and its velocity was determined (Fig 2). By extrapolating its trajectory to the back sheet position, the time window for useful data collection can be estimated.

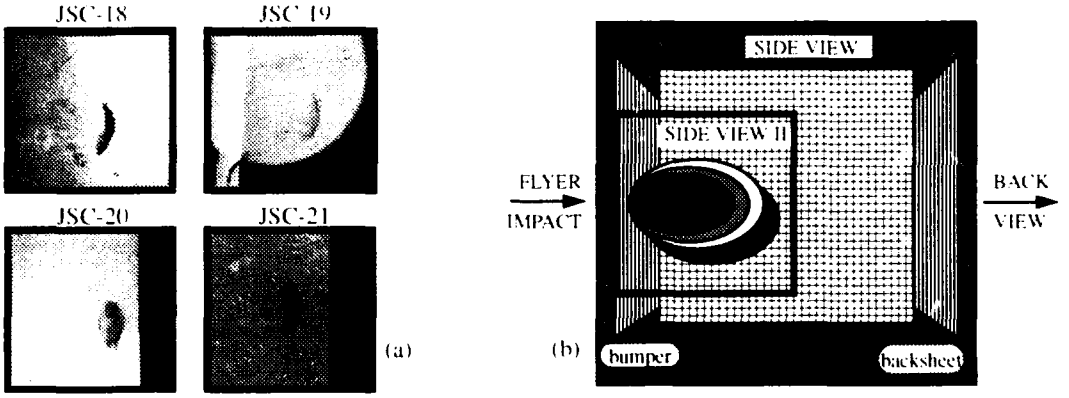


Fig. 3. (a) Flash x-ray photographs of flyers, (b) schematic of framing camera fields of view.

3.3 Framing Photographs

In most of the experiments, two framing cameras viewed the shield assembly from the side. Because the framing camera images are emphasized in this paper, a schematic representation of the view from each camera is depicted in Fig. 3(b). In this example, the Whipple shield configuration is shown. The effect of perspective from the cameras is seen, and it is clear that the grid in the background cannot be used as a direct scale for position of the debris. The debris front is assumed to lie along an extension of the boreline of the gun, and is therefore closer to the cameras and has a different magnification factor. Calibration images were taken with a ruler on the boreline to determine the ratio of magnification factor on the boreline to that on the gridplane. Since the gridplane is visible in the shot images, it can be used with the measured ratio to determine the appropriate magnification factor. The schematic nature of Fig. 3(b) should be emphasized; the perspective is exaggerated, and in reality the two side cameras view the scene from different angles.

4. RESULTS AND DISCUSSION

Numerous experiments have been performed on the three different debris shield configurations; parameters that were varied included flyer material, mass, and velocity. Not all these experiments are discussed in detail here; instead several were chosen to highlight the effects of particular differences in either the experimental results or the impact configuration. In this section, the test results at impact velocities of about 7 and 10 km/s are summarized in detail for the selected experiments. The impact conditions are given in Table 1. Whenever a given test resulted in a rupture of the back sheet due to interaction with the debris generated by the impact of the flyer on the bumper, the test was classified as "fail". When the back sheet remained undisturbed, or was deformed without rupturing over the useful duration of the experiment, then it was classified as "pass". In a few tests we observed minor "pinhole" penetrations that did not continue to grow. These were classified as "threshold" tests.

4.1 Whipple Bumper Shield

4.1.1 Experiment JSC-5. This experiment examined the response of a Whipple bumper shield to the impact of a 0.781 g aluminum flyer at 7.10 km/s. The bumper thickness was 0.30 mm, which was chosen on the basis of calculated full melting of a 0.8 g, 19 mm diameter, 1 mm flat flyer impacting normal to the bumper surfaces. The back sheet thickness was 4.06 mm, and the distance between the two aluminum sheets was 305 mm. In Fig. 4, the side view framing sequence of images is shown. The times associated with each frame are relative to the estimated time of impact on the

Table 1. Summary of Experiments Performed on Debris Shields.

Shot No.	Shield type	Flyer Material	Initial Flyer Thickness (mm)	Initial Flyer Diameter (mm)	Initial Flyer Mass (g)	Impact Velocity (km/s)	Debris Shield Variable[a]	Back Sheet Thickness (mm)	Pass/Fail
JSC-3	WBS	Aluminum	1.02	19.3	0.781	7.08	0.305	4.06	Fail
JSC-5	WBS	Aluminum	1.04	19.3	0.793	7.19	1.27	4.06	Pass
JSC-9	WBS	Aluminum	1.03	19.0	0.777	9.52	0.305	4.06	Fail
JSC-12	WBS	Magnesium	1.01	19.1	0.503	9.92	1.27	4.06	Threshold
JSC-15	MSS	Aluminum	1.04	19.1	0.790	9.60	BF54	2.03	Pass
JSC-18	MSS	Aluminum	1.00	17.0	0.599	9.85	BF54	2.03	Pass
JSC-19	MSS	Aluminum	1.06	17.0	0.624	9.97	BF54	2.03	Pass
JSC-20	MSS	Aluminum	0.99	16.9	0.594	10.12	AF62	2.03	Pass
JSC-6	MDB	Aluminum	1.03	19.0	0.766	7.46	4	1.59	Threshold
PII-3	MDB	Aluminum	1.05	19.0	0.794	9.60	5	2.03	Pass

a. Bumper Thickness (mm) for WBS, Nextel™ type for MSS, number of Kevlar® layers in third bumper for MDB

bumper. A rapidly expanding debris cloud can be seen propagating to the right from the point of impact. The front edge of the debris is well-defined, and the apex is lined up with the centerline of the experiment. A thin envelope of bright material appears to have separated from the darker, main mass of debris, and moved ahead at higher velocity. By measuring the position of the fronts of these debris clouds as a function of time, the velocity of the leading edge of each front can be determined by means of linear regression. This method assumes that no acceleration of the debris front takes place after impact. This assumption is valid within the precision of position measurement and the velocity is about 5.5 km/s for the dark, main mass and 7.0 km/s for the brighter envelope. The debris velocities determined from framing images in this way are termed "photo-visual" velocities, to distinguish them from velocities determined via flash x-rays which were included in some experiments. The photo-visual velocities tend to be somewhat different than x-ray velocities because in the former method visible light that is reflected or radiated from x-ray-transparent matter can be measured. In the final (42 μs) frame, the debris cloud has already impacted on the back sheet, as indicated by the resulting flash. In Fig. 5, the side view (II) data are shown. Common features can be seen, but from a different angle. In Fig. 6(a), the back surface view framing sequence is shown. The framing interval is 5 μs, and the first frame time is 44.7 μs after bumper impact. It is clear that by this time the back sheet has already been deformed by the debris cloud that was seen impacting it a few microseconds earlier in the side view. In the following frames, a secondary debris cloud continues to grow, indicating that the back sheet has ruptured.

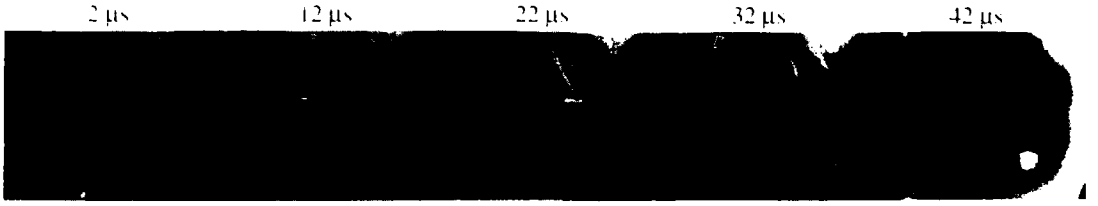


Fig. 4. JSC-3--Side View.

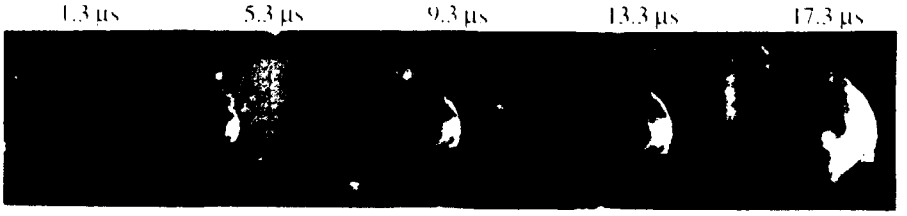


Fig. 5. JSC-3--Side View (II).

The information in these images can be conveniently presented as time vs. position in an "x-t" diagram, as shown in Fig. 6(b). In this diagram, δx is the distance behind the bumper, and δt is the time after estimated impact at the bumper. Symbols indicate time-position data as determined from the framing images. The solid line is the best fitting debris front trajectory. The debris front velocity is the reciprocal of the slope of this line. For reference, the extension of the

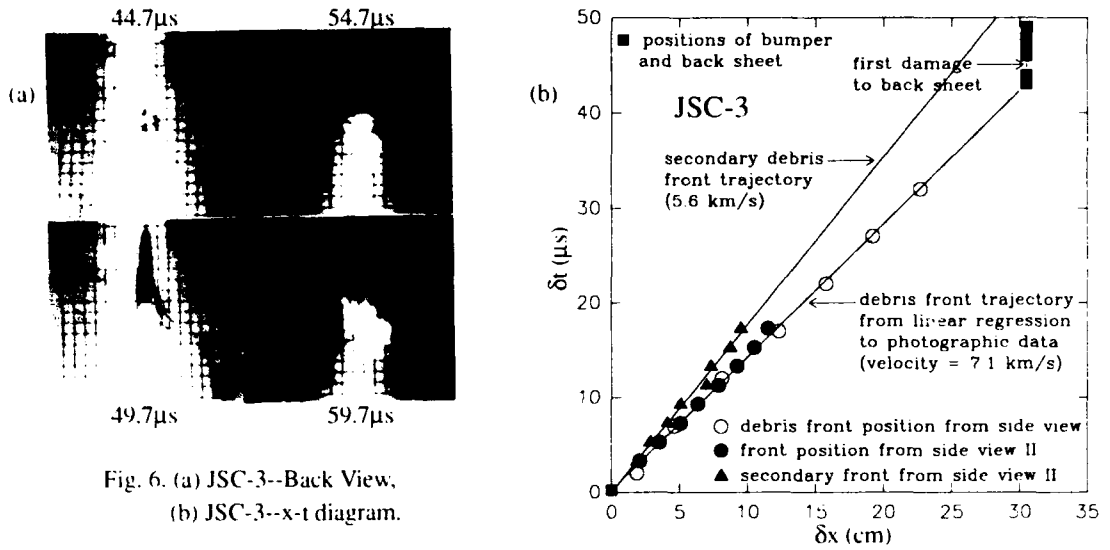


Fig. 6. (a) JSC-3--Back View, (b) JSC-3--x-t diagram.

flyer velocity is also plotted (this would be the trajectory of the flyer in the absence of the shield). Because the back sheet clearly ruptured at an early time, JSC-3 was classified as a "fail" in Table 1.

4.1.2 Experiment JSC-5. Because flash x-ray images of flyers show that they tend to be tilted as well as bowed, their areal densities are higher than if they had remained flat. For this reason, a thicker bumper than that used in JSC-3 would be required to provide the same amount of irreversible shock energy per unit flyer mass, thereby completely melting the flyer. In JSC-5, the bumper thickness was increased to 1.27 mm. The debris structure and evolution was similar to that noted for JSC-3, with a separation into a dark mass and a brighter, faster envelope. Side and back views were shown by Ang *et al.* (1992), where the leading edge of the outer layer could be seen to impact the backsheet between 37.8 and 42.8 μs after bumper impact. The photo-visual velocity of this debris was about 6.8 km/s, and that of the dark mass was 5.6 km/s. The back surface view of the back sheet showed that some deformation had taken place by 57.4 μs, but 45 μs later the sheet was still intact. Because the back sheet remained intact up to 100 μs after bumper impact, JSC-5 was classified as a "pass".

4.1.3 Experiment JSC-9. For this test, we returned to the original Whipple bumper thickness of 0.30 mm, but the impact velocity was increased significantly to 9.52 km/s. The debris cloud developed very rapidly (see Ang *et al.*, 1992), with the outer, brighter cloud expanding more rapidly, at about 12 km/s. It remained roughly spherical, and was tenuous enough to be transparent. The inner, darker cloud expanded more slowly, at 9.7 km/s and retained a more prolate shape. It appeared to be more dense, as it obscured the view of the grid in the background. The structure of the debris was qualitatively different from that generated by lower velocity impacts, but the outer envelope seen in those experiments may be related to the outer cloud observed in this one. The most reasonable interpretation is that the outer cloud is vapor and small droplets of liquid condensing from it, while the inner cloud consists of dense, mostly liquid debris. The back view framing sequence indicated that the backsheet was not penetrated until δt=40.4 μs, after which damage proceeded very rapidly compared to shot JSC-3. This is 18 μs after the outer low density debris cloud arrived at the backsheet, and is consistent with the arrival of the dark, inner cloud. The results of test JSC-9 were clearly classified as "fail".

4.1.4 Experiment JSC-12. For JSC-12, the thick (1.27 mm) Whipple bumper was used with a high velocity (9.92 km/s) flyer. In this case, the flyer mass was reduced to 0.503 g, by using a magnesium plate. The side view sequence (Fig. 7) shows that, like JSC-9, there is a clear separation of the debris cloud into two distinct components. Also as with JSC-9, the perforation of the backsheet appears to take place significantly later than arrival of the faster cloud. The outer debris velocity for JSC-12 was determined to be over 15 km/s, and that of the inner cloud was about 10.6 km/s. Because there was no apparent growth of the hole after the plate was penetrated, JSC-12 was classified as "threshold".

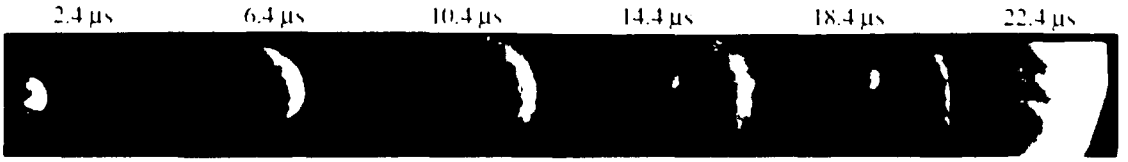


Fig. 7. JSC-12--side view (II).

4.2 Multi-Shock Shield

4.2.1 Experiment JSC-15. This was the first test involving the MSS configuration made up of the BF54 Nextel® fabric as described in section 2.2. The flyer was 0.790 g of aluminum, and it was launched to a velocity of 9.60 km/s. The final x-ray radiograph of the flyer before impact indicates that it consisted of a large piece with some small trailing fragments. The side view framing images shown in Fig. 8 indicate a somewhat different debris cloud development and evolution than was observed in the Whipple bumper experiments. Most noteworthy is the fact that the debris front velocity slows down with each subsequent shield interaction. For example, at δt=6.5 μs, the debris from impact on the first shield has just arrived at the second shield, as indicated by the brightly glowing area on the downrange side of the second shield. By 16.5 μs, debris has arrived at the third shield, but it is another 30 μs or so before the main mass of debris hits the fourth shield Another feature of note is the apparent generation of multiple debris fronts that behave differently upon interaction with the shield layers. In the 16.5 μs frame (when the debris is between shields 2 and 3), two distinct debris types can be seen which have much in common with those identified for shot JSC-9 and JSC-12. The behavior of the debris fronts when they arrive at the Nextel® shields supports the previous identification of the diffuse, faster front with vapor and mist, and the slower front with dense solid and liquid. The debris in the faster front appears to pass though the holes in the fabric with little interaction. This effect can most readily be seen in upper part of the 26.5 μs frame, where the faster front is approximately continuous across shield 3, whereas the bright, slower front shows a discontinuity. These phenomena are discussed further in section 4.2.5. In the back view sequence (not shown), the first indication of damage is not until about 146 μs, so JSC-15 is a "pass".

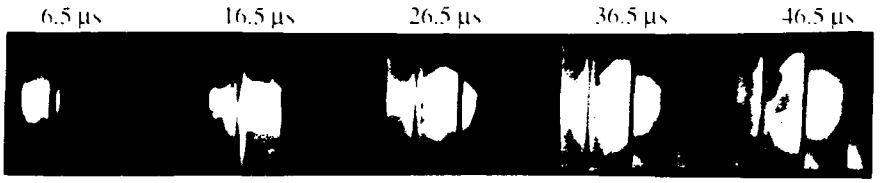


Fig. 8. JSC-15--side view.

4.2.2 Experiment JSC-18. The only difference between this test and JSC-15 was the lower flyer mass (0.599 g), the slightly higher impact velocity (9.85 km/s), and the condition of the flyer before impact (fully intact but bowed-see Fig. 3). The debris cloud images (Fig. 9) are qualitatively similar, but have a greater degree of axial symmetry, possibly due to the more symmetric condition of the flyer at impact. The discontinuity of the debris front on either side of each shield is more extreme (giving rise to a "wedding cake" like structure). In this case the diffuse, faster front also appears to be discontinuous. There is some evidence for a third component of debris; a roughly spherical bubble centered about a point moving downrange. One such bubble can be seen growing and moving downrange in the third intershield space between 23.6 and 38.6 μs. After 38.6 μs, a similar bubble evolves in the last intershield space; it is sharpest in the 43.6 μs image. The JSC-18 data were divided into four sets, each corresponding to front measurements within one of the four 76 mm-wide intershield spaces. Each set of data (some containing only two points) were independently fit to a straight line to estimate the velocity. The approximate velocities determined in this way were, in chronological order: 15, 9, 4, and 6 km/s. Because of the small data sets and the relatively large uncertainties these velocities are estimates, but the general trend indicates a decrease in velocity with each shield interaction. In this experiment, there was a long delay between the estimated time of arrival of debris upon the back sheet and the first sign of damage, so JSC-18 is a "pass"; the rupture was caused by the ancillary "launch" debris.

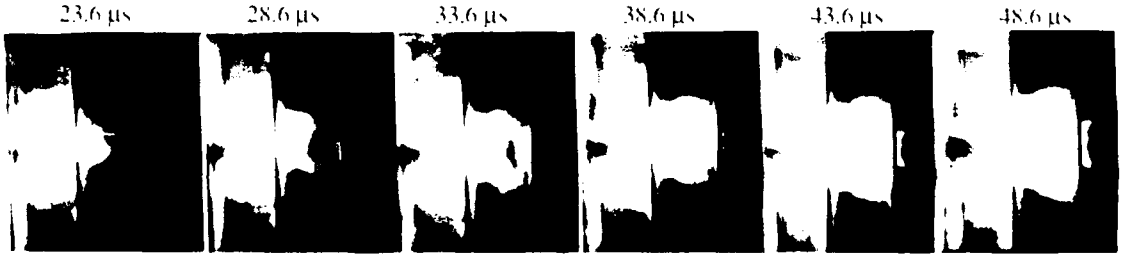


Fig. 9. JSC-18--side view (II).

4.2.3 Experiment JSC-19. The only substantive difference between this test and JSC-18 was in the choice of Nextel®. In this case it was BF54 "sized", *i.e.* heated with an anti-irritant coating so that it can be handled manually). The mass and velocity of the aluminum flyer were almost the same, at 0.634g and 9.97 km/s, respectively. The evolution and shape of the debris clouds are remarkably similar for both experiments (Fig. 10). The growth and motion of the debris bubble at 24.8 and 29.8 μs is particularly clear and sharp. Another feature can also be seen in the JSC-19 images. A

uniformly-spaced pattern appears just aft of at the third shield (approximate center of field-of-view). The horizontal streaking of these features is consistent with debris streaming through a periodic pattern of holes in the woven fabric shield. Position-time histories are plotted in Fig. 2, with optimal linear fits indicating a decrease in debris velocity from 14 km/s behind the first shield to 5 km/s behind the third, in general agreement with JSC-18. Also plotted in Fig. 2 is the time of the last image of the back surface of the back sheet before the first indication of penetration.These images show no damage to the back sheet until about 180 μs after the flyer impacts on the first bumper, so JSC-19 is a "pass".



Fig. 10. JSC-19--side view (II).

4.2.4 Experiment JSC-20. This test was similar to the previous two, but made use of lighter-weight AF62 Nextel™. The aluminum flyer mass was 0.594 g, and the velocity was 10.12 km/s. The flyer was intact just before impact (Fig. 3), but it appears be quite irregular in shape compared to the previous two experiments. This irregularity is probably the reason for the somewhat less symmetric debris cloud form seen in the side view sequence (Fig. 11, 12a).However, the main features noted before are still present. Between 13.5 and 17.5 μs, a moving debris bubble can be seen in addition to an outer diffuse and inner, denser cloud. Further downrange, it can be seen that there is actually more than one diffuse debris cloud. This is most apparent at 40.6 μs in Fig. 12(a).

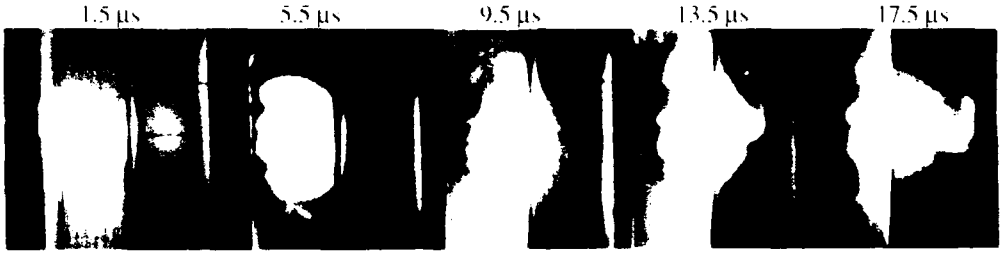


Fig. 11. JSC-20--side view.

For this experiment, an attempt was made to determine time-position data for all the debris fronts. These are plotted in Fig. 12(b), where different symbols are used to denote different debris fronts, and the calculated velocities correspond only to the fastest, outermost front. The back view of the back sheet shows that it is still fully intact as of 160 μs after impact on the first bumper, so this test was a "pass".

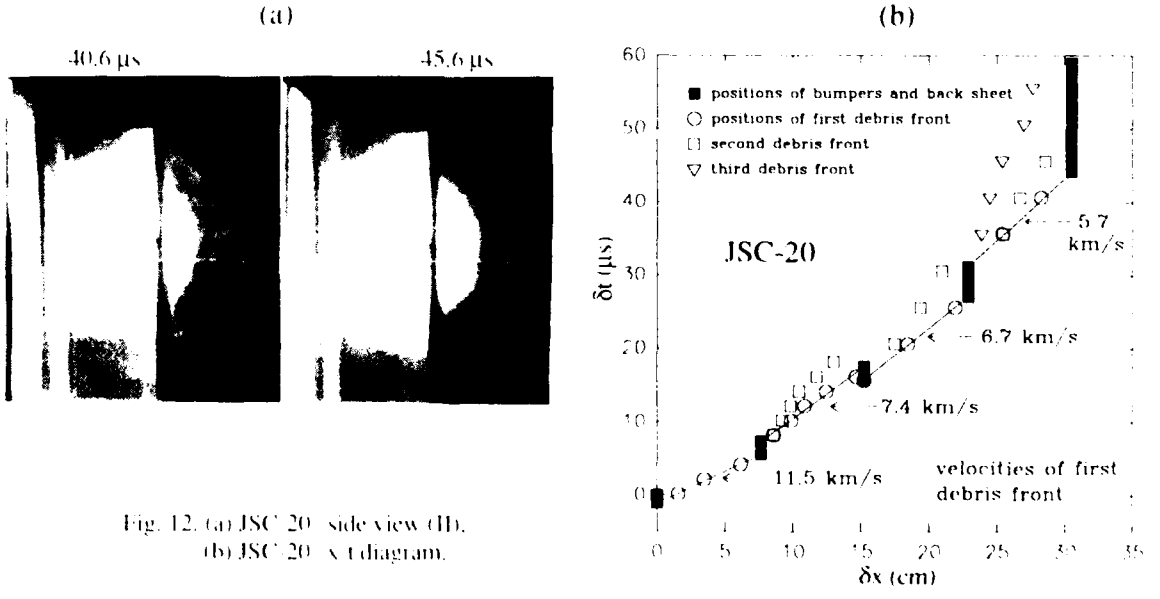


Fig. 12. (a) JSC-20--side view (II). (b) JSC-20--x-t diagram.

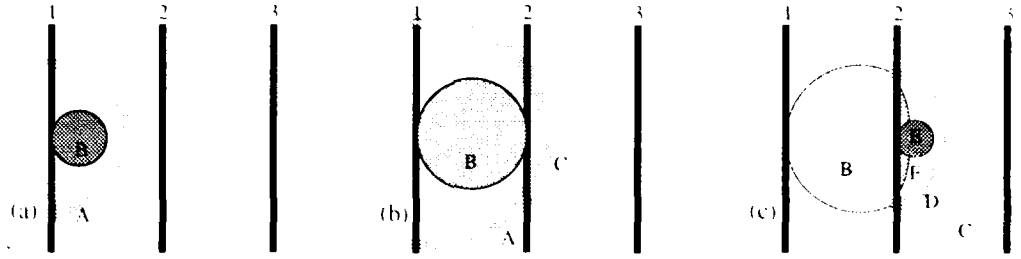


Fig. 13. Hypothetical evolution of MSS debris cloud.

4.2.5 Discussion of MSS Debris Evolution. The flyer impact and subsequent interaction between debris fronts and additional shield layers clearly leads to a richer, more complicated structure and evolution of debris for this shield assembly in comparison to that for the simple metallic WBS. Fig. 13 depicts a highly simplified interpretation of the origin of the various parts of the debris cloud. The figure shows a sequence of schematic snapshots of the development of an idealized debris cloud as it progresses through the first two shields. Figure 13(a) shows the structure of the debris shortly after impact at which time it has separated into two components: *A*, the vapor cloud, and *B*, the dense solid/liquid debris bubble. The situation shown in Fig. 13(b) is the instant the dense debris bubble arrives at the second shield. A portion of the vapor cloud *A* has already passed through the porous fabric, giving rise to vapor cloud *C* in the second space. Figure 13(c) depicts the situation after the main bubble *B* has collided with the second shield. The vapor cloud *C* has propagated downrange, and the mass concentration of flyer material at the apex of bubble *B* generates a pair of debris components, *D* and *E*, that are analogous to *A* and *B* from the original impact. Finally, the "skin" of bubble *B* interacts with the second shield, generating debris front *F*. Obviously, if a similar set of interactions takes place at each shield, the number of debris components will increase much more rapidly than the number observed in the framing images. However, this picture does provide a conceptual framework for identification of various debris fronts.

4.3 Mesh Double Bumper

4.3.1 Experiment JSC-6. In this test, an MDB shield such as that described in section 2.2 was subjected to impact by a 0.766 g aluminum flyer at 7.46 km/s. The flash x-ray image of the flyer before impact indicates that it was intact and bowed, but was tilted at impact. It is very difficult to see the form of the debris between the mesh and the second bumper in the framing sequence because of impact flash (Fig. 14), and it is not possible to make any quantitative statements about it. However, the debris cloud that forms immediately downrange from the second bumper has a very well-defined leading edge from which it was easy to determine a velocity of about 6.5 km/s. This debris cloud is quite different from that generated by the Whipple bumper, in that the outer envelope of faster material is not present.

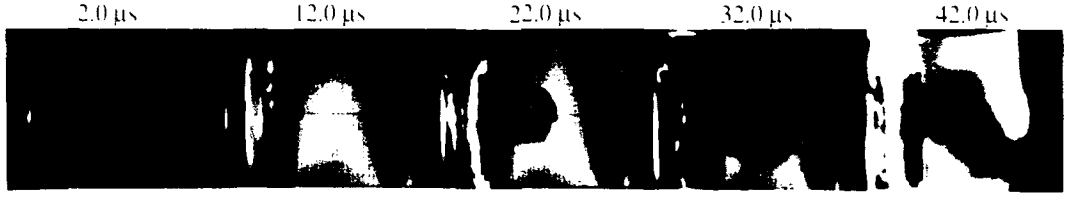


Fig. 14. JSC-6—side view.

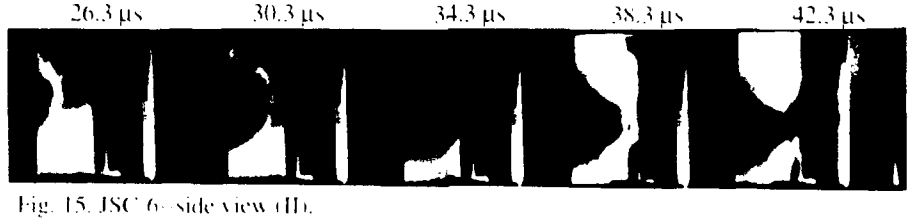


Fig. 15. JSC-6—side view (II).

This cloud can be seen colliding with the third (Kevlar®) bumper in Fig. 15, generating another debris cloud in the following space with a velocity of roughly 8 km/sec. This increase in velocity after interaction with a bumper was not observed in any of the MSS tests (within the uncertainty of measurement). However, there are valid reasons why metal debris impacting a polymer-containing composite could generate a secondary debris cloud with a higher expansion velocity as observed. The sequence of back surface images (not shown) demonstrate that the backsheet is perforated quite early by the debris, but the perforations do not appear to grow very much. For this reason, JSC-6 was classified as being on the threshold of failure.

4.3.2 Experiment PII-3. In this test, a 0.794 aluminum flyer hit an MDB at 9.6 km/s. A more massive MDB was used, with five layers of Kevlar in place of the four layers used in the previous experiments, and with the aluminum backsheet increased in thickness to 2.03 mm. The framing images in Fig. 16(a) show the debris approaching and impacting the second (solid aluminum) bumper, and the debris cloud that is generated from that impact. The velocity of the debris in the first intershield spacing was about 7.5 km/s. However, a faster, more tenuous front is also visible. The debris in the second spacing was moving at a remarkably high velocity of nearly 16 km/s. This increase in velocity at the second bumper for 10 km/s impacts has since been confirmed by other experiments on MDB's. The lower, post-Kevlar debris velocity of about 5 km/s is a lower bound. Because the backsheet did not suffer damage until well after arrival of ancillary launch debris, experiment PII-3 is listed as a "pass".

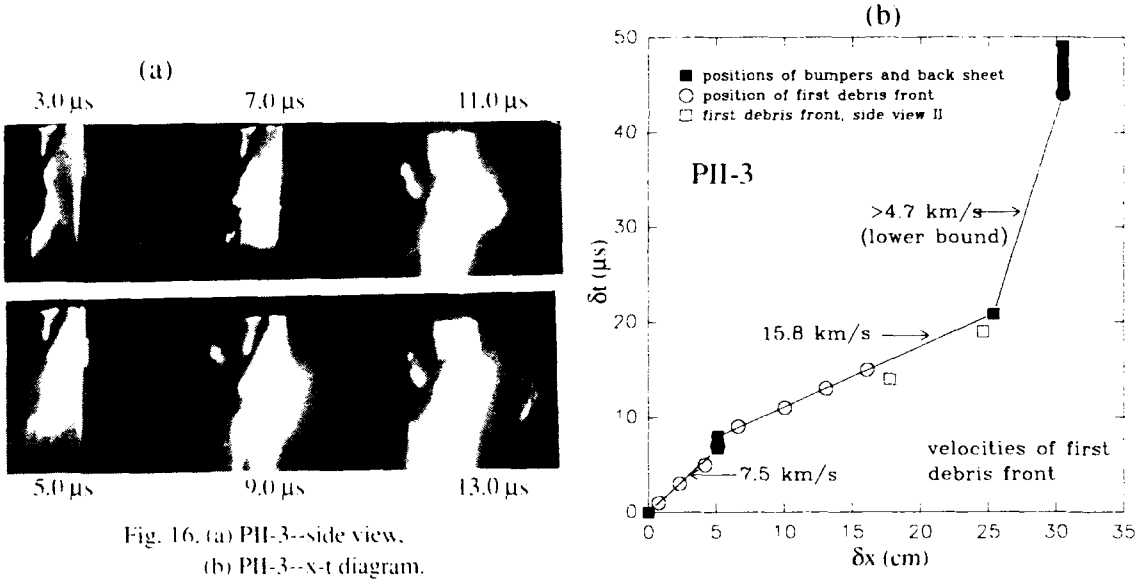


Fig. 16. (a) PII-3--side view, (b) PII-3--x-t diagram.

5. ANALYSIS AND COMPARISON OF RESULTS

The analysis of the shielding concepts reported in this section is preliminary because the flyers are bowed in shape as opposed to the flat disks that have been considered analytically. In some experiments, the bowed disks are skewed or tilted as well (Fig. 3), so the initial impact is no longer an axially symmetric process. Irregular impacts are far more likely than geometrically simple impacts to occur in orbit, but they are more difficult to simulate with computer codes. Some modelling of the flyer and first bumper interaction is needed to understand the complex fragmentation that takes place. The purpose of the present test series was to extend the shield development undertaken with spherical aluminum flyers at 7 km/s (Cour-Palais *et al.*, 1992) to higher velocities. However, it is possible to glean some interesting results if we consider the relative areal densities of the intact flyers and the shields.

Radiographs of the flyers taken prior to impact (Fig. 3) show that the curvature of the disks reduces their effective diameter. Given a disk thickness of 1 mm and diameter of 19 mm, the mass of an aluminum flyer is 0.77 g and its areal density is about 0.27 g/cm^3. If the curvature decreases its diameter to a chord of 17 mm, the areal density increases to a mean of about 0.34 g/cm^3. The diameters of a number of flyers were measured from the x-ray images, and their known masses (Table 1) were used to determine the areal densities at impact (see Table 2). These numbers are based on the assumption that the single radiographic projection available is representative, *i.e.* that flyers are approximately symmetric. In a few of the experiments, orthogonal x-rays taken prior to impact show that the flyer is still approximately circular (for those experiments, the mean diameter is given). This interpretation is also supported by the symmetric and smooth appearance of most of the flyers in the radiographs. However, flyers may be tilted and their areal projection on the plane perpendicular to the velocity vector will not be circular, giving rise to significant uncertainty. The resulting flyer areal densities were used to calculate several shield parameters (Table 2) that can be compared directly with similar results obtained with undeformed spheres and disks launched by a light-gas gun to 7 km/s.

The WBS tests can be summarized as follows: JSC-3 failed, JSC-5 passed but the back sheet experienced two small dimples, JSC-9 failed and JSC-12 had one small perforation and was on the threshold of failure. Thus the ballistic limit for a total shield areal-density (A-D) of 1.44 g/cm^2 is an initial impact momentum between the 5.7 x 10^5 dyne-seconds for JSC-5 and 5.0x 10^5 dyne-seconds for JSC-12 (Table 2). However, in JSC-12, the flyer had a ring of fragments, so its effective A-D was lower. It is possible that a fragment escaped bumper impact and did further damage, or that there were more solid bumper fragments for the lower-momentum impact (JSC-12).

The four MSS tests (JSC-15,18, 19, and 20) all passed. The first thing to note is that the total shield A-D's are much lower than for the WBS shields. The total A-D is 31% less for the MSS tested in JSC-18 compared to the WBS in JSC-12, yet the MSS survived a higher-momentum impact than the WBS, which was on the threshold. A comparison of JSC-15 and JSC-19 with JSC-12 shows that the MSS also passes with a 31% lower A-D for a heavier, denser flyer. Finally, JSC-20 can be compared with JSC-18 to show that the total shield A-D can be further reduced to 33% lighter than the heavy WBS. The MSS shields tested in JSC-18 and 19 were slightly lighter than the "baseline" shields that were derived in previous tests (Cour-Palais *et al.*, 1992). In those tests a 1.27 g spherical aluminum projectile at 6.73 km/s was the ballistic limit for an impact momentum of 8.5×10^5 dyne seconds. The limited results of these tests suggest that a 10 km/s bowed disk projectile is more damaging than a spherical projectile for a given momentum and areal density, in agreement with Hertel *et al.*, 1992 who showed that for a "plate" impact (unlike a spherical impact) the resulting debris cloud tends to be more channelled and focussed. The corrections to allow for shape effects in the predictive equations derived from light-gas gun tests with spheres at 7 km/s must await the further tests that are planned at this facility.

The two MDB experiments were selected to show the effect of bumper areal density on survival of this design, and to compare their effectiveness to heavier WBS's. JSC-6 was of the lightest-weight design, and was just on the threshold of failure. It is noteworthy that the bumper/flyer A-D ratio was lower by a factor of 3, and the total shield A-D was about 43% less than the WBS tested in JSC-3, which clearly failed under similar impact conditions (the flyer was highly tilted for JSC-6, giving it a high average areal density). PII-3 was a test of an MDB design with an areal density of 0.94 g/cm^2, slightly less than the MSS's, and 35% lighter than the WBS that barely survived similar loading conditions in test JSC-12. The flyer was highly deformed with a small radius of curvature, giving it a relatively high A-D. Nevertheless, the shield survived an impact with the largest flyer momentum test, with a lower bumper/flyer A-D ratio than any of the MSS tests.

Table 2. Debris Shield Test Parameters.

Shot No.	Flyer momentum (10^5 dyne·sec)	Effective flyer diam. (mm)	Mean flyer A-D, m_f (g/cm^2)	Bumper A-D, m_b (g/cm^2)	Backsheet A-D, m_{bs} (g/cm^2)	Total Shield A-D, m_s (g/cm^2)	Bumper/flyer A-D Ratio, m_b/m_f	Shield/flyer A-D Ratio, m_s/m_f
JSC-3	5.53	18.9	0.28	0.085	1.101	1.18	0.31	4.3
JSC-5	5.70	16.9	0.35	0.343	1.101	1.44	0.97	4.1
JSC-9	7.40	16.7[a]	0.36	0.085	1.101	1.18	0.24	3.3
JSC-12	4.99	20.2[b]	0.16	0.343	1.101	1.44	2.18	9.2
JSC-15	7.58	14.9	0.45	0.432	0.551	0.98	0.95	2.2
JSC-18	5.90	16.5	0.28	0.432	0.551	0.98	1.54	3.5
JSC-19	6.32	15.8	0.32	0.432	0.551	0.98	1.34	3.0
JSC-20	6.01	16.0	0.30	0.400	0.551	0.95	1.36	3.2
JSC-6	5.71	13.5	0.54	0.350	0.322	0.67	0.65	1.3
PII-3	7.62	14.3	0.49	0.382	0.555	0.94	0.77	1.9

a. Flyer is broken and has trailing fragments.
b. Includes diameter of fragment ring.

6. SUMMARY

Experiments have been performed on the Sandia's Hypervelocity Launcher to characterize and evaluate both simple and advanced shielding concepts that are proposed for use with spacecraft in low earth orbit, such as Space Station Freedom. Experiments were conducted over a velocity range of 7 to 10 km/s, a range heretofore not accessible by conventional smooth bore launchers. Orbital debris impact is simulated by launching a plate-like projectile at the proposed shield designs. The simple shield concepts make use of an aluminum Whipple Bumper Shield placed at a distance from its protective structure. Concepts for advanced shielding include both the Mesh Double Bumper and Multi-Shock Shields. Results and conclusions from these experiments may be summarized as follows:

Whipple Bumper Shield:

- A WBS whose bumper thickness is 0.3 mm is not sufficient to protect a back wall about 4 mm thick placed 305 mm away when an 0.78 g plate in the shape of a bowed disk initially about 19 mm in diameter by about 1 mm thick impacts it over a velocity range of 7 to 10 km/s.

- A similar WBS whose bumper thickness is increased to 1.3 mm is sufficient to protect a back wall about 4 mm thick placed 305 mm away under similar loading conditions at about 7 km/s, even when the total shield-to-projectile A-D ratio is slightly lower.

Multi-Shock Shield:

- The MSS is effective at dispersing incoming bowed disk flyers with masses up to 0.79 g (about 19 mm diameter by 1 mm thick) at velocities up to about 10 km/s. It consistently prevents rupture of a 2 mm thick back sheet located 305 mm from the front bumper shield.
- With an areal density reduction of up to 33%, the MSS is more effective than the WBS against impact by bowed disk aluminum plates at up to 10 km/s.
- The MSS disperses debris in both space and time, generating multiple debris fronts at each successive bumper. As the debris fronts propagate through the shield assembly, they slow down.

Mesh Double Bumper:

- An MDB with a back sheet 0.16 mm thick placed 305 mm from the first mesh location appears to be on the survival threshold when impacted by a 0.75 g bowed disk about 19 mm in diameter and 1 mm thick. This shield was about 43% lighter than a WBS that clearly ruptured under less severe impact conditions.
- With an areal density reduction of up to 35%, the MDB is more effective than the WBS against impact by bowed disk aluminum plates at up to 10 km/s.

General:

- A comparison of x-ray measurements and photographic measurements of the debris cloud suggest that the fastest photovisual debris is very low density.
- For normal impacts, bowed-plate or flat-plate projectiles are more damaging than spherical projectiles for a given momentum and areal density.

7. ACKNOWLEDGMENTS

This work was performed at Sandia National Laboratories supported by the U.S. Department of Energy under contract DE AC04-76DP00789. We thank NASA for their interest and support. Brian Abeyta participated as a summer student by helping determine debris velocities from framing camera images.

REFERENCES

Ang, J. A., L. C. Chhabildas, B. G. Cour-Palais, E. C. Christiansen and J. L. Crews (1992). Evaluation of Whipple Bumper Shields at 7 and 10 km/s. In: *Space Programs and Technologies Conference*, AIAA Paper #92-1590.

Boslough, M. B., L. C. Chhabildas, R. D. Reinhart and C. A. Hall (1993). Hypervelocity Testing of Debris Shields against Impacts to 10 km/s. *Sandia Report*, in preparation.

Charters, A. C. (1987). Development of the High-Velocity Gas-Dynamics Gun. *Int. J.of Impact Engng.*, 5, 181-203.

Chhabildas, L. C., L. M. Barker, J. R. Asay, T. G. Trucano, G. I. Kerley and J. E. Dunn (1992a). Launch Capabilities to over 10 km/s. In: *Shock Waves in Condensed Matter--1991* (S. C. Schmidt *et al.*, eds.), pp. 1025-1031. Elsevier Science Publishers, B.V., Amsterdam.

Chhabildas, L. C., J. E. Dunn, W. D. Reinhart and J.M. Miller. (1992b) An Impact Technique to Accelerate Flier Plates to Over 12 km/s. *Int. J.of Impact Engng.*, this volume.

Chhabildas, L. C., E. S. Hertel and S. A. Hill, (1992c) Whipple Bumper Shield Tests at over 10 km/s. In: *Shock Waves in Condensed Matter--1991*, (S. C. Schmidt *et al.*, eds.), pp. 991-994. Elsevier Science Publishers, B.V., Amsterdam.

Christiansen, E. L. (1990) Advanced Meteoroid and Debris Shielding Concepts" In: *Procs. Orbital Debris Conf.*, AIAA Paper #90-1336.

Cour-Palais, B. G. (1969) Meteoroid Protection by Multi-Wall Structures. AIAA Paper No. 69-372.

Cour-Palais, B. G. and J. L. Crews, (1990) A Multi-Shock Concept for Spacecraft Shielding. *Int. J. Impact Engng.*, 10, 135-146.

Cour-Palais, B. G., A. J. Piekutowski, K. V. Dahl, and K. L. Poormon (1992) Analysis of the UDRI Tests on Nextel Multi-Shock Shields. *Int. J.of Impact Engng.*, this volume.

Hertel, E. S., L. C. Chhabildas, and S. A. Hill, (1992) Whipple Bumper Shield Simulations. In: *Shock Waves in Condensed Matter--1991*, (S. C. Schmidt *et al.*, eds.), pp. 987-990. Elsevier Science Publishers, B.V., Amsterdam.

Interagency Group (Space), (1989) Report for National Security Council, Washington, D.C.

Kessler, D. J., R. C. Reynolds, and P. D. Anz-Meador, (1989) Orbital Debris Environment for Spacecraft Designed to Operate in Low Earth Orbit. NASA TM 100-471.

Whipple, F. L. (1947) Meteorites and Space Travel. *Astronomical J.* 52, 131.

Wilkinson J. P. D. (1969) A Penetration Criterion for Double-Walled Structures Subject to Meteoroid Impact, *AIAA J.* 7, 1937-1943.

Int. J. Impact Engng Vol.14, pp.107–120, 1993
Printed in Great Britain

0734-743X/93 $6.00+0.00
1993 Pergamon Press Ltd

RHALE: A MMALE SHOCK PHYSICS CODE WRITTEN IN C++*

K.G. BUDGE and J.S. PEERY

Computational Physics Research and Development (1431)
Sandia National Laboratories
Albuquerque, NM 87185

ABSTRACT

This paper describes RHALE, a multi-material arbitrary Lagrangian-Eulerian (MMALE) shock physics code. RHALE is the successor to CTH, Sandia's 3-D Eulerian shock physics code, and will be capable of solving problems that CTH cannot adequately address.

We discuss the new Lagrangian capabilities of RHALE, which include arbitrary mesh connectivity, superior artificial viscosity, and improved equations of state. We also discuss some of the issues we have encountered in the choice of an axisymmetric element technology and our resolution of these issues.

We discuss the MMALE algorithms that have been extended for arbitrary grids in both two and three dimensions and present the results of calculations that are of interest to the hypervelocity impact community. The MMALE addition to RHALE provides the accuracy of a Lagrangian code while allowing a calculation to proceed under very large distortions. Coupling an arbitrary quadrilateral or hexahedral grid to the MMALE solution facilitates modeling of complex shapes with a minimum number of computational cells.

RHALE allows regions of a problem to be modeled with Lagrangian, Eulerian or ALE meshes. In addition, regions can switch from Lagrangian to ALE to Eulerian based on user input or mesh distortion. For ALE meshes, new node locations are determined with equipotential schemes. Element quantities are advected with donor, van Leer, or Super-B algorithms. Nodal quantities are advected with the second order SHALE or HIS algorithms. Currently, material interfaces are determined with the SLIC algorithm; however, both two and three dimensional versions of Youngs' interface tracker are being investigated.

To facilitate the development of such a lengthy code, we choose to write in the C++ programming language. We feel that object-oriented programming techniques are superior to conventional programming techniques. However, we discuss a few of the efficiency problems we have encountered using these techniques and how we have addressed these problems.

*This work performed at Sandia National Laboratories supported by the U.S. Department of Energy under contract number DH-AC04-76DP00789.

INTRODUCTION

Theoretical studies of hypervelocity impact phenomena make heavy use of computer simulations. The computational kernel of these simulation codes (frequently called "shock codes", "hydro codes", or "wave codes") must be highly efficient and capable of handling strong shocks and large deformations.

The strong shock code CTH (McGlaun *et al.* 1986) is used extensively in the simulation of hypervelocity impacts. This code uses an Eulerian finite-volume formulation of the equations of motion, includes sophisticated equations of state, and has strength and fracture models. Its results have been extensively checked against experimental data for regimes where such data are available and have been shown to be remarkably accurate for many classes of problems. It is heavily supported and widely used throughout the DOE, DoD, and NASA communities and its capabilities continue to be enhanced; for example, a version suitable for massively parallel computers, PCTH, is currently in development (Robinson *et al.*, 1992).

However, CTH suffers from the limitations inherent in any shock code based on a purely Eulerian formulation. Since material flows through a fixed mesh, advection algorithms are required which introduce numerical dispersion and dissipation. Sliding between surfaces is difficult to model. Since Eulerian formulations generally use a regular mesh, the size of mesh elements can be varied only in limited ways, which means that element dimensions tend towards the smallest length scale of interest in the calculation. Large regions of empty space must also be included in many grids. The latter two limitations make many interesting calculations prohibitively expensive.

Shock codes based on Lagrangian formulations avoid these difficulties. Since the mesh moves with the material, no advection takes place and the associated numerical dispersion and dissipation is avoided. Sliding is handled much more accurately than in an Eulerian code. Element connectivities and volumes are arbitrary and can more easily reflect the very different length scales in different portions of the problem. Lagrangian codes are thus preferred for problems requiring high numerical accuracy or where differing length scales are important and in which large deformations do not take place. They fail whenever large deformations are present, since highly distorted elements lose accuracy or may even invert (thus halting the calculation).

The RHALE code uses an arbitrary Lagrangian-Eulerian (ALE) formulation in an effort to get the best of both worlds. Although users can specify a purely Lagrangian or purely Eulerian calculation for portions of the problem domain, the normal mode of operation is for a calculation to proceed in Lagrangian fashion until elements become highly distorted (as measured by various criteria specifiable by the user). At this point, material is permitted to flow between elements in the most deformed portion of the mesh so as to reduce the distortion to acceptable levels. This formulation permits accurate treatment of contact surfaces and has less numerical dissipation than a purely Eulerian calculation (since less advection takes place). Quite large deformations can take place without the calculation failing, unlike a purely Lagrangian calculation. We are currently developing ALE algorithms that also preserve variable mesh scaling.

Another innovative feature of the RHALE development project is that the code is being written in C++. We feel that the object-oriented programming paradigm, which C++ supports, is the best approach to the development of such a lengthy code. We are addressing some of the known efficiency problems with C++ through a variety of programming techniques, including reference counting, deferred expression evaluation, and hidden calls to assembly language routines.

RHALE is being developed in parallel with PCTH and the two projects are expected to share much of their coding. However, RHALE represents the next generation of strong shock codes and may eventually replace CTH and PCTH. It should be capable of performing any calculation that CTH can perform (though perhaps somewhat less efficiently) and will execute additional calculations that CTH cannot currently treat.

FUNCTIONALITY OF RHALE

RHALE supports three types of meshes: pure Lagrangian, pure Eulerian, and ALE. All meshes may have arbitrary

connectivity between elements. An arbitrary connectivity mesh allows an arbitrary number of elements to share a common node. The user may specify different mesh types for different regions of a problem, so that, for example, the projectile and target region in an impact calculation may be calculated in ALE mode while the far-field target calculation may take place in pure Lagrangian mode.

We have experimented extensively with a variety of artificial viscosity formulations. None has proven consistently superior to the scalar bulk viscosity formulation that has been used for over thirty years. However, we are continuing to experiment with the spurious vorticity correction methods discussed by Dukowicz and Meltz (1992) and may eventually incorporate a spurious vorticity control method in RHALE.

The finite element technology of RHALE consists of uniform-strain quadrilaterals (in 2-D) or hexahedrons (in 3-D). Frame invariance for the constitutive models is achieved by using a corotational frame formulation similar to that of the PRONTO finite-element code (Taylor and Flanagan, 1987). The row-summed lumped mass is used to diagonalize the mass matrix (avoiding large matrix inversions) and the time integration is carried out using an explicit central-difference method (Hughes, 1987). Thus, individual time steps are computationally efficient but the maximum time increment is limited by a Courant condition.

Since RHALE uses a uniform-strain quadrilateral, spurious zero-energy modes (hourglass modes) exist and must be damped. We provide both the control method used in PRONTO (Taylor and Flanagan, 1987), which is applicable to materials with strength, and a version of the Margolin-Pyun method (Margolin and Pyun, 1987), which is applicable to fluids.

RHALE uses the equation of state library being developed for both RHALE and PCTH. This library includes several Mie-Gruneisen models, ideal gas, JWL equations of state for explosives, and SESAME tabular equations of state. It also has sophisticated strength models for the deviatoric response, including the Johnson-Cook plasticity model.

RHALE can handle 2-D Cartesian, 2-D axisymmetric, and 3-D Cartesian geometries. We use a volume-weighted rather than an area-weighted axisymmetric element (Taylor and Flanagan, 1987). The former has the advantages that the nodal lumped masses are only slightly time dependent and that the element passes a restricted patch test. The latter formulation has the advantages of a closer correspondence between the 2-D Cartesian and axisymmetric formulations and of being better conditioned for implicit methods. Since RHALE currently uses an explicit time integration method, the latter consideration is not important.

MMALE ALGORITHMS

The MMALE addition to RHALE involves remeshing to relieve distortion and remapping velocities and state variables to the new mesh while conserving global quantities. These steps and their substeps are described below.

Remesh

The remeshing phase of the MMALE method determines new node locations that will partially alleviate the associated elements' distortion. In RHALE, a node can be of type Lagrangian, ALE, or Eulerian, reflecting the type of mesh of which it is part. Nodes on boundaries between meshes of different type are given the more restrictive type (Lagrangian rather than ALE; ALE rather than Eulerian).

Remeshing is a three step process. First, nodes that meet the criteria for being moved are tagged. Next, new positions are calculated for candidate nodes. Eulerian nodes are moved to their original location, Lagrangian nodes remain fixed in the remesh/remap phase, and ALE nodes are moved based on distortion criteria. Finally, the actually movement of the selected ALE nodes is limited to some fraction of their calculated movement.

One set of criteria for moving an ALE node is given in the HEMP code (Sharp and Barton, 1981). Barton's criteria amount to two tests: an angle test and a volume test. For these nodes, the angles that are form by the element edge

vectors that originate at the node are calculated. The ideal situation is for the angles to be 90 degrees. Additionally, the volumes of each of the elements that are connected to a node are compared. Ideally, they should all be equal. These calculations must be performed for each of the elements that surround a tagged node. To determine if an ALE node should move, a user defined minimum angle and minimum to maximum volume ratio criteria are used.

Node and Element Ordering. Determining element and node neighbors is trivial for logically regular meshes. However, for arbitrary meshes, determining this information requires sophisticated algorithms and logic.

The most robust algorithms for determining new node locations require the coordinates of node neighbors. The identification of a node's closest neighbors is not a trivial problem. Explicitly storing this information or using a searching algorithm would make the ALE formulation unrealistic if not impossible due to the enormous memory and CPU burden. To overcome this problem in two dimensions, the methods of element and node ordering described by Benson (1989) were adopted. Benson's method relies solely on counterclockwise ordering of nodes within an element, and of elements about a node. Given an array that contains the nodes listed in counterclockwise order within each element, Benson's method generates a hash table to describe the relative orientation of a node within each of its connecting elements. Since in two dimensions there are only four possible node locations within an element, a node can have a hash value of 4^{nc} where nc is the number of element connections. With an arbitrary mesh, nc can be large (four or greater) and thus only unique hash values for a mesh are stored. There is no known extension of this concept to three dimensions, where we must develop more general (but less robust) methods.

For the advection algorithms, an element must not only know the nodes on its vertices but also its element neighbors. This is relatively easy to determine by matching node lists. This element neighbor information plays a pivotal role in the second order advection algorithms.

Applying Equipotential Solutions to the Mesh. In order to perform the remeshing phase of MMALE, one must determine where an ALE node is to be moved. There are many techniques for deciding where to move a node, but one of the most successful and the one used in this MMALE algorithm for two dimensional problems is a method based on equipotential smoothing (Winslow and Barton, 1982). Winslow's method is based on inverting Laplace's equation. This is given as

$$\alpha x_{\phi\phi} - 2\beta x_{\phi\varphi} + \gamma x_{\varphi\varphi} = 0 \tag{1}$$

$$\alpha y_{\phi\phi} - 2\beta y_{\phi\varphi} + \gamma y_{\varphi\varphi} = 0 \tag{2}$$

where

$$\alpha = x_{\varphi}^2 + y_{\varphi}^2 \tag{3}$$

$$\beta = x_{\phi} x_{\varphi} + y_{\phi} y_{\varphi} \tag{4}$$

$$\gamma = x_{\phi}^2 + y_{\phi}^2 \tag{5}$$

These equations can be approximated with second order central differencing techniques and are given as

$$x' = \frac{1}{2(\alpha+\gamma)} \left(\alpha (x_4 + x_8) + \gamma (x_2 + x_6) - \frac{1}{2}\beta (x_3 - x_5 + x_7 - x_9) \right) \tag{6}$$

$$y' = \frac{1}{2(\alpha+\gamma)} \left(\alpha (y_4 + y_8) + \gamma (y_2 + y_6) - \frac{1}{2}\beta (y_3 - y_5 + y_7 - y_9) \right) \tag{7}$$

where

$$x_{\phi} = \frac{1}{2}(x_4 - x_8) \tag{8}$$

$$x_{\varphi} = \frac{1}{2}(x_2 - x_6) \tag{9}$$

$$x_{\phi\varphi} = \frac{1}{4}(x_3 - x_5 + x_7 - x_9) \tag{10}$$

and equations for the y coordinate are similarly developed.

These equations can be applied for nodes connected to four elements. For the other nodes, a method developed by Budge (1991) is used.

Finding the x and y coordinates for all the nodes that satisfy Laplace's equation or the method developed by Budge is an iterative procedure. Jacobi iteration (Press *et al.*, 1986) can be used to solve these equations; however, MMALE algorithms are interested in making small changes to the mesh and therefore these equations are generally solved only once per remap step. In RHALE, the user is allowed to control the number of iterations performed on these equations.

Limiting Node Movement. Currently, RHALE has no limiting criteria placed on the coordinates determined from the equipotential solution. In other words, the displacement from the old to new coordinates is multiplied by a fraction of one. One should be concerned about a node being moved such that its new position overlaps the old position of one of its neighbors. Test cases have not shown this to be a problem primarily because only one iteration is being performed with the equipotential equations. In the future, node movement will be limited since multiple iterations on the equipotential equations is allowed and Courant stability limits in the advection could be exceeded.

Remap

The explicit relocation of nodes creates an advection problem. Since time is not involved, the advection problem simplifies to a remapping problem. The remap phase consists of determining volumes fluxes, determining material fluxes from volume fluxes through the use of an interface tracker, and advecting material variables and velocities. The various aspects of the remap phase will be discussed in the following sections.

Determining Volume Fluxes. The first step in any advection scheme is to determine the volume fluxes created by the movement of nodes. When a node is moved, volume fluxes are generated through the faces/sides of the elements. The volume flux through an element face is given by the change in volume produced by the movement of nodes on that face. With this definition of volume flux, the new volume of an element is given by

$$V^{new} = V^{old} + \sum_{i=1}^{ns} \Delta V_i \tag{11}$$

where i refers to an element's face and ns refers number of element faces (four in two dimensions and six in three dimensions).

Material Fluxes. In MMALE, a simulation generally begins with single material elements. If a problem remained Lagrangian, the elements would remain single material; however, for problems of interest, elements quickly become distorted and remeshing/remapping is used to relieve distortion. The remeshing/remapping phase creates multi-material elements and thus, the volume of each material within the volume fluxes must be determined.

Currently, RHALE determines material volume fluxes with the SLIC interface tracking algorithm (Noh and Woodward, 1976). This algorithm places materials within a cell in an order from left to right by determining the materials contained in neighboring cells and assuming a planer interface between materials. The material order determines the precedence of materials to be used in the material makeup of the volume flux. In the future, Young's (1987) interface tracker will be added to RHALE.

Element Centered Advection. Once the nodes have been moved, the element centered variables must be advected to their new locations. Isotropic advection assumes that the material is advected through all faces of the element simultaneously. This discussion will assume that advection occurs isotropically, however, RHALE makes one-dimensional remap sweeps through the mesh to aid in corner coupling.

Advection algorithms are expressed in volume and mass coordinates. Using the above definition of volume flux, a newly advected element centered variable is given by

$$f_j^{new} = \frac{f_j^{old} V_j^{old} + \sum_{i=1}^{ns} \tilde{f}_i \Delta V_{ji}}{V_j^{new}} \tag{12}$$

where the $\tilde{f}_i$'s are determined by the type and order of the advection algorithm and V represents either volume or mass. Most intensive quantities are fluxed with mass.

The simplest advection scheme is a first order advection method since it does not involve evaluating derivatives; however, it is also the most diffusive. The advecting material is assumed to carry the average value of an element centered variable from which the material originated. This is analogous to first order upwinding in finite difference methods. For a first order method, the $\tilde{f}_i$'s are given by

$$\tilde{f}_i = \begin{cases} f_n \text{ if } \Delta V_{ji} > 0 \ (influx) \\ f_i \text{ if } \Delta V_{ji} < 0 \ (outflux) \end{cases} \tag{13}$$

where n is the neighbor's value.

Two second order advection methods are available in RHALE, van Leer (1984) and Super-B (Christensen, 1991). Both are based on slopes among the donor, acceptor and behind elements. For van Leer, this relationship is shown in the figure below where the x-axis represents volume or mass and the y-axis represents a quantity to be fluxed.

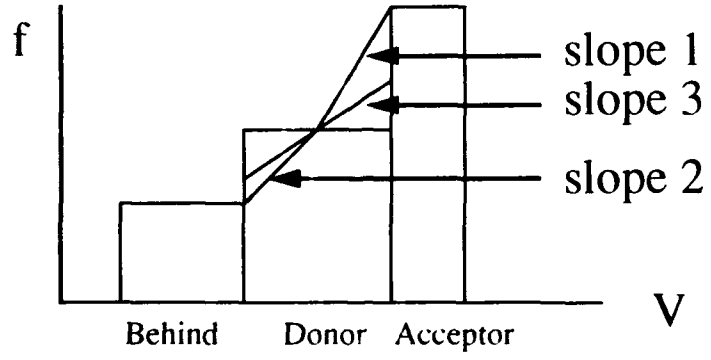


Fig. 1. Slopes Used in van Leer Advection Algorithm

The three slopes are given by

$$s1 = (2(f_{i+1} - f_i))/X_i \tag{14}$$

$$s2 = (2(f_i - f_{i-1}))/X_i \tag{15}$$

$$s3 = (2(f_{i+1} - f_i))/(X_{i+1} + X_i) + (2(f_i - f_{i-1}))/(X_i + X_{i-1}) \tag{16}$$

For the van Leer scheme, the slope used is given by

$$slope' = \begin{cases} 0 \text{ if } \left| \dfrac{sign(s1) + sign(s2) + sign(s3)}{3} \right| \neq 1 \\ sign(s1)\, min(|s1|, |s2|, |s3|) \end{cases} \tag{17}$$

and the value used for $\tilde{f}_i$ is given as

$$\tilde{f}_i = \begin{cases} f_n + \dfrac{slope'}{2}(V_n - \Delta V_{ni}) \text{ if } \Delta V_{ni} > 0 & \text{(inflow)} \\ f_i + \dfrac{slope'}{2}(V_i + \Delta V_{ni}) \text{ if } \Delta V_{ni} < 0 & \text{(outflow)} \end{cases} \tag{18}$$

Vertex Centered Advection. Vertex centered advection is very similar in concept to element centered advection and is required for advecting nodal quantities such as momentum. For vertex centered variables, however, a staggered grid exists with vertices at the center. For a logically connected grid, donor, acceptor and behind nodes are known for each direction and staggered fluxes and advection quantities can be determined. Amsden and Hirt (1973) developed the YAQUI algorithm for this type of mesh. However, determining staggered mesh quantities can be very expensive. In addition, for an arbitrary mesh, the staggered mesh can have a very odd shape and advection quantities are difficult if not impossible to calculate. Attempts to eliminating these problems have resulted in several element centered methods for advecting vertex centered variables.

In RHALE there are three element centered options for nodal vertex centered variables, SALE (Amsden *et al.*, 1980), SHALE (Margolin and Beason, 1988), and HIS (Benson 1992). All of these methods project nodal variables to element centers, advect the new element centered variables with the element centered methods described above, and project these values back to the nodes. SALE simply averages nodal variables to calculate element centered quantities and thus is first order. SHALE averages both the nodal variable and its derivatives and thus is second order. Both SALE and SHALE are monotonic with respect to the element centered advection but not with respect to the nodal variables. This can lead to new maxima or minima for nodal quantities. Benson's HIS algorithm is second order and monotonic. The HIS algorithm places nodal variables at element centers, advects the element quantities and assembles the values back at the nodes. The HIS method has been extended to arbitrary meshes in RHALE.

C++ EFFICIENCY AND OPTIMIZATION

To facilitate code development and maintenance, we have chosen to write RHALE in C++ (Ellis and Stroustrup, 1990). We feel that the object-oriented programming paradigm provides superior reliability, reusability, and portability. Some of our coding is being developed in common with PCTH, which is also being written in C++.

Our basic classes represent scalar, vector, and tensor fields. Various operations between objects of these classes are

represented by the usual C operators, so that, for example, the equation

$$\vec{f} = \vec{\nabla}_x \bullet \mathbf{T} + \vec{b} \qquad \text{(EQ 19)}$$

can be coded as

```
f = Div(T,X) + b;
```

where `X`, `f` and `b` are objects of a vector field class and `T` is an object of a tensor field class. These objects contain both the data representing the field and a pointer to a data structure describing the mesh topology. Thus, indexes and loops are hidden in the class definition.

We find that considerable care is required in developing the basic classes to avoid inefficiencies. For example, many unnecessary copy operations take place unless reference counting techniques are used. In memory-critical applications, unacceptably large amounts of memory may be allocated for intermediate results of expression evaluation unless deferred expression evaluation is also implemented. Finally, the large number of memory allocation/deallocation operations that are necessary for field operations can be very expensive on certain architectures or operating systems; it is then necessary to take control of heap management, using the C++ language features provided for that purpose.

Reference Counting

This refers to the technique of allowing different field objects to make use of the same array of data (Coplien, 1992). A count of the number of fields using a data array is maintained. If a field operation is called that would modify the data, a private copy of the data is first generated for the particular field in question. Assignment operations consist simply of giving a field object access to a data array; no copy operation takes place. Once the number of fields using a given data array drops to zero, the data array is deleted and its memory returned to the heap.

Deferred Expression Evaluation

This refers to the technique of building a parse tree for an expression at run time, rather than immediately evaluating each sub-expression (Quinlan, 1991). When an assignment operation is reached, the parse tree is evaluated recursively. This allows the programmer to control the use of temporary scratch memory and (in principle) to apply optimizations to the parse tree without relying on compiler support. In practice, deferred expression evaluation reduces memory usage at the expense of computational efficiency. In many applications memory usage is critical, but for most others deferred expression evaluation is not worth the overhead entailed. Deferred expression evaluation is not currently used in our field library.

Heap Management

This is possible in C++ because operators are provided to obtain or free heap memory. Since many C++ implementations must make an expensive system call to obtain or release heap memory, application-specific memory management often dramatically improves efficiency. The usual approach is to obtain heap memory from the system using the standard system call, but without ever returning the memory to the operating system. The overloaded memory management operators reuse this memory for subsequent memory requests, circumventing the expensive system calls.

The value of these techniques is illustrated in Table 1. The test calculation consists of the repeated evaluation of a

Table 1: CPU time (seconds) for matrix test case (rank 100, 10,000 iterations)

Language	SUN CPU time	CRAY CPU time (MFlops)	nCUBE CPU time (assembly language libraries)
FORTRAN	110.1	0.71 (140)	185.8 (no)
C	108.4	0.77 (130)	150.8 (no)
C++ (default)	328.5	2.43 (41)	458.9 (yes)
C++ (rc)	131.9	1.06 (94)	82.8 (yes)
C++ (rc and mm)	130.4	0.83 (121)	81.4 (yes)

simple matrix expression (involving matrix addition and multiplication) for a 100x100 matrix. The expression is evaluated 10000 times. Note that coding using a naive C++ implementation of a matrix class is very inefficient, but that when reference counting (rc) and memory management (mm) are added to the class, the CPU time is within 20% of that of FORTRAN or C coding. In the case of the nCUBE, calls to vendor assembly language libraries were used in the class definition, which resulted in code that was actually more efficient than FORTRAN.

Table 2. Performance of Field Classes (no deferred expression evaluation)

# of elements	Sun Sparc-2 (MFlops)	Cray YMP, 1 CPU (MFlops)
1	0.15	0.10
10	0.75	1.03
100	1.22	9.5
1000	1.07	58.8
10000	0.88	121.5
100000	insufficient memory	140.0
50% peak	6 elements	1380 elements

We have benchmarked our field class library on Sandia's CRAY-YMP and obtained the results illustrated in Table 2. The test calculation consisted of the polar decomposition of a tensor field, which is a very realistic application. The final row of the table shows the number of elements in the array for which the performance drops to half of its peak value. We see that high efficiency is reached for very large arrays, but that the overhead becomes significant on the CRAY for moderate array sizes. In the case of the Sun workstation, the higher cost of floating operations makes the overhead insignificant even for rather small arrays. We are working to further reduce the overhead in these class libraries

LONG ROD PENETRATOR CALCULATION

One problem of interest to the hypervelocity impact community is long rod penetrators. An example of this type of problem in axisymmetric geometry is shown in Figure 2. (Note that all units are CGS.) RHALE has the ability

through its MMALE algorithm to zone this problem with Eulerian, ALE and Lagrangian sub-regions as shown in Figure 2. With this type of zoning, the structural response at the ends of the plates can be studied.

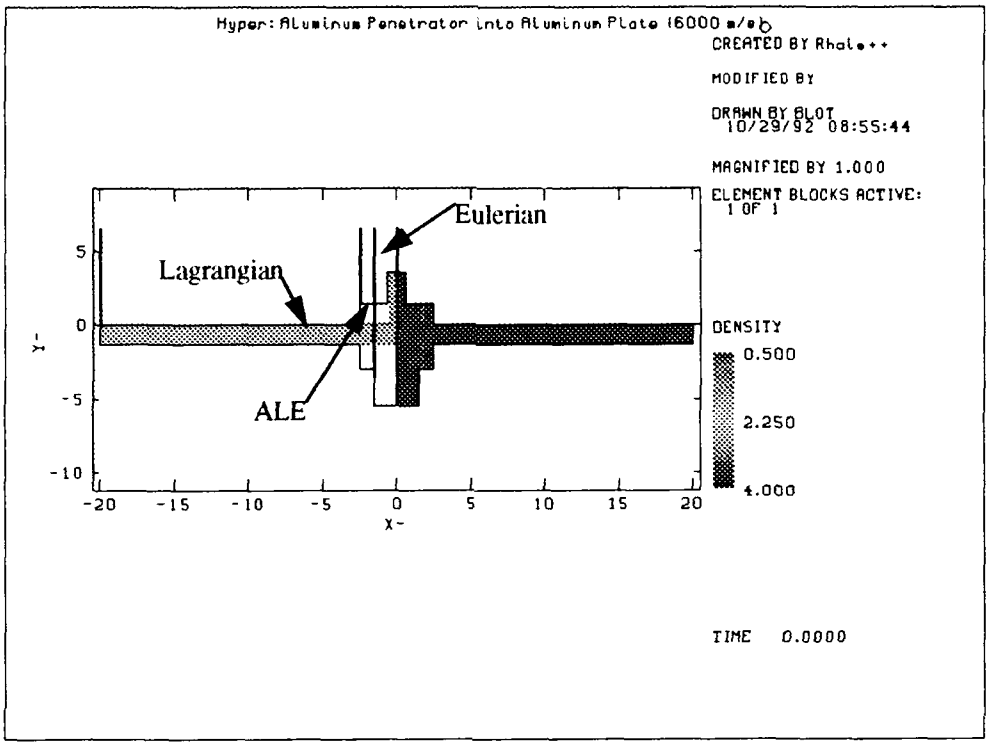


Fig. 2. Initial State of Long Rod Penetrator Simulation

The problem shown in Figure 2 was initialized with an aluminum rod moving at 6 km/s into an aluminum plate. Both the rod and the plate were modelled with an elastic-plastic constitutive model and a Mie-Gruniesen equation-of-state. The parameters used for the elastic-plastic model are given in Table 3.

Table 3: Elastic-Plastic and Mie-Gruniesen Parameters for Long Rod Penetrator Calculation

Parameter	Aluminum
Young's Modulus (dyne/cm^2)	73.0×10^{10}
Poissons Ratio	0.3225
Yield Stress (dyne/cm^2)	2.9×10^9
Hardening Modulus (dyne/cm^2)	1.0×10^9
Initial Density (g/cm^3)	2.66
Initial Temperature (K)	298.0
Initial Pressure (dyne/cm^2)	0.0
Initial Sound Speed (cm/s)	5.328×10^5
s	1.338
gamma0	2.18
Specific Heat (erg/g/K)	1.034×10^7
Pressure Cutoff (dyne/cm^2)	-3.0×10^{10}

Density contours and mesh plots are shown at 3.0, 6.2, and 10μs in Figures 3, 4, and 5, respectively. As one can see in Figure 5, the rod has punched through the plate and the ALE region has undergone significant deformation. Figure 6 shows the history of displacement of the first five Lagrangian nodes on the top of the plate. This figure shows the vibrational modes the plate is undergoing far from the impact.

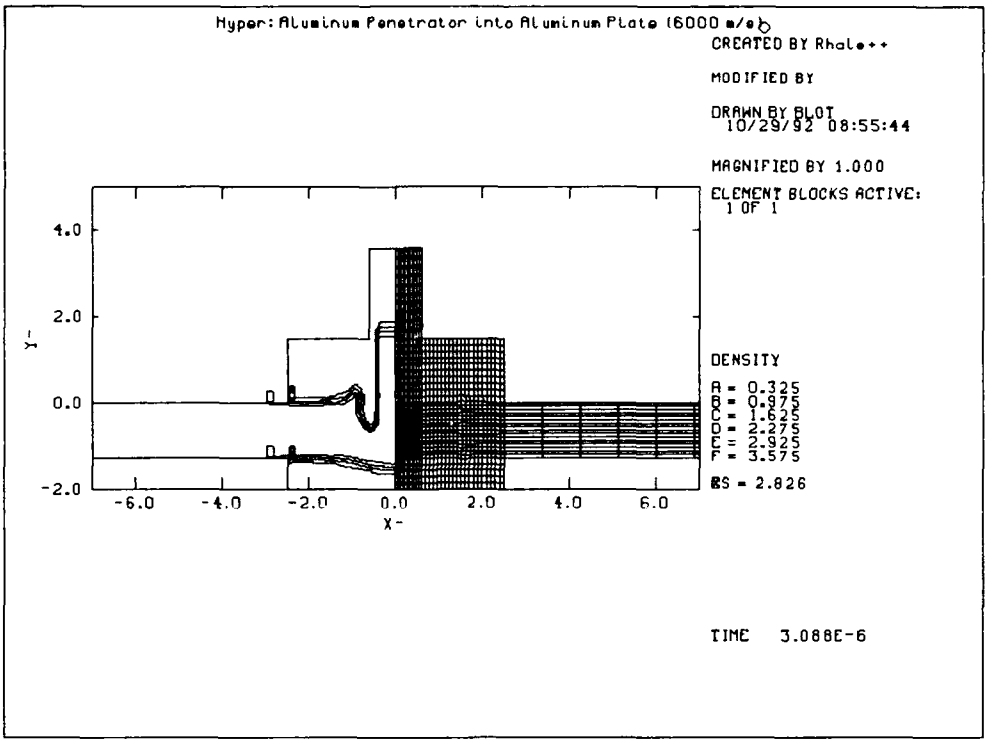


Fig. 3. Density Contours and Mesh Deformation at 3.2 ms.

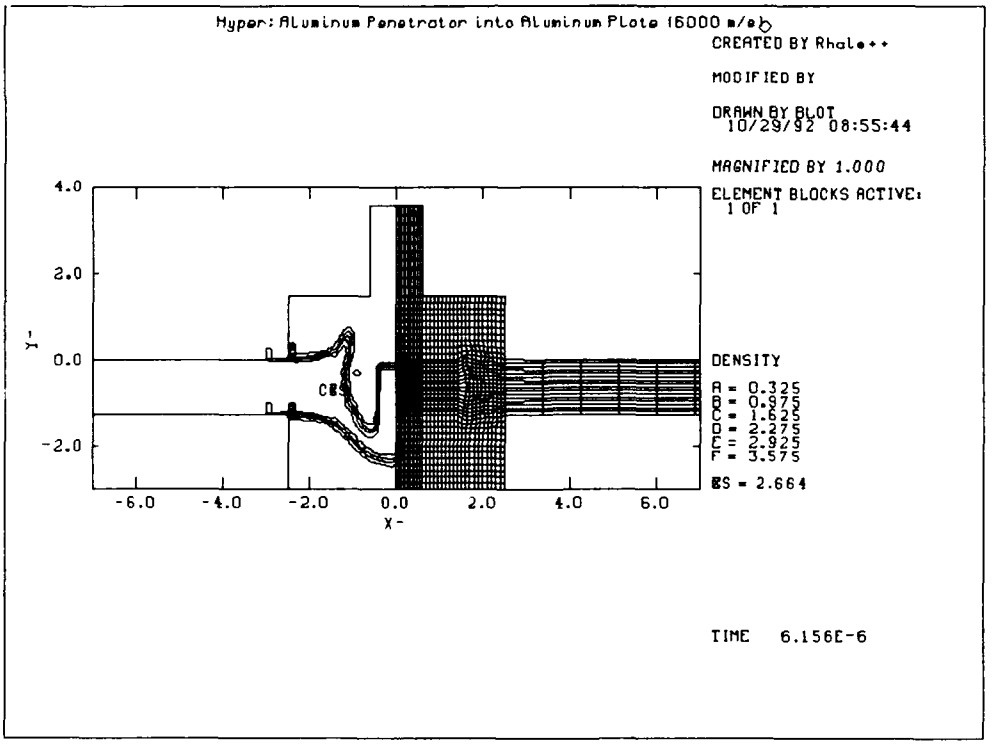


Fig. 4. Density Contours and Mesh Deformation at 6.2 ms.

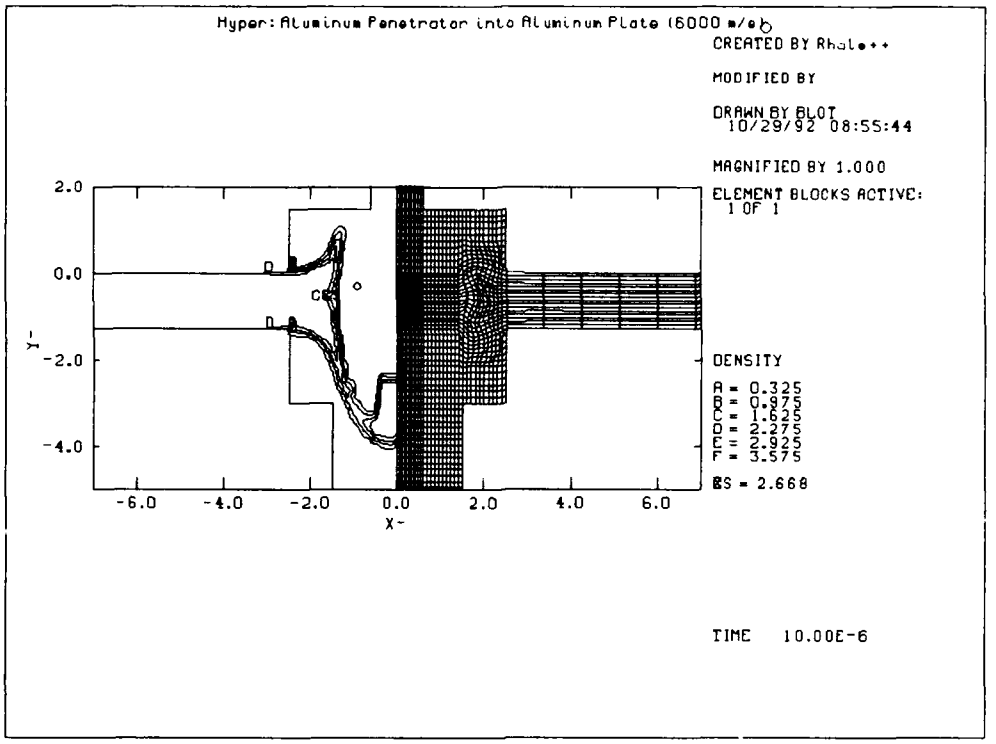


Fig. 5. Density Contours and Mesh Deformation at 10 ms.

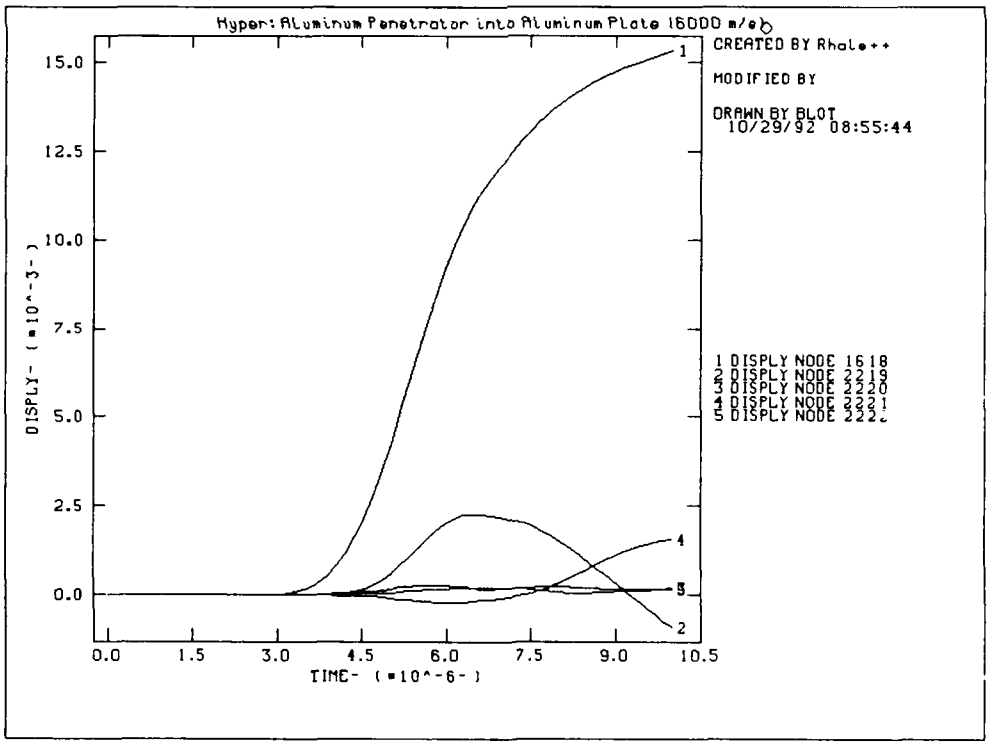


Fig. 6. Displacement in the Lagrangian Region of the Plate Far from Impact.

REFERENCES

Amsden, A.A. and C.W. Hirt (1973). Los Alamos Scientific Report LA-5100. Los Alamos National Laboratory, Los Alamos, New Mexico.

Amsden, A.A., H.M. Ruppel, and C.W. Hirt (1980). Los Alamos Scientific Report LA-8095. Los Alamos National Laboratory, Los Alamos, New Mexico.

Benson, D.J. (1989). An efficient, accurate, simple ALE method for nonlinear finite element programs. *Comp. Meth. Appl. Mech. Eng. 72*, 309-350.

Benson, D.J. (1992) Momentum advection on a staggered mesh. *J. Comp. Phys. 100*, 143-162.

Budge, K.G. (1991). ALE shock calculations using a stabilized serendipity rezoning scheme. *1991 APS Topical Conference on Shock Compression of Condensed Matter.*

Christensen, R. (1991). Private communication.

Coplien, J.O. (1992). *Advanced C++*. Addison-Wesley Publishing Company, Reading, Massachusetts.

Dukowicz, J.K. and B.J.A. Meltz (1992). Vorticity errors in multidimensional Lagrangian codes. *J. Comp. Phys. 99*, 115-134.

Ellis, M.A. and B.Stroustrup (1990). *The Annotated C++ Reference Manual*. Addison-Wesley Publishing Company, Reading, Massachusetts.

Hughes, T.J.R., 1987. *The Finite Element Method*. Prentice-Hall, Inc., Englewood Cliffs, New Jersey

McGlaun, J.M., S.L. Thompson, and M.G. Elrick (1989). *A Brief Description of the Three-Dimensional Shock Wave Physics Code CTH*. SAND89-0607. Sandia Corporation, Albuquerque, New Mexico

Margolin, L.G. and C.W. Beason (1988). Remapping on the staggered mesh. *Fifth Nuclear Code Developers' Conference*, Boulder, CO., October 11-14, 1988.

Margolin, L.G. and J.J. Pyun (1987). A method for treating hourglass patterns. *Proceedings of the Fifth International Conference on Numerical Methods in Laminar and Turbulent Flow*, Montreal, Canada.

Noh, W.F. and P. Woodward (1976). SLIC (simple line interface calculation). *Proceedings of the Fifth International Conference on Numerical Methods in Fluid Dynamics*, Twente University, Enschede, June 28 - July 2, 1976.

Press, W.H., B.F. Flannery, S.A. Teukolsky, and W.T. Vetterling (1986). *Numerical Recipes*, Cambridge University Press, Cambridge, pp. 653-655.

Quinlan, D. (1991). Private communication.

Robinson, A.C. *et al.* (1992). Massively parallel computing, C++, and hydrocode algorithms. ASCE 8th Conference on Computing, June 10-12, 1992.

Sharp, R.W. and R.T. Barton (1981). *HEMP Advection Model*, UCID-17609. Lawrence Livermore National Laboratory, Livermore, California.

Taylor, L.M. and D.P. Flanagan (1987). *PRONTO-2D: A Two-Dimensional Transient Solid Dynamics Program*. SAND86-0594. Sandia Corporation, Albuquerque, New Mexico.

Van Leer, B. (1984). *Comp. Meth. Appl. Phys. Eng., 6.*

Winslow, A.M. and R.T. Barton (1982). *Rescaling of Equipotential Smoothing*. UCID-19846. Lawrence Livermore National Laboratory, Livermore, California.

Youngs, D.L. (1987). *An Interface Tracking Method for a 3D Eulerian Hydrodynamics Code*, AWRE/44/92/35. Atomic Weapons Research Establishment.

Int. J. Impact Engng Vol. 14, pp. 121 - 132, 1993
Printed in Great Britain

0734-743X/93 $6.00 + 0.00
1993 Pergamon Press Ltd

AN IMPACT TECHNIQUE TO ACCELERATE FLIER PLATES TO VELOCITIES OVER 12 KM/S*

L. C. CHHABILDAS*, J. E. DUNN**, W. D. REINHART* and J. M. MILLER*

*Sandia National Laboratories, Albuquerque, New Mexico 87185
**University of Nebraska, Lincoln, Nebraska, 68588

ABSTRACT

Very high pressure and acceleration is necessary to launch flier plates to hypervelocities. In addition, the high pressure loading must be uniform, structured, and shockless, *i.e.*, time-dependent to prevent the flier plate from either fracturing or melting. In this paper, a novel technique is described which allows the use of 100 GPa megabar loading pressures and 10^9-g acceleration to launch intact flier plates to velocities of 12.2 km/s. The technique has been used to launch nominally 1-mm thick aluminum, magnesium, and titanium alloy plates to velocities over 10 km/s, and 0.5-mm thick aluminum and titanium alloy plates to velocities of 12.2 km/s.

INTRODUCTION

The history of early launch capabilities and the developments of various launcher techniques up to the late sixties, which include the developments of explosive lenses (Taylor, 1984), explosive liners (Wenzell, 1987), smooth-bore guns (Asay *et al.*, 1985, Charters, 1987, Chhabildas, 1992) has been well documented. An explosive lens (Taylor, 1984) is routinely capable of launching flier plates up to 6 km/s, while among smooth-bore guns, a two-stage light-gas gun propels projectiles the fastest. Current two-stage light-gas gun technology (Asay *et al.*, 1985, Charters, 1987, Chhabildas, 1992) allows routine launching of 10 gm to 20 gm projectile mass to a velocity of ~ 8 km/s, although velocities in excess of 10 km/s have been reported for ten milligram size particles (Seigel, 1979, Stilp, 1987).

The interest in increased velocity launch capabilities was renewed in the early eighties. Techniques that are either available or are in progress include (i) Van de Graaff accelerators (Keaton *et al.*, 1990), which can launch sub-micron size (10^{-13} gm) particles to over 100 km/s, (ii) plasma accelerators (Igenbergs *et al.*, 1987), which can launch micron size (10^{-6} gm) glass beads to velocities of 18 km/s, (iii) electrical discharge techniques such as the electric gun (Osher *et al.*, 1987), which can launch 43 mg kapton flier plates to 18 km/s, (iv) electromagnetic techniques such as the rail-gun (Asay *et al.*, 1990), which can launch a few grams to 7.5 km/s, (v) explosive techniques (Marsh and Tan, 1992), which can launch 1-mm thick steel plates to ~ 9 km/s, (vi) inhibited shaped-charge techniques (Grosch *et al.*, 1991) that can launch a shaped charge jet tip of 0.4 gm to velocities of 11 km/s, and (vii) an impact technique (Chhabildas *et al.*, 1991, 1992a) in which a time-dependent structured high pressure pulse is generated (upon impact) to launch 0.5-mm to 1.0-mm thick flier plates to velocities up to 12.2 km/s. It is the purpose of this paper to describe this impact technique to launch/accelerate flier plates to hypervelocities.

There are two main requirements to launch flier plates to hypervelocities. First, very high pressures are needed to launch the flier plate, and second, this loading must be nearly *shockless* and *uniform* over the entire surface. To achieve both these criteria, a graded-density material referred to as a "pillow" (Barker, 1984) or a "multi-ply" (Chhabildas and Barker, 1988, Chhabildas *et al.*, 1988) is used to impact the flier plate. When this graded-density material is used to impact a flier plate at high velocities on a two-stage light-gas gun, nearly shockless 100 GPa pressure pulses (Chhabildas *et al.*, 1990a, Chhabildas and Asay, 1992) are introduced into the flier plate. Since the loading on the flier plate is shockless, excessive heating is minimized to prevent melting of the flier plate (Chhabildas *et al.*, 1990a, Chhabildas and Asay, 1992). The method has been used (Chhabildas *et al.*, 1991, 1992a) to launch a 2-mm thick tita-

nium alloy plate to a velocity of 8.1 km/s, and 1-mm thick aluminum, magnesium, and titanium alloy plates to velocities in excess of 10 km/s, and 0.5 mm thick titanium and aluminum alloy plates intact to 12.2 km/s. With further improvements to this technique launch velocities approaching 14 km/s are expected (Chhabildas *et al.*, 1991, 1992a).

TECHNICAL ISSUES

The principle of gun operation is primarily based on using the energy release from high pressure compressed gases to propel projectiles to high velocities and is schematically depicted in Figure 1. If $P(t)$ is the time dependent driving pressure history used to propel a projectile of mass M in a gun barrel (of length L) having a cross sectional area A, then it can be shown that the projectile's terminal velocity V can be represented by

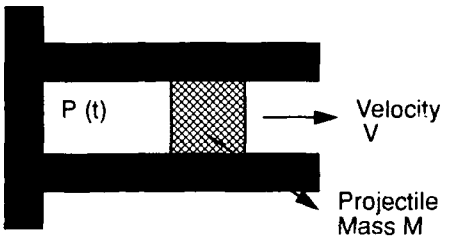


Fig. 1. Schematic of a gun launcher.

$$V = \frac{A}{M}\int_0^t P(t)\,dt. \tag{1}$$

This principle of gun operation is being used in the operations of smooth-bore gun launchers developed for controlled impact studies. Specifically, in a single-stage compressed-gas gun a 0.04-GPa gas pressure is used to drive a projectile weighing approximately 1 kg to a terminal velocity of ~ 1.1 km/s, while the combustion gaseous products from nitrocellulose propellants in a powder gun will yield a pressure of 0.3 GPa and propel a ~ 1 kg projectile mass to a velocity of over 2.3 km/s. In a two-stage light-gas gun the hydrogen propellant is dynamically compressed to a peak pressure of ~ 0.7 GPa to 1.0 GPa to launch a projectile mass of 10 gm to 20 gm to a velocity approaching 8 km/s (Asay *et al.*, 1985). To achieve higher velocities the mass of the projectile is decreased, while the average driving pressure is increased. This is also indicated in Figure 2 as a plot of projectile velocity *vs.* peak projectile acceleration.

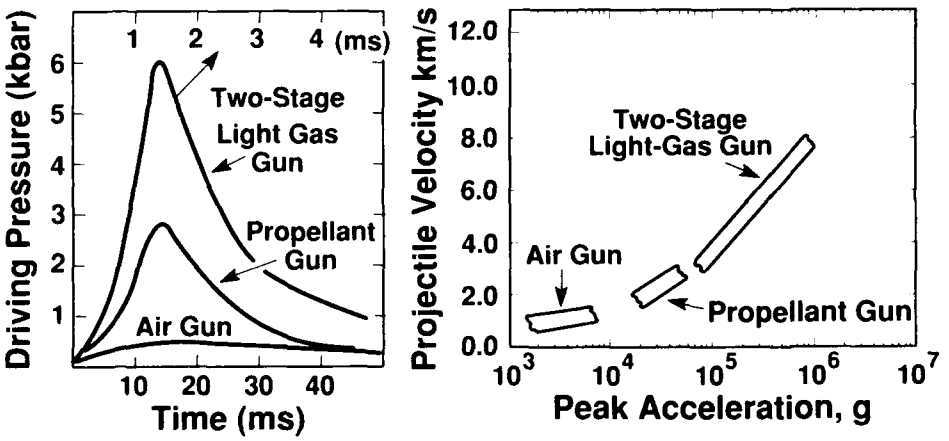


Fig. 2. Driving pressure history *vs* time and the relationship of velocity vs acceleration of projectiles for smooth bore guns

It would seem, therefore, (see Eq. 1) that either gas loading pressures be sustained for a longer duration, or yet higher driving gas pressure and higher acceleration be used to accelerate projectiles to hypervelocities. The former has been attempted on the two-stage light-gas gun by using collapsible launch tubes (using explosive techniques) to achieve lexan projectile velocities in excess of 11 km/s (Baum, 1973). However, attempts to launch flier plates to high velocities using higher gas pressures of ~ 100 GPa (Barker *et al.*, 1990a, 1990b) and higher acceleration have resulted in plate

fragmentation (Chhabildas *et al.*, 1990a, 1990b). Under these loading conditions the flier plate is subjected to (nonuniform) driving pressures which are orders of magnitude above its elastic limit, resulting in severe deformation. Because the flier plate has limited tensile strength, the non-uniformity in gas pressure loading over the entire face of the flier plate can be sufficiently large to cause flier fragmentation (Chhabildas *et al.*, 1990a, 1990b). Thus, the non uniformity in gas pressure loading over the entire face of the flier plate should not exceed the fracture strength of the plate.

First, very high pressures are needed to launch the flier plate to hypervelocity, and second, this loading must be nearly shockless, structured, and uniform over the entire surface. Shockless acceleration of the plate is crucial to prevent shock-induced heating and subsequent melting of the flier (Chhabildas *et al.*, 1990a, Chhabildas and Asay, 1992) during the loading process. A structured release pressure pulse is needed to prevent tensile failure of the flier plate. Uniform loading over its entire face is necessary to prevent plate fragmentation. To satisfy these criteria, a graded-density material is used to propel the flier plate. When this graded-density material is used to impact a flier plate at high velocities with a two-stage light-gas gun, nearly shockless 100-GPa pressure pulses are introduced into the flier plate. This time-dependent pressure pulse subsequently propels the flier plates to hypervelocities. The resultant acceleration of these flier plates, launched using impact techniques, is 10^{12} cm/s^2 (10^9 g).

EXPERIMENTAL TECHNIQUE

This section briefly describes the experimental techniques employed to augment the launch capabilities of Sandia's two-stage light-gas gun. The experimental impact configuration is indicated in Figure 3. The two-stage light-gas gun used in these studies had a bore diameter of 29 mm. As indicated in the figure, a two-stage light-gas gun projectile faced with a graded-density impactor is made to impact a thin flier plate located at the muzzle end of the barrel. Implementation of these techniques require that the barrel of the two-stage light-gas gun be extended (Barker *et al.*, 1990a, 1990b) by adding an expendable section, and also that the flier plate be laterally confined to minimize two-dimensional effects (Chhabildas *et al.*, 1991, 1992a).

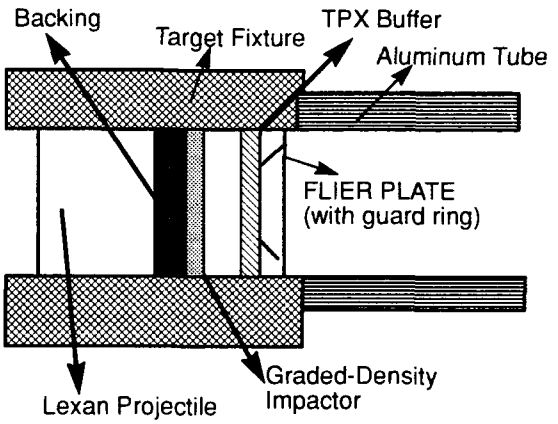


Fig. 3. Schematic of a graded-density impactor/flier-plate experiment

Flier Plate Configuration

As shown in Figure 3, the flier plate used in these experiments consists of a center plate made to fit exactly into a guard ring. The outside diameter of the guard ring used in these studies was 29 mm, while the inner diameter of the guard ring and the diameter of the center plate was 19 mm. The ratio of the center flier plate thickness (1-mm) to its diameter (19 mm) is approximately 0.05. Two-dimensional effects due to radial release waves (generated upon impact) emanating from the edges of the plate would cause a velocity gradient across the radius of the plate. Large velocity gradients across the radius of the plate would cause the flier plate to bend and, perhaps, even fragment. The guard ring geometry indicated in Figure 3 allows a *controlled* separation of the center plate from its edges without causing the entire flier plate to fragment. Confinement in a tungsten target fixture is desirable for maximizing the diameter of intact flier (Chhabildas *et al.*, 1991). It may not be essential for launching the central region of the flier, however. But, this central region must then be isolated from the edge interactions with guard-rings. This prevents wave-propagation induced fractures from propagating in from the outer radius, and allows the intact core of the flier to separate in a controlled fashion

as the flier plate bends during launch and flight. Tungsten makes a good confinement fixture, but calculations have indicated that a material such as steel (Chhabildas *et al.*, 1991) could provide a satisfactory confinement.

The flier plate materials used in this study consisted of titanium (Ti-6Al-4V), aluminum (6061-T6) or magnesium (AZ31) alloys. As indicated in Figure 3, a TPX or a lexan plastic buffer is used in most experiments. (TPX is a registered plastic product purchased from the Polymer Corporation, Pamona, California, and has an approximate density of 0.82 gm/cm^3.) The plastic buffers will further cushion the input pressure pulse and will have a tendency to minimize the tensile strength induced in the flier plate (Chhabildas *et al.*, 1991, 1992a)

Table 1. Summary of Graded-Density Impactor/Flier-Plate Experiments

Experiment No.	Graded-Density Material	Pillow/Backing or Multi-ply Assembly Thicknesses (mm)	Buffer/ Flier- Plate Thickness (mm)	Impact Velocity (km/s)	Flier-Plate Material/ Velocity (km/s)
Ti40	Pillow	2.206/2.00	0.0/2.050	6.3	Ti6/8.1
WS6	Pillow	4.58/1.00	1.50/0.98	6.3	Ti6/9.5
JSC12	Multi-ply	1.00/0.61/0.47/0.41/0.30/0.92	1.53//1.01	6.0	Mg/9.92
JSC18	Multi-ply	1.11/0.60/0.55/0.43/0.30/0.91	1.51/0.998	6.3	Al/9.85
EHVL1	Multi-ply	0.64/0.33/0.28/0.31/0.19/0.52	0.81/0.41	7.2	Al/11.6
EHVL2	Multi-ply	0.61/0.30/0.24/0.32/0.20/0.44	1.21/0.43	7.35	Ti6/11.9
EHVL3	Multi-ply	0.62/0.30/0.23/0.33/0.19/0.44	1.25/0.42	7.35	Al/12.2
EHVL4	Multi-ply	0.65/0.28/0.23/0.30/0.15/0.43	1.48/0.74	7.35	Ti6l/10.6-10.4

Projectile Design

A lexan projectile which has a facing of a graded-density material such as a pillow or a multi-ply impactor backed by tantalum is used in these studies. A 'pillow' impactor is fabricated using powder metallurgical techniques (Barker, 1984) such that a smooth variation in its shock impedance occurs through its thickness. The shock impedance of the impact surface of the graded-density material is that of polyolefin, and the shock impedance of the back surface of the pillow resembles copper or tantalum. A 'multi-ply' impactor (Chhabildas and Barker, 1988) is fabricated by bonding a series of thin plates in order of increasing shock-impedance from the impact surface. The series of layered materials used in these studies consisted of a plastic TPX, magnesium, aluminum, titanium, copper, and tantalum. The thickness of each layer is precisely controlled to tailor the time-dependent stress pulse required to launch the flier plate intact, and is indicated for each experiment in Table 1. When these graded-density materials are used to impact a titanium alloy flier plate at a velocity of ~ 6.3 km/s, an initial shock of approximately 50 GPa, followed by a ramp wave to over 100 GPa is introduced into the flier plate. At higher impact velocities the input pressure profile would result in a higher peak pressure pulse resulting in launching flier plates to yet faster velocities. This is indicated in Table 1. The diameter of the graded density materials (either pillows or multi-ply impactors) used in this study was ~ 27 mm.

Diagnostics

Following impact, seven flash X-rays are taken of the flier plate while it is in motion. They are used to estimate the velocity of the flier plate and also to check its integrity following impact and subsequent acceleration by the shockless pressure pulse. Four of these flash X-rays are taken while the flier plate is in the aluminum barrel extension, usually a few microseconds after impact. The energy of the first four X-rays is 600 keV, and the pulse duration is 3 ns. The pulse duration is sufficiently small to "freeze" the motion at the present velocities. The other 3 X-rays are taken after the flier plate has exited from the muzzle and are located ~ 80 mm, 170 mm, and 350 mm from the impact position. These X-rays sources have a 300-450 keV energy and a 25 ns pulse duration. Due to the hypervelocities achieved in this study, the 25 ns pulse duration can cause a 250 μm blurring of the flier plate while in flight. Radiographic pictures of the flier plate taken in flight over these large distances allow an accurate measurement of its velocity. The flier plate velocity is determined to within 1%.

RESULTS

In all the experiments performed to date, the graded-density projectile driver is allowed to impact the buffer-flier plate combination. The impact velocities are indicated in Table 1. The impact velocities are not measured but are estimates based on the two-stage light-gas gun performance data and are accurate to ~ 2%. As mentioned above plastic buffers were used in most experiments in an attempt to further cushion the launch. The plastic buffer will also reduce the magnitude of the tensile states generated in the flier plate material that result from wave interactions (Chhabildas *et al.*, 1991, 1992). Titanium and aluminum alloy flier plates were used in this study, because of their high-fracture resistance properties (Chhabildas *et al.*, 1990a, 1990b). At an impact velocity of ~ 6.3 km/s, this technique has launched intact a 1-mm thick Ti-6Al-4V titanium alloy plate to 9.5 km/s, a 1-mm thick 6061-T6 aluminum alloy plate to 10.4 km/s, and a 1-mm thick magnesium alloy plate to 10 km/s. Radiographs of some of these experiments are shown in Figures 4, and 5. As the impact velocity is increased to ~ 7.4 km/s, flier plate velocities of 0.5-mm thick aluminum and titanium plates have been increased to over 12 km/s. Radiographs of these latter experiments are summarized in Figure 6.

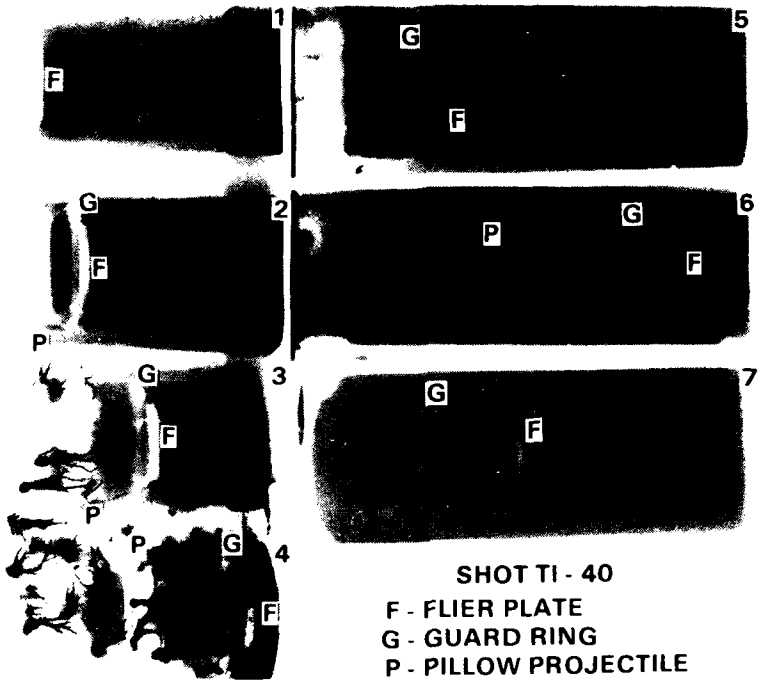
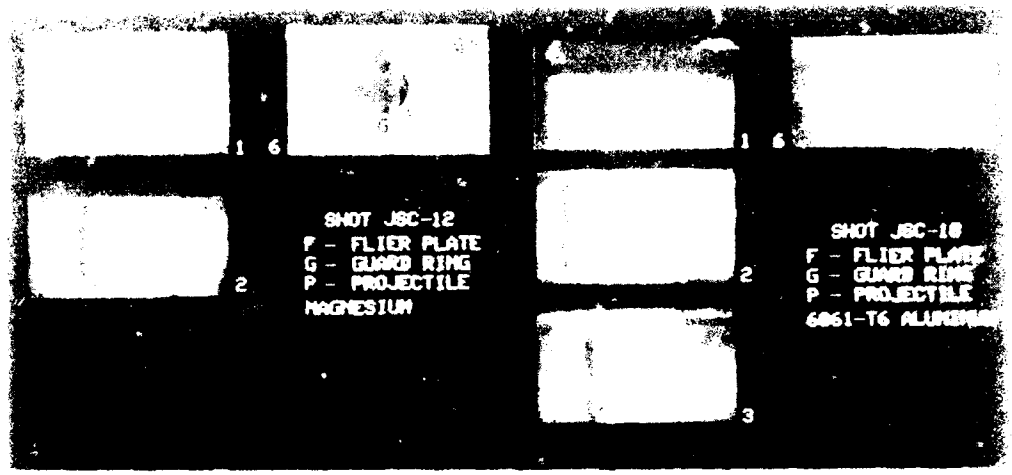


Fig. 4. Radiographs of experiment Ti40. The titanium flier plate is moving from left to right at a velocity of 8.1 km/s.

Radiographs of a 2.05-mm thick Ti-6Al-4V flier plate moving at a velocity of 8.1 km/s as a result of impact by a graded-density driver at ~ 6.4 km/s are indicated in Figure 4. A copper backing was used in this experiment. The sequence of radiographs indicated on the left in Figure 4 is taken over the first 60 mm from launch impact position. The radiographs on the right are taken after exit from the aluminum muzzle, after a total travel distance of 85 mm, 152 mm and 357 mm from impact, respectively. As indicated in the figure, the flier plate is extremely flat even after a propagation distance of 357 mm. This is believed to be due to optimal experimental impact conditions, such as (i) extremely good impact with very little impact misalignment (tilt), (ii) a good (uniform) pillow, and (iii) the thicker flier plate dimension in this experiment. This is evidenced by the symmetry of the projectile/pillow debris trailing the flier plate at a velocity of ~ 5.5 km/s. The mass of the center plate (flier plate) is 2.6 gm. A similar experiment with a 1-mm thick titanium flier-plate (experiment WS6 in Table 1) yields a velocity of 9.5 km/s.

Radiographs of experiment JSC12 are indicated in Figure 5. In this experiment a nominally 1.0-mm thick magnesium flier plate was impacted by the multi-ply impactor at a velocity of approximately 6 km/s. A 1.5 mm thick TPX plastic buffer was also used in the experiment. The first two radiographs shown on the left in Figure 5 are taken over a flight distance of 60 mm while the flier plate is in the extended aluminum muzzle, and the radiograph indicated on the right is taken at a flight distance of ~ 160 mm from impact location. The mass of the center plate without the guard ring is 0.5 gm and the magnesium flier plate is moving at a velocity of 9.92 km/s in this experiment.


1 6
2
SHOT JBC-12
F - FLIER PLATE
G - GUARD RING
P - PROJECTILE
MAGNESIUM
1 6
2
3
SHOT JBC-18
F - FLIER PLATE
G - GUARD RING
P - PROJECTILE
6061-T6 ALUMINUM

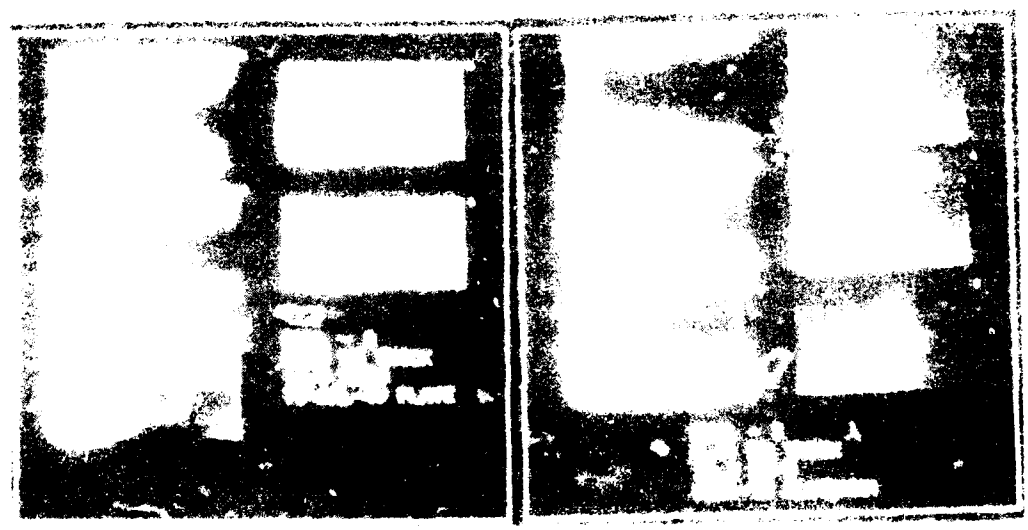


Figure 6 also indicates the radiographs of an aluminum flier plate launched at 12.2 km/s. In this experiment the multi-ply impactor impacts the stationary aluminum flier plate at a velocity of 7.35 km/s. A 1.25-mm thick plastic buffer was used in this experiment. The sequence of radiographs shown on the left are taken over a transit distance of 60 mm. The flier plate appears to be intact as it is exiting the muzzle. However, after a flight distance of 350 mm, the flier plate appears to have lost its shape and appears to have transformed into a "*slug*" of material. This is attributed to the melting of the flier plate. At a higher impact velocity *i.e.*, at 7.35 km/s, the magnitude of the first shock transmitted into the aluminum flier plate is sufficiently high to cause it to melt upon release.

DISCUSSION

As mentioned in Equation 1, the velocity V of the flier plate can be represented by $V = \frac{A}{M}\int P(t)\,dt$. The time-dependent, high-pressure, shockless loading pressure pulse $P(t)$ that is needed to launch the flier plate to high velocities is provided upon impact and is represented by the term $\int P(t)\,dt$. This is indicated in Figure 7 for the experiment EHVL 2 shown in Figure 6. An impact velocity of 7 km/s was assumed in the calculation, instead of the experimental impact velocity of 7.35 km/s. Numerical simulations of the graded-density impact experiments were performed using a version of the Lagrangian code, WONDY which uses a tabular equation-of-state (EOS) option (Kerley, 1988). The calculational model treats the pillow as a series of zones having impedances that increase from that of a polymer approximating polyolefin at the impact surface, to that of the copper or tantalum backing plate. The zone thicknesses are chosen so

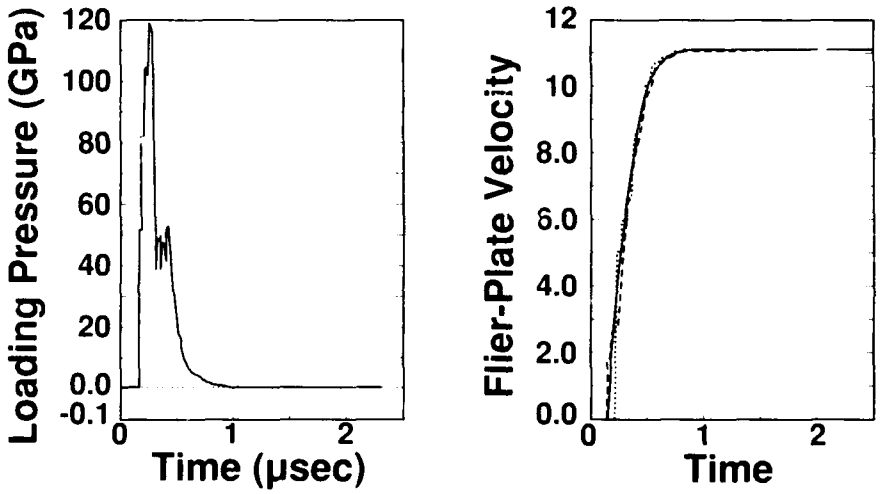


Fig. 7. Calculated stress history on the base of the EHVL2 flier-plate experiment shown in Figure 6 is indicated on the left. Predicted velocity history for the flier plate is shown on the right.

that the impact generates a sequence of multiple shocks in the target; both experiments and calculations have shown that a calculational model of this type gives a loading history that closely approximates the smooth quais-isentropic loading of a pillow (Chhabildas and Barker, 1988, Chhabildas *et al.*, 1988). When a multi-ply material is used as a graded-density impactor then the zones represent the exact thickness of the materials used. The titanium alloy experiment shown in Figure 6 for EHVL2 had a 1.21 mm plastic buffer and an impactor backed with tantalum. As indicated in Figure 7, the calculated driving stress history is a 50 GPa shock followed by a relatively shockless loading from approximately 53 GPa to 120 GPa over a time duration of ~ 0.2 μs. The entire loading pressure pulse is applied over a duration of ~ 0.5 μs. The calculated velocity history resulting from this driving pressure pulse is also shown in Figure 7. The calculations predict a terminal velocity of approximately 11.1 km/s for the flier-plate when impacted by the graded-density impactor at 7 km/s. A calculation using 7.4 km/s as impact velocity would have predicted a flier-plate velocity of 11.7 km/s. In the experiment, impact by the graded density impactor was at a velocity of ~ 7.4 km/s, launching the titanium flier plate at 11.9 km/s, in excellent agreement with predicted values. Calculations also indicate that due to the time-dependent loading, the residual temperature of the titanium flier plate after it is compressed to 1.2 M bar and launched at 11.9 km/s is expected to be ~ 800 K. When compared to its melt temperature of ~ 2000 K, the flier plate is relatively "cool" and well below its melt temperature.

The aluminum flier plate experiment identified as EHVL3, and indicated in Figure 6 is launched at 12.2 km/s. The flier plate appears to have lost its shape due to a loss in shear strength. The experiment suggests that the thermal state of the

aluminum plate is very near its melt boundary and this is confirmed by calculations. A WONDY calculation as mentioned above indicates that the driving stress history is a shock in excess of 50 GPa followed by a relatively shockless loading from approximately 50 GPa to 120 GPa. The magnitude of the first shock (over 50 GPa) transmitted into the aluminum flier plate at an impact velocity of 7.4 km/s is sufficiently high to cause it to melt upon release. Flier plate materials that have higher melting points than aluminum, such as titanium, steel, tantalum, or molybdenum are not expected to exhibit this behavior. Thus, impact velocities less than 7.4 km/s are expected to launch aluminum plates intact *i.e.*, without melting if the current design for the graded-density impactor is used. An alternate technique is to use a lower-density material such as plastic foams, either as a buffer or as the first layer of the graded-density impactor, so that the magnitude of the first shock generated upon impact in aluminum is considerably less than 50 GPa.

Very high time-dependent and structured pressure pulses are used to launch intact flier plates in this study. The loading pressure is applied over a duration of 0.5 μs to 1 μs to launch flier plates to velocities up to 12.2 km/s. The acceleration of the flier plates launched to hypervelocities is on the order of 10^{12} cm/s^2, (10^9g) and is at least three to four orders of magnitude higher than that used on current two-stage light-gas guns. This is indicated in Figure 8, where the acceleration of the current hypervelocity launcher (HVL) is compared to those from other smooth bore guns. Unlike two-stage light-gas guns in which the projectile is accelerated over 200 times its bore diameter (caliber) dimensions (Charters, 1987) the flier plate is accelerated in this study over distances of tens of millimeters.

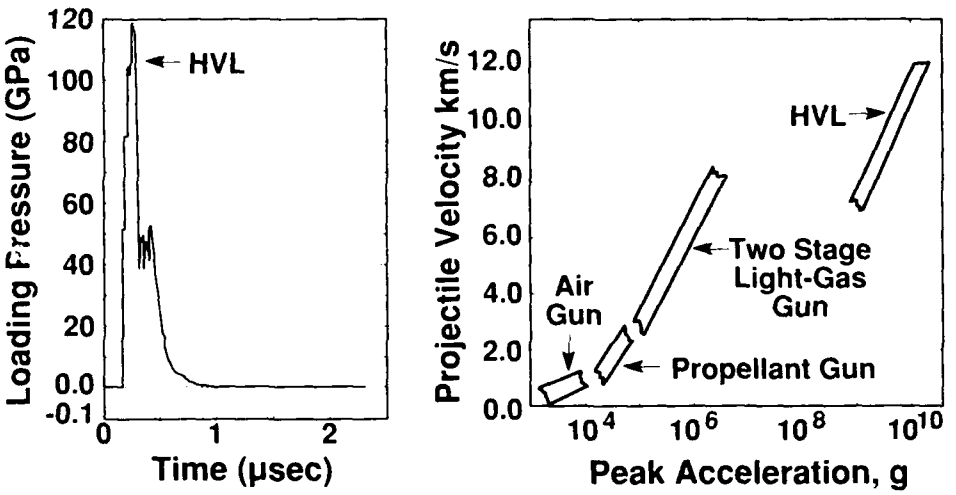


Fig. 8. The stress history on the base of the EHVL2 titanium flier-plate shown in Figure 6 propels the flier plate at an acceleration of over 10^9g.

The mass of the plate can be represented by $M = \rho x A$, where ρ is the density of the plate, x its thickness and A its cross sectional area. Equation (1) can therefore be expressed as

$$V = \frac{1}{\rho x}\int_0^t P(t)\,dt. \tag{2}$$

Equation 2 suggests that the velocity of the flier plate is independent of its cross sectional area and depends only on its thickness and the time-dependent driving pressure pulse. This would be true if two-dimensional effects were not present in these experiments. The maximum mass that could be launched in the absence of any two-dimensional effects would be the diameter over which the graded-density driver impacts the flier plate. This impact interaction occurs over a 27-mm diameter in this study. Two-dimensional effects due to radial release waves (generated upon impact) emanating from the edges of the plate would cause a velocity gradient across the radius of the plate, thus limiting the one dimensionality of the experiment. In this study, a guard-ring geometry indicated in Figure 3 allows the launching of a 19 mm diameter center plate. It is therefore useful to express the velocity of the flier plate as a function of its mass density (ρx) and this is plotted in Figure 9 for the series of experiments performed in this study. As indicated in the figure the terminal velocity of the flier plate is dependent on the impact velocity of the graded-density driver. Also, as shown in Figure 9, the presence of plastic buffers further augment the terminal velocity of the flier plates.

To increase the velocity of the flier plate one needs to decrease the thickness of the plate or increase the time dependent pressure loading pulse. In this investigation (see experiments EHVL in Table 1) we decreased the flier-plate thickness

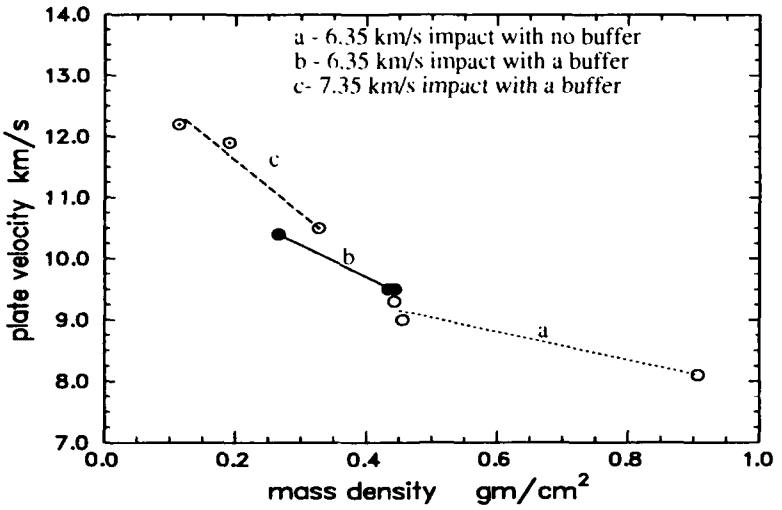


Fig. 9. Hypervelocity performance of the graded-density impactor/flier plate experiment plotted as plate velocity vs mass density of the plate.

by a factor of two and increased the graded-density driver velocity. These results are indicated as dashed lines in Figure 9. Since we also decreased the graded-density impactor thickness also by a factor of two (see Table 1) the quantity $\frac{1}{\rho}\int P(t)\,dt$ remains an invariant. This suggests that if the pillow dimension is increased by a factor of two, then there should be no velocity penalty in increasing the flier plate dimension by a factor of two *i.e.*, one should be able to launch twice as heavy a mass to the same velocity provided the graded-density impact velocity is kept the same.

Results of the present studies are also shown in Figure 10 plotted as the maximum mass that can be launched on a 29-mm bore gun in the absence of any two-dimensional effects *vs* the mass that is currently launched as a 19-mm diameter plate. At higher loading pressures, however, since the sample thickness is approximately one-half of the ones launched the two-dimensional loading times are reduced by a factor of ~ one-half, resulting in minimal two-dimensional effects. Also, because the thermal state of aluminum is close to its melt boundary the guard ring does not separate distinctly from its center flier plate as effectively as it does at lower impact pressures. This is particularly true for aluminum flier

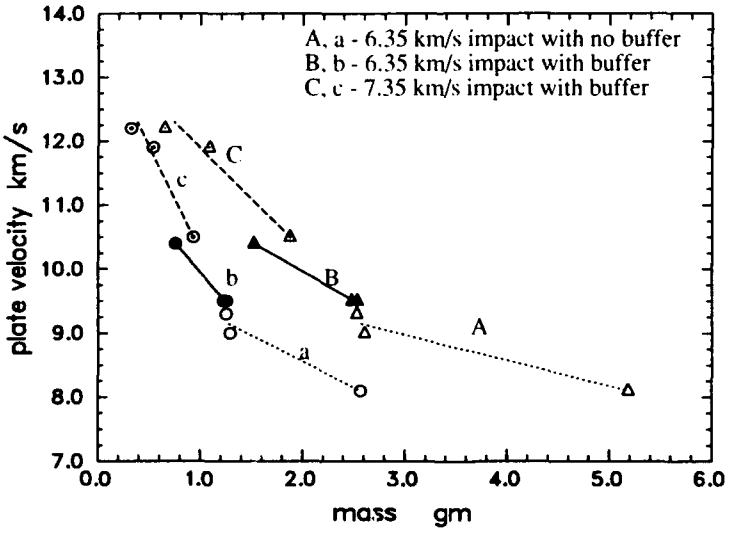


Fig. 10. Performance of the graded-density impactor/flier-plate experiments plotted as mass vs velocity of the flier-plate. A, B, C indicate the ideal mass possible that can be launched on the current 29-mm bore gun *while* a, b, c indicate the mass that is launched as a 19 mm plate.

plates. This allows launching of heavier *i.e.*, larger diameter flier plates. Nevertheless, as indicated in Figure 10, first, a mass of approximately 0.5 gm can be launched to velocities of 12.2 km/s, and second, if techniques were introduced to mitigate two-dimensional effects then the potential of launching heavier *i.e.*, massive flier plates exist for the same bore diameter.

As indicated in this study a graded-density impactor material has been used as a driver to launch nominally 1-mm thick aluminum, titanium and magnesium alloy plates intact to velocities over 10 km/s, and 0.5-mm thick titanium and aluminum alloy plates (see Figures 4 to 6) to velocities over 12 km/s. The flier plate integrity may be summarized as follows. For propagation distances of approximately tens of millimeters, the plate seems to be flat while in the aluminum muzzle. For propagation distances of hundreds of millimeters, the flier plate appears to be bowed, which can be attributed to two-dimensional effects. The flier plate materials undergo a volume strain of 0.3 to 0.4 during high pressure (megabar) compression and are not expected to return to their original shape. Effects due to tilt, gas blowby, and non-uniformity in graded-density driver materials are expected to enhance non-uniform loading and two-dimensional effects, and would result in flier-plate fragmentation.

Plastic buffers are used to reduce the magnitude of tensile stress states induced in the material. They also have the net effect of augmenting the flier plate velocities as indicated in Figures 9 and 10. It is crucial that the graded-density driver dimensions and also those of the buffered flier plate be optimized to prevent spall fracture of the plate. This is shown in Figure 11 for experiment EHVL4 in which a 0.74-mm titanium flier plate is impacted by the graded-density driver at 7.35 km/s. Calculations have suggested a tensile state of approximately 4.8 GPa in the flier plate, and as indicated in the figure, was sufficient to fracture the plate.



Fig. 11. Radiographs of experiment EHVL4 in which a spalled titanium flier plate is moving from left to right. The leading spall plate is propelled at 10.6 km/s while the second plate is coasting at 10.4 km/s. The flier plate radiographs are taken over a flight distance of 360 mm.

ENHANCED CAPABILITIES

Materials

Because of the softer loading history produced with a buffer layer, a computational study was made to see if the same system could be used to launch flier plates made of other materials. WONDY calculations were made for the same configuration as reported in this paper except with 1-gm target plates of tantalum, molybdenum, iron, and a tungsten alloy. In all four cases, a terminal velocity of over 10 km/s was predicted (Chhabildas *et al.*, 1991, 1992a) without either melting or fracture. Experiments have not been conducted to date.

Velocity

Studies in the present program have also focussed on exploring methods to achieve even higher plate velocities. Some of the possible velocity enhancement methods are discussed in this section. Studies using the WONDY code show that increased flier velocities could be obtained using buffer layers of plastic, explosive, or hydrogen on the impact surface. Calculations have indicated, that as a result of high-pressure compression and decompression these materials behave "energetically" in that the expansion velocities of these materials are extremely high. This results in an efficient "push" on the flier and can further enhance its velocity. This concept has been tested through the successful launch of the aluminum and titanium flier plates using plastic buffers (see Figures 9 and 10). Additional calculational studies

were made to see if hydrogen, with its high sound speed, could be used to further enhance flier velocities. By replacing the plastic buffer with a 10-mm layer of liquid hydrogen, the velocity of the aluminum flier was predicted to increase from 10.4 km/s to 11.3 km/s (Chhabildas *et al.*, 1991, 1992a). If the impact velocity is further increased to 8 km/s, then the calculation predicts a final velocity of 14.0 km/s for this design (Chhabildas *et al.*, 1991, 1992a). Hence hydrogen buffers in combination with higher impact velocities appear to offer a way to achieve the extremely high flier velocities.

Applications

The capability to launch flier-plates to hypervelocities will allow well-controlled equation of state studies to be conducted in materials to high pressure and temperature regimes that have never before accessible in the laboratory before. As an example a symmetric impact experiment in high-impedance materials such as tungsten at 12.2 km/s will allow Hugoniot states to be determined at stresses of 1.4 TPa (14 Mbar) and temperatures of 7 eV. Isentropic expansion of these materials from a high pressure molten state is expected to partially vaporize the material. Techniques employed on two-stage light-gas guns (Asay *et al.*, 1990) can be used to determine the kinetics of shock-induced vaporization in materials such as lead to higher degrees of vaporization. These techniques can now be extended to include materials such as aluminum which has a low vapor pressure *i.e.*, a high boiling point. With the increasing threat to space voyagers from man-made orbital debris the technique can be used to hurl plates at either a single shield (Ang *et al.*, 1992, Chhabildas *et al.*, 1992b) or multiple shields (Boslough *et al.*, 1992) to help design and understand the operations of the proposed protection shields.

SUMMARY

A systematic study has been described in which an impact technique is used to launch gram-size plates to hypervelocities. The high pressures that are needed to launch flier plates intact have been achieved by using graded-density impactor materials to impact stationary flier plates, over the velocity of range of ~ 6.3 km/s to 7.4 km/s on the two-stage light-gas gun. Upon impact, a shockless *i.e.*, a time-dependent high pressure (100 GPa) pulse is produced at the flier-plate/impact interface. This allows shockless acceleration of the flier plates to hypervelocities without causing excessive heating leading to melt or vaporization. The pressure pulse must be tailored, however, to prevent spall fracture of the plate. The successful use of this technique has been demonstrated by launching intact 1-mm thick aluminum, magnesium, and titanium plates to velocities over 10 km/s, and 0.5 mm thick aluminum and titanium alloy plates to velocities over 12 km/s. Although the technique has been used currently to launch Ti-6Al-4V alloy and 6061-T6 aluminum alloy plates, calculations suggest that this technique can be extended to include other (high-density) materials.

The flier plate velocities can be further enhanced either by using explosives, plastics, or hydrogen as a first layer of the graded-density impactor or on the flier plate itself. Calculations have indicated that as a result of high-pressure compression and decompression these materials behave "energetically," in that the expansion velocities of these materials are extremely high. This results in an efficient "push" on the flier plate and can further enhance the flier plate velocity. This concept has been verified by successfully launching a plastic buffered aluminum and titanium plates and is indicated in figures 9 and 10. The buffer has the added advantage in that it can mitigate spall fracture from occurring in the flier plate. Calculations also suggest that hydrogen buffers in combination with higher impact velocities appear to offer a way to achieve the extremely high flier velocities in excess of 14 km/s.

ACKNOWLEDGMENTS

The author wishes to acknowledge J. R. Asay, T. N. Tsai and J. Connell for the many technical discussions and their interest and support during the course of this study. Gun code simulations by M. Shahinpoor are also acknowledged.This work performed at Sandia National Laboratories supported by the U.S. Department of Energy under contract number DE-AC04-76DP00789.

REFERENCES

Ang, J. A., L. C. Chhabildas, B. G. Cour-Palais, E. C. Christenen and J. L. Crews, (1992). Evaluation of Whipple Bumper Shields at 7 and 10 km/s. *AIAA Paper No*, 92-1590 1-4.

Asay, J. R., L. C. Chhabildas and L. M. Barker, (1985). Projectile and impactor designs for plate-impact experiments. *Sandia National Laboratories Report*, SAND85-2009, unpublished.

Asay, J. R., T. G. Trucano, and R. S. Hawke, (1990). The use of hypervelocity launchers to explore previously inaccessible states of matter. *Int'l. J. of Impact Engng.*, 10, 51-66.

Barker, L. M., (1984). High pressure quasi-isentropic impact experiments. In: *Shock Waves in Condensed Matter - 1983*, (J. R. Asay, R. A. Graham, and G. K. Straub, eds.), pp 217-224. Elsevier Science Publishers, B.V.,

Barker, L. M., L. C. Chhabildas, and T. G. Trucano, and J. R. Asay, (1990a). High gas pressure acceleration of flier-plates - experimental techniques. *J. Impact Engng.*, 10, 67-80.

Barker, L. M., L. C. Chhabildas, T. G. Trucano, and J. R. Asay, (1990b). Gas accelerated plate stability study. In *Shock Waves in Condensed Matter -1989*, (S. C. Schmidt, J. N. Johnson, and L. W. Davison, eds.), pp 989-991.Elsevier Science Publisher, B.V..

Baum, D. W., (1973). Explosively driven hypervelocity launcher - second stage augmentation techniques. *Physics International Report No.* PIFR-245-1, unpublished.

Boslough, M. A., J. A. Ang, L. C. Chhabildas, B. G. Cour-Palais, E. C. Christenen and J. L. Crews, (1992). Hypervelocity Testing of Advanced Shielding Concepts for Spacecraft against Impact at 10 km/s. This volume.

Charters, A. C., (1987). Development of the high-velocity gas-dynamic gun. *Int'l. J. of Impact Engr.*, 5, 181-203.

Chhabildas, L. C. (1992). Hypervelocity Launch Capabilities to over 10 km/s. In *Recent Trends in High Pressure research*, (A. K. Singh, ed.) pp. 739-746. Oxford & IBH Publishing, New Delhi.

Chhabildas, L. C., and J. R. Asay, (1992). Dynamic yield strength and spall strength measurements under quasi-isentropic loading. In *Shock-Wave and High-Strain-Rate Phenomena in Materials*, (M. A. Meyers, L. E. Murr, K. P. Staudhammer, eds.), pp 947-955. Marcel Dekker Inc., New York.

Chhabildas, L. C., J. R. Asay, and L. M. Barker, (1988). Shear Strength of Tungsten Under Shock- and Quasi-Isentropic Loading to 250 GPa. *Sandia National Laboratories Report No.*, SAND88-0306, unpublished.

Chhabildas, L. C., and L. M. Barker, (1988). Dynamic Quasi-Isentropic Compression of Tungsten. In *Shock Waves in Condensed Matter 1987*, (S. C. Schmidt and N. C. Holmes eds.), pp. 111-114. Elsevier Science Publishers B. V..

Chhabildas, L. C., L. M. Barker, J. R. Asay, and T. G. Trucano, (1990a). Relationship of fragment size to normalized spall strength for materials. *J. Impact Engng.*, 10, 107-124.

Chhabildas, L. C., L. M. Barker, T. G. Trucano, and J. R. Asay, (1990b). Spall strength measurements on shock-loaded refractory metals. In *Shock Waves in Condensed Matter - 1989*, (S. C. Schmidt, J. N. Johnson, and L. W. Davison, eds.), pp. 429-432. Elsevier Science Publishers B.V..

Chhabildas, L. C., L. M. Barker, J. R. Asay, T. G. Trucano, G. I. Kerley, (1991). Sandia's new hypervelocity launcher-HVL. *Sandia National Laboratories Report* SAND91-0657, unpublished.

Chhabildas, L. C., L. M. Barker, J. R. Asay, T. G. Trucano, G. I. Kerley and J. E. Dunn, (1992a). Launch capabilities to over 10 km/s. In *Shock Waves in Condensed Matter - 1991*, (S. C. Schmidt, R. D. Dick, J. W. Forbes, D. G. Tasker, eds.), pp 1025-1031. Elsevier Science Publishers B. V..

Chhabildas, L. C., E. S. Hertel, S. A. Hill, (1992b). Whipple bumper shield tests at 10 km/s. In *Shock Waves in Condensed Matter - 1991*, (S. C. Schmidt, R. D. Dick, J. W. Forbes, D. G. Tasker, eds.), pp 991-994. Elsevier Science Publishers B. V..

Grosch, D., J. Walker, S. A. Mullin, R. Tullos, (1991). Development of an Inhibited Explosive Hypervelocity Launcher. *Southwest Reasearch Institute Report No.* 06-3513, unpublished.

Igenbergs, E., S. Aigner, A. Hudepohl, H. Iglesder, H. Kuczerz, M. Rott, and U. Weishaupt, (1987). Launcher technology, in-flight measurement and impact diagnostics at the TUM/LRT. *Int'l. J. of Impact Engng.*, 5, 371-380.

Keaton, P. W., G. C. Idzork, L. J. Rowton, J. D. Seagrave, G. L. Stradling, S. D. Bergeson, M. T. Collopy, H. L. Curling, D. B. McColl, and J. D. Smith, (1990). A hypervelocity microparticle impacts laboratory with 100 km/s projectiles. *Int'l. J. of Impact Engng.*, 10, 295-308.

Kerley, G. I., (1988). A Tabular Equation of State Option for the WONDY Code. *Sandia National Laboratories Report* SAND88-0831, unpublished.

Marsh, S. P., and T. H. Tan, (1992). Hypervelocity plate Acceleration. In *Shock Waves in Condensed Matter - 1991*, (S. C. Schmidt, R. D. Dick, J. W. Forbes, D. G. Tasker, eds.), pp 1031-1039. Elsevier Science Publishers B. V..

Osher, J. E., H. H. Chau, G. R. Gathers, R. S. Lee and R. C. Weingart, (1987). Applications of a 100-kV electric gun for hypervelocity impact studies. *Int'l. J. of Impact Engng.*, 5, 501-507.

Seigel, A. E., (1979). In *Interior Ballistics of Guns*, (H. Krier and M. Summerfield, eds.), pp135. AIAA Publishers, New York.

Stilp, A. J., (1987). Review of modern hypervelocity impact facilities. *Int'l. J. of Impact Engng.*, 5, 613-621.

Taylor, J. W., (1984). Thunder in the Mountains. In *Shock Waves in Condensed Matter - 1983*, (J. R. Asay, R. A. Graham, G. K. Straub, eds.), pp 1- 15. Elsevier Science Publishers B. V..

Wenzell, A. B., (1987). A Review of Explosive Accelerators for Hypervelocity Impact. *Int'l. J. of Impact Engng.*, 5, 681-692.

Int. J. Impact Engng Vol 14, pp 133–144, 1993
Printed in Great Britain

0734-743X/93 $6.00 + 0.00
1993 Pergamon Press Ltd

HYPERVELOCITY IMPACT TESTS AND SIMULATIONS OF SINGLE WHIPPLE BUMPER SHIELD CONCEPTS AT 10 KM/S

L. C. CHHABILDAS[1], E. S. HERTEL[1], AND S. A. HILL[2]

1: Sandia National Laboratories, Albuquerque, New Mexico
2: Marshall Space Flight Center, Huntsville, Alabama

ABSTRACT

A series of experiments has been performed to evaluate the effectiveness of a Whipple bumper shield to orbital space debris at impact velocities of ~10 km/s. Upon impact by a 19 mm (0.87 mm thick, L/D ~0.5) flier plate, the thin aluminum bumper shield disintegrates into a debris cloud. The debris cloud front propagates axially at velocities of ~14 km/s and expands radially at a velocity of ~7 km/s. Subsequent loading by the debris on a 3.2 mm thick aluminum substructure placed 114 mm from the bumper penetrates the substructure completely. However, when the diameter of the flier plate is reduced to 12.7 mm, the substructure, although damaged, is not perforated. Numerical simulations performed using the multi-dimensional hydrodynamics code CTH also predict complete perforation of the substructure by the subsequent debris cloud for the larger flier plate. The numerical simulation for a 12.7 mm flier plate, however, shows a strong dependence on assumed impact geometry, i. e., a spherical projectile impact geometry does not result in perforation of the substructure by the debris cloud, while the flat plate impact geometry results in perforation.

INTRODUCTION

It is well known that the principal threat to orbiting space structures results from impact damage caused by orbiting space debris (Kessler, 1985, Kessler, 1989). Presently, conventional laboratory facilities are not generally available for evaluating damage mechanisms or the effectiveness of protective structures against this debris. Although analytic methods (Cour-Palais, 1969, Wilkinson, 1969) for predicting impact damage and hydrodynamics code simulations (Hertel *et al.*, 1992) of impact events have progressed to the point of providing damage assessments, these analyses or models have not been validated over the velocity range of 7 to 10 km/s, primarily due to lack of experimental capabilities to launch gram-size plates or particles over that velocity range.

A requirement for an effective shielding system is that it must protect the spacecraft from impacts both from the micrometeoroid and orbital debris environment. The micrometeoroid environment is thought to result from dust-size particles having an average velocity of 18 km/s, while the most probable threat from the orbital debris environment is believed to be millimeter or centimeter size particles weighing approximately a gram with average velocities of ~10 km/s. It is generally assumed that orbital debris is metallic (Kessler, 1985, Kessler, 1989) with a density of ~2.8 g/cm^3, and therefore can be represented by the material properties of aluminum. The orbital debris, which is man-made, is hazardous because of the abundance and relatively large mass of the debris particles. This makes the design requirements for an adequate bumper shield difficult to establish. In addition, the requirements for an adequate bumper shield design are demanding due to: (i) the uncertainty in the size, shape and density of the orbital debris particulates; (ii) the inability of hydrodynamics codes to accurately represent impact phenomena due to uncertainties in material properties as well as computational difficulties associated with the propagation of fragmented (molten and partially vaporized) debris; (iii) the lack of an impact test capability with launcher mass-velocity capabilities of approximately a gram and in excess of 8 km/s to test design concepts.

With the development of a hypervelocity launch capability (Chhabildas *et al.*, 1991, Chhabildas *et al.*, 1992, Chhabil-

das *et al.*, 1993) at Sandia, it is now possible to perform experiments over the velocity range of 7 to 12 km/s, a range not accessible previously for impacts of gram-size plates. This meets the requisite mass-velocity criteria established for the orbital debris environment. In this paper, impact experiments have been performed for a single Whipple bumper shield configuration. Simulations of these experiments using the multi-dimensional finite-volume code CTH are also described in this paper. The mass of the aluminum flier plate which is supposed to represent the orbital debris particle has been varied from 0.318 g to 0.652 g by varying the diameter of the plate from 12.7 to 19 mm.

Results of these experiments indicate that the thin aluminum bumper at the impact location completely disintegrates into a debris cloud upon impact at ~10 km/s by the aluminum flier plate. The debris cloud front propagates at velocities in excess of 14 km/s and expands radially at a velocity of ~7 km/s. Subsequent loading on the rear panel by the debris cloud generated by the 0.652 g particle (19 mm plate) penetrates the substructure completely. However, when the mass of the flier plate is reduced to 0.318 g (12.7 mm plate) the substructure, although "damaged," is not punctured over the duration of the experiment. CTH simulations of these experiments predict the results of the experiments qualitatively in that penetration or no penetration of the substructure is replicated. However, the propagation characteristics of the debris cloud are not replicated quantitatively.

In the next section the experimental technique used to launch hypervelocity plates is briefly described. The experimental set up used to simulate the orbital debris impact condition is also described in detail in a subsequent section followed by a discussion and a summary of the results. CTH simulations of the experiments are also described in later sections.

EXPERIMENTAL TECHNIQUE

The principle of operation of Sandia's newly developed hypervelocity launcher is briefly described here. It is based on the principle that structured, time-dependent (shockless), megabar driving pressures are needed to launch a plate without melting or fracturing the plate. This is accomplished by using a graded-density material to impact a stationary flier plate. When this graded-density material is used to impact a stationary flier plate on a two-stage light-gas gun over impact velocities of 6 to 7.4 km/s, a nearly shockless, structured, and uniform high-pressure pulse will be introduced in the flier plate. Since the loading on the flier plate is nearly shockless, excess heating is minimized to prevent melting of the flier plate. The structured pressure pulse is also necessary to prevent the flier plate from fracturing. This method has been used to launch a nominally 1-mm thick aluminum flier plate to a velocity of 10.4 km/s (Chhabildas *et al.*, 1992a, Chhabildas *et al.*, 1991), and 0.5-mm thick aluminum and titanium flier plates to velocities in excess of 12 km/s (Chhabildas *et al.*, 1993).

The experimental impact configuration used to simulate orbital debris impact is indicated in Figure 1. Radiographs of

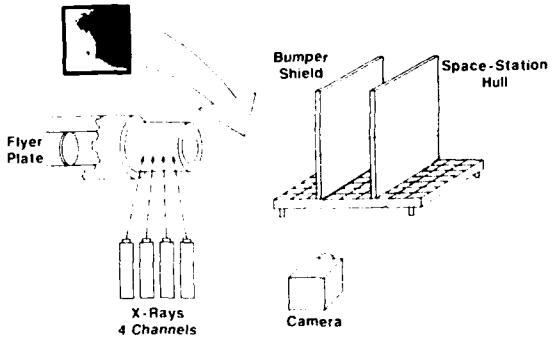


Fig. 1. Experimental configuration to simulate orbital debris impacts

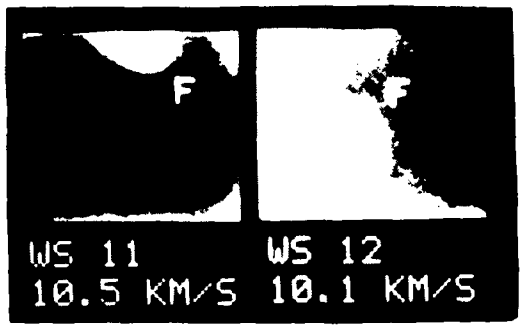


Fig. 2. Radiographs of the flier plates in experiments WS11 and WS12 prior to impact

the flier plates prior to impact are depicted in Figure 2. The bumper shield material used in these studies was a 305 mm × 305 mm 6061 T6 aluminum alloy sheet, 1.27 mm ± 0.025 mm thick. The rear panel was represented by a 305 mm × 305 mm 2219-T87 aluminum alloy panel. The thickness of the rear panel employed for both experiments was 3.20 mm ± 0.03 mm. In both experiments, the stand-off distance between the bumper shield and the rear panel was 114 mm. The debris shield and rear panel assembly was placed at a minimum distance of 550 mm from the plate launch position. This ensures that a minimum of 55 μs reading time is available for fast framing photography.

Fast framing photography was used to record the propagation of the debris cloud generated upon impact of the bumper shield. Xenon lamps were used for a light source and the images indicated in the framing pictures are front-lit photographs. Front-lit photography was chosen to determine the structure of the debris cloud. In most experiments the side view *i.e.*, the view between the bumper shield and the rear panel was monitored; the back surface view of the rear panel was also photographed. The time separation of each frame is indicated in the figure. An example of the photographs recorded for both the side and back view is shown in Figure 3 and 4 for experiment WS11. The cameras were located

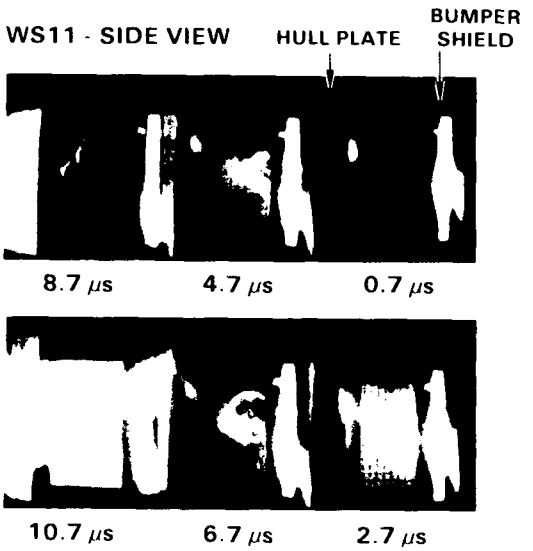


Fig. 3. Side view of the debris cloud in experiment WS11

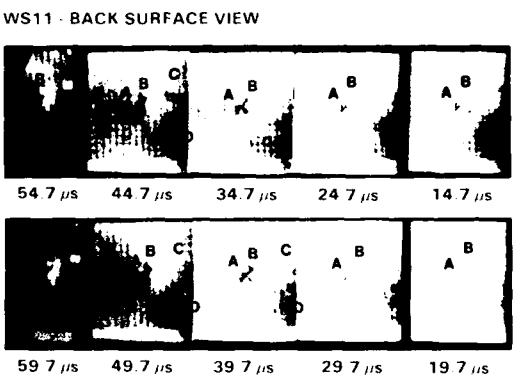


Fig. 4. Back view of the rear panel in experiment WS11

approximately 1500 mm away from the center of the debris cloud. The grid is positioned ~100 mm from the center of the line of flight. The grid markings indicated on the figures have a spacing of 1 cm.

EXPERIMENTAL RESULTS

The results of these two experiments are summarized in this section as a collection of framing photographic pictures. Impact of the flier plate with the bumper is referenced as time t = 0 in this paper.

Experiment WS11 Side View

In this experiment, impact on the shield occurred at a velocity of 10.5 km/s with a mass of 0.318 g for a 12.7 mm flier plate. Figure 3 depicts framing photographs of the debris cloud generated upon impact of the bumper shield by the flier plate. The first frame was taken at 0.7 μs after impact. The debris is not observed in the first frame since the camera is not exactly normal to the plane of view. At 8.7 μs, impact of the rear panel has already occurred. This would suggest a propagation velocity of the leading edge of the debris front to be greater than 13.1 km/s. The debris cloud expands laterally as it propagates towards the rear panel at a radial expansion velocity of over 7 km/s.

Experiment WS11 Back Surface View

The back surface view of the rear panel is indicated in the framing photographs shown in Figure 4. The deformation of the rear panel is evident at 14.7 μs after impact of the bumper shield. Note the loading of the rear panel occurs at ~8.5 μs, suggesting that at early times impulse loading by the low density mass is not damaging to the plate. As indicated in the figure, the characteristics of the deformation at A on the rear panel appear to be relatively unchanged with time up to ~60 μs. The deformation at B appears to increase at least up to 40 μs after impact of the bumper shield. There is evidence of further deformation identified as C and D in the figure occurring at ~40 to 45 μs. They appear to be more pronounced in later frames. Since the characteristics of the deformation at C and D do not seem to change significantly, rupture of the rear panel appears to have been prevented at least up to 60 μs after impact of the bumper shield. It seems,

therefore, that the mass threshold for penetration of this type of Whipple bumper shield concept is at least 0.32 g when the projectile is shaped as a 12.7-mm diameter plate 0.95 mm thick, at an impact velocity of 10.5 km/s. This does not, however, imply that there are no spall planes or cracks formed in the rear panel, thereby weakening the substructure.

Experiment WS12 Side View

In this experiment a flier plate (0.65 g) 19 mm in diameter, 0.868 mm thick impacted the bumper shield at 10.1 km/s. Framing photographs of the debris cloud generated upon impact of the bumper shield by the flier plate are shown in Figure 5. Although the flier plate is bowed prior to impact, the bowing appears to be symmetric in this experiment. As indicated in the figure, the expansion of the debris cloud appears to be very nearly spherical as it propagates towards the rear panel. A longitudinal debris front velocity is calculated to be ~14.1 km/s, while the radial expansion velocity of the debris cloud is estimated to be ~7.3 km/s. This does not however mean that the entire debris cloud is propagating at this velocity. The structure of the debris cloud at 7 μs suggest an approximate dispersion of 50 mm, suggesting a velocity distribution from a maximum of over 14 km/s to ~7 km/s. Impact of the rear panel is evidenced by the impact flash signature observed in the photographic frame at 8 μs. Note that the debris cloud is over 120 mm in diameter prior to impacting the rear panel.

Experiment WS12 Back Surface View

The set of framing photographs depicted in Figure 6 displays the back surface view of the rear panel. The first frame

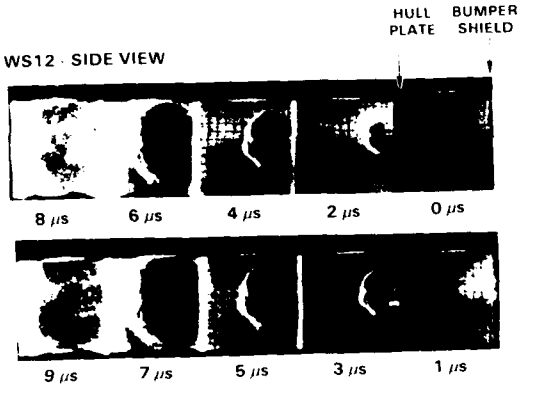


Fig. 5. Side view of the debris cloud in experiment WS12

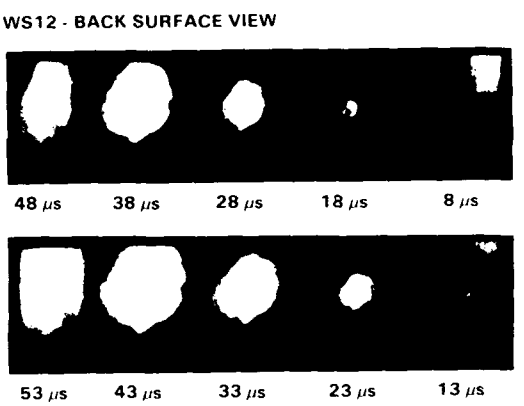


Fig. 6. Back surface view of the rear panel in experiment WS12

is taken at 8 μs, which is approximately the time at which the leading edge of the debris cloud arrives at the rear panel. No deformation of the rear panel is observed until the subsequent frame at 13 μs, in which a deformation bulge ~15 mm in diameter is observed. Perforation is observed in the next frame at 18 μs. The exact size of the rupture of the rear panel cannot be estimated, since it is obscured by the penetrating debris. The radial expansion of the penetrating debris occurs approximately at a velocity of 2 km/s.

CTH SIMULATIONS

The CTH (McGlaun, *et al.*, 1990) code was developed to model a wide range of solid dynamics problems involving shock wave propagation and material motion in one, two, or three dimensions. CTH has several thermodynamic models that are used for simulating strong shock, large deformation events. CTH can model elastic-plastic behavior, high explosive detonation, fracture, and motion of fragments smaller than a computational cell.

Numerical simulations of experiments WS11 and WS12 were performed using CTH. Due to the bowed shape of the impacting flier plate, three CTH simulations were completed for each of the experiments described in this report. Two of the CTH configurations were meant to bracket the actual impact and the third was an attempt at matching the actual impact configuration. The bracketing calculations are characterized as a flat plate identical to the experimental plate prior to acceleration and a sphere of mass equal to the experimental plate. In addition to the bracketing simulations, a section of a spherical shell that roughly approximates the accelerated plate prior to impact was chosen as the projectile. For the spherical shell, the radius refers to the outer radius of the sphere, the thickness refers to the difference between the inner and outer shell radius, and the diameter is the distance along the surface of the shell. The Table 1 lists the relevant properties of the six CTH simulations. These simulations also allow us to evaluate numerically the effects of shape on the performance of a simple Whipple bumper shield.

Table 1. Projectile Parameters for the CTH Simulations

CTH Model	Experiment	Form	Mass (g)	Diameter (mm)	Thickness (mm)	Shell Radius (cm)
na12-s	WS11	Sphere	0.318	0.608		
na12-p	WS11	Plate	0.318	12.7	0.953	
na12-c	WS11	Cap	0.318	12.7	1.0	1.33
na19-s	WS12	Sphere	0.652	0.723		
na19-p	WS12	Plate	0.652	19.0	0.868	
na19-c	WS12	Cap	0.652	19.0	1.0	1.33

The CTH simulations assumed normal impacts which were modelled with the two-dimensional axisymmetric geometry option. All of the simulations used identical zoning, material strength models, and equations-of-state. The zoning was chosen so that good resolution (~10 zones across the axial dimension) of the shock front in the relatively thin bumper and excellent resolution (~25 zones across the axial dimension) in the rear panel was achieved. In addition, to ensure second order accuracy, the zoning is square in those regions of primary importance (the bumper and the rear panel). The zoning is allowed to grow and the contract axially in the region between the bumper and rear panel.

The projectile and bumper, both 6061-T6 aluminum, were represented by the equation-of-state developed by Kerley and validated against experimental data for pressures below 80 GPa (Kerley, 1987). The rear panel (2219 T-87 aluminum) was represented using the 6061-T6 aluminum equation-of-state with an adjustment made to reflect the higher initial density. This equation-of-state for aluminum represents the solid-liquid and liquid-vapor phase changes (Kerley and Wise, 1985).

The materials were treated using a linearly-elastic perfectly-plastic material strength model with a Von Mises yield surface. Principal stress was used to trigger the void insertion fracture model for all materials. The yield and tensile strengths used for 6061-T6 and 2219-T87 were 5.0×10^9, 17.0×10^9 and 6.0×10^9, 15.0×10^9 dynes/cm^2, respectively. The values that were used reflect the well known increase in yield and fracture strength in a dynamic loading environment. (Asay *et al.* 1985, Ek and Asay, 1985).

COMPUTATIONAL RESULTS

The CTH simulations will be discussed separately in their respective sections. However, several key results from the CTH simulations pertain to all computational permutations. Experimentally, the debris cloud generated by the impact of the flier plate on the bumper is characterized by a diffuse leading edge. This diffuse leading edge is traveling at velocities of 13-14 km/s. A large radial velocity is also noted from the experimental photographs. Only the flat plate CTH simulations predict an enhancement in axial velocity of the debris front as generated by the impact, although at a lower velocity than the experiment. The CTH simulations also predict radial velocities lower than the experimental data. In general, the simulations do not predict the diffuse vapor-like nature of the debris cloud as noted in the experimental photographs.

To assess the sensitivity of the results on resolution in a limit domain, a series of one-dimensional calculations were also performed. The zoning was increased by a factor of 100 over the axial zoning in the two-dimensional simulations. For this very finely resolved simulation, the debris front velocity was only slightly greater (< 5%) than that noted for the flat plate simulations. In addition, a similar highly resolved one-dimensional Lagrangian calculation was performed. The Lagrangian simulation also gave results similar to the CTH predictions. Therefore, it is concluded that mesh resolution is not a significant contributor to the under-prediction in debris front velocity by the CTH simulations.

WS11 Simulation Spherical Projectile

Figure 7 shows a representation of the debris cloud resulting from CTH simulations just prior to impact with the rear panel. The right side of Figure 7 shows the density (resulting from the impact of a spherical projectile) of all materials

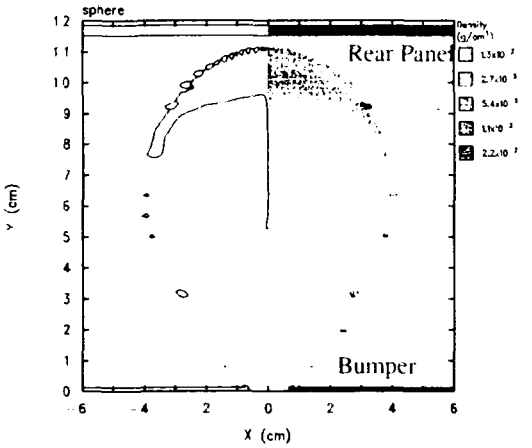


Fig. 7. Cross-section of debris cloud for the WS11/sphere simulation at 11 μs

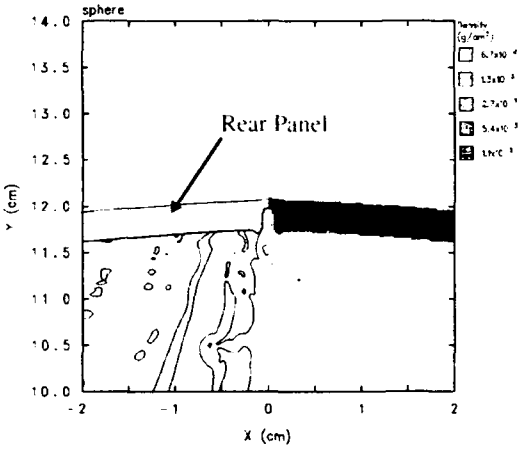


Fig. 8. Cross-section of the rear panel for the WS11/sphere simulation at 25 μs

in the simulation. The density referred to here is that of a computational cell and should not be confused with the linear density as determined from a radiograph. The left side of Figure 7 shows the interface lines between different materials. Remnants of the bumper appear in the left side of the figure as small masses of material being swept along by the remains of the spherical projectile. The simulations predict that the debris front axial velocity is ~10.2 km/s and the radial velocity is ~3.6 km/s with a spray angle of ~31°. Figure 8 shows a representation of the rear panel at 25 μs, which is the end of the computational record. For the spherical projectile, the rear panel is not perforated by the debris generated from the initial impact. From this single perspective, the CTH simulation agrees with the experimental results.

WS11 Simulation Flat Plate Projectile

Figure 9 shows a representation of the debris cloud from CTH just prior to impact with the rear panel for the simulation of experiment WS11. In this simulation, the bumper material leads the remains of the plate and has expanded axially compared with the spherical assumption (compare this to Figure 7). The simulations predict that the debris front axial velocity is ~12.5 km/s and the radial velocity is ~1.8 km/s with a spray angle of ~10°. Unlike the simulation of a spherical projectile, the mass appears to be "focused" into a column, resulting in less dispersion. Figure 10 shows the CTH representation of the rear panel just after perforation by the debris cloud. An ~15 mm diameter rupture is predicted for the flat plate projectile.

WS11 Simulation Spherical Cap Projectile

Figure 11 shows a representation of the debris cloud from CTH just prior to impact with the rear panel. In this simulation and unlike the flat plate prediction, a section of the bumper has separated from the projectile material and is leading the bulk of the debris cloud. The simulations predict that the debris front axial velocity is ~11.1 km/s and the radial velocity is ~2.5 km/s with a spray angle of ~13°. Figure 12 shows a representation of the rear panel just after perforation by the debris cloud. An inspection of the complete computational record shows that perforation of the rear panel occurs at ~24 μs after initial impact. From this figure, one can note the perforation diameter is ~5 mm. Perforation is not observed in experiment WS11 (see Figure 4).

Figures 13 and 14 show the calculated density as a function of axial (y-axis computationally) and radial (x-axis com-

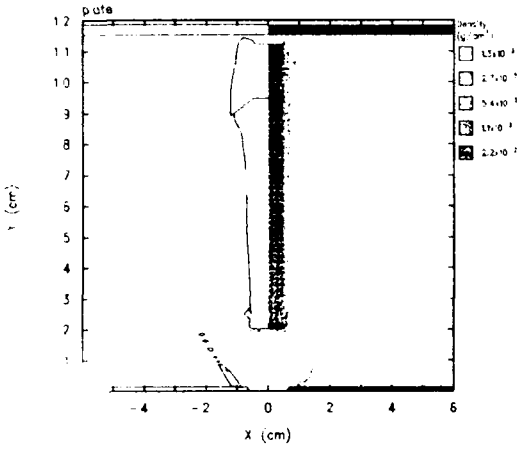


Fig. 9. Cross-section of the debris cloud for the WS11/plate simulation at 9 μs

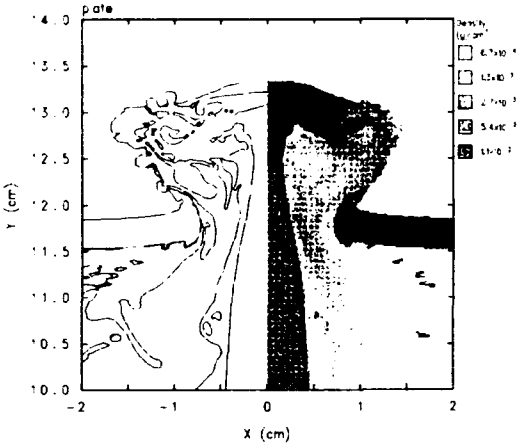


Fig. 10. Cross-section of the rear panel for the WS11/plate simulation at 19 μs

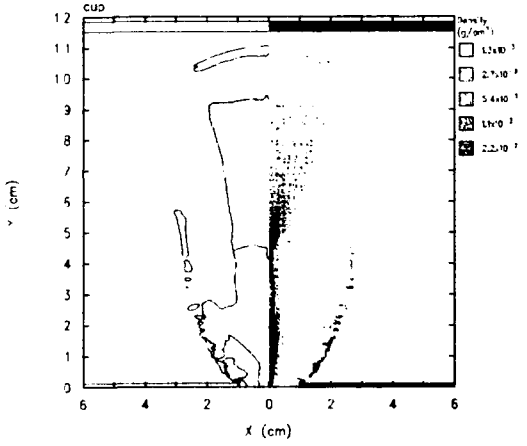


Fig. 11. Cross-section of the debris cloud for the WS11/cap simulation at 11 μs

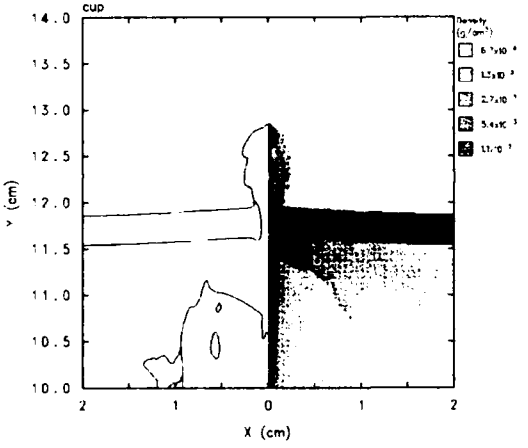


Fig. 12. Cross-section of the rear panel for the WS11/cap simulation at 25 μs

putationally) position, respectively, for the three projectile approximations. Both figures contain information just prior to impact (9 - 11 μs) with the rear panel. The axial locations used in Figure 13 are not identical for the three projectile approximations, but are taken to illustrate the differences in the radial mass distribution. In general, the density of the debris cloud is ~100 times below ambient aluminum density. For the spherical projectile, the two figures show the debris cloud to have a relatively high density leading edge axially with a somewhat lower density leading edge radially. The radial density plot (Figure 14) shows a density spike along the centerline. This is thought to be an artifact of the axisymmetric approximation. Mass has a tendency to accumulate along the centerline because of the boundary condition applied there. For the flat plate projectile, the two figures show the debris cloud to have a slightly higher density leading edge axially for both the bumper and projectile material. The radial density plot shows a density plateau roughly equal to the initial plate radius (0.6 cm) with an exponential decrease off of that plateau. For the spherical cap projectile, the two figures show the debris cloud to have a distinctly separated regions, the leading cloud is low density with the trailing material ~3 times higher density.

WS12 Simulation Spherical Projectile

Figure 15 shows a representation of the debris cloud from CTH simulation just prior to impact with the rear panel. The right side of Figure 15 shows the density of all materials in the simulation. The left side of Figure 15 shows the interface

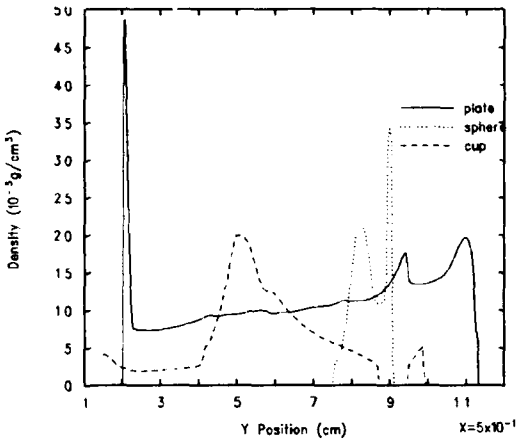


Fig. 13. Density along the symmetry axis (y-axis) for the WS11 simulations

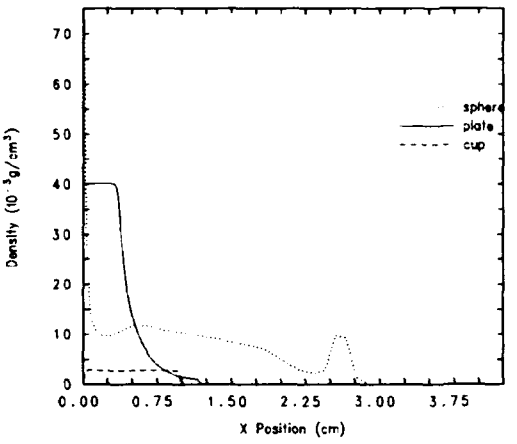


Fig. 14. Density as a function of radius (x-axis) for the WS11 simulations

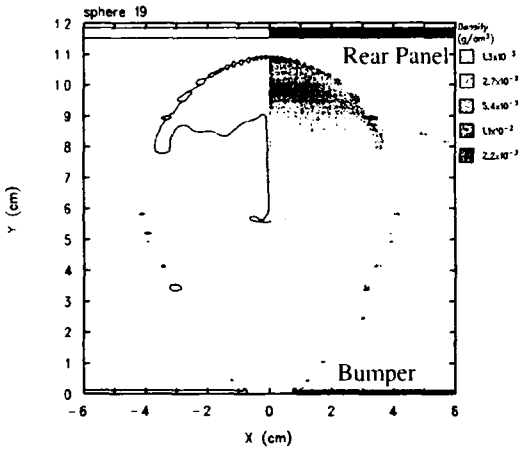


Fig. 15. Cross-section of the debris cloud for the WS12/sphere simulation at 11 μs

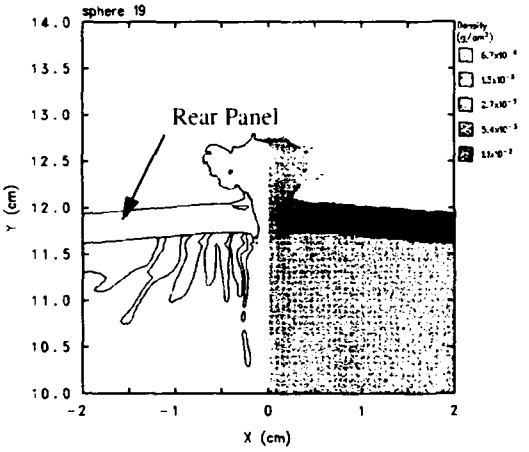


Fig. 16. Cross-section of the rear panel for the WS12/sphere simulation at 18 μs

lines between different materials. Remnants of the bumper appear in the left side of the figure as small masses of material being swept along by the remains of the spherical projectile. The simulations predict that the debris front axial velocity is ~10.0 km/s and the radial velocity is ~3.4 km/s with a spray angle of ~30°. Figure 16 shows a representation of the rear panel just after perforation by the debris cloud. An inspection of the complete computational record shows that perforation of the rear panel occurs at ~15 μs after initial impact. From this figure, one can note the perforation diameter to be ~2.5 mm.

WS12 Simulation Flat Plate Projectile

Figure 17 shows a representation of the debris cloud from CTH just prior to impact with the rear panel. In this simulation, the bumper material leads the remains of the plate and has expanded substantially compared with the spherical assumption (compare this to Figure 15). The simulations predict that the debris front axial velocity is ~12.1 km/s and the radial velocity is ~2.1 km/s with a spray angle of ~13°. Figure 18 shows a representation of the rear panel just after perforation by the debris cloud. An inspection of the complete computational record shows that perforation of the rear panel occurs at ~20 μs after initial impact. From this figure, one can note the perforation diameter is ~22 mm. Note that the photographic records for experiment WS12 (see Figure 6) indicate a deformation bulge of ~15 mm prior to rupture of the rear panel.

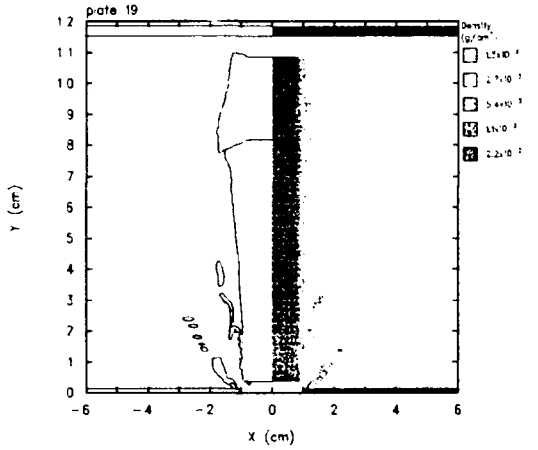


Fig. 17. Cross-section of the debris cloud for the WS12/plate simulation at 9 μs

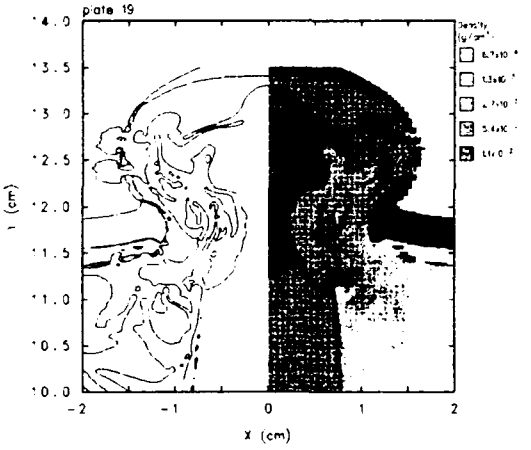


Fig. 18. Cross-section of the rear panel for the WS12/plate simulation at 19 μs

WS12 Simulation Spherical Cap Projectile

Figure 19 shows a representation of the debris cloud from CTH just prior to impact with the rear panel. In this simula-

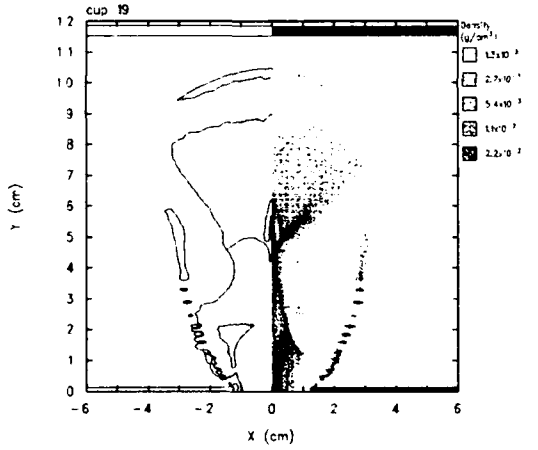


Fig. 19. Cross-section of the debris cloud for the WS12/cap simulation at 10 μs

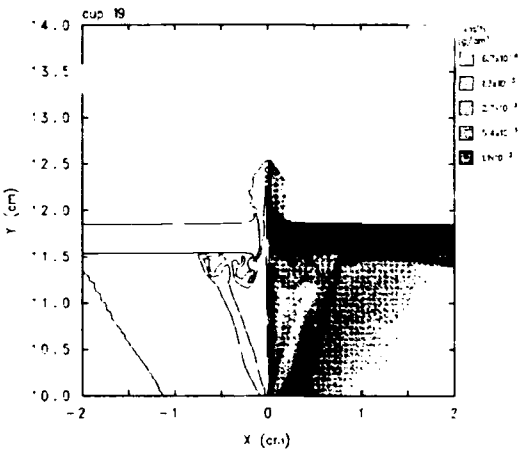


Fig. 20. Cross-section of the rear panel for the WS12/cap simulation at 25 μs

tion, a section of the bumper has separated from the projectile material and is leading the bulk of the debris cloud. The simulations predict that the debris front axial velocity is ~10.5 km/s and the radial velocity is ~3.2 km/s with a spray angle of ~24°. Figure 20 shows a representation of the rear panel just after perforation by the debris cloud at 25 μs after impact. An inspection of the complete computational record shows that perforation of the rear panel occurs at ~20 μs after initial impact. From this figure, one can note the perforation diameter is ~2 mm. Perforation of the rear panel occurs when a relatively slow moving slug of centerline-material impacts the rear panel. This slug of centerline-material can be seen in Figure 19 at y = 5-6 cm.

Figures 21 and 22 show the density as a function of axial and radial position, respectively, for the three projectile approximations. Both figures contain information just prior to impact (9 - 11 μs) with the rear panel. The axial locations used in Figure 22 are not identical for the three projectile approximations, but are taken to illustrate the differences in the radial mass distribution.In general, the density of the debris cloud is ~100 times below ambient aluminum density. For the spherical projectile, the two figures show the debris cloud to have a relatively high density leading edge axially

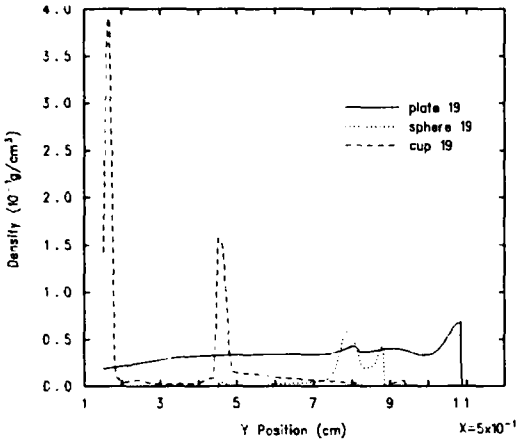


Fig. 21. Density along the symmetry axis (y-axis) for the WS12 simulations

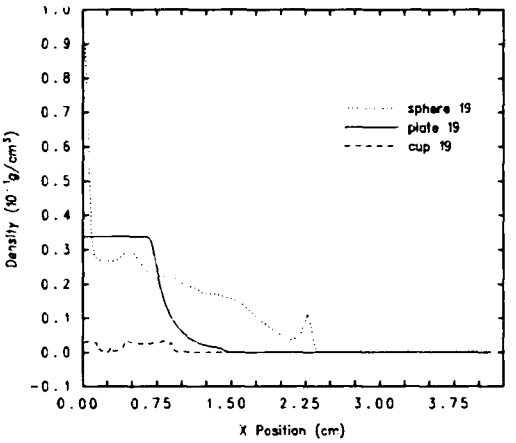


Fig. 22. Density as a function of radius (x-axis) for the WS12 simulations

with a somewhat lower density leading edge radially. The radial density plot shows a density spike along the centerline. These features were also seen in the CTH simulations of experiment WS11. Again, this is most likely an artifact of the axis-symmetric approximation. For the flat plate, the two figures show the debris cloud to have a slightly higher density leading edge axially for both the bumper and projectile material. The radial density plot shows a density plateau roughly equal to the initial plate radius (0.95 cm) with an exponential decrease off of that plateau. For the spherical cap projectile, the two figures show the debris cloud to have distinctly separated regions. The leading cloud is low density with the trailing material ~3 times higher density.

DISCUSSION

In this study, impact of the flier plate on the bumper shield occurs at velocities over 10 km/s. This generates stresses in excess of 160 GPa in both the impacting flier plate and the bumper shield. Aluminum melts at ~120 GPa in the shocked state. Therefore upon release from 160 GPa the entire plate and the bumper shield will be molten with the final release temperature ~3000 K. Since the boiling point for aluminum is ~2700 K, partial vaporization is also anticipated. The debris cloud generated upon impact is therefore expected to be completely molten with partial vaporization.

As mentioned previously, the debris cloud is observed to expand almost spherically as it propagates longitudinally. The leading edge of the debris cloud is presumed to be low-density material probably vapor, travelling at velocities of 13 to 14 km/s, with a density gradient across the debris cloud in that the higher density material is travelling slower at velocities approximating 6 to 7 km/s. The debris cloud expands radially at a rate of ~7 km/s. This implies a spray angle of ~45°. This is indicated schematically in Figure 23. The subsequent loading on the rear panel is both spatial and time-dependent in that the loading is distributed over a considerable portion of the rear panel and spans a time interval of approximately 8 μs. This is also consistent with the result that the rear panel usually ruptures approximately 5 μs after initial loading.

The total mass in the debris cloud is composed of the mass of the flier plate and the fraction of the mass of the bumper shield that was penetrated upon impact. As a first-order approximation, we assume that the flier plate punches an equivalent diameter hole in the bumper shield upon impact and we neglect any mass ejected from the impacting surface of the bumper. For a 19 mm diameter plate impact, the contributing mass to the debris cloud from the bumper shield will be approximately 0.96 g. Specifically, in experiment WS12 the total mass in the debris cloud will be 1.61 g. If the entire mass is distributed uniformly in a sphere of ~11 cm diameter prior to impact (see Figure 5) of the rear panel, then the density of the debris cloud is calculated to be ~0.002 g/cm^3. However, as indicated in Figure 5, the mass appears to be distributed towards the "front" of the cloud within a finite shell thickness. On an average the density of the rest of the cloud should therefore be less than 0.002 g/cm^3.

The agreement with experiment is relatively good if the criteria of penetration/no-penetration is used. However, the nature of the debris cloud (front velocity, radial dispersion, and mass distribution) is not consistently simulated by CTH. In general, the assumption that the projectile is a spherical object of mass equal to the mass of the experimental flier plate gives the best agreement with experiment for the distribution of mass in the debris cloud, the general shape of the cloud, and the penetration characteristics of the debris cloud. The flat plate assumption predicts the highest axial velocity of the debris cloud but a very small spray angle. This assumption also overpredicts perforation numerically.

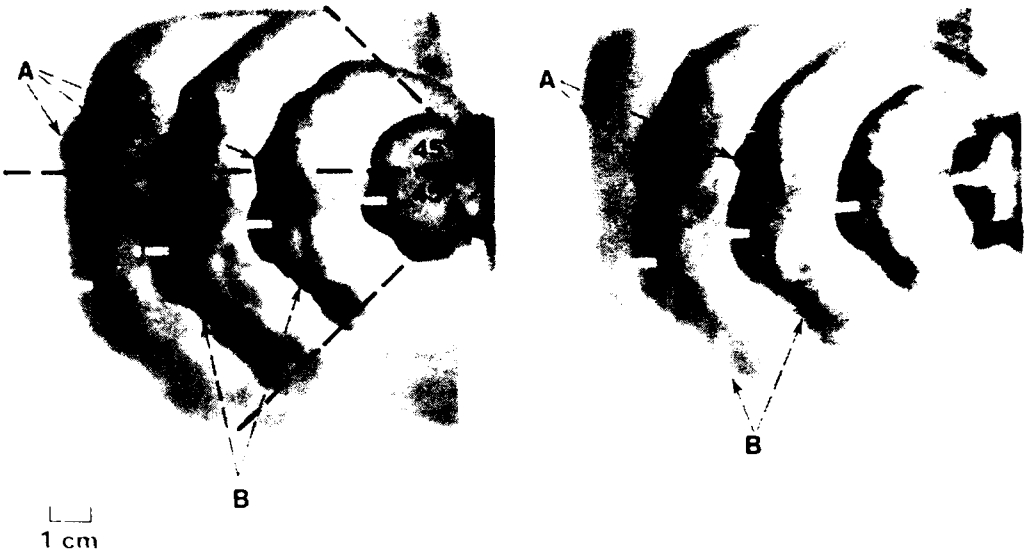


Fig. 23. Spray Angle for WS12

The spherical cap assumption predicts some features of the two bracketing cases. The predicted debris cloud does have a larger spray angle than the flat plate assumption, but is still less than the experimentally observed value. The axial velocity is also lower than the flat plate value but higher than the spherical assumption. However, the penetration predictions from the spherical cap assumption do not match the experimental results. The spherical cap impact produces a density concentration on the axis of symmetry (see Figures 11 and 19). For the WS11 simulation, the computational penetration occurs at ~20 μs and is a result of this axial mass impacting the rear panel. For the WS12 simulation, the computational penetration occurs at ~15 μs and is also a result of the leading edge of the debris cloud impacting the rear panel. The simulations exhibit perfect symmetry and tend to abnormally concentrate mass along the axis. We believe that the overprediction of perforation for WS11 with the spherical cap assumption is due to concentration of this mass. Removing the computational symmetry would disperse the mass radially and most likely improve the predictive capabilities of CTH. Three dimensional calculations would allow further exploration of this phenomena, however, these calculations would be prohibitively expensive given the current state of computing technology.

Table 2 lists an estimate of the state properties of the debris cloud using data from CTH. All material below 900 K was

Table 2. Solid liquid vapor estimates based on temperature predictions from CTH

CTH Simulation	Solid (B) (%)	Solid (P) (%)	Liquid (B) (%)	Liquid (P) (%)	Vapor (B) (%)	Vapor (P) (%)
ta12.s	0.0	0.0	75.5	59.0	24.5	41.0
ta12.p	0.0	0.0	26.5	21.0	73.5	79.0
ta12.c	0.0	2.0	0.0	65.0	100.0	33.0
ta19.s	0.0	0.0	82.5	79.0	17.5	21.0
ta19.p	0.0	0.0	4.0	12.5	97.0	87.5
ta19.c	0.0	0.0	0.0	59.0	100.0	41.0

assumed to be solid, all material between 900 and 2700 K was assumed to be liquid, and all material above 2700 K was assumed to be vapor. No other parameters were used to screen the state determination, so the results in Table 2 should be considered an estimate only. The CTH simulations are labeled using the nomenclature from Table 1. The symbol (B) refers to the original bumper material and the symbol (P) refers to the original projectile material. From an inspection of Table 2, one can note that the debris clouds are composed of liquid and vapor with virtually no solid material as would be expected from the initial impact generated state in both materials. The spherical projectile simulations have the lowest amounts of vapor with the bumper material being mostly condensed phase. The spherical cap projectile com

pletely vaporizes the bumper material but maintains it's own state as mostly liquid. The flat plate projectile simulations produce the highest amounts of vapor for both bumper and projectile.

The mass threshold for penetration at ~10 km/s for a Whipple-like bumper shield design concept described in this study is ~0.32 g for a plate 12.7 mm in diameter, and 0.953 mm thick, as the results of experiment WS11 suggest. Experiments with intermediate diameter plates are required to determine a threshold for perforation or ballistic limit. Although the deformation of the rear panel is observed in this experiment, rear panel perforation is prevented at least up to 60 μs after impact of the bumper shield. This does not, however, imply that there is no structural damage to the rear panel, such as spall planes, voids or cracks, or that late time structural response does not cause rupture.

As mentioned above, the leading edge of the debris cloud is low-density material, presumably vapor, travelling at velocities of 13 to 14 km/s, with a density gradient across the debris cloud since the higher density material is travelling at velocities approximating 6 to 7 km/s. The density distribution of the debris cloud cannot be quantitatively estimated. Low energy x-ray studies on the propagation of debris cloud would complement the current measurements, and would yield quantitative measurements on the density distribution of the debris cloud. Alternately, we have used the multi-dimensional hydrodynamics code CTH to numerically estimate the density distribution and the temperature distribution of the cloud.

In general, the CTH simulations show tantalizing glimpses of the reality of the experimental results. In no case does CTH fully predict the relevant experimental results. However, this is the first attempt at validating CTH to an experiment of this type. The evidence indicates that the equation-of-state used does not contain some key physics, such as phase separation, that is important for the conditions generated by ~10 km/s impacts. Since this velocity regime has not been previously accessible to experiment, the inadequacy of the equation-of-state should not be surprising.

These calculations do, however, suggest that a thin flat plate impact on a thin shield will cause the most damage to the rear plate, primarily due to the "one-dimensional" nature of the propagating debris that is generated upon impact. For a spherical projectile, the debris tends to disperse laterally, causing the impulse loading to be distributed over a wider area, thereby minimizing the damage to the rear panel when compared to the flat plate configuration.

REFERENCES

Asay, J. R., L. C. Chhabildas, G. I. Kerley, and T. G. Trucano (1985). High Pressure Strength of Shocked Aluminum. Shock Waves in Condensed Matter - 1985 Edited by Y. P. Gupra, Plenum Publishers.

Chhabildas, L. C., L. M. Barker, J. R. Asay, T. G. Trucano, and G. I. Kerley (1991). Sandia's New Hypervelocity Launcher - HVL. Sandia National Laboratories Report SAND91-0657.

Chhabildas, L. C., L. M. Barker, J. R. Asay, T. G. Trucano, G. I. Kerley, and J. E. Dunn (1992a). Launch Capabilities to Over 10 km/s. Shock Waves in Condensed Matter - 1991 Eds., S. C. Schmidt, J. W. Forbes, R. D. Dick, Elsevier Science Publishers B.V.

Chhabildas, L. C., E. S. Hertel, S. A. Hill (1992b). Whipple Bumper Shield Tests at over 10 km/s. Shockwaves in Condensed Matter - 1991 Eds. S. C. Schmidt, J. W. Forbes, R. D. Dick, Elsevier Science Publishers B. V.

Chhabildas, L. C. (1993). An Impact Technique to Accelerate Flier Plates to Velocities Over 12 km/s. This Volume.

Cour-Palais, B. G. (1969). Meteoroid Protection by Multi-Wall Structures. AIAA Paper No. 69-372.

Ek, D. R. and J. R. Asay (1985). The Stress and Strain-Rate Dependence of Spall Strength in Two Aluminum Alloys. Shock Waves in Condensed Matter - 1985 Edited by Y. P. Gupra, Plenum Publishers.

Hertel, E. S., L. C. Chhabildas, and S. A. Hill (1992). Whipple Bumper Shield Simulations. Shock Waves in Condensed Matter - 1991, Eds., S. C. Schmidt, J. W. Forbes, R. D. Dick, Elsevier Science Publishers B.V., 1992.

McGlaun, J. M., S. L. Thompson, L. N. Kmetyk, and M. G. Elrick (1990). A Brief Description of the Three-Dimensional Shock Wave Physics Code CTH. Sandia National Laboratories Report SAND89-0607.

Kerley, G. I. (1987). Theoretical Equation of State for Aluminum. Int. J. Impact. Engng., 5, 441-449.

Kerley, G. I. and J. Wise (1985). Shock-Induced Vaporization of Porous Aluminum. Int. J. Impact. Engng., 5, 441-449.

Kessler, D. J. (1985). Orbital Debris Issues. Adv. Space Res., 5, 3-10.

Kessler, D. J., R. C. Reynolds, and P. D. Anz-Meador (1989). Orbital Debris Environment for Spacecraft Designed to Operate in Low Earth Orbit. NASA Technical Memorandum 100-471.

Wilkinson, J. P. D. (1969). A Penetration Criterion for Double-Walled Structures Subject to Meteoroid Impact. AIAA Journal, 7, 1937-1943.

Int. J. Impact Engng Vol.14, pp.145 - 156, 1993
Printed in Great Britain

0734-743X/93 $6.00+0.00
Pergamon Press Ltd

DESIGN AND PERFORMANCE EQUATIONS FOR ADVANCED METEOROID AND DEBRIS SHIELDS

ERIC L. CHRISTIANSEN

NASA Johnson Space Center, Mail Code SN3, Houston, Texas 77058

ABSTRACT

This paper provides equations defining the performance capability of various types of meteoroid and debris shielding systems. These equations have been developed at the NASA Johnson Space Center (JSC) Hypervelocity Impact Test Facility (HIT-F). Equations are included that are applicable for aluminum Whipple shields, Nextel® Multi-Shock (MS) shields, hybrid Nextel®/Aluminum MS shields, and Mesh Double-Bumper (MDB) shields. The MS and MDB shields are advanced shields with demonstrated weight and performance advantages over conventional Whipple shields.

NOMENCLATURE

C	Speed of sound in target (km/sec)
d	projectile diameter (cm)
d_c	critical projectile diameter (cm) causing failure
ρ	density (g/cm^3)
H	Brinell hardness of target (BHN)
m	areal density (g/cm^2)
M	projectile mass (g)
P	penetration depth (cm)
S	overall spacing between outer bumper and rear wall (cm)
σ	rear wall yield stress (ksi)
t	thickness (cm)
θ	impact angle (deg) measured from surface normal
V	projectile velocity (km/sec)
V_n	normal component of proj. velocity (km/sec) = V cos θ

Subscripts:

b	bumper(s) [all bumpers in Multi-Shock (MS) shield, first & second bumper in Mesh Double-Bumper (MDB) shield]
I	intermediate layer in MDB shield
p	projectile
t	target
w	rear wall
1,2,3,4	individual bumpers and spacings

INTRODUCTION

Research at the NASA Johnson Space Center (JSC) Hypervelocity Impact Test Facility (HIT-F) has resulted in a number of low-weight, state-of-the-art shielding concepts for spacecraft protection from meteoroid and orbital debris impact (Crews and Christiansen, 1992). One such concept, the Multi-Shock (MS) Shield, uses a spaced array of 4-5 thin sheets of aluminum, ceramic fabric or other materials to repeatedly shock and disintegrate impacting projectiles followed by a rear-wall to react the loading from the debris cloud (Cour-Palais and Crews, 1990). Another concept, the mesh double-bumper (MDB) consists of four elements: a mesh, a continuous aluminum sheet, high-strength fabric, and rear wall (Christiansen, 1990). Both the MS and MDB shields provide weight savings of approximately 50% at light gas gun velocities compared with conventional dual-sheet aluminum Whipple shields (Table 1). NASA is currently assessing the potential application of advanced shield concepts to Space Station *Freedom* (SSF), including hybrid forms of the MS and MDB shields that combine ceramic cloth and aluminum layers in various multi-bumper configurations to optimize performance capabilities within established design constraints. Results of HVI testing and performance assessments for one of many hybrid shield configurations under consideration are presented in this paper.

Table 1. Hypervelocity impact data for Whipple, Nextel® Multi-Shock (MS), and Mesh Double-Bumper (MDB) shields

Shield mass per unit area for no perforation or detached spall (All impacts at 6-7 km/sec)

Impact Angle	Overall Spacing (cm)	Shield Areal Density (g/cm^2) and (Test Number) Whipple	Multi-Shock	MDB
3.2 mm (45 mg) Aluminum Projectile				
0°	5	1.12 (JSC-A1464)	0.53 (JSC-A624)	0.41 (JSC-A963)
0°	10	0.60 (JSC-A235)	0.29 (JSC-A1231)	0.25 (JSC-A1285)
45°	10	1.50 (JSC-A1195)	0.31 (JSC-A1317)	0.36 (JSC-A1069)
6.4 mm (0.37 g) Aluminum Projectile				
0°	10	2.07 (JSC-B128)	1.10 (JSC-B112)	0.94 (JSC-B77)
0°	20	0.96 (JSC-B31)	0.63 (JSC-B70)	0.64 (JSC-B27)
9.5 mm (1.3 g) Aluminum Projectile				
0°	30	1.35 (ARC-1895)	1.02 (UDRI 4-1293)	1.08 (UDRI 4-1172)

For assessments of the vulnerability of spacecraft from meteoroids and debris, equations have been developed that define Whipple, MS, and MDB shield protection capabilities as a function of projectile diameter, velocity, impact angle, density, etc. These equations are updates of previous work (Cour-Palais, 1969; Cour-Palais and Crews, 1990; Christiansen, 1990). The shield performance equations are based on hypervelocity impact tests and analyses to cover the full range of expected on-orbit impact conditions. Orbital debris in low Earth orbit can impact at speeds exceeding 14 km/sec, with an average of ~10.3 km/sec. Meteoroids range from 11 to 72 km/sec. Most on-orbit impacts will be oblique, and only a fraction (<15% typically) will be within 10° to 20° of perpendicular (i.e., normal) to the spacecraft surface. Impact tests are used to derive the penetration equations up to the highest velocity attainable in the laboratory, and analytical/numerical techniques are used to determine shield response beyond test capabilities. Impact data to validate the equations is limited by light gas gun performance to approximately 8 km/sec. NASA has been actively supporting launcher development to extend the database to 10-12 km/sec.

The equations in this paper are presented in two parts: (1) sizing equations to determine preliminary estimates of shielding thicknesses and weights, and (2) performance (or "ballistic limit") equations to define the impact conditions, such as projectile size, velocity, density, and impact angle, that define the

maximum protection capability for a particular shield. The penetration or ballistic limit equations given in this paper are based on a failure criteria defined as perforation or detached spall of the rear wall of the shield. Other ballistic limit curves could be developed based on other failure modes. The ballistic limit equations are used in computer programs to calculate probabilities of damage from meteoroid and debris impacts (Christiansen and Hyde, 1992). These equations continue to be updated periodically as warranted by the results of additional hypervelocity impact (HVI) tests, analyses, and impact modelling.

SINGLE SHEET PROTECTION

In some cases, spacecraft components (such as electronic boxes, etc.) are "protected" by a single, monolithic material. To assess protection capabilities for single-sheet aluminum alloy "shields", penetration and perforation threshold equations were developed by Cour-Palais (1985, 1987). For projectile density ($\rho_p/\rho_t < 1.5$), the penetration depth into a semi-infinite target is:

$$P_\infty = 5.24\, d^{19/18}\, H^{-0.25}\, (\rho_p/\rho_t)^{0.5}\, (V_n/C)^{2/3} \tag{1a}$$

For projectile density ($\rho_p/\rho_t \geq 1.5$):

$$P_\infty = 5.24\, d^{19/18}\, H^{-0.25}\, (\rho_p/\rho_t)^{2/3}\, (V_n/C)^{2/3} \tag{1b}$$

If there is attached spall, the penetration depth is greater than into a semi-infinite target:

$$P = 1.05\, P_\infty \tag{2}$$

If there is detached spall, penetration depth can vary between 1.08 and 1.5 times the semi-infinite target penetration, that is

$$P = 1.08\, P_\infty \text{ to } 1.5\, P_\infty \tag{3}$$

The plate thickness to prevent perforation, but not detached spall is approximately 1.8 times the semi-infinite target penetration (this includes the detached spall thickness):

$$t = 1.8\, P_\infty \tag{4}$$

Plate thickness to prevent perforation and detached spall, but would allow attached spall is

$$t = 2.2\, P_\infty \tag{5}$$

Plate thickness to prevent perforation and incipient spall is

$$t = 3\, P_\infty \tag{6}$$

EQUATIONS FOR PRELIMINARY SHIELDING DESIGN

A simplified method is sometimes used (Cour-Palais, 1979; Christiansen, 1992) to roughly size the thicknesses of the bumper(s) and rear wall of meteoroid/debris shields and estimate shielding weights. A "design" particle size is calculated for each surface of a critical element from probability of no-failure requirements, environment models, surface area, and orientation considerations. Thicknesses and spacings for the various shield layers are then determined based on defeating the "design" particle at its average impact velocity, density, and impact angle. Although adequate for developing estimates of shielding weights and for performing quick trade studies, a more comprehensive approach is used for verifying design adequacy by considering the complete meteoroid/debris impact angle and velocity distributions.

EQUATIONS FOR PROBABILITY ANALYSES

Shielding protection capability is assessed by probability analyses which account for the directional nature of orbital debris and meteoroids, the complex response of the shielding to oblique and low speed

impact, and shadowing from nearby equipment (Christiansen et al., 1992; Crews and Christiansen, 1992).

The ballistic limit equations for Whipple, Multi-Shock (MS), and Mesh Double-Bumper (MDB) shields are in a form that relates critical particle diameter (d_c) with impact velocity, impact angle, particle density, and target parameters. Impacts larger than the critical particle size cause shield failure (i.e., perforation or detached spall of the rear wall of the hybrid shield), while those smaller do not. The equations are consistent with the equations given for shield sizing purposes, although additional equations are given to cover the full range of on-orbit impact velocities and impact angles.

DERIVATION OF EQUATIONS

The shielding equations in this paper are based on a number of HVI tests performed in the JSC Hypervelocity Impact Test Facility (HIT-F) and other facilities. The damage classification system of Dahl and Cour-Palais (1991) was used to standardize the shield damage observed in these hypervelocity impact tests. The criteria for shielding success in these tests was no perforation or detached spall from the in-board wall (or "rear wall") of the shield protection system. Over 200 tests on Whipple shields and 150 tests on Multi-Shock and Mesh Double-Bumper shields provide the basis of the performance equations. The tests used spherical projectiles up to ~8 km/sec. The velocity in the databases is limited by the capability of two-stage light gas guns, the workhorses of hypervelocity impact research. Although velocities less than 8 km/sec represent only ~25% of the debris threat, the HVI data includes the more damaging low velocity impacts for these particular shields (typically 2-3 km/sec) and therefore represents a higher percentage of the penetrating flux (Christiansen et al., 1992). In addition, the JSC HIT-F is currently evaluating data provided from a new generation of launchers such as an inhibited shaped charge launcher developed by Southwest Research Institute for NASA (Tullos et al., 1990) and Sandia National Laboratories' Hypervelocity Launcher (Chhabildis, 1992). Although these launchers can fire aluminum particles in excess of 10 km/sec, test analysis is complicated by the fact that the projectiles are non-spherical and subject to variations in impact orientation, size and shape. A primary use for the advanced launchers is for comparison with hydrocode results and calibration of the material models used in hydrocodes. The hydrocodes are then used to predict shield performance for >10 km/sec spherical particle impacts.

The equations for application beyond test capabilities have built on formulations originally developed for Whipple shields in the 1960's and 1970's which have been applied in evaluating meteoroid threats (Cour-Palais, 1969), as well as previously developed MS and MDB equations (Cour-Palais and Crews, 1990; Christiansen, 1990). Generally, a simple analytical relationship forms the basis of scaling to velocities beyond 8 km/sec, although JSC HIT-F applies more sophisticated analysis techniques such as hydrodynamic computer codes to evaluate the velocity scaling relations (Crews and Christiansen, 1992). These evaluations are still in progress.

ALUMINUM WHIPPLE SHIELDS

Figure 1 illustrates the Whipple shield concept which consists of a front bumper at some stand-off distance from a rear wall. The following equations are based on aluminum alloy shielding materials. Bumper and rear wall thicknesses for defeating a given particle threat can be determined by the following equations:

$$t_b = c_b\, m_p/\rho_b = c_b\, d\, \rho_p/\rho_b \tag{7}$$

$$t_w = c_w\, d^{0.5}\, (\rho_p\, \rho_b)^{1/6}\, M^{1/3}\, V_n/S^{0.5}\, (70/\sigma)^{0.5} \tag{8}$$

For aluminum on aluminum impacts (i.e., $\rho_p = \rho_b$), $c_b = 0.25$ when $S/d<30$ and $c_b = 0.20$ when $S/d\geq 30$. In equation (8), $c_w = 0.16$ $cm^2\text{-}sec/g^{2/3}\text{-}km$. The coefficient c_b is increased to 0.25 to reduce the possibility of underestimating the required rear wall thickness with small standoff distances. These equations are based on a ballistic limit criterion defined as no perforation or detached spall of the rear wall of the shield.

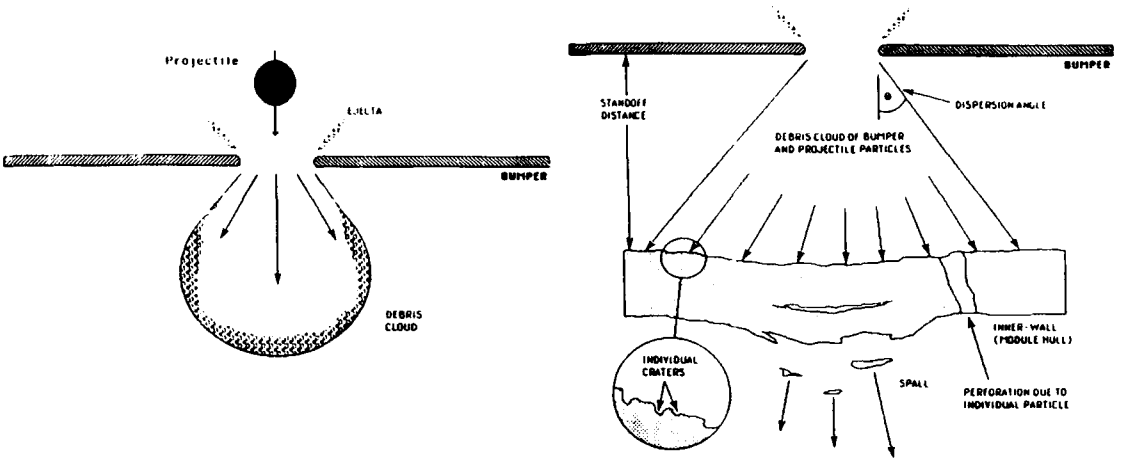


Figure 1. Whipple Shield (after Rajendran and Elfer, 1989)

Equation (8) is valid for particles impacting at a normal component velocity (V_n) of greater than 7 km/sec. The rear wall thickness relation is a slightly modified version of the Cour-Palais Whipple equation ("non-optimum") which was used in the Apollo program to extrapolate test data to meteoroid impact conditions (Cour-Palais, 1969). Coefficient c_w was derived from HVI testing with aluminum, glass, and nylon projectiles that varied in diameter from 0.04 cm to 1.9 cm (Christiansen, 1991b). If the S/d ratio is less than 15 for aluminum on aluminum impacts ($\rho_p = \rho_b$), or $(t_b \rho_b)/(d \rho_p)$ is less than 0.18 for normal impacts (not oblique) with V>7 km/sec, equation (8) potentially underpredicts rear wall thickness. Bumper fragments become the primary source of rear wall damage at impact angles greater than 65°. Therefore, above 65°, the calculated rear wall thickness should be constrained to 65°. More information on the derivation and applicability of these equations is contained elsewhere (Christiansen, 1991a; Cour-Palais, 1969).

The following equations define the protection capability limits for a Whipple shield in terms of a critical particle size (d_c) that causes shield failure (complete penetration or detached spall). Three penetration regimes are defined based on normal component velocity. At low velocities, below 3 km/sec, impact shock pressures are low and the projectile remains essentially intact after impact on the bumper. The shield's rear wall is then impacted by a deformed but substantially intact projectile. The critical particle size for $V_n \leq 3$ km/sec is given by

$$d_c = [(t_w (\sigma/40)^{0.5} + t_b)/(0.6 (\cos \theta)^{5/3} \rho_p^{0.5} V^{2/3})]^{(18/19)} \quad (9)$$

The projectile is more damaging as velocity increases in the low velocity regime, thus critical particle size decreases as velocity increases. At velocities above V_n=3 km/sec, the projectile fragments on the bumper and will begin to melt above V_n = ~5.5 km/sec for aluminum on aluminum impacts (Swift, 1982). A fragmenting or partially molten projectile is less damaging to the rear wall, thus critical particle size increases in the intermediate velocity range.

For 3 km/sec < V_n < 7 km/sec:

$$d_c = \{[(t_w (\sigma/40)^{0.5} + t_b)/(1.248 \rho_p^{0.5} \cos \theta)]^{(18/19)} \times$$

$$(1.75 - (V \cos \theta)/4)\} + \{[1.071 t_w^{2/3} \rho_p^{-1/3} \rho_b^{-1/9} S^{1/3} (\sigma/70)^{1/3}] \times$$

$$((V \cos \theta)/4 - 0.75)\} \quad (10)$$

At velocities above 7 km/sec, the debris cloud impacting the rear wall will contain various fractions of solid, liquid, and vapor components of the projectile and bumper depending on impact conditions (projectile shape, obliquity, density, etc.). For $V_n \geq 7$ km/sec, critical particle size is given by

$$d_c = 3.918\, t_w^{2/3}\, \rho_p^{-1/3}\, \rho_b^{-1/9}\, (V \cos\theta)^{-2/3}\, S^{1/3}\, (\sigma/70)^{1/3} \qquad (11)$$

For oblique impact angles over 65°, critical particle sizes should be set to the critical particle sizes for 65° impact, because of the increased damage to the rear wall from bumper fragments; i.e.,

$$d_c^{\theta>65} = d_c^{\theta=65} \qquad (12)$$

An example of set of ballistic limit curves for a 10 cm standoff Whipple shield (1.25 g/cm^2 total areal density) is shown in Figure 2. The plot is of particle diameter to fail the shield as a function of impact speed for different impact angles (failure of the shield occurs above the curves). This shows low speed (~2-3 km/sec) and higher speed (~7 km/sec) oblique impacts can be more damaging (i.e., they have lower critical diameters) than higher speed (~7 km/sec) normal impacts. A key factor governing the performance of Whipple shields is the "state" of the debris cloud projected from the bumper toward the rear wall. Whipple shields are less effective at low impact velocities and certain oblique impact angles at higher speeds because these are the conditions which generate low impact pressures in the projectile and bumper that result in solid, more penetrating fragments impacting the rear wall.

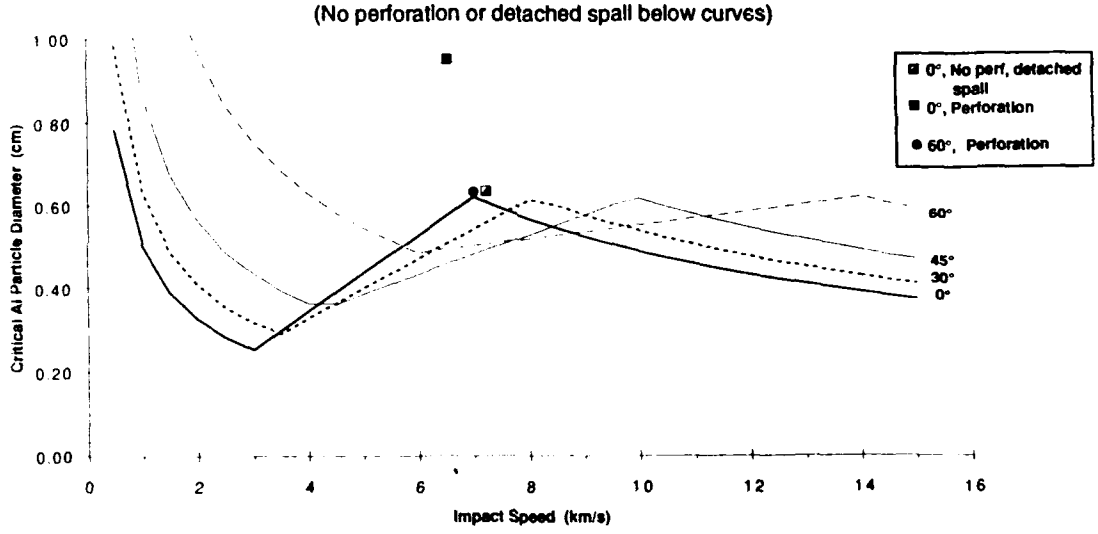


Figure 2. Whipple Shield Ballistic Limit Curves: 0.127 cm Al 6061-T6 bumper, 10.2 cm spacing, 0.32 cm Al 2219-T87 rear wall, total shield areal density = 1.25 g/cm^2

NEXTEL MULTI-SHOCK (MS) SHIELD

The multi-shock (MS) shield (Figure 3) is a low-weight shielding alternative to the Whipple shield. Sizing equations for two types of MS shield are given below: (1) Four equally spaced ceramic fabric bumpers with an aluminum rear wall, and (2) An all-flexible shield consisting of four equally spaced ceramic fabric bumpers with a ceramic fabric rear wall. A ceramic fabric that has been tested extensively at the JSC HIT-F is Nextel®, an alumina, boron oxide, silica ceramic product made by 3M Corporation. In these equations, the combined areal density of all four Nextel® bumpers is given by "m_b", and the overall spacing (from outermost bumper to the rear wall) is given by "S". The areal density of all four MS bumpers is approximately equal to the areal density of the single bumper in a Whipple shield. Major weight savings occur in reducing the rear wall thickness required to stop a given threat particle.

For MS ceramic fabric bumpers and aluminum wall:

$$m_b = 0.19\, m_p = 0.19\, d\, \rho_p \qquad (13)$$

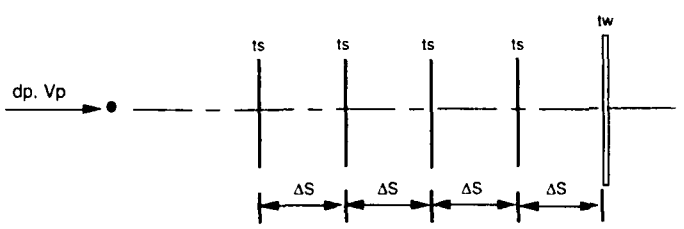
$$m_w = 41.7\ M\ V_n/S^2\ (40/\sigma)^{0.5} \quad (14)$$

For MS ceramic fabric bumpers and ceramic fabric wall:

$$m_b = 0.19\ m_p = 0.19\ d\ \rho_p \quad (15)$$

$$m_w = 43.6\ M\ V_n/S^2 \quad (16)$$

These equations are slightly modified version from the MS equations presented by Cour-Palais and Crews (1990). The wall areal densities calculated by Equations 14 and 16 are based on the ballistic limit criteria of preventing perforation and detached spall. HVI testing with aluminum projectiles up to 1 cm have been performed on the Nextel® bumper and aluminum wall MS configuration. These equations can be applied for a component velocity ($V \times \cos^{0.25}\theta$) of greater than 6.4 km/sec and S/d ratio of greater than 15. These equations are valid for all impact angles.



- Multiple, ultra-thin, spaced sheets (TS/DP <03)
- Successive shocks raise thermal state of projectile
- Flexible or rigid shields materials
- Flexible material: ceramic fabric
  - Nextel (3M brand name): 62% Al2O3, 24 SiO2, 14% B2O3
  - Versatile. Many on-orbit augmentation options.
- Augmentation shield using deployable concepts.

Figure 3. Multi-Shock Shield (Cour-Palais and Crews, 1990)

No limits are necessary on oblique impacts because the ceramic fabric bumpers do not produce damaging fragments. Particles produced by impacts on the ceramic fabrics are short fibers up to several millimeters long but only 10-12 microns in diameter. Nextel® bumper particles ejected normal to the bumper during oblique impact generally do not penetrate subsequent bumper layers and therefore do not damage the rear wall. Bumper fragments from a Whipple shield are far more damaging to the rear wall for two reasons: (1) an oblique impact on the bumper of the Whipple shield (which is ~4 times heavier than a MS bumper) produces bumper fragments that are larger and more penetrating than the tiny fiber particles from a MS fabric bumper and (2) these bumper particles impinge directly on the rear wall of the Whipple shield in contrast with the MS shield where bumper particles are stopped by lower layers of the MS shield before reaching the rear wall.

The following MS shield ballistic limit equations are valid for a shield consisting of 4 Nextel® bumpers and an aluminum rear wall, with equal spacing between sheets. In these equations, the overall spacing from the first, outer-most, bumper to the rear wall is given by "S".

For $V \geq 6.4/(\cos\theta)^{0.25}$:

$$d_c = 0.358\ (t_w\ \rho_w)^{1/3}\ \rho_p^{-1/3}\ V^{-1/3}\ (\cos\theta)^{-1/3}\ S^{2/3}\ (\sigma/40)^{1/6} \quad (17)$$

For $2.4/(\cos\theta)^{0.5} < V < 6.4/(\cos\theta)^{0.25}$:

$$d_c = 1.12\ \rho_p^{-0.5}\ [t_w\ (\sigma/40)^{0.5} + 0.37\ m_b]\ (\cos\theta)^{-1}$$

$$[(6.4/(\cos\theta)^{0.25} - V)/(6.4/(\cos\theta)^{0.25} - 2.4/(\cos\theta)^{0.5})]$$

$$+ 0.193\ (t_w\ \rho_w)^{1/3}\ \rho_p^{-1/3}\ (\cos\theta)^{-1/4}\ S^{2/3}\ (\sigma/40)^{1/6}$$

$$[(V - 2.4/(\cos\theta)^{0.5})/(6.4/(\cos\theta)^{0.25} - 2.4/(\cos\theta)^{0.5})] \quad (18)$$

For $V \leq 2.4/(\cos\theta)^{0.5}$:

$$d_c = 2\,[t_w\,(\sigma/40)^{0.5} + 0.37\,m_b]/[(\cos\theta)^{4/3}\,\rho_p^{0.5}\,V^{2/3}] \qquad (19)$$

Figure 4 illustrates the results of applying the above equations for a small-scale MS shield (0.31 g/cm^2 shield areal density, 10 cm overall spacing). This plot shows that a 3.2 mm aluminum projectile impacting at 6.5 km/sec and normal impact angle will be on the ballistic limit of the shield, while the shield will stop a 1.25 mm projectile in a normal impact at 3 km/sec.

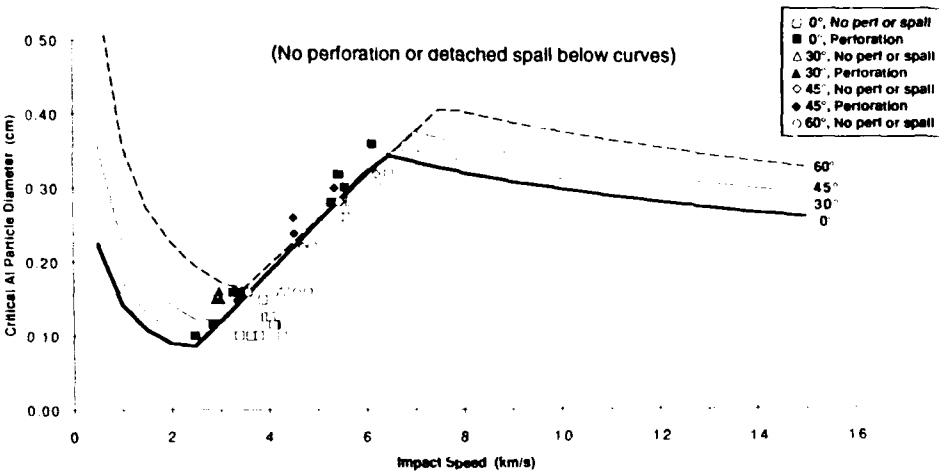
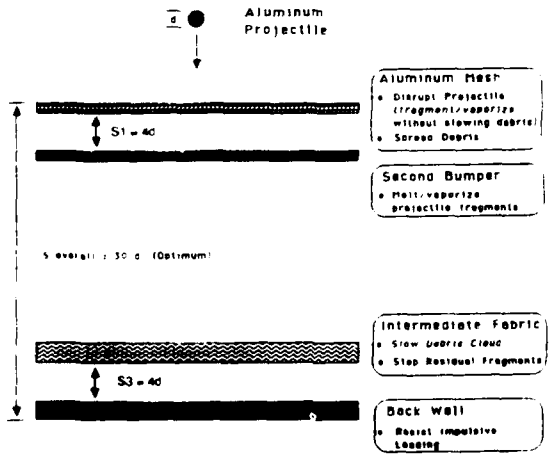


Figure 4. Multi-Shock Shield Ballistic Limit Curves: MS consists of four Nextel® AF26 bumpers (0.043 g/cm^2 each) and a 0.0508 cm Al 2024-T3 rear wall, with 2.54 cm between each sheet, 10.16 cm overall spacing, 0.31 g/cm^2 total

MESH DOUBLE-BUMPER (MDB) SHIELD

The Mesh Double-Bumper (MDB) is another advanced shield that provides similar protection and weight savings benefits as the MS shield. A schematic of the MDB shield is given in Figure 5. It was developed to show major improvements in the shielding protection capability of a Whipple shield could be made simply by adding a mesh a short distance in front of the Whipple bumper and putting a high-strength fabric layer (Kevlar®, Spectra®, or ceramic cloth) between the Whipple bumper and rear wall. Impact testing at the JSC HIT-F has shown that a double bumper system with a mesh outer bumper exhibits superior performance than the same weight double bumper consisting of two continuous aluminum sheets. Equations for sizing MDB shields and predicting performance are given by Christiansen and Kerr (1992).



- Aluminum mesh:
  - Mass efficient method to disrupt projectile
  - Greater spread of debris cloud results from impacts on mesh; reduces performance degradation at smaller spacings.
  - Fine mesh used. Small projectiles passing unhindered through mesh easily defeated by remaining shield elements.
  - Improvement over equal-weight aluminum double bumpers.
- Second bumper used to deliver second shock to remaining fragments.
- Intermediate layer of high-strength fabric (Spectra, Kevlar, Nextel, etc.) used to decrease impulsive loading on back sheet.

Figure 5. Mesh Double-Bumper Shield (Christiansen, 1990)

HYBRID NEXTEL/ALUMINUM MULTI-SHOCK SHIELDS

Hybrid MS shields are defined as a MS combination of Nextel® and aluminum bumpers and aluminum rear wall. Hybridized MS (and MDB) shields are being considered for application on SSF because it is relatively uncomplicated to improve the protection capability of certain Whipple shields by adding 2 to 3 Nextel® layers in the hybrid shield configuration (i.e., over the Whipple shield). The hybrid shield considered in this section is a triple-bumper shield containing two layers of Nextel® ceramic cloth over an aluminum 2-sheet Whipple shield (Figure 6). The 2 outer Nextel® bumpers and the aluminum bumper are all equally spaced from each other. The spacing between the aluminum bumper and aluminum rear wall is twice the inter-bumper spacing. Both Nextel® sheets together contain approximately the same areal density as the aluminum bumper, while the rear wall is approximately twice the areal density of the aluminum bumper. HVI testing investigated a range of different hybrid MS shields, including:

(1) A 20 cm overall standoff (1.05 g/cm^2) hybrid shield (100% scale model) with 2 Nextel® BF54 bumpers (0.108 g/cm^2 each), a 0.1 cm Al 6061-T6 bumper, and a 0.18 cm Al 6061-T6 rear wall.

(2) A 40% model of the hybrid shield in (1): A 7.6 cm overall standoff (0.42 g/cm^2) hybrid shield with 2 Nextel® AF26 bumpers (0.043 g/cm^2 each), a 0.041 cm Al 6061-T6 bumper, and a 0.081 cm Al 6061-T6 rear wall.

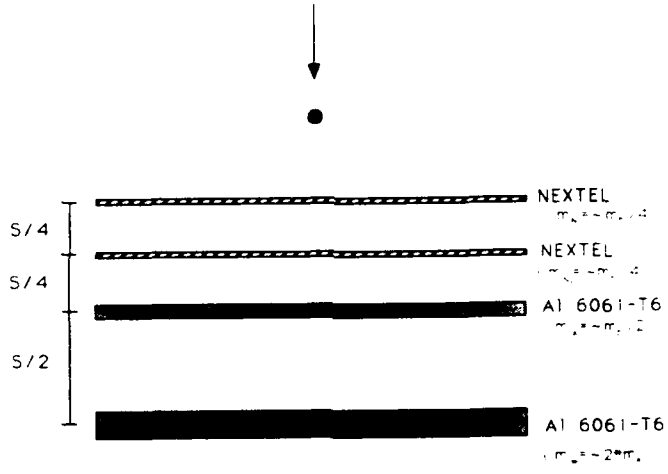


Figure 6. Hybrid Nextel®/Aluminum Multishock Shield

Ballistic limit equations for the hybrid shield are given below based on analysis of the ~50 HVI tests completed at the JSC HIT-F on hybrid shields. The impact tests demonstrated dimensional scaling over target sizes varied by 2.5 times (i.e., a 40% scale model that defeats a 2.5 mm particle was scaled to a 100% model that defeats a 6.3 mm particle).

For $V \geq 6.5/(\cos\theta)^{2/3}$:

$$d_c = 2.4\,(t_w\,\rho_w)^{2/3}\,\rho_p^{-1/3}\,\rho_A^{-1/9}\,(V\cos\theta)^{-2/3}\,S^{1/3}\,(\sigma/40)^{1/3} \qquad (20)$$

For $2.7/(\cos\theta)^{0.5} < V < 6.5/(\cos\theta)^{2/3}$:

$$d_c = 1.031\,\rho_p^{-0.5}\,[t_w\,(\sigma/40)^{0.5} + 0.37\,m_b]\,(\cos\theta)^{(1/3-x)}$$

$$[(6.5/(\cos\theta)^{2/3} - V)/(6.5/(\cos\theta)^{2/3} - 2.7/(\cos\theta)^{0.5})]$$

$$+ 0.689\,(t_w\,\rho_w)^{2/3}\,\rho_p^{-1/3}\,\rho_A^{-1/9}\,(\cos\theta)^{-2/9}\,S^{1/3}\,(\sigma/40)^{1/3}$$

$$[(V - 2.7/(\cos\theta)^{0.5})/(6.5/(\cos\theta)^{2/3} - 2.7/(\cos\theta)^{0.5})] \qquad (21)$$

For $V \leq 2.7/(\cos\theta)^{0.5}$:

$$d_c = 2\,[t_w\,(\sigma/40)^{0.5} + 0.37\,m_b]/[(\cos\theta)^x\,\rho_p^{0.5}\,V^{2/3}] \qquad (22)$$

where,

$x = 7/3$ when $\theta \leq 45°$

$x = 2$ when $\theta > 45°$

$m_b = m_N + t_A\,\rho_A$ (N = Nextel bumpers, A = Aluminum bumper)

For oblique impact angles over 75°, use the d_c calculated at 75°; i.e., for $\theta > 75°$:

$d_c^{\theta>75} = d_c^{\theta=75}$

Figure 7 shows the ballistic limit curves for a hybrid shield with the same layup as the 40% scale model (i.e., the second configuration discussed above).

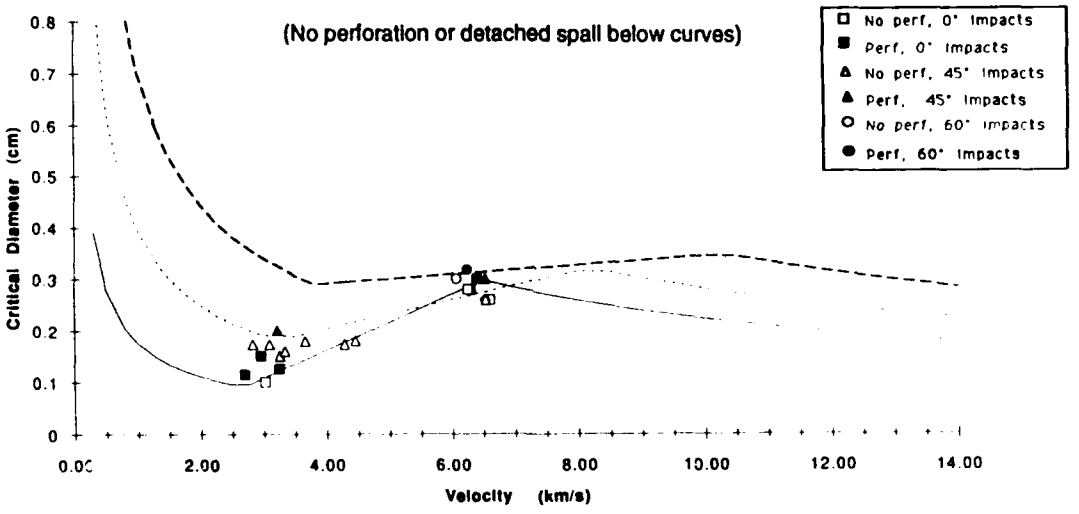


Figure 7. Hybrid Nextel®/Aluminum MS Ballistic Limit Curves: Two Nextel® AF26 bumpers (0.043 g/cm^2 each), 1.9 cm between bumpers, 0.041 cm Al 6061T6 third bumper, 3.8 cm spacing, 0.08 cm Al 6061T6 rear wall, 7.6 cm overall spacing, 0.42 g/cm^2 total

SUMMARY OF ADVANTAGES FOR MULTI-BUMPER SHIELDS

Besides improved performance, multi-bumper shields (such as the MS, MDB, and hybrid MS shields) offer a number of advantages over conventional Whipple shields that are not completely evident from the performance and design equations given above, including:

(1) *Less damaging external secondary debris (ejecta)*: The thin Nextel® bumpers in MS shields, and mesh bumpers in MDB shields, generate less external secondary ejecta in oblique impacts. The secondaries that are produced are fine grained and result in little damage into witness plates compared to Whipple shields.

(2) *More efficient at converting projectile's initial kinetic energy to internal thermal energy*: Alme et al. (1991) has demonstrated by numerical simulation that a series of shocks produced by multi-bumper shields increases the heating of the projectile compared to the single shock provided in impacts with the bumper of a Whipple shield.

(3) *Less sensitive to projectile shape*: Multi-bumper shields are less prone to perforation by disks, cylinders and other non-spherical projectiles than Whipple shields because the multiple shocks disrupt

the projectile to a greater extent. Numerical simulations at the JSC HIT-F and by Williamsen and Tipton (1990) support this conclusion.

(4) *Less sensitive to oblique impacts*: HVI tests and the equations in this paper indicate that oblique impacts can be more damaging on Whipple shields than multi-bumper shields. Multiple shocks from multiple bumpers cause greater projectile fragmentation and heating than a single bumper Whipple shield, which suffers from less projectile fragmentation in oblique impacts (up to 60°) in the 4-8 km/sec range. Also, multi-bumper systems have several layers that slow the expansion of the debris cloud before it collides with the rear wall, whereas the Whipple shield has no intervening bumpers to slow debris cloud expansion (Boslough et al., 1992). This reduction in the debris cloud expansion speed is even more pronounced in oblique impacts on multi-bumper systems, because of the greater spread and increased bumper contact area as impact obliquity angle increases.

(5) *Less cumulative damage to the shield's rear wall*: Over time, bumper fragments from numerous small strikes will crater and damage the rear wall of a Whipple shield more often than multi-bumper systems. The outer bumpers of the Whipple and multi-bumper shields will be perforated and spalled by relatively small particles. In multi-bumper shields, the intermediate layers of the shield stop bumper fragments from impacting and damaging the rear wall; whereas, the Whipple shield has no such protection. This can be a maintenance/inspection consideration for long duration spacecraft.

CONCLUSIONS

This paper gives sizing and ballistic limit equations that are applicable for a variety of spacecraft materials and shielding systems. Data and analyses supporting these equations were discussed (also see references to Christiansen, Cour-Palais and Crews). Tests and analyses on these and other promising shielding systems are continuing at the JSC Hypervelocity Impact Test Facility (HIT-F) and these equations will continue to evolve.

ACKNOWLEDGEMENTS

The author appreciates the many contributions to this work from Jeanne Lee Crews, Manager of the NASA JSC Hypervelocity Impact Research Laboratory (HIRL), and Burton G. Cour-Palais, McDonnell Douglas Space Systems Company. The excellent support from HIT-F personnel, including Lu Borrego, Earl Brownfield, Ed Cykowski, Joe Falcon, Jim Hyde, Jay Laughman, Javier Ortega, Ken Oser, Pat White, and Jim Whitney, is also appreciated.

REFERENCES

Alme, M.L., Christiansen, E.L., and Cour-Palais, B.G. (1991). Hydrocode Simulations of the Multi-Shock Meteoroid and Debris Shield. Proceedings of the APS 1991 Topical Conference on Shock Compression on Condensed Matter, Williamsburg, VA, June 17-20, 1991.

Boslough, M.B., Ang, J.A., Chhabildas, L.C., Cour-Palais, B.G., Christiansen, E.L., and Crews, J.L. (1992). Hypervelocity Testing of Advanced Shielding for Spacecraft Against Impacts to 10 km/s. *Int. J. Impact Engng*, to be published.

Chhablidis, L. (1992). A New Hypervelocity Launcher (HVL) for Space Science Application. AIAA Paper Number 92-1639.

Christiansen, E.L. (1990). Advanced Meteoroid and Debris Shielding Concepts. AIAA Paper No. 90-1336, presented at AIAA/NASA/DOD Orbital Debris Conference, Baltimore, MD, April 16-19, 1990.

Christiansen, E.L. (1991a). Whipple Shield Sizing Equations. NASA JSC Memorandum SN3-91-19, March 1, 1991. NASA TM-105539.

Christiansen, E.L. (1991b). Whipple, Multi-Shock, and Mesh Double- Bumper Shield Hypervelocity Impact Data. NASA JSC Memorandum SN3- 91-95, June 19, 1991. NASA Technical Memorandum to be published.

Christiansen, E.L. (1992). Performance Equations for Advanced Orbital Debris Shields. AIAA Paper No. 92-1462, presented at the AAIA Space Programs and Technologies Conference, Huntsville, AL, March 24-27, 1992.

Christiansen, E.L., Hyde, J. and Snell, G. (1992). Spacecraft Survivability in the Meteoroid and Debris Environment. AIAA Paper Number 92-1409.

Christiansen, E.L. and Kerr, J.H. (1992). Mesh Double-Bumper Shield: A Low-Weight Alternative for Spacecraft Meteoroid and Orbital Debris Protection. *Int. J. Impact Engng*, to be published.

Cour-Palais, B.G. (1969). Meteoroid Protection by Multi-Wall Structures. AIAA Hypervelocity Impact Conference, AIAA Paper Number 69-372.

Cour-Palais, B.G. (1979). Space Vehicle Meteoroid Shielding Design. ESA SP-153, pp.85-92.

Cour-Palais, B.G. (1985). Hypervelocity Impact Investigations and Meteoroid Shielding Experience Related to Apollo and Skylab. NASA Conference Publication 2360, Orbital Debris, pp.247-275.

Cour-Palais, B.G. (1987). Hypervelocity Impact in Metals, Glass and Composites. *Int. J. Impact Engng* Vol.5, pp.221-237.

Cour-Palais, B.G. and Crews, J.L. (1990). A Multi-Shock Concept for Spacecraft Shielding. *International Journal of Impact Engineering*, Vol.10, pp.135-146.

Crews, J.L. and Christiansen, E.L. (1992). NASA Johnson Space Center Hypervelocity Impact Test Facility (HITF). AIAA Paper Number 92-1640.

Dahl, K.V. and Cour-Palais, B.G. (1991). Standardization of Impact Damage Classification and Measurements for Metallic Targets. To be published at the 1992 Hypervelocity Impact Symposium.

Rajendran, A.M. and Elfer, N. (1989). Debris Impact Protection of Space Structures. In: *Structural Failure* (Wierzbicki, ed.), John Wiley & Sons.

Swift, H.F. (1982). Hypervelocity Impact Mechanics. In: *Impact Dynamics* (Zukas, ed.), John Wiley & Sons.

Tullos, R., Grosch, D., and Walker, J. (1990). An Explosive Hypervelocity Launcher for Orbital Debris Impact Simulations at 11.4-11.9 km/s. Southwest Research Institute, Report 06-2880, San Antonio, TX.

Williamsen, J.E. and Tipton, J.P. (1990). *Freedom* Station Wall Design Using Hydrodynamic Modelling. AIAA Paper No. 90-3664.

Int. J. Impact Engng Vol.14, pp 157 168, 1993
Printed in Great Britain

0734-743X/93 $6.00+0.00
Pergamon Press Ltd

HIGHLY OBLIQUE IMPACTS INTO THICK AND THIN TARGETS

ERIC L. CHRISTIANSEN*, ED CYKOWSKI ^, AND JAVIER ORTEGA^

*NASA Johnson Space Center, Houston, Texas 77058
^Lockheed Engineering and Sciences Company, Houston, Texas 77058

ABSTRACT

Hypervelocity impact (HV tests have been conducted at the JSC Hypervelocity Impact Test Facility (HIT-F) with aluminum projectiles impacting semi-infinite (thick) and thin aluminum plates (with plate thickness to projectile diameter ratios of 6.4 and 0.14, respectively) at impact angles ranging from normal to the plate (0°) to highly oblique (88°). The targets were impacted by solid homogeneous aluminum spheres from 1 mm to 3.6 mm diameter. Results of the HVI tests were not unusual up to ~65°, where impact damage is characterized as smooth craters and holes that become progressively elliptical and distended along the projectile flight path. Above 65° angles, however, a transition occurs to an irregularly shaped hole in thin materials and rough bottomed crater in thick targets. Above ~80°, multiple damage sites in the targets were formed with the damage areas separated by variable distances of undamaged target surface. Analytical and numerical simulations of the impact process at oblique angles above 65° demonstrates that shock compression and release of the projectile into multiple fragments occurs before the projectile fully engages the target. The resulting projectile fragments are then responsible for the multiple impact sites observed on the targets.

NOMENCLATURE

C	Speed of sound in target (km/sec)
d	projectile diameter (cm)
ρ	density (g/cm^3)
H	Brinell hardness of target (BHN)
P	penetration depth (cm)
t	thickness (cm)
θ	impact angle (deg) measured from surface normal
V	projectile velocity (km/sec)
V_n	normal component of proj. velocity (km/sec) = V cos θ

INTRODUCTION

Oblique impact studies into thick monolithic and thin bumper shield targets have been reported in the past (Eichelberger and Gehring, 1962; Schonberg, 1989). In addition, considerable work has been done to assess the effects of oblique impacts on a planetary scale through laboratory testing (Gault and Wedekind, 1978; Schultz and Gault, 1989; Schultz and Gault, 1990; Schultz and Beatty, 1992; Schultz and Lianza, 1992). This paper provides additional investigation of the physics and phenomenology of oblique impacts. These results are relevant to current spacecraft programs. For instance, a portion of the hypervelocity impact craters found on the LDEF (Long Duration Exposure Facility) satellite aluminum surfaces showed a pronounced multiple-crater morphology. An explanation offered for these multi-crater impact features is that the impacting particle was non-homogeneous; possibly a meteoroid consisting of a lightly-bound collection of individual particles (See et al., 1990). In this paper, we will show that a homogeneous projectile impacting at a highly oblique angle (>65°) can also cause an

irregular, multiple-pit crater. In a highly oblique impact, the initial shock wave can travel through the projectile causing the projectile to fragment before it has completely impacted the target material. The resulting crater in a thick target, or hole in a thin target, will be irregular and can show multiple impact sites. These results support the results previously observed and reported by Gault and Wedekind (1978), Schultz and Gault (1990) and Schultz and Lianza (1992), especially for planetary cratering.

In addition, the results of our testing and analysis provide an explanation for the "critical angle" observed in the oblique impact experiments on thin bumper shield plates by Schonberg (1989). Schonberg found that for impacts at angles above the critical angle (60°-65°), impact damage occurred primarily to external ejecta witness plates rather then the pressure wall plate mounted behind the bumper plate. However, analytical models of the process were not advanced. In this paper, we show analytically that in highly oblique impacts (above ~65° at 6 km/sec and ~70° at 7 km/sec) the projectile will fragment first from the propagation of the initial shock front before the projectile has traveled completely through the bumper. The remaining projectile fragments from the top of the projectile are shocked a second time as they contact the bumper. At these high obliquity angles, some of the remaining projectile fragments cannot penetrate through the bumper, and instead are projected along the exterior surface of the bumper plate. These effects combine to substantially reduce the impact damage on the pressure wall as observed by Schonberg (1989) for high obliquity impacts.

EXPERIMENTAL DESIGN

A series of HVI tests were performed at the NASA Johnson Space Center (JSC) Hypervelocity Impact Test Facility (HIT-F) to study oblique impacts on semi-infinite (thick) and thin aluminum plates. The HIT-F's .07 caliber and .17 caliber light-gas guns were used in the study. The HIT-F is described in detail elsewhere (Crews and Christiansen, 1992).

Definition of "Thin" and "Thick"

Projectiles were solid aluminum (2017-T4 alloy) spheres as were the targets (6061-T6 alloy). The speed of the projectiles was maintained between 6.5 and 7 km/sec in 18 tests on semi-infinite targets. A 6.4 mm aluminum 6061-T6 plate was used as the "thick" target and the projectiles were 1 mm diameter spheres (t/d=6.4). Impact angles were varied from 0° (normal to the surface) to 88°, starting with coarse increments at the low obliquity angles and making finer adjustments in impact angle at the more oblique angles. The targets were adjusted in the target chamber to achieve the desired angle to the horizontal flight path of the projectile. Impact angles were measured by an inclinometer to ± 0.5°. In addition, 10 oblique angle tests on 0.051 cm aluminum 6061-T6 plates were conducted to characterize perforation hole size and shape for "thin" plates. Projectiles were 0.357 cm diameter aluminum 2017-T4 spheres impacting at 5.5 to 6.2 km/sec (t/d=0.14). Impact angles of 60° to 88° were investigated. The test data is given elsewhere (Christiansen, 1992b).

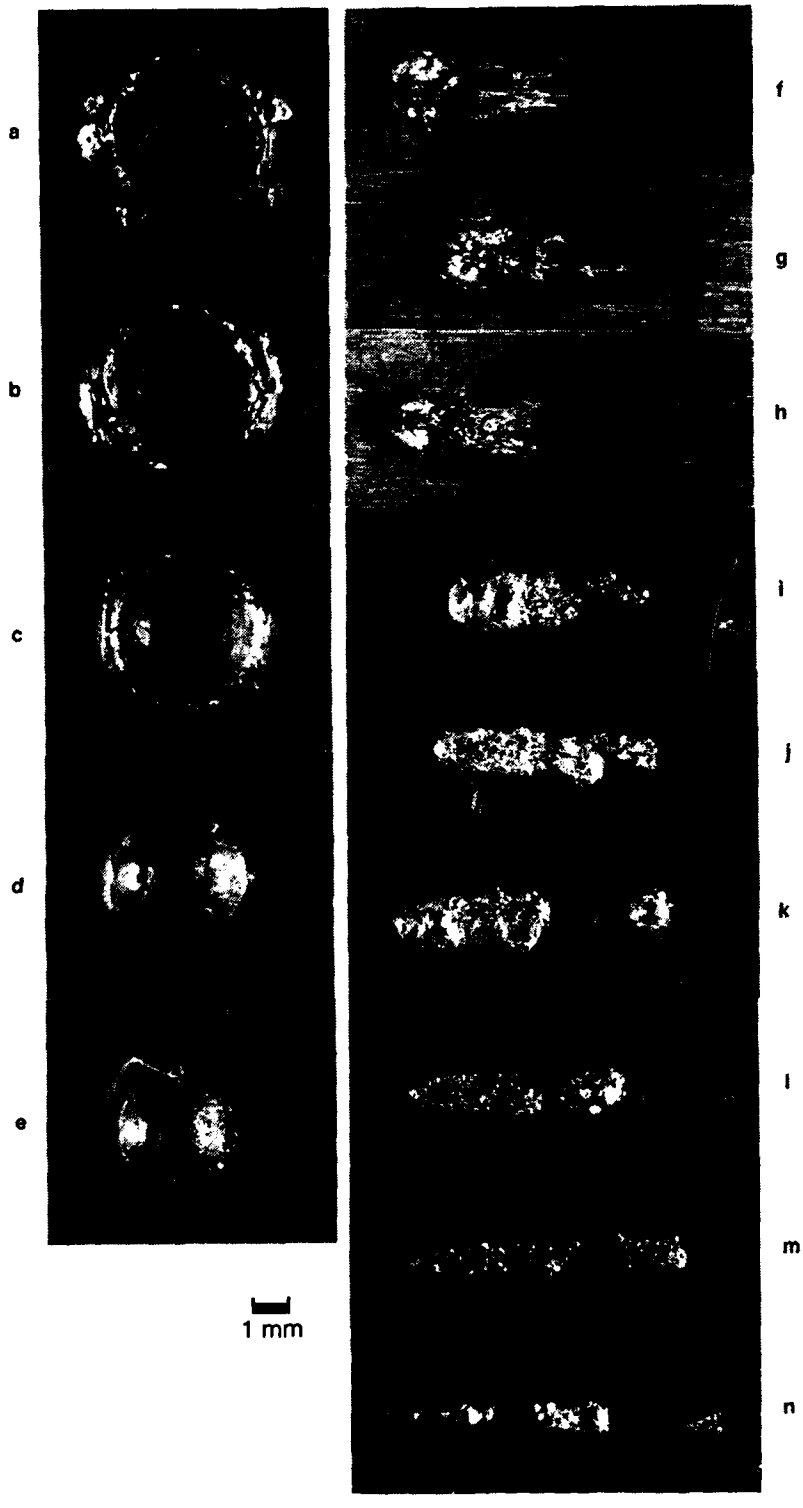
EXPERIMENTAL RESULTS

Craters were formed in the thick plates, whereas the thin plates were perforated. The following paragraphs describe the morphology of the impact damage in more detail.

Crater Data

The photographs in Figure 1 show the craters formed by 6.5-7 km/sec impacts into monolithic aluminum plates as a function of impact angle. Figure 1f shows the impact site resulting from a 1 mm spherical aluminum projectile impacting at 6.6 km/sec into the aluminum target at a 72° impact angle (from normal). The crater is elliptical, with an irregular (non-smooth) crater floor. Measurements indicated the deepest part of the crater is on the entry side. There are a few small secondary craters located along the projectile flight path, down range from the main crater (greater than a projectile diameter away). Schultz and Gault (1990) introduce the term "sibling craters" to distinguish these "secondary craters" formed by fragments of the original projectile from secondary cratering caused by ejecta following ballistic trajectories. In addition, dark streaks and a spray of molten aluminum is found on the surface of the target for many projectile diameters downrange of the impact crater.

Craters from impacts above 72° have a more pronounced multi-crater appearance as shown by Figures 1g through 1n. The main crater of the 76° impact is becoming more multi-pit like in appearance and the



(a): JSC Shot 2012, θ=0°, V=6.83 km/sec
(b): JSC Shot 1948, θ=30°, V=6.88 km/sec
(c): JSC Shot 1946, θ=45°, V=6.93 km/sec
(d): JSC Shot 1947, θ=60°, V=6.57 km/sec
(e): JSC Shot 1897, θ=70°, V=6.86 km/sec
(f): JSC Shot 2095, θ=72°, V=6.59 km/sec
(g): JSC Shot 2093, θ=74°, V=6.79 km/sec
(h): JSC Shot 2094, θ=76°, V=6.62 km/sec
(i): JSC Shot 2072, θ=78°, V=6.53 km/sec
(j): JSC Shot 2074, θ=80°, V=6.60 km/sec
(k): JSC Shot 2076, θ=82°, V=6.79 km/sec
(l): JSC Shot 2077, θ=84°, V=6.72 km/sec
(m): JSC Shot 2079, θ=86°, V=6.94 km/sec
(n): JSC Shot 2084, θ=88°, V=6.72 km/sec

Figure 1. Crater from a 1 mm aluminum sphere impacting at 6.5 to 7.0 km/sec on monolithic aluminum 6061-T6. Impact direction from left to right.

down-range sibling craters are becoming more noticeable. The spray of dark material and molten metal observed on the surface of the target increases in extent as the impact angle becomes more oblique.A double crater is formed with impact angles of 82°-84° (Figures 1k and 1l). The deeper of the two craters switches from the up-range to down-range crater for the 84° impact.

Figure 2 shows penetration depth decreasing in semi-infinite targets as impact angle becomes more oblique; an unsurprising result (Gehring, 1970). The data indicates that for a normal impact at ~7 km/sec, the ratio of penetration depth to projectile diameter (P/d) is ~2.1, and becomes less than unity (i.e., P/d < 1) for impact angles greater than 65°.

Experimental and predicted penetration depths are presented in Figure 3. The predictions were made using the Cour-Palais (1987) cratering equation which had been derived in the 1960's for the Apollo program. The Cour-Palais equation adequately predicts the decreasing trend in penetration depth with increasing impact obliquity. It slightly underpredicts penetration depth at near normal (0°) angles (high V_n) while somewhat overpredicting penetration depth at high obliquity angles (low V_n). The Cour-Palais equation used here (also given in Christiansen, 1992a) is valid for aluminum alloy targets and for a projectile density to target density ratio of less than 1.5 ($\rho_p/\rho_t < 1.5$). Penetration depth into a semi-infinite target is:

$$P_\infty = 5.24\, d^{19/18}\, H^{-0.25}\, (\rho_p/\rho_t)^{0.5}\, (V_n/C)^{2/3} \qquad (1)$$

If there is attached spall, the penetration depth is greater than into a semi-infinite target: $P = 1.05\, P_\infty$ (only the normal and near normal impacts showed any spall bulging in this study).

The ratio of total damage length to projectile diameter given in Figure 4 shows that for impact angles between 0° and 65°, the damage size becomes slightly smaller in length as obliquity increases. This probably reflects the decrease in the energy deposited in the target as the impact becomes more oblique (i.e., lower normal component kinetic energy). But above 65°, the damage length begins to increase with the cratering damage stretching out to well over 10 times the projectile diameter at angles over 85°. The ratio of damage width (or diameter) to projectile diameter steadily decreases as impact obliquity angle increases (Figure 5). Figure 6 shows that the aspect ratio of the craters increase in a non-linear fashion; that is, the craters become longer and thinner as obliquity increases, with the most significant aspect ratio changes occurring above 65° impact angles.

Perforation (Hole) Data

Figures 7a, 7b, and 7c show the irregular hole resulting from 65° (JSC shot no. A1488), 80° (JSC shot no. A1485) and 85° (JSC shot no. A1486) oblique impacts on 0.5 mm thin aluminum plates. The tests were performed with a 3.6 mm aluminum projectile at ~6 km/sec. All impacts resulted in one or more perforations in the target plate. The target plate resembles the bumper (or first sheet) of dual-sheet Whipple meteoroid/debris protection shields. The edges of the perforation are smooth where the projectile initially contacts the bumper, but become more irregular and ragged as the projectile moves through the bumper (on the down-range side of the impact hole). This is because the projectile has already fragmented from transition of the initial shock wave prior to passing across the plane of the bumper. In effect, a multi-shock process occurs with only a single bumper in highly oblique impacts on thin materials. This multiple shock has the effect of increasing the thermal state of the projectile above that which would be achieved by a single shock. The result is to increase the possibility that at least a portion of the projectile will melt. In all thin plate oblique impact experiments, molten metal and darker looking material were deposited on the target surface in a fan-shaped region down-range from the projectile impact point.

The thin plate perforations followed similar trends as with the oblique impacts on the semi-infinite plate. The 65° impact holes were slightly irregular in shape (Figure 7a) but became conspicuously irregular at 80° (Figure 7b), and a double perforation was formed at an 85° impact angle (Figure 7c).

ANALYTICAL RESULTS

Thick Target Simulation. Hydrocode simulations of JSC shot 2074 (1 mm aluminum projectile at 6.6 km/sec and 80° obliquity on a semi-infinite aluminum plate) were performed by the JSC HIT-F using the

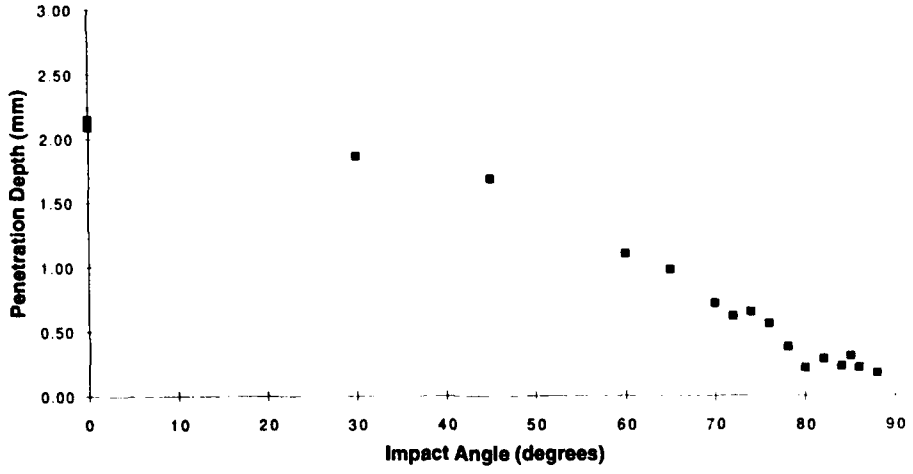


Figure 2. Impact Angle Effect on Penetration Depth for 1 mm Al projectile impacting at 6.5-7 km/sec into Al 6061-T6

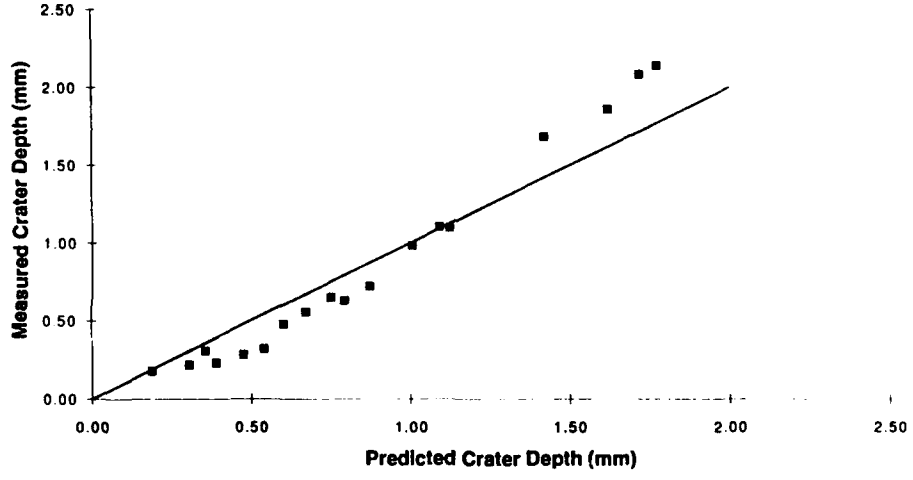


Figure 3. Comparison of Experimental Penetration Depth (Pexp) and Calculated Penetration Depth (P_{calc}) for oblique Al into Al impacts

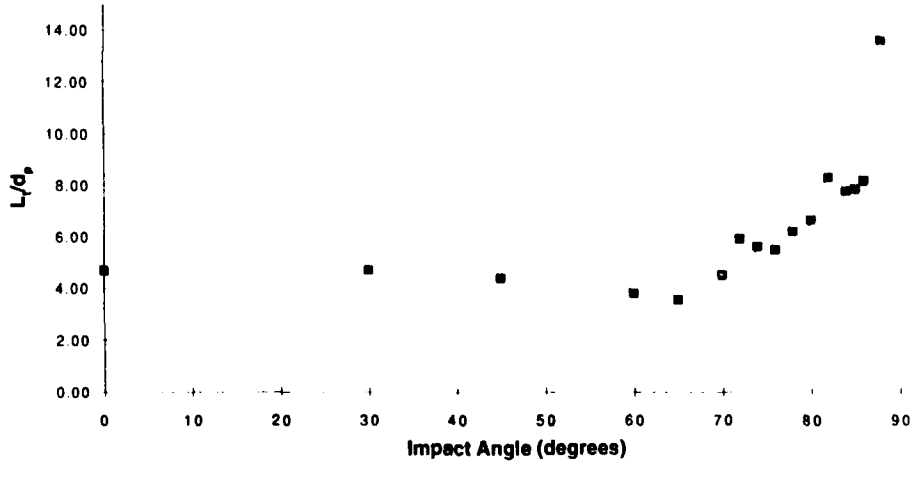


Figure 4. Ratio of total length of cratering damage to projectile diameter (L_t/d_p) versus impact angle (for Al into Al impacts)

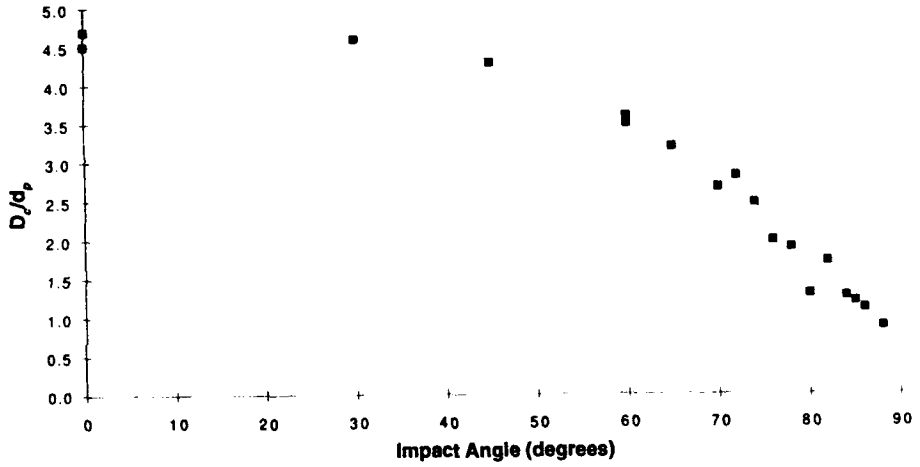


Figure 5. Ratio of maximum crater diameter to projectile diameter (D_c/d_p) versus impact angle (for Al into Al impacts)

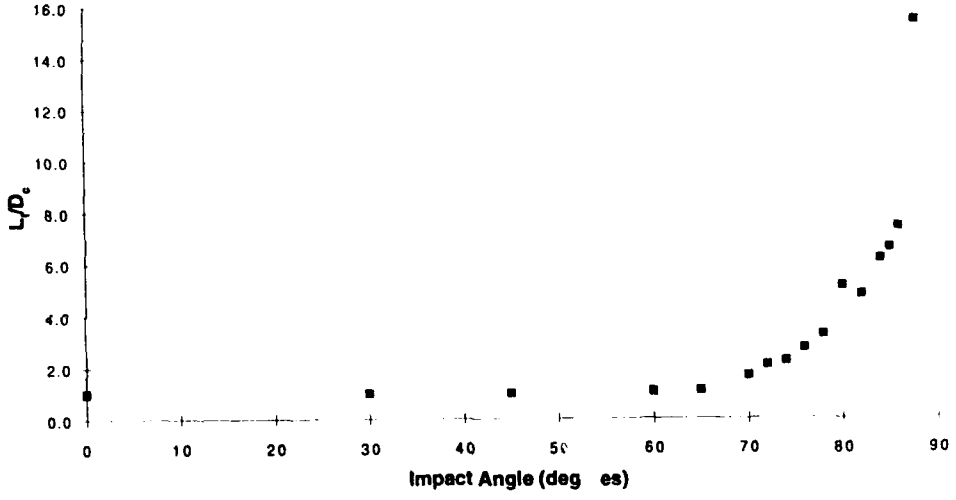


Figure 6. Aspect ratio of crater damage (total length to maximum diameter of damage, L_t/D_c) for Al into Al impacts

CTH Eulerian code from Sandia National Laboratories (McGlaun et al., 1990) and ZeuS. ZeuS is a Lagrangian impact analysis code with sliding interface logic developed by Computational Mechanics Consultants for personal computers (Zukas, 1990). Both calculations were performed in a two-dimensional, plane strain mode to demonstrate some features of the oblique impact process. The 2-D calculations are approximations of the 3-D oblique impact, and are essentially of an infinite length aluminum cylinder impacting the target, with the cylinder's longitudinal axis oriented in the third dimension.

*The CTH simulation used the SNL-SESAME Equation of State (EOS) tables and Steinberg-Guinan-*Lund viscoplastic model. The Mie-Gruneisen equation of state was used to model the high pressure material response in ZeuS. In the ZeuS code, material failure modeling is based on effective plastic strain, volumetric strain, and maximum tensile stress (spall limit). Material yielding is simulated with the von Mises criterion implemented to allow for strain and strain rate hardening, as well as pressure and thermal effects. With ZeuS, the user generally adjusts some of the dynamic material and failure parameters to tune the model results to the experimental observations (after which the "tuned" model is used to predict results outside of the experimental data base).

The CTH and ZeuS predictions of crater depth and down-range length were generally close to each other and the shot 2074 experimental results:

Data Source	Max. Depth (mm)	Crater(s) Length (mm)
Measured	0.32	6.9
CTH	0.33	7
ZeuS	0.4	6

A series of Lagrangian tracer particles were employed in the CTH calculation to follow stress wave dynamics. The maximum pressure recorded at the tracer points was ~170 kbar at a tracer located initially 0.5 mm from the initial contact point at the original surface (compared to ~880 kbar for a normal impact at 6.6 km/sec).

The ZeuS results of the simulation are illustrated in a series of plots contained in Figure 8 encompassing 1522 computational cycles and 1 μsec of the impact event. The plots are read from top to bottom starting on the left side. Each plot shows nine pressure contours in units of dynes/cm^2 ranging from the material spall limits to 10^{12} dynes/cm^2 (1 Mbar). The plot axes are in units of centimeters. The simulation time is indicated in the upper left hand corner of each plot frame.

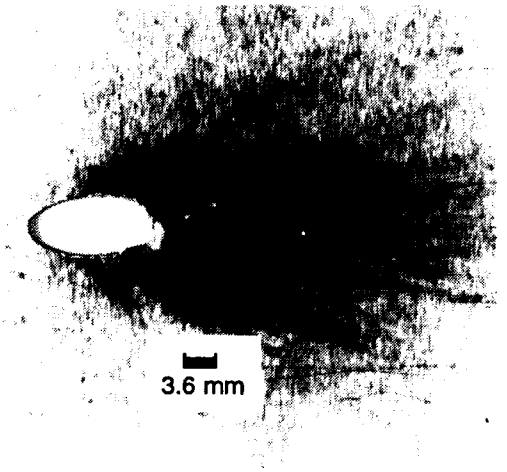


Figure 7 (a). JSC Shot A1488: 3.6 mm Al 2017T4 projectile at 6 km/sec and 65° into 0.51 mm Al 6061T6 plate

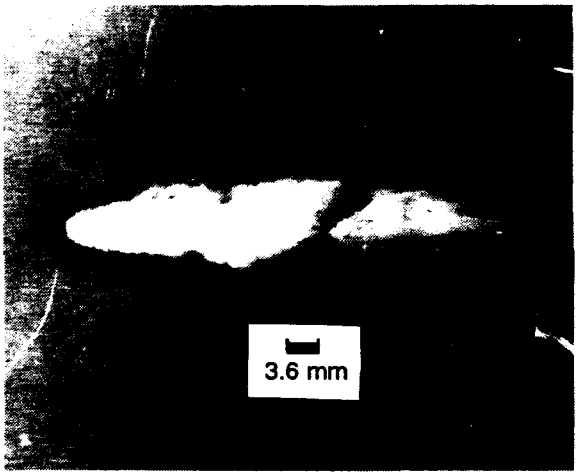


Figure 7 (b). JSC Shot A1485: 3.6 mm Al 2017T4 projectile at 6.2 km/sec and 80° into 0.51 mm Al 6061T6 plate

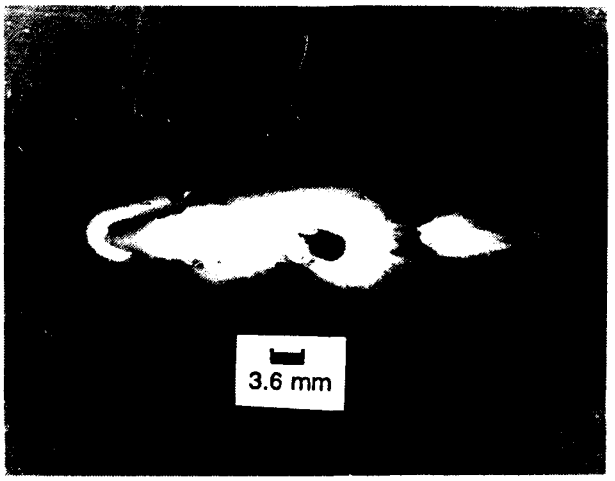


Figure 7 (c). JSC Shot A1486: 3.6 mm Al 2017T4 projectile at 5.5 km/sec and 85° into 0.51 mm Al 6061T6 plate

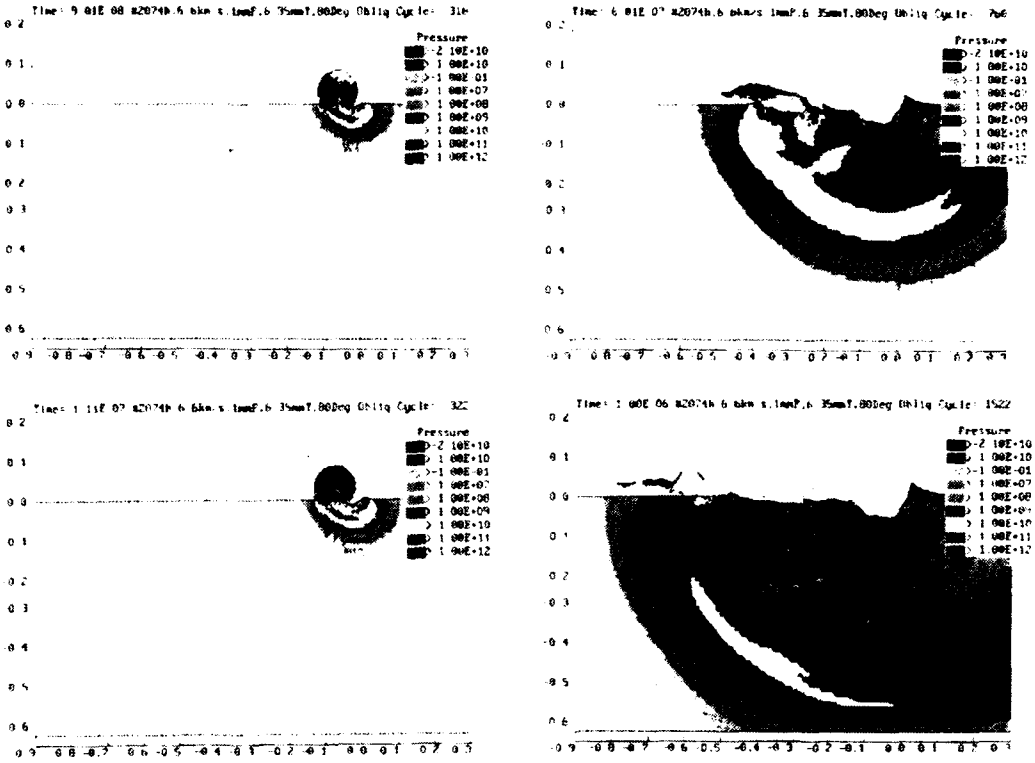


Figure 8. ZeuS Hydrocode Simulation of JSC Shot 2074 (at .09 μs, .11 μs, .6 μs, 1μs after impact)

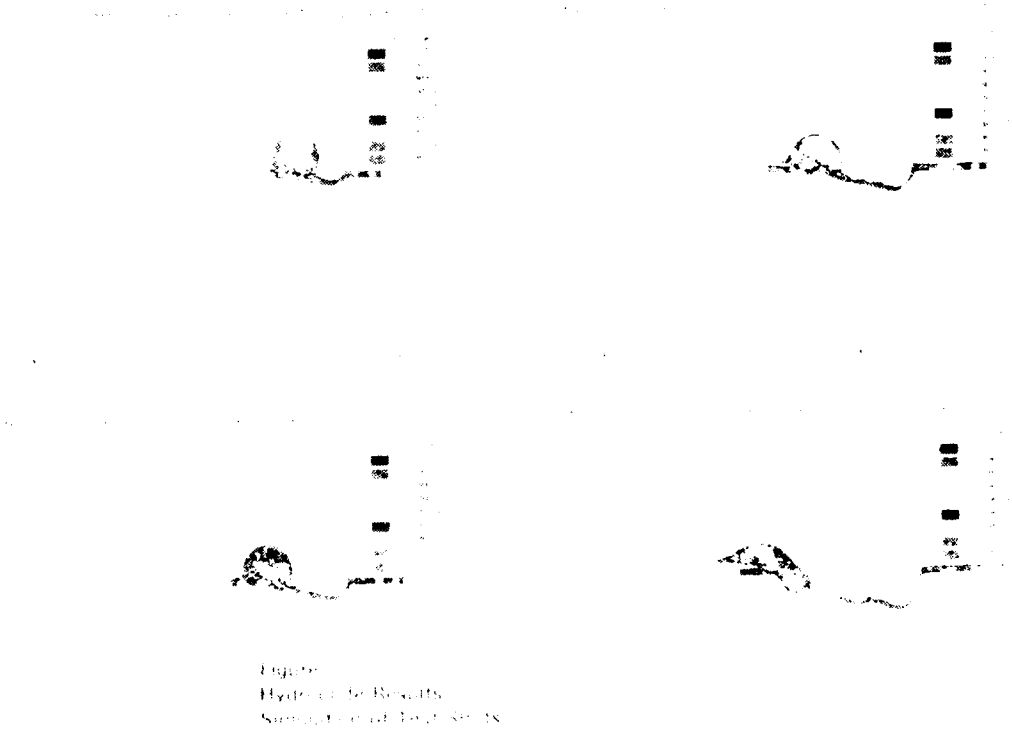


Figure 9. ZeuS Hydrocode Simulation of JSC Shot A1485 (at .6 μs, 1 μs, 1.2 μs, 2 μs after impact)

In the simulation of shot 2074, the compressive wave reaches the back of projectile at about 0.091 μsec after impact. The back of the projectile has unloaded from the initial shock at 0.11 μsec after impact and projectile breakup has begun. This occurs well before the projectile has fully engaged the target and the remnant projectile fragments begin to form a second crater in the target 0.11 μsec after impact. By 0.3 μsec after impact, the remnant projectile is undergoing a second compressive shock from its repeated contact with the target. This second shock is of importance in determining the state of the remnant projectile, as it has many similarities to the multiple shock strategy applied by several new, improved shielding techniques such as the Multi-Shock Shield (Cour-Palais and Crews, 1990). Multiple shocks have been shown experimentally (Cour-Palais and Crews, 1990; Christiansen, 1990) and computationally (Alme et al., 1991) to be more effective at elevating the thermal state of the projectile and to increase the extent of projectile fragmentation. The hydrocode calculations indicate that multiple compression/release cycles of the projectile are possible in highly oblique impacts which contribute to projectile disruption and thermal processing.

In the ZeuS calculation, several secondary craters have developed between 0.4 and 0.7 μsec after impact. Parts of the projectile remain intact and continue to move with a velocity vector parallel to the surface of the target at the conclusion of the calculation at 1 μsec. The calculation matches the test shot in general characteristics. In particular, the simulation illustrates how multiple, rough bottom craters can be generated by the impact of a single projectile into a thick plate target at an oblique impact angle.

Thin Target Impact Simulations (A1485). The perforation length in the CTH simulation of A1485 is 14.4 mm at 5 μsec after impact compared to a final experimental value of 20.1 mm. However, the CTH perforation was still increasing when the simulation was terminated. The peak pressure is 125 kbar 1mm from the impact point, and 86 kbar at the initial contact point.

The results of ZeuS simulation of thin plate test number A1485 impacted at 80° with a 0.36 cm particle are displayed in Figure 9. The plots illustrate the pressure contours in the projectile and target up to 2 μsec after impact. The initial compressive wave reaches the back of the projectile about 0.6 μsec after impact and the projectile begins to fragment. As the remnant projectile contacts the plate again, a second shock wave is initiated in the projectile between 1 and 1.2 μsec after impact. At 2 μsec, the target is perforated and a portion of the projectile still remains intact but it is traveling down-range on the outside of the target. If the thin target was the bumper of a Whipple shield, most of the material in the debris cloud traveling toward the back plate of the shield would be bumper fragments.

The "external" secondary ejecta is composed of a major fraction of the original projectile and includes additional bumper (target) material. The ZeuS simulation was run to show the late time results of the secondary ejecta impacts on a 0.51 mm aluminum witness plate mounted normal to the bumper (target) plate. The witness plate is perforated as observed in the experiment at 22.5 μsec illustrating the damaging effects of secondary ejecta debris.

Criteria for Formation of Multi-Craters in Oblique Impacts

The experimental evidence, supported by numerical calculations, shows that multiple-crater damage can be created by a single, homogenous, regularly shaped (e.g., spherical) projectile impacting at an oblique angle. A criteria is required that can be used to define the impact conditions that lead to the creation of multiple- crater damage sites instead of a single recognizable crater. The criteria offered here is that the creation of a multi-crater will be likely when:

(A) the impact angle is oblique enough to allow time for the initial compressive shock wave to travel across the impacting particle, and:

(B) the rarefaction wave has time to travel back through and unload sufficient projectile material (assumed here when the rarefaction nears the center of the projectile) to cause fragmentation of the upper part of the projectile, before:

(C) the center of the projectile has traveled to the original surface level of the target.

With this criteria, a curve can be constructed for the "critical" impact angle as a function of impact speed based on estimates of shock wave and rarefaction wave speed in various materials of various thicknesses. Such a curve is plotted in Figure 10 that defines the critical impact angle above which oblique impacts

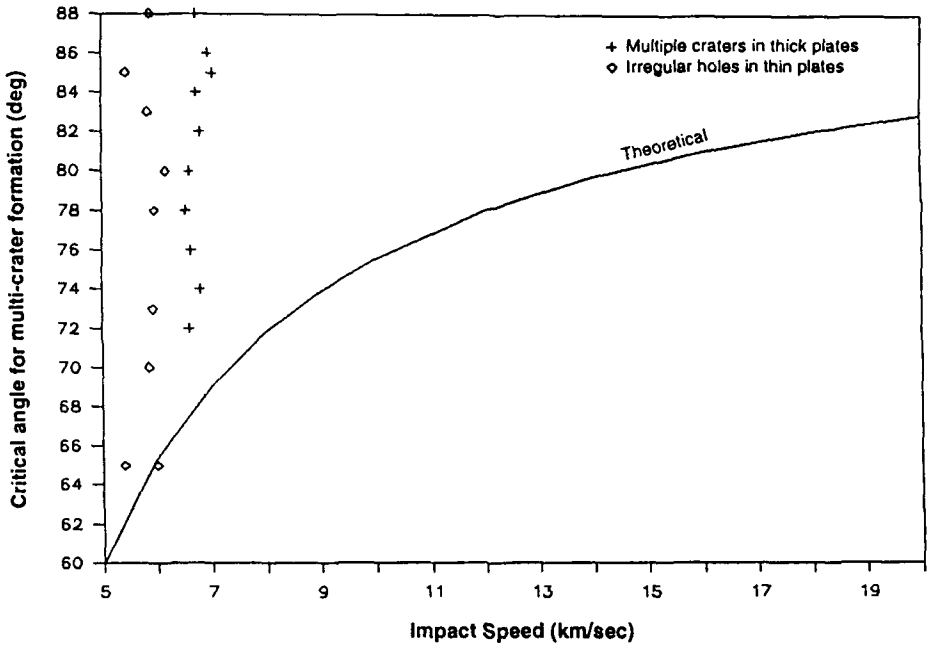


Figure 10. "Critical" impact angle (deg) above which oblique impacts form multiple-crater features (for aluminum into aluminum impacts)

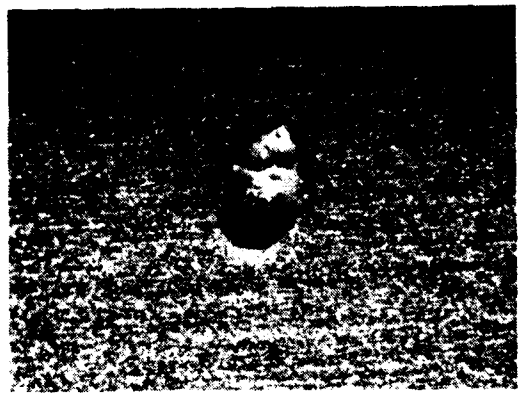


Figure 11. Impact on LDEF aluminum surface (compliments Zolensky, M., 1992; See et al., 1990)

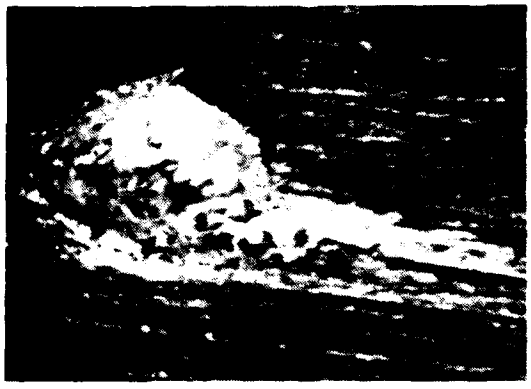


Figure 12. Impact on LDEF aluminum surface (compliments Zolensky, M., 1992; See et al., 1990)

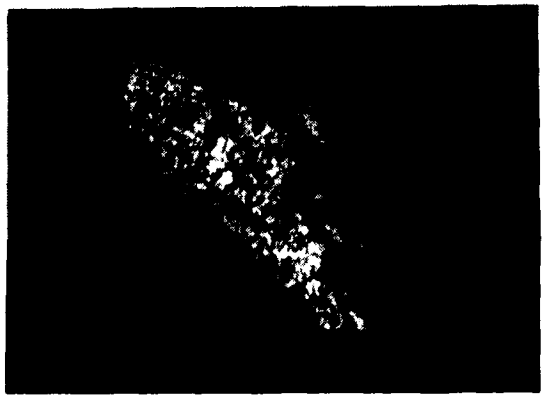


Figure 13. Impact on LDEF experiment-tray flange (aluminum) of an A0178 tray (compliments Zolensky, M., 1992; See et al., 1990)



Figure 14. Messier crater (left) and Messier A (right) showing topography (Gault, 1974)

will produce a multi-crater for aluminum on aluminum impacts. A one-dimensional shock wave analysis was used to construct the curve in Figure 10, although it is recognized to be a rather coarse approximation given the complex geometry of even 2-dimensional problems. The formulas of Gehring (1970b) for shock and release wave speeds were used in the 1-D analysis, in the same manner they had been applied to previous bumper shield analyses (Christiansen, 1987).

Figure 10 shows that as impact speed increases, the impact angle must become more oblique to see any evidence of multi-crater impact damage. Less than 3 km/sec impacts should not be considered because speeds less than 3 km/sec would produce weaker shocks that may be insufficient to fragment the projectile (which is prerequisite for multi-crater formation).

Data from the experimental work has been plotted against the theoretical curve. The HVI data indicates multi-craters form in monolithic targets at impact angles of ~72° and average speed of ~6.8 km/sec. This point falls somewhat above the theoretical critical angle curve, but it is close considering the assumptions in the 1-D analysis. The 3.6 mm impact data with an average speed of ~5.8 km/sec suggests irregular perforations form in thin targets (an indication of "multi-craters" in thick targets) at ~65°. This point falls very nearly on the theoretical curve.

EVIDENCE OF OBLIQUE IMPACT ON EXPOSED SPACE SURFACES

LDEF. The Long Duration Exposure Facility (LDEF) satellite was returned after nearly 6 years in space with a large collection (> 5000) of ≥ 0.5 mm diameter craters and ≥ 0.3 mm diameter perforations on its surface as reported by See et al. (1990). Some of the LDEF craters display unusual morphologies as evidenced by the craters in Figures 11, 12, and 13 which show strong multi-crater characteristics. A possible explanation is an impact, probably at an oblique angle, from a friable and/or multi-grain aggregate of natural (meteoroid) particles (See et al., 1990).

However, this study has indicated another possible alternative: an impact from a homogeneous particle at an oblique impact angle (that lies above the critical impact angle versus velocity curve in Figure 10) which creates a complex multiple-crater morphology. For reference, the LDEF craters in Figures 11, 12, and 13 can be compared with craters created by single, solid spherical projectiles impacting at 74° to 80° (and ~7 km/sec) in Figures 1g, 1h, and 1j.

Lunar Craters. Various lunar craters have been identified by Gault and Wedekind (1978) and Schultz and Gault (1992) as likely oblique impact candidates including the craters Messier and Messier A (Figure 14). Comparing the Messier craters to the double-crater impacts in Figures 1k and 1l, supports the view that a single impact at a very oblique angle created both craters; either by a particularly slow meteoroid (7-10 km/sec) impacting at 80°-85°, or a faster (20 km/sec) impactor at >87°.

CONCLUSIONS

A hypervelocity impact test and analysis study conducted by the JSC Hypervelocity Impact Test Facility (HIT-F) has demonstrated that multiple craters can be produced by a single, solid, spherical projectile impacting at an oblique angle (typically greater than 65° at 6 km/sec). A criteria was developed and applied to predict, for any impact speed, the critical impact angle causing impact damage with a multiple crater morphology. This information was used to suggest possible alternative sources of peculiar multi-crater features found on the Long Duration Exposure Facility, and provides an explanation for the "critical angle" observations obtained from thin plate penetration experiments (Schonberg, 1989).

ACKNOWLEDGEMENTS

The authors wish to express their gratitude to the Hypervelocity Impact Research Laboratory (HIRL) Manager, Jeanne Lee Crews, and to the personnel of the HIT-F for their support of this work, including Lu Borrego, Earl Brownfield, Joe Falcon, and Jay Laughman.

REFERENCES

Christiansen, E.L. (1987). Evaluation of Space Station Meteoroid/Debris Shielding Materials. Eagle Engineering Report No. 87-163.

Christiansen, E.L. (1990). Advanced Meteoroid and Debris Shielding Concepts. AIAA Paper No. 90-1336. Presented at AIAA/NASA/DOD Orbital Debris Conference, Baltimore, MD, April 16-19, 1990.

Christiansen, E.L. (1992a). Performance Equations for Advanced Orbital Debris Shields. AIAA Paper No. 92-1462.

Christiansen, E.L. (1992b). Oblique Impact Data. NASA Internal Memorandum SN3-92-177, June 30, 1992.

Crews, J.L. and Christiansen, E.L. (1992). The NASA JSC Hypervelocity Impact Test Facility (HIT-F). AIAA Paper No. 92-1640. Presented at the AIAA Space Programs and Technologies Conference, Huntsville, AL, March 24-27, 1992.

Cour-Palais, B.G. (1987). Hypervelocity impact in metals, glass and composites. *Int. J. Impact Engng.*, Vol.5, No.1-4, pp.221-237.

Gault, D.E. (1974). Impact Cratering. In: *A Primer in Lunar Geology*, NASA publication, pp.137-175.

Gault, D.E. and Wedekind, J.A. (1978). Experimental studies of oblique impact. Proc. Lunar Planet. Sci. Conf. 9th, pp. 3843-3875.

Gehring, J.W. (1970). Engineering Considerations in Hypervelocity Impact. In: *High-Velocity Impact Phenomena* (Kinslow, ed.), Academic Press.

Gehring, J.W. (1970b). Theory of Impact on Thin Targets and Shields and Correlation with Experiment. In: High-Velocity Impact Phenomena (Kinslow, ed.), Academic Press.

Eichelberger, R.L. and Gehring, J.W. (1962). Effects of Meteoroid Impacts on Space Vehicles. *ARS Journal*, pp.1583-1591, October, 1962.

McGlaun J.M, Thompson, S.L., Kmetyk, L.N. and Elrick, M.G. (1990). A Brief Description of the Three-Dimensional Shock Wave Physics Code CTH. SNL report SAND99-0607.

Schonberg, W.P. (1989). Penetration and Ricochet Phenomena in Oblique Hypervelocity Impact. *AIAA Journal*, Vol.27, No.5, May 1989.

Schultz, P.H. and Beatty, J.K. (1992). Teardrops on the Pampas. *Sky & Telescope*, April, 1992.

Schultz, P.H. and Gault, D.E. (1987). Oblique Impact: Projectile Richochet, Concomitant Ejecta and Momentum Transfer. Proc. Lunar Planet. Sci. Conf.

Schultz, P.H. and Gault, D.E. (1990). Global Catastrophes in Earth History: Interdisciplinary Conf. Impacts, Volcanism and Mass Mortality, In *Geol. Soc. Amer. Special Paper 247*, pp.239-261.

Schultz, P.H. and Lianza, R.E. (1992). Recent grazing impacts on the Earth recorded in the Rio Cuarto crater field, Argentina. *Nature*, Vol. 355, pp. 234-237, January 16, 1992.

See, T., Allbrooks, M., Atkinson, D., Simon, C., Zolensky, M. (1990). Meteoroid and Debris Impact Features Documented on the Long Duration Exposure Facility: A Preliminary Report. NASA JSC #24608, August 1990.

Zukas, J.A. (1990). Survey of Computer Codes for Impact Simulation. In: *High Velocity Impact Dynamics* (Zukas, ed), John Wiley & Sons.

Int. J. Impact Engng Vol. 14, pp. 169–180, 1993
Printed in Great Britain

0734-743X/93 $6.00 + 0.00
Pergamon Press Ltd

MESH DOUBLE-BUMPER SHIELD: A LOW-WEIGHT ALTERNATIVE FOR SPACECRAFT METEOROID AND ORBITAL DEBRIS PROTECTION

ERIC L. CHRISTIANSEN AND JUSTIN H. KERR

NASA Johnson Space Center, Mail Code SN3, Houston, Texas 77058

ABSTRACT

A number of new, innovative, low-weight shielding concepts have resulted from a decade of research at the NASA Johnson Space Center (JSC) Hypervelocity Impact Test Facility (HIT-F). One such concept, the mesh double-bumper (MDB) shield is a highly efficient method to provide protection from meteoroid and orbital debris impacts. Hypervelocity impact (HVI) testing of the MDB shield at the HIT-F and other facilities have demonstrated weight savings of approximately 30% to 50% at light gas gun velocities compared with conventional dual-sheet aluminum Whipple shields at normal impact angles. Even larger weight savings, approximately 70%, have been achieved at 45 degree oblique angles. The MDB shield was developed to demonstrate that a Whipple shield could be "augmented" or modified to substantially improve protection by adding a mesh a short distance in front of the Whipple bumper and inserting a layer of high strength fabric between the second bumper and rear wall. From the test results, formulas have been developed that allow the design engineer to size MDB shield elements for spacecraft applications.

GLOSSARY OF SYMBOLS USED

C	equation coefficient
d	diameter (cm)
d_c	projectile diameter causing failure (cm)
ρ	density (g/cc)
m	areal density (g/cm^2)
S	overall spacing between outer bumper and rear wall (cm)
σ	rear wall allowable yield stress (ksi)
t	thickness (cm)
θ	impact angle measured from surface normal (deg)
V	projectile velocity (km/sec)
V_n	normal component of projectile velocity (km/sec) = V cos θ

Subscripts:

b	bumpers [first & second bumper in mesh double-bumper shield]
I	intermediate fabric layer in MDB shield
p	projectile
w	rear wall

INTRODUCTION

NASA and other agencies have historically constructed spacecraft with requirements for protection from meteoroid impact (NASA SP-8042, 1970). A relatively recent design consideration has been the growth

of the orbital debris environment in low Earth orbit which now exceeds the natural meteoroid environment for the important size regime of particle diameters greater than ~1 mm (NASA, 1991). Due to weight constraints on spacecraft designers, there is a need for higher performance shielding concepts that provide greater protection for less weight than the conventional two-sheet aluminum Whipple shield.

This paper describes work in progress on characterizing the impact protection performance of an innovative new shield concept: the Mesh Double-Bumper (MDB) shield. The MDB shield is one of several advanced shielding concepts that have resulted from research at the NASA JSC Hypervelocity Impact Test Facility (HIT-F). Weight reductions of 30% to 70% for equivalent hypervelocity impact protection are achieved by the MDB compared to conventional dual-sheet Whipple shields. Hypervelocity impact (HVI) tests, supported by numerical and analytical calculations, have been instrumental in developing the optimum MDB shield configuration. Distinguishing features of the MDB are the combination wire mesh and continuous sheet double-bumper, and a high-strength fabric layer that reduces particulate impacts and impulsive loading on the rear wall.

The MDB shield technology indicates that the protection performance of a Whipple shield can be significantly enhanced by adding a mesh a short distance in front of the standard Whipple bumper and by incorporating a fabric layer (of Kevlar®, Spectra®, Nextel® or other fabric) in front of the rear wall. The mesh bumper provides additional benefits as well, such as reduction of damaging secondary ejecta debris (Crews and Christiansen, 1992).

THE MESH DOUBLE-BUMPER SHIELD

The mesh double-bumper (MDB) shield consists of a spaced array of four distinct layers as shown in Figure 1: (1) wire mesh first bumper, (2) continuous second bumper, (3) high-strength fabric intermediate layer, and (4) a back plate or rear wall. Each has a different function as discussed below.

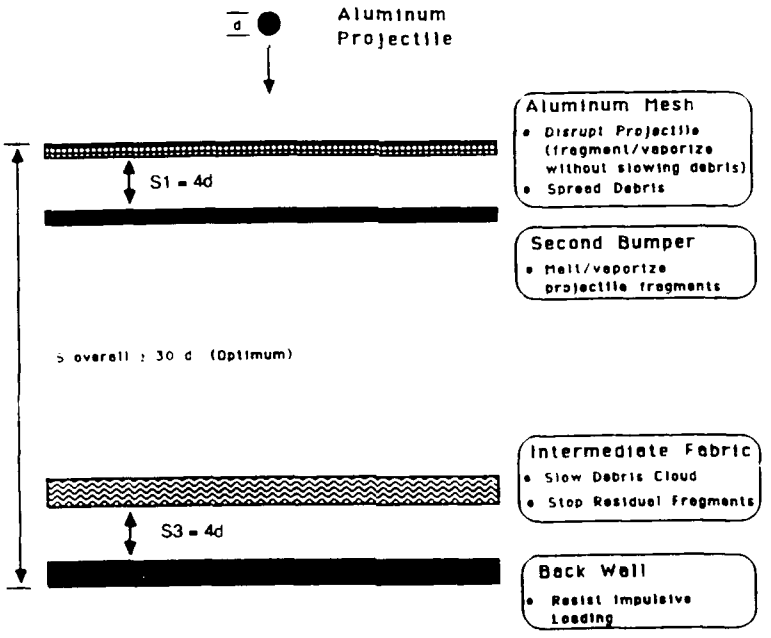


Figure 1. Mesh Double-Bumper Shield (Christiansen, 1990)

Wire Mesh

The wire mesh bumper provides a weight efficient method of breaking up the projectile into smaller fragments which are subsequently shocked by the second bumper. The mesh is composed of overlapping wires in a square pattern. Where the wires overlap, the mesh thickness to projectile diameter ratio is double the wire to projectile diameter ratio. This effectively creates localized mesh areas with greater bumper thickness. These thick areas contribute to the disruptive forces exerted on the projectile by increasing the shock duration in the projectile during the impact event. By removing

"excess" bumper material, the mesh bumper is as capable of disrupting a projectile as a heavier continuous bumper.

Based on evidence from high-speed framing camera photography provided in impact tests at the JSC HIT-F, the mesh does not substantially reduce the speed of fragments resulting from the initial impact. Because the velocity of the fragments remains high after the incident particle breaks up on the mesh, the second bumper is more effective in shocking the remaining fragments to a high stress level that will, upon unloading, cause the remnant projectile fragments to release into liquid, vapor or finer solid particles that are less penetrating to the back sheet of the shield.

Less damaging secondary ejecta (external debris) is produced by the MDB shield, with its relatively thin outer mesh bumper, compared to an equivalent performance Whipple shield. Tests have demonstrated that secondary ejecta from mesh bumpers consist of fine, mist-like particles that do not significantly damage witness plates (Christiansen, 1987).

Another observation from the impact tests is that the fragmentation of the projectile on a wire mesh is more dispersive than an impact into the same areal density continuous bumper (Christiansen, 1987, 1990). The debris cloud exiting from a wire mesh bumper spreads laterally to a greater extent than from the same weight per unit area continuous bumper. A recent research study (Horz et al., 1992) substantiates this conclusion. The resulting greater spread in the debris cloud reduces performance degradation at smaller bumper standoffs. This translates into greater weight savings for the MDB shield as overall shield standoff distance is reduced, compared to an equivalent performance Whipple shield.

Second Bumper

The purpose of the second bumper is to produce a second shock in the projectile fragments produced from impact with the initial mesh bumper. The impacting fragments become further pulverized after unloading from the shock on the second bumper, and their thermal state increases which can melt or vaporize them. The second bumper is a continuous sheet that is sized to completely shock the largest particle in the debris cloud from the projectile impact on the mesh. A continuous bumper insures that any small particles passing unhindered through the first mesh are disrupted well before contacting the intermediate layer and rear wall.

Intermediate Fabric Layer and Back Plate

The intermediate fabric layer is used to increase shielding performance by stopping or slowing any remaining solid fragments before they contact the back plate. In addition, the fabric layer slows the expansion of the debris cloud by absorbing energy through stretching and breaking of the fabric fibers, thereby decreasing the momentum loading on the back plate. The purpose of the back plate (or "rear wall") is to resist penetration of any solid fragments and react the impulsive loading from the debris cloud.

EXPERIMENTAL DESIGN AND RESULTS

The concept of using a mesh as a bumper material for shielding has been investigated since the early 1980's by personnel at the NASA JSC Hypervelocity Impact Test Facility (HIT-F). Numerous tests were performed on wire mesh bumper systems before the MDB shield design was perfected (Christiansen, 1987; Crews and Christiansen, 1992). The MDB shield has performance characteristics comparable to the Multi-Shock (MS) Shield described by Cour-Palais and Crews (1990).

Testing of the MDB concept occurred in several distinct phases: (1) research testing to select and optimize the materials, spacings, and weight distribution between the different shield layers, (2) scaling studies to assess thicknesses of the various shield elements as a function of projectile impact conditions (size, velocity, etc.), and (3) development testing to derive equations for predicting overall MDB shield performance as a function of impact velocity, impact angle, and projectile density.

MDB Optimization and Scaling Studies

Results of the MDB optimization studies using 0.32 cm diameter aluminum projectiles have been reported by Christiansen (1987, 1990). This work has been extended to scaling up the MDB shield concept to 0.64 cm, 0.79 cm, and 0.95 cm diameter aluminum projectiles. Scaling equations were developed (reported later in this paper) and verified in the scale-up studies.

Spacing between first and second bumper is a key variable that was evaluated in the impact testing. It is desirable to keep the first and second intra-bumper spacing as small as possible to allow the greatest expansion in the debris cloud that exits the second bumper before impact with the back plate. However, spacing is required between bumpers to allow sufficient material contact with the second bumper to fully shock the debris fragments. The minimum weight MDB configuration was found when first to second bumper spacing was 3 to 4 times the projectile diameter (Christiansen, 1990, 1992).

Hydrocode calculations show residual stresses cause further flattening of the projectile fragments as they travel from first bumper to second bumper (Alme, 1991). The change in aspect ratio of the fragments (to thinner, more disk like shapes) is an advantage upon impact with the second bumper, allowing a thinner second bumper to fully shock the fragments.

The optimization studies investigated the required mesh areal density and mesh geometry parameters. Figure 2 shows some of the aluminum mesh types used in the study. The mesh is composed of overlapping wires in a square pattern with a wire diameter to projectile diameter ratio of from 0.07 to 0.10. Generally, from 4 to 6 wires are "cut" by the diameter of the projectile. Open area of the meshes varies from 20% to 40%. Since a fine mesh is used, small projectiles passing unhindered through the mesh are easily defeated by remaining shield elements.

Aluminum meshes have been extensively tested since they are effective against orbital debris which until 1991 has been defined as having the density of aluminum (NASA, 1991). However, some tests have been performed with steel projectiles on steel meshes and fabrics. Tests with higher density projectiles were conducted since they may be included in future debris environment definitions. It has been found that a higher density mesh bumper is more effective against higher density impacting projectiles.

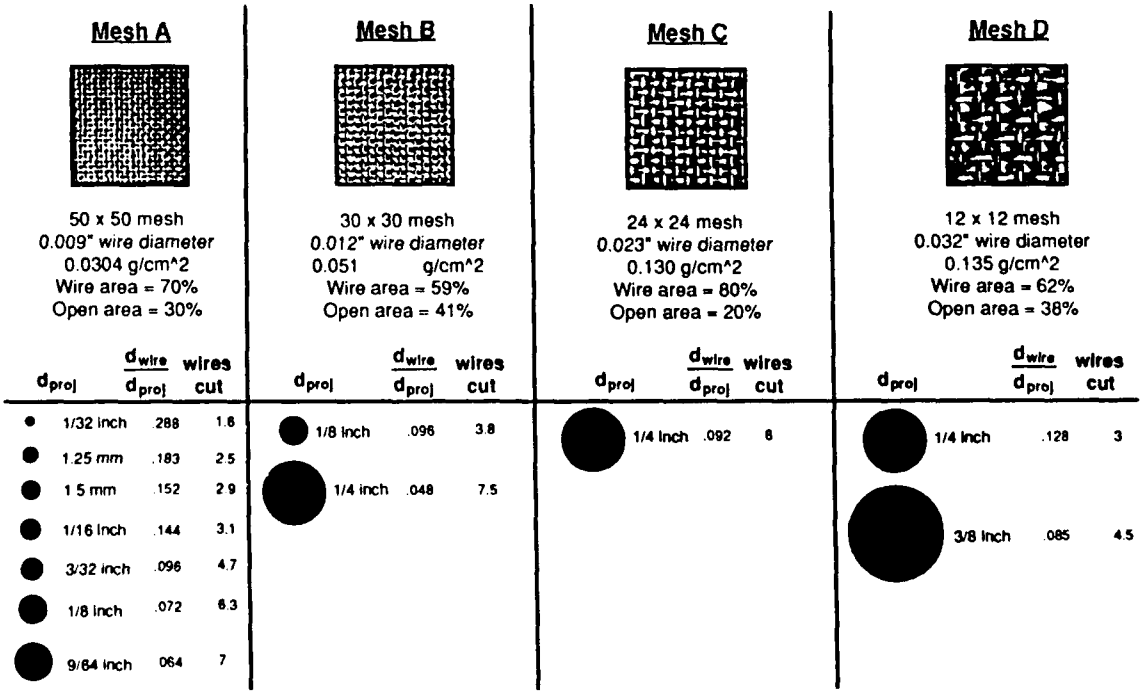


Figure 2. Aluminum Mesh Types Evaluated in HVI Tests

Different materials for the second bumper were evaluated analytically and experimentally (Christiansen, 1990), including various aluminum alloys, graphite-epoxy, and Nextel® ceramic fabric. Although graphite-epoxy and Nextel® performed as well or better than aluminum, aluminum (6061 alloy) was used for the second bumper in the later development testing because the emphasis was on methods to upgrade the protection of typical Whipple shield designs. A series of flash X-ray photographs in Figure 3 from the University of Dayton Research Institute (UDRI) shows a 0.95 cm aluminum impact at 6.8 km/sec on the first two sheets of a mesh double-bumper. After impact with the mesh, the remnant projectile is fractured and flattened. Also of note are precursor "jets" of very fine material that correlate with the gaps between the mesh wires. The projectile fragments are totally broken up into a cloud of very fine particles after impacting the second continuous bumper sheet.

Location of the intermediate fabric layer is a significant parameter influencing the effectiveness of the MDB shield. The optimum fabric layer location is dictated by mounting as far from the bumpers as possible to attain the maximum debris cloud expansion while allowing sufficient clear space to insure the cloth fibers stretch and tear to slow the debris cloud velocity before contacting the rear wall. Testing showed greater impulsive loading damage occurred to the back plate if the fabric layer was mounted directly to the back plate surface (Christiansen, 1990). It was found that the optimum location for the cloth layer was at a short distance, approximately 3 to 4 times the projectile diameter, from the back plate.

A number of different types of fabric materials were considered for the intermediate cloth layer. Impact tests were used to evaluate Kevlar® and Spectra® intermediate layers, primarily because they have high strength to weight ratios giving them excellent ability to absorb energy. Kevlar® is a DuPont product made from aramid fibers while Spectra® is a high modulus polyethylene fabric produced by Allied Signal. Nextel® 312 (made by 3M) ceramic cloth was also tested because it has good high-temperature strength characteristics. Spectra® 900 and Kevlar® 29 fabrics performed somewhat better than Nextel® 312 cloth, although all fabrics increased shielding performance over not having a fabric layer and adding the equivalent mass of the fabric to the back plate.

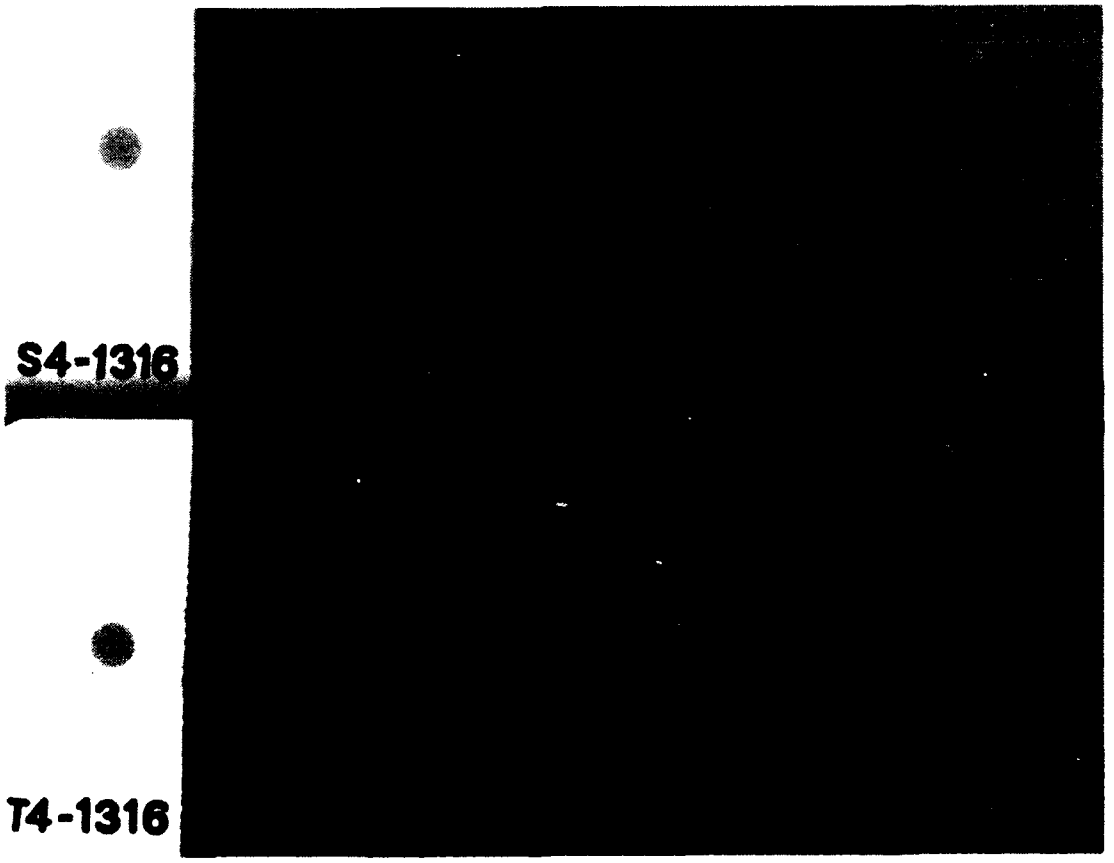
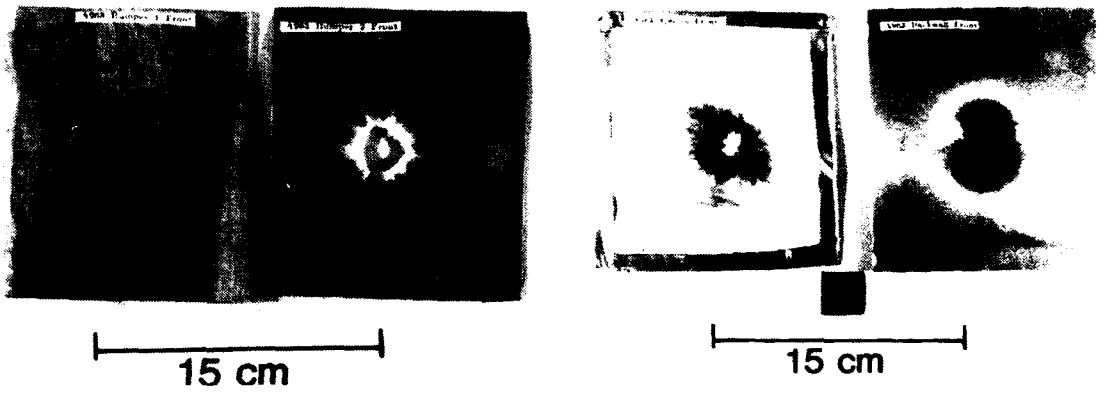


Figure 3. UDRI flash X-ray series of 1 cm, 6.8 km/sec aluminum impact on a mesh double-bumper shield (Mesh Type D)

Alternative back plate materials and configurations, such as laminates, honeycomb, composites and fabrics, have been tested and could potentially provide more protection for less weight than aluminum alloys.

Figure 4 shows typical results of a hypervelocity impact test (JSC Shot No. A963) on an aluminum mesh double-bumper system using a type B mesh (see Figure 2). The projectile was a 3.2 mm aluminum sphere impacting at 6.35 km/sec normal to the shield. This particular test was evaluating small standoffs, with a 5 cm total spacing used in this test (S/d = 16). Spectra® 900 cloth (2 layers of Style 618 fabric) was used in the intermediate layer (0.056 g/cm^2). No perforations or detached spall occurred to the 0.08 cm Al 2024-T3 back plate, which was permanently deformed and bulged by a purely impulsive load. No cratering from solid fragments was evident on the back plate. The total areal density of this MDB shield is 0.41 g/cm^2. This weight is ~60% less than an aluminum Whipple shield providing equivalent protection (no penetration or spall) with the same standoff (1.1 g/cm^2). For this threat case (0.32 cm aluminum with S/d=16), the MDB shield shows a slight improvement over the 0.525 g/cm^2 Nextel® MS shield with a 5 cm total spacing reported by Cour-Palais and Crews (1990). Impact testing at the JSC HIT-F has shown that a double bumper system with a mesh outer bumper exhibits superior performance over the same weight double bumper consisting of two continuous aluminum sheets (Christiansen, 1990).



a) Double-Bumper Front

b) Intermediate Layer and Wall Front

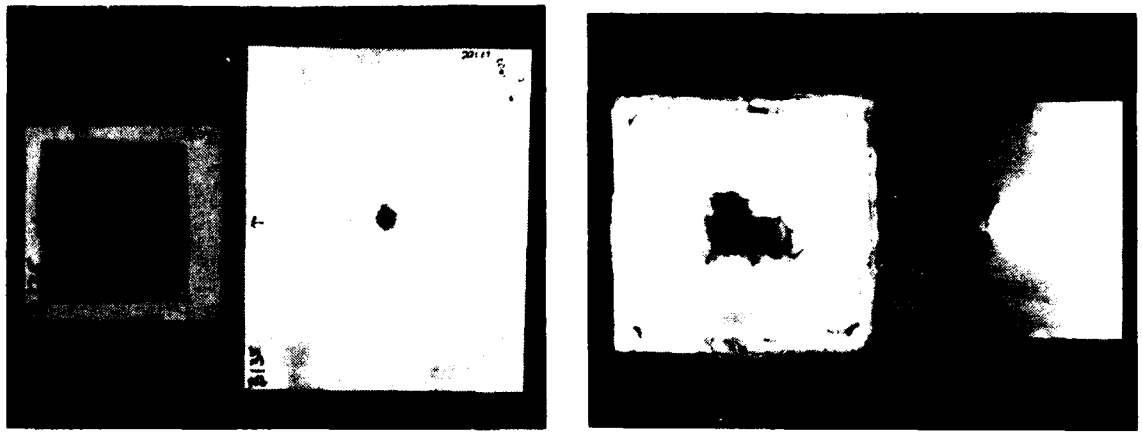
Projectile: 0.32 cm Al 2017T4, 6.35 km/sec, 0°
Target: Mesh Type B first bumper (0.03 cm wire diameter), 0.03 cm Al 6061 second bumper, 0.056 g/cm^2 Spectra® 900 Layer (2 Style 618 fabric), 0.08 cm Al 2024T3 rear wall, 5.08 cm overall spacing

Figure 4. JSC HIT-F Shot No. A963: Performance of MDB Shield with 5 cm overall spacing against 0.32 cm Al projectile.

Figure 5 demonstrates a scaled-up mesh double-bumper that was tested with a 7.9 mm diameter aluminum (2017T4) projectile at 7.43 km/sec (JSC Shot No. B135). For this test, a type A mesh was used (Figure 2) for the first bumper and five sheets of Kevlar® 29 fabric (style 710) with an areal density of 0.16 g/cm^2 was used for the intermediate layer. The Kevlar® was securely mounted to a rigid frame located 3.8 cm in front of the back plate. Overall spacing from first bumper to back plate was 25.4 cm. Total shield areal density for this MDB configuration was 0.766 g/cm^2. In comparison, a Whipple shield with 25.4 cm spacing would weigh 1.3 g/cm^2 to provide similar protection (Christiansen, 1992).

Development Testing

Development testing concentrated on specific MDB configurations to derive MDB shield sizing formulas and performance assessment equations suitable for spacecraft shield design application. In particular, MDB shield performance as a function of projectile size, impact velocity, density, and impact angle was assessed. The basis of the testing was a MDB configuration with an aluminum mesh bumper, Al 6061 second bumper, Kevlar® 49 and Spectra® fabric intermediate layers, and aluminum alloy rear wall.



Mesh Bumper and Second Bumper (front) Kevlar Intermediate Layer and Back Plate (back)

Projectile: 0.79 cm Al 2024T3, 7.43 km/sec, 0°
Target: Mesh Type A first bumper (0.023 cm wire diameter), 0.08 cm Al 6061T6 second bumper, 0.16 g/cm^2 Kevlar® 29 Layer (5 Style 710 fabric), 0.127 cm Al 2024T3 rear wall, 25.4 cm overall spacing

Figure 5. JSC HIT-F Shot No. B135: Performance of MDB Shield with 25 cm overall spacing against 0.79 cm Al projectile.

Over 100 tests on shields utilizing wire mesh bumpers have been performed. Table 1 lists selected hypervelocity impact data on MDB shields from the research and development testing. The criteria for shielding success in these tests was no perforation or detached spall from the rear wall of the shield protection system. Damage to the rear wall of the MDB was classified with the damage classification system promulgated by Dahl and Cour-Palais (1991) as given by the "Damage Class" column in Table 1. Development tests were performed primarily at the JSC HIT-F using spherical projectiles up to ~8 km/sec, although other facilities were utilized to supplement the required test data (University of Dayton Research Institute and Sandia National Laboratory). Although the test velocities represent only ~25% of the debris threat, the HVI data includes the more damaging low velocity impacts for these particular shields (typically 2-3 km/sec) and therefore represents a higher percentage of the penetrating flux (Christiansen et al., 1992).

ANALYSIS AND DISCUSSION

The equations in this paper are presented in two parts: (1) sizing equations to determine preliminary estimates of shielding thicknesses and weights, and (2) ballistic limit equations that define the impact conditions causing shield failure (perforation or detached spall).

Shield Sizing Equations

The following equations have been modified slightly from those given previously (Christiansen, 1990). These equations have been developed for preliminary shield sizing purposes using a "design" particle method (Christiansen, 1992). A "design" particle (size, average impact velocity and angle) can be determined for each surface of a shielded element from probability of no-failure requirements, meteoroid/debris environment models, surface area, and orientation considerations. The bumper and rear wall thicknesses for each surface can then be calculated from equations (1) through (5). This simplified method is useful for deriving estimates of shielding weights and for performing trade studies. A more detailed approach is used for verifying design adequacy by extending the analysis to include the full distribution of meteoroid and orbital debris impact velocities and angles.

The mesh areal density is given by:

$$m_1 = c_m d \rho_p \qquad (1)$$

Table 1: MDB Hypervelocity Impact Test Data

JSC Shot No.	Projectile Diameter (cm)	Vel. (km/sec)	Impact Angle (deg)	Intermediate Layer Material (# of sheets)	Back-Wall Mat'l	Wall Thick (cm)	Overall Spacing (cm)	Total Ar. Density (g/cm^2)	Damage Class	Wall Damage (P=Perforation, S=Detached Spall)
					Type A Aluminum 5051 Mesh					
A1276	0.318	6.20	0	Kevlar 095(2)	Al2024T3	0.041	10.16	0.283	F3	No P or S, bulge
A1285	0.318	6.42	0	Kevlar 095(2)	A12024T3	0.030	10.16	0.254	F3	No P or S, bulge
A1289	0.318	6.24	0	Spectra 618(2)	A12024T3	0.030	10.16	0.254	F3	No P or S, bulge
A1351	0.239	4.46	45	Kevlar 710(2)	A12024T3	0.051	10.16	0.319	C4	4 Ps, 1.5xlmm max
A1364	0.357	6.00	75	Kevlar 710(2)	A12024T3	0.051	5.08	0.319	C1	No P or S, sm.dmpls
1414	0.079	3.50	0	Spectra 618 (2)	A12024T3	0.030	10.16	0.275	C0	No P or S, No damage
1651	0.149	2.63	0	Kevlar 710(2)	A!2024T3	0.051	10.16	0.319	C4	1 P,0.8mm
1652	0.160	3.44	45	Kevlar 710(2)	A12024T3	0.051	10.16	0.319	C2	No P or S, dmpls
1654	0.160	3.41	60	Kevlar 710(2)	A12024T3	0.051	10.16	0.319	C1	No P or S, no dmpls
1660	0.160	4.81	45	Kevlar 710(2)	A12024T3	0.051	10.16	0.319	C2	No P or S, dmpls
1661	0.160	5.74	60	Kevlar 710(2)	A12024T3	0.051	10.16	0.319	C0	No P or S, No damage
					Type B Aluminum 5051 Mesh					
A954	0.318	6.39	0	Spectra 618 (2)	A12024T3	0.079	5.08	0.439	F3	No P or S, some dimples
A963	0.320	6.35	0	Spectra 618 (2)	A12024T3	0.079	5.08	0.412	F3	No P or S, bulge
A971	0.317	6.62	0	Spectra 618 (2)	A13003H12	0.064	10.16	0.364	F3	No P or S, bulge
A978	0.318	6.58	0	Spectra 618 (2)	A16061-0	0.064	10.16	0.362	F3	No P or S, bulge
A1061	0.318	6.11	45	Spectra 618 (2)	A12024T3	0.079	10.16	0.412	C2	No P or S, dmpls
A1068	0.318	5.87	60	Spectra 618 (2)	A13003H12	0.064	10.16	0.364	C4	1 P, 1.3mm
A1069	0.318	6.08	45	Spectra 618 (2)	A13003H12	0.064	10.16	0.364	C2	No P or S, dmpls
A1111	0.318	6.02	60	Spectra 618 (3)	A12024T3	0.064	10.16	0.395	C2	No P or S, dmpls
A1275	0.318	5.90	0	Spectra 618 (2)	A12024T3	0.041	10.16	0.309	F3	No P or S, bulge
B201	0.635	7.46	0	Kevlar 710 (4)	A12024T3	0.102	20.30	0.635	F3	No P or S, bulge
					Type C Aluminum 5051 Mesh					
B27	0.635	6.69	0	Spectra 618(4)	A12024T3	0.079	20.32	0.638	F3	No P or S, bulge
B77	0.635	7.53	0	Kevlar 710(4)	A12024T3	0.180	10.16	0.935	F3	No P or S, bulge
B204	0.635	7.50	0	Kevlar 710 (4)	A12024T3	0.102	20.30	0.714	F3	No P or S, bulge
					Type D Aluminum 5051 Mesh					
B203	0.635	7.25	0	Kevlar 710 (4)	Al2024T3	0.102	20.30	0.719	F3	No P or S,bulge
4-1172(UDRI)	0.053	6.65	0	Kevlar 903 (7)	A12024T3	0.180	30.48	1.084	F3	No P or S, s. bulge

Where c_m can range from 0.035 to 0.057 without changing the accuracy of the following equations. The mesh has wires in a square pattern with a wire diameter to projectile diameter ratio of from 0.07 to 0.10. The first to second bumper spacing is four times the projectile diameter: $S_1 = 4\ d$.

The second bumper is a continuous aluminum sheet that is sized by the following equation:

$$m_2 = 0.093\ d\ \rho_p \tag{2}$$

A high strength fabric intermediate layer (Spectra®, Kevlar®, Nextel®, etc.) is mounted a distance of $S_3 = 4\ d$ in front of the rear wall. For Spectra® or Kevlar®, the sizing equation is:

$$m_I = 0.064\ d\ \rho_p \tag{3}$$

If Nextel® is used, the sizing equation is:

$$m_I = 0.095\ d\ \rho_p \tag{4}$$

The rear wall sizing equation is:

$$m_W = 9\ M\ V_n/S^{3/2}\ (40/\sigma)^{0.5} \tag{5}$$

These equations can be applied for a component velocity ($V \times \cos^{1/3}\theta$) of greater than 6.4 km/sec and S/d ratios of more than 15. The wall areal density calculated by (5) is based on the ballistic limit criterion of preventing perforation and detached spall.

The equations are valid for all impact angles. Bumper materials are ejected normal to the bumper in oblique impacts. Bumper particles from oblique impacts on a wire mesh consist of fine mist-like particles that are stopped by the second bumper. Bumper particles from the second bumper are stopped or slowed considerably by the intermediate fabric layer protecting the rear wall. On the other hand, bumper fragments from a Whipple shield are far more damaging to the rear wall for two reasons: (1) an oblique impact on the bumper of the Whipple shield produces bumper fragments that are larger and more penetrating than from the thinner MDB bumpers and (2) these bumper particles can impinge directly on the rear wall of the Whipple shield.

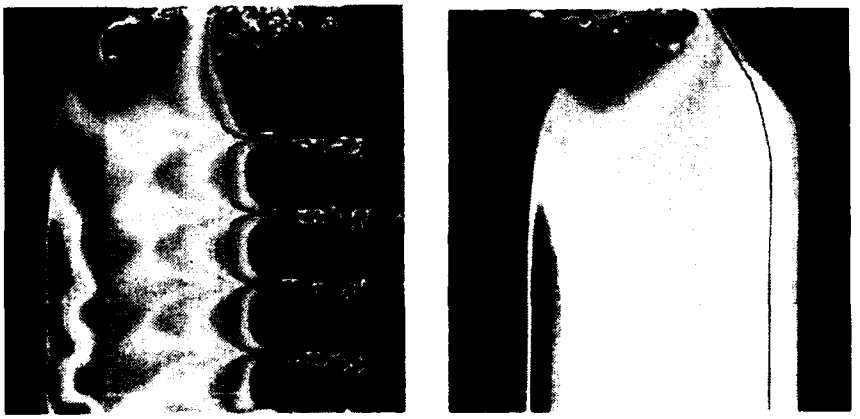


Figure 6. CALE Simulation of impact on discontinuous grid (left) and continuous bumper (right) (Alme, 1991). Impact occurs left to right. Projectile and target boundaries are outlined. Specific energy distribution at 0.4 μs. Scale varies linearly from zero to 0.03 Mb-cc/g on left and to 0.025 Mb-cc/g on right.

For applications to velocities beyond test capabilities, these formulations build on equations originally developed in the 1960's and 1970's for predicting optimum Whipple shield performance against 11-72 km/sec meteoroid threats (Cour-Palais, 1969; Cour-Palais and Crews, 1990). JSC HIT-F applies additional analysis techniques such as hydrodynamic computer codes to evaluate the velocity scaling relations. For example, Figure 6 shows a hydrocode simulation of an impact into equal areal density

continuous and discontinuous bumpers. This impact sequence was performed with the CALE hydrocode (Alme, 1991). The discontinuous bumper represents a 50% filled wire grid (a linear pattern of square cross-section wires), with a wire thickness to projectile diameter ratio of 0.08. The pressure contours after 0.35 μsec shows that localized areas of the projectile impacting the grid bumper have been shocked to somewhat higher pressures than the continuous bumper because the duration and extent of the shock wave has been changed by mesh geometry. The code also predicts that areas of the projectile that impacts the grid have a 20% higher thermal energy content than with the impact on the continuous bumper (Figure 6). The simulation shows "jets" of molten material form in the gaps of the grid. The hydrocode evaluations of the MDB are still in progress.

Ballistic Limit Equations

The following ballistic limit equations define MDB shield performance for a configuration using either Kevlar® or Spectra® cloth as an intermediate layer, and aluminum mesh and continuous bumpers and rear wall. The equations are in a form that relates critical particle diameter with impact velocity, impact angle, particle density, and target parameters. Impacts larger than the critical particle size cause shield failure (i.e., perforation or detached spall of the rear wall of the hybrid shield), while those smaller do not. The equations are consistent with the equations given previously, but additional equations are given to cover low and intermediate impact velocities.

These equations predict MDB performance across the full range of impact conditions expected on-orbit and are used in meteoroid/debris probability analyses, such as BUMPER, a computer program that is used by the JSC HIT-F to calculate probabilities of meteoroid and debris impact damage (Christiansen et al., 1992; Crews and Christiansen, 1992).

For $V \geq 6.4/(\cos\theta)^{1/3}$:

$$d_c = 0.6\,(t_w\,\rho_w)^{1/3}\,\rho_p^{-1/3}\,V^{-1/3}\,(\cos\theta)^{-1/3}\,S^{1/2}\,(\sigma/40)^{1/6} \tag{6}$$

For $2.8/(\cos\theta)^{0.5} < V < 6.4/(\cos\theta)^{1/3}$:

$$d_c = 1.11\,\rho_p^{-0.5}\,[t_w\,(\sigma/40)^{0.5} + 0.37\,(m_b+m_l)]\,(\cos\theta)^{-4/3}$$

$$[(6.4/(\cos\theta)^{1/3} - V)/(6.4/(\cos\theta)^{1/3} - 2.8/(\cos\theta)^{0.5})]$$

$$+ 0.323\,(t_w\,\rho_w)^{1/3}\,\rho_p^{-1/3}\,(\cos\theta)^{-2/9}\,S^{1/2}\,(\sigma/40)^{1/6}$$

$$[(V - 2.8/(\cos\theta)^{0.5})/(6.4/(\cos\theta)^{1/3} - 2.8/(\cos\theta)^{0.5})] \tag{7}$$

For $V \leq 2.8/(\cos\theta)^{0.5}$:

$$d_c = 2.2\,[t_w\,(\sigma/40)^{0.5} + 0.37\,(m_b+m_l)]/[(\cos\theta)^{5/3}\,\rho_p^{0.5}\,V^{2/3}] \tag{8}$$

An application of these equations to a typical MDB shield configuration is shown in Figure 7. Figure 8 shows a comparison between the HVI test data and predicted shielding performance using (6) through (8) for impact tests on different MDB configurations.

SUMMARY AND CONCLUSIONS

The impact testing and analysis work at the JSC HIT-F has resulted in an alternative low-weight shielding concept: the mesh double- bumper shield. MDB shields offer ~50% weight savings compared to conventional Whipple shields, while reducing the amount of damaging secondary ejecta debris. Impact performance of the MDB has been assessed for the full range of impact conditions assessable in the laboratory (up to 8 km/sec and at normal and oblique impact angles). Equations have been formulated to allow designers to apply the MDB concept to spacecraft meteoroid/debris protection. Aluminum mesh bumpers offer some unique advantages in augmenting conventional Whipple shield meteoroid/debris protection. Work to date indicates that the addition of a mesh to the exterior of equipment items protected by Whipple shields will greatly increase their resistance to penetration.

Ballistic protection can be improved even more if an intermediate fabric layer (of Kevlar®, Spectra®, or Nextel®) is attached near, but not on, the rear wall.

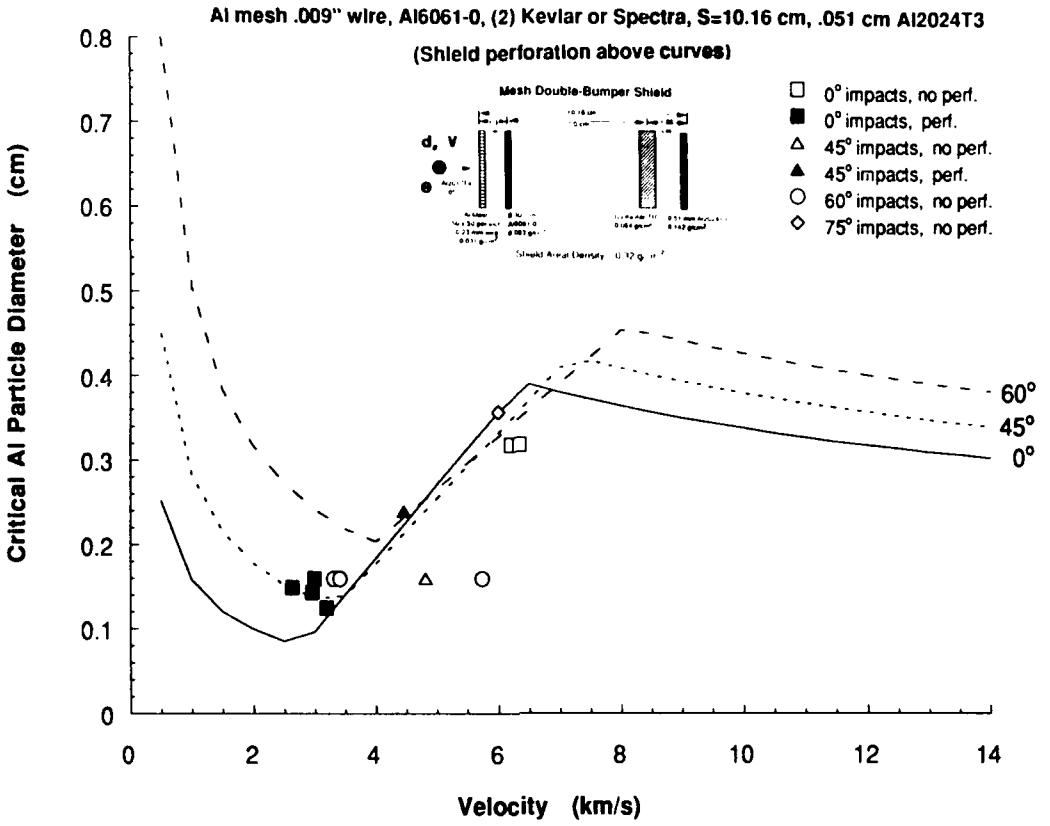


Figure 7. Mesh Double-Bumper Shield Ballistic Limit Curves

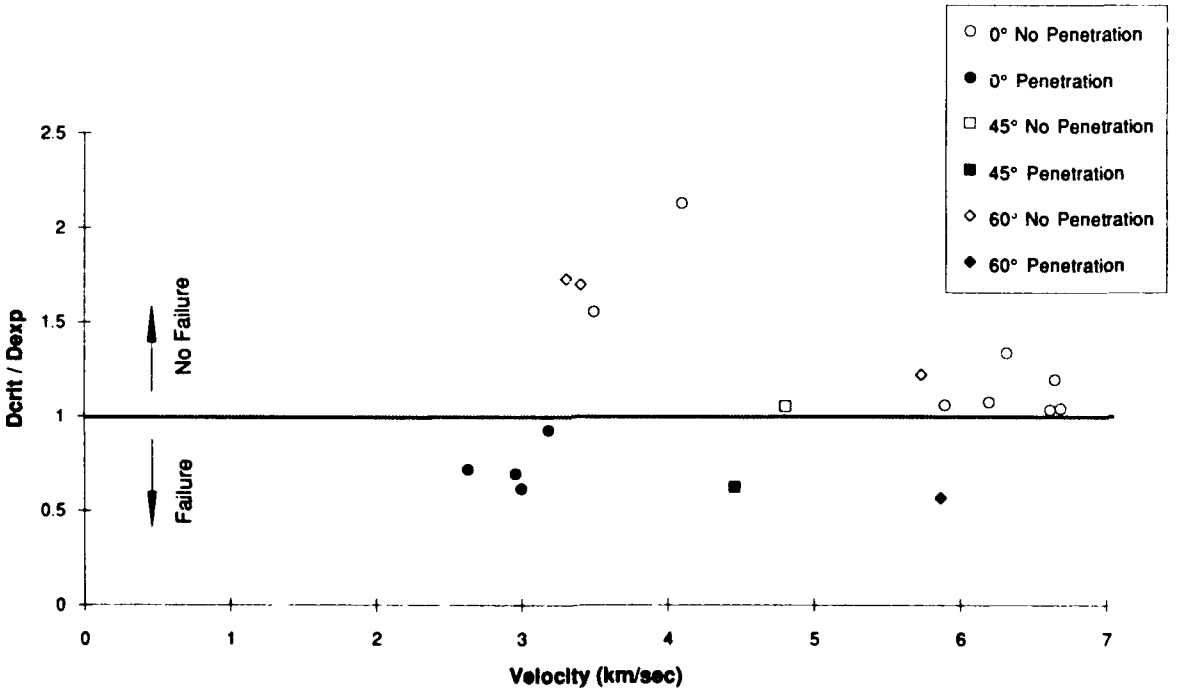


Figure 8. Comparison of MDB Shield Predicted Perfomance with HVI Data

ACKNOWLEDGEMENTS

The authors wish to express their gratitude to Jeanne Lee Crews, Manager of the NASA JSC Hypervelocity Impact Research Laboratory (HIRL) for her contributions to this work. The authors appreciate the excellent efforts on the part of the HIT-F personnel supporting this work, including Lu Borrego, Earl Brownfield, Joe Falcon, Jay Laughman, Javier Ortega, Ken Oser, Pat White, and Jim Whitney.

REFERENCES

Alme, M.L. (1991). Hydrocode Simulations in Support of the Development of Advanced Shielding Concepts. RDA Associates. Sponsored by NASA Johnson Space Center.

Alme, M.L., Christiansen, E.L., and Cour-Palais, B.G. (1991). Hydrocode Simulations of the Multi-Shock Meteoroid and Debris Shield. Proceedings of the APS 1991 Topical Conference on Shock Compression on Condensed Matter, Williamsburg, VA, June 17-20, 1991.

Christiansen, E.L. (1987). Evaluation of Space Station Meteoroid/Debris Shielding Materials. Eagle Engineering Report No. 87-163.

Christiansen, E.L. (1990). Advanced Meteoroid and Debris Shielding Concepts. AIAA Paper No. 90-1336. Presented at AIAA/NASA/DOD Orbital Debris Conference, Baltimore, MD, April 16-19, 1990.

Christiansen, E.L., Horn, J.R., and Crews, J.L. (1990). Augmentation of Orbital Debris Shielding for Space Station Freedom. AIAA Paper No. 90-3665. Presented at the AIAA Space Programs and Technologies Conference, Huntsville, AL, September 25-28, 1990.

Christiansen, E.L. (1992). Performance Equations for Advanced Orbital Debris Shields. AIAA Paper No. 92-1462. Presented at the AIAA Space Programs and Technologies Conference, Huntsville, AL, March 24-27, 1992.

Cour-Palais, B.G. (1969). Meteoroid Protection by Multi-Wall Structures. AIAA Hypervelocity Impact Conference, AIAA Paper Number 69-372.

Cour-Palais, B.G. and Crews, J.L. (1990). A Multi-Shock Concept for Spacecraft Shielding. *Int. J. Impact Engng.*, Vol.10, pp.135-146.

Cour-Palais, B.G. (1992). Multi-Shock Shield Testing and Analysis (Title TBD). Paper presented to the 1992 HVIS, to be published in the *Int. J. Impact Engng.*

Crews, J.L. and Christiansen, E.L. (1992). The NASA JSC Hypervelocity Impact Test Facility (HIT-F). AIAA Paper No. 92- 1640. Presented at the AIAA Space Programs and Technologies Conference, Huntsville, AL, March 24-27, 1992.

Dahl, K.V. and Cour-Palais, B.G. (1991). Standardization of Impact Damage Classification and Measurements for Metallic Targets. To be published in the 1992 Hypervelocity Impact Symposium proceedings.

Horz, F. et al. (1992). Comparison of Continuous and Discontinuous Collisional Bumpers: Dimensionally Scaled Impact Experiments into Single Wire Meshes. NASA Technical Memorandum 104749.

NASA SP-8042 (1970). Meteoroid Damage Assessment. Space Vehicle Design Criteria (Structures). May 1970.

NASA (1991). Space Station Program Environment Definition for Design. NASA SSP 30425, Revision A, June 1991.

Int. J. Impact Engng Vol. 14, pp. 181–192, 1993
Printed in Great Britain

0734-743X/93 $6.00+0.00
1993 Pergamon Press Ltd

A NOVEL METHOD FOR LAUNCHING FLYER PLATES

T. COOPER

SRI International, 333 Ravenswood Avenue, Menlo Park, CA 94025

ABSTRACT

We describe a potential method for launching flat flyer plates by using explosives in complete cylindrical convergence. The basic problem we study in this computational analysis is how to turn the cylindrically convergent shock wave from the explosive into a flat front shock wave running parallel to the cylinder axis. We use a two-dimensional Lagrangian finite difference code to simulate the device. The code uses a free Lagrange method for dealing with mesh distortions.

The calculations predict that the method could launch relatively flat metal plates at velocities up to 14 km/s, but computational uncertainties make experimental verification mandatory.

INTRODUCTION

Explosively-launched high velocity flyer plates are useful for high pressure equation-of-state measurements and other applications. However, usual designs attain plate velocities of only a few km/s. This paper addresses the problem of producing plate velocities in excess of 10 km/s. The work here was inspired by a Russian design communicated by Fortov et al. (1990). As shown in Fig. 1, the Russian design uses a hollow cone of explosive initiated simultaneously on the outside. The explosive will drive a hollow cone of copper onto a solid cone of copper. The Mach stem that develops in the solid cone finally impacts an aluminum plate at the base of the solid copper cone. The Mach stem should be able to throw a center portion of the aluminum plate as a flat plate, the Mach stem being flat itself. When we tried to computationally simulate this configuration we got a glob of aluminum going at an impressively high velocity of 10-15 km/s, but we were not able to preserve a flat plate. The problem might be that we did not do the calculation with sufficient resolution or that we did not have sufficient detail about the design. The information we had was somewhat meager. If a flat flyer plate cannot be produced, the performance is not attractive since Leyrat et al. (1991) have shown that one can throw a glob of material potentially at 20-21 km/s by using complete cylindrical convergence. The Russian design has the deficiency that the momentum vector of the explosive is not completely at right angles to the cylinder axis. The configuration by Leyrat et al. has complete convergence, but since it works generally like a shaped-charge device, it inherently throws a glob of material. Our incremental invention is to use complete cylindrical convergence, but still be able to throw a flat plate.

FLYER PLATE DESIGN

The basic configuration is shown in Fig. 2. The symmetry is cylindrical with the Z axis the axis of symmetry. We have a circular aluminum plate, then a cone of Al_2O_3, outside that a hollow cylinder of tungsten, and finally, a hollow cylinder of high explosive. The explosive continues out to a radius of

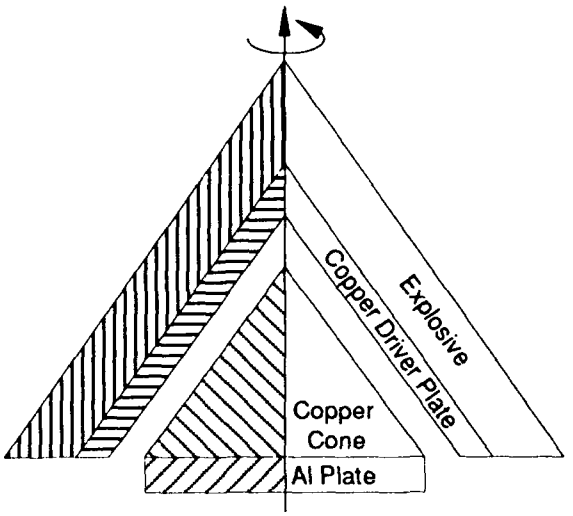


Fig. 1. Russian device for throwing a flat plate. Cross section of cylinder symmetry.

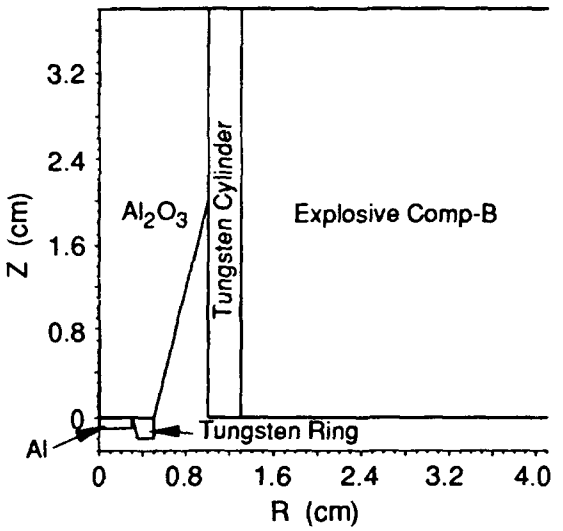


Fig. 2. Configuration for throwing a flat aluminum plate. Cylinder symmetry with Z the axis of symmetry.

7.5 cm (not shown in plot). There is also a ring of tungsten around the aluminum plate to keep the aluminum from expanding radially. The upper and lower boundaries at 0 and 3.8 cm are symmetry boundaries to simulate confinement. We omitted the confinement from the calculation to simplify things. The explosive is initiated uniformly at the outside surface at 7.5 cm radius. We could probably have reduced the amount of explosive needed by putting confinement on this boundary, too. The uniform initiation of the explosive produces a cylindrically convergent detonation wave that will arrive simultaneously all along the tungsten/explosive interface. The tungsten cylinder in its turn will start collapsing radially inward.

When the wave hits the Al_2O_3/tungsten interface at R = 1 cm, we get a wave converging on the axis, but we also get a wave going downward in the Z direction. This downward wave will be reinforced when the radial shock wave in the Al_2O_3 is reflected at the cylinder axis. The purpose of the sloped outside boundary of the Al_2O_3 cone is to time the closure of the tungsten cylinder with the Al_2O_3 cone, so that the downward wave gets side support. This closure point must move vertically with a speed that is equal to the shock wave speed of the vertical wave in the Al_2O_3. The radial wave in the Al_2O_3 will bounce back and forth between the cylinder axis and the tungsten, gradually equilibrating the wave front of the vertical wave into a flat front. The higher the wave speed in the cone material, the faster the equilibration of the vertical wave front. It is for this reason that we chose Al_2O_3: it has an unusually high wave speed, starting out at about 10 km/s and going up to about double that at several megabars.

The material properties for the solids were taken from the Lawrence Livermore National Laboratory (LLNL) shock compendia (Van Thiel, 1977). The equation of state is a Mie-Gruneisen expression with the Hugoniot as the reference line. The Hugoniot is based on a straight line Us-Up fit. The material strength is modeled as a simple elastic-plastic with a Von Mises yield model. It is only for the Al_2O_3 that the material strength can conceivably have any importance. For the Al_2O_3, we use a constant shear modulus of 1.6 Mbar and a Von Mises yield of 0.1 Mbar. The explosive in all cases was Comp-B with a JWL equation of state. When it comes to material properties, the following calculations can be viewed only as feasibility studies. Actual part dimensions must, unfortunately, be determined by iterative experiments. For instance, the data in the LLNL shock compendia for Al_2O_3 go only up to 1.5 Mbar, while in the calculation, significant pressure peaks go up to 3-4 Mbar.

Let us first look at what parameters we can vary. For a given radius of the aluminum plate, we can vary the thickness of the explosive, the thickness of the tungsten cylinder, and the thickness (in the Z direction) of the aluminum plate. We must also vary the cone angle of the Al_2O_3 to make the closure point between the Al_2O_3 and the tungsten move at the same speed as the vertical shock wave in the Al_2O_3. In addition, before we reached the present state of knowledge, we also had to vary the materials

involved to figure out the optimum combination of materials. Note that the materials we have chosen are no more esoteric or expensive than those feasible for use in real experiments.

The explosive thickness will influence the inward radial velocity of the tungsten cylinder. The outside radius we used, 7.5 cm, was the point of diminishing return: as the explosive thickness increases, a further increase brings less and less increase in the radial velocity of the tungsten. In retrospect, we could have reduced the amount of explosive by putting a confining cylinder of material outside the explosive. No material can give perfect confinement in a real experiment, but a dense, stiff material like steel would have helped.

For the tungsten cylinder (the compression cylinder), we must recognize that the pressure driven into the Al_2O_3 increases for both an increase in the radial velocity of this cylinder and an increase in the density of the cylinder. At the same time, an increase in density will decrease the radial velocity. The radial velocity of the compression cylinder will determine the vertical velocity of the closure point for a given cone angle. We can, of course, compensate for an increased radial velocity by tilting the cone angle outward so as to keep the velocity of the closure point the same. However, there are limits to how far we can tilt the cone. Particularly, the bigger the cone angle, the fewer the number of times the radial wave in the cone will bounce back and forth before the vertical wave reaches the aluminum plate. It is this bouncing back and forth of the radial wave in the cone that flattens out the vertical wave front. For this reason, it is generally favorable to increase the density of the compression cylinder. The Rankine-Hugoniot equation

$$\sigma = \rho_o U_s U_p \qquad (1)$$

indicates that, for the same shock velocity Us, there is an exact trade-off between density and particle velocity. In reality, shock velocity will change when one changes the material. We designed one configuration using copper in the compression cylinder instead of tungsten. We say design because one cannot just change from one material to another. One must also change the cone angle of the Al_2O_3. We found that the velocity of the aluminum plate was lower for copper, for the same flatness of the plate. We always strive to maintain flatness of the aluminum plate because the ability to throw a flat plate is the main advantage claimed for the present device.

For the cone, there was only one choice of material: some high wave speed ceramic. One could possibly use B_4C instead of Al_2O_3; however, the data for that material indicate that its constitutive relationship has a somewhat anomalous behaviour. One thing we cannot afford in a complex parameter variation exercise like this is a material that behaves vastly different for different pressure ranges. That pretty much left us with Al_2O_3. It is relatively well characterized, and it is available in good quality batches.

We tried using copper for the cone material. For any reasonable cone angle, the radial shock did not have time to reverberate even once before the vertical shock reached the aluminum plate. The smaller (closer to a straight cylinder) the cone angle, the more time available for radial equilibration of the vertical wave in the cone. The problem is that, for a given radial velocity of the compression cylinder, the closure point moves faster and faster as the cone angle grows smaller. To keep the closure point velocity the same as the vertical shock velocity in the cone, one would have to decrease the radial velocity of the compression cylinder as one decreased the cone angle. This, in turn, would decrease the pressure in the cone, thus decreasing the plate velocity.

Time did not permit us to vary the thickness of the aluminum plate. Up to a certain plate thickness, the velocity of the aluminum plate will tend to remain constant. This thickness will reasonably relate to the pulse width of the vertical shock in the Al_2O_3. There are two problems with the integrity of this plate: the radial expansion of the plate and spallation in the vertical direction. The radial expansion can probably be checked by putting a ring of protective material around the aluminum plate. The tungsten ring around the aluminum plate in Fig. 2 was not successful. We will look at a more successful design below. To keep the plate intact from vertical spallation, it will probably be necessary to put a buffer between the plate and Al_2O_3 cone so as to load the plate semi-isentropically. The buffer, however, might decrease the velocity of the plate.

THE SIMULATIONS

We used the two-dimensional Lagrangian finite difference code L2D for the simulations (Cooper, 1980). It uses a so called free Lagrange rezoning scheme to deal with the mesh distortions. A good description of the method, albeit applied to incompressible water hydrodynamics, can be found in Fritts and Boris (1979). As opposed to most free Lagrange methods, we use quadrilaterals rather than triangles. It turns out to be perfectly feasible to do general rezonings on quadrilateral elements as long as you allow combinations of quadrilaterals and triangles to solve mesh topological problems. Figure 3 shows the initial mesh for a typical simulation, showing that we have used triangles to accommodate the sloping right boundary of the cone. During the simulation, triangles will be created when rezoning operations like creation or deletion of nodes are done. Then a kind of garbage collector will sweep the mesh and reduce well-shaped pairs of triangles to quadrilaterals. The result of the operations is that one gets a mesh dominated by quadrilaterals with a sprinkling of lone triangles. Figure 8 below shows an example.

We try to minimize the number of triangles for two reasons. First, a triangular mesh has roughly double the number of cells that a quadilateral one has. Second, a badly elongated triangle generates unrealistically high stresses, the so-called stiffness effect of triangles. With continuous rezoning, the triangles will tend to stay equilateral, of course, but code skeptics will find less reason to criticize the calculation if the mesh is mainly quadrilateral.

As shown in Fig. 3, the cells in the tungsten cylinder and in the explosive have 2 - 1 aspect ratios. We did this to save mesh. We need resolution only in the radial direction for those two parts (the calculation is one-dimensional until you hit the Al_2O_3). One of the rezoning criteria is cell size. This will make the rezoner strive to keep the cells square, contradicting our mesh layout. In the first place, we do not turn on the rezoner until the shock wave enters the Al_2O_3. In the second place, the rezoner will not rezone a quadrilateral that is close to right angle even if it has an aspect ratio different from 1.

The finite difference equations are based on a force-mass method. Instead of calculating accelerations directly from stresses and densities, we calculate an explicit node mass that remains fixed except for rezonings. On every timestep, we calculate a net force on the node by integrating the stresses into forces with a spatial contour integral around the node. One simple advantage of the method is that we can verify conservation of momentum directly. A good description of the method is found in Hancock (1976). In the literature they often call it a finite element method. Hancock's equations are essentially the same as the DYNA2D equations (Goudreau and Hallquist, 1982).

Tungsten Cylinder Configuration

The configuration in Fig. 2 is the one we found to be optimal, given aluminum plate, Al_2O_3 for the cone, and tungsten for the compression cylinder. The variations in the cell sizes in Fig. 3 are designed to give roughly constant cell transit times for a wave. The simple rule for matching cell sizes, at the interface between two materials, is to adjust for wave velocity so that you get equal transit time through the cells. Since shock velocities vary a lot because of the strong nonlinearities, it is not worthwhile (or possible) to match the cell sizes that carefully. Also, the nonlinearities tend to quench the noise from mismatches quickly. When it comes to resolution, we have not made a rigorous doubling of the resolu-tion to evaluate resolution effects. The mesh is what the machine can handle (a Sun workstation). There are about 10-20 cells across the cone radius. With a quadratic Von Neumann-Richtmyer viscosity, that spreads a shock over 3-4 cells, which should be enough to resolve the radial shock in a respectable way.

Figure 4 shows the initial positions of the Lagrangian time histories we sampled. We focus on time histories 1 through 15 and refer to the time histories by these numbers in the following. Please understand the meaning of Lagrangian: the time history is a history of what happens to the material particle that was initially at the position indicated in Fig. 4. As the particle moves, the time history moves with it.

Figure 5 shows radial velocities for histories 7, 11, 15. Time zero is at initiation of the explosive in all plots. The velocity is initially one-dimensional. For histories 11 and 15, it changes when the particle

hits the Al_2O_3. For history 7, a further increase in the radial velocity occurs when the second compression wave arrives at the free surface of the tungsten. When the initial shock from the explosive arrives at the free surface, you get a rarefaction traveling back. When that rarefaction hits the tungsten/explosive interface, a new compression wave travels back into the tungsten. This stagewise increase in the radial velocity will make the closure point move with a varying vertical velocity. Our design criterion for the slope of the cone has always been to make the closure point arrive at Z = 0 at the same moment that the vertical shock in the cone arrives there. It is unavoidable that the closure point will be out of sync, at times, with the vertical shock wave in the cone. This is one inherent limitation on our ability to equilibrate the vertical shock in the cone.

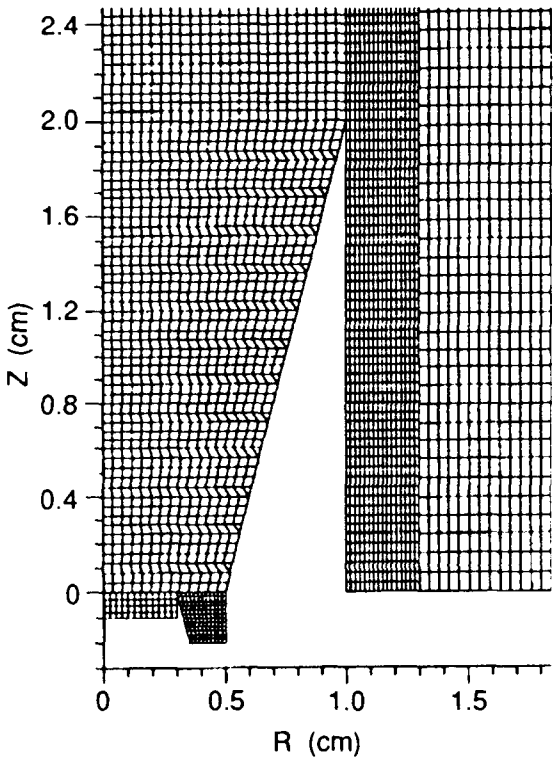


Fig. 3. Mesh layout for basic configuration.

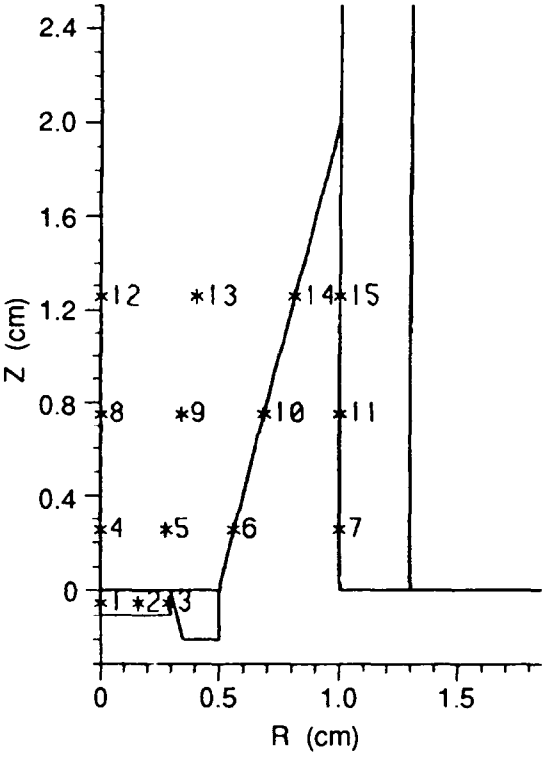


Fig. 4. Initial positions for Lagrangian time histories.

Figure 6 (a), (b), (c) shows vertical stress Al_2O_3 for histories 12, 13, 14 and 8, 9, 10 and 4, 5, 6 respectively. We can see how the time of arrival gradually creeps together as we move downwards. Figure 7 shows contours of vertical stress at 10.2 μs. The wave front of the vertical wave is satisfactorily flat, but there is a complex stress state behind the front. Some of this complexity will have time to interact with the aluminum plate. Figure 8 shows the mesh at 10.2 μs. Notice how the rezoner has introduced uneven cell sizes at scattered spots. In principle, this unevenness disturbs subsequent shocks running through the mesh behind the main wave. In practice, it is not important in a strongly nonlinear problem like this. A specific device in the code suppresses rezoning in a shock front, because distortions of the mesh are typically not a problem in the shock front. The mesh distortions develop due to the long-term particle displacements behind the shock, rather. The cells may get considerably compressed inside a shock front. However, this is really an advantage of Lagrangian methods over Eulerian methods. With a Lagrangian method, one tends to get an automatic refinement of the spatial resolution inside a sharp gradient.

Figure 9 shows vertical velocity for histories 1, 2, and 3. Notice that the fringe of the plate wants to separate from the center. Also, there is a velocity difference of about 0.1 cm/μs between histories 1 and 2. It would take about 1 μs for this velocity difference to generate a shear displacement of 0.1 cm, i.e., the thickness of the plate. In 1 μs, the plate would travel about 1.4 cm. Figure 10 shows material boundaries at 11.2 μs. Figure 11 shows the mesh at 11.2 μs. These two figures are somewhat busy. It

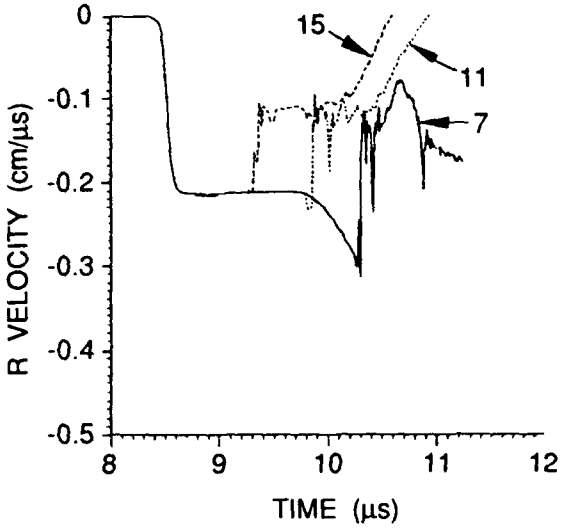


Fig. 5. Radial velocities of tungsten cylinder for time histories 7, 11 and 15. History number 7 shows a further increase in velocity from a second reflection off the explosive.

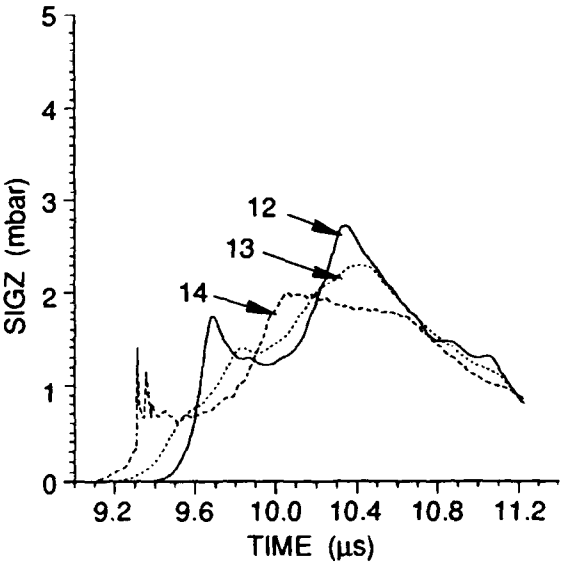


Fig. 6a. Vertical stress in Al_2O_3 for time histories 12, 13, 14.

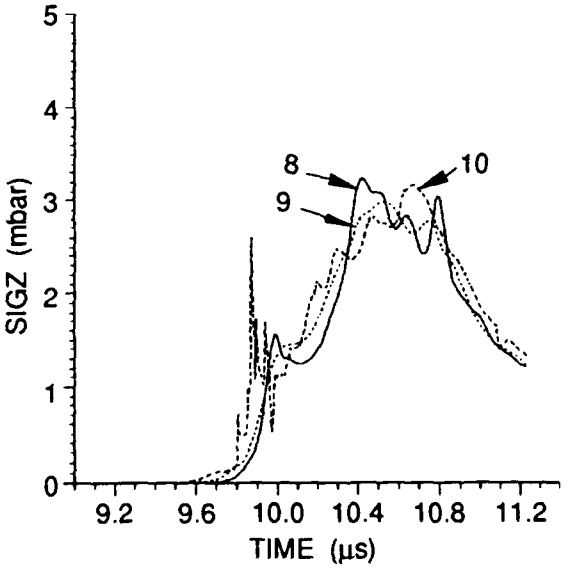


Fig. 6b. Vertical stress in Al_2O_3 for time histories 8, 9, 10.

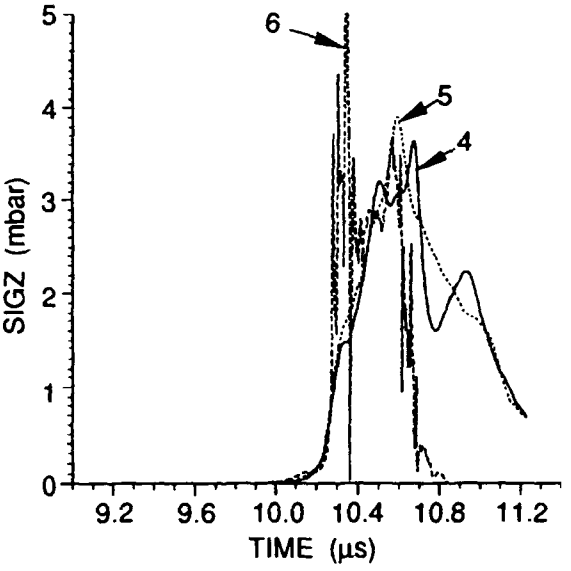


Fig. 6c. Vertical stress in Al_2O_3 for time histories 4, 5, 6.

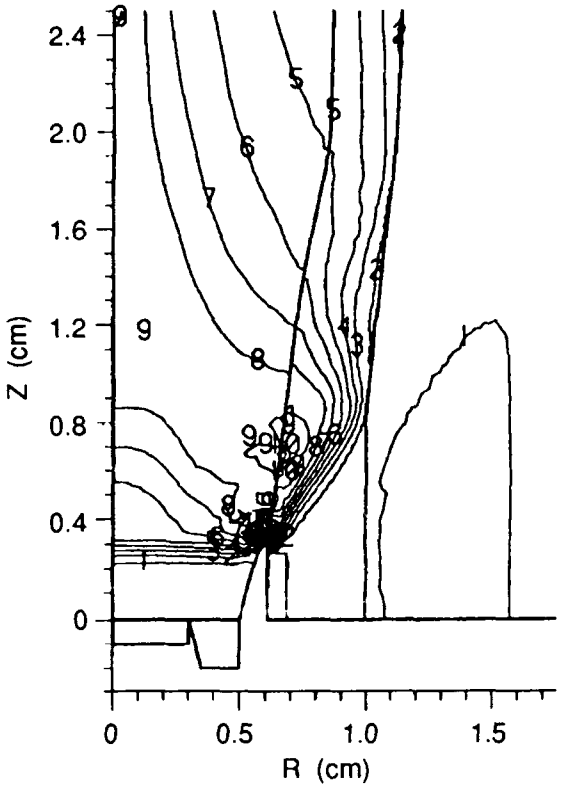


Fig. 7. Contours of vertical stress at 10.2 μs, 0.25 Mbar per contour. Showing a relatively flat shock front in the Al_2O_3.

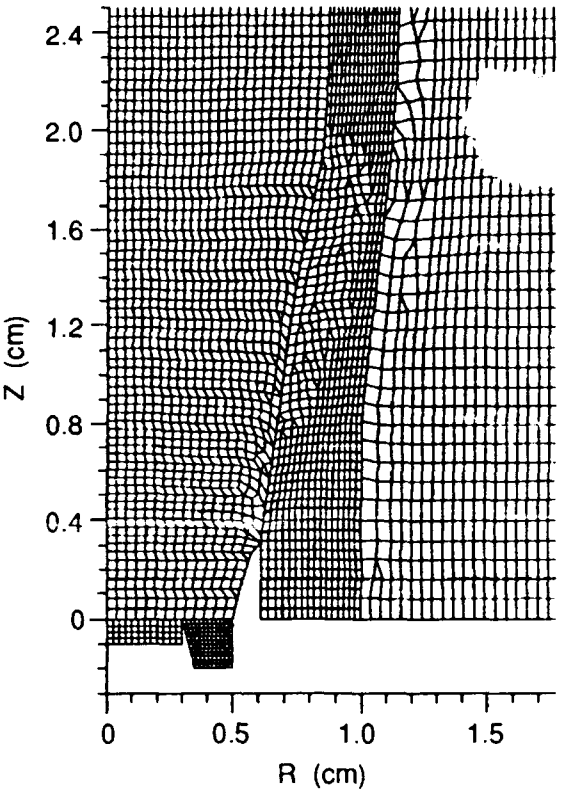


Fig. 8. Mesh at 10.2 μs.

might help the reader to remember that there are three pieces of material below Z = 0: the aluminum plate, the tungsten ring that was around the aluminum plate, and the expansion products from the Al_2O_3.

We varied the thickness of the tungsten cylinder between 0.2 and 0.45 cm to evaluate the optimum thickness of the cylinder. When we change the thickness of the tungsten cylinder, we must also change the slope of the Al_2O_3 cone. Because of all the nonlinearities involved, it is not possible to hand-calculate the correct slope. Instead, we must try different slopes, doing iterative calculations. The process is somewhat tedious, but after some accumulation of experience, it is usually possible to fix the slope in two to three iterations. Figure 12 shows vertical plate velocities for histories 1, 2, and 3 for a tungsten cylinder of 0.2-cm thickness. Figure 13 shows same for a thickness of 0.45 cm. The smaller thickness did not lead to any significant increase in the velocity for the aluminum plate, but the breakup of the plate is if anything worse. The thicker tungsten cylinder, 0.45 cm, gave a clearly lower plate velocity even though the integrity of the plate improved somewhat. For the 0.45-cm-thick tungsten cylinder, we could keep the cone angle the same as for 0.3 cm (because we were not completely fastidious in fine-tuning the cone angle). This indicates a certain insensitivity to the cone angle, which is beneficial.

Thus, it appears that the concept has the potential for throwing a relatively flat aluminum plate at about 14 km/s over distances of a few millimeters before plate distortion becomes severe. Such high velocity flyer plates would be very useful for high pressure equation-of-state measurements.

There is one further problem that we are not addressing here. Namely, melting and spallation of the target plate. In order to simplify the calculations, we did not model the melting of the aluminum plate. The amount of irreversible internal energy caused by the shock dissipation should be enough to melt the

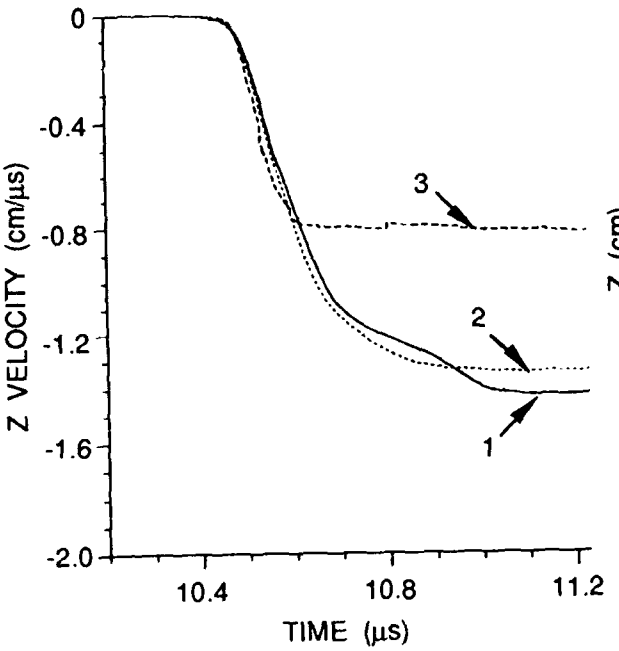


Fig. 9. Vertical velocity of aluminum plate for time histories 1, 2, and 3.

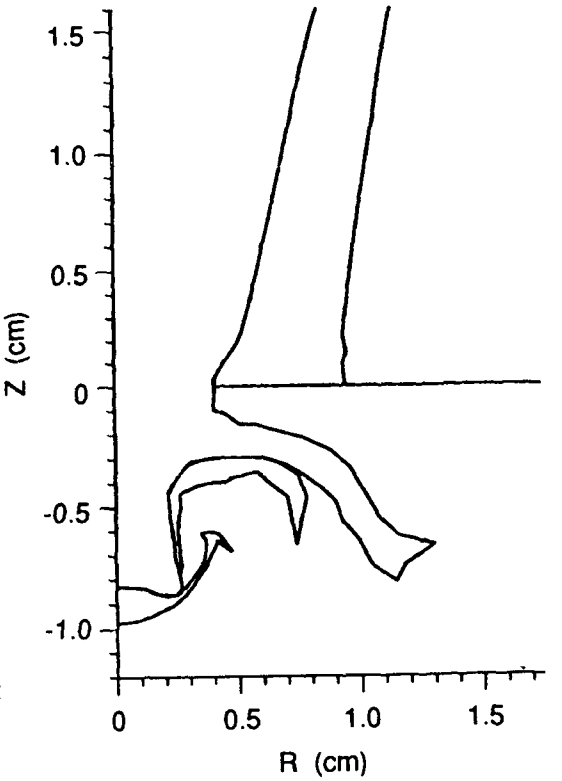


Fig. 10. Material boundaries at 11.2 μs.

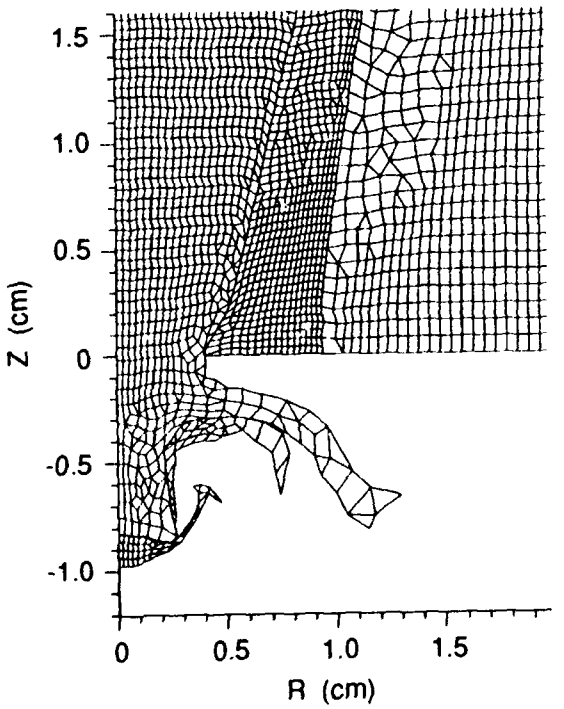


Fig. 11. Mesh at 11.2 μs.

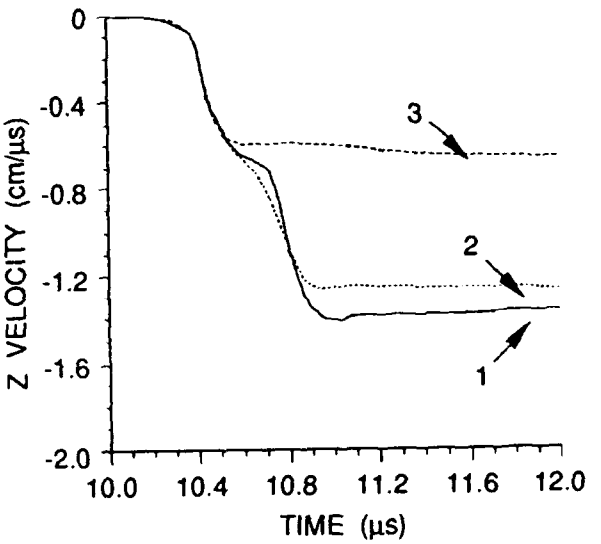


Fig. 12. Vertical velocity of aluminum plate with a 0.2 cm tungsten cylinder for time histories 1, 2, and 3. There is no noticeable improvement compared to Fig. 9.

aluminum. Also, we used a Von Mises model for the yielding with a constant yield stress of 2.95 Kbar. For the stress levels we are studying, this means the aluminum plate behaves essentially as a fluid. As mentioned above, a possible solution to the problem of the integrity of the target plate is to insert a buffer material between the plate and the Al_2O_3 cone, so as to load the plate semi-isentropically. However, it is beyond the scope of the present effort to investigate cures for the problems with the target plate integrity.

Copper Cylinder Configuration

We also made one calculation using copper for the compression cylinder. According to equation (1), we should expect a higher radial particle velocity since copper has a density of 8.93 g/cm^3 compared with 17.8 g/cm^3 for tungsten. Figure 14 shows part dimensions. Figure 15 shows radial velocities for histories 7, 11, and 15. Figure 16 shows vertical velocities for histories 1, 2, and 3. With the copper cylinder, we get lower peak velocity of the aluminum plate with no real improvement in plate integrity. The main reason we get lower output is probably because the bigger cone angle gives less convergence effect due to the larger radius.

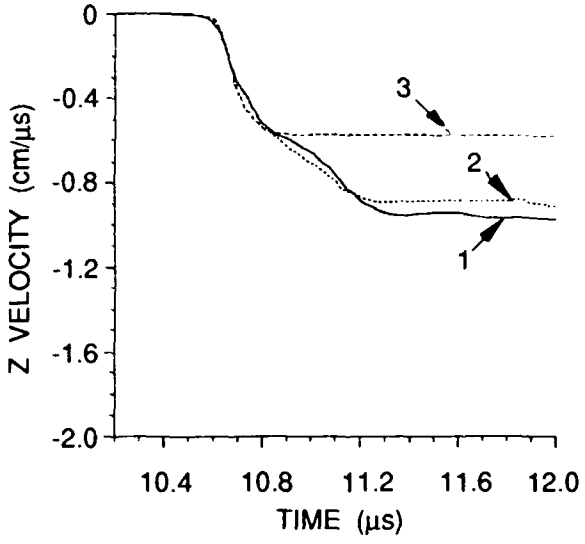


Fig. 13. Vertical velocity of aluminum plate with a 0.45-cm tungsten cylinder for time histories 1, 2 and 3. The plate integrity has improved somewhat, but the velocity has decreased.

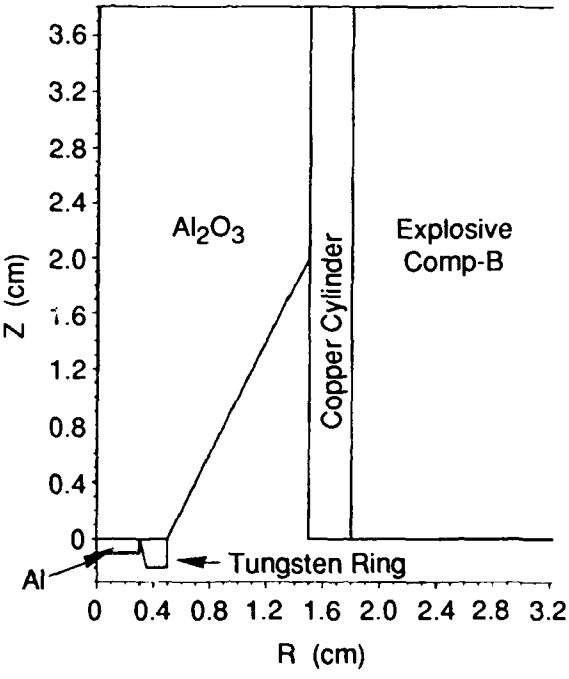


Fig. 14. Configuration for throwing a flat aluminum plate using a 0.3 cm copper cylinder. Cylinder symmetry, with Z the axis of symmetry.

According to this reasoning, the ideal material for the compression cylinder should have high density so as to lower the radial particle velocity, which in its turn reduces the cone angle, which leads to stronger cylindrical convergence, a purely geometrical effect. From equation (1), we can see that a higher shock velocity will also increase the pressure, holding everything else constant. Tungsten is unfavorable in this respect compared with copper; at least the initial shock velocity is lower for tungsten. To judge from our simulations, one gains more from the increase in density, using tungsten, than one loses from the lower shock velocity.

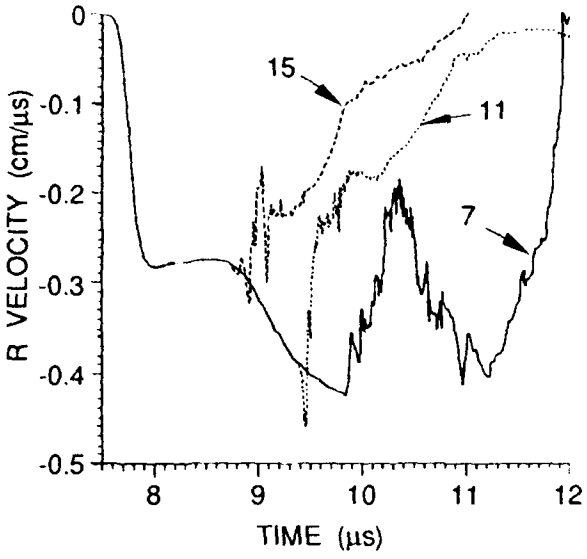


Fig. 15. Radial velocities of copper cylinder for time histories 7, 11 and 15.

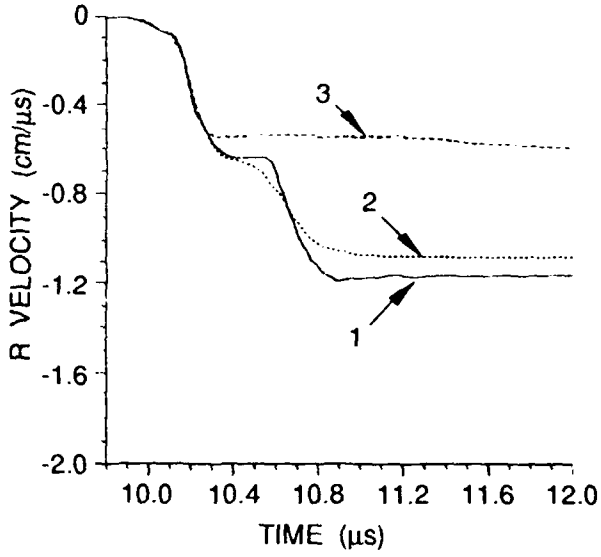


Fig. 16. Vertical velocity of aluminum plate, using a copper cylinder, for time histories 1, 2 and 3.

Multiple Stage Configuration

We designed one more configuration, considerably more complex, as shown in Fig. 17. It is similar to a Russian concept (Fortov et al., 1990) of having several stages of accelerators. First, we modified our radial support for the aluminum plate to create a ring of aluminum, with varying thickness, around the plate. We first tried to taper the ring so that it was thickest at the outside edge. However, there is a focusing of the stress at about (R, Z) = (0.5, 0) cm that makes the ring compress the aluminum plate radially. The present taper keeps the radius of the plate roughly constant. We also designed a large ring of tungsten to act as a gun barrel. A layer of Comp-B is inserted between Z = -0.6 and Z = -0.8. The final tungsten plate is 0.5 mm thick with a tapered tungsten ring around it as confinement. Here the taper has the orientation one intuitively expects.

Figure 18 shows material boundaries at 10.7 μs. The ring support for the aluminum plate is reasonably successful at keeping the radius of the plate constant at 0.3 cm. Figure 19 shows material boundaries at 12.5 μs. The final tungsten plate is very distorted, although the center portion has attained the impressive speed of about 16 km/s. Overall, the design was not successful, but time has not permitted optimization of this design. The calculation is very hypothetical. For one thing, because the Comp-B in the second stage reaches pressures of about 2 Mbar, it is not to be expected that the JWL equation of state extrapolates that far, the C-J pressure of Comp-B is actually 0.295 Mbar! Figure 20 shows histories of vertical velocities in the final tungsten plate. The histories are positioned the same way as for the aluminum plate.

DISCUSSION

The calculations suggest that single or multiple staged launchers of the type proposed could launch relatively flat metal plates at velocities of about 14 km/s. The primary question is whether it is feasible to make a functioning experiment. In the first place, exact dimensions must be determined by iterative experiments because we must extrapolate in all the material models we use in the simulation. A gradual modification of properties, such as whether a certain Us-Up curve has exactly the slope we assume,is

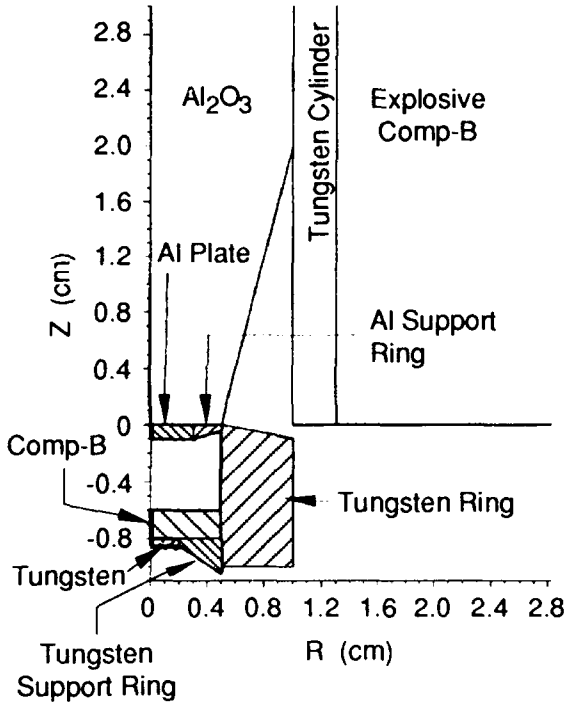


Fig. 17. Configuration with two stages. Cylinder symmetry, with Z the axis of symmetry.

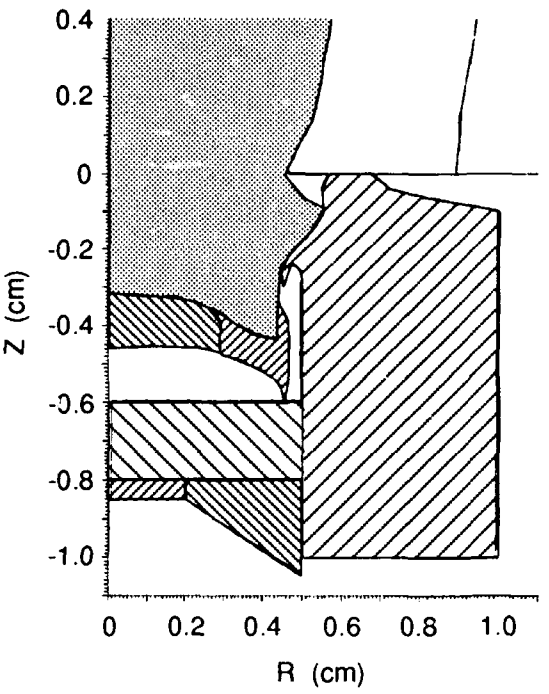


Fig. 18. Material boundaries of multiple-stage configuration at 10.7 μs.

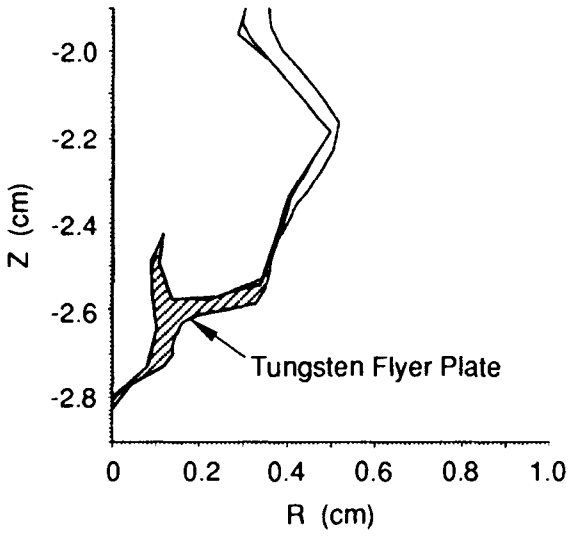


Fig. 19. Material boundaries of multiple-stage configuration at 12.5 μs.

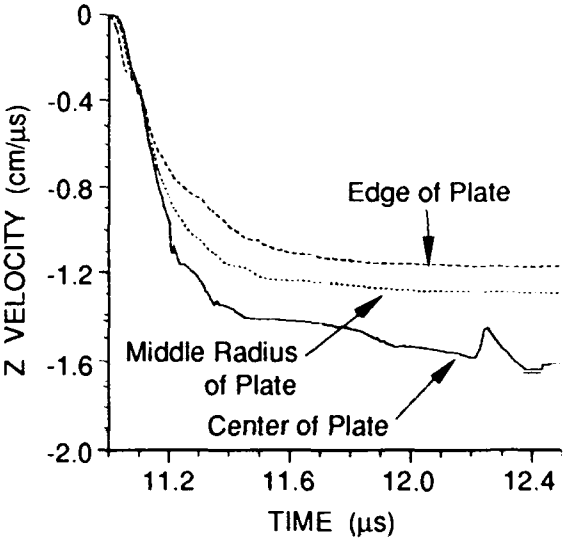


Fig. 20. Vertical velocity of tungsten plate of multiple-stage device for three time histories.

not a problem. However, a complete change in properties can pose a big problem. For instance, the Al_2O_3 might have a phase change at high pressure that radically reduces the wave speed. The Al_2O_3 is the critical component. For all the other materials, we can easily adjust dimensions to compensate for an unexpected material model. Actually, the slope of the cone is the only variable we need to adjust because the results are relatively insensitive to the thickness of the tungsten cylinder. There is a good chance that a tungsten cylinder thickness of 0.3 cm is not too far from optimal. We did not optimize the thickness of the aluminum plate, but it should be possible to optimize it sufficiently by computer alone.

One question we have not addressed here is the problem of maintaining a cylindrically symmetric detonation in the explosive. Our calculations are inherently symmetric. At present, we do not have enough knowledge to answer that question. Even if a lack of symmetry does not destroy the experiment, it might, for instance, reduce convergence effects.

Finally, even though uncertainties in the material models for the tungsten and the explosive may not prevent the design from working, they might generate a different ultimate velocity of the aluminum plate. Because this might work for us as well as against us, it is more of an uncertainty than a problem.

ACKNOWLEDGMENT

Thanks are due to D. R. Curran for suggesting the problem and for helpful discussions.

REFERENCES

Cooper, T. (1980). A Computer Code for Numerical Simulation of Shock Waves in Fluids and Solids. Swedish Detonic Res. Foundation, Report DS 1980:16.

Fortov, V. E., G. I. Kanel, and Y. Alexander (1990). Personal communication by Fortov.

Fritts, M. J. and J. P. Boris (1979). The Lagrangian Solution of Transient Problems in Hydrodynamics using a Triangular Mesh. J. Computational Physics, Vol. 31, pp. 173-215.

Goudreau, G. L. and J. O. Hallquist (1982). Recent Developments in Large-Scale Finite Element Lagrangian Hydrocode Technology. Computer Methods in Applied Mechanics and Engineering, Vol. 33, pp. 725-757.

Hancock, S. L. (1976). Finite Difference Equations for PISCES 2DELK, A Coupled Euler Lagrange Continuum Mechanics Computer Program. Physics International Technical Memo TCAM 76-2.

Leyrat, J. P., E. Charvet, M. Mace, and H. C. Pujols (1991). Creation et Simulation de Jets Hyperveloces, Vol. c3, pp. 253, Journal de Physique IV (proceedings).

Van Thiel, M. (Ed.) (1977). Compendium of Shock Wave Data. Lawrence Livermore Laboratory, UCRL-50108.

Int. J. Impact Engng Vol 14, pp 193–204, 1993
Printed in Great Britain

0734-743X/93 $6.00 + 0.00
1993 Pergamon Press Ltd

ANALYSIS OF THE UDRI TESTS ON NEXTEL MULTI-SHOCK SHIELDS

B.G. COUR-PALAIS(1), A.J. PIEKUTOWSKI(2), K.V. DAHL(1) AND K.L. POORMON(2)

(1) McDonnell Douglas Space Systems Company, Space Systems Division, Houston, TX U.S.A.
(2) University of Dayton Research Institute, Dayton, OH, U.S.A.

ABSTRACT

This paper analyzes the results of further development of the Nextel ceramic cloth, multiple-bumper or multi-shock shield, first presented at the 1989 HVIS and published as Cour-Palais and Crews (1990). The supporting hypervelocity impact testing was done by the University of Dayton Research Institute, Dayton, Ohio, in their Impact Physics Laboratory, using 0.953cm aluminum spheres and equal-mass (l/d=0.16) aluminum discs. The projectiles were launched at 6.6 to 6.9km/s by a 50/20mm, two-stage light gas gun, normal to the targets. The objective of this development project was to investigate light-weight, flexible, multiple-bumper shields for possible use as protection for some elements of Space Station Freedom. The analysis discusses the performance of shields consisting of different combinations of Nextel ceramic cloth bumpers and aluminum rear sheets. Several Nextel fiber strengths and weaves were investigated as bumpers and a baseline, light-weight shield that met the failure criteria was established using the spherical aluminum projectiles. This same target was then tested against the aluminum discs to investigate the effect of projectile shape. The multi-shock phenomena was also investigated during this project using the UDRI multiple, orthogonal x-ray system to observe the first three or four sequential impacts of the projectile fragments. Some of these are reproduced in the paper, together with views of the associated rear sheet damage. Similarities between the shock effects of the Nextel and thin aluminum bumpers are shown, and the aluminum multiple-bumper shield results are used to further understand the multi-shock process. Finally, the paper modifies the equation constants given by Cour-Palais and Crews (1990), adds constants for the l/d=0.'6 disc, and provides evidence that they scale with momentum to 10km/s.

GLOSSARY OF SYMBOLS:

	C	coefficient
	M	mass; g
	S	total spacing; cm
	ΔS	inter-bumper spacing; cm
	V	velocity; km/s
	Y	yield stress; N/m^2
	Σ	summation
	d	diameter; cm
	l	disc/cylinder length; cm
	t	thickness; cm
	m	areal density; g/cm^2
	n	number of bumpers
	ρ	mass density, g/cm^3
Subscripts:	b;	bumper
	p;	projectile
	r;	rear sheet
	t;	tensile

INTRODUCTION

Since the multi-shock shield concept for spacecraft shielding was first presented, the interest in using the Nextel multiple-bumper shield on certain elements of Space Station Freedom has increased. In addition, the orbital debris environment definition has been refined and is accepted as a threat to be considered. The flexible, Nextel multiple-bumper shield by itself or in combination with the Whipple shield, is being seriously considered as a means to achieve the lightest, acceptable degree of protection against orbital debris impacts. This paper presents the results of a series of tests conducted at the University of Dayton Research Institute (UDRI) on the Nextel multiple-bumper shield. Nextel is a ceramic cloth produced by the 3M company which is available in several different fiber strengths, weaves and areal

densities. The intent of these tests was to simplify the shield construction, to optimize the shield's performance in terms of total areal density, and to determine the most effective distribution of the bumper and rear sheet areal densities. At this point, it is necessary to define the term "shield" as referring to the complete system, i.e., multiple bumpers plus the rear sheet or other final element that is to perform the shielding function.

In addition to the Nextel optimization tests, the tests at UDRI included thin aluminum multiple-bumper shields, to assist in modelling the physics relating to the multiple shock process, several miscellaneous tests to investigate specific uses of Nextel multiple-bumper shields, and one Whipple shield test with the disc.

EXPERIMENTAL PROCEDURE

The tests were performed in the UDRI Impact Physics Laboratory, using 0.953cm aluminum spheres and equal mass, (l/d=0.16), aluminum discs launched at 6.6 to 6.9km/s by a 50/20mm, two-stage, light gas gun. All the impacts in this series were at normal inclination to the targets. The debris produced by the first three impacts on the multiple bumpers were observed by simultaneous, orthogonal, soft flash x-rays, with a fourth pair of x-rays positioned in front of the first bumper to show the condition of the projectile prior to impact. A more detailed discussion of the test setup and a sequence of x-ray views is given in the paper to be published as Piekutowski (1993).

In almost all of the tests, the rear sheet was an aluminum 6061-T6 plate, with an aluminum witness sheet placed behind it. Figure 1 shows a typical multiple shield target assembly prior to impact. As the purpose of this series was to study the effect of the Nextel fabrics on the ballistic limits, the number of bumpers and the spacing between them, and also the space between the last bumper and the rear sheet, was held constant during the optimizing phase. The constants were five bumpers for the aluminum shield; four bumpers for the Nextel shield, and a distance of 7.62cm for all the spaces. After a baseline shield was identified, other combinations of spacing and number of shields were tested. Finally, the equal mass aluminum disc projectiles were tested against the baseline shield for comparison with the spherical projectile results.

Four Nextel fabrics were selected for this series which were as follows:

1. AF26; areal density of 0.043g/cm^2, woven from Nextel 312 fiber (62% aluminum oxide; 24% silicon dioxide; 14% boric oxide). This was the original ceramic fabric used for the multiple bumpers reported in Cour-Palais and Crews (1990).
2. AF40; areal density of 0.08g/cm^2, woven from the same fiber as AF26.
3. AF62; areal density of 0.1g/cm^2, also woven from the Nextel 312 fiber but having a different weave pattern than the above.
4. BF54; areal density of 0.108g/cm^2, woven from Nextel's 440 fiber (70% aluminum oxide; 28% silicon dioxide; 2% boric oxide). BF54 has the same weave as the AF62, however the fiber has a 20% higher tensile strength.

With these four fabrics it was possible to investigate the effect of the bumper make-up on the total shield performance, as previously mentioned.

TEST RESULTS

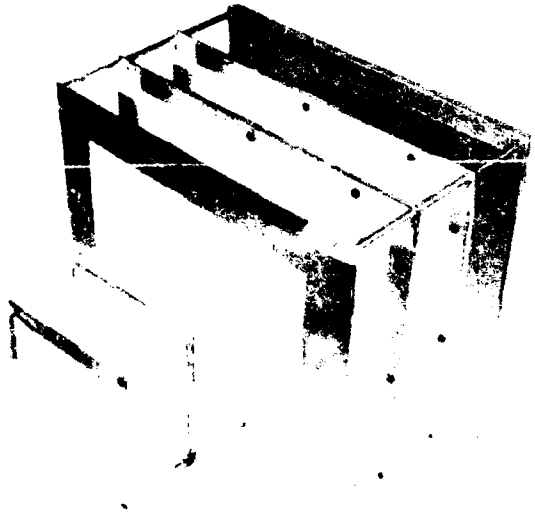
The test matrices and results are shown in Table 1 for the Nextel shield optimization study, and in Table 2 for the other tests. This next portion of the report will describe the reason for each test and the result.

Tests UDRI 4-1149 (aluminum) and UDRI 4-1150 (Nextel) were run to establish the validity of the earlier results obtained at the Ames Research Center facility, Cour-Palais and Crews (1992), using the same shields projectile material, mass and velocity. However, the bulge was not as pronounced as in the Ames result in these tests, due to a difference in the rear sheet mounting. The frame supporting the rear sheet deflected under impulsive loading on the plate and was permanently bowed as shown in Fig. 2. As a result, the rear sheet mounting frame was thickened for all the remainder of the tests.

In the next test, UDRI 4-1151, the four triple AF26 bumper elements used in UDRI 4-1150 were replaced with five single element AF62 bumpers of approximately the same total areal density, using the same wall element. The success of this test led to the elimination of one bumper and the substitution of the BF54 fabric for each element in the next test, UDRI 4-1152. Using the same rear sheet thickness, the bulge in the wall element was deeper, and the total areal density was reduced to 1.054g/cm^2 from 1.148g/cm^2 for UDRI 4-1150.

Tests UDRI 4-1153 and UDRI 4-1154 investigated the reduction of the rear sheet thickness and combinations of the AF62 and the BF54 Nextels. In the first of these, two AF62 bumpers were placed in front of two BF54 bumpers to examine the effect of having the higher strength Nextel 440 fibers for the rear bumpers, where the impulsive loading was greatest. The second test examined the effect of having the higher areal density BF54 in the first two bumpers, to enhance projectile breakup. There was no difference in the performance of either shield, and the lower total areal density of 0.968g/cm^2, resulted in a shield that was just below the ballistic limit.

Several attempts at investigating lower areal density shields are represented by the tests numbered UDRI 4-1170, 4-1174, 4-1251 and 4-1253. In these tests the AF40 and AF26 Nextel materials were used in several combinations of bumpers and rear sheet thicknesses. All of them resulted in rear sheet failures ranging from marginal to catastrophic.



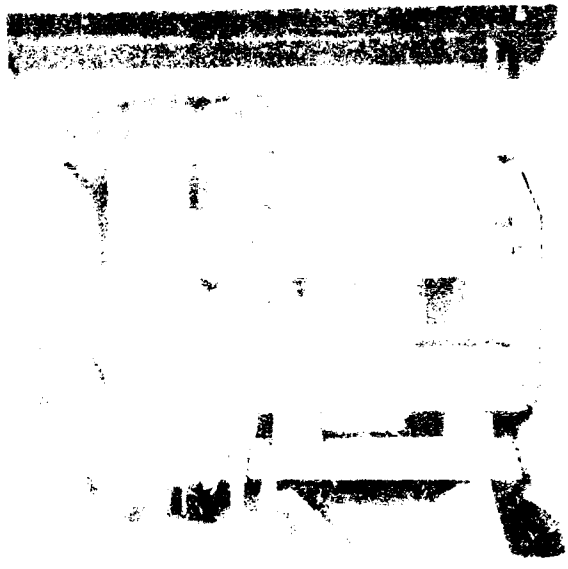


Table 1. Multiple-Bumper Optimization Test Results
Projectile: AL 2017-T4 Diameter: 0.953 (cm); Mass: 1.27 (g) Nominal; Impact Angle: 0

Shot #	Shielding Material for Each Bumper	Total Number of Bumpers	Spacing Between Bumpers (cm)	Rear Sheet Material	Rear Sheet Thickness (cm)	Total Mass Per Unit Area (gm/cm^2)	Velocity (Km/s)	Shield to Rear Sheet Weight Ratio	Description of Rear Sheet Damage
UDRI 4-1149	AL1100-0	5	7.62 Equal 38.1 Total	AL 6061-T6	0.229	1.136	6.69	0.83	No Perforation; Slight Bulge; Molten Splash
UDRI 4-1150	NEXTEL AF26	4	7.62 Equal 30.48 Total	AL 6061-T6	0.229	1.148	6.77	0.85	No Perforation; Slight Bulge; Molten Splash
UDRI 4-1151	NEXTEL AF62	5	7.62 Equal 38.1 Total	AL 6061-T6	0.229	1.120	6.78	0.80	No Perforation; Slight Bulge; Molten Splash
UDRI 4-1152	NEXTEL BF54	4	7.62 Equal 30.48 Total	AL 6061-T6	0.229	1.054	6.78	0.70	No Perforation, Deep Bulge; Molten Splash
UDRI 4-1153	NEXTEL AF62 + BF54	4	7.62 Equal 30.48 Total	AL 6061-T6	0.203	0.968	6.75	0.76	1 Small Perforation; Deep Bulge; Molten Splash
UDRI 4-1154	NEXTEL BF54 + AF62	4	7.62 Equal 30.48 Total	AL 6061-T6	0.203	0.968	6.75	0.76	1 Small Perforation; Deep Bulge; Molten Splash
UDRI 4-1170	NEXTEL AF40	4	7.62 Equal 30.48 Total	AL 6061-T6	0.203	0.893	6.72	0.62	Large Petalled Hole; Molten Splash on Witness Sheet
UDRI 4-1174	NEXTEL AF40	5	7.62 Equal 38.1 Total	AL 6061-T6	0.203	0.978	6.57	0.78	1 Small Perforation; Deep Bulge, Molten Splash
UDRI 4-1250	NEXTEL BF54	4	7.62 Equal 30.48 Total	AL 6061-T6	0.203	0.984	6.73	0.79	1 Small Perforation; Deep Bulge, Molten Splash
UDRI 4-1251	NEXTEL AF40	5	5.08+5.08+ 5.08+7.62+ 7.62 30.48 Total	AL 6061-T6	0.203	0.978	6.80	0.78	3 Cracks; Deep Bulge, Large Hole in the Witness Sheet; Molten Fragment
UDRI 4-1253	3xNEXTEL AF26	4	7.62 Equal 30.48 Total	AL 6061-T6	0.160	0.962	6.76	1.22	3 Perforations; Deep Bulge; Small Hole in Witness Sheet
UDRI 4-1292	AL 1100-0	5	7.62 Equal 38.1 Total	AL 6061-T6	0.203	0.964	6.69	0.15	No Perforation; Deep Bulge; Molten Splash
UDRI 4-1293	NEXTEL AF62	4	7.62 Equal 30.48 Total	AL 6061-T6	0.229	1.020	6.67	0.64	No Perforation; Deep Bulge; Molten Splash

Table 2. Special Purpose Multiple-Bumper Test Results

Shot #	Shielding Material for Each Bumper	Total Number of Bumpers	Spacing Between Bumpers (cm)	Rear Sheet Material	Rear Sheet Thickness (cm)	Total Mass Per Unit Area (gm/cm^2)	Velocity (Km/s)	Shield to Rear Sheet Weight Ratio	Description of Rear Sheet Damage
UDRI 4-1295	NEXTEL BF54	4	7.62 Equal 30.48 Total	AL 6061-T6	0.229	1.054	6.36	Disc 1.262	H[illegible] with 3 Cracks Disc Hit at 45 ^{0}
UDRI 4-1307	NEXTEL BF54	4	7.62 Equal 30.48 Total	AL 6061-T6	0.229	1.054	5.93	Disc 1.252	Large Hole: Disc Hit Edge-On
UDRI 4-1308	NEXTEL BF54	4	7.62 Equal 30.48 Total	AL 6061-T6	0.229	1.054	6.22	Disc 1.252	No Penetration: Disc Hit Flat
UDRI 4-1309	NEXTEL AF62 (1:2:1)	3	10.16 Equal 30.48 Total	AL 6061-T6	0.229	1.021	6.65	Sphere 1.275	Large Split in Deep Bulge; Vapor Deposit on Witness Sheet
UDRI 4-1312	NEXTEL AF62 (Lapped Seam)	4	7.62 Equal 30.48 Total	AL 6061-T6	0.229	1.021	6.82	Sphere 1.275	1 Small Perforation Deep Bulge; Molten Splash
UDRI 4-1313	2 NEXTEL AF62 1 NEXTEL AF26 2 NEXTEL BF54	3	3.81 + 3.81 + 2.54 10.16 Total	AL 6061-T6	0.180	0.966	6.82	Sphere 0.373	Deep Bulge Split Wide Open; 1 Small Perf. in Witness Sheet
UDRI 4-1314	AL6061-T6 (0.155 cm)	1	30.48	AL 6061-T6	0.318	1.280	6.52	Disc 1.253	Large Elongated Hole; Disc Hit Edge On
UDRI 4-1315	NEXTEL BF54	4	7.62 Equal 30.48 Total	AL 6061-T6	0.229	1.054	6.57	Disc 1.253	Shallow Bulge; No Perforations. Seven Small Bumps; Disc Hit Flat
UDRI 4 1317	3 NEXTEL AF62 + 1 AL6061-T6 (0.127 cm)	4	7.62 + 7.62+ 7.62 + 10.16 33.02 Total	AL 2219-T87	0.318	1.550	6.82	Sphere 1.275	No Perforation; Attached Spall; Shallow Bulge

clearly. The first part of this section will address this process as it applies to the various shields and projectiles tested.

Multi-shock Shield Phenomenology

Cour-Palais and Crews (1992) showed that the performance of multi-shock shields made from very thin aluminum sheets and low areal density Nextel fabric was essentially the same, on the basis of the total areal density to prevent perforation of a rear sheet. The x-ray photographs of the debris after the first two impacts show a marked similarity in the debris-cloud composition and thermal state for an aluminum and a Nextel multiple-bumper shield, as seen in Figs. 3 and 4, respectively. At this point, let us examine the aluminum multiple-bumper in some detail, to establish the fundamentals of the phenomena observed in the sequential x-ray radiography.

Four tests were conducted strictly for the purpose of better understanding the interaction between the 0.953cm projectiles and the 0.0305cm aluminum bumpers used in UDRI 4-1149. The first test, UDRI 4-1290, was done with just one bumper, t/d=0.032, to observe the initial impact shock compression and subsequent expansion of the projectile



Fig. 3. Aluminum Multi-shock Bumper Interactions. UDRI 4-1292.



Fig. 4. Nextel Multi-shock Bumper Sequences: UDRI 4-1293

and shield debris. Flash x-ray views of the shocked projectile at 6.7 micro-secs and 19.9 micro-secs after impact are shown in Fig. 5(a). In UDRI 4-1288, a second bumper was added 7.62cm behind the first, to observe it's effect on the debris cloud. These two views are shown in Fig. 5(b), with a one-to-one time correspondence with Fig. 5(a). The debris cloud from a single aluminum bumper, equal in thickness to the two bumpers used in UDRI 4-1288, is shown in Fig. 5(c) for UDRI 4-1359, again at the same times after initial impact and magnification. This test was part of a series conducted for Martin Marietta Manned Space Systems by UDRI and is discussed further in Piekutowski (1993). The t/d is 0.062 and the greater dispersion and finer particulates in the debris, compared with Fig. 5(a), is obvious. The damage done to 0.635cm, 6061-T651 aluminum witness sheets, placed approximately 38cm behind the initial bumpers, is shown in Fig. 6(a), 6(b) and 6(c). The damage is nearly the same, in terms of the equivalent hole diameter, for the double bumper of UDRI 4-1288, (Fig. 6b), and the single bumper of UDRI 4-1359, (Fig. 6c). The differences in the debris particulate number density and size distribution are also evident.

UDRI 4-1292 was the final test in this series and the debris-cloud expansion was previously shown in Fig. 3. There were two other bumpers in UDRI 4-1292 and a 0.203cm, 6061-T6 thick aluminum rear sheet, with the same 7.62cm spacing between them. The impulsive load caused a 1.9cm deep rear surface bulge, with no indication of a split or a perforation, and a molten aluminum splash on the front surface. The typical features of the debris seen after the initial impact of a projectile on a very thin bumper, for the aluminum cases shown in Figs. 3 and 5, have been analyzed by Piekutowski (1993). He describes them as: (1) an ejecta veil consisting almost entirely of bumper fragments created during the initial contact, (2) an expanding bubble of debris from the remainder of the bumper, and (3) projectile debris inside and at the front of the bumper debris bubble. The projectile debris is further subdivided by Piekutowski into a front element consisting of finely divided, molten droplets of bumper and projectile material; a central disc-like element made up of a large number of projectile fragments; and a rear element which is a hemispherical shell of fragments spalled from the rear of the spherical projectile surface. These features are clearly visible in the figures.

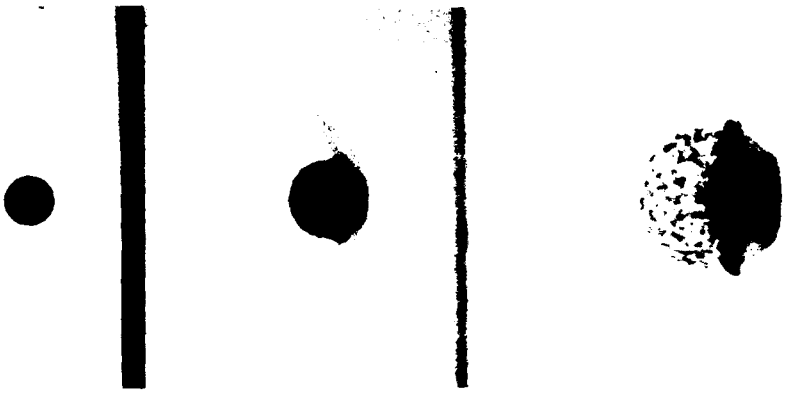


Fig. 5a. Aluminum Bumper: UDRI 4-1290.

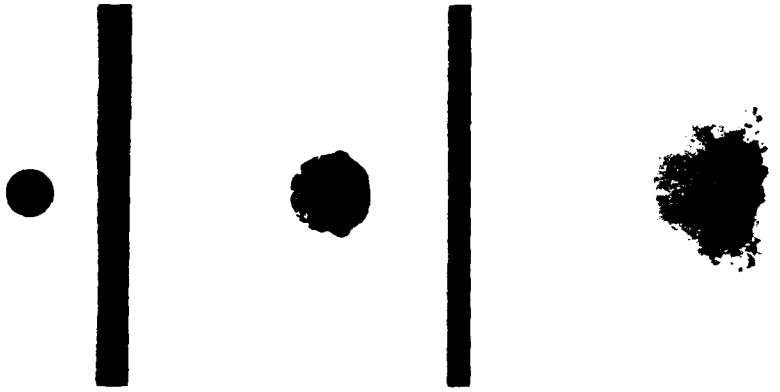


Fig. 5b. Aluminum Bumper: UDRI 4-1288.

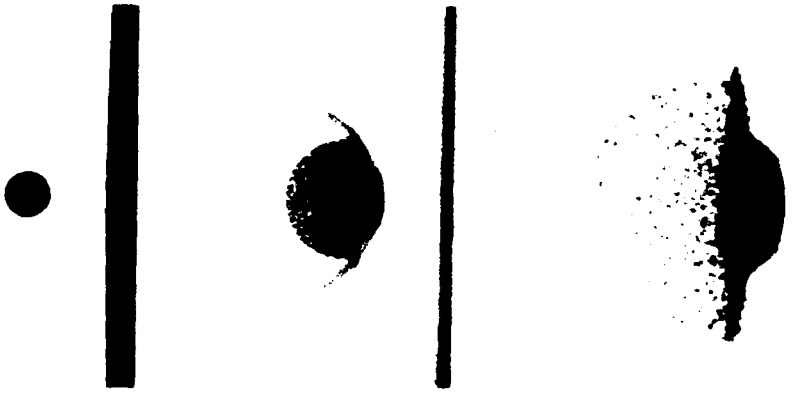


Fig. 5c. Single Aluminum Bumper: UDRI 4-1359.

Figure 4 shows the condition of the debris after the first two bumpers in UDRI 4-1293 for the 0.953cm aluminum sphere at 6.67km/s. The bumpers were Nextel AF62, and the spacing also 7.62cm. The noticeable difference in Fig. 4 from Fig. 3 is the presence of radial spikes well ahead of the main projectile mass shown in the second frame. This is projectile material jetting through the voids in the Nextel weave at speeds greater than the main body of the debris. The central disc of projectile fragments, and the rear hemispherical shell of spalled fragments are very similar for the same exposure time in Fig. 3 and Fig. 4. However, the Nextel bumper debris is too fine to be visible in this case.

The debris after the second bumper impact in both cases, with 0.0305cm aluminum in Fig. 3 and Nextel AF62 in Fig. 4, show a very similar pattern of the further breakup and radial expansion of the projectile debris. Both debris clouds indicate the presence of finer solid fragments at the front trailed by liquid and possibly vaporized material.

It was not possible for the debris to be photographed after the impact on the third Nextel bumper, due to the target setup, but this was not the case for the aluminum shield. The last frame of Fig. 3 shows that after the third impact, there are very few dense particles left and the trailing cloud is definitely a mixture of highly molten and possibly vaporous



Fig. 6a. Witness Sheet Damage for UDRI 4-1290.

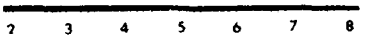


Fig. 6b. Witness Sheet Damage for UDRI 4-1288.



Fig. 6c. Witness Sheet Damage for UDRI 4-1359.

material. One would assume that the third Nextel bumper is more effective than the third aluminum bumper. This is because the same degree of melt and vaporization is seen on the rear sheet, together with the deep bulge formed by an impulsive load, with four Nextel AF62 shock surfaces as for the five for aluminum. The rear sheets for UDRI 4-1292 and UDRI 4-1293 show the typical melt and vapor deposits associated with the multiple shock process seen in Cour-Palais and Crews (1990) and Cour Palais et al (1992). Also, the areal density of each of the AF62 bumpers is 0.1g/cm^2, compared with 0.083g/cm^2 for each of the aluminum bumpers.

The bumper efficiency of the other Nextel fabrics tested was also investigated using orthogonal x-rays. For the AF40 bumper material of UDRI 4-1170, which has an areal density of 0.085g/cm^2, the projectile breakup pattern is the same as seen in Fig. 4. However, the radial expansion of the disc-element and the hemispherical shell does not occur as a result of the first impact. After the second impact the disc expands and the material in it is finer. The hemispherical shell has additional particulate matter in it and expands also, but there is little evidence of molten or vaporous material.

In the case of UDRI 4-1252, which has each bumper surface composed of three layers of AF26 for an areal density of 0.132g/cm^2, the disc element is comprised of the majority of the projectile material after the first impact. There is very little rear spallation, and evidence of the jetting noticed in Fig. 4. After the second impact, there is a further breakup and dispersal of the particulates in the disc, and evidence of a trailing molten and vaporous cloud. The BF54 bumper used in UDRI 4-1250 performs very much like the AF62 shown in Fig. 4. Both of these bumpers, with areal densities about 0.1g/cm^2, disperse the projectile debris over a larger frontal area than the AF26 in the first impact. After the second impact on the BF54 bumper, there is a larger diameter cloud of tenuous material, with a more centrally located but lesser number of particulates than the AF26 bumper.

Figures 7(a), (b) and (c) show x-ray views of the l/d=0.16 discs interacting with the first two BF54 bumpers of the three multiple-bumper shield tests, UDRI 4-1308, UDRI 4-1295, and UDRI 4-1307. In Fig. 7(a), the disc is seen to impact at a slight tilt to the surface of the first bumper; in Fig. 7(b), the disc is tilted at about 60 degrees to the bumper; and in Fig. 7(c), the disc is tilted at almost 90 degrees prior to impact. It is obvious that the severely tilted discs are only partially destroyed by the first two shields. However, the disc that strikes close to flat has exploded into a ring of small particulate matter, preceded by streamers of very fine molten or vaporous material. Behind it is a cloud of material from the rear of the projectile which appears to be composed of particulates, and molten or vaporized residue from the bumper. There appears to be a Nextel "veil" like the one for the aluminum bumper described by Piekutowski (1993). The particulate in front of the main debris cloud is from the piece of launch debris seen prior to impact. After the second impact there are a few particulates remaining in what seems to be a vapor cloud.

The shield in each of the three tests described above was the baseline mentioned previously, i.e. a four-Nextel BF54 bumper and a 0.229cm 6061-T6 aluminum rear sheet that was the ballistic limit for the 0.953cm aluminum sphere. The front surfaces of these rear sheets are shown in Figs. 8a, 8b and 8c, from which it appears that the four bumpers did not completely breakup the tilted disc(s). However, the flat on disc was easily defeated as may be seen from the molten deposit on the front face of Fig. 8a. There was a shallow bulge on the rear side of the sheet and no split or perforations.

Alme et al (1991) demonstrated the increased projectile heating produced by the multi-shock concept as compared to a single bumper or Whipple shield. These simulations were performed with the Lawrence Livermore National Laboratory CALE hydrocode, and used the aluminum multiple bumper test UDRI 4-1155 as the model. This test is not listed in Table 1 of this report, because it was performed by UDRI for x-ray test purposes. However, the work reported by Alme et al (1991) is applicable to the aluminum shields discussed in this paper. These authors concluded that thinner sheets more efficiently convert the center of mass kinetic energy to projectile internal energy, and therefore, the multi-shock shield produces significantly more projectile heating than an equivalent mass Whipple shield. The CALE simulations also show that multiple shocks can produce higher temperatures in the projectile than single sheet bumpers. A more detailed description of the test program, with additional debris cloud x-ray evidence is given in Cour Palais et al (1992).



Fig. 7a. BF54 Nextel Bumpers with l/d = 0.16 Disc at 0^0: UDRI 4-1308.



Fig. 7b. BF54 Nextel Bumpers with l/d = 0.16 Disc at 60^0 : UDRI 4-1295



Fig. 7c. BF54 Nextel Bumpers with l/d = 0.16 Disc at 90^0 : UDRI 4-1307.

Multi-Shock Performance

The results of the Nextel multiple bumper shield optimization tests, shown in Table 1, were condensed into two others. In Table 3, significant parameters for the targets in which the rear sheet was not perforated at the same ballistic limit velocity are compared. These turn out to be two aluminum and two Nextel shields. In Table 4, the same parameters for the remainder of the tests, which resulted in penetrations, are compared with the aluminum multiple bumper shield, UDRI 4-1292, of Table 3. UDRI 4-1292 resulted in the lowest ballistic limit achieved in this series, and is used as the standard for comparisons.

One trend that is apparent in the comparisons in Table 3 is that a lower total shield areal density, (a-d), is associated with a lower total bumper a-d to rear sheet a-d ratio. Areal density (or mass per unit cross-sectional area) is defined as 2/3 the product of the projectile diameter and mass density, in this paper. With reference to the two aluminum shields in Table 3, UDRI 4-1149 and UDRI 4-1292, a 15% reduction in total shield a-d was obtained when this ratio was reduced from 0.83 to 0.75. Most of this reduction was due to thinning the individual bumpers. It was also worth noting that as a result, the rear sheet had a much deeper bulge in UDRI 4-1292 than in UDRI 4-1149. This would indicate a more efficient use of the inherent 6061-T6 alloy strain before failure property.

Turning to the two Nextel shields in Table 3, UDRI 4-1151 and UDRI 4-1293, the total bumper a-d was decreased by removing one of the bumpers. This resulted in lowering the bumper to rear sheet a-d ratio from 0.81 to 0.64, and a 8.9% lower total shield a-d. The rear sheet in UDRI 4-1293 had a deeper bulge than the rear sheet for UDRI 4-1151, which is a measure of the higher efficiency of the lighter shield. However, it is highly probable that a 0.216cm rear sheet, if it had been available, would not be perforated, judging by the other tests shown in Table 4. This would make the total shield a-d ratio 0.68, which brings the Nextel and aluminum low weight shields closer together.



Fig. Sc Damage to Rear Sheet by the Ed 0.16 Disc at 0° UDRI 4 1808

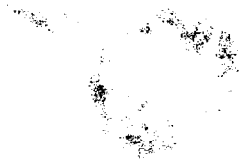


Fig. Sc Damage to Rear Sheet by the Ed 0.16 Disc at 60° UDRI 4 1258



Fig. Sc Damage to Rear Sheet by the Ed 0.16 Disc at 90° UDRI 4 1807

Table 4 lists the same parameters as [illegible] Next[illegible] sheets tested and compares them to the previously mentioned aluminum shields. Although these shields failed to meet the no perforations, they can be used to develop the trade-offs between [illegible]. The shield that came closest to matching the aluminum standard in terms of [illegible] UDRI 4 1258 and UDRI 4 1284. Both of these had the mixed Al-62 and BF54 Nextel bumpers, with 0.250" rear sheets. The rear sheets did not spall or let the projectile load, but they both were regarded as failures because of [illegible] perforations. UDRI 4 1284, which has the BF54 as the initial bumper surfaces, has a slightly higher BL than UDRI 4 1258 which has the Al-62 initial layers.

Further attempts to lower the total bumper to rear sheet areal density and the total areal density shown in Table 4. UDRI 4 1170 and UDRI 4 1174 used the Al-60 Nextel bumpers with 0.250" rear sheets. The only difference being four and five bumpers, respectively. UDRI 4 1170 had a total areal density of 0.62 g/cm² with the bumper to rear sheet areal ratio of 0.62 and was well over the ballistic limit. With the areal density per a total shield areal density of 0.78 g/cm² and a bumper to rear sheet areal ratio of 0.78, UDRI 4 1174 was [illegible] limit. It failed from use of [illegible] perforations, like UDRI 4 1183 and UDRI 4 1284. With the [illegible] and the deep craters on the rear sheets signifying shield effectiveness as previously mentioned. Finally, UDRI 4 1255 represented an attempt to lower the total shield areal density by increasing the bumper to rear sheet areal ratio. It had four bumpers composed of three layers of Nextel Al-26 stitched together, and a rear sheet 0.268" thick. This combination gave a total shield areal density of 0.902 g/cm², consistent with the aluminum standard, but the bumper to rear sheet areal ratio was 1.22. The target had the deep craters associated with the others of the same total shield areal density, but failed because of the perforations.

The trend that the maximum effectiveness of [illegible] bumper to rear sheet areal density ratio of 0.7" to 0.9 kms BL is obtained when the bumper to rear sheet areal ratio is [illegible] 0.4 for a Nextel bumper and 0.6 for a rear sheet shield, was most evident. Each [illegible] was conducted at NASA Johnson Space Center Hypervelocity Impact Research Laboratory (HIRL) was used to [illegible] Nextel multiple bumper shields.

Table 5 [illegible] Shield Parameters BL Results

d_p = 0.058 cm, ρ_p = 2.02 g/cm³, Al = Al 2024-T4, M = M 1.27 g/cm², ρ_{bp} = 1.78 g/cm²

[illegible] No.	[illegible]	[illegible]	[illegible]	[illegible]
[illegible]	[illegible]	[illegible]	[illegible]	[illegible]

Table 4. Comparison of Shield Parameters: Non BL Results
d_p = 0.953 cm; 2017-T4 AL; M =1.27 g; m_p = 1.78 g/cm^2

TEST NUMBER	UDRI 4-1292	UDRI 4-1153	UDRI 4-1154	UDRI 4-1250	UDRI 1170	UDRI 1174	UDRI 1253
BUMPERS	5xAL1100-0	2AF62 2BF54	2BF54 2AF62	4xBF54	4xAF40	5xAF40	12xAF26
V_p (Km/s)	6.70	6.75	6.90	6.70	6.70	6.60	6.80
BUMPER a-d; Σm_b (g/cm^2)	0.413	0.417	0.417	0.433	0.342	0.427	0.528
REAR SHEET; t_r (cm)	0.203	0.203	0.203	0.203	0.203	0.203	0.528
REAR SHEET a-d; m_r (g/cm^2)	0.551	0.551	0.551	0.551	0.551	0.551	0.160
SHIELD a-d; m_{tot} (g/cm^2)	0.964	0.968	0.968	0.984	0.893	0.978	0.962
$\frac{\Sigma m_b}{m_r}$	0.750	0.757	0.757	0.786	0.621	0.775	1.217
$\frac{m_{b1}}{m_p}$	0.046	0.056	0.061	0.061	0.048	0.048	0.074
$\frac{m_r}{m_p}$	0.310	0.310	0.310	0.310	0.310	0.310	0.244
$\frac{\Sigma m_b}{m_p}$	0.232	0.234	0.234	0.243	0.192	0.240	0.297
REAR SHEET DAMAGE	NO PERF: DEEP BULGE	1 PERF: DEEP BULGE	1 PERF: DEEP BULGE	1 PERF: DEEP BULGE	LARGE PETALLED HOLE	1 PERF: DEEP BULGE	3 PERFS: DEEP BULGE

These are shown in Table 5.

The first two tests, HIRL B-192 and HIRL B-193, had four Nextel AF40 bumpers with 0.051cm and 0.064cm, 6061-T6 aluminum rear sheets, respectively. All the spaces between the elements were 3.81cm. HIRL B-193 was the BL for the AF40 bumper shields with a total a-d of 0.517g/cm^2 and a bumper to rear sheet ratio of 2.0. It's rear sheet had a deep, lumpy bulge with two very small surface spalls.

The third test shown in Table 5, HIRL B-195, had four AF26 bumpers and a 0.127cm rear sheet, with the same spacing between elements. In this test the total shield a-d was 0.516g/cm^2 and the bumper to rear sheet a-d ratio, 0.5. The rear sheet had a deep smooth bulge and no perforations and was probably slightly over the BL. In any case the two tests HIRL B-193 and B-195, with the same total shield a-d, illustrate the trend observed in the UDRI series, that it is more efficient to concentrate the total a-d in the aluminum rear sheet than in the multiple bumpers. This holds true for Nextel as well as the aluminum bumpers. HIRL tests B-214 and B-192 have the same total shield weight, but with opposite emphasis on the bumper and rear-sheet areal densities. Both rear sheets failed, B-192 by perforation and B-214 by impulsive loading. This is not all due to the 6% higher velocity.

Table 5. Comparison of Bumper to Rear Sheet a-d Ratio
d_p = 0.476 cm; 2024-T4 AL; M =0.16 g; m_p = 0.889 g/cm^2

TEST NUMBER	HIRL B-192	HIRL B-193	HIRL B-195	HIRL B-214
BUMPERS	4xAF40	4xAF40	4xAF26	4xAF26
V_p (Km/s)	7.00	7.15	7.06	7.43
BUMPER a-d; Σm_b (g/cm^2)	0.345	0.345	0.172	0.172
REAR SHEET; t_r (cm)	0.051	0.064	0.127	0.102
REAR SHEET a-d; m_r (g/cm^2)	0.138	0.172	0.344	0.275
SHIELD a-d; m_{tot} (g/cm^2)	0.483	0.517	0.516	0.447
$\frac{\Sigma m_b}{m_r}$	2.500	2.000	0.500	0.630
$\frac{m_{b1}}{m_p}$	0.097	0.097	0.048	0.048
$\frac{m_r}{m_p}$	0.155	0.193	0.383	0.310
$\frac{\Sigma m_b}{m_p}$	0.388	0.388	0.191	0.193
REAR SHEET DAMAGE	2 PERFS:DEEP LUMPY BULGE	NO PERFS: 2 SPALLS DEEP, LUMPY BULGE	NO PERFS: DEEP SMOOTH BULGE	DEEP DRAWN AND SPLIT INTO 3 SEGMENTS

In keeping with the equations developed by Cour-Palais and Crews (1990), the constants C_3 and C_4 were calculated for the UDRI ballistic limits shown in Table 1 and the HIRL ballistic limits given in Table 5. These are listed in Table 6 and compared with the values given in the referenced paper for the aluminum and Nextel multiple-bumper tests conducted with the 0.318cm aluminum spheres, HIRL A-965 and HIRL A-433. It is apparent that the optimized aluminum multi-bumper shield URDI 4-1292 and the HIRL A-965 of Cour-Palais and Crews (1990), obtained with the 0.318cm sphere, have almost identical C_3 and C_4 values. Notice also the three-to-one diameter scaling in the individual and total a-d values and that the bumper to rear sheet a-d ratios are close, for almost the same BL. The optimized Nextel multi-bumper shield UDRI 4-1293, with the 0.953cm sphere, has very nearly the same C_3 and C_4 values as the 0.476cm sphere results for HIRL B-195. Although the a-d values for the rear sheet and the total shield are in good agreement for the two-to-one diameter ratio, the total bumper a-d values are further off. As this is born out by the bumper to rear sheet a-d ratios, it implies that another Nextel, with an a-d of 0.05g/cm^2 was needed for the individual bumpers for HIRL B-195. This was not available at the time.

Table 6. Ballistic Limit Constants

	12XAF26	5XAF62	4XBF54	4XAF62	5XAL1100	4XAF40	4XAF26	5X1100	4XAF26
TEST NUMBER	UDRI 4-1150	UDRI 4-1151	UDRI 4-1152	UDRI 4-1293	UDRI 4-1292	HIRL B-193	HIRL B-195	HIRL A-965	HIRL A-433
d_p (cm)	0.953	0.953	0.953	0.953	0.953	0.476	0.476	0.318	0.318
M_p (g/m)	1.270	1.270	1.270	1.270	1.270	0.159	0.159	0.047	0.047
V_p (Km/s)	6.80	6.80	6.80	6.80	6.70	7.15	7.060	6.50	6.60
Σm_b (g/cm^2)	0.528	0.500	0.433	0.400	0.413	0.345	0.172	0.138	0.172
m_r (g/cm^2)	0.621	0.621	0.621	0.621	0.551	0.172	0.344	0.173	0.214
m_{tot} (g/cm^2)	1.149	1.121	1.054	1.021	0.964	0.517	0.516	0.311	0.386
$\frac{\Sigma m_b}{m_r}$	0.850	0.810	0.700	0.640	0.750	2.000	0.500	0.800	0.800
C_3 (SHIELD)	124.2	189.0	113.7	112.0	164.7	106.0	107.1	164.7	128.4
C_4 (REAR SHEET)	67.1	104.7	67.0	68.1	94.1	35.2	71.4	91.6	71.2

Some other facts shown in Table 6 need to be mentioned at this time. UDRI 4-1150 and HIRL A-433 also scale with the three-to-one diameter ratio in every category. As neither test was optimized, the equation constants are given for reference only. The five-element Nextel multiple-bumper shield, UDRI 4-1151, was included for comparison with its aluminum equivalent, UDRI 4-1292, and four-element Nextel, UDRI 4-1293.

It is now possible to give average constants for equations 3 and 4 given by Cour-Palais and Crews (1990), reproduced below as (1) and (2), that will be valid for diameters between 0.318 and 0.953cm at 6.7 to 7.15km/s. The equations are:

$$\left\{\Sigma_1^n m_b + m_r\right\} = \frac{C_3 x M_p x V_p}{(\Sigma_1^n \Delta S)^2} x \left\{\frac{2.76x10^8}{Y_t}\right\}^{\frac{1}{2}}, \text{ gm/cm}^2 \qquad (1)$$

and,

$$m_r = \frac{C_4 x M_p x V_p}{(\Sigma^n \Delta S)^2} x \left\{\frac{2.76x10^8}{Y_t}\right\}^{\frac{1}{2}}, \text{ gm/cm}^2 \qquad (2)$$

For Nextel multiple-bumpers with aluminum rear sheets:

$$C_3 = 110\text{s/km and } C_4 = 70\text{s/km}$$

For aluminum multiple-bumpers with aluminum rear sheets:

$$C_3 = 165\text{s/km and } C_4 = 93\text{s/km}$$

The constants are for s=8d and n=4 for the Nextel bumpers, and s=8d and n=5 for the aluminum bumpers.

The comparable constants for the Nextel multiple-bumper with the l/d=0.16 disc impacting flat are obtained from UDRI 4-1315 as:

$$C_3 = 119\text{s/km and } C_4 = 70\text{s/km}$$

These are close to the spherical projectile values shown above. This could mean that a sphere and equal mass disc, if it impacts on it's flat side, require the same a-d shields and rear sheets. If there had been the time to optimize the disc result, it would probably have the same values of C_3 and C_4 as the optimized Nextel multiple-bumper impacted by the spherical projectile given above.

Christiansen (1992) presents a modified form of equations 1 and 2 for the Nextel multiple-bumper with the aluminum rear sheet. The constant used in equation 3 of the referenced paper for the total bumper areal density, is equivalent to 2/3 the values given in this paper, due to the differences in definition. Also, the constant in equation 4 reflects the optimization of the previously mentioned HIRL A-433, shown in Table 6, by NASA Johnson Space Center. The shield approach given in Christiansen (1992) exemplifies the high bumper to rear sheet a-d which gives approximately the same total a-d as the opposite approach, as discussed above. Christiansen also discusses the effect of obliquity and low velocity impact on the Nextel multiple-bumper shield described in the same reference.

Further studies with Nextel multi-shock shields are reported by Boslough et al (1993), using the Sandia National Laboratories flat plate launcher. These were at velocities between 9.85 and 10.22km/s with nominally 0.6g aluminum thin discs which were slightly bowed prior to impact. The targets were the same as UDRI 4-1250, with BF54 Nextel bumpers and the 0.203cm, 6061-T6 aluminum rear sheet. In one test the BF54 was replaced by the AF62 Nextel. Coefficients were calculated for three tests that survived the process, which are as follows:

$$C_3 = 150\text{s/km and } C_4 = 84\text{s/km}$$

The average momentum of the three Nextel multi-shock tests in Boslough et al (1993) referred to is 6.1x10^5dyne-secs and for UDRI 4-1315 it was 8.23x10^5dyne-secs. If constants obtained from UDRI 4-1315 are momentum-scaled, the Sandia values would have been 161s/km and 95s/km respectively. Considering the differences in the tests, i.e., launch technique, projectile shape and mass calculation, and target damage verification, it would seem, on the basis of the disc tests, that the UDRI test results can be scaled by momentum with reasonable accuracy to orbital debris velocities.

CONCLUSIONS

The series of development hypervelocity impact tests conducted at UDRI explored the properties of Nextel multiple-bumper shields with the use of multiple-exposure, orthogonal x-radiography. Successive views of the projectile and fragments after impact with the first three bumpers clearly showed the shock excitation of the debris to higher energy states. In addition, light-weight orbital debris shields, comprising various Nextel fabric multiple-bumpers and aluminum rear sheets, were investigated using 1.27g aluminum spheres at 6.7km/s and equal mass L/D = 0.16 aluminum discs at 6.2km/s. The areal density required to prevent perforation of the rear sheet for the sphere was approximately 1g/cm^2, using either the BF 54 or the AF62 Nextels. It was also found that using a combination in which two BF54 bumpers preceded two AF62 bumpers was slightly superior to the reverse case, in terms of increasing the ballistic limit. Also, there are two ways to obtain a light-weight Nextel-aluminum shield for the same ballistic limit; making the bumpers a higher areal density than the rear sheet areal density or vice-versa. The more efficient shield, from the view-point of maximizing the material properties of the rear sheet and a lower overall weight, is the second choice, obtained by using a Nextel multi-bumper to rear sheet areal density ratio of 0.64. It was also found that the disc would penetrate the 1g/cm^2 shield if it struck at a tilt angle other than about 5 degrees.

An all aluminum multiple-bumper shield, with five 0.03cm, 1100-0 bumpers and a 0.203cm 6061-T6 rear sheet, had an areal density of 0.964g/cm^2 for the same ballistic limit as the Nextels mentioned previously. It is interesting, from the physical process involved, that the total bumper areal densities (0.4g/cm^2) and the total shield areal densities of the two shields are almost identical. However, the aluminum shield requires a lower areal density rear sheet than the Nextel for the same ballistic limit, because it has five shock surfaces versus the four for the Nextel.

Constants for the equations given previously by Cour-Palais and Crews (1990) have been refined and it has been shown that the multiple-bumper scales with projectile momentum between 6 and 10km/s. The extension to 10km/s relies on the results of the Nextel BF54 and AF62 multiple-bumper tests done at the Sandia National Laboratories flat-plate launcher facility on the same configurations that were successfully tested at UDRI.

ACKNOWLEDGEMENTS

The authors wish to acknowledge the support for this work provided by NASA Johnson Space Center under Contract No. NAS9-18200, Exhibit "C" and the Office of the Director of the University of Dayton Research Institute.

REFERENCES

Alme, M.L., E.L. Christiansen and B.G. Cour-Palais (1991). Hydrocode Simulations of the Multi-shock Meteoroid and Debris Shield, Shock Compression of Condensed Matter 1991, 975-978, Elsevier Science Publishers, B.V. (North Holland).

Boslough, M.B., J.A. Ang, L.C. Chhabildas, B.G. Cour-Palais, E.L. Christiansen and J.L. Crews (1993). Hypervelocity Testing of Advanced Shielding Concepts for Spacecraft Against Impacts to 10km/s, Int. J. Impact Engng., 14.

Christiansen, E.L. (1992). Performance Equations for Advanced Orbital Debris Shields, AIAA 92-1462.

Cour-Palais, B.G. and J.L. Crews (1990). A Multi-shock Concept for Spacecraft Shielding, Int. J. Impact Engng. 10, 135-146.

Cour-Palais, B.G., A.J. Piekutowski, K.V. Dahl and K.L. Poormon (1992). The Nextel Multi-shock Shield Tests: 1990-1991. MDC 92H0432. McDonnell Douglas Space Systems Co.

Piekutowski, A.J. (1993). Characteristics of Debris Clouds Produced by Hypervelocity Impact of Aluminum Spheres with Thin Aluminum Sheets, Int. J. Impact Engng., 14.

Int. J. Impact Engng Vol.14, pp.205–216, 1993
Printed in Great Britain

0734-743X/93 $6.00+0.00
1993 Pergamon Press Ltd

THE PRODUCTION AND EVOLUTION OF IMPACT-GENERATED MAGNETIC FIELDS

David A. Crawford and Peter H. Schultz

Department of Geological Sciences, Brown University, Providence, RI 02912

ABSTRACT

The production of magnetic fields within impact-generated plasma may explain magnetic fields that have been observed during hypervelocity impact experiments at the NASA Ames Vertical Gun Range. The effect of impact angle on the production and subsequent evolution of impact-generated magnetic fields is assessed using magnetic field data obtained during macroscopic hypervelocity impacts conducted within two ambient magnetic field environments. The configuration and duration of spontaneous impact-generated magnetic fields are found to have a strong dependence on impact angle, exhibiting a smooth transition from a cylindrically symmetric field configuration at vertical incidence to a strong bilaterally anti-symmetric field configuration at high obliquity; hence, crater-related paleomagnetic fields may yield a diagnostic signature of impact angle where other clues (shape, ejecta pattern) are absent or ambiguous. As a direct result of some surprising experimental results, a first-order model of field generation during the cavitation regime of high incidence angle hypervelocity impacts is explored. A possible consequence of this model is that magnetic fields produced during hypervelocity impacts (especially those that form large craters) may be an important component of planetary magnetism—especially lunar magnetism during the last ~3.6 billion years.

INTRODUCTION

The production of transient magnetic fields associated with plasma produced by hypervelocity meteoroid impacts has been invoked to possibly explain the remnant magnetization of certain "young" (3 Ma - 1.5 Ga) lunar samples (Sugiura *et al.*, 1979; Collinson, 1984), as well as broad areas of the lunar surface (Gold and Soter, 1976; Martelli and Newton, 1977; Srnka *et al.*, 1979; Schultz and Srnka, 1980; Srnka and Schultz, 1980; Hood and Vickery, 1984; Lin *et al.*, 1988; Hood and Huang, 1991). Dachille (1978) proposed that transient magnetic fields could be produced during hypervelocity impacts by inertial charge separation occurring in the initial moments of plasma production. Srnka (1977) and Srnka *et al.* (1979) proposed that magnetic fields could be generated in quasi-neutral plasma produced during the early stages of hypervelocity impacts. The proposed mechanism is similar to the self-generation of magnetic fields in plasma produced by pulsed laser experiments as discussed by Pert (1977, 1981). The formulation is the magnetohydrodynamic (MHD) equation of a low temperature plasma with a source term arising from electron thermal pressure gradients:

$$\frac{\partial \mathbf{B}}{\partial t} = \nabla \times \mathbf{v} \times \mathbf{B} + \frac{c^2}{4\pi\sigma} \nabla \times \nabla \times \mathbf{B} + \frac{ck}{ne} \nabla T \times \nabla n \qquad (1)$$

$$= \text{advection} + \text{diffusion} + \text{source}$$

where **v** and σ are the plasma's fluid velocity and electrical conductivity respectively; c is the speed of light; k is Boltzmann's constant; and n, T and e are the electron number density, temperature and charge, respectively. The first term on the right of (1) represents advection of **B** due to fluid motion; the second represents diffusion of **B** through the electrically conductive plasma. The third term is a source term which arises from drift currents due to thermal pressure gradients (∇nkT) and is non-zero when the electron temperature and density gradients are not aligned. On the relatively short time scale of projectile penetration and cavitation, the diffusion term is generally neglected (Srnka, 1977).

The production and evolution of magnetic fields associated with plasma produced by experimental hypervelocity impacts may be attributed to many processes including, but not limited to, field generation from nonaligned electron density and temperature gradients within plasma (Srnka 1977; Srnka *et al.* 1979), field generation from charge separation and transport (e.g. Dachille, 1978), field amplification that can occur during cavitation, field decay that occurs as the plasma expands freely, and field rarefaction that occurs as the electrically conductive plasma expands into the ambient magnetic field environment (Crawford and Schultz, 1992). In the interpretation of magnetic fields associated with quasi-neutral plasma generated by experimental hypervelocity impacts, a two component magnetic field model can be used (Fig. 1). One component is due to rarefaction of the ambient field as the "diamagnetic" plasma expands into the ambient magnetic field; the other is the plasma's internal field (seen outside the plasma as a leakage field) that arises from spontaneous field generation, amplification and/or decay during the projectile penetration, cavitation and late-time expansion regimes.

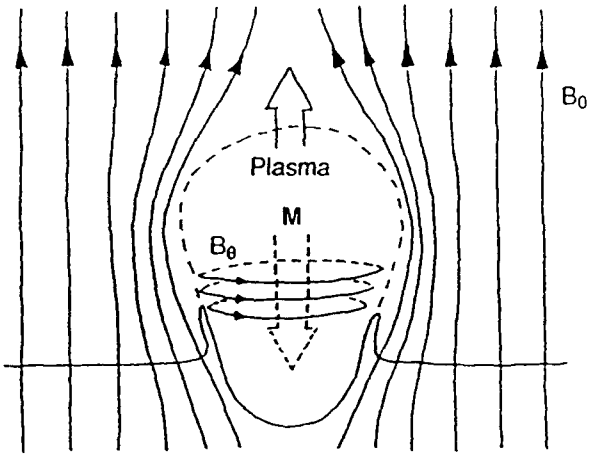


Fig. 1. First-order model of impact-generated magnetic fields (after Srnka *et al.*, 1979). The radially expanding quasi-neutral plasma can be approximated as a diamagnetic material with dipole moment **M**, reducing the intensity of the ambient field ($\mathbf{B_0}$) below the impact point. Nonaligned electron density and temperature gradients can produce a toroidal field (B_θ) confined to the plasma although leakage fields may penetrate into the target.

Magnetic field rarefaction appears as the plasma excludes the ambient magnetic field while expanding above the impact point. In this way, it acts as a diamagnetic material (Rayzer, 1964) producing a zone about the point of impact where the magnetic field is temporarily reduced from its initial value. Magnetic field generation arises from the source term on the right side of equation (1) and is independent of the initial magnetic field strength provided that this initial value is lower than the limit imposed by finite energy density. Magnetic field amplification and decay occur due to advective processes within impact-generated plasma. For a brief period of time after the projectile has penetrated the target, vapor/plasma production is greatest along the sides of the projectile and cavitation occurs, i.e., a portion of the plasma is directed inward upon itself as the plasma converges above the rear of the greatly deformed projectile (see O'Keefe and Ahrens, 1977). Due to the convergence of the flow field during this time, amplification of the ambient and/or generated field can occur. This process may explain a brief enhancement of the ambient magnetic field that we observed during many high incidence angle experimental impacts. In the discussion section of this paper, a first-order, one-

dimensional model of this process is considered. During late-time plasma expansion, the plasma fluid velocity is directed outward and the field decays.

EXPERIMENTS

Experimental investigation of magnetic field generation and evolution during hypervelocity impacts has been performed at the NASA Ames Vertical Gun Range, Moffett Field, California (Crawford and Schultz, 1988, 1991). The vertical gun is a two-stage hydrogen light gas gun capable of launching macroscopic projectiles at up to 7 km/s with the angle of impact varying from nearly horizontal to vertical in increments of 15° (see Gault and Wedekind, 1978). The large impact chamber is large enough to accommodate, surrounding the impact point, a mu-metal shield that reduces the 0.35 G ambient (terrestrial) magnetic field to levels comparable with the free solar wind value of lunar surface field strengths. Impacts of aluminum projectiles into powdered dolomite ($Mg_{0.5}Ca_{0.5}CO_3$) targets have demonstrated repeatability and readily produce a self-luminescent, slightly ionized vapor cloud that we infer to be the source of impact-generated magnetic fields. Through the use of high frame-rate photography, the vapor's fluid velocity, total mass and energy can be characterized (Schultz, 1988; Schultz and Gault, 1990a).

Magnetic field production was observed during laboratory hypervelocity impacts conducted within two different ambient magnetic field environments in order to separate spontaneous field generation from the interactions of the expanding, electrically conductive plasma with the ambient magnetic field. A moderate field environment of 34±6 mG intensity, oriented ~45° from horizontal within the plane of the projectile trajectory was produced by using a single layer mu-metal shield in a capped cylindrical configuration (1 m diameter by 1 m high, see Fig. 2). A low field environment of 4.5±0.8 mG intensity (comparable to lunar surface strength: 0-5 mG), oriented vertically, was produced by adding an inner mu-metal layer to the shield. The inner layer was degaussed periodically by application of a ramped 60-Hz vertical magnetic field.

Impact-generated magnetic fields were measured by 15 magnetic search coils (Fig. 2), each capable of measuring a single component of $\partial B/\partial t$. Each coil consisted of several hundred turns of 30 gauge copper magnet wire wound helically on a plastic form approximately 8 cm in diameter. All the coils and leads were electrostatically shielded by 1-mm-thick grounded aluminum foil. The signals from the

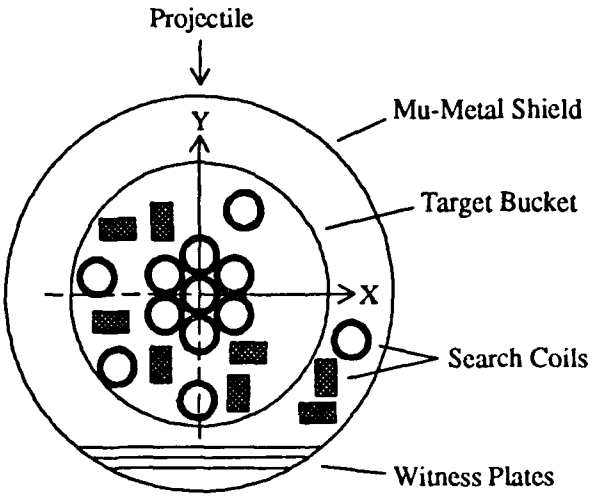


Fig. 2. Experimental setup for the measurement of impact-generated magnetic fields. View from above. The mu-metal shield is a pair of concentric capped cylinders approximately 1 m in diameter by 1 m high. The projectile impacts the target at the origin. Coils that measure the magnetic field are located above and below the target surface (usually buried in the target). The witness plates break up and contain ricochet fragments produced by oblique (<30°) impacts.

coils were amplified by instrumentation amplifiers and sent to a multichannel digital acquisition system where they were simultaneously converted into 8-bit digital form at a rate of 500 kHz (2 μs per conversion) for later computer readout. The data from each channel were integrated with a robust technique developed using known magnetic field waveforms.

Thirty-three experimental impacts have been used to map the spatial and temporal character of impact-generated magnetic fields. The experiments used 0.64-cm-aluminum spherical projectiles impacting a powdered dolomite target. Dependence on impact angle and the ambient field environment were explored whereas the impact velocity was held as constant as possible from shot to shot. Fifteen magnetic search coils were buried within the target, arrayed horizontally (but measuring the three field components) 7-9 cm below the impact point. The coils are laid out using a Cartesian coordinate system where the origin is the impact point, the z axis is vertical and the y axis defines the horizontal projection of the projectile trajectory (but oriented uprange) prior to oblique impacts. Each magnetic search coil is oriented parallel (e.g. $+x$, $+y$ or $+z$) or anti-parallel (e.g. $-x$, $-y$ or $-z$) to the x, y or z axes. During the low field experiments (19 experimental impacts), the ambient magnetic field was oriented vertically (B_x, $B_y < 0.5$ mG, $B_z = 4.5 \pm 0.8$ mG).

Maps of the 3-D impact-generated magnetic field (Fig. 3) were formed by combining the data from experiments with complementary coil locations and orientations. The data were linearly time-shifted to account for slight variations of impact velocity and then combined using a three-dimensional Gaussian spatial filter to produce plots showing the configuration of the magnetic field at particular times. No attempt is made to force the result to be divergence free. Instead, the relatively weak non-zero divergence in the resulting plots can be used as an estimate of the accuracy of the interpolation.

Dependence on Impact Angle

Results from experiments conducted in the low field environment (4.5±0.8 mG), described above, are shown in the plots of Fig. 3. Magnetic field observations are shown for six different impact angles: 90°, 75°, 60°, 45°, 30°, and 15° from horizontal. Each plot is a compilation of data collected in 2-5 impact experiments (30-75 measurement locations/orientations) and depicts a 2-D slice (in a horizontal plane ~9 cm below the target surface) of the average magnetic field observed 0.3-0.5 ms after impact.

At early time, the magnetic field within the impact-generated plasma is probably very intense, as predicted by theory, but because it is confined to such a small region (within 1-3 projectile radii of the impact point), its intensity rapidly diminishes with distance and is difficult to observe. At late time, the magnetic field is spread over a large region within the expanding plasma, so that it can be readily measured, but is relatively weak. With this in mind, the magnetic fields produced by vertical impacts and shown in Fig. 3 are consistent with the two component magnetic field model discussed earlier.

The azimuthal (spiral) magnetic field pattern that appears during vertical impacts at relatively early times is consistent with spontaneous field generation arising from the source term of equation (1). The radial and vertical field components are consistent with a first-order plasma magnetic dipole moment oriented in the same direction as the ambient field and may be due to ambient field amplification during cavitation. Rarefaction of the ambient field is also likely to occur, but, due to the relatively weak lateral expansion of the plasma, never appears as a significant component of the overall field pattern.

During impacts at 75° and 60° from horizontal, the vertical field pattern is initially in the same direction as the ambient field but then develops into a rarefaction field with opposite polarity (Fig. 3). The early time field pattern is, again, consistent with ambient field amplification during cavitation. At later time the plasma is directed away from vertical by the configuration of the transient cavity resulting in a more efficient interaction with the ambient field and, therefore, a stronger rarefaction component.

During impacts at 45°, 30° and 15° from horizontal, ambient field amplification cannot be seen in the observations, yet the spontaneous magnetic field is enhanced overall. The field is stronger downrange and exhibits bilateral anti-symmetry across the plane containing the projectile trajectory. The strength of the anti-symmetric part of the field patterns, especially for low angle impacts, strongly suggests that much of the field observed in these experiments is spontaneous and is consistent with earlier work that demonstrated the repeatability of impact-generated magnetic fields in various ambient field environments (Crawford and Schultz, 1988, 1991).

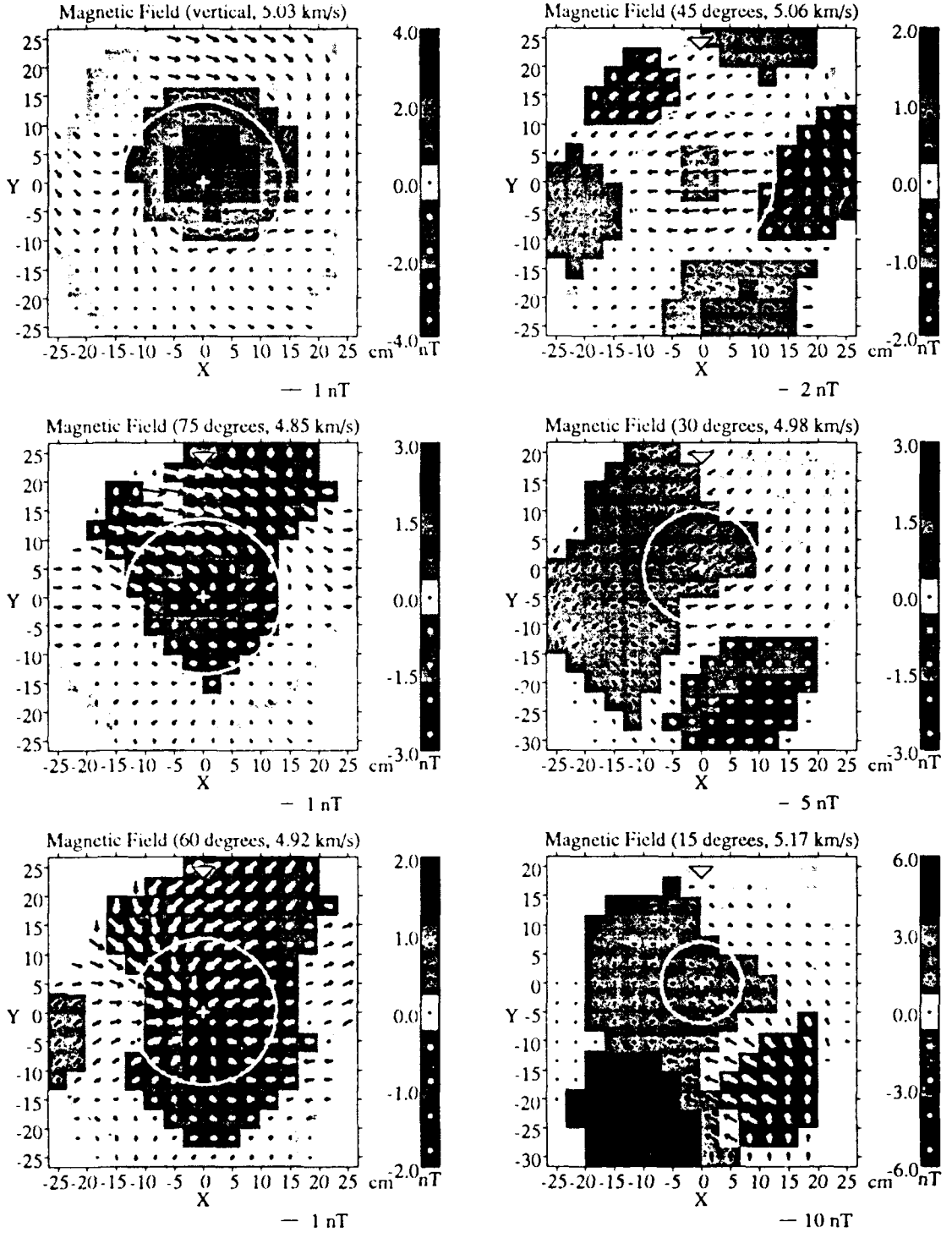


Fig. 3. Magnetic field dependence on impact angle as observed in a low magnetic field environment (4.5±0.8 mG oriented vertically—up) 0.3-0.5 ms after hypervelocity impacts of 0.64-cm aluminum projectiles into a powdered dolomite target. The observations were made in a horizontal plane ~9 cm below the impact point. Magnetic field units are nT (1 nT = 10^{-5} G). The impact angle was varied between 90° from horizontal (upper left) and 15° (lower right) in 15° increments. Shading represents the vertical component of the magnetic field whereas vectors represent the horizontal component with white vectors appearing where the field is directed into the page (down). The impact point is shown by the white cross and crater extent is shown by the white circle. The white triangle indicates the projectile trajectory prior to impact. Note the changes in scale.

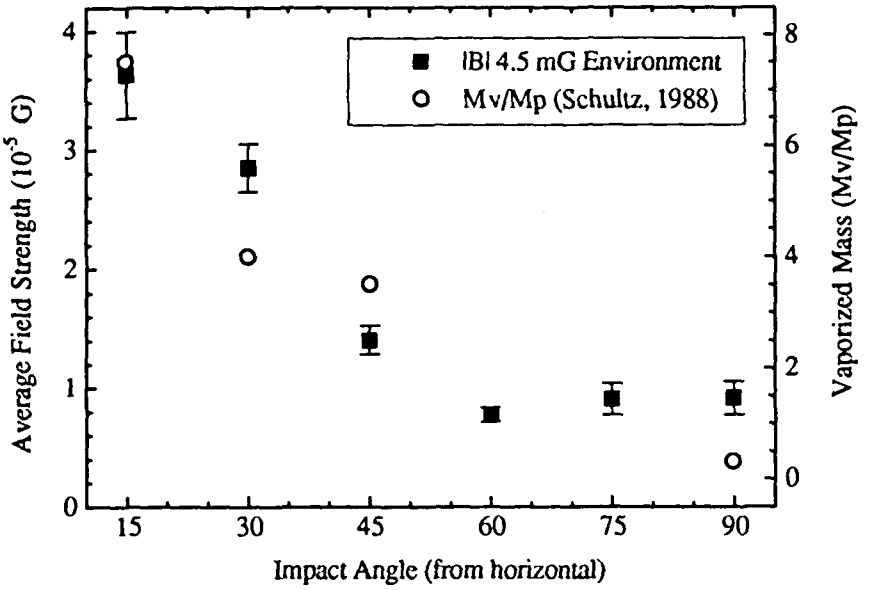


Fig. 4. Average magnetic field strength (squares) as a function of impact angle measured during the time interval 0.3-0.5 ms after impact. Error bars are the standard error of the mean. Overall vaporization efficiency (M_v/M_p, circles) is plotted for impact angles of 15°, 30°, 45° and 90° from horizontal for comparison (from Schultz, 1988).

Figure 4 shows the average magnetic field strength as a function of impact angle 0.3-0.5 ms after impact corresponding to the time interval shown in the plots of Fig 3. The error bars are the standard errors of the mean which primarily reflect the variance from shot-to-shot. The figure includes experimental vaporization data for the same target material (dolomite) from Schultz (1988) as a comparison. Although not conclusive, the consistency of the data suggests that impact-generated magnetic field strength has a similar impact-angle dependence to overall vapor production. As plasma generated by low-angle impacts generally expands downrange against the target surface, part of the enhancement at low impact angles may be due to the plasma's close proximity to the target surface.

DISCUSSION

To help interpret the experimental data, we start with equation (1) and develop a first-order, one-dimensional model of impact-generated plasma that incorporates advection of the electrically conductive plasma as well as electron density and temperature gradients that are expected to appear within the plasma during the early stages of vertical meteoroid impact. Because the thermal pressure gradients that generate the magnetic field of equation (1) also change the electron kinetic energy, the evolution of electron specific (kinetic) energy (W) needs to be evaluated (Pert, 1977; Srnka *et al.*, 1979; Crawford and Schultz, 1992). By expressing electron temperature (T) in terms of the electron specific energy (W) a system of coupled partial differential equations is obtained that relates the evolving electron energy (W) with the magnetic field:

$$\frac{\partial \mathbf{B}}{\partial t} = \nabla \times \mathbf{v} \times \mathbf{B} + \frac{2m_i c}{3Ze}\frac{1}{n}\nabla W \times \nabla n \qquad (2)$$

$$\frac{\partial W}{\partial t} = -\nabla \cdot (W\mathbf{v}) - \frac{m_i c}{6\pi Zde}\frac{1}{n} W \nabla n \cdot \nabla \times \mathbf{B} \qquad (3)$$

$$= \text{advection} + \text{source}$$

where d is the ion mass density, and Z and m_i are the average ion charge and mass respectively. This system of differential equations will, under certain conditions, exhibit unstable growth primarily limited by the finite thermal energy density (Pert, 1977; Srnka *et al.*, 1979). It may well be that

magnetic field growth reaches the limit imposed by finite thermal energy density during projectile penetration and/or cavitation as will be shown. Although energy density in the plasma is at most weakly dependent on projectile size, the ratio of projectile diameter to crater diameter for gravity-limited crater growth increases. Consequently, impact-generated magnetic fields as measured (or experienced) at the same diameter-scaled distance may have significance for impact craters (especially large craters) on Earth, the Moon and planetary surfaces.

Because vertical impacts exhibit azimuthal symmetry, a cylindrical coordinate system is appropriate. For a first-order semi-analytical treatment, we consider the case where velocity and the electron specific energy (W) vary only as functions of r and electron number density (n) varies only as a function of z (which may occur at the interface between the projectile and target materials). Under cylindrical symmetry, azimuthal gradients can be neglected. Provided the initial magnetic field (**B**) is homogeneous under these conditions, it will vary only radially at later time; hence:

$$\frac{\partial B_r}{\partial t} = 0 \tag{4a}$$

$$\frac{\partial B_z}{\partial t} = -\frac{1}{r}\frac{\partial}{\partial r}(r v_r B_z) \tag{4b}$$

$$\frac{\partial B_\theta}{\partial t} = -\frac{\partial}{\partial r}(v_r B_\theta) - \frac{\alpha}{n}\frac{\partial n}{\partial z}\frac{\partial W}{\partial r} \tag{4c}$$

$$\frac{\partial W}{\partial t} = -\frac{W}{r}\frac{\partial}{\partial r}(r v_r) - v_r\frac{\partial W}{\partial r} - \frac{\alpha}{4\pi n d}\frac{\partial n}{\partial z}\frac{W}{r}\frac{\partial}{\partial r}(r B_\theta) \tag{4d}$$

where

$$\alpha = \frac{2 m_i c}{3 Z e},$$

and v_r is the radial velocity component. To first order, the radial component of the magnetic field does not change with time. Provided a velocity field can be imposed, the vertical component, described by equation (4b) only depends on the initial conditions and can be treated independently. The azimuthal component, equation (4c), is coupled with the energy equation (4d) via the last (source) terms on the right hand side of the equations. We look for a self-similar model solution to equations (4c) and (4d).

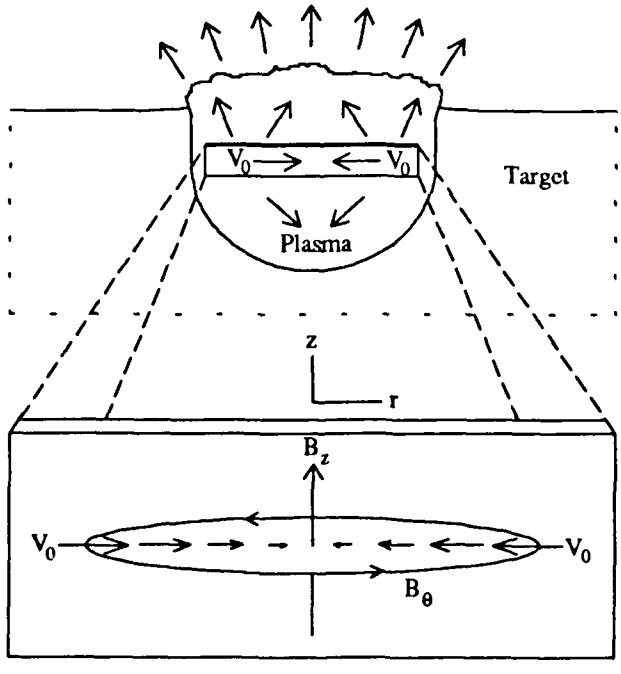


Fig. 5. Idealized model of impact-generated plasma—configuration during cavitation. Within the transient cavity, the plasma fluid velocity (characterized by V_0) is directed inward potentially leading to azimuthal (B_θ) and vertical (B_z) field growth as described in the text.

In an idealized model of impact-generated plasma (Fig. 5), the electron specific energy has a radial dependence due to the curvature of the projectile whereas the electron density primarily has a vertical dependence due to vertical compositional variations (e.g. the compositional contrast between projectile and target or compositional layers within the projectile and/or target).

The coordinates t, r and z can be expressed with their dimensionless forms (t', r' and z') as:

$$t = t' R_p / V_p \tag{5a}$$

$$r = r' R_p \Psi(t') \qquad 0 \le r' \le 1 \tag{5b}$$

$$z = z' L \Psi(t') \qquad 0 \le z' \le 1 \tag{5c}$$

and thereby:

$$dt = dt' R_p / V_p \tag{6a}$$

$$dr = dr' R_p \Psi(t') \tag{6b}$$

$$dz = dz' L \Psi(t') \tag{6c}$$

where R_p is projectile radius, V_p is projectile velocity, L is the length scale over which significant vertical gradients in electron density occur and $\Psi(t')$ is a dimensionless scaling factor.

A straightforward dimensional analysis of equations (4c) and (4d) yields a unique, self-similar radial dependence for the radial fluid velocity (v_r), the azimuthal magnetic field (B_θ) and the electron specific energy (W). These self-similar solutions have the form:

$$v_r(r') = V_0 r' \tag{7a}$$

$$B_\theta(r',t') = b(t') r' \tag{7b}$$

$$W(r',t') = \varepsilon(t') r'^2 \tag{7c}$$

with $0 \le r' \le 1$. Applying the coordinate transformations described in equations (5) and (6) and substituting equations (7) into (4c) and (4d), we find:

$$\frac{db}{dt'} = -2\eta b - \kappa\varepsilon \tag{8a}$$

$$\frac{d\varepsilon}{dt'} = -4\eta\varepsilon - \frac{\kappa}{2\pi d}\varepsilon b \tag{8b}$$

$$= \text{advection} + \text{source}$$

where

$$\eta = \frac{V_0}{\Psi V_p}, \tag{9}$$

and

$$\kappa = \frac{\alpha}{L\Psi^2 V_p}\frac{1}{n}\frac{\partial n}{\partial z'} \approx \frac{\alpha}{L\Psi^2 V_p}. \tag{10}$$

During the cavitation phase of crater growth(<10-30 R_p/V_p for vertical impacts), the impact-generated vapor/plasma is confined to a cavity (Fig. 5) with characteristic dimension $R_0 \propto R_p$ (see O'Keefe and Ahrens, 1977). Much of the fluid flow field is directed inward with characteristic radial velocity $-V_0$ so that $\eta < 0$. Since the plasma is confined to a small cavity, $R_0 = \Psi R_p$, with $\Psi(t)$ a constant on the order of 2-3 (estimated from O'Keefe and Ahrens, 1977). Hence, for this first-order model, η is a constant during cavitation. In reality, η is dependent on the growth rate of the transient cavity and the velocity distribution within the plasma as realized by the range of η values given in Table 1. If, during cavitation, fluid motion acts to homogenize the plasma, then the effective electron density gradient ($\sim 1/L$) would decrease from a scale invariant starting value (initially strongest across the contact between the projectile and target materials) to a value proportional to $\sim 1/R_p$ and κ would decrease proportionately. For the following calculations, we use the latter definition of κ.

Table 1. Parameters of the first-order cavitation model.

Parameter	Value	Units	Definition
R_p	$1\text{-}10^7$	cm	projectile radius
V_p	10^6	cm/s	projectile velocity
R_0	$2\text{-}3R_p$	cm	transient cavity size (during cavitation)
V_0	3×10^5	cm/s	characteristic fluid velocity
L	10^{-1} - 10^6	cm	vertical gradient length scale (see text)
Ψ	2-3	dimensionless	R_0/R_p (during cavitation)
α	10^{-3}	g·cm/esu·s	see equation (4)
η	-0.2 - 0.5	dimensionless	normalized fluid velocity ($V_0/\Psi V_p$)
κ	10^{-16} - 10^{-9}	g/esu·cm	$\sim\alpha/L\Psi^2V_p$ (see text)
d	10^{-6}	g·cm^{-3}	plasma density (ionic mass per cm^3)
$b(0)$	0	G	initial magnetic field strength
b_{max}	$1\text{-}10^3$	G	energy-limited field strength ~ $(nkT)^{1/2}$
$\varepsilon(0)$	10^{11}	ergs/g	initial plasma specific energy

Equations (8a) and (8b) were numerically integrated with fourth-order Runge-Kutta using the parameters shown in Table 1. With no initial magnetic field ($b(0) = 0$), exponential field growth occurs with time (Fig. 6). Many solutions ($\eta < 0.2$) eventually reach a singularity where infinite field growth can occur (in reality, limited by conservation of energy). Pert (1977) studied this instability for the advectionless case ($\eta = 0$). As shown by the cavitation solutions ($\eta = -0.1$; $10^{-16} \le \kappa \le 10^{-9}$ g/esu·cm) depicted in Fig. 6, the magnetic field generally reaches an energy-limited value ($b_{max} \sim (nkT)^{1/2}$) or leaves the cavitation regime prior to reaching the region of instability. It is important to note that the time required for the magnetic field to reach its energy-limited value has only a weak dependence on κ. Varying κ from 10^{-9} (~0.1-1 cm projectiles) to 10^{-16} (~10-100 km projectiles) delays attainment of the energy-limited field level by only a factor of ~80. It is likely that only for the largest impacts will field growth not achieve the energy-limited value during cavitation.

Cavitation may also induce (nonlinear) amplification of the ambient field as shown schematically in Fig. 5. Due to azimuthal symmetry, the source term of equation (4) will contribute to growth of the azimuthal magnetic field. The advection term, however, can contribute to the vertical field as well. By only considering the advection terms of equations (4), the azimuthal field component (B_θ) and the vertical field component (B_z) can be treated independently by considering solutions of the form:

$$v_r(r') = -V_0 r' \tag{11a}$$

$$B_\theta(r',t') = b_\theta(t')\, r'^m \tag{11b}$$

$$B_z(r',t') = b_z(t')\, r'^n \tag{11c}$$

Substituting (11) into (4) and applying the coordinate transformations of equations (6), we obtain

$$\frac{db_\theta}{dt'} = -(m+1)\eta b_\theta \tag{12a}$$

$$\frac{db_z}{dt'} = -(n+2)\eta b_z \tag{12b}$$

where η was defined previously in equation (9). During cavitation ($\eta < 0$), the magnetic field will grow exponentially as:

$$b_\theta = b_1 \exp[-(m+1)\eta t'] \tag{13a}$$

$$b_z = b_2 \exp[-(n+2)\eta t'] \tag{13b}$$

hence the amplification factor depends on η, m and n. To first order, the ambient vertical field is flat, $n = 0$, and the azimuthal field has the self-similar form of equation (7b), $m = 1$. With $\eta \sim -0.1$ and $t \cdot V_p/R_p \sim 20$ (during cavitation), the initial field will be amplified ~50 times. More amplification is possible with higher cavitation velocities and/or longer cavitation times. On the lunar surface, where the ambient field is 0-5 mG, amplified vertical fields of up to 0.2 G may be produced in this way.

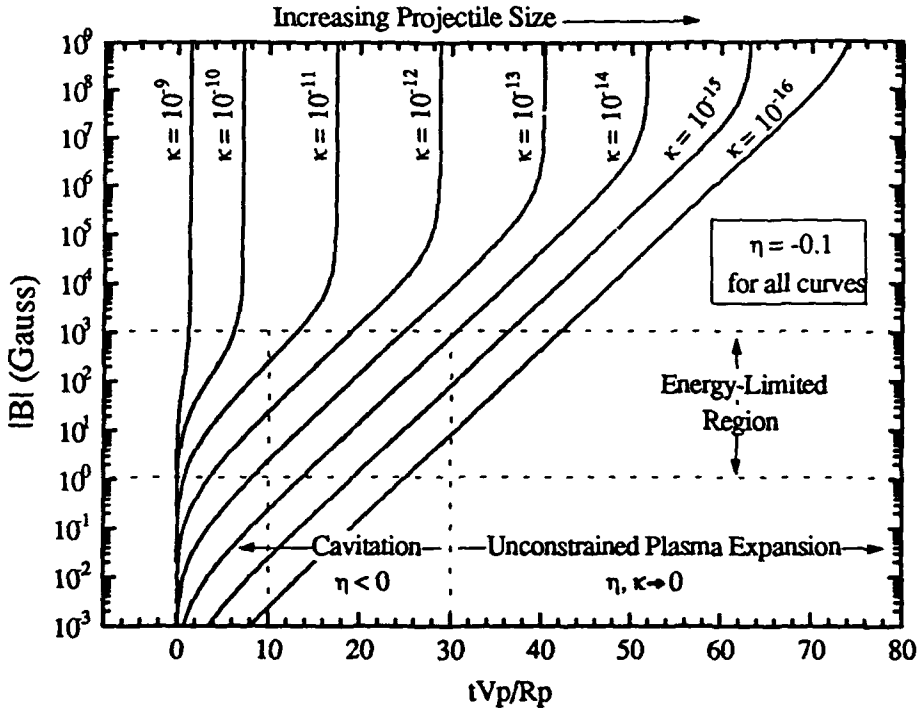


Fig. 6. The azimuthal component of the plasma's internal magnetic field as a function of dimensionless time during cavitation. The field has been plotted for $\eta = -0.1$ and a range of κ values ($\kappa = 10^{-9}$ corresponds to 0.1-1 cm projectiles and $\kappa = 10^{-16}$, 10-100 km projectiles). In reality, field intensity will not increase beyond the energy-limited region (horizontal dashed lines) nor beyond the time of cavitation (10-30 R_p/V_p, vertical dashed lines). Later, during plasma expansion, the field will decay as discussed below (not shown).

At late time (i.e., after projectile penetration/cavitation) the plasma is freely expanding with velocity V_0. We consider solutions of the form described by equations (11a), (11b) and (11c) with:

$$\Psi(t') = 1 + \frac{V_0}{V_p} t' = \frac{V_0}{V_p}\left(t' + \frac{V_p}{V_0}\right) = \frac{V_0}{V_p}(t' + t_0) . \tag{14}$$

At late time, the source term can be neglected and the azimuthal and vertical magnetic field components can be described by a pair of ordinary differential equations:

$$\frac{db_\theta}{dt'} \sim -(m+1)\frac{b_\theta}{(t' + t_0)} \quad \rightarrow \quad b_\theta = b_1(t' + t_0)^{-(m+1)} \tag{15a}$$

$$\frac{db_z}{dt'} = -(n+2)\frac{b_z}{(t' + t_0)} \quad \rightarrow \quad b_z = b_2(t' + t_0)^{-(n+2)} \tag{15b}$$

where the constants b_1 and b_2 are determined by the magnetic field strength achieved at the end of projectile penetration/cavitation. Strictly speaking, the decay rates are dependent on the radial distribution of B_θ and B_z at the end of projectile penetration/cavitation. To first order, B_θ has a linear dependence on r (m=1) due to the self-similar form of equation (7b), whereas B_z, ultimately, depends on the distribution of the ambient field (which will likely be flat over the typical impact scale, n=0). Hence, the azimuthal and vertical fields will exhibit late-time ($t >> t_0$) decay proportional to r^{-2}.

In summary, first-order theoretical modeling predicts that during projectile penetration spontaneous magnetic fields can be produced from nonaligned electron density and temperature gradients. Due to the inward directed flow that appears in portions of the impact-generated plasma during cavitation, amplification of the ambient and spontaneous fields also may occur. Ultimately, the exponential field

growth is limited by the finite duration of projectile penetration/cavitation or by the finite electron energy density. At late time, impact-generated plasma expands freely thereby leading to decay of the magnetic field proportional to r^{ξ} where ξ is a constant that depends on the field's radial dependence. A self-similar, one-dimensional solution for radially expanding plasma predicts $\xi = 2$.

CONCLUSION

The configuration and duration of impact-generated magnetic fields have a strong dependence on impact angle, as demonstrated in Fig. 3. Impact-generated magnetic fields exhibit a regular transition from a cylindrically symmetric field configuration at vertical incidence to a strong bilaterally anti-symmetric field configuration at high obliquity. During oblique impacts, stronger fields within the target could result simply from the close proximity of impact-generated plasma to the target surface, from a fundamental change in the field production mechanism within the plasma, or from increased vaporization (Schultz, 1988; Schultz and Gault, 1990a) yielding a greater volume of magnetized plasma. Although this could not be directly resolved with the data obtained, the correlation with increased vaporization at low angles is intriguing (e.g. Fig. 4). In addition, the configuration and duration of impact-generated magnetic fields have been shown to depend on impact velocity and projectile and/or target composition (Crawford and Schultz, 1991).

With the expected increase of vapor and plasma production at higher velocities (O'Keefe and Ahrens, 1977; Kissel and Krueger, 1987), it is reasonable that magnetic fields produced by 25 km/s impacts may be ten times stronger than those from 5 km/s experimental impacts. Provided this assumption holds true, the data in Fig. 3 can be extrapolated using gravity scaling coupled with the self-similar field decay model of equation (15). For 10-100 km craters formed by 25 km/s impacts, magnetic field strengths of perhaps 0.03-0.3 G lasting several minutes or more are possible at a distance of 1-2 crater diameters from the impact point. Because cavitation may occur for the majority of impacts on the lunar surface (with impact angles greater than ~15° from horizontal), amplification of the local ambient magnetic field may occur as well. These first-order estimates of magnetic field intensities are within the range of paleointensity values determined for certain relatively young (3 Ma - 1.5 Ga) lunar samples (Sugiura *et al.*, 1979; Cisowski *et al.*, 1983; Collinson, 1984) and more generally may help account for part of the lunar magnetic record, especially during the last ~3.6 billion years. Ongoing experimental work is being conducted to more precisely determine the scaling dependence.

A remnant of the impact-generated magnetic field can be induced within the target material by the passage of the impact-induced shock wave (Cisowski *et al.*, 1975, 1976; Wasilewski, 1981) or by cooling through the Curie point of small portions of impact melt or hot target material. During oblique impacts, spalled fragments of the projectile may impact further downrange, thereby inducing an additional shock and/or thermal remanence (Schultz and Gault, 1990a, b). Because of these dependencies, remnant impact-generated magnetic fields could be a useful geophysical tool for the study of impact craters on the Earth and planetary surfaces by helping to determine the impact angle, direction and composition of the impactors. Furthermore, an understanding of the complex contribution of impact-induced magnetism to the magnetic state of solid body surfaces, in general, and the lunar surface, in particular, is necessary to assess the role of internally derived fields such as that due to a core dynamo and may help to define future magnetic survey missions to the solid surface planets, satellites and asteroids.

Acknowledgments. We would like to thank the members of the NASA Ames Vertical Gun Crew (Ben Langedyk, John Vongray and Wayne Logsdon) for their expertise and effort and the constructive reviews of two anonymous reviewers. This research was supported by NASA Grant NAGW-705.

REFERENCES

Cisowski, S. M., M. D. Fuller, Y. M. Wu, M. F. Rose and P. J. Wasilewski (1975). Magnetic effects of shock and their implications for magnetism of lunar samples, *Proc. Lunar Sci. Conf.*, 6, 3123-3141.

Cisowski, S. M., J. R. Dunn, M. Fuller, Y. M. Wu, M. F. Rose and P. J. Wasilewski (1976). Magnetic effects of shock and their implications for lunar magnetism (II), *Proc. Lunar Sci. Conf.*, 7, 3299-3320.

Cisowski, S. M., D. W. Collinson, S. K. Runcorn, A. Stephenson and M. Fuller (1983). A review of lunar paleointensity data and implications for the origin of lunar magnetism, *Proc. 13th Lunar Planet. Sci. Conf., J. Geophys. Res.*, 88, suppl., A691-A704.

Collinson, D. W. (1984). On the existence of magnetic fields on the Moon between 3.6 Ga ago and the present, *Phys. Earth Planet. Interiors*, 34, 102-116.

Crawford, D. A., and P. H. Schultz (1988). Laboratory observations of impact-generated magnetic fields, *Nature*, 336, 50-52.

Crawford, D. A., and P. H. Schultz (1991). Laboratory investigations of impact-generated plasma, *J. Geophys. Res.*, 96, 18,807-18,817.

Crawford, D. A. and P. H. Schultz (1992). The Production and Evolution of Magnetic Fields During Hypervelocity Impacts, *Lunar and Plan. Sci.*, 23 .

Dachille, F. (1978). Electromagnetic Effects of Collisions at Meteoritical Velocities: Experimental and Theoretical Results, *Meteoritics* 13, 430-433.

Gault, D. E. and J. A. Wedekind (1978). Experimental studies of oblique impact, *Proc. Lunar Sci. Conf.*, 9, 3843-3875.

Gold, T., and S. Soter (1976). Cometary impact and the magnetization of the Moon, *Planet. Space Sci.*, 24, 45-54.

Hood, L. L., and Z. Huang (1991). Formation of magnetic anomalies antipodal to lunar impact basins: two-dimensional model calculations, *J. Geophys. Res.*, 96, 9837-9846.

Hood, L. L., and A. Vickery (1984). Magnetic field amplification and generation in hypervelocity meteoroid impacts with application to lunar paleomagnetism, *Proc. 15th Lunar Planet. Sci. Conf.*, Part 1, *J. Geophys. Res.*, 89, suppl., C211-C223.

Kissel, J., and F. R. Krueger (1987). Ion formation by impact of fast dust particles and comparison with related techniques, *Appl. Phys. A*, 42, 69-85.

Lin, R. P., K. A. Anderson and L. L. Hood (1988). Lunar Surface Magnetic Field Concentrations Antipodal to Young Large Impact Basins, *Icarus*, 74, 529-541.

Martelli, G., and G. Newton (1977). Hypervelocity cratering and impact magnetisation of basalt, *Nature*, 269, 478-480.

O'Keefe, J. D. and Ahrens, T. J. (1977). Impact-induced energy partitioning, melting, and vaporization on terrestrial planets, *Proc. Lunar Sci. Conf.*, 8, 3357-3374.

Pert, G. J. (1977). Self-generated magnetic fields in plasmas, *J. Plasma Phys.*, 18, 227-241.

Pert, G. J. (1981). Algorithms for the self-consistent generation of magnetic fields in plasmas, *J. Comput. Phys.*, 43, 111-163.

Rayzer, Y. P. (1964). The Deceleration and Energy Conversions of a Plasma Expanding in a Vacuum in the Presence of a Magnetic Field, *NASA TT F-239*, National Aeronautics and Space Administration, Washington, D.C., 20 pp.

Schultz, P. H. (1988). Impact vaporization of easily volatized targets: experimental results and implications, *Lunar Planet. Sci.*, 19, 1039-1040.

Schultz, P. H., and D. E. Gault (1990a). Prolonged global catastrophes from oblique impacts, in *Global Catastrophes in Earth History: An Interdisciplinary Conference on Impacts, Volcanism, and Mass Mortality*, edited by V. L. Sharpton, and P. D. Ward, *Geol. Soc. Am. Spec. Pap.*, 247, 239-260.

Schultz, P. H., and D. E. Gault (1990b). Decapitated impactors in the laboratory and on the planets, *Lunar Planet. Sci.*, 21, 1099-1100.

Schultz, P. H., and L. J. Srnka (1980). Cometary collisions on the Moon and Mercury, *Nature*, 284, 22-26.

Srnka, L. J. (1977). Spontaneous magnetic field generation in hypervelocity impacts, *Proc. Lunar Sci. Conf.*, 8, 893-895.

Srnka, L. J., G. Martelli, G. Newton, S. M. Cisowski, M. D. Fuller and R. B. Schaal (1979). Magnetic field and shock effects and remanent magnetization in a hypervelocity impact experiment, *Earth Planet. Sci. Lett.*, 42, 127-137.

Srnka, L. J. and P. H. Schultz (1980). A Cometary Origin of Reiner-Gamma Magnetic Anomalies, *Lunar Planet. Sci.* 11, 1076-1078.

Sugiura, N., Y. M. Wu, D. W. Strangway, G. W. Pearce and L. A. Taylor (1979). A new magnetic paleointensity value for a "young lunar glass", *Proc. Lunar Planet. Sci. Conf.*, 10, 2189-2197.

Wasilewski, P. J. (1981). Magnetic Properties and Microstructures Associated with the Shock Induced Transformation of fcc Iron to bcc Iron, in *Shock Waves and High-Strain-Rate Phenomena in Metals*, Plenum Pub., NY, 779-793.

Int. J. Impact Engng Vol.14, pp.217–228, 1993
Printed in Great Britain

0734-743X/93 $6.00+0.00
1993 Pergamon Press Ltd

THE EFFECTS OF A RANDOM OFF-AXIS VELOCITY COMPONENT ON THE PENETRATION ACHIEVED BY LONG ROD KINETIC ENERGY PENETRATORS AND SHAPED CHARGE JETS

J P CURTIS

EDS-Scicon Ltd, 49 Berners Street, London W1P4AQ

ABSTRACT

The impact of long rod kinetic energy penetrators and shaped charge jets on homogeneous targets is investigated. In particular the effects of a random off-axis velocity component on the penetration achieved are analyzed. The aim of this study is to consider the case where the off-axis velocity component takes a uniform value W along the rod or jet.

It is assumed that penetration takes place according to the classical hydrodynamic penetration law, and that it continues either until the projectile material is exhausted or until a side wall collision occurs. The penetration is evaluated as a function of a reference coordinate q defined along the projectile, and the corresponding crater radius distribution R(q) calculated, on the assumption that W is zero. The locus of the penetration stagnation point S corresponding to the true value of W is then determined as a function of q and a revised crater profile is calculated with radius R(q), centred on S. We determine whether a side-wall collision occurs, and calculate the final penetration, P. The probability that P exceeds a given value P_0 is found. We then determine the expected value of P and investigate parameter variations to maximize this value.

INTRODUCTION

Over the last decade there has been increasing interest in identifying the causes of degraded penetration performance of long rod penetrators and shaped charge jets impacting on homogeneous targets (Brown, 1990). For the latter type of penetrator it has emerged that the main cause appears to be the tendency of the jet to collide with the side wall of the crater it is in the process of forming. Such collisions can occur in principle when the jet is still intact or after the onset of break-up. They arise because there is a distribution of off-axis velocity along the length of the jet caused by small asymmetries introduced in the manufacturing process or by inherent imhomogeneities in the explosive. The effect of these side wall impacts is to reduce the penetration, because all or part of the contribution that a particle hitting the side would have made at the bottom of the crater is lost. We believe this accounts for the characteristic penetration versus stand-off curve observed experimentally, which rises rather like a sinusoidal function from a non-zero value at zero stand-off to reach a maximum value before eventually decaying (Brown, 1990) like an exponential or

hyperbolic function .

This problem of the decrease in penetration with increasing stand-off has been considered previously by Smith (1981), who applied the Monte Carlo technique to the effects of tumbling, off-axis motion (wavering), and break-up. All three phenomena were treated as stochastic processes. Appropriate choices of the statistical parameters enabled the prediction of penetration versus stand-off curves in good agreement with experimental results. Recent studies reported by Brown (1990) show that it is sufficient to consider only the latter two phenomena to obtain a satisfactory fit of the experimental data.

In the light of the above considerations it seemed logical to investigate the effects of off-axis motion in isolation as a step towards a full understanding of the processes underlying the degradation phenomenon. Moreover, it is natural to commence with the analysis of an ideal jet which does not break up, to gain a clear understanding of the basic ideas. The same motivation led us to consider first the simplest possible case of a non-stretching jet - essentially a long rod kinetic energy penetrator. We follow Smith (1981) in considering the off-axis speed as a random variable. However, we perform analytical studies without recourse to the technique of Monte-Carlo simulation, for both the long rod and the idealized jet.

This strategy yields several important benefits. In each case it is possible to derive explicit analytical formulae for the probability that the penetration will exceed a given arbitrary value P_O and for the expected value of the penetration. Once the formula for the expected value of the penetration is available it is then possible to consider parametric variations to maximise this value. In other words, it becomes possible to seek to optimize the penetration performance with respect to such variations. In this paper, we confine our attention to what we consider to be the most important parameter - namely the initial ratio of the penetrator length to penetrator diameter.

The means of optimizing the penetration achieved by a shaped charge jet has been sought previously without success - we believe because the significance of the off-axis effects was not understood. In the absence of any treatment of off-axis motion the penetration achieved by both rod and jet can be made arbitrarily large for a given volume simply by reducing the ratio of the diameter to the length, if the hydrodynamic penetration law holds. Once off-axis motion can occur then this may no longer be true.

There is only a limited amount of data available on the off-axis motion of shaped charge jets. The reason for this is the high cost of conducting experiments using the available techniques of flash X-ray radiography and synchro-streak photography. Accordingly, in this preliminary analysis the simple choice of a constant value for the off-axis speed along the rod or jet is a natural one. We also assume that penetration occurs according to the classical hydrodynamic law first proposed by Hill, Mott and Pack (1944), modified by our treatment of the collisions on the side wall of the crater. The dynamic yield strength of the penetrator and target materials is assumed negligible in comparison with the pressures generated at the interface between the penetrator and the target. An energy-volume constant is used for predicting the radius of the crater made by the penetrator.

PENETRATION OF A LONG ROD WITH A UNIFORMLY DISTRIBUTED OFF-AXIS VELOCITY

Consider a long rod impacting on a homogeneous metal target. Suppose that the rod is cylindrical in shape and that it moves with components of velocity of V in the axial direction and W in the off-axis direction. Let its density be denoted by ρ_J, and let its length and radius be L and r_J respectively. The geometry of the impact is shown in Fig.1.

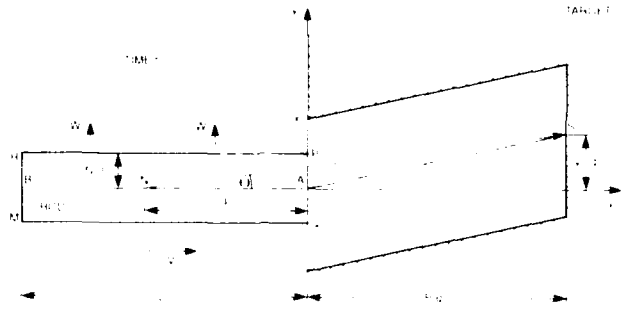


Fig.1 Penetration of a long rod with a uniform off-axis velocity component W into an homogeneous target. The element initially at N contributes to the penetration at S, the stagnation point.

Let the point where the centre of the circular front cross-section of the rod hits the target of density ρ_T be A. It is convenient to define a Cartesian coordinate system with the x-direction parallel to the axis of the rod, the y-direction parallel to the off-axis velocity component W, and the origin at A. It is also convenient to define a length coordinate q measuring the distance from the tip of the rod at the time of impact.

We assume that, in spite of the presence of the off-axis velocity component, the rod penetrates in the x-direction according to the classical hydrodynamic root density law first proposed by Hill, Mott and Pack (1944). We use this simple law in this preliminary exploration of the theory, with the intention of investigating other long rod penetration algorithms, particularly that of Tate (1967) later. Figure 1 depicts the way the crater formed by the rod is displaced in the y-direction. The point N on the rod axis initially at the distance q from A arrives at the so-called stagnation point S with coordinates $(P(q),y_s(q))$ at a time t, say, after the impact. Here P(q) is the penetration achieved by the portion AN of the rod. The equation describing the locus of this point is

$$y = \tan\theta\,(x+q) \quad . \tag{1}$$

The angle θ between NS and the x-axis must take as its tangent the ratio of the velocity components.

Thus

$$\tan\theta = \frac{W}{V} \quad . \tag{2}$$

Use of the hydrodynamic penetration law given by

$$P(q) = \left(\frac{\rho_J}{\rho_T}\right)^{1/2} q \tag{3}$$

yields

$$y_s(q) = \frac{Wq}{V}\left[1+\left(\frac{\rho_J}{\rho_T}\right)^{1/2}\right] = \frac{WP(q)}{U} \quad , \tag{4}$$

where the speed of penetration U is given by

$$V = U\left[1+\left(\frac{\rho_T}{\rho_J}\right)^{1/2}\right] \quad . \tag{5}$$

We suppose that the crater made by the rod is of circular cross-section for all sections taken normal to the x-axis. We apply the concept of the hole-volume constant to derive a relationship between the radii of the rod and crater in the form

$$R_C = DVr_J = \lambda r_J \quad , \tag{6}$$

where D is a constant.

With the above basic equations established we now perform an analysis to determine whether a side-wall collision can occur. In this simple case it is clear that if a side wall collision happens then it must occur at the point X when W is greater than zero (cf.Fig.1.). This is because the line RP is always parallel to the x-axis and X is the point having the lowest y-coordinate on the side wall which the rod is moving towards. The equation describing the straight line along which the point R moves is

$$y_R = \frac{W}{V}(x+L) + r_J \quad . \tag{7}$$

The condition that the rod will pass down the hole it makes without fouling on X is found by setting x to zero in this equation and imposing the inequality that y_R is less than the radius R_C of the crater. Thus

$$y_R(0) = \frac{WL}{V} + r_J < R_C \quad . \tag{8}$$

There is a corresponding condition that holds when W is less than zero, namely

$$\frac{-WL}{V} < R_C - r_J \quad . \tag{9}$$

Equations (8) and (9) may be combined to yield the following condition that the rod penetrate to its full length:

$$|W| < \frac{V}{L}(R_C - r_J) = W_A \quad , \tag{10}$$

where W_A is defined by the equality. If W is uniformly distributed in the range $[-W_U, W_U]$ then the probability p_A that all the rod contributes is given by

$$P_A = \begin{cases} \dfrac{W_A}{W_U} & W_A \le W_U \\ 1 & W_A > W_U \end{cases} \tag{11}$$

We now derive a general expression for the penetration in the event that a side wall collision occurs. We suppose that once a collision has happened then no further penetration may take place. This assumption is made looking ahead to the treatment of the shaped charge jet for which it is known to be a reasonable working hypothesis (Brown, 1990). It may be desirable to enhance this approach when treating long rods themselves. Let the element of the rod initially at a distance q_0 from A collide with the wall at X. Then q_0 satisfies

$$y_s(q_0) + r_J = R_C \tag{12}$$

and after use of eq.(4) we have

$$q_0 = \frac{V(R_C - r_J)}{W\left[1 + \left(\frac{\rho_J}{\rho_T}\right)^{1/2}\right]} \quad . \tag{13}$$

This equation has a solution only when $W \ge W_A$, that is when the inequality

$$\frac{V(R_C - r_J)}{W} \le L \tag{14}$$

is satisfied. This is written as

$$q_0 \leq \frac{L}{\left[1+\left(\frac{\rho_J}{\rho_T}\right)^{1/2}\right]} \quad . \tag{15}$$

or

$$q_0+P(q_0) \leq L \quad , \tag{16}$$

where the latter form is perhaps the more readily interpreted when one considers Fig.2.

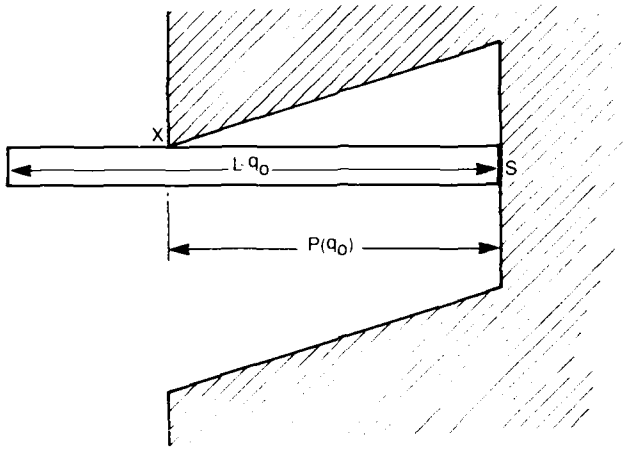


Fig.2 The geometry of the side wall collision for the rod.

The sought general expression for the penetration is given by

$$P(q_0) = \begin{cases} \mu q_0 & W_U \geq |W| \geq W_A \\ \mu L & |W| < W_A < W_U \\ \mu L & W_A > W_U \end{cases} \tag{17}$$

where we have introduced the parameter μ given by

$$\mu = \left(\frac{\rho_J}{\rho_T}\right)^{1/2} \quad . \tag{18}$$

There is a discontinuity in the penetration at $W = W_A$. This arises as a result of our assumption that the penetration process ceases as soon as a side wall collision occurs. Through the use of eqs.(6), (13) and (18) eq.(17) may be written in terms of r_J, W and λ as

$$P(q_0) = \begin{cases} \dfrac{\mu V(\lambda-1) r_J}{(1+\mu) W} & W_U \geq |W| \geq W_A \\ \mu L & |W| < W_A < W_U \\ \mu L & W_A > W_U \end{cases} \tag{19}$$

The above expression for the penetration will be used to calculate the expected penetration for several probability distributions. However, we first calculate the probability that the penetration exceeds a given arbitrary value.

PROBABILITY THAT A GIVEN DEPTH BE EXCEEDED

For the consideration of the calculation of the probability that an arbitrary depth of penetration be

exceeded it is convenient to work with eq.(19) in the form

$$P = \begin{cases} \dfrac{\mu L W_A}{(1+\mu)W} & W_U \geq |W| \geq W_A \\ \mu L & |W| < W_A \leq W_U \\ \mu L & W_A > W_U \end{cases} , \tag{20}$$

since we are concerned here only with the random variable W. The cases of $W_A > W_U$ and $W_A \leq W_U$ must be treated separately. For the former case the penetration is always given by

$$P = \mu L \quad . \tag{21}$$

Thus the probability that P exceeds P_O is given by

$$P(P \geq P_O) = \begin{cases} 1 & P_0 \leq \mu L \\ 0 & P_0 > \mu L \end{cases} . \tag{22}$$

Where $W_A \leq W_U$ the first two cases of eq.(20) apply. For the first of these two the penetration lies in the range

$$\frac{\mu L W_A}{(1+\mu)W_U} \leq P \leq \frac{\mu L}{(1+\mu)} . \tag{23}$$

For the second the penetration takes the value stated in eq.(20). The minimum value that P may take is given by the lower limit of the two-sided inequality (23). Therefore if P_O is less than or equal to this value then the penetration P will always exceed P_O. Now consider the circumstances in which the upper limit of the inequality (23) is exceeded by P. This can only occur when the second case of eq.(20) applies, when P satisfies eq.(21). The probability of this case holding is given by

$$P(|W| < W_A) = \frac{W_A}{W_U} . \tag{24}$$

Here we have assumed that W is uniformly distributed as before, and have availed ourselves of the symmetry of the distribution as convenient. It remains to consider the case where P_O lies within the range (23). Let us define a critical value of W, w_O, given by

$$w_O = \frac{\mu L W_A}{(1+\mu)P_O} . \tag{25}$$

Then the probability that P lies between P_O and the upper limit of the range (23) is given by

$$P\left(\frac{\mu L}{1+\mu} \geq P \geq P_O\right) = P(W_A \leq |W| \leq w_O) = \frac{w_O - W_A}{W_U} = \left(\frac{\mu L}{(1+\mu)P_O} - 1\right)\frac{W_A}{W_U} . \tag{26}$$

The probability that P exceeds P_O is simply the sum of the probabilities (24) and (26).

All of the above information can be summarised in the following single equation giving the desired probability for each of the four possible ranges of values for P_O:

$$P(P \geq P_O) = \begin{cases} 0 & P_O > \mu L \\ \dfrac{W_A}{W_U} & \mu L \geq P_O > \dfrac{\mu L}{(1+\mu)} \\ \dfrac{\mu L W_A}{(1+\mu)P_O W_U} & \dfrac{\mu L}{1+\mu} \geq P_O \geq \dfrac{\mu L W_A}{(1+\mu)W_U} \\ 1 & \dfrac{\mu L W_A}{(1+\mu)W_U} > P_O \end{cases} \tag{27}$$

Equations (22) ($W_A > W_U$) and (27) ($W_A \leq W_U$) cover all the possibilities.

We may consider the same problem but with W distributed according to a truncated normal distribution. The derivations of the probability that the entire rod contributes to the penetration and of the probability that P exceeds P_O are directly analogous to those for the uniform distribution.

The results of this section show how an understanding of the statistics of the random off-axis component of velocity can be used to calculate the probability of penetrating a given depth into a chosen target material.

CALCULATION AND MAXIMIZATION OF THE EXPECTED PENETRATION OF THE ROD

Consider the calculation of the expected penetration and the problem of maximising it by varying the radius and length of the rod so as to keep its volume V_R, and hence mass and kinetic energy, constant. The same eq.(19) for the penetration is used for both the uniform and truncated normal distributions. The forms of the expected value are of course dependent on the particular choice of distribution.

For both distributions we note that W_A is dependent on r_J and L through eq.(10). Let us consider first the third case in eq.(19). Substituting the expression for W_A into the inequality $W_A > W_U$ holding for this case and using the constant volume relation

$$\pi r_J^2 L = V_R \quad , \tag{28}$$

we obtain after simple manipulation the inequality

$$r_J > \left(\frac{W_U V_R}{\pi V(\lambda-1)}\right)^{1/3} \quad . \tag{29}$$

This inequality provides a lower bound above which r_J must lie in order that all the rod contribute to the penetration. Below this bound side wall collisions occur at X in Fig.1, and one of the first two cases in eq.(19) applies. Corresponding to the above lower bound on r_J is an upper bound on L, since eq.(28) must be satisfied. Since the penetration is directly proportional to L through the third of the cases in eq.(19) it also must be bounded above. The bound may be written explicitly as

$$P = E[P] < \mu\left(\frac{V_R V^2(\lambda-1)^2}{\pi W_U^2}\right)^{1/3} \quad . \tag{30}$$

As the expected penetration and all possible values of the penetration are one and the same for this case we have included this equality in eq.(30). It gives the maximum penetration that can be obtained by reducing the radius of the rod, ie increasing the length/diameter ratio, before a side wall collision occurs.

The question arises naturally, whether it is possible for this value to be exceeded even if a side wall collision occurs. To answer this question we must write down the expected value of the penetration when $W_A \leq W_U$ for both of the distributions. For both the expected value is found by integrating the product of the appropriate form of the penetration (given in the first two cases of eq.(19)) with the probability density function. Commencing with the uniform distribution we have

$$E[P] = \frac{\mu V(\lambda-1) r_J}{(1+\mu)} \int_{W_A}^{W_U} \frac{1}{W W_U} \, dw + \mu L \int_0^{W_A} \frac{1}{W_U} \, dw \quad , \tag{31}$$

where we have used the symmetry of the distribution to allow us to consider positive values of W only. After evaluating the integrals the expected value reduces to

$$E[P] = \frac{\mu V(\lambda-1) r_J}{W_U(1+\mu)} \ln\left(\frac{W_U}{W_A}\right) + \frac{\mu L W_A}{W_U} \quad . \tag{32}$$

Elimination of L using eq.(28), of W_A by eq.(10), and of R_C enables us to write the right-hand side of this equation as a function of r_J as the only variable, so that it reduces to

$$E[P] = \mu V(\lambda-1) r_J \left[\frac{1}{W_U(1+\mu)} \ln\left(\frac{W_U V_R}{\pi V(\lambda-1) r_J^3}\right) + 1\right] . \tag{33}$$

It is now straightforward to seek a maximum of E[P] by differentiating the right-hand side of eq.(33) with respect to r_J, equating the resulting expression to zero, and solving for r_J. The solution must lie in the range that is complementary to (29), namely

$$r_J \le \left(\frac{W_U V_R}{\pi V(\lambda-1)}\right)^{1/3} , \tag{34}$$

in order that it be meaningful, if we are seeking it in the case where $W_A \le W_U$. In fact we find that

$$r_J = \left(\frac{W_U V_R}{\pi V(\lambda-1)} \exp(\mu-2)\right)^{1/3} , \tag{35}$$

so that the inequality is satisfied provided $\mu \le 2$. Substituting this result into eq.(33) yields the following result for the maximum expected penetration:

$$E[P]_{max} = \frac{3\mu}{(\mu+1)} \left(\frac{V_R V^2 (\lambda-1)^2 \exp(\mu-2)}{\pi W_U^2}\right)^{1/3} . \tag{36}$$

Dividing the right-hand side of this result by the right-hand side of the inequality (30) we observe that the maximum penetration with a side wall collision exceeds that without one provided the following inequality holds:

$$\frac{3}{(\mu+1)} (\exp(\mu-2))^{1/3} > 1 \quad . \tag{37}$$

Let us consider some examples. Suppose first that the rod and target materials are the same. Then $\mu = 1$ and the left-hand side of the inequality (37) takes the value 1.0747, confirming that for maximum penetration a side wall collision occurs. Now consider a copper long rod and steel target. Taking 8900kg/m^3 and 7860kg/m^3 as the densities of copper and steel respectively, we find that $\mu = 1.0641$ and that the left-hand side of the inequality (37) takes the value 1.0639. Once again the penetration is made greater by allowing the side wall collision to occur.

It is of interest to consider the sensitivity of these results to the choice of probability distribution. therefore we repeat our analysis, this time using the truncated normal distribution.

Again it is found that the maximum penetration with a side wall collision exceeds that without one provided the ratio analogous to the left hand side of inequality (37) exceeds unity.

As an example a plot of this ratio is shown in Fig.3 for values of the standard deviation σ of the underlying normal distribution ranging from 5m/s to 100m/s where the truncation limit is 50m/s. Here the rod is made of copper and the target of steel. We observe that for small values of σ the maximum achievable penetration with a side wall collision exceeds the maximum possible with no collision eg by a factor of 4 for σ = 5m/s. The curve asymptotically approaches the result given above for the uniform distribution, namely 1.0639, as σ increases, demonstrating the consistency of the analysis.

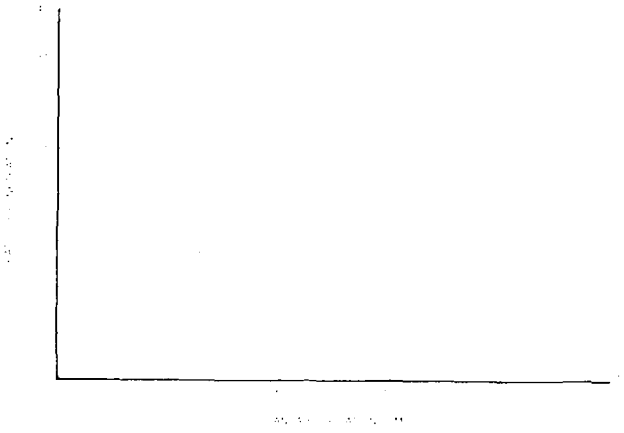


Fig.3. Plot of the ratio of the maximum expected penetration with a side wall collision to the maximum penetration with no collision, as a function of the standard deviation σ of the normal distribution prior to truncation. The figure shows that the results for the uniform distribution are approached asymptotically as σ increases.

PENETRATION OF A SHAPED CHARGE JET WITH UNIFORM OFF-AXIS VELOCITY DISTRIBUTION

Consider the impact of a stretching shaped charge jet on a homogeneous target as shown in Fig.4. The stretching brings about a diminution of the radius of the crater as the penetration increases. We retain the assumptions about the penetration process made above for the rod, but take account of an assumed linear decrease in the axial velocity of the jet with increasing length coordinate q, defined as before for the initial state

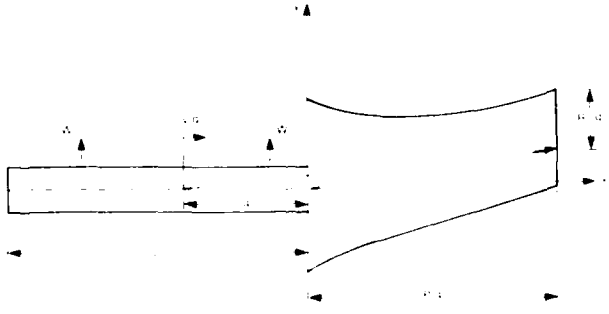


Fig.4 Penetration of a stretching shaped charge jet with a uniform off-axis velocity component W into a homogeneous target. Note that the velocity of each element is a function of q, and that the crater radius is not constant.

Let the axial velocity components of the front and back of the jet be v_0 and v_L respectively. Then the penetration P(q) achieved by a length q of the jet is given by use of the analysis of Abrahamson and Goodier (1963) as

$$P(q) = \left\{\frac{L}{V^{\beta}}\left[\frac{V_0^{\beta+1}-V^{\beta+1}}{V_0-V_L}\right] - q\right\} \quad . \tag{38}$$

Here $v = v(q)$ is the velocity of the element of the jet initially at distance q from the tip of the jet.

The investigation of side wall collisions is more complicated than for the rod, since it is not clear which point of the crater wall will be the first to be hit. Indeed it is likely that the location of this point will be a function of all the jet and target parameters.

An element of the jet colliding with the side wall will do so at a depth $P(q_A)$ into the target, at time t_o given by

$$t_O = [q_O + P(q_O)] \; / \; v(q_O) \quad , \tag{39}$$

where q_o is the initial coordinate of the element penetrating at the time of the side wall collision, so that $P(q_A) < P(q_o)$. The coordinate q_A is the initial distance from the tip of the jet of the infinitesimal element that made the infinitesimal increment to the crater at depth $P(q_A)$ at time t_A given by eq.(39) with q_O replaced by q_A. If the collision is the very first to occur then the off-axis displacement of the jet at time t_O plus its radius at time t_O must equal the off-axis displacement $y_S(q_A)$ of the crater plus its radius R_C at depth $P(q_A)$. Here we assume that all displacements are in the positive y-direction. An analogous result holds for negative displacements. The condition for first impact is thus

$$R_C(q_A) + y_s(q_A) = |W| t_O + r_J(t_O) \quad . \tag{40}$$

This may be written in terms of q_A and q_O as

$$Dv(q_A)\, r_J(q_A) + \frac{|W|(q_A + P(q_A))}{v(q_A)} = r_J(q_O) + \frac{|W|(q_O + P(q_O))}{v(q_O)} \quad , \tag{41}$$

where we have used eq.(6) and evaluated $y_S(q_A)$ as the product of W and t_A. Henceforth we denote the left-hand side of this equation by $f_1(q_A,W)$ and the right-hand side by $f_2(q_O,W)$. The functional dependence of r_J on q is given by

$$r_J(q) = r_J(O)\left[1 + \frac{\eta(q + P(q))}{v(q)}\right]^{-1/2} \quad , \tag{42}$$

where η is the strain rate given by

$$\eta = (v_O - v_L)/L \quad . \tag{43}$$

Let us now define a new function $F(q_A,q_O,W)$ given by

$$F(q_A, q_O, W) = f_1(q_A, W) - f_2(q_O, W) \quad . \tag{44}$$

For a given value of W if F > O then the jet elements within distance q_o of the tip pass through the crater cross-section at depth $P(q_A)$. If, however, a collision occurs then its location is determined by seeking the minimum value of q_O such that F = O. This minimum value and the corresponding value of q_A are both functions of W. Just as for the rod there will be a critical value W_A for W below which all of the jet contributes to the penetration. This value can be determined by gradually increasing W until a value of q_O is found for which F = O. Again there are three cases to consider in determining the penetration, which is given by

$$P = \begin{cases} P(q_O(W)) & W_A \le |W| \le W_U \\ P(L) & |W| < W_A \le W \\ P(L) & W_A > W_U \end{cases} \tag{45}$$

Note that we have indicated explicitly the dependence of the minimum value of q_O on W in the case of a collision. As before we suppose that W falls in the range $[-W_U, W_U]$.

PROBABILITY THAT JET PENETRATION EXCEEDS AN ARBITRARY DEPTH

The probability that the penetration exceeds an arbitrary value P_O, given that the jet is of radius r_J depends on the relative sizes of W_A and W_U, as for the rod. For $W_A > W_U$ it is given by

$$P(P \geq P_O) = \begin{cases} 0 & P_O > P(L) \\ 1 & P_O \leq P(L) \end{cases} . \tag{46}$$

Where $W_A \leq W_U$ it is given for a uniform distribution by

$$P(P \geq P_O) = \begin{cases} 0 & P_O > P(L) \\ W_A/W_U & P(q_O(W_A)) \leq P_O \leq P(L) \\ (W_A+W_U-w_O)/W_u & P(q_O(W_U)) \leq P_O \leq P(q_O(W_A)) \\ 1 & P_O < P(q_O(W_U)) \end{cases} . \tag{47}$$

Here the value w_O is defined such that $P(q_O(w_O)) = P_O$. Since P(q) increases strictly with q this definition is unique.

CALCULATION OF THE EXPECTED PENETRATION

If we adopt the convention that $q_O = L$ in the second and third cases of eq.(45), the expected penetration may be written as:

$$E[P] = \int_0^{W_U} \frac{P(q_O(W))}{W_U}\, dw . \tag{48}$$

This is a convenient form for numerical computation. Several examples have been investigated over a range of values of the jet radius while keeping the volume and kinetic energy of the jet constant. The following set of nominal parameter values has been taken:

v_O = 8000 m/s — Density of steel target = 7860 kg/m^3

v_L = 1000 m/s — Volume of jet = 0.31416 x 10^{-6} m^3

W_U = 50 m/s — Radius of jet from 0.27 mm to 1.0 mm

Density of copper jet = 8900 kg/m^3 — Non-dimensionalized crater radius constant D/v_O = 3

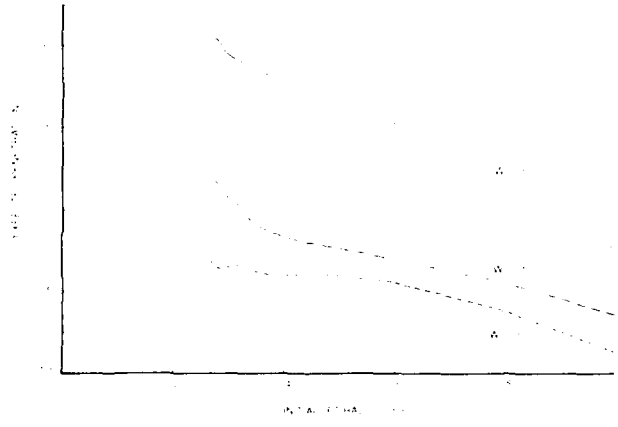


Fig.5 Expected penetration of a shaped charge jet as a function of off-axis velocity distribution parameter W_U.

Figure 5 shows that the effect of increasing the value of W_U first to 100m/s and then to 500m/s is to reduce the penetration over the entire range of values of the radius of the jet considered.

CONCLUSIONS

The effects of a random off-axis velocity component on the penetration achieved by long rod kinetic energy penetrators and shaped charge jets have been investigated. After making several simple assumptions about the penetration process calculations were made of the expected penetration for a long rod. The assumption was made that the off-axis velocity is uniformly distributed or that it has a truncated normal distribution. For some examples of materials in common use, the maximum expected penetration for a given volume is achieved when the radius of the rod is reduced or, in other words, the length to diameter ratio is increased, to an extent that the rod collides with the side wall of the cavity. This is true for both of the probability distributions considered. The probability that the penetration achieved by the rod exceeds an arbitrary value was also calculated.

We have also pursued the analysis for the case of a stretching shaped charge jet which does not break up. We have derived a means of determining the location of a side wall collision and written a computer program to exploit this analysis to make calculations of the expected penetration. The results obtained show that the penetration for a given volume of the jet increases with decreasing jet radius. No global maximum of the penetration was found, in contrast to the case of the long rod.

ACKNOWLEDGMENT

The author is very grateful for the support of the Defence Research Agency, Fort Halstead, Sevenoaks, United Kingdom, in preparing this paper.

REFERENCES

Abrahamson, G.R. and J.M. Goodier (1963). Penetration by Shaped Charge Jets of Nonuniform Velocity. J.Appl.Phys. 34, 195-199.

Brown, J. (1990). Modelling and Experimental Studies of a Family of Shaped Charges in a European Collaborative Forum. In: Proceedings of the 12th International Symposium on Ballistics, San Antonio, Texas. Vol I, pp27-41.

Hill, R., N. Mott and D. Pack (1944). A.R.D. Theoretical Research Reports Nos 2/44 (January) and 12/44 (March). UK Ministry of Defence Reports.

Smith, J. (1981). Shaped Charge Penetration at Long Stand-off. US Air Force Armament Laboratory Report No. AFATL-TR-81-25.

Tate, A. (1967). A Theory for the Deceleration of Long Rods after Impact. J.Mech.Phys.Solids, 17, 387-399.

Int. J. Impact Engng Vol. 14, pp. 229–240, 1993
Printed in Great Britain

0734-743X/93 $6.00+0.00
© 1993 Pergamon Press Ltd

A LAGRANGIAN MODEL FOR DEBRIS CLOUD DYNAMICS SIMULATION

E.P. Fahrenthold

Department of Mechanical Engineering, University of Texas
Austin, TX 78712

ABSTRACT

A new modeling approach has been developed for computer simulation of hypervelocity impacts on multi-plate orbital debris shields. This approach links an Eulerian finite difference code for shield perforation calculations to a Lagrangian finite element code for debris cloud evolution simulations. Mixture theory is used to account for the presence of void space in the debris cloud.

INTRODUCTION

Most numerical simulations of hypervelocity impact problems have employed Eulerian hydrocodes [e.g. CSQ (Thompson, 1990a) and CTH (McGlaun et al., 1990)], well suited to model perforation and erosion effects. However application of Eulerian codes in the design of multi-plate space debris shields (Cour-Palais and Crews, 1990 and Christiansen, 1990) suggests that they are not well suited to modeling debris cloud evolution, even in two dimensions. This is apparently due to basic mass dispersion problems associated with the use of Eulerian analysis methods to model very low density debris. Although rezoning, periodic deletion of low density debris, or other techniques may improve the efficiency of Eulerian codes in two dimensional debris modeling problems, such techniques can involve significant requirements for user intervention in the simulation. In addition, three dimensional Eulerian hydrocode analysis of debris cloud evolution appears to be impractical, given current supercomputer capabilities. Hence the present paper describes the development and application of a Lagrangian modeling approach to debris cloud dynamics simulation.

Previous work comparing the accuracy of Lagrangian and Eulerian codes in one-dimensional modeling of debris cloud dynamics has indicated that Lagrangian models can provide an accurate description of experimental data (Asay and Trucano, 1990). However the extension of this modeling approach to general debris shielding design problems presents two major difficulties. First, the initial (perforation) portion of the impact problem is very difficult to model accurately with Lagrangian codes. Second, generating a conventional finite element mesh description of the debris cloud is extremely difficult or impractical. As a result, the author is not aware of any previous attempts to extrapolate the one-dimensional work of Asay and Trucano (1990) to the general case.

Recognizing the inherent suitability of Eulerian codes for modeling perforation and and the apparent accuracy of Lagrangian codes in modeling debris cloud evolution, the present paper describes a systematic linking of the codes CTH (McGlaun et al., 1990) and DYNA2D (Hallquist, 1987) for the simulation of two dimensional space debris shield impact problems. In the approach described here, the mass and velocity distribution data obtained from a CTH model of initial perforation is post-processed to provide a DYNA2D model of the debris cloud behind the perforated plate. The Lagrangian debris cloud model is then used to simulate the transport of dispersing debris toward the next shield, or the shielded structure.

To simulate the perforation of the next shield in a multi-plate assembly, the DYNA2D model of the expanded debris cloud is post-processed to initiate a new CTH simulation. This process is repeated to progress though the multi-plate shield system and finally model impact on the protected structure. Automated post-processing and mesh generation for the sequence of calculations is performed using newly developed routines written to interface the the DYNA2D and CTH codes.

In order to solve the difficult problem of Lagrangian mesh generation for the impact debris cloud, the basic DYNA2D code has been augmented with a mixture theory based (Drumheller and Bedford, 1980) constitutive model of a solid or fluid medium containing voids, including a rate dependent law for void space evolution (Drumheller, 1987). The result is a thermodynamically consistent model of debris cloud evolution for use in space shield design applications. Simulation results show that that the outlined work improves upon existing capabilities for direct hydrocode modeling of such problems.

METHODOLOGY

The paragraphs which follow outline the methodology used in developing a combined Eulerian-Lagrangian approach to debris cloud dynamics simulation. The Appendix discusses the analysis procedure in detail, while this and later sections present an overview and example simulations. The series of routines written to link the codes CTH and DYNA2D is referred to under the title DCT2D (Debris Cloud Translator 2-Dimensional). The series of routines written to augment the standard DYNA2D code for debris cloud simulation is referred to under the title DCA2D (Debris Cloud Augmentation 2-Dimensional). All code development and analysis was performed on a Cray Y-MP/864. The CTH-DYNA interface and DYNA augmentations presented here are currently limited to two dimensional problems, although the general modeling methodology may be implemented in a three-dimensional form.

To illustrate the analysis procedure, consider the representative problem of a 0.32 cm diameter aluminum sphere impacting upon a 0.081 cm thick aluminum plate at a velocity of 6.58 km/sec (Fig. 1a). At a standoff distance of 10.16 cm, this plate represents a ballistic limit Whipple shield for an aluminum wall of 0.127 cm thickness (Cour-Palais and Crews, 1990). CTH simulation of the initial impact in this problem was performed with mesh dimensions $\Delta x = \Delta y = 0.004$ cm. This mesh density exceeds by a factor of 6.25 that used by the CTH code development group in their published study of a canonical debris cloud problem (Trucano and McGlaun, 1990). Transmitting boundary conditions (McGlaun, 1982) were used to accommodate backsplash and debris transport outside the modeled region. The simulation employed the first momentum advection option (CONV=1, Trucano and McGlaun, 1990) in the CTH code. This option conserves momentum in mapping the deformed material mesh to the space-fixed mesh, while discarding any kinetic energy error associated with the remap, and is recommended by the CTH code development group (Trucano and McGlaun, 1990). The ANEOS (Thompson, 1990b) library equation of state for aluminum, with melting, was employed. The calculation required 3,135 CPU seconds.

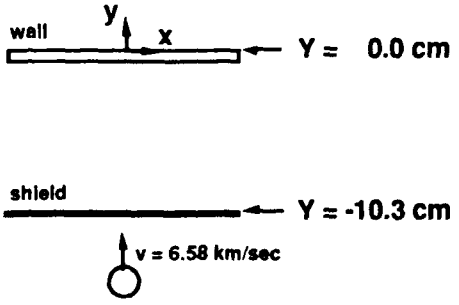


Fig.1a. Whipple shield impact problem

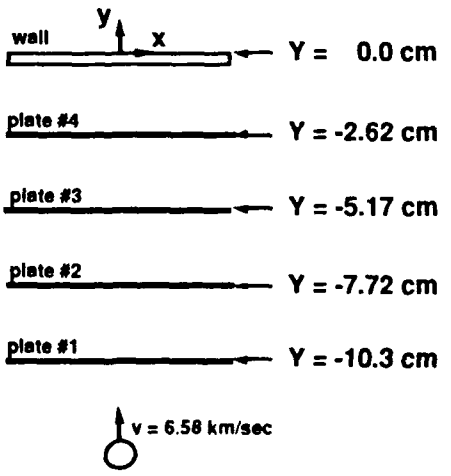


Fig. 1b. Multi-plate shield impact problem

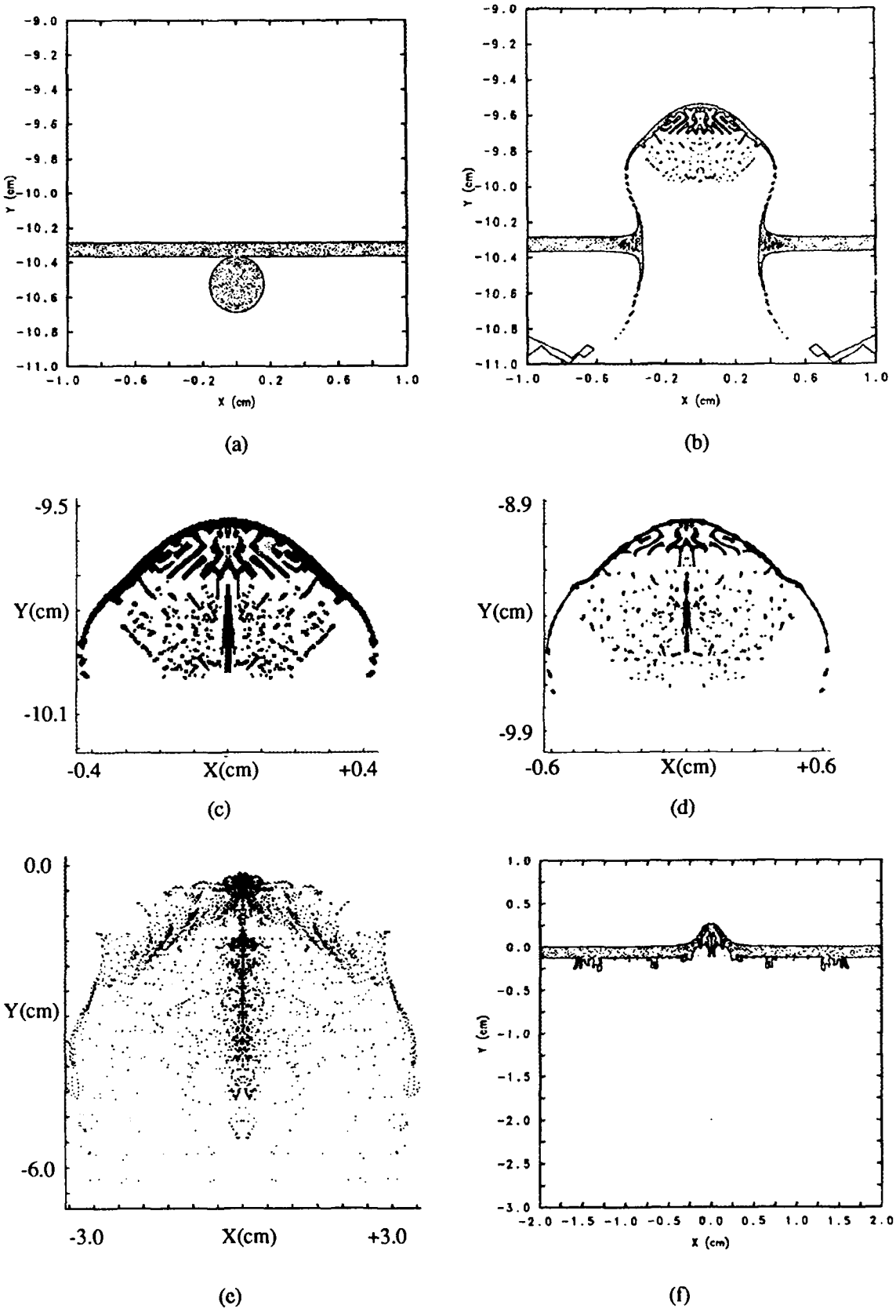


Fig. 2. Whipple shield impact simulation

Figures 2a and 2b show the results of the CTH simulation, in the form of mesh density plots at impact and at one and one-half microseconds after impact. The plot in Fig. 2b shows a clearly defined debris cloud at one and one-half microseconds after impact, extending approximately over the region -10.0 cm < Y < -9.5 cm and 0.0 cm < X < 0.5 cm, where X is a radial coordinate in this axisymmetric problem, and Y = 0 defines the axial location of the shielded structure (not modeled in this calculation). At this point in time the CTH calculation was terminated and the post-processor CTHED was used to write information on the debris cloud region to a data file for use in constructing a DYNA2D debris model.

Next the program DCT2D was run to prepare a DYNA2D input file describing the debris cloud mass, geometry, and velocity distribution, in a Lagrangian finite element form. All elements in the initial mesh containing over ninety-nine percent void space were deleted, resulting in the debris model shown in Fig. 2c. Comparison of the Lagrangian debris cloud model (Fig. 2c) with the debris cloud state at the end of the Eulerian simulation (Fig. 2b) illustrates the accuracy of the model translation procedure. Mass and kinetic energy error associated with the model translation process was approximately one percent. Since the Lagrangian elements contain variable amounts of void space, as determined by the CTH mass distribution data, caution should be exercised in interpreting the finite element geometry plot of Fig. 2c as a direct representation of the debris cloud mass.

Given an initial density, velocity, and void fraction distribution obtained from the CTH simulation, the Lagrangian model (DYNA2D augmented by the DCA2D routines) was then integrated to propagate the debris. In this example the DYNA2D model of the debris was composed of 2,181 elements, and required 4,297 CPU seconds to simulate the first microsecond of debris cloud evolution. It is important to note that the Lagrangian calculation must be started with a low user-specified time step, since the default DYNA2D calculation for the initial time step will not account for void space effects.

At two and one-half microseconds after impact, one microsecond after ending the Eulerian simulation, the debris cloud has evolved to the form shown in Fig. 2d (note the change in scale as compared to Fig. 2c). The radius of the debris cloud has increased significantly, and the leading edge of the debris cloud has translated along the impact centerline. The shell of the debris cloud has thinned as it expands, while the spreading of debris particles within the shell illustrates the presence of velocity variations across the debris cloud. The analysis reflects (qualitatively) results observed in impact experiments.

The Lagrangian simulation of debris cloud evolution shown in Figures 2c and 2d assumed that adjacent finite elements composing the debris cloud were interconnected, i.e. that the debris cloud deforms as a cohesive body, retaining its mechanical strength after impact. An alternative modeling option incorporated in the DCT2D routines takes each finite element to represent a discrete debris cloud fragment, i.e. assumes that the debris cloud lacks any cohesive strength after impact. This is often a more realistic description of hypervelocity impact effects on Whipple shield structures. Consider again the representative Whipple shield impact problem depicted in Figures 2a and 2b. Starting with the initial Lagrangian debris cloud model (Fig. 2c), and neglecting any cohesive coupling of the motion of the deforming elements, the augmented version of DYNA2D was used to propagate the impact debris towards a wall plate located at axial position Y = 0. At 17.5 microseconds after impact the leading edge of the debris cloud has reached the wall plate, with the expanded debris cloud taking the form shown in Fig. 2e. This simulation required 13,320 CPU seconds. Comparing Figures 2c and 2e, the debris cloud has expanded radially by a factor of eight and axially by a factor of thirteen. The predicted angle of expansion of the cone of debris is approximately thirty-six degrees. Qualitatively the debris cloud shown in Fig. 2e is consistent with experimental observations of Whipple shield impacts.

To complete the simulation and model debris impact on the wall plate, the mass, position, and velocity data from the DYNA2D simulation at 17.5 microseconds after impact (Fig. 2e) was input to DCT2D to generate a CTH input file. CTH was then used to simulate impact of the debris on the wall structure. The wall plate was modeled as aluminum with a yield strength of 0.966×10^9 dynes/cm^2. Figure 2f shows the wall at 19.5 microseconds after initial impact on the bumper shield, or 2.0 microseconds after initial impact of the debris on the wall. This CTH simulation required 3,035 CPU seconds. Overall the simulation predicts perforation of the wall plate for this nominally ballistic limit shield configuration.

Comparison of the preceding simulation results with the corresponding experiment (Cour-Palais and Crews, 1990) suggests that the analysis results are conservative, i.e. that the lethality of the debris cloud has been overestimated. However the results indicate that the proposed analysis procedure provides a

stable and realistic transformation of the Eulerian impact modeling results to a Lagrangian form well adapted for debris cloud evolution calculations. General use of the simulation approach just discussed in debris shield design applications requires further evaluation of the methods employed. A later section describes a series of calculations conducted to simulate a multi-plate shield impact experiment.

MIXTURE THEORY MODEL

The preceding discussion noted the development of a new constitutive augmentation of the DYNA2D code, describing a solid or fluid continuum with voids, in order to make practical the use of this code in multi-dimensional debris modeling applications. The following paragraphs outline briefly the formulation and implementation of a mixture theory based model for debris cloud simulation. This model has been coded (as a user-defined, history dependent equation of state) in a Cray (UNICOS) version of DYNA2D. The model is currently implemented in an isothermal, hydrodynamic form, although extension to include non-isothermal and deviatoric stress effects is possible. For a discussion of mixture theory concepts, see Drumheller and Bedford (1980).

Consider a solid or fluid continuum with voids, described by a bulk density ρ, a true density γ, a void fraction ϕ, a bulk pressure P, and a true pressure P_S. The parameters γ and P_S represent the thermodynamic state of the material of interest, while the parameters P and ρ are corresponding average values for a Lagrangian finite element of fixed mass M and variable volume V. The preceding parameters are related by

$$P = (1-\phi)\, P_S \;;\; \rho = (1-\phi)\,\gamma \;;\; \rho = M/V \;;\; P_S = P_S(\gamma) \qquad (1a,b,c,d)$$

where the expression (1d) represents the true isothermal equation of state for the material of interest. The history dependent element equation of state which is required for the Lagrangian finite element code has the functional form

$$P = P(\gamma, \phi) \qquad (2)$$

In order to define the element state an additional equation is needed for ϕ. Consistent with Drumheller's (1987) work on hypervelocity impact of mixtures, a rate equation will be employed here. The rate equation may be formulated with the aid of the general isothermal entropy inequality (Malvern, 1969)

$$-\dot{\Psi} + (1/\rho)\, \mathrm{tr}[\mathbf{TD}] \geq 0 \qquad (3)$$

where Ψ is the Helmholtz free energy density, **T** is the Cauchy stress tensor, **D** is the rate of deformation tensor, and "tr" is the trace operator. Considering only volumetric deformation, let

$$\mathbf{T} = -P\mathbf{I} \;;\; \mathrm{tr}(\mathbf{D}) = -\dot{\rho}/\rho \qquad (4a,b)$$

where **I** is the identity tensor. The entropy inequality then reduces to

$$-\dot{\Psi} + (P/\rho)\,[\dot{\rho}/\rho] \geq 0 \qquad (5a)$$

Using equations (1) and the conventional free energy density assumption $\Psi = \Psi(\gamma)$, the inequality (5a) reduces to

$$[(1-\phi)P/\rho^2 - \partial\Psi/\partial\gamma]\,\dot{\gamma} - (P\gamma/\rho^2)\,\dot{\phi} \geq 0 \qquad (5b)$$

If a rate law is assumed for $\dot{\phi}$, as previously discussed, this implies constitutive relations of a general functional form

$$\partial\Psi/\partial\gamma = (1-\phi)P/\rho^2 \;;\; \dot{\phi} = \dot{\phi}\,[P\gamma/\rho^2] \;;\; P\gamma/\rho^2 = P_S/\rho \;;\; (1-\phi)P/\rho^2 = P_S/\gamma^2 \qquad (6a,b\ \&\ 7a,b)$$

where the brackets in equation (6b) indicate functional dependence. Numerical implementation in DYNA2D of the mixture model just described assumed the following particular functional form for equation (6a)

$$P_s = c_1 \mu + c_2 \max(\mu,0) + c_3 \mu^2 + (c_4 + c_5\mu + c_6 \mu^2) E \; ; \; \mu = (\gamma/\gamma_0) - 1 \qquad (8a,b)$$

where the parameters c_i (i=1,2,...6) are constants, E is the internal energy, and γ_0 is the reference density. Consistent with the derived entropy inequality, the void fraction evolution equation was taken as

$$\dot{\phi} = - [\alpha/(\gamma_0/\rho)^2] \{ P/[(1-\phi)\rho] \} \qquad (8c)$$

where α is a constant which determines the rate of change of the void fraction in response to imposed pressure or deformation. The case $\alpha = 0$ represents a constant void fraction, whereas for the "shifting equilibrium" case (Bowen, 1982) represented by $\alpha \rightarrow \infty$ the void fraction adjusts instantaneously to changes in the bulk density. The latter case is representative of classical porous media models. A total of fourteen FORTRAN routines were added to DYNA2D or modified from their basic DYNA2D form in order to incorporate the mixture model just discussed into that code.

MODEL TRANSLATION PROCEDURE

The Eulerian-to-Lagrangian and Lagrangian-to-Eulerian model conversions used here require proper translation of mass, void fraction, and velocity distributions. Certain aspects of the model translation process warrant elaboration.

In the Eulerian-to-Lagrangian (CTH to DYNA2D) model translation process, each Eulerian cell is mapped to a Lagrangian finite element of the same size and geometry. Of course this exact geometric correspondence holds only at the start of the Lagrangian calculation, since the finite elements move and deform during the simulation, while the Eulerian cells are space fixed. The true density and void fraction for each cell at the end of the Eulerian simulation are assigned directly to a corresponding Lagrangian finite element. Translation of the velocity data is complicated slightly by the fact that the finite difference scheme used in CTH provides velocity data at the midpoints of the cell boundaries, while the finite element scheme in DYNA2D requires initial conditions data at nodal points corresponding to the Eulerian cell corners. Hence the following formulas were used to assign the initial Lagrangian nodal velocities $V_x^{(i,j)}$ and $V_y^{(i,j)}$ at the point located by the position coordinates $x^{(i)}$ and $y^{(j)}$:

$$V_x^{(i,j)} = [\, w_x^{(i,j-1)} v_x^{(i,j-1)} + w_x^{(i,j)} v_x^{(i,j)} \,] / [\, w_x^{(i,j-1)} + w_x^{(i,j)} \,] \qquad (9a)$$

$$V_y^{(i,j)} = [\, w_y^{(i-1,j)} v_y^{(i-1,j)} + w_y^{(i,j)} v_y^{(i,j)} \,] / [\, w_y^{(i-1,j)} + w_y^{(i,j)} \,] \qquad (9b)$$

where the $v_x^{(i,j)}$ and $v_y^{(i,j)}$ are the Eulerian velocity data, the superscripts (i), (j), and (i,j) denote logical (index) coordinates in the CTH mesh (McGlaun et al., 1990), and

$$w_x^{(i,j)} = (1/2) [\, m^{(i-1,j)} + m^{(i,j)} \,] \; ; \; w_y^{(i,j)} = (1/2) [\, m^{(i,j-1)} + m^{(i,j)} \,] \qquad (9c,d)$$

with $m^{(i,j)}$ denoting the mass in cell (i,j). The weighting factors $w_x^{(i,j)}$ and $w_y^{(i,j)}$ are appropriate for the uniform mesh used here, and are required in order to account for spatial variations in the true density and void fraction.

In the Lagrangian-to-Eulerian (DYNA2D to CTH) model translation process, one or two mass insertion packages for each finite element are written to the CTH input file. Triangular elements require one insertion package while quadrilateral elements require two, one for each of two triangular parts into which the quadrilateral is bisected. (The DCT2D routines provide an option for the use of either quadrilateral or triangular finite elements.) The material in each insertion package is assigned a velocity equal to the average of the associated nodal velocities, and a density equal to the true density of the solid material in

the associated finite element. The latter quantity is calculated using the element void fraction, which is maintained as a history variable in the Lagrangian simulation. Each triangular insert package is located in space as follows. First the coordinates of the centroid of the triangular insertion package (X_c,Y_c) are calculated from the associated nodal coordinates at the end of the Lagrangian simulation(X_i,Y_i). Then the coordinates of the corners of the triangular insertion package (x_i,y_i) are calculated using the formulas:

$$x_i = c\,X_i + (1-c)\,X_c \;;\; y_i = c\,Y_i + (1-c)\,Y_c \;;\; c = (1-\phi)^{1/2} \;;\; i \in \{1,2,3\} \qquad (10a,b,c)$$

The mapping of equations (10) represents a uniform dilatation, as seen in the element cross section, and was adopted in order to conserve both mass and true density in the model translation process. A subdivision of quadrilateral elements into two triangles is employed in the Lagrangian-to-Eulerian model translation process, so that in the case of radial symmetry the centroidal (cross section) coordinates of the element subdivisions and their associated insertion packages are identical.

MULTI-PLATE SPACE DEBRIS SHIELDING

This section describes a representative multi-plate shield impact modeling problem, simulated using the coordinated Eulerian-Lagrangian approach previously outlined. Parameters of the simulations are listed in Table 1. The problem involves normal impact of a 0.32 cm diameter sphere on a series of four bumper plates of thickness 0.0102 cm, followed by a wall of thickness 0.079 cm (Fig. 1b). The plate-to-plate and plate-to-wall spacing was 2.54 cm. The corresponding experiment is described by Cour-Palais and Crews (1990).

The CTH simulations were performed using the same mesh density, boundary conditions, and other modeling options previously discussed. The DYNA2D simulations were performed using models composed of up to 6,944 finite elements. The debris cloud was modeled as an isotropic, elastic-plastic hydrodynamic material (aluminum) with voids, and the following material properties: shear modulus = 0.250 g/(cm-μsec^2), bulk modulus = 6.52 x 10^{-1}g/(cm-μsec^2), yield strength = 3.45 x 10^{-3}g/(cm-μsec^2), plastic hardening modulus = 6.67 x 10^{-2}g/(cm-μsec^2), and values of α over the range $10^{-1} < \alpha < 10^{+3}$ (μsec/cm^2) as indicated in Table 1. Variations in the parameter α were considered in order to investigate the results on the simulations. Analyses to date indicate that the results are insensitive to the choice of values for α, although numerical stability requirements appear to place an upper limit on allowable values for α in the explicit DYNA2D code.

The following paragraphs briefly outline the series of nine Eulerian and Lagrangian simulations required to model perforation of all four shields and impact on the protected structure. The simulations are referred to by the codes listed in the first column of Table 1. The total required CPU time was 18.8 hours, for a simulation time of 20.8 microseconds.

The first CTH simulation ("plate #1" in Table 1) modeled perforation of the the first shield plate (Fig. 3a). Figure 3b shows a mass density plot at 1.5 microseconds after impact. At that time the CTH simulation was terminated and a DYNA2D model of the debris cloud was generated (Fig. 3c). This model ("debris #1" in Table 1) was used to simulate motion of the debris cloud towards the second plate, requiring a simulation time of 2.4 microseconds. The state of the debris cloud at 3.9 microseconds after impact, i.e. at the end of this Lagrangian simulation, is shown in Fig. 3d. At this point the results of the Lagrangian calculation were used to generate a new Eulerian model of impact on the second plate (Fig. 3e).

The results of the second CTH simulation ("plate #2" in Table 1) are shown in Fig. 3f, a mass density plot at 5.5 microseconds after impact on the first shield. Comparison of the debris cloud models at the end of the first Lagrangian simulation (Fig. 3d) and the start of the second Eulerian simulation (Fig. 3e) illustrates the model translation process. Note that in the interest of reducing CPU time requirements, some of the widely dispersed debris present at the end of the first DYNA2D simulation (Fig. 3d) is neglected in the Lagrangian-to-Eulerian remap. CTH simulation of the second shield impact was followed by a second Lagrangian simulation of debris cloud evolution towards the third shield ("debris #2" in Table 1). As indicated in Table 1, this sequence of calculations was repeated to proceed through the entire multi-

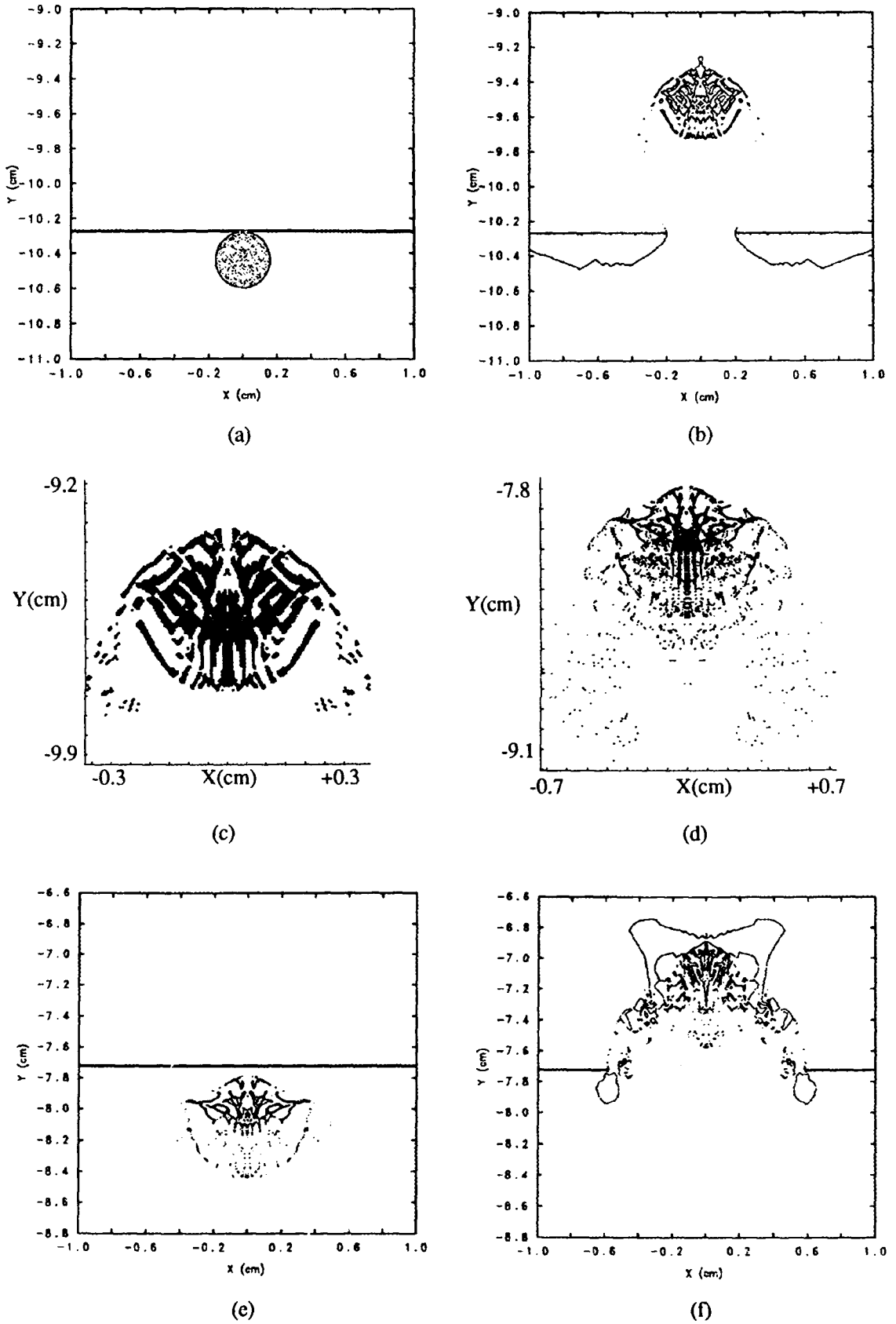


Fig. 3. Multi-plate shield impact simulation

plate structure. To reduce CPU time requirements, only the central core of the debris cloud was propagated towards the wall plate. That is debris subject to wide radial dispersion was dropped from the simulation during the Eulerian-to-Lagrangian or Lagrangian-to-Eulerian rezones. No Lagrangian-to-Lagrangian rezones were required to complete the analysis.

Final simulation of debris cloud impact on the wall structure is depicted in Fig. 4, which shows a mass density plot at 20.8 microseconds after initial impact on the first shield. As indicated by the plot in Fig. 4, the predicted result is a hole in the protected structure with an approximate diameter of 0.16 cm. This compares favorably with the experimental result of a torn wall plate, with damage dimensions approximately 0.2 cm x 0.5 cm (Cour-Palais and Crews, 1990).

Simulation title	Simulation type E=Eulerian L=Lagrangian	Start time (micro-seconds)	End time (micro-seconds)	CPU time (seconds) Cray Y-MP/864	Alpha (micro-seconds per cm squared)	maximum element void fraction (%)	Number of Eulerian or Lagrangian zones
plate #1	E	0.0	1.5	2,913	-	-	250 x 500
debris #1	L	1.5	3.9	7,481	0.1	99	2,423
plate #2	E	3.9	5.9	6,249	-	-	250 x 500
debris #2	L	5.9	8.3	8,168	1000.0	98	6,944
plate #3	E	8.3	10.1	5,860	-	-	250 x 750
debris #3	L	10.1	12.1	10,360	1.0	99	6,510
plate #4	E	12.1	14.8	8,676	-	-	250 x 750
debris #4	L	14.8	17.8	11,850	1.0	99	4,462
wall plate	E	17.8	20.8	6 [illegible]5	-	-	250 x 750

Table 1. Simulation parameters: multi-plate shield impact problem

CONCLUSIONS

A number of analytical models have been developed for projectile impact on Whipple shields (see e.g. Grady and Passman, 1990). These models typically adopt a number of very basic assumptions regarding the debris cloud shape, mass distribution, velocity distribution, and other properties. These assumptions have been motivated in part by difficulties experienced in modeling debris cloud evolution with Eulerian hydrocodes. The modeling methodology presented here avoids both the major assumptions of analytical models and mass dispersion problems which may be encountered with purely Eulerian simulations.

The results presented here suggest two conclusions regarding the use of a combined Eulerian-Lagrangian hydrocode modeling approach to space debris shield design :

(1) Mixture theory based models for solid and fluid materials with voids provide a suitable means for extending the use of Lagrangian hydrocodes to multidimensional debris cloud modeling problems.

(2) Lagrangian debris cloud models can offer acceptable CPU time requirements for direct computer simulation of multi-plate impact experiments, at least in two dimensions, while requiring minimal user intervention in the simulation.

Future work can profitably focus on two areas. First, additional simulation work is needed, to further critique the modeling methodology used here against a range of hypervelocity impact experiments. Of particular importance is the effect of variations in material properties and constitutive equations on model predictions at various impact velocities. Second, additional software development work is needed to provide the capability for three dimensional simulation of oblique impact effects on proposed space debris shield designs. Extension of the modeling approach presented here to three dimensions is direct, and well motivated by the extremely large computer time requirements of three dimensional Eulerian hydrocode simulations.

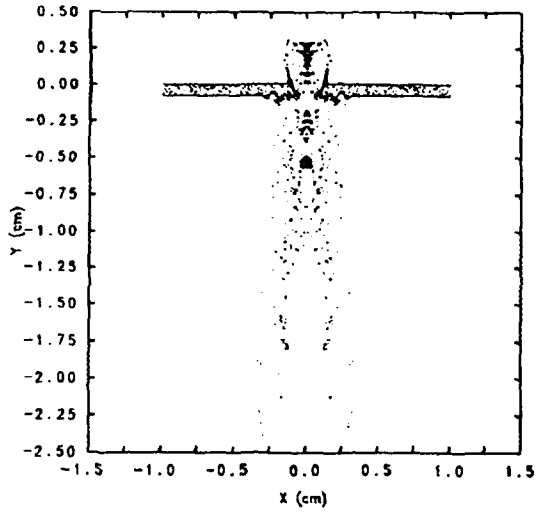


Fig. 4. Wall impact for the multi-plate shield impact simulation

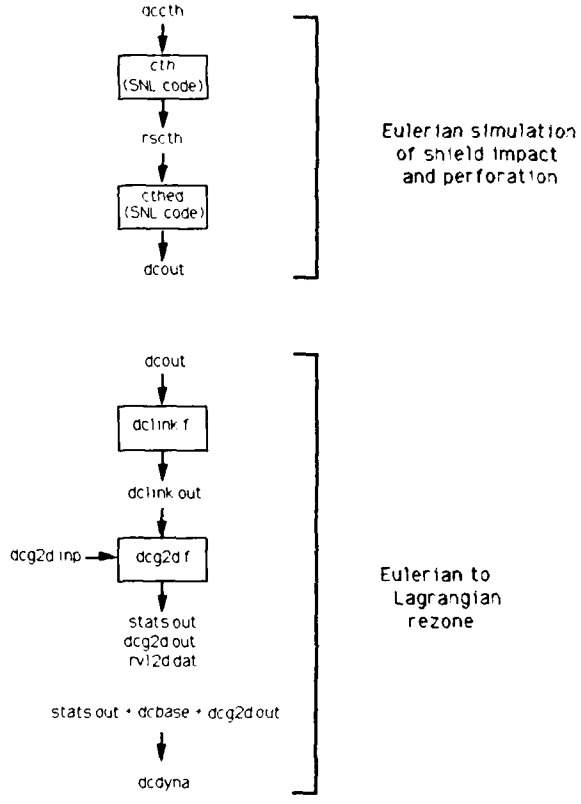


Fig. A-1. Eulerian simulation and rezone procedure

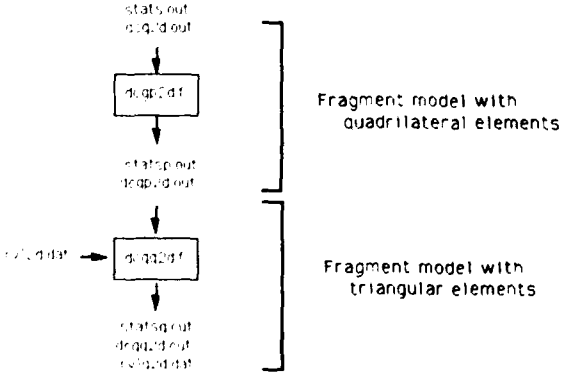


Fig. A-2. Fragmented debris cloud model generation procedure

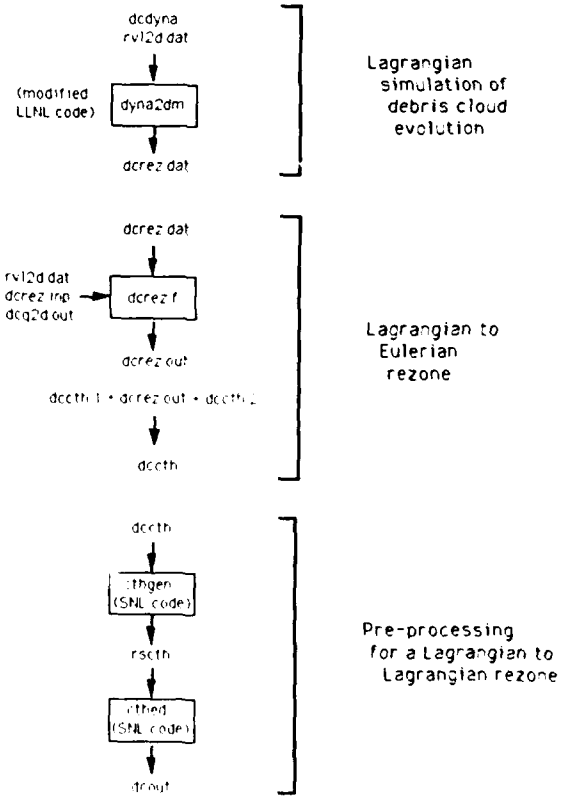


Fig. A-3. Lagrangian simulation and rezone procedure

ACKNOWLEDGEMENTS

This work was supported under the NASA Regional Universities Grant Program. The assistance of Eric L. Christiansen (NASA Technical Officer) and Jeanne Lee Crews of Johnson Space Center is gratefully acknowledged. Additional funding was provided by Cray Research, Inc. under the Cray University Research and Development Grant Program. Computer time was provided by the University of Texas System Center for High Performance Computing.

REFERENCES

Asay, J.R. and T.C. Trucano (1990). Studies of Density Distributions in One-Dimensional Shock-Induced Debris Clouds. *Int. J. of Impact Engineering*, 10, 35-50.

Bowen, R.M. (1982). Compressible Porous Media Models by Use of the Theory of Mixtures. *Int. J. of Engineering Science*, 20, 697-735.

Christiansen, E.L. (1990). Advanced Meteoroid and Debris Shielding Concepts. AIAA 90-1336, AIAA/NASA/DOD Orbital Debris Conference, Baltimore, April 16-19.

Cour-Palais, B.G. and J.L. Crews (1990). A Multi-Shock Concept for Spacecraft Shielding. *Int. J. of Impact Engineering*, 10, 135-146.

Drumheller, D.S. (1987). Hypervelocity Impact of Mixtures. *Int. J. of Impact Engineering*, 5, 261-268.

Drumheller, D.S. and A. Bedford (1980). A Thermomechanical Theory for Reacting Immiscible Mixtures. *Archives for Rational Mechanics and Analysis*, 73, 257-284.

Grady, D.E. and S.L. Passman (1990). Stability and Fragmentation of Ejecta in Hypervelocity Impact. *Int. J. of Impact Engineering*, 10, 197-212.

Hallquist, J.O. (1987). *User's Manual for DYNA2D*. UCID 18756 (Rev. 3), Lawrence Livermore National Laboratory, Livermore, California.

Malvern, L.E. (1969). *Introduction to the Mechanics of a Continuous Medium*. Prentice-Hall, Englewood Cliffs, New Jersey.

McGlaun, J.M. (1982). *Improvements in CSQ:A Transmitting Boundary Condition*. SAND82-1248, Sandia National Laboratories, Albuquerque, New Mexico.

McGlaun, J.M., S.L. Thompson and M.G. Elrick (1990). CTH: A Three Dimensional Shock Wave Physics Code. *Int. J. of Impact Engineering*, 10, 351-360.

Thompson, S.L. (1990a). *CSQ III: An Eulerian Finite Difference Program for Two-Dimensional Material Response: User's Manual*. SAND87-2763, Sandia National Laboratories, Albuquerque, New Mexico.

Thompson, S.L. (1990b). *ANEOS - Analytic Equations of State for Shock Physics Codes: Input Manual*. SAND89-2951, Sandia National Laboratories, Albuquerque, New Mexico.

Trucano, T.G. and J.M. McGlaun (1990). Hypervelocity Impact Simulations Using CTH: Case Studies. *Int. J. of Impact Engineering*, 10, 601-614.

APPENDIX

This appendix provides a detailed description of the structure and use of the software written to link CTH and DYNA2D. The general analysis procedure is represented by the flow charts shown in Figures A-1 through A-3. As presently formulated, the procedure models two-dimensional (axisymmetric) impact of like materials. Mass, kinetic energy, void fraction, and density are conserved in Eulerian-to-Lagrangian or Lagrangian-to-Eulerian translations of debris cloud data. Thermal energy is discarded. Generalization of this analysis procedure is possible, given additional development work.

A typical impact simulation proceeds as follows. A standard Eulerian model of the projectile impact on the first debris shield is formulated using CTH (Fig. A-1). Geometry, material properties, initial velocities, and other input data are specified in the input file *dccth*. The simulation is halted after perforation of the plate and initial formation of the debris cloud, but before the bulk debris cloud density is reduced to a level at which the Eulerian mesh density becomes inadequate. The output file (*rscth*) from the CTH simulation is then input to the post-processor CTHED. The standard CTH post-processor CTHED is then used to write an output data file which describes the state (mass, velocity, etc.) of all Eulerian cells in a rectangular region of space behind the shield. (The user selects the region of space containing the debris which must be propagated to the next shield, by viewing the CTH simulation

results.) The mass, velocity, and pressure distribution in the debris cloud is contained in the post-processor output file *dcout*.

Next (Fig. A-1) the routines *dclink.f* and *dcg2d.f* are used to generate a Lagrangian model of the debris cloud (*dcdyna*), given the Eulerian simulation results (*dcout*) and the geometry, material, and control data contained in the user input files *dcg2d.inp* and *dcbase*. Specifically, the output data file *dcout*, which is quite extensive and is written in a specific CTHED format, is read and screened by *dclink.f*, which writes an output data file *dclink.out* that contains only the position, mass, velocity, void fraction, and other data needed to construct the Lagrangian finite element mesh with appropriate initial conditions. Then the program *dcg2d.f* is invoked, which reads the data file *dclink.out* and performs the following three functions:

(1) Defines the nodes, elements, element connectivities, and initial velocities for the Lagrangian finite element mesh used to model the debris cloud. Initial velocities are assigned to the finite element nodes based on interpolation of the CTH cell velocity data. The user may choose to delete all element interconnections, essentially simulating the debris cloud as a collection of noninteracting deforming elements ("fragments") with voids (Fig. A-2). The use of this option, well suited to many hypervelocity problems, is illustrated in the example simulations discussed in the text.

(2) Screens the preliminary finite element mesh to identify and delete all elements with void space percentages above a user-specified level. This necessitates a somewhat complex renumbering of nodes and elements to satisfy DYNA2D input format requirements. This step is important to avoid the inclusion of very low mass, high void space elements which may greatly slow the computation while representing very little debris mass. The preceding results are written to *dcg2d.out* in a format suitable for direct inclusion in a DYNA2D input file.

(3) Defines the initial void space associated with each finite element in the Lagrangian model, writing the results to *rvl2d.dat* which becomes an auxiliary input data file for the DYNA2D code. Combined with the new constitutive modeling routines previously discussed, this procedure provides a mass and kinetic energy consistent interface between the CTH and DYNA2D codes without requiring that each debris particle be explicitly modeled by the Lagrangian mesh. Such a requirement would in general be impractical from both a model generation and CPU time consumption point of view.

The output file *dcg2d.out* is appended to a short user-prepared control file *dcdata* (written in a DYNA2D specified format) which provides standard information on material properties, time step size, etc. needed to perform the Lagrangian simulation. The resulting file *dcdyna* is input to an augmented version of the Lagrangian code DYNA2D (Fig. A-3), which incorporates a mixture equation of state for a continuum with voids, as well as a void fraction evolution equation. The auxiliary input file *rvl2d.dat* created by *dcg2d.f* is required to properly initialize the DYNA2D calculation. A Lagrangian simulation is then used to propagate the debris to the next shield. An auxiliary output file *dcrez.dat* is created by the modified version of DYNA2D for use in initializing the next Eulerian shield impact calculation.

The results of the Lagrangian simulation of the debris cloud evolution (*dcrez.dat*) are input to the routine *dcrez.f* (Fig. A-3), to develop an Eulerian description of the debris cloud impacting the next shield. The routine *dcrez.f* also requires as input certain geometry, mesh connectivity, and mass distribution data contained in the files *dcrez.inp*, *rvl2d.dat*, and *dcg2d.out*, the latter two having been previously generated by *dcg2d.f*. The output from *dcrez.f*, contained in the file *dcrez.out*, is combined directly with standard CTH specified geometry, material, and control data (*dccth.1* and *dccth.2*) describing the next shield (or wall) impact calculation to be performed. The resulting CTH input file (*dccth*) is used to initiate a repeat cycle of calculations.

In some cases, one or more rezones of the Lagrangian mesh may be required to propagate the debris between two adjacent shields. In this case (Fig. A-3), the file *dccth* is created as previously discussed, but without a new shield model, and then input to the CTH pre-processor CTHGEN. The resulting output file (*rscth*) is then processed as previously described in order to create a rezoned Lagrangian model. This Lagrangian rezone procedure is well suited to mixture theory based debris models, although a special (direct) rezone routine could be written for this purpose. Note that the standard DYNA2D rezoner cannot be used in this case, due to the presence of void space in the Lagrangian finite elements. In any case, conventional Lagrangian rezone procedures are ill-suited to this application, due to the extremely complex geometry of the debris clouds.

In summary, the programs DCT2D and DCA2D provide a highly automated coupling of CTH and DYNA2D for use in debris cloud modeling problems.

Int. J. Impact Engng Vol.14, pp.241 - 254, 1993
Printed in Great Britain

0734-743X/93 $6.00+0.00
© 1993 Pergamon Press Ltd

IMPACT-INDUCED DELAYED DETONATION IN AN ENERGETIC MATERIAL DEBRIS BUBBLE FORMED AT AN AIR GAP

S. A. FINNEGAN, J. K. PRINGLE, J. C. SCHULZ,
O. E. R. HEIMDAHL, and A. J. LINDFORS

Research Department, Naval Air Warfare Center - Weapons Division,
China Lake, CA 93555-6001

ABSTRACT

A planar model of a rocket motor has been developed that allows reaction in a central bore perforated by a projectile to be viewed with high-speed photography. Earlier work with this model showed that a "bubble" of propellant debris forms in the air gap between energetic material layers (bore region) as a result of projectile penetration of one of the layers. Ignition of the bubble occurs upon impact with the second layer, followed by a reaction ranging from mild burning to delayed detonation, depending on the width of the air gap, properties of the energetic material, and degree of confinement. The present paper presents the results of experimental and hydrocode studies to characterize the latter (delayed detonation) reaction. Results show that reaction initiates in the frontal portion of the bubble wall through mechanical (impact) shock. It then propagates backward through the bubble wall towards the first layer which then detonates. Detonation of the second layer occurs sympathetically. The reaction is bounded by a lower velocity limit and confined within a range of air gaps that increases with impact velocity. The upper-air-gap limit roughly coincides with the maximum expansion distance for the bubble before breakup, while the lower limit represents the minimum (threshold) damage level for detonation.

INTRODUCTION

Projectile impact at sufficient velocity against energetic material (propellant or explosive) can cause the material to detonate (Mellor *et al.*, 1988). Detonation may occur almost immediately on contact (prompt detonation) or at a later time (delayed detonation).

Prompt detonation can be explained in terms of the so-called shock-to-detonation transition (SDT). Delayed detonation is any detonation occurring after the time for prompt detonation. One type of delayed detonation involves the deflagration-to-detonation transition (DDT). An initial burning reaction increases the pressure in a porous bed of energetic material. Increased pressure "feeds" the reaction. In the presence of sufficient confinement, transition to detonation occurs. Another type of delayed detonation has been termed unknown-mechanism-to-detonation transition (XDT). XDT involves recompression of impact-damaged material, although, as the name implies, the exact mechanism is not clear (Mellor *et al.*, 1988).

There has been a renewed interest in XDT reactions as a result of some recent bullet impact tests of cylindrical rocket motor sections containing center bores. In these tests, XDT reactions were observed for impacts through the bore center under certain conditions. Initiation occurred in the rear portion of the web (i.e., opposite from the impact side) during projectile penetration of that region. Reaction was attributed to propellant damaged as a result of stress wave interactions (Nouguez *et al.*, 1989).

Because of the direct relationship between damage and reaction sensitivity, there has also been a large interest in failure processes in energetic materials, particularly under dynamic loading conditions. Recently, a comprehensive study of damage processes in an explosive simulant impacted by cylindrical projectiles was conducted (Yuan *et al.*, 1992a, b, c). Fragmentation was induced by impacting planar targets at sufficiently high velocities so that a cloud of debris (i.e., debris bubble) was ejected from the rear surface. Fragmentation characterizations were made as a function of both impact velocity and layer thickness.

In experiments similar to those conducted by Yuan *et al.* (1992a, b, c), we have observed a type of XDT reaction resulting from impact of an energetic material debris bubble on a layer of either inert or energetic material. The

purpose of the present paper is to present experimental and hydrocode studies that we have performed to characterize this delayed detonation phenomenon.

EXPERIMENTAL STUDIES

Experimental Arrangement

Planar Rocket Motor Test Model. Our interest in impact-induced detonation phenomena is related primarily to the prevention of bullet or fragment initiation of propellant in solid rocket motors. The study of detonation phenomena in rocket motors is complicated by the fact that the initiating processes are hidden within the cylindrical case. A planar rocket motor test model has been developed as an aid in the visualization of these processes (Finnegan *et al.*, 1990).

The planar model consists of a steel plate, a layer of propellant, an air gap, a second layer of propellant, and a second steel plate, as shown in Fig. 1. The air gap simulates an inner bore in the rocket motor. A spherical steel projectile impacts the target perpendicular to the plates and layers. The plates can be omitted and tests run against bare propellant. Also, the second plate and layer can be omitted to produce an infinite air gap The addition of transparent Plexiglas sidewalls provides a degree of lateral confinement. The open architecture allows impact and reaction events in the air gap to be recorded photographically.

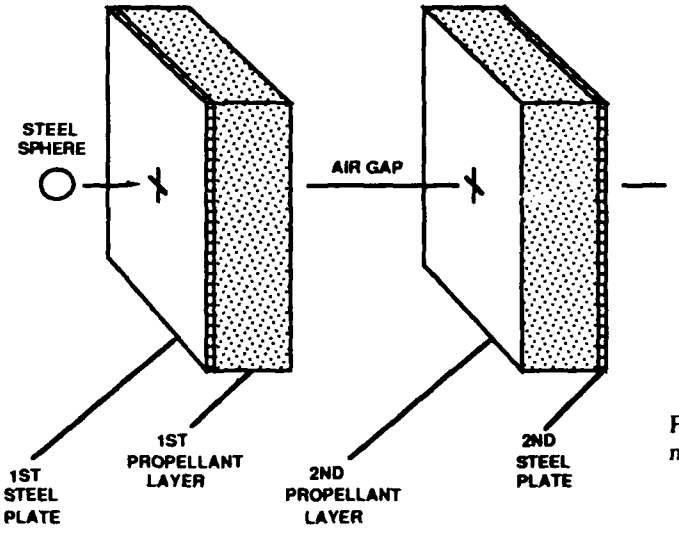


Fig. 1. Planar rocket motor test model.

Target/Projectile Parameters. Energetic materials used in the present study included two nonmetallized, high-energy, nitramine propellants (called HEP-1 and HEP-2) and an explosive (Composition B). An inert propellant simulant was also used as second layer material, in a few tests. Mechanical properties for these materials are listed in Table 1. Cover plate materials consisted of either hardened (370 BHN) or mild (95 BHN) steel. Energetic material layer and cover plate thicknesses were 38.1 and 1.59 mm, respectively. Fast-setting urethane adhesive (Hardman Inc, Belleville, NJ) was used to bond the two together. The air gap was varied between 12.7 mm and "infinity". Projectiles were 19.0-mm-diameter mild steel spheres or ogival-nosed cylinders. Tests of Composition B were included to examine the influence of material brittleness on detonation behavior, while tests of ogival projectiles were done to determine the effects of nose geometry.

Table 1. Uniaxial tensile properties of energetic and simulant materials.

Test Material	Initial Density, ρ g/cm^3	Stress, σ MPa[a]	Strain, ε %[b]	Young's Modulus, E GPa
Simulant	1.73	0.67[c]	30	0.00401
HEP-1	1.61	0.46[c]	43	0.00182
HEP-2	1.70	0.39[c]	327	0.00184
Comp B	1.71	1.43[d]	0.015	11.69

[a] Engineering maximum.
[b] At maximum stress.
[c] Test rate 2 in/min.
[d] Test rate 0.05 in/min.

Projectile Launcher/Photographic Setup. Saboted projectiles were fired from a 20 mm smooth-bore gun. Sabots for spherical projectiles were designed to separate from the projectile during flight and were stopped by a stripper plate. Sabots for ogival projectiles were rigidly attached to provide greater stability during flight and target penetration. In-flight velocities were measured using a Photec high-speed camera running at 16,000 frames/s in conjunction with a backlighting system consisting of an array of flash lamps and a diffusing screen. Impact processes and propellant reactions were observed using a Fastax high-speed camera running at 32,000 frames/s along with a separate, similar backlighting system. Launch velocities ranged from 500-1,250 m/s.

Experimental Results

Bubble Breakup Elongation Measurements. Bubble breakup elongation estimates were obtained from the high-speed photographs by noting the film frame at which "feathering" of the edge of the bubble first occurs. These estimates, listed in Table 2, probably represent upper bounds to the actual breakup elongations. A high-speed photographic sequence showing the expansion and breakup of a debris bubble in an infinite air gap, is seen in Fig. 2. (Sequence runs from top to bottom and left to right.)

Table 2. Summary of experimentally-measured debris bubble breakup elongations.

Cover Plate[a]	Propellant Type	Propellant Layer Thickness, mm	Projectile	Impact Velocity, m/s	Bubble Velocity, m/s	Bubble Breakup Elongation, mm[b]
steel[c]	HEP-1	25.4	sphere	1188	905	53.3
steel[c]	HEP-1	34.9	sphere	1177	897	63.5
steel[d]	HEP-2	38.1	sphere	706	473	53.3
steel[d]	HEP-2	38.1	sphere	820	561	66.0
steel[d]	HEP-2	38.1	sphere	1007	673	81.3
steel[d]	HEP-2	38.1	sphere	1233	791	88.9
none	HEP-2	38.1	sphere	978	718	55.9
none	HEP-2	38.1	sphere	1171	938	63.5

a 1.59 mm thickness.
b Measured normal to propellant layer, from exit side to front of bubble.
c 95 BHN hardness.
d 370 BHN hardness.

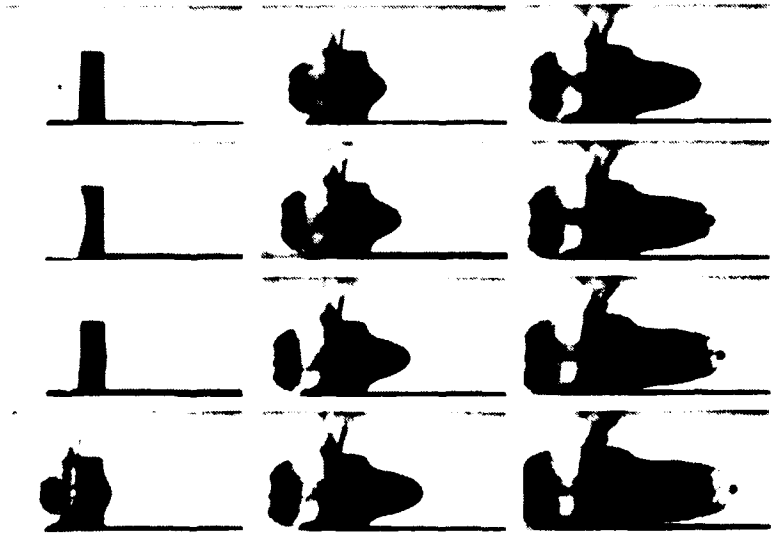


Fig. 2. Photographic sequence of sphere/planar model impact at 1233 m/s. (29 μs interframe time) Planar model configuration: hard steel, HEP-2, infinite air gap.

Delayed Detonation Limit Measurements. Delayed detonation limits were established by testing through a range of air gaps and impact velocities. Testing of HEP-1 and Composition B was limited to a single impact velocity, projectile shape and target condition, while testing of HEP-2 was more extensive. A total of 30 tests were run, the results of which are summarized in Table 3.

Table 3. Summary of delayed detonation reaction tests.

1st Steel Plate[a]	1st Prop. Layer	Air Gap, mm	2nd Prop. Layer	2nd Steel Plate[a]	Projectile[b]	Impact Vel., m/s	Bubble Vel., m/s	Reaction
hard	HEP-1	12.7	HEP-1	hard	sphere	1163	[c]	delayed detonation
hard	HEP-1	25.4	HEP-1	mild	sphere	1210	[c]	delayed detonation
hard	HEP-1	38.1	HEP-1	mild	sphere	1216	[c]	slight burning
mild	HEP-1	38.1	HEP-1	mild	sphere	1174	[c]	slight burning
mild	HEP-1	38.1[d]	HEP-1	mild	sphere	1219	737	mild burning
mild	HEP-1	50.8[d]	HEP-1	mild	sphere	1221	731	mild burning
mild	HEP-1[e]	76.2[d]	HEP-1	mild	sphere	1177	897	moderate burning
none	HEP-2	25.4	HEP-2	none	sphere	818	560	delayed detonation
none	HEP-2	38.1	HEP-2	none	sphere	829	576	delayed detonation
none	HEP-2	50.8	HEP-2	none	sphere	870	631	slight burning
none	HEP-2	38.1	HEP-2	none	sphere	1234	916	delayed detonation
none	HEP-2	50.8	HEP-2	none	sphere	1192	903	slight burning
none	HEP-2	25.4	HEP-2	none	ogive	1201	[c]	delayed detonation
none	HEP-2	38.1	HEP-2	none	ogive	1172	1082	slight burning
hard	HEP-2	31.8	HEP-2	hard	sphere	534	283	delayed detonation
hard	HEP-2	38.1	HEP-2	hard	sphere	523	269	delayed detonation
hard	HEP-2	44.4	HEP-2	hard	sphere	552	318	very slight burning
hard	HEP-2	12.7	HEP-2	hard	sphere	628	[c]	none visible
hard	HEP-2	25.4	HEP-2	hard	sphere	646	376	none visible
hard	HEP-2	38.1	HEP-2	hard	sphere	674	404	delayed detonation
hard	HEP-2	50.8	HEP-2	hard	sphere	785	498	very slight burning
hard	HEP-2	50.8	HEP-2	hard	sphere	1011	605	delayed detonation
hard	HEP-2	63.5	HEP-2	hard	sphere	1042	648	delayed detonation
hard	HEP-2[f]	25.4[d]	simulant	hard	sphere	1153	[c]	moderate burning
hard	HEP-2[f]	38.1[d]	simulant	hard	sphere	1182	[c]	delayed detonation
hard	HEP-2[f]	50.8[d]	HEP-2[f]	hard	sphere	1186	700	delayed detonation
hard	HEP-2[f]	63.5[d]	HEP-2[f]	hard	sphere	1209	[c]	delayed detonation
hard	HEP-2[f]	76.2[d]	HEP-2[f]	hard	sphere	1263	769	moderate burning
hard	Comp B	25.4	Comp B	mild	sphere	1211	[c]	delayed detonation
hard	Comp B	50.8	Comp B	mild	sphere	1206	717	slight burning

[a] 1.59 mm, 95 BHN (mild) or 370 BHN (hard) steel.
[b] Sphere mass: 28.2 g. Ogive mass: ~40 g.
[c] Velocity could not be measured.
[d] Confined with Plexiglas sidewalls.
[e] 34.9 mm thickness.
[f] Propellant contained numerous large voids.

Bubble Breakup Elongation/Delayed Detonation Limit Comparison. A comparison of measured bubble breakup elongations with upper-air-gap detonation limits (i.e., average of largest air gap for detonation and smallest for burning) is shown in Table 4. In all cases, detonation limits are considerably lower than measured breakup elongations. As mentioned, measured estimates of breakup elongation represent upper bounds to the actual breakup elongations.

Table 4. Comparison of detonation limits with experimentally-measured bubble breakup elongations.

Projectile[a]	Target Configuration	Detonation Limit, mm[b]	Bubble Breakup Elongation, mm[c]
sphere	covered HEP-1[d]	31.8	63.5
sphere	covered HEP-2	69.9	88.9
sphere	covered Comp B	38.1	[e]
sphere	bare HEP-2	44.4	63.5
ogive	bare HEP-2	31.8	[e]

[a] Impact velocity approximately 1200 m/s.
[b] Average of largest air gap for detonation and smallest for burning.
[c] Measured normal to propellant layer, from exit side to front of bubble.
[d] 34.9 mm thickness.
[e] Not measured.

The lower detonation limits for HEP-1 and Composition B as compared to HEP-2 are consistent with the smaller breakup elongations expected for less tough materials (Grady and Passman, 1990). The lower detonation limit for an ogival projectile as compared to a spherical one reflects the lower penetration resistance for this nose shape that allows easier penetration of the bubble wall.

Delayed Detonation Limit Map For HEP-2 Propellant. Although most of the effort was directed towards determining upper (air gap) limits for the delayed detonation reaction, sufficient tests were conducted on HEP-2 to allow lower limits to be established also. Establishing a lower limit was relatively straightforward at the lower impact velocities. At the highest impact velocities, the process was complicated by the onset of a second delayed detonation reaction that initiated at the smaller air gaps (Finnegan *et al.*, 1992). Fortunately, the much longer delay times for the second reaction allowed the two reactions to be separated.

Combining upper and lower limit data allows a more complete boundary map to be constructed for the delayed detonation reaction in this propellant, as shown in Fig. 3. (Individual test results, rather than average limit values, were used for Fig. 3.) An interesting feature is the apparent invariance of the lower limit within this velocity range. The reason for this invariance was not established, although it may be the result of experimental limitations considering the small amount and limited accuracy of these data.

Delayed Detonation Mechanistic Study. Based on initial tests, a mechanism for delayed detonation was proposed involving initiation at the front of the bubble upon impact with the second propellant layer and propagation of a reaction backwards through the bubble to the first layer. The evidence for this mechanism was indirect, consisting of high-speed photographs showing ignition beginning at the point of impact of the bubble on the second propellant layer and showing the first propellant layer detonating ahead of the second. In recent tests, a number of photographs were obtained showing the reaction front at various locations within the air gap. One example is shown in Fig. 4. In Fig. 4 (top), the bubble has not yet impacted the second layer. In Fig. 4 (bottom), which was taken about 9 μs after impact with the second layer, the reaction, as indicated by the products boundary (dashed for clarity), has almost crossed the air gap. (The projectile is traveling from left to right. The lower part of the boundary is not visible due to light reflection from the base.)

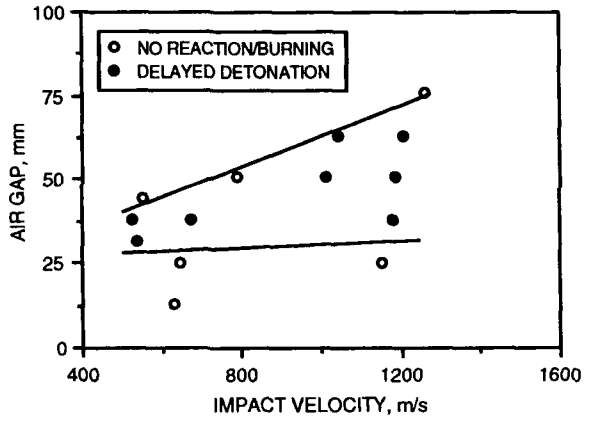


Fig. 3. Upper- and lower-air-gap detonation limits as a function of impact velocity for covered HEP-2 propellant

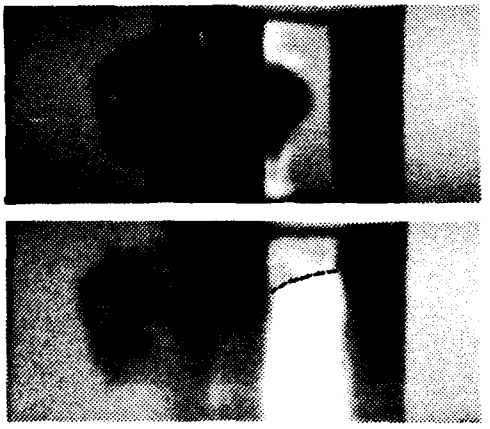


Fig. 4. Photographs showing propagating delayed detonation.

Evidence for detonation of the main propellant layers was provided by velocity measurements of cover plate fragments and, for the test involving Composition B, by a comparison with the theoretical Gurney velocity (Table 5). The Gurney velocity was calculated from data contained in a report by Henry (1967). (A discussion of the Gurney relationship is contained in a report by Stronge *et al.* (1989)). For Composition B, the Gurney velocity agrees quite well with exit-side (second layer) velocities, but is lower than impact-side values. The reason for the much higher impact-side fragment velocities, compared to exit-side values, for HEP-2 was not established. Jensen *et al.* (1981) have shown that blast overpressures from XDT reactions are, on average, higher than for SDT. This increase in reaction violence has been attributed to collision of detonation waves from adjacent hot spots (Dienes, 1986). It is possible that reaction of the more-heavily-damaged first layer involves XDT, while detonation of the second layer (which appears to occur sympathetically from experimental data) involves SDT, in this case.

Table 5. Cover plate fragment velocity comparison.

Energetic Material	Impact Vel., m/s	1st Plate Vel., m/s	2nd Plate Vel., m/s	Gurney Vel., m/s
HEP-2	1200[a]	4400[a]	2800[a]	[b]
Comp. B	1211	>3470	3256	3219

[a] Average for several tests.
[b] Not calculated.

Tests of covered HEP-2 propellant at lower impact velocities provided some significant information regarding the initiation mechanism responsible for the delayed detonation process. At impact velocities below about 900 m/s, there was virtually no visible propellant reaction in the absence of detonation. The absence of surface combustion processes during the initial bubble impact stage demonstrated that these processes were not responsible for the detonation reaction. These differences are illustrated in three high-speed photographic sequences, shown in Fig. 5-7, of tests at similar impact velocities but for air gaps below, within, and above the detonation regime. In these three sequences, the only visible reaction, other than the one associated with the detonation process, in Fig. 6, is the slight "puff" of reaction seen in propellant debris emanating from within the penetration cavity on the impact side in Fig. 7. This reaction, seen at even lower impact velocities, is associated with impacts of fragmented bubble debris. This impact condition typically results in a reaction that propagates backward through the center of the remaining incoming material (Finnegan *et al.*, 1990). That the debris bubble was fragmented for this test can be seen by an inspection of the bubble impact pattern on the inner surface of the second propellant layer (Fig. 8 - lower right side). The pockmarked pattern of that surface is characteristic of an impact involving fragmented bubble material, while the circular crater with the concentric, ring-like surface morphology (Fig. 8 - upper right side) is characteristic of one involving an unbroken bubble.

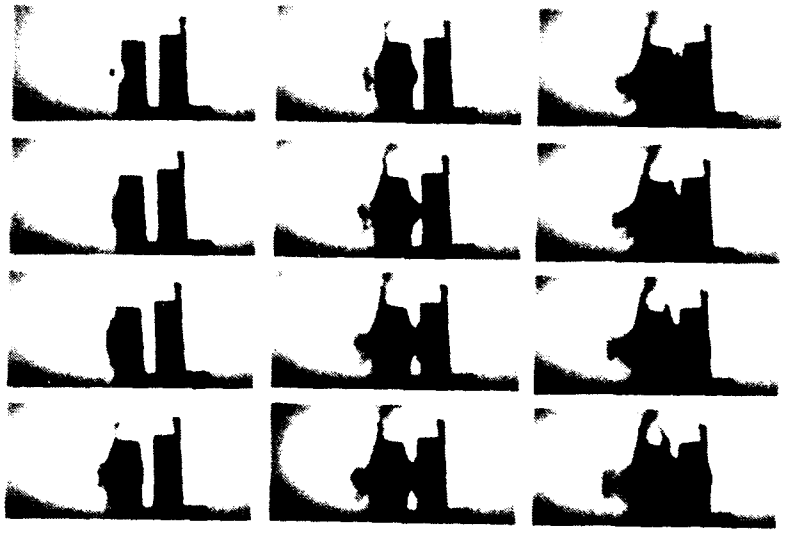


Fig. 5. Photographic sequence of sphere/ planar model impact at 646 m/s. (28 μs interframe time) Planar model configuration: hard steel, HEP-2, 25.4 mm air gap, HEP-2, hard steel.

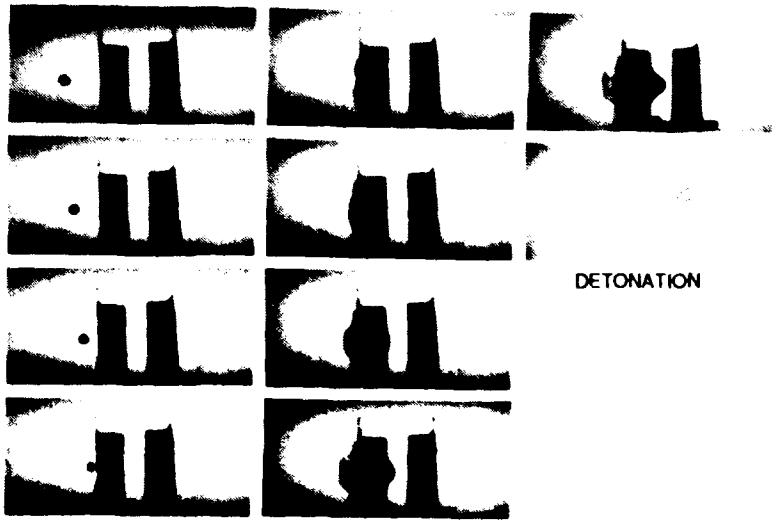


Fig. 6. Photographic sequence of sphere/ planar model impact at 674 m/s. (29 μs interframe time) Planar model configuration: hard steel, HEP-2, 38.1 mm air gap, HEP-2, hard steel.

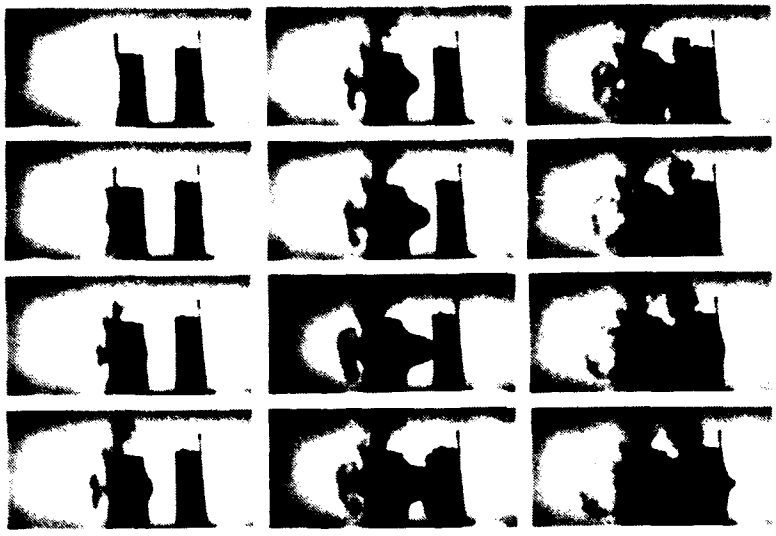


Fig. 7. Photographic sequence of sphere/planar model impact at 785 m/s. (28 μs interframe time) Planar model configuration: hard steel, HEP-2, 50.8 mm air gap, HEP-2, hard steel.

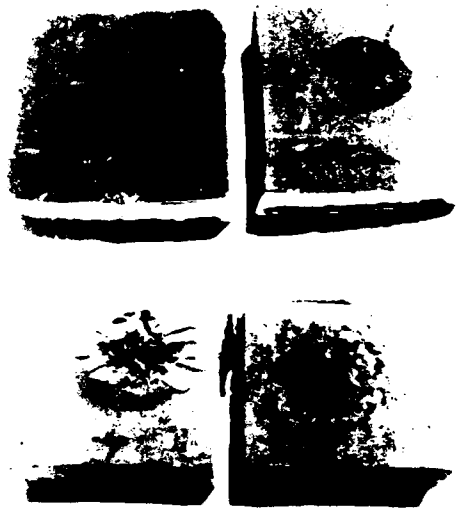


Fig. 8. Postmortem photographs of inner surfaces of front (left) and rear (right) propellant layers for tests shown in Fig. 5 (upper) and 7 (lower).

The ring-like crater pattern produced by the unbroken bubble results from contact surface jetting during impact (Lazari and Al-Hassani, 1986). The wave-like interfacial structure created by this process (responsible for the crater pattern) has been studied extensively in explosive welding and a number of theories have been advanced to explain it (El-Sobky, 1983). An interesting feature of this wavy interface is the frequent association of shear deformations/fractures with the wave tips. This phenomenon, observed frequently in both explosively welded and ballistically impacted metals (Salam and Al-Hassani, 1981, and Finnegan *et al.*, 1987), was noticed in both crater and bubble fragments from some of the propellant tests. An illustrative sketch of the interfacial wave and shear patterns found along the debris bubble/second layer contact surface is shown in Fig. 9.

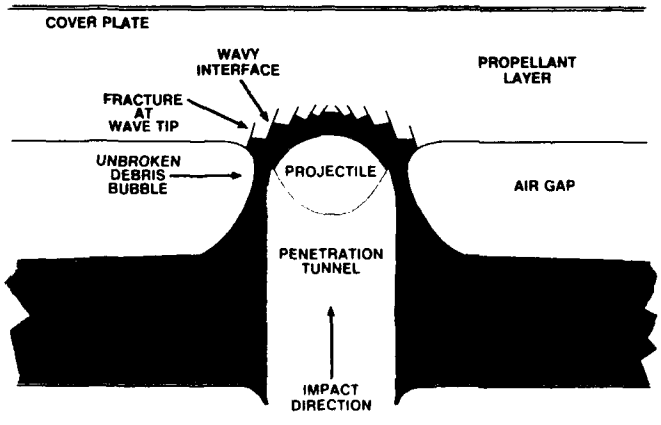


Fig. 9. Sketch of debris bubble/propellant layer impact interface showing interfacial wave structure and shear fracture system.

The presence of this impact jetting pattern suggested a method for determining the initiation stimulus for the detonation reaction found at the larger air gaps. Briefly, a minimum angle between two colliding bodies is required to initiate jetting, hence a wavy interface. Above the minimum, wave amplitude and period both increase with angle. For axially-symmetric impacts of curved and planar surfaces, where the collision angle increases continuously with time, wave size will be a maximum near the crater edge. Since shear length increases roughly with wave size (Finnegan *et al.*, 1987), maximum shearing should also occur in that region as shown in Fig. 9. By using a concave-curved impact surface shaped to match that of the bubble, the collision angle everywhere is reduced below this minimum, preventing formation of the wavy interface and associated shears. This shape also results in more uniform loading of the bubble wall. Conversely, using a convex-curved impact surface of the same shape reverses these effects (i.e., minimizes the initial contact area while increases shearing of the bubble wall by loading the bubble incrementally and by shifting the minimum angle for jetting towards the center of the contact area).

Two similar-velocity impacts of debris bubbles on concave- and convex-curved surfaces were conducted to test this idea. To reduce cost, impact surfaces were hemispherical in shape rather than shaped to match that of the bubble, and were machined out of inert simulant rather than live propellant. The upper edge of the concave one was rounded to match the edge of the bubble. Surfaces were identical in size; both were 50.8 mm in diameter. The air gap for both was 34.9 mm (to point of impact). The impact velocity, for both, was the minimum for which detonations were observed previously in HEP-2 propellant. The low impact velocity was chosen to minimize the initial shock pressure, hence reduce the probability that detonation would occur for both impact conditions. Results for these tests are summarized in Table 6 and also shown in Fig. 10 and 11.

Table 6. Summary of debris bubble/curved surface impact tests.

1st Steel Plate[a]	1st Propellant Layer	Air Gap, mm	2nd Propellant Layer	2nd Steel Plate[a]	Projectile[b]	Impact Velocity, m/s	Bubble Velocity, m/s	Reaction
hard	HEP-2	34.9	simulant[c]	mild	sphere	519	299	no visible reaction
hard	HEP-2	34.9	simulant[d]	mild	sphere	500	*e*	delayed detonation

[a] 1.59 mm, 95 BHN (mild) or 370 BHN (hard) steel.
[b] Sphere mass: 28.2 g.
[c] 50.8-mm-diameter, convex-curved hemispherical impact surface.
[d] 50.8-mm-diameter, concave-curved hemispherical impact surface.
[e] Velocity could not be measured.

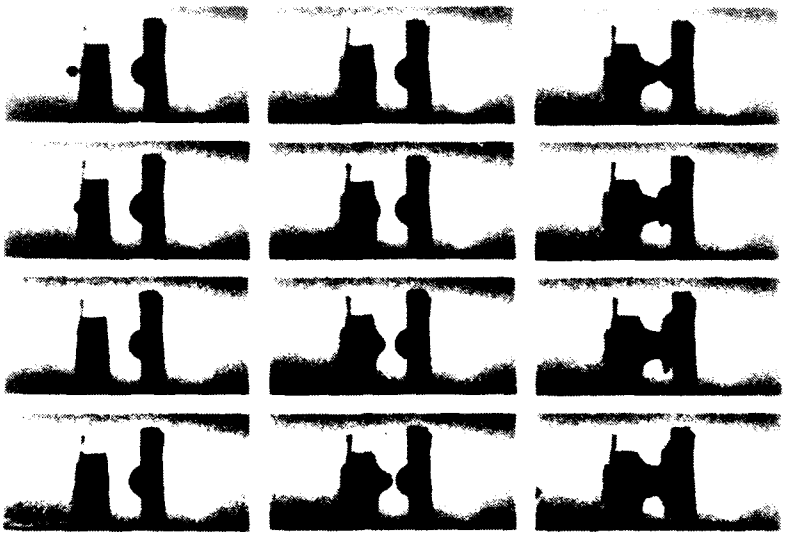


Fig. 10. Photographic sequence for debris bubble impact on convex-curved surface. (28 μs interframe time)

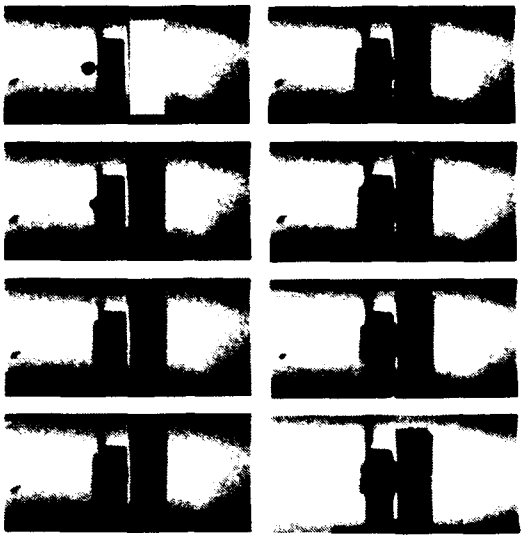


Fig. 11. Photographic sequence for debris bubble impact on concave-curved surface. (28 μs interframe time)

As seen in the two high-speed photographic sequences (Fig. 10 and 11), impact against the concave surface resulted in detonation, whereas impact against the convex surface resulted in no reaction. These tests indicate that the reaction mechanism, in this case, is the initial shock entering the bubble rather than another mechanical process. This explanation is consistent with observations indicating very short (<3 μs) reaction delay times after bubble impact. It also provides an explanation for the reaction observed with the ogival projectile. Projectile shape is irrelevant in this situation as the projectile only serves to propel the bubble across the air gap. This mechanism has been proposed by other investigators as an explanation for XDT reactions (Green *et al.*, 1985).

HYDROCODE STUDIES

Two hydrocode studies were conducted as part of the program. One, a study of debris bubble expansion and breakup processes, was done using an Eulerian hydrocode, CSQ III, developed at Sandia National Laboratories (Thompson, 1979). The other, a study of bubble impact and reaction processes, was done using an Eulerian hydrocode, SMERF, originally developed at the New Mexico Institute of Mining and Technology, Socorro, NM (Libersky and Lundstrom, 1992).

CSQ III Hydrocode Study

As an aid to understanding the debris bubble expansion and breakup process, a parametric study was conducted using an Eulerian hydrocode, CSQ III. An earlier version of this code, CSQ II, had been used successfully to model debris bubble breakup processes in hypervelocity impacts (Grady and Passman, 1990). The study was performed to establish the basic character of the debris bubble and to establish bubble breakup elongation trends as a function of various target and impact parameters. The parameters that were varied included impact velocity, propellant layer thickness, and plate material. Runs were made against "half targets" only; impact against a second propellant layer was not considered.

Hydrocode Model of Debris Bubble Expansion/Breakup Process. The output of each hydrocode run consisted of a sequence of computer plots showing the deformed cross-sections of the projectile and target layers at constant time intervals. Such a sequence, for a 38.1-mm-thick propellant layer with a 1.59-mm-thick steel cover plate impacted by a 19.0-mm-diameter steel sphere at 1158 m/s, is shown in Fig. 12. At 30 μs the projectile has perforated the plate and is penetrating through the propellant layer. By 60 μs a bubble has started to form at the rear surface of this layer. The layer elongates and thins down and starts to fragment at some time prior to 150 μs. By 180 μs fragmentation is complete and the projectile has started to exit from the solution space. The plots indicate that the debris bubble can be regarded as an expanding hollow shell, similar to those occurring in hypervelocity impacts (Swift *et al.*, 1970). The exterior shape closely matches that seen experimentally at distances out to 75-100 mm (Finnegan *et al.*, 1990).

From the computer plots, debris bubble elongation as a function of time and at breakup can be determined. A series of debris bubble measurements, made from the hydrocode runs at the time of breakup, is contained in Table 7. An examination of breakup elongation data in Table 7 shows that breakup elongation increases with impact velocity, propellant layer thickness, and plate density.

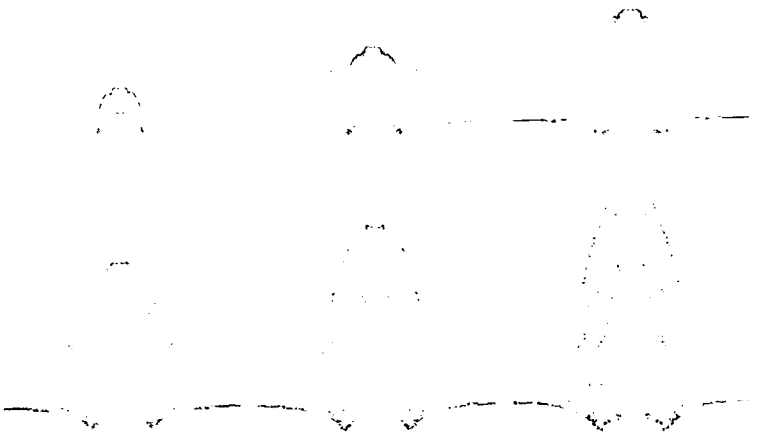


Fig. 12. Hydrocode plots for 19.0 mm steel sphere impacting 38.1 mm propellant layer with 1.59 mm steel cover plate at 1158 m/s. (30 μs intervals)

Table 7. Summary of hydrocode-calculated debris bubble breakup elongations.

Cover Plate[a]	Propellant Layer Thickness, mm	Projectile[b]	Impact Velocity, m/s	Bubble Velocity, m/s	Bubble Breakup Elongation, mm[c]	Bubble Breakup Thickness, mm[d]
steel	12.7	sphere	1158	921	38.4	1.8
steel	25.4	sphere	1158	813	54.9	2.0
steel	38.1	sphere	1158	715	71.9	1.5
steel	38.1	sphere	975	584	60.5[e]	1.8
steel	38.1	sphere	1341	813	77.0	1.8
steel	38.1	sphere	1524	952	85.6[e]	1.3
aluminum	38.1	sphere	1158	813	65.3	1.5
none	12.7	sphere	1158	1016	32.1	2.8
none	25.4	sphere	1158	908	44.7	2.3
none	38.1	sphere	1158	855	54.6	1.8
none	38.1	sphere	975	737	48.5	2.0
none	38.1	sphere	1341	991	57.8	1.5
none	38.1	sphere	1524	1124	57.8	2.0
none	38.1	ogive	1158	914	48.1	1.8

[a] 1.59 mm thickness.
[b] 28.2 g. mass.
[c] Measured normal to propellant layer, from exit side to front of bubble.
[d] Measured 25.4 mm behind front of bubble.
[e] Estimated.

Debris Bubble Mechanics. It should be pointed out that the debris bubble is not a spall. A spall is the result of tensile failure when a shock wave is reflected back into the material as a rarefaction at a free surface. Bubble formation in the present case is a much longer term process produced by the mechanical interaction of the projectile with the propellant layer. This is clearly shown by the modeling results. Impedance matching can be used to determine the initial shock pressure in the propellant (Jones, 1972). For a steel projectile impacting at 1158 m/s, the shock pressures for several case materials are compared with breakup elongation values in Table 8. It is apparent that there is no correlation, indicating that the initial shock is not responsible for breakup of the bubble. Grady and Passman (1990) have postulated that breakup is the result of instabilities that develop on the bubble surface.

Table 8. Comparison of initial shock pressures in propellant with bubble breakup elongations.

Plate Material	Pressure, GPa[a]	Breakup Elongation, mm[b]
none	8.9	54.6
aluminum	9.9	65.3
steel	8.9	71.9

[a] Initial shock pressure in propellant from impact of steel sphere at 1158 m/s.
[b] Measured normal to propellant layer, from exit side to front of bubble.

Hydrocode/Experimental Bubble Breakup Elongation Comparison. A comparison of hydrocode-calculated bubble breakup elongations with measured values (from Table 2) for different thicknesses of bare and covered HEP-1 propellant is shown in Fig. 13. Agreement is quite good. A similar comparison for 38.1 mm slabs of bare and covered HEP-2 propellant at different impact velocities is shown in in Fig. 14. Measured values for this propellant are somewhat higher and differences between bare and covered material are larger than predicted. Data trends for both targets are about the same as predicted ones, however.

Hydrocode Bubble Breakup Elongation/Detonation Limit Comparison. A comparison of hydrocode-calculated bubble breakup elongations with upper-air-gap detonation limit values (from Table 3) for bare and covered HEP-2 propellant, as a function of impact velocity, is shown in Fig. 15. Agreement between experimental and hydrocode measurements is quite good for covered propellant but less so for bare material. The poor agreement for the latter is apparently caused by excessive projectile deformation, during penetration, for the hydrocode model. Trend differences for the two conditions appear to reflect differences in projectile deformation. A comparison of projectile deformation levels, at the two velocity extremes, shows little difference for bare propellant impacts, but large differences for covered propellant impacts.

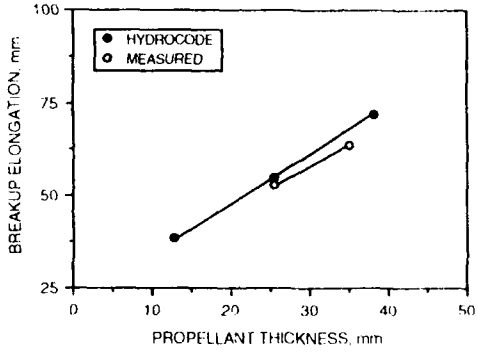


Fig. 13. Bubble breakup elongation versus propellant layer thickness for HEP-1 propellant.

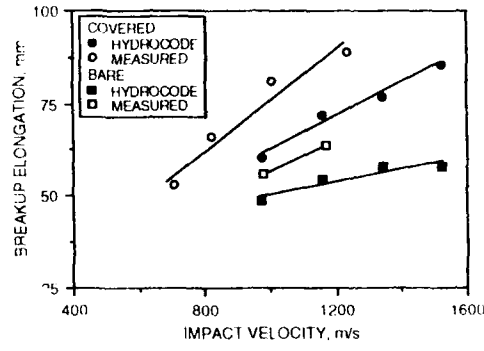


Fig. 14. Bubble breakup elongation versus impact velocity for HEP-2 propellant.

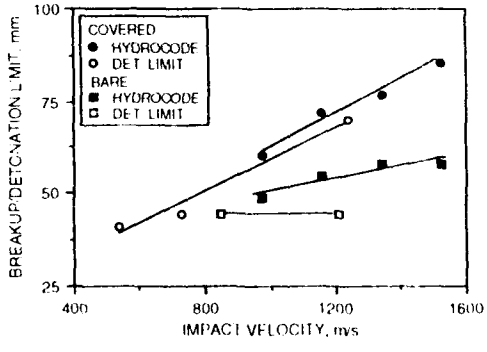


Fig. 15. Comparison of upper-air-gap detonation limits with hydrocode-calculated bubble breakup elongations for covered and bare HEP-2 propellant.

SMERF Hydrocode Study

To examine the shock initiation mechanism, debris bubble impact and reaction processes were studied using an Eulerian hydrocode, SMERF, and the Forest Fire reactive burn model. To simplify the analysis, only impacts against bare propellant were considered. The target consisted of two 38.1-mm-thick propellant layers separated by a 25.4 mm air gap. The air gap was chosen so that the debris bubble was unbroken at impact. Impact was by a 19.0 mm steel sphere traveling at 1158 m/s.

Modeling Conditions. Four debris bubble/second layer conditions, listed in Table 9, were modeled. To reduce costs, the last set of computer iterations prior to impact of the bubble, in the first run (Run 1), was saved and used as the starting point for the other runs (Runs 2-4). Bubble "sensitization" was achieved by shifting the Pop plot, for the undamaged propellant, downward until detonation occurred (Fig. 16). (The Pop plot, a power law fit of run distance to detonation versus input pressure, is a method for plotting data from a wedge test (Dienes and Dick, 1984)). Although there is evidence that the slope changes for damaged (porous) material (Lindstrom, 1970), the amount of change required in the present circumstance was unknown. Based on this uncertainty, it was decided to use the original slope as a first approximation for the damaged material.

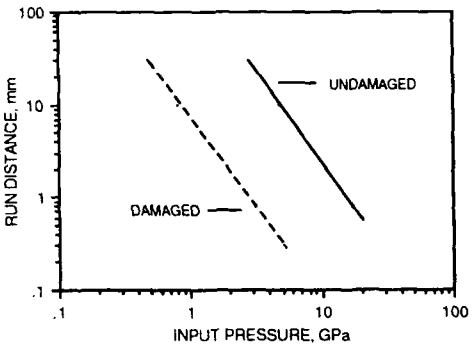


Fig. 16. Pop plot used in SMERF hydrocode study.

Table 9. Modeling conditions for debris bubble/ second propellant layer impacts.

Hydrocode Run	Debris Bubble	2nd Propellant Layer
1	inert	inert
2	live/sensitized	inert
3	live/sensitized[a]	inert
4	live/sensitized	live

[a] Projectile removed prior to bubble impact.

Hydrocode Model of Impact Pressure Distribution. The first impact condition (Run 1), shown in Fig. 17, was done primarily to examine the pressure distributions within the bubble wall after impact. Consequently, the burn model was not activated. From Fig. 17, there appears to be no significant recompression of the bubble wall except in the frontal portion between the projectile and the second layer.

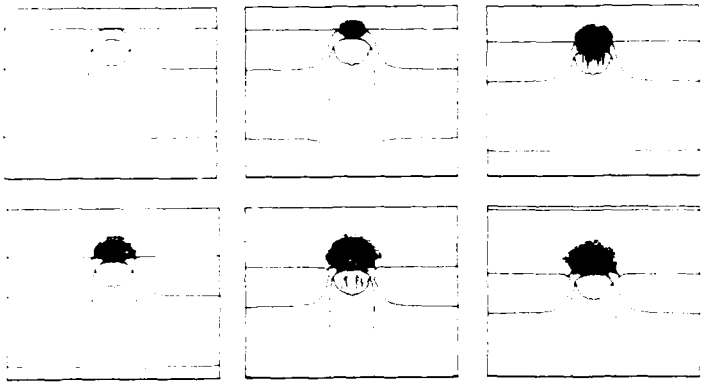


Fig. 17. Hydrocode plots for impact of inert debris bubble (with projectile) on inert propellant layer. (2 μs intervals)

Hydrocode Models of Detonation Process. The second condition (Run 2), shown in Fig. 18, was done to establish threshold conditions for initiation of reaction and transition to detonation in the bubble wall. Minimum conditions were met by the lower Pop plot in Fig. 16. The six-fold pressure reduction required is within the range of values reported by other investigators (Weirick, 1990). As seen in Fig. 18, reaction begins at the debris bubble/second layer contact surface.

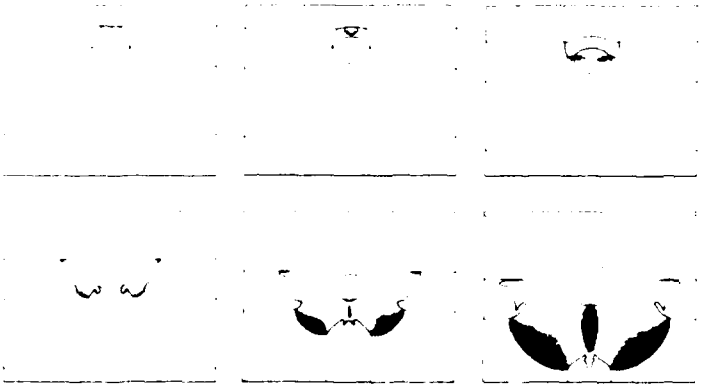


Fig. 18. Hydrocode plots for impact of sensitized debris bubble (with projectile) on inert propellant layer. (2 μs intervals)

The third condition (Run 3), shown in Fig. 19, was done to examine the influence of the projectile on the detonation process. For this run, the projectile was removed just before impact and the bubble allowed to impact alone. The result, essentially unchanged from the run made with the projectile in place (Fig. 18), indicated that the reaction was caused by the initial shock and not the reflected (compressional) shock from the projectile front surface.

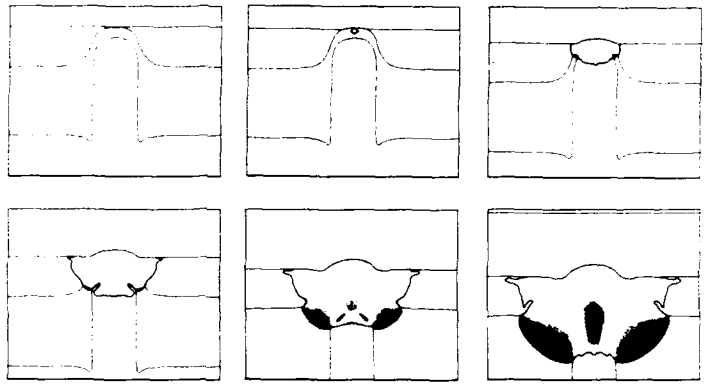


Fig. 19. Hydrocode plots for impact of sensitized debris bubble (without projectile) on inert propellant layer. (2 μs intervals)

The fourth condition (Run 4), shown in Fig. 20, was done to examine the effects of a live second layer. In this situation, reaction in the bubble was able to initiate reaction in the second layer that transitioned to detonation. This result indicates that direct transfer of reaction from bubble to second layer can occur for sufficiently sensitive materials.

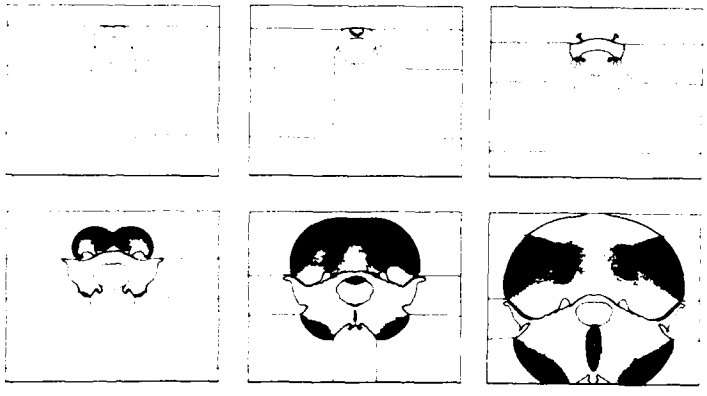


Fig. 20. Hydrocode plots for impact of sensitized debris (with projectile) on live propellant layer. (2 μs intervals)

CONCLUSIONS

The main conclusions to be drawn from this study, involving the normal impact of spheres and ogival cylinders on a planar model of a solid rocket motor containing high-energy propellant and a center bore, are:

1. A projectile impacting and penetrating a layer of energetic material at a sufficiently high velocity creates a "bubble" of material at the rear surface. Impact of the expanding bubble on a second layer of energetic material results in reaction that, under certain conditions and for sufficiently energetic material, transitions into a detonation wave that propagates back through the wall of the bubble.
2. From experimental and hydrocode studies, the initiation mechanism for this delayed detonation reaction has been identified as the initial shock entering the bubble after impact on the second propellant layer.
3. The reaction is bounded by a lower velocity limit and by a range of air gaps (i.e., distance between the two layers of energetic material). The maximum air gap for detonation roughly coincides with the maximum expansion distance for the bubble before breakup (i.e., breakup elongation). The minimum air gap represents a lower damage threshold level for detonation.
4. The use of hydrocode models greatly enhances the interpretation of the experimental data by providing information not easily obtainable otherwise (e.g., debris bubble characteristics) and by providing confirmation of experimental evidence.

ACKNOWLEDGEMENT

The planar rocket motor impact tests were done by the Warhead Test Branch (Code 6214), Naval Air Warfare Center, Weapons Division, China Lake, California. Their efforts are gratefully acknowledged.

REFERENCES

Dienes, J. K. and J. J. Dick (1984). Shock and impact response of solid rocket propellants: experimental and theoretical. In: *Hazard Studies for Solid Propellant Rocket Motors*, AGARD-CP-367, pp. 16-1 to 16-16. NATO Advisory Group for Aerospace Research and Development.

Dienes, J. K. (1986). Progress in the theory of fragmentation and analysis of XDT. In: *Proc. 1986 JANNAF Propulsion Systems Hazards Subcommittee Meeting*, CPIA Pub. 446, Vol. 1, pp. 507-512. JHU/Chemical Propulsion Information Agency, Columbia MD.

El-Sobky, H. (1983). In: *Explosive Welding, Forming and Compaction* (T. Z. Blazynski, ed.), Chap. 6, pp. 189-217. Applied Science Publishers, London.

Finnegan, S. A., J. C. Schulz and O. E. R. Heimdahl (1987). Fragmentation characterization techniques for ordnance speed impacts. In: *Proc. Tenth International Symposium on Ballistics*, Vol. II, American Defense Prepardness Association, Alexandria, VA.

Finnegan, S. A., J. K. Pringle, J. C. Schulz and M. D. Alexander (1990). The effect of impact damage on violent reaction in cased propellant. In: *Proc. 12th International Symposium on Ballistics*, Vol III, pp. 149-158, American Defense Prepardness Association, Alexandria, VA.

Finnegan, S. A., J. K. Pringle, O. E. R. Heimdahl and J. C. Schulz (1992). Impact-induced delayed reactions in rocket motors: Further studies with a planar model. In: *1992 JANNAF Propulsion Hazards Subcommittee Meeting*, CPIA Pub. 582, Vol. 1, pp. 267-283. JHU/Chemical Propulsion Information Agency, Columbia, MD.

Grady, D. E. and S. L. Passman (1990). Stability and fragmentation of ejecta in hypervelocity impact. *Int. J. Impact Engng.*, 10, 197-212.

Green, L., E. James and E. Lee (1985). Energetic response of propellants to high velocity impact. In: *Eighth Symposium (International) on Detonation*, pp. 284-293. Naval Surface Weapons Center, White Oak, Silver Spring, MD.

Henry, I. G. (1967). The Gurney formula and related approximations for the high-explosive deployment of fragments. Report No. PUB-189. Hughes Aircraft Company, Culver City, CA.

Jensen, R. C., E. J. Blommer and B. Brown (1981). An instrumented shotgun facility to study impact initiated explosive reactions. In: *Seventh Symposium (International) on Detonation*, NSWC MP 82-334, pp. 299-307. Naval Surface Weapons Center, White Oak, Silver Spring, MD.

Jones, O. E. (1972). Metal response under explosive loading. In: *Proc. 12th Symposium on Behavior and Utilization of Explosives in Engineering Design*, pp. 125-148. New Mexico Section, ASME and University of New Mexico, Albuquerque, NM.

Lazari, L. and S. T. S. Al-Hassan (1986). Explosive welding of variable thickness plates. In: *Metallurgical Applications of Shock-Wave and High-Strain-Rate Phenomena* (L. E. Murr, K. P. Staudhammer and M. A. Meyers, ed.), pp. 969-989. Marcel Dekker, New York.

Libersky, L. and E. Lundstrom (1992). The SMERF code. NAWC WPNS TM (in preparation). Naval Air Warfare Center - Weapons Division, China Lake, CA.

Lindstrom, I. E. (1970). Planar shock initiation of porous Tetryl. *J. Appl. Phys.* 41, 337-350.

Mellor, A. M., T. L. Boggs, J. Covino, C. W. Dickinson, D. Dreitzler, L. B. Thorm, R. B. Frey, P. W. Gibson, W. E. Roe, M. Kirshenbaum and D. M. Mann (1988). Hazard initiation in solid rocket and gun propellants and explosives. *Prog. Energy Combust. Sci.*, 14, 213-244.

Nouguez, B., H. Gerger, B. Gondouin and J. Brunet (1989). An odd bore effect on bullet induced detonation of high energy propellant grains. In: *Proc. Joint International Symposium on Compatibility of Plastics and Other Materials with Explosives, Propellants, Pyrotechnics and Processing of Explosives*. American Defense Prepardness Association, Alexandria, VA.

Salam, S. A. L. and S. T. S. Al-Hassani (1981). Interfacial wave generation in explosive welding of multi-laminates. In: *Shock Waves and High-Strain-Rate Phenomena in Metals* (M. A. Meyers and L. E. Murr, ed.), pp. 1003-1018. Plenum Press, New York.

Stronge, W. J., Ma Xiaoqing and Zhao Lanting (1989). Fragmentation of explosively expanded steel cylinders. *Int. J. Mech. Sci.*, 31, 811-823.

Swift, H. F., D. D. Preonas and W. C. Turpin (1970). Dissection methods for measuring the characteristics of expanding clouds. *Rev. Sci. Instr.*, 41, 746-751.

Thompson, S. L. (1979). CSQ II - An Eulerian finite difference program for two-dimensional material response. SAND77-1339. Sandia National Laboratories, Albuquerque, NM.

Weirick, L. J. (1990). Shock initiation sensitivity of damaged TP-H1207C composite propellant. In: *Proc. 1990 JANNAF Propulsion Systems Hazards Subcommittee Meeting*, CPIA Pub. 538, Vol. I, pp. 325-333. JHU/Chemical Propulsion Information Agency, Columbia MD.

Yuan, W., W. Goldsmith, J. Radin and Z. Tauber (1992a). Response of simulated propellant and explosives to projectile impact—I. Material behavior and penetration studies. *Int. J. Impact Engng.*, 12 (in press).

Yuan, W. and W. Goldsmith (1992b). Response of simulated propellant and explosives to projectile impact—II. Fragmentaton. *Int. J. Impact Engng.*, 12 (in press).

Yuan, W. and W. Goldsmith (1992c). Response of simulated propellant and explosives to projectile impact—III. Experimental and numerical results of warhead penetration and fragmentation. *Int. J. Impact Engng.*, 12 (in press).

Int. J. Impact Engng Vol.14, pp.255–265, 1993
Printed in Great Britain

0734-743X/93 $6.00+0.00
1993 Pergamon Press Ltd

THE VALIDATION OF HYDROCODES FOR ORBITAL DEBRIS IMPACT SIMULATION

J.D. Frey, F. Janicot, X. Garaud, P. Groenenboom
Engineering Systems International
20, rue Saarinen, Silic 270, 94578 Rungis Cedex (France)

M. Lambert
ESA, European Space Agency
P.O. Box 292, 2200 AG Noordwijk (The Netherlands)

ABSTRACT

Orbital debris pose a danger for spacecraft in orbit. Protection against this threat is obtained by shielding. One or more shields placed at some distance from the structure to be protected can minimize the damage inflicted by projectiles at high velocity. The range of velocity between 0 and 8 km/s is well covered by tests. Unfortunately, the average velocity of debris in low earth orbit is above 10 km/s with a maximum velocity around 15 km/s. The methodology presented in this paper aims to validate the numerical approach. It will predict and extrapolate the behavior of multishock shields in the velocity range between 8 and 15km/s. The formation and propagation of the debris cloud, after perforation of the shields and the generation of damage in the backwall, are key factors. These phenomena are examined, discussed and illustrated with correlation between numerical simulation with EFHYD™ analytical formulae and test results.

Keywords : Hypervelocity, Impact, Orbital debris, Damage, Hydrocode.

INTRODUCTION

Orbital debris belongs to a man-made environment. It is generated by the destruction of payloads, upper stages or any hardware in orbit. The number and the size of debris is a function of the destruction mode: explosion or collision. The size ranges from tiny particles to huge chunks of satellites.

The debris size of interest is defined by the size of the spacecraft, the mission characteristics, and the associated system requirements. For manned craft, safety aspects of orbital debris are most relevant. Projectiles to be considered are generally between 1 and 10 mm in diameter. The density of aluminum is accepted as representative.

The literally most striking characteristics of debris is their potentially high relative velocity. Maximum relative velocity in low earth orbit is approximately 15 km/s with an average around 11 km/s. In order to arrest such high velocity particles, often a dual shield system is imployed, that consists of a first bumper plate, a spacing and a second backup plate. While the bumper plate may well be perforated by a striking debris, the backup plate must definitively arrest the debris cloud, formed after perforation of the bumper plate. Sometimes the bumper plate is replaced by two bumper plates. Because tests cannot be readily performed above 8 km/s, computer simulation is necessary to investigate the upper velocity range. Before these simulations can be believed, an acceptable level of confidence in the computer results has to be established. The following report addresses this subject.

HYPERVELOCITY IMPACT PHYSICS

When solids collide at speeds of the order of several kilometers per second, megabar pressures are generated (Zukas, 1982). Because these pressures exceed the strength of materials by many factors of ten, this is a regime where it is possible to neglect the effect of strength and to treat the solid as an inviscid compressible fluid. The pressures eventually decay and the material strength then becomes the dominant factor, determining the final configuration in which the material comes to rest.

If the target is thick enough, only cratering will occur. This complex process is driven by mechanical and metallurgical properties of the target as well as projectile characteristics.

When a particle strikes a plate at high velocity, the compressive shock is attenuated as it travels through the plate and is generally reflected off the rear surface as a rarefaction wave.

If the plate is thin enough, the reflected wave will be so intense that a portion of the rear surface of the plate may be ejected with a momentum sufficient to damage other parts of the structure. This phenomenon is called spalling.

Perforation results from the combination of cratering and spalling. A detailed study of these mechanisms show that perforation can occur for plate thicknesses significantly greater than the expected depth of penetration when calculated as a semi-infinite target.

The hypervelocity impact of a projectile upon a thin metal plate produces a subsequent formation of back surface debris. At sufficiently high impact velocities, roughly greater than 3 km/s for aluminum (depending upon the shock impedances of the materials involved), shock formation and interaction dominate and control the overall response of both the projectile and the target plate. For relatively high velocities (> 6 km/s) shock heating can produce melting and vaporization of both, projectile and target and the formation of a debris cloud. Because of the complexity of the physical interactions, numerical simulation of such problems is necessary to draw quantitative conclusions about the cloud configuration in order to be able to design and predict the behavior of the backup plate (spalling, cratering). The first major area of interest in the simulation field are the equations of state which describe the behavior of the shocked material. A review of the literature and a comparison and explanation of the different models has been carried out. A second major area of interest concerning low impact velocities (2-5 km/s for aluminum on aluminum) for the bumper and particle interaction as well as residual cloud impact on the backup plate for higher striking velocity, is the dynamic fracture and fragmentation of both projectile and target.

The capability for computing the disintegration behavior under hypervelocity impact conditions, in general, must include mathematical models with accurate spalling and fragmentation capabilities as well as adequate high pressure equations of state for melting and vaporization. In fact, the damage of the backwall depends on the state, mass and velocity of the debris. Vaporized materials produce a distributed load that may buckle, collapse or spall the plate. Solid fragments or droplets, on the other hand, produce more point loads where they impact and may penetrate the backwall (local cratering).

The significance of a shield is that it can fragment the projectile, spread the fragments radially and significantly reduce size, density and velocity of many of the fragments (Fig.1).

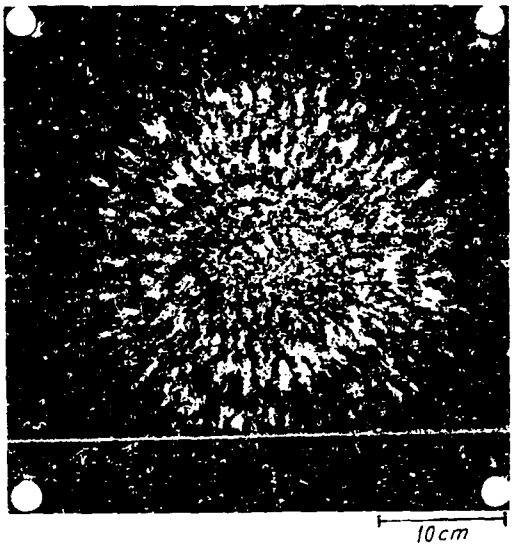


Figure 1 : Backwall impact damage
4 mm diameter aluminum projectile, V = 7 km/s, normal impact, 2 mm aluminum bumper, 1.5 mm aluminum backwall, 200 mm spacing

If the conditions are adequate, released fragments are liquefied and distributed fairly homogeneously at the front of the debris cloud. Splashes of molten material are produced as well as plastified droplets, collapsing upon hitting the back-up structure (Fig.2). This allows a better distribution of the loading on the structure protected by the shield.

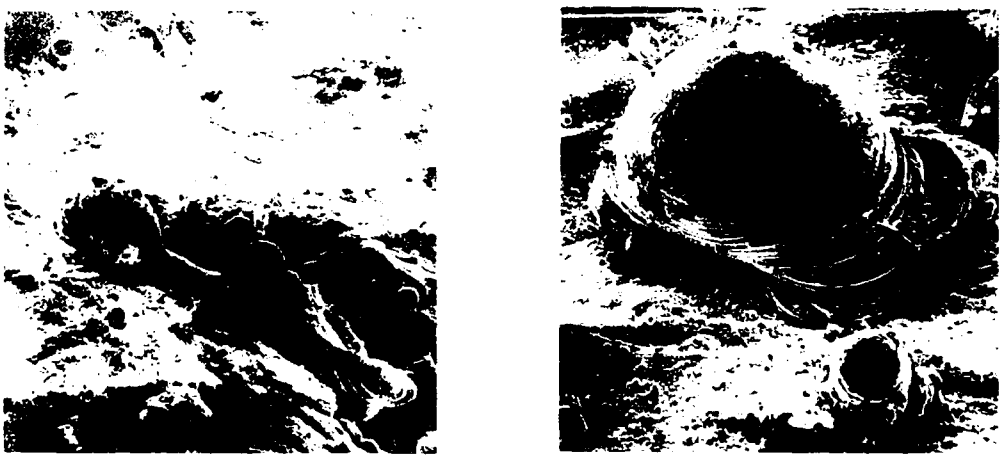


Figure 2 : Examples of material splashes and plastified droplets after impact (Electron scanning microscope, magnification - 100, 200 x)

The debris cloud can thus induce in the structure three main types of loading :

- cratering,
- spalling,
- impulse inducing gross deformations.

BACKGROUND WORK

The reported technological work has been undertaken to support the design of the COLUMBUS pressurized modules. Certain parameters, like projectile characteristics, shield spacing and material selections, are controlled by project requirements. The baseline shielding is considered here (Fig.3).

Once the configuration is chosen, the basic need of the designer is to be able to predict if the pressurized wall of the spacecraft will be perforated or not by a certain projectile. Projectiles to be considered according to project requirements range from 1 to 10mm aluminum spheres.

Considering a Whipple shield concept, and illustrating the hypervelocity impact physics, the required backwall thickness shows (Fig.4) a first peak around 3 km/s, associated with a poor fragmentation of the projectile. The curve goes down from the peak to a minimum at around 8km/s. It highlights the effects of the improved fragmentation with increasing velocity. The minimum corresponds roughly to the beginning of the liquid phase for the debris cloud. For higher velocities, the required thickness must increase again as the projectile momentum continues to grow.

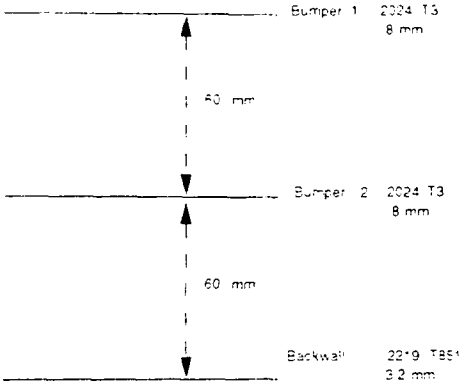


Figure 3 : COLUMBUS attached pressurized module Meteoroids and orbital debris protection configuration

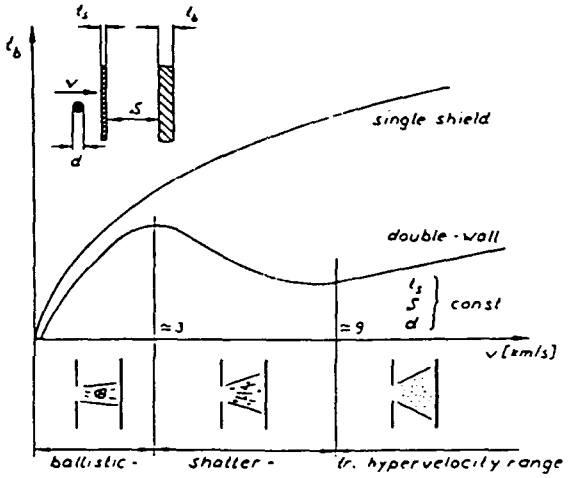


Figure 4 : Ballistic limit curves of a single shield and a double wall meteroids and orbital debris protection

Unfortunately, projectile accelerators are limited in performance. Technologies other than the commonly used light gas gun can be considered. They can only accelerate projectiles with aspect ratios that do not correspond to the considered particles. For example, shaped charges are considered, however, getting an adequate projectile is not yet fully demonstrated and documented.

Experimental data are available in the velocity range defined by the accelerator performances (Fig.5). The exploration of the velocity range above 8 km/s is thus limited to computer simulation.

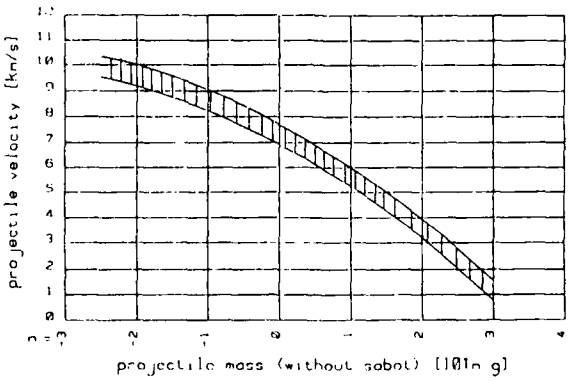


Figure 5 : Define light gas gun performances (from Ernst Mach Institute, Germany)

THE CODE

EFHYD-2/3D™ is a finite element Arbitrary Lagrange-Euler (ALE) code for the elastoplastic and hydrodynamic analysis of multimaterial continua and structural systems. The code handles in two and three dimensions solid and shell elements with impact sliding surfaces and various boundary conditions. Manual and automatic rezoning as well as complete remeshing coupled with ALE or Eulerian capabilities are available to perform simulations for the highly distorted shapes typical of hypervelocity impacts (Fig.7).

EFHYD has been extensively used and validated in a wide range of hydrodynamic applications for defence and space industries especially considering fragmentation phenomena.

Key features of a hydrodynamic code are the material descriptions (Anderson, 1987) :

- equations of state (EOS) (High pressure and phase changes),
- constitutive modelling (strength),
- failure modelling (damage).

The velocity range (8-15 km/s) considered here covers all 3 states (solid, liquid, vapour) for aluminum and the associated phase changes. A correct description of this transition is thus a must for the selection of the equations of state.

Many simple equations of state (Mie-Gruneisen EOS or Tillotson EOS) do not cover the whole pressure range encountered here. More sophisticated EOS, like the ANEOS package (Sandia) or SESAME tables (Los Alamos), including several analytical models and experimental data enable the numerical simulations for a large range of densities, temperatures and phase transitions. The tabulated Sesame EOS is used here. It is well correlated with experiments and its accuracy is acceptable for most of the applications.

The constitutive model has to cope with the elastoplastic behavior at high strain rates and pressure : Johnson-Cook or Steinberg models in which the plastic flow depends on pressure, strain rates, and temperature are incorporated in the code and are used for the description of the elastoplastic regime.

Satisfactory ductile fracture models have to incorporate the contribution of 3 distinct mechanisms :

- crack and void nucleation,
- crack and void growth,
- coalescence and propagation of cracks and voids.

A detailed description of these mechanisms, as in the SRI model (Curran, 1987), requires the determination of many material parameters. This approach would require many experiments to precisely characterize the material, and would be difficult to integrate in a global modeling of the phenomena from an engineering viewpoint. For this reason, the SRI model is not considered. The simpler Sandia Model (Grady et al.), based on energy balance and statistical considerations is incorporated in the code. It accounts for material degradation due to damage and includes a fragmentation model. The model has been used to describe dynamic fragmentation occurring in brittle and ductile solids with reasonable success (Trucano,1989).

VALIDATION PROCEDURE

As no direct and full scale testing is possible with the current test capabilities, the validation beyond 8km/s has to include the verification of two important features :

- each key physical phenomenon involved in the backwall loading has to be validated ; the cloud density and the spreading angle, the cratering, spalling and gross deformation have to be checked for various equivalent cloud impinging conditions ;
- the trends observed with increasing velocity have to be predicted by the code, which can be determined indirectly by assessing the pressure on the backwall (high velocity cases).

Reference cases

The purpose of this investigation is to confirm the ability of the code to predict, for the actual geometry, the main features of the shielding with a projectile representative of those expected for COLUMBUS.

The velocity chosen must be compatible with the experimental device but high enough to produce the debris cloud in a liquid phase which is representative of the velocity range of concern. Parametric analysis has shown that apart from mass, velocity and spreading, the density of the debris cloud impinging on the backwall is a key element. For this purpose, bumper hole diameter, spray angle and backwall pressure have to be cross-checked with test results.

Piezoresistive pressure transducers have been mounted within back-up plates in a sandwich arrangement. In this way, a pressure-time record can be obtained on the back-up plate at the center of the fragment cloud impact area (Fig.13). Pressure pulses of the order of some tens of kilobars have been detected. Similar measurement set-ups are used for all validation phases.

Visualisation of fragment clouds has been achieved by means of X-ray flash techniques as well as image converter camera photo series. Both methods are appropriate to derive fragment cloud expansion velocities (Fig.6).

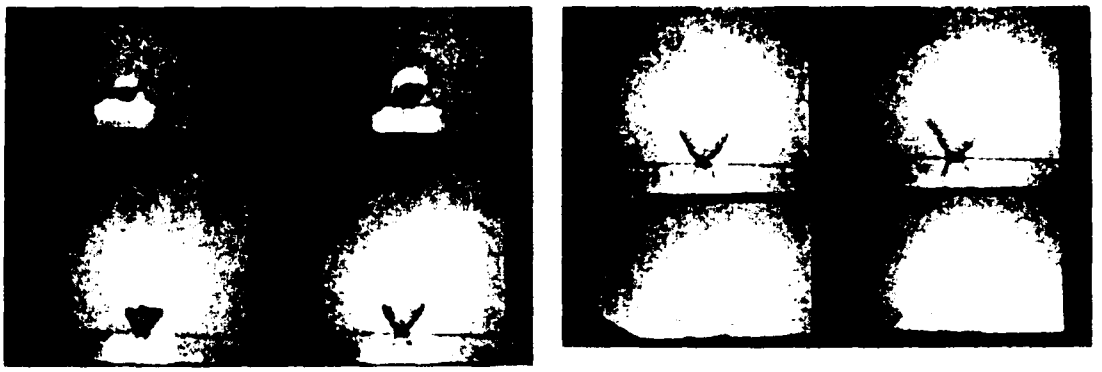


Figure 6 : Kinematics of fragment cloud visualized by an image converter camera. 5 mm aluminum bumper. 2 mm diameter projectile. 8.1 km/s
Photos time step : 1 ms. Fragment cloud velocity 7.1km/s

An additional case with different thicknesses for the second bumper is considered to explore the effect of the debris cloud variations on the backwall.

Material validation cases

A relation has to be established between the shock wave amplitude and the debris cloud density on the one hand and the cratering and spalling on the other hand.

As some degree of shock wave uniformity is needed to correlate the test results with the calculations, the projectiles are made of circular flat plates impacting the target on a surface significantly larger than the measurement gauges.

Different projectile materials and sizes are used to explore the effects of the debris cloud density and geometry. Detailed simulations of the damage in the plate have been undertaken.

As spalling can be influenced by the time duration of the pulse, the projectile thickness allows a parametric investigation of this important impact characteristic.

High velocity cases

The object of this investigation is to demonstrate the extrapolation capabilities of the code for very high velocities.

For this task, at least two conditions in the upper velocity range have to be investigated. As the accelerators have limited performances, a small projectile diameter is used to allow to cover conditions leading to liquid debris clouds. With small projectiles, a reasonable damage pattern on the backwall can only be obtained after scaling of the configuration.

The validity of the geometrical scaling, at least for modest ratios, has been demonstrated (Westine, 1986/87).

COMPARISON BETWEEN EXPERIMENTS AND NUMERICAL SIMULATIONS

Description of the methodology

Comparisons with experiments are made on different parameters : *kinematic parameters* (residual velocity of the cloud, hole diameters in the bumpers, spray angles and cloud parameters like the shape of the cloud with exploitation of X ray pictures), but also on *pressure measurements* on the backwall which can be thought of as an indirect measurement for the density of the cloud.

2D numerical simulations are performed for the Whipple concept as well as for multishock shield concepts (3 plates). Due to the relative complexity of such calculations and the need of parametric analyses to understand the physics, a simplified 1D methodology is also calibrated and used to predict the cloud state and the backwall behavior. This mixed approach, using 2D simulations and a simplified 1D calculation, has already been validated for typical cases and will be necessary to define design curves for the studied configuration.

Description of a triple plate simulation

The numerical simulation of the triple plate configuration (Fig. 7) involves the knowledge of several impact phenomena depending on the state of the projectile and the behavior of the impacted target.

The simulation is divided into 5 steps as follows :

(a) impact on the first bumper,
(b) flight and expansion of the debris cloud to the second bumper,

(c) impact on the second bumper,
(d) flight and expansion of the debris cloud to the backwall,
(e) impact on the backwall.

Using a remeshing technique and an ALE processor, it becomes possible to simulate these successive phenomena (Fig.7).

(a) **Impact on the first bumper (B1).** The first impact simulation has already been validated (Dubois, 1988). It leads with high accuracy (less than a few percent w.r.t. the experiment) to the determination of the hole diameter and the residual velocity of the debris cloud (Table 1.1). This phenomenon lasts about 2.5 microseconds (Fig.7) for the considered configuration.

(b) **Flight and expansion of the debris cloud to the second bumper (B2).** From the time of the first impact to the impact on the second target (bumper in case of multishock shield concept or backwall in case of a Whipple concept), which occurs at about 8 microseconds, one can observe a release phenomenon with an expansion of the cloud, resulting in a heterogeneous distribution of mass (sharp gradient of density).

In particular, one can see in front of the cloud a thin liquid zone of relatively high density. For this impact velocity (8 km/s) a density of about 0.56 g/cm3 is found, which is significantly greater than in the internal part of the cloud (Fig.8).

(c) **Impact on the second bumper.** For a striking velocity of 8 km/s, physical phenomena involved in this second impact are quite different from those resulting from the first bumper impact. A relatively low density projectile, made of vapour, liquid and fragments, impacts the second bumper with a velocity close to the initial velocity. Apart from the melting at the interface, vaporisation occurs during the compression of the impacting cloud. This impact is no longer purely hydrodynamic.

The impacted bumper undergoes deformations under applied pressure and the use of an adequate failure law is necessary to obtain good results for the residual velocity of the secondary cloud and for the hole diameter. A simple EOS model alone is no longer valid. The correlation between the simulation and the experiment shows a good agreement concerning the residual velocity and the hole diameter in the bumper (Table 1.1).

(d) **Flight and expansion of the debris cloud to the backwall.** After perforation, the cloud continues to spread behind the second bumper. Only a small part of the total mass flying to the backwall appears to come from the initial debris cloud. This kinematic phase is quite similar to the previous phase between B1 and B2 at a lower velocity level.

(e) **Impact on the backwall.** The last stage of the simulation is the impact of the resulting cloud on the backwall. Measurements of the pressure were performed with a Manganin gauge, and the correlation between the calculation and the experiments is quite good (see Tables 1.1 and 1.2).

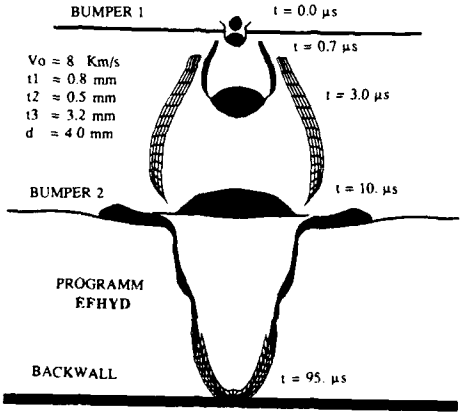


Figure 7 : History of a high velocity projectile perforation of a triple plate

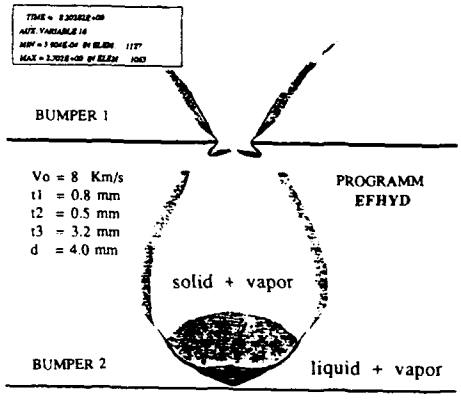


Figure 8 : Debris cloud material state and density before second impact

Material validation cases

Objectives. The early objectives of the material test cases were to reproduce the behavior of the backup-plate, impacted by a debris cloud, generated by a very high velocity projectile (up to 15 km/s). Up to 10 km/s and for the studied configuration, the average residual velocity after the second bumper appears to be less than 1 km/s. Such a velocity level can be reached with the current facility but experiments are now restricted by the low density and large radii inherent to an equivalent flat load.

Materials with densities lower than .9 g/cm3 tend to collapse under acceleration imposed by a light gas gun. Considering these experimental limitations, it is difficult to reproduce a peak pressure resulting from a density representative of such a debris cloud. However, it is possible to observe the cratering and spalling processes in order to validate the material models implemented in the code. The selected configuration includes a flat projectile (Radius : 15 mm, thickness = 5 mm) impacting at about 1 km/s an aluminum target 11.6 mm thick.

		Vb_1 (km/s)	Vb_2 (km/s)	$øb_1$ (mm)	$øb_2$ (mm)	γ_1/γ_2 (in °)	γ'_1/γ'_2 (in °)
R1	Experiment	6.76	0.75	7.80	33	29/56	8/25
	2D calculation	6.90	0.70	8.00	38	3,)/45	10/
	1D calculation	5.85	5.00				
R2	Experiment	6.76	0.975	7.80	70	30/56	14/37
	2D calculation	6.90	0.90	8.00		30/45	
	1D calculation	5.85	5.45				

Legend :

R1 ø = 4 mm, V = 8 km/s, t1 = 0.8 mm, t2 = 0.8 mm; t3 = 3.2 mm; S1 = S2 = 60 mm
R2 ø = 4 mm, V = 8 km/s, t1 = 0.8 mm, t2 = 0.5 mm; t3 = 3.2 mm; S1 = S2 = 60 mm

ø particle diameter
Vb_1 debris cloud velocity after 1st bumper
Vb_2 debris cloud velocity after 2d bumper
$øb_1$ diameter of 1st bumper perforation hole
$øb_2$ diameter of 2d bumper perforation hole
γ_1/γ_2 main and total spray angle behind 1st bumper
γ'_1/γ'_2 main and total spray angle behind 2nd bumper

Table 1.1. Reference cases : Comparison between experiments and computer simulations

	pressure on	B1	B2	Backwall
R1	Experiment	-	-	-
	2D calculation	1.2 Mbars	75.0 Kbars	3.5 Kbars
	1D calculation	1.2 Mbars	95.0 Kbars	4.0 Kbars
R2	Experiment	-	-	6.00 Kbars*
	2D calculation	1.2 Mbars	80.0 Kbars	5.75 Kbars
	1D calculation	1.2 Mbars	85.0 Kbars	6.00 Kbars

**Due to the relatively low pressure on the backwall in both cases, no significant damage appears on the backwall for this velocity.*

Table 1.2. Reference cases : Comparison between experiments and computer simulations

Physical phenomena related to the impact. In the case of a planar normal impact of a flyer plate (equivalent flat load) on a target plate, a state of purely one dimensional strain is produced in both projectile and target. One great advantage of this geometry is that it is relatively amenable to analysis. However, the presence of lateral boundaries can result in a substantial alteration of the strain history of the material.

At the moment of the impact the shock begins to propagate into both the flyer plate and the target plate. At the same moment, rarefactions originating at the lateral boundaries begin to propagate into the target and the flyer. These rarefactions can cause both a rapid stress release and a transition to triaxial strain. These simple experiments are used to evaluate and validate the numerical tool for compression (cratering), for tension (spalling) and gross deformations of the plate.

Numerical modeling. The material models used for the aluminum alloy are the same as for the simulation of the previous reference cases. A Mie-Gruneisen equation of state is used for the Makrolon and Cellotex, combined with a Johnson-Cook/Steinberg-Guinan model.

The plate and the projectile are discretized with four node brick elements. The total number of elements is about 2000. Several numerical simulations were carried out and compared with experimental results.

Cases	V (km/s)	Peak pressure (Kbars)	Bubble on rear plate (spallation) ø (mm)	Bubble on rear plate (spallation) h (mm)	Crater on rear plate ø (mm)	Crater on rear plate h (mm)
M1 exp	1.3	72/38	-	-	18.5	2.8
M1	1.3	80/75	-	2	20.5	2.6
M2 exp*	1.7	70/24	8.5	-	20.0	4.0
M2	1.7	80/85	8.0	< 5.2	23.0	3.7
M3 exp	1.1	-	-	< 1.0	20.3	1.9
M3	1.1	65/58	-	1.3	17.0	2.1
M4 exp	1.1	51/40	-	< 0.8	20.0	2.0
M4	1.1	54/46	-	1.0	16.0	2.0

	exp	*run*
** ejecta velocity*	*2.3 km/s*	*2.0 km/s*
spalling velocity	*140 m/s*	*140 m/s*

Legend :

(1) projectile of 5 mm length (Makrolon)
(2) projectile of 8 mm length (Makrolon)
(3) projectile of 8 mm length, 4 mm Makrolon + 4 Cellotex

Table 2 : Material validation cases

Discussion. The deformation of both projectile and target is shown on Fig.9. For all four tests, numerical results are in good agreement with available experimental data. All expected physical trends concerning the influence of the impact velocity, the material properties and the geometrical data are well predicted by the simulation. Moreover, the implemented material model in EFHYD gives good results concerning the spallation bubble as well as the global deformation process (see Table 2).

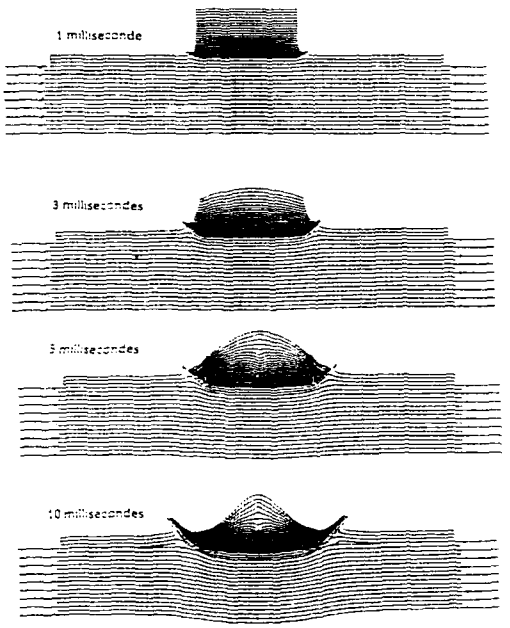


Figure 9: Scenario of deformation for one material validation case

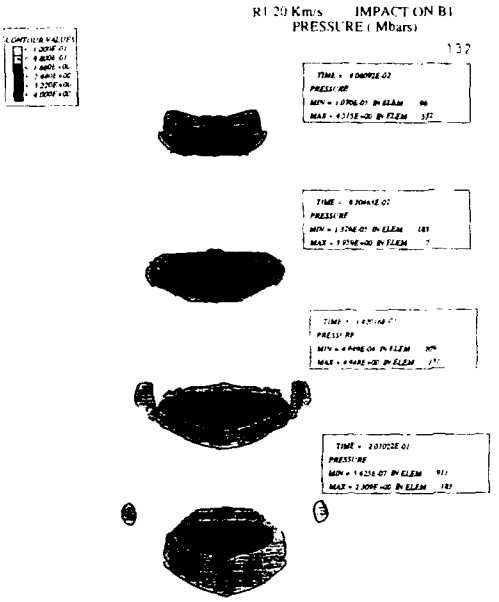


Figure 10 : Pressure contours in Mbar during the first bumper impact (velocity : 20 km/s) (diameter of the particle : 4 mm)

High velocity cases

Numerical simulations give detailed information not directly measurable from tests, like local density, temperature and state of the projectile, the bumper and the debris cloud (Fig.10). During the second impact, the rebound of the debris cloud (Fig.11) is typical of the rebound observed in the test. The backwall impact damage is sensitive to projectile conditions and to shielding configuration. At 7 km/s, craters generated by solid fragments are still present (Fig.1). At 8 km/s, for the triple plate configuration, no crater can be identified (Fig.12).

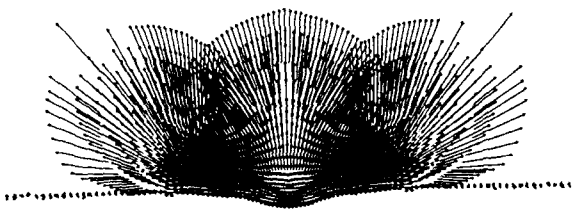


Figure 11 : Velocity field after impact on second bumper

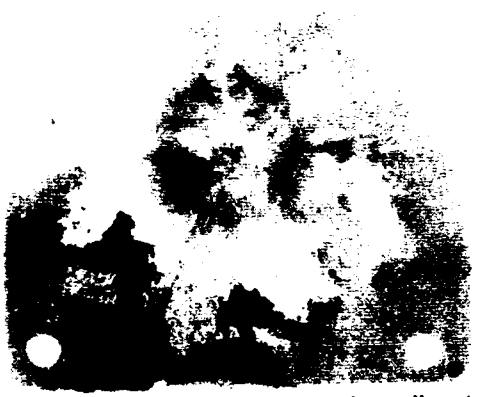


Figure 12 : Backwall impact damage 4 mm diameter aluminum projectile, V = 8 km/s, normal impact 0.8 mm aluminium 1st bumper / 0.5 mm aluminum 2d bumper, 3.2 mm aluminum backwall, 120 mm spacing

According to the performance curves of the experimental facility, the maximum velocity cases are performed at approximately 9.5 km/s. This velocity is well inside the liquid phase regime for aluminum alloys.

The maximum pressure induced by the debris cloud on the backwall is correctly predicted by the code (Fig.13). Two calculations have been performed and validated on a Whipple concept, two more have been performed and validated on a muti shock shield concept. In Tables 2A and 2B, the principal numerical results as well as the available experimental data are given. One can notice the good correlation between both set of data.

			Backwall pressure	Pressure B1	Pressure B2
Whipple concept	V1	Experiment 8 km/s, ø = 2mm 2D calculation 1D calculation	59 kbars 60 kbars 58 kbars	- 1.2 Mbars 1.2 Mbars	N.A.
	V2	Experiment 10 km/s, ø = 2mm 2D calculation 1D calculation	- 40 kbars 40 kbars	- 1.6 Mbars 1.6 Mbars	N.A.
Multi shock shield concept	V3 *	Experiment 8 km/s, ø = 2mm 2D calculation 1D calculation	 N.A.	- 1.2 Mbars 1.2 Mbars	 25 kbars
	V4	Experiment 10 km/s, ø = 2mm 2D calculation 1D calculation	- 2.2 kbars -	- 1.6 Mbars 1.6 Mbars	 5.5kbars

Table 2A : Comparative table for pressure values

			Vb1 (km/s)	Vb2 (km/s)	øb1 (mm)	øb2 (mm)	γ1/γ2 (en °)	γ'1/γ'2 (en °)
Whipple concept	V1	Experiment 8 km/s,ø = 2mm 2D calculation 1D calculation	7.1 6.8 6.2	N.A.	- 4.1 -	N.A.	- 30/47 -	N.A.
	V2	Experiment 10 km/s, ø = 2mm 2D calculation 1D calculation	- 8.4 -	N.A.	- 4.8 -	N.A.	- 35/50 -	N.A.
Multi shock shield concept	V3 *	Experiment 8 km/s, ø = 2mm 2D calculation 1D calculation	7.1 6.8 6.2	N.A.	- 4.1 -	N.A.	- 30/47 -	N.A.
	V4	Experiment 10 km/s, ø = 2mm 2D calculation 1D calculation	- 8.4 -	- 0.1 -	- 4.8 -	- 75 -	- 35/50 -	- 19/38.5 -

**no perforation of the second bumper*

Table 2B : Comparative table for kinematics values

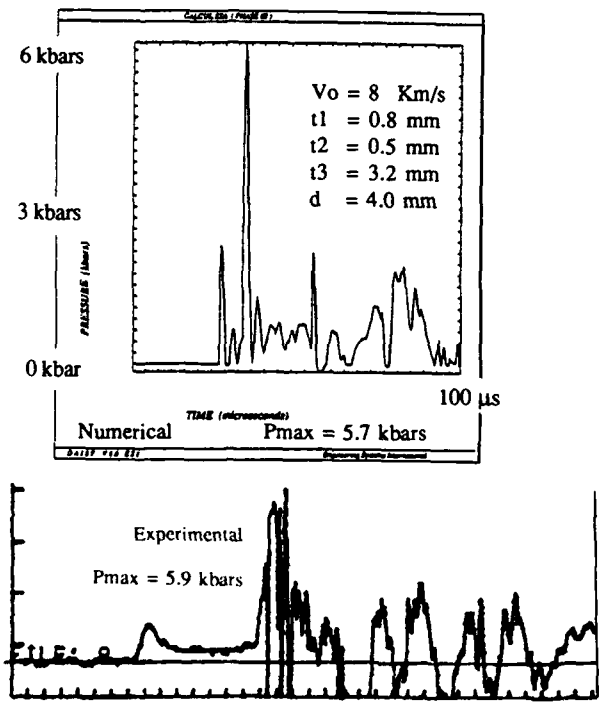


Figure 13 : Comparison of numerical and experimental backwall pressure

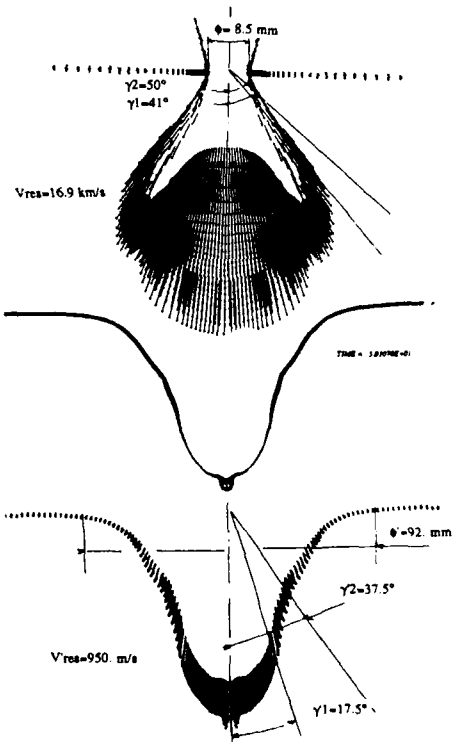


Figure 14 : Geometrical results

EXTRAPOLATION BEYOND TEST CAPABILITIES

Extrapolation to higher velocities

The correlation between experiments and calculations shown in the previous paragraphs gives confidence in the possibility to extrapolate with the numerical code the behavior of triple plate shieldings at higher velocity. Three simulations with impact velocities of 10, 15 and 20 km/s are analyzed to estimate the behavior of the actual multi-shields concept. The previously calibrated and validated material models are used. Figures 14 and 15 represent the evolution of the phenomena during all impacts (first bumper, second bumper and backwall) for an impact at 20 km/s. Typically, for this velocity, the pressure peak is about 25 kbars on the backwall (see Fig.15).

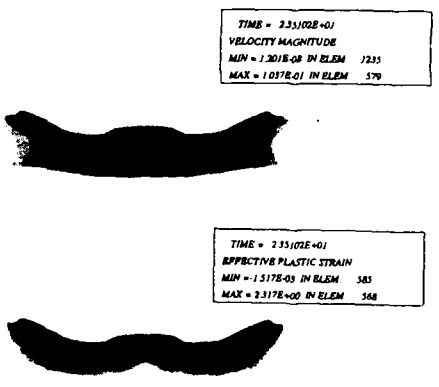


Figure 15 : Typical backwall impact with a projectile diameter of 5 mm at 20 km/s

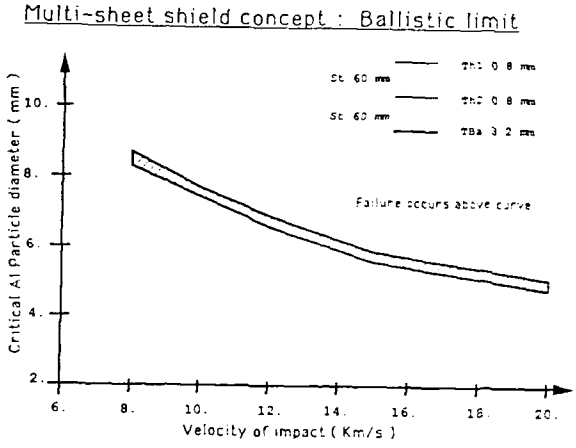


Figure 16 : Multi-sheet shield concept : ballistic limit

Elaboration of a design curve

In order to be able to establish a design curve for the given configuration of the protection system, a 1D/2D simplified methodology has been established and validated against full 2D simulations. Several calculations are carried out for different velocitites and for different diameters of impacting particles.

The evaluation of the ballistic limit for a given velocity, is obtained in making iterative calculations around the diameter which leads to the perforation of the protection system. Five velocities between 8 and 20 km/s are analyzed. The table below summarizes these simulations.

PROJECTILE DIAMETER	PROJECTILE VELOCITY (km/s)				
(MM)	8	10	12	15	20
4	X*	X*		X*	X*
5				X	X
6			X	X	X
7	X	X	X	X	
8	X	X	X		
9	X				

** validated against full 2D analysis*

Results : Establishment of the design curve

For all the simulations carried out for the establishment of the design curve, the damage observed in the backup plate is mainly due to gross deformations under shear and pressure loading. One can observe that the line describing the design curve (Fig.16) presents a certain level of uncertainties. As the calculation is performed with a finite element code, EFHYD, representing a continuous medium, individual fragments generated during the impact cannot be simulated. In order to verify whether or not a generated fragment can perforate the backup plate, a formula relating crater diameter and impactor diameter, density and velocity is used (Klopps, 1990).

CONCLUSIONS

The objective of this work was to analyze the current meteoroid debris protection system in a velocity range between 8 km/s and 20 km/s which is practically not covered by tests. After specific adaptations and validation, the numerical tool of ESI, EFHYD™, has been used for the extrapolations beyond the present test capabilities.

The following main conclusions can be drawn :

(i) The principal physical phenomena occurring during a hypervelocity impact, as well as the different models being able to accurately represent this complex physics in the whole range of impact velocity under consideration, has been discussed and compared. The most suitable models for the above mentioned problem were implemented in the numerical simulation tool EFHYD™ for spalling, cratering, gross deformations and EOS.

(ii) In order to validate EFHYD™, different experiments have been carried out with the following logic :
- comparison of the simulations with the experiments on a configuration as close as possible to the actual geometry.
- calibration and validation of the implemented material laws with flat load experiments.
- indirect validation of the cloud density with the pressure measurement of the backwall on a Whipple concept.
- extrapolation for higher velocities (up to 9.2 km/s) on a multi sheet shield concept.

All simulations carried out were in good agreement with the different experiments concerning the observed physical trends but also concerning kinematic values like hole diameter in the plates, residual velocity of the cloud, spray angles, etc., and pressure values on the backwall.

(iii) After direct and indirect validations in the test range, the validated numerical tool EFHYD, is used to perform extrapolation calculations beyond 10 km/s with realistic projectile sizes. Three extrapolation calculations are performed on the current MDPS configuration at 10 km/s, 15 km/s, and 20 km/s. A simplified 1D/2D numerical methodology is developed and validated against full 2D numerical simulations. This simplified methodology is then used to obtain the design curve of the current MDPS configuration between 8 km/s and 20 km/s. However, and in order to be more general, this methodology should be validated for other MDPS configurations and/or other particle diameters. A number of tests could be suggested for this purpose. Shaped charge fragments impact with reasonable L/D aspect ratio could also be performed in order to extend the direct validation range of the simulation tool.
Concerning an indirect validation of a cloud in a vapor state, lead material could be used instead of aluminum and pressure measurement could be made on the backwall. Similar but simplified validation methodology could be applied for non normal impacts (with possibility of rebound) in order to validate the 3D simulation tool as well as to obtain design curves for different incidence angles.

REFERENCES

Anderson Charles E. Jr., An overview of the theory of hydrocodes. International Journal of Impact Engineering, Vol.5, 1987.

Curran, D.R., Seaman, L. and Shockey, D.A., Dynamic Failure of Solids. Physics Reports, A Review Section of Physics Letters, Vol.147, Nbrs 5 & 6, March 1987, ISSN 0 370-1573, PRPLCM 147(5&6) 253-388 (1987).

Dubois, J. & al. Numerical simulation of micrometeroids and debris hypervelocity impacts on COLUMBUS pressurised module. ESA SP 289, 1988.

Klopps, R.W., Shockey, D.A. (SRI), Osher, J.E., Chare, H.H. (LLNL). Characteristics of hypervelocity impact debris clouds, 1990.

Smith, D. and Adams, N.G. Studies of Plasma Production at Hypervelocity microparticle impact. J. Phys. D. App. Phys, vol 6., 1973.

Trucano, T.G., Grady, D.E., Mc Glaun, J.M., Fragmentation statistics from hydrocodes calculations. P.O. Box 5800, Div. 1534, Albuquerque, New Mexico 87185- 5800, 1989.

Westine P. & Mullin S., Scale Modelling of Hypervelocity impact. Proceedings of the Hypervelocity Impact Symposium. International Journal of Impact Engineering. vol 5, 1986, 1987.

Zukas, J.A., Nicholas, T., Swift, H.F., Greszczuk, L.B., Curran, D.R., Impact Dynamics. John Wiley & Sons, 1982.

Int. J. Impact Engng Vol. 14, pp. 267–277, 1993
Printed in Great Britain

0734-743X/93 $6.00 + 0.00
Pergamon Press Ltd

RECENT ADVANCES IN METHODS FOR MEASURING THE DYNAMIC RESPONSE OF GEOLOGICAL MATERIALS TO 100 GPA

Michael D. Furnish

Sandia National Laboratories
Albuquerque, New Mexico 87185-5800

ABSTRACT

Modeling certain classes of hypervelocity impact events requires laboratory materials data for benchmarking purposes. These data include Hugoniot states, release path and strength. Two classes of impact techniques have been employed for measuring equation-of-state properties for rocks and rock simulants These techniques both use velocity interferometer diagnostics. One, employing a sample-in-projectile geometry, provides high-precision Hugoniot data and continuous release trajectories for dry or water-saturated materials. The majority of the present experiments have been performed with this geometry. The other, employing a sample-in-target geometry, provides loading path and Hugoniot data as well as limited release data. Materials studied by these two techniques have included a variety of tuffs, rhyolites, carbonates, grouts and an epoxy-alumina mixture. Uncertainties in the results from these techniques have been estimated by analyzing the effects of errors in observables and ancillary material properties.

INTRODUCTION

In a hypervelocity event such as meteoroid impact cratering, shocks strong enough to melt or vaporize geological media may be found in the immediate vicinity of the impactor. However, much of the interesting physics of the cratering process occurs at the lower stress levels seen outside of this relatively small volume. Material ejection is significantly affected by material behavior in the region <100 GPa (Öpik, 1971). For relatively low velocity impacts (up to about 10 km/sec for silicates), pressures generally do not exceed 100 GPa anywhere in the system.

Modeling these events (Ahrens and O'Keefe, 1987, Hardage, 1967, Roddy *et al*, 1987) requires appropriate material descriptions. The most commonly used description for the solid components of the system has been the Mie-Grüneisen-based model of Tillotson (1982) although other models have been employed (Roddy *et al*, 1987) such as that of Schuster and Isenberg (1972). These models may be benchmarked by laboratory gas-gun tests designed to elucidate material properties of interest.

The main properties of interest include Hugoniot conditions, loading history and release behavior (continuous unloading trajectories where possible). Material strength is of interest for small events, but not for such large-scale problems as asteroid impact. Where loading conditions are uniaxial (as with the present shock-wave experiments), axial stress, motion, wave velocity (compression and release) and density (or axial strain) are the characteristics of interest. Hugoniot states alone (e.g. Marsh, 1980, McQueen *et al*, 1970) do not sufficiently constrain material models.

In the present paper, techniques for measuring these properties over the range 0 - 100 GPa with gas-gun tests instrumented with VISAR (Velocity Interferometry System for Any Reflector) (Barker and Hollenbach, 1972) are discussed. How the data may be used and what appropriate error bounds may be placed on the data will also be discussed.

Natural geological materials and artificial simulants (e.g. grouts) pose several problems for obtaining meaningful dynamic data. Scales of heterogeneities tend to be significantly larger than the spot size for which data is returned to a VISAR. These materials also often have a moisture content which must be preserved if *in situ* properties are to be measured. Finally, such materials as rock materials with significant ice content must be tested (and preferably preserved) under refrigerated conditions.

Two impact techniques have been developed to measure the requisite dynamic properties of geological materials. Both of these are used with laboratory gun systems and use VISAR for time-resolved waveform measurements. One

(referred to as reverse-ballistic) has the sample in the projectile and gives Hugoniot and continuous release information. The other (referred to as forward-ballistic) has the sample in the target. The sample is backed by a window material. This configuration is especially useful for measuring loading and Hugoniot information. The somewhat lower-resolution piezoresistive and electroinductive gauge techniques (e.g. Murri *et al*, 1975) have contributed to this field of study as well, although these techniques will not be discussed.

There are several experimental constraints of special interest for testing geological materials. Sample sizes generally are 4 - 10 mm thick and 6 -7 cm diameter (2 - 2.2 cm diameter for impact velocities of 2.5 - 7 km/sec, where a two-stage light-gas gun must be used). Hugoniot stresses available depend on the exact configuration, but range to about 25 GPa for the larger samples and 100 GPa for the smaller samples, assuming shock impedances of typical geological materials. Impact velocities may range from several tens of meters/second to about 7 km/sec. The present configurations preserve water saturation states, although care must be taken during sample preparation to maintain saturation levels. It is quite difficult to preserve a saturation level intermediate between fully saturated and air-dried. As well, many geological materials (such as zeolitized tuffs) may be irreversibly dewatered by simple evaporation.

REVERSE-BALLISTIC TECHNIQUE FOR EVALUATING HUGONIOT AND RELEASE OF GEOLOGICAL MATERIALS

Consider an impact experiment with the design shown in Fig. 1. The wave interactions and observed velocity history for this design are also shown in Fig. 1. The sample is mounted in the projectile, contained in an aluminum cup to protect it from gun vacuum and backed by a closed-cell, high strength foam. In this way water saturation is maintained during the experiment. Upon impact, a shock propagates through the aluminum cup, through the sample and into the foam backer. A release is reflected forward through the sample, the aluminum cup and target components and into the lithium fluoride window. A VISAR monitors the velocity history of the aluminum/lithium fluoride interface.

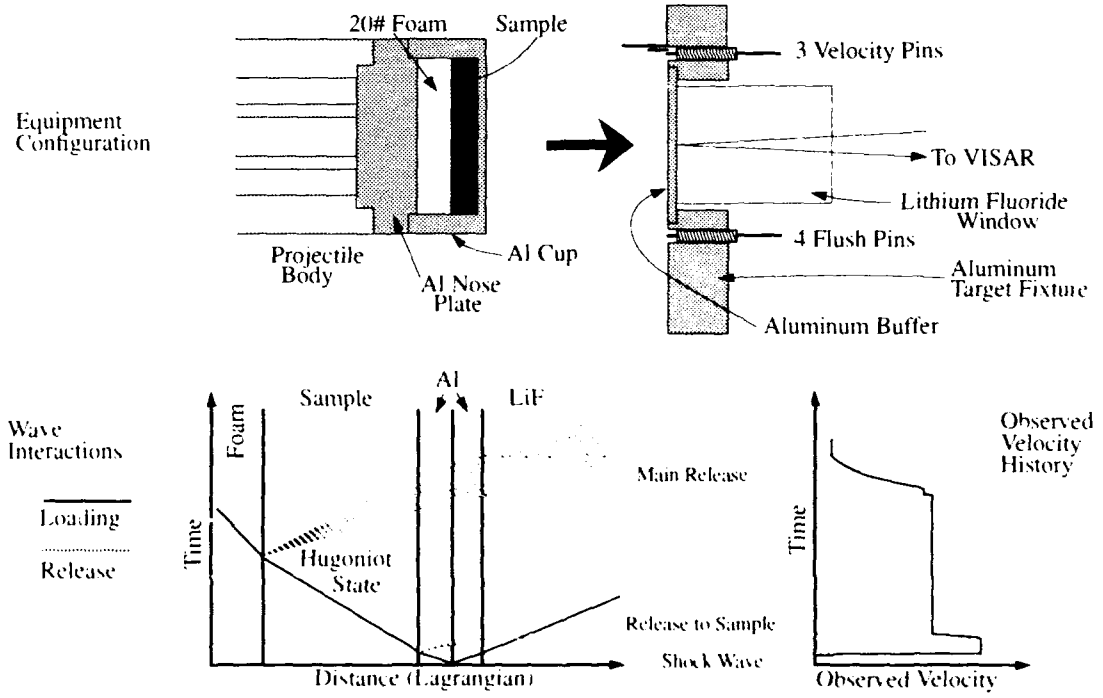


Fig. 1. Configuration of Reverse-Ballistics Configuration (Powder gun adaptation shown)

Information Available from the Reverse-Ballistic Method

The most basic form of generally usable data produced by this experiment is a velocity profile. Material models may be validated by comparing computer code simulations of the experiment with the observed wave profiles. Utilizing these data requires a detailed knowledge of such experimental particulars as component dimensions and projectile velocity.

Hugoniot data are derived from these profiles by standard impedance-match methods (McQueen *et al*, 1970, see Grady and Furnish, 1988, for details about the present technique) (Fig. 2). Information required is the projectile velocity, the initial sample density and the velocity level of the long plateau in the observed velocity profile. In addition, the Hugoniot and release properties of the cup and window materials are required, although these are known to good precision for materials such as aluminum and lithium fluoride (better than 1 percent stress at a given particle velocity).

Release trajectories are derived by modeling the experiment computationally (Grady and Furnish, 1988). Hugoniot data are also redundantly provided from the computer analysis. We have used the wavecode WONDY V, a one-dimensional Lagrangian wavecode. After the Hugoniot state has been determined, an empirical model of the sample is constructed with a Mie-Grüneisen loading behavior and a Lagrangian release modulus described by:

$$(-V_0)\left.\frac{\partial\sigma}{\partial V}\right|_S \equiv B_S = B_0(1+\chi B_1+\chi^2 B_2+\chi^3 B_3) \qquad \left(\text{where } \chi \equiv \frac{\sigma}{\sigma_H}-1\right) \qquad \text{(Eq. 1)}.$$

Here, B_0 has units of pressure and the other B_i (i = 1, 2, 3) are nondimensional. B_0 is adjusted to match the observed release arrival time on the VISAR record; the Eulerian sound speed at the Hugoniot state may be expressed as $C_h = (\rho_0/\rho)\sqrt{B_S/\rho_0}$. Next, B_1 is adjusted to match the initial slope of the release signature; then B_2 and B_3 are adjusted to match the observed curvature of the release curve signature. Within the uncertainties of the fitting process, B_0 and B_1 are generally determined accurately, while B_2 and B_3 are less well constrained. The release path in stress versus density space may then be determined by integrating Eq. 1; particle velocity may be obtained by integrating the differential $dU_p = \sqrt{d\sigma dV}|_S$ over volume from the Hugoniot state ($|_S$ indicates integration along the release). In practice, this fitting process is iterative, requiring 3 - 15 runs of the wavecode. About 600 zones are used for typical models.

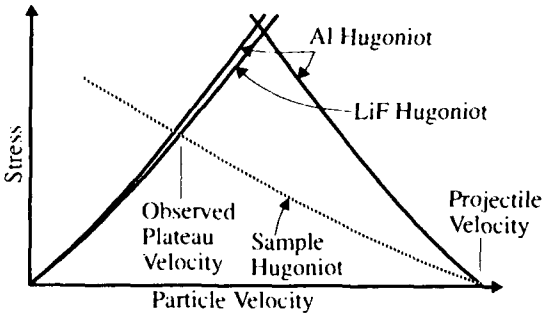


Fig. 2.
Impedance match diagram for standard reverse-ballistics configuration.

Provides σ, U_p
If loading wave is steady, then:
$U_S = \sigma/\rho_0 U_p$
$\rho = \rho_0 U_S/(U_S - U_p)$

Fig. 3 gives an indication of the role of each of the B_i in fitting the profile, and the relation between fitting precision and effects on the calculated release trajectories in various spaces. The particular example is for a test on a rhyolite (density 2.276 Mg/m^3) shocked to a Hugoniot stress of 11.6 GPa. The initial arrival of the release wave corresponds to the sound speed, which may be calculated as discussed by Furnish (1990a). Empirical material models may be derived directly from a set of Hugoniot points and release curves. Consider the axial release modulus, $K \equiv -V(\partial\sigma/\partial V)|_S$, and its first three stress derivatives, $K^{(n)} \equiv (\partial^n K/\partial\sigma^n)|_S$. These are functions of stress along the release. Their values at the Hugoniot stress may be expressed (Furnish, 1990b)in terms of the B_i described above, the Hugoniot stress P_H, and the ratio of initial to Hugoniot density, ρ_0/ρ_H. Each of the $K^{(n)}$ may then be expressed as a function of Hugoniot stress (each experiment generates one set of the $K^{(n)}|_{\sigma_H}$; this then gives an experiment-based description of the release behavior of the material for shocks of arbitrary strength within the experimental range. This technique has been used to estimate errors caused by using an approximation that a grout release lies along the Hugoniot when correcting gauge stress or particle velocity to *in-situ* conditions (Wise and Chhabildas, 1986).

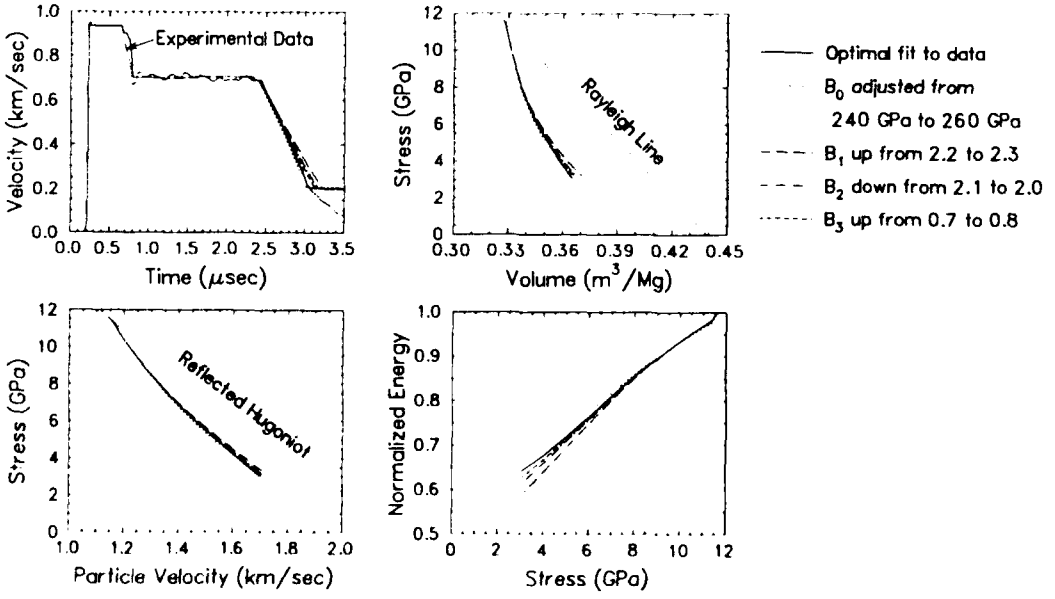


Fig. 3. Effects of changing respective B_i coefficients in WONDY fits (rhyolite, 11.6 GPa). Normalized energy is the specific energy on the release divided by the Hugoniot specific energy

Limitations of the Reverse-Ballistic Method

With this technique, releases are limited by the nonzero shock impedance of the foam. In turn, the foam selected is governed by strength requirements: it must support the acceleration of the sample and cup during launch. Releases may thus be measured down to as low as 20 percent of the Hugoniot stress for low-velocity launches (up to 0.7 km/sec; Hugoniot stresses up to ~3 GPa, depending on the impedance of the test material). On the other hand, tests with the 2-stage gun at 4 - 7 km/sec only provide releases down to 60-75 percent of the Hugoniot stress, since a relatively dense (0.7 gm/cm^3) plastic/glass microballoon composite must be used for the 1 - 2 mega-G launch environment.

From such data, geologic materials may be characterized by the fraction of the Hugoniot specific energy retained at half-stress on the release. Higher fractions correspond to greater shock attenuation rates.

The sample must also be able to withstand the launch. For most rock materials studied, this has not been a problem. More distended materials, however, may present problems with this technique.

The Grüneisen gamma, an important parameter in many material models, can be only approximately determined from these data. There are two reasons for this. The first is experimental: this technique is optimized to measure a release trajectory and single Hugoniot state rather than a difference between the Hugoniot and the release trajectory. Any flexibility in choosing a Hugoniot corresponds to an uncertainty in progressing from a release curve to a Grüneisen parameter. The second reason, common to uniaxial experiments, lies with the inability of this technique to distinguish between the strength of the material and the effects of shock heating or phase changes.

Finally, such properties of the loading wave as precursors (e.g. an elastic wave or a phase-transition induced precursor) and the rise time are not measured by this method. For many tuffs, rhyolites and silicate-based grouts, this is not a significant concern because the strengths (substantially less than 0.1 GPa) are very small compared to the Hugoniot stresses (1 to 100 GPa). More competent materials, such as granites, dunites or many single-crystalline samples, do show multiwave structures in forward-ballistic experiments (shock transmitted through sample to window; see later section discussing the forward ballistics method). Carbonates may show precursors related to the $CaCO_3$ $I \rightarrow II \rightarrow III$ transitions. Reverse-ballistic testing of these materials must be interpreted in light of the multi-wave structure. Impedance-match calculations in the stress-particle velocity plane give the correct Hugoniot stress and particle velocity, but the shock velocity and Hugoniot density must be calculated to account for the wave structure. Releases may be derived by the iterative wavecode modeling method described above if the description of the loading behavior in the wavecode is correct. The version of WONDY V used is written to accommodate a two-wave loading structure and variable-modulus release simultaneously in the sample material

Strengths of the Reverse-Ballistic Method

There are three primary reasons for using the reverse-ballistic configuration where possible. First, it is very robust against experimental error. Information about absolute timing of the trace and projectile velocity is supplied redundantly, affording cross-checking. This advantage is due to the first part of the experiment being an aluminum/aluminum impact, where 6061-T6 aluminum properties are well-known.

Second, the wave interactions are relatively simple. This is partly due to the very good impedance match between the aluminum buffer and the lithium fluoride window. While the experimental analyses makes corrections for all wave interactions, it is useful to know that the sample has been subjected to a simple load/unload path with little in the way of extraneous wave interactions. In particular, the main release wave travels through an almost uncontaminated Hugoniot state for the entire sample thickness (compare with the case for forward-ballistic VISAR experiments, below). This second advantage does not hold if a high-impedance buffer, such as tantalum, is used instead of aluminum so as to achieve higher shock stresses. As mentioned below, it also may not hold for forward-ballistics geometries.

Third, the use of a buffer and cup provides an intrinsic averaging of the response of a heterogeneous material not afforded by experiments with high time-resolution stress gauges, while providing a high time resolution not afforded by larger stress gauges. Not only is the data more representative of the whole sample, but the reflecting interface is more likely to survive long enough to allow data to be recorded until the simple load/unload cycles are complete (3 - 6 μsec). In recent experiments to measure transient loading effects in sapphire, the sample was impacted directly onto a reflecting surface of a lithium fluoride window and the reflecting surface typically was lost within 50 - 100 nsec, probably due to a combination of heterogeneous sample yielding (cleavage?) and bow shock. Hence, even where a cup is not used (such as with samples that do not need to be isolated from gun vacuum) a buffer is normally used in this configuration.

Uncertainties Associated with Reverse Ballistic Data

Consider the data as reduced and reported in three stages: wave profile, Hugoniot data and release trajectories. Uncertainties in each stage of reduction affect that and subsequent stages.

The wave profile is uncertain in timing and amplitude. Impact time (which is defined as zero time) may be established by two methods: an electronic fiducial generated by a flush pin, and assumed shock velocities through the buffer separating the impact surface from the window and the interface monitored by VISAR. For these experiments, assumed buffer shock transit times have generally been used, with an uncertainty estimated at about 10 nsec (mainly due to uncertainty in interpreting the low VISAR fringes). Fiducial time determinations have exhibited appreciable

discrepancies with the buffer transit time determinations (up to 200 nsec); this is ascribed to small bowing of projectile components.

Wave profile amplitudes are uncertain insofar as the velocity-per-fringe (VPF) is uncertain. This error in turn is a combination of errors in calibrating of the VISAR leg delay and in the assumed index-of-refraction correction for the window $(1+\Delta v/v_0)$ (about 1.28 for LiF, 0.99 to 1.00 for PMMA, 1.03-1.06 for fused silica and 1.75-1.78 for sapphire (Wise and Chhabildas, 1986; Barker and Hollenbach, 1970)). The combined errors here are limited to about 1 percent.

The Hugoniot point is calculated as discussed above. The principal uncertainties are the projectile velocity (about 0.5 - 1 percent), the average value of the velocity plateau on the VISAR record, the initial density, and errors in the assumed equations of state for the ancillary materials (aluminum, lithium fluoride, and (where appropriate) tantalum or copper. Errors in ancillary material EOS have been taken arbitrarily as 1 percent in stress at a given particle velocity; this may understate the error somewhat at stress levels $\sigma_{xx} \lesssim 4$ GPa, where strength becomes important. Projectile velocities are measured by pins (1 or 2 independent measurements per shot) and from the first (short) plateau in the velocity history; uncertainties are taken as 0.5 percent unless the spread of these readings justifies a larger uncertainty. Often the most difficult uncertainty to assign is the (Hugoniot) plateau velocity. When there is an apparent step in the middle, an average value is taken, with uncertainties sufficient to bracket both elevations. If a high-impedance buffer is used, a clean step may correspond to aluminum ringing, and the two elevations may be used separately (Grady and Furnish, 1988). A large hump at the end of the plateau, as found in some tests, is not included in any averaging.

As an example, errors for Hugoniot calculations in a series of experiments on a tuff are broken down according to principal causes in Fig. 4, for each of the four Hugoniot quantities. The principal contributions to overall Hugoniot uncertainties are projectile velocity and velocity plateau level for typical tests. The initial density error is a far less

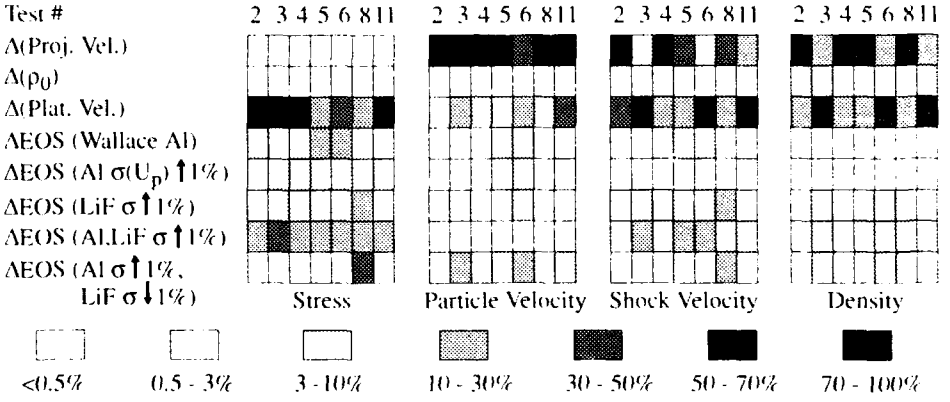


Fig. 4. Fractional error contributions to a tuff Hugoniot error by various uncertainties.

important quantity in this analysis. Release uncertainties are difficult to present explicitly. We have assessed them by performing a perturbation-type analysis (Grady and Furnish, 1988). The principal uncertainties (broken down as observables) are the projectile velocity, the plateau velocity (hence the Hugoniot state), the profile timing relative to impact and the fitting of the calculated profile to the experimental profile in the release interval. Other uncertainties are less important: ancillary material equations of state (which tend to "cancel out"), initial density, and sample thickness (which may be measured very closely prior to the experiment). Fig. 5 shows the effects of perturbations of the observed plateau velocity on the reported release curve (Test # 5 for the material of Fig. 4). A 2σ error in plateau velocity (taken here loosely as meaning about an 80 percent confidence interval) gives approximately a 4 percent error in $f = E(\sigma_H/2)/E(\sigma_H)$ (normalized energy at half of the Hugoniot stress). This is for a typical test, and can vary depending on the oscillation amplitude of the VISAR record in the plateau region and the existence/absence of such anomalies as a two-plateau structure or a large bump at the end of the plateau. Similar analyses for errors in impact velocity, timing and in fitting the release profile show 2σ contributions of about 2 percent, 1 percent and 1 percent, respectively. The fitting error, of course, is difficult to estimate for the general case. Adding these in quadrature, and including small uncertainties for the other observables and the ancillary materials, a total 3σ error in f of 7-10 percent for a given test may be assumed

Example of Reverse-Ballistic Data

A set of reverse-ballistic experiments was conducted on samples of Indiana Limestone (18% porosity; both water-saturated and dry). This material is nearly pure $CaCO_3$. These experiments are chosen as representative illustrations of this technique, which has also been applied to a wide variety of tuffs, granites, grouts, other carbonates, ceramics, single-crystals and metals. Sample sizes were about 7 cm diameter and 6 mm thick.

Wave profiles for this limestone (fully saturated) are shown in Fig. 6. Only profiles from tests with aluminum buffers and cups and lithium fluoride windows are shown. Timing was calculated from the known shock speed in aluminum for these impact conditions (impact is zero time)

Three features of interest should be noted. The basic waveform of Fig. 1 is followed, although there is a short-duration velocity drop after the initial plateau in some of these velocity histories. This drop is almost certainly due to a

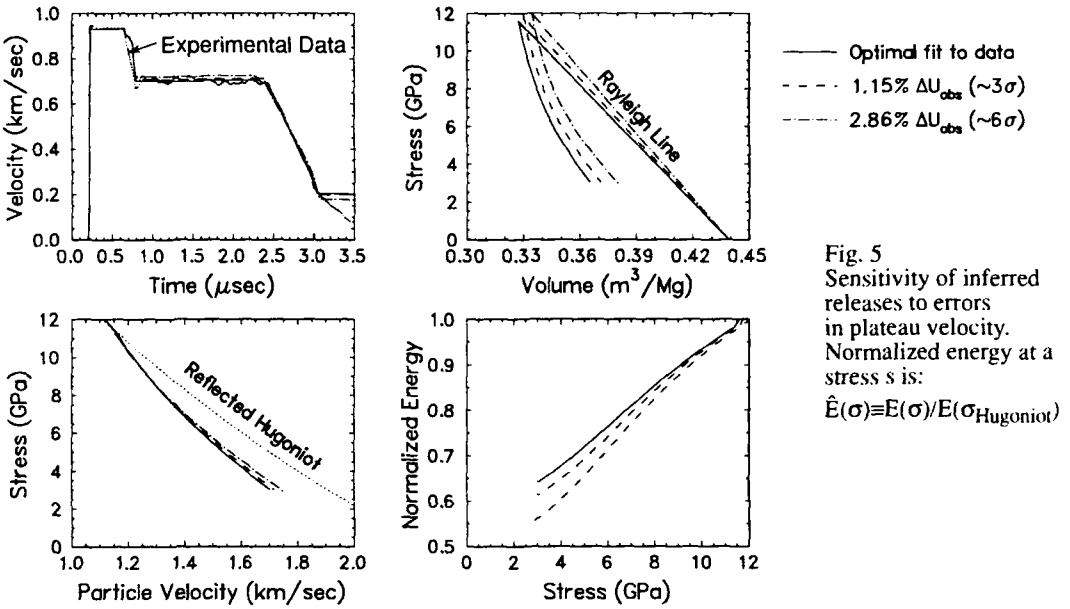


Fig. 5
Sensitivity of inferred releases to errors in plateau velocity. Normalized energy at a stress s is:
$\hat{E}(\sigma) \equiv E(\sigma)/E(\sigma_{Hugoniot})$

gap (in some cases of infinitesimal width) between the sample and the cup. A zero-width gap can still cause such a signature; any forward-running release will outrun a following reshock to give a finite-duration signature on the observed waveform. This has a very minor effect on the calculation of the Hugoniot state. As well, it can be explicitly taken into account in the WONDY runs to determine release trajectories.

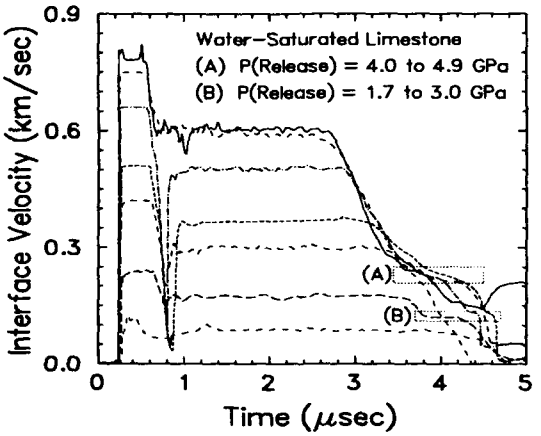


Fig. 6. Velocity histories for Indiana Limestone (18% porosity)

The second feature is the form and structure on the release. The overall release is dispersive (consistent for almost all materials studied). This corresponds to a strong curvature in stress vs. volume space. Steps at stresses corresponding to about 4.5 GP and 2.5 GPa (at the aluminum/lithium fluoride interface) appear consistently. Wavecode calculations (Furnish, 1990c)show that these are consistent with a $CaCO_3$ III $\rightarrow$ I transition (and a concomitant multiwave unloading structure), and not consistent with simple strength effects. Forward-ballistic experiments (Furnish, 1990c) and theoretical calculations by Kerley (1990) suggest that a multiwave loading structure is not produced in these samples due to the large initial porosity.

Finally, the irregularities in the long plateau almost certainly correspond to sample inhomogeneities. We have not observed such irregularities for homogeneous samples.

Hugoniot values with uncertainties and release curves are plotted in Fig. 7. Theoretical curves are due to Kerley (1990) The data strongly suggest that a hydration reaction ($CaCO_3 + 6H_2O$ › $CaCO_3{\cdot}6H_2O$ (Ikaite)) occurs during shock loading to greater than 4 GPa. Release curves are very slightly hysteretic. Lower-stress tests show a two-part release as required by the wave profile; for these different polynomials were used in the different stress ranges for the Lagrangian release modulus B.

Uncertainties shown are typical for this type of experiment, although they tend to be slightly greater where very small samples are used as on a two stage light-gas-gun (2.5 cm diameter and 4 mm thick).

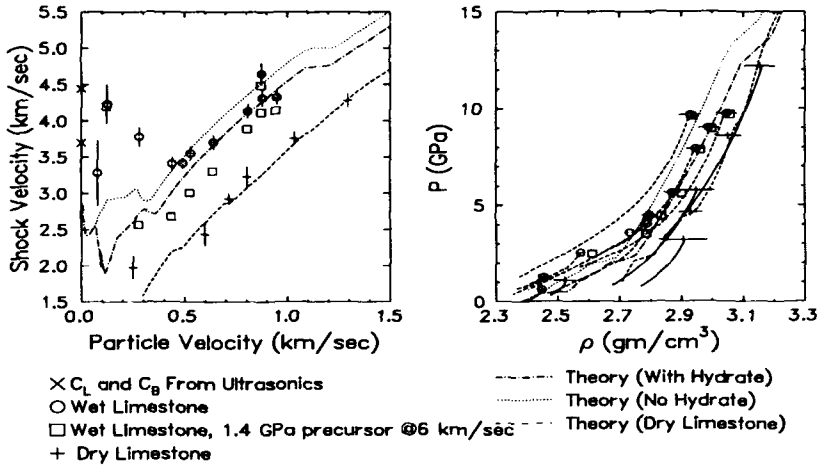


Fig. 7. Hugoniot points and release trajectories from reverse-ballistics experiments compared with theoretical equations-of-state (Kerley, 1990) for Indiana Limestone (18% porosity).

In general, the geological materials tested have been found to give slightly hysteretic releases (below the Hugoniot) for stresses up to 40 - 60 GPa, and releases above the Hugoniot for higher shock stresses. If thermal effects alone were operative (normal Mie-Grüneisen behavior), these releases would consistently lie above the Hugoniot. Since the slope of the release is related to the axial sound velocity at the Hugoniot state C_x by $C_x=\sqrt{V(\delta\sigma_{xx}/\delta\varepsilon_{xx})|_s}$, a steeper (more hysteretic) release corresponds to a higher sound velocity. Sound velocity data at the Hugoniot state of a zeolitized tuff are shown in Fig. 8. For low Hugoniot stresses (to about 50 GPa), the observed sound velocities are higher than those predicted for release along the Hugoniot; for high stresses they are lower.

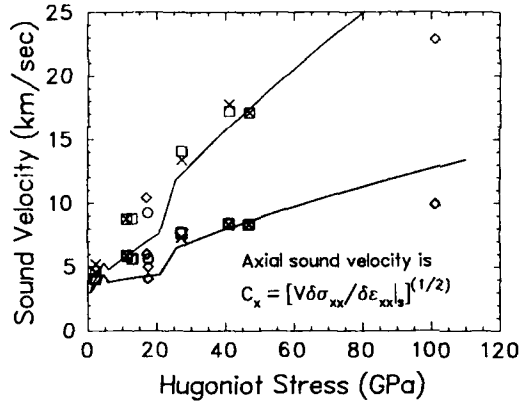


Fig. 8. Sound (release) velocities observed for a zeolitized tuff.

As a check of the credibility of the WONDY method described above for calculating releases, releases were calculated for archived waveforms from experiments with a thick aluminum flyer backed by vacuum impacting an aluminum buffer backed by lithium fluoride (Hugoniot stresses of 50 and 90 GPa). The releases for these cases were above the Hugoniot and agreed closely with those calculated by more conventional Lagrangian means.

FORWARD BALLISTICS METHOD USING VISAR

Details of Technique

There are many situations where the reverse-ballistics configuration is unsuitable. For example, experiments with refrigerated or heated samples, or fragile samples, must be done with the sample in the target. Any material tested under conditions where a precursor (elastic or phase-transition) exists at a large fraction of the Hugoniot stress will not give a simple centered release wave in a reverse-ballistics experiment; the precursor will reflect a strong release wave before the plastic loading wave has finished traversing the sample. If the shock state of the precursor is not known, the Hugoniot shock velocity and density cannot be calculated from the results of the reverse-ballistic experiment. For these situations, a forward-ballistic experiment is required

The information available from such experiments varies with the particular experiment. Usually it includes a loading history (including strain rate and the shock states of any precursors), the Hugoniot state, either a reshock state or a partial release state of the sample, and a release or recompression trajectory from this state. In some cases it is possi-

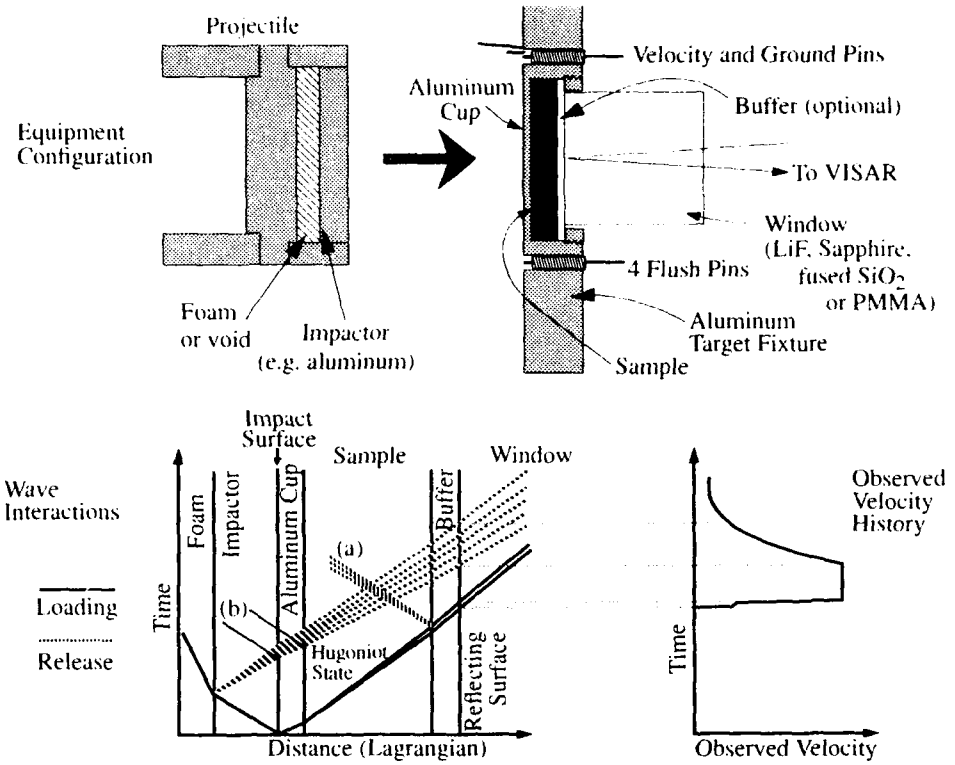


Fig. 9. Forward-Ballistics Configuration (Gas gun adaptation shown)
(a) Release or reshock from sample/buffer interface
(b) Reshock(s) from sample/cup/impactor interfaces

ble to measure a release directly from the Hugoniot state.

Consider the configuration of Figure 9. This is the most practical geometry for use with VISAR since a window must be used (free surfaces of geological materials are not adequate reflectors after shock arrival). Often a buffer is desirable or essential for studies of geological materials. It averages the effects of heterogeneities, provides better survivability for the reflecting surface during the experiment and protects the reflecting surface from chemical attack during preparation. Very low-porosity materials (e.g. granites and marbles) may be used without buffers. The advantage of avoiding the use of a buffer is that an explicit Lagrangian analysis method may be used to give relationships between stress, strain, strain rate, particle velocity and wavespeed through compression and release (e.g. Furnish and Chhabildas, 1992).

The best available window materials for use with geological materials are PMMA, lithium fluoride and fused silica (although Z-cut sapphire may be used in its elastic regime below ~12 GPa for extremely high-impedance samples such as iron). If an inappropriate window is chosen, an excessively large reshock or a release wave is sent back into the sample (see Fig. 9 releases labeled (a)) and the primary release is contaminated by the affected volume of sample. In this respect, *in-situ* stress or particle velocity gauges hold advantages over VISAR diagnostics: sandwiching the gauge between disks of the sample will give a perfect impedance match.

Available shock stresses may be increased by choosing higher-impedance impactors such as tantalum or tungsten carbide. However, if an impactor of higher impedance than the sample or cup is used, the release will be abbreviated by the wave interaction leading to the reshock labeled (b) in Fig. 9.

Calculation of the Hugoniot and partial release/reshock states proceeds as illustrated in Fig. 10. For this configuration, the Hugoniot state in stress/particle velocity space is calculated from the shock arrival time at the window (hence the shock velocity in the material). Assuming there is no precursor, this state lies at the junction between the line $\sigma = (\rho_0 U_S) U_P$ and the aluminum release from the Al/Al impact state. This is based on the requirement that axial stress and particle velocity must be continuous across an interface. If there is a precursor, both the shock velocity U_{S1} and particle velocity U_{P1} of the precursor state must be determined. U_{P1} may be estimated from the observed interface velocity after passage of the precursor, using the fact that the precursor state must lie on the line $\sigma_1 = (\rho_0 U_{S1}) U_{P1}$ and assuming that a release of the same slope magnitude connects this state to the observed precursor state transmitted into the PMMA. The Hugoniot state then lies on the intersection of the line $\sigma = \sigma_1 + [\rho_p (U_{S2} - U_{P2})](U_P - U_{P1})$ with the same aluminum release as before.This is depicted in Fig. 11. If a buffer is used, care must be taken to calculate the sample shock velocities correctly because the buffer shock transit times are different for the precursor and final wave. For the experiment of Fig. 10, the sample was immediately released to approximately half of the Hugoniot stress by the release (a) (in Fig. 9). The stress/particle-velocity state of this release lies on the PMMA Hugoniot, as shown in Fig. 10. The density of this state cannot be determined from this experiment because

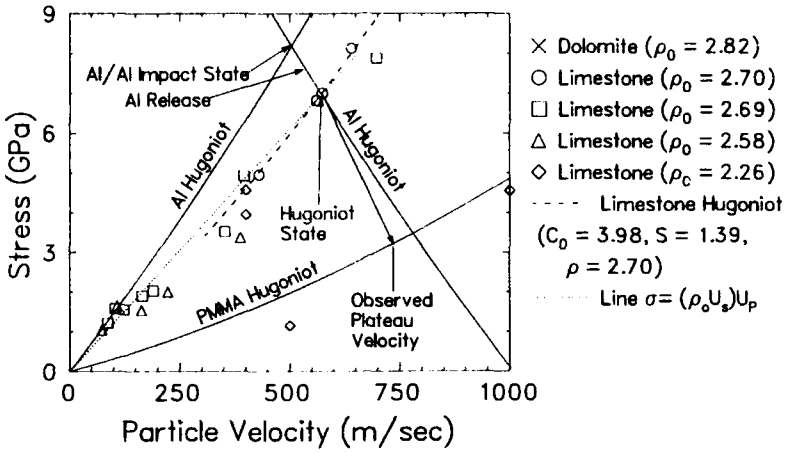


Fig. 10. Calculation of Hugoniot and partial released states for forward-ballistics experiment. Sample used is a dolomitized limestone (ρ_0 = 2.786 gm/cm^3); aluminum impactor and cup; PMMA buffer and window; 1008 m/sec impact velocity

a continuous stress/particle velocity curve from the Hugoniot point to the partially released state is not available and the necessary Riemann integration cannot be performed:

$$\int_{\sigma_{Hug}}^{\sigma_{Rel}} \left.\frac{\partial U_P}{\partial \sigma}\right|_S d\sigma = -\int_{U_{P(Hug)}}^{U_{P(Rel)}} \left.\frac{\partial V}{\partial U_P}\right|_S dU_P = V_{Rel} - V_{Hug} \qquad \text{(Eq. 2)}$$

In this particular experiment, a lithium fluoride buffer and window might have been used in place of the PMMA, and would have been a better impedance match for the sample. It would have caused a slight reload of the sample instead of the marked release for PMMA. For a lower-density sample, however, the reload would have been large for a lithium fluoride window and release properties from this reloaded state could not reliably have been related to release properties from the Hugoniot state.

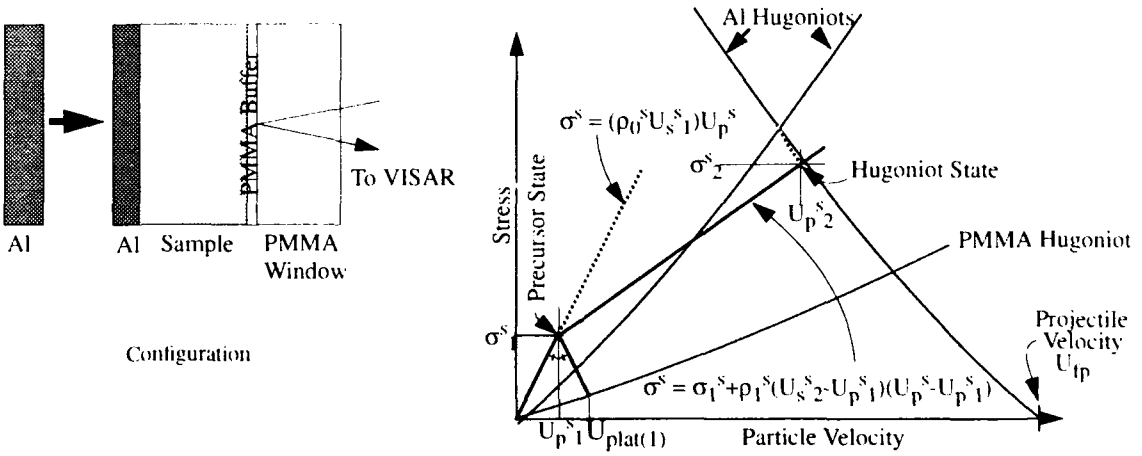


Fig. 11. Calculation of Shock States, Forward-Ballistic, 2-Wave Case. Nomenclature: Superscript S refers to sample, subscripts 1 and 2 refer to first and second shocked states; "U_{Plat}" refers to plateau velocity. Observables are (1) transit times of two waves, and consequent wave speeds ($\Delta t_1{}^S$ and Δt_2, giving $U_S{}^S{}_1$ and $U_S{}^S{}_2$), (2) plateau velocities, $U_{plat(1)}$ and $U_{plat(2)}$, and (3) projectile velocity. Note that $U_S{}^S{}_2$ is referenced to the compressed medium; i.e. is Lagrangian.

Examples of Data Acquired by the Forward-Ballistic Method

Two sets of waveforms acquired by this method are shown in Fig. 12 and will serve as exhibits. Both are for relatively low-porosity carbonates: dolomitized limestones (porosities 2-3%) and a nonporous marble. The higher-stress tests (conducted on the dolomitized limestones) generally show sharp shocks and flat following plateaus. The less dolomitized samples (Jeffersonville) in general show precursors, while the more dolomitized samples (Louisville) do not, except at the lowest stresses. This is consistent with the smaller elastic-plastic velocity difference of dolomite

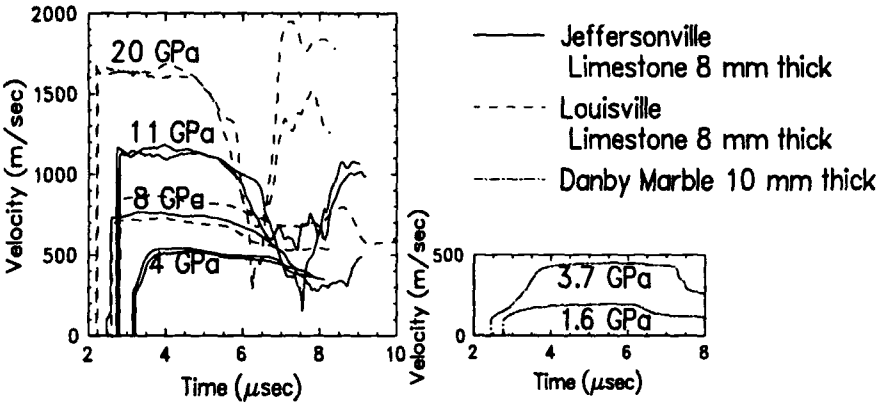


Fig. 12. Wave profiles for Jeffersonville and Louisville Limestones (left) and Danby Marble (right)

relative to calcite (e.g. Grady *et. al.*, 1976) and the effect of porosity in suppressing precursors. The pure marble samples show precursors and ramp loading waves.

As mentioned earlier, calculation of the Hugoniot state depends on an accurate measurement of time-of-arrival. We are generally able to establish the proper timing of the trace to within 5 - 10 nsec using electronic fiducials generated by a flush or rear-surface pin. The dominant uncertainty often arises from the ramp nature of low-stress waves. Uncertainty in measuring the precursor plays a small role in this calculation. Uncertainties in the partial release states (per Fig. 10) arise from uncertainties in the plateau velocity, the PMMA Hugoniot and the sample Hugoniot state. For the present series, they are summarized in Fig. 13.

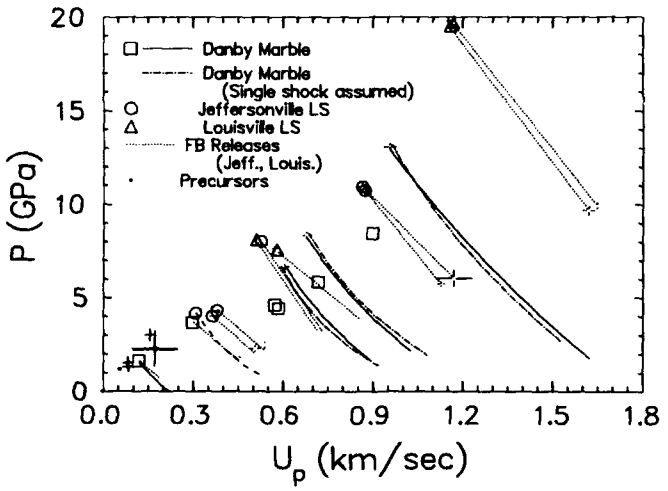


Fig. 13. Hugoniot and partial release states for Jeffersonville and Louisville Limestones and Danby Marble. Curved releases are from reverse-ballistic experiments; straight are from forward-ballistic (endpoints only are known).

CONCLUDING REMARKS

There are several limitations of laboratory techniques for characterizing the response of rocks to dynamic loading and release. Any such method is limited by how well the samples represent the true rock, which may have larger-scale flaws and variability. Equally important is the question of whether the loading waves in a geological event such as a meteoroid impact are as sharp as the shocks produced in these experiments, and thus whether the physics of the two environments is comparable. Questions such as the nature of phase transitions must be addressed in this context.

Within these limitations, several techniques have been developed that have considerable utility in characterizing the response of hand samples of geological material and of various underdense materials to shock loading and release.

ACKNOWLEDGEMENTS

I am grateful to Ron McIntosh and Carl Konrad for handling the myriads of details associated with building up the shots and operating the guns and instruments. I am also grateful for numerous discussions with Eric Rinehart (DNA/

FCTP). Finally, I thank Dennis Grady who collaborated with me during the early part of this work and has continued to be a valuable resource and sounding board. Portions of this work were sponsored by the Defense Nuclear Agency (Point of contact: Eric Rinehart, FCTP), and other portions by the U. S. Department of Energy, and the entire work was conducted under the auspices of the U. S. Department of Energy under Contract DE-AC04-76DP00789.

REFERENCES

Ahrens, T. J. and J. D. O'Keefe (1987). Impact on the Earth, Ocean and Atmosphere, *Int. J. Impact Eng.*, 5, 13-32. Also see J. D. O'Keefe and T. J. Ahrens (1982), The interaction of the Cretaceous/Tertiary bolide with the atmosphere, ocean and solid earth, pp. 103 - 120 in L. T. Silver and P. H. Schultz (eds), *Geological Implications of Impacts of Large Asteroids and Comets on the Earth*, Geological Society of America, Inc.

Barker, L. M. and R. E. Hollenbach (1970). Shock-wave studies of PMMA, fused silica, and sapphire, *Journal of Applied Physics*, 41, pp. 4208-4226.

Barker, L. M. and R. E. Hollenbach (1972). Laser interferometer for measuring high velocities of any reflecting surface, *J. Appl. Phys*, 43, 4669-4675.

Furnish, M. D. (1990a). Measuring the dynamic compression and release behavior of the Paintbrush and Tunnel Bed (NTS) Tuffs over the range 1-13 GPa, Sandia Report SAND90-1317. Aluminum sound velocity calculations (pp. 54-55) are based on data supplied by L. C. Chhabildas (personal communication).

Furnish, M. D. (1990b). Using power series expansions of moduli to interpolate between release curves from dynamic tests: technique and application, Sandia Report, SAND90-1291.

Furnish, M. D. (1990c). Dynamical compression and release experiments on Indiana limestone, pp. 625-629 in *Shock Compression of Condensed Matter* - 1989, S. C. Schmidt, J.N. Johnson and L. W. Davison (eds)., Elsevier.

Furnish, M. D. and L. C. Chhabildas (1992). Dynamic Material Properties of Refractory Materials: Molybdenum, pp. 229-240 in *High Strain Rate Behavior of Refractory Metals and Alloys*, R. Asfahani, E. Chen and A. Crowson, eds., The Minerals, Metals and Materials Society

Grady, D. E, W. J. Murri and K. D. Mahrer (1976). Shock compression of dolomite, *J. Geophys. Res.*, 81, 889-893.

Grady, D. E. and M. D. Furnish (1988). Shock- and Release-Wave Properties of MJ-2 Grout, Sandia report SAND88-1642.

Hardage, Bob A. (1967). Hypervelocity impact with flow and shock penetration through fluid, plastic and elastic zones, Ph.D. thesis, Oklahoma State University, 163 pp.

Kerley, G. I. (1990). Theory of calcite equation of state, pp. 613 - 616 in *Shock Compression of Condensed Matter* - 1989, S. C. Schmidt, J.N. Johnson and L. W. Davison (eds)., Elsevier.

Marsh, S. P. (ed.) (1980), *LASL Shock Hugoniot Data*, University of California Press.

McQueen, R. G., S. P. Marsh, J. W. Taylor, J. N. Fritz and W. J. Carter (1970), The equation of state of solids from shock wave studies, pp. 293 - 417 in R. Kinslow (ed.), *High Velocity Impact Phenomena*, Academic Press.

Murri, W. J., D.E. Grady and K. D. Mahrer (July, 1975). Equation of state of rock, Stanford Research Institute Report.

Öpik, E. J. (1971). Cratering and the moon's surface, pp. 112 - 130 in Z. Kopal (ed.), *Advances in Astronomy and Astrophysics*, v. 8, Academic Press.

Roddy, D. J., S. H. Schuster, M. Rosenblatt, L. B.Grant, P. J. Hassig and K. N. Kreyenhagen (1987). Computer simulations of large asteroid impacts into oceanic and continental sites -- preliminary results on atmospheric, cratering and ejecta dynamics, *Int. J. Impact Eng.*, 5, 525 - 541.

Schuster, S. H. and Isenberg, J. (1972), Equations of state for geologic materials, *DNA 2925Z Report*, Defense Nuclear Agency, Washington D.C.

Tillotson, J. H. (1982). Metallic equations of state for hypervelocity impact, *General Atomic Report GA 3216*.

Wise, J. L. and L. C. Chhabildas (1986). Laser interferometer measurements of refractive index in shock compressed materials, pp. 441-454 in *Shock Waves in Condensed Matter*, Y. M. Gupta (ed.), Plenum.

Int. J. Impact Engng Vol.14, pp.279 - 289, 1993
Printed in Great Britain

0734-743X/93 $6.00+0.00
1993 Pergamon Press Ltd

MATERIAL RESPONSE AT HYPERVELOCITY IMPACT CONDITIONS USING LASER INDUCED SHOCK WAVES

I. Gilath[a], S. Eliezer[b], T. Bar-Noy[c], R. Englman[a] and Z. Jaeger[a]

a) Applied Physics and Mathematics Dept. Soreq NRC, Yavne 70600, Israel, b) Electrothermic Propulsion Lab., Soreq NRC, Yavne 70600, Israel, c) Physics Dept., NRC Negev, Beer Sheva, Israel

ABSTRACT

Dynamic fracture at hypervelocity impact conditions was investigated in different materials using short pulsed laser induced shock waves. All stages of damage evolution were identified for one dimensional or spherical shock wave impact geometry. A new experimental method is presented to estimate the shock pressure decay in materials. In the theoretical section we obtain the damage induced in the target, as follows: The shock wave is modeled by an expanding stress front, which creates micro-damage in the laser impacted layer and extrudes a bulge at the far surface. The calculated bulge geometry compares well with that observed by us for metal-adhesive-metal sandwiches. The micro-defects coalesce into macro- damage or fracture by a mechanism which is described by percolation theory.

INTRODUCTION

Shock loads can be generated by intense short time energy deposition. While in most high speed experiments the impact time is in the microsecond range, laser pulse times are in the nanosecond regime. Thus, high irradiance short pulsed laser induced shock waves offer unique experimental method to study material behavior at conditions of hypervelocity impact in controlled laboratory experiments.

Absorbtion of laser radiation by a target takes place within a very thin layer near the irradiated surface. The rapid temperature increase causes plasma ejection into the vacuum. This expansion drives a strong shock wave into the material. The shock wave pressure P_a is related to the laser pulse intensity I, as $P_a \sim I^{0.7}$. When this compression wave reaches the back surface of the target a tensile wave of increasing negative amplitude is reflected from the back surface or the interface in a multilayer structure. When this tensile stress becomes larger (more negative) than the tensile strength of the target, spall occurs (Gilath et al., a,b,c,d, 1988, Eliezer et al., 1990, Salzmann et al .,1988, 1989). Spall is defined as a planar separation of material, parallel to the wave front, as a result of dynamic tensile stress components perpendicular to this plane. The various stages of material failure were identified with increasing laser intensities from incipient spall, spall layer breaking and target perforation for metals, alloys, composites, alumina and adhesive joints (Gilath et al., 1988, 1989, 1990, 1991, 1992, Eliezer et al., 1990, Salzmann et al., 1988, 1989).

EXPERIMENTAL

The high power Nd:glass system at Soreq N.R.C. (1.06 μm wavelength) is capable of delivering up to 100 J energy in 3-8 nsec corresponding to 10^9 - 10^{14} Watt/cm^2. The ablation pressures obtained on the target for the above irradiances are in the range of kbar-Mbar. The laser spot was changed from small diameter beam (0.1 mm) to large spots (3 mm). By using a large spot compared to overall sample thickness, experimental conditions can be considered as one dimensional; for focused beam, spherical shock waves are obtained. By changing stepwise the laser intensities, the damage threshold till complete material failure can be obtained for the two shock wave configurations. The spall was observed and evaluated by microscopy on sectioned targets.

Diagnostics of high pressures in the range of kbars-Mbars on a nanosecond time scale is still a challenge, therefore calculations of these effects are achieved by large laser-matter hydrodynamic codes. These codes require a full understanding on many parameters and are therefore a major effort. A new approach was found to estimate experimentally the spall stress and the pressure gradient in different materials using the effect of laser induced shock waves to produce spall in targets of different width (Eliezer et al., 1990).

RESULTS

Impact Experiments

The controlled stepwise increase in laser energies allowed us to find the stages of damage evolution from incipient spall to complete perforation of the target materials. The incipient spall for ductile metals was identified from the level of separate voids, while in brittle metals from the level of cracks. Those voids or cracks coalesce and this results in a continuous spall layer. For higher laser intensities the spall layer breaks away and target penetration is observed for specific high intensities. A few examples illustrate the damage evolution on metallurgical sectioned and polished samples. In fig. 1 a cross section is shown of the incipient spall in iron for one dimensional (1-D) impact configuration. The damage extent is equivalent to the impact area, i.e. three times the sample thickness (Salzmann et al.,1988). Spall layer formation with extensive deformation of the spall layer can be seen in ductile materials. In fig. 2, the maximum elongation of the spall layer before break-away can be seen in aluminum.

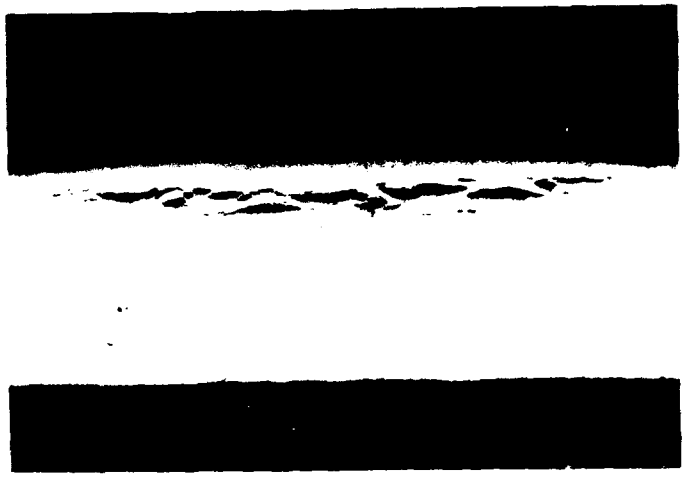


Fig. 1. Incipient spall in iron at 2.4 KJ/cm2, (cross section, x 140).



Fig. 2. Maximum spall layer elongation in aluminium at 3.25 KJ/cm2 (cross section, x 110).







Shock pressure decay in different materials.

At incipient spall for different target widths, similar shock parameters prevail at the rear side of the target (Eliezer et al., 1990). In thicker targets, higher energies (pressures) have to be applied on the front surface of the target, to make up for the energy and peak-pressure decay (ablation pressure) while the shock wave travels through the target. This pressure decay in the target, dP/dx, leads to a dependence of the threshold ablation pressure on the target width, while the fracture stress is constant for the same material.

The peak value of the laser shock pressure (ablation pressure) Pa, depends on the laser intensity I_L, in a 1-D case, in the form (Harrach et al., 1981, Thompson et al., 1984):

$$P_a(\text{Mbar}) = a\left(\frac{I_L}{10^{14}\text{W/cm}^2}\right)^n , \qquad (1)$$

where a=8 and $0.7 < n < 0.8$. If the laser spot is small compared to the target width, a correction for 2-D effects should be used (Harrach et al., 1981). This correction in the limit of very small spots (<0.1 mm) reduces the ablation pressure by a constant factor of 1.8, without changing its 1-D intensity-dependence (Thompson et al. 1984). A linear dependence was obtained for the pressure as a function of target thickness for aluminum, copper, and carbon fiber epoxy unidirectional composites for 1-D impact geometry: (see Figure 7). The experimentally determined spall pressure and pressure gradients are summarized in Table 1.

Table 1. The spall pressure and pressure gradient in different materials.

Material	Pspall (kb)	Pgradient (kb/mm)
Copper	20	180
Aluminum	25	60
CF/epoxy (perp.to fiber) ⊥	0.3	15
CF/epoxy (parallel to fiber) ∥	7	100

Table 2. Threshold laser energy for spall (E_L), laser intensity (I_L) and the ablation pressure (P_a) for different target width (d).

d (mm)	E_L (J)	T_L (10^{14} W/cm^2)	P_a (Mbar)
0.5	11±2	0.47±0.1	2.4±0.4
0.6	15±2	0.64±0.1	3.1±0.4
1.0	49±5	2.1±0.2	6.9±0.7
1.3	105±7	4.5±0.3	11.7±0.8

The spall stress values for aluminum and copper obtained by this method are in good accordance with the values obtained by simulation (Eliezer et al., 1990)

The case for a 2-D hemispherical shock wave, is somewhat different. The pressure decay while the shock wave travels through the foil is much steeper. A linear relationship between the laser energy and the cubic target width was obtained for aluminum. The experimental data for Fig. 8 can be fitted by:

$$E_L = P_o d^3 + E_o \qquad (2)$$

where $P_o = 45.3$ J/mm^3 and $E_o = 4.9$, and d is in mm.

Since in the limit of a very small spot the ablation pressure dependence on the laser intensity is the same as in the 1D case, then

$$P \sim I_L^{0.7} \sim E_L^{0.7} \quad d^{2.1} \qquad (3)$$

The graphical representation of this result for aluminum (based on the numerical values ofTable 2) yielded: $P_a(\text{Mbar}) = 6.46\, d^{2.1} + 0.54$, where the distance d is in mm.

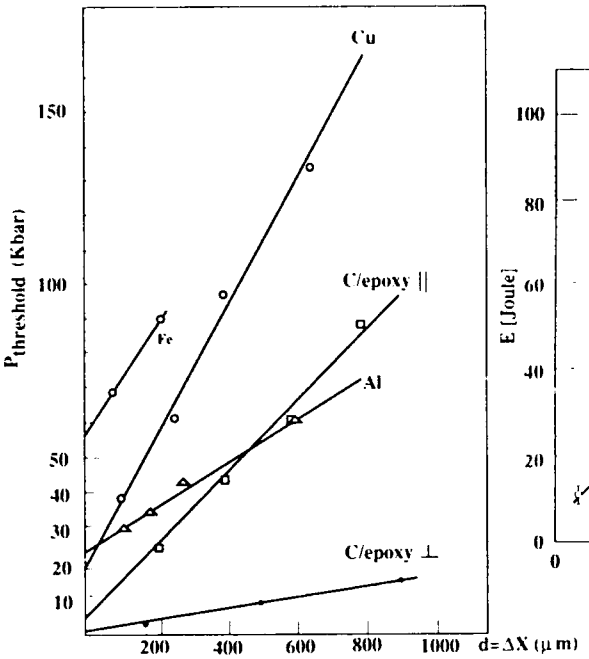


Fig. 7. Plasma threshold ablation pressure for spall as a function of target thickness (one-dimensional shock waves).

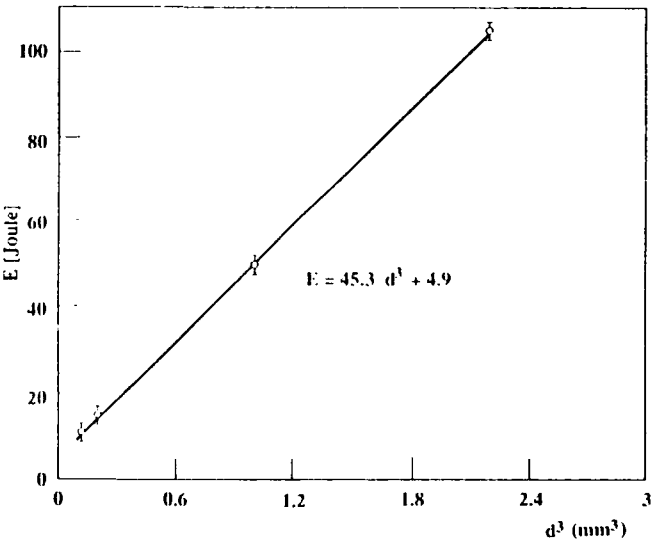


Fig. 8. Laser energy as a function of cubic distance for threshold spall conditions for aluminum (hemispherical shock waves)

THEORY OF LASER-DAMAGE MORPHOLOGY

Preliminaries

The theoretical analysis is concerned with the different types of damage present in the laser- irradiated target and made visible in micro-photographs. The mechanical damage is due to laser generated shock, which results in cracking of brittle compounds, or the creation of voids in ductile in materials and in the appearance of a spall surface near the rear of a finite target. The types of damage can be classified according to their density and connectivity as (a) fragmented, (b) connected and (c) sparse. Percolation theoretical concepts and numerical simulations can be used to identify the various regions and to assess the energy requirements for the formation of each zone, namely how much of the energy input present in the beam is expended on the creation of the damage. The sizes of the various zones are clearly linked to the variation of the laser power. The theoretical prediction is found to agree with size-determinations obtained from experiments.

This theoretical effort forms a link between damage created at the micro-damage level under conditions of ultra-high loading rates and the macroscopic showings of the damage, eventually reaching a local material-failure stage (as in spall). The stochasticity of the micro-damage population leads perforce to a statistical approach, which is provided in our work by the use of percolation theory. The damage development has three interconnected stages: The propagation of stress-waves into the target, the creation of microdamage centers, and the development of these into complete material failure (frequently, the fragmented stage).

Stress-wave development

Here the treatment is based on a model for a stress wave in the target that is valid after an initial stage of laser impact. The model leads to an analytical description of the pressure-wave intensity and, in the next subsection, of the damage formed in the medium. For simplicity a point-like impact (rather than a planar one) was assumed and the propagating stress-wave has a semi-spherical shape. More precisely, this shape becomes distorted because of boundaries at the front and rear faces of the target.

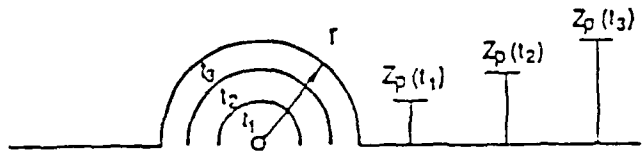


Fig. 9. Hemi-spherical stress wave expanding into semi-infinite targets.

The stress-wave propagating in the medium (without boundary effects) is shown in Fig. 9. The penetration distance $Z_p(t)$ of the stress-wave precursor as time t (where t = 0 signifies the start of the pressure wave) is shown in the figure and satisfies for $t_1 < t_2 < t_3 < \ldots$

$$Z_p(t_1) < Z_p(t_2) < Z_p(t_3) < \ldots$$

Though the medium may be compressible it is simpler to start with an incompressible target, for which one can immediately write the equation of mass conservation and derive from it the following expression for the material velocity field (namely, the material velocity V_m at time t and position r)

$$V_m(r,t) = \dot{Z}(t-r/v_s)\, Z^2(t-r/v_s)/r^2 \tag{4}$$

where $Z(\equiv Zp)$ and $\dot{Z}(\equiv \dot{Z}p)$ are the positions and velocities of the stress-wave front penetrating into the target, v_s is the sound velocity. We shall later see that the strain rate $\dot{\varepsilon}$ plays a dominant role in the creation of damage. It can be given using (4) and the relation

$$\varepsilon(r,t) = V_m(r,t)/r \tag{5}$$

For a compressible material the previous relations, (4) - (5), become modified and $\dot{\varepsilon}$ takes the form (Johnson, 1972, Perrett and Brass, 1974).

$$\dot{\varepsilon}(r,t) = V_m(r,t)/r^{1+\zeta} \qquad \text{(compressible)} \tag{6}$$

in which the exponent ζ satisfies

$$0 < \zeta = 2 - n < 1 \tag{7}$$

It is known that in certain materials

$$\zeta \sim 0.2,\ n \sim 1.8 \tag{8}$$

The presence of boundaries modifies (4). The change can be easily made for planar boundaries and by use of the method of images. Here image sources of stress are placed at distances Z* such that the total stress field (consisting of the true and image stresses) takes at the boundaries the values required by the boundary condition (e.g., zero normal stress on a free surface, zero tangential stress on a perfectly rigid one). In Fig. 10 we illustrate the method of images for a flat slab of thickness d. By the use of this method one gets the following expression for the material velocity (with neglect of additional sources, whose importance is marginal):

$$V_m(r,t) = \frac{1}{4} R_0^2 \left[\frac{\dot{Z}(\tau)(r-z)}{|r-z|^{3-\zeta}} + \frac{\dot{Z}^*(\tau^*)(r^*-z^*)}{|r^*-z^*|^{3-\zeta}} \right] \tag{9}$$

The bulge in the rear face

With the approach of the stress wave to the far face of the slab, a bulge is formed that grows with time. This is shown schematically in Fig. 11.

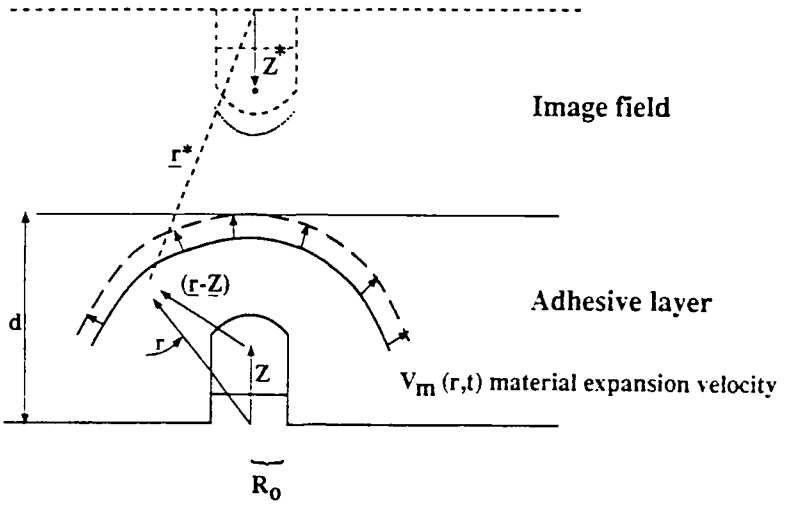


Fig. 10. Definition of symbols in the method of images. The symbols with asterisks relate to the image source

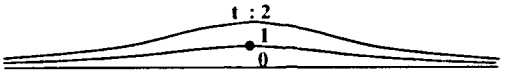


Fig. 11. Schematic description of bulge development at far face of adhesive.

The bulge will continue to grow until there is either a perforation of the slab, or the stress wave expansion stops because the available pulse energy is exhausted. The following illustration (Fig. 12) shows the bulge dimension r_b as function of δr_s, the distance of approach of the stress-wave front to the rear-face, obtained from observations by one of us (I. Gilath) on epoxy sandwiched between Al layers. For energies exceeding 30 J, δr_s is "negative", meaning that the stress wave transpasses the original rear plane boundary. In this situation our theory requires extension. For positive values of δr_s the experimental data, shown in Fig. 12 by crosses, are quite close to the values (represented by dots) that were obtained from our theory of stress wave expansion with some simplifying approximation.

In Fig. 13, one sees the bulge at subsequent times as obtained by calculating the predictions of the model. The computed bulge differs somewhat from those seen in laser-pulse experiments: The computed contours are excessively peaked near the center and extend so far in the wings. The source of the discrepancy is probably that the elasticity of the metallic layer (that borders on the adhesive layer) has not been properly included in the model.

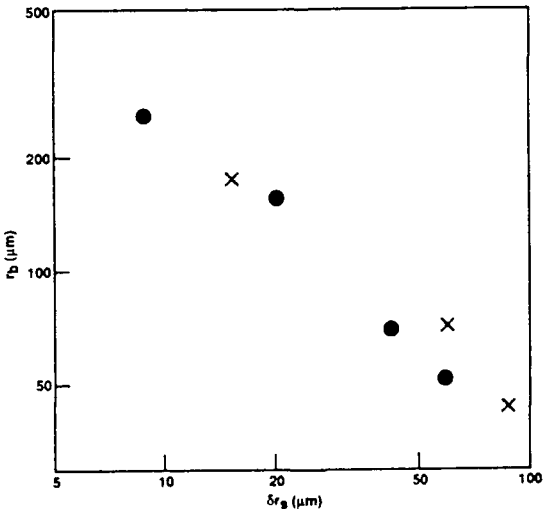


Fig. 12. Bulge height r_b against distance of approach δr_s of the stress front to the rear slab surface. Computed values (dots) are compared with experimental data-points (crosses), taken from adhesive bulges in laser impact with different energies on metal-adhesive-metal sandwiches.

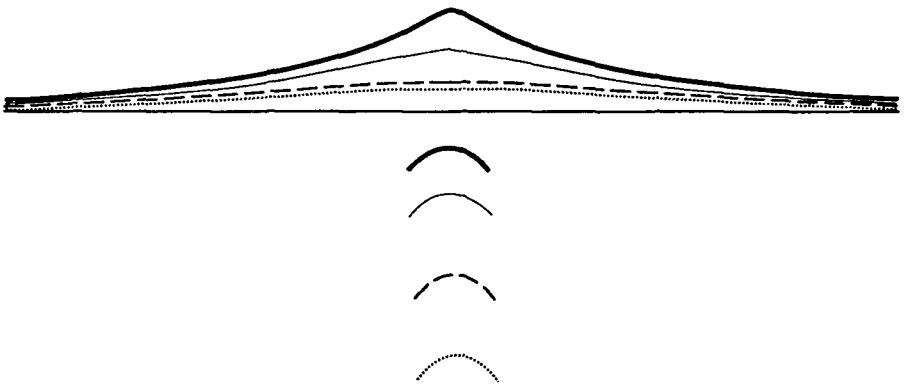


Fig. 13. Bulge shapes at subsequent instances. The bulge contours correspond to the advancing pressure fronts drawn with the same lines.

Dynamics of defect-formation

The rate of energy deposition in the region of the expanding stress-wave is given by

$$\frac{\partial Q}{\partial t} = P_r \cdot 2\pi Z^2 V_m \tag{10}$$

where P_r is the radial stress on the expanding sphere. V_m is the material velocity and Z the radius of the sphere. Assuming that (before defect formation) all the energy is expended on the motion of the particles of the slab (this includes strain waves, elastic or otherwise, and even thermal motion of the atoms) we obtain for the energy investment up to time t:

$$Q(t) = \frac{1}{2}\int \rho_T V_m^2(r,t) d^3r \tag{11}$$

where ρ_T is the target mass-density and the integration is over the target volume (Yatom and Ruppin, 1989). Clearly, the integrand

$$\frac{1}{2}\rho_T V_m^2(r,t)$$

is the energy density. If we consider a small portion in the target (say of linear dimension a that is much smaller than the target size), we observe that the velocity $V_m(r,t)$ contains both the center of mass velocity of the small volume (of the order a^3) and the relative velocities in this volume. The latter is $r\,\dot{\epsilon}(r,t)$ ($\dot{\epsilon}$ being the local strain rate) and it is this part (rather than the full velocity V_m) that causes fracture. Suppose now that defects of size a are created. Then the deformation energy that goes into defect formation is

$$1/2\ \rho_T a^2 \dot{\epsilon}^2(r,t) \tag{12}$$

On condition that the strain exceeds threshold for permanent defect formation. (The threshold differs for compression, tension or shear.) Let us now suppose spherically shaped defects of size a and number density n_a, where both quantities depend on position r and time t. Following the approach of Grady (1978) and Glenn and Chudnovsky (1986) we can write the energy density input in the creation of defects as:

$$2\pi/5\ n_a(r,t)\rho_T \dot{\epsilon}^2(r,t) a^5(r,t) \tag{13}$$

We can equate this to the energy density of formation of free surfaces, namely:

$$2\pi\ \gamma n_a a^2 \tag{14}$$

where γ is the energy for creating a unit surface. Further using (4) and (5) we obtain the characteristic size a of the defects as:

$$a(r,t) = (5\gamma/\rho_T\, \dot{\varepsilon}^2(r,t))^{1/3} = (5\gamma/\rho_T)^{1/3}\, [\dot{Z}_p(t) Z_p{}^2(t)]^{-1/3}\, r^{2(n+1)/3} \qquad (15)$$

This leads to the following functional relation for an incompresible target, n=2:

$$a(r,t) \propto r^2 \qquad (16)$$

The number density of defects is obtained from equating (13) or (14) to (12)

$$n_a(r,t) = \frac{5}{4\pi}\,\frac{r^2}{a^5} = \frac{5}{4\pi}\left[\frac{\rho_T}{5\gamma}\right]^{5/3} \dot{\varepsilon}^{10/3}\, r^2 =$$

$$= \frac{5}{4\pi}\left[\frac{\rho_T}{5\gamma}\right]^{5/3} [\dot{Z}_p(t) Z_p^2(t)]^{10/3}\, r^{-4/3-10/3n} \qquad (17)$$

which gives for an incompressible solid: $n_a(r,t) \propto r^{-8}$

Structured damage in brittle materials

We now describe the defect morphology with a percolation model on a three dimensional lattice. (The model does not impute a lattice structure to the target material, only enables the defect statistics to be made in a discrete, countable manner. Later we go over to a continuous limit or potential defect sites). Supposing a brittle solid in which circularly shaped cracks can be prescribed on the faces of a cell (of size 2a x 2a) in a simple cubic lattice, let us denote by G the number of cells (of size $8a^3$) in the target. Then the number of faces (of area $4a^2$) is (6/2)G = 3G. The number of actual (rather than potential) cracks is $8n_a a^3 G$ (supposing that each crack is placed on a single face. The occupation probability is the ratio of actual to potential crack numbers, or

$$8n_a a^3/3 \qquad (18)$$

which represents the occupation probability (conventionally denoted by p) on a discrete lattice. In a continuum we have to take into account the "Lebensraum"or excluded volume of one planar crack (or plaquette) with respect to another, given by $8a^3$, and we obtain the following probability for the crack occupation:

$$p = 1 - e^{-8/3 n_a a^3} = 1 - e^{-Cr^{-2}} \qquad (19)$$

for an incompressible lattice, where C is a constant. Interpreting the above results, we note that for low values of r the cracks will mainly be isolated, for somewhat higher values but still lower than about $1/3 \sim p_{C1}$ (the 3D percolation probability) the crack system will be complex but non-pervasive (over the whole target), for values of p between p_{C1} and p_{C2} (~ 2/3) chains of plaquette-complexes will span the whole material space but will not yet fragment it. Fragmentation will occur for $p > p_{C2}$ (Aharony et al., 1986) In this region the characteristic fragment sizes (or coherence distances) ξ will depend on the occupation number through

$$\xi \propto (p - p_{C2})^{-\nu_2} \qquad (20)$$

where the critical index $\nu_2 \sim 0.88$. The quantities a, p, ξ all depend on distance r, and time t, as shown earlier in the development. The fragment sizes are distributed in a manner described in percolation theory. For finitely sized targets one needs to apply finite size scaling (Stauffer, 1985). For a non-uniform, space varying stress distribution the fragment-size distribution is affected by the finiteness of the region where $p \sim p_{C2}$ and is calculated as described by Murat et al., (1980).

Ductile Failure

Here one needs to modify details of the percolation approach. The discontinuities formed by the stress are mainly voids. Let their characteristic radii be denoted by a. The space and time variations of a and of n_a are as before. The occupation probability p is calculated as follows: Suppose that voids arise at lattice points of an FCC lattice. Then in G cells (each of volume $16\sqrt{2}\,a^3$) there can be 4G voids. In actuality the number of voids on the lattice is $16\sqrt{2}\,n_a a^3 G$ and the site occupation probability $4\sqrt{2}\,n_a a^3 = 5.66 a^3 n_a$. In a continuum, where there is overlap of voids, the occupation probability is

$$p = 1 - e^{-5.66\,a^3 n_a} \tag{21}$$

If we start with a BCC lattice

$$p = 1 - e^{-6.16 a^3 n_a}$$

Obviously the difference is small. The critical void occupation probabilities are for a pervasive void-chain $p_{C1} = 0.311$, and for a void-complex that is dense enough to fragment the target $p_{C2} = 1 - p_{C1} = 0.689$.

Substituting this value in the left-hand side of (21) yields the critical value of the void density n_a [as in Eq. (17)] and the times and positions in the material where fragmentation will occur.

CONCLUSIONS

It can be concluded that short pulsed laser induced shock waves is a very suitable method to study material response at hypervelocity impact conditions. All stages of material failure were identified from incipient spall through complete target penetration.

One dimensional and hemispherical pulsed laser-induced shock-wave experiments confirmed the expected spall formation and the theoretical decay of the ablation pressure in different materials.

The modeling of events that take place upon laser impact in the ablated region of the material requires a knowledge of many details, including equations of state under widely ranging pressure conditions. Here we have shown that beyond that region, the pressure pulse wave can be calculated in a simple way and the bulge development estimated in a way that is supported by experiment. The extent of micro-damage can be estimated as function of position in the target and of time. A theory of percolation can describe the development of the micro defect population into large scale macroscopic damage, perforation of the impacted target and (eventually) fragment formation.

Research partly supported by USAFOSR Grant Number 89-0374.

REFERENCES

Aharony, A., A. Levi, R. Englman and Z. Jaeger (1986). Percolation model calculations of fragment properties. Ann. Israel Phys. Soc., 8, 112-118.

Eliezer, S., I. Gilath and T. Bar Noy (1990a). Laser induced spall in metals experiment and simulation. J.Appl. Phys., 67 (2), 715-724.

Eliezer, S., Y. Gazit, and I. Gilath (1990b). Shock wave decay and spall strength in laser - matter interaction. J. Appl. Phys., 68, (1) 356-8.

Gilath, I., D. Salzmann, M. Givon, M.P. Dariel, L. Kornblith and T. Bar-Noy (1988a). Spallation as an effect of laser induced shock waves. J. of Materials Science, 23, 1825.

Gilath, I., S. Eliezer, M.P. Dariel and L. Kornblith (1988b). Total elongation at fracture at ultra-high strain rates. J. of Mat. Science Letters, 7, 915-7.

Gilath, I., S. Eliezer, M.P. Dariel and L. Kornblith (1988c). Brittle - to ductile transition in laser induced spall at ultra high strain rate, in the 6061-T6 aluminum alloy. Appl. Phys. Letters, 52, 1207.

Gilath, I., S. Eliezer, M.P. Dariel, L. Kornblith and T. Barnoy (1988d. Laser induced spall in aluminum and copper. Journal de Physique C3, 49, 191.

Gilath, I., S. Eliezer and H. Weisshaus, (1989). Damage in 2D carbon-carbon composites by short pulsed laser induced shock waves. J. of Reinforced Plastics and Composites, 8, 259-269.

Gilath, I., S. Eliezer and S. Shkolnik (1990). Spall behavior of carbon epoxy unidirectional composites as compared to aluminum and iron. J. of Composites, 24, 1138-51.

Gilath, I., S. Eliezer and Y. Gazit (1991). Fracture modes in alumina at hypervelocity impact conditions, J. of Mat. Science 26, 2023 - 2025.

Gilath, I., R. Englman, Z. Jaeger, A. Buchman, E. Segal and H. Dodiuk (1992). Dynamic behaviour of adhesive joints. I.A. Report No. 2148.

Grady, D.E. (1982). Local inertial effects in dynamic fragmentation, J. Appl. Phys. 53 , 322-8.

Glenn, L.A. and A. Chudnovsky (1986). Strain energy effects on dynamic fragmentation, J. Appl. Phys. 59, 322-5..

Harrach, R.J., Y.T. Lee P.J. Trainor, N.C. Holmes, M.D. Rosen, D.L. Banner and R.J. Olness (1981). Livermore National Lab. (U.S.A.) preprint UCRL-86301.

Johnson, R.C. (1972), Explosive Excavation Technology. Report NCG-TR-21.

Murat, M., A. Aharony and Z. Jaeger,1980. Fragmentation in a percolation model with radically decaying crack concentration. Ann. Israel Phys. Soc. 8, 182-8.

Perret, W.E. and R.C. Brass (1974). Report SAND - 74 - 0252.

Salzmann, D., I. Gilath and B. Arad (1988). Experimental measurements of the conditions for the planarity of laser-driven shock waves. Appl. Phys. Lett. 52, 1128-.

Salzmann, D., I. Gilath, M. Givon and T. Bar Noy (1989). Measurement of the tensile strength of aluminum at a strain rate of $2 \times 10^{7}\ s^{-1}$. J. Phys. D. : Appl. Phys. 22, 1271-.

Stauffer, D. (1985). Introduction to Percolation Theory. Taylor and Francis, London.

Thompson, P.C. and P.D. Roberts (1984). Laser and Particle Beams, 2, 13.

Yatom, H. and R. Ruppin (1988). Dynamic fragmentation model with inertial damage. J. Appl. Phys. 65, 112-6.

Int. J. Impact Engng Vol.14, pp.291–302, 1993
Printed in Great Britain

0734-743X/93 $6.00+0.00
Pergamon Press Ltd

METALLIZATION AND INSULIZATION DURING IMPACT

John J. Gilman

Lawrence Berkeley Laboratory
One Cyclotron Road
Berkeley, CA 94720

ABSTRACT

It is pointed out that the large strains produced by hypervelocity impacts can be expected to produce dramatic changes in the chemical bonding (electronic structures) of materials. This will change the mechanical behavior towards increased ductility when a semi-conductor is compressed until it becomes metallic; and towards increased brittleness when a transition metal is expanded so as to localize its d-band electrons. Both isotropic compression (expansion) and shear strains can cause these transformations. Critical deformation criteria are given based on the observed cubic to tetragonal transformations in compressed semiconductors.

INTRODUCTION

Ideal impact deformations begin with uniaxial compression. As shown in Figure 1, this consists of a combination of a volume change (isotropic compres-sion) and a shearing distortion. In plastic materials, if the yield stress is exceeded, the stresses causing the shear distortion will tend to relax. This requires a finite amount of time which depends inversely on the difference between the local applied stress and the yield stress. The relaxation time is finite because the process requires dislocations which have finite inertial masses to be generated, multiplied, and moved.

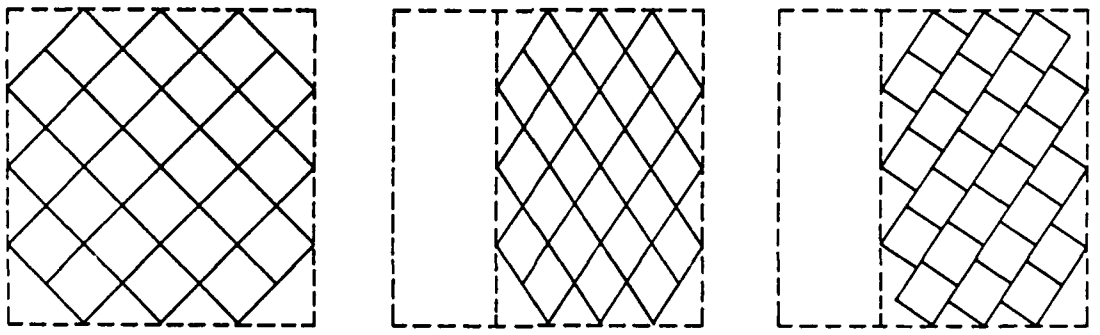


Figure 1 - Uniaxial shock compression induces both dilatation and shear in an impacted target. Left - target before impact. Middle - target compressed uniaxially (deformation consists of a combination of volume reduction and shear). Right - Shear strains relaxed, only volume change remains.

As a result of the interaction of impact-generated compression waves with free surfaces and/or other interfaces, large amplitude rarefactions may develop. These will put the material into a state of uniaxial expansion. The deformation consists of a combination of isotropic expansion and shear, but with the signs reversed. In strong impacts the strains in the compressions and

expansions are large, so shock fronts develop in the compressive case and instabilities (spalls) develop in the expansion case.

The local strains may far exceed the usual elastic range. This is illustrated by the schematic shock front of Fig. 2 where the deformation starts at zero on one side of the front passes through an indefinitely large maximum at the front and then becomes $\Delta l/l = 1/2$ on the other side. Such large strains can be expected (in some cases) not only to distort the pattern of atoms in a material, but also to cause enough distortion of the pattern of electrons (bonds) to induce electronic phase transitions. These transitions will in turn cause changes of the mechanical behavior. Note that even when the shear strains relax quickly behind the front they are very large within it.

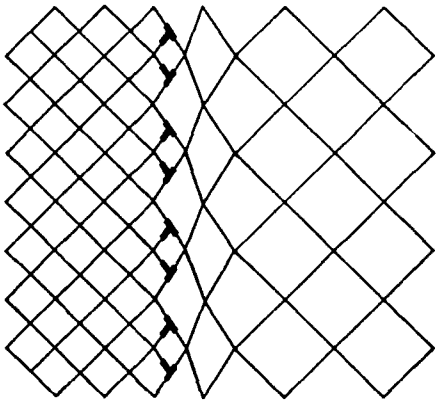


Figure 2 - Sharp shock front moving from left to right. The structural pattern is the same before and after, but at the front there are large shear distortions and a high concentration of broken "bonds" (that is, of interface dislocations).

STRAIN-INDUCED TRANSFORMATIONS

It will be shown that both compressions and shears can induce transforma-tions. Both crystal structures and transport types (semiconduction to metallic conduction and inversely) may change. Specific (albeit approximate) criteria for these transitions will be given, and compared with the available experimental data.

After an electronic transformation has occurred the material may become more ductile in the compression case; or more brittle in the tension case. Thus these transformation are relevant to hypervelocity impact phenomena because they can dramatically change the flow and fracture behavior. As an example, silicon which is normally as brittle as window glass becomes as ductile as a soft metal like lead. On the other hand a very ductile metal like copper when subjected to a strong rarefaction may exhibit cleavage-like fracture.

In the compression case (metallization), the change in mechanical proper-ties results from delocalization of the valence electrons. This enhances dislocation motion in the material by allowing the dislocation cores to spread out along the glide-planes. Prior to the transformation the atoms of the material are connected by very localized covalent bonds which localize and immobilize the dislocation cores.

In the expansion case, the s-band electrons of a metal are not expected to be affected much, but the electrons in the d-bands may become more localized. This may inhibit the motions of dislocations which may make the material more brittle.

Both of these effects mean that the properties of the material in the highly strained state may

be substantially different from those in the unstrained state. Furthermore, they may not be directly deducible from a knowledge of the initial state of the material. In some cases they must play a significant role in the behavior of materials that are subjected to hypervelocity impacts.

All materials become metallic at sufficiently large compressions. However, the transformation strains are smaller for semiconductors than for large band-gap insulators; so this discussion will be limited to the former.

COVALENTLY BONDED MATERIALS

The most straightforward case is that of covalent bonding. This type yields open crystal structures (the diamond structure is the prototype), and to chemical bonds with distinct lengths and bond angles. Changing the lengths or the angles causes increases in the energies of the bonding orbitals, and decreases in the energies of the anti-bonding orbitals. In the language of solid-state physics, the valence band-edge increases in energy, while the conduction band-edge decreases. Thus the energy gap decreases (for large strains; in some cases it increases for small strains). When it vanishes, the electrons at the top of the valence band become delocalized, and the material is said to have metallized.

In general both dilating and shearing are asymmetric. Lengthening a bond is clearly not the same as shortening one. Shearing may be symmetric, but often it is not. For example, increasing a right angle making it obtuse is not the same as making it acute by decreasing it. On the other hand increasing, or decreasing, a 180° angle is symmetric. Thus, depending on the sense of a particular deformation, the electrons may become either more, or less, localized.

It is well-known that insulators become metallic if they are compressed a critical amount (Cottrell, 1988). Volumetric compression criteria for this transition have been proposed by various authors, starting with Herzfeld (1927); and later by Mott (1949); and further developed by Edwards and Sienko (1983). The proposed criteria which are well-corroborated by experiments are based on changes in the overlapping of atomic wave-functions as compression occurs. That is, on changes in bond-lengths. However, in the case of semiconductors, there is substantial experimental evidence that bond-angle changes are more important than length changes. In open structures, either bond-length or angle changes can cause the overall volume changes that have been reported as experimental results.

One pertinent fact is that uniaxial compression (a combination of dilatation and shear strains) induces the transition to the metallic state at much lower stresses than those required for triaxial compression. This has been noted in passing by various authors, but largely ignored. In the case of silicon the difference can be 40% or more, so the effect is not small (Gupta and Ruoff, 1980). Further evidence is provided by the crystallographic data to be presented here.

COVALENT ELEMENTS

A prototype transformation for semiconductors is the conversion of the diamond-framework, tetrahedrally-bonded crystals (Group IV, III-V, and II-VI substances). For eight of the known cases this converts the cubic diamond-framework into the tetragonal β-tin framework (Fig. 3). In the latter structure, the crystals are metallic (for tin itself the resistivity is not isotropic, being different parallel and perpendicular to the tetragonal axis).

The crystallographic data (Table I) show that the observed shear deformations of the bonds, $\Delta\theta/\theta$ are numerically much larger than the bond compressions $-\Delta l/l$. Thus, the bond-angle changes are much larger than the bond-length changes. The angle changes reduce the symmetry from cubic to tetragonal. These crystallographic facts indicate that although these

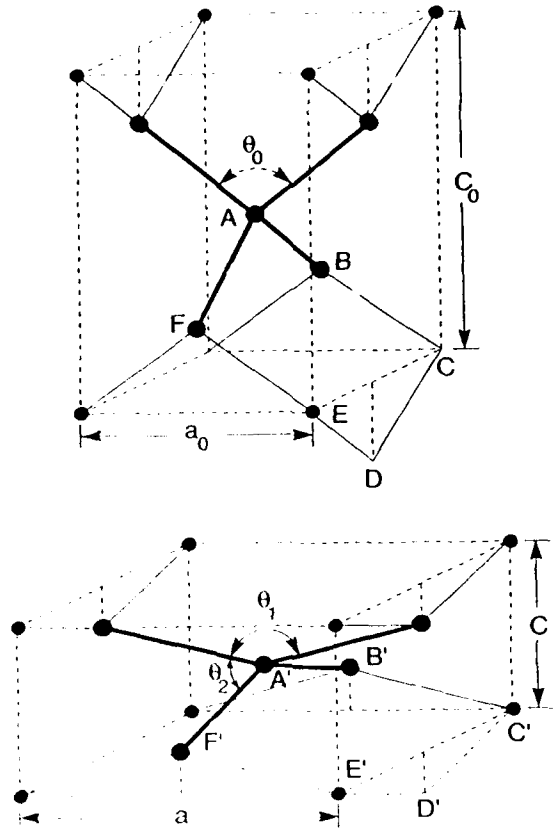


Figure 3 - Schematic relationships between the diamond and β-tin frameworks. For Sn: θ_0 = 109.5°; θ_1 = 149.5°; θ_2 = 94°. Note that the "boat-ring", ABCDEF which has equal sides and equal angles in the diamond framework becomes the ring A'B'C'D'E'F' which has equal sides but two sets of three angles in the β-tin structure. Also note that the next-nearest-neighbor distance, c, in the β-tin structure is 3.18 Å, compared with 3.01 Å for the nearest-neighbor bond length.

transitions are commonly said to be "pressure-induced"; in reality the whole deformation tensor governs them, not just the isotropic compression scalar. Thus they are "deformation-induced"; or perhaps shear alone induces them.

Several of the other III-V compounds transform to the rock-salt, instead of the β-tin, structure. This can also happen through shearing, but will not be discussed here because it is not as straightforward as the β-tin case.

As Musgrave and Pople (1962) have pointed out, the β-tin framework can be reached by compressing the diamond framework along its cube edge while allowing it to expand laterally (Fig. 3). The elementary deformation consists of compressing a tetrahedral bonding unit along an axis that passes through its center and bisects the opposite edges; plus the topological constraint that "bond rings" such as ABCDEF which becomes A'B'C'D'E'F' are conserved; i.e., they remain closed. In order for them to close while the nearest neighbor bond lengths remain equal, the ring symmetry must change from three-fold to two-fold. This occurs more readily than symmetry preserving triaxial compression because the bending force constants are substantially smaller than the stretching constants.

For tin itself, the fractional changes in the crystallographic parameters are given at the top of Table I. Since the contraction of the c-axis is nearly twice the expansion of the a-axes, the

Table I
Per Cent Changes During the Transformation of the Diamond to the β-Tin Framework (Elements and III-V Compounds)

	Lattice Parameter (A) -tetragonal cells-		Bond Length(A)	Bond Angles	Cell Volume
	a	c	d	θ(deg.)	V
Sn	+27.4	-50.9	+7.9	+37; -14	-20.3
Ge	+22.3	-52.4	+3.2	+35; -14	-28.8
Si	+22.0	-52.4	+3.4	+36; -14	-29.1
C	(+22)	(-51.9)	(+3.2)	(+36;-14)	(-28.6)
InSb	+20.9	-51	+6.8	+37; -14	-22
GaSb	+24.1	-51.8	+4.9	+36; -14	-25.8
AlSb	+24.1	-52.8	+4.5	+37; -14	-27.6
InAs	+22.0	-57.0	+2.7	+39; -15	-36
GaP	+22.5	-54.7	+3.4	+38; -14	-32.1

Table data references:
Sn, Ge, Si - Landolt-Bornstein Tables
C - Estimate of uniaxial transformation strain from O. Nielson, Phys. Rev., 34B, 5808 (1986).
InSb - R.E.Hanneman, M.D.Banus and H.C.Gatos, J.Phys.Chem.Solids, 25, 293 (1964).
InAs - J.C.Jamieson, Science, 139, 762, 845 (1963).
AlSb - M.A.Baublitz and A.L.Ruoff, J.Appl.Phys., 53, 6179 (1982).
GaSb - C.Yu, I.L.Spain and E.F.Skelton, Sol.St.Comm., 25, 49 (1978).
GaP - A. L. Ruoff and M. A. Baublitz, Phys.Solids High Pressure, Ed. by Schilling and Shelton, North-Holland Publ.Co., p.81 (1981).

volume change is modest. A point that is particularly noteworthy is that the fractional bond-angle changes are much larger (5-10X) than the bond-length changes. Furthermore, the table indicates that the critical bond-angle change (and therefore the critical bond-angle) is essentially invariant for all eight of the known cases. Also, the bond length changes are small in all cases. Thus the crystallography as well as the mechanics indicates that shear predominantly induces the transition; not isotropic compression. It will be shown shortly that this is also consistent with the theory of chemical bonds.

Notice that the first nearest-neighbor distance in the β-tin structure is 3.01 A. while the second nearest-neighbor distance is 3.18 A. So the difference is only 5.6%. This has led many authors to assert that the coordination number is 6, rather than 4, in β-Sn. However, conservation of orbital continuity requires that it be 4 as suggested by Fig. 3.

It has become commonplace to discuss these semiconductor transitions in terms of energy vs. density diagrams (Yin and Cohen, 1980), but Fig. 3 and the text above indicates that this obscures the nature of the change. The change is primarily one of shape; and only secondarily of specific volume. The same comment applies to other substances. For example, it applies to the transformations in silicates and phosphates which also involve covalent bonds. In such cases, volume change is not an adequate descriptor of either the structural, or the energetic, factors.

Little is known experimentally about the state of deformation at the start of the transformation. Typically, only the "pressure" is reported; and/or the "volume". But it is not clear whether the material still has cubic symmetry; and to what level of precision.

BOND-BENDING CRITERION FOR TRANSFORMATION

A simple criterion for shear metallization can be derived from Pauling's original (approximate)

theory of the chemical bond (Glasstone, 1944). In the most simple version of this theory, the form of the wave-function for a hybrid sp^3 orbital is (angular dependence only; the radial part is assumed to be unchanged by hybridization):

$$\psi_h = 1/2(1 + 3\cos\theta)$$

where θ is the angle with respect to the direction of the bond. The first term represents the s-part of the orbital while the second represents the p-part. The bond energy is proportional to the square of this; and the anti-bonding orbital has a similar form except that its energy decreases with increasing bond-angle. The energy difference, or gap, between the bonding and anti-bonding energies decreases toward zero as the bond angle increases from its initial value. The gap becomes zero when the bond angle becomes 148.5° which is close to the 149.5° observed for tin. The excellent agreement may be fortuitous, but the calculation illustrates the principle that there is a strong dependence of bond energy on bond angle, and that there is a critical angle at which the bonding becomes metallic. Numerical band-theory calculations are consistent with this (Chelikowsky, 1987).

Further support can be given to this geometric criterion by showing that it yields the correct energy condition. That is, by showing that the work done in changing the bond-angle equals the energy needed to close the energy gap.

Imagine a bond of length, b that is held in place at one end and acted on by a tangential force, f at the other end. The force tends to change the bond angle, θ, and is resisted by a bond-bending force-constant, k_θ (d-cm). For a small change of the angle, the incremental work, dW done by the force is: $fbd\theta = k_\theta\theta d\theta$. Integration yields:

$$W = K_\theta(\Delta\theta)^2/2$$

and since the observed value of $\Delta\theta$ is 0.7 radians, $W = k_\theta/4$. This is to be compared with one-half of the energy gap $k\theta$ has been defined in various ways, but most convenient is Harrison's (1980) definition: $k_\theta = (3b^3/8)(C_{11} - C_{12})$ which relates it to the standard elastic constants, C_{ij}.

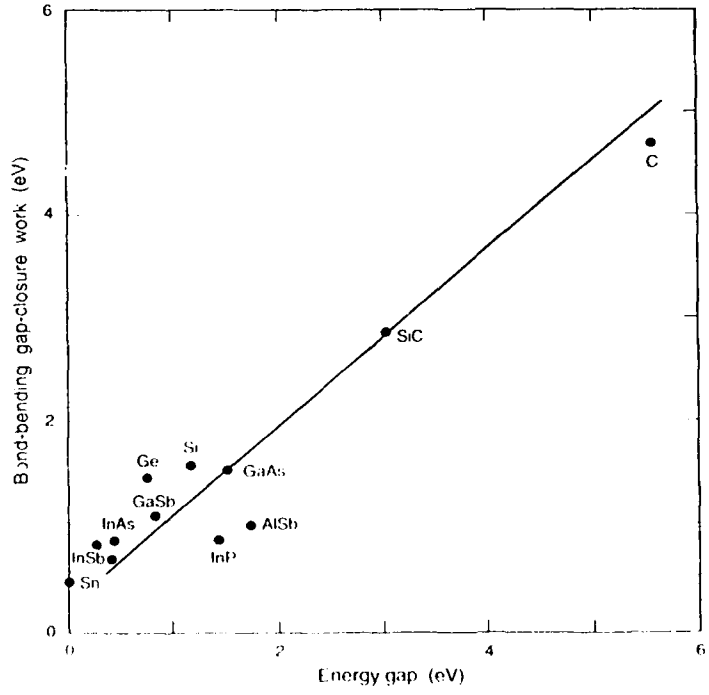


Figure 4 - Work required to bend bonds from their initial tetrahedral angles up to the critical transformation angle plotted against the average energy gap of the material.

If the bond-bending hypothesis is valid the force constant should be related to the band-gap, and Fig. 4 shows that indeed it is. Thus, as the gap increases, so does the force constant, and the angle change needed to close the gap remains approximately constant.

CONSEQUENCES OF METALLIZATION AND HYPERVELOCITY IMPACTS

For states of uniaxial compression such as those experienced in the inertial confinement of strong shock waves, or in the confined static compression of indentations, bond-angle changes are accompanied by bond-length decreases, and metallization is induced by the combination. However, since the stretching force constants are much larger than the bending force constants (by a factor of ~4) they provide most of the resistance to the loading, and bending accommodates most of the deformation. This may account for the correlations that have been found between transformation pressures and indentation hardnesses (Gilman, 1992). An example of this correlation is shown in Fig. 5. This indicates quite strongly that there is a connection between flow under conditions of high deformation and electronic transitions in these materials. It should then be expected that hard materials that are impacted at hypervelocities will transform through delocalization of their bonding electrons into states that will flow more readily than might otherwise be expected.

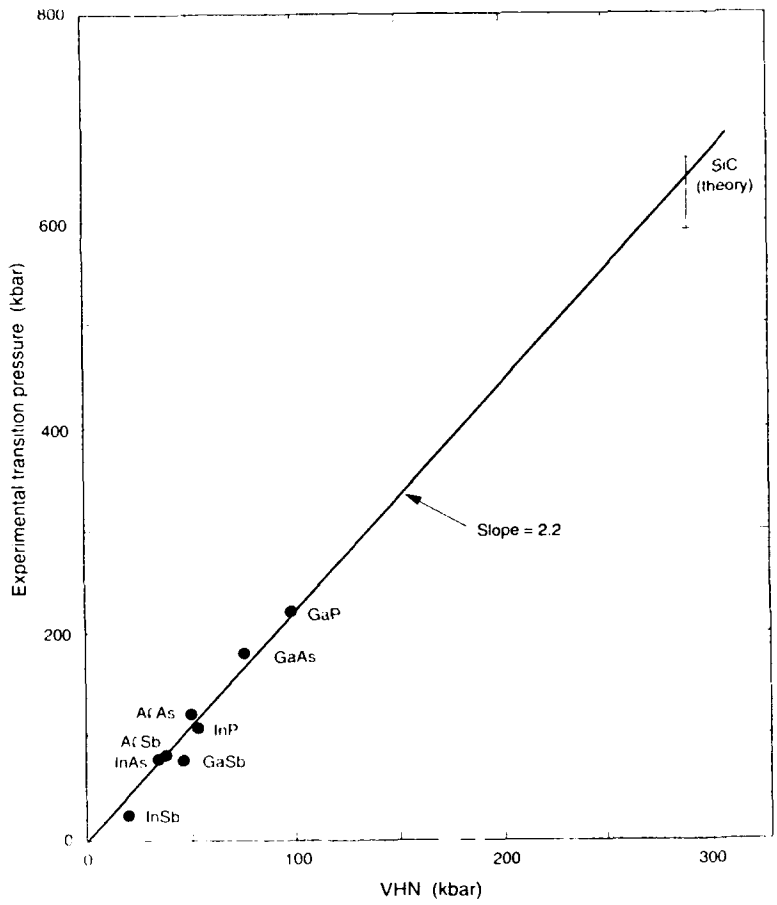


Figure 5 - Insulator-metal transition pressures correlated with Vickers hardness numbers (VHN). The correlation suggests that bond-bending plays an important role in both processes.

If it is accepted that shear can induce metallization, there are implications for many situations that do not appear to have been appreciated in the past. These include: point-contact diodes and transistors (Clarke et al.,1988), various allotropic transformations including those involving

the d-shell bonding in metals, chemical reactivity by facilitating electron-transfers(Gilman, 1992), the core structures of dislocations and dislocation-dipoles, the mechanisms of machining and grinding, Mode III crack propagation, reversible compression-induced transitions in silicate-like frameworks, impacts and shock fronts, friction and wear phenomena, and indentations (Gilman, 1992).

In the last case, a dramatic photograph has been obtained by Pharr, Oliver, and Harding (1991). This shows material extruding out from under a diamond pyramid as it indents silicon. An interpretation is that the compression created by the indentation has metallized the silicon locally thereby allowing it to extrude like a metal. This observation has led to the proposal that this is a common phenomena when similar states of deformation are present.

A connection between impact yield stresses (Hugoniot elastic limits) for hard materials was demonstrated by the author previously (Gilman, 1970; 1975). The connection is illustrated by Fig. 6. In the light of the evidence presented here for the sp^3 bonded semiconductors, it is natural to wonder whether impact has a large effect on the electronic (bonding) structures of hard compounds like B_4C. Does the Hugoniot elastic limit represent a phase transition? Or does it represent the stress needed to move low mobility dislocations? What is the role of shear deformation compared with that of isotropic compression? How might one answer these interesting questions?

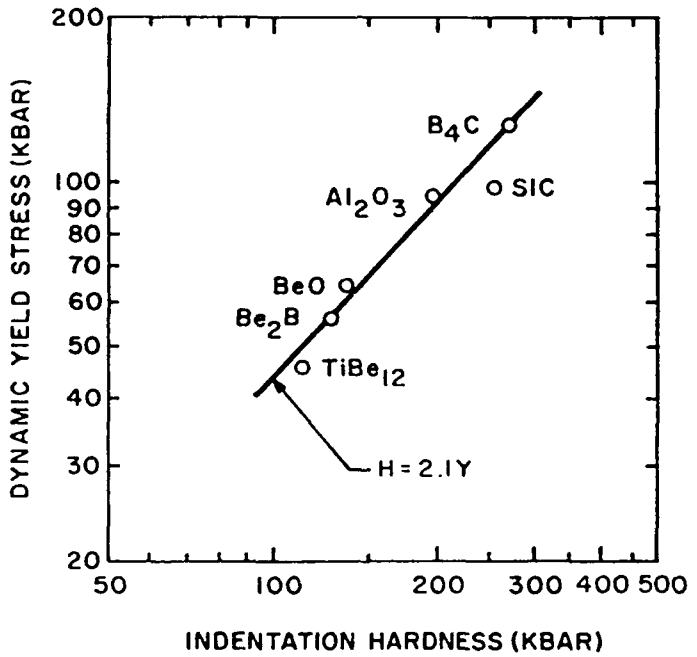


Figure 6 - Relationship of dynamic (explosive impact) yield stresses to static yield stresses (from indentation hardness) for various hard compounds. The ratio of these yield stresses to the elastic shear stiffnesses for these compounds is the same as for those of Figure 8. The data are from C. F. Cline.

Since all solids become metallic when compressed sufficiently, they will all metallize at sufficiently high impact velocities. So the question is not whether hypervelocity impact causes changes in the electronic structures of solids (or liquids); the question is when? And when does shear deformation facilitate the process?

The velocity needed to transform silicon, for example, in an impact with itself is about 1.3 km/sec. This assumes a critical strain of about 0.2; a bulk modulus of 2.24 Mb; and a specific gravity of 2.33. For SiC the critical impact velocity is about 1.6 km/sec. Thus the transformation can be expected under typical hypervelocity conditions.

INSULIZATION, THE INVERSE OF METALLIZATION

For tensile states of strain in metals, metallization is not expected, but the inverse; that is "insulization", is. It is expected that insulization will be deformation dependent (i.e., dependent on both dilatation and shear). This would change the metallic bonding from a delocalized mode to a localized one. Therefore, it might well play a role in such phenomena as crack propagation in which large tensile strains exist near crack tips. It might also account for why the spalling of metals that is associated with strong reflected shock waves is often very localized. And it may account in part for the weakening effects of large concentrations of dislocations; as well as the hardening effects of dilatational dislocation dipoles in metals. Localization of the bonding would be expected to have a strong influence on the microscopic mechanisms of these various phenomena.

Bonding in most of the metals that are used to build engineering structures is associated with interactions of the d-type electrons (3d, 4d, and 5d). These interactions are responsible for the high cohesive energies, the high stiffnesses, and melting points of the structural metals. Ductility in these metals is associated with small (relatively) shear moduli. That is, with low values of the ratio of the shear to the bulk modulus (Gilman, Cunningham and Holt, 1990). This, in turn, is related to delocalization of the bonding electrons, particularly the d-electrons since the s- and p-electrons contribute relatively little to either the bonding or the shear resistance. These comments apply to the pure metals; alloying may also play a crucial role.

One manifestation of the importance of the d-bonding is the fact that iron cleaves on its (100) planes rather than the most close-packed (110) planes. Another direct manifestation is the role that it plays in determining dislocation mobility in the "hard metals"; carbides, borides, and nitrides (Gilman, 1970).

The d-orbitals tend to be more compact than the s- or p-orbitals so only their tip regions tend to overlap in transition metal crystals (Cottrell, 1988). The more the overlap the more the delocalization. Thus, if such a crystal is extended so the overlap is reduced, localization (and bond directionality) increases, and properties such as dislocation mobility tend to decrease, while crack tip localization tends to increase.

The standard localization parameter is called the "hopping Integral" which measures how fast electrons tend to hop from one atom to another (Cottrell, 1988). In other words how readily they move away from any particular locality. For the strongest d-bonds (called ddσ-bonds), it has the following form:

$$\text{hopping integral} = \beta = -2.4\, w\, (r_s/b)^5$$

where w = d-band width, r_s = Wigner-Seitz radius, and b = bond length. The inverse fifth-power dependence of β indicates that small extensions can cause large increases in localization. For example, extending the bond length by 25% decreases the hopping integral by a factor of ~3.

Very large extensions of metals will convert them into insulators when the s and p-electrons become localized. However, these extensions are so large that they will rarely be consequential in practice. However, localization will tend to increase shear stiffness relative to extensional stiffness, and this will change the overall mechanical response.

POSSIBLE ROLE OF DELOCALIZATION IN DISLOCATION MOTION

Hard materials may be divided into two hardness classes; intrinsic and extrinsic. The extrinsic ones are those in which dislocations move readily through perfect crystals of the base composition, but are inhibited by defects such as other dislocations, dipoles, impurities, grain

boundaries, and precipitates. Most crystalline metals and many ionic compounds belong to this class. Intrinsic ones are those in which dislocation mobilities are low even in perfect crystals. Examples of these are semiconductors, interstitial metal compounds, and metallic glasses. In the intrinsic class, the behavior suggests that electronic structure plays an important, and intrinsic, role. Some of the facts leading to this conclusion are:

a. the correlation between the thermal activation energy for dislocation motion and electronic energy gaps (Fig. 7) (Gilman, 1975).

b. the large ratio of the hardness number and/or the Hugoniot elastic limit to the elastic shear stiffness (Figs. 6 and 8) (Gilman, 1973).

c. the connection between the critical transformation pressure and the hardness number (Fig. 5).

d. the influence of light and other electrical disturbances on hardness, and plastic flow, including surface effects (McColm, 1990).

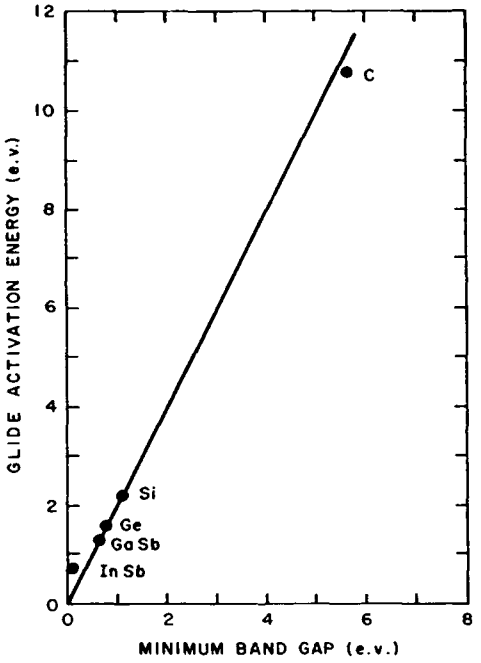


Figure 7 - Activation energy for the motion of dislocations versus the minimum energy gap for various covalently bonded crystals.

The connection between the mechanics and the electronics occurs through the bond-bending effects at the cores of dislocations and cracks. On the glide plane of a dislocation, the shear strain is a maximum at the center of the core and falls away to zero on both sides. At the center, if the spacing of the glide planes is h, and the Burgers displacement is δ, the maximum shear strain is $\delta/2h$.

Then, taking semiconductors as an example, in the diamond framework h = b, and δ = 1.63 b, so the maximum strain is 0.82 and the bond-bending angle is the inverse tangent of this or 39.2°. This plus the tetrahedral angle (109.5°) yields 148.7° which is the angle at which the energy gap closes. Closing the gap is equivalent to "breaking" the bond, and being an irreversible process, it limits the dislocation motion. Similarly, it is equivalent to the band-to-band tunneling process that was proposed previously (Gilman, 1975) to account for low-

temperature dislocation mobility. At higher temperatures, it is expected that phonons will assist the bond-bending process, thereby increasing dislocation mobility.

Impact loading causes countervailing effects which complicate interpretations. On one side, the high strain-rates minimize the time available for strain-relaxation through dislocation motion and multiplication. On the other side, high stresses tend to be present which delocalize bonding electrons and thereby enhance mobilities.

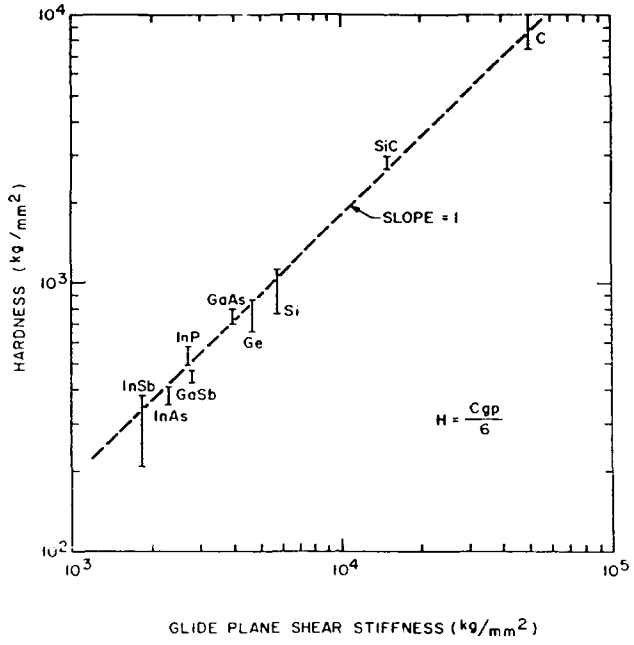


Figure 8 - Showing that the ratio of the Vickers hardnesses of a variety of tetrahedrally bonded crystals to their elastic shear stiffnesses is 1/6. Thus the corresponding ratio for their shear flow stresses is ≃1/18.

CONCLUSION

Evidence has been presented showing that the large shear deformations that occur during impact can cause semiconductors to transform into metals. Thus materials that are normally quite brittle can become ductile. Their yield stresses can decrease dramatically. Criteria for this phenomenon are given that are derived from the theory of chemical bonding. The transformation occurs when covalent bonds are bent from their normal angles by a critical amount (for tetrahedral bonds, when the bond angle goes from 109.5° to 149.5°). Compression must also be present.

Expansion causes the opposite of metallization; namely, insulization. That is localization of bonding electrons. This may be important in the behavior of expanded transition metals. Localization of the bonding d-electrons will modify the behavior of dislocations and cracks in these expanded metals.

REFERENCES

Chelikowsky, J. R., Phys. Rev., 35B, 1174 (1987).
Clarke, D. R., Kroll, M. C., Kirchner, P. D., Cook, R. F. and Hockey, B. J., Phys.Rev.Lett., 60, 2156 (1988).
Cottrell, A. H. (1988), Introduction to the Modern Theory of Metals, Chapter 1, Institute of Metals, London.
Edwards, P. P. and Sienko, M. J., Int. Rev. Phys. Chem., 3, 83 (1983).
Gilman, J. J., J. Appl. Phys., 41, 1664 (1970).
Gilman, J. J., in The Science of Hardness Testing and Its Research Applications, Ed. by Westbrook and Conrad, Chapter 4, p.60, American Society for Metals, Metals Park, Ohio (1973).
Gilman, J, J., J. Appl. Phys., 46, 5110 (1975).
Gilman, J. J., Cunningham, B. J., and Holt, A. C., Mater. Sci. and Eng., A125, 39 (1990).
Gilman, J. J., "Detonation via Metallization in Solids", Bull. Amer. Phys. Soc., 37, 361 (1992).
Gilman, J. J., J. Mater. Res., 7, 535 (1992).
Glasstone, S. S., Theoretical Chemistry, p.97ff, Van Nostrand Company, New York (1944).
Gupta, M. C. and Ruoff, A. L., J. Appl. Phys., 51, 1072 (1980).
Harrison, W. A., Electronic Structure and Properties of Solids, p.193ff, W. H. Freeman, San Francisco (1980).
Herzfeld, K. F., Phys. Rev., 29, 701 (1927).
McColm, I. J., Ceramic Hardness, p.135, Plenum Press, New York (1990).
Mott, N. F., Proc. Phys. Soc., 62A, 416 (1949).
Musgrave, M. P. J. and Pople, J. A., J.Phys.Chem.Solids, 23, 321 (1962).
Pharr, G. M., Oliver, W. C., and Harding, J. Mater. Res., 6, 1129 (1991).
Yin, M. T. and Cohen, M. L., Phys.Rev. Lett., 45, 1004 (1980).

ACKNOWLEDGMENT

This work was supported by the Director, Office of Energy Research, Office of Basic Energy Sciences, Materials Sciences Division, of the U.S. Department of Energy under Contract No. DE-AC03-76F00098.

Int. J. Impact Engng Vol.14, pp.303–314, 1993
Printed in Great Britain

0734-743X/93 $6.00+0.00
Pergamon Press Ltd

NONSTEADY PENETRATION OF LONG RODS INTO SEMI-INFINITE TARGETS

F. I. GRACE

U.S. Army Research Laboratory,
Aberdeen Proving Ground, MD 21005-5066

ABSTRACT

This paper describes a new one-dimensional theory of nonsteady penetration of long rods into semi-infinite targets. The target is viewed as a "finite mass" that resides within the semi-infinite target space. Thus, an equation of motion for the target was constructed so that together with erosion and penetrator deceleration equations, expressions for penetration rates and depths were obtained. Forces acting on the target and penetrator are defined in terms of only ordinary strength levels usually associated with dynamic properties or work-hardened material states. Also, the concept of critical impact velocity was used to establish the onset of penetration in this formulation. This penetration equation corresponds in exact form to hydrodynamic theory in the limits of small strengths and/or high impact velocity. Results for penetration rates agree well with hydrocode calculations, and predicted penetrations agree with experimental data over an impact velocity range of 0–5,000 m/s.

NOTATION

A	empirical constant
A_p, A_t	rod and target cross-sectional areas
C_o	sound velocity
d	rod diameter
f, g	empirical functions
l_o, l, l_a, l_b	initial, intermediate and final rod lengths
M_p, M_t	intermediate rod and target masses
P	depth of penetration
Q	angle related to velocity ratio
S_p, S_t	strengths of rod and target
t	time
u_o, u, u_c, u_h	initial, intermediate, critical and hydrodynamic penetration velocities
v_s, v, v_c	initial, intermediate and critical rod velocities
x_o, x	initial and intermediate target lengths
α	constant related to erosion rates
γ	square root of density ratio
ρ_p, ρ_t	densities of rod and target

INTRODUCTION

Current descriptions of long-rod penetration contain combinations of simple theories and complex models. These often attempt to include appropriate material strength effects. For example, Belyakov *et al.* (1962) extended the Poncelet approach for soft targets to short penetrators striking solid targets. More recently, Dehn (1987) developed a unified theory of penetration that addresses, in principle, short and long penetrators and wide ranges of penetrator and target characteristics through various assumed force laws. In nearly all such cases, it has been necessary to include empirical adjustments in the application.

Another approach for penetration of long rods developed from hydrodynamic theory of jet penetration. For this, Birkhoff *et al.* (1948) successfully applied Bernoulli's equation for steady streamline flow to the jet penetration process. For long-rod penetration at lower impact velocity, Alexveeskii (1966) and Tate (1967, 1969) developed

a "modified" Bernoulli equation wherein penetrator and target material strengths were introduced as Bernoulli pressures. Wright (1983) examined difficulties posed by this procedure including nonsteady flow associated with penetration by retarding rods. In further development, Tate (1986a, 1986b) relates the high strength factors required in the model to actual dynamic material properties.

Despite various shortcomings, when appropriate models and adjusted material properties are included, both the Poncelet and modified Bernoulli equation approaches provide one-dimensional models for long-rod penetration mechanics. An example of the complexities encountered can be seen in the work of Luk and Piekutowski (1991). Recently, comprehensive surveys of the subject have been provided by Anderson and Bodner (1988) and Zukas (1990). Frank and Zook (1987) have commented on the utility of several currently utilized models and described procedures to optimize penetrator design with success.

In this paper, the author presents a new theory for nonsteady penetration of long rods into semi-infinite targets. In this development, Newton's laws are applied to obtain solutions to various problems given initial conditions and more normal values for material strengths. Further, in the appropriate limits, the theory corresponds to hydrodynamic penetration and, therefore, has application to both jets and long-rod penetrators.

FORMULATION OF NONSTEADY PENETRATION THEORY

In this theoretical development, the target is defined as a "finite mass" that resides within the semi-infinite target space. Such target definition is implied in the hydrodynamic theory of jet penetration (Birkhoff *et al.*, 1948). Further, Batra and Wright (1986) noted that for a rigid perfectly plastic target, target material adjacent to the penetrator extrudes rearward in a uniform block that is separated from the bulk of the stationary target by a sharp velocity gradient. Thus, for present purposes, target mass is considered to be that which occupies a right circular cylinder extending into the target from the front surface to a depth that equals or exceeds the expected penetration. The geometry of the penetration problem is given in Fig. 1. Initial values are defined as penetrator length l_o, effective target length x_o, penetrator striking velocity v_s and penetration velocity u_o. Current values at any intermediate time t are noted as uneroded penetrator length l, penetrator mass M_p, uneroded target length x, target mass M_t, penetrator velocity v and penetration velocity u. Also, densities for penetrator and target are denoted ρ_p and ρ_t, respectively.

The coordinate system chosen is located at the penetrator-target interface. In this system, target material flows into the reference point with velocity u, while penetrator material flows at a rate (v-u). For a one-dimensional problem, erosion products are removed from the axis as flow takes place. Any turning of the products (radial acceleration) would be due to off-axis interactions with target material in a two-dimensional sense and need not be considered here. Relative to the reference point, the equation of motion for the penetrator is

$$M_p \frac{d}{dt}(v - u) = - S_p A_p , \tag{1}$$

where S_p is a measure of rod strength, A_p is rod original cross-sectional area such that $-S_pA_p$ is the force applied to the penetrator. If the target mass is isolated completely from its surroundings, then there would be no force associated with the action of shearing stresses on its cylindrical surface so that, in this case, the time rate of change of momentum for the target system would be

$$M_t \frac{du}{dt} = - S_t A_t , \tag{2}$$

where S_t is target strength, A_t is the target cross-sectional area (not final cavity area) and $-S_tA_t$ is the force applied to the target. Also, penetrator mass $M_p = \rho_pA_pl$ and target mass $M_t = \rho_tA_tx$ so quantities for rod and target are independent of their respective areas. Since time derivatives of Eqs. (1) and (2) are nonzero, the represented flow is clearly nonsteady. Conservation of mass provides expressions for rod and target erosion (Birkhoff *et al.*, 1948), respectively, as

$$\frac{dl}{dt} = - (v - u) , \tag{3}$$

$$\frac{dx}{dt} = - u. \tag{4}$$

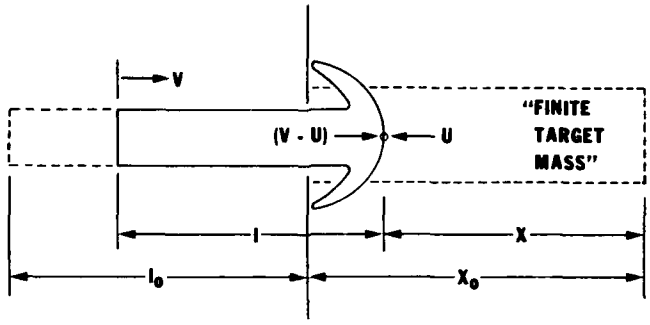


Fig. 1. Impact geometry defining "finite target mass" and variables used for nonsteady penetration.

Eqs. (1) and (2) have the following forms when Eqs. (3) and (4) are used to eliminate explicit dependence on time as follows:

$$(v - u)\, d(v - u) = \frac{S_p}{\rho_p} \frac{dl}{l} , \tag{5}$$

$$u\, du = \frac{S_t}{\rho_t} \frac{dx}{x} . \tag{6}$$

Eqs. (5) and (6) are integrated to provide velocity dependencies on l and x. These give independent trajectories for the two masses as

$$v - u = (v_s - u_o)\left[1 + \frac{2S_p}{\rho_p (v_s - u_o)^2} \ln (l/l_o) \right]^{1/2} , \tag{7}$$

$$u = u_o \left[1 + \frac{2S_t}{\rho_t u_o^2} \ln (x/x_o) \right]^{1/2} , \tag{8}$$

In general, the penetration depth P at any point in the penetration process is $(x_o\text{-}x)$ and is obtained by integrating u/(v-u) over the rod length l. This gives

$$P = - \int_{l_o}^{l} \frac{u}{v - u}\, dl . \tag{9}$$

Eqs. (1) through (9) represent a general formulation for the nonsteady penetration problem. The first integrals of motion are obtained in closed form as shown in Eqs. (7) and (8). The second integral of motion, namely penetration, will require additional assumptions to obtain solutions. These are provided in the next two sections. Summary of the assumptions thus far include 1) the target is considered a finite mass embedded in, but isolated from, the semi-infinite target space, 2) both penetrator and target undergo erosion and retardation and 3) penetrator and target are acted upon by constant forces which are related to their respective strengths.

IDEALIZED PENETRATION PROCESS

Since x_o is unknown for the semi-infinite target problem, it will be necessary to establish a relationship between x and l before Eq. (9) can be solved. If the forces of collision are assumed to be equal ($S_t A_t = S_p A_p$), then x can be obtained by equating (1) and (2) after substituting ($\rho_p A_p l$) and ($\rho_t A_t x$) for the rod and target masses respectively. Also, Eqs. (3) and (4) provide an additional expression for x. Together these result in

$$\int_{l_o}^{l} \frac{u}{v - u}\, dl = \frac{\rho_p}{S_p} \frac{S_t}{\rho_t} \frac{d(v - u)}{du} l - x_o . \tag{10}$$

A possible solution for Eq. (10) is

$$\frac{u}{v-u} = \frac{1}{\alpha} , \tag{11}$$

where α is a constant. Substituting (11) into (10) gives

$$\left(\frac{1}{\alpha} - \frac{\rho_p}{S_p}\frac{S_t}{\rho_t}\alpha\right) l = \left(\frac{1}{\alpha} l_o - x_o\right) , \tag{12}$$

where the right hand side of Eq. (12) is a constant. Since Eq. (12) must hold at any value of l, the quantity $[(1/\alpha) - (\rho_p/S_p)(S_t/\rho_t)\alpha] = 0$, so that

$$\alpha = \sqrt{\frac{S_p}{\rho_p}\frac{\rho_t}{S_t}} . \tag{13}$$

Eqs. (11) and (13) provide additional relationships as

$$u = \frac{v}{1+\alpha} , \qquad v-u = \frac{\alpha}{1+\alpha} v , \tag{14}$$

$$\frac{dx}{x} = \frac{dl}{l}, \qquad \frac{x}{x_o} = \frac{l}{l_o} , \tag{15}$$

where Eqs. (14) hold for initial values u_o, (v_s-u_o) and v_s as well. Eq. (15) allows (8) to be expressed in terms of l giving

$$u = u_o \left[1 + \frac{2S_t}{\rho_t u_o^2} \ln (l/l_o) \right]^{1/2} \tag{16}$$

Using (14) for u and v-u, and (16) for l/l_o forms the integrand for Eq. (9) in this ideal case. Integration gives

$$P = \frac{l_o}{\alpha}\left\{ 1 - \exp\left[- \frac{\rho_t}{2S_t(1+\alpha)^2}\left(v_s^2 - v^2\right)\right]\right\} . \tag{17}$$

A case of interest is where $\rho/S = \rho_p/S_p = \rho_t/S_t$. Associated values given by (13) and (14) are

$$\alpha = 1, \qquad u = \frac{1}{2} v, \qquad v - u = \frac{1}{2} v . \tag{18}$$

In this case, penetration is obtained by (17) and (18) to give

$$P = l_o \left\{ 1 - \exp\left[- \frac{\rho}{4(2S)}\left(v_s^2 - v^2\right)\right]\right\} \tag{19}$$

which is, of course, restricted to cases where the target and penetrator have equal strength-to-density ratios. Eq. (19) is somewhat less restrictive than the special case $\rho = \rho_p = \rho_t$ and $S = S_p = S_t$, although it applies there as well. When compared to Walters and Segletes (1991) closed form solution to Tate's equation in this special case, Eq. (19) contains an additional factor of two in the denominator of the exponential term. Thus, the present equation indicates a greater material strength influence in the penetration process than does the Tate solution. The ideal penetration as given by Eq. (17) results from the general formulation of the previous section under the additional assumption that the forces of collision between the penetrator and target are equal.

GENERALIZED PENETRATION PROCESS

For the more general penetration problem, it will be necessary to introduce additional considerations. Here, the relationship between x and l will not be given by a constant α but will be allowed to vary throughout the penetration process. This is expressed as

$$x = \frac{1}{\alpha(l)}\, l\,, \tag{20}$$

where $\alpha(l)$ is a slowly varying function whose derivatives may vary considerably. In this case, x is given at two points as

$$\frac{x}{x_o} = \frac{\alpha(l_o)}{\alpha(l)}\,\frac{l}{l_o} \simeq \frac{l}{l_o}\,, \tag{21}$$

where $\alpha(l_o)/\alpha(l)$ is approximated by the value of one. Thus, l/l_o becomes a useful metric of x/x_o so that Eq. (16) is valid in the general case. The derivative of x with respect to l is

$$dx = \left\{ \frac{1}{\alpha(l)} + l\,\frac{d\,[1/\alpha(l)]}{dl} \right\} dl\,, \tag{22}$$

and dividing by dt together with (3) and (4) provides

$$u = \left\{ \frac{1}{\alpha(l)} + l\,\frac{d\,[1/\alpha(l)]}{dl} \right\} (v - u)\,. \tag{23}$$

The time scale dt as given by (3) and (4) is preserved since by (22) and (23)

$$dt = -\frac{dx}{u} = -\frac{dl}{(v-u)}\,. \tag{24}$$

For the general penetration process, Eqs. (7) and (16) provide the integrand to be used in Eq. (9). This gives a general expression for penetration as

$$P = -\frac{u_o}{v_s - u_o} \int_{l_o}^{l} \frac{\left[1 + \dfrac{2S_t}{\rho_t u_o^2} \ln (l/l_o) \right]^{1/2}}{\left[1 + \dfrac{2S_p}{\rho_p (v_s - u_o)^2} \ln (l/l_o) \right]^{1/2}}\, dl\,. \tag{25}$$

It will not be necessary to specify $\alpha(l)$. The quasi-independent nature of the u and v-u equations given by (7) and (16) generates variations in the flow variables during the penetration process. These are such that u/(v-u) is not constant in this general case, and, therefore, the flow is consistent with Eq. (23). In addition, the initial conditions u_o and v_s-u_o are determined from other sources (next section) where factors related to the onset of penetration have been included. The time t during penetration can be obtained from (3) and (7), where $t_o = 0$ at impact of the rod with the target front surface. This gives

$$t = -\frac{1}{v_s - u_o} \int_{l_o}^{l} \left[1 + \frac{2S_p}{\rho_p (v_s - u_o)^2} \ln (l/l_o) \right]^{-1/2} dl\,. \tag{26}$$

The solution for the entire penetration process from impact to where penetration stops requires integration of Eq. (25) over the interval l_o to l_a where l_a is rod length when u = 0. Eq. (16) gives rod length l_a as

$$l_a = l_o \exp\left[-\frac{\rho_t}{2S_t} u_o^2 \right]\,. \tag{27}$$

In some cases when penetration ceases, rod erosion continues until the erosion rate v-u = 0. In this situation, uneroded rod length l_b is given by (7) as

$$l_b = l_o \exp\left[-\frac{\rho_p}{2S_p} (v_s - u_o)^2 \right]\,. \tag{28}$$

The behavior of (25), (27) and (28) implies two distinct penetration possibilities. The first corresponds to the case where target penetration ceases while rod erosion continues. The second occurs when rod erosion ceases before target penetration is completed. The two cases are defined when eqs. (27) and (28) meet the following conditions:

$$\text{Case 1:} \quad l_a > l_b \,, \quad \text{Case 2:} \quad l_a < l_b \,. \tag{29}$$

In Case 1, penetration depth is given by integration of Eq. (25) since (v-u) is finite throughout the interval l_o to l_a. In Case 2, the function can only be integrated up to l_b since at and beyond l_b, the integral is undefined. Penetration beyond $l = l_b$ is considered to be that of a rigid body.

Eq. (25) becomes identical to hydrodynamic theory of penetration in the appropriate limits. For example, when S_p and S_t equal zero, or as u_o (through v_s) approaches a high value, the integrand of Eq. (25) becomes equal to one. Also, the upper limit of the integral becomes $l = 0$ under these same conditions through Eqs. (27) and (28). In these limits, the penetration Eq. (25) corresponds to the hydrodynamic penetration equation as

$$P = -\frac{u_o}{v_s - u_o} \int_{l_o}^{0} dl = \sqrt{\frac{\rho_p}{\rho_t}}\, l_o \,, \tag{30}$$

where the constant $u_o/(v_s-u_o)$ can be seen to equal $\sqrt{\rho_p/\rho_t}$ at the hydrodynamic limit (see Eq. [38], next section).

Eqs. (7), (16), (25), (26), (27), and (28) constitute a complete set of solutions for long-rod penetration problems. In present form, variables are expressed as functions of rod length l, which is the independent variable. Eq. (26) allows variables to be expressed as numerical functions of time t after impact. This provides time histories of the flow process as well. The relative magnitudes of l_a and l_b as given by (27) and (28) define two distinct penetration cases and also determine whether or not rigid body penetration occurs in a particular problem. Eq. (28) provides the length of uneroded rod expected to be present at the very end of the rod erosion process. The assumptions involved in the general solution as given by Eq. (25) include those summarized in the general formulation of the nonsteady penetration problem, together with the additional assumption that the ratio u/(v-u) varies slowly throughout the penetration process and that the ratio is given by Eq. (16) divided by Eq. (7).

A SEMI-EMPIRICAL METHOD TO DETERMINE u_o

For the general impact problem, experimental data and hydrocode calculations indicate that u_o, can differ markedly from the hydrodynamic value $u_h = v_s/(1+\gamma)$, where γ is $\sqrt{\rho_t/\rho_p}$. As a general rule, target strength significantly decreases u_o while penetrator strength tends to only modestly increase u_o relative to u_h. Also, introducing onset of penetration through a critical impact velocity alters u_o significantly, particularly at low impact velocity. Values for u_o under a number of impact conditions are provided by hydrocode calculations where u_o was obtained by extrapolating u(t) back to the target front surface (ignoring the transient). Figure 2. presents u_o and u_h as a function of striking velocity where the plotted points are results of CTH calculations (Kimsey, 1992). The established concept of critical impact velocity provides a means to estimate onset of penetration (Wilkins and Guinan, 1973). This is extended to include both target erosion (penetration) and penetrator erosion. These give

$$\frac{1}{2}\,\rho_p\, v_c^2 = S_t \,, \qquad \frac{1}{2}\,\rho_t\, u_c^2 = S_p \,, \tag{31}$$

where v_c is a critical striking velocity and u_c is a critical penetration rate. The intercept on the v_s axis of Fig 2. is given by v_c. For a tungsten alloy penetrator of density 17.3 g/cm^3 and steel armor target strength of 1.3 GPa, v_c is 387 m/s. This agrees with data of Zook *et al.* (1992), indicating a critical impact velocity for tungsten of from 245 to 424 m/s. For steel penetrator impact on steel targets, v_c = 575 m/s. Figure 2. suggests a near linear dependence of u_o on v_s with varied amounts of offset from u_h as v_s is increased.

In view of the previous discussion and the plotted results of Fig. 2., u_o will be formed as a linear combination of involved velocities given by

$$(1+\gamma)\, u_o = v_s - f(v_s)\, v_c + g(v_s)\, u_c \,, \tag{32}$$

where $f(v_s)$ and $g(v_s)$ are functions to be determined. The functions need to be defined such that u_o can avoid being positive when v_s is zero, for example. Also, although not necessary, it is desired to force the functions to

zero as v_s approaches infinity. This will enable u_o to correspond to the hydrodynamic value in the appropriate limit. For present purposes, the following values are taken for the functions:

$$\begin{aligned} v_s \le v_c &: \quad f(v_s) = 1, \ g(v_s) = 0 \\ v_s > v_c &: \quad f(v_s) > 0, \ g(v_s) > 0 \\ v_s \to \infty &: \quad f(v_s) = 0, \ g(v_s) = 0 . \end{aligned} \tag{33}$$

The sound speed for the target C_o is used to determine when the striking velocity approaches infinity. Thus, an angle Q is defined as

$$Q = \frac{\pi}{2}\left[\frac{v_s - v_c}{C_o - v_c} \right] . \tag{34}$$

Eq. (34) can satisfy the requirements of (33) when

$$f(v_s) = \mathrm{Cos}(Q) \quad \text{and} \quad g(v_s) = A\ \mathrm{Cos}(Q)\ \mathrm{Sin}(Q). \tag{35}$$

The definitions of (33), (34), and (35) are applied to Eq. (32) to give u_o in terms of values used to define the penetration problem. A good fit was found for $A = 1.1\gamma$. The three velocity ranges of Fig. 2. are described by the following:

$$(0 \le v_s \le v_c): \quad u_o = 0 , \tag{36}$$

$$(v_c < v_s < C_o): \quad u_o = \frac{v_s}{1+\gamma} - \frac{\mathrm{Cos}(Q)}{1+\gamma}\left[\sqrt{\frac{2S_t}{\rho_p}} - A\ \mathrm{Sin}(Q) \sqrt{\frac{2S_p}{\rho_t}} \right] , \tag{37}$$

$$(C_o \le v_s): \quad u_o = \frac{v_s}{1+\gamma} . \tag{38}$$

The first term on the right-hand side of (37) can be recognized as the penetration rate associated with hydrodynamic penetration. The second term reduces the hydrodynamic value by a factor involving target strength to rod density ratio, while the third term enhances penetration rates according to penetrator strength to target density ratio. Penetrator strength is a weaker function and only enhances penetration rates in the mid-range of striking velocities. The dashed lines of Fig. 2. represent u_o as determined by Eq. (37) using the same strength values that were used in the CTH calculations.

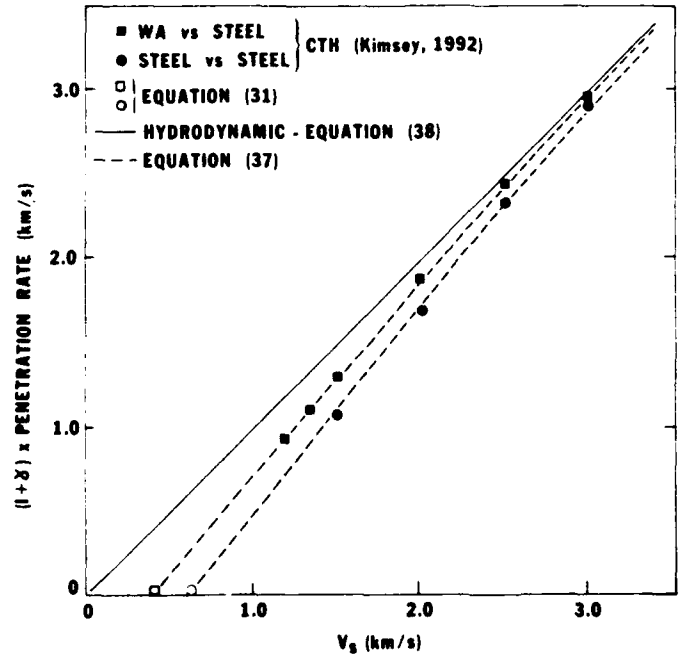


Fig. 2. Penetration velocity plotted as a function of striking velocity.

CALCULATED RESULTS

This section provides some general results of the long-rod penetration equations, while detailed comparisons to experimental data are deferred. Calculations are presented for flow variables u, v, and (v-u) as functions of rod length and time. Also, penetration depth for combinations of striking velocity, rod and target strengths are examined, especially where $S_p > S_t$, $S_p = S_t$ and $S_p < S_t$. There are some comments regarding computational methods used in this work. Eqs. (7) and (16) are exact with respect to rod length variable l. However, the time Eq. (26) and penetration depth Eq. (25) were numerically integrated using Simpson's rule. An IBM AT PC, a single precision BASIC program, and forty-eight rod length intervals were used for the numerical integration.

Initially, three examples were examined for steel penetrators impacting steel targets where densities were 7.86 g/cm^3, and C_0 was 5,170 m/s. The material strengths utilized are given in Table 1. The first set of calculations was done for a striking velocity of 1,500 m/s. Results are presented in Fig. 3., where velocities u, v and (v-u) are plotted as functions of l. The curves exhibit logarithmic reductions in velocity variables as expected. Examples 1 and 2 show that when penetration ceases (u = 0), rod motion and erosion continue (i.e., v > 0 and |v-u| > 0). In Example 3, the opposite occurs. Here, erosion ceases (v-u = 0) before penetration has been completed.

A second set of calculations was made for the three examples of interest over a wide range of striking velocity. These are shown in Fig. 4. The results are consistent with known rod penetration behavior. The first is that in the three examples, rod penetrations approach the hydrodynamic limit at high striking velocity. Secondly, a critical impact velocity must be reached before any penetration is realized. Thirdly, high penetrator strength can produce penetration depths which exceed hydrodynamic expectations. These occur primarily in a mid-velocity range of 1,500 to 3,000 m/s. Finally, characteristic S-shaped curves result when calculations are presented as P/L versus striking velocity. The shape is not due to Eq. (37) since it provides a nearly linear dependence of u_0 on v_s.

Comparisons are made between present calculations, CTH results and the Tate model. The latter are taken from the work of Anderson *et al.* (1992). Of interest is a tungsten alloy penetrator (l_0 = 31.6 mm) impacting a steel target. Impact velocity was 1,500 m/s. Material strengths used in the current calculations are those used in the above work and are given in Table 2. Results for three computational methods are provided in Fig. 5. For the Tate model, target resistance was adjusted to a value of 5.43 GPa so that results agreed with CTH at the point u = 0. For the present equations, strength values given in Table 2 were used without further adjustment. Also, u_0 was taken to be 765 m/s as obtained from CTH (Anderson *et al.*, 1992).

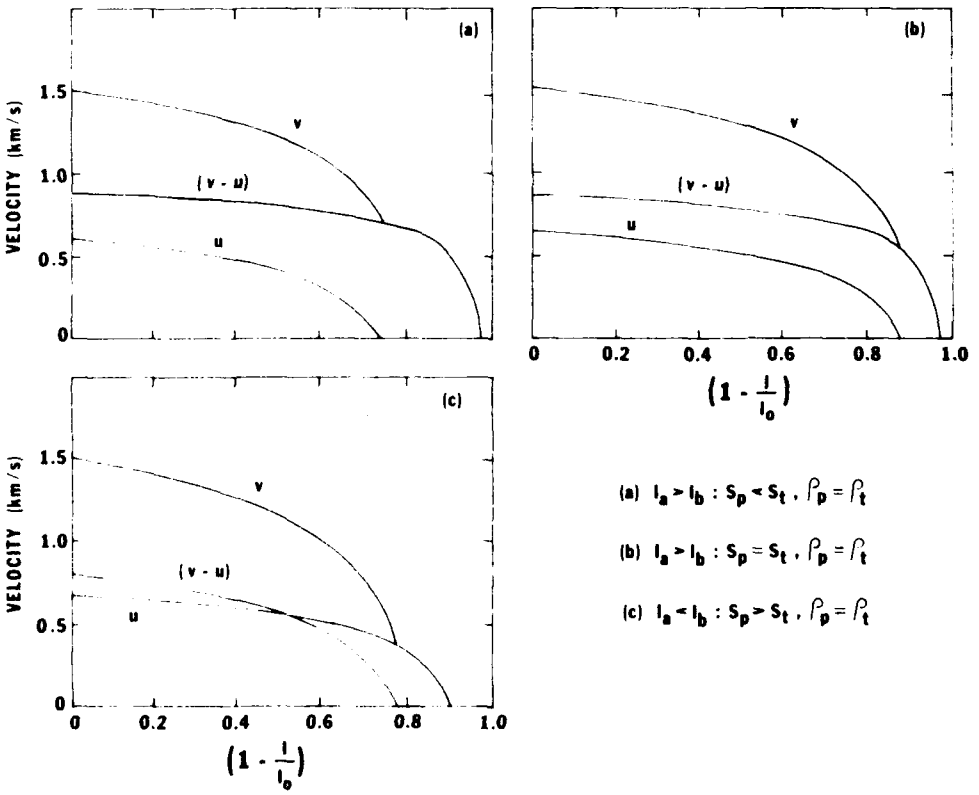


Fig. 3. Penetration velocity, rod velocity and erosion rate as functions of rod length.

Table 1. Material Properties Used in Examples 1–3

Example	S_p (GPa)	S_t (GPa)
1	0.8	1.1
2	0.8	0.8
3	1.8	0.8

Table 2. Material Properties for u(t) Calculations

Material	Density (g/cm^3)	Strength (GPa)
Tungsten Alloy	17.2	1.51
S-7 Steel	7.84	1.26

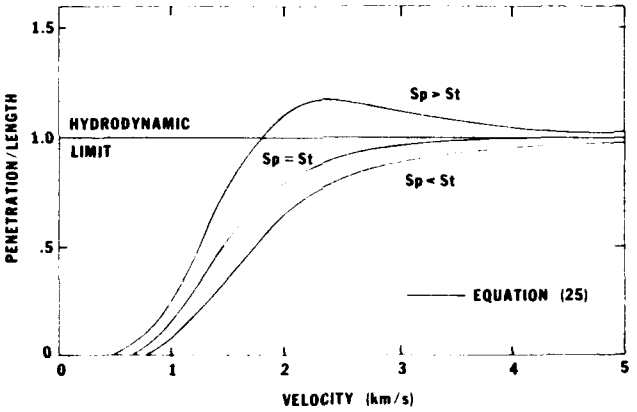


Fig. 4. Calculated P/L curves for three conditions of impact versus striking velocity.

A most important comparison is that of u = u(t) since it is a basis for penetration. In this regard, the good agreement with CTH results is an important test of Eqs. (2) and (16). On the other hand, comparisons of penetrator velocity differ somewhat. This could result from approximations in the general formulation or differences between rod body and rod tail velocities due to velocity gradients along the rod length.

COMPARISONS WITH EXPERIMENTAL DATA

The present equations were used to predict uneroded rod lengths and penetration depths for long rod penetrators ($l/d \geq 10$) impacting semi-infinite targets. Data from Anderson *et al.* (1992) are examined since experimental shots were conducted to compare with CTH calculations. For the problem shown in Fig. 5., CTH gave 25.1 mm, Eq. (25) gave 23.2 mm while the experimental penetration depth was 22.6 mm. The good agreement suggests an integrated accuracy of Eq. (25) despite approximations in the general procedure.

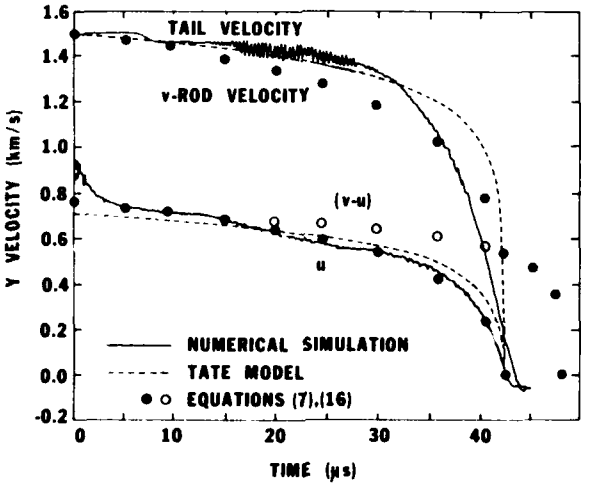


Fig. 5. Penetration, erosion and rod velocities versus time as calculated by CTH, Tate model and current equations.

Data for tungsten alloy and steel rods striking steel targets over a wide range of striking velocities have been reported by Tate (1967, 1969), Tate (1978), Hohler and Stilp (1984), Silsby (1984) and Zook *et al.* (1992). The last cited work also provides uneroded rod lengths for tungsten penetrators versus RHA at low striking velocities. Calculations corresponding to experimental results used material properties presented in Table 3.

Table 3. Material Properties Used in Predicting Penetration Versus Striking Velocity

Material	Density (g/cm^3)	Strength (GPa)	C_0 (m/s)
WA Rod	17.3	1.51	—
Steel Target	7.84	1.3	5,170
Steel Rod	7.85	1.2	—
Steel Target	7.85	1.3	5,170

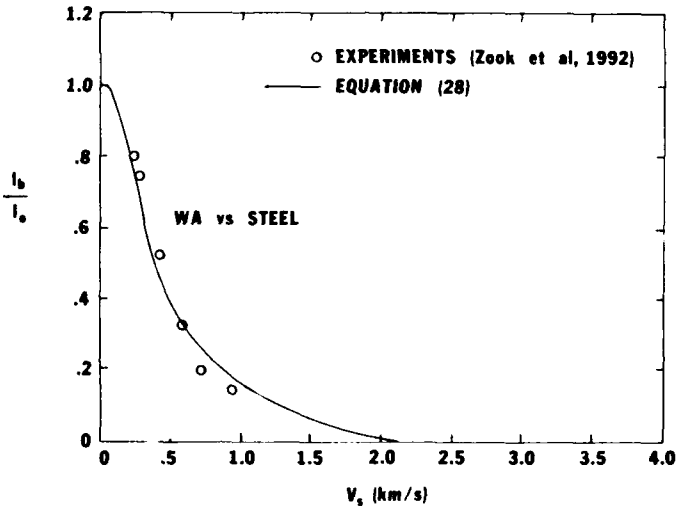


Fig. 6. Uneroded rod length versus striking velocity.

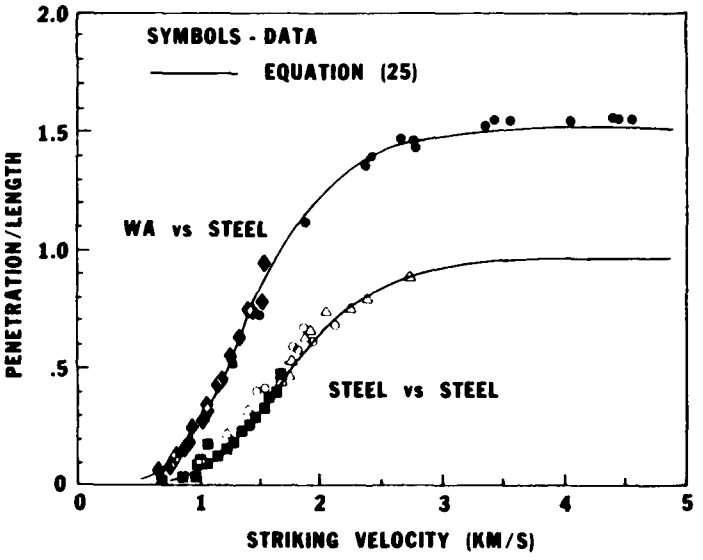


Fig. 7. Comparison of predicted and experimental penetration results on the basis of P/L versus striking velocity.

Good agreement between predicted uneroded rod length and the data is shown in Fig. 6. The agreement is a test of Eqs. (1), (7) and (28) under two very different conditions. The first is where impact is below v_c, (387 m/s) and only penetrator erosion is involved (u=0), while the second relates to flow above v_c where both penetrator and target undergo erosion (u>0).

Theoretical results are compared to data on the basis of P/L versus striking velocity in Fig. 7. Good agreement can be seen over much of the data range, particularly at the onset of penetration, over the region of rapid increase in penetration depth at low velocity and throughout the intermediate velocity range (linear region). In the high velocity range, the theory predicts expected asymptotic behavior, although data in this range is somewhat higher. The theory suggests that such additional penetration is not due to rigid body penetration since $l_a > l_b$ in these calculations and only small rod lengths are expected at the end of the erosion phase. General agreement at the high end of the striking velocity range is expected since the equations correspond to hydrodynamic theory of penetration there. Also, agreement at the lowest possible impact velocity was expected since that point is given by the critical impact velocity. The overall agreement suggests that the present development takes into account major material strength influences in the nonsteady penetration process.

SUMMARY AND CONCLUSIONS

As seen in previous sections, the present development provides a theory of nonsteady penetration for long rods. The theory differs from previous formulations in that Newton's law is used rather than Bernoulli's equation. The formulation considers both rod and target erosion and retardation in the penetration process. Material strengths are included in the force laws that govern rod and target motion. The theory applies throughout the entire range of striking velocity to include hydrodynamic penetration at the limit of very high impact velocity.

From a single formulation, two distinct penetration possibilities are predicted. The criteria depends on whether or not target erosion ceases before penetrator erosion is complete. This depends on initial erosion rates, relative strengths and relative densities of the rod and target. For both cases, penetration during the target erosion phase is given by Eq. (25). When rod erosion ceases first, an *ad hoc* contribution due to rigid body penetration can be included but this lies outside the present theory. However, as seen in Fig. 4., application of Eq. (25) indicates that some penetration beyond the hydrodynamic limit can result from the erosion/retardation process inherent in the theory under certain strength-density conditions.

Final penetration depths and also penetration histories have been calculated from the theory. On the basis of a single comparison, penetration rates agree very well with calculations obtained with the CTH hydrocode. Theoretical calculations for tungsten alloy and steel rods impacting steel targets showed excellent agreement with experimental data of penetration depth taken from several sources. Uneroded rod lengths as given by the theory agreed quite well with data for impacts of tungsten alloy rods on steel targets.

The present theory includes equations of motion (nonsteady) for both penetrator, giving v-u, and target, giving u. With these erosion rates, a penetration solution is obtained. In contrast, Tate's theory provides an equation of motion only for the penetrator, giving v, while an assumed modified steady-state Bernoulli equation is used to determine u from v. These differences in approach give rise to differences in erosion rates and consequently differences in penetration formulations, especially with regard to dependencies of penetration upon initial conditions and material strengths. From cases examined in this work, it appears that for comparable results, the Tate approach requires target strength multiplication factors ranging from 2, as in the special case, to 4.3, as seen in the more general case of tungsten alloy penetrators striking steel targets. The present theory appears to be accurate when material strengths utilized are the ordinary values generally associated with dynamic properties or work-hardened material states.

ACKNOWLEDGEMENT

The author would like to thank the following associates for valuable discussion during the course of this work: Professor James Coughlin, Towson State University, MD, and Miles Lampson, Konrad Frank, James Dehn, Evan Walker, Drew Dietrich and Nevin Rupert, U.S. Army Research Laboratory (ARL), MD. Also, thanks are due Kent Kimsey of the ARL for providing a consistent set of CTH hydrocode calculations to support this work.

REFERENCES

Alexseevskii, V. P. (1966). Penetration of a rod into a target at high velocity. *Fizika Goreniya i Vzryva*, Vol. 2, No. 2, pp. 99–106 (Combustion, Explosion and Shock Waves, pp. 63–66).

Anderson, C. E., and S. R. Bodner (1988). Ballistic impact: The status of analytical and numerical modeling. *Int. J. Impact Engng.*, Vol. 7, pp. 9–35.

Anderson, C. E., J. D. Walker, and G. E. Hauver (1992). Target resistance for long-rod penetration into semi-infinite targets. *Nuclear Engineering and Design*, in publication.

Batra, R. C., and T. W. Wright (1986). Steady-state penetration of rigid perfectly plastic targets. *Int. J. Engng. Sci.*, Vol. 24, pp. 41–54.

Belyakov, L. V., F. F. Vitman, and N. A. Zlatin (1962). Collision of deformable bodies and its modelling: II. The modelling of the impact of a sphere and a half-space. *Zhurnal Technicheskoi Fiziki*, Vol. 33, No. 8, pp. 990–195.

Birkhoff, G., D. P. MacDougall, E. M. Pugh, and G. Taylor (1948). Explosives with lined cavities. *J. Appl. Phys.*, Vol. 19, No. 6, pp. 563–582.

Dehn, J. T. (1987). A unified theory of penetration. *Int. J. Impact Engng.*, Vol. 5, pp. 239–248.

Frank, K., and J. A. Zook (1987). Energy efficient penetration and of perforation of targets in the hypervelocity regime. *Int. J. Impact Engng.*, Vol. 5, pp. 277–284.

Hohler, V., and A. Stilp (1984). Influence of length-to-diameter ratio in the range of 1 to 32 on the penetration performance of rod projectiles. *Proc. 8th Int. Symp. Ballistics*, Orlando, FL.

Kimsey, K. D. (1992). Unpublished work, U.S. Army Research Laboratory, Aberdeen Proving Ground, MD.

Luk, V. K., and A. J. Piekutowski (1991). An analytical model on penetration of eroding long rods into metallic targets. *Int. J. Impact Engng.*, Vol. 11, pp. 323–340.

Silsby, G. F. (1984). Penetration by semi-infinite steel targets by tungsten long rods. *Proc. 8th Int. Symp. Ballistics*, Orlando, FL.

Tate, A. (1967). A Theory for the deceleration of long rods after impact. *J. Mech. Phys. Solids*, Vol. 15, pp. 387–399.

Tate, A. (1969). Further results in the theory of long rod penetration. *J. Mech. Phys. Solids*, Vol. 17, pp. 141–150.

Tate, A., K. E. B. Green, P. G. Chamberlain, and R. G. Baker (1978). Model scale experiments on long rod penetration. *Proc. 4th Int. Symp. Ballistics*, Monterey, CA.

Tate, A. (1986). Long rod penetration models - Part I. A flow field model for high speed long rod penetration. *Int. J. Mech. Sci.*, Vol. 28, pp. 535–548.

Tate, A. (1986). Long rod penetration models - Part II. Extensions to the hydrodynamic theory of penetration. *Int. J. Mech. Sci.*, Vol. 28, pp. 599–612.

Walters, W. P. and S. Segletes (1991). An exact solution of the long rod penetration equations. *Int. J. Impact Engng.*, Vol. 11, pp. 225–231.

Wilkins, M. L., and M. W. Guinan (1973). Impact of cylinders on a rigid boundary. *J. Appl. Phys.*, Vol. 44, pp. 1200.

Wright, T. W. (1983). A survey of penetration mechanics for long rods. BRL-TR-02496, U.S. Army Ballistic Research Laboratory, Aberdeen Proving Ground, MD.

Zook, J. A., K. Frank, and G. F. Silsby (1992). Terminal ballistics test and analysis guidelines for the penetration branch. BRL-MR-3960, U.S. Army Ballistic Research Laboratory, Aberdeen Proving Ground, MD.

Zukas, J. A. (Editor) (1990). *High Velocity Impact Dynamics*. John Wiley and Sons, Inc., New York.

Int. J. Impact Engng Vol.14, pp.315–324, 1993
Printed in Great Britain

0734-743X/93 $6.00+0.00
1993 Pergamon Press Ltd

DEVELOPMENT AND OPTIMIZATION OF A "MICRO" TWO-STAGE LIGHT-GAS GUN

DONALD J. GROSCH and JACK P. RIEGEL

Southwest Research Institute
6220 Culebra Road, San Antonio, TX 78238

ABSTRACT

This paper details the steps taken to develop and optimize a "micro" two-stage light-gas gun system. The micro gun described in this paper has a 5.56-millimeter (mm) pump tube and a 1.78-mm launch tube. The original gun configuration is presented, followed by a description of our analysis and revision of the gun system. The modifications to the micro gun system and their effect on the performance of the gun are discussed.

INTRODUCTION

An ever-growing threat to spacecraft is the impact of micrometeoroids and man-made orbital debris. Within 2000 kilometers (km) of the Earth's surface, there exists 200 kilograms (kg) of meteoroid mass, most of it concentrated in 0.1-mm micrometeoroids. In this same envelope around the earth, there exists 300 kg of orbital debris less than 1 mm in diameter. Although these particles are small, they can travel at velocities between 10 and 20 kilometers per second (km/s) relative to orbiting spacecraft (Kessler, *et al.*, 1989). At these extremely high impact velocities these particles pose a very real threat to spacecraft and astronauts.

The ability to test advanced materials and shielding concepts against these threats is very important. Simulating extremely high velocity threats in a laboratory has historically been done using a two-stage light-gas gun system. These gun systems can produce velocities approaching those seen by micro-particles in space. However, the majority of existing gun systems launch particles much larger than the 0.1 to 1.0-mm particles mentioned above.

BACKGROUND

To study the impact effects of these extremely small particles, Southwest Research Institute (SwRI) developed a "micro" two-stage light-gas gun. The development of this gun was funded as part of SwRI's Internal Research Program. In an effort to minimize the cost of developing the new gun system, a number of gun components were used from an existing light-gas gun that had been donated in the early 1980's to SwRI by NASA. The integration of old parts into a new design prevented optimization of the system in terms of fabrication costs and functionality.

Initial firings of the gun system were only marginally successful. Launch velocities of no more than 5.0 km/s were achieved. Attempts to improve the maximum achievable projectile launch velocity experimentally were unsuccessful. It was decided that a systematic approach had to be taken to optimize performance. This approach began with the examination of the gun performance using a two-stage light-gas gun computer code. Experimental procedures were also examined to determine if changes were required. This systematic examination of the gun system resulted in a number of changes to both the gun firing procedures and the configuration of the gun.

ORIGINAL GUN CONFIGURATION

A schematic of the original gun configuration is given in Fig. 1. The breech was designed for an 11.63-mm (0.458 inch) standard rifle case (Tullos, *et al.*, 1990). A mechanically operated firing pin impacted a percussion primer that initiated the burning of a smokeless propellant in the case.

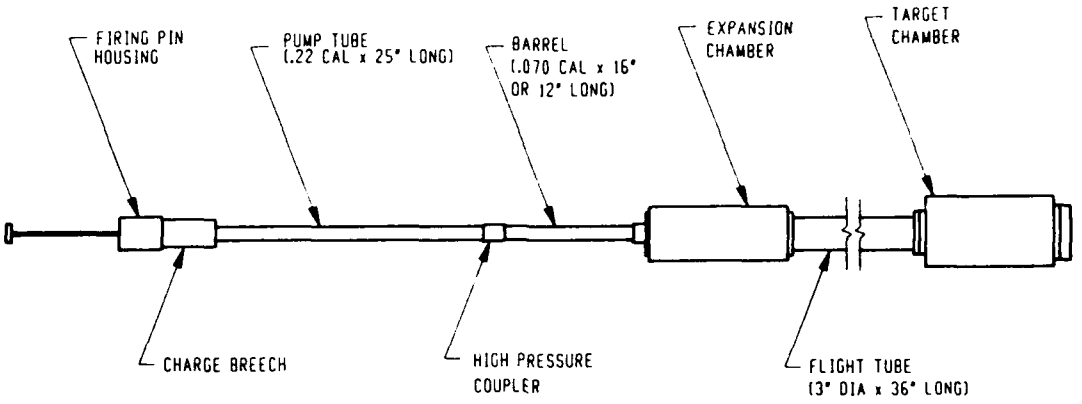


Fig. 1. Original Gun Configuration.

The pump tube had a bore diameter of 5.56 mm (0.22 inch) and a length of 711 mm (28.0 inches). The launch tube had a bore of 1.78 mm (0.070 inch) and a length of 376 mm (14.8 inches). Between the pump and launch tubes was the accelerated reservoir (AR) section, whose total length was 50.8 mm (2.0 inches). Flanges, which threaded onto the pump tube and launch tube, clamped the AR section in place.

The launch tube was interfaced with a flight tube with a total length of 1.2 meters. A 15 by 15 by 30 cm rectangular target chamber was located at the end of the flight tube. The overall length of the gun system was 2.6 meters.

ORIGINAL GUN PERFORMANCE

The performance of the gun system in its original condition was inadequate. The maximum velocity achieved with the original configuration was 5.0 km/s. The gun displayed signs of excessive wear in the areas of the breech, pump tube, and AR section. The wear in the pump tube resulted in an extremely rough and expanded inner diameter near the breech end of the tube. Inner diameter enlargement and cracks developed in the bore of the AR section. The remainder of this section describes some of the gun system problems that were addressed.

It was determined that gas leakage was occurring at the interface of the AR section and the launch tube. This interface is also the location of a rupture disk. The leak of pressure outside the gun system could be heard during each test as a loud "pop." It could also be detected by visual inspection of the rupture disk after a test. This pressure release was occurring at the location in the gun system where the high pressure hydrogen gas begins acting on the projectile. Any pressure loss in this area reduces the efficiency of the gun.

Several components of the original gun design contributed to the lack of performance. The most obvious problem involved the launch tube arrangement. The launch tube for the original gun consisted of a piece of stainless steal tubing that formed the actual bore of the gun. The tubing had an inner diameter of 1.78 mm and a wall thickness of 2.29 mm. This tubing, which was meant to be replaced after each test, was inserted inside a thick-walled tube for support. The intent of the design was to permit interior ballistics parameters to be pushed to extremes, resulting in plastic deformation of the launch tube. The deformed tube could then be replaced, but the more expensive outer shell remained undamaged. In practice, deformation of the outside diameter of the steel tubing insert made it difficult, and in some cases impossible, to remove the inner tube.

Another problem with the system was the short length of the flight tube (1.2 meters). In the micro gun system, the flight range (launch tube, flight tube, and target chamber) is evacuated to achieve higher velocities and to avoid atmospheric ablation of the projectile. However, when launching saboted spheres, some amount of atmosphere is required in the flight range to achieve aerodynamic separation of the sabot from the projectile. A large amount of atmosphere was required in the range to open the sabot halves in such a short distance. This excessive amount of atmosphere reduced the accuracy and the maximum velocity achievable with saboted projectiles.

The usefulness of the overall gun system was further limited by the target chamber. The small size of the chamber greatly limited the size and configuration of targets that could be tested. The small target chamber also made placing targets, sabot stripper plates, and witness plates difficult.

MODIFICATIONS

A systematic analysis of the gun system was initiated to develop a better understanding of the variation in performance as a function of design and firing parameters with the expectation that we would be able to greatly improve its performance. The approach involved the use of a computer code designed to model the interior ballistics of two-stage light-gas guns. SwRI obtained a code written by A. C. Charters and D. K. Sangster for this purpose (Charters, *et al.*, 1973).

The first requirement when running the code is to accurately describe the geometric parameters of the gun system. The size and shape of the breech, pump tube, AR section, and launch tube are required. Once the gun system is dimensionally modelled, the parameters used to fire the gun are entered. These parameters include the amount of propellant, the type of propellant, the shot-start pressure, the initial light-gas pressure, the rupture disk release pressure, and the projectile size. The input includes the equations of states and the physical properties of these items. The program then utilizes the information to perform a one-dimensional analysis of the interior ballistics. The output provided by the code includes projectile launch velocity, piston velocities at various user-defined locations, maximum projectile acceleration, maximum breech and base pressures and temperatures, and other information useful in the evaluation of the gun system.

An immediate difficulty arose in defining the gun system. The propellant is analyzed using a burn rate equation of the form $\frac{dB}{dt} = -\beta P^{\alpha}$, where α and β are two coefficients that vary with propellant composition and geometry. Unfortunately, these coefficients are not readily available for most powders and must be determined experimentally. The first coefficient, β, is the linear burn rate of the propellant and the second, α, is the exponent on the pressure term of the burn rate equation.

The accuracy of these two coefficients can be important when using the code to estimate real gun performance. The significance of these coefficients to the overall performance depends on a combination of gun geometry and test conditions. It is possible to compute approximately the same final velocity using a number of burn coefficients. Likewise, it is possible to compute approximately the same peak pressure in the breech for a number of coefficient combinations. It appears that for small powder charges (relative to full chamber volume) these coefficients do not have to be very precise. This is because the pressures in the chamber remain relatively low, minimizing the effect of the exponent term. The linear coefficient is fairly consistent for a large number of powders, and the code calculations are not very sensitive to small changes in the coefficient.

In order to estimate the two burn rate coefficients without undertaking a series of burn rate tests, the gun code option of analyzing a straight-through, single-stage gun system was utilized. A 0.357-caliber (9.07 mm) rifle was modelled according to the specifications given in a hand-loading manual. This manual gave launch velocity data using the same propellant type used in the micro-gun. The two propellant coefficients were estimated by comparing calculated velocities from the gun code with tabulated experimental data in the hand-loading manual.

The code was now ready to simulate the performance of the micro-gun. However, the only parameter that could be checked against the many outputs of the code was the projectile launch velocity. With the large number of variables used in the code, it is possible that the projectile velocity obtained experimentally could be the same as the code prediction, while other output parameters that may be important are incorrect. For example, the same final projectile velocity can be achieved with a wide range of peak accelerations on the projectile. This is important since the peak acceleration was used as a relative performance guide during part of our study. Results of the peak acceleration analysis are discussed later.

A solution to this problem would be to obtain an additional experimentally measured quantity to check against the code predictions and increase confidence levels. Since the travel of the piston is very critical to the overall performance of the gun, we decided this would be a good second quantity to measure experimentally. However, because a smooth, undisturbed piston motion is desirable, the use of break or make wires to measure piston velocity was not considered an option. Also, the addition of ports for lasers or other optical measuring methods would create a disturbance in the pump tube bore that might affect the piston motion. Therefore, in order to measure the piston velocity without disturbing the piston, strain gauges were placed at three locations along the outside of the pump tube length. The high breech pressures that act on the base of the piston create a slight elastic deformation in the pump tube. This slight deformation is detected by the strain gauge as the piston passes each location. The peak strain expected was on the order of 30 micro-strain. Therefore, two single-axis strain gauges were placed at each station and configured to obtain the additive output of both gauges in order to increase the signal-to-noise ratio. The analog output from the gauges is recorded on a tape recorder and reviewed on a Hewlett Packard Model 54501A Oscilloscope. The piston velocity is calculated using the times between traces and distances between gauges. This provided a second value that could be compared to the output of the gun code to determine if the code was indeed accurately estimating the performance of the gun.

Once the gun was being modelled correctly and the code was accurately estimating its performance, various parameters were modified to determine their effects. The main goal of this procedure was to increase the achievable launch velocity. This procedure and the use of the gun code proved invaluable to the optimization of the gun.

The first items modified in the gun model were the size of the breech and the amount of propellant used. These changes were based on an assumption that there was too much ullage, or void space, in the breech. The volume of the ullage in the breech was approximately three times the volume taken up by the propellant. Based on the code calculation, this ullage was reducing performance substantially. The code also suggested that if a smaller breech volume was utilized, much less powder could be used to produce the same results.

Based on these findings, the 0.458-caliber (11.63 mm) breech was replaced with a .22-250-caliber (5.59 mm) firing action. This breech is approximately 1/5 the volume of the previous one. The propellant mass was reduced from 40 grains (2.60 g) to about 10 grains (0.65 g). After this change was made, the pump tube and AR section no longer sustained the high amount of erosion seen previously. Another benefit of the reduced propellant mass was a reduction in the amount of cleaning required between tests.

In addition to these changes, the mass of the piston was reduced from over one gram to 0.4 grams. The lower piston mass reduced its kinetic energy, thus reducing the amount of wear in the AR section. Also, the smaller pistons are easier to make and easier to extract from the AR section after a test.

The code also suggested that the initial hydrogen pressure should be lowered from 150 pounds per square inch (psi) (1.030 MPa) to 120 psi (0.827 MPa). Once this final change was made, performance was increased substantially. The initial test performed after these modifications achieved a launch velocity of 6.2 km/s, over a thousand meters per second faster than the previous maximum velocity. This value was improved upon even more by several iterations between the computer code and experiments.

TESTING IMPROVEMENTS

In order to further improve the performance of the gun, design and assembly procedure changes were made to some of the gun components. The problem that had the most adverse affect on the performance of the gun was the blow-by at the AR section interface with the launch tube. A possible source of this problem was the manner in which the AR section was held in place between the pump and launch tubes (see Fig. 2). The distance between centers of the 1/4 inch (6.35 mm) bolts is 11.1 cm. If these bolts were not strong enough or if the spacing was too large, this configuration could possibly yield elastically under the high pressure loading produced as the piston comes to rest in the AR section. This yielding would allow some of the high pressure gas to escape the system.

To eliminate this blow-by the flange connection was modified (see Fig. 3). The size of four bolts was increased from 1/4-inch (6.35 mm) to 1/2-inch (12.70 mm) diameter. The distance between centers of the bolt pattern was decreased to 6.9 cm to help prevent any bending of the flanges. These changes increased the clamping pressure on the AR section. To insure consistency and proper clamping pressure, the bolts were torqued to a specified value before each test. Also, to avoid the need of working with nuts and an additional wrench, one of the flanges was threaded. These modifications resulted in an increase in performance. The loud "pop" associated with blow-by no longer occurred and launch velocities increased. The ease and consistency of the clamping procedure also increased.

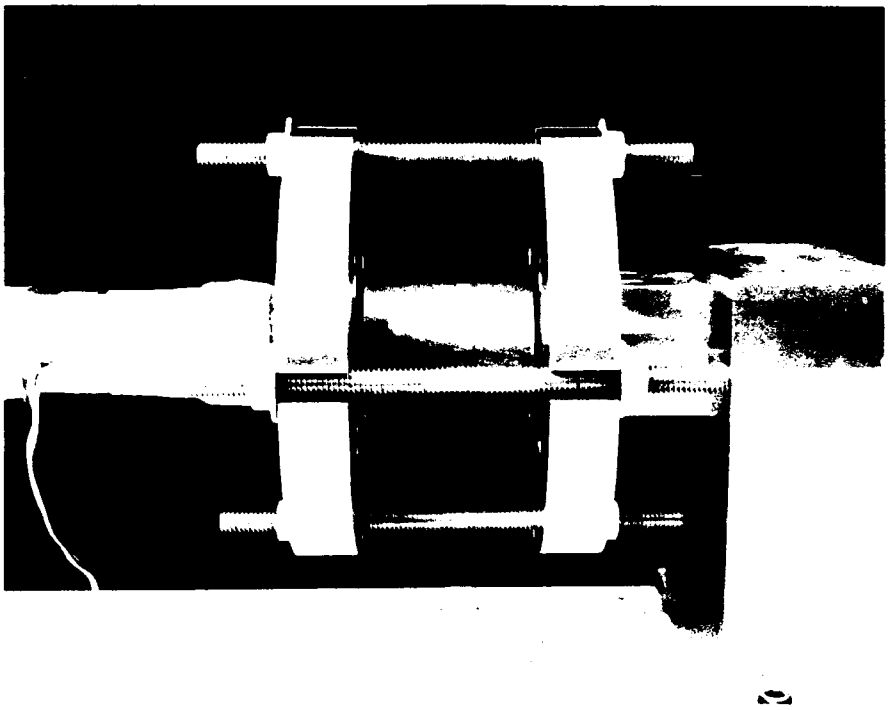


Fig. 2. Original Accelerated Reservoir (AR) Section Connection.
(From left to right: Pump Tube, Clamped AR Section, Launch Tube)

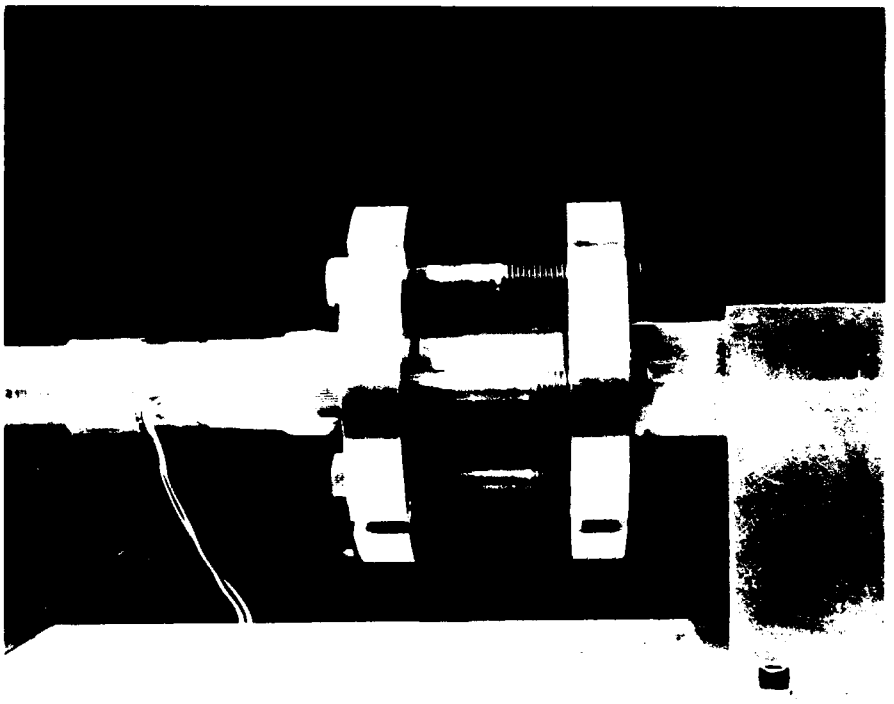


Fig. 3. Modified Accelerated Reservoir (AR) Section Connection.
(From left to right: Pump Tube, Clamped AR Section, Launch Tube)

To ease the insertion and extraction of the expendable launch tube, the outer support tube design was changed. The thick-walled support tube was replaced with a two-piece, clam-shell arrangement (see Fig. 4). This piece supports the expendable tube in the same manner as the outer tube did; however, the clam shell can be taken apart, which makes the placement and removal of the inner tube extremely easy.

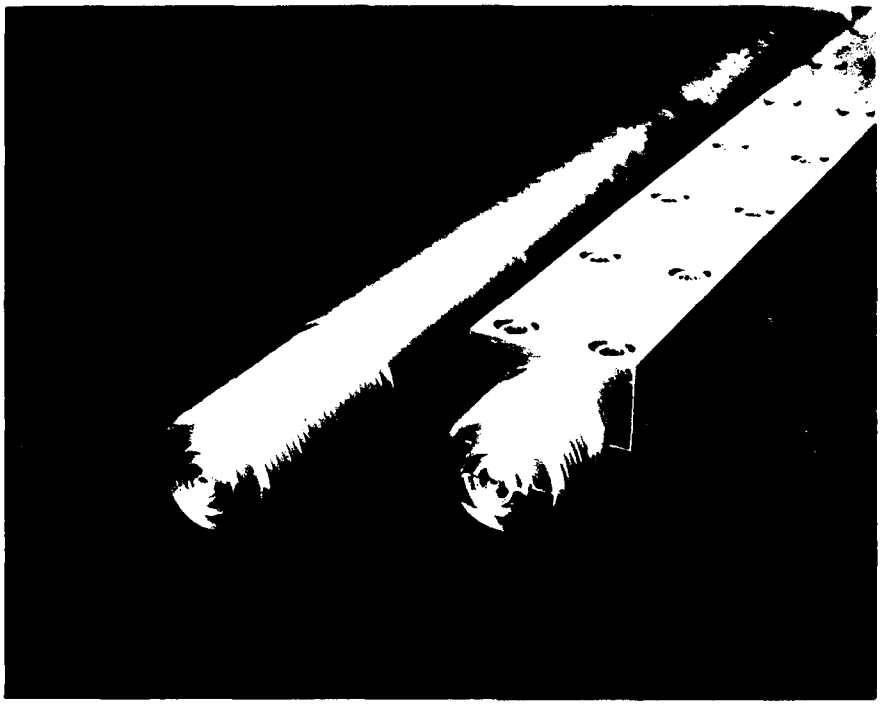


Fig. 4. Original and Modified Launch Tubes.

To improve the sabot launching abilities of the gun system, the flight tube length was increased to slightly over three meters. Also, the gun system was made more versatile by increasing the target chamber size to a box with dimensions of 30.5 cm by 30.5 cm by 61.0 cm. This size target chamber allows the testing of up to a 25 cm square target. The larger chamber also eases the placement of targets, sabot strippers, and witness plates.

SABOT LAUNCHING IMPROVEMENTS

Most of the work mentioned above was performed using nylon, right-circular cylinders as the projectile. Results of some of these tests are shown in Fig. 5, which compares penetration depth (corrected for projectile mass) versus launch velocity. This work led to a gun system that was capable of launching nylon cylinders with masses between 3.0 and 4.5 mg at velocities of 7.5 to 9.5 km/s. However, it is often important to observe the hypervelocity impact effects of various materials, such as aluminum.

Launching such a material requires the use of a sabot. The sabot we use with the micro gun is a two-piece, lexan sabot (see Fig. 6). The outer diameter of the sabot is machined to fit the bore of the gun. A "pocket" is machined into the sabot to hold the projectile as it travels down the gun barrel. The leading edge is machined so that as the sabot interacts with the air in the flight chamber, the two halves will be stripped away from the projectile. This is a typical sabot configuration for use in light-gas guns (Berggren, *et al.*, 1970).

The same gun parameters used to launch the nylon, right-circular cylinders to velocities above 9 km/s were used to launch saboted aluminum spheres. The saboted spheres did not behave in the same manner as the nylon projectiles. The three objects being launched (two sabot halves and one aluminum sphere) did not fly straight and often missed the target area completely. Often, the target would show signs that the package "shot-gunned," or broke apart into small pieces.

Since the nylon projectiles had been launched effectively using the current gun loading parameters, we began looking at the quality of the sabot as a cause of the inconsistent launches. In order to increase this sabot quality, the rotational speed of the lathe used to fabricate them was examined. Increasing the rotational speed of the lathe increases the relative cutting tool-to-material surface speed, which is extremely critical when machining plastics.

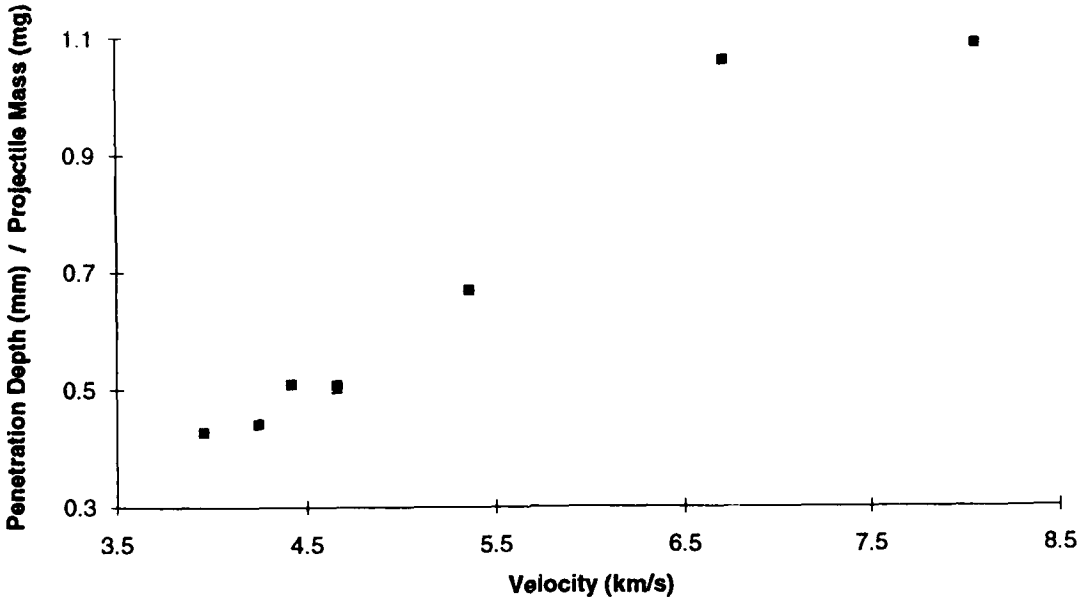


Fig. 5. Penetration Depth vs. Velocity (Corrected by Projectile Mass).

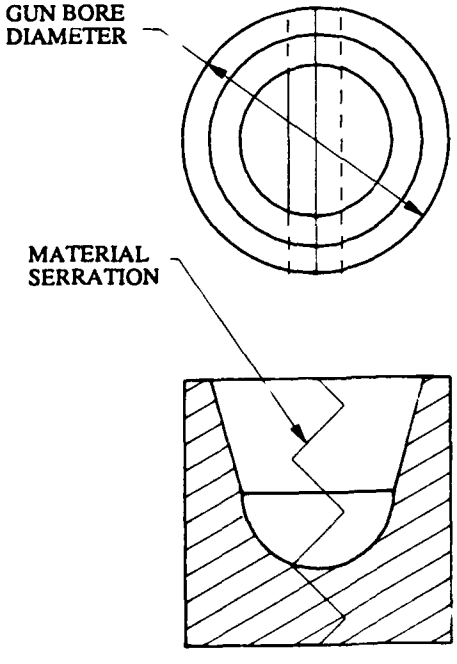


Fig. 6. Typical Sabot Configuration.

The minimum recommended surface speed for machining plastics is 183 meters per minute. This value is difficult to obtain when the diameter of the sabot is only 1.78 mm. This diameter produces a revolution rate of 5.59 mm per revolution (mm/rev), which results in a required lathe rotational speed of almost 33,000 revolutions per minute (rpm).

To maximize the rotational speed of the lathe, a speed doubler kit was purchased. This device increased the rotational speed of the lathe to 3000 rpm. Although this speed is an order of magnitude less than the recommended value, the quality of the sabot increased as did its launch performance.

Although the increase in sabot quality improved its performance, sabot launches were still not optimal. It was decided that the three-piece sabot package could not be accelerated as rapidly as the homogeneous nylon cylinder. Examination of the gun code results revealed that the projectile is subjected to extremely high values of base pressure and acceleration (Chavez, *et al.*, 1991). The high accelerations seen by the projectile are due to its low mass and extremely high final velocity. Figure 7 compares constant accelerations (the lowest possible) versus accelerations predicted by the gun code at various launch velocities. The figure demonstrates that as the velocity increases, the acceleration forces seen by the projectile increase dramatically.

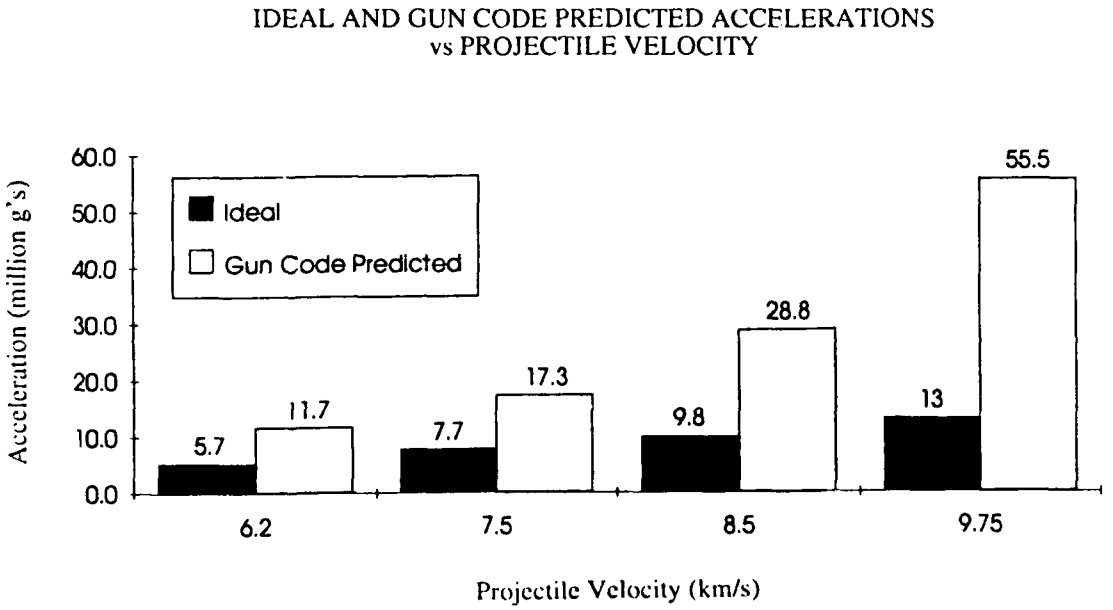


Fig. 7. Ideal and Actual Accelerations vs. Projectile Velocity.

It appeared the two-piece sabot was failing due to these high loads. Therefore, the gun code was utilized to reduce the load on the projectile while maintaining the high launch velocities. Interpretation of the code results led to changes in the initial hydrogen pressure, propellant mass, and piston mass. These changes, coupled with the improved sabot machining, produced substantially improved sabot launches. The pattern produced on the target was typical of sabot launches; two sabot halve impacts radially separated from the projectile impact.

The amount of sabot separation depends on the amount of atmosphere in the flight chamber. Figure 8 shows the spacing between sabot halves at various values of flight chamber pressure. The figure shows that only slight changes in the pressure produces large changes in the amount of sabot separation. Based on this matrix of tests, a value of 15 torr became the flight chamber pressure for saboted launches.

The maximum achievable velocity using saboted spheres is less than the maximum velocity achieved using nylon cylinders. However, SwRI is continuing attempts to push the parameters of the micro gun to achieve ever higher velocities. Additional use of the gun code along with experimentation should lead to higher velocities using saboted spheres.

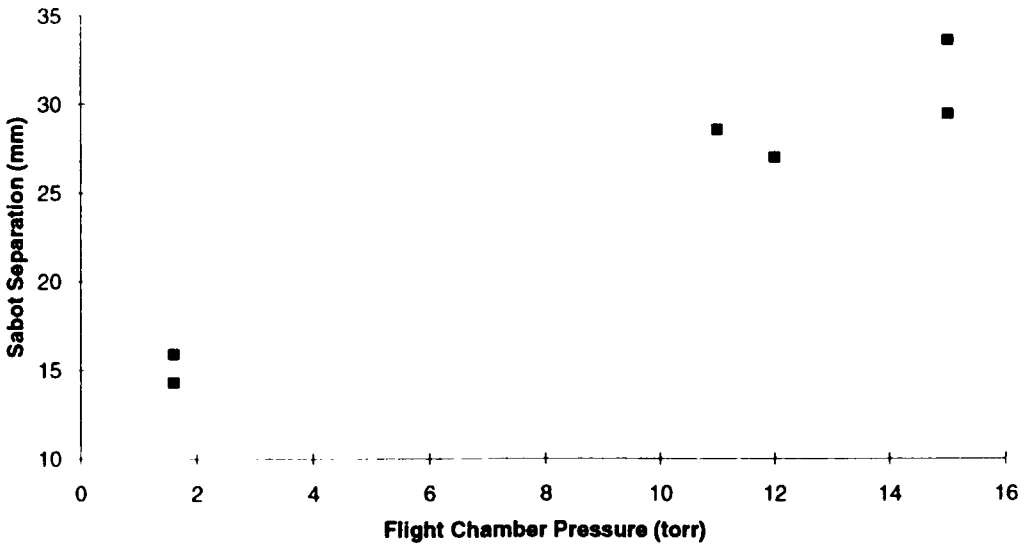


Fig. 8. Sabot Separation vs. Flight Chamber Pressure.

CONCLUSION

A systematic approach to the examination of the performance of the gun and the use of the computer code proved invaluable to the optimization of the micro gun system. The gun system was closely examined to determine which components and firing procedures required change. The code suggested a number of changes in both the gun configuration and loading parameters. These changes led to a gun that can consistently launch 1 mm or smaller aluminum spheres (with masses between 0.3 to 0.9 mg) above 7.5 km/s and nylon, right-circular cylinders (with masses around 3.0 mg) above 9.0 km/s (see Fig. 9). Complex gun systems such as our micro gun or larger two-stage gas guns should be optimized with a combination of experimental and analytical/numerical procedures. The benefits of using a combined approach include greater understanding of the operation and limitations of the system.

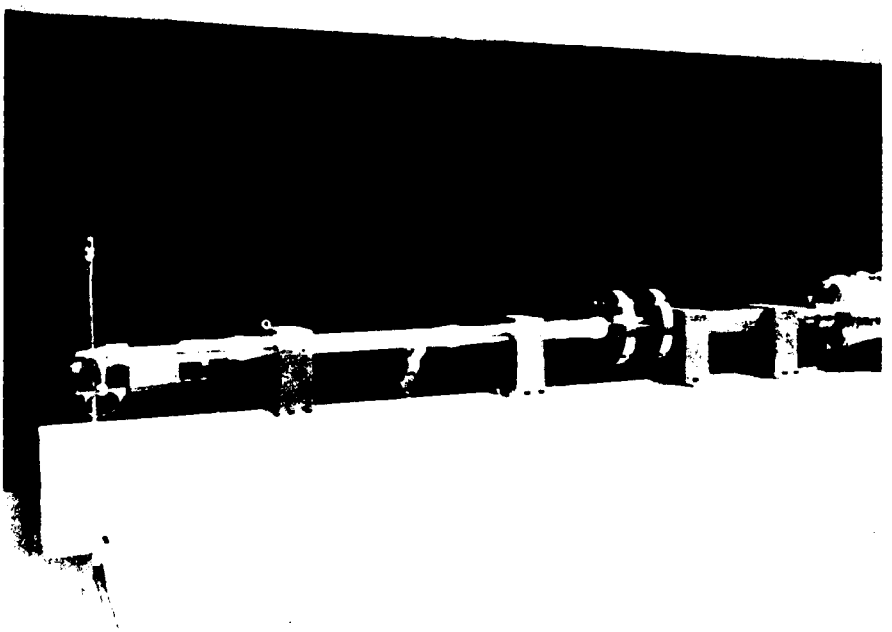


Fig. 9. View of Modified Gun System. (From left to right: Firing Action, Pump Tube, AR Section, Launch Tube, Start of Flight Tube)

REFERENCES

Berggren, R. E. and R. M. Reynolds (1970). The Light-Gas-Gun Model Launcher. *AGARDograph No. 138 on Ballistic Range Technology.*

Charters, A. C. and David K. Sangster (1973). Fortran Computer Program for the Interior Ballistic Analysis of Light-Gas Guns.

Chavez, D. J., C. C. King, and L. J. Linley (1991). A Study to Optimize a 7.6-MM (30-Caliber) Two-Stage Light Gas Gun. *42nd Aeroballistic Range Association Meeting Proceedings.*

Kessler, D. J., R. C. Reynolds, and P. D. Anz-Meader (1989). Orbital Debris Environment for Spacecraft Designed to Operate in Low Earth Orbit. *NASA Technical Memorandum 100471.*

Tullos, R. J. and C. E. Anderson (1990). The Development of a Two-Stage Light-Gas Micro-Gun Facility. *SwRI Final Report.*

Int. J. Impact Engng Vol.14, pp.325–334, 1993
Printed in Great Britain

0734-743X/93 $6.00+0.00
1993 Pergamon Press Ltd

EXPERIMENTAL AND NUMERICAL SIMULATION OF HIGH VELOCITY IMPACT ON STEEL TARGETS

V. HOHLER, H. NAHME, R. THAM, A. STILP, K. WEBER
Y.-K. YEH, J.-P. WANG, T.-S. LEE*

Ernst-Mach-Institut, Eckerstr. 4, 7800 Freiburg, Germany
*Chung Shan Institute of Science and Technology, Lung-Tan, Taiwan 32500, R.O.C.

ABSTRACT

The perforation process of steel plates at normal impact by cylindrical steel fragments together with the debris cloud expansion have been studied in the velocity range 2 - 3 km/s. The fragments have a length-to-diameter ratio of 1.035 and a mass of 51g. Fragment and target materials are 9SMn28 and C45, respectively. Two plate thicknesses of 20 and 30 mm have been tested. These thicknesses are in the order of the penetration depth in the semi-infinite target. In addition the cratering in the semi-infinite target has been investigated. The crater dimensions on the target front side are comparable for both, the plate targets and the semi-infinite targets. The degree of fragmentation in the debris cloud increases with velocity and is smaller in case of the 30 mm target. The ratio of longitudinal to lateral dimensions of the debris clouds is independent of the target thickness, but dependent on the distance from the plate rear side. This ratio increases with distance and converges at larger distances versus nearly hemispherical expansion. A further goal of this paper is the application of a Lagrangian code to the numerical simulation of the impact process in the semi-infinite target. For this purpose the LS-DYNA2D code with a new erosion option has been used. Material input data are the static material properties as well as shock wave data determined from planar impact tests for the steels used here. LS-DYNA2D with its new erosion option can predict in a good agreement the particle velocity history of the planar impact tests and the crater shapes in the semi-infinite target.

NOTATION

b	lateral dimension of debris cloud
c_b	bulk sound speed
c_l	longitudinal sound speed
d, d_a, d_i, d_{i1}, d_{i2}, d_{sp}	damage diameter of craters s. Figs. 8 and 12
d_{min}, d_{max}	damage diameters on witness plate s. Fig. 13
m_p	fragment mass
p	crater depth
pl	plastic (index)
sp	spallation (index)
t	time
tr	true (index)
t_{pl}	plate thickness
u	particle velocity
v_P	impact velocity
v_R	residual debris cloud velocity
x	debris cloud distance from plate
A_5	elongation at fracture
D	fragment diameter
E	Young modulus
G	shear modulus
HEL	Hugoniot elastic limit
HV20	Vickers hardness
L	fragment length
R_{eL}	lower yield strength
R_{eH}	upper yield strength
$R_{p0.2}$	flow stress at 0.2 % strain
R_m	ultimate tensile strength
S	slope of U-u-relation
U	shock velocity
V_T	crater volume
V_P	fragment volume
α	tilt angle
ϵ	strain
ϵ_{el}	elastic strain
ϵ_{pl}	plastic strain
$\epsilon_{pl,f}$	effective plastic strain at failure
ρ	material density
t	Poisson ratio
σ	stress
σ_0	uniaxial yield strength
Γ_0	Grüneisen parameter

INTRODUCTION

In case of hypervelocity impact of spheres, cubes or short cylinder fragments against thin shields, a debris cloud of nearly spherical geometry is formed. A model exists (Swift et al., 1970) that describes this cloud as a symmetrically expanding sphere and all material is assumed to be concentrated at its surface. Experiments done by Piekutowski (1990) show, that mainly the fragment material distribution in the debris cloud can differ from this model and special material distribution patterns are observed for different fragment geometries. At lower velocities the fragmentation in the cloud decreases and the material patterns disappear (Dickinson et al., 1987; Finnegan et al., 1990)). This paper deals with the geometrical features of the debris cloud expansion behind "thick steel shields", impacted normally and flat on by cylindrical steel fragments in the velocity range of 2 to 3 km/s. The fragment material is 9SMn28, the target material C45. The fragments have dimensions of L = 20.7 mm and D = 20 mm. Thick shield targets with t_{PL}/D-values of 1 and 1.5 are considered as plate thicknesses, which are in the order of the penetration depth p in the semi-infinite target. In addition the cratering in the semi-infinite C45 target has been investigated and compared with the damage on the perforated target plates. A further topic of this paper is the numerical simulation of the cratering in the semi-infinite target by the Lagrangian code LS-DYNA2D. In the past simulation of hypervelocity impact by Lagrangian codes often failed. The new erosion option makes such a simulation possible for the Lagrangian code LS-DYNA2D (Hallquist, 1990, 1991; Sewell et al., 1990). Static material properties and the dynamic behaviour under planar shock loading measured with a VISAR for both the fragment and target material serve as input data for the numerical simulation of the cratering. As a test for the code the particle velocity history also has been simulated.

STATIC AND DYNAMIC MATERIAL DESCRIPTION

In order to describe the penetration behaviour by means of the LS-DYNA2D code, static as well as dynamic material properties of both target and projectile material have to be determined.

Static Material Properties

Uniaxial tension tests have been performed at quasi-static strain rates. The test rods were made according to the standard DIN 50125 type A 10 x 50 with smooth cylindrical heads or type B 10 x 50 with threaded heads. A double strain gauge with two crossed 90°-elements served to measure the transverse and axial strain in the elastic regime. The true stress-strain curve was determined by measurements of the actual diameter in the neck of the probe and the radius of curvature of the neck. For this purpose photographs of the plastically deforming specimen were taken. The mechanical data are listed in Table 1.

Table 1. Measured mechanical data of the tested steels

	C45-para.	C45-perp.	9SMn28
R_{eL}/MPa	383	360	-
R_{eH}/MPa	421	375	-
$R_{p0.2}$/MPa	-	-	526
R_m/MPa	673	667	552
A_5/%	33.5	19.5	10.7
E/GPa	208	-	209
G/GPa	80.7	-	81.3
ν	0.288	-	0.285
HV 20		190	185

While the steel quality 9SMn28 was cold drawn and specimens were only loaded in the direction of drawing, the probes of the steel C 45 were made out of rolled plate material. Therefore, specimens of C45 with the load axis parallel as well as perpendicular to the direction of rolling were examined.

The true stress-strain data are fitted very well by the Ludwik equation

$$\sigma_{tr} = K_L \cdot \epsilon_{tr}^n \tag{1}$$

with K_L = 1077 MPa and n = 0.1785 for C45 and with K_L = 641 MPa and n = 0.04383 for 9SMn28, respectively.

Dynamic Material Properties

The dynamic properties of the two steel qualities have been determined by planar plate impact technique in connection with a velocity interferometer VISAR (Barker and Hollenbach, 1965). The steel samples have been mounted in a precisely adjustable sample holder (Fig. 1). The tilt angle α between projectile and target plate

has been measured in previous tests to be $\alpha < 1.5$ mrad. The target and projectile plate were always made of the same material. The time resolution of the VISAR is 2 ns. Due to elastic-plastic material response to shock loading, this shock wave is split into an elastic part, propagating with the longitudinal sound velocity c_l and a plastic part propagating with the shock velocity U. The waves are reflected at the free surfaces of target and of projectile as release waves. Superposition of the waves inside the targets results in tension stress causing spallation. The free surface motion of the target is recorded by the VISAR. Figure 2 shows examples of velocity history curves for the material C45. All curves exhibit the velocity increase due to the elastic precursor followed by the steep velocity increase caused by the plastic wave. After about 3 μs the spall signal is observed. From these curves the Hugoniot elastic limit HEL has been determined according to

$$\sigma_{HEL} = \tfrac{1}{2}\, \rho\, c_l\, u_{HEL} \tag{2}$$

From the velocity decrease u_{sp} of the spall signal the spall strength of the materials is calculated using

$$\sigma_{sp} = \tfrac{1}{2}\, \rho\, c_l\, u_{sp} \tag{3}$$

c_l, σ_{HEL} and σ_{sp} are listed in Table 2.

Table 2. Longitudinal sound velocity c_l, HEL-stress σ_{HEL} and spall strength σ_{sp}

	c_l/m/s	σ_{HEL}/GPa	σ_{sp}/GPa
C45	5828 ± 60	1.81 ± 0.12	1.97 ± 0.28
9SMn28	5818 ± 60	1.4 ± 0.07	1.82 ± 0.08

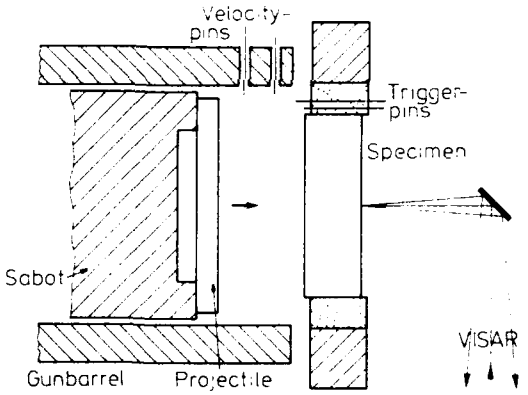


Fig. 1. Schematic experimental setup

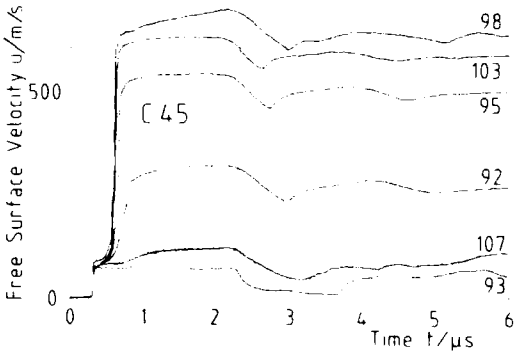


Fig. 2. Velocity history curves for C45-steel

With the known target thickness t_{pl} and the time intervall dt between the arrival of the elastic and plastic wave at the target rear surface the shock velocity U is calculated according to

$$U = c_l / (1 + c_l\, dt/t_{pl}) \tag{4}$$

The maximum stresses inside the target plates have been calculated using

$$\sigma_{max} = \sigma_{HEL} + \tfrac{1}{2}\, \rho\, U\, (u_{max} - u_{HEL}) \tag{5}$$

and the strains are derived from

$$\epsilon_{el} = u_{HEL} / (2\, c_l);\ \epsilon_{pl} = (u_{max} - u_{HEL}) / (2\, U);\ \epsilon_{tot} = \epsilon_{el} + \epsilon_{pl} \tag{6}$$

Finally the strain rates are derived from

$$\dot{\epsilon} = (du_{pl}/dt) / 2\, U \tag{7}$$

with du_{pl}/dt the slope of the velocity curve at its steepest part during the plastic velocity increase. Figure 3 shows the U-u-data, Fig. 4 the σ-ϵ-data and finally Fig. 5 the σ-$\dot{\epsilon}$-data.

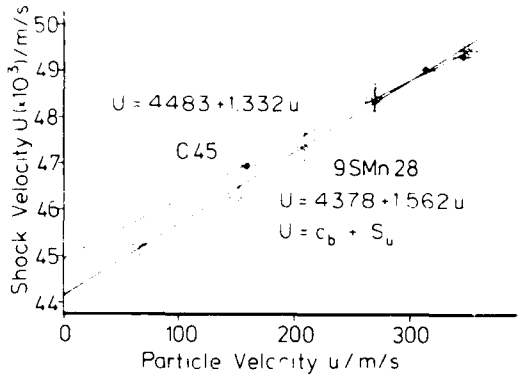


Fig. 3. Shock velocity vs particle velocity

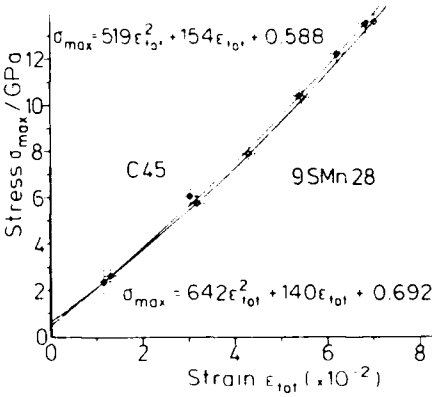


Fig. 4. Stress-strain diagram

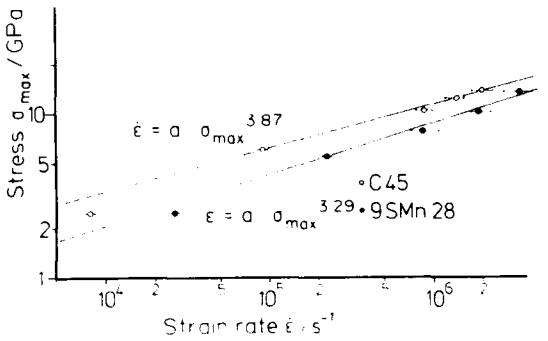


Fig. 5. Stress-strain rate diagram

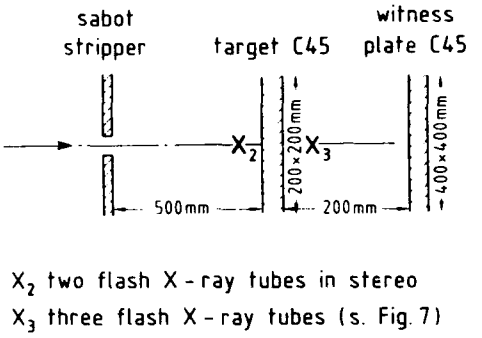


Fig. 6. Test setup

For C45 the slope of the fitted curve in Fig. 5 is in quite good agreement with the $\dot{\varepsilon} = a \cdot \sigma_{max}^4$ rule reported by Swegle and Grady (1985) for homogeneous solids. The deviation in the case of 9SMn28 seems to be based on the more inhomogeneous nature of this steel, that has been observed during metallographic inspection of the samples in recovery experiments.

IMPACT IN SEMI-INFINITE AND SINGLE PLATE TARGETS

Projectile, Targets and Measurement Technique

Cylindrical steel projectiles (L = 20.7 mm, D = 20 mm, material 9SMn28) have been launched by a two stage light gas gun in the velocity range v_P = 2 - 3 km/s, applying the sabot technique. Semi-infinite targets and single plate targets with thicknesses t_{pl} of 20 and 30 mm of steel C45 are impacted at normal incidence. The experimental test setup is demonstrated in Fig. 6. Two flash X-rays control in stereo the yaw angle of the impacting cylinder in front of the target. Yaw angles of $\pm$ 2° have been accepted. In case of plate targets the debris cloud expansion is observed by the flash X-ray arrangement, shown in Fig. 7. One flash intensity is weakened by an Al-absorber and so, two pictures of the cloud taken at different times on the same film can be distinguished. There is a witness plate behind the target to visualize the impact pattern of the debris cloud.

Cratering in Semi-Infinite Targets

Craters in the semi-infinite target are shown in Fig. 8. The crater geometry is roughly hemispherical and the crater lips are broken out. This indicates a relatively brittle behavior of the target steel C45. Some projectile material remains in the crater ground area, the amount of which decreases with velocity. The crater data penetration p, diameter d and volume V_T are plotted in Figs. 9, 10 and 11 versus the impact velocity. The most frequently used normalizations are applied, i.e. p/L, d/D and V_T/V_P. For comparison and to demonstrate in a better way the velocity dependence also penetration data for cylindrical C110W2 steel projectiles (L/D = 1) into semi-infinite RHA targets are given with Vickers hardnesses HV = 230 and 295 kp/mm^2, respectively (Hohler and Stilp, 1977). The data demonstrate the influence of the material hardness. In case of RHA targets there is no breaking out of the crater lips. So d_a does not exist and d_i = d. In the diagram V_T/Vp with the double logarithmic scale, the slope of the curves converges at high velocities roughly versus two, which means proportionality of V_T to the kinetic energy of the projectile 1/2 m_P v_P^2.

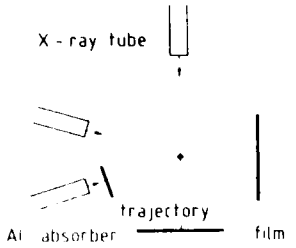


Fig. 7. Flash X-ray arrangement X_3 (s. Fig. 6)



Fig. 8. Craters in semi-infinite C45 targets. The mark indicates the crater depth p. v_p = 2104 m/s, 2478 m/s and 2892 m/s

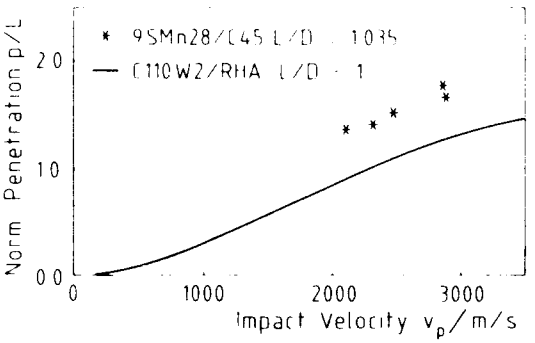


Fig. 9. Penetration into the semi-infinite target

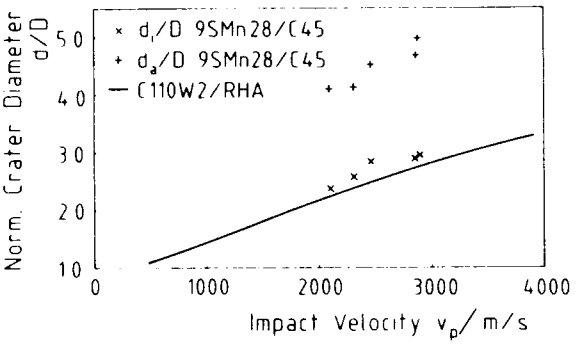


Fig. 10. Crater diameters in the semi-infinite target

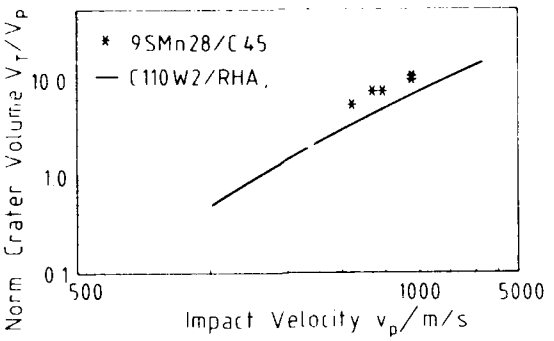


Fig. 11. Crater volumes in the semi-inifinite target

Debris Cloud Expansion Behind Perforated Target Plates

Flash X-ray pictures of the debris cloud expansion are shown in Figs. 12 and 13. The clouds are roughly spherical. The fragmentation increases with velocity and is smaller in case of the 30 mm plates. The damage on the target front is comparable to that on the semi-infinite target. d_{i1}/d_i-data of 0.83 - 0.9 and 0.92 - 1.0 are observed for the 20 and 30 mm target, respectively. This is in agreement with the fact, that the d_{i1}-values are expected to increase with shield thickness and converge for thick shields ($t_{Pl} \approx p$) versus the crater diameter d_i in the semi-infinite target (Vitali et al., 1960). In addition there is a strong spallation damage at the target rear side that confirms the relatively brittle behavior of the C45 steel. The spallation ring limits the boundary line of the cloud near the target rear side. This ring is ejected with a diameter of about $(d_{sp} + d_{i2})/2$. For the inner diameter d_{i2} at the crater exit side $d_{i1} = d_{i2}$ is observed in case of the 20 mm target and $d_{i1} > d_{i2}$ for the 30 mm target. This means a decrease of d_{i2} with plate thickness in the area of thick shields.

Figure 14 shows a sketch of an expanding cloud together with the damage on the witness plate. This damage consists of an inner area of high debris concentration with diameter d_{min} and an outer area of low concentration with diameter d_{max}. It seems that the inner area is impacted by the main part of the debris cloud whereas the particles in the outer area are partly coming from the rear of the cloud. The geometry of a cloud can be characterized by the ratio of distance x and the maximum lateral diameter b (s. Fig. 14). b is only

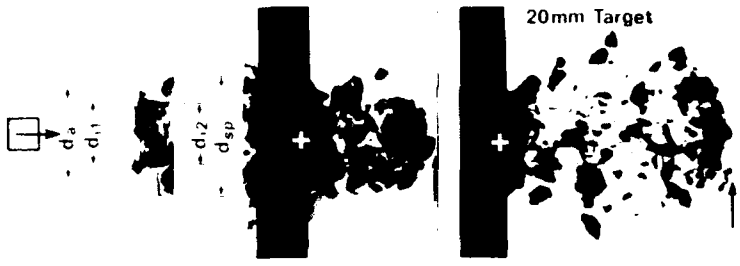


Fig. 12a. x_i = distance between front of the cloud (↑) and target rear side (+); t_i = corresponding time with $t_i = 0$ = moment of impact. $v_p = 1929$ m/s; $x_1 = 82.9$ mm, $x_3 = 143.8$ mm; $t_1 = 100\ \mu s$, $t_3 = 165.6\ \mu s$

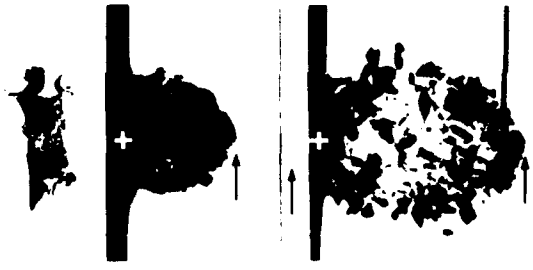


Fig. 12b. $v_p = 2529$ m/s; $x_1 = 65.5$ mm, $x_2 = 99.5$ mm, $x_3 = 123$ mm; $t_1 = 80\ \mu s$, $t_2 = 109.9\ \mu s$, $t_3 = 130.6\ \mu s$

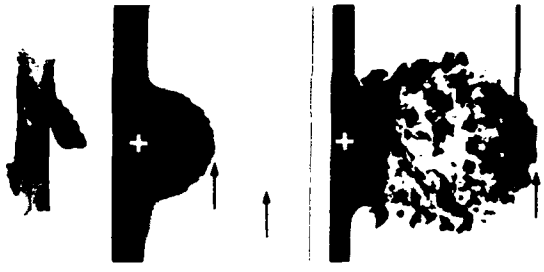


Fig. 12c. $v_p = 2911$ m/s; $x_1 = 44.9$ mm, $x_2 = 76$ mm, $x_3 = 115.1$ mm; $t_1 = 50\ \mu s$, $t_2 = 74.7\ \mu s$, $t_3 = 105.5\ \mu s$

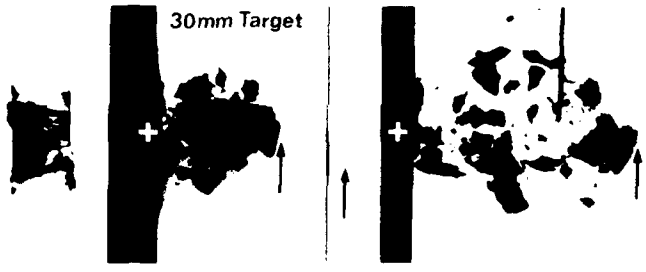


Fig. 13a. $v_p = 1927$ m/s; $x_1 = 70.6$ mm, $x_2 = 107.5$ mm, $x_3 = 133$ mm; $t_1 = 150\ \mu s$, $t_2 = 219.8\ \mu s$, $t_3 = 260.6\ \mu s$



Fig. 13b. $v_p = 2535$ m/s; $x_1 = 70.2$ mm, $x_2 = 112$ mm, $x_3 = 134.4$ mm; $t_1 = 110\ \mu s$, $t_2 = 169.8\ \mu s$, $t_3 = 200.6\ \mu s$

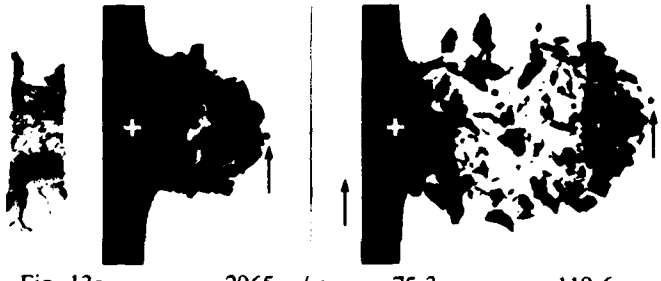


Fig. 13c. $v_p = 2965$ m/s; $x_1 = 75.3$ mm, $x_2 = 119.6$ mm, $x_3 = 156.1$ mm; $t_1 = 90\ \mu s$, $t_2 = 134.8\ \mu s$, $t_3 = 170.7\ \mu s$

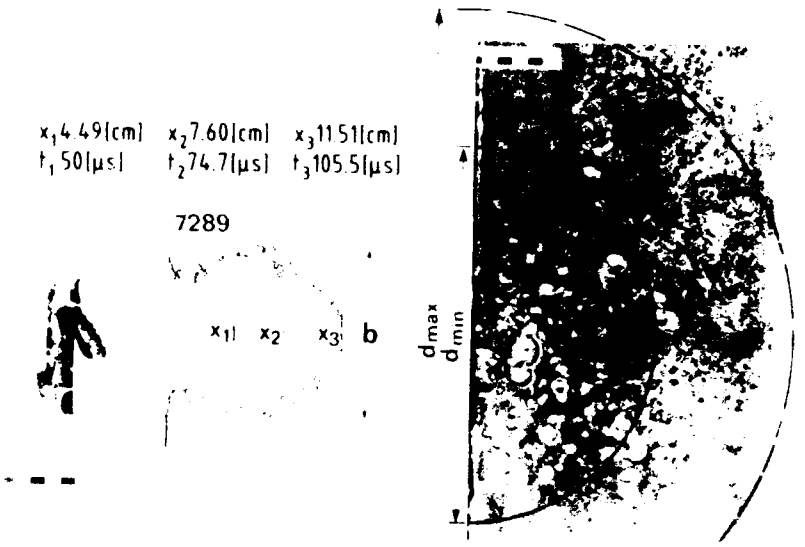


Fig. 14. Debris cloud behind a 20 mm steel target with witness plate

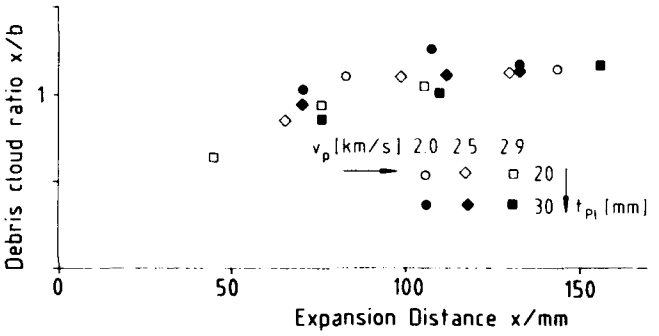


Fig. 15. Debris cloud ratio x/b versus x

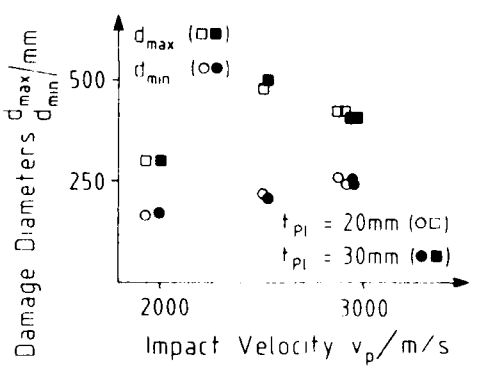


Fig. 16. Damage diameters d_{min} and d_{max} on the witness plates

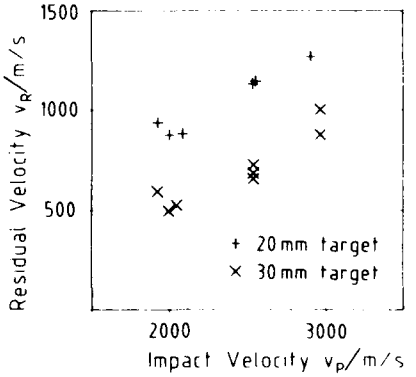


Fig. 17. Cloud front velocity v_R versus v_p

defined for $b \geq (d_{sp} + d_{i2})/2$. For small x-values during early bulging $b = (d_{sp} + d_{i2})/2$ is used. Figure 15 shows x/b as a function of x. x/b increases at small distances strongly with x, becomes one at about x = 4 D and converges at larger distances versus x/b = 1.1 - 1.2. This behavior can only be explained by the fact, that the fragments are not ejected from a central point in the target. The origin of the fragments is spread over the total damage area in the target and causes a dependence of x/b on x near the target rear side. At larger distances this dependence disappears and x/b becomes constant, which means in this case a roughly spherical expansion of the cloud. x/b is nearly equal for both plate thicknesses, tested here, i.e. nearly independent of the residual velocity v_R of the cloud front. Only a small decrease of x/b with v_P is observed. This indicates a weakly growing lateral spread of the clouds with impact velocity. This behavior is confirmed by the plot of d_{min} and d_{max} in Fig. 16. Both parameters weakly increase with v_P and do not depend on v_R. v_R-data are given in Fig. 17.

SIMULATION OF THE CRATERS IN THE SEMI-INFINITE TARGET BY THE LAGRANGIAN CODE LS-DYNA2D

LS-DYNA2D has been used to simulate the cratering in the semi-infinite target. Due to the restriction, LS-DYNA2D cannot be applied to numerical analysis of debris cloud forming. The material property measurements already presented supply the basic material parameters for numerical analysis. LS-DYNA2D is a well-known hydrodynamic Lagrangian finite element code. Based on its contact-impact algorithm, it is able to solve many impact problems. For high strain rate, elasto-plastic deformation topics such as planar impact tests, the code can produce excellent results. However, for hypervelocity impact, the elements are subjected to a large amount of compression and deformation. To get stable results the time step size has to be reduced and so the computer cpu time becomes too long. The new erosion option can overcome this restriction. It defines the overcompressed elements as the failed elements, kills them and neglects their energy. Through the auto-contact algorithm the contact surfaces are maintained. So the time step size and the cpu-time can be controlled by users. However, the neglection of the failed elements can influence the result. A failure criterion is needed to determine which elements should be deleted during computation. In this paper the effective plastic strain $\epsilon_{pl,f}$ at failure is used to be the criterion. But this failure strain is not a physical quantity and cannot be evaluated from laboratory tests. The choice of $\epsilon_{pl,f}$ directly influences the numerical result.

Material Parameters in Simulations

LS-DYNA2D supplies many kinds of material models and equations of state. Here the isotropic-elastic-plastic hydrodynamic material model with the Grüneisen equation of state is used. Based on the laboratory planar impact tests and sound speed measurement the material parameters of Table 3 have been used.

Table 3. Material parameters used in the simulation

	ν	G/GPa	ρ/g/cm^3	σ_{HEL}/GPa	σ_0/GPa	c_h/mm/μs	S
9SMn28	0.259	85.8	7.8	1.4 (Test 102)	0.915	4.378	1.562
C45	0.279	81.3	7.8	1.71 (Test 95)	1.05	4.483	1.332

c_h and S are taken from Fig. 3. G and ν have been derived from measured c_l- and c_h-values and are very close to the static data in Table 1. σ_0 was calculated from HEL-data in Table 2 and a Grüneisen parameter Γ_0 of 2.0 for both steel materials has been inserted.

Simulation Results

By applying LS-DYNA2D, the planar impact tests have been simulated. Examples of the velocity histories of the rear surfaces are shown in Fig. 18. The computed results are fairly in agreement with the experimental curves.

Based on the measured material parameters, the craters in the semi-infinite target have been simulated. Without the erosion option, the computation will not be carried forward. The negative area elements will terminate the computation. By using the erosion option, the effective plastic strain $\epsilon_{pl,f}$ at failure is needed to specify the criterion of the failed elements. Because 9SMn28 and C45 are both similar steels, identical $\epsilon_{pl,f}$-values have been assumed. Beside the choice of $\epsilon_{pl,f}$, the plastic hardening modulus E_h influences the computed crater size. Best results have been found with $\epsilon_{pl,f}$ = 1.8 cm/cm and E_h = 1.8 and 0.0 GPa for 9SMn28 and C45, respectively. 2420 mesh elements and 2586 mesh nodes are used in these finite element analyses. To overcome the instability problem, a scale factor for computed time step size has been used to control the initial computed time step size. 40 μsec after projectile-target contact the projectile's velocity decreased from the initial value v_p to zero and the final crater shape is formed. The calculations were carried out on the Alliant FX/80 super mini-computer. The computed crater shapes are compared with the experimental craters in Fig. 19. The data are listed in Table 4.

Table 4. Simulated and measured crater depth p and crater diameter d_i in the semi-infinite C45-target

v_p/m/s	p/mm		d_i/mm	
	simulation	test	simulation	test
2104	24.0	27.9	44.7	47.2
2478	25.7	31.5	49.7	56.3
2892	27.6	34.2	48.7	58.6

The calculated craters are in a good agreement with the measured craters. Residual fragment material in the crater ground has also been simulated. The breakup of the crater lips cannot be verified. The new erosion option of LS-DYNA2D needs large computer's cpu time, but with the new option the hypervelocity impact problem can be solved by means of a Lagrangian code.

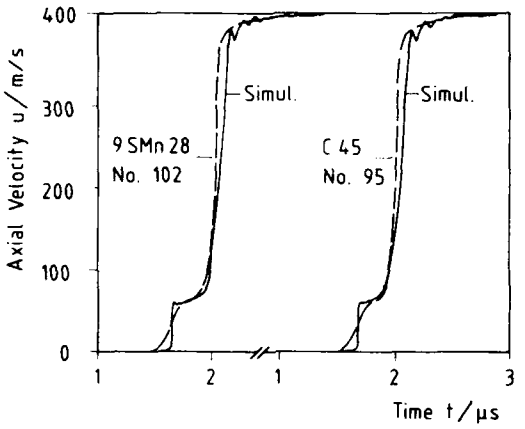


Fig. 18. Simulated and measured velocity history curves

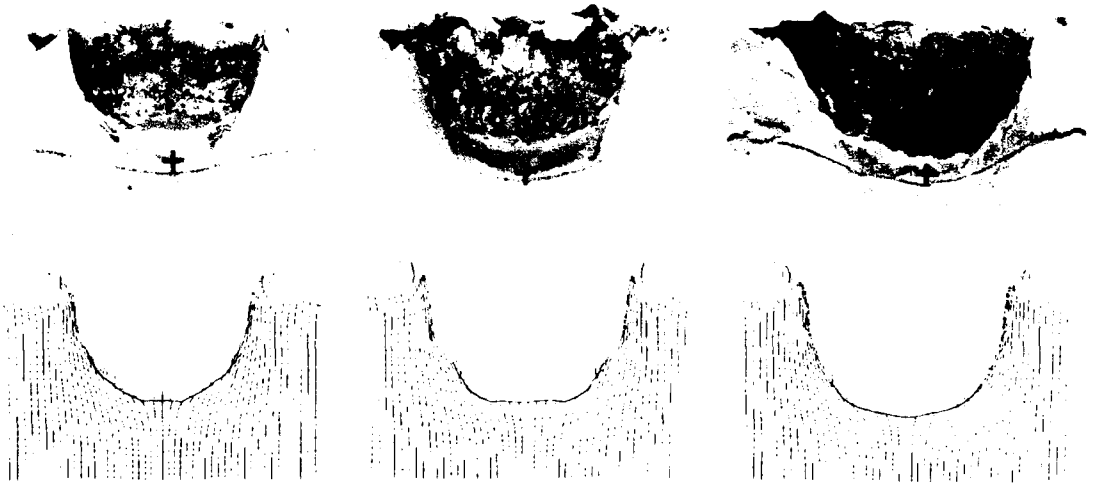


Fig. 19. Measured and simulated craters (v_p = 2104, 2478 and 2892 m/s)

CONCLUSIONS

The cratering in semi-infinite targets and the perforation of thick shields with the debris cloud expansion has been investigated for short cylinder fragments in the velocity range of 2 -3 km/s. Projectile and target materials are steel 9SMn28 and C45,respectively. Thick shields are understood to be targets with thicknesses in the order of the semi-infinite penetration depths. The damage on the target front side is comparable to that on the semi-infinite target. At the beginning of it's formation the debris cloud exhibits a flat shape that is determined by the origin of the cloud material from all over the impact region. During expansion the cloud approaches nearly hemispherical shape. The cratering in the semi-infinite target has been simulated numerically by the Langrangian code LS-DYNA2D with the new erosion option. Input data are static material properties as well as shock wave data obtained from planar impact tests. The simulation of the particle velocity history of planar impact tests and of the crater shapes is in fairly good agreement with the experimental data. Only some minor deviations between experimental result and simulations still have to be improved.

REFERENCES

Barker, L.M. and R.E. Hollenbach (1965). Interferometer technique for measuring the dynamic mechanical properties of materials. *Rev. Sci. Instrum.*, 36, 1617 - 1620.

Dickinson, D.L., J.D. Yatteau and R.F. Recht (1987). Fragment breakup. *Int. J. Impact Engng*, 5, 249 - 260.

Finnegan, S.A., J.C. Schulz and O.E.R. Heimdahl (1990). Spatial fragment mass and velocity distributions for ordnance and ultra-ordnance speed impacts. *Int. J. Impact Engng*, 10, 159 - 170.

Hallquist, J.O. (1990). LS-DYNA2D - An explicit two-dimensional hydrodynamic finite element code with interactive rezoning and graphical display. *Technical Report LSTC Report 1004*, Livermore Software Technology Corporation, Livermore, CA, USA.

Hallquist, J.O. and D.W. Stillman (1991). VEC/DYNA3D USER`S MANUAL - Nonlinear dynamic analysis of structures in three dimensions. *Technical Report LSTC Report 1018*, Livermore Software Technology Corporation, Livermore, CA, USA.

Hohler, V. and A.J. Stilp (1977). Penetration of steel and high density rods in semi-infinite steel targets. *Proc. 3rd Int. Symp. Ballistics*, Karlsruhe, Germany

Piekutowski, A.J. (1990). A simple dynamic model for the formation of debris clouds. *Int. J. Impact Engng*, 10, 453 - 471

Sewell, D.A., A.C.J. Ong and J.O. Hallquist (1990). Penetration calculations using an erosion algorithm in DYNA. *Proc. 12th Int. Symp. Ballistics*, San Antonio, TX, USA.

Swegle, J.W. and D.E. Grady (1985). Shock viscosity and the prediction of shock wave rise times. *J. Appl. Phys.*, 58, 692 - 701

Swift, H.F., D.D. Preonas and W.C. Turpin (1970). Dissection methods for measuring the characteristics of expanding clouds. *Rev. Scientific Instruments*, 41, 746 - 751

Vitali, R., K.R. Becker and R.W. Watson (1960). Perforation of finite targets by high velcity projectiles. *5th Symp. Hypervelocity Impact*, Denver, CO, USA

Int. J. Impact Engng Vol.14, pp.335 - 345, 1993
Printed in Great Britain

0734-743X/93 $6.00+0.00
Pergamon Press Ltd

HYPERVELOCITY IMPACT EXPERIMENTS IN SURROGATE MATERIALS

K. A. HOLSAPPLE

Aeronautics and Astronautics FS-10, University of Washington, Seattle, WA 98195;
Consultant, Boeing Defense and Space Group, Seattle, WA

ABSTRACT

A requirement to perform experiments for hypervelocity impacts in substitute materials arises from the need for data at velocity ranges inaccessible in the laboratory. The role of melt and vapor in hypervelocity shielding designs cannot be assessed with the maximum velocity of approximately 8 km/sec that is achievable. As a consequence, there is interest in performing experiments in materials where the melt and vapor regimes occur at lower velocities.

Such surrogate experiments can in principle be exact. A process in a surrogate material will be dynamically similar to one in the material of interest if the constitutive equations are the same to within three arbitrary scale factors given by the ratios of the natural mass densities, sound speeds and viscosities. Then experiments can be performed at scaled size, velocity and time.

Cadmium and zinc are considered as candidates to substitute for aluminum to allow velocity scaling. Their thermodynamic equations of state are constructed from existing data and the ANEOS analytical equation of state model. They are recast in a scaled form in which the satisfaction of the scaling requirements can be assessed. Reasonable matching is attained. Testing in cadmium at a velocity of *6 km/sec* is approximately dynamically similar to experiments in aluminum at *18.6 km/sec*, a velocity factor of *3.1*.

INTRODUCTION

Hypervelocity impacts occur at velocities unattainable by normal experimental methods. Impacts at velocities up to *15 km/sec* are important for vehicles in the space environment. At these velocities, significant melt and vapor are generated from impacts into typical aerospace structural materials such as aluminum. Unfortunately, the usual experimental techniques have been limited for some time to an upper velocity of about *8 km/sec*.

A natural question arises: what is the possibility of using materials for which melt and vapor occur at lower velocities to test the physics that would occur in aluminum at the higher velocities? Historically, such approaches were based on heuristic arguments. In the early 1960's, cratering experiments were performed into lead targets in order to achieve melt states. Are the results merely qualitative, or are they also quantitative? The theoretical and practical answers to those questions are the basis for this paper.

DYNAMIC SIMILARITY IN EXPERIMENTS

A dynamic process consists of time and space dependent fields for the fields of continuum mechanics. Those fields include, collectively $\{\boldsymbol{x},\boldsymbol{v},\boldsymbol{a},\boldsymbol{F},\rho,\rho_0,\boldsymbol{T},\boldsymbol{b},e,\boldsymbol{L},r,\boldsymbol{q}\}$, where $\boldsymbol{x}$ is the spatial position at time t of the particle occupying $\boldsymbol{X}$ in the reference configuration,

$$\boldsymbol{x} = \boldsymbol{x}(\boldsymbol{X},t) \tag{1a}$$

the tensor $\boldsymbol{F}$ is the material gradient

$$\boldsymbol{F} = \text{Grad}\,\boldsymbol{x}(\boldsymbol{X},t) \tag{1b}$$

of that motion, $\boldsymbol{a}$ is the acceleration vector, $\boldsymbol{v}$ is the velocity, and $\boldsymbol{L}$ denotes the spatial gradient of the velocity vector $\boldsymbol{v}$:

$$\boldsymbol{L} = \text{grad}\,\boldsymbol{v}(\boldsymbol{X},t)\,. \tag{1c}$$

Further, $\boldsymbol{T}$ is the symmetric stress tensor, $\boldsymbol{b}$ is the body force vector, r is the heat supply, ρ is the mass density, ρ_0 is the initial mass density, and e is the specific internal energy. The internal energy is arbitrary to within an additive constant. Here it is assumed that $e=0$ in some initial state.

Consider two processes (perhaps with different materials) where the fields for the first process are related to those of the second in some simple way. A similarity transformation is a relationship between those two different processes which is characterized by simple "scale factor" scalar constants of proportionality for each of the time and space-dependent fields, and for which the three balance equations of mass, momentum and energy are invariant. Suppose the time and space-dependent fields in the first process are given. Then all of the fields in the second process will be denoted by primes, and will be related to those of the first:

$$\begin{aligned}
&\boldsymbol{x}'(\boldsymbol{X}',t') = \alpha_x \boldsymbol{x}(\boldsymbol{X},t) && \rho'(\boldsymbol{X}',t') = \alpha_\rho \rho(\boldsymbol{X},t) && \boldsymbol{T}'(\boldsymbol{X}',t') = \alpha_T \boldsymbol{T}(\boldsymbol{X},t)\\
&\boldsymbol{b}'(\boldsymbol{X}',t') = \alpha_b \boldsymbol{b}(\boldsymbol{X},t) && e'(\boldsymbol{X}',t') = \alpha_e e(\boldsymbol{X},t) && r'(\boldsymbol{X}',t') = \alpha_r r(\boldsymbol{X},t)\\
&\boldsymbol{q}'(\boldsymbol{X}',t') = \alpha_q \boldsymbol{q}(\boldsymbol{X},t)
\end{aligned} \tag{2a}$$

at so-called homologous points and times defined also by constants of proportionality:

$$\boldsymbol{X}' = \alpha_X \boldsymbol{X} \qquad \boldsymbol{x}' = \alpha_x \boldsymbol{x} \qquad t' = \alpha_t t \tag{2b}$$

The derived fields as a consequence of their definitions satisfy:

$$\begin{aligned}
&\boldsymbol{v}'(\boldsymbol{X}',t') = \alpha_v \boldsymbol{v}(\boldsymbol{X},t) = \frac{\alpha_x}{\alpha_t}\boldsymbol{v}(\boldsymbol{X},t) && \boldsymbol{a}'(\boldsymbol{X}',t') = \alpha_a \boldsymbol{a}(\boldsymbol{X},t) = \frac{\alpha_x}{(\alpha_t)^2}\boldsymbol{a}(\boldsymbol{X},t)\\
&\boldsymbol{F}'(\boldsymbol{X}',t') = \alpha_F \boldsymbol{F}(\boldsymbol{X},t) = \frac{\alpha_x}{\alpha_X}\boldsymbol{F}(\boldsymbol{X},t) && \boldsymbol{L}'(\boldsymbol{X}',t') = \alpha_L \boldsymbol{L}(\boldsymbol{X},t) = \frac{1}{\alpha_t}\boldsymbol{L}(\boldsymbol{X},t)
\end{aligned} \tag{2c}$$

There are nine independent scale factor constants in these equations. It is assumed that the material position $\boldsymbol{X}$ is taken as the initial spatial position $\boldsymbol{x}$. Then the two length scalar factors α_x and α_X must be equal, leaving only eight remaining independent constants. In this case the deformation gradients $\boldsymbol{F}$ and $\boldsymbol{F}'$ (and hence strains) are the same at homologous points in the two materials.

Assume that the fields in the first process satisfies the general balance equations of mass, momentum and energy. In order that the second also satisfy the equations these eight scale constants cannot be arbitrary, but five must be determined by the remaining three. That can be easily proved by a substitution of the un-primed fields into the balance equations (Schmidt and Holsapple, 1980). (That also follows from the fact that there are three independent dimensions in the balance equations to which this transformation is to be invariant. (Holsapple,1992).

If one chooses the mass density, velocity and length scales as fundamental then it is necessary that the others satisfy:

$$\alpha_t = \frac{\alpha_x}{\alpha_v} \qquad \alpha_T = \alpha_\rho (\alpha_v)^2 \qquad \alpha_b = \frac{\alpha_v^2}{\alpha_x}$$
$$\alpha_\varepsilon = (\alpha_v)^2 \qquad \alpha_r = \frac{(\alpha_v)^3}{\alpha_x} \qquad \alpha_q = \alpha_\rho (\alpha_v)^3 \tag{3}$$

The two processes are called dynamically similar when these relations hold. Thus, the balance equations of continuum thermophysics are invariant to a similarity transformation determined by three independent scale factors, which can be taken to be those of velocity, mass density and length. In the present case, the interest is in a scaling of the velocity field. The possibility of the invariance of constitutive equations to such transformations is now examined.

GENERAL THERMODYNAMIC CONSTITUTIVE THEORIES

A very general class of material behavior termed "simple materials" has been defined by Truesdell and Noll (1965). Heat conduction can be ignored for the processes of interest here. Then simple materials have constitutive equations given by:

$$\boldsymbol{T}(t) = \mathcal{F}\left[\underset{\tau\ -\infty}{\boldsymbol{F}^{t}(\tau)}, \underset{\tau\ -\infty}{e^{t}(\tau)}\right] \tag{4}$$

where the value of the stress tensor at the present time t is determined by the entire past history over times $-\infty \le \tau \le t$ of the deformation gradient and the internal energy. It is assumed that a stress-free initial state with $\boldsymbol{F}=\boldsymbol{I}$ and $e=0$ is chosen for the reference state.

The variables with units in this equation include the stress tensor $\boldsymbol{T}$ and the internal energy e. The histories have the time variable t. There are then the three independent dimensions of stress, length and time; or, equally, of mass density, velocity and time. Therefore, there must exist a natural material mass density scale ρ_l, a velocity scale c_l and a temporal scale s_l (or a viscous scale η_l) defined by the constitutive equation. Those natural material scales can be used to write (4) in a nondimensional form

$$\frac{1}{\rho_l c_l^2}\boldsymbol{T}(t) = \bar{\mathcal{F}}\left[\underset{\bar{\tau}\ -\infty}{F^{t}(\bar{\tau})}, \underset{\bar{\tau}\ -\infty}{\frac{e^{t}(\bar{\tau})}{c_l^2}}\right], \quad \bar{\tau} = \frac{\tau}{s_l} \tag{5}$$

For processes that satisfy both the transformations (3) and the constitutive relation (5), the natural material mass density, velocity and time scales must be scaled between the experiment and the prototype case, which implies different materials for those processes. Only in the case that one or more material scales is missing is there a possibility of constitutive equation invariance to one or more scale factors of the similarity transformation for a fixed material (Holsapple, 1992).

Consequently, *one cannot perform surrogate tests in the same simple material in the general case.* Further, while many special classes of materials have one or more natural material scales missing, and as a consequence allow surrogate tests in that same material (Holsapple, 1992); no common class of materials has the velocity scale missing for fully dynamic processes. As a consequence, *surrogate materials will be required for velocity scaled experiments.*

In the case that a surrogate material is used for the experiment, the scale factors will be determined from the mass density, velocity, and time natural material scale ratios of the prototype and surrogate material. The experimenter must choose the surrogate material to satisfy the specific constraints and needs for experimentation. (If one or more material scales are not a part of the material constitution, then those missing scales can be chosen at the convenience of the experimenter). Then experiments in that surrogate material are related to the case of interest by the similarity transformation, *if the scaled form of the constitutive equation (5) above is identical for the prototype and surrogate material.* If the material

constitution has all three natural material scales, then the material velocity and time scales will determine the size scale using the first of (3). For example, if a surrogate material velocity scale is a factor of *1/3* compared to the material of the application, and the time scale is the same, then the experiment would have to be conducted at a reduction of *1/3* in the size scale. If there is a velocity but no time scale in the material, the size scale can remain arbitrary.

The practicality of these requirements can be assessed by a consideration of the type of constitutive equations appropriate for hypervelocity impact processes, and by a perusal of the materials available.

CONSTITUTIVE EQUATIONS FOR IMPACT PHENOMENA

Descriptions of materials for hypervelocity impact studies are commonly written in two parts. First, the pressure p (*1/3* of the negative of the trace of the stress tensor), the internal energy and the mass density are related by equations of state of equilibrium thermodynamics:

$$e = \boldsymbol{e}(p,\rho) \tag{6}$$

at each material point and time.

The equation (6) relates three quantities, but there are only two independent dimensions, which can be chosen as any two of stress, velocity and mass density. Therefore, this material has a natural material mass density ρ_l and velocity scale c_l but it has no time scale. There cannot exist any other material constants defined from (6) with units independent from these two. The velocity scale can be taken, for example, as the reference condition sound speed c_0 . The mass density scale can be taken as the initial mass density ρ_0. Other choices may also be made. All other material properties inherent in (6) can be expressed as dimensionless ratios using these two as basic.

The equivalent nondimensional form of (6) is given by using the two natural material scales:

$$\frac{e}{c_l^2} = \phi\left(\frac{p}{\rho_l c_l^2}, \frac{\rho}{\rho_l}\right) \tag{7}$$

where the function ϕ is nondimensional.

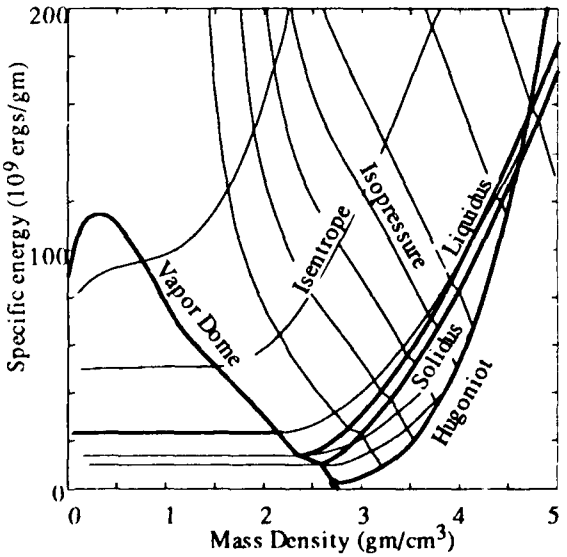


Fig. 1. The Equation of State for Aluminum, with The Hugoniot and Phase Boundaries

This equation of state (eos) description typically includes the different regimes of solid, liquid and vapor. A typical case is shown as Fig. 1, which was generated for aluminum using the ANEOS analytical description (Thompson and Lawson, 1972). (In this plot, the zero energy state is taken at zero temperature, it could be shifted to the atmospheric point at room temperature shown as a circle at the beginning of the Hugoniot by simply subtracting a constant.) The various curves are identified as the melt curves (solidus and liquidus), the vapor dome, the Hugoniot, and various isopressure and isentropic curves.

The second part of the material description is a relation giving the stress deviator tensor as a functional in terms of the past deformation gradient and internal energy histories:

$$\boldsymbol{T}_d(t) = \mathcal{F}\left[\boldsymbol{F}(\tau), e(\tau)\right]_{\tau=0}^{t} \tag{8}$$

At this level of generality, this functional includes theories of nonlinear viscoelasticity, plasticity,

viscosity, fracture and elasticity as special cases. It is common to make the additional assumption that the material is rate-independent, which rules out viscoelastic and viscous effects, but retains still all rate-independent theories of elasticity, plasticity and fracture. Then the equation must be invariant to the time scale factor α_t, but still allows a history dependence where the stress is invariant to how fast that history occurred.

The values of the functional (8) are stresses and the internal energy has the units of *velocity*^{2}. The nondimensional form is obtained using the same two material scales ρ_l and c_l that came from the equation of state relation (6):

$$\frac{1}{\rho_l c_l^2}\boldsymbol{T}_d(t) = \mathcal{F}\left[\boldsymbol{F}(-), \frac{1}{c_l^2}e(-)\right] \tag{9}$$

where the replacement of the time variable by the dashes is meant to indicate the rate independence. Therefore, all stress values determined by this equation (typically including modulii, yield stresses, fracture stresses and so on) are made nondimensional using the same material scales as before. (In most cases, there is no dependence on the past internal energy history, and the dependence on the present internal energy is represented as a dependence on the present temperature. It is easily converted to this form using a specific heat constant.)

Thus, for the equations normally used to describe materials in hypervelocity processes, there are only natural material scales of mass density and velocity. Given a prototype material, and with a choice of a surrogate material, the two material scales (denoted with and without primes) determine two of the scale factors for the similarity transformation by

$$\alpha_\rho = \frac{\rho_l'}{\rho_l}, \quad \alpha_v = \frac{c_l'}{c_l} \tag{10}$$

The remaining problem scales are then given by equations (3). Note specifically that the internal energy scale is the square of the velocity scale. There is no material time or length scale, so that the size scale α_x is entirely arbitrary for tests in this class of problems, and can be chosen for the convenience of the experimenter. For more general material models with a time scale, the experiment would have to be conducted at the size scale determined by the time and velocity scales.

Thus, in summary, *for two different materials to have impact processes that are dynamically similar the scale factors are determined by the ratios of those materials mass density and sound speeds.* It is necessary that, when scaled by those constants, *their entire equation of state surfaces be identical.* In addition, the stress constitutive equations must be invariant to that scaling, so that all stress measures must scale as the pressure, using (10) and the second of (3).

The requirement for equality of the entire scaled eos description has many individual components and measures (indeed, an infinite number). Included are static properties related to derivatives of (6) such as the reference state bulk modulus, sound speed and Grunеisen parameter. Other measures include the shape of the Hugoniot curve, the position and shape of the melt and vapor boundaries, and ad-infinitum. Here, rather than attempting to list any finite number of those individual properties, it will be the entire plot of that eos description that will be considered. Then a few particularly key properties will be identified for quantification.

One might expect that a complete match of an equation of state surface, even crudely, is too much to expect. What physical basis is there to even expect it? Motivation lies in simple models of solid state structure of metals.

A simple model has atoms at the corners of a rectangular three dimensional structure, with interatomic metallic bonds appropriate to the metals considered here. While various metals actually have different crystal structures (face centered cubic for aluminum, close packed hexagonal for cadmium and zinc), the essence of the behavior for any one can be depicted by this simple structure. Then the important physical properties of the structure are the atomic masses, the interatomic spacing and the interatomic forces, which depend on the interatomic spacing and the interatomic potential. An analysis of this model shows

that there is a compressibility modulus determined by the second derivative of the interatomic potential, divided by the interatomic spacing (Ashby and Jones, 1980). The atom masses and interatomic space also give the effective bulk mass density. Thermal agitation of this structure is governed by that same modulus and mass density. All macroscopic properties of this simple model are determined by that modulus and the macroscopic mass density, so that the material behavior is determined by only two fundamental material properties. If the interatomic potentials have the same shape, then second order and nonlinear properties will also match. While different metals have different modulii and mass density, and there are many complexities not addressed by this simple model, one might expect some kind of correlation of material behavior based on only two natural material scales.

In tabulations of the material properties of the elements, certain correlations of this type are also noted. For example, Gschneidner, 1964 discusses a number of correlations of the properties of elements including near constancy of Poison's ratio, relations between the linear and the second order terms of compressibility, correlation of the bulk modulus with the energy of sublimation, constancy of the entropy of fusion, the Slater relation between the compressibility and the Gruneisen constant and the Bragg and Lindeman laws for the heat of fusion. In all of these cases, the properties of the elements point to an underlying simplicity based on only two fundamental material scales for any one material.

In shock wave studies, researchers have also noted a similar fact. Many solid materials have the same equations of state when nondimensionalized with the initial sound speed and the initial density, with only the nondimensional Gruneisen parameter remaining as an additional parameter (see Rae, 1970 for a discussion and references to the older studies). If the Gruneisen is similar between two metals (which is common), then a complete first order match in a scaled sense is obtained.

Finally, there have also been successes in correlating cratering results in a variety of metals using only the mass density and a single stress-valued strength measure (see Holsapple and Schmidt, 1982).

AN EXAMPLE: SUB-VELOCITY SCALING OF ALUMINUM

An examination of the material properties of metals was made, with a comparison to those for the aluminum used for space vehicle shielding designs. The primary interest is in the dynamic properties, with pressures and particle velocities appropriate to impacts at several *km/sec*. Furthermore, it is not the entirety of the equation of state description that will be important in the impact processes of interest. The impact generates a shock wave in the material that propagates into the interior, decays as it propagates, and may reflect from free surfaces. A typical material particle will experience this shock at some time and the pressure will jump to a value along the Hugoniot curve. Particles near the impact point will be subjected to higher pressure than those further away. Behind the shock the process is adiabatic, the pressure decays, and the material particle follows an isentrope in the equation of state surface. Eventually, all material points will return to the ambient pressure.

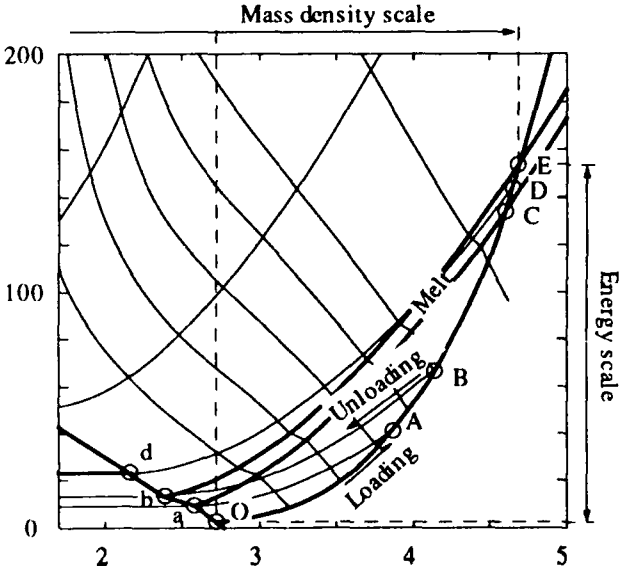


Fig 2. The Region of Interest for Aluminum, Showing the Material Specific Energy and Mass Density Scales

As a consequence, the primary region of concern is the region bounded below by the Hugoniot, and above by the isentrope unloading from the highest pressure generated at the impact point. For aluminum, that is on the order of a few megabars. An expanded view of that region for aluminum is shown in the adjacent Fig. 2.

Several points of particular interest on the Hugoniot curve are also shown on this Fig. The point labeled "A" is the first point where the unloading isentrope back to ambient pressure at point "a" will reach any part of the melt regime. Particles loaded to the point "B" will have complete melt on unloading to point

"b". Point "C" is the point where there will be partial melt at the shock wave, then complete melt will occur on unloading. Material reaching point "D" will vaporize upon unloading to point "d". Finally, material reaching point "E" will have complete melt at the shock, and will vaporize upon unloading.

For aluminum impacts into aluminum, the table 1 quantifies these points. It shows the peak pressure for a one-dimensional impacts as predicted by the ANEOS model, and identifies other significant points of impact velocity and pressure that give various levels of melt and vapor.

Table 1. Pressures generated for aluminum impacts into aluminum

Velocity	Peak Pressure	Notes
5 km/sec	600 kbar	
8 km/sec	1.17 megabar	
10 km/sec	1.65 megabar	
12 km/sec	2.21 megabar	
15 km/sec	3.16 megabar	
20 km/sec	5.13 megabar	
5.6 km/sec	700 kbar	Point A: Some melt on unloading
7.2 km/sec	1.0 megabar	Point B: Complete melt on unloading
10.4 km/sec	1.76 megabar	Point C: Some melt at shock
10.9 km/sec	1.90 megabar	Point D: Vapor on unloading
11.0 km/sec	1.93 megabar	Point E: Complete melt at shock

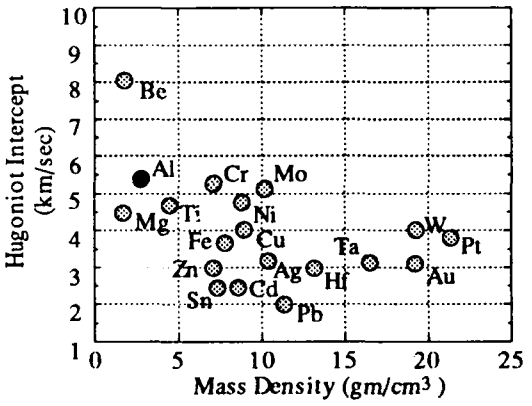


Fig. 3. Wave Speed and Mass Density of some metals.

In order to choose materials suitable for scaling studies, other metals were considered. It is desired to scale the velocity, so that any measure determined from the velocity scale can be examined, including the natural sound speed and any internal energy measures. As a first measure, material wave speeds were examined. Specifically, the zero pressure intercept of the linear fit to the shock velocity-particle velocity Hugoniot was chosen for actual comparison. (If that linear fit were exact, that intercept would be the sound speed.)

That material velocity measure is shown in Fig. 3 plotted versus the mass density for a number of metals. Most metals have a lower wave speed than aluminum. There are several candidates for which the velocity scaling is about the desired factor of *1/2* or so compared to aluminum; including cadmium, gold, hafnium, lead, silver, tantalum, tin and zinc.

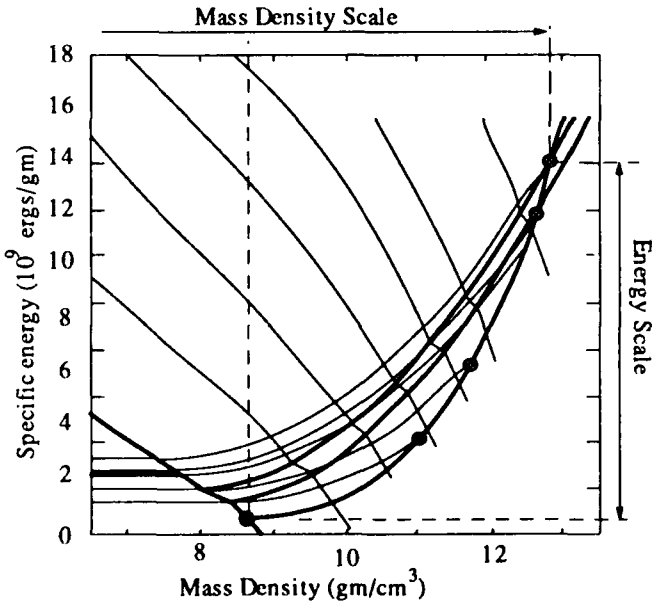


Fig. 4. The Equation of State for Cadmium

Cadmium and zinc were chosen for further study. (Future examination of several others is appropriate, including tin, and silver which has the same crystal structure as aluminum.) Complete three phase equations of state were then generated for those two metals, again using the ANEOS analytical eos package. To make detailed comparisons between these three equation of state descriptions, an expansion of the pertinent region is shown for cadmium in Fig. 4 and for zinc in Fig. 5. The question is whether in a scaled form, the equations of state of either of these metals matches that of aluminum. Using any material velocity scale c_l and a mass scale ρ_l, the

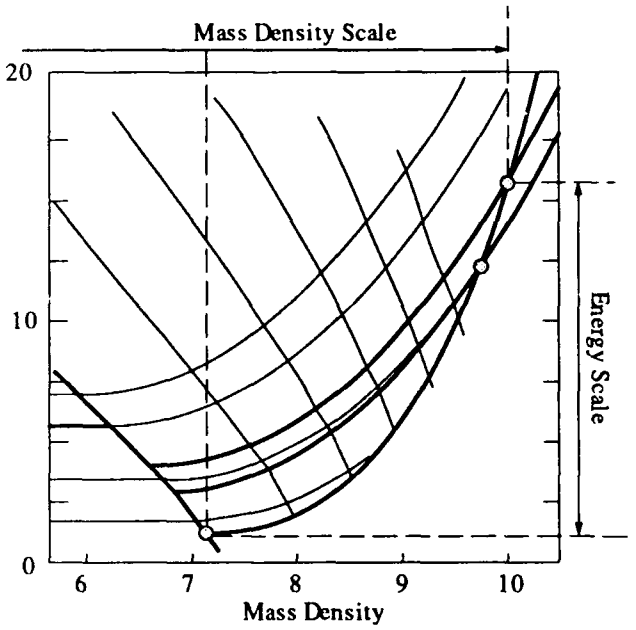


Fig. 5. The Equation of State for Zinc.

scaling of the internal energy and density axes are given by (3) as the ratios of the square of the velocity scales, and the ratio of the mass density scales, respectively.

The important points are those identified as "A" to "E" in Fig. 2, as well as the unloading from those states. In a qualitative way, one can answer the question of the equivalence in a scaled sense by a simple overlay of the figures 2, 4 and 5 as presented, since the actual physical size chosen for the display here was exactly scaled by appropriate factors to match the reference points "O" and the dynamic point "E" where the Hugoniot reaches complete melt. (Note that the absolute value of the internal energy is of no consequence, therefore the matching of the vertical offset for the axes does not matter.) The overlay shows reasonably good agreement of all of the pertinent points.

The scaling determined by that comparison of the reference points and the points "E"; as well as certain other significant points can be determined by a comparison of the ratios of the internal energy (velocity scale squared) and the mass densities at those key points on these figures. An exact match of scaled properties would give a single velocity and mass density scale for all points considered. The actual scale factors based on a number of those points is shown in the Table 2 for the implied velocity scales, and in Table 3 for the implied mass density scales. The static properties are those found in handbooks for properties at one atmosphere pressure in quasi-static processes. The dynamic properties are determined by the Hugoniot curve, which governs the shock propagation in the material.

Table 2. Ratios of Energy Properties for Aluminum, Cadmium and Zinc, and the Resulting Velocity Scale Factors. (Energies are ergs/gm, sound speed in km/sec.)

	Alum	Cad	Zinc	Ratio Al/Cd	Vel. Ratio	Ratio Al/Zn	Vel. Ratio
STATIC PROPERTIES							
Energy to Begin Melt	6.40E+09	7.10E+08	1.60E+09	9.0	3.0	4.0	2.0
Heat of Fusion	4.00E+09	5.50E+08	1.13E+09	7.3	2.7	3.5	1.9
Energy to Begin Vaporization	1.06E+10	1.92E+09	4.59E+09	5.5	2.3	2.3	1.5
Vapor Energy	1.19E+11	1.00E+10	2.00E+10	11.9	3.4	6.0	2.4
Reference Sound Speed	5.3	2.48	3.03		2.13		1.75
DYNAMIC PROPERTIES							
Energy for Some Melt on Unloading (Point A)	3.90E+10	3.90E+09	9.60E+09	10.0	3.2	4.1	2.0
Energy for Complete Melt on Unloading (Point B)	6.20E+10	7.00E+09	1.52E+10	8.9	3.0	4.1	2.0
Energy to Begin Melt at Shock (Point C)	1.34E+11	1.30E+10	1.24E+10	10.3	3.2	10.8	3.3
Energy to Vaporize Some on Unloading (Point D)	1.42E+11	1.20E+10	2.41E+10	11.8	3.4	5.9	2.4
Energy to Completely Melt at Shock (Point E)	1.52E+11	1.50E+10	1.61E+10	10.1	3.2	9.4	3.1

Table 3. Ratios of Mass Density Properties for Aluminum, Cadmium and Zinc.

	Alum	Cad	Zinc	RatioAl/ Cd	Ratio Al/Zn
STATIC PROPERTIES					
Initial Mass Density	2.70	8.648	7.13	3.20	2.64
Mass density at Melt Beginning	2.57	8.42	6.84	3.28	2.66
Mass Density at Complete Melt	2.38	8.02	6.60	3.37	2.77
Mass Density at Vaporization Beginning	2.15	7.73	6.24	3.59	2.90
DYNAMIC PROPERTIES					
Mass Density at Hugoniot Point A	3.87	11.12	9.49	2.87	2.45
Mass Density at Hugoniot Point B	4.12	11.79	9.98	2.86	2.42
Mass Density at Hugoniot Point C	4.61	12.64	9.74	2.74	2.11
Mass Density at Hugoniot Point D	4.65	12.39	10.52	2.67	2.26
Mass Density at Hugoniot Point E	4.69	12.82	10.04	2.74	2.14

With regard to the internal energy and the implied velocity scales in Table 2, it is seen that all energy ratios are much more consistent for the dynamic properties than for the purely static properties. Furthermore, they are all quite different than the simple reference-value sound speeds. Insofar as that sound speed value is determined by the initial slope of an isentrope at the reference conditions, it is not particularly indicative of the global behavior. Thus, it is probably not the best measure to determine the effective velocity scaling. All dynamic energy scales give effective velocity scales of about *1:3.1* for cadmium, with variations within 10%. There is much more spread for zinc, centering around about *1:2.5*.

For the scales of the mass density, again the static are different than the dynamic. The dynamic mass density scales for cadmium are about *2.8:1* compared to aluminum, and are about *2.3:1* for zinc. Again, the zinc is much more variable, and appears not to be as good a choice for scaling experiments for an aluminum prototype.

In summary, with respect to these thermodynamic properties it would appear that cadmium is a good candidate for velocity scaled experiments for aluminum. The necessary curves in the equation of state surface match to within perhaps 10% in the regions of interest.

The second aspect of matched behavior deals with the stress scales that govern the behavior of the deviators in the solid regime. Those include a modulus of elasticity, yield strengths and fracture strengths. (Note however, that as a material particle approaches a melted state, those finite strength effects go away.)

The compressibility in bulk is determined by the equation of state description already considered. The additional shear behavior is determined by that bulk modulus and the Poisson ratio, which is about 1/3 for all common metals. Therefore, with respect to the compressibility aspects in the solid regime, the matching of the equation of state should suffice. With regard to the metals above, the compressibility at the atmospheric pressure state, as determined by the bulk modulus, $K_0=\rho_0 c_0^2$, does not scale particularly well. Both cadmium and zinc have values well above the scale reductions calculated from the mass densities and internal energies. That follows directly from the fact the reference sound speeds also do not scale very well. However, for the total compressibility along points well up the Hugoniot, the matching is quite good.

The scaling of the strength effects is quite a different matter from that of the compressibility. While the crystal structure dominates the thermodynamics and compressibility, the strength of a crystalline solid is never more than a small percentage of that predicted from the crystal structure and interatomic potentials. Instead, it is governed by defects in that crystalline structure such as dislocations and grain boundaries. Therefore, one cannot expect the strength measures between two metals to scale as simply as the behavior based on the fundamental crystalline structure.

However, there are two factors that alleviate this potential problem. First, many aspects of the behavior of processes of interest are not affected by the strength of the metal, particularly those dominated by melt

and vapor where that strength goes away. For example, the spray cloud emanating from behind an impact into a thin metal sheet at high velocity is undoubtedly not affected significantly by any strength aspects of that sheet.

Secondly, in those cases where some strength measure is important, the strength of metals can be tailored a great deal by alloying, annealing and by work hardening without significant effect on the other bulk properties. Aluminum, as an example, comes in alloys and states with the yield strengths varying by over an order of magnitude, but with essentially the same melting point, compressibility and other thermodynamic properties. It is not out of the question that, for phenomena where it is thought to be important, specific alloys or states of cadmium or zinc could be found with the scaled strength measures down the factor of about *3.4* compared to a specific aluminum alloy of interest.

HYBRID SURROGATE MATERIAL TESTING

A hybrid approach to surrogate material testing for space debris shielding for the space station has been advocated by others (Schmidt and Housen,1992). In their approach, there is a replacement of a front shield of aluminum by a cadmium sheet of equal geometry, but the back wall, modeling the space station wall, is retained in its original aluminum thickness and type.

This approach has advantages and drawbacks. It is probable that it is only the back wall material for which any strength measures matter. When using aluminum those strengths clearly are as desired.

The function of the front shield at velocities over about *6 km/sec* is to break up, melt and vaporize an incoming hypervelocity projectile. The net effect is a dispersed spray of fine, strengthless particles hitting the back structural wall over a circular area at high speed. That produces some pressure loading as a function of radial position and time on the back wall. (Any remaining coherent dense particles could create concentrations in that loading.)

With a surrogate cadmium front shield, the theory predicts that the pressure on the back wall will be a factor scaled by the ratio of $\rho_1 c_1^2$, (a factor of *3.4* less) over a period of time scaled by $1/c_1$, (a factor of *3.1* times longer) and with the same radial distribution. That pressure history loading can cause failure by mechanisms of back surface spall due to stress waves and governed by spall fracture strength, by "punch-through" of individual competent particles, or by over-all structural deformation and petalling governed by yield and fracture strengths. Clearly there is little hope of matching failures governed by stress wave magnitudes or punch through with such tests, these threats are substantially reduced in seriousness. However, since the loading times are relatively short compared to structural response times, it may not be the entire pressure history that matters. Instead, it is commonly assumed that such failures can be characterized by the area under the pressure-time history: the impulse (per unit area) of the loading. The impulse scales as the product $\rho_0 c_0$. Serendipitously, that product is almost the same for cadmium and aluminum, the cadmium gives an impulse that is within 90% of that of aluminum. (This value is to first order unity, the scaling of the material behavior is not accurate to any better than perhaps 10%.) Thus, failures by impulsive loading are modeled correctly in this hybrid approach.

What is gained in this hybrid approach is the elimination of the requirement to scale the back wall strength and fracture values, which may be difficult to achieve for cadmium or other surrogate materials. What is lost is the ability in principle to correctly model all types of failure. A separate assumption of the appropriate measure of the loading on that back wall is required to free the experimenter from using the surrogate material for all parts of the problem.

SUMMARY

The use of surrogate materials is necessary for any dynamically similar tests at reduced velocity. In principle such tests can be exact, with a scaling of all velocities, mass densities, and sizes determined from three natural material scales. Using those three material scales to non-dimensionalize, the entire remaining constitutive behavior of the surrogate material must match that of the prototype. For the common material models for hypervelocity impacts, using equilibrium thermodynamics and rate independent stress functionals, there are only mass density and stress scales, so that surrogate material tests at the prototype or any other size scale are possible.

There are simple solid-state models that would predict matching of equation of state descriptions using only two material scales that give some basis for expecting actual first order matching with common metals. The equations of state of both cadmium and zinc do give first-order matching, more so for the overall dynamic properties than for the detailed properties at atmospheric pressure that govern static tests. For cadmium, the properties predict that a test scaled with a velocity scale reduced by a factor of *3.1* and a mass density scale increased by *2.8* will give a good match to tests in aluminum. Any strength scale that is important in the test would have to be reduced by the factor of *3.4*.

With additional assumptions about the governing measure of part of the problem, such as impulsively loaded failures of back walls in shielding designs, the requirement to scale strength values of the back wall may be eliminated by using the actual prototype material.

REFERENCES

Ashby, M.F. and D.R.H. Jones (1980), Engineering Materials 1: An Introduction to their Properties and Applications, *Intl. Series on Mat. and Tech.* **34**, Pergamon Press.

Gschneidner, K.A. Jr.(1964), "Physical Properties and Interrelationships of Metallic and Semimetallic Elements", in *Solid State Physics* **16**, ed. by Seitz F. and D. Turnbull.

Holsapple, K.A. and R.M. Schmidt (1982), "On the Scaling of Crater Dimensions 2. Impact Processes", *J. Geophy. Res., 87, No. B3*, 1849-1870.

Holsapple, K.A.(1992), "On Dynamic Similarity, Scaling and Experiments in Continuum Mechanics", *Submitted for publication.*

Rae, W.J. (1970), "Analytical Studies of Impact-Generated Shock Propagation: Survey and New Results", in High-Velocity Impact Phenomena, ed. by Kinslow, R., Academic Press.

Schmidt, R.M. and K.A. Holsapple (1980), "Theory and Experiments on Centrifuge Cratering", *J. Geophys. Res. 85*, 235-252.

Schmidt, R.M. and K.R. Housen (1992), "Cadmium Simulations of Orbital Debris Shields Performance to *18 km/sec*" (These Proceedings)

Thompson, S.L.and H.S. Lauson (1972), "Improvements in the Chart D Radiation-Hydrodynamics Code III: Revised Analytical Equations of State", Sandia Report SC-RR-710714.

Truesdell, C. and W. Noll (1965) "The Non-Linear Field Theories of Mechanics", in *Handbuch der Physik*, Volume III/3, Springer-Verlag.

Int. J. Impact Engng Vol 14, pp.347 - 358, 1993
Printed in Great Britain

0734-743X/93 $6.00 + 0.00
Pergamon Press Ltd

DIMENSIONALLY SCALED PENETRATION EXPERIMENTS TO EXTRACT PROJECTILE SIZES FROM SPACE EXPOSED SURFACES

FRIEDRICH HÖRZ and MARK J. CINTALA
NASA Johnson Space Center, SN4
Houston, Texas 77058

RONALD P. BERNHARD and THOMAS H. SEE
Lockheed - ESC, C23
2400 NASA Road 1
Houston, Texas 77058

ABSTRACT

Impact experiments were conducted which employed soda-lime glass projectiles (50, 150, 1000 and 3175 μm in diameter; D_p) and aluminum (1100 series) and Teflon (FEP) targets of variable thickness (T; ranging from thick infinite halfspace targets [$D_p/T < 0.1$] to foil thicknesses of a few microns [$D_p/T > 100$]). The objectives of these impact experiments were to determine, at constant impact velocity, the relationships between the diameter of the resulting penetration hole (D_h), the foil thickness (T) and the projectile size (D_p). We found that D_h, and other morphologic features such as rim structures in aluminum or spall phenomena in Teflon exhibit a systematic relationship to the target thickness. This relationship is described by polynomial fits which permit unique solutions for unknown projectile sizes (D_p) from the measurement of T and D_h on space-exposed surfaces.

INTRODUCTION

Reconstructing the size of a projectile from measured crater or penetration-hole dimensions on surfaces tha. were exposed in low-Earth orbit (LEO) is not a straightforward task, yet it is critical to the understanding of the collisional hazards to spacecraft. (*e.g.*, Levine, 1992, 1993). Projectile masses vary by more than ten orders of magnitude, while encounter velocities may range from essentially zero to tens of km/s at arbitrary impact angles, and projectile densities can range from <1 g/cm^3 to as high as 8 g/cm^3 (steel). Even if reasonable average conditions were applied to any set of measured craters or penetrations, substantial uncertainties would still remain in deriving projectile sizes and masses because the critical, initial conditions cannot readily be duplicated in the experimental impact laboratory. As a consequence, an apparent discrepancy exists between cratering and penetration formulas when interpreting the populations of impact features on space-retrieved surfaces.

Specifically, when extracting projectile diameters from craters and penetrations on the same 125 μm thick aluminum foils from the Solar Maximum Mission (SSM), the resulting projectile size frequencies display a pronounced offset at the transition from cratering to penetration regimes (Warren *et al.*, 1989). Similarly, Humes (1991) reported internal inconsistencies between cratering and penetration formalisms during his analysis of Long Duration Exposure Facility (LDEF) surfaces. Note that both

investigations refer to aluminum targets, whose impact behavior has been extensively investigated (*e.g.*, Carey *et al.*, 1985; Cour-Palais, 1987; Herrmann and Wilbeck, 1987).

The objective of this study was to experimentally determine the relationship between the penetration-hole size (D_h) and the impactor diameter (D_p) by employing targets of thickness (T) that systematically ranged from infinite halfspace ($D_p/T << 1$) to thin films ($D_p/T > 100$). This wide range in target thickness not only permits investigation of the transition between the cratering and penetration regimes, but it also enables characterization of the target thickness which yields $D_h = D_p$. Thus, such an experimental approach corresponds to satellites/instruments in LEO which typically expose materials of fixed thicknesses and which encounter an enormous range of projectile sizes, as evidenced by substantial populations of (small) craters and (relatively large) penetration holes on many space-exposed surfaces (*e.g.*, Warren *et al.*, 1989; See *et al.*, 1990; Levine, 1992, 1993).

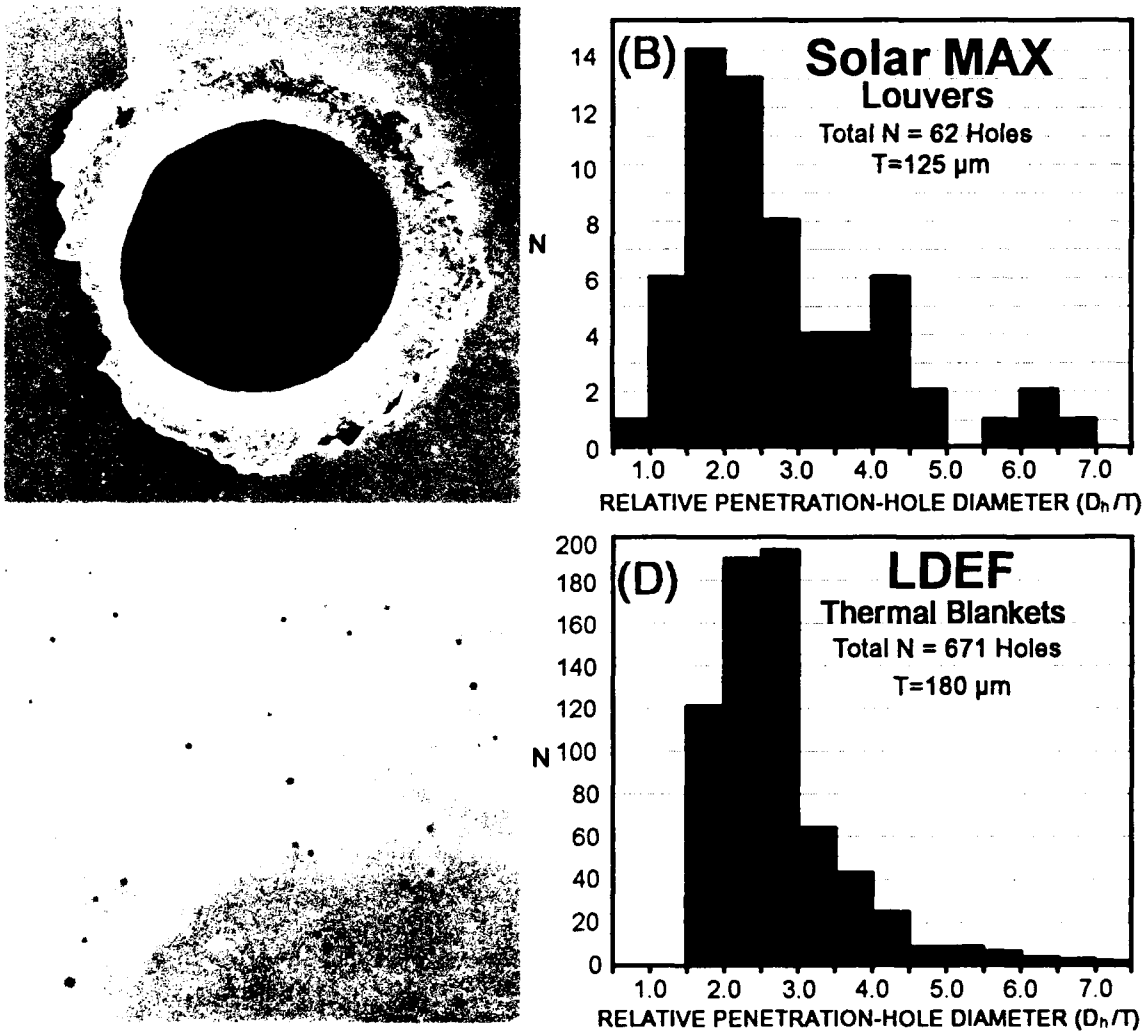


Fig. 1. Typical results from SMM (Warren *et al.*, 1989) and LDEF (See *et al.*, 1990). (A) Penetration of a 125 µm aluminum louver from SMM (D_h = 435 µm), (B) Frequency distribution of normalized (D_h/T) penetration-hole diameters in the SMM louvers, (C) LDEF thermal blanket. Each black dot represents a penetration, but the actual penetration-hole size is typically order of magnitude smaller than the low-albedo ring features; field-of-view = ~35 cm (D) Frequency distribution of penetration holes >300 µm in all LDEF blankets.

EXPERIMENTS

The rationale for selecting the specific materials employed in this study (*i.e.*, annealed, 1100 aluminum and FEP Teflon as targets and soda-lime glass spheres as projectiles) is as follows:

Aluminum thin films, ~500-1000 Å thick, are being contemplated for use on future dust-collection instruments on the Space Station *Freedom* (CDCF, 1990). However, various aluminum materials have already been exposed and returned from space (*e.g.*, Warren *et al.*, 1989; McDonnell, 1991; Humes, 1991; Hörz *et al.*, 1992a; See *et al.*, 1992). Fig. 1a displays a typical penetration feature on a SMM aluminum louver, while Fig. 1b shows the frequency of the entire population of penetration holes observed on all louvers, where the hole diameter has been normalized to the target thickness (125 μm; Warren *et al.*, 1989).

On LDEF, a specific type of protective thermal blanket covered ~20 m^2 of surface area and represents, next to the aluminum surfaces on LDEF, the most substantial opportunity to characterize the cumulative particle environment in LEO at constant target properties (*e.g.*, See *et al.*, 1990). These blankets consisted of an ~125 μm thick outer layer of Teflon, backed by vapor-deposited metal mirrors, organic binders and thermal protective paint resulting in a total blanket thickness of ~180-200 μm. We are aware that pure FEP Teflon, as used in this study, may be a somewhat deficient analog to these composite LDEF blankets, but we consider it suitable in order to obtain first order insights into Teflon's behavior. Fig. 1c shows a typical LDEF thermal blanket containing numerous penetrations, while Fig. 1d plots the measured frequency distribution of all penetrations >300 μm in diameter (See *et al.*, 1990), again normalized to target thickness (180 μm).

The use of soda-lime glass projectiles relates to the dominance of natural silicates in LEO, at least for projectiles 10 to 500 μm in size, as demonstrated by the chemical analysis of projectile residues in LDEF impact craters (Bernhard *et al.*, 1992). Such projectiles also reflect our primary interests which are the development and analysis of cosmic-dust experiments. Within the context of the hypervelocity particle environment in LEO, our silicate impactors also provide complementary and useful contrast to most of the previous and ongoing penetration studies which generally employ metal projectiles.

An important part of understanding the wide diameter range of (LEO) penetrations in targets that vary from microns to millimeters in thickness relates to an understanding of the effects of absolute projectile size. Cour-Palais (1987) demonstrated that there is a modest dependence of crater diameter (D_c) on absolute projectile size (D_p). Similar dependency may exist for penetration holes, and is the reason why glass spheres 50, 150, 1000 and 3175 μm in diameter were employed.

EXPERIMENTAL RESULTS

Projectile velocities for the aluminum-foil experiments ranged from 5.8-6.2 km/s, with the majority clustering between 5.9 and 6.1 km/s; we refer to them as representing a nominal 6 km/s. Similarly, the Teflon-experiment projectile velocities ranged from 6.2-6.5 km/s, with the majority clustering at a nominal 6.3 km/s. All experiments were performed with a 5 mm light-gas gun at normal incidence to the target surface.

Morphologic Trends in Aluminum Targets

The types of craters and penetration holes produced by soda-lime glass projectiles in aluminum targets are illustrated in Fig. 2. Each vertical column is at the same scale, given at the bottom. Each column is arranged such that the "standard" crater (infinite halfspace target) is at the top, with target thickness decreasing downward. The actual target thickness is identified for each image/experiment by the normalized thickness ratio D_p/T. When comparing absolute and relative dimensions a convenient, internal scale is presented by the penetration hole in the thinnest foil (bottom), which approaches or corresponds to the condition of $D_h = D_p$. For clarity, not all experiments are illustrated.

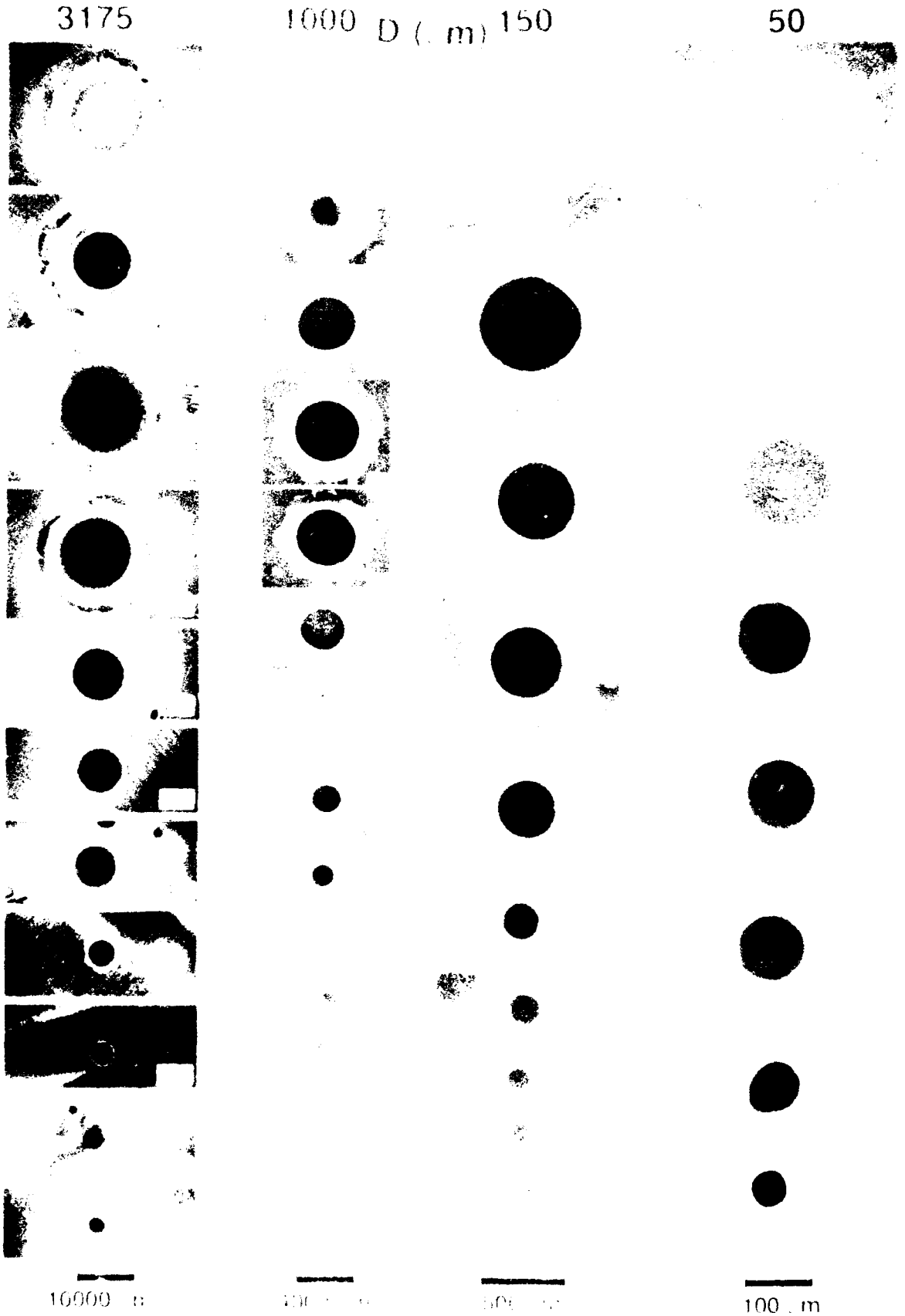


Fig. 2. Craters and penetration holes resulting from glass projectiles in increasingly thinner aluminum targets of normalized thickness D_p/T (given for each frame). Note: $D_h = D_p$ at $D_p/T > 50$

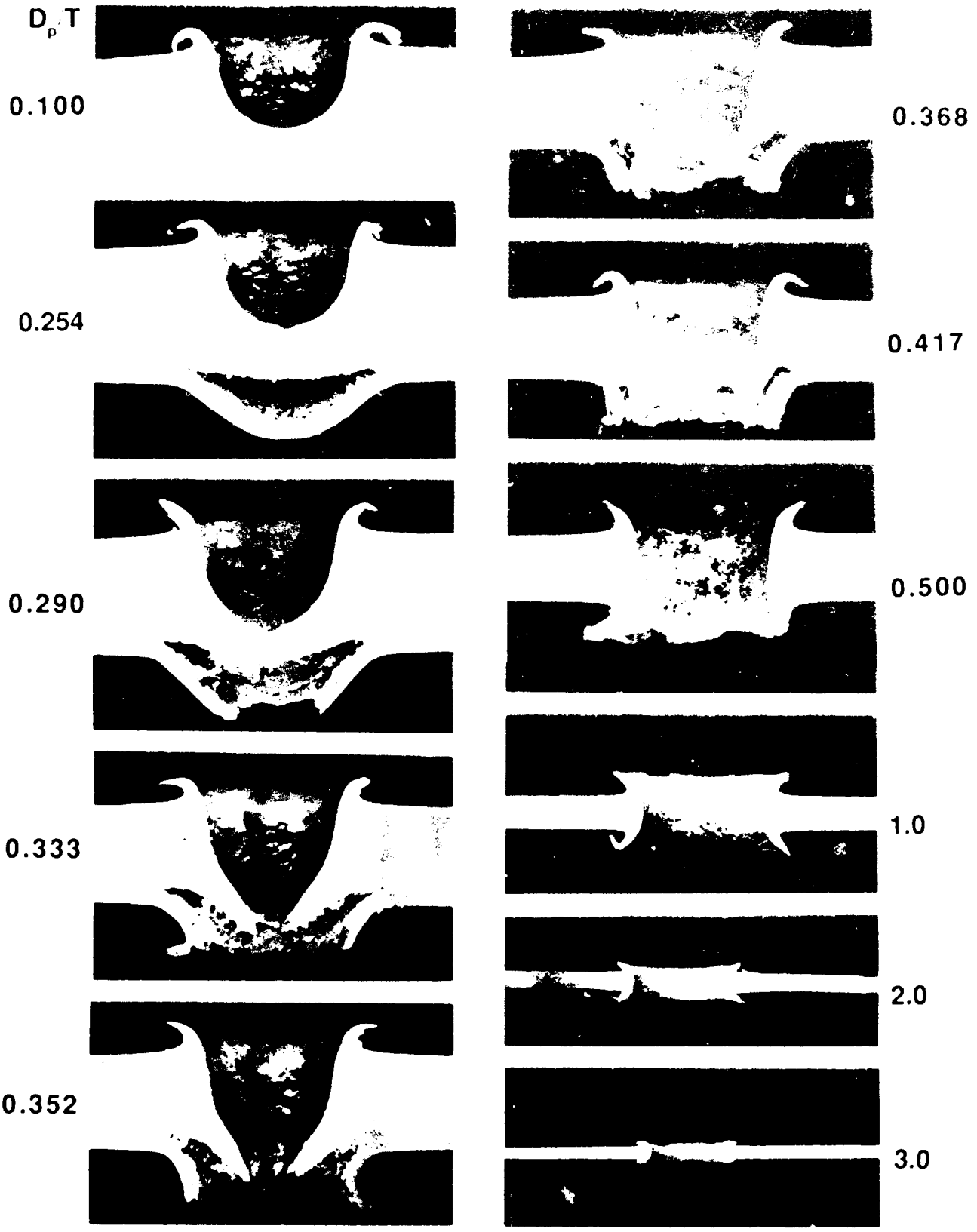


Fig. 3. Cross-sections of aluminum targets penetrated by 3175 μm glass projectiles traveling at ~6 km/s. $D_p/T = 1$ provides convenient comparison of relative and absolute dimensions because $T = D_p$.

It can be seen in Fig. 2 that craters and penetration holes found in massive targets ($D_p/T < 1$) possess typical dimensions measured in multiple projectile diameters. As increasingly thinner targets are encountered, the hole diameter progressively shrinks until sufficiently thin foils permit D_h to approach D_p; this typically occurs at $D_p/T > 50$. The transition from cratering to penetration events is gradual and systematic, as are other morphologic changes. This systematic behavior must be viewed as a continuum. This conclusion is reinforced when examining the penetrations in cross-section, as summarized for the aluminum targets and the 3175 μm projectiles in Fig. 3.

Note in both Figs. 2 and 3 that the diameters of the craters and penetrations, if measured at the initial target surface, remain essentially constant at $D_p/T < 1$. The penetrations resemble truncated cratering events in that the flow of the target material at or close to the front surface responded in a fashion typical for cratering. If anything, the diameters measured at the very target surface are subtly larger for the penetrations at $D_p/T < 1$ compared to the standard crater diameter, suggesting somewhat increased lateral flow and deformation. While these crater diameters remain relatively constant, the diameter of the penetration hole (see Fig. 3) undergoes a dramatic change from sizes smaller than D_p, at or close to the ballistic limit ($D_p/T = 0.3$), to dimensions measured in multiple projectile diameters at $D_p/T > 0.35$. Figure 3 also shows that the depth of the crater increases when incipient spallation occurs and that there are systematic changes in the slope(s) of the crater walls until $D_p/T > 0.5$ is reached.

Observations of the witness plates associated with these experiments (Hörz *et al.*, 1992b) corroborate the view that these penetrations represent truncated cratering events because no projectile material reaches the witness plate until $D_p/T > 0.6$-0.7. Without exception, this projectile material is molten and deposited on the witness plate in the form of subtle, webb-like stringers. These melt stringers appear for the first time at target thicknesses which are thinner than the depth (P) of the standard crater (*i.e.*, at $T < 0.8P$). This implies that in spite of the gaping holes at $D_p/T = 0.4$ to 0.6, all of the projectile is entrained in cratering-related flows, and is quantitatively ejected uprange.

Note from Figs. 2 and 3 that it takes $D_p/T > 1$ to generate penetration holes that are smaller in diameter than the standard crater, regardless of where the actual hole diameter is measured (at the target surface or at the narrowest points). This decrease in D_h is systematically related to T until a threshold foil thickness is reached where $D_h = D_p$ (see actual measurements below). We do not have a good physical model for the small penetrations in thin targets ($D_p/T >> 1$). Obviously, progressively thinner targets will lead to increasingly shorter arrival times of the rarefaction waves from the rear surfaces (*e.g.*, Gehring, 1970). The rarefaction waves will terminate any incipient cratering flow at increasingly earlier times, thereby arresting radial crater growth.

The morphology and dimensions of the crater lips develop in a fashion that is systematically related to the target thickness as well. The lip diameter, measured from crest to crest (Figs. 2 and 3), can be modestly larger at $D_p/T < 0.5$ than that of the standard crater, yet it systematically decreases with decreasing foil thickness. Furthermore, the average extent of the entire lip (D_l; average periphery to periphery diameter accounting for the lobate nature of the lip by multiple diameter measurements) systematically decreases as T decreases, as does the height of the lip above the original target surface. In summary, the detailed lip morphology is also a sensitive indicator for scaled dimensions (D_p/T) and is an auxiliary criterion to aid in solving for D_p (Hörz *et al.*, 1992b).

Finally, Fig. 2 illustrates that the above described morphologic continuum applies to impact events of dramatically different sizes, having employed projectiles that differed in diameter by almost two orders of magnitude. These observations provide substantial confidence in the linear scaling of dimensional relationships to either smaller or larger projectile sizes and/or to thinner or thicker targets. In detail, and as described in Hörz *et al.*, (1992b), the crater diameters at very small scales (D_p = 50 μm) seem relatively smaller than those produced by millimeter-sized impactors, consistent with the observations of Cour-Palais (1987). In contrast, the penetration holes produced in very thin foils ($D_p/T > 20$) by 50 μm impactors are subtly larger than their counterparts from large projectiles. Thus, there is evidence of subtle, scale-dependent phenomena in our aluminum penetration experiments (Hörz *et al.*, 1992b).

Morphologic Trends In Teflon Targets

Teflon responds to shock stresses largely by brittle failure yielding crater and penetration-hole morphologies that differ dramatically from those of the 1100-series aluminum. Fig. 4 summarizes the crater and penetration-holes produced by ~175 and 1000 μm diameter glass projectiles into Teflon. A few experiments which employed 150 μm diameter projectiles exist, but are not illustrated. Fig. 5 shows the cross-sections of penetrations in Teflon targets resulting from 3175 μm glass projectiles. Akin to Figs. 2 and 3, the penetration holes in the thinnest targets of Fig. 4 and the $D_p/T = 1$ case in Fig. 5 represent convenient scales for projectile dimensions.

Referring to Figs. 4 and 5 we observe that Teflon undergoes significant spallation on both the front and rear surfaces. Furthermore, the "standard" crater in Teflon (*e.g.*, $D_p/T = 0.125$ for $D_p = 3175$ μm) is difficult to precisely define because of the highly irregular fashion in which Teflon tends to fail. The walls and bottoms of the craters are formed by highly irregular protrusions that are associated with a substantial set of radial cracks which approach a crater radius in length. Nevertheless, the overriding impression from Figs. 4 and 5 is again one of continuous, systematic and gradual changes of all morphologic elements with decreasing target thickness. The general conclusion seems inescapable that penetration holes are systematically related to D_p/T, no matter what target material, and that they form a morphologic continuum over a wide range of D_p/T, including a smooth transition from cratering to penetrations in massive targets.

The geometry of the rear-surface spall zone in Teflon is fairly constant for the more massive targets (see Fig. 5). For experiments with $D_p/T < 0.75$, the spalls appear to truncate a full crater at increasingly shallower depth (relative to the target's front surface). Note that most of the penetrations have wedge-shaped cross-sections. The crater walls are prominent at $D_p/T < 0.25$, yet they are gradually being replaced by free surfaces associated with spall processes emanating from the rear ($D_p/T > 0.25$-0.5). Apparently, an increasingly larger fraction of the total target cavity is being generated by the removal of material from the rear as D_p/T increases from ~0.2 to 0.5. These observations extend our general view that penetrations of massive targets reflect truncated cratering events.

Referring to Fig. 4 we also note that the average diameter of the front spall zone (D_s; obtained from multiple measurements of their irregular, scalloped diameter) stays relatively constant at all $D_p/T < 0.75$, resembling that of the standard crater. Again, similar to the crater lips in aluminum, subtle increases of D_s seem typical for penetrations at $D_p/T = 0.15$-0.5. Substantial decreases of D_s occur at $D_p/T > 0.75$ which is simultaneously accompanied by a rapid decrease of relative spall width (D_s/D_h). Rear-surface spallation processes are already occurring in the Teflon targets at $D_p/T = 0.15$, and are substantial at $D_p/T > 0.2$. Note in Fig. 5 that at $D_p/T = 0.2$-0.5, the rear-surface spallation can be substantially more pronounced than that associated with the front side. Specifically, over a relatively narrow range of target thickness ($D_p/T = 0.2$-0.3), the rear-surface spall diameters are substantially larger than D_s and go through a maximum at $D_p/T = 0.2$-0.3. Furthermore, the rear-surface spallation at $D_p/T > 0.5$-0.7 is so prominent that it controls the physical size of the penetration hole, producing a distinct maximum for D_h at $D_p/T > 0.6$-0.7, a phenomena which was verified and reproduced by a number of duplicate experiments.

CRATER AND HOLE DIAMETER MEASUREMENTS

Detailed measurements of the crater diameter (D_c, wall intercept with the target surface), the rim-diameter (D_r, rim-crest-to-rim-crest), the of lip width (D_l, average radial extend of lobate and irregular periphery of lips) and the hole diameter (D_h, smallest physical hole size) for all aluminum targets are described by Hörz *et al.* (1992b). Comparable data was obtained for the Teflon targets (*e.g.*, D_c, D_h, D_s). However, we only present D_h measurements below, because they represent the most prominent feature of thin targets and because they frequently constitute the only measurement obtained in systematic fashion from space-exposed surfaces (*e.g.*, See *et al.*, 1990).

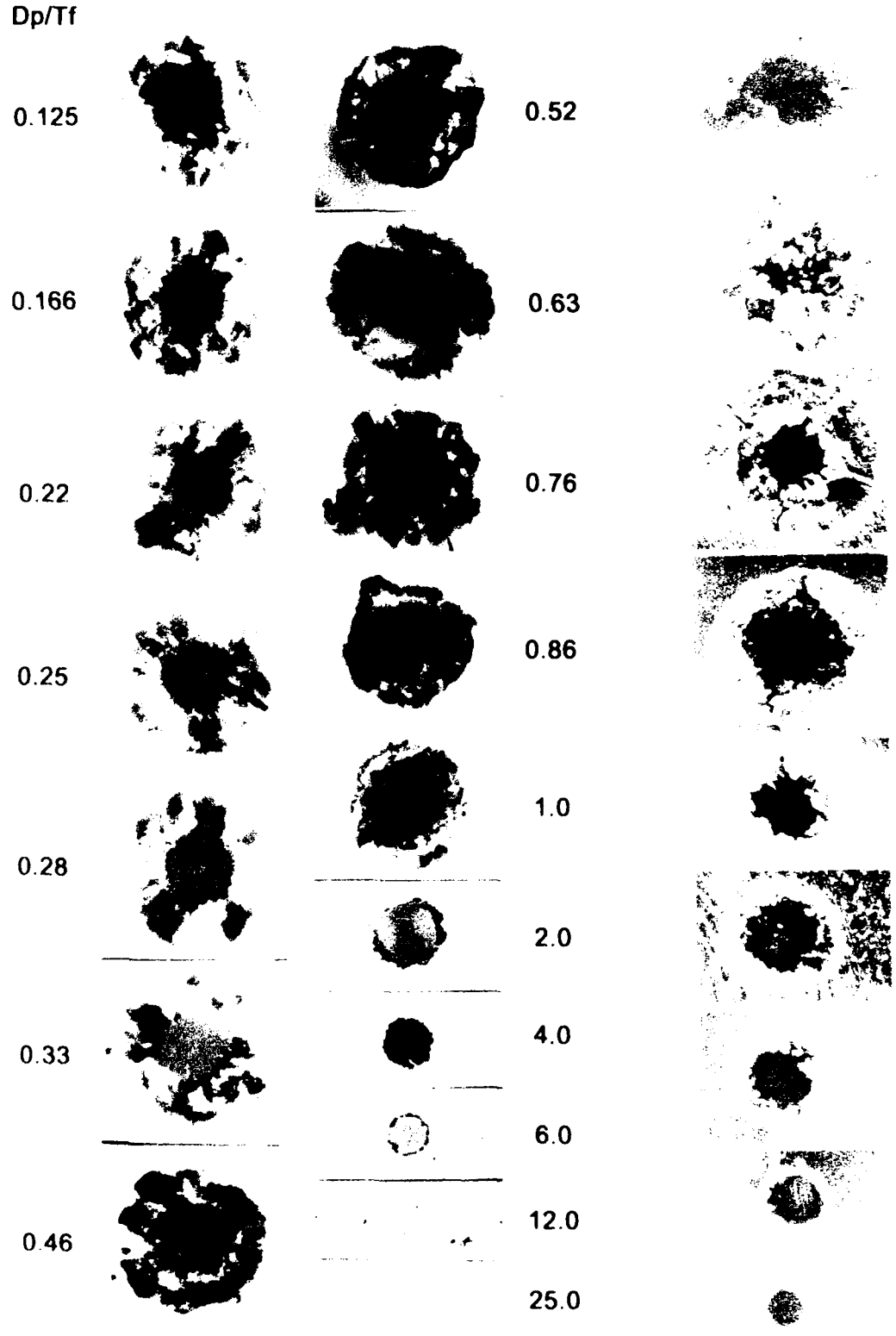


Fig. 4. The morphology of craters and penetration holes in Teflon targets with relative target thickness (D_p/T) systematically decreasing in vertical order. (Left and middle: D_p = 3175 μm at ~6.3 km/s; right: D_p = 1000 μm at ~5.9 km/s; $D_h \equiv D_p$ for the thinnest foils).

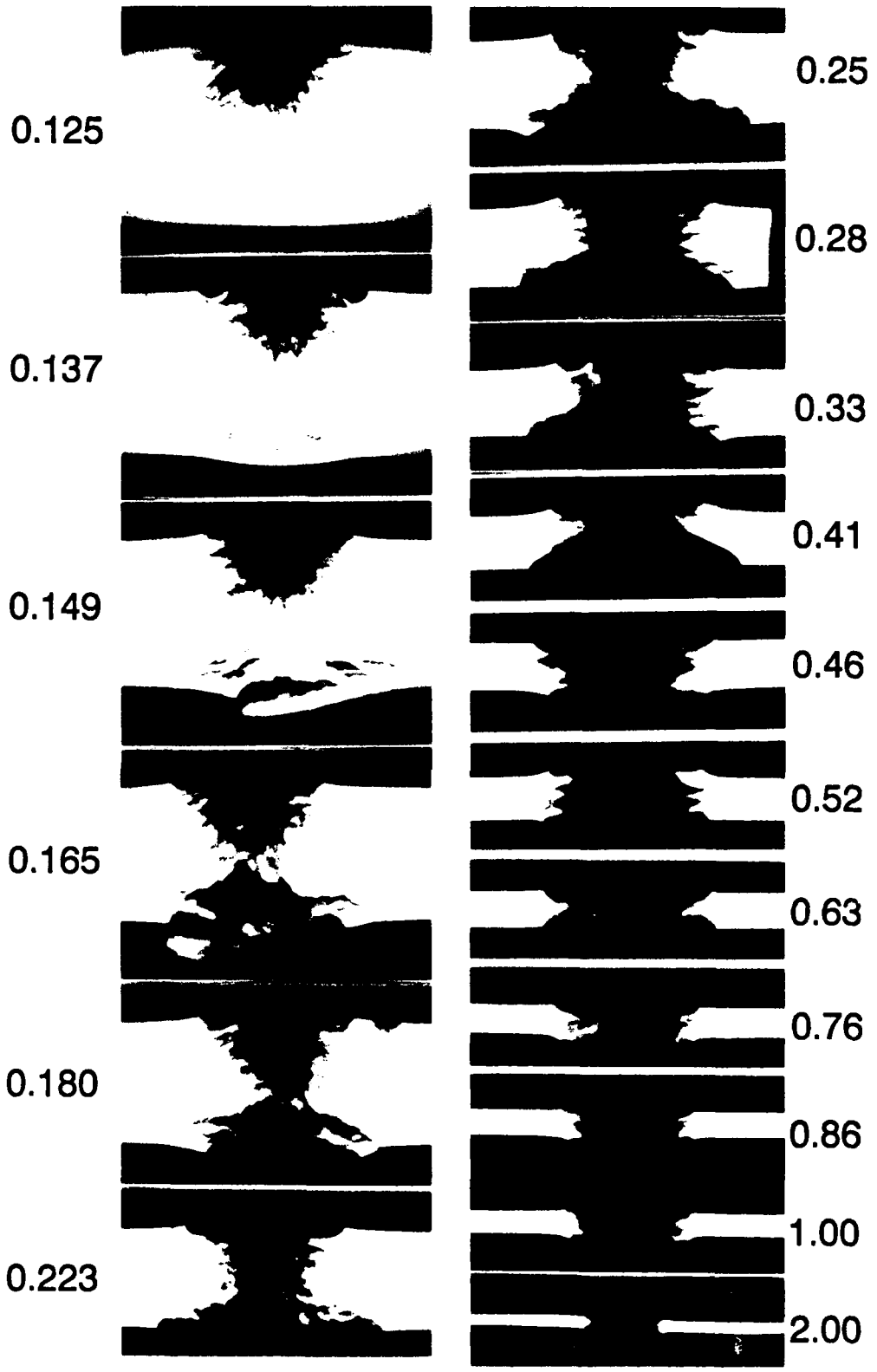


Fig. 5. Cross-sections trough Teflon targets which were impacted with 3175 μm glass projectiles traveling at ~6.3 km/s.

As can be seen in Fig. 6, the size of the penetration hole in both materials is systematically related to the target thickness. In fact, the plot is purposefully designed to serve as a "calibration curve" for the determination of an unknown D_p from measurable dimensions (D_h and T) on space-exposed targets. Assuming some unit velocity, such as the experimental 6 km/s, one may obtain unique solutions of D_p for individual penetrations. This is a substantial improvement over previous efforts that largely employed ballistic-limit considerations and that could only define a minimum projectile size, leading to cumulative statements that all penetrations must have been caused by projectiles larger than this threshold impactor.

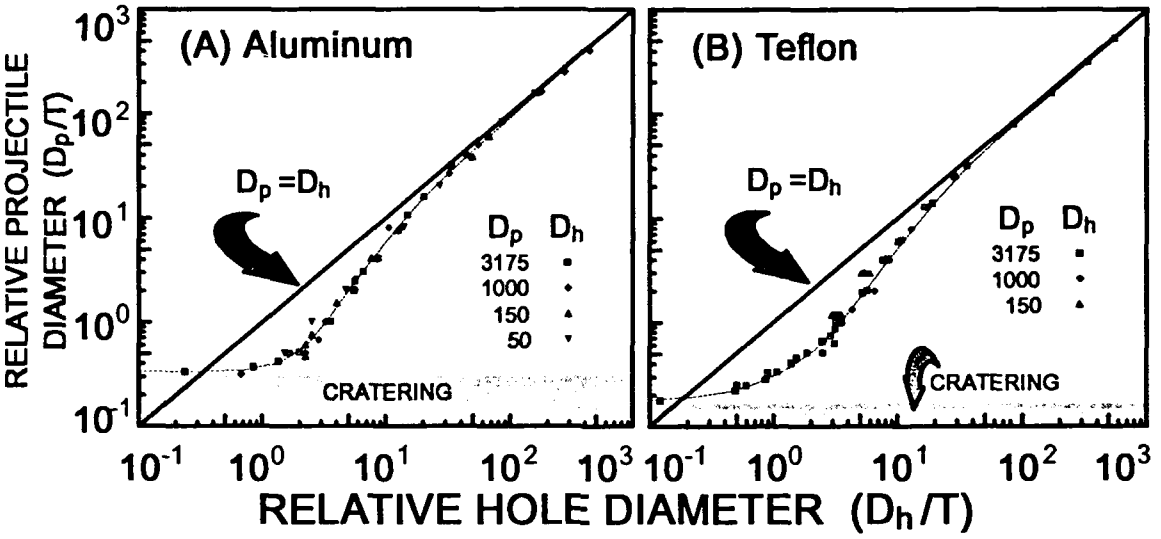


Fig. 6. Plot of penetration-hole diameters (D_h) in (A) aluminum and (B) Teflon targets plotted as a function projectile diameter (D_p), both normalized to target thickness (T).

Note from Fig. 6 that experiments conducted with a wide range of projectiles sizes combine to define a single curve, the form of which is similar for both the aluminum and Teflon targets. This validates the scaling of target and penetration-hole dimensions as a suitable approach to solve for first-order projectile dimensions from the measurements of D_h and T on space-exposed (aluminum and Teflon) targets that may be substantially thinner or thicker than those employed in these experiments. We have performed various curve-fitting procedures and find that a polynomial fit of the form $\log_{10} y = a_o + a_1(\log_{10}x) + a_2(\log_{10}x)^2 + a_3(\log_{10}x)^3 + a_n(\log_{10}x)^n$ (where $y = D_p/T$ and $x = D_h/T$) best describes and generalizes our experimental results (as summarized in Table 1).

TABLE 1. Coefficients for the formula (see above) that best describe the curve fits to the data plotted in Fig. 6.

	a_0	a_1	a_2	a_3	a_4	a_5	a_6	a_7	a_8
ALUMINUM (1100)	-0.458	0.175	1.008	1.199	-1.131	-0.800	1.152	-0.434	0.546
TEFLON (FEP)	-0.485	0.667	0.562	-0.230	0.518	0.021	-0.661	0.415	-0.075

DISCUSSION

This is an experimental effort aimed at delineating the transition between cratering and penetration in aluminum and Teflon targets, as well as at improving the more general understanding of penetrations of thin targets, including the ultra-thin case where penetration-hole dimensions mimic those of the projectile. The motivation for such efforts evolved from the analysis of space-exposed surfaces, both present and future. Detailed comparison with previous work exceeds the scope of this report, especially since we are not aware of other penetration experiments utilizing Teflon targets.

Some comparisons with existing aluminum data were offered by Hörz *et al.*, (1992b). Generally, after adapting existing formalisms to the present experimental conditions (*i.e.*, glass projectiles at ~6 km/s), the aluminum results agree to the first order with previous efforts (Maiden *et al.*, 1963; Nysmith and Denardo, 1969; Pailer and Grun, 1980; or the summary of Carey *et al.*, 1985). Nevertheless existing penetration formulas may disagree by 50% (either too large or too small) in the determination of D_p, at D_p/T = 1-10. Application of existing data to massive targets ($D_p/T < 0.7$) can yield discrepancies as large as a factor of two in D_p, and still larger discrepancies with some models are noted at $D_p/T > 20$. The best agreement of our data with that of others, over most of the target thicknesses employed in this study, is with Maiden *et al.*, (1963) and Carey *et al.*, (1985).

Extensive comparison with previous work is not warranted because our current data only pertain to a constant impact velocity, thus prohibiting tests of and comparisons with previous suggestions regarding velocity scaling, which is a crucial and integral aspect in the interpretation of penetration features on space-exposed surfaces. Without question, we must perform duplicate experiments over as wide a range of velocities as possible before formulating generalizations of space-produced penetrations, most of which result from projectiles traveling at >10 km/s. However, on the basis of our present data, we do suggest that penetrations of relative dimensions $D_h < T$ should be considered as truncated craters. Consequently, these penetrations may be interpreted with suitable crater-scaling laws, including applicable velocity scaling, with the proviso that the impact feature was characterized by D_c rather than by D_h. On the other hand, the case of ultra-thin foils, yielding $D_h = D_p$, most likely displays little, if any, velocity dependence. Therefore, penetrations of targets possessing relative thicknesses between the limiting cases of truncated craters in massive targets and the $D_h = D_p$ case for *very* thin films must have velocity exponents that vary as a function of foil thickness.

Lastly, we return to Figs. 1b, 1d and 6 all plotting penetration-hole diameters normalized to the target thickness. Note that the vast majority of space-retrieved penetrations (Fig. 1) have normalized diameters $D_h/T < 5$. Therefore, they fall exactly into that category of D_h/T values in Fig. 6 for which we suggest appreciable differences with cratering equations, as well as substantial deviations from the simple assumption of $D_h = D_p$. These observations emphasize the need for a more detailed understanding of penetration processes, both experimental and theoretical, to properly interpret the majority of targets that were penetrated by natural or man-made hypervelocity particles in near-Earth space.

ACKNOWLEDGMENTS

We appreciate the creative and skillful production of these experiments by F. Cardenas, B. Davidson, G. Haynes and J. Winkler, all of Lockheed-ESC, and many useful discussions with D. Atkinson, D. Humes, A. Watts, M. Zolensky and H. Zook. This work was sponsored by NASA's Extraterrestrial Materials Program under CDCF Flight Instrument Development and LDEF Post-Flight Analysis project funds.

REFERENCES

Bernhard, R. P., T. H. See, and F. Hörz (1992). Projectile Compositions and Modal Frequencies on the "Chemistry of Micrometeoroids" LDEF Experiment. In: *LDEF - 69 Months in Space, Second Post Retrieval Symposium, NASA CP*, in press.

Carey, W. C., J. A. M. McDonnell, and D. G. Dixon (1985). An Empirical Penetration Equation for Thin Metallic Films used in Capture Cell Techniques. In: *Properties and Interactions of Interplanetary Dust* (R. H. Giese and P. Lamy, eds.), pp. 131-136. Reidel Publishing Co., Dodrecht/Boston.

CDCF (1990). *Cosmic Dust Collection Facility: Scientific Objectives and Programmatic Relations, CDCF Committee Report NASA TM 102169* (F. Hörz, ed.) 14 p.

Cour-Palais, B. G. (1987). Hypervelocity Impact in Metal, Glass, and Composites, *Int. J. Impact Engrg. 5*, 681-692.

Gehring, J. W. (1970). Theory of Impact on Thin Targets and Shields and Correlation with Experiment. In: *High Velocity Impact Phenomena* (A. Kinslow, ed.), pp. 105-156. Academic Press, New York.

Herrmann, W. and J. Wilbeck (1986). *Review of Hypervelocity Penetration Theories, Sandia National Laboratories Report, SAND--86-1884C.*

Hörz, F., R. P. Bernhard, J. L. Warren, T. H. See, D. E. Brownlee, M. R. Laurance, M. R. and S. Messenger (1992a). Preliminary Analysis of LDEF Instrument A0-187-1: The Chemistry of Micrometeoroids Experiment (CME). In: *LDEF - 69 Months in Space, First Post Retrieval Symposium, NASA CP-3134*, (A. E. Levine, ed.), p. 487-501.

Hörz, F., M. J. Cintala, R. P. Bernhard and T. H. See (1992b). Dimensionally Scaled Penetration Experiments: Aluminum Targets and Glass Projectiles 50 μm to 3.2 mm in Diameter, *Int. J. Impact Engrg.*, submitted.

Humes, D. (1992). Large Craters on the Meteoroid and Debris Experiment. In: *LDEF - 69 Months in Space, First Post Retrieval Symposium, NASA CP-3134*, (A. E. Levine, ed.), pp. 399-418.

Levine, A. E. ed. (1992) *LDEF - 69 Months in Space, First Post Retrieval Symposium, NASA CP-3134*, 1712 p.

Levine, A. E. ed. (1992) *LDEF - 69 Months in Space, Second Post Retrieval Symposium, NASA CP*, in preparation.

Maiden, C. J., J. W. Gehring and A. R. McMillan (1963). *Investi, ition of Fundamental Mechanisms and Damage to Thin Targets by Hypervelocity Projectiles, NASA TR-63-22.*

McDonnell, J. A. M. (1991). Impact Cratering from LDEF's 5.75 Year Exposure: Decoding of the Interplanetary and Earth-Orbital Population. *Proc. 22nd Lunar Planet. Sci. Conf.*, 185-193.

Nysmith, C. R. and B. P. Denardo (1969). *Experimental Investigation of the Momentum Transfer Associated with Impact into Thin Aluminum Targets, NASA TN D-549.*

Pailer, N. and E. Grun (1980). The Penetration Limit of Thin Films, *Planet. Space Sci., 28*, 321-331.

See, T. H., M. K. Allbrooks, D. R. Atkinson, C. G. Simon and M. E. Zolensky (1990). *Meteoroid and Debris Impact Features Documented on the Long Duration Exposure Facility, NASA-JSC Report # 24608*, 561 p.

See, T. H., K. S. Mack, J. L .Warren, M. E. Zolensky and H. A. Zook (1993). Continued Investigation Of LDEF's Structural Frame And Thermal Blankets By The Meteoroid & Debris Special Investigation Group. In: *LDEF - 69 Months in Space, Second Post Retrieval Symposium, NASA CP*, in press.

Warren, J. L. H. A. Zook, J. H. Allton, U. S. Clanton, C. B. Dardano, J. A Holder, R. R. Marlow, R. A. Schultz, L. A. Watts and S. J. Wentworth (1989). The Detection and Observation of Meteoroid and Space Debris Impact Features on the Solar Maximum Satellite. *Proc. 19th Lunar Planet. Sci. Conf.*, 641-657.

Int. J. Impact Engng Vol.14, pp.359–372, 1993
Printed in Great Britain

0734-743X/93 $6.00+0.00
© 1993 Pergamon Press Ltd

HYPERVELOCITY RESEARCH AND THE GROWING PROBLEM OF SPACE DEBRIS

WILLIAM M. ISBELL

General Research Corporation
5383 Hollister Ave., Santa Barbara CA 93111

WILLIAM J. TEDESCHI

Defense Nuclear Agency
6301 Telegraph Rd., Alexandria VA 23310

ABSTRACT

Man-made orbital debris has increased in number so that it poses a potential barrier to the exploration of space. The ever-increasing number of objects in space has created an increasing hazard to all spacecraft, including manned shuttles, unmanned satellites, and manned space stations. Although international efforts are underway to reduce the proliferation of space debris, the number of objects continues to climb.

The majority of debris tracked by earth observation is classed either as "operational debris" (spent boosters and satellites, discarded hardware from manned flight, etc.) or as "fragmentation debris" (debris created by explosions aboard boosters or satellites or by impacts between objects in orbit). While there is considerable information available about operational debris, statistics on fragmentation debris are more suspect, since it is difficult to predict with any accuracy the fragments resulting from an explosion or impact on a space structure.

As realization of the importance of the problem grows, the hypervelocity launcher and impact communities are becoming increasingly involved. This paper defines the major problems to be solved and outlines the requirements for launchers, diagnostics, and modeling. A new U.S space program to model the fragmentation of satellites impacted by space debris is described. The results of tests against actual satellites are described in terms of their importance to the modeling effort.

BACKGROUND

Space voyagers of the late 1950's and early 1960's were concerned that the meteorite flux in near-Earth and trans-lunar space might be sufficiently high that spacecraft would be in great danger of being struck and destroyed (Charters, 1964; Bjork, 1961). Pre-1963 estimates of the meteoroid flux (Fig. 1) and data returned from the Explorer XVI spacecraft were cause for concern among spacecraft designers. Sufficient data existed on the effects of hypervelocity impact on lightweight structures to indicate that even very small particles represented a danger to spacecraft and satellites (Eichelberger and Gehring, 1962; Herrmann and Jones, 1961; Kornhauser, 1960; Christman and McMillan, 1966)

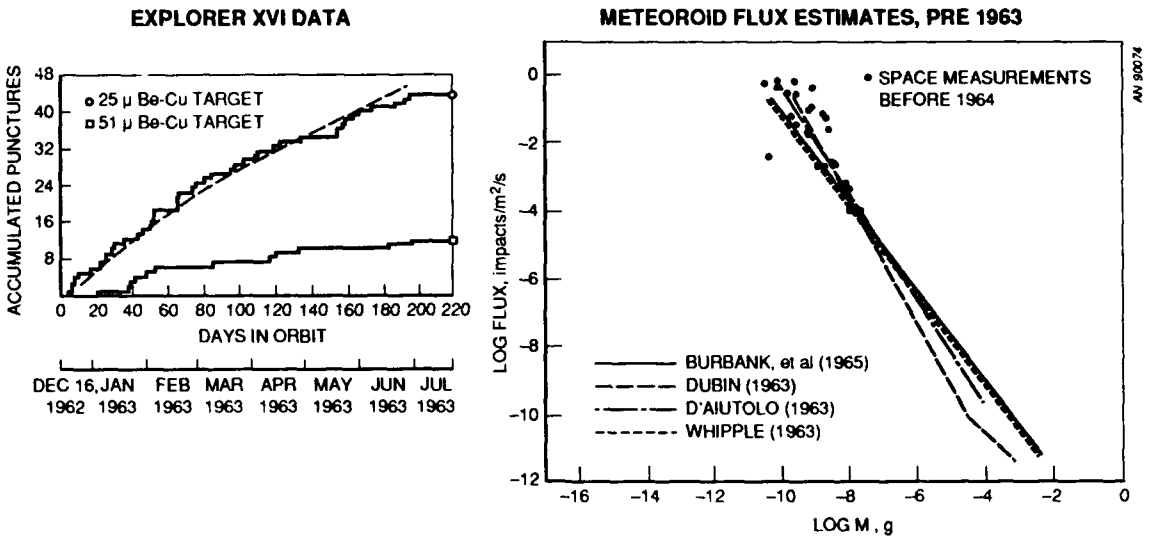


Fig. 1. Early data suggested a significant hazard to spacecraft.

At the request of NACA (NASA's predecessor), an effort was begun to design lightweight shields for spacecraft, utilizing the hypervelocity guns that had been developed for the anti-ICBM program (Charters, 1960). Thus was created the "Whipple Bumper", named for Fred C. Whipple of Harvard University, its originator (Whipple and Hughes, 1955; Whipple, 1963) (Fig. 2). This concept of shattering the incoming particle into small pieces with an externally-mounted shield and thus spreading the impulse over a large area of the spacecraft skin has persisted, in many forms, to this day (Maiden et al, 1963; Cour-Palais, 1979; Olsen and Nolan, 1992; Hertel et al, 1991).

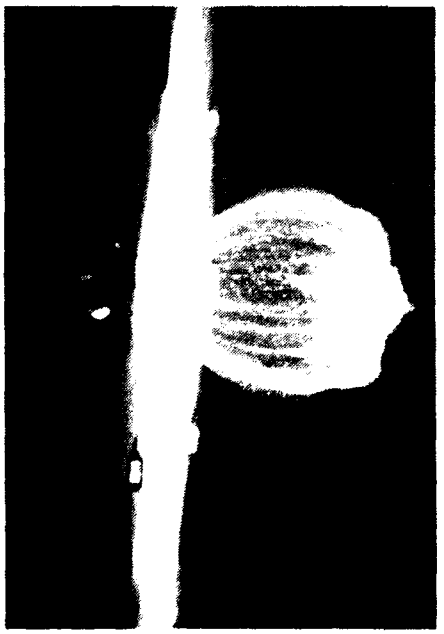


Fig. 2. Spacecraft shield design became an active area of research.

With the advent of man into space, however, statistics from satellites soon proved that the likelihood of meteorite impact was small. Note the decrease in measured flux shown in Fig. 3 (Grun et al, 1985). Decisions were made early in the manned spaceflight program not to employ external shields in space module design.

By the 1970's, interest (and funding) had waned considerably for hypervelocity impact studies relating to protecting spacecraft. Interest in hypervelocity impact for use as a warhead mechanism for ABM

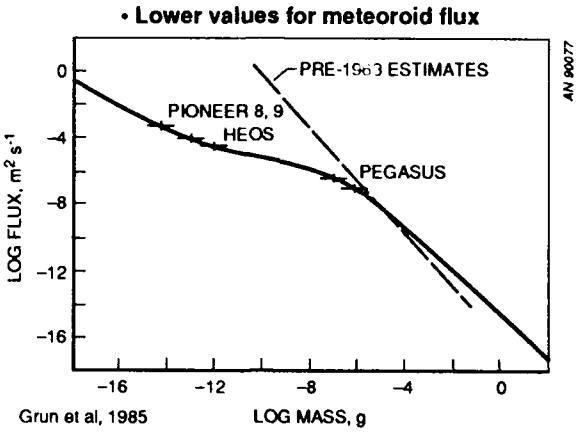


Fig. 3. During the late 1960's and early 1970's, new data indicated a lesser hazard existed. Interest (and funding) in hypervelocity research waned.

systems also declined because of the inability of early projectile guidance systems to intercept incoming reentry vehicles with miss distances measured in meters. The effect of lack of accuracy was to increase the size of the fragmenting warhead and thus the size and cost of the missile. As a result, the U.S. anti-ballistic missile developers considered for a time equipping their missiles with nuclear warheads, where larger miss distances were acceptable.

THE SITUATION CHANGES

The reduced interest in hypervelocity impact phenomena remained until the 1980's, when the situation changed substantially. First, guidance system technology improved to the point where fragmenting warhead and hit-to-kill projectiles became feasible for ballistic missile defense. This increased capability produced a vigorous program under the Strategic Defense Initiative to understand how enemy missiles and reentry vehicles could be destroyed by ground and space-based kinetic energy weapons.

Second, because man-made debris in space had increased dramatically, the likelihood of a dangerous encounter in space became a subject of worldwide concern. Figure 4 presents a 1976 estimate of the expected increase in orbital debris, assuming an input rate of 510 fragments per year and neglecting fragment demise by reentry into the atmosphere occasioned by atmospheric drag (Kessler and Cour-Palais, 1978). The probability that a spacecraft might be damaged by the impact of orbital debris could no longer be ignored.

As the fragment population continued to increase, a new phenomenon was postulated to occur, further exacerbating the problem. In a process termed "cascading", impacts between fragments in orbit create many more fragments. Figure 5 indicates that, even if no new fragments are added (0% increase line), the total population continues to grow (Su, 1985). Moreover, if even a modest 5-10% per year increase occurs in the number of new objects added to orbit, the population can grow geometrically, making space exploration a risky business, indeed.

(It should be noted here that there remains disagreement within debris growth modelers on the statistics and severity of the problem of debris cascading.)

Space debris thus became a matter of international concern and international agreements were accorded to mitigate the proliferation of new objects in space. A resurgence of interest soon followed in hypervelocity impact phenomenology for spacecraft shields and for techniques to mitigate and clean up the orbital debris environment.

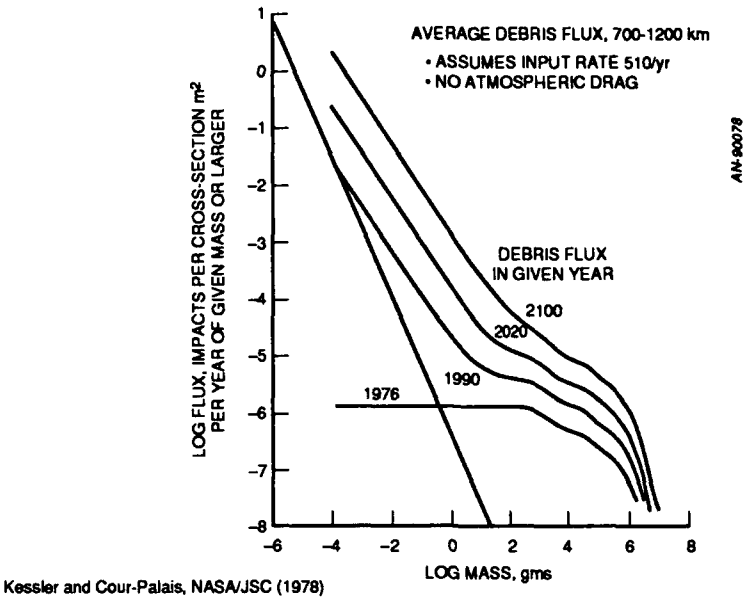


Fig. 4. In the 1980's, the situation changed as man-made debris in space increased dramatically.

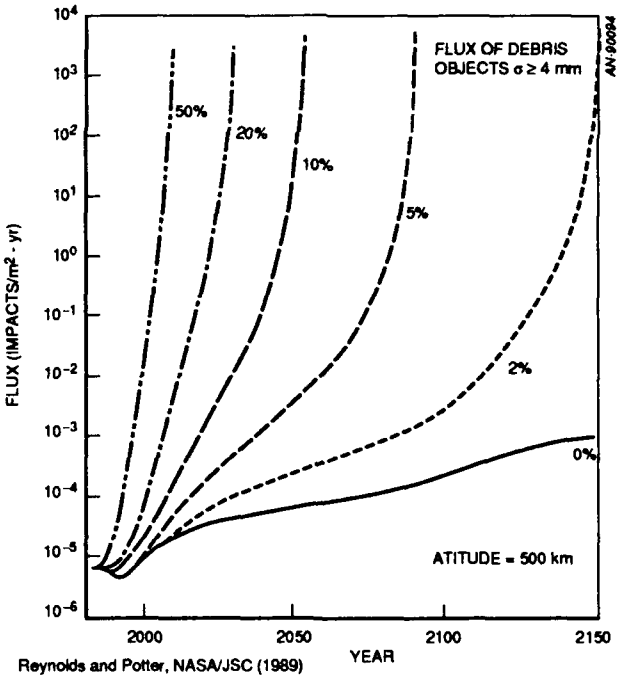


Fig. 5. A 1989 estimate by NASA indicated that collisions between debris in orbit could cause a geometrical increase in numbers of fragments.

The decade of disinterest has taken its toll, however. Because of current inadequacies in both experimental and calculational capabilities, hypervelocity impact researchers presently have only limited means to conduct the necessary research. National and international programs have been initiated to close the technology gap. These programs are being directed toward:

A more fundamental understanding of the fragmentation process, including the development of the capability to predict the number, size, velocity, and direction of fragments,

The development of launchers and diagnostics capable of simulating and recording impacts in the 10-15 km/s range,

An understanding of the results of fragment impact on spacecraft so that efficient shields can be constructed.

This paper discusses the requirements for research into the growing problem of space debris, the new launchers and diagnostic systems to be brought to bear, and the status of the impact and breakup models that will be used to predict the generation and spread of debris in space. The paper begins with a definition of the debris environment and the experimental and calculational capabilities required to conduct research.

DESCRIPTION OF THE PROBLEM

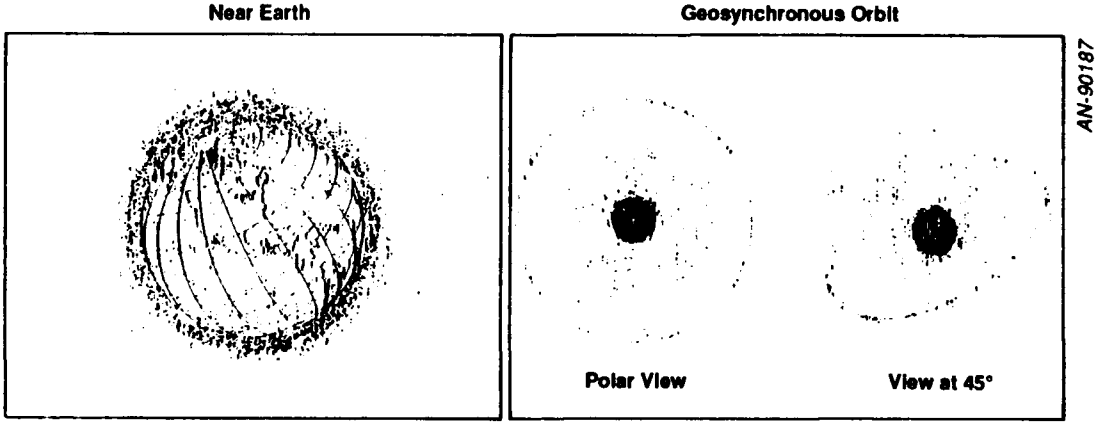
There has always been a flux of particles passing near the Earth. These meteoroids arise from several sources - asteroids, cometary debris, and occasional interstellar particles. Since the beginning of the "Space Age", however, there has been an enormous increase in the number of particles large enough to do serious damage to space assets - 1 cm or more in size.

The problems before the space community are therefore, "Can lightweight shields be designed to counter the threat? Can the threat be mitigated or eliminated?"

The corresponding problems before the hypervelocity impact community are, "Can predictions be made of the generation and propagation of space debris? Can the insight from this community into hypervelocity phenomena and fragmentation of structures be used to devise shields, fragmentation mitigators, and debris cleanup methods?"

There remains the question of how accurate the predictive models and data need to be, especially for very small particles. There seems to be consensus in the space debris community that the range of greatest interest is for fragments 1 mm to 10 cm in length. While the numbers of objects in space undoubtedly continues to increase as fragment size decreases, shielding for debris < 1 mm is possible. Conversely, while weight-effective shielding for fragments > 10 cm is not likely to be available in the near term, the number of fragments and their probability of striking a space asset is now quite small.

Figure 6 depict the locations of orbital debris, as seen from near Earth and from near geosynchronous orbit (Teledyne-Brown Engineering, 1988). They comprise some 7,000 objects with dimensions greater than about 10 cm and many more objects too small to be tracked from ground stations. Figure 7 shows the growth vs time for these objects over the thirty year period 1960-1990.



Courtesy of Teledyne-Brown Engineering

Fig. 6. The debris population is most extensive in near Earth orbits, but includes a sizeable number of extremely long-lived fragments in geosynchronous orbit.

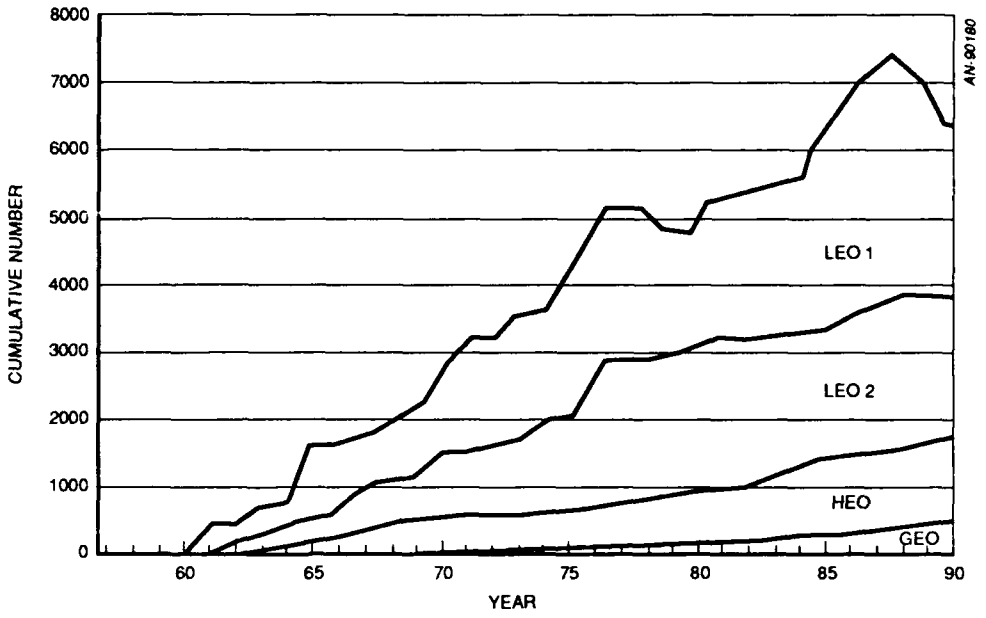


Fig. 7. Growtl of NORAD Cataloged Objects > 10 cm in Size over the Period 1960-1990.

A 1990 assessment of hazards to spacecraft (objects > 1 cm in size) estimated that natural hazards and operational payloads comprise only 7% of the total number of objects in orbit, while operational debris and fragmentation debris account for 50% and 40%, respectively.

Orbital debris is thought to originate from two main sources. First, propellants left aboard spent boosters and satellites can leak past seals, resulting in an energetic hypergolic reaction which fragments the spacecraft. Second, fragment-satellite and satellite-satellite impacts fracture create substantial debris. Thousands to millions of particles are created by these scenarios.

In order to determine solutions to the problem of orbital debris, it is necessary to understand the fragmentation processes in sufficient detail to be able to predict the statistics of debris generation. At present, both explosive fragmentation and impact fragmentation stress the ability to perform such predictions.

The estimated relative impact velocity distribution for debris impact on objects in a space station orbit is shown in Fig. 8 (Mog, 1990). The probability distribution peaks at ~13 km/s, making it necessary to extrapolate test results by nearly a factor of two in velocity, since current launchers are limited to 6-8 km/s for projectiles of substantial mass (>30 g).

The problem is made even more difficult by the fact that secondary debris fragments undergo changes in phase from solid to melt to vapor as the impact velocity is increased over the range of interest. Inaccuracies in the formulations of three phase equations of state make the prediction of impact damage even more uncertain.

REQUIREMENTS FOR TESTING

For an adequate space debris program it will be necessary to provide launch capabilities over the entire mass-velocity range of concern to the orbital debris community. Figure 9a demonstrates the parameter space required to be covered. When contrasted with the current capabilities of modern launch systems (Fig. 9b), the problem becomes clear.

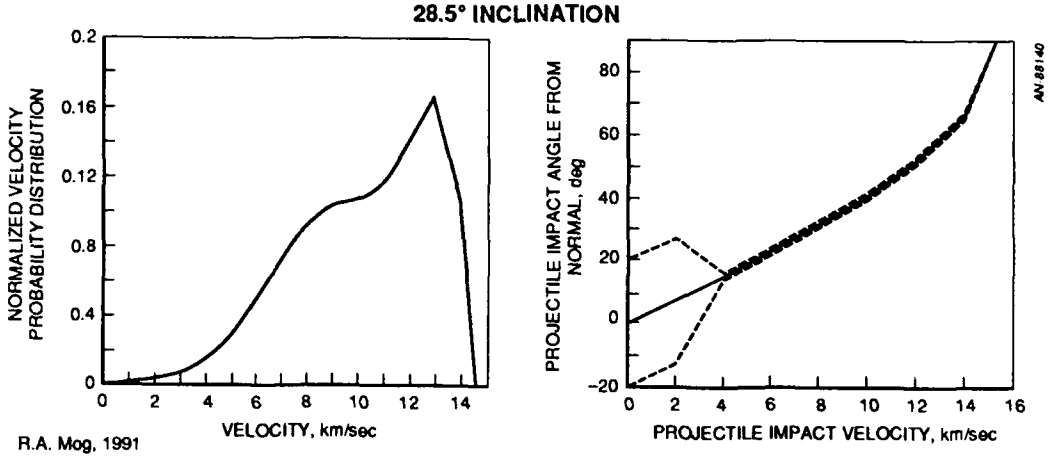


Fig. 8. Estimated Engagement Conditions for Space Station Orbit.

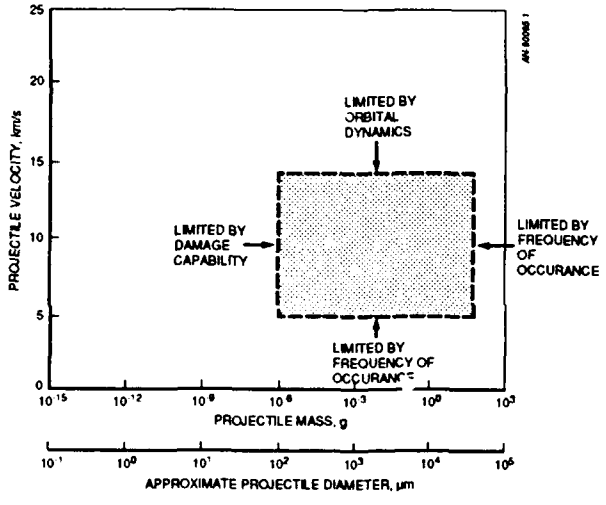


Fig. 9a

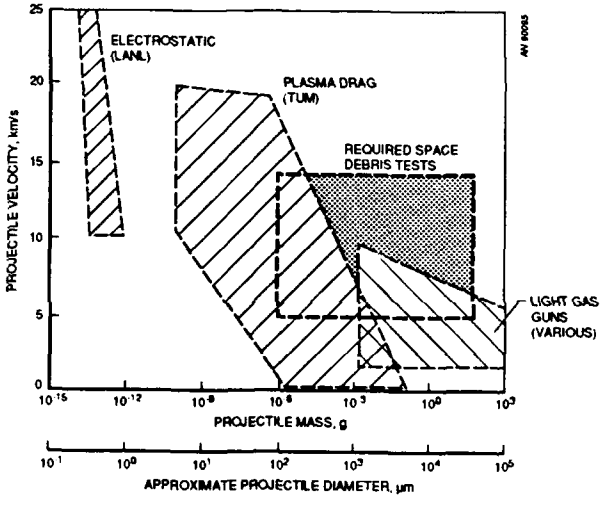


Fig. 9b

Fig. 9. Comparison of Mass-Velocity Launch Requirements for Space Debris Studies with the Capabilities of Various High velocity Launchers.

While electrostatic and plasma-drag launchers cover the appropriate velocity range, only the lowest mass range is covered. In addition, particles launched by these facilities are primarily spherical, while orbital debris fragments are generally more plate-like. It has been shown that flat plate fragments can cause substantially more damage than spheres of an equal mass (see, for instance, Chhabildas et al, 1991a).

Light gas guns, the mainstay of hypervelocity impact testing, can launch fragments of the required sizes and shapes, but only at velocities of 6-8 km/s, leaving unexamined the most damaging and most difficult to calculate regions of parameter space.

Thus, the requirements for testing will stress the current state of the art in most areas of hypervelocity research. Certain advances must be made:

> The velocity range must be extended to 12-15 km/s. Because of current weaknesses in fragmentation models, data obtained on complex structures at 6-8 km/s usually cannot be extrapolated with confidence to much higher velocities.

Since fragment shape can have an influence in satellite penetration and fragmentation, irregular fragments must be launched which simulate the actual debris. This requirement and the requirement for fragment impacts at specified angles are difficult for current launch systems.

The necessity of determining the vulnerability to impact of hazardous energetic materials will require specialized impact chambers, capable of testing hypergolic and non-hypergolic liquid and solid propellants and pressurized batteries, gas bottles, and fuel cells.

Actual satellites should be tested, if possible. Current tests on mock, full scale satellites have demonstrated that, for satellites with complex geometries and filled interiors, many more fragments are created by impact than for a simplified mockup.

If actual satellites are to be impacted, impact chambers of large dimensions must be available. Current impact chambers are limited to structures of approximately two meters in length. If scaled models are to be used, it must be shown that the fragment statistics are accurate.

For future use on satellites and space stations, on-orbit debris sensors must be developed that are capable of remotely sensing, recording, assessing, and communicating information on potential debris impacts in near real-time.

The impact testing program will require a large number of tests, because of the inherently statistical nature of the problem. Lowered launcher costs are desirable, a requirement which runs counter to the need for higher velocities.

Details of the impact process must be measured on very complex targets. Typically, hypervelocity impact experiments have been made on idealized targets, where access for optical and electronic measurements has been relatively easy, and where x-rays can penetrate through the target, revealing details of interactions. These procedures must now be adapted to targets in which complex, multiple-dimension interactions make many currently used x-ray systems, gages, and sensors inapplicable.

Debris recovery and tracking techniques are fundamental to the success of the debris program. In general, the current soft recovery techniques are insufficient to determine the fragment numbers, directions, and velocities. New techniques and adaptations of previous techniques are being developed.

While this is an imposing list of deficiencies, solutions to most or all of the problems described above have been proposed. Some of these solutions are described below.

ADVANCES IN LAUNCH SYSTEMS

Papers presented at the 1992 Hypervelocity Impact Symposium show promise of launchers attaining the requisite velocities and masses.

The three stage light gas gun at Sandia National Laboratories (Chhabildas, 1991b) launches 1 gram, thin flat discs at velocities over 12 km/s, with the possibility of launching both higher masses (to several grams), at higher velocities (to 14 km/s), and with projectiles of lower L/D.

Shaped charge launchers have been able to reach the appropriate velocities for several decades, although they produce multiple projectiles with rather ill-defined shapes and masses. Both eccentrically-initiated and inhibited shaped charge designs are now available which separate the first fragment from the remainder of the jet, making these techniques more applicable and thus more attractive (Held, 1992a; Walker et al, 1992). Shaped charges are

currently capable of launching 10 gram fragments at 10-11 km/s. Scaling of these devices to 100 gram fragments at similar or slightly higher velocities appears feasible (Held, 1992b).

Plasma-drag devices, which have been used extensively for space debris studies at microgram masses (Igleseder and Igenbergs, 1989) may also be capable of achieving somewhat higher masses, using a first stage injection device (Igenbergs, 1992).

Electromagnetic launchers, while holding great promise for achieving the requisite velocities have, as yet, been unable to perform launches of greater than 6-8 km/s. Funding for achieving still higher velocities is currently in the decline, with efforts being primarily devoted to velocities <5 km/s.

"Electric guns" throwing thin, flat sheets of dielectric material, can reach (and exceed) the necessary velocity range for space debris studies (Osher et al, 1989). While testing with these launchers will be valuable, their applicability is limited by their inability to launch "typical" debris materials and shapes.

Electrostatically-launched particles have been measured with velocities >100 km/s (Keaton et al, 1989). Particle masses, however, are in the range of femtograms to micrograms. Useful phenomenology studies are possible with this technique and, if scaling studies indicate a relationship with the much larger particles of interest to space debris, the information obtainable may be directly useful.

It is obvious that providing launch facilities for space debris research must be approached from several directions, and that no one launch technique will cover the entire parameter range of interest.

DIAGNOSTIC SYSTEMS

While launcher development has been emphasized for the last decade, at least to some degree, the development of diagnostic systems for complex targets has not kept pace. Considerable additional improvements are necessary.

There are promising new diagnostic techniques which can be applied to the problem of instrumenting complex targets. Among these are:

Very penetrating pulsed x-ray sources

Pulsed laser holographic techniques for fragment visualization and counting (Hough, 1989; Ang, 1992)

Fiber optic and conducting wire "break wire" grids for target fragmentation (Naumann and Isbell, 1992)

X-ray cinematography systems

Miniaturized, shock hardened on-board recorders and telemetry units (Menna et al 1992)

Foam recovery materials which are calibrated for velocity and fragment shape (Cunningham et al, 1992; Dahlen et al 1992)

High pressure "water lathe" systems for simplifying the tedious task of separating fragments from the recovery foam (Venditto, 1992)

TESTING AND MODELING EFFORTS FOR DEBRIS GENERATION

In the absence of substantial data and validated first-principles models for debris creation, the space debris community has developed and used simple empirical spacecraft and booster breakup models for debris calculations. Programs now being initiated will expand significantly the experimental breakup database for use in semi-analytic breakup models and in complex, state-of-the-art, physics-based models, including hydrocodes and finite element structural response codes.

Current spacecraft breakup models are empirical in nature and are based on test data from a handful of partially characterized tests. The output from these empirical models is consequently of low fidelity and accuracy. Typically, the debris impactor/target structure interaction is modeled in terms of the masses involved and the relative velocity and, therefore, the kinetic energy of impact. The structures are assumed to fragment into isotopically expanding debris clouds. The specific model output consists of debris mass and velocity distributions.

These models are considered accurate to within only an order of magnitude, since no explicit accounting is made of the structure geometries and materials. The models are routinely used outside the parameter space upon which they were developed.

As part of an Orbital Debris Technology Transfer Program conducted by the Defense Nuclear Agency (DNA) and their agent, Wright Laboratories of Eglin AFB (WL/MNSA), carefully-controlled hypervelocity impact tests are being conducted on various complex spacecraft structures to provide accurate and complete debris mass and velocity distribution data. The first test series, called the Federal Republic of Germany Impact Test Series (FRGITS), was conducted in November 1991 and involved three scaled, complex satellite structures and one complex satellite electronics box, impacted by 8-15 g aluminum debris fragments at 10 km/s.

Details of the FRGITS test series are contained in Hunt et al (1992).

The second test series, named the Satellite Orbital Debris Characterization Impact Test (SOCIT), was conducted from September 1991 through January 1992 and involved the flight-ready OSCAR 22 Navy satellite, obtained from the U.S. Navy by D. McKnight, then at the United States Air Force Academy. In addition to the test on an actual satellite, tests were also conducted on two structural mockups of OSCAR, a solar panel, and a fourth-stage adapter section (Cunningham et al, 1992).

The projectile was a 150 g sphere of aluminum, impacting at 6 km/s. A full suite of instrumentation, including debris capture foams, X-rays, cine and pulsed laser photography, and numerous onboard time of arrival and motion sensors were used to capture the debris field generated.

Figure 10 shows the OSCAR satellite target. Impact tests were performed on a solar panel and on the satellite body. Data reduction and analysis are described in detail in a companion paper.

These recent tests are significant in that they represent a substantial increase in the statistical data on satellite breakup available to modelers. In the SOCIT series, in particular, a substantial effort was made to recover and characterize the debris in terms of number, size, material, direction, and (to some degree) velocity. The recovery techniques used by General Research Corp., the test conductor, ensured that greater than 90% of all debris was recovered. The recovery process protected the debris in an manner such that secondary damage from the recovery process did not affect the data.

Debris specimens were processed and subsets of the debris were supplied to groups at the University of Colorado and California Institute of Technology for additional detailed examination.

Significant improvements are being made in the ability of semi-analytic and complex models to determine the breakup of complex spacecraft structures (see, for instance, McNight and Brechin, 1990;

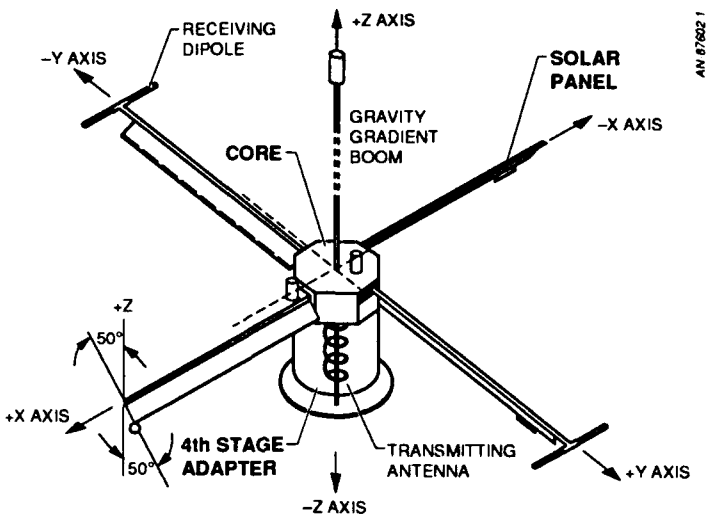


Fig. 10. External View of OSCAR Satellite Impacted in Debris Generation Test Series.

McNight, 1987). The new models include analytical descriptions of the target and impactor structures, material constitutive properties, and fragmentation algorithms. These improvements are producing more accurate definitions of the debris fields generated by impact. Such a capability is of importance in determining not only the number and size of fragments, but how the debris propagates in space and thus how it will affect the long term, on-orbit debris environment.

In addition to the rapidly-advancing capabilities of "traditional" hydrocode models (CTH, MESA, JOY, HULL, DYNA, etc.), a different approach to computer formulation has been taken by the developers of the Smoothed Particle Hydrodynamics (SPH) model - Los Alamos National Laboratory, the Air Force Phillips Laboratory, and the New Mexico Institute of Technology, among others (Tedeschi et al, 1991).

The SPH model is based on a Lagrangian formulation which offers the advantage of being able to track the formation and propagation of debris over large distances and times. SPH has been used to calculate the effects of projectile impacts on satellites, on complex military targets, and on the simulated hull of Space Station Freedom.

INTERNATIONAL PROGRAMS

The space debris problem is international in scope and research is underway in several countries. There have been attempts at the international level to develop orbital debris generation and mitigation "standards" for all space-faring nations. These attempts have been both informal - at the working level (e.g., technical interchanges between scientists at technical conferences and information exchange meetings) and formal - at the United Nations level (e.g., legal definitions of debris and methods to mitigate debris generation).

These efforts are currently meeting with varying levels of success. While most countries appear to be cognizant of the debris threat and are acting responsibly to minimize the likelihood of on-orbit debris generation, a consensus has yet to be reached on implementing potentially very expensive debris mitigation schemes. Most space-faring countries recognize the need to conduct debris related research, including hypervelocity impact breakup testing and modeling, to understand this growing threat.

In the United States, member organizations of the DoD/NASA/DOT Interagency Group (Space) are conducting orbital debris research in a cooperative and coordinated environment. Orbital debris

research has taken the form of projections of future debris environments, studies of impact phenomenology and shielding, concepts for debris mitigation techniques, and hypervelocity breakup testing and modeling. The results of these efforts are being documented throughout the open literature.

Internationally, research efforts have taken a similar form. The Former Soviet Union has obtained considerable orbital debris-related information, e.g., on-orbit and ground-based measurements, hypervelocity launcher techniques, and spacecraft breakup data. When made available, this information will be an invaluable contribution to the field.

The European Space Agency member countries, the Japanese, and the Canadians also are active in orbital debris research in most of the areas mentioned above. Through technical publications, they have made major contributions to the international orbital debris space community.

SUMMARY

There is a sense of urgency in defining and solving the problem of man-made debris in space. Although the rate of debris increase is slowing as nations implement debris mitigation schemes in their operations, the total number of fragments in orbit continues to increase. Without these efforts, the risk to both manned and unmanned space exploitation could become unacceptable. Only through continued orbital debris research and continued open cooperation between nations can nations understand the magnitude of the orbital debris problem and work to correct it in a timely manner.

REFERENCES

Alfriend, K.T., and D.L. Lewis, "Estimation of the Low Earth Orbit Debris Population and Distribution", Paper No. 92-4444, Presented at the 1992 AIAA Astrodynamics Conference. General Research Corporation.

Bjork, R.L., "Effects of a Meteoroid Impact on Steel and Aluminum in Space," The Rand Corporation Report TR P-1662, 16 Dec. 1958; see also, "Meteoroids vs Space Vehicles," *ARS J.*, 31, 6, June 1961, pp. 803-807.

Charters, A.C., "The Use of Shrapnel as an Anti-ICBM Countermeasure", NASA Technical Memorandum X-112, 1960.

Charters, A.C., J.W. Gehring, and C.J. Maiden, "Impact Physics, Meteoroids, and Spacecraft Structures", AGARDOgraph 87, Vol. 1, 1964.

Chhabildas, Lalit C., E.S. Hertel, and S.A. Hill, "Whipple Bumper Shield Tests at Over 10 km/s". Proceedings of the American Physical Society Topical Conference held in Williamsburg, VA, June 17-20, 1991.

Chhabildas, L.C., L.M. Barker, J.R. Asay, et al, "Launch Capabilities to Over 10 km/s", Sandia National Laboratories, Albuquerque, NM. Published in *Shock Compression of Condensed Matter*, 1991.

Christman, D.R. and A.R. McMillan, "The Meteoroid Environment and its Consequences to Spacecraft Structures", published in *The Journal of Environmental Sciences*, February 1966.

Cour-Palais, Burton G., "Space Vehicle Meteoroid Shielding Design," ESA JP-153, April 1979.

Cunningham, T.M., W.M. Isbell, D.M. Hogg, and W.J. Tedeschi, "Results from the Satellite Orbital Debris Characterization Impact Test Series".

Dahlen, G.A., T.M. Cunningham, M.R. Good, and H.H. King, "Characterization of Polyurethane Foam as a Debris Catcher Medium", General Research Corp., Report CR-91-1264, October 1991.

Eichelberger, R.J. and Gehring, J.W., "Effects of Meteoroid Impacts on Space Vehicles," *ARSJ.*, 32, 10, 1962, p. 1583.

Grun, E., H.A. Zook, H. Fechtig, and R.H. Giese, (1985) Collisional Balance of the Meteoritic Complex. *Icarus*, 62, 244-272.

Held, M. et al, "Development of an Eccentrically Initiated Shaped Charge Hypervelocity Launcher Technique", Proceedings, Hypervelocity Impact Symposium, 1992, Austin, Texas.

Held, M., Private Communication, 1992.

Herrmann, W. and A.H. Jones, "Survey of Hypervelocity Impact Information," Massachusetts Institute of Technology, Aeroelastic and Structures Research Laboratory, ASRL Report No. 99-1, Sep. 1961.

Hunt, R., M. Fry, M. Held, and W. Tedeschi, "Test Results at 10 km/s Using an Eccentrically Initiated Shaped Charge Hypervelocity Launcher Technique".

Igenbergs, Private Communication, 1992.

Iglseder, H., and E. Igenbergs, "Crater Morphology at Impact Velocities Between 8 and 17 km/s", ZARM, Universitat Bremen, Badgasteinerstr. IW1, Federal Republic of Germany. *Int. J. Impact Engng.* Vol. 10, pp. 271-280, 1990.

Keaton, P.W., G.C. Idzorek and eight co-authors (1990). A Hypervelocity-Microprojectile Impacts Laboratory with 100-km/s Projectiles. Proceedings of the 1989 Hypervelocity Impact Symposium. *Int. J. Impact Eng.* 10, 295-308, 1990.

Kessler, D.J., and B.G. Cour-Palais, "Collision Frequency of Artificial Satellites: The Creation of a Debris Belt. *Journal of Geophysical Research*, Vol. 83, 1978, pp. 2637-2646.

Maiden, C.J. J.W. Gehring, and A.R. McMillan, "Investigation of Fundamental Mechanism of Damage to Thin Targets by Hypervelocity Projectiles," General Motors Defense Research Lab., Santa Barbara, CA, Rept. GM-DRL-TR-63-225, Sept. 1963.

McKnight, D.S., "Classification of Satellite Breakups by Debris Fragment Lifetimes", Department of Physics, U.S. Air Force Academy, (Presented at the AAS/AIAA Astrodynamics Specialist Conference).

McKnight, D., and C. Brechin, "Debris Creation Via Hypervelocity Impact", U.S. Air Force Academy, Colorado Springs, CO. 28th Aerospace Sciences Meeting, January 8-11, 1990/Reno, Nevada AIAA 90-0084.

Menna, T.L., J.L. Swann, and H.H. King, "A Technique for In-Target Digital Recording during High Shock Events. General Research Corporation, 1992. (To be submitted to 39th International Instrumentation Symposium, 1993.)

Mog, Robert A., "Spacecraft Protective Structures Design Optimization", Science Applications International Corporation, Hunstville, AL. Published in *Journal of Spacecraft*, Vol. 28, No. 1, Jan.-Feb. 1991.

Naumann, W.J. and W.M. Isbell, "The Break Wire Array", Technical Memorandum CR92-1540, General Research Corporation, July 1992.

Olsen, G.D., and A.M. Nolen, "Advanced Shield Design for Space Station Freedom".

Osher, J. et al (1990). Hypervelocity acceleration and impact experiments with the LLNL electric guns. Proceedings of the 1989 Hypervelocity Impact Symposium. Int. *J. Impact Eng.* 10, 439-452.

Su, S.Y., "Contribution of Explosion and Future Collision Fragments to the Orbital Debris Environment. *Advances in Space Research*, 5, 2, 25, 1985.

Venditto, V.A., "Water Lathe Technique for Removing Debris Embedded in Foam:, VAV Industries, Technical Report submitted to General Research Corporation, 1992.

Walker, J.D., D.J. Grosch, and S.A. Mullin, "A Hypervelocity Fragment Launcher Based on an Inhibited Shaped Charge".

Whipple, F.L. and Hughes, R.F., "On the Velocities and Orbits of Meteors, Fireballs, and Meteorites," in *Meteors*, Pergamon Press Ltd., 1955, pp. 149-156.

Whipple, F.L., "On Meteoroids and Penetration," *J. of Geophysical Research*, 68, 17, Sep. 1, 1963, pp. 4929-4938.

Int. J. Impact Engng Vol.14, pp.373–383, 1993
Printed in Great Britain

0734-743X/93 $6.00+0.00
1993 Pergamon Press Ltd

LAGRANGIAN EPIC CODE COMPUTATIONS FOR OBLIQUE, YAWED-ROD IMPACTS ONTO THIN-PLATE AND SPACED-PLATE TARGETS AT VARIOUS VELOCITIES

Gordon R. Johnson
Alliant Techsystems Inc.
Brooklyn Park, Minnesota

and

William H. Cook
Wright Laboratory, Armament Directorate
Eglin Air Force Base, Florida

ABSTRACT

This paper presents Lagrangian EPIC code computations for oblique, yawed-rod impacts onto thin-plate and spaced-plate targets at various velocities. The baseline set of computations considers a nominal obliquity of 65 degrees and a nominal impact velocity of 1300 m/s, onto thin-plate targets at nominal yaw angles of 0, –10, and +10 degrees. The yaw angles are achieved by inducing velocities into the plates. These results are compared to test data and MESA code results published previously. Additional sets of computations are presented to show the effect of increased impact velocities at nominal values of 2600 m/s and 5200 m/s. Some spaced-plate computations are also included.

INTRODUCTION

Computer codes are now available to perform a variety of two- and three-dimensional computations for high-velocity impact problems. Although two-dimensional computations have been performed routinely for many years, a relatively small number of three-dimensional computations have been performed. Current three-dimensional computing capabilities now allow for the examination of many interesting three-dimensional effects.

This paper presents a variety of three-dimensional EPIC computations. They are intended to examine the following factors:

- The accuracy and efficiency of EPIC code computations, as compared to MESA code computations and test data, for oblique, yawed-rod impacts onto thin plates.
- The effect of increasing the impact velocity by factors of two and four such that the nominal impact velocities are 1300, 2600, and 5200 m/s.
- The effect of initial yaw and impact velocity for spaced-plate targets.

COMPARISON TO TEST DATA AND MESA COMPUTATIONS

Figure 1 shows three impact conditions for a depleted uranium (DU) rod impacting a steel plate. These problems are presented and discussed by Cagliostro, *et al.* (1990). The obliquity, γ, is the angle between the rod velocity vector and the plate normal, in a coordinate system fixed to the plate. The yaw angle is $\alpha = \gamma - \beta$, where β is the angle between the rod axis and the plate normal. These problems represent a rod velocity of 1290 m/s relative to the plate, an obliquity of $\gamma = 65$ degrees, and three nominal yaw angles of 0, –10, and +10 degrees. The conditions on the left side of Fig. 1 are for a stationary plate. Those on the right side are essentially equivalent, except that the yaws are obtained by inducing velocities into the plates. This allows the rod velocity vectors to act along the longitudinal axes of the rods.

Figure 2 shows EPIC three-dimensional computations for these three conditions. A constant flow stress of 1790 MPa was used for the rod, and a constant flow stress of 1000 MPa was used for the steel plate. These strengths were used so that a direct comparison with MESA code computations (Cagliostro, *et al.*, 1990) could be made. The materials were not allowed to fracture, and the erosion strain was 1.5.

When a Lagrangian material erodes, the element essentially disappears, except that mass is retained at the nodes. This is necessary to allow the sliding interface to be continuously updated, such that the projectile can erode through the top surface of the target plate. This provides the capability to penetrate and perforate thick target plates (Johnson and Stryk, 1987).

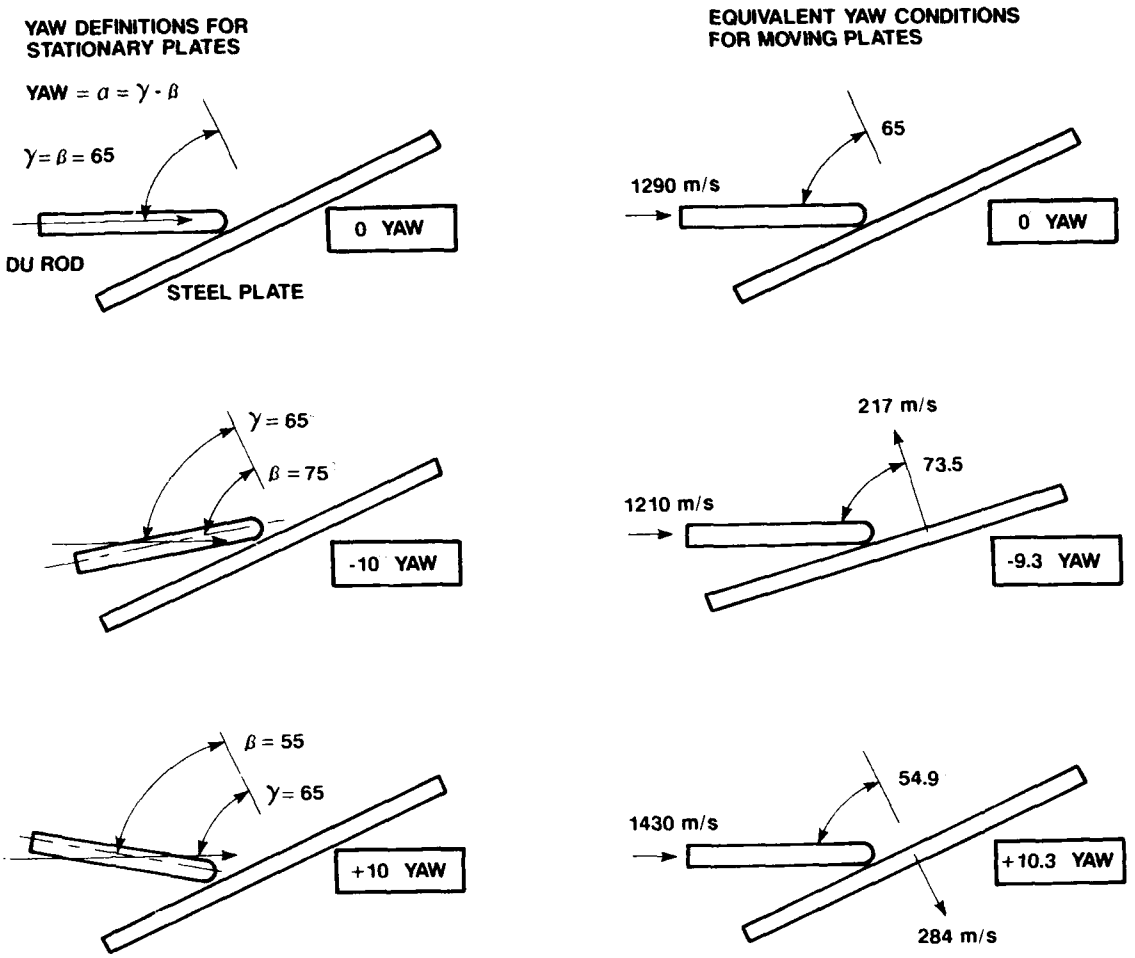


Fig. 1. Baseline Yaw Conditions for Stationary Plates and Equivalent Yaw Conditions for Moving Plates

Figure 3 shows the EPIC results compared to Eulerian MESA code computations (Cagliostro, *et al.*, 1990) and to experimental test data (Fugelso and Taylor, 1978). In general, the EPIC results are in good agreement with the trends of experimental data and they are as accurate as the MESA results. Due to the scatter in the test results, it is difficult to quantify the differences between the computed results and the test results. Some of the differences between the computations and the test data may be due to effects of fracture and friction, which were not included in the computations. It should be noted that the MESA results for the net velocity are improved when the constant flow stress is replaced with a thermal softening model and/or a fracture model (Cagliostro, 1990).

There are two sets of EPIC results shown in Fig. 3. The EPIC (PREVIOUS) results were presented earlier by Johnson and Schonhardt (1991), and these were based on a coarser grid and a slightly different sliding interface algorithm. The EPIC (PRESENT) results, shown in Fig. 2, have a finer grid which is similar to that used for the MESA computations. The volume of the MESA cells and the volume of the EPIC elements are both equal to 1.0 mm^3 in the uniform regions of the grid. Because the Lagrangian grid is only embedded into the rod and the plate, it requires only 20,112 elements. The Eulerian grid, however, must include the entire region, and it required 202,752 cells, for essentially the same grid size as the Lagrangian computation.

This effect is clearly shown in the comparative computing times. The Lagrangian EPIC computations required only 13 CPU minutes on a CRAY Y-MP computer for 100 μs, whereas the Eulerian MESA computations required 3 hours for the same 100 μs on a CRAY X-MP. Even though the CRAY Y-MP is about twice as fast as the CRAY X-MP, the Lagrangian computations are definitely much faster. As a point of reference, the EPIC (PREVIOUS) results used a coarser grid of only 10,368 elements, and it required only 6 CPU minutes on a CRAY Y-MP.

These results cannot be generalized for all problems. For penetration into thick plates, the accuracy of the Lagrangian erosion algorithm can decrease (Johnson and Stryk, 1987), and the CPU difference may not be as great. For spaced-plate computations, however, the CPU advantage may be further increased for the Lagrangian codes.

It is not the purpose of this paper to argue the relative merits of Lagrangian and Eulerian codes, because both have advantages and disadvantages for different classes of problems. It is intended instead to show that Lagrangian codes can be effectively used for high-velocity impact computations.

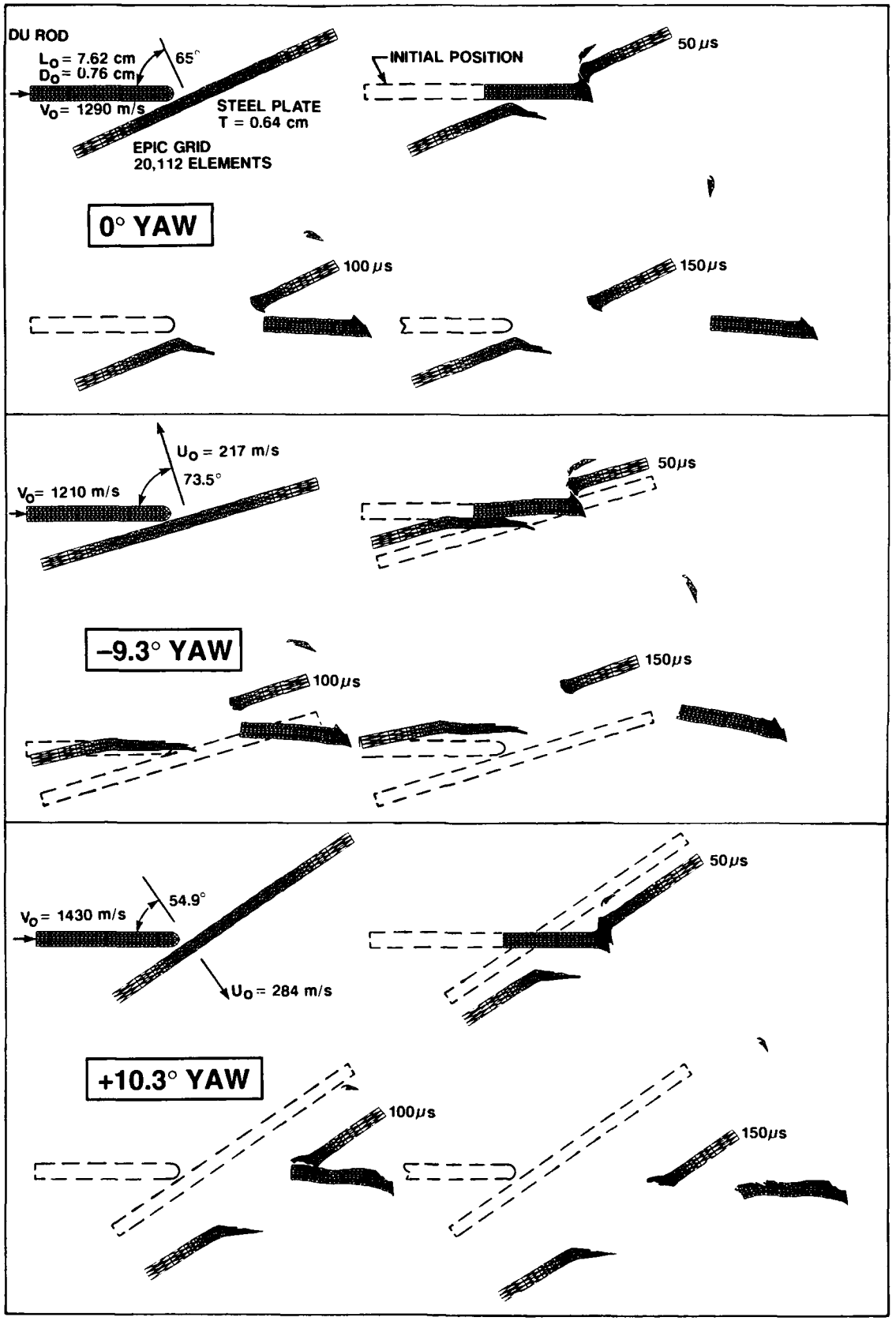


Fig. 2. Baseline EPIC Computations at 0, –9.3, and +10.3 Degree Initial Yaw

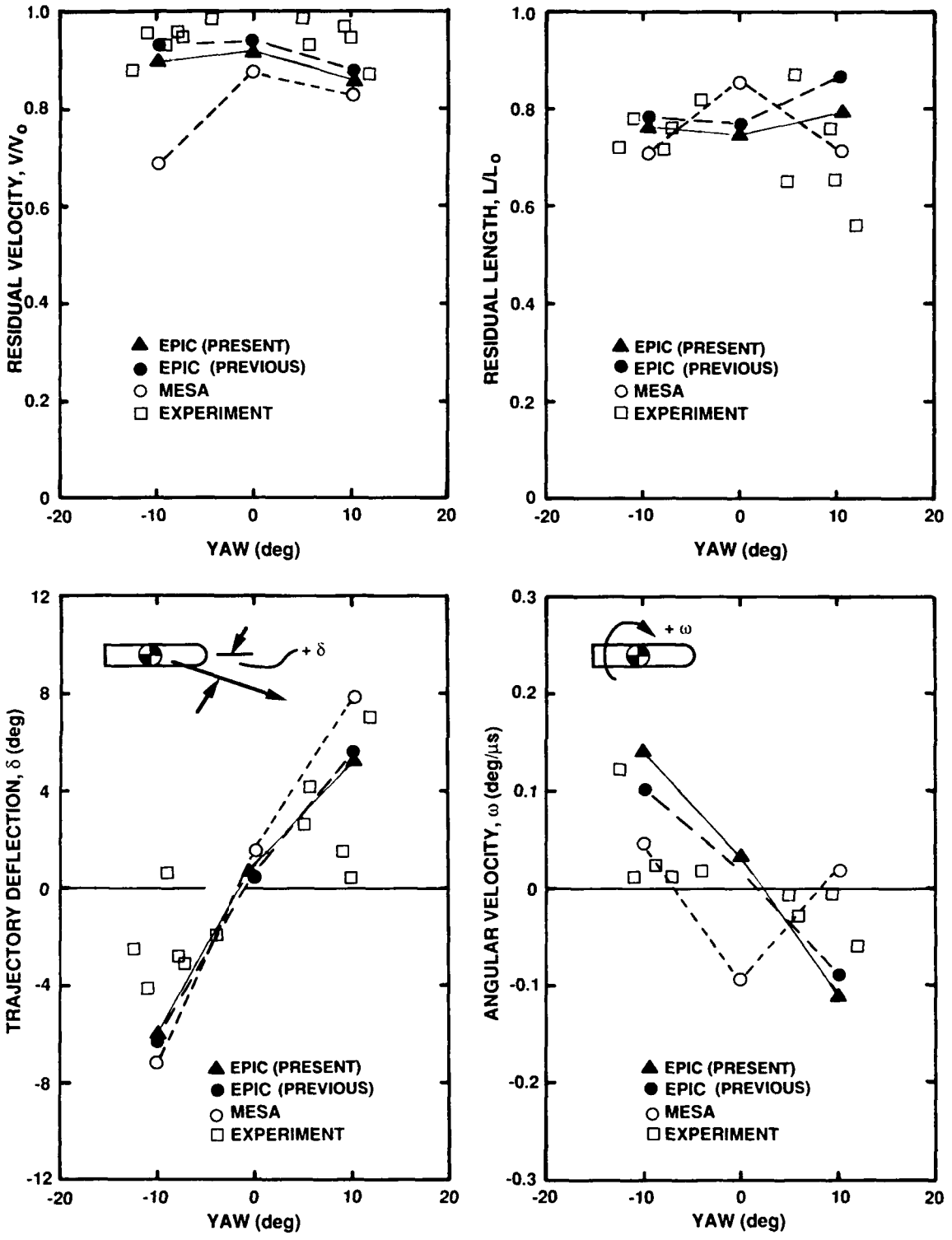


Fig. 3. Comparison of EPIC Computations with MESA Computations and Test Data

EFFECT OF INCREASED PROJECTILE VELOCITY

Now that the accuracy of the EPIC computations has been partially assessed by comparing to test data, it is of interest to examine the effects of other variables. Figures 4 and 5 show the effects of increasing the baseline rod velocities by factors of two and four. The plate velocities remain the same as for the baseline conditions so that the yaw is decreased. The times at which the results are shown are decreased by factors of two and four so that meaningful comparisons can be made. Although there is no experimental verification of these higher-velocity computed results, there is no reason to believe that the accuracy should be different than that of the lower-velocity baseline results.

Figure 6 shows residual rod characteristics as a function of impact velocity for the various yaw conditions. These results are complicated by the fact that the obliquity is not constant for the different yaw conditions. For the residual velocity (V/V_O) and the trajectory deflection (δ), the effects of yaw are almost eliminated at the nominal increased velocities of 2600 and 5200 m/s. The residual lengths (L/L_O) for the negative-yaw cases at the increased velocities are less than the other yaw conditions. This may be due to the increased line-of-sight distance (because the obliquity is higher) the negative-yaw rod must travel to perforate the plate.

The angular velocity (ω) results are very interesting. For the baseline conditions in Fig. 2, the early angular velocities are negative (nose up) when the rod first impacts the plate (Cagliostro, *et al.*, 1990). The magnitude of the early rotation is greatest for the negative yaw case because the obliquity is greater and the plate is moving upward. After the negative-yaw rod perforates the plate, the plate pushes the aft end of the rod upward (at 50 μs), thus imparting a large positive angular velocity (nose down). For the baseline positive-yaw case, the plate pushes the aft end of the rod downward (at 100 μs) resulting in a negative angular velocity (nose up).

As the impact velocities are increased, the negative-yaw cases behave in a similar manner, except the magnitudes of the angular velocities are reduced. For the positive yaw cases, however, the plate does not push on the aft end of the rod at the higher velocities. This results in a positive (nose down) final angular velocity as the rod follows the path of least resistance through the normal thickness of the plate.

SPACED-PLATE COMPUTATIONS

As noted previously, Lagrangian computations are well-suited for spaced-plate computations. This is because the grid is embedded in the material only, and the grid is not required for the spaces. Figure 7 shows a three-dimension view of the baseline, no-yaw case at 200 μs, after an additional thick plate has been added at 150 μs. The face of the second plate is about 20 cm from the face of the first plate, along the path of the rod. Both plates are of identical steel material.

Figure 8 shows cross-sectional views of the rod and two plates at 200 μs, as well as the second plate at 250 μs and 350 μs. The negative-yaw rod does not perforate because of the lower velocity and higher angle at impact. The positive yaw does perforate, and it is probably because of the higher velocity.

Figure 9 shows results for increased rod velocities of approximately 2600 m/s. Here, the increased velocities and decreased impact angles allow the rods for all three cases to readily perforate the second plate.

SUMMARY AND CONCLUSIONS

This paper has demonstrated that Lagrangian EPIC code computations can provide reasonably accurate, efficient, and useful results for a class of problems involving rods (at various obliquities, yaws, and velocities) impacting targets composed of thin and spaced plates. It also has shown the effects of varying these parameters and has provided insight into understanding the complicated interactions which occur during the course of the events.

ACKNOWLEDGEMENTS

This work was partially funded by Contract F08635-89-C-0074 from Wright Laboratory, Armament Directorate, Eglin Air Force Base. J.A. Schonhardt and R.A. Stryk also provided assistance in performing the computations.

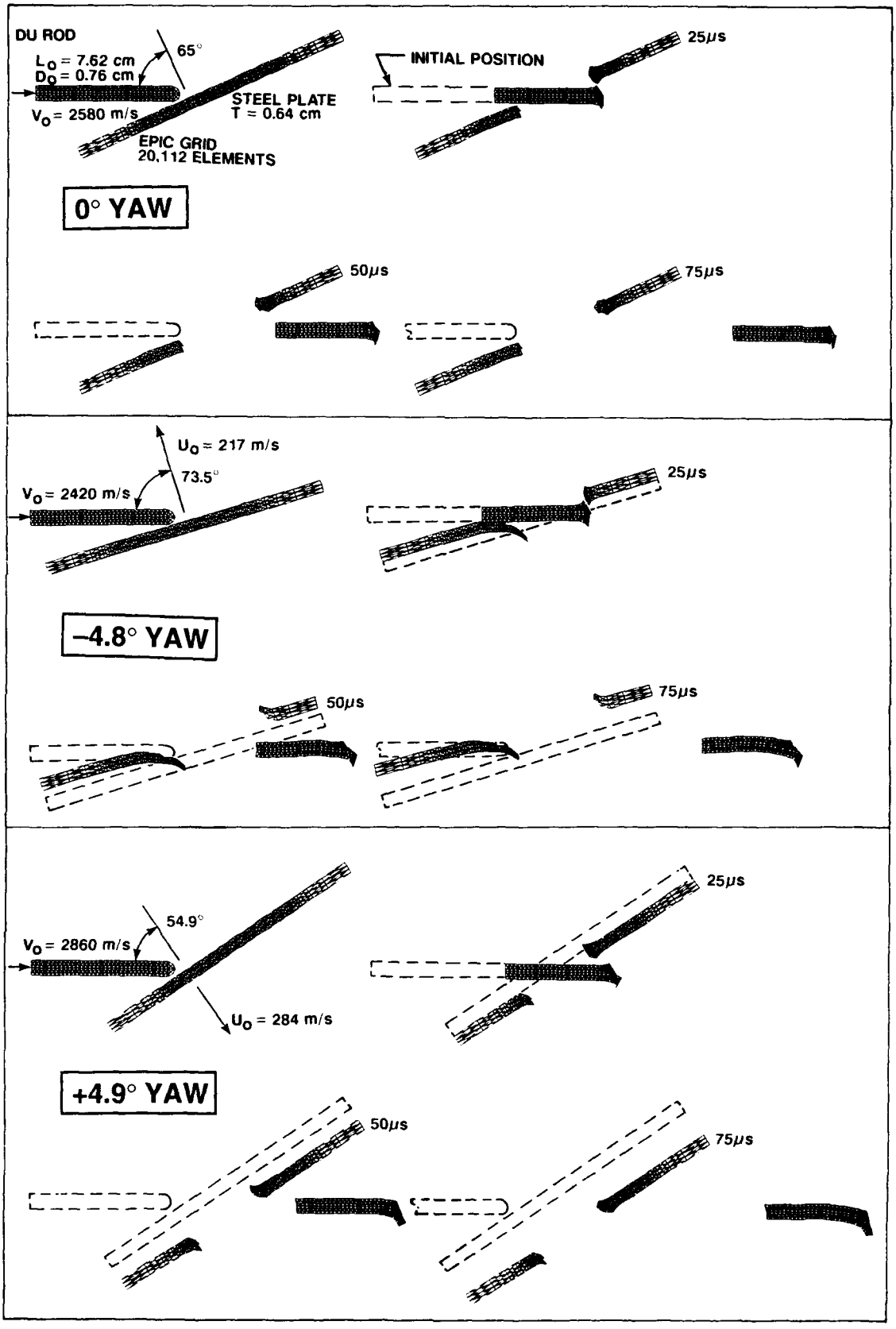


Fig. 4. EPIC Computations for Increased Rod Velocities (2x Baseline) at 0, −4.8, and +4.9 Degree Initial Yaw

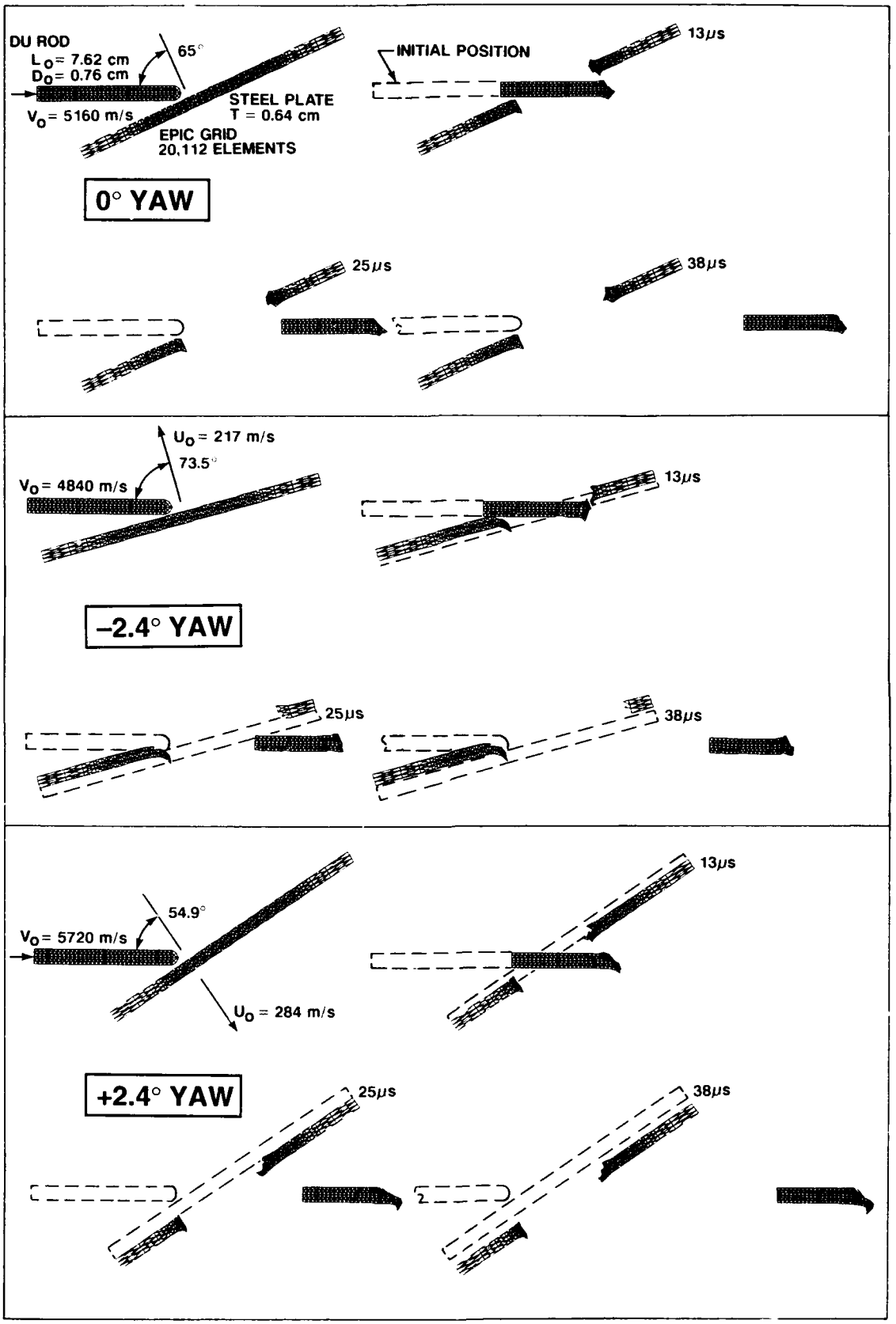


Fig. 5. EPIC Computations for Increased Rod Velocities (4x Baseline) at 0, −2.4, and +2.4 Degree Initial Yaw

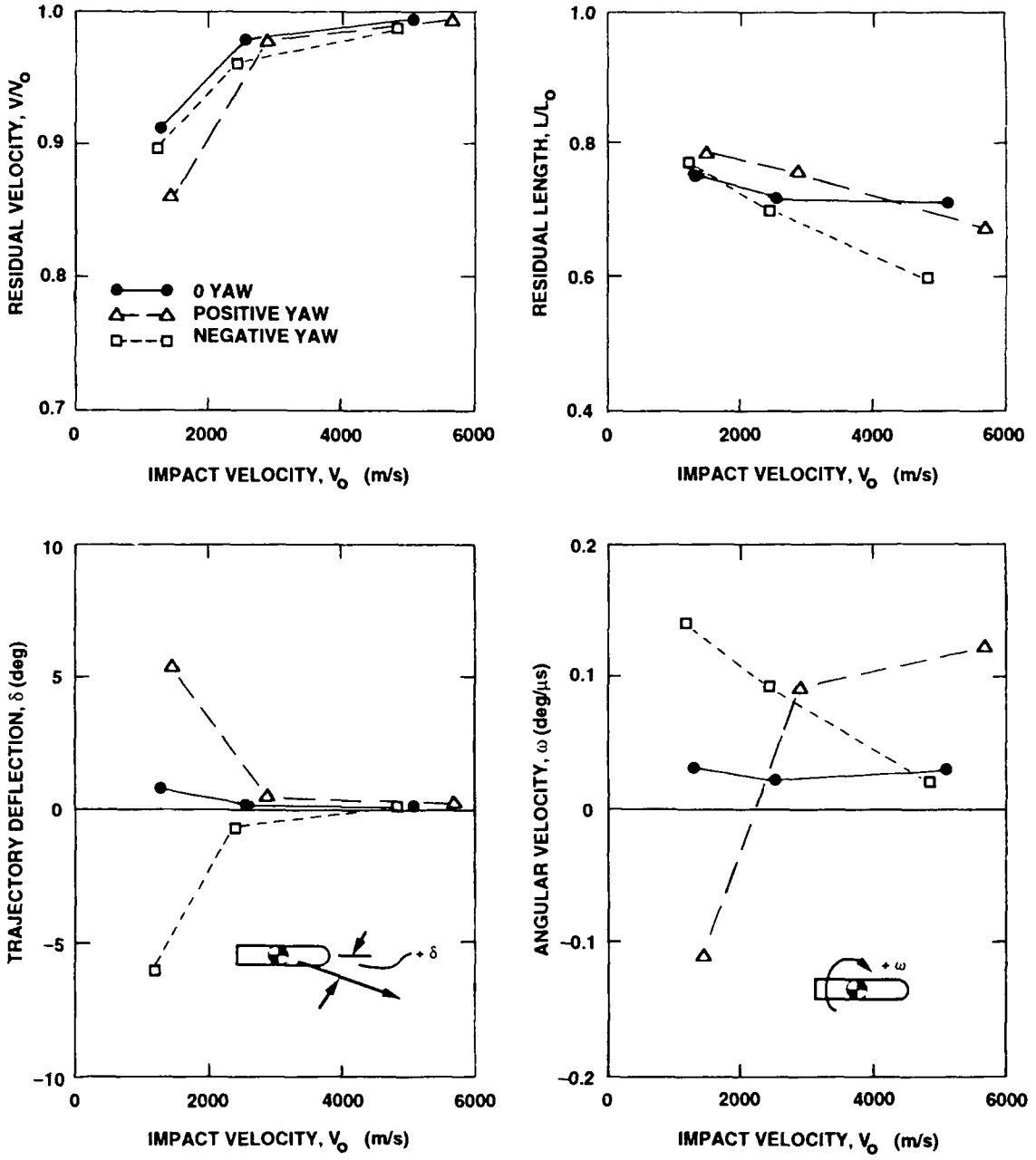


Fig. 6. Results of EPIC Computations Which Show the Effect of Rod Impact Velocity for the Various Initial Yaw Conditions

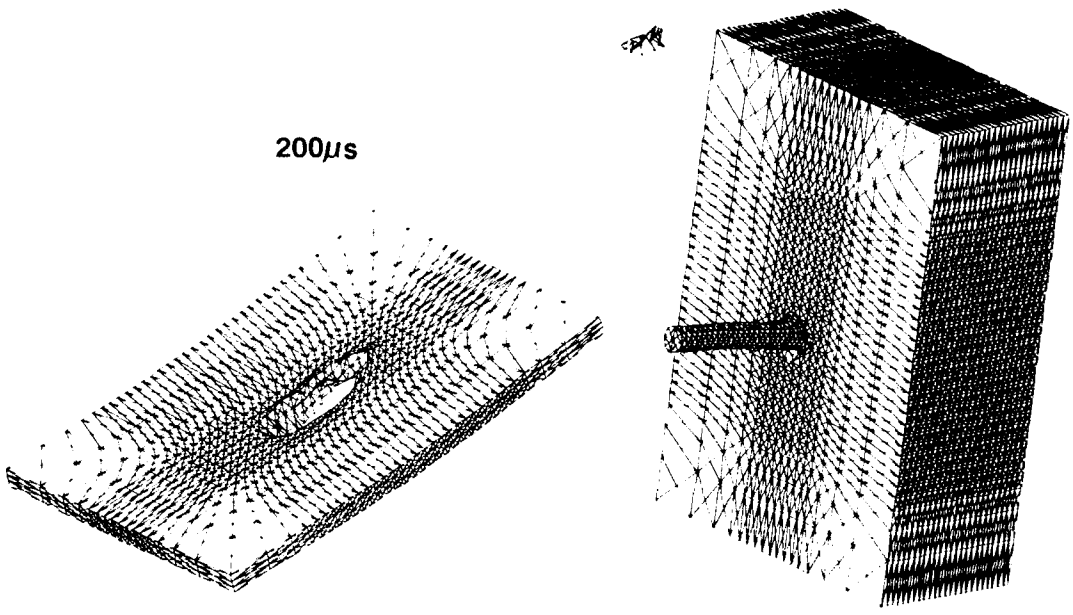


Fig. 7. Three-Dimensional View of Spaced-Plate Baseline Computation with 0 Degree Initial Yaw

REFERENCES

Cagliostro, D.J., Personal Communication, 1990.

Cagliostro, D.J., D.A. Mandell, L.A. Schwalbe, T.F. Adams, and E.J. Chapyak, "MESA 3-D Calculations of Armor Penetration by Projectiles with Combined Obliquity and Yaw," *Intl. J. of Imp. Eng.*, 10, 1990.

Fugelso, E. and J.W. Taylor, *Evaluation of Obliquity and Yaw for U 0.75 wt % Ti Penetrators*, Los Alamos Scientific Laboratory Report LA-7402-MS, 1978.

Johnson, G.R. and J.A. Schonhardt, "Some Parametric Sensitivity Analyses for High Velocity Impact Computations," *Proceedings of Impact III (Post SMiRT 11 Conference)*, Tokyo, Japan, 1991.

Johnson, G.R. and R.A. Stryk, "Eroding Interface and Improved Tetrahedral Element Algorithms for High Velocity Impact Computations in Three Dimensions," *Intl. J. of Imp. Eng.*, 5, 1987.

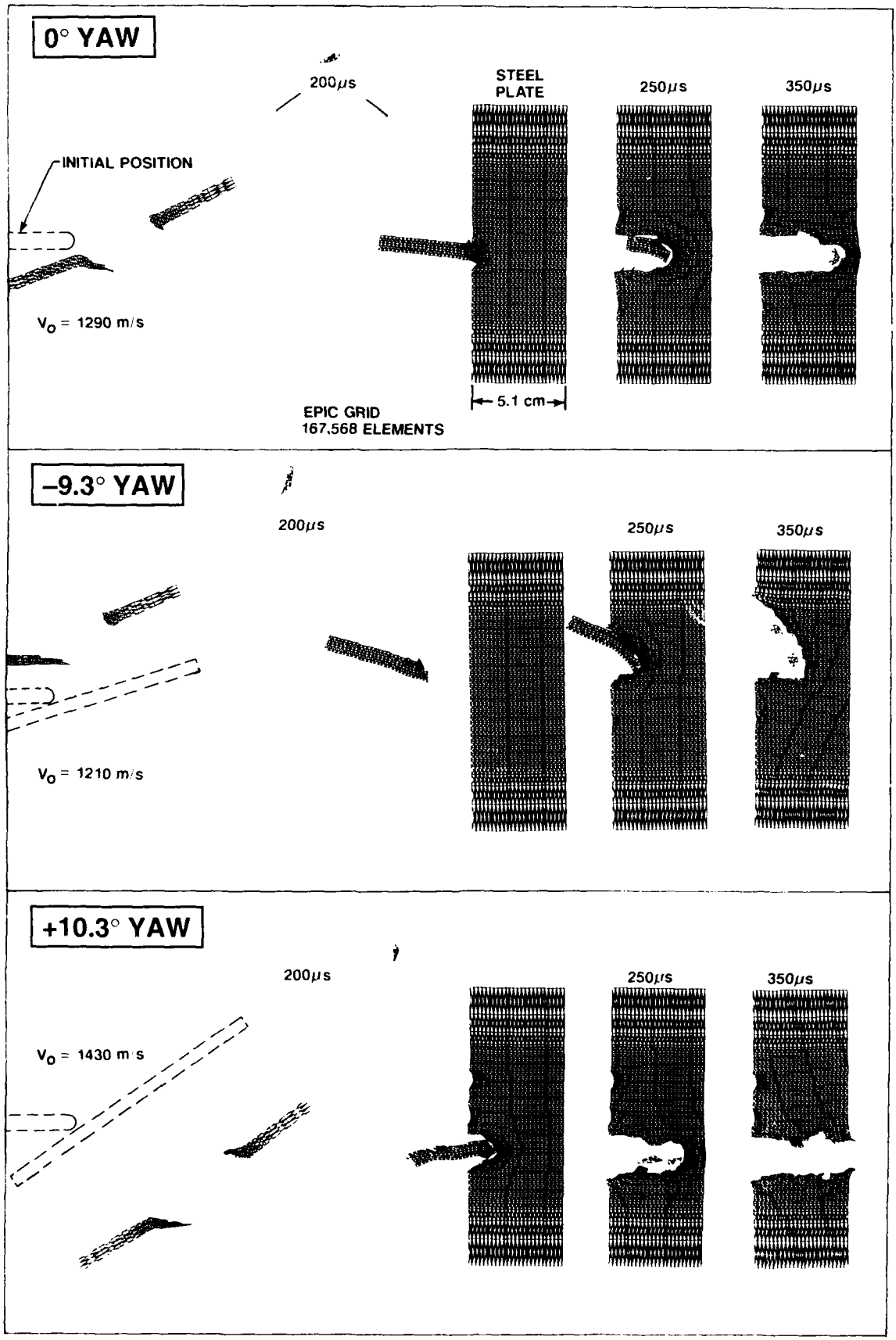


Fig. 8. Spaced-Plate Computations for the Baseline Projectile Velocities at 0, –9.3, and +10.3 Degree Initial Yaw

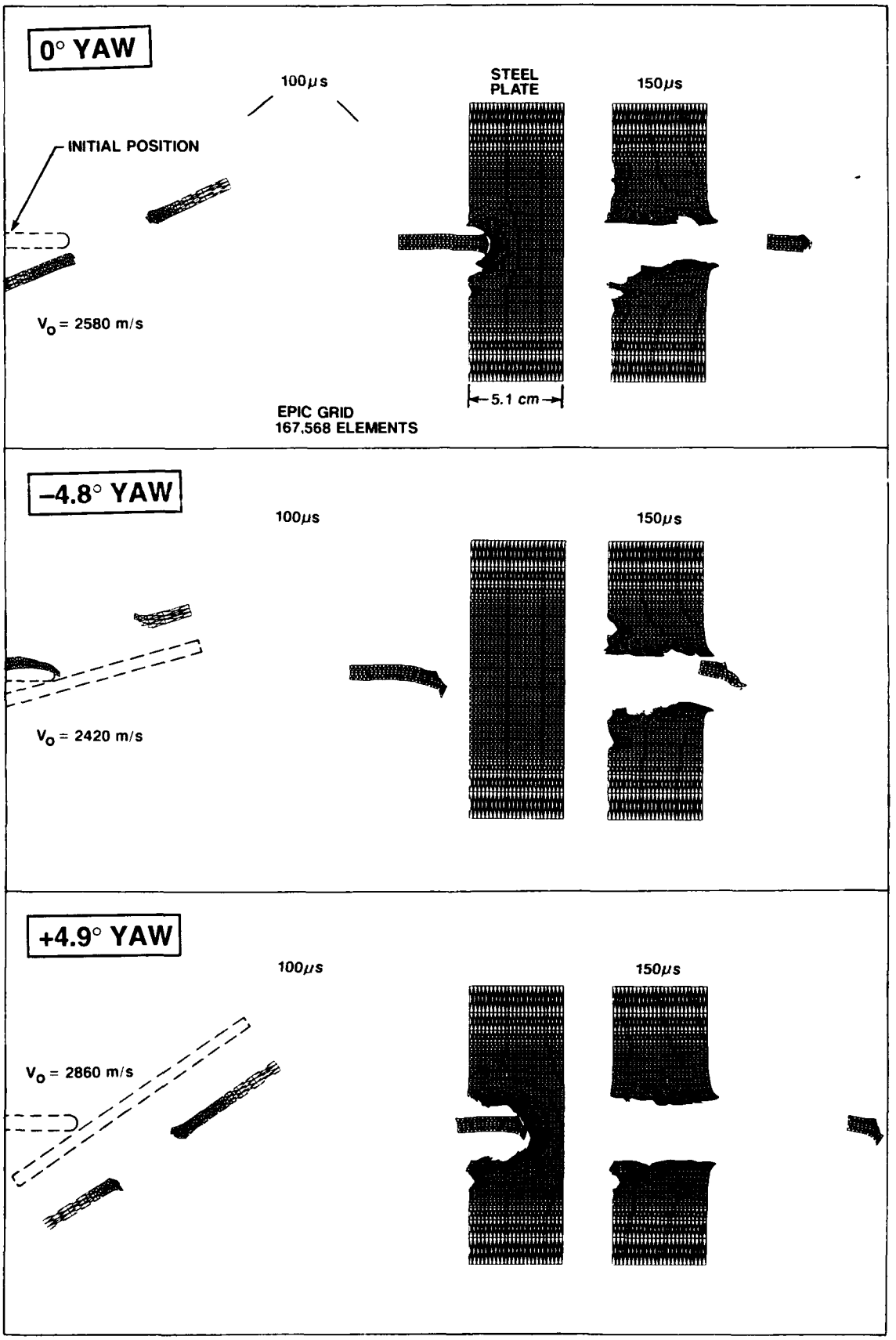


Fig. 9. Spaced-Plate Computations for Increased Velocities (2x Baseline) at 0, –4.8, and +4.9 Degree Initial Yaw

Int. J. Impact Engng Vol 14, pp.385–394, 1993
Printed in Great Britain

0734-743X/93 $6.00+0.00
1993 Pergamon Press Ltd

INCORPORATION OF AN SPH OPTION INTO THE EPIC CODE FOR A WIDE RANGE OF HIGH VELOCITY IMPACT COMPUTATIONS

Gordon R. Johnson, Eric H. Petersen, and Robert A. Stryk

Alliant Techsystems Inc.
Brooklyn Park, Minnesota

ABSTRACT

This paper describes and demonstrates how a Smooth Particle Hydrodynamics (SPH) algorithm can be incorporated into a standard Lagrangian code such as EPIC. The SPH technique is also Lagrangian, but it has variable nodal connectivity and can handle severe distortions in a manner comparable with Eulerian codes. Included is the SPH algorithm for axisymmetric geometry, example problems using only the SPH option, and example problems where the SPH grid is coupled to the standard EPIC grid. The coupling techniques allow for attachment, sliding, and automatic generation of SPH nodes.

INTRODUCTION

The Smooth Particle Hydrodynamics (SPH) technique was first introduced by Lucy (1977) and Gingold and Monaghan (1977). Since then, further contributions have been made by Schüssler and Schmidt (1981), Monaghan (1982), Gingold and Monaghan (1982), Monaghan and Gingold (1983), and Benz (1989). Many of the early applications were directed at astrophysics problems.

Recently, Cloutman (1990), Libersky and Petschek (1990), and Stellingwerf (1990) presented SPH computations for high velocity impact problems. The effect of material strength, for elastic-plastic flow in two-dimensional plane strain geometry, was also presented by Libersky and Petschek (1990). A closely related approach, using variable connectivity NABOR nodes, was provided by Johnson, Stryk, and Dodd (1986) and Johnson and Stryk (1989).

The primary motivation for this work has been a desire to perform severe distortion computations in a Lagrangian framework. Because there are no elements or fixed grids in these variable connectivity approaches, highly distorted flow can be represented. Although it has yet to be demonstrated or proven, the hope is that the SPH techniques can provide sufficiently accurate and efficient results to improve on the current capabilities of standard finite element Lagrangian and finite difference Eulerian approaches.

This paper describes how an SPH option has been incorporated into the EPIC code. Because both the standard elements and SPH nodes are Lagrangian, both the SPH nodes and standard elements can be included in a specific problem. This feature allows for the capability to obtain solutions for a wide range of problems.

SPH ALGORITHM FOR AXISYMMETRIC GEOMETRY

The derivation and theoretical discussion of the SPH approach is not provided in this paper. It will instead be an extension of the work of Libersky and Petschek (1990). In some cases, the SPH algorithm reported herein has been modified to allow it to fit into the framework of the EPIC code. The axisymmetric algorithm is included because it is not a straightforward extension of the plane strain algorithm.

Before presenting the specific algorithm, a few comments should be made to show how the SPH option fits into the structure of a standard Lagrangian code. The following four steps represent the primary computational activities:

- Step 1 – Update the velocities and displacements of the nodes, based on the nodal forces generated during the previous cycle. This includes both the standard nodes and the SPH nodes. The forces can come from both the standard elements and the SPH nodes.
- Step 2 – Update the velocities and displacements of the nodes (standard and SPH) on the sliding interfaces.

- Step 3 – Determine strain rates and strains in the standard elements. From these and other variables, the pressures, deviator stresses, and net stresses are obtained with various material models. The net stresses are then converted to equivalent forces acting on the nodes.
- Step 4 – Determine strain rates and strains in the SPH nodes. The net stresses are obtained in exactly the same manner as they are for the standard elements. These nodal stresses are then converted to equivalent forces acting on the nodes.

It should be emphasized that the forces in Step 1 can come from either the standard elements or the SPH nodes. Another important observation is that the same material models can be used for both the standard elements and the SPH nodes.

Finally, there is another powerful possibility that can be exercised. This consists of converting highly distorted standard elements into SPH nodes as the computation progresses. This, and other coupling approaches, will be demonstrated later.

Figure 1 represents some features of the SPH technique. Node i is designated as the center node and the neighbor nodes are designated as nodes j. The distance between nodes is r_{ij}, the diameters of the nodes are d_i and d_j, and the masses of the nodes are M_i and M_j. The masses remain constant throughout the computation, and are obtained from $M = \rho_o V_o$ where ρ_o and V_o represent the initial density of the material and the initial volume represented by the node.

The smoothing function used in this work is identical to the plane strain smoothing function used by Libersky and Petschek (1990). It is shown in Fig. 1 and exhibits the characteristics of a Dirac delta function as h_{ij} approaches zero.

$$W_{ij} = \frac{1}{\pi h_{ij}^2}\left[\frac{15}{7}\left(\frac{2}{3} - v_{ij}^2 + \frac{1}{2}v_{ij}^3\right)\right] \qquad 0 \le v_{ij} \le 1 \tag{1}$$

$$W_{ij} = \frac{1}{\pi h_{ij}^2}\left[\frac{5}{14}\left(2 - v_{ij}^3\right)\right] \qquad 1 \le v_{ij} \le 2$$

where $v_{ij} = r_{ij}/h_{ij}$, and the smoothing distance is

$$h_{ij} = \alpha(d_i + d_j)/2 \tag{2}$$

The dimensionless constant, α, is a user supplied input. The examples in this paper are for $\alpha = 1.0$.

The diameters, d_i and d_j, can be obtained from

$$d = d_o \sqrt{(1 + \varepsilon_v)\, x_o/x} \tag{3}$$

where ε_v is the volumetric strain, d_o is the initial node diameter, and x_o and x are the initial and current X (radial) coordinates.

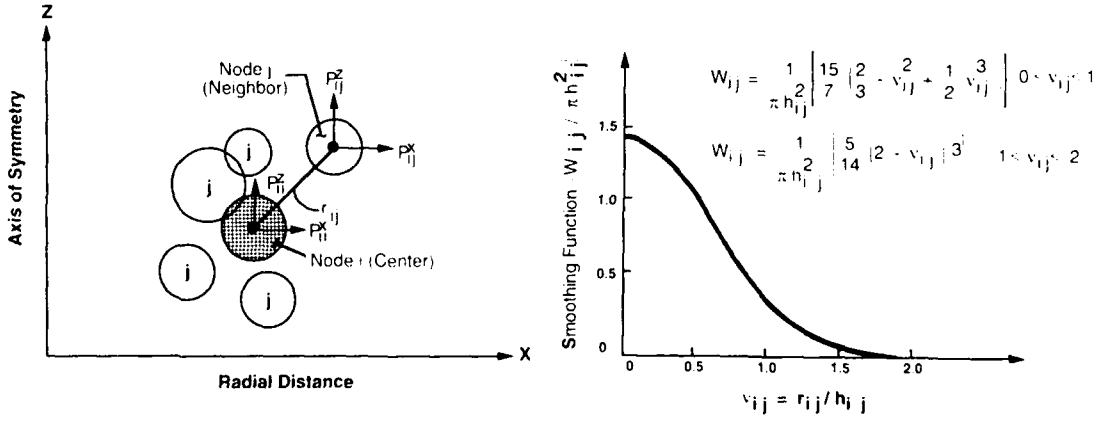


Fig. 1. Description of SPH Characteristics

The volumetric strain rate of node i, based on the current configuration, is given by

$$\dot{\varepsilon}_v = \sum_j - W'_{ij} V_j \left[(\dot{u}_j - \dot{u}_i) l_x + (\dot{v}_j - \dot{v}_i) l_z + \frac{r_{ij}\dot{u}_j}{2x_j} \right] \Big/ 2\pi x_j \tag{4}$$

where $W'_{ij} = \partial W_{ij}/\partial r$ is the derivative of the smoothing function, V_j is the current volume of the node j, $\dot{u}_i$ and $\dot{u}_j$ are the X velocities of nodes i and j, $\dot{v}_i$ and $\dot{v}_j$ are the Z velocities, l_x and l_z are the direction cosines from node i to node j, and x_j is the X coordinate of node j.

The in-plane contribution of Equation 4 is provided by

$$\sum_j - W'_{ij} V_j \left[(\dot{u}_j - \dot{u}_i) l_x - (\dot{v}_j - \dot{v}_i) l_z \right] \Big/ 2\pi x_j \tag{4a}$$

where the division by $2\pi x_j$ adjusts the volume, V_j, to what it would be in plane strain geometry.

The hoop contribution of Equation 4 is provided by

$$\sum_j - W'_{ij} V_j \left(\frac{r_{ij}\dot{u}_j}{2x_j} \right) \Big/ 2\pi x_j \tag{4b}$$

For a fully surrounded center node i, and neighbor nodes j, moving at a constant radial velocity $\dot{u}_i = \dot{u}_j$, the hoop contribution must be equal to $\dot{u}/x$. Also, it can be demonstrated that for a fully surrounded node i

$$\sum_j - W'_{ij} V_j \left(\frac{r_{ij}}{2} \right) \Big/ 2\pi x_j = 1 \tag{5}$$

Therefore, Equation 5 acts as a weighting function to sum the contribution of the neighbor nodes j. This formulation allows for both the in-plane and hoop contributions to be provided by the identical neighbor nodes j. This is especially important for a radial collapsing or expanding free surface.

The updated volumetric strain can be obtained from

$$\varepsilon_v^{t+\Delta t} = \varepsilon_v^t + \dot{\varepsilon}_v^t \Delta t \left(1 + \varepsilon_v^t \right) \tag{6}$$

where Δt is the integration time increment and the factor $(1 + \varepsilon_v^t)$ converts the strain rate from the current configuration back to the initial configuration.

The nodal pressure, P_i, and bulk artificial viscosity, Q_i, can be determined from the same material models used for the standard elements, now that ε_v and $\dot{\varepsilon}_v$ are known.

To incorporate elastic-plastic material strength, it is necessary to compute the three normal strain rates ($\dot{\varepsilon}_x$, $\dot{\varepsilon}_z$, $\dot{\varepsilon}_\theta$), the shear strain rate, $\dot{\gamma}_{xz}$, and the rotational rate, ω_{xz} (Johnson, 1979).

$$\dot{\varepsilon}_x = \sum_j - W'_{ij} V_j (\dot{u}_j - \dot{u}_i) l_x / 2\pi x_j \tag{7}$$

$$\dot{\varepsilon}_z = \sum_j - W'_{ij} V_j (\dot{v}_j - \dot{v}_i) l_z / 2\pi x_j \tag{8}$$

$$\dot{\varepsilon}_\theta = \sum_j - W'_{ij} V_j \left(\frac{r_{ij}\dot{u}_j}{2x_j} \right) \Big/ 2\pi x_j \tag{9}$$

$$\dot{\gamma}_{xz} = \sum_j - W'_{ij} V_j \left[(\dot{u}_j - \dot{u}_i) l_z + (\dot{v}_j - \dot{v}_i) l_x \right] / 2\pi x_j \tag{10}$$

$$\omega_{xz} = \sum_j W'_{ij} V_j \left[(\dot{u}_j - \dot{u}_i) l_z - (\dot{v}_j - \dot{v}_i) l_x \right] / 4\pi x_j \tag{11}$$

The effects of axisymmetric geometry are similar to those for the volumetric strain rate. Again, the SPH nodes can use the same constitutive models as used for the standard elements.

The nodal forces on node i and nodes j, for the stresses of node i, can now be determined.

$$P^x_{ij} = P^x_{ij\ (plane)} + P^x_{ij\ (hoop)} \tag{12}$$

where P^x_{ij} is the force on node j due to stresses in node i. The force due to the in-plane stresses is

$$P^x_{ij\ (plane)} = M_i M_j W'_{ij} \left\{ \left[\left(\sigma^x_i - Q_{ij} \right) l_x + \tau^{xz}_i l_z \right] / \rho^2_i \right\} / 2\pi x_j \tag{13}$$

where $\sigma^x_i = s^x_i - (P_i + Q_i)$ is the net normal stress in the X direction, composed of the deviator stress, pressure and bulk artificial viscosity. The shear stress is τ^{xz}_i and the density of node i is ρ_i.

There is also an artificial viscosity, Q_{ij}, which is dependent on the relative velocities of nodes i and j (Monaghan and Gingold, 1983). It is intended to keep adjacent nodes from becoming too close to one another. This has been expanded by the authors to include a relatively soft resistance spring which begins to act when two nodes approach one another within a user-specified distance.

The axisymmetric effect in Equation 13 comes from dividing M_i by $2\pi x_i$ and M_j by $2\pi x_j$ to get equivalent masses for plane strain. The plane strain forces from node i must be multiplied by $2\pi x_i$, however, to account for the axisymmetric circumferential effect. The net result is a division by $2\pi x_j$.

The force due to the hoop stress is

$$P^x_{ij\ (hoop)} = W'_{ij} V_j \left[\left(\frac{r_{ij}}{2} \right) / 2\pi x_j \right] \left[\sigma^\theta_i V_j / x_j \right] \tag{14}$$

where $\sigma^\theta_i = s^\theta_i - (P_i + Q_i)$ is the net hoop stress and the weighting is done in a manner similar to that used previously. This is consistent with the volumetric and normal strain rate formulations inasmuch as the nodes which determine the strain rates, are the nodes which receive the forces.

The force in the Z direction is

$$P^z_{ij} = M_i M_j W'_{ij} \left\{ \left[\left(\sigma^z_i - Q_{ij} \right) l_z + \tau^{xz}_i l_x \right] / \rho^2_i \right\} / 2\pi x_j \tag{15}$$

Equations 12 and 15 provide the forces only on the neighbor nodes j. The forces on center node i, due to the stresses in node i, are equal and opposite to the in-plane forces in the X and Z directions.

$$P^x_{ii} = - \sum_j P^x_{ij\ (plane)} \tag{16}$$

$$P^z_{ii} = - \sum_j P^z_{ij} \tag{17}$$

It is interesting that node i gets no force from the hoop stresses in node i. This entire process is repeated for each node such that the neighbor j nodes become central i nodes, and the central i nodes become neighbor j nodes.

EXAMPLES

Figure 2 shows four examples of SPH results compared to standard EPIC results. The grid and/or plastic strain contours on the left side of the axisymmetric cylinder are for the standard element computations. The SPH nodes are on the right side of the cylinder. They are shown as circles with diameters of 90 percent of their actual diameters. The outline, on both the left and right sides of the cylinder, is for the standard elements.

The explosive detonation uses the same JWL Equation of State for both the standard elements and the SPH nodes. The deformed shapes show good general agreement at 3 μs, but the outer SPH nodes are too small, and there are large voids between SPH nodes. This occurs because the nodes achieve a much greater spacing in the X direction than they do in the Z direction. The rapid velocity separation in the X direction initially causes the volumetric strain to grow rapidly. Later, however, these nodes escape beyond the smoothing distance and no longer contribute to the expanding volume.

The OFHC copper and Armco iron cylinder impact computations use the Mie-Gruneisen Equation of State and the constitutive model of Johnson and Cook (1983). A comparison of the deformed geometries shows the standard element outline on the right side to provide almost perfect agreement with the outer surface of the SPH nodes. Equivalent plastic strains are also shown for regions of $0.1 \le \bar{\varepsilon}_p \le 0.2$ and $0.5 \le \bar{\varepsilon}_p \le 1.0$, and these results are in good general agreement.

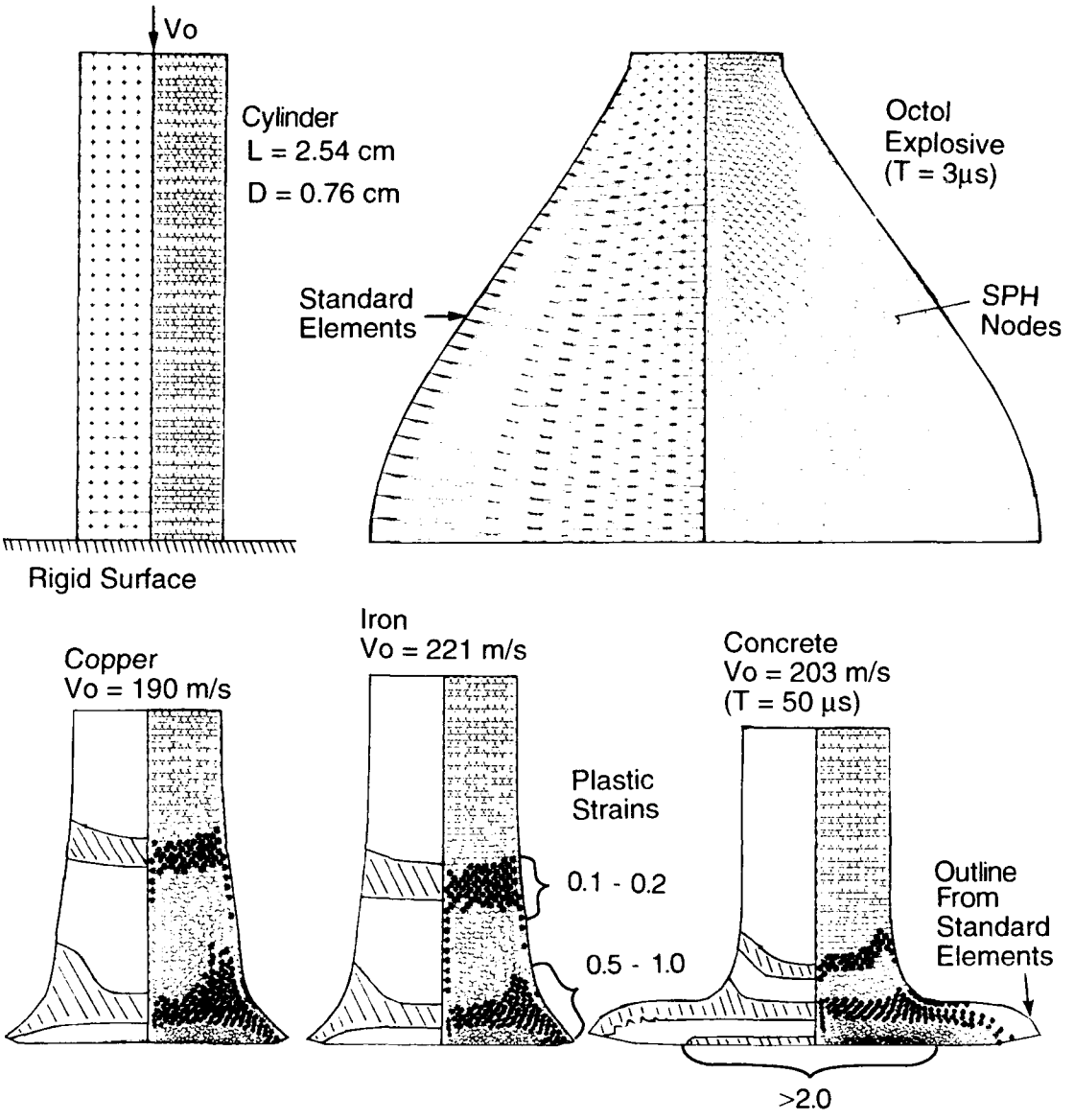
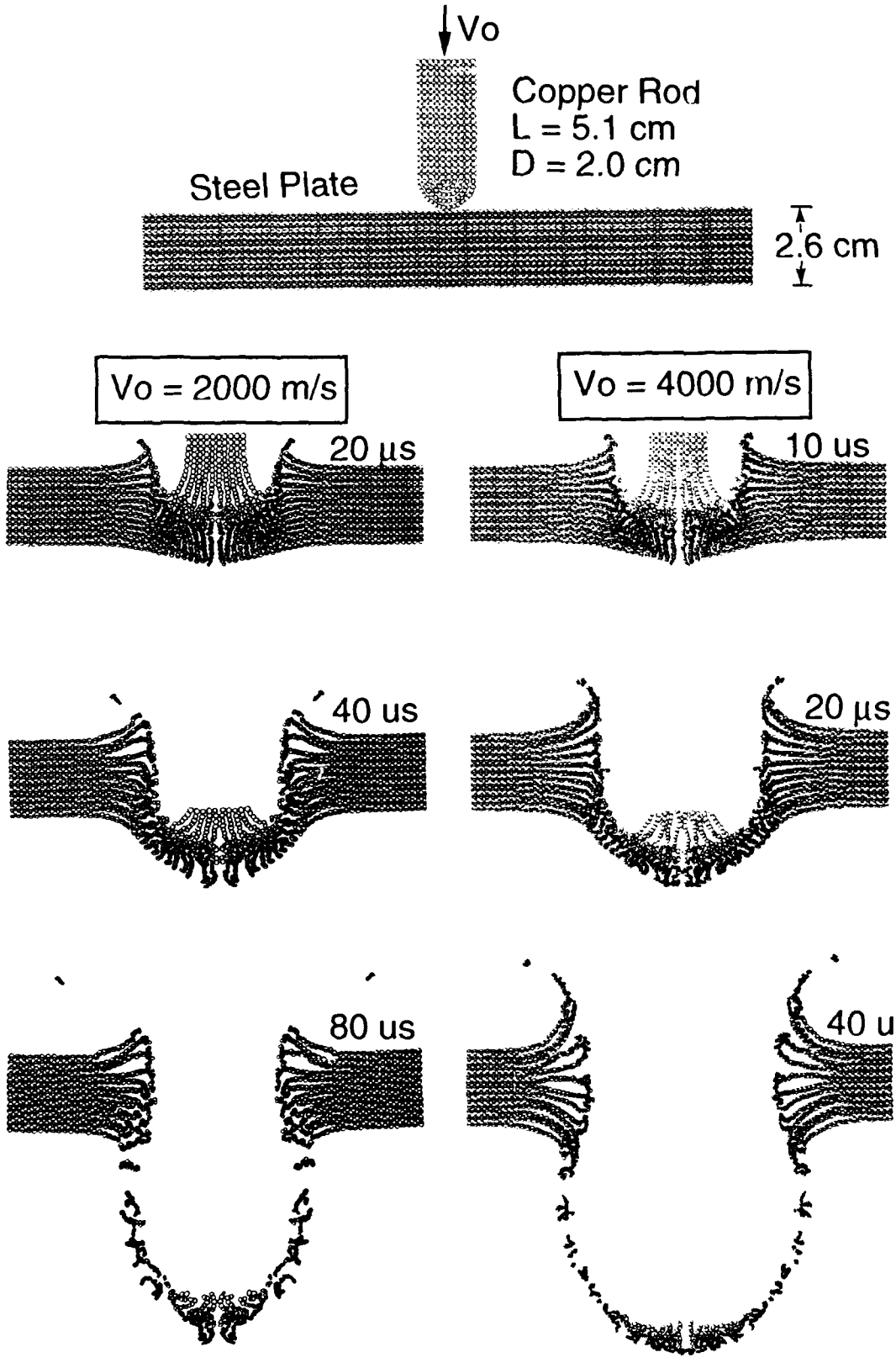


Fig. 2. Comparison of SPH Computations with Standard EPIC Computations for Various Materials

The concrete cylinder impact example uses a crushable pressure-volume relationship and a pressure-dependent strength similar to that presented by Matuska, Durret, and Osborn (1982). In general, the comparison of the computations in Fig. 2 shows the SPH results to be in good agreement with the standard EPIC results for a range of material types and models.

Figure 3 shows two SPH perforation computations for impact velocities of 2000 m/s and 4000 m/s, and Fig. 4 shows an SPH penetration computation for an impact velocity of 5000 m/s. All three results appear to be reasonable and well-behaved.

Figure 5 shows an SPH spall computation using the fracture model of Johnson and Cook (1985). At 1.0 μs, the aluminum projectile is compressed and shows only limited fracture of one node on the outer diameter. At 2.0 μs, the compression has released and the entire projectile has fractured. When a node fractures, the material behaves like a liquid inasmuch as it cannot develop any shear or deviator stresses, and it cannot develop any tensile hydrostatic pressure.


Vo
Copper Rod
L = 5.1 cm
D = 2.0 cm
Steel Plate
2.6 cm
Vo = 2000 m/s
Vo = 4000 m/s
20 μs
10 us
40 us
20 μs
80 us
40 us

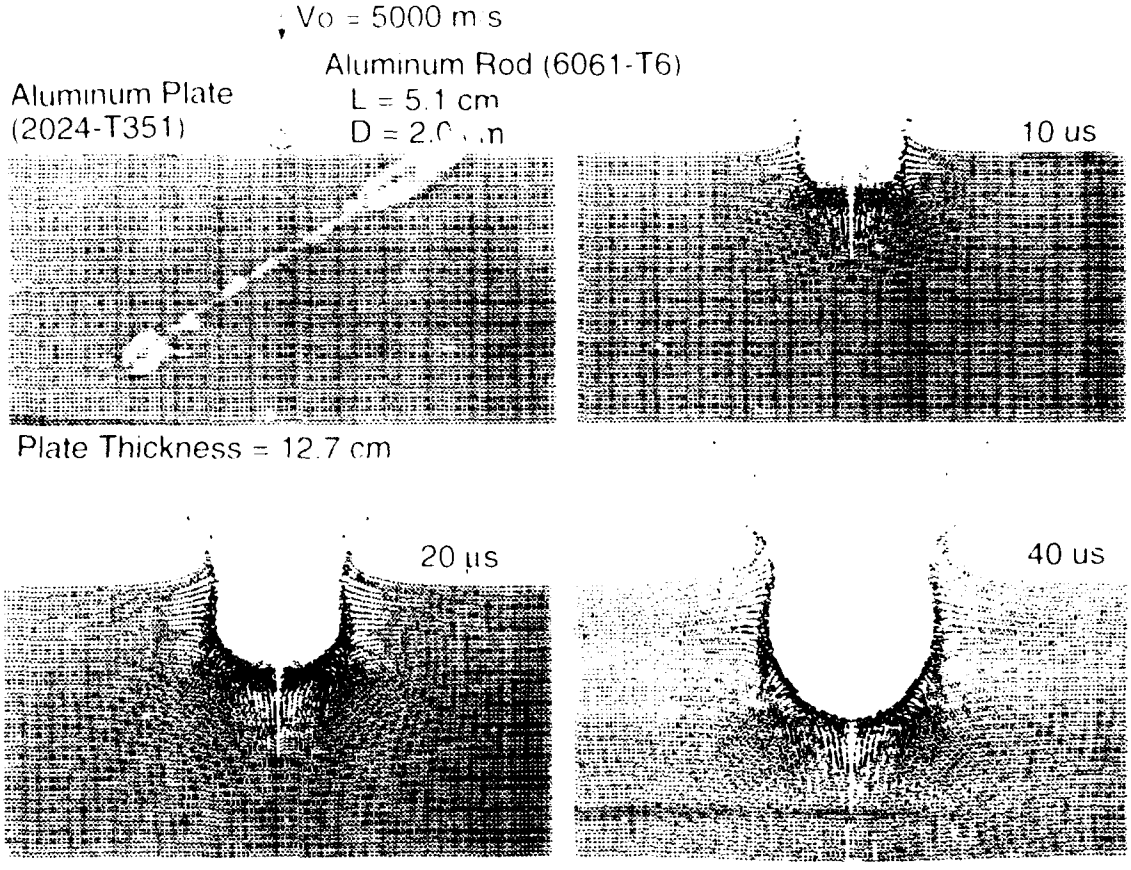


Fig. 4. SPH Penetration Computation for an Impact Velocity of 5000 m/s

The interesting fracture occurs as a spall plane near the bottom of the plate at 12.0 µs. The spall area opens clearly between the adjacent rows of fractured nodes. Again, the fracture model and constants are identical to those used for the standard grid.

The computation in Fig. 6 shows how SPH nodes can be coupled to a standard grid. This concept was demonstrated previously in two dimensions by Johnson, Stryk, and Dodd (1986), and in three dimensions by Johnson and Stryk (1989), using NABOR nodes. This approach allows a relatively soft material, such as concrete, to slide and interact with a much stronger material, such as steel. Because the SPH computations generally require more CPU time than standard element computations, limiting the SPH nodes to the region of high distortion can improve the efficiency of the computation. This approach can also be used to transfer shocks into a structural, standard element grid at later times.

The final example in Fig. 7 shows the powerful potential of the SPH technique when coupled to a standard grid. This problem is identical to that of Fig. 4 except that the initial grid is composed entirely of standard elements. As the computation progresses, however, the highly strained elements on the interface are automatically converted to SPH nodes. When they are converted, they take on the identical characteristics (stress, strain, energy, damage, etc.) of the replaced standard elements. The results of Figs. 4 and 7 are almost identical. Eventually, it may be possible to set up almost any problem with a standard Lagrangian grid, and then have the code decide where and when the SPH nodes should be inserted to provide the best solution.

SUMMARY AND CONCLUSIONS

This paper has shown how an SPH option can be incorporated into a standard Lagrangian code such as EPIC. An axisymmetric algorithm has been incorporated and shown to provide good agreement with standard EPIC computations. The capability to use various Equations of State (EOS) and fracture models, for both SPH and standard element computations, has been demonstrated. Finally, contact logic and the automatic generation of SPH nodes have also been demonstrated through example computations. The results achieved to date are very encouraging, and it would appear as though the SPH technique and the associated coupling techniques will be widely used in the future.

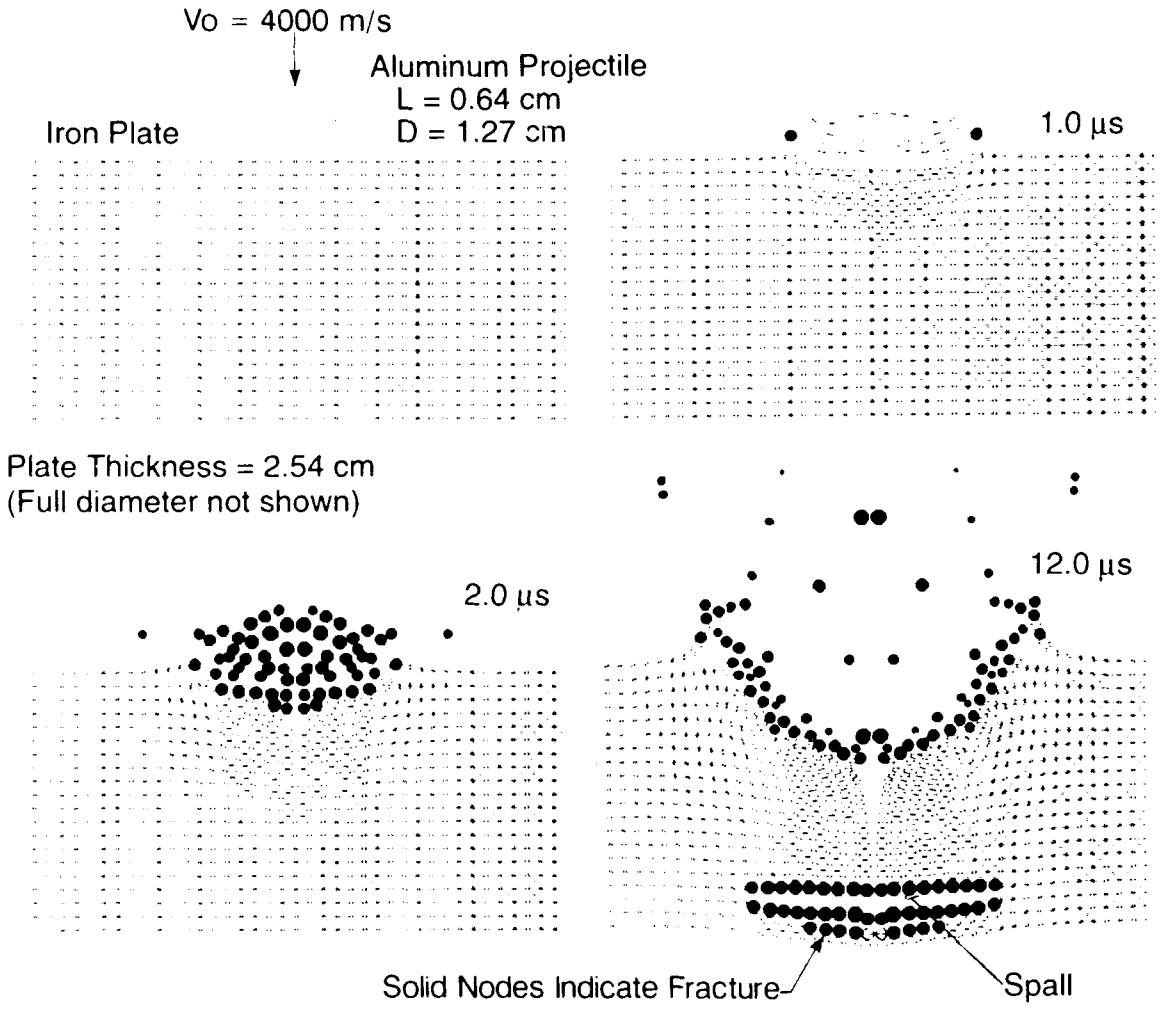


Fig. 5. SPH Spall Computation (Using the Johnson-Cook Fracture Model) for an Impact Velocity of 4000 m/s

ACKNOWLEDGEMENT

This work was funded by DARPA (Defense Advanced Research Projects Agency).

REFERENCES

Benz, W., "Smooth Particle Hydrodynamics: A Review," Harvard-Smithsonian Center for Astrophysics (Preprint 2884), 1989.

Cloutman, L.D., "An Evaluation of Smooth Particle Hydrodynamics," *Advances in the Free-Lagrange Method*," Lecture Notes in Physics, 395, 1990.

Gingold, R.A. and J.J. Monaghan, "Smoothed Particle Hydrodynamics: Theory and Application to Non-spherical Stars," *Monthly Notices Royal Astr. Soc.*, 181, 1977.

Gingold, R.A. and J.J. Monaghan, "Kernel Estimates as a Basis for General Particle Methods in Hydrodynamics," *J. Comp. Phys.*, 46, 1982.

Johnson, G.R., "Dynamic Response of Solids Subjected to Impact and Spin," *AIAA Journal* 17, 1979.

Johnson, G.R. and W.H. Cook, "A Constitutive Model and Data for Metals Subjected to Large Strains, High Strain Rates and High Temperatures," *Proceedings of Seventh International Symposium on Ballistics*, The Hague, The Netherlands, 1983.

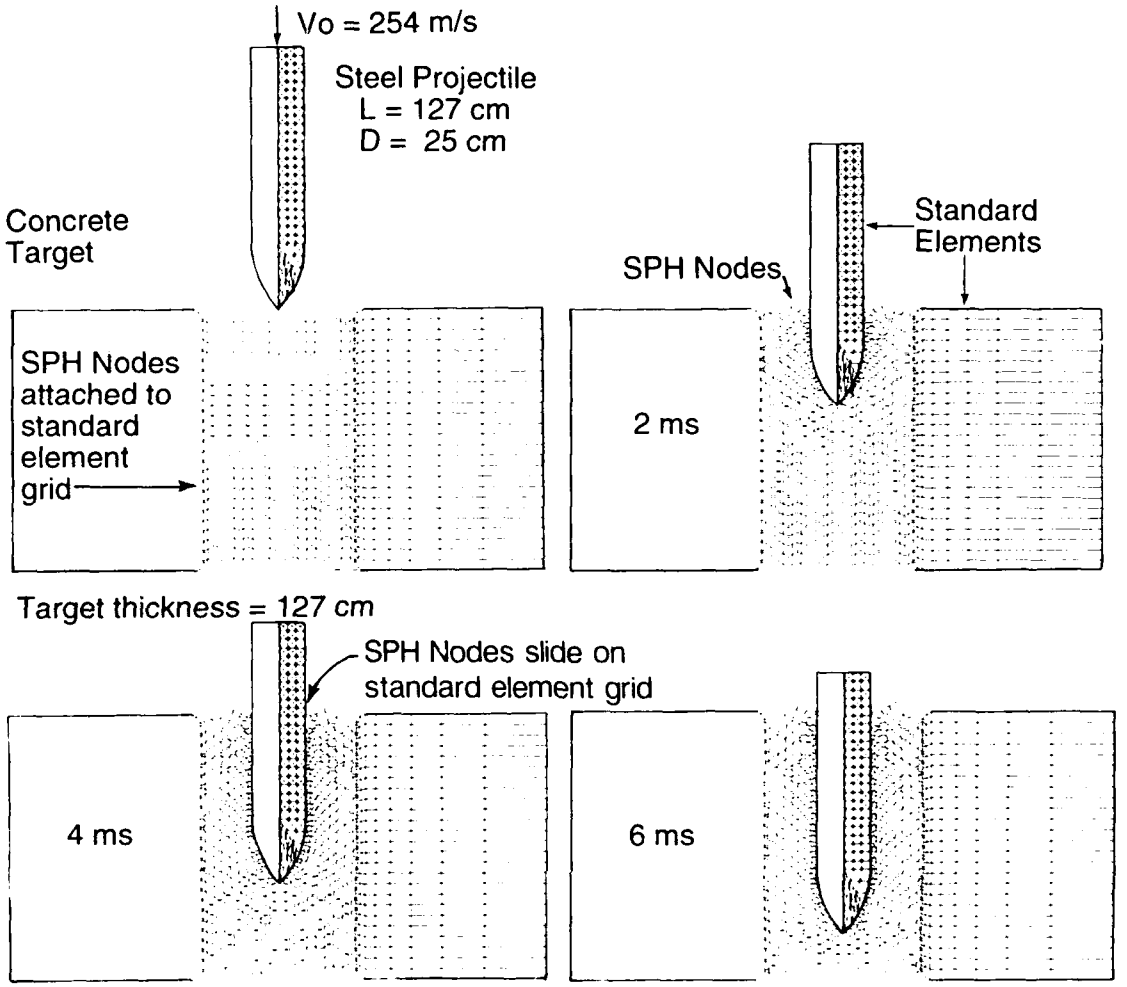


Fig. 6. Coupled Penetration Computation with SPH Nodes Attached to, and Sliding on, Standard Element Grid

Johnson, G.R. and W.H. Cook, "Fracture Characteristics of Three Metals Subjected to Various Strains, Strain Rates, Temperatures and Pressures," *Eng. Fract. Mech.*, 21, 1985.

Johnson, G.R, R.A. Stryk, and J.G. Dodd, "Dynamic Lagrangian Computations for Solids, with Variable Connectivity for Severe Distortions," *Intl. J. Numer. Meth. Eng.*, 23, 1986.

Johnson, G.R. and R.A. Stryk, "Dynamic Three Dimensional Computations for Solids, with Variable Nodal Connectivity for Severe Distortions," *Intl. J. Numer. Meth. Eng.*, 28, 1989.

Matuska, D.A., R.E. Durret, and J.J. Osborn, *Hull User Guide for Three Dimensional Linking with EPIC-3*, ARBRL-CR-00484, 1982.

Lucy, L.B., "A Numerical Approach to the Testing of the Fission Hypothesis," *The Astro. J.*, 82, 1977.

Libersky, L.D. and A.G. Petschek, "Smooth Particle Hydrodynamics with Strength of Materials," *Advances in the Free-Lagrange Method*, Lecture Notes in Physics, 395, 1990.

Monaghan, J.J., "Why Particle Methods Work," *SIAM J. Sci. Stat. Comp.*, 3, 1982.

Monaghan, J.J. and R.A. Gingold, "Shock Simulation by the Particle Method SPH," *J. Comp. Phys.*, 52, 1983.

Schüssler, M. and D. Schmidt, "Comments on Smoothed Particle Hydrodynamics," *Astron. Astrophys.*, 97, 1981.

Stellingwerf, R.F., "Smooth Particle Hydrodynamics," *Advances in the Free-Lagrange Method*, Lecture Notes in Physics, 395, 1990.

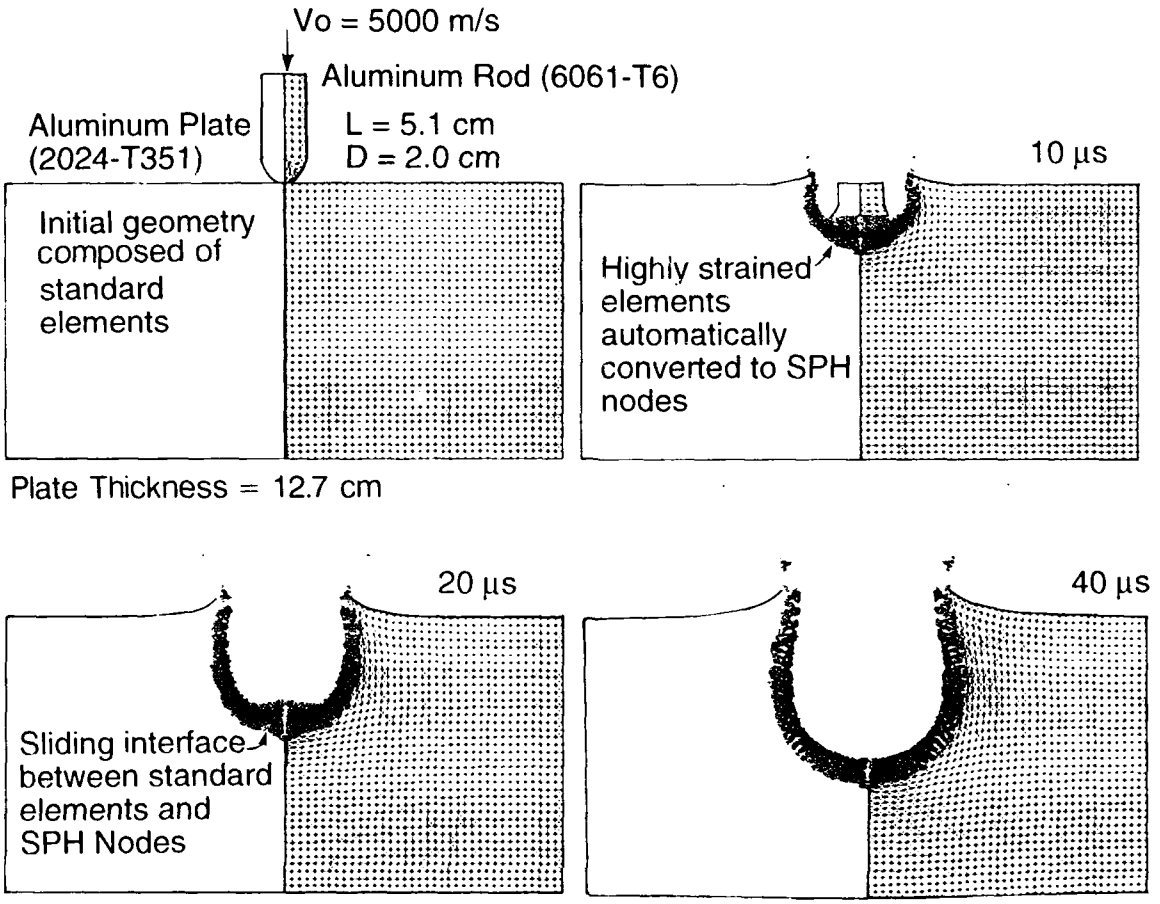


Fig. 7. Coupled Penetration Computation Where Highly Strained Standard Elements are Automatically Converted to SPH Nodes

Int. J. Impact Engng Vol 14, pp 395–406, 1993
Printed in Great Britain

0734-743X/93 $6.00 + 0.00
Pergamon Press Ltd

STATISTICAL BALLISTIC LIMIT CURVE REGRESSION FOR SPACE STATION FREEDOM METEOROID/ORBITAL DEBRIS SHIELDING

William H. Jolly†[1] and Joel E. Williamsen‡

†Kaman Sciences Corporation, Huntsville, AL
‡NASA-Marshall Space Flight Center, AL

ABSTRACT

Relationships defining the ballistic limit of Space Station Freedom's dual wall protection systems have been determined. These functions were regressed from empirical data found in Marshall Space Flight Center's Hypervelocity Impact Testing Summary (HITS) for the velocity range between three and seven kilometers per second. A stepwise linear least squares regression was used to determine the coefficients of several expressions that define a ballistic limit surface. Using statistical significance indicators and graphical comparisons to other limit curves, a final set of expressions is recommended for potential use in Probability of No Critical Failure calculations for Space Station.

INTRODUCTION

Meteoroid and space debris impacts are anticipated to occur on the exterior of the Space Station during its service life in a low earth orbit (LEO). As a result, the external walls are required to be designed to minimize the risks associated with these impacts. The SSF requirements document [8] states that the probability of an anticipated impact to cause failure of the pressure wall will be less than 0.45% over a ten year period. In order to calculate this probability, ballistic limits must be determined.

Hypervelocity impact testing has been performed in the Light Gas Gun Facility at Marshall Space Flight Center (MSFC) since 1985. This testing has been directed toward the development of a meteoroid and space debris protection system design for Space Station Freedom. The information gathered from this testing has been formally recorded in a Lotus database entitled Hypervelocity Impact Testing Summary (HITS).

The purpose of this analysis is to determine the ballistic limit of a dual wall meteoroid and space debris protection system similar to the proposed system for SSF, using HITS data. The empirical relationships derived are intended for use in the design and verification of the SSF protection system. These regression equations are only applicable over bumper thicknesses between 0.040" and 0.080" and obliquities[2] up to 65° for the SSF manned module dual wall.

An Analysis of Variations (ANOVA) is performed to indicate the statistical significance of these curves. In order to quantify the scatter in the test data, confidence intervals are determined for each regression.

The definition of a ballistic limit varies depending on the method of analysis being employed. For this analysis, the ballistic limit is defined as the velocity at which a specified projectile will just barely penetrate the second wall (or rear wall) of a dual wall structure. Failure of the second wall by cracking or spalling is considered penetration since pressure loss would occur under those circumstances.

The ballistic limit for dual wall structures is governed by processes whose phenomenologies change as the impact velocity increases. Specifically, the ballistic limits can be subdivided into three velocity regimes: ordinance, shatter, and hypervelocity. These regimes are differentiated by the relative strengths of the projectile and target for given impact pressures. The velocity range considered for this analysis is the shatter regime and, for aluminum spheres impacting aluminum targets, that regime is roughly between two and eight kilometers per second (km/sec). In this velocity range, the mechanics of penetration changes from impacts at lower velocities where projectiles remain intact

[1] Formerly with Sverdrup Technology, Inc., MSFC Group.
[2] Obliquity is the angle between the projectile velocity vector and the outward normal of the target.

throughout the penetration event, to impacts at higher velocities where the projectile becomes completely vaporized during penetration of the first wall or bumper, as it will be referred to in this report. This section of the ballistic limit curve is highly nonlinear due to the randomness of the shatter mechanisms causing the projectile to breakup. However, Burch indicated in [1] that the general shape of the ballistic limit curve, in this velocity range for this target configuration and normal obliquity, is monotonically increasing with velocity. This indicates a reduction in damage (or penetration) as velocity increases.

TEST AND DATA DESCRIPTION

All data considered in this analysis was generated in testing performed in the Light Gas Gun Facility at Marshall Space Flight Center. Since this analysis and desired ballistic limits are specific to Space Station, only shots made against targets similar to its proposed dual wall configuration were considered. This reduces the required complexity of the ballistic limit expressions and, in theory, should increase the accuracy of the regression. The following discussion provides more specific information about the tests used to generate the ballistic limit curves.

Projectile Configuration

The only projectile type considered for this analysis was a pure aluminum sphere. 1100-O (pure annealed aluminum) was used extensively in testing because its average density is very near the estimated average density of space debris as specified in [6]. Since only one material is considered in this analysis, spherical diameter and projectile mass are directly related and diameter can be used to convey ballistic limit information. In this report, a critical projectile diameter is plotted as a function of impact velocity to portray a ballistic limit against a specific target.

Target Configuration

Fig. 1. shows a dual wall target configuration composed of two walls spaced 4.0" apart with a Multi-Layered Insulation (MLI) blanket located between the walls. The bumper is 6061-T6 aluminum sheet that ranges in thickness between .032" and .080". The rear wall is 0.125" thick 2219-T87 aluminum sheet. The actual pressure wall of a SSF manned module is proposed to consist of waffle plate; however, it is 0.125" thick between the ribs and would be expected to behave similar to plain sheet stock for penetrations near the ballistic limit. The target is usually backed up by three 0.020" 7075 aluminum witness plates; however, more plates are often used for high momentum shots.

The bumper thickness varies depending upon the specific requirements for the particular SSF component. In fact, this is the predominant parameter of variance to be considered in design optimization of the protection system. Therefore, bumper thickness will be handled in the regression analysis as an independent variable and the BLCs will be applicable over the range of bumper thicknesses indicated.

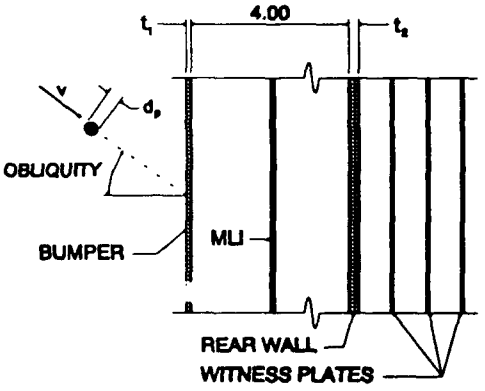


Fig. 1. Dual-wall target configuration Simulates the proposed Space Station Configuration.

Data Summary

The HITS database was searched for tests on dual wall targets with 6061-T6 bumpers and 0.125" 2219-T87 rear walls spaced four inches apart, impacted with 1100-O pure aluminum spheres at any available obliquity, MLI position, and bumper thickness. In addition to the geometric search parameters, other search parameters included base line requirements on the information available for each shot. For instance, shots that penetrated the rear wall must have witness plate damage information and shots that did not penetrate the rear wall must have crater depth information. If a test record indicated multiple holes in the bumper, then the projectile was assumed to have broken up before impacting the target. This was found to be the case in four tests and the shots were removed from the regression dataset.

A total of 385 hypervelocity impact tests, fired at velocities between two and eight km/sec, were found to comply with these search parameters

Shot Summary of the Regression Dataset

Tables 1 through 6 summarize shot diversity for the 385 shots used in this analysis. The majority of the data is for targets where MLI was placed near the bumper or against the rear wall. In the actual SSF configuration the MLI is centered between the walls. Nineteen shots, applicable to this regression, have been made against targets with MLI centered between the walls, but all of them were fired at normal obliquity on 0.063" bumpers. The 221 shots used in the final analysis are indicated by the asterisks.

Fig. 2 is a sample plot of some of the shot results indicating the final condition of the rear wall.

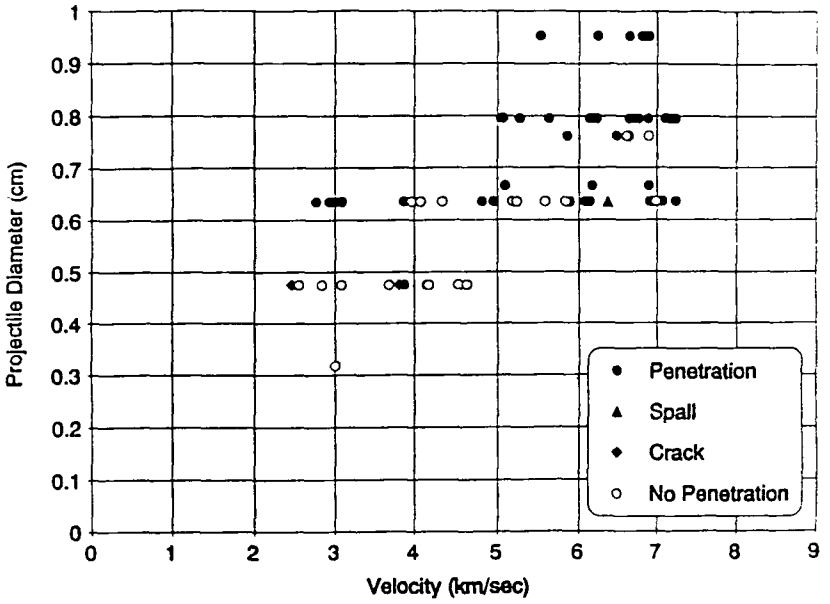


Fig. 2 Raw data plot for 0.063" bumper impacted normally by a 0.250" projectile

Table 1. Shot occurrences with no MLI present

Bumper Thickness (in.)	Diameter (in.)	Number of Shots (above/below 4.75 km/sec)						
		Obliquity						
		0°	30°	45°	55°	60°	65°	75°
.080	.375					0/1		0/1
	.350	0/1		1/1		1/1		
	.313			0/1				
	.300	0/1						
	.250			0/1				
	.187	5/1						
.063	.313	0/3	0/1	0/2		0/1	0/1	0/3
	.300	0/2						
	.262	0/2						
	.250	2/9	0/6	0/4	0/3		2/3	
	.187	3/0	0/2	2/6		0/2	2/0	
	.125	1/0						
.040	.250	3					4	
	.187			8				
	.125			3				
.032	.300			1				

Table 2. Shot occurrences with MLI near the bumper.

Bumper Thickness (in.)	Diameter (in.)	Number of Shots (above/below 4.75 km/sec)						
		Obliquity						
		0°	30°	45°	55°	60°	65°	75°
.080	.313	3*						
	.250	4*						
.063	.375	0/1*						

* Shots used in final regression analysis.

Table 3. Shot occurrences with MLI at 3.75" from the rear wall.

Bumper Thickness (in.)	Diameter (in.)	Number of Shots (above/below 4.75 km/sec)						
		Obliquity						
		0°	30°	45°	55°	60°	65°	75°
.080	.313	0/1*		6/6*		2/2		5/6
	.250	0/1*		2/6*		2/2		2/2
	.187			2/5*		2/2		2/2
.063	.313	0/5*						0/1
	.250	2/6*		0/3*				
	.187	3/0*		0/2*				
.050	.313			1/0*		3/2		3/1
	.250			2/10*		2/2		2/2
	.187			2/2*		4/2		2/2

* Shots used in final regression analysis.

Table 4. Shot occurrences with MLI at 0.90" from the rear wall.

Bumper Thickness (in.)	Diameter (in.)	Number of Shots (above/below 4.75 km/sec)						
		Obliquity						
		0°	30°	45°	55°	60°	65°	75°
.063	.375	0/1*						

* Shots used in final regression analysis.

Table 5. Shot occurrences with MLI centered between walls.

Bumper Thickness (in.)	Diameter (in.)	Number of Shots (above/below 4.75 km/sec)						
		Obliquity						
		0°	30°	45°	55°	60°	65°	75°
.063	.375	0/4*						
	.313	0/8*						
	.250	4/3*						

* Shots used in final regression analysis.

Table 6. Shot occurrences with ML1 on the rear wall.

Bumper Thickness (in.)	Diameter (in.)	Number of Shots (above/below 4.75 km/sec)						
		Obliquity						
		0°	30°	45°	55°	60°	65°	75°
.080	.313	3*		4*			1*	
	.300	4*						
	.250			1*			2*	
	.187			1*				
.063	.375	1*						
	.350			2*			2*	
	.313	5*	1	5*				
	.300	3*		1*			3*	
	.262	1*						
	.250	4*		5*			3*	
	.187	5*	1	2*				
.040	.375			1*				
	.350						2*	
	.313	2*		5*			6*	
	.300						5*	
	.250	5*	1	7*			3*	
	.187	5*	3	6*				
.032	.313			1*			3*	
	.250	1*		3*			4*	
	.187	4*		3*			2*	

* Shots used in final regression analysis.

ANALYSIS DESCRIPTION

The following sections provide a detailed description of the linear regression method used in this analysis to derive ballistic limit curve (BLC) expressions from the HITS database. Since there were so many regressions performed, a single Analysis of Variations (ANOVA) was performed to determine the level of confidence for the final set of curves generated.

Penetration Parameter

No matter which regression method is used, a dependent penetration parameter is required to provide a dependent variable that relates the penetration process to the independent test variables. The penetration parameter (P) is a calculated variable that characterizes the amount of damage sustained by the target.

For this analysis, the penetration parameter is defined as, "the total areal density penetrated plus one". The areal density is incremented by one so that the natural logarithm does not go to negative infinity when the bumper completely defeats the projectile (i.e., when $P = 0$). The reason for taking the logarithm depends upon the regression model and will become apparent later. The Penetration Parameter may be written as

$$P^* = P + 1 \tag{1}$$

The total areal density is defined as a step function with respect to rear wall penetration. For shots that did not penetrate the rear wall, the total areal density is the product of the depth of the deepest crater found on the wall and the density of the rear wall (2.851 gm/cc for 2219-T87 aluminum). Equation (2) represents this quantity.

$$P = h\rho_2 \tag{2}$$

For shots where penetration of the rear wall did occur, the number of witness plates penetrated indicates the amount of damage. It was assumed that, if a witness plate was penetrated, then half of the next witness plate was also penetrated. Therefore, the penetration parameter becomes the areal density of the rear wall plus the areal density of the number of witness plates penetrated plus one half. This may be written as

$$P = t_2\rho_2 + (n_{wp} + \frac{1}{2})\rho_{wp}t_{wp} \tag{3}$$

Critical penetration corresponds to the value of the penetration parameter equal to the areal density of the rear wall. When this occurs, the rear wall should, theoretically, be "just" penetrated. The following equations define this parameter and the numerical values given correspond to the SSF dual wall target configuration.

$$P_c = t_2\rho_2 = 0.3175cm(2.851\frac{gm}{cm^3}) = 0.9052\frac{gm}{cm^2} \tag{4}$$

$$P_c^* = P_c + 1 = 1.9052 \tag{5}$$

Multiple Regression Analysis Technique

Multiple Regression refers to a multivariate linear least squares regression of a non-linear equation mapped into linear space. In this analysis, mapping was performed by imposing algebraic laws of logarithms on a monomial and expanding.

Assume a general monomial form such as:

$$P^* = e^{c_1}v^{c_2}t_1^{c_3}(\cos\theta)^{c_4}d^{c_5} \tag{6}$$

where,

P^* is Penetration Parameter

e is the exponential function

v is the Impact Velocity

t_1 is the Bumper Thickness

θ is the Obliquity of the Projectile's Trajectory

d is the Projectile Diameter

c_i is the i^{th} Regression Coefficient.

Then, map the form into linear space by taking the natural logarithm and expanding to get the polynomial expression shown below:

$$\ln(P^*) = c_1 + c_2\ln(v) + c_3\ln(t_1) + c_4\ln(\cos\theta) + c_5\ln(d) \tag{7}$$

Apply linear least squares regression techniques to determine the coefficients. This method is outlined in [4] and is similar to the method used by Burch to generate the widely accepted work presented in [1]. Also, Dr. Robert Mog used this method in his work on posynomial regression analysis [7].

The primary limitation of this method, or any method of regression, is the correctness of the assumption of the model form. The monomial form assumed in this analysis forces the relationships between the dependent variable and the independent variables to be monotonic. This is desirable when the overall relationship is not known, because trends can be studied to assist in the development of more precise models. An unfortunate consequence of assuming monotonic relationships is their inability to predict periodic phenomena. To minimize problems associated with choosing correct forms, stepwise regressions can be performed where the model is reduced to lower forms eliminating the effects of the more generalized assumptions. This is done by sorting the data into groups where one variable is held constant and performing the regression with that variable removed. A FORTRAN algorithm was written to perform a complete stepwise regression for a given generalized relationship. Three monomials were regressed,

the first for constant bumper thickness,

$$P^* = e^{c_1}v^{c_2}(\cos\theta)^{c_3}d^{c_4} \tag{8}$$

the second for constant obliquity,

$$P^* = e^{c_1}v^{c_2}t_1^{c_3}d^{c_4} \tag{9}$$

the third for constant bumper thickness and obliquity,

$$P^* = e^{c_1}v^{c_2}d^{c_3} \tag{10}$$

The most complex form of this equation, (6), will provide a very general expression for the ballistic limit, however, this generality is usually gained at the expense of fidelity and, consequently, may fail to produce accurate damage predictions, therefore, all forms should be investigated.

Statistical Analysis

The statistical routines from which the all statistical parameters were determined, including the ANOVA, were generated from theoretical derivations found in [3] and, subsequently verified by hand calculation and modeling of idealized examples.

The multiple regression program specified correlation coefficient and F statistic only for each stepwise regression fit. This allowed a reasonable determination of the significance of each curve. High correlation coefficients do not always indicate the best fits, they only indicate how well the prediction estimates the observation at the specified position. For higher order polynomials this result is pronounced. Likewise, high values of F statistic may not necessarily indicate a reasonable confidence level. The combination of the two parameters, however, does appear to provide a set of statistical parameters that indicate adequate fits.

RESULTS AND DISCUSSION

In the following sections, the results of this analysis are presented. In addition, a comparison is made to the baseline ballistic limits (generated by Boeing) shown in Fig. 7, and to the equations proposed by Burch [1] without MLI effects.

Multiple Regression

A generic stepwise regression was performed on the complete set of 385 shots. The coefficients of the curves were not consistent with respect to sign and did not agree with currently accepted theory (i.e., the slope of the velocity curves varied randomly with obliquity and bumper thickness). Inconsistent shapes would not be expected with varying bumper thickness and, the velocity exponent for the ballistic limit curve is expected to be positive. Therefore, a detailed study of the data was made by performing a series of regressions on various groupings of the shots.

The model used in the regression was not constructed to include dependence upon the position of the MLI between the shield and the rear wall. Therefore, several regressions were made to study the effects of MLI position in the stack-up. After regressing the sorted data and plotting penetration parameter versus velocity for constant bumper thickness, obliquity, and projectile diameter for various MLI positions, a dependency was established. Tests made with targets having 0.063" bumpers impacted normally with 0.250" projectiles comprised the largest single group of shots. Fig. 3 shows this group together with the predicted solution using the applicable equations[3] in [1] and a regression through the associated groups of data. The comparison between the curves indicates the proper functional relationship (or curve shape) results from the regression. Fig. 5. is a plot of the regressions of shots with MLI near the bumper, near the rear wall and centered between the walls. This plot indicates that ballistic performance is a function of MLI position and that the presence of MLI tends to reduce the amount of damage incurred by the rear wall. The damage decreases as the distance between the bumper and the rear wall increases.[4] The curves shown in Fig. 5. indicate a monotonic relationship between shield performance and MLI position, with the "MLI centered" damage roughly "centered" in severity between "MLI on bumper" and "MLI on wall" damage. This observation fits well with previous qualitative test observations.

Having noted this effect, all shots where MLI was present were grouped into a single regression model. This decision was made because 1) data on the "MLI centered" and "MLI on bumper" test configuration was sparse, and 2) the limited existing data for 0.063" bumpers lead to the observation that MLI position, while affecting shield performance somewhat, did not affect the general slope of the final BLCs, significantly. Because the preponderance of data was from "MLI on wall" tests, it is reasonable to assume that the final regression most closely models the "MLI on wall" test configuration.

Fig. 4 illustrates one set of BLCs suggested by the analysis corresponding to the more general equation

$$P^{*} = e^{0.8533} v^{-0.0547} t_1^{-0.0815} (\cos\theta)^{0.2238} d^{0.5268} \qquad (11)$$

[3] The Burch equation is plotted to indicate the functional relationship. Since there is no direct means of including MLI in this prediction, the results correspond to the case where MLI is not present in the target configuration.

[4] Although this is true, shots made against targets with MLI placed against the rear wall generally result in massive pedalling failures. These failures are worse than similar events where MLI was not present. Therefore, the current SSF configuration is near optimum with respect to MLI position.

Substituting $P^* = P_c^* = 1.9052$ and solving for the projectile diameter results in the ballistic surface described by:

$$d_c = 0.6729 v^{0.1038} t_1^{0.1546} (\cos\theta)^{-0.4249} \tag{12}$$

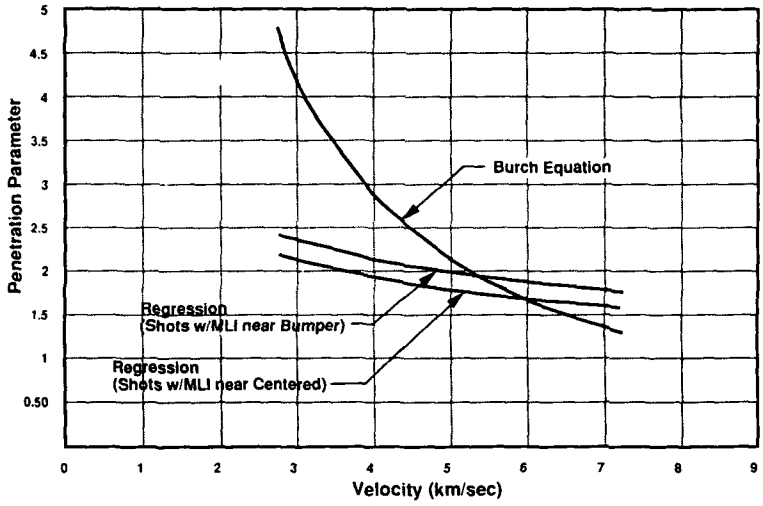


Fig 3. Penetration parameter versus velocity for 0.063" bumper, normal impact, and 0.250" projectile diameter.

Fig. 5. was generated using equation (12) with the bumper thickness set to 0.050" to represent the proposed Space Station dual wall manned module configuration.

One notable problem with this general regression was that it generated somewhat inaccurate results for high obliquity shots. In studying the high obliquity shot data, the ricochet test series was found to be relatively independent of impact velocity. This appears to be due to the fact that the majority of the shots were fired well in excess of the ballistic limit. This data would, therefore, exhibit a skewed distribution about a ballistic limit function and violate the normal distribution assumption for the derivation of the least squares regression.

These anomalies were remedied by filtering the data. Grouping shots fired at 0°, 45°, and 65° obliquities together and discarding shots where MLI was not present reduced the total number of shots used in the regression to 221, and increased the accuracy of the final regressions.

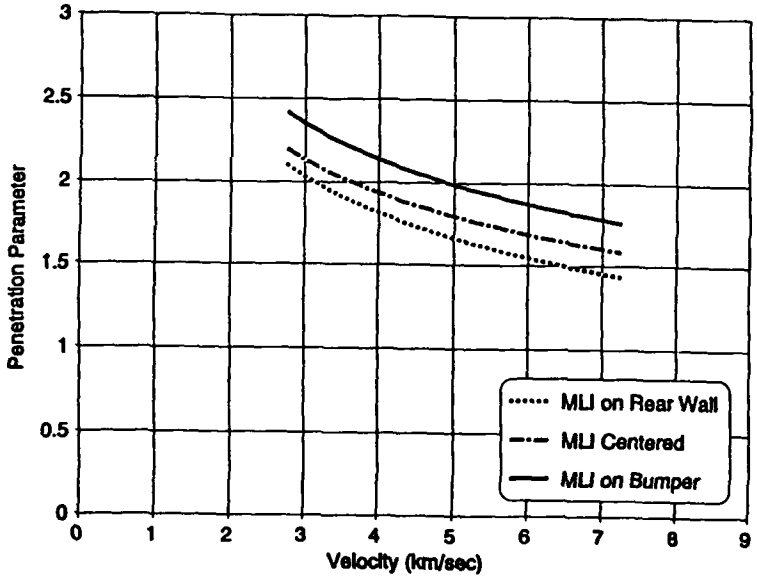


Fig 4. Penetration parameter versus velocity for 0.063" bumper, normal impact, 0.250" projectile diameter for three MLI positions

Therefore, another set of BLCs were regressed from the same data, one for each obliquity; for normal impacts,

$$P^* = e^{0.6160} v^{-0.1699} t_1^{-0.2977} d^{0.5694} \tag{13}$$

for 45° impacts,

$$P^* = e^{0.7627} v^{-0.0333} t_1^{-0.1605} d^{0.7783} \tag{14}$$

for 65° impacts,

$$P^* = e^{1.3686} v^{-0.1137} t_1^{-0.2218} d^{0.5726} \tag{15}$$

Substituting $P^* = P_c^* = 1.9052$ and solving for the projectile diameter results in the ballistic surface described by:

$$d_c = 1.0514 v^{0.2983} t_1^{0.5228} \tag{16}$$

$$d_c = 0.8591 v^{0.0428} t_1^{0.2063} \tag{17}$$

$$d_c = 0.2824 v^{0.1986} t_1^{-0.3874} \tag{18}$$

These functions are illustrated in Fig. 6. Equations (11) through (18) are valid for the dual wall protection system shown in Fig. 1 with bumpers between 0.032" and 0.080" thick impacted by aluminum spheres at velocities between three and seven km/sec.

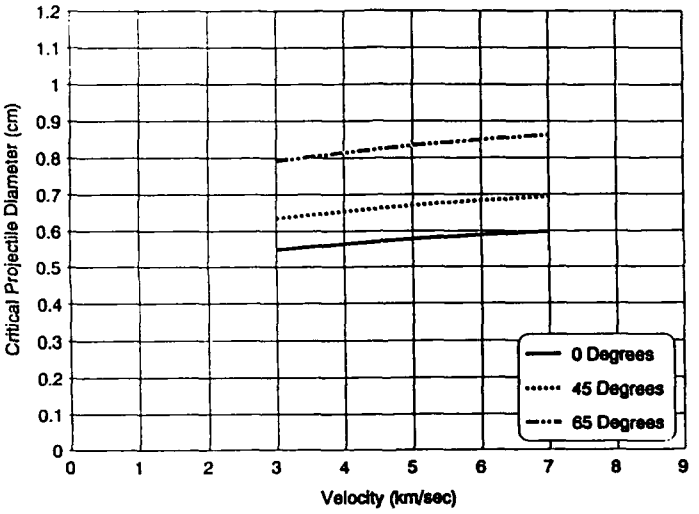


Fig. 5 Generalized regression curves for the proposed SSF dual wall configuration with a 0.050" bumper

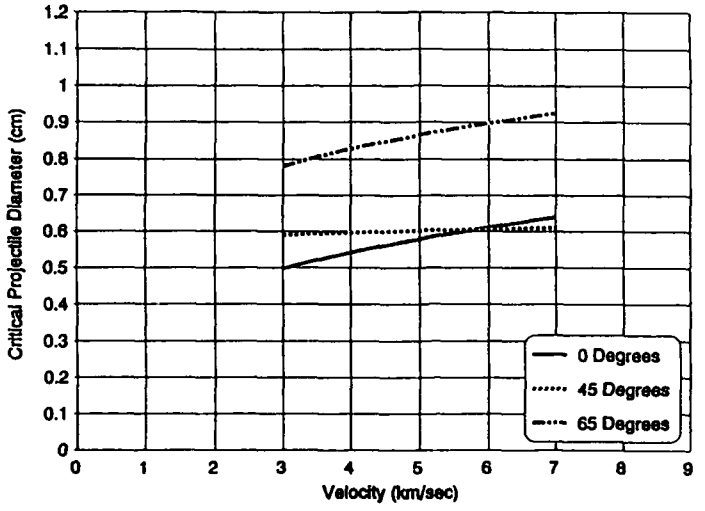


Fig. 6 Ballistic limit curves regressed at constant obliquity for the proposed SSF dual wall configuration with a 0.050" bumper

In an effort to choose the most accurate expression for use in the determination of PNCF, a brief study of the dataset was made to look for shots that might indicate a ballistic limit. A series of three tests was found where 0.187" projectiles impacted a 0.063" bumper at 0° obliquity with velocities between 3.9 and 4.5 km/sec. This velocity range appears to be very near the ballistic limit because in two cases the rear wall was penetrated without penetrating witness plates and in the third case 50% of the rear wall was penetrated. If we assume a ballistic limit for a 0.475 cm projectile to be ~4.0 km/sec, then the more general expression makes a better prediction of 0.5883 cm, as compared to the normal impact equation's prediction of 0.6189 cm. Both regressions are noted as being anti-conservative. It must be understood that these are P_{50} (or 50% probability of prediction) curves and that the lower bounds provide estimations based on the confidence intervals.

Table 7. Comparison Statistics Parameters.

Regression Equation	F-Distribution Value	Correlation Coefficient (r)	
	Upper 5%	5% Significance	1% Significance
Generalized	5.63	.379	.449
Constant Obliquity 0°	8.56	.336	.410
Constant Obliquity 45°	8.56	.336	.410
Constant Obliquity 65°	8.61	.397	.481

Table 8. ANOVA for Generalized Regression

Source	Degrees of Freedom	SS	MS	F Value
Regression	4	2.821	0.705	23.064
Residual	216	6.605	0.031	
Total Corrected	220	9.426		
Multiple Correlation Coefficient (r^2) =		0.299	(r = .547)	
Reduced Ballistic Equation Multiplier =		1.045	(95% Confidence Interval)	

Table 9. ANOVA for 0° Constant Obliquity Regression

Source	Degrees of Freedom	SS	MS	F Value
Regression	3	0.655	0.218	6.001
Residual	85	3.095	0.036	
Total Corrected	88	3.751		
Multiple Correlation Coefficient (r^2) =		0.175	(r = .418)	
Reduced Ballistic Equation Multiplier =		1.073	(95% Confidence Interval)	

Table 10. ANOVA for 45° Constant Obliquity Regression

Source	Degrees of Freedom	SS	MS	F Value
Regression	3	2.348	0.782	55.402
Residual	92	1.300	0.014	
Total Corrected	95	3.647		
Multiple Correlation Coefficient (r^2) =		0.644	(r = .802)	
Reduced Ballistic Equation Multiplier =		1.031	(95% Confidence Interval)	

Table 11. ANOVA for 65° Constant Obliquity Regression

Source	Degrees of Freedom	SS	MS	F Value
Regression	3	0.479	0.160	6.428
Residual	32	0.795	0.025	
Total Corrected	35	1.274		
Multiple Correlation Coefficient (r^2) =		0.376	(r = .613)	
Reduced Ballistic Equation Multiplier =		1.098	(95% Confidence Interval)	

Statistical Significance

All regressions made had statistical parameters generated for them, however, the full ANOVA was reserved for only the final set of equations, (11) through (18) For the generalized regression, the F value of 23 064 is in excess of 5 63, the 5% level of significance value for the F-distribution, which allows the rejection of the null hypothesis According to [5], the "acceptable" value of the correlation coefficient (r) for 50 degrees of freedom and 4 predictor variables is 379 for 5% level of significance and 449 for 1% level of significance The generalized regression resulted in an ($r = \sqrt{0\ 299} = 0\ 547$), indicating adequate fit for the number of variables involved Table 7 is a compilation of similar values for the constant obliquity regressions Note that in every case (0°, 45°, and 65°) the F test was successful and the correlation coefficient indicated a "good fit" to at least a one percent level of significance Tables 8 through 11 provide statistical parameters for each regression equation presented

Baseline Ballistic Limits

Fig 7 is an interpolation of the "baseline" (preliminary) ballistic limit curves currently used to calculate PNCF for SSF These curves are proposed for use in [9] and are presented here to indicate the relative shift in the ballistic limit proposed by this analysis for Space Station protective structures

An alternative viewpoint is that this analysis may be viewed as a verification of the baseline curves

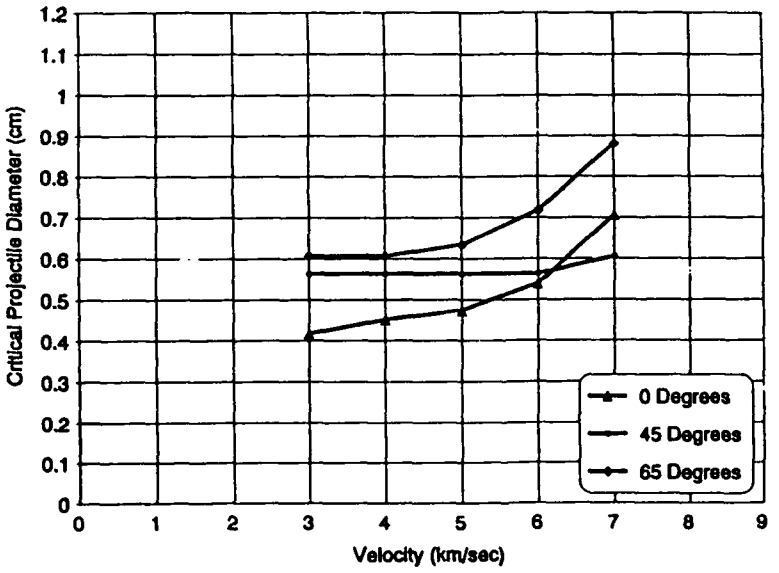


Fig 7 Baseline ballistic limit curves interpolated for a 0 050" bumper

CONCLUSIONS

The following sections contain some of the conclusions that can be drawn from the data studied during this analysis

Dual Wall Ballistic Limit Curve

The curves shown in Fig 6 , where obliquity was held constant in the regression model appear to match the curves generated by Boeing (Fig 7) These curves are recommended for use as limit curves for Space Station Freedom protection systems They may, on the other hand, be considered as verification of baseline curves because of similarity in the predicted diameters

The generalized curves, shown in Fig 5 , indicate closer agreement with Burch's expressions with respect to the sign and magnitude of the velocity exponent and indicate lower overall statistical variance The major difference

between the sets of equations is how the target performance varies with obliquity. In the generalized curves, performance increases monotonically with obliquity. The curves regressed over constant obliquity indicate that a monotonic relationship may not be correct and are therefore preferred over the generalized regressions.

Another observation is that the constant obliquity curves are more conservative than the generalized curves at lower obliquities but both are anti-conservative when compared to ballistic limits indicated by the results of specific shots.

Statistical Significance

F test values and correlation coefficients have been determined for the all sets of ballistic limit curves presented in Tables 7 through 10. Note that in every case (0°, 45°, and 65°) the F test was successful and the correlation coefficient indicated a "good fit" to at least a one percent level of significance.

REFERENCES

1. G. T. Burch,"Multiplate-Damage Study (U)", The Boeing Company, AFATL-TR-67-116, September 1967.
2. K. B. Hyashida and J. H. Robinson, "Single Wall Penetration Equations", National Aeronautics and Space Administration, TM not released, 1990.
3. William J. Hemmerle, "Statistical Computations on a Digital Computer", Blaisdell Publishing Co., 1967.
4. R. R. Umarji, "Probability and Statistical Methods", Asia Publishing House, 1962, pp 138.
5. N. R. Draper and H. Smith, "Applied Regression Analysis" second ed., John Wiley and Sons, 1981, pp 141.
6. Space Station Program Natural Environment Definition for Design, JSC 30425.
7. Robert A. Mog, "Posynomial Regression Analysis for Hypervelocity Impact Prediction", White Paper prepared for George C. Marshall Space Flight Center, September 1989, Science Applications International Corporation.
8. Space Station Freedom Program Definition and Requirements, SS-SRD-0001C, SEC. 3.0, 17 April 1990, Marshall Space Flight Center, Huntsville, Alabama.
9. Boeing Areospace Company, "Results of the Ballistic Limit Testing of Aluminum M/D Shields," Document No. D683-10578-1, Preliminary.
10. Sverdrup Technology, Inc., MSFC Group, Ballistic Limit Regression Analysis for Space Station Freedom Meteoroid and Debris Protection System, Final Report No. 661-001-92-008, Prepared under NASA Contract NAS 8-37814.

Int. J. Impact Engng Vol 14, pp 407–416, 1993
Printed in Great Britain

0734-743X/93 $6.00+0.00
1993 Pergamon Press Ltd

A ONE-DIMENSIONAL ANALYSIS OF THE PENETRATION OF SEMI-INFINITE 1100-0 ALUMINUM TARGETS BY RODS

S. E. Jones and Rhett B. Marlow
College of Engineering
The University of Alabama 35487

and

J. W. House and L. L. Wilson
Wright Laboratories, Armament Directorate
Eglin AFB, Florida 32542

ABSTRACT

The one-dimensional analysis of normal rod penetration, recently presented by Cinnamon, et al, 1992, is applied to a very soft target, 1100-0 aluminum. The results are shown to be satisfactory for impact velocities under about 2.5 km/sec. Since the analysis is based on the initial transient stage of penetration, the theory can be applied to impacts by rods with very low L/D ratios. The theory is entirely algebraic and the depths of penetration are predicted from crater volume/kinetic energy curves. To extend the theory to higher velocity impacts, a new distribution of pressure is introduced. These results are promising.

NOTATION

A	initial cross-sectional area of the penetrator
a	slope of the crater volume-kinetic energy line
b	intercept of the crater volume-kinetic energy line
e	engineering strain in the mushroom of the penetrator
e_0	engineering strain in the mushroom at impact
e_1	engineering strain in the mushroom at steady state
E_0	kinetic energy of the penetrator at impact
ℓ	current undeformed section length
n	pressure distribution exponent

P average pressure on the penetrator tip
P_1 average pressure on the penetrator tip at the end of the transient stage
p pressure distribution on the penetrator tip
P_a pressure on the axis of the penetrator tip
q uniform pressure component
r radial distance from the axis of the penetrator
R radius of the undeformed penetrator
R_t dynamic strength of the target
t time elapsed since impact
u current penetration velocity
u_0 penetration velocity at impact
V_c volume of the crater
v current velocity of the undeformed section
v_0 impact velocity
Y_p dynamic strength of the penetrator
Z penetration depth
α dimensionless constant related to n
β constant related to n with the dimension of MPa
ρ penetrator density
μ^2 ratio of target density to penetrator density

INTRODUCTION

Jones, et al., 1987, presented an alternative formulation of the classic theory of Tate, 1967, and Alekseevskii, 1966, theory for normal penetration of semi- infinite targets by long rods. The new formulation contained a relative velocity term to account for mass loss from the undeformed section and an infinitesimally thin mushroom with an enlarged cross-sectional area. A new equation to account for conservation of mass across the plastic wave front of the penetrator was added by Wilson, et al., 1989. The penetration depths predicted by this theory were shown to be in fairly good agreement with experiment when the mean strain in the mushroom was estimated from the profile diameters of recovered targets. It should be pointed out, at this juncture, that all dynamic material properties were estimated by laboratory tests (e.g., Taylor impact tests, Split Hopkinson Bar tests, etc.) at high strain rates. The results were encouraging. However, there are several defects in the modeling process. One is that the entire penetration process is treated as steady, while the mushroom has constant strain. The constant strain assumption may be appropriate for the steady portion of the penetration process, but not for the entire event. This stimulated Cinnamon, et al., 1992, a, b, to investigate the initial transient stage of penetration. In this case, the initial transient stage shall refer to everything that precedes steady penetration. This includes the shock/impact stage in both the penetrator and the target and the complete mushrooming of the penetrator. By considering the pressure distribution p on the penetrator tip to be nonuniform

$$p = p_a \left(1 - \frac{r^2}{R^2}\right)^n \tag{1}$$

where p_a is the pressure on the rod axis, r/R is the dimensionless radial distance from the axis, R is the undeformed rod radius, and n is a dimensionless exponent, Cinnamon, et al., 1992, a, b, developed a one-dimensional analysis of penetration that was completely algebraic. The pressure distribution in equation (1) is referred to the original configuration of the rod, but is extended over the deformed configuration in the equation of motion by means of the mean mushroom strain, e. The equation of motion for the undeformed section of length ℓ can now be shown to take the form

$$\ell\dot{v} + \dot{\ell}(v - u) = \frac{-p_a}{\rho(n+1)(1+e)} \tag{2}$$

where v is the current velocity of the undeformed section. u is the penetration velocity, and ρ is the density of the penetrator. Dots over symbols denotes differentiation with respect to time t. When equation (2) is coupled with the equation for conservation of mass for the mushrooming material introduced by Wilson, et al [4]

$$e\dot{\ell} = v - u \tag{3}$$

and elementary theory for mushrooming was produced. It was shown that n was basically a function of target strength for the low to intermediate impact velocities, say 1 km/sec to 3 km/sec. Specifically,

$$n = \alpha + \frac{\beta}{R_t} \tag{4}$$

where α and β are constants and R_t is the dynamic strength of the target at a strain- rate appropriate to the penetration event. A good correlation was achieved for $\alpha = 9.2117 \times 10^{-2}$ and $\beta = 1835.117$ MPa. This hypothesis was tested for several target materials in [5]. The targets were: 2024-T4 Aluminum, 7075-T6 Aluminum, and 4340 Steel in hard and annealed states. The penetrators were of the same materials. In Cinnamon, et al., 1992, b, the hypothesis was shown to be valid for OFHC copper, 4340 steel, and tantalum penetrators into rolled homogeneous armor and 4340 steel targets.

The pressure exponent n rapidly increases with decreasing target strength. It is interesting to apply this reasoning to a very soft target, say 1100-0 aluminum.

PENETRATION OF 1100-0 ALUMINUM TARGETS

Christman, et al., 1964, reported penetration data for 1100-0 Aluminum targets. Their data will be used for comparison in this section. A static yield strength for 1100-0 aluminum is approximately 70 MPa. However, for strain-rates appropriate to mushroom formation, 250 MPa is acceptable. For $R_t = 250$ MPa, equation (4) indicates that $n = 7.41$. Figure 1 shows graphically the relationship between

n and target strength for all of the targets considered. Figures 2 and 3 show the engineering strain in the target e_1 when steady state is reached for 2024-T3 aluminum and C1015 steel penetrators. The dynamic yield stresses for the penetrator materials are assumed to be 750 MPa for 2024-T3 aluminum and 1000 MPa for C1015 steel. The strain e_1 has been estimated from [5] by

$$e_1 = \frac{-(v_0 - u_0)^2}{(v_0 - u_0)^2 + \frac{P_1}{\rho(n+1)}} \tag{5}$$

P_1 is the pressure at the initiation of steady penetration that can be estimated by the Modified Bernoulli Equation (e.g., Tate, 1967).

$$P_1 = \frac{1}{2}\mu^2 \rho u_0^2 + R_t = \frac{1}{2}\rho (v_0 - u_0)^2 + Y_p \tag{6}$$

In this equation, Y_p is the dynamic strength of the penetrator, v_0 is the impact velocity, u_0 is the penetration velocity during mushroom formation (assumed to be approximately constant), and $\mu^2\rho$ is the target density. These equations can be used to find u_0 in terms of v_0 and the other physical parameters, as well as the pressure P_1.

Penetration depths can be estimated by assuming that the crater in the target is approximately a cylinder whose cross-sectional area can be computed from the engineering strain e_1 in equation (5). Experimental evidence suggests that in the range of impact velocities in question, the relationship between crater volume V_c and kinetic energy on impact E_0 is approximately linear.

$$V_c = aE_0 + b \tag{7}$$

This means that the penetration depth z can be estimated from

$$z = \frac{1}{A}(1 + e_1) V_c = \frac{1}{A}(1 + e_1)(aE_0 + b) \tag{8}$$

where A is the original cross-sectional area of the rod penetrator. The constants a and b are determined experimentally. Figures 4 and 5 show the penetration depth curve predicted by equation (7) for 2024- T3 aluminum and C1015 steel penetrators. The results are good up to impacts of about 2.5 km/sec. They deteriorate rapidly at velocities higher than that. This is partly due to the simple pressure distribution presented in equation (1). In the next section, we introduce a more general pressure distribution.

A DIFFERENT DISTRIBUTION OF PRESSURE

Following a suggestion made by Anderson, 1991, we consider an alternative form for the pressure distribution in equation (1). A uniform component q is added to the variable distribution in equation (1). The new distribution has the form

$$p = q + (p_s - q)\left(1 - \frac{r^2}{R^2}\right)^n \tag{9}$$

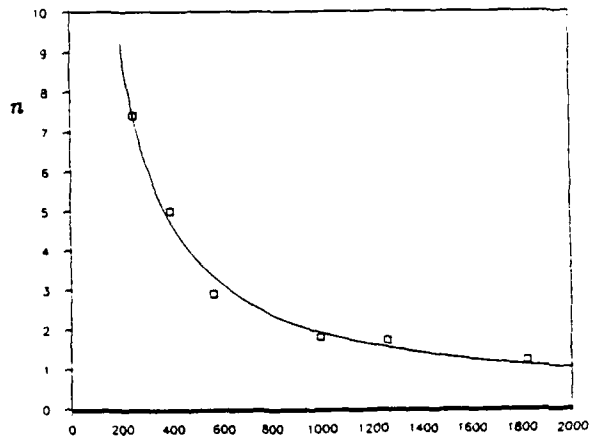


Fig. 1. n vs. target strength R (MPa). The relationship between them is approximately given by $n = 8.544 \times 10^{-2} + 1830 / R$. ❑ denotes a fit to experimental data.

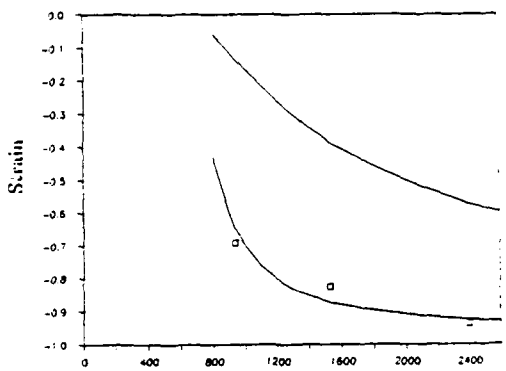


Fig. 2. Strain vs. impact velocity (m/s) for 2024-T3 Al (750 MPa) penetrators against 1100-0 Al (250 MPa) targets. ❑ denotes experimental data points. e_1 (lower solid curve) is the predicted strain at the beginning of steady state and e_o (upper solid curve) is the predicted strain at impact.

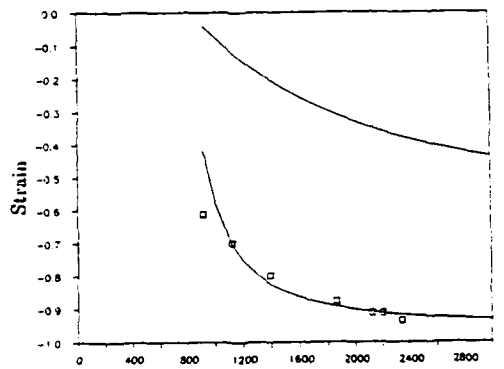


Fig. 3. Strain vs. impact velocity (m/s) for C 1015 st. (1000 MPa) penetrators against 1100-0 Al (250 MPa) targets. ❑ denotes experimental data points. e_1 (lower solid curve) is the predicted strain at the beginning of steady state and e_o (upper solid curve) is the predicted strain at impact.

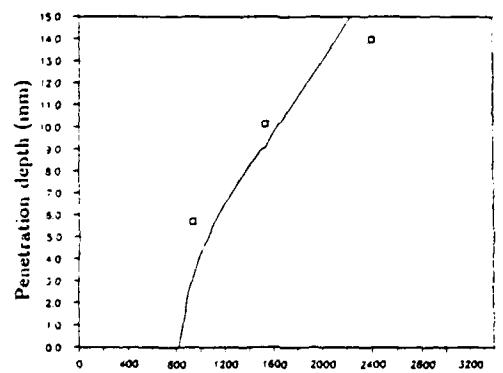


Fig. 4. Penetration depth (mm) vs. impact velocity for 2024-T3 Al penetrators impacting 1100-0 Al targets. ❑ denotes experimental data points for L/D=3 penetrators. The solid curve is a prediction based on the crater volume/kinetic energy relationship.

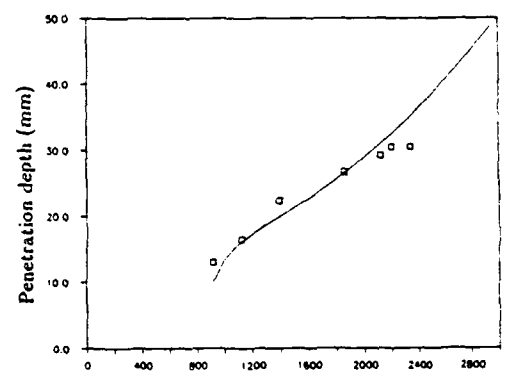


Fig. 5. Penetration depth (mm) vs. impact velocity (m/s) for C 1015 st. penetrators impacting 1100-0 Al targets. ❑ denotes experimental data points for L/D=3 penetrators. The solid curve is a prediction based on the crater volume/kinetic energy relationship.

where p_a is the total pressure on the axis of the penetrator. Now, the average pressure P which appears in the equation of motion of Jones, et al [1], is easily shown to be

$$P = \frac{1}{A}\int_A p\,dA = \frac{nq}{n+1} + \frac{p_a}{n+1} \tag{10}$$

where A is the undeformed cross-sectional area of the penetrator. Using equation (10) for the average pressure revises the equation of motion for the undeformed section into the form

$$\ell\dot{v} + \dot{\ell}(v-u) = \frac{-1}{\rho(1+e)(1+n)}(nq + p_a) \tag{11}$$

This equation, coupled with equation (3), given a new system from which we can estimate the initial transient behavior of the penetrator in terms of two parameters, n and q. It should be noted, however, that n will no longer have the simple interpretation afforded by equation (4).

THE INITIAL TRANSIENT STAGE

Equations (3) and (11) can be used to estimate the initial transient behavior of the penetrator when suitable assumptions are made about the velocity of the undeformed section v and the penetration velocity u. Equation (5) was developed by Cinnamon, et al., 1992, a, by assuming that $v \approx v_0$ and $u \approx u_0$ (const.) during the mushrooming of the penetrator. These assumptions force equations (3) and (11) to take the form

$$e\dot{\ell} = v_0 - u_0 \tag{12}$$

and

$$\dot{\ell}(v_0 - u_0) = \frac{-1}{\rho(1+e)(1+n)}(nq + p_a) \tag{13}$$

When $\dot{\ell}$ is algebraically eliminated between these equations, we get a single equation for the mushroom strain, e.

$$e = \frac{-\rho(n+1)(v_0-u_0)^2}{\rho(n+1)(v_0-u_0)^2 + p_a + nq} \tag{14}$$

This equation expresses e in terms of the time- dependent pressure p_a, the uniform pressure component q, and the parameter n. The uniform pressure q could vary with time, but for this analysis we will assume that it is constant.

Equation (14) is valid throughout the mushrooming stage. At the transition point between mushrooming and steady state, we assume that the Modified Bernoulli Equation (6) applies. This suggests that equation (14) should reduce to

$$e_1 = \frac{-\rho(n+1)(v_0-u_0)^2}{\rho(n+1)(v_0-u_0)^2 + P_1 + nq} \tag{15}$$

and P_1 is taken from equation (6).

The two parameter strain equation (15) is used to match experimental data at high and low velocities. The parameters q and n are then determined algebraically. For C1015 steel penetrators impacting 1100-0 aluminum targets, the results are shown in Figure 6. In this instance, $n = 15.14$ and $q = 105.17$ MPa. The estimates for penetration depth using equation (8) are shown in Figure 7. They are somewhat disappointing, because even a slight variation in strain at percentages as high as those given in Figure 6, can produce considerable discrepancy in the penetration depth predicted by equation (8).

The two parameter strain equation was also applied to some of the cases for which only low velocity data was available. The results for hard 4340 steel penetrators impacting hard 4340 steel targets are shown in Figures 8 and 9. In this case, $n = 3.07$ and $q = 344.8$ MPa. For annealed 4340 steel penetrators impacting annealed 4340 steel targets, the results are shown in Figures 10 and 11. In this instance, $n = 2.58$ and $q = 705.89$ MPa.

Figures 12 and 13 show the results of tungsten (W10) penetrators impacting RHA targets at velocities between 1 km/sec and 3km/sec. The experimental comparison is taken from Silsby, 1984. For this comparison, $n = 8.42$ and $q = 1790$ MPa.

CONCLUSIONS

The results of Cinnamon, et al., 1992, a, have been extended to the penetration of 1100-0 aluminum targets. For lower impact velocities, say those under 2.5 km/sec, the correlation of pressure exponent n in equation (1), predicted by equation (4), produces very reasonable results. However, for higher impact velocities the results deteriorate rapidly. To accommodate higher velocities, the pressure was generalized in equation (9) and the strain at steady state e_1 was shown to correlate very well with independently reported experimental results [7] for two penetrators impacting 1100-0 aluminum targets. The penetration depth predictions using the elementary algebraic method introduced by Cinnamon, et al., 1992, a, are somewhat disappointing. However, this is understandable. At very large strains, even minor deviations from the experimental results will produce significant deviations in the cross-sectional area of the crater. As a result, equation (8) will produce estimates that differ from experiment. Such differences are not as visible at low velocities because the strains are smaller in magnitude. Future efforts will be directed toward improvement in this area. Future efforts will also center on other forms for the pressure distribution in equation (9). Some progress has already been made in the area.

A project of some interest to us is the physical interpretation of n and q. For the simple pressure distribution in equation (1), a low velocity interpretation can be provided by equation (4). However, for $q = 0$ and velocities higher than about 3 km/sec., n does not have this interpretation. It remains to be seen whether a

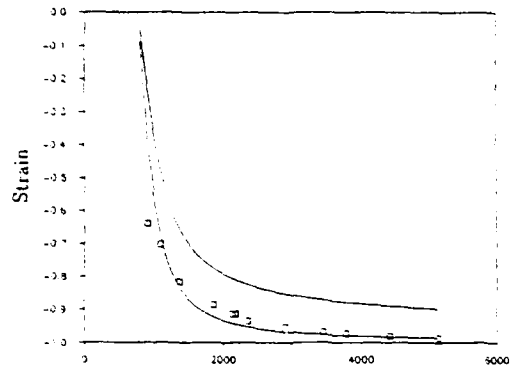


Fig. 6. Strain vs. impact velocity (m/s) for C 1015 st. (1000 MPa) penetrators against 1100-0 Al (250 MPa) targets. ❑ denotes experimental data points. e_1 (lower solid curve) is the predicted strain at the beginning of steady state and e_0 (upper solid curve) is the predicted strain at impact.

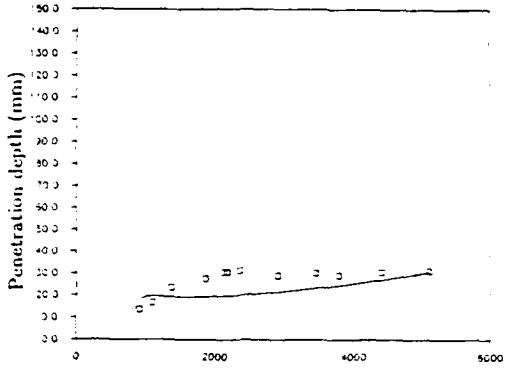


Fig. 7. Penetration depth (mm) vs. impact velocity (m/s) for C 1015 st. penetrators impacting 1100-0 Al targets. ❑ denotes experimental data points for L/D=3 penetrators. The solid curve is a prediction based on the crater volume/kinetic energy relationship. The disparity noted for the intermediate velocities is caused by small deviations in the predicted strain which can result in large deviations in the predicted cross-sectional area of the crater.

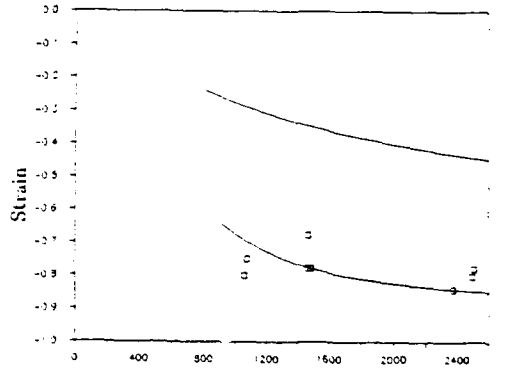


Fig. 8. Strain vs. impact velocity (m/s) for hard 4340 st. (1825 MPa) penetrators against hard 4340 st. (1825 MPa) targets. ❑ denotes experimental data points. e_1 (lower solid curve) is the predicted strain at the beginning of steady state and e_0 (upper solid curve) is the predicted strain at impact.

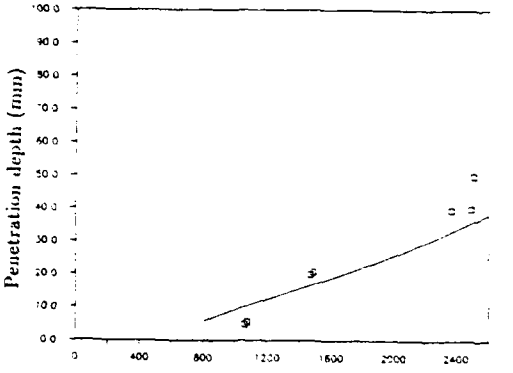


Fig. 9. Penetration depth (mm) vs. impact velocity (m/s) for hard 4340 st. penetrators impacting hard 4340 st. targets. ❑ denotes experimental data points for L/D=10 penetrators. The solid curve is a prediction based on the crater volume/kinetic energy relationship.

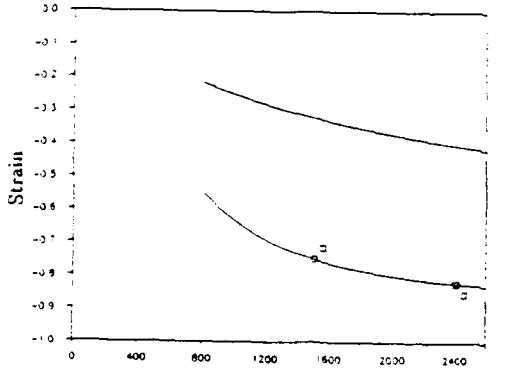


Fig. 10. Strain vs. impact velocity (m/s) for annealed 4340 st. (1263 MPa) penetrators against annealed 4340 st. (1263 MPa) targets. ❑ denotes experimental data points. e_1 (lower solid curve) is the predicted strain at the beginning of steady state and e_0 (upper solid curve) is the predicted strain at impact.

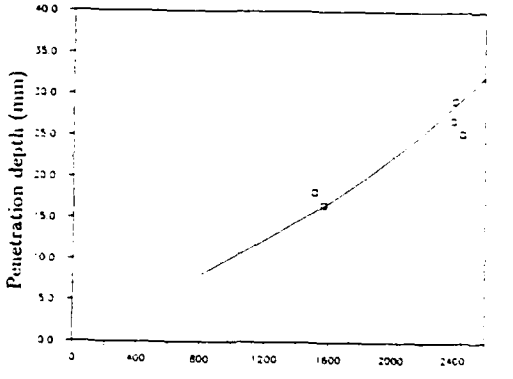


Fig. 11. Penetration depth (mm) vs. impact velocity (m/s) for annealed 4340 st. penetrators impacting annealed 4340 st. targets. ❑ denotes experimental data points for L/D=5 penetrators. The solid curve is a prediction based on the crater volume/kinetic energy relationship.

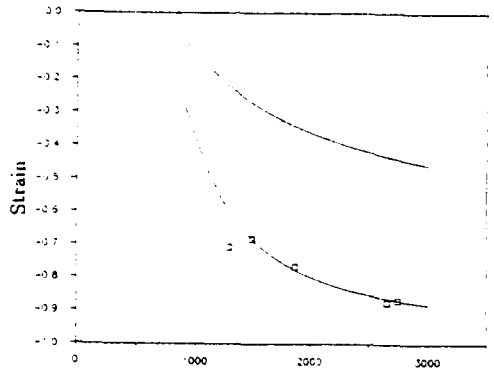


Fig. 12. Strain vs. impa[illegible]elocity [illegible]m/s) for tungsten W 10 (2500 MPa) penet[illegible] against RHA (1000 MPa) targets. ❑ denotes [illegible]perimental data points. e_1 (lower solid curve) is the predicted strain at the beginning of steady state and e_0 (upper solid curve) is the predicted strain at impact.

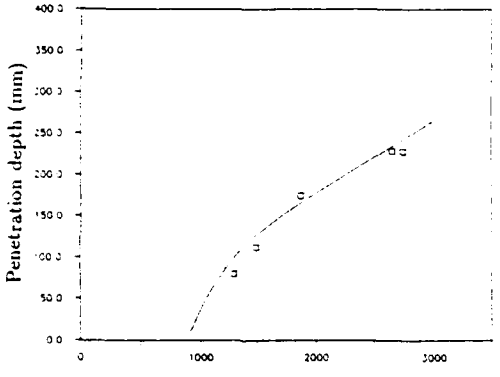


Fig. 13. Penetration depth (mm) vs. impact velocity (m/s) for Tungsten W 10 penetrators impacting RHA targets. ❑ denotes experimental data points for L/D=3 penetrators. The solid curve is a prediction based on the crater volume/kinetic energy relationship.

physically based understanding of these parameters can be found.

REFERENCES

1. Alekseevskii, V. D. (1966) Penetration of a rod into a target at high velocity," *Combustion, Explosion, and Shock Waves.*

2. Anderson, C. E. (1991) Southwest Research Institute, San Antonio, Texas, private communication.

3. Christman, D. R., A. B. Wenzel, and J. W. Gehring. (1964). Penetration mechanisms of high velocity rods. *Proceedings of the Seventh Hypervelocity Impact Symposium*, Tampa, Florida.

4. Cinnamon, J. D., S. E. Jones, J. W. House, and L. L. Wilson. (1992a). A one-dimensional analysis of rod penetration. *International Journal of Impact Engineering*, 12, 2, 145-166..

5. Cinnamon, J. D., S. E. Jones, L. L. Wilson, and J. W. House. (1992b). Further results in the one-dimensional analysis of rod penetration. *Developments in Theoretical and Applied Mechanics, Vol. XVI*, (B. Antar, R. Engels, A. A. Prinaris, and T. H. Moulden, eds.), Nashville, Tennessee.

6. Jones, S. E., P. P. Gillis, and Joseph C. Foster, Jr., (1987). On the penetration of semi-infinite targets by long rods. *J. Mech. Phys. Solids*, 35, 121.

7. Silsby, G. F. (1984). Penetration of semi-infinite steel targets by tungsten long rods at 1.3 to 4.5 km/sec. In: *Proceedings of the Eighth International Symposium on Ballistics*, Orlando FL.

8. Tate, A. A theory for the deceleration of long rods after impact. *J. Mech. Phys. Solids*, 15, 387.

9. Wilson, L. L.,Joseph C. Foster, Jr., S. E. Jones, and Peter P. Gillis. (1989). Experimental rod impact results. *Int. J. Impact Engng*, 8, 15.

Int. J. Impact Engng Vol. 14, pp. 417–426, 1993
Printed in Great Britain

0734-743X/93 $6.00 + 0.00
Pergamon Press Ltd

PROBLEMS ASSOCIATED WITH LAUNCHING HYPERVELOCITY PROJECTILES FROM THE FAST SHOCK TUBE

J. F. Kerrisk and J. K. Meier

Los Alamos National Laboratory
Mail Stop F663
Los Alamos, New Mexico 87545

ABSTRACT

Modeling and experiments are being done with the goal of understanding the physics of projectile acceleration at high driving pressures (megabar range) and short acceleration times (a few microseconds) well enough to design and test successful hypervelocity launch systems. The Fast Shock Tube, a cylindrically convergent high-explosive driver, has been used to accelerate projectiles. Detailed modeling of the experiments, including high-pressure gas flow, projectile instability, and projectile fracture, has been done with the MESA/2D code. Modeling results show quantitative agreement with the average behavior of the system. However, details of projectile behavior are not predicted well. Observed velocity distributions across the diameter of a projectile or projectile shapes are only in qualitative agreement with calculations. This, then, presents the major constraint on the successful design of a launch system: that the processes that limit projectile integrity depend on the details of the drive conditions, and these details are not quantitatively modeled at this time.

INTRODUCTION

The Fast Shock Tube (FST) is a cylindrically convergent high-explosive (HE) system for driving a flat axial shock in a polystyrene foam core inside the HE (Marsh and Tan, 1992; Meier and Kerrisk, 1992; Kerrisk and Meier, 1992). The shocked foam, which acts like a gas, is used as a driver for gas-flow or projectile-acceleration tests. Drive conditions much higher than direct HE drive can be obtained in the FST. Projectiles can be shock accelerated (in direct contact with the foam) or accelerated more gently by expanding the foam before acceleration. Peak driving pressures on flat-plate projectiles have ranged from 0.3-1 Mbar. Intact plates have been accelerated up to ~0.9 cm/μs over distances of a few centimeters.

The work discussed here represents an attempt to probe limits of projectile acceleration under the high-pressure drive conditions attainable in the FST. The initial problem, that of achieving a source of high-pressure gas with uniform conditions (pressure, density, velocity) over an area of at least a few square centimeters, has been solved by the FST driver (Meier and Kerrisk, 1992; Menikoff et al., 1991). However, the use of this driver gas presents a number of additional problems. If projectile acceleration were one dimensional, problems of shock formation and spall fracture would still occur. These problems can be mitigated by tailoring the pressure/time history of the drive with an expansion region between the initial location of the drive gas and the projectile. However, one-dimensional drive is an oversimplification. With a uniform, two-dimensional drive but with ideal (rigid, reflecting) boundaries, the additional problems of projectile instability, stresses associated with exit from a barrel, and two-dimensional fracture would occur. These problems become more difficult to solve as the driving pressure increases. With the FST, however, even this is an oversimplification. Driving pressures in the FST are well above any material strengths. Thus, real boundaries (for example, the barrel wall) deform during projectile acceleration. Deformation of boundaries leads to flow perturbations and nonuniform

drive conditions. This, in turn, intensifies the instability and fracture problems inherent in the two-dimensional system.

These problems are being investigated through a combination of experiments and two-dimensional modeling. Our goal is to understand the physics underlying the process of projectile acceleration with a high-pressure gas well enough to design and test successful launch systems.

DESCRIPTION OF THE FAST SHOCK TUBE

Figure 1 shows one of a number of related FST systems that has been built and tested. The initiator section insures a uniform initiation of the driver HE around the outer periphery. The detonation front moves axially along the HE/foam interface in the driver at the detonation velocity (0.88 cm/μs for PBX 9501), forming a flat, normal shock in the foam. The design parameters of the driver section (diameters, lengths, type of HE, foam density) must be chosen properly to achieve the flat shock and uniform flow conditions behind the shock in the foam core (Meier and Kerrisk, 1992; Menikoff et al., 1991). In the system shown in Fig. 1, an initial foam density of 0.5 g/cm^3 gives a pressure of ~0.3 Mbar and a particle velocity of ~0.66 cm/μs behind the shock in the foam. Figure 2 shows calculated material interfaces and pressure contours in the HE and foam of the driver from Fig. 1 when the shock is ~1 cm from the end of the driver. The calculations (all hydrodynamic calculations discussed here were done with MESA/2D (Cagliostro et al., 1990)) are in good agreement with radiographs showing the detonation front and flat shock in the foam. The lack of radial variation of the pressure (also density and axial velocity) contours behind the shock shows that this flow is radially uniform. This condition is necessary to achieve a sustained, uniform acceleration.

An experimental section consisting of a barrel, an expansion region for the shocked foam, and a projectile (plate) is also shown in Fig. 1. A variety of other experiments, including driver diagnostics or direct acceleration of plates, have been used on the end of the driver. Projectiles in the form of plates of stainless steel, Ti, and Ta with diameters of 10-25 mm and thicknesses of 0.7-3.5 mm have been accelerated.

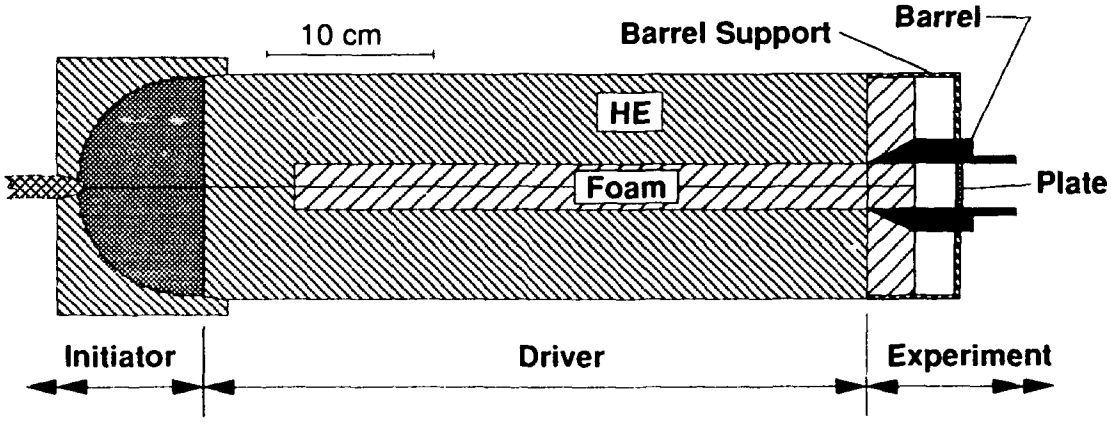


Fig. 1 Sketch of the Fast Shock Tube.

EXPANSION OF THE DRIVING GAS

Projectiles can be accelerated by placing the projectile in direct contact with the foam. However, this method shocks the projectile up to pressures of ~1 Mbar. Although these shock pressures are not high enough to melt the materials tested, they result in high temperatures and the possibility of spalling. For these reasons, a short expansion down a barrel has been used to modify the pressure/time history driving the plate (Fig. 1). Although expansion can eliminate shocks in the projectile, the high pressures and velocities of the expanding foam deform the barrel walls during expansion and acceleration. Flow past the deformed walls disturbs the initially uniform flow from the driver and results in increasingly nonuniform drive conditions. Figure 3 shows material interfaces and vector velocities in the vicinity of

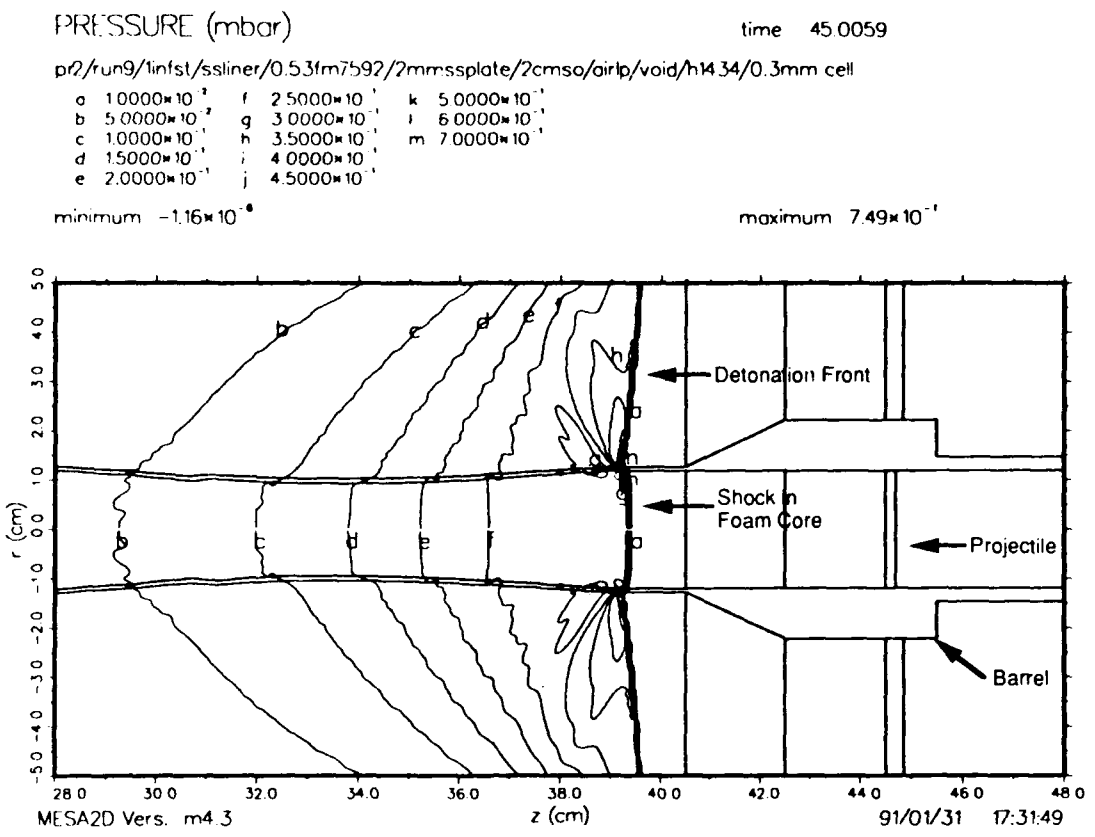


Fig. 2 Material interfaces and pressure contours in the FST at 45 μs after initiation of the driver HE.

the barrel (stainless steel) and projectile (2-mm thick stainless steel) ~5 μs after the start of motion of the projectile. The distorted barrel walls (compare with Figs. 1 and 2) and radially nonuniform flow behind the projectile are evident.

MESA/2D calculations of initially uniform flow entering and flowing down a stainless steel barrel show flow perturbations starting at the barrel wall and moving radially out into the gas stream. The most prominent deformations of the barrel wall occur at the entrance, at any discontinuities such as the interface between the foam and expansion region, and at the initial axial location of the plate (see Fig. 3). The design of the barrel entrance shown in Fig. 1 represents an attempt to minimize flow perturbations from the entrance.

Flow that is essentially uniform 1-2 μs after the start of expansion develops density perturbations of 10-20% by 5 μs after the start of flow. The magnitude of a perturbation also tends to increase as it converges radially. These perturbations result in nonuniform drive conditions. The details of when and where (radially) the flow perturbations influence the plate depend, among other parameters, on the sound speed in the shocked and expanding foam. Attempts to calculate the effects of these flow perturbations on projectile velocity have shown only qualitative agreement with observations (see discussion of LINE VISAR measurements, below). Uncertainties in the equation of state (EOS) of the foam are thought to be mostly responsible for these differences.

EARLY PROJECTILE ACCELERATION

The early motion of 2-mm-thick stainless steel plates has been observed in systems like Fig. 1 using a LINE VISAR to measure velocity across a diameter of the plate (Hemsing et al., 1992). This technique provides velocity data for 2-4 μs after the start of motion. After that time, gas blowby around the edges of the plate disrupts the VISAR signal. Figure 4 shows plots of the axial velocity of the front surface of

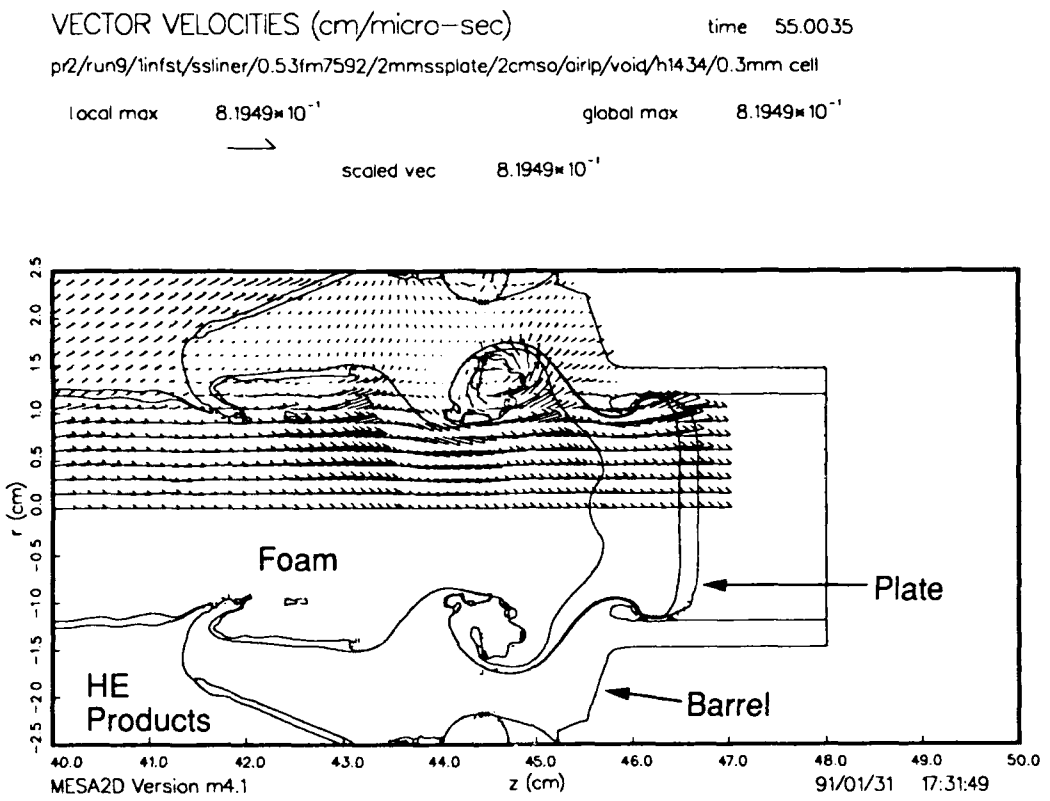


Fig. 3 Material interfaces and velocity vectors in the FST ~5 μs after start of motion of the projectile (plate).

the plate as a function of the distance across a diameter. At each time observed and calculated velocity profiles are shown. At 50.5 μs (~0.1 μs after the start of motion), the observed data show the edges of the plate moving faster than the center; the calculations show the center moving faster. By 50.9 μs, the observed and calculated velocities are in good agreement. At later times, some show good agreement between observations and calculations and others show poor agreement.

An examination of the observed velocity profiles in Fig. 4 shows that a perturbation (an increase in velocity) starts at the edges of the plate at ~50.7 μs and moves toward the center, reaching the r = 0 axis between 51.6 and 52 μs. This disturbance in the velocity is probably caused by a flow perturbation in the driving gas. The calculations indicate a much smaller perturbation of a similar nature. The discrepancy between these observations and calculations is an example of our inability to calculate the details of the flow perturbations and their effects on the plate at this time.

Calculated average projectile velocities depend to a large extent on the EOS of the foam. Figure 5 is a plot of calculated projectile velocity (2-mm thick by 25-mm-diameter stainless steel plate) using ideal-gas and SESAME (Holian, 1984) EOSs for the foam compared with the measured average velocities obtained from three radiographs and impact on a witness plate. These two EOSs were chosen based on comparisons of the observed and calculated shock positions in the FST driver. In that comparison and for projectile velocities, they tend to bracket the observed behavior. A single suitable EOS has not been found.

PROJECTILE STABILITY

During acceleration, the driving gas that is pushing the projectile is of lower density than the projectile material. This leads to the possibility of instabilities that are similar to the Rayleigh-Taylor instability at the interface between two fluids of different density in a gravitational field. Previous examinations of

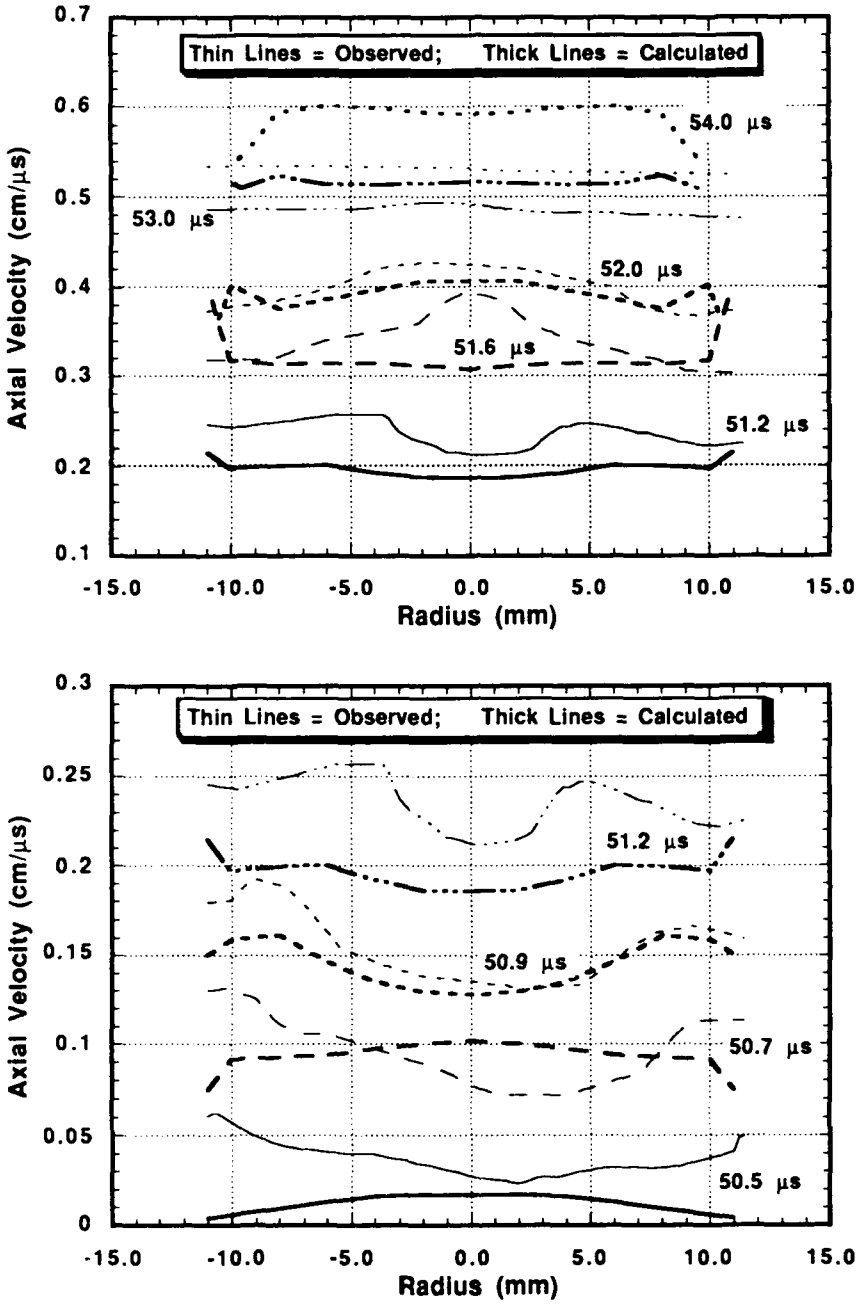


Fig. 4 Observed (LINE VISAR) and calculated (MESA/2D) velocity profiles of the front surface of a 2-mm-thick stainless steel plate accelerated in the FST (test H1434). The lower plot shows times from 50.5 to 51.2 μs on an expanded scale; the upper plot shows times from 51.2 to 54 μs.

the stability of accelerated plates involved Lagrangian numerical calculations (Swegle and Robinson, 1989) or experiments (Barnes et al., 1974; Barnes et al., 1980) on plates with prescribed initial surface perturbations. This work would be applicable if the driving pressure were uniform across the diameter of a plate. However, experiments and calculations indicate that nonuniformities exist in the FST drive. The calculations described here were Eulerian (with MESA/2D, the same code used for other FST calculations) and used a prescribed driving-pressure perturbation on a plate that had an initially uniform surface. Perturbations that varied only spatially and that varied with space and time were used.

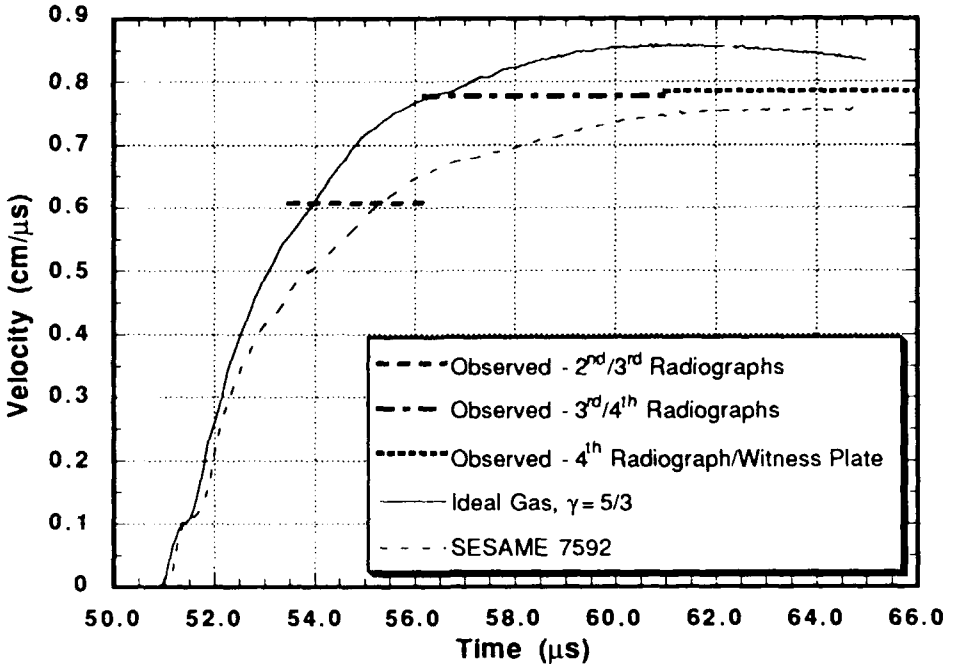


Fig. 5 Observed average projectile velocities obtained from radiographs and a witness plate compared with calculated (MESA/2D) velocities using two foam EOSs (test E6035).

A group of calculations was done initially to compare the MESA/2D results with the Lagrangian calculations of Swegle and Robinson (1989). The agreement was good except for one case in which the system was on the boundary between stability and instability. Swegle and Robinson predicted the plate was just stable, but MESA/2D predicted it was marginally unstable. Trends in the susceptibility of plates to instability were observed from calculations in which various parameters were systematically varied. Increasing the wavelength to plate thickness ratio, increasing the relative magnitude of the perturbation, increasing the driving pressure, or decreasing the yield strength of the plate all led to greater tendency for instability. These same trends were observed whether produced by an initial surface perturbation on the plate or by a driving-pressure perturbation.

A simple analytical argument can be made to show that these two types of perturbations are equivalent after an initiation period. In the limit of small perturbations and for a steady-state pressure gradient, there is a relation between the initial relative surface perturbation ($\Delta h_0/h$) and the relative pressure perturbation ($\Delta P/P$) that gives the same axial pressure gradient. For this analysis, h is the plate thickness, Δh is the peak-to-peak surface variation, Δh_0 is the initial value of Δh, P is the pressure, and ΔP is the peak-to-peak pressure variation. Figure 6 shows sketches of the pressure gradient through a plate of thickness h. On the left, the driving pressure is uniform and the gradients for two different plate thicknesses [h and $(h - \Delta h_0)$] are shown. On the right, the plate thickness is uniform and the gradients for two different driving pressures [$(P + 1/2\Delta P)$ and $(P - 1/2\Delta P)$] are shown. For the ratio of these two gradients to be the same in the two cases, Fig. 6 shows that $\Delta h_0/h = \Delta P/P$. That is, the ratio of the pressure gradients would be the same if the magnitude of the relative initial surface perturbation ($\Delta h_0/h$) is the same as the magnitude of the relative pressure perturbation ($\Delta P/P$). Because the axial pressure or stress gradient drives the instability (Swegle and Robinson, 1989), the behavior of plates should be similar under these conditions.

Figure 7 is a plot of Δh as a function of time that compares three calculations in which a uniform drive pressure and initial surface perturbation were used ($\Delta h_0/h = 0.2\%$) with three otherwise identical calculations in which a uniform plate and a perturbation ($\Delta P/P = 0.2\%$) in the driving pressure were used. For these calculations, the average driving pressure for a 2-mm-thick tungsten plate rose to 1 Mbar in 0.1, 1.0, or 10.0 μs and then was held constant. At early time there is a large difference between the two sets of calculations because it takes some time for plates that have $\Delta h_0 = 0$ to catch up

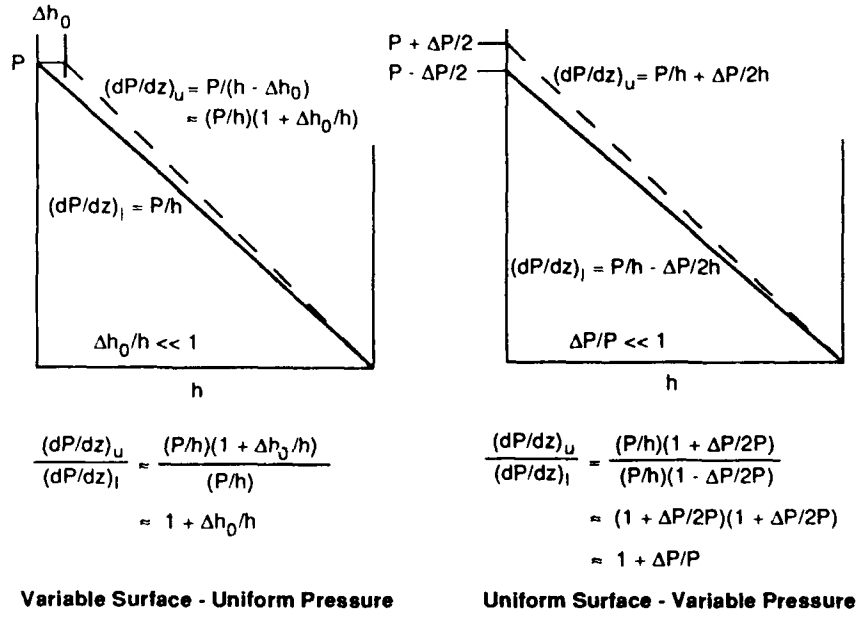


Fig. 6 Sketch of pressure gradients formed by a uniform pressure on a variable surface (left) and a variable pressure on a uniform surface (right).

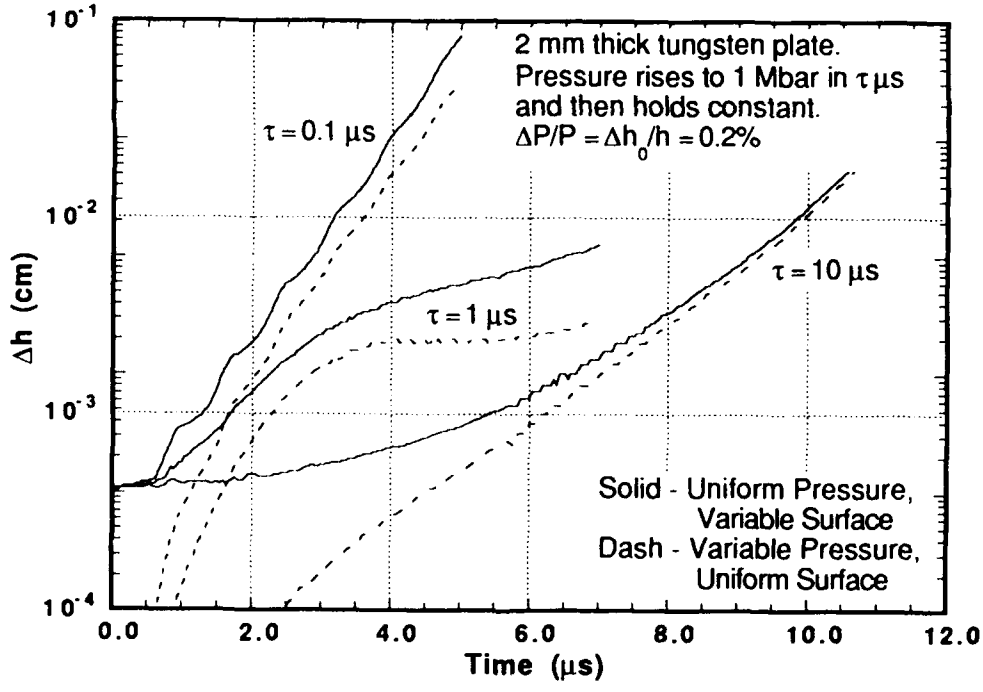


Fig. 7 Δh as a function of time for six calculations that compare the effects of initial surface perturbations with those of pressure perturbations on an initially uniform surface.

with the plates that have $\Delta h_0 = 0.0004$ cm. At later time, the best agreement is for the problem with the longest rise time (10 μs); this problem best meets the assumption of a steady-state pressure gradient. However, the agreement is reasonable in the case of the shortest rise time (0.1 μs) even though the pressure gradient is far from steady state. The problem with the intermediate rise time (1 μs) is on the boundary between stability and instability and shows the poorest late-time agreement of the three.

Stability calculations that are more characteristic of the type of perturbations seen in the FST were also done. For these calculations the average driving pressure on a 24-mm diameter by 2-mm-thick stainless steel plate rose to a maximum (P_m) of 0.4, 0.7, or 1 Mbar in 1 μs, held constant for 1 μs, and then dropped to zero over 6 μs. A pressure perturbation that started near the edge of the plate and moved toward the r = 0 axis at 0.5 cm/μs was superimposed on the average pressure. The perturbation was assumed to decay to zero after it reached the r = 0 axis. A series of calculations was done to find the magnitude of the pressure perturbation (ΔP/P) that produced the same maximum plate deformation (Δh_m) at a particular time in the calculation. Figure 8 is a plot of ΔP/P as a function of P_m that produces Δh_m = 0.5 mm at 12 μs and Δh_m = 5 mm at 12 μs. The lines represent contours of constant Δh_m in ΔP/P - P_m space. The velocities shown are the final plate velocities. Figure 8 indicates that as the maximum driving pressure in the FST increases, the allowable ΔP/P for some fixed maximum plate deformation decreases. The relation is nonlinear so that the decrease in allowable ΔP/P is occurring faster than the proportionate increase in pressure. Larger levels of ΔP/P can be tolerated if larger maximum plate deformations are acceptable.

PROJECTILE INTEGRITY

Radiographs have often shown breakup of projectiles that have exited the barrel of the FST (Marsh and Tan, 1992). This breakup is probably caused by conditions (time-varying, localized tensile stresses within the projectile that lead to fracture. The ability of two fracture models in MESA/2D to describe this behavior was examined with calculations of the acceleration of a 19-mm-diameter by 2.66-mm-thick Ti-6Al-4V plate. This material was highly fragmented in test radiographs (Marsh and Tan, 1992). Parameters for the Johnson-Cook Damage (JCD) model (Johnson and Cook, 1985) were originally obtained from Johnson and Holmquist (1989). However, use of these parameters to model a one-dimensional spall test (Me-Bar et al. 1987) did not predict spall when it was observed. Values of s_{spall} and e_{min} were varied in a series of one-dimensional calculations until the calculated stress matched the observed data. The other model parameters (D_1 - D_5) were held fixed at the values given by Johnson and Holmquist. Parameters for the Johnson Spall (JS) model (Johnson, 1981) were determined by matching the same spall-test data.

As a measure of damage, the JCD model uses a damage fraction ($0 \le D \le 1$) that is accumulated from the ratio of the incremental plastic strain to a predicted strain to failure at each time step. The JS model calculates a material porosity ($0 \le \alpha \le 1$). Although the ranges of these two damage measures are the same, they are probably not directly comparable. There is also a difference in how damage is communicated to the strength model. With the JCD model, there is no communication until D = 1, at which time the yield strength and shear modulus are set to zero. In the JS model, the yield strength and shear modulus are continuously degraded as porosity increases (Johnson, 1981).

Figure 9 shows a plot of plastic strain, damage fraction, and porosity at r = 0 and the mid plane of the plate for three calculations of the acceleration of the Ti-6Al-4V plate, one without fracture, one using the JS model, and one using the JCD model. The accumulated plastic strain differs significantly among the three calculations. With the JCD model, plastic strain is no longer accumulated after ~23.1 μs, when D is 1 at this location. (The earlier rise of D above 1 (at 20.5 μs) and its subsequent drift downward were caused by numerical diffusion in this Eulerian calculation.) Although there is a difference in the magnitude of damage fraction and porosity, the two models tend to show sharp increases at about the same time. This is when the local tensile stresses are highest. Looking at damage patterns over the entire plate, the two models predict the most damage in the same regions, near the axis (r = 0) toward the front of the plate (where spall is most likely) and near the intersection of the plate with the barrel walls (where considerable plastic strain occurs). Neither model predicts the complete fragmentation observed in the test.

LIMITATIONS ON PROJECTILE ACCELERATION

The goal of this work is to understand the physics underlying projectile acceleration well enough to design and test successful hypervelocity launch systems. A qualitative understanding of the problems associated with projectile acceleration at high driving pressures and short acceleration times has been attained. The major problems encountered have been shock formation in the projectile, projectile

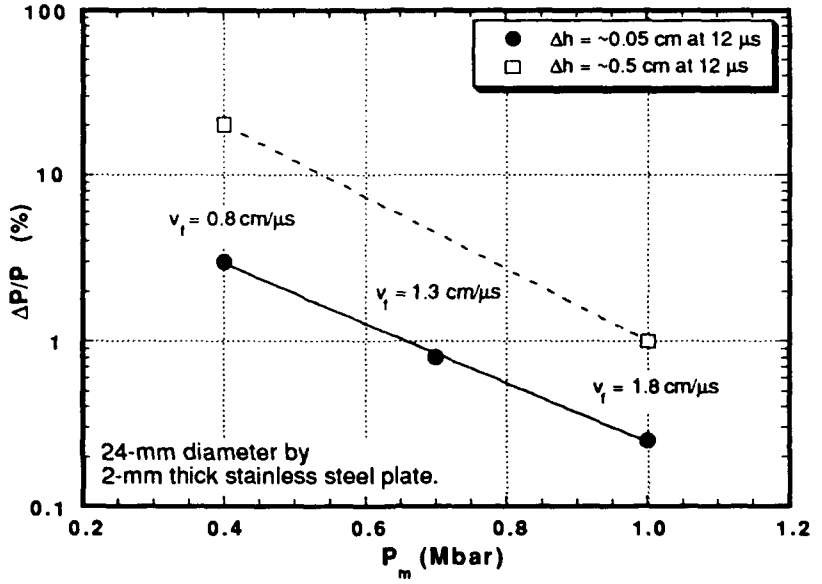


Fig. 8 Contour lines of constant Δh_m at 12 μs as a function of $\Delta P/P$ and P_m for the acceleration of a 2-mm-thick stainless steel plate in the FST. The velocities are final plate velocities at peak driving pressures of 0.4, 0.7, and 1.0 Mbar.

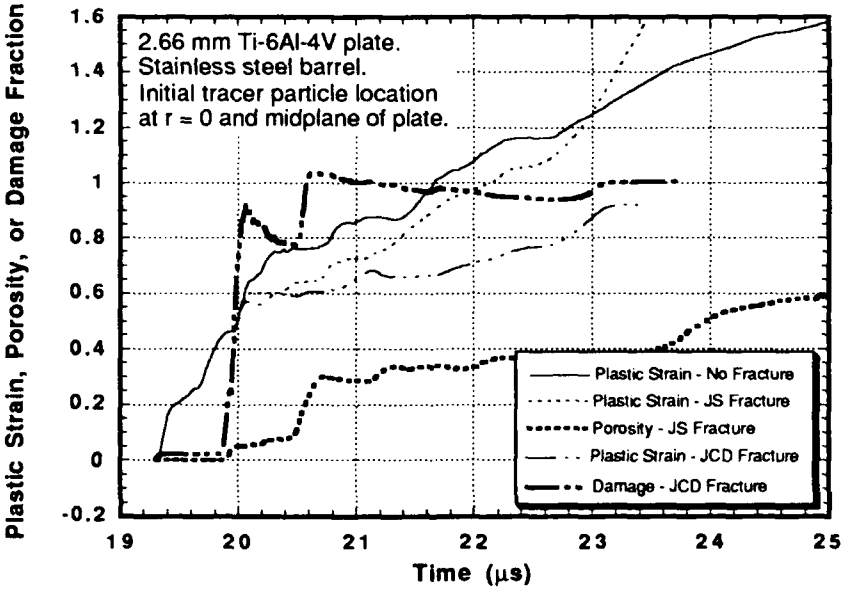


Fig. 9 Plastic strain, porosity (JS model), and damage fraction (JCD model) as a function of time for three calculations (without fracture, the JS model, and the JCD model) of the acceleration of a 2.66-mm-thick Ti-6Al-4V plate. The three thin curves show plastic strains for the three calculations. The two thick curves show damage measures for the calculations using the JS and JCD models.

instability, and projectile fracture. Shock formation in the projectile can be limited by tailoring the pressure/time profile on the projectile. In the FST, an expansion region between the foam core and the projectile limits shock formation. However, flow in the expansion region leads to flow perturbations that

result in nonuniform driving pressures on the projectile. The likelihood of instabilities leading to projectile distortion or breakup increases as the drive becomes more nonuniform. Projectile fragmentation, probably from localized tensile stresses, has been shown to be a material-dependent problem (Marsh and Tan, 1992).

Modeling of FST tests has shown quantitative agreement with the average behavior of the system. For example, calculated average projectile velocities are normally in good agreement with observations. However, details of projectile behavior are not predicted well. Observed velocity distributions across the diameter of a projectile (LINE VISAR data) or projectile shapes (radiographs) are only in qualitative agreement with calculations. This presents the major constraint on the successful design of a launch system: that the processes that limit projectile integrity depend on the details of the drive conditions, and these details are not quantitatively modeled at this time. The need for two-dimensional modeling is a consequence of the kinds of problems encountered. The nonuniformities in driving pressure, material distortions, and plate instabilities and fracture are all two-dimensional effects that would be missed in one-dimensional modeling.

ACKNOWLEDGMENTS

The authors would like to thank other researchers at Los Alamos National Laboratory for their assistance in this work. They include M. George, W. Hemsing, M. Holder, and S. Marsh for their test data; and J. Shaner, T. H. Tan, and R. Godwin for their comments and support.

REFERENCES

Barnes, J. F., P. J. Blewett, R. G. McQueen, K. A. Meyer, and D. Venable (1974). Taylor instability in solids. *J. Appl. Phys.*, 45, 727-732.

Barnes, J. F., D. J. Janney, R. K. London, K. A. Meyer, and D. H. Sharpe (1980). Further experimentation on Taylor instability in solids. *J. Appl. Phys.*, 51, 4678-4679.

Cagliostro, D. J., D. A. Mandell, L. A. Schwalbe, T. F. Adams, and E. J. Chapyak (1990). MESA-3D calculations of armor penetration by projectiles with combined obliquity and yaw. *Int. J. Impact Eng.*, 10, 81-92.

Hemsing, W. F., A. R. Mathews, R. H. Warnes, and G. R. Whittemore (1992). VISAR: Line-imaging velocity interferometer. *Shock Compression of Condensed Matter 1991* (S. C. Schmidt, R. D. Dick, J. W. Forbes and D. G. Tasker, ed.), pp. 767-770. Elsevier Sci. Publishers B. V., Amsterdam.

Holian, K. S. (ed) (1984). T-4 handbook of material properties data base. Vol. Ic: equations of state. Los Alamos National Laboratory report LA-10160-MS.

Johnson, G. R. and W. H. Cook (1985). Fracture characteristics of three metals subjected to various strains, strain rates, temperatures, and pressures. *Eng. Fracture Mech.*, 21, 31-48.

Johnson, G. R. and T. J. Holmquist (1989). Test data and computational strength and fracture model constants for 23 materials subjected to large strains, high strain rates, and high temperatures. Los Alamos National Laboratory report LA-11463-MS.

Johnson, J. N. (1981). Dynamic fracture and spallation in ductile solids. *J. Appl. Phys.*, 52, 2812-2825.

Kerrisk, J. F. and J. K. Meier (1992). Comparisons between Fast Shock Tube calculations and tests. *Shock Compression of Condensed Matter 1991* (S. C. Schmidt, R. D. Dick, J. W. Forbes and D. G. Tasker, ed.), pp. 1049-1052. Elsevier Sci. Publishers B. V., Amsterdam.

Marsh, S. P. and T. H. Tan (1992). Hypervelocity plate acceleration. *Shock Compression of Condensed Matter 1991* (S. C. Schmidt, R. D. Dick, J. W. Forbes and D. G. Tasker, ed.), pp. 1033-1039. Elsevier Sci. Publishers B. V., Amsterdam.

Me-Bar, Y., M. Boas, and Z. Rosenberg (1987). Spall studies on Ti-6Al-4V. *Materials Sci. and Eng.*, 85, 77-84.

Meier, J. K. and J. F. Kerrisk (1992). An introduction to the Fast Shock Tube (FST). *Shock Compression of Condensed Matter 1991* (S. C. Schmidt, R. D. Dick, J. W. Forbes and D. G. Tasker, ed.), pp. 1045-1048. Elsevier Sci. Publishers B. V., Amsterdam..

Menikoff, R., K. S. Lackner, N. L. Johnson, S. A. Colgate, J. M. Hyman, and G. A. Miranda (1991). Shock wave driven by a phased implosion. *Phys. Fluids*, A3, 201-218.

Swegle, J. W. and A. C. Robinson (1989). Acceleration instability in elastic-plastic solids. *J. Appl. Phys.* 66, 2838-2858.

Int. J. Impact Engng Vol 14, pp. 427–438, 1993
Printed in Great Britain

0734-743X/93 $6.00 + 0.00
Pergamon Press Ltd

NUMERICAL AND EXPERIMENTAL STUDIES OF HIGH-VELOCITY IMPACT FRAGMENTATION

M. E. KIPP, D. E. GRADY, and J. W. SWEGLE

Sandia National Laboratories
Albuquerque, New Mexico 87185-5800

ABSTRACT

Developments are reported in both numerical and experimental capabilities for characterizing the debris spray produced in penetration events. We have performed a series of high-velocity experiments specifically designed to examine the fragmentation of the projectile during impact. High-strength, well-characterized steel spheres (6.35 mm diameter) were launched with a two-stage light-gas gun to velocities in the range of 3 to 5 km/s. Normal impact with PMMA plates, thicknesses of 0.6 to 11 mm, applied impulsive loads of various amplitudes and durations to the steel sphere. The extent of fragmentation, loss in momentum, and divergence of the debris are shown to correspond to the impact conditions. Multiple flash radiography was used to monitor material motion and fragmentation of the steel sphere during the impact event. Dynamic fragmentation theories, based on energy-balance principles, were used to evaluate local material deformation and fracture state information from CTH, a three-dimensional Eulerian solid dynamics shock wave propagation code. The local fragment characterization of the material defines a weighted fragment size distribution, and the sum of these distributions provides a composite particle size distribution for the steel sphere. The calculated axial and radial velocity changes agree well with experimental data, and the calculated fragment sizes for a specific experiment are in qualitative agreement with the radiographic data.

INTRODUCTION

Some basic theories have emerged within the past decade for predicting the consequences of dynamic fragmentation brought about by high-velocity impact or explosive events. These theories have focused principally on the prediction of mean fragment size through energy and momentum balance principals (*e.g.* Grady, 1982; Kipp and Grady, 1985; Glenn and Chudnovsky, 1986) and on the statistical issues of fragment size distributions (*e.g.* Brown, 1989; Englman, *et al.*, 1984; Grady and Kipp, 1985). This theoretical basis has provided the underlying framework for a number of computational algorithms employed to analyze complex fragmentation events (*e.g.* Johnson, *et al.*, 1990; Melosh, *et al.*, 1992; Smith, 1989).

The present studies focus on the development of both numerical and experimental capabilities for characterizing the debris spray produced in penetration events. A systematic fragment debris database is essential for the continued development of a theoretical understanding of fragmentation and the associated computational model development and verification. This investigation of impact-induced fragmentation was undertaken to provide such an experimental base of high-resolution impact fragmentation data for evaluating models and the accuracy of current computational fragmentation analysis techniques.

The primary experimental objective in this study was to investigate the dynamic fragmentation characteristics of a high-strength steel, through controlled impact experiments, using flash-radiography diagnostics. Experiments of this type usually involve the high-velocity interaction of a metal projectile with a stationary target (plate) of similar or dissimilar metals. Radiographic diagnostics of the fragmentation event cannot readily discriminate projectile fragments from target fragments. In each of the present experiments, a high-velocity steel sphere, accelerated to a velocity in the range of 3 to 5 km/s, undergoes normal impact on a thin stationary plastic plate. The plate imparts a controlled impulse to the steel sphere of magnitude and duration determined by impact velocity and plate thickness. The radiographic diagnostic exclusively images the fragmented steel sphere, since the target plastic is transparent to the x-ray beam. This technique offers useful analysis and interpretation features of the fragmentation event not available in multi-metal impact experiments, foremost of which is the association of the known mass of the sphere with the debris in the radiograph.

The numerical tool chosen for development of fragmentation prediction capability is the three-dimensional Eulerian wave propagation code, CTH (McGlaun, *et al.*, 1990). A post-processor was developed to determine local average fragment sizes from strain-rate and temperature information, using the dynamic fragmentation theories mentioned previously.

EXPERIMENTAL CONFIGURATION AND MATERIALS

The experimental configuration for the series of impact fragmentation tests is shown in Fig. 1. Saboted steel spheres were launched at velocities between about 3 to 5 km/s with a two-stage light-gas gun system. The launch tube diameter was 12 mm. Plastic sabots were separated from the steel spheres through forces produced by a slight back pressure in the gun range section. Sabot segments are trapped upstream and do not reach the target impact chamber. Velocity of the steel spheres is measured to ±1% accuracy by recording the time interval during passage between two magnetic coils of known separation. Normal impact occurred in the target chamber at the center of a 75 mm by 75 mm square plastic target plate of thickness between 0.6 and 11 mm. The plastic is PMMA (polymethyl-methacrylate) Rohm and Haas Type II UVA, and has a nominal density of 1186 kg/m^3.

In all experiments a steel sphere 6.35 mm (1/4 in.) in diameter was used. The measured mass was 1.027 ± 0.001 grams. The steel was AISI E52100 high-carbon chromium steel, heat treated to a Rockwell-C hardness of 60 to 67. The density of the steel is 7837 kg/m^3, yield strength is 2.03 GPa, fracture toughness is 30 to 40 MPa m$^{1/2}$, and elastic modulus (Young's) is 200 GPa, with a Poisson ratio of 0.29.

Fragment debris is diagnosed at two stations (approximately 150 mm and 300 mm) downstream from the input point. Two 150 keV flash x-ray tubes, placed approximately 400 mm from the line of debris travel, provided orthogonal shadow graphs of the fragment debris, as shown in Fig. 1. Appropriate delay times were calculated from the predicted impact velocity and x-ray tubes independently triggered from the second magnetic velocity coil. The x-ray film cassette, using Kodak Direct Exposure film backed by a Quanta Fast Detail screen, was stationed about 100 mm from the debris trajectory.

For two experiments (Test 1 and Test 2), the x-ray tubes and film cassette were oriented to obtain an oblique shadow graph of the fragment debris (an angle significantly less than the 90 degree orientation to the line of travel used in the majority of the experiments).

An aluminum target plate 152.4 mm (6 in.) on a side and either 6.35 mm (1/4 in.) or 12.7 mm (1/2 in.) in thickness was placed on axis approximately 400 mm down stream from the PMMA primary target plate to intercept the flux of steel fragments. This witness plate, prepared from 6061-T6 aluminum plate stock, was recovered after each experiment, and provided a post-test passive diagnostic of secondary fragmentation effects.

The primary configuration parameters for all experiments in the present study are provided in the first two columns of Table 1, where h is the PMMA plate thickness, V_i is the impact velocity, ΔV is the difference between the incident sphere velocity and the debris cloud velocity, and V_e is the radial expansion velocity of the debris cloud periphery.

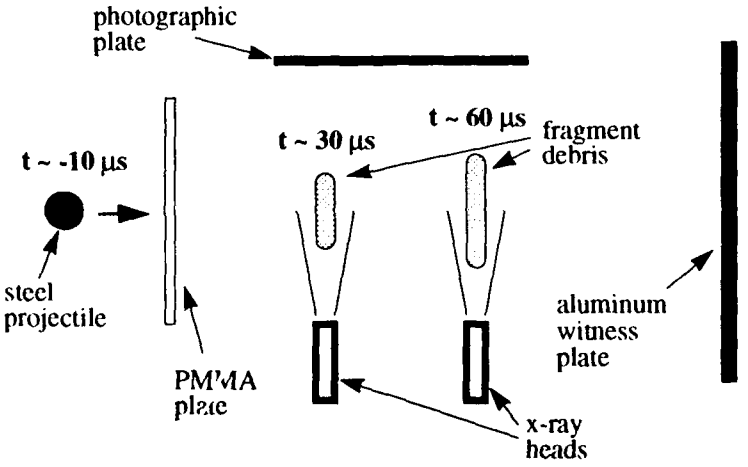


Fig. 1. Experimental configuration for radiographic and witness plate diagnostic of impact fragmentation experiment. (Timing is representative of a 5 km/s impact.)

Table 1: Experimental Impact Parameters and Summary of Results

Test #	h (mm)	V_i (m/s)	ΔV (m/s)	V_e (m/s)	Test #	h (mm)	V_i (m/s)	ΔV (m/s)	V_e (m/s)
1	3.28	4460	a	a	13	5.37	4430	460	290
2	3.28	4460	a	a	14	5.36	4060	330	183
3	1.74	4450	b	200	15	5.38	3310	240	50
4	1.74	4700	150	147	16	5.37	4080	330	164
5	3.38	4570	270	271	17	3.25	4520	195	223
6	3.28	3460	200	52	18	4.71	4430	345	219
7	3.44	4160	250	171	19	5.39	4610	410	660[d]
8	1.49	3950	130	105	20	4.75	4040	295	158
9	1.51	3460	170	44	21	4.78	3750	270	82
10	0.63	3410	50	0	22	0.99	4700	85	72
11	0.64	3920	60	0	23	11.23	4060	785[c]	580[d]
12	0.69	4470	90	0	24	9.47	4030	680[c]	540[d]

[a] Oblique angle radiograph — parameters not determined.
[b] Not determined
[c] Velocity of debris cloud front
[d] Diffused

FRAGMENT DEBRIS EXPERIMENTAL RESULTS

A total of 24 experiments of the basic impact configuration described in the previous section were performed in this investigation. The principal experimental variables were the impact velocity, V_i, and the thickness, h, of the primary target plate (PMMA), which defined the amplitude and duration of the impulse transmitted to the steel sphere, and consequently, the intensity of fragmentation of the steel projectile.

An example of the experimental radiographic results is shown in Fig. 2, where the images for Test 5 are displayed. These images qualitatively illustrate the nature of the fragmentation process observed in all of the experiments in the present study, with the exception of several tests in which parameter extremes were reached. The steel fragments remain well grouped and continue to move along the original trajectory at velocities somewhat less than the initial impact velocity, having been slowed by the impulse delivered to the sphere by the plate. Axial dispersion of the fragment debris is quite limited, with fairly well-defined, nearly planar boundaries forming. Radial dispersion is significant, but still the fragments are contained by rather well-defined limits. These observations hold in general except for the very largest of target thicknesses. Since the PMMA is not recorded in the radiograph, we are assured that only the mass of the original steel sphere is represented in each image.

The foremost objective of the experimental study was to assess, through radiographic diagnostics, the kinematic and structural characteristics of the steel fragment debris produced by the impact of the PMMA plate with the steel sphere. Several experimental parameters have been extracted from the data and are included in Table 1. First is the axial velocity decrease, ΔV, of the fragment debris from the initial impact velocity, V_i. Residual velocity, V_r, of the debris is readily calculated from $\Delta V = V_i - V_r$. The magnitude of ΔV can also be regarded as the change in axial velocity of a stationary sphere due to momentum imparted by the impacting plate. This velocity change is determined from the motion of the geometric center of mass of the debris cloud observed in the radiograph. The most accurate value is calculated by using the separation of the two radiographic images and the times at which the images were made. Corrections are made for magnification and parallax in the radiographic measurement.

As noted earlier, axial dispersion of the fragment debris is small. The axial extent for all of the tests is not more than several sphere diameters at the later radiograph image. The induced radial expansion velocity, V_e, is substantial, however, and varies systematically with initial impact parameters. A radial expansion velocity was determined for the experiments in which this is a reasonably well-defined property. It represents the radial velocity of the outer fringe of the fragment cloud from the center-line and is determined from the change in diameter of the successive radiographic images. Although an errant fragment at the cloud fringe can lead to a degree of subjectivity, the expansion velocity is determined with an accuracy of about ± 20 m/s. In a few cases, at the higher impact velocities, data scatter was somewhat larger. In three experiments (Test 19, Test 23, and Test 24) the fragment debris pattern included a sparse



Fig. 2. Radiographic images from Test 5 illustrating the general fragmentation character observed in the majority of experiments in the present study. (Time interval between images: 33.2 μs.)

spray of high velocity peripheral fragments. For these tests, radial expansion velocities in Table 1 represent the extreme of spray fragments observed on the radiographs. Quantitative measurements of fragment size data have not yet been determined from the radiographs. Preliminary examination of the images shown in Fig. 2 for Test 5 indicates about 200 particles, with a typical fragment size of about 1 mm and a largest fragment size of about 2 mm.

It is apparent from the radiograph in Fig. 2 that the impulse imparted to the steel sphere by the PMMA plate partitions the initial kinetic energy of the steel sphere into kinetic energies of axial translation and radial expansion of the steel fragments, kinetic energy of the PMMA debris, and energy expended in the various dissipative processes active during the impact process. The axial velocity change, ΔV, recorded for the experimental series in Table 1, provides a measure of the translational momentum lost by the steel sphere upon impact. These results are plotted against the product of the PMMA plate thickness and the steel sphere impact velocity, hV_i, in Fig. 3. This latter parameter provides a measure of the impulse delivered to the sphere by the PMMA target. Within experimental scatter, the ΔV data are found to be a single-valued function of the parameter hV_i.

The trend of the data in Fig. 3 can be reasonably well understood in terms of a relatively basic hydrodynamic description of the sphere and target interaction (*e.g.* Backman and Goldsmith, 1978). The acceleration of the steel sphere of mass m, is determined from,

$$m\frac{dV}{dt} = \frac{1}{2}\rho V^2 A, \tag{1}$$

where $\rho V^2/2$ is the Bernoulli pressure applied by the PMMA target material, of density ρ, under steady flow conditions, and is assumed to apply over the projected geometric area, A, of the sphere. The velocity V is the equilibrated velocity of the PMMA and the steel sphere. The relatively low target impedance of PMMA compared with that of the steel projectile permits this approximation. Integration of eq. (1) leads to a predicted exponential change in projectile velocity with plate perforation thickness. For target plate thicknesses (h) on the order of the sphere diameter, a first order solution of eq. (1) provides the functional relationship of the decrease in velocity with the impact velocity and target thickness,

$$\Delta V = \frac{\rho A}{2m} hV_i. \tag{2}$$

Comparison of eq. (2) with the measured velocity decrease data, tabulated in Table 1, is shown in Fig. 3 and demonstrates excellent agreement.

Interesting features are also observed in the radial expansion characteristics of the steel fragment debris following target impact. Several distinct regions of behavior were noted to occur within the parameter range of the present study. First, impulses for which there was no radial expansion of the steel spheres were observed in three experiments performed on target plates approximately 0.6 mm in thickness. The steel sphere remained intact at impact velocities of 3400 and 3900 m/s. A small fragment was spalled off the rear surface of the sphere at a velocity of 4500 m/s. One of several possible representations of debris formation data is provided in Fig. 4. Points identify the impact velocity and the target plate thickness, on the vertical and horizontal axes, respectively, the product of which provides an approximate measure of the impulse imparted to the steel sphere. Curves of constant impulse are used to identify boundaries between three regions of behavior in the fragmentation process: Region I - No Fragmentation; Region II -

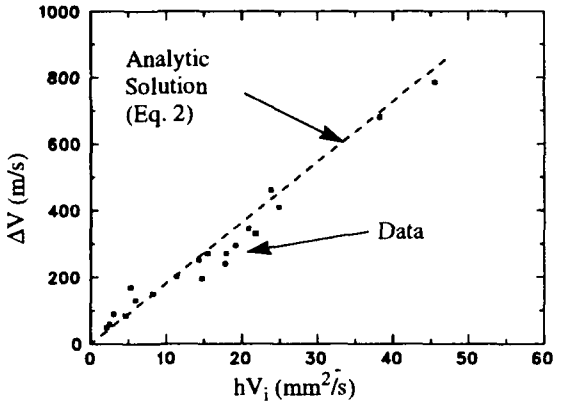


Fig. 3. Translational velocity reduction data. Dependence on product of target plate thickness and impact velocity.

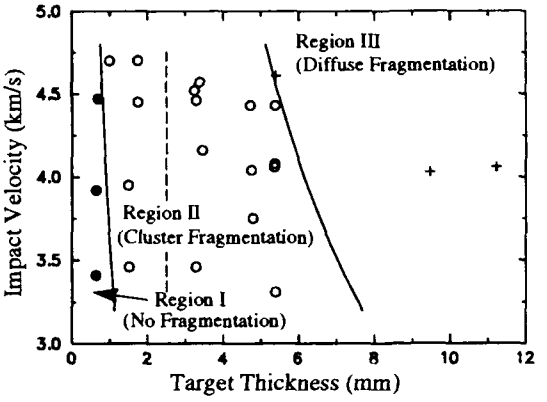


Fig. 4. Plot of impact velocity versus target thickness. Different regions of fragment debris characteristics are identified and separated by iso-impulsive curves. The vertical dashed line separates distinct fragment pattern differences in Region II.



Fig. 5. Radiograph of steel debris using oblique x-ray diagnostics (Test 2). Note the continuous spatial distribution of the fragments.

Cluster Fragmentation; and Region III - Diffuse Fragmentation. In Region I, the impulse was insufficient to cause fragmentation. Region II identifies the tests in which fragment debris was clearly clustered in the sense described previously. Within this cluster region, two fairly distinct patterns were observed in the debris cloud; they were most likely a consequence of the target plate thickness relative to sphere diameter. For plate thicknesses less than about 2 mm, distinct spall debris from the back of the sphere leads to some axial divergence and a shallow conical shape to the debris pattern (for example Test 4 and Test 8). For plate thicknesses closer to the sphere diameter (3 to 6 mm) a distinct plate or disc shape is observed for the debris pattern.

Also appearing in Region II are two experiments (Test 1 and Test 2) in which an oblique x-ray orientation was used (47 ± 2 degrees from the shot line) to establish how fragments were distributed through the diameter of the debris disc. The radiograph for Test 2 is shown in Fig. 5. The debris is moving obliquely away from the point of observation. The radiograph establishes that fragment debris is in fact distributed fairly uniformly through the diameter, and a distinct regular structure in the pattern of the peripheral fragments is observed.

Finally, a clear transition in debris characteristics was observed in several tests in which parameter extremes were achieved (Region III). The impact velocity in Test 19 was in excess of 4600 m/s for the steel sphere on a 5.4 mm plate,

and the spheres in Test 23 and Test 24 impacted at slightly lower velocities on plates in excess of 9 mm in thickness. Rather than an abrupt transition in the fragment density, as observed in Region II, there is a more gradual thinning in the density toward the cloud perimeter. The perimeter fragments in Region III have significantly higher expansion velocities (see Table 1) than those achieved in Region II. The debris pattern was umbrella shaped with perimeter fragments lagging behind the central cloud.

For the tests which have Region II behavior for their fragment debris pattern, expansion velocity data from Table 1 are plotted as a function of impact velocity, as shown in Fig. 6. In this graph, tests of nominally the same plate thickness are identified by a common symbol. Although data scatter tends to obscure detailed trends, some observations can be made. First, at similar impact velocities, the expansion velocity increases with plate thickness but becomes less sensitive at increased plate thickness. This trend is most noticeable at the higher impact velocities. Second, there is a critical impact velocity below which fragmentation and subsequent expansion do not occur. This velocity limit is outside of the range of the data for the 0.6 mm plate and is probably around 4000 m/s for a 1.0 mm plate. For thicker plates (1.6 mm and above) this critical velocity (about 3000 m/s) becomes independent of plate thickness.

In Fig. 7, an alternative representation of the expansion velocity data is shown. Expansion velocity is plotted against plate thicknesses at nominally similar impact velocities. Increased expansion velocity with increasing impact velocity is seen. Flattening of the curves for plate thicknesses above about 2 mm is clearly observed.

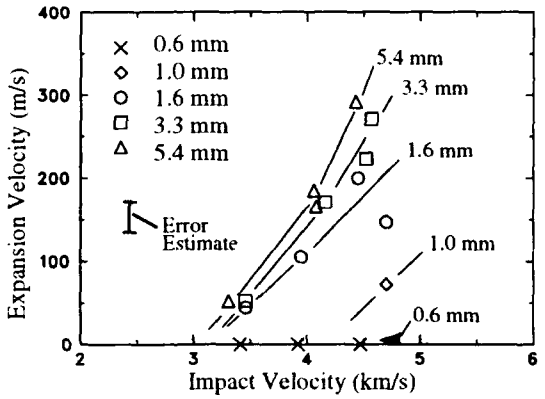


Fig. 6. Radial expansion velocity of fragment debris. Tests with nominally similar target-plate thicknesses are plotted against the impact velocity.

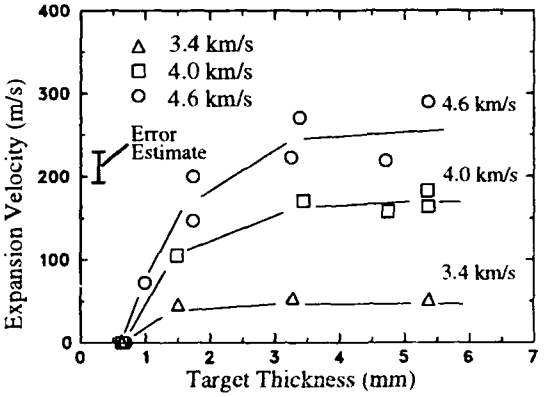


Fig. 7. Radial expansion velocity of fragment debris. Tests at nominally similar impact velocities are plotted against target plate thickness.

The translational impulse imparted to the fragment debris appears to be a consequence of the momentum exchanged during hydrodynamic penetration of the target plate. This conclusion is supported by the nearly linear dependence on plate thickness, in agreement with the analytic expression given in eq. (2) and our numerical computations to be described later. In contrast, the evidence displayed in Figs. 6 and 7 would suggest that radial impulse acquired by the impacting sphere is a consequence of the early shock phase of the interaction and is little affected by the later hydrodynamic penetration phase.

SUMMARY OF FRAGMENTATION THEORY AND CODE IMPLEMENTATION

A capability has been developed to produce fragment size predictions from calculations using wave propagation codes that solve the equations expressing conservation of mass, momentum, and energy for a continuum. Although plots produced from standard wavecode calculations sometimes appear to depict a collection of discrete fragments, the physical mechanisms that control these processes, such as surface tension or real physical heterogeneities and microstructure, are not currently included in the codes. It is not feasible for continuum mechanics wavecodes, except perhaps in one dimension (Kipp and Grady, 1985), to account for the complete, explicit formation of discrete fragments. But extensive work has demonstrated that continuum models of various levels of sophistication can successfully address the damage processes of void and crack growth leading to material failure (*e.g.* Grady and Kipp, 1989).

Previous work (Grady, *et al.*, 1990b) has produced dynamic fragmentation theories that are based on the assumption that strain rate and temperature at the time of failure control subsequent fragmentation. Considerable progress has been made in extracting this information from Lagrangian wavecodes (Grady, *et al.*, 1990b; Johnson, *et al.*, 1990), which are excellent at tracking the history associated with each material element and can easily save the required information at the time of fracture. It is a much more difficult task for an Eulerian wavecode to maintain accurate values of this

information because of the degradation accumulated by the repetitive rezoning used in the convection process. However, the extensive deformation associated with these impact and penetration events encourages the use of an Eulerian wave propagation code.

The wavecode that was used for the calculations was the Eulerian finite-difference shock wave propagation code CTH (McGlaun, *et al.*, 1990). This code has a general internal state variable capability which allows information to be saved in variables that are advected with the material as it crosses the cell boundaries. Significant modifications were made to the fracture algorithm in the code to locate each time and location at which the tensile stress criterion for a single material, rather than a mixed-material cell, was exceeded and material fracture was judged to occur. All diagonal components of the strain-rate tensor, $\dot{\varepsilon}_i = \partial v_i/\partial x_i$, including the hoop component in cylindrical coordinates, $\dot{\varepsilon}_R = v_R/R$, where v_i and x_i are velocity and position components and R refers to radius, were then calculated and the maximum value was stored as an internal state variable. While the internal state variables provide storage locations for the strain rate and temperature information that must be saved from the calculation, there is a problem with diffusion of these quantities as material motion occurs. For instance, even though a calculation may be performed in which only a single fracture of a material cell takes place during the entire calculation, subsequent material motion may result in spurious values of strain rate appearing in all cells through which the material has passed. Fortunately, these values typically have a very small magnitude except in the region of the mesh containing the bulk of the fractured material. However, diffusion does result in some spreading and loss of localization of the fractured material, so extreme care was taken to assess such effects and ensure that reasonable fragment size distributions were obtained. Since most fractures occurred at high strain rates on the order of 10^3 to 10^6 per second, it was possible to discard significantly lower strain rates as having been produced by diffusion. Mass fraction weighting was used to maintain the proper convected amplitudes of the strain rates and temperatures.

Files containing strain rate and temperature at the time of fracture are saved periodically during the simulation of the impact, and these are examined to determine the extent of the fractured regions as time progressed. When the fracture process is complete, the data are post-processed outside the wavecode to produce fragment size distributions. Dynamic fragmentation theories predict an average local fragment size at a given strain rate and temperature, and the number of fragments with this average size is determined by the local mass of the material that fractures. The dynamic fragmentation theories that were used to process the strain rate and temperature information have been described in detail elsewhere (Grady, 1988; Grady, *et al.*, 1990a; Grady, *et al.*, 1990b), and they will only be summarized here. Various types of fragmentation mechanisms have been identified, depending on the strain rate and temperature at fracture. The data can also be used to determine the mass distribution of fractured material in the solid, liquid, and vapor phases.

For the present purposes, the average fragment diameter S will be determined in three different fragmentation regimes. These are:
(1) solid spall dominated by fracture toughness, for which

$$S = \left(\frac{\sqrt{24}K_c}{\rho c\dot{\varepsilon}}\right)^{2/3}, \tag{3}$$

(2) solid spall dominated by the flow stress, for which

$$S = \left(\frac{1.2Y}{\rho\dot{\varepsilon}^2}\right)^{1/2}, \tag{4}$$

and (3) liquid spall above the melt temperature, for which

$$S = \left(\frac{48\gamma}{\rho\dot{\varepsilon}^2}\right)^{1/3}. \tag{5}$$

In these equations, ρ is the density, $\dot{\varepsilon}$ is the strain rate, c is the sound speed, and γ is the constant value of the surface tension. The temperature and strain-rate dependent yield strength, Y, is given by

$$Y = Y_0\left(1 - \frac{T}{T_m}\right)^n \left(\frac{\dot{\varepsilon}}{\dot{\varepsilon}_0}\right)^m, \tag{6}$$

and the temperature dependent fracture toughness, K_c, is given by

$$K_c = K_{c0}\left(1 - \frac{T}{T_m}\right)^{n'} \tag{7}$$

where Y_0 is the reference yield strength, K_{c0} is the reference fracture toughness, T is the temperature, T_m is the melt temperature, $\dot{\varepsilon}_0$ is a reference value of the strain rate (one per second), and n, m, and n' are constants. In the solid regime, the transition from fracture toughness to flow stress dominated spall occurs at a strain rate given by

$$\dot{\varepsilon}_t = \sqrt{\frac{0.003\rho c^4 Y^3}{K_c^4}}. \tag{8}$$

Appropriate material properties were obtained for the steel sphere for the fragmentation regimes of brittle, ductile, and liquid spall, as shown in Table 2. Application of the above formulas allows each point in the strain rate - temperature plane to be mapped into a fragment size for a given material.

Table 2: Fragmentation Material Properties

	Hard Steel
Surface Tension γ (N/m)	1.5
Yield Strength Y_0 (GPa)	2.0
Fracture Toughness K_{c0} (MPa $m^{1/2}$)	40
Melt Temperature T_m (K)	1800
n	1
m	0.1
n'	-1

Table 3: Material Parameters Used For Calculations

	PMMA	Hard Steel
Density (kg/m^3)	1186	7850
Bulk sound speed (m/s)	2598	4570
Linear shock velocity-particle velocity slope	1.516	1.49
Gruneisen coefficient	0.97	2.17
Yield strength (GPa)	0.2	2.0
Poisson ratio	0.32	0.29
Fracture stress (GPa)	0.15	4.0

The fragmentation theories described above are derived assuming spall induced by uniform volumetric dilatation, so they are most applicable to the prompt fragmentation of the steel sphere induced by the impact. The fracture process is complete within a few microseconds following impact. The strain rate and temperature files generated by each of the calculations that were produced immediately after this time were used for the fragment size predictions.

To obtain the fragment size distribution from the analysis, files are generated by the wavecode calculations that contain the strain rate and temperature at the time of fracture for each cell containing fractured material. There is thus a mass associated with each strain rate - temperature pair, which is just the total mass, m, of the material in the cell. The simplest assumption to make when determining fragment size distributions is that all of the mass in the cell produces equal particles of size S, given by the appropriate one of eqs. (3) to (5). Thus, letting i be the cell index, where $i = 1, N$ and N is the total number of cells containing fractured material, the cell data consist of N pairs m_i, S_i where m_i is the mass of material in cell i and S_i is the size of all the particles in the cell. If the data are arranged in order of increasing fragment size, so that $S_i \le S_{i+1}$, then the cumulative mass of fragments less than or equal to size S_i is

$$M(S_i) = \sum_{j=1}^{i} m_j \qquad (9)$$

However, as previously described (Grady and Kipp, 1985), statistical considerations indicate that a distribution of fragment sizes should be obtained for each cell. The mean value of each distribution is assumed to be S_i. The form of the distribution is obtained by assuming that fragments in the mass m_i are Poisson-distributed. This leads to a probability distribution of finding a fragment of mass μ in the cell within a tolerance $d\mu$ given by

$$dP(\mu) = \frac{1}{\mu_a} e^{-\mu/\mu_a} d\mu, \qquad (10)$$

where μ_a is the average, or mean, value of the fragment mass in the cell. Integrating from 0 to μ and multiplying by the total mass m_i of the cell gives the cumulative mass of fragments of mass less than or equal to μ in the cell

$$M(\mu) = m_i \left[1 - e^{-\mu/\mu_a}\right]. \qquad (11)$$

Now, assuming that the mass of the fragment is related to the cube of the fragment size (such as for cubic or spherical particles) and noting that the average mass μ_a corresponds to a fragment having the average size S_i,

$$\frac{\mu}{\mu_a} = \left(\frac{S}{S_i}\right)^3. \qquad (12)$$

Therefore, the cumulative mass of fragments in cell i having a size less than or equal to S is

$$M(S) = m_i \left[1 - e^{-(S/S_i)^3}\right]. \qquad (13)$$

Finally, the total cumulative mass of all fragments in all cells having a size less than or equal to S is

$$M_T(S) = \sum_{i=1}^{N} m_i \left[1 - e^{-(S/S_i)^3}\right]. \qquad (14)$$

It was found that if the original distribution is sharply peaked, a large spread is generated by the statistical relations. However, if the original distribution already contains a large range of fragment sizes, the additional statistical spread

is minimal. The statistical distributions do show the addition of a tail at small, possibly aerosol-sized, fragments, but the total additional mass in the aerosol source term so generated is negligible. In application, the cell data is grouped into "bins" of a chosen fragment size increment.

NUMERICAL SIMULATIONS OF STEEL SPHERE IMPACT ON PMMA TARGETS

Impact simulations of a steel sphere onto a PMMA target plate were made with a physical space that was partitioned into uniform square cells, with a resolution of 0.05 mm (about 60 cells in the radius of the sphere). The two-dimensional, axisymmetric geometry encompassed a 20 mm radius and a 20 mm axial length, requiring 160,000 computational cells. This radius is sufficiently large that edge effects of the target do not influence the fragmentation behavior of the steel sphere. The steel and PMMA were both represented as low temperature Mie-Gruneisen solids, in which the Hugoniot was described with a linear shock velocity - particle velocity relationship. The properties used in the calculations are listed in Table 3. The fragmentation parameters for the steel are listed in Table 2. The mass of the sphere used in the calculations was 1.052 gm, slightly larger than the experimental mass of 1.027 gm.

As an example, consider the case of Test 5, in which a steel sphere impacts a 3.38 mm PMMA target plate at a velocity of 4570 m/s (*cf* Table 1). The computed sequence of penetration that occurs is plotted in Fig. 8. Note that the sphere deforms as it progresses through the plate, with the leading surface undergoing significant flattening. The impact pressure is about 30 GPa, well above the 2 GPa yield strength of the steel. Just after 1 μs, void is beginning to be inserted into the sphere as spall fracture commences. It is apparent from these plots that the PMMA material in front of the sphere has been accelerated to a higher velocity than the exit velocity of the sphere, as is easily confirmed from a one-dimensional pressure - particle velocity diagram of the impact. Flash laser photographs of similar events also clearly show the dispersed PMMA debris leading the clustered steel debris (Ang, 1992). We note in passing that the appearance of the calculated PMMA target plate residual hole is that of a rather ductile material; the experiments indicate a far more distinctive residual hole surrounded by large fractured rings that have been removed, suggesting that there are equation of state and plastic fracture issues to be pursued.

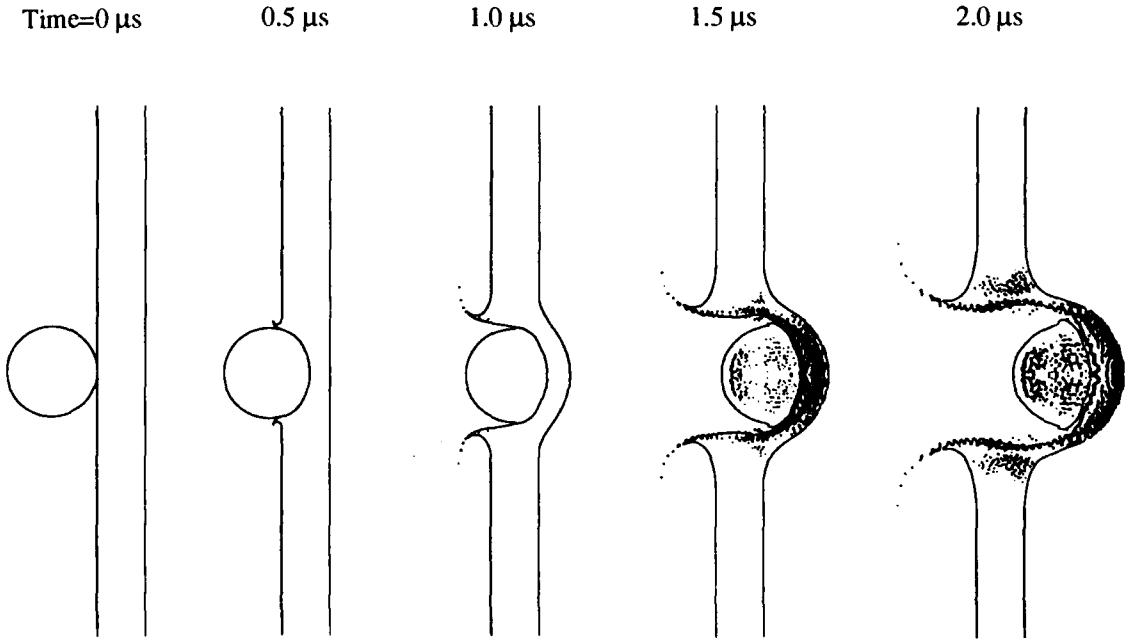


Fig. 8. Calculated sequence of a 6.35 mm steel sphere, with normal incidence velocity of 4570 m/s, perforating a 3.38 mm PMMA target plate (Test 5).

Tracer particles, embedded in the sphere to provide point histories of computed variables, indicate that fracture is completed between 1.5 and 2 μs. After this time, the PMMA imparts very little impulse to the steel sphere. This response is illustrated in Fig. 9, where the minimum principal stresses through the axial diameter of the sphere are plotted. (The first pulse is recorded at the impact surface, and the final pulse at the trailing surface.) The tensile stress is observed to reach a limit of about 4 GPa, then unload as void is added to the local cells to relieve the state of tension.

As the shock pulse transits the axis of the sphere, the amplitude decays from an initial peak of about 30 GPa to less than 10 GPa. The immediate consequence of this decay in impulse is a larger decrease in particle velocity at the leading edge of the sphere than at the trailing edge, so that the trailing material in the sphere has a relative velocity towards the leading edge of the sphere. This relative velocity of the leading and trailing surfaces of the sphere explains the

tendency of the particles to stay clustered in a thin disk, as seen in the radiographs (*cf* Figs. 2 and 5). As a consequence of the impulse delivery being completed by about 2 μs, the formation of fragments has also been completed by then, and the fragmentation post-analysis calculations can be made. The debris is basically in free flight by this time, expanding as seen in the radiographs (in Fig. 2) at much later times (*e.g.*, 30 and 60 μs).

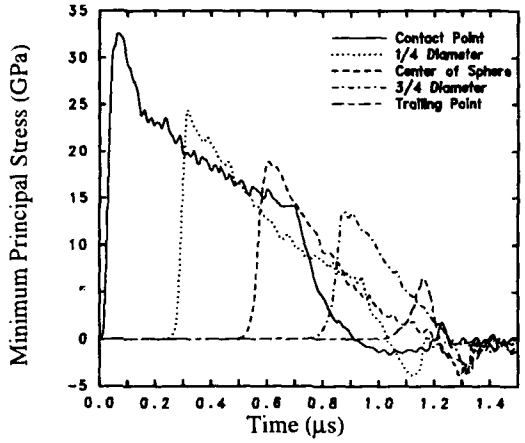


Fig. 9. Histories of minimum principal stress at points along the axis of the steel sphere.

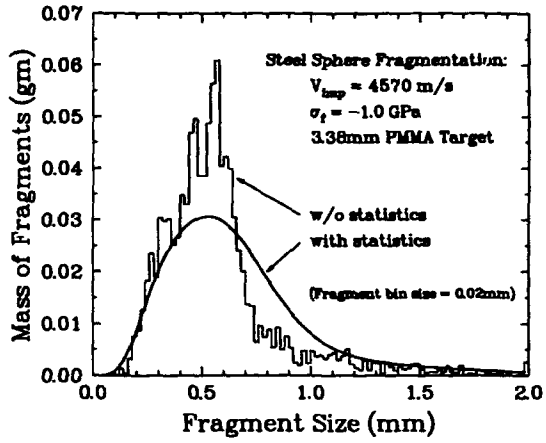


Fig. 10. Mass distribution of steel fragments *vs.* fragment size resulting from the impact of a 6.35 mm steel sphere with a 3.38 mm PMMA target plate (Test 5).

When the steel fragmentation characteristics were computed for this example, it was found that less than 25% of the mass of the steel sphere had fragmented. That is, the fracture stress of 4.0 GPa was exceeded in only a quarter of the volume of the sphere. Examination of the tensile strain rates that occur throughout the sphere indicate a range from about 6×10^4 per second to over 10^6 per second. Under these conditions, the expected spall stress would range from 2.2 GPa to 5.6 GPa, based on derived expressions by Grady (1988) for brittle fracture. Recalculating this example with a fracture stress of 2.0 GPa results in about 80% of the sphere fracturing; with a fracture stress of 1.0 GPa, 100% of the sphere fractures. It is clear that fracture conditions based on exceeding a tensile stress limit are not adequate to accurately represent the fracture behavior of this steel. As a working basis for this example, the fragmentation process was permitted to proceed using the 1.0 GPa fracture stress limit. The resulting computed steel fragment size distribution is shown in Fig. 10, labelled "w/o statistics". This distribution sums the masses of fragments in each material cell, where the average fragment size is calculated from the local strain rate, as defined in eqs. (3) to (9). The figure plots the total steel fragment mass determined for each fragment size "bin", summed throughout the sphere. Each bin includes a fragment size increment of 0.02 mm. The largest mass of fragments have an average fragment size of about 0.6 mm. The temperature in the steel has increased only about 100 K, so that the majority of the material falls in the brittle, or fracture toughness dominated, region of fragmentation. The average fragment size is qualitatively consistent with what can be seen in the radiographs. It has also been observed that the strain rates, and consequently the average calculated fragment sizes, depend on the equation of state being used for the materials.

As discussed in the previous section, the fragment size calculated for a given strain rate represents the average fragment in an exponential (Poisson) distribution of sizes. The masses associated with each of the fragment sizes shown in Fig. 10 (curve labelled "w/o statistics") can be modified to account for this statistical spread by employing the concepts expressed in eqs. (10) to (14). When these equations are applied to the current example, the mass associated with each particle size results in the distribution labelled "with statistics" in Fig. 10. The Poisson statistics (in which the same size "bins" were used) tend to broaden the distribution up to about 1.1 mm fragment sizes, and do not significantly affect the upper and lower extremes of sizes. The integral of the mass with size, as described by eq. (14), results in the cumulative mass as a function of fragment size. Fig. 11 contains both the original calculated cumulative mass distribution and the associated statistical cumulative mass distribution as a function of fragment size. The total mass of steel accounted for up through particle sizes of 2 mm is 1.01 gm, or about 96% of the 1.05 gm mass of the sphere used in the calculations. The corresponding distributions that show the number of fragments at each fragment size are plotted in Fig. 12. Now the broadening effect of the Poisson statistics is apparent for the small size particles. The largest number of particles are of size 0.2 mm; the largest mass of particles are of size 0.6 mm.

To examine trends of the behavior resulting from target thickness variations, a suite of eight impact calculations was made in which the impact velocity was fixed at 4500 m/s. Variations in PMMA target thickness from 0.76 mm (1/32 inch) to 6.35 mm (1/4 inch) covered most of the range of the experiments, providing a large spread in the amplitude of the impulse imparted to the steel sphere. From these calculations, comparisons can be made with experimental data for the loss in axial momentum, and the expansion velocity of the particles debris cloud.

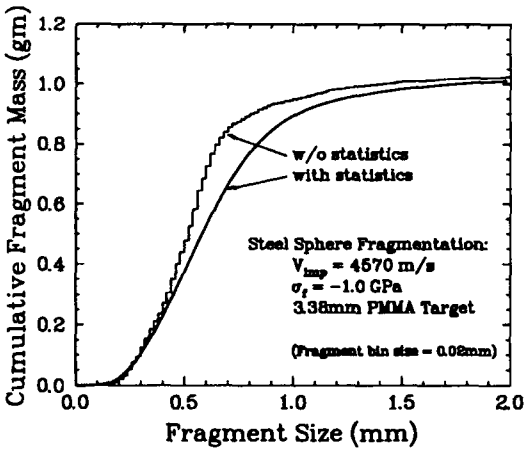


Fig. 11. Cumulative mass distribution of steel fragments *vs.* fragment size resulting from the impact of a 6.35 mm steel sphere with a 3.38 mm PMMA target plate (Test 5).

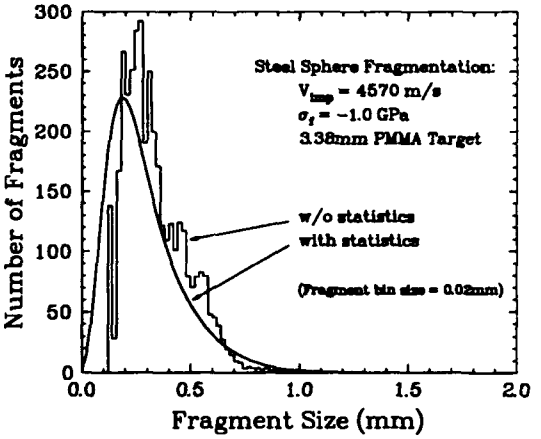


Fig. 12. Final number distribution of steel fragments *vs.* fragment size resulting from the impact of a 6.35 mm steel sphere with a 3.38 mm PMMA target plate (Test 5).

The loss in axial velocity as a function of target plate thickness is plotted in Fig. 13, and the numerical data clearly compares well with the experimental data. This figure can be compared with Fig. 3, noting that the numerical simulations are representing the experimental data in much the same way as the analytic expression. The calculated curve in Fig. 13 is not quite linear, and tends to have an upward curvature as the PMMA target thickness increases beyond 3 mm. The expansion velocity of the outer debris edge is plotted in Fig. 14 as a function of PMMA target plate thickness. The computed points were determined by evaluating the maximum radial momentum acquired by the steel during penetration. The computed values generally fall within the range of the experimental data. This figure can be compared to Fig. 7, in which three curves of constant impact velocity are included. In the present figure, only an impact

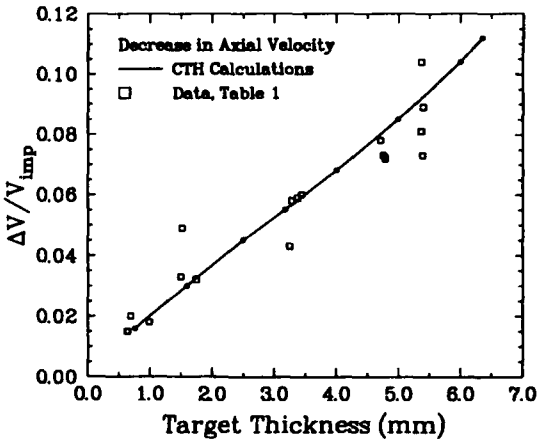


Fig. 13. Decrease in axial velocity of the steel sphere as a function of PMMA target plate thickness. Data is from Table 1.

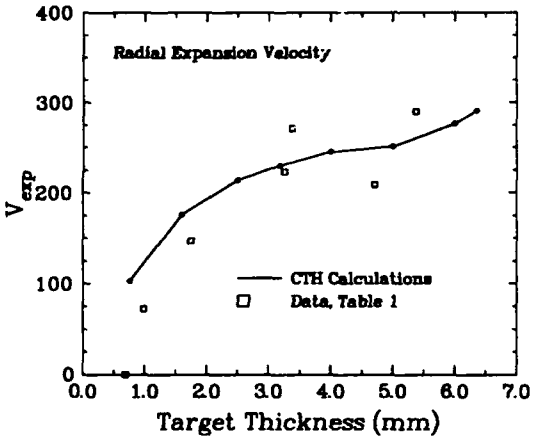


Fig. 14. Variation of maximum steel particle debris cloud expansion velocity with PMMA target plate thickness. Data is from Table 1.

velocity of 4500 m/s has been tabulated. In principle, the source of the particles in the debris cloud can be determined from velocity histories at points distributed throughout the sphere. Along the initial surface of the sphere, the amplitude of the maximum lateral velocity varies from zero at the leading impact point to a maximum near the equator, returning to zero at the trailing point on the axis. Analysis of the velocity histories on a cross-section at the equator of the sphere indicates a linear increase in velocity from zero on the axis to maximum on the surface, resulting in the distribution of fragments throughout the disk seen in the radiographs. This continuous spatial distribution of particles is in contrast to the commonly observed hollow debris cloud that forms when a target imparts a larger energy to the projectile (*e.g.* Grady and Passman, 1990; Piekutowski, 1992). We note that as the thickness increases, the calculated expansion velocity begins to increase again, an effect that requires some additional analysis

CONCLUSIONS

The experiments reported here provide a clear definition of the steel debris cloud formed by the impact of a steel sphere with PMMA targets. The spectrum of impact velocities and target thicknesses provide sufficient basis to establish trends in debris cloud formation. Some aspects of the fragmenting steel sphere data are represented quite well by the calculations, particularly the axial velocity decrease and the radially divergent velocity imparted to the sphere. The ability to calculate detailed fragment size distributions is the first step in defining quantitative properties of debris clouds for subsequent interactions. The quantitative comparisons of debris characterization will require some additional refinement of the data from the radiographs. The simulations have also demonstrated that there is additional work required on the fracture model used here to more precisely determine the time of fracture and the condition of the steel at breakup.

REFERENCES

Ang, J. A. (1992). Sandia National Laboratories, Personal communication.

Backman, M. E. and W. Goldsmith (1978). The mechanics of penetration of projectiles and targets. *Int. J. Engng. Sci.*, 16, 1-99.

Brown, W. K. (1989). *J. Astrophys. Astr.*, 10, 89-112.

Englman, R., Z. Jaeger, and A. Levi (1984). Percolation theoretical treatment of two-dimensional fragmentation in solids. *Phil. Mag. B*, 50, 307-315.

Glenn, L. A. and A. Chudnovsky (1986). Strain energy effects on dynamic fragmentation. *J. Appl. Phys.*, 59, 1379-1380.

Grady, D. E. (1982). Local inertia effects in dynamic fragmentation. *J. Appl. Phys.*, 53, 322-325.

Grady, D. E. and M. E. Kipp (1985). Geometric statistics and dynamic fragmentation. *J. Appl. Phys.*, 58, 1210-1222.

Grady, D. E. (1988). The spall strength of condensed matter. *J. Mech. Phys. Solids*, 36, 353-384.

Grady, D. E. and M. E. Kipp (1989). Fragmentation of solids under dynamic loading, *Structural Failure*, (ed. T. Wierzbicki & N. Jones), John Wiley & Sons, Inc.

Grady, D. E. and S. L. Passman (1990). Stability and fragmentation of ejecta in hypervelocity impact. *Int. J. Impact Engng.*, 10, 197-212.

Grady, D. E., J. E. Dunn, J. L. Wise, and S. L. Passman (1990a). Analysis of prompt fragmentation. Sandia National Laboratories Report, SAND90-2015.

Grady, D. E., J. W. Swegle, and J. A. Ang (1990b). Analysis of prompt fragmentation Oct 89-Sept. 90. Sandia National Laboratories Report, SAND91-0483.

Johnson, G. R., R. A. Stryk, T. J. Holmquist, and O. A. Souka (1990). Recent EPIC code developments for high velocity impact: 3D element arrangements and 2D fragment distributions. *Int. J. Impact Engng.*, 10, 281-294.

Kipp, M. E. and D. E. Grady (1985). Dynamic fracture growth and interaction in one dimension. *J. Mech. Phys. Solids*, 33, 399-415.

McGlaun, J. M., S. L. Thompson, and M. G. Elrick (1990). CTH: A three-dimensional shock wave physics code. *Int. J. Impact Engng.*, 10, 351-360.

Melosh, H. J., E. V. Ryan, and E. Asphaug (1992). Dynamic fragmentation in impacts: hydrocode simulation of laboratory impacts. *J. Geophys. Res. - Planets*, 97, No. E9.

Piekutowski, A. J. (1992). Properties of largest fragment produced by hypervelocity impact of aluminum spheres with thin aluminum sheets, AIAA 92-1588, AIAA Space Programs and Technologies Conference, March 24-27, 1992, Huntsville, Alabama.

Smith, V. (1989). Kaman Sciences Corporation, Personal communication.

Int. J. Impact Engng Vol. 14, pp. 439–449, 1993
Printed in Great Britain

0734-743X/93 $6.00 + 0.00
Pergamon Press Ltd

THEORETICAL ANALYSIS OF A PULSED-LASER-DRIVEN HYPERVELOCITY FLYER LAUNCHER*

R. Jeffery LAWRENCE and Wayne M. TROTT

Computational Physics Research and Development Department
Sandia National Laboratories
Albuquerque, New Mexico 87185-5800

ABSTRACT

High-power but low-total-energy pulsed lasers can be used to accelerate small-diameter, thin flyers to velocities in excess of several kilometers per second. The geometry under consideration involves placing the flyer on the end of an optical fiber through which the laser pulse is delivered. The blowoff products driving the flyer are thus fully tamped. A model, based on the Gurney theory for explosively driven plates, is derived for predicting the final velocity of these flyers. All but two of the required input parameters are readily available; those two can be extracted from one limited set of experimental measurements. Data on aluminum flyers illustrate that once the input parameters have been determined, the model predicts changes resulting from variations of laser fluence and pulse duration as well as flyer thickness and diameter. Additional data on copper and magnesium indicate that the energy-coupling efficiency can vary by at least 50%, depending on the flyer material.

INTRODUCTION

Many different approaches for accelerating projectiles to hypervelocities have been considered. Some of them have been only conceptual in nature, whereas others have proven eminently successful in practice. Examples include conventional powder and gas guns as well as electrically driven rail and coil guns. Among the more innovative techniques is the use of lasers, either pulsed or continuous, to provide the requisite driving energy. On a large scale, lasers have even been considered as ground-based power sources for launching various types of satellites into low earth orbits (Lawrence *et al.*, 1992). On a more modest scale, the present investigation uses small pulsed lasers to drive thin flyers to velocities of several kilometers per second or more (Trott and Meeks, 1990). Here we describe in detail a model that can be used to predict and analyze many aspects of the latter arrangement.

The basic geometry under consideration involves thin flyers, from a few to several tens of microns thick, placed on the ends of fused silica optical fibers that are typically several hundred microns in diameter. A short, high-intensity laser pulse is transmitted down the fiber and deposited on the inner surface of the flyer, vaporizing a thin layer and driving the remaining portion to high velocities. It is interesting to note that the power losses in propagating through these optical fibers can be measured in terms of decibels per kilometer; hence, the laser can be located at a considerable distance from the end with the flyer. Because of the modest scale of the system, the total laser energies are no more than several tens of millijoules. In contrast, a typical rifle bullet will have a kinetic energy of several kilojoules or more. The system is thus small enough that elaborate and extensive facilities are not required for laboratory installations and applications.

It has been shown previously that simple models can be effective and accurate for predicting integral-like quantities, such as flyer momentum or velocity, that result from laser interactions

*This work was supported by the U.S. Department of Energy under contract DE-AC04-76DP00789.

(Lawrence, 1988). In most previous work of this type, the blowoff products have been free to expand into a vacuum. Here we assume that the optical fiber, which carries the laser pulse to the flyer, is transparent to the laser energy but mechanically rigid with respect to the blowoff. Hence, the vaporization process is fully constrained or tamped. To model this latter situation, we use conservation of energy in the framework of the well-known Gurney theory (Gurney, 1943) to predict the final flyer velocity. In this context, the vaporized portion of the flyer is treated as analogous to the high explosive in the Gurney theory. Not only does the model predict the flyer velocity, but it is also easy to extract the effective thickness of the layer vaporized by the laser pulse, the energy-coupling efficiency, and the momentum-coupling coefficient. By noting the general behavior of the latter two quantities, a limited set of experimental results can be used to define the only two model parameters not easily determined or readily available from standard compilations.

From early experiments we determined all of the required parameters for aluminum flyers operating with a laser at a wavelength of 1.06 μm. In subsequent tests it was established that the model accurately reproduces the results arising from changes in laser fluence, laser pulse duration, flyer diameter, and flyer thickness. Specific features that the model accurately predicts include the energy threshold for flyer motion, and, well above this threshold, the square-root dependence of the flyer velocity on the fluence. It also shows, and is well verified by experiment, that the momentum-coupling coefficient peaks at a fluence several times that of the threshold. This suggests that this intermediate fluence would be the most efficient for maximizing the flyer velocity. Experiments on other flyer materials, magnesium and copper in particular, have also been performed. They indicate that both the energy threshold and the energy-coupling efficiency can be varied substantially by changing the flyer material. In a broader sense then, the model provides insight into the physical phenomena so that materials and parameters can be chosen for overall optimum performance.

In the succeeding sections we describe the model and its various features. We then derive a number of scaling relations that follow and that can be used to describe the general behavior of this type of laser-driven flyer system. The model is then applied by comparing its predictions with experimental measurements spanning a large range of conditions and three different flyer materials.

MODEL DESCRIPTION

The general configuration we are employing is illustrated schematically in Fig. 1. To generate a model that is easy to use and that will describe all major features of the dynamic response of this system, we must make a number of simplifying assumptions. The most basic is that the energy deposition in the flyer, the vaporization and blowoff phenomena, and the forces driving the flyer are all one dimensional. This is comparable to saying that the flyer is thin compared to its lateral dimensions, and that the laser fluence is uniform across the fiber diameter. These are probably reasonable approximations for the experiments we have conducted. We next assume that the optical fiber is transparent to the incident laser radiation, but mechanically rigid with respect to the blowoff products from the flyer—that is, the explosive vaporization of the inner surface of the flyer is fully tamped. Although other approaches are possible, the deposition of the laser energy in the flyer is approximated with a standard exponential profile controlled by an effective absorption coefficient. This coefficient is a function of the true laser absorption coefficient and, through the thermal diffusivity, the laser pulse duration. In applying the basic conservation laws, we implicitly allow the deposited energy to equilibrate over the blowoff depth during the pulse width. Finally, while the blowoff products are accelerating the flyer, we represent their spatial velocity distribution as a linear function, extending from zero at the rigid fiber end to the actual flyer velocity at the blowoff-solid interface. It is this last approximation that is a key part of the Gurney theory.

To apply the Gurney theory, we note that because of the rigid fiber end, the present configuration is one-half of a "symmetric sandwich" as described by Kennedy (1970). In this planar geometry, the vaporized portion of the flyer replaces the high explosive of the original theory and the fiber end serves as the plane of symmetry. For an asymmetric situation, conservation of momentum would have to be invoked, but here energy conservation alone suffices. Equating the "potential" energy deposited in the flyer by the laser with the kinetic energy of both the blowoff products and the remaining solid portion of the plate, we have

$$\rho\, x_d\, E = (\rho/2)\,(x_o - x_d)\, v_o^2 + (\rho/2) \int_0^{x_d} (v_o\, x/x_d)^2\, dx \,. \tag{1}$$

The left-hand side represents the energy available in the blowoff for accelerating the flyer, where ρ is the flyer density, x_d is the thickness of the layer that is vaporized by the laser pulse, and E is the so-called Gurney energy. The first term on the right is the kinetic energy of the flyer, which has an original thickness x_o and a final uniform velocity v_o. The remaining term on the right is the kinetic

energy of the blowoff material, where we have assumed a linear Lagrangian velocity profile of the form

$$v(x) = (v_o/x_d)\,x\ , \qquad 0 \le x \le x_d\ , \tag{2}$$

as suggested above. Because of the one-dimensional planar geometry, each term in Eq (1) has units of energy per unit area. This expression can be solved easily for the flyer velocity v_o, obtaining

$$v_o = \sqrt{\frac{3\,E}{3x_o/2x_d - 1}}\ . \tag{3}$$

There are no difficulties with this equation unless $x_d \ge 3x_o/2$, an impossible situation since generally $x_d \ll x_o$, and always, for meaningful conditions, $x_d < x_o$.

To use Eq (3), definitions must be provided for both the Gurney energy E and the blowoff depth x_d. We first assume that the energy in the laser pulse is deposited exponentially in the flyer according to an effective absorption coefficient μ_{eff}. Since the velocity of the flyer is relatively insensitive to the details of the energy deposition profile (Lawrence, 1992), alternate approximations could easily be used (e.g., a uniform deposition over a depth governed by μ_{eff}); however, we have chosen Lambert's Law because it is physically the most realistic. The energy per unit mass in the flyer $\varepsilon(x)$ is then

$$\varepsilon(x) = \mu_{eff} F_o\ (1 - r)\ \exp(-\mu_{eff}\ \rho\ x\ ), \tag{4}$$

where F_o is the laser fluence incident on the flyer, and r is the effective fractional energy loss. The latter includes losses due to both reflection and radiation and is integrated over the entire time of the interaction. This deposition profile is illustrated in Fig. 2, where we note that the energy at the inner surface of the flyer is $\varepsilon_o = \mu_{eff} F_o (1 - r)$.

Pulse-width dependence is incorporated into the model by taking μ_{eff} to be a function of both the true mass absorption coefficient μ_a and the laser pulse duration τ. The form chosen is

$$\mu_{eff} = \frac{\mu_a}{1 + k\ \mu_a\ \rho\ \sqrt{\alpha\ \tau}}\ , \tag{5}$$

where α is the thermal diffusivity of the flyer. It is related to more common thermal properties through $\alpha = K/\rho c_p$, where K is the thermal conductivity and c_p is the specific heat. The constant k is not an additional parameter, but it is included to allow for uncertainties in the handbook values for μ_a and α. To contrast direct energy deposition with that controlled by thermal effects, we note that the effective mean free path is $1/\mu_{eff}\,\rho$. In the limit of short pulse durations this is a true mean free path of $1/\mu_a\,\rho$, while for long pulse widths such that $\tau \gg \tau_o = 1/\alpha(k\mu_a\,\rho)^2$, the problem is thermally dominated, and the energy can be considered to be deposited on or near the front surface as a thermal load. In this case Eq (5) leads to an effective mean free path of $k(\alpha\tau)^{1/2}$, which is a characteristic diffusion length for the pulse width τ. Anticipating our experimental results, we find that for the metallic flyers we are using, μ_a is in the vicinity of 10^5 cm^2/g, k is about 0.3, and α is typically $\sim$1 cm^2/s. The transition pulse width τ_o is thus no larger than a small fraction of a nanosecond. Since all of our laser pulse widths are greater than this by at least an order of magnitude, all the interactions considered here are clearly dominated by thermal diffusion, and the precise value for μ_a is not particularly important.

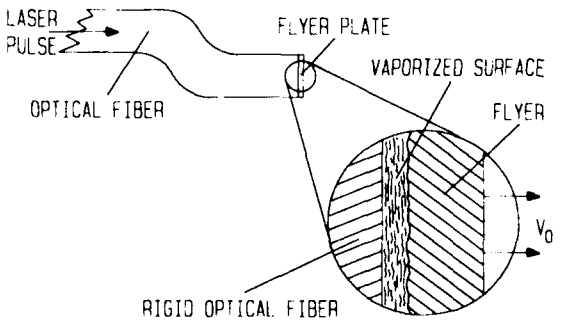


Fig. 1. Schematic for fully tamped, laser-driven flyer configuration.

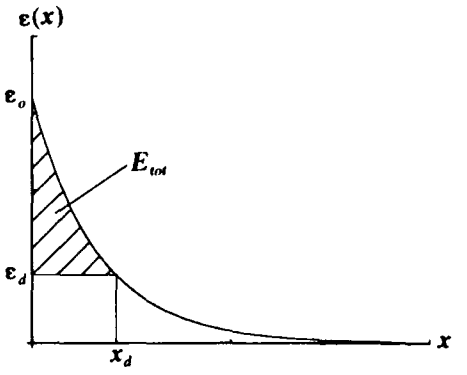


Fig. 2. Exponential energy deposition profile.

The thickness x_d of the layer vaporized from the flyer is determined by finding the depth at which the deposited energy is equal to the decomposition or vaporization energy ε_d. Thus we solve Eq (4) in the form $\varepsilon(x_d) = \varepsilon_d$, obtaining

$$x_d = \frac{1}{\mu_{eff}\,\rho} \ln\left(\frac{\mu_{eff} F_o (1 - r)}{\varepsilon_d}\right), \tag{6}$$

as suggested in Fig. 2. Now the amount of energy available for accelerating the flyer is that in excess of ε_d and contained in the blowoff layer, as indicated by E_{tot} in the figure. It can be found from

$$E_{tot} = \int_0^{x_d} [\varepsilon(x) - \varepsilon_d]\, dx, \tag{7}$$

where $\varepsilon(x)$ and x_d are obtained from Eqs (4) and (6). This leads to

$$E_{tot} = \frac{F_o (1 - r)}{\rho} - \varepsilon_d \left(\frac{1}{\mu_{eff}\,\rho} + x_d\right). \tag{8}$$

In this expression the first term on the right is the total deposited energy, and the second term represents the amount that cannot be converted into kinetic energy. The latter has two parts, the energy lost to deposition beyond the blowoff depth, $\varepsilon_d/\mu_{eff}\rho$, and the energy used for vaporization, $\varepsilon_d x_d$. Finally, we define the Gurney energy as this latter value, E_{tot}, averaged over the thickness of the blowoff layer, $E = E_{tot}/x_d$, or

$$E = \frac{F_o (1 - r)}{\rho\, x_d} - \varepsilon_d \left(1 + \frac{1}{\mu_{eff}\,\rho\, x_d}\right). \tag{9}$$

To use the model for predicting the flyer velocity, we first calculate the effective absorption coefficient μ_{eff} from Eq (5). Then, for each laser fluence of interest, we find x_d from Eq (6), and E from Eq (9). The flyer velocity v_o then follows from Eq (3).

MODEL CHARACTERISTICS AND SCALING LAWS

A number of features and characteristics predicted by the model have been borne out well by all the experiments conducted to date. The first is that there is a threshold laser fluence F_{th} below which none of the flyer is vaporized and no flyer motion will take place. Its value can be determined by setting $x_d = 0$ in Eq (6) and solving for the fluence, yielding

$$F_{th} = \frac{\varepsilon_d}{\mu_{eff}\,(1 - r)}. \tag{10}$$

When the problem is thermally dominated, as is generally true for our current configuration, the laser pulse width can be considered long, and using Eq (5), the threshold becomes

$$F_{th} \approx \frac{k\,\rho\,\varepsilon_d \sqrt{\alpha\,\tau}}{1 - r}, \qquad \tau \gg \frac{1}{\alpha\,(k\,\mu_a\,\rho)^2}. \tag{11}$$

In this case F_{th} will scale with the square root of pulse duration. If τ were much shorter than the transition value, then F_{th} would be independent of τ.

To illustrate the general behavior of the system, Fig. 3 contains plots of several of the important parameters as a function of the laser fluence, where the latter has been non-dimensionalized by the threshold F_{th}. The threshold is clearly evident in each of the plots. Figure 3(a) shows how the model predicts the variation of flyer velocity with fluence. We see that after the threshold and knee of the curve, the velocity appears to increase with the square root of the fluence. This simple scaling arises from the fact that, in general, the blowoff layer is a small fraction of the total flyer thickness, i.e., $x_d \ll x_o$. That this is true can be shown by substituting Eq (9) into Eq (3), letting F_o get large relative to F_{th}, and keeping x_d small with respect to x_o. The result is

$$v_o \approx \sqrt{\frac{2\,F_o\,(1 - r)}{\rho\,x_o}}, \qquad F_o \gg F_{th}, \qquad x_d \ll x_o. \tag{12}$$

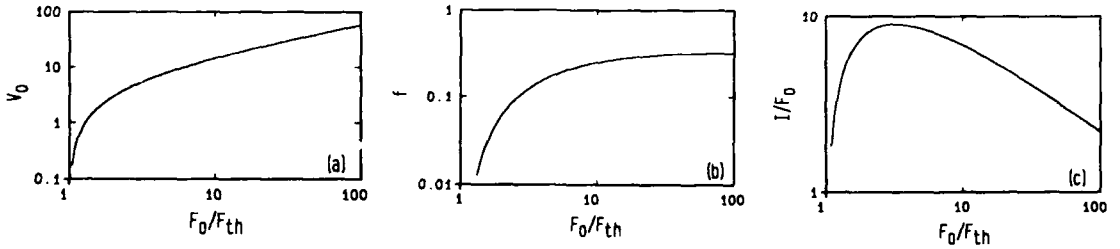


Fig. 3. Model predictions for (a) flyer velocity v_o, (b) energy-coupling efficiency f, and (c) impulse- or momentum-coupling coefficient I/F_o. The fluence is non-dimensionalized with respect to the threshold F_{th}, and in all cases the ordinate units are arbitrary.

Not only does this indicate how the velocity scales with fluence, but it shows that under these limits it also scales with $x_o^{1/2}$, $\rho^{1/2}$, and $(1 - r)^{1/2}$, but is independent of both τ and ϵ_d.

Next we define the energy-coupling efficiency f as the kinetic energy of the flyer divided by the energy fluence in the laser pulse,

$$f = \frac{\rho (x_o - x_d) v_o^2}{2 F_o} . \tag{13}$$

Using Eqs (3), (6), and (9) this becomes

$$f = \frac{3\left(\frac{x_o}{x_d} - 1\right)}{2 F_o\left(\frac{3x_o}{2x_d} - 1\right)} \frac{\epsilon_d}{\mu_{eff}} [F^* - (1 + \ln F^*)] , \tag{14}$$

where $F^* = F_o/F_{th} = \mu_{eff} F_o(1 - r)/\epsilon_d$, and is the laser fluence non-dimensionalized with respect to the threshold fluence. We can show that as F^* gets large, $1 + \ln F^*$ gets small relative to F^*. Hence the latter term can be dropped from Eq (14), and we have

$$f \approx \frac{3\left(\frac{x_o}{x_d} - 1\right)}{2\left(\frac{3x_o}{2x_d} - 1\right)} (1 - r) , \qquad F_o \gg F_{th} , \tag{15}$$

and f is independent of the fluence. If, in addition, $x_d \ll x_o$, then the efficiency becomes

$$f \approx (1 - r) , \qquad F_o \gg F_{th} , \qquad x_d \ll x_o \tag{16}$$

and it is dependent only on the energy loss r. This is evident in Fig. 3(b) where the curve asymptotically approaches its maximum value as the fluence gets large. This last result is extremely valuable because it will allow us to determine r from a limited set of high-fluence experimental data.

Another parameter of importance is the momentum- or impulse-coupling coefficient I/F_o. It is defined as the momentum per unit area in the flyer divided by the laser fluence, and is shown in Fig. 3(c), again plotted as a function of F_o/F_{th}. From the figure we see that I/F_o peaks at an intermediate fluence and then falls off as the fluence increases further. The specific nature of this behavior can be examined by looking at the actual form of I/F_o, which can be written as

$$\frac{I}{F_o} = \frac{\rho (x_o - x_d) v_o}{F_o} . \tag{17}$$

In this case, we first expand and then approximate the resulting expression in the limit $x_d \ll x_o$, which leads to

$$\frac{I}{F_o} \approx \sqrt{\frac{2 \rho x_o \mu_{eff}}{\epsilon_d}} (1 - r) \sqrt{\frac{1}{F^*} - \frac{1}{F^{*2}} - \frac{\ln F^*}{F^{*2}}} , \qquad x_d \ll x_o . \tag{18}$$

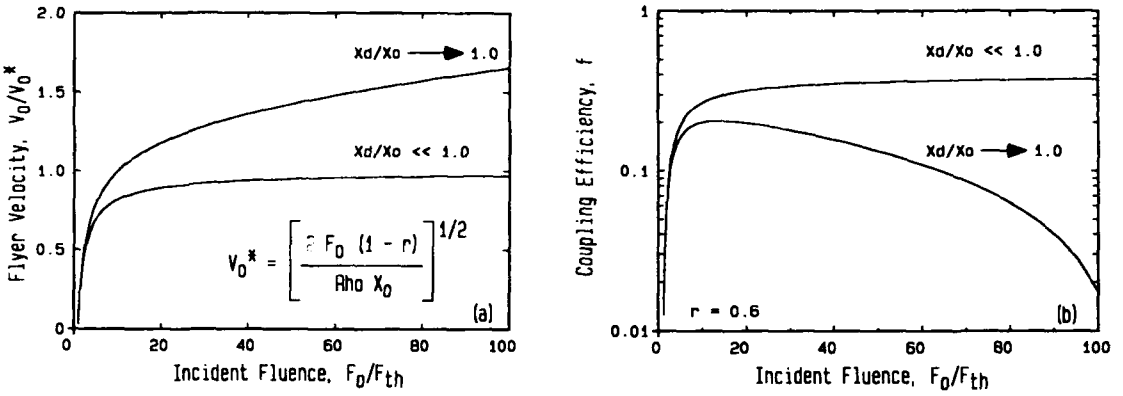


Fig. 4. The effect of flyer thickness on (a) flyer velocity and (b) energy-coupling efficiency. The flyer velocity is non-dimensionalized with respect to the scaled value given by Eq (12).

The second square-root term on the right, which is a function of F^* only, controls the shape of the curve; the other factors are simply dimensionalizing constants. Examining this term, we find that it has a maximum value of 0.319 at $F^* = 3.51$. If we can experimentally locate this point at $(I/F_o)_{max}$ and $(F_o)_{opt}$, we then have

$$\frac{\mu_{eff}}{\varepsilon_d} = \frac{(I/F_o)^2_{max}}{2 \times 0.319^2 \times \rho\, x_o\, (1 - r)^2}, \qquad \text{or} \qquad \frac{\mu_{eff}}{\varepsilon_d} = \frac{3.51}{(F_o)_{opt}\,(1 - r)}, \tag{19}$$

as long as $x_d \ll x_o$. Along with Eq (16), these results will be used to specify fully all the parameters required by the model. In the high-fluence limit, I/F_o further reduces to

$$\frac{I}{F_o} \approx \sqrt{\frac{2\,\rho\, x_o\,(1 - r)}{F_o}}, \qquad x_d \ll x_o, \qquad F_o \gg F_{th}, \tag{20}$$

and we see that it falls off as the square root of F_o, as suggested in the figure.

The scaling laws and relations that we have developed here, especially Eqs (10), (12), (16), and (20), can be used to provide rapid but approximate results for the behavior of this class of laser-driven flyer launchers. The only restriction is that we observe the appropriate limits in terms of fluence and flyer thickness.

An interesting question remains: What happens when these limiting conditions are not realized? With respect to the fluence the answer is simple. The threshold is approached from above and then achieved; there is then no flyer motion, and both the energy and momentum coupling become zero. On the other hand, if x_o is small enough so that a significant fraction of the flyer is vaporized by the laser pulse, then the relevant scaling laws, in particular Eqs (12), (16), (18), and (20), no longer apply. To illustrate, Fig. 4 shows plots of both v_o and f using their full forms, Eqs (3) and (13). In Fig. 4(a), we show how the flyer velocity behaves for these two cases. To emphasize the differences, v_o is non-dimensionalized with respect to the scaled value given by Eq (12); in other words, for the ordinate we plot v_o/v_o^*, where $v_o^* = [2\,F_o(1 - r)/\rho x_o]^{1/2}$. Hence, the curve for the thick flyer ($x_d/x_o \ll 1$) approaches a value of one as the fluence gets large. In contrast, when the flyer is thin ($x_d/x_o \to 1$), we see that the velocity becomes much larger than the scaled value. For the energy-coupling efficiency f, we show similar curves in Fig. 4(b). For thick flyers f asymptotically approaches $1 - r$ or 0.4 at large fluences (the calculations were performed with $r = 0.6$), whereas for thin flyers f drops off rapidly when x_d exceeds roughly half of the initial thickness x_o. Thus, although the velocity can be driven higher by using thin flyers, the efficiency with which the energy can be coupled into the flyers is reduced by an even greater factor. These thin-flyer effects have not been experimentally verified, but assuming that adequate diagnostics could be employed, there is little doubt that these trends would be observed.

PARAMETER DETERMINATION

In the previous section we suggested that a limited set of experimental data could be used to define all the parameters required by the model. Here we will describe the appropriate procedure, using measurements taken with aluminum flyers as an example. We first assemble the characteristics of the system with which we are working, specifically the laser fluence F_o, the pulse width τ, and the flyer

thickness x_o. Knowing the flyer material, we should be able to obtain readily the flyer density ρ, the thermal diffusivity α, and the vaporization energy ϵ_d. Although it is not particularly important for the present configuration, we should also be able to find at least an estimate for the true absorption coefficient μ_a for the laser wavelength being used. This leaves only two parameters, the integrated fractional energy loss r, and the effective absorption coefficient μ_{eff}.

To generate values for these last two model inputs, we need one set of velocity measurements spanning a range of fluences starting near the threshold but with the other variables held constant. If the flyer thickness is great enough so that $x_o \gg x_d$, these data can be converted to energy-coupling efficiencies f through

$$f \approx \frac{\rho\, x_o\, v_o^2}{2\, F_o} , \qquad x_o \gg x_d , \tag{21}$$

and into impulse-coupling coefficients I/F_o with

$$\frac{I}{F_o} \approx \frac{\rho\, x_o\, v_o}{F_o} , \qquad x_o \gg x_d . \tag{22}$$

If the data are plotted as f versus F_o, they should approach a constant value as the fluence is increased, and if they are plotted as I/F_o, they should peak at a fluence several times the threshold. The limiting value of f will lead to r through Eq (16), and the maximum value of I/F_o will yield μ_{eff} through Eq (19).

As an example, we will consider one of our earlier sets of data employing aluminum flyers, for which the relevant system parameters are $x_o = 25$ μm for the flyer thickness, and $\tau = 25$ ns for the laser pulse width. For the aluminum flyers, we have $\rho = 2.7$ g/cm^3 for the density, $\epsilon_d = 12$ kJ/g for the vaporization energy, $\alpha = 0.8$ cm^2/s for the thermal diffusivity, and $\mu_a = 4.4 \times 10^5$ cm^2/g for the true absorption coefficient at the laser wavelength of $\lambda = 1.06$ μm (Hultgren *et al.*, 1963; Touloukian *et al.*, 1973; Weber, 1986). Converting the measured velocity data with Eqs (21) and (22), we obtain the results shown in Figs. 5(a) and 5(b).

Looking first at the energy-coupling efficiency, it appears that f is asymptotically approaching a value of about 0.4. Using Eq (16), this leads to a value for the energy loss of $r = 0.6$. Next, an estimate for the coordinates of the peak impulse-coupling coefficient can be made from Fig. 5(b). For these data we find $(I/F_o)_{max} \approx 43$ dyne s/J at a fluence of $F_o \approx 10.4$ J/cm^2. With $r = 0.6$, both parts of Eq (19) then give $\mu_{eff} \approx 1.01 \times 10^4$ cm^2/g for the effective absorption coefficient. In the actual implementation of the model, μ_{eff} is not used directly but is computed from Eq (5). To find the required constant k, we simply invert this expression, obtaining

$$k = \frac{\mu_a - \mu_{eff}}{\mu_a\, \mu_{eff}\, \rho\, \sqrt{\alpha\, \tau}} , \tag{23}$$

where, as was mentioned earlier, k is not an additional parameter but provides for uncertainties in the other constants contributing to μ_{eff}. The value thus obtained is $k = 0.253$. The curves in both parts of Fig. 5 were plotted using Eqs (3) and (17) with this result and the other constants mentioned above.

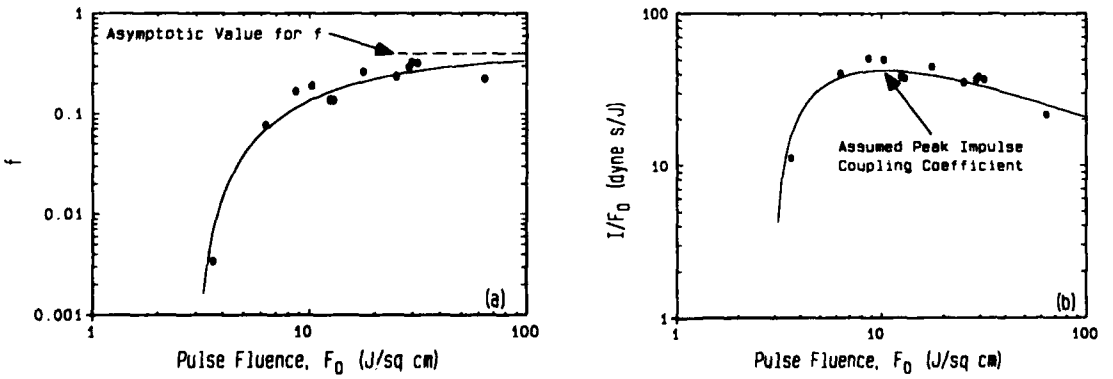


Fig. 5. Experimental data for aluminum flyers with $\tau = 25$ ns and $x_o = 25$ μm plotted in terms of (a) energy-coupling efficiency f, and (b) impulse-coupling coefficient I/F_o. The curves were calculated from the model using the constants derived from these data.

Note that through Eq (10) an independent determination of μ_{eff} could have been found from an experimental estimate of the threshold fluence F_{th}. For the present data set an estimate of $F_{th} \approx 3$ J/cm^2 would have been very close to the value predicted by Eq (10) and the above constants, 2.97 J/cm^2. All these final values for the material constants are summarized in Table 1.

Table 1. Flyer Material Properties

	Aluminum	Copper	Magnesium
Material density, ρ (g/cm^3)	2.7	8.93	1.74
Decomposition energy, ε_d (kJ/g)	12.0	6.2	7.0
Thermal diffusivity, α (cm^2/s)	0.8	1.0	0.86
True absorption coefficient, μ_a (cm^2/g)	4.4×10^5	9.3×10^4	1.0×10^5
Absorption coefficient constant, k (dimensionless)	0.253	0.252	0.30
Effective energy loss, r (dimensionless)	0.60	0.45	0.40

MODEL APPLICATIONS

Two major areas will be used for applying the model to actual experimental results. For the first, we will analyze a range of parameter variations using aluminum flyers; for the second, we will look at more limited sets of data on two alternate metallic flyer materials, copper and magnesium.

To illustrate the accuracy of the model, as well as the range of parameters over which we can reliably extrapolate its predictions, we will examine experimental variations in flyer diameter and thickness, laser pulse duration, and coupling method. For the initial comparison, we combine the data used to determine the parameters for aluminum flyers with additional measurements taken with other optical fiber and flyer diameters. The results are shown in Fig. 6. It is clear that all the data lie very close to the single curve generated by the model. The fact that the flyer diameter makes no significant difference in the flyer velocity shows that our original assumption of one dimensionality is, for all practical purposes, fully justified. The plot also shows that the high-fluence square-root scaling of v_{fl} with F_{fl} predicted by Eq (12) is well obeyed.

The next example considers a set of shots that did not use the optical fiber to couple the laser energy to the flyer, but instead employed a thick plate of fused silica on which the flyer was mounted, and that provided the tamping for the blowoff products. A lens was then used to focus the laser beam on the inner surface of the flyer, through the quartz plate. In addition, the aluminum flyer was considerably thicker, with $x_{fl} = 66$ μm, and the pulse width was $\tau = 18$ ns. It was anticipated that the laser fluence would be somewhat less uniform across the flyer diameter than with the optical fiber, but if this were true, it did not lead to any significant anomalies in the flyer response. Because of the different coupling method, the delivery of the laser energy to the flyer is less efficient than with the fiber, and it was found that an energy loss fraction of $r = 0.78$ was needed to match these data. All the other input constants were, however, the same as before. The results, which are plotted in Fig. 7, show excellent agreement between theory and experiment.

Returning to the fiber-coupled configuration, we next consider the interaction of the laser pulse with thin flyers. The measurements and calculations shown in Fig. 8 used a pulse duration of $\tau = 18$ ns and a flyer thickness x_{fl} of only 5 μm. This is only one-fifth the thickness of the flyers used for the Fig. 6 data and less than one-tenth that represented in Fig. 7. Again, with no changes to the basic input parameters, the model reproduces the data very closely. With flyers this thin, there is some question as to the thickness of the blowoff layer x_d, and whether the limiting condition, $x_d \ll x_{fl}$, is maintained. Although this restriction is not a requirement for applying the model, a departure from the velocity scaling suggested by Eq (12) and illustrated in Fig. 4(a) might be expected. No such deviation is observed, and in fact for the maximum fluence in this experimental series, $F_{fl} = 26$ J/cm^2, Eq (6) leads to $x_d/x_{fl} \approx 0.14$. Apparently this value is adequate to meet the limiting case requirements.

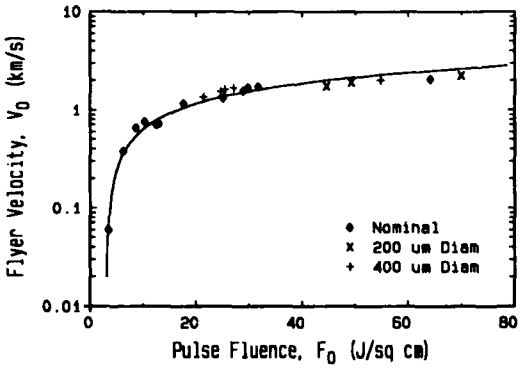


Fig. 6 Comparison of model predictions with experimental results for aluminum flyers. The various symbols represent different flyer diameters and, by their agreement with a single theoretical curve, they indicate that the interaction is one dimensional. In these experiments, the flyer thickness was $x_0 = 25$ μm and the pulse width was $\tau = 25$ ns.

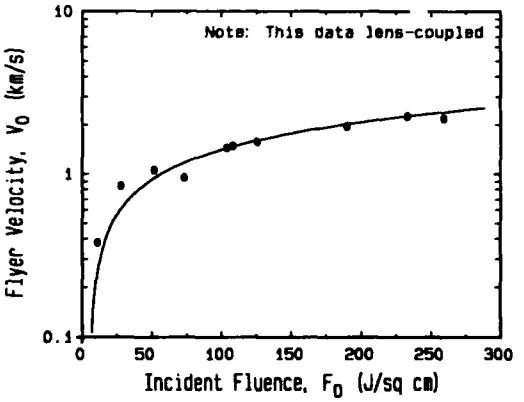


Fig. 7. Comparisons between theory and experiment for lens-coupled aluminum flyers. Here the flyer thickness was $x_0 = 66$ μm and the pulse width was $\tau = 18$ ns. Because of the coupling method, a value of $r = 0.78$ was required to match these data; otherwise, the standard parameters were used.

For a final parametric variation using aluminum flyers, we analyze a series of experiments in which all the parameters were held roughly constant except for the laser pulse duration. In this case we used a flyer thickness of $x_0 = 12.7$ μm and a nominal fluence of $F_0 \approx 27$ J/cm^2. The pulse width τ was allowed to vary over more than an order of magnitude, ranging from 4 ns to 48 ns. Both the experiments and the model predictions are plotted in Fig. 9. Again, the theory matches the data quite well. There is, however, some evidence in the data of a structure not exhibited by the model, but it is difficult to ascertain whether this is real or just an artifact of experimental uncertainties.

Although most of our efforts have concentrated on aluminum flyers, several other materials have been examined. For the second basic model application, experimental results were obtained from both copper and magnesium flyers, and the data are shown in Fig. 10. For copper (Paisley, 1991), the required material properties were determined in the same manner as with aluminum, and are listed, along with the constants for the other materials, in Table 1. As with aluminum, the agreement between theory and experiment is very good over the entire range of fluences examined. In a similar fashion, we have analyzed and then plotted the results for magnesium flyers. As with the other materials, the model matches the data very well, and any discrepancies could easily be attributed to experimental scatter.

The major difference among the three flyer materials shows up in terms of the overall energy loss r. For aluminum at high fluences, only 40% of the input laser fluence is ultimately converted into kinetic energy of the flyer, whereas for magnesium the process is 60% efficient. Copper is almost as good as magnesium, with a value of $r = 0.45$ for the energy loss. These material differences can probably be best

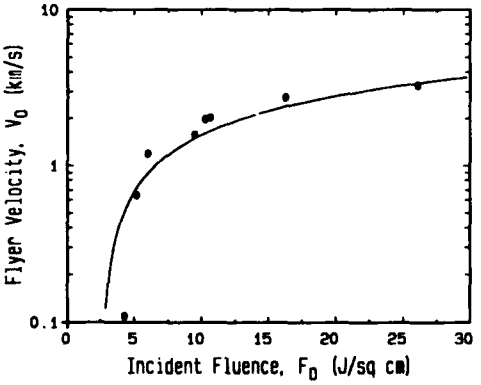


Fig. 8. Model predictions and experimental results for thin aluminum flyers. For these shots, the flyer thickness was $x_0 = 5$ μm and the pulse duration was $\tau = 18$ ns. For all the experiments shown here, $x_d/x_0 \leq 0.14$.

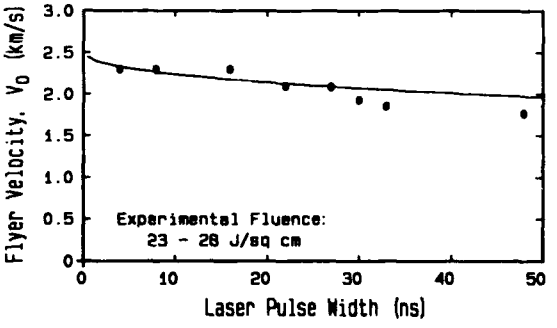


Fig. 9 Comparison between theory and experiment for flyer velocity as a function of laser pulse width. For these shots the flyer thickness was held constant at $x_0 = 12.7$ μm and the laser fluence was maintained at $F_0 \approx 27$ J/cm^2. The model calculations used $F_0 = 28$ J/cm^2.

illustrated by using the model to look at both the energy-coupling efficiency and the impulse-coupling coefficient, which we have done in Fig. 11. To keep these comparisons on a common basis, we have held the flyer thicknesses constant at a nominal value of 15 μm. We could also have allowed x_0 to vary and kept the areal density constant, but it was felt that the former was a more realistic operational constraint. A constant pulse duration of $\tau = 20$ ns was also assumed for these calculations.

From these figures we see immediately that the threshold fluence for magnesium is about one-third of that for aluminum and roughly one-fourth that of copper. F_{th} could also have been determined directly from Eq (11) and the respective input constants. The coupling efficiency, in Fig. 11(a), is greater for magnesium at all fluences. However, because of the dependence of f on the other parameters, as indicated in Eq (14), the efficiencies for aluminum and copper are similar, crossing each other at an intermediate fluence. Examining the impulse-coupling coefficient in Fig. 11(b), we see that both magnesium and copper are about twice as good as aluminum, with magnesium achieving its peak I/F_0 at a fluence almost one-fourth that of either of the other materials. This could also have been determined with a direct application of Eq (18). These results suggest that, barring other considerations, magnesium would be the best choice for the flyer material in this type of laser-driven system.

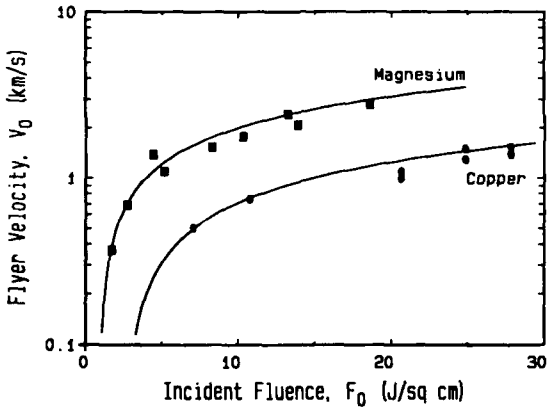


Fig. 10. Flyer velocity as a function of laser fluence for copper and magnesium flyers. The experiments on copper (Paisley, 1991), shown on the lower curve, employed a pulse width of $\tau = 8.8$ ns and a flyer thickness of $x_0 = 10$ μm. The magnesium data, on the upper curve, were taken with $\tau = 18$ ns and $x_0 = 12.5$ μm. The other model parameters, for both materials, are listed in Table 1.

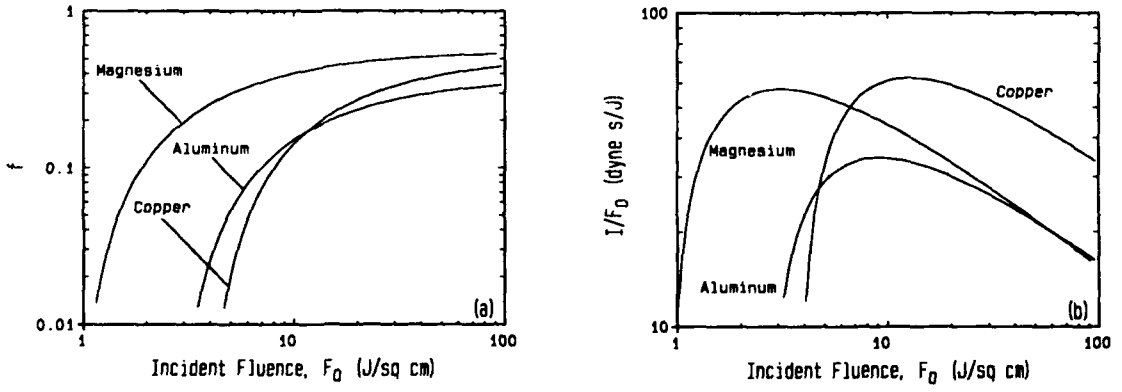


Fig. 11. Model comparisons among the three tested flyer materials. In (a) we show the energy-coupling efficiency f, and in (b) we plot the impulse-coupling coefficient I/F_0. In both cases the flyer thickness was kept constant at $x_0 = 15$ μm, and a pulse width of $\tau = 20$ ns was employed.

CLOSURE

In the course of this study we have developed a simple model for predicting the late-time velocity of thin flyers driven by high-power pulsed lasers under conditions where the blowoff products are fully tamped. Once all the required constants are established through the use of an initial set of data, we have found that the model is capable of accurate extrapolations to other conditions involving changes in energy fluence, laser pulse width, and flyer thickness. In fact, each of these parameters has been varied by more than an order of magnitude, with no significant loss in this accuracy. Variation of flyer diameter with no resulting velocity change shows that the response of the system is indeed one dimensional. By comparing different materials, we have seen that the energy-coupling efficiencies can be altered substantially, and that these differences are manifested as shifts in both threshold fluence and peak impulse-coupling coefficients.

More specifically, we have derived a number of expressions that can be used to describe most features of the system. In fact, we can easily predict not only the flyer velocity, but also the energy-coupling efficiency, the impulse-coupling coefficient, the effective blowoff depth, and the threshold fluence. In the limits of high fluence and thick flyers, these relations become particularly simple scaling laws.

A more general but important conclusion from this work is that simple engineering models, such as the one described here, provide fast and economical approaches for studying many aspects of problems involving dynamic interactions. This is true as long as the variables of principal interest are integral quantities such as momentum or flyer velocity as opposed to non-integral variables such as pressure.

REFERENCES

Gurney, R. W. (1943). *The Initial Velocities of Fragments From Bombs, Shell, and Grenades*. Report No. 405. Ballistic Research Laboratories, Aberdeen Proving Ground, MD.

Hultgren, R., R. L. Orr, P. D. Anderson, and K. K. Kelley (1963). *Selected Values of Thermodynamic Properties of Metals and Alloys*. John Wiley and Sons, Inc., New York.

Kennedy, J. E. (1970). *Gurney Energy of Explosives: Estimation of the Velocity and Impulse Imparted to Driven Metal*. Report No. SC-RR-70-790. Sandia Laboratories, Albuquerque, NM.

Lawrence, R. J. (1988). *An Effective Properties Model for Pulsed Radiation Interactions*. Report No. SAND88-0245. Sandia National Laboratories, Albuquerque, NM.

Lawrence, R. J. (1992). The equivalence of simple models for radiation-induced impulse. In: *Shock Compression of Condensed Matter - 1991* (S. C. Schmidt *et al.*, eds.). Elsevier Science Publishers B.V., Amsterdam.

Lawrence, R. J., J. T. Kare, R. M. Zazworsky, and D. K. Monroe (1992). System requirements for low-earth-orbit launch using laser propulsion. In: *Proceedings of the 6th International Conference on Emerging Nuclear Energy Systems (ICENES '91)*. American Nuclear Society, La Grange Park, IL (in publication).

Paisley, D. L. (1991). Private communication. Los Alamos National Laboratory, Los Alamos, NM.

Touloukian, Y. S., R. W. Powell, C. Y. Ho, and M. C. Nicolaou (1973). *Thermophysical Properties of Matter, Vol. 10, Thermal Diffusivity*. IFI/Plenum, New York.

Trott, W. M. and K. D. Meeks (1990). Acceleration of thin foil targets using fiber-coupled optical pulses. In: *Shock Compression of Condensed Matter - 1989* (S. C. Schmidt *et al.*, eds.). Elsevier Science Publishers B.V., Amsterdam.

Weber, M. J. (1986). *CRC Handbook of Laser Science and Technology*, Vol. IV. CRC Press, Boca Raton, FL.

Int. J. Impact Engng Vol.14, pp.451–465, 1993
Printed in Great Britain

0734-743X/93 $6.00+0.00
Pergamon Press Ltd

THE IMPACT OF FLAT, THIN PLATES ON ALUMINUM TARGETS IN THE 5-10 km/s VELOCITY RANGE*

R. Lee, J. Osher, H. Chau, M. Gerassimenko, G. Pomykal and R. Speer

Lawrence Livermore National Laboratory
P.O. Box 808, Livermore, CA 94550

ABSTRACT

The purpose of the study was to investigate the effect of the impact of a thin membrane on aluminum in the velocity range 6-10 km/s. The impulsive load delivered by a membrane impact will exceed the momentum/area of the membrane because of rebound, blow-off of vaporized membrane material, and ejection of molten and fractured material from the target (impulse gain). One of the objectives of the study was to quantify the impulse gain in the velocity range of interest. Also of interest was the physical damage to the target including spall, melting and fracture. Understanding these damage mechanisms is important for protecting spacecraft from the impact of space debris and meteoroids.

Simple theories account for the flyer rebound, but hydrodynamic modeling is required to treat the blow-off of target material. At lower velocities, the blow-off is negligible, but at 10 km/s calculations show it to be equal to the rebound momentum for one-dimensional (1-D) impacts. The modeling of three-dimensional (3-D) experiments revealed large effects at the edge of an impacting membrane, prompting an emphasis on 1-D pressure profile experiments.

87 kJ ELECTRIC GUN FACILITY:

The LLNL electric gun systems operate by discharging a capacitor bank through a thin metallic foil as is shown schematically in Figure 1. Ohmic heating of the foil deposits a significant portion of the stored capacitor bank energy into the foil causing the foil to explode. The explosion of the foil drives a thin plate of material, placed on top of the foil, down a barrel to impact a target. LLNL operates several electric gun systems with stored electrical energy up to 1 MJ. The work described here was performed on an 87 kJ electric gun which has been described in detail in Reference [1].

The heart of the 87-kJ electric gun is a 17.6-uF, 25-nH capacitor bank which has a peak charging voltage of 100 kV and maximum stored energy of about 87 kJ. Electrical current from the bank flows through Maxwell rail gap switches into the exploding foil load, a disposable, low-inductance, parallel-plate transmission line "laminate" which is clamped into a permanent transmission line coming from the bank, as shown schematically in Figure 1.

* *This work was done under the auspices of the U.S. Department of Energy by Lawrence Livermore National Laboratory under Contract No. W-7405-Eng-48. Funding was provided by SDIO through DNA and managed by the U.S. Army Defense Command.*

The transmission line from the capacitor bank passes into a steel target chamber. The target chamber contains any shrapnel from the shot and is purged with air after the shot, so the smoke and fumes from firing do not enter the room. The disposable laminate is clamped into the transmission line and the barrel and target are mounted on top of the transmission line. If experiments are to be conducted in vacuum, a disposable, Lucite (PMMA) vacuum fixture is mounted over the barrel and target and evacuated. An optical port provides optical access for a laser beam and a line of sight for two electronic streak cameras. Two flash x-ray (FXR) tubes can be independently triggered to measure the motion of the target and debris over a prescribed time interval.

Diagnostics include measurement of current and voltage waveforms to monitor bank performance, FXR photos, an electronic streak camera, and a Fabry-Perot (FP) laser velocimeter. For the FP velocimeter measurements, the beam from an argon ion laser is focused onto a spot on a diffusely-reflected surface, typically aluminum or silver paint. The diffusely-reflected laser light is collected and passed through cylindrical optics and then through a Fabry-Perot etalon. For a collimated beam, the F-P etalon produces a series of circular fringes whose angular separation depends on the wavelength of the return light. Placing the cylindrical optics ahead of the etalon collapses the fringe pattern into a series of dots which are focused onto the streak camera slit. If the diffusely-reflecting surface remains stationary, the streak record is a series of parallel lines, but if the surface moves, the return light is Doppler shifted, changing the angular separation of the dots. The velocity-time history of the surface may be determined by measuring the change in spacing of the lines recorded on the streak record. Flyer velocity was measured by painting a small dot of silver paint onto the surface of the flyer and monitoring the motion with the FP velocimeter. The FP velocimeter was also used to measure impulse gain using the LiF technique, which will be described later.

EXPERIMENTAL ARRANGEMENT:

Impulse Gain - In these experiments, a thin flyer plate moving at velocity v strikes a target at rest. From Newton's second law, we know that the impulse delivered to the target is equal to the change in target momentum. If the flyer plate rebounds or vaporizes, and if material is ejected from the target surface, the final momentum of the target may be greater than the initial momentum of the flyer plate, hence the impulse delivered to the target is greater than the initial momentum of the plate. This is called an impulse gain. It is convenient to define quantities in terms of unit area of impact, so we define impulse to be the momentum imparted to the target per unit area of impact. With this definition, impulse is the time integral of pressure. The unit of

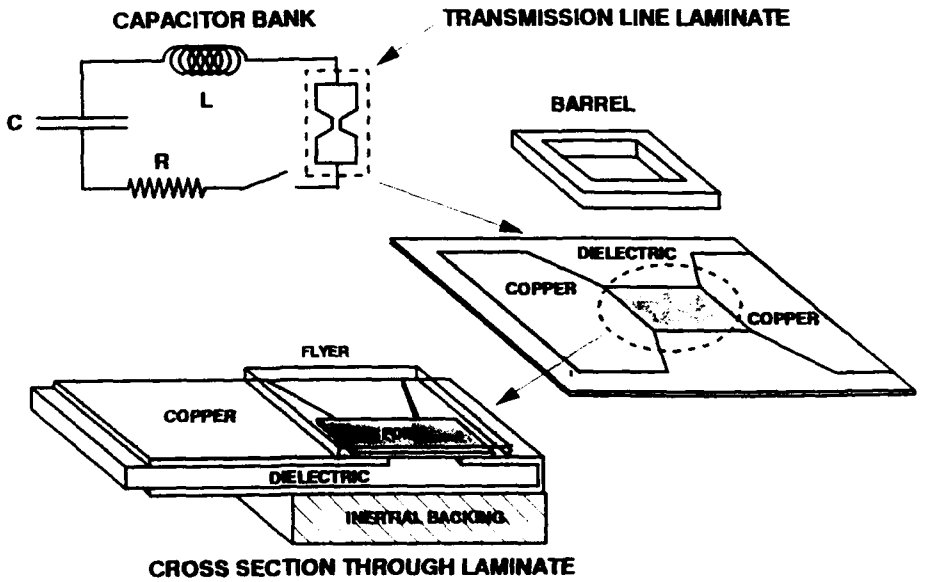


Figure 1. Schematic drawing of an electric gun laminate. A barrel is placed on top of the flyer and foil, and the explosion of the foil drives the flyer down the barrel to impact a target.

impulse is the kilotap, where 1 ktap = 1000 dyne-s/cm^2. The definition of impulse gain is the ratio of the impulse delivered to the target to the momentum/area of the incident flyer plate.

Ballistic Technique - One way to measure impulse gain is to measure the ratio of the target momentum, after the flyer has struck and rebounded, to the incident flyer plate momentum. The flyer plate thickness determines the mass/area of the flyer plate. Flyers with a diameter of 22.2mm were used for most of this work. Flyers were either 0.20mm thick Mylar or 0.30mm thick Kapton. Both Mylar and Kapton have a density of 1.4g/cm^3. Flyer velocity was measured as a function of capacitor bank charging voltage using the FP laser velocimeter described above.

The incident flyer momentum, p_f, is thus:

$$p_f = DdAv_f, \tag{1}$$

where D is the flyer density, d is the flyer thickness, A is the flyer area, and v_f is the flyer velocity.

The final velocity, v_t, of the aluminum target was measured by using the FXR to photograph the target position at two different times after the impact. v_t is taken to be the displacement of the target (measured in the FXR photos) divided by the time interval between the x-ray flashes. The target is recovered, its final mass, M_t is measured and the final target momentum, p_t, is given by

$$p_t = M_t v_t. \tag{2}$$

Impulse gain, G, is thus

$$G = (M_t v_t)/DdAv_f). \tag{3}$$

The targets were aluminum, typically 2.54cm thick and 4.45cm square. It was necessary to drill two rows of holes, through the target, parallel to the rear target surface (opposite the impact surface) to suppress spall from the back surface, as is shown in Figure 2. These holes attenuate the shock wave produced by the flyer plate impact and spall, if it occurs, occurs internally in the holes. Otherwise, one or more spall scabs will separate from the rear surface, greatly complicating the task of keeping track of the impulse delivered by the flyer plate impact. It is advantageous to keep the target mass as low as possible, to maximize the target velocity after impact, but the lateral dimensions are limited by the need to suppress spall. Had a target of smaller lateral dimensions been used, spall would have occurred from the sides of the target. Measurements were made at approximately 5,8, and 10km/s.

There are a number of experimental difficulties associated with this type of measurement. The metallic target must be shielded from the magnetic field produced by the exploding foil, otherwise eddy currents will interact with the magnetic field and give an additional momentum component to the target. Exploratory experiments without magnetic shielding yielded spuriously high impulse gains. A layer of copper and a layer of steel, with holes for the flyer plate to pass through, were used to shield the target from the magnetic fields, as shown in Figure 3. This shielding arrangement was tested by using the FXR to monitor the motion of a 45mm square, 25.4mm thick, aluminum target after discharging the bank with a dielectric barrier interposed to prevent the flyer from striking the target. No motion was detected in the picture taken 18 μs after the current start. The period of the capacitor bank is about 4 μs, and the damping is such that after two periods the next current peak is only about 20% of the initial current peak. It can be safely assumed that the magnetic contribution is over after the first two periods (recall that the magnetic force is proportional to the square of the current) so the FXR picture indicates that the magnetic shields are effective in eliminating the magnetic contribution to impulse gain.

The flight distance of the flyer plate to the target was about 5cm. The long flight distance helps to minimize magnetic effects, and to delay the impact of slow-moving debris on the target, e.g. pieces of the barrel. It is difficult, however, to track the flyer velocity over such a large distance. Attempts to

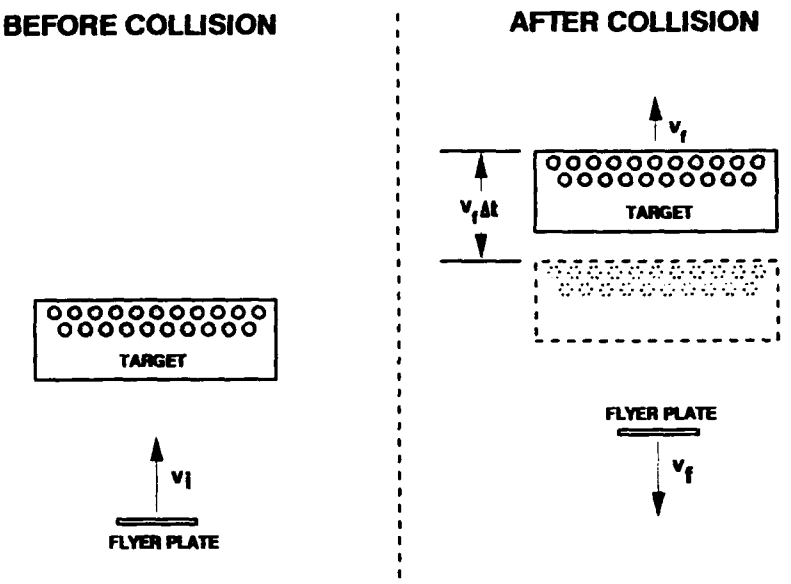


Figure 2. Schematic drawing of an impulse gain experiment, using the ballistic technique. The dashed drawing on the right represents the position of the target during the first x-ray flash, the upper drawing represents the position of the target during the second flash. The holes at the top of the target are to suppress spall.

obtain a good flyer velocity measurement near the maximum charging voltage (95 kV) were unsuccessful until an electronic streak camera was used to measure the arrival time of the flyer at the target. The FP measurement of velocity over the first several mm of flight and the time of arrival, measured by the streak camera, were then combined to get a good measurement of impact velocity.

Another concern is the contribution to the momentum gain from the aluminum plasma which accelerates the flyer. The material velocity in the plasma is equal to the flyer velocity, v_f just behind the flyer, whose position we denote by z_f ($z = 0$ before the flyer is launched). If it is assumed that the flyer velocity varies linearly from v_f at $z = z_f$ to 0 at $z = 0$, and further assumed that the plasma density is uniform, the plasma momentum can be computed. Let C and M be the mass/area of the bridgefoil and flyer respectively. The flyer momentum is thus Mv_f and one can show by integration that the plasma momentum is $1/2Cv_f$. The ratio of plasma to flyer momentum is thus 1/2 (C/M). For many of these experiments a 0.2mm thick Mylar flyer and a 0.1mm thick bridgefoil were used, so the plasma carries approximately half the momentum of the flyer. Not all of this momentum contributes to the impulse delivered to the target, however, because of the long flight path and the magnetic shield. Figure 3 shows a sketch of the geometry used for the shots. If it is assumed that the plasma spreads laterally at a velocity equal to the flyer velocity, it will spread at a 45° angle and from the experimental geometry it is calculated that the order of 10% of the plasma mass actually strikes the target, which would contribute the order of 5% to the impulse. The impulse from the plasma contributes directly to the measurement error in the ballistic technique, but is less important in the LiF technique described below.

Final target velocities were rather low, in the 10 m/s range, and target displacements were small over the FXR delay times that were used. The FXR flashes could not be delayed more than 400 microseconds because debris from the barrel could strike the target and change the momentum at later times. The primary limitation on accuracy was the error in measuring the small target displacements. In some of the later experiments, a hole was drilled through the center of mass of the target into which a lead sphere, which could be more easily resolved on the film, was inserted. Measurements using this technique had estimated errors of about ±10% in the measurement of sample position. Errors in x-ray timing and target

mass were negligible, so the major remaining error is the systematic contribution from the plasma impulse, estimated above at about 5%.

A difficulty with the ballistic technique is that the experiment is inherently two or three dimensional. There is an unavoidable edge effect due to the finite size of the flyer plate. The extent to which edge-effects contribute to impulse gain is difficult to quantify experimentally, but impact craters on recovered samples show more material removal around the edges of the impact than at the center. Modeling calculations show the edge effect to be large for 10 km/s impacts.

LiF Technique - Another way of measuring the impulse delivered to the target is to measure the time variation of the pressure at a point in the target as the pressure wave from the impact passes that point. Impulse is the time integral of the pressure, so this is a rather direct and fundamental way of measuring impulse.

To achieve this the arrangement shown in Figure 4 was used. The flyer plate strikes a 1mm thick aluminum target and produces a pressure wave in the target. A 5mm thick LiF crystal is in contact with the rear surface of the aluminum and the FP laser beam passes through the LiF to strike the aluminum and be diffusely reflected. The FP velocimeter thus monitors the motion of the Al/LiF interface during the passage of the pressure wave produced by flyer impact.

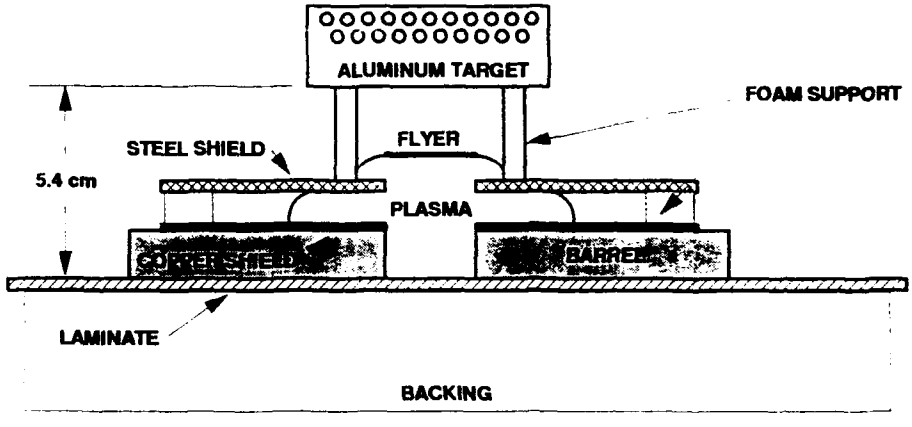


Figure 3. Schematic drawing of the magnetic shielding arrangement. The steel shield was about 3mm thick, the copper shield was about 0.25mm thick. The steel shield prevents part of the plasma from reaching the target.

Generally, two shots were required for each impulse gain measurement. The first shot, which is called a timing shot, launched the flyer so as to strike a glass cover slip, mounted at the position of the impact surface of the target. The F-P velocimeter recorded the flyer velocity and the streak camera recorded the arrival time of the flyer at the target. This allowed the timing window to be set for the following impulse gain shot with the F-P velocimeter, and also provided the impact velocity of the flyer. Measurements were made at approximately 5,8, and 10 km/s. For the impulse gain shots some of the return light from the laser beam was split off and focused on the slit of the streak camera. This recorded a speckle pattern which is very sensitive to motion of the target. No motion due to magnetic forces was detected, but a short time before the arrival of the shock wave at the interface, changes in the speckle pattern were observed. This was attributed to the arrival of a small amount of gas from the foil explosion which had gotten ahead of the flyer. No motion was recorded by the velocimeter before the arrival of the main shock, so it was concluded that precursor gas contributes negligible momentum.

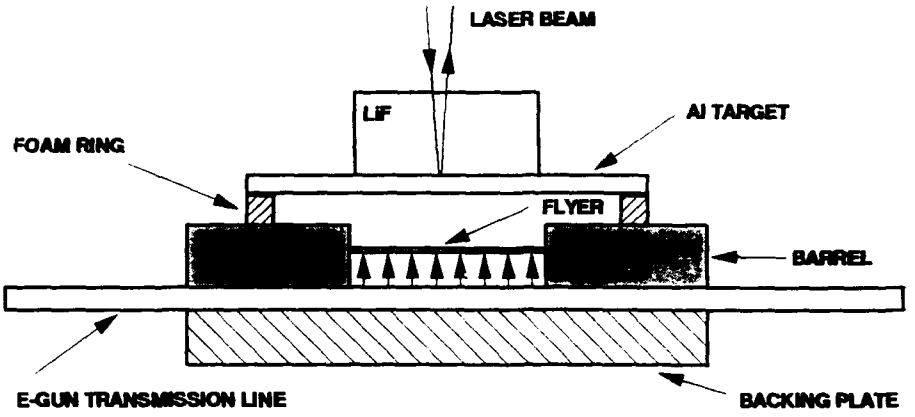


Figure 4. Schematic drawing of a LiF-technique experiment.

Mass and momentum conservation require the pressure and material velocity to be the same on both sides of the interface and, knowing the material velocity, the pressure can be computed using the well-known U_S-u_p Hugoniot curve for LiF. The Hugoniot curves for aluminum and LiF are nearly the same, so there is little reflection of the shock wave as it passes through the interface. A graphical construction shows that a 100 GPa shock wave passing from aluminum to LiF will only drop about 2% in amplitude. Lateral dimensions of the flyer and the LiF crystal are chosen large enough to ensure that the flow remains one dimensional over the time of interest.

Once the pressure-time curve at the interface has been computed from the F-P record of the interface velocity, it is a simple matter to compute the impulse delivered to the target by integrating the pressure wave. The error due to the impedance mismatch at the interface is 2% or less.

The LiF technique is a much more accurate way measuring impulse, eliminates edge effects and it has the additional advantage of being one-dimensional. The one dimensionality makes the results much easier to compare with calculations.

A disadvantage of the LiF technique is in accounting for late-time effects, e.g. the ejection of molten and vaporized material from the target. One can increase the recording time by using a large-diameter flyer and a larger and thicker LiF crystal.

EXPERIMENTAL RESULTS AND DISCUSSION

Impulse Gain Results:

The results of the impulse gain experiments are shown in Figure 5. Four sets of data are displayed. The inverted triangles represent impulse gain measured using the ballistic technique. The rest of the data are obtained using the LiF technique described above. The squares are data for 0.2mm thick Mylar, the right-side-up triangles are for 0.3mm thick Kapton and the crosses are from earlier measurements made with 0.3mm thick Kapton. The Hugoniot curves of Kapton and Mylar can be used interchangeably.

Examination of Figure 5 shows a systematic difference between the results obtained using the ballistic and LiF techniques. The ballistic results show a pronounced rise at the highest impact velocities, while the LiF results are essentially flat. It is not surprising that the ballistic experiments show a momentum gain rising with impact velocity, because of the contribution to impulse gain from ejecta from the impact region. Examination of recovered targets shows a substantial edge effect, which would not be present in a 1-dimensional (1-D) impact. A 3-D simulation of a ballistic-technique experiment, discussed in a later section, show that some of the impulse is delivered over a time span which is large compared to the

pressure pulse produced by the impact, with the target momentum increasing for 3 microseconds after impact. The late time effects are presumably due to material being ejected from the impact crater.

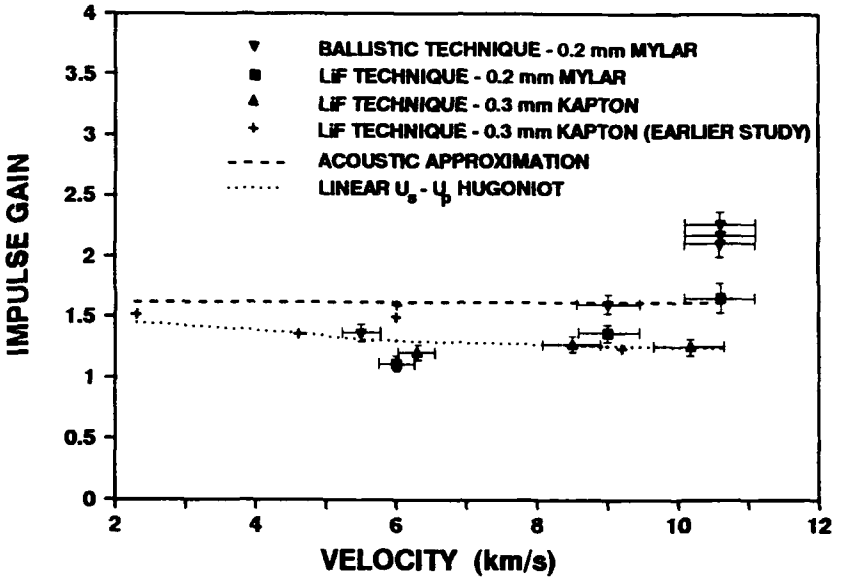


Figure 5. Summary of the impulse gain data.

In contrast, the LiF technique is inherently 1-D, so it does not include an edge contribution. A factor which must be considered in understanding the LiF results is the relatively short duration of the measurement, typically a few hundred nanoseconds. Contributions to the impulse due to late-time ejection of material after the flyer has rebounded are not measured so it is not surprising to measure a larger impulse gain with the ballistic technique, where edge effects result in a large quantity of ejected material, and where the measurement is integrated over hundreds of microseconds. Recording time can be increased by using a larger-diameter flyer and a thicker LiF crystal.

Because of the long flight distance, velocity calibration was difficult to obtain, especially near 10 km/s. The F-P velocimeter would follow the motion of the flyer only part of the way to the target and then the signal was lost. This was finally resolved when we used a streak camera to record the impact of the flyer plate on a glass plate. Knowing the impact time and distance, we could extrapolate the early velocity-time record to give us the proper impact time and distance. Estimated errors in impact velocity are shown by the horizontal error bars in Figure 5.

The long flight distance also adversely affects the flatness of the flyer impact. Streak camera records of flyer impact after 5cm of flight show that impact is not simultaneous across the width of the flyer. We believe that most of the difference between measured and calculated pressures is due to this. Calculations show that if the portion of the flyer surface which strikes near the laser spot has a ridge, the pressure-time records will depend on the distance from the ridge to the laser spot, accounting for most of the scatter in the LiF technique results.

Sample Recovery:

All of the samples from the ballistic-technique experiments were recovered, and for some of the velocity calibration shots 3mm aluminum plates were used as witness plates to show the effect of the impact on a thinner target. At ~5 km/s, an impact crater was formed showing considerable plastic flow, but little melting except around the edges of the impact. At ~8 km/s and above, considerable melting was evident. The mass of the targets was measured before and after impact and a crude estimate can be made of the

depth of melt from these data. If we assume an idealized crater with a flat bottom and the same area as the 22.2mm square flyer, we obtain the estimate of average melt depth produced by the impact of 0.2mm thick Mylar flyers which is shown in Figure 6.

A LiF shot at 10 km/s with a 0.2mm thick Mylar flyer impacting a 1mm thick aluminum target recorded a peak pressure of 67 GPa at the Al/LiF interface. Figure 7 shows the calculated release temperature of shocked 2024 aluminum [3], with melt occurring at release from about 67 GPa, so the 9 km/s impact must melt the Al target to a depth of at least 1mm. This result is quite consistent with the estimated melt depths shown in Figure 6.

When 3mm thick Al plates were used in velocity calibration experiments at 10 km/s, a 0.2mm thick Mylar flyer simply blew a hole in the plates. When a second plate was added, spaced 6mm behind the first plate, the 0.2mm flyer also made a hole in the second plate. It should be noted that these plates had a small hole in them to pass the laser beam for velocity calibration, so these shots should be repeated with intact plates to confirm the results.

Simple Theories of Impulse Gain:

Some of the gain in impulse, which is observed when a flyer plate strikes a target, is due to the rebound of the flyer plate after the collision. If some simplifying assumptions are made about the material properties of the flyer and target, the momentum carried by the rebounding flyer is easy to compute. For example, if the flyer rebounded elastically from a much heavier target, the momentum gain would be nearly two. For non-elastic collisions, the Hugoniot jump conditions are used to compute the final state of the flyer at the instant it separates from the target.

The simplest model is one put forth by John Huntington [4] where one assumes that shock waves propagate in the target and flyer at the sound of speed, c. This will be referred to as the acoustic approximation. The Rankine-Hugoniot jump condition requires that

$$P = D_0 uc \tag{4}$$

where P is the pressure behind the shock waveD_0 is the initial density of a shocked material and u is the material velocity behind the shock wave. This can be expressed in terms of the shock impedance, x, of the material as

$$P = xu \tag{5}$$

where $x = D_0 c$. In this approximation, the (P,u) Hugoniot is linear with slope x. To compute the impulse gain in a collision, an impedance-matching calculation is done first to determine the state (P,u) which is produced at the collision interface. If it is further assumed that the materials release to zero pressure along an isentrope identical to the Hugoniot, one can compute the final state of the flyer, (o,u_r), where u_r is the rebound velocity. Using momentum conservation, one can then show that the momentum gain, G, is

$$G = 2X/(1+X) \tag{6}$$

where X is the ratio of target impedance to flyer impedance. This result predicts that the momentum gain in a collision between Kapton or Mylar and aluminum should be 1.61, shown as the dashed line in Figure 5. The agreement with the measured gains is quite good, considering the crudeness of the assumptions.

To refine the model, one can improve the assumption of a constant shock speed. Most materials exhibit a Hugoniot where the shock velocity, U, is a linear function of the material velocity, u.

$$U = c_0 + su, \tag{7}$$

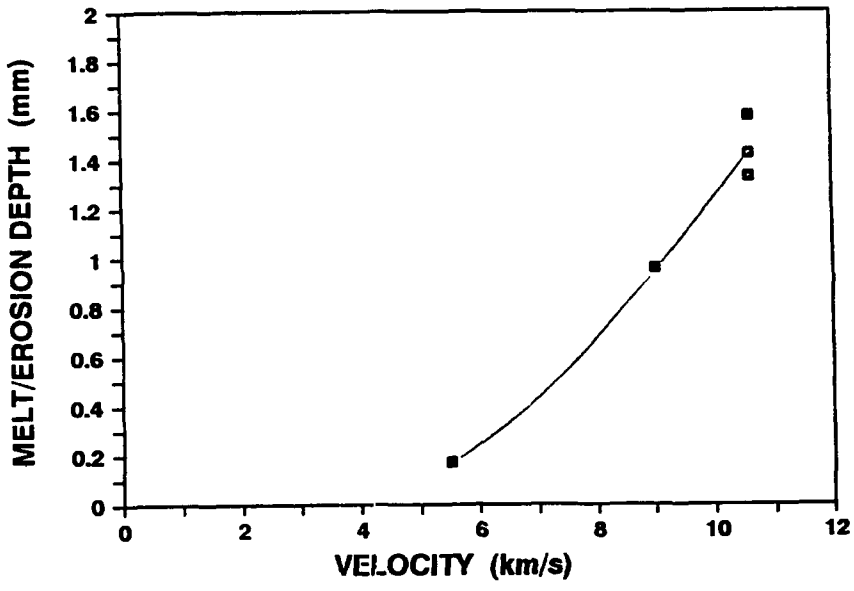


Figure 6. Average melt/erosion depth for aluminum samples impacted by 22.2mm, square, 0.2mm thick Mylar flyer plates.

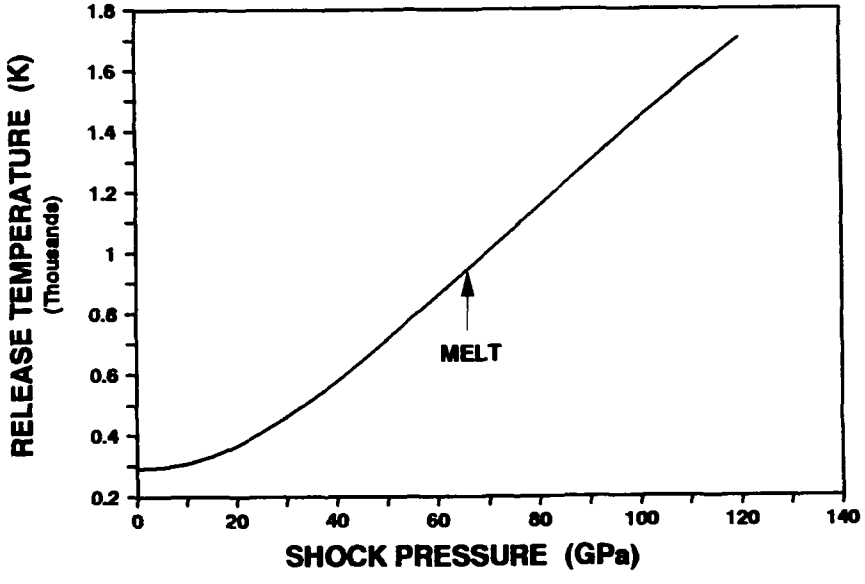


Figure 7. Calculated release temperature of 2024 aluminum [3].

where c_0 and s can be measured experimentally. If one again assumes that the release isentrope is identical to the Hugoniot, one can show that

$$G = 2(1-u/v_f), \tag{8}$$

where u is the initial velocity of the collision interface and v_f is the flyer impact velocity. The predicted impulse gain for a material with a linear (U,u) Hugoniot is shown in Figure 5 as the dotted line. The predicted impulse is somewhat lower than for the acoustic approximation and is in good agreement with most of the LiF data.

There are other effects which cannot be included in these simple models, and as the velocity of impact increases, these effects will become more important. The assumption that the release isentrope is identical to the Hugoniot becomes invalid at higher pressures. The simple models also cannot include the contribution of blow-off from the target surface or the vaporized flyer. The simple theories give a reasonable estimate of the flyer rebound which is a major contributor to impulse gain for the velocity range we have studied, but one would expect them to fail to account for an increasing fraction of impulse gain as the impact velocity continues to increase.

HYDROCODE CALCULATIONS

Modeling Considerations

Modeling is prompted by several factors. There is a need to relate the 3-D experiments to the 1-D operational case of greatest interest. Furthermore, experimental investigation of all eventualities is neither realistic nor affordable and therefore calculations must address many scenarios of interest. There is also an interplay between calculations and experiments. Carefully designed experiments benchmark code calculations and calculations provide a check on the reliability of experimental data. Calculations are credible to the extent that they incorporate all the relevant physics. Reasonable agreement enhances the credibility of both. The components that contribute to impulse gain are the incoming flyer momentum, the flyer rebound momentum, and the momentum of the melted or failed material ejected from the target. Hydrocode calculations treat all of the components and are the most powerful calculational means of simulating and understanding the impact of a membrane on a satellite structure at hypervelocities.

Modeling Calculations:

The JOY, Eulerian hydrodynamics code was selected because it is a well-documented code with 3-D capability that was developed for impact modeling. The equations of state (EOS) for the materials in the problem are an essential part of the calculation. For the 6061 aluminum targets and for LiF, a Gruneisen EOS was chosen from the LLNL EOS library which includes models for work hardening and melting. A Gruneisen EOS from the tabulation by Marsh [2] was used for the Kapton and Mylar flyers. EOS parameters are listed in Table I.

TABLE I. EOS PARAMETERS

Parameter	6061 Al	Kapton	Mylar	LiF
Density (g/cm^3)	2.7	1.43	1.40	2.63
Yield Str.(GPa)	0.29	0.2	0.2	0.36
Shear Mod. (GPa)	27.6	2	2	49.0
Gamma	1.97	0.5	0.5	1.69
Gamma Vol. Coeff.	0.48			0.34
c_0 (km/s)	5.24	2.66	2.57	5.15
s (km/s)	1.40	1.48	1.49	1.35

Before proceeding with the 3-D calculations, which are very costly in computer time, 1-D calculations were performed to explore parameter dependence and establish zoning requirements. First, the parameters of the Kapton EOS were varied. Changing c_0 and s in the (U,u) Hugoniot by ±20% had virtually no effect on the computed pulse gain. The flyer rebound momentum changes by ±10%, but this change was canceled by a corresponding and opposite change in the momentum carried by the ejecta from the target. Changing the initial value of the Gruneisen coefficient by 100% (from 0.5 to 1) increases the flyer rebound momentum by about 20%, the ejecta momentum by 10%, and the impulse gain by 4%. Thus a very weak dependence of impulse gain on the Gruneisen coefficient is observed.

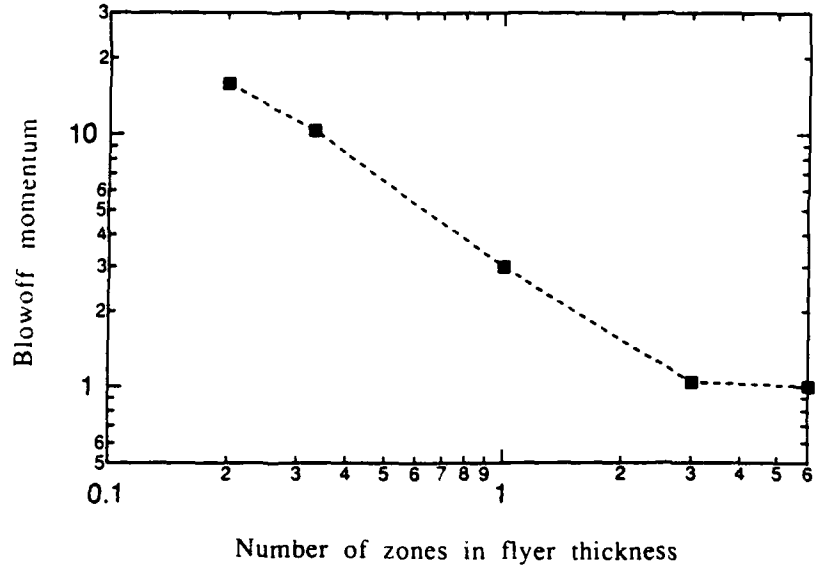


Figure 8. Calculated momentum of the ejecta as a function of the number of zones in the flyer. (1-D JOY calculation, 0.2mm Kapton flyer on aluminum at 10 km/s normal incidence).

Turning to zoning requirements, one first notes that accurate modeling of the shock as it moves through the target precludes varying the zone size along any direction in the calculation. Linear changes in the zone dimension produce spurious reflections if they are large enough to have an appreciable effect on the computational burden. Logarithmic changes do not faithfully preserve the shock profile. The flyer thickness needs to include enough zones to provide an adequate representation of the shock produced by the flyer impact. The normal impact of a 0.02cm thick Kapton flyer on aluminum was modeled and the number of zones was varied. The total momentum of the ejecta from the target as a function of zone thickness is shown in Figure 8. It is clear that the flyer needs to be at least 3 zones thick. A spuriously high value of ejecta momentum is obtained if the flyer is less than a zone thick. While zone dimensions greater than the zone thickness may seem a poor choice, such calculations have been presented and should not be taken seriously unless it can be demonstrated that the zoning is adequate to represent the problem of interest.

The experiments modeled in 3-D used a 0.03cm thick flyer to impact a 4.4 x 4.4 x 2.5cm aluminum target. The maximum zone dimension in the direction of the flyer thickness is 0.01cm, so approximately 400 zones were needed to cover the target and ejecta region. In the other directions, practicality and computer usage considerations prompt the use of 0.1cm resolution. The symmetries of the problem allow 1/4 of the target to be modeled by using reflecting boundaries. This implies about 24 zones in each of the other two directions, since there are boundary zones assigned by the code. A 3-D calculation involves ~200k zones, which takes 300 minutes of Cray YMP/8-128 time to run the problem to 5 microseconds after impact.

Failure of the target material is modeled to occur when one of the following conditions is met: When the tension is greater than 0.68 GPa, the density is less than 10% of the initial density, or the effective plastic strain exceeds a critical value, eps_{crit}. The first condition is the well-known spall strength of 6061-T6 aluminum. The density condition is the one used in the equation-of-state (EOS). Changing the density condition by 50% has a negligible effect on the results. The value chosen for eps_{crit} has negligible effect on the calculated impulse gain, but does influence the calculated ejecta mass.

Comparison of 3-D Calculational Results With Data:

A full 3-D calculation was run of a 0.030cm thick, 1.6cm square Kapton flyer impacting a 4.4 x 4.4 x 2.5cm aluminum target at 10 km/s. The experimentally measured quantities were target momentum after it moves as a rigid body and mass loss from the target. In addition, the shape of the crater left by the flyer impact was measured. In the calculation, the flyer breaks up after impact, but rebounds with a momentum about 0.3 of the incident momentum. Mass ejection causes the target momentum to increase, reaching a steady value of about 3 microseconds after impact, as shown in Figure 9. At 3 microseconds the calculated impulse gain is 2.7. It is difficult to calculate target mass loss, because much of the failed material is surrounded by non-failed material, corresponding to the cracks and voids observed in sectioned, recovered targets. In the calculations and the experiments, the crater depth did not exceed 0.5cm. Taking $eps_{crit} = 0.3$, the mass of aluminum which failed in the first 0.5cm of the target was about 15 times the flyer mass.

Early experiments gave large values of impulse gain, but after adjustments to mitigate magnetic effects, the experimental values for the conditions modeled were in the range 2.5-3. Experimental mass loss was 13 times the flyer mass. The level of agreement between calculations and the data is heartening.

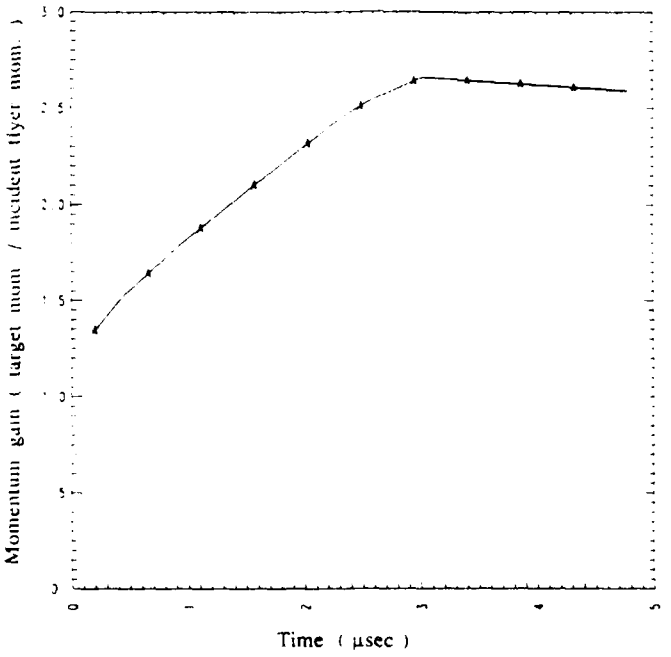


Figure 9. Target momentum as a function of time in the direction of the incident momentum.

The last comparison between the 3-D calculations and data is the impact crater profile. In JOY there is an easy way to determine the boundary between failed and unfailed material, since the effective plastic strain is set to zero after the material fails. Figure 10 is a photograph of the target sectioned through its center. The slight asymmetry of the measured crater is removed by averaging the profile about the plane of symmetry, allowing the comparison between the calculated and measured profiles shown in Figure 11. The calculated crated is deeper near the edge of the flyer impact boundary, which is not obvious in the measured profile shown in Figure 16, but the agreement is generally quite good.

Comparison of 3-D and 1-D Calculations:

Now that the calculations have been shown to be in good agreement with the data, they can be used to relate the 3-D experimental situation to the 1-D case of interest. The comparison is straight-forward, but some care needs to be taken since the spall-suppression holes cannot be modeled in 1-D. For a 2.5cm thick target, the shock has not reached the rear at 3 microseconds, so spall is not an issue, and 1-D and 3-D calculations give the same flyer rebound momentum (0.3). The target ejecta momentum is much lower for the 1-D case and the calculated impulse gain is ~1.6, compared to ~2.7 for the 3-D calculation. This is an interesting result which suggests that there is a significant edge effect in the 3-D calculations. An edge effect is obvious in the flyer impact craters, and the ~2.7 impulse gain agrees quite well with the measured gains in the ballistic experiments at 10 km/s.

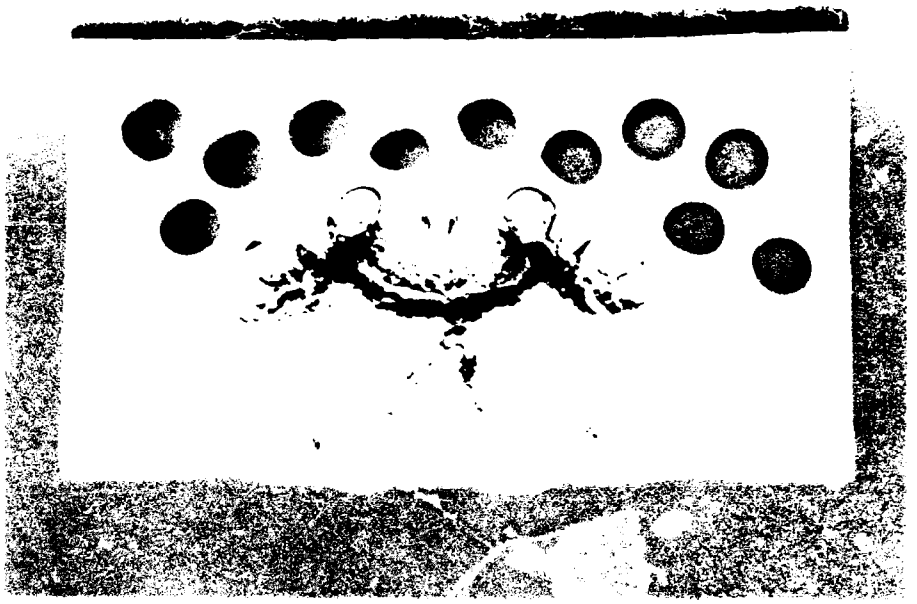


Figure 10. Central section through a recovered aluminum target.

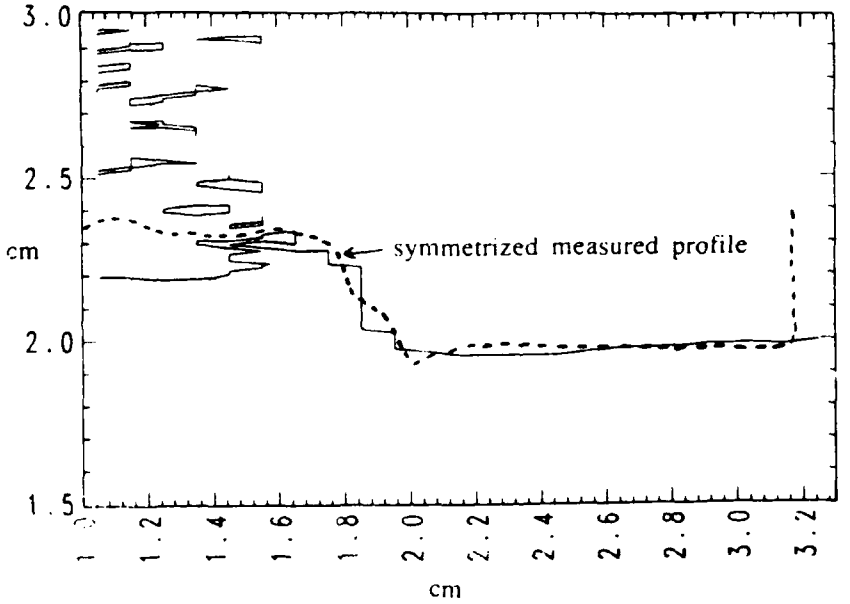


Figure 11. Comparison of measured and calculated crater profiles for central section through the target.

Pressure Profile Calculations:

The difference between the 1-D and 3-D results can be better understood if we compare the 1-D calculations with 1-D experiments using the LiF technique, discussed above. Impulse gains measured with the 1-D technique are in excellent agreement with the 1-D calculational results (see Figure 6). The JOY code was used to calculate pressure profiles at the aluminum/LiF interface in the LiF-technique experiments. Very fine zoning was needed to capture the peak of the profile. A zone thickness of 10 microns was used. Propagation of shocks in hydrocodes requires the use of artificial viscosity. The JOY default values were used: no linear term and a coefficient of 2 for the quadratic term. Experimental and calculated pressure profiles at a depth of 1mm in aluminum impacted by a 0.2mm thick Mylar flyer are shown in Figure 12 for a flyer velocity of 9 km/s.

Comparison of Calculated and Measured Pressure Profiles:

The integrals of the pressure profiles, which represent the target impulse, were also computed. The data shown in Figure 12 represents the best agreement between calculated and experimental results. For all of the shots, the measured impulses were within 18% of the calculated values, while the differences in peak pressure were somewhat larger. Table II lists peak pressures, impulses and impulse gains.

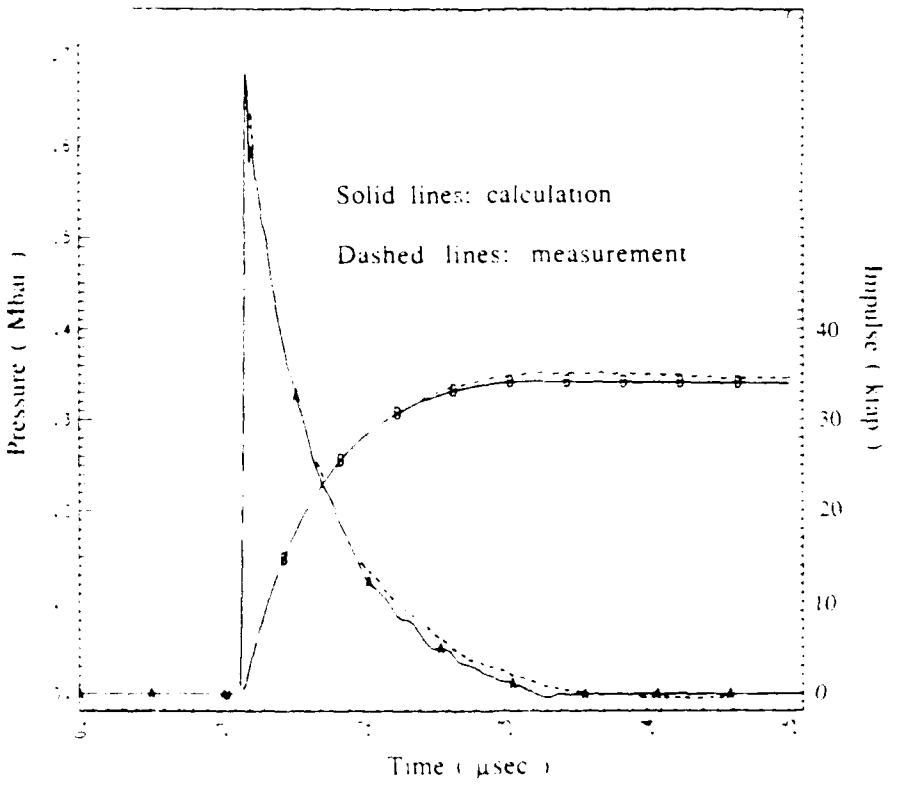


Figure 12. Pressure-time profile and impulse (integral of pressure-time) at 1mm depth in aluminum normally impacted by a 0.2mm Mylar flyer at 9.0 km/s.

TABLE II.

Comparison of measured and calculated peak pressure, impulse and impulse gain. Type 1 flyers were 0.2mm thick Mylar, Type 2 flyers were 0.3mm thick Kapton.

	MEASURED				CALCULATED		
Type	VEl. (km/s)	pk. Press (GPa)	Imp. (kTap)	Gain	Pk. Press. (GPa)	Imp. (kTap)	Gain
1	5.5	23	19	1.2	41	19	1.2
1	9	67	35	1.4	68	34	1.4
1	10.4	96	48	1.7	80	41	1.4
2	6.3	39	31	1.2	53	34	1.3
2	8.5	65	47	1.3	81	48	1.3
2	10.2	79	52	1.2	108	59	1.4

There may be evidence for a systematic trend, the measured gains for the Mylar flyers are all equal to, or higher than, the calculated ones - the reverse is true for the Kapton flyers. Differences between calculations and measurements may be due to several factors. On the calculational side, there may be physics processes not included in the code. On the experimental side there are uncertainties in measurement of the sharply spiked pressure profile, flyer velocity, and deviations from flatness in the impact. Calculations show that if there is a significant bulge in the flyer at impact near the measurement point (laser spot), significant deviation in peak pressure and impulse may be measured, relative to a flat impact. This, along with velocity calibration errors, are the most significant sources of experimental error, as reflected by differences between calculated and measured values in Table II.

CONCLUSIONS

At impact velocities up to 10 km/s, impulse gain for Mylar and Kapton flyers is consistent with predictions of simple theories for the rebound of the flyer and with hydrocode calculations. The rise in impulse gain at 10 km/s we observed using the ballistic technique is probably due to edge effects in the 3-D interaction between the flyer and target. Targets recovery showed that a 0.2mm Mylar flyer moving at 10 km/s causes almost total failure of a 3mm thick aluminum target. The impact melts the aluminum to a depth of 1mm or greater, produces spall from the back, and the remaining material fails at the edges of the impact region.

ACKNOWLEDGMENTS

We gratefully acknowledge the work of Jim Wade and Art McAlice for their hard work and dedication in building and firing the shots.

REFERENCES

1. J.E. Osher et al., "Operating Characteristics and Modeling of the LLNL 100-kV Electric Gun", IEEE Trans. on Plasma Science, 17, 1989.

2. S.P. Marsh, Ed., LASL Shock Hugoniot Data, University of California Press, Berkeley, 1980.

3. R. Kinslow, Ed., High Velocity Impact Phenomena, Academic Press, New York, 1970, pp.530-531.

4. J. Huntington, Huntington Research and Engineering, San Jose, CA, Private Communication.

Int. J. Impact Engng Vol 14, pp 467 - 477, 1993
Printed in Great Britain

0734-743X/93 $6.00 + 0.00
1993 Pergamon Press Ltd

CREATION AND SIMULATION OF VERY FAST JETS

J.P. LEYRAT* - E. CHARVET** - H.C. PUJOLS***

*C.E.A - Centre d'Etudes de Vaujours-Moronvilliers - B.P. 7 - 77181 - Courtry - France
**C.E.A - Centre d'Etudes de Limeil-Valenton - 94195 - Villeneuve St Georges Cedex - France
***C.E.A. - Centre d'Etudes scientifiques et techniques d'Aquitaine -BP 2 - 33114 - Le Barp - France

ABSTRACT

We propose a concept in order to produce very fast metallic jets (which speed could exceed 20 km/s). It uses the detonation wave of an explosive cylinder to initiate a high compression on the rear face of a metallic target ; the jet is created on the front surface, in a cylindrical cavity. Many experiments were performed, in which we tested different metals and various geometries of cavity. Numerical calculations with PLEXUS (finite element 2D or 3D code) and CEL (finite difference 2D code) were used to understand the phenomenology of the creation and propagation of these jets ; the correlation with the experimental results (about the shape of the jets and their speed) is good.

The experimental device described in this paper was patented (patent n° 90 11684 - 09/26/1990)

INTRODUCTION

In a classical shaped charge with a metallic liner, the velocity of the jet cannot exceed a limit (Defourneau, 1970, Walter and Zukas, 1989) which is proportional to the sound speed of the liner material. For instance, the maximum velocity of an aluminum jet is about 13 km/s ; for a copper jet, it is 10 km/s. Therefore, an improvement of these performances requires other charges concepts.

In this study, we propose a device to generate very fast jets, which velocity could sometimes exceed 20 km/s. The principle of operations, previously mentioned by Asay *et al.* (1976) consists in transmitting a shock wave to a metallic target in which a cylindrical cavity is bored, so that we combine two effects : the increase of velocity in the material at the bottom of the cavity and the implosion of this cavity.

In a first section, we describe the experimental facility and the main results obtained with it ; afterwards, we present a numerical study, which purposes are a correlation with the experiments, the understanding of the mechanisms of jet creation and the optimization of these jets.

EXPERIMENTS

The experimental device

The experimental device we use to generate fast jets (fig. 1) is composed of an explosive cylinder (diameter 120 mm, height 150 mm), where a plane detonation wave is initiated. In a first configuration (fig. 1-a), this wave transmits a shock to a thin copper plate, which is projected upon a metallic target (thickness e) with a cylindrical cavity characterized by its diameter D, its depth h and the radius of curvature at the bottom r (equal to D/2 for an hemispherical bottom). The jet is obtained when the compression wave due to impact reaches the bottom of the cavity. Another experimental configuration (fig. 1-b) consists in using directly the detonation of the explosive cylinder to produce a shock wave in the target.

The jets are vizualised by using high speed cinematography, with argon flashes put close to the jet. Dimensional markers are located on the front side of the flashes, in order to measure the jet velocity.

Experimental results

About 30 shots were performed with different target materials (copper, aluminum alloy 2024, uranium alloy) and various cavity geometries (diameter D between 10 and 80 mm, depth h between 3 and 90 mm, radius of curvature r between D/2 and ≈0).

The jets were very fast, and velocity increased as r decreased. For instance in an aluminum target with an hemispherical bottom (D 20 mm, h 20 mm, r 10 mm), the maximum speed of the jet was 9.7 km/s ; with a "flat" bottom (D 20 mm, h 20 mm, r 1 mm), it was 21.5 km/s (figure 2). With a copper target, similar effects were obtained, although the jet velocities were smaller : in a cavity D 30 mm, h 30 mm, we measured 5.3 km/s with an hemispherical bottom, and 15.5 km/s with r = 3 mm.
Furthermore, we noticed a large difference in the shape of these jets, according to the geometry of the cavity (fig. 2). The jets created in cavities with hemispherical bottom (fig. 2-a) were relatively thick and generally topped by a protuberance (more visible with 2024 Al jets). On the contrary, with "flat bottom cavities" (fig. 2-b and 2-c), we observed three different zones in the jets : a thick and relatively slow backward part, very similar to the jets obtained in hemispherical bottom cavities, a larger protuberance in the middle and, before it, a thin dart, which make up the high speed part of the jet.

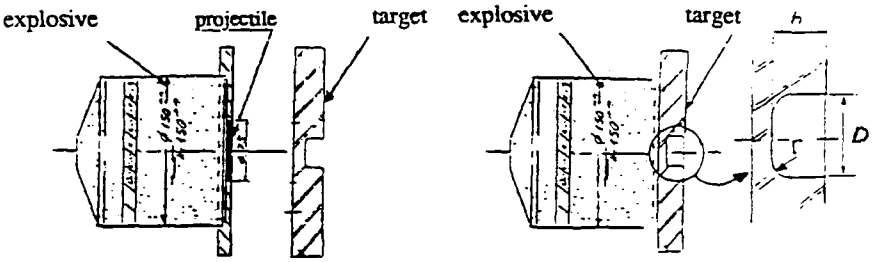
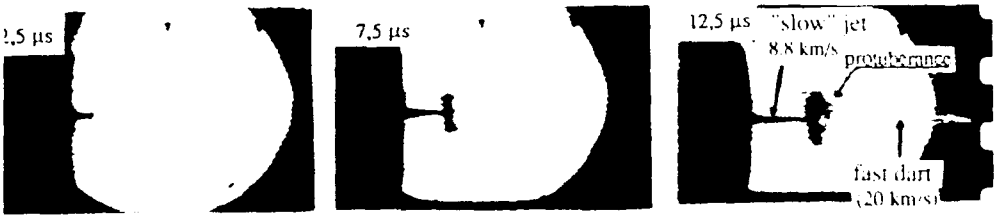


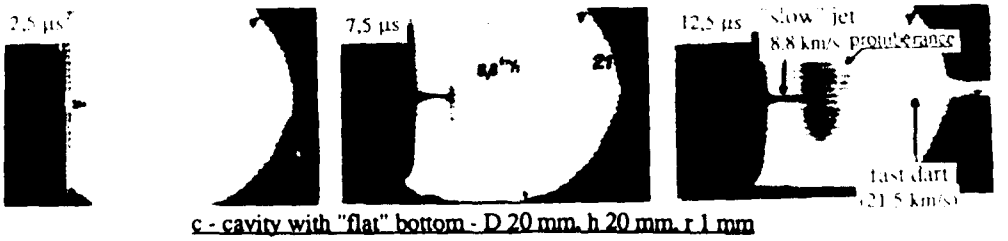
Figure 1 - The experimental device



a - cavity with hemispherical bottom - D 20 mm, h 20 mm, r 10 mm



b - cavity with "flat" bottom D 20 mm, h 20 mm, r 5 mm



c - cavity with "flat" bottom - D 20 mm, h 20 mm, r 1 mm

Figure 2 - Visualization of the jets (2024Al targets)
zero time = the instant where the jet spouts out the cavity)

The coherence of these jets seems to be quite good, since they are able to induce significant damages at long distances. For instance, an aluminum jet (cavity D 20 mm, h 20 mm, r 5 mm) can perforate 80 mm of steel at a distance of 400 mm ; a copper jet (cavity D 50 mm, h 40 mm, r 20 mm) go through 400 mm of high strength steel at 500 mm.

NUMERICAL CORRELATIONS

Numerical codes

A correct simulation of these experimental results requires numerical codes with appropriate equations of state and dynamic behaviour laws : a purely hydrodynamic model seems correct to describe the actual jet (where temperature is sufficiently high to obtain melting and, sometimes, partly vaporization), but not the periphery of the cavity, which is mostly solid, and where elastoplasticity must be taken into account.

Two codes were used in this study : PLEXUS and CEL (Leyrat *et al.*, 1991).

PLEXUS is a finite element 2D or 3D code, with an explicit time-algorithm. Consequently, it is appropriate for solving mechanical problems at high strain rate, and with large deformations. In this code, we can use the Wilkins equation of state, a 2-phases EOS with a Mie-Grüneisen formulation in compression, and a Puff one in tension :

$$\rho>\rho_0 : P = K\mu + D\mu^2 + S\mu^3 + \Gamma\rho E \quad (1)$$

$$\rho<\rho_0 : P = \rho[H+(\Gamma-H)\sqrt{\eta}]\left\{E-E_s\left[1-\exp\frac{K}{\Gamma\rho E_s}\frac{1}{\eta}\left(1-\frac{1}{\eta}\right)\right]\right\} \quad (2)$$

P is the hydrostatic pressure, ρ the density, E the energy per unit mass ; μ and η characterize the "compression" of the material (η = ρ/ρ0 , μ = η − 1). Γ is the Grüneisen ratio, K the bulk modulus, D and S are the quadratic and cubic coefficients of the polynomial development of P ; Es is the vaporization enthalpy ; H = γ - 1, with γ : polytropic coefficient of gas.

Various behaviour laws are available in PLEXUS. For metals, we use the classical SCG model developed by Steinberg *et al.* (1980), which takes into account the variation of the shear modulus G and of the flow stress Y with temperature, hydrostatic pressure and equivalent plastic strain ε_p :

$$G = G_{PE}\left(\frac{p}{\eta^{1/3}}\right) + G_0\left[G_{PE}(T - 300) + 1\right] \quad (3)$$

$$Y = (\beta_1 + \beta\varepsilon_p)^r\left[Y_0(1 + G_{PTE}(T - 300)) + Y_{PE}\left(\frac{p}{\eta^{1/3}}\right)\right] \quad (4)$$

with : $$(\beta_1 + \beta_{ep}) \le Y_{max} \quad (5)$$

This model is available until the "actual" melting temperature T_{fm} defined with a Lindemann law :

$$T_{fm} = T_m\eta^{2(\gamma_0-a-1/3)}\exp\left[2a\left(1 - \frac{1}{\eta}\right)\right] \quad (6)$$

T_m is the melting temperature for $\rho = \rho_0$; at higher temperatures, calculations are performed in hydrodynamic conditions. The 11 parameters of the SCG model were determined from high strain rate experiments, especially Taylor tests (Steinberg *et al.*, 1980, Gust, 1982).

The finite differences 2D code CEL has a mixed Eulerian and Lagrangian scheme. Different EOS can be used for jet simulations : the Wilkins equation above mentioned, multiphasis EOS or Sesame EOS. Moreover, it is possible to use the SCG model, with the same formulation as in PLEXUS.

The results obtained with these 2 codes are very similar. For instance, with a 2024 Al target D 20 mm, h 20 mm, r 1 mm, the maximum jet velocity is 21 km/s if calculated with PLEXUS, and 23 km/s with CEL (with Eulerian or Lagrangian mesh). For a copper target D 30 mm, h 30 mm, r 3 mm, we found 13 km/s with PLEXUS and 13.5 km/s with CEL.

Correlation with experimental data

The drawings of the distorted meshes at different times (figure 3 and 4) correlate well to the photographs of fig. 2, and especially the difference upon the shape of jets created in cavities with hemis-pherical or flat bottom.

Table 1 summarizes the comparison between experiments and calculations upon the maximum jet speed ; the correlation seems quite good. However, the numerical values slightly underestimate the experimental velocities for copper targets, and overestimate them for 2024 Al. In point of fact, the most important discrepancies (10 to 20%) are always observed for experimental configuration as described in fig. 1-b : in this case, the initial condition in target (a pressure versus time transmitted at the rear surface) is not so well known as for fig. 1-a configuration (where the velocity of the flying plate can be accurately mesured).

Therefore, we might consider that the numerical simulations correctly describe the experimental results, and we tried to specify the mechanism of the jet creation through a phenomenological study presented as follows.

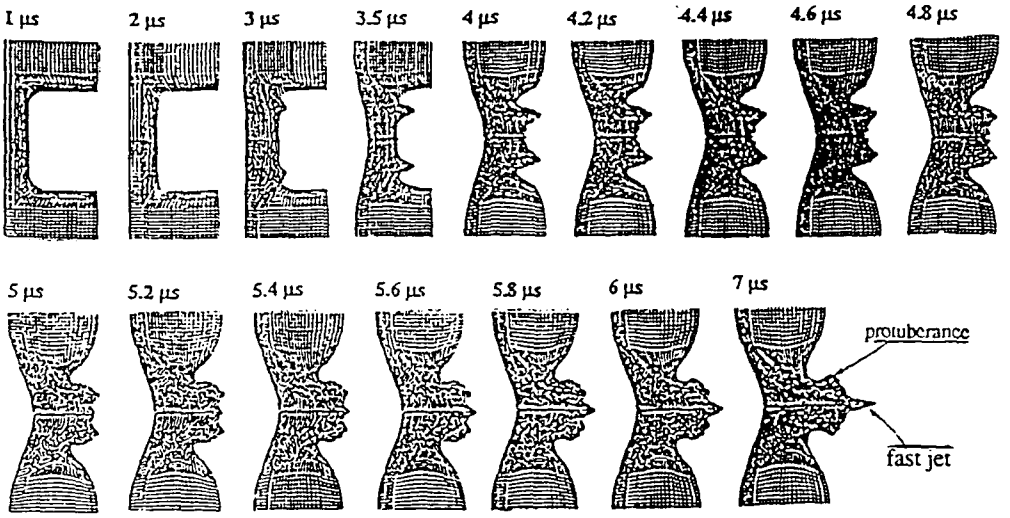
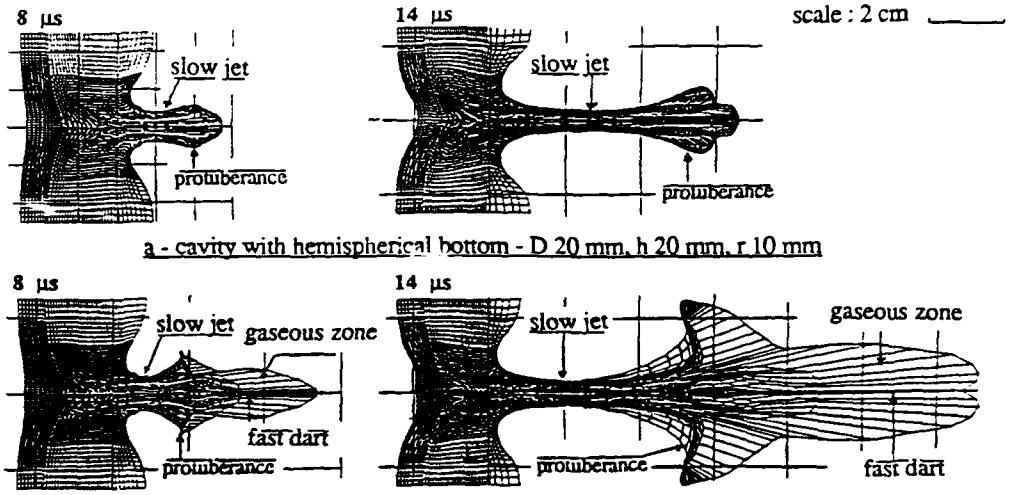


Figure 3 - Visualization of jet formation (2024Al target D 20 mm, h 20 mm, r 5 mm)
Lagrangian calculations with PLEXUS - zero time = initiation of the shock wave in the target



a - cavity with hemispherical bottom - D 20 mm, h 20 mm, r 10 mm

b - cavity with "flat" bottom - D 20 mm, h 20 mm, r 1 mm

Figure 4 - Distorsion of the mesh (2024Al targets)
Lagrangian calculations with CEL - zero time = initiation of the shock wave in the target

Table 1. Correlation between experiments and calculations
(calculations were performed with CEL * or PLEXUS **)

Target matl	e (mm)	D (mm)	h (mm)	r (mm)	V exp (km/s)	Vcalc (km/s)
2024 Al	30	20	20	1	21.5	23*, 21**
	30	20	20	5	20	20*, 18**
	30	20	20	10	9.7	11.6*
	37.5	30	30	15	9.3	11.6*
Copper	30	20	20	1	19	15.5*
	30	20	20	5	14.5	12**
	40	30	30	3	15.5	13.5*,13**
	40	30	30	15	5.3	5*

PHENOMENOLOGICAL STUDY

We studied with CEL the jet creation in 2024Al targets (e 33 mm, D 20 mm, h 20mm, r 10 or 1 mm); the initial condition is here a calibrated pressure curve P(t) on the rear surface of the target (maximum pressure : 423 kilobars). We visualized the phenomenon with isobar drawings until 5 µs (fig. 5) and velocities curves vs time for different points of the cavity (fig. 6). It is not possible to simulate the whole extension of the jets (because of mesh distortions in Lagrangian simulations, and of too long computation times in Eulerian ones). So, we limited the jet propagation study at 20 µs.

Cavity with hemispherical bottom (r = 10 mm)

The plane shock wave due to the detonation of explosive go through the plate at the sound velocity of aluminum (≈ 5 to 6 km/s) ; the pressure intensity is about 500 kilobars. At 1.7 µs, the shock wave reaches the bottom of the cavity on the axis, which begins to move forward (velocity ≈ 4 km/s). A release goes back to the rear surface, and diminishes the pressure.

Near the axis, the shock wave has still not reached the free surface of the cavity ; this zone is in compression, and tends to release in the direction of the axis, where pressure is lower. A shaped charge effect is produced, with two consequences :

- the velocities of the points out of the axis have a centripetal component ;
- thus, there is an accumulation of matter on the axis, which tends to reduce the intensity of the release and to increase the jet velocity.

The phenomenon expands step by step ; as soon as the points of the free surface are reached by the shock wave, they are ejected forward and toward the axis. At 2 µs, the hemispherical part of the cavity is entirely in motion, and, at 4 µs, the whole plate is reached by the initial shock.

Therefore, the jet velocity (very homegeneous) uniformly increases until 5 µs ; its maximum is then 9 to 10 km/s. The jet is dense ($\rho \approx 3$ g/cm^3 in the front part, 3.5 g/cm^3 in the rear part) and partly liquid.

At 5 µs, this "implosion" is over. The velocities in jet have no more centripetal component ; we even observe a centrifugal movement at the periphery and in the front part of the jet, due to the rebound of the matter upon the jet axis, which is denser ; this explains the protuberance visualized both in experiments and calculations.

After 5 µs, the jet is progressively extending. Its velocity and diameter remain constant (v_{max} = 10 km/s, Φ = 8 mm in the thinner part), while the protuberance becomes larger (Φ = 10 mm at 9 µs, Φ = 24 mm at 20 µs). The jet, which homogeneity diminishes, is schematically composed of two parts (fig. 7) :

- a central liquid core, very coherent and at nearly nominal density ($\rho \approx 2.5$ g/cm^3) ; its diameter is about 3 mm, and it is composed of matter initially near the axis of the plate ;
- a peripheral sheath, very heterogeneous, which density progressively decreases from the jet base (where it is of the same order as on the axis) to the protuberance (≈ 0.5 g/cm^3 at 20 µs).

Cavity with flat bottom (r = 1 mm)

As for previous configuration, the shock wave reaches the bottom of the cavity at 1.7 µs, but here, the whole "flat" part of the cavity moves forward, and the reflected release is almost one-dimensional, except near the "curved" zone, where the shaped charge effect appears. In this zone, we observe roughly the same phenomena as for an hemispherical bottom : first, a rapid increase of velocity (4 km/s), then a progressive acceleration. However, the concentration of matter is obtained on a circular crown, so that a "torus" jet is induced ($\rho \approx 2.2$ g/cm^3, longitudinal velocity ≈ 6 km/s).

Near the axis, since the release is not immediately disturbed by the shaped charge effect, the pressure decays to zero, and the velocity remains unchanged (4 km/s). Afterwards, the centripetal compression wave (initiated at the periphery of the cavity, and due to the release of the side zone of the plate) is focused at 3.6 µs ; the pressure and the density increase then rapidly and highly (P > 400 kbar, $\rho > 4$ g/cm^3), and an axial jet appears (velocity ≈ 8 km/s).

Meanwhile, the torus jet tends to converge on the axis, because of the centripetal component of velocity. At 4.6 µs, its implosion is sufficient to confine the axial jet, later but faster : the convergence of these two jets gives rise to an hyperfast jet, composed of the front part of the axial jet, and the inner part of the torus jet. The velocity increases highly (21 km/s), and the maximum temperature (> 3000 °C) is sufficient to partly vaporized the jet.

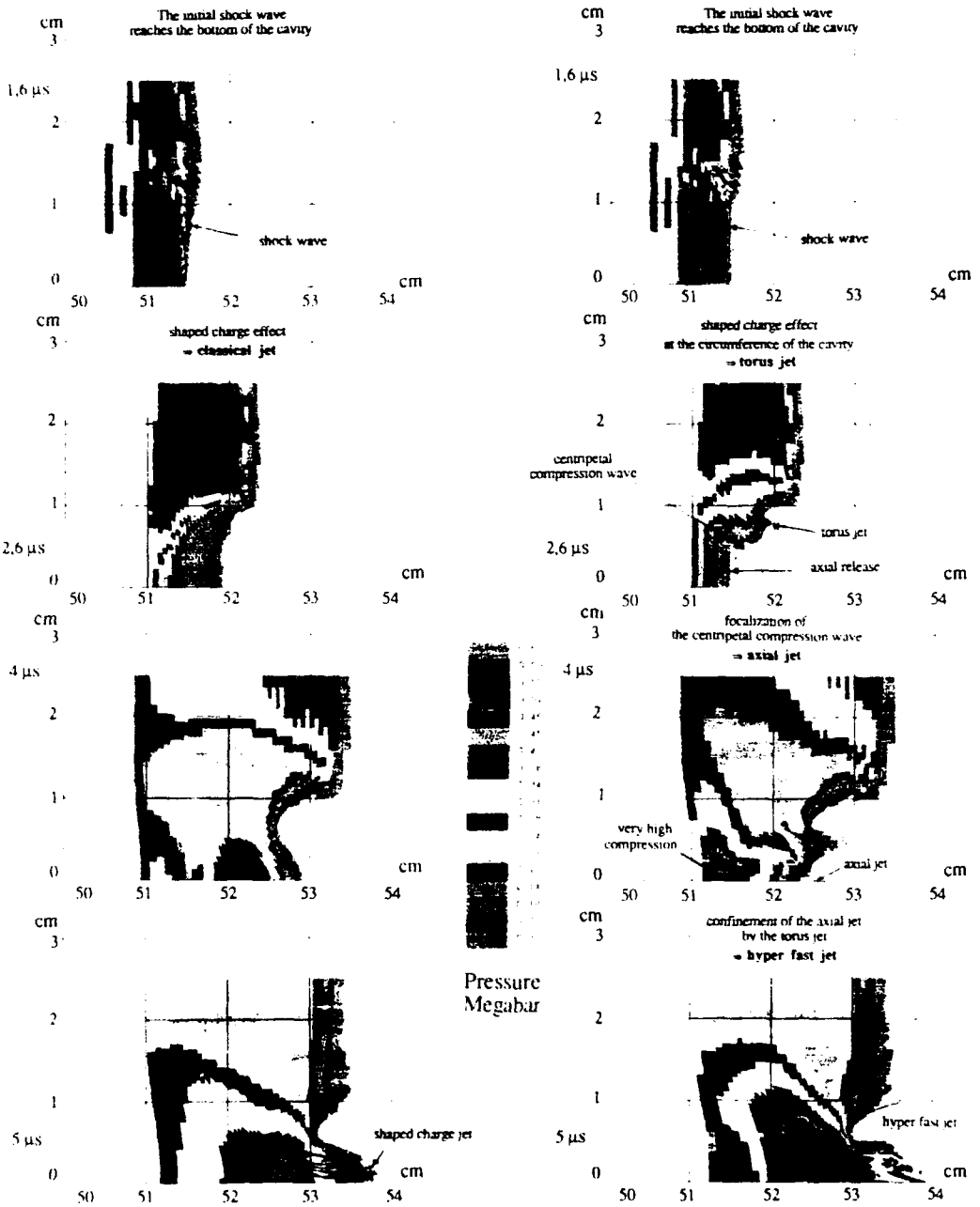


Figure 5 - Visualization of jet formation - Evolution of the pressure
2024Al target - Lagrangian calculation with CEL

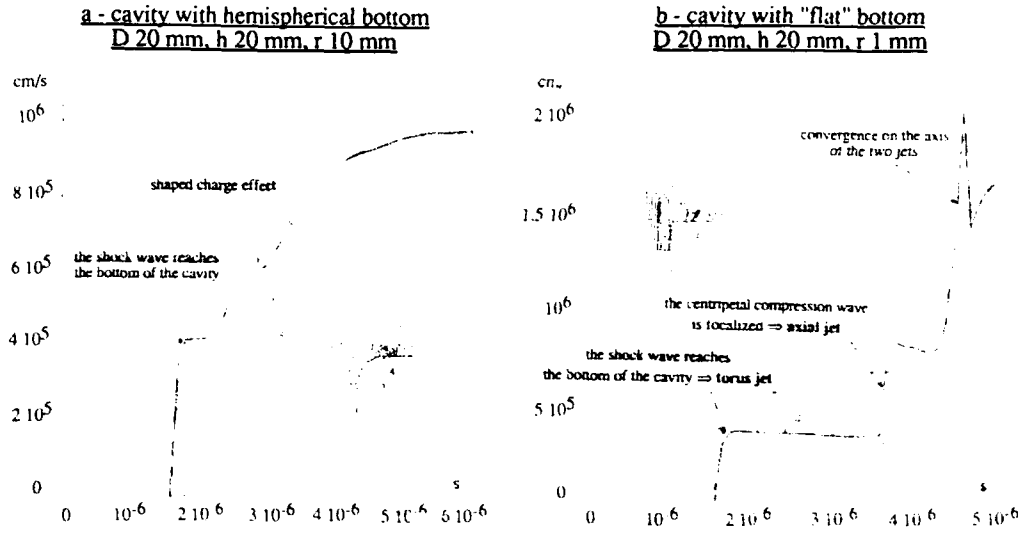


Figure 6 - Longitudinal velocity versus time for different points at the bottom of the cavity (2024Al targets) - Calculations with CEL

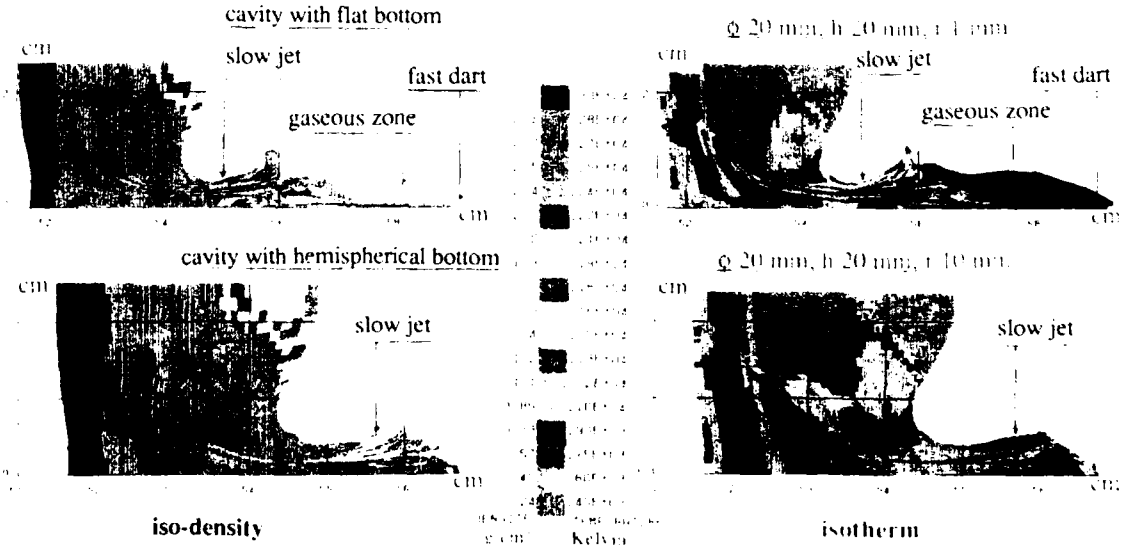


Figure 7 - Comparison between 2024Al jets created in cavities with hemispherical or flat bottom Iso-density and isotherm diagrams 8 µs after impact -Lagrangian calculations with CEL

The external part of the torus jet rebounds upon the dense layers of the axis, and creates a large protuberance, while the back part of the axial jet (which is behind the focused zone) is not so much accelerated ; this explains the three part-shape of the jet ("slow" jet - protuberance - hyperfast jet) observed in experiments.

The propagation of these three zones is very different (fig. 7) :

- the slow jet is very similar to those obtained with "hemispherical bottom cavities", although the central core and the peripheral sheath are here separated by a thin very hot zone, which appears when the axial and torus jets converge. The core is rather dense, and its very homogeneous speed tends to increase slightly (8 km/s at 9 μs, 11 km/s at 20 μs) : this is due partly to the good confining by the peripheral zone, and to an"entrainment" of the hyperfast jet.
- the protuberance expands more rapidly than in hemispherical bottom configurations, because of the release of the hottest zone (Φ = 15 mm at 9 μs, Φ = 80 mm at 20 μs).
- the hyperfast jet is composed of a central thin dart (Φ = 1 mm), liquid and relatively dense ($\rho \approx 2$ g/cm^3), and of a gaseous very hot zone (T > 3000 °C, $\rho < 0.1$ g/cm^3) which diameter increases (Φ = 10 mm at 9 μs, Φ > 60 mm at 20 μs) ; because of its low density, this "cloud" cannot be observed in experiments. The velocities in the dart become more and more homogeneous : the maximum speed at the tip decreases (21 km/s at 5 μs, 16 km/s at 20 μs : this decrease is probably overevaluated with a Lagrangian mesh), while a slight acceleration is visible near the protuberance (10 km/s at 5 μs, 12 km/s at 20 μs).

The main points of comparison between the two types of jets are summarized on tables 2 (jet creation) and 3 (jet composition).

Table 2. Jet creation - comparison between cavities with hemispherical or flat bottom

	Hemispherical bottom D 20 mm, h 20 mm r 10 mm	Flat bottom D 20 mm, h 20 mm r 1 mm
Jet creation	1) Initial velocity due to shock wave on the axis t = 1.7 μs → v = 4 km/s 2) Progressive increase of velocity at periphery : → shaped charge effect ; → concentration of matter on the axis ; → Progressive increase of v : t = 1.7 to 5 μs → v = 9 km/s	1) Initial velocity due to shock wave on the "flat" part : t = 1.7 μs → v = 4 km/s 2) Shaped charge effect in the "curved" zone : → torus jet v = 6 km/s ; → centripetal compression wave focused on the axis at 3.6 μs : → axial jet v = 8 km/s ; 3) Convergence of the 2 jets : t = 4.3 μs → v = 21 km/s
Velocity *after 5 μs*	9 to 10 km/s *very homogeneous*	21 km/s (hyperfast jet) 10 km/s ("slow" jet)
Density at 5 μs	2.8 to 3.5 g/cm^3	0.8 to 3.5 g/cm^3
Temp. at 5 μs	200 to 1300 °C	400 to > 3000 °C

Table 3. Jet composition - comparison between cavities with hemispherical or flat bottom

	Hemispherical bottom D 20 mm, h 20 mm r 10 mm	Flat bottom D 20 mm, h 20 mm r 1 mm
Back part	1) Constant velocity at all points and vs time v = 9 to 10 km/s 2) Constant Φ = 8 mm 3) Central liquid core : Φ 3 mm ρ 2.5 g/cm^3 + Heterogeneous peripheral zone	1) Constant velocity at all points slightly increasing vs time : v = 8 km/s at 9 μs, 11 km/s at 20 μs 2) Φ diminishes vs time : Φ = 8 mm at 9 μs, 7 mm at 20 μs 3) Same composition as opposite + very hot layer between core and periphery
Protuberance	1) Constant velocity v = 9 km/s 2) Φ increases vs time : Φ = 10 mm at 9 μs, 24 mm at 20 μs 3) Very heterogeneous zone	1) Roughly constant velocity v ≈ 10 km/s 2) Φ highly increases vs time : Φ = 15 mm at 9 μs, 80 mm at 20 μs 3) Very heterogeneous zone
Hyperfast part of the jet	non-existent	1) more and more homogeneous velocities $v_{max} \approx 21$ km/s $v_{lim} \approx 15$ km/s 2) Central liquid dart Φ 1 mm ρ 2.5 g/cm^3 + Gaseous peripheral zone $\rho < 0.1$ g/cm^3 Φ rapidly increases : 10 mm at 9 μs, > 60 mm at 20 μs

OPTIMIZATION OF JET PERFORMANCES

Evaluation of jet penetration

The performance of a given jet can be defined as its penetration ability in a thick plate, i.e. with two parameters : the **penetration depth** ℓ and the **crater volume** ϑ. Various models were built up to evaluate the influence of the characteristics of an homogeneous, cylindrical jet of uniform velocity. The simplest one is a purely hydrodynamic model (Birkhoff, 1948). Other authors (Szendrei, 1983) took into account various effects (elastoplasticity in the plate, crushing of the jet upon the plate...). The main result of all these models is :

- a variation of ℓ as $\Omega = L\sqrt{\rho}$, where L and ρ are the length and density of the jet ;
- a variation of ϑ as the kinetic energy in the jet $Ec = 0{,}5\ V\ \rho\ v^2$ (V : jet volume, v : jet velocity).

In the case of the "real" jets obtained in our experiments, let us neglect the effect of the peripheral heterogeneous zones ; that amounts to saying that the performances of these jets are due to their "axial" part only (liquid core with hemispherical bottom cavities, core + hyperfast dart with flat bottom cavities). Then, the above conclusions are still valid, and we may estimate the penetration power for the two types of jets with parameters Ω and E_c.

Since it is not possible to simulate numerically the total extension of the jets, we cannot estimate directly Ω and E_c when the jets are completely shaped. Nevertheless, the results obtained at 20 µs (table 4) are sufficient to compare the jets capacities.

Table 4. Energetic balance in 2024 Al jets at 20 µs
(* we neglect the mass of the gaseous part of the jet)

	Hemispherical bottom cavity D 20 mm, h 20 mm	Flat bottom cavity D 20 mm, h 20 mm, r 1 mm
Jet length (cm)	9.2	18.0 (dart : 10.2)
Jet velocity (km/s)	10.0	dart : 16.0, core : 12.0
Jet mass (g)	2.8 (core : 0.6)	2.5* (dart : 0.15, core : 0.6)
Ω ($g^{1/2}cm^{-1/2}$)	core : 14.5	dart : 14.4, core : 12.3
Kinetic energy (kJ)	core : 30.0	dart : 20.0, core : 43.0

We observe that Ω and E_c at 20 µs are about two times higher for jets created in flat bottom cavities than for "classical" jets obtained in "equivalent" hemispherical bottom cavities (with identical thickness e, diameter D and depth h).
Furthermore, if we admit :

- that the jet remains coherent even for important elongations ;
- that the velocity distribution does not significantly vary during the jet elongation (this assumption is valid for hemispherical bottom cavities, rougher for flat bottom cavities) ;
- that the mass ratio between the different parts of the jet is constant ;
- that the volume of plate material ejected in the jet is limited, as for shaped charges, by the cavity volume (here $\approx 6\ cm^3$) ;

we can estimate a "theoretical" maximum kinetic energy in a 2024 Al jet with a cavity D 20 mm h 20 mm : ≈ 200 kJ with an hemispherical bottom, 370 kJ with a flat bottom, which points out the great advantage of these hyperfast jets.

From these results, we shall now numerically evaluate the influence upon the jet performance of the initial shock, the geometry of the cavity, and the jet material.

Influence of the initial shock

The initial conditions - a pressure curve P(t) - can be schematically described by a pressure peak Pmax and a "characteristic duration", for instance the time τ during which $P > 0.5\ Pmax$.

Pmax has a strong influence upon the jet velocity. However, an important difference exists between the jets created in cavities with hemispherical and flat bottom, as shown on fig. 8 for 2024Al jets :

- for hemipherical bottom cavities, as for shaped charges, the maximum jet speed tends towards a limit of ≈ 12 km/s ; this limit is obtained for a pressure peak of 500 kilobars ;
- on the contrary, for flat bottom cavities, there is no saturation effect for the hyperfast dart velocity (we only notice a more important decrease vs time of the velocity for very high initial compressions). Thus, in this case, it is theoretically possible to improve without limit the performance of the jet by increasing Pmax, i.e. the capacity of the explosive launcher.

As for the parameter τ, it has an influence upon the ejected mass, but only if it is significantly smaller than the time necessary for the shock wave to go through the target thickness : in that case, the release reflected at the bottom of the cavity will induce tensions, which will disturb the jet creation. For higher values of τ, its influence is negligible.

Influence of the geometry of the cavity

The influence upon the jet velocity v of diameter D, depth h and radius of curvature r of the cavity are summarized on fig. 9.

Diameter D : all other parameters being unchanged, when D increases, the duration of the torus jet implosion increases ; thus, the mass of this part of the jet is higher, and will better confine the axial jet. Consequently, the jet velocity v, and also the jet mass, grow with D. However, a large increase of D implies an increase of all target dimensions, especially its diameter, in order to avoid a possible disturbance of the jet implosion by the lateral releases.

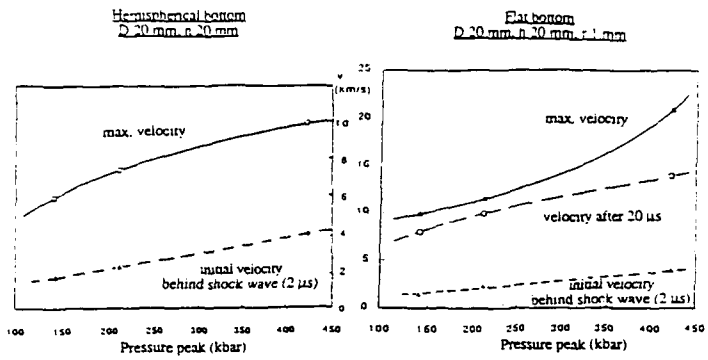


Figure 8 - Influence of the initial shock wave intensity upon the 2024Al jet velocity
Calculations with CEL

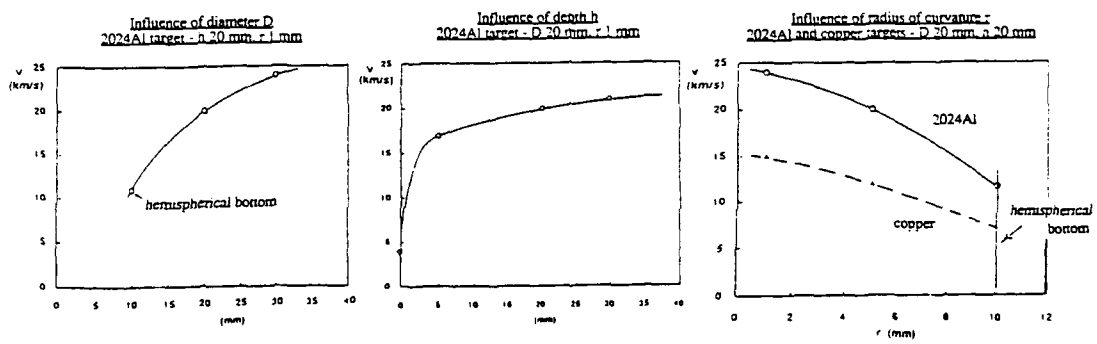


Figure 9 - Influence of the geometry of the cavity upon the jet velocity
Calculations with CEL

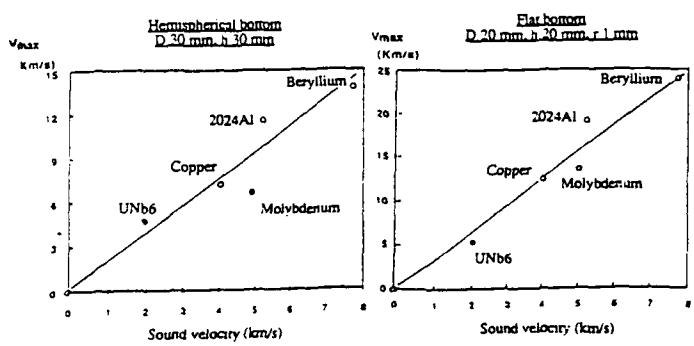


Figure 10 - Influence of the sound velocity of the target material upon the max. jet velocity
Calculations with CEL

Depth h : the calculations show that the points located at the circumference of the cavity will integrate the slower part of the jet, mostly in the peripheral sheath ; therefore, a variation of h will only slightly modify the dart velocity, except for "not very deep" cavities, i.e. when $h < D$.

Radius of curvature r : for given values of D and h, if r diminishes, the centripetal compression wave has a steeper front (for $r = 0$ it is a step) ; at the focalization, the increase of pressure and, consequently, the axial jet speed, will be higher. On the other hand, the surface of the flat area at the bottom of the cavity increases, and the implosion of the torus jet will be longer ; thus, the axial jet will be faster and better confined, and the hyperfast dart velocity will therefore increase.

All these results are proved by the experiments. Hence, with given launcher and target material, we can define an "optimal" geometry of the cavity :

- D as large as possible, the problem of the lateral releases being taken into account ;
- h = D ;
- r as small as possible.

Influence of the jet material

We present the influence of the material of the jet upon its velocity on fig. 10, for cavities with hemispherical or flat bottom. Five materials were tested with equivalent initial conditions : copper, beryllium, molybdenum, aluminum alloy 2024 and uranium alloy UNb6. We observe, for the two types of cavities, that the jet speed is roughly proportional to the sound velocity C of the material (evaluated with hydrodynamic assumption : $C = [K/\rho]^{1/2}$). This will help us to determine "optima" jet materials.

We first examine a classical jet created in an hemispherical bottom cavity. Since the jet speed v is nearly constant versus time, its length L is equal to vt ; therefore, at a given time t, Ω varies as $v\,\rho^{1/2}$, or (because of the linear variation of v with C), as the square root of the bulk modulus K. The penetration depth will consequently be optimized by choosing a very incompressible material (as tungsten or molybdenum).

As for jets obtained in flat bottom cavities, the same conclusions may be obtained both for the "slow" core and the hyperfast dart, although here there is a slight variation of v versus time.
In fact, other parameters must be taken into account to define a "good" jet material ; for instance, to maintain coherence during the jet elongation requires (as for shaped charges) a ductile material with fine grains.

A further improvement of the jet performance will be obtained :

- for the penetration P, by extending the duration of the jet ;
- for the crater volume ϑ, which varies as $V\rho v^2$, by increasing the volume V of the projected material, the quantity ρv^2 (proportional to K) being already optimized.

This requires a sufficiently high "time parameter" τ and a large diameter of cavity D, as mentioned above.

CONCLUSION

These studies point out a new concept of jet creation, using the implosion of a cavity with a flat bottom. Since the jet is obtained in three steps:

- shaped charge effect at the periphery of the cavity, hence, creation of a torus jet ;
- focalization of a centripetal compression wave, and creation of an axial jet ;
- confinement of the axial jet by the torus one,

it is possible to get faster jets than those created by a simple shaped charge effect.

Moreover, the experiments prove that the propagation of these jets is very regular (their coherence remains good even for high elongation), and the calculations seems to indicate that their penetration ability is higher than for classical jets.
Other experiments are planned to verify these theoritical results and to specify the actual performances of these jets.

REFERENCES

J.P. Asay, L.P. Mix, C. Perry (1976). In : Applied PhysicsLetters, 29 (5), 284-285.
G. Birkhoff, E.M. Pugh (1948). In : J. of Applied Physics, 19,. 563.
M. Defourneau (1970). Sciences et Techniques de l'armement. In : Mémorial de l'artillerie française, 44(2).
W.H. Gust (1982). High impact deformation of metal cylinders at elevated temperatures. In : Journal of applied physics, 53 (5), 3566-3575.
J.P. Levrat, E. Charvet, M. Lacomme, P. Massard, H.C. Pujols (1991). Simulation des effets des impacts à hypervitesse. In : Journal de Physique III, 1, 155-162.
D.J. Steinberg,S.G. Cochran , M.W. Guinan (1980). A constitutive model applicable at high strain rate. In : Journal of applied physics, 51 (3).
T. Szendrei (1983). Analytical model of crater formation by jet impact and its application to calculation of penetration curves and holes profiles. In : Proc. of the 7th Int. Symp. on Ballistics - La Hague.
W.P. Walters, J.A. Zukas (1989). In : Fondamentals of shaped charges (John Wiley and Sons, Ed.).

Int. J. Impact Engng Vol 14, pp 479–489, 1993
Printed in Great Britain

0734-743X/93 $6.00+0.00
1993 Pergamon Press Ltd

TOPOGRAPHICALLY MODIFIED BUMPER CONCEPTS FOR SPACECRAFT SHIELDING

T.D. MACLAY*, R.D. CULP*, L. BAREISS†, T.G. GILLESPIE†, and F.M. KUSTAS†

*CCAR, CB 431, Dep't of Aerospace Eng. Sciences, U. of Colorado, Boulder, CO 80309
†Martin Marietta Space Systems, P.O. Box 179, Denver, Colorado 80201

ABSTRACT

This paper introduces the concept of Topographically Modified Bumpers, or TMB's, for spacecraft shielding. By milling geometric patterns onto the front face of a flat plate bumper, ribs are formed which create multiple contact points with a projectile during impact. As the generated shock waves travel through the projectile, they overlap causing a superposition and amplification of the shock. Several different TMB designs are considered and results from experimental tests conducted at low (1.5 to 3.5 $\frac{km}{sec}$) and medium (6 to 8 $\frac{km}{sec}$) velocities are presented. At higher velocities, a parametric study of topography dimensions is performed to show optimizing trends. It is found that TMB's with tall ribs, thin backing plate, and small rib separation should perform best.

INTRODUCTION

The untrackable orbital debris environment is becoming increasingly inhospitable to satellite operations in low-Earth orbit. This is especially true for large spacecraft and satellites with long missions. The Space Shuttle Discovery's collision avoidance maneuver in September, 1991, marked the Shuttle fleet's first debris avoidance maneuver, and is a prime example of how debris is beginning to disrupt mission operations. Experiments had to be temporarily shut down while the Shuttle steered clear of a 1440 kg discarded rocket body (McKnight, 1991). Atlantis found itself in a similar situation fewer than three months later.

These encounters are isolated incidences, and generally do not end in catastrophe because of USSPACECOM's tracking and warning capabilities. But impacts from smaller, more plentiful objects are not uncommon, as the Long Duration Exposure Facility can attest. LDEF was struck more than 34,000 times by meteoroids and debris during its 5.7 year flight (See *et al.*, 1990). More than 3,000 of these strikes resulted in craters with diameters of at least .5 mm across; the largest measured over one half centimeter across. Looking toward future programs, it has been estimated that Space Station Freedom will encounter tens of thousands of debris particulates larger than .1 mm and 10's to 100's bigger than 1 mm over its 30 year life (Maclay *et al.*, 1991).

Impact damage from sub-millimeter size particles may only influence the performance of sensitive instruments and solar panels, but debris larger than a few millimeters could pose a serious threat

to a manned vessel or fuel tank. As a consequence of this hazard, much attention has been focused on shielding techniques and design. Specifically, researchers have been devising innovative ways of defeating larger projectiles with lower shielding weights.

Present shield designs are typically based on the Whipple bumper shield concept of placing a thin aluminum bumper plate some distance in front of the spacecraft wall. The purpose of this plate is to shock incoming projectiles sufficiently to shatter, melt, or even vaporize them, thereby reducing the impulsive load on the spacecraft hull. Some variations on this theme have been the use of different materials (e.g. Kevlar, ceramics, foam, mesh, and composites), inclusion of multiple bumpers, and optimization of plate spacing and thicknesses.

This paper offers an advanced bumper design which involves modifying the bumper's front surface topography by milling out rows of grooves from a flat plate. By creating these ribs, the effectiveness of the bumper can be enhanced without increasing its weight. As part of an experimental test series being conducted by Martin Marietta's Defensive Shields Demonstration (DSD) Program, these Topographically Modified Bumpers (TMBs) are being evaluated under low (1.5 to 3.5 $\frac{km}{sec}$) and medium (6 to 8 $\frac{km}{sec}$) impact conditions. At the higher velocities more typical of orbital encounters, the TMB is evaluated through numerical simulation using the CTH hydrocode, provided by Sandia National Laboratory. By exploring the effects of varying rib height, width, and spacing, trends are identified that lead to a partially optimized TMB configuration.

CURRENT SHIELDING DESIGNS

Thin Plate Theory

The easiest way to assure that a spacecraft can withstand meteoroid and debris impacts is to increase its wall thickness. However, by doing so, the satellite's weight, and therefore its cost of delivery, are driven up dramatically. It was first proposed by Whipple (1947) that a spacecraft wall subjected to hypervelocity impact would be afforded more protection by a thin sheet spaced some distance in front of the wall than by adding the same weight of material to the wall itself.

The purpose of this bumper sheet is to break up the projectile into an expanding cloud of debris, thereby reducing the impulsive load that the hull wall would otherwise have experienced. A complete mathematical description of how the projectile and bumper materials behave during impact is quite complex, but a general understanding of the processes involved can be gained by looking at two important mechanisms: spalling and heating.

At the time of impact, shock waves are initiated in both the projectile and bumper which propagate away from their common interface. Figure 1a depicts this situation using a spherical projectile. The compression waves travel through the material and reflect off the free surface at the back of the sphere as tensile waves. If the tensile amplitude is sufficiently high to fail the material, the rear surface will fracture, or spall (Fig. 1b). This process may continue as new free surfaces are created and rarefaction waves are generated to satisfy stress boundary conditions. The size of these spalled debris particles varies inversely with the magnitude of the original shock, or impact velocity (Anderson *et al.*, 1990). Dispersion of debris cloud particulates also depends on the shock strength, but is a function of the shape of the shock front and the free surface geometry as well. These two parameters are controlled primarily by the projectile's shape and orientation during impact (Morrison, 1972; Piekutowski, 1987; Chhabildas and Hertel, 1991; Hertel *et al., 1991*).

Another mechanism that aids in the dispersion of the debris cloud is heating. The projectile and bumper materials undergo a state of high compression when the shock wave arrives, and are released from this state as it passes. This is an irreversible process which leaves behind residual energy in the form of heat. The amount of heating increases with the shock amplitude, and for

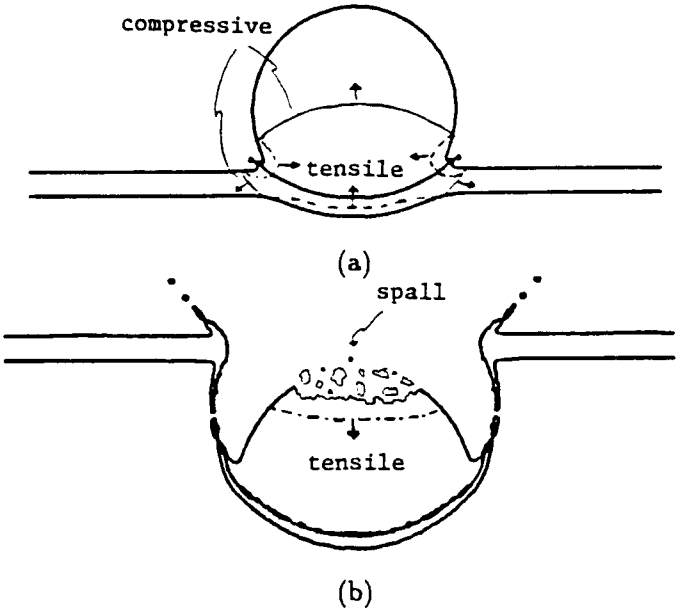


Fig. 1. (a) Shock waves are initiated during impact and propagate through the projectile and plate. (b) Rear surface spall occurs if the shock strength is sufficient.

sufficiently high impact speeds will melt or even vaporize the projectile and bumper. Melting is beneficial because then the cloud expansion is hindered only by the surface tensions of the liquid, and small droplets are formed which continue to spread. A solid particle, on the other hand, would remain intact (assuming no spall). Vaporization is even more advantageous since the density of vapor is low compared to liquid or solid material. In this case, even surface tensions disappear, and phase separation effects help disperse the cloud (Hertel, 1992).

Experimental testing of the Whipple shield concept at the NASA Johnson Space Center Hypervelocity Impact Research Laboratory (HIRL) has demonstrated a substantial weight savings over single-walled structures. For example, Christiansen (1990) reports that at 7 $\frac{km}{sec}$, a single sheet of aluminum must be more than five times heavier than an aluminum Whipple shield to defeat the same threat. Researchers have been working to further improve this weight savings. The next two sections describe successful designs that are being considered for Space Station Freedom.

Multi-Shock Shield

A Multi-Shock (MS) shield, as proposed by Cour-Palais and Crews (1990), consists of multiple layers of an ultra-thin, flexible ceramic fabric, called Nextel. Nextel is used instead of continuous metallic sheets because less shield debris is generated. A schematic is shown in Fig. 2a. As in the single sheet bumper, the first sheet disperses the projectile into an expanding debris cloud while increasing the fragments' temperatures. Subsequent layers then reshock these fragments, further reducing their sizes and increasing their temperatures. Thus, the debris is raised to substantially higher pressures and thermal states with the MS shield than with a single layer shield.

MS tests performed at 6.3 $\frac{km}{sec}$ have shown amounts of melting and vaporization equivalent to that found at 10 $\frac{km}{sec}$ with a standard Whipple shield (Cour-Palais and Crews, 1990). Ongoing experiments conducted at HIRL show that the level of protection provided by a single sheet Whipple shield can be achieved at more than a 40% weight savings with a Multi-Shock shield (Crews and Christiansen, 1992).

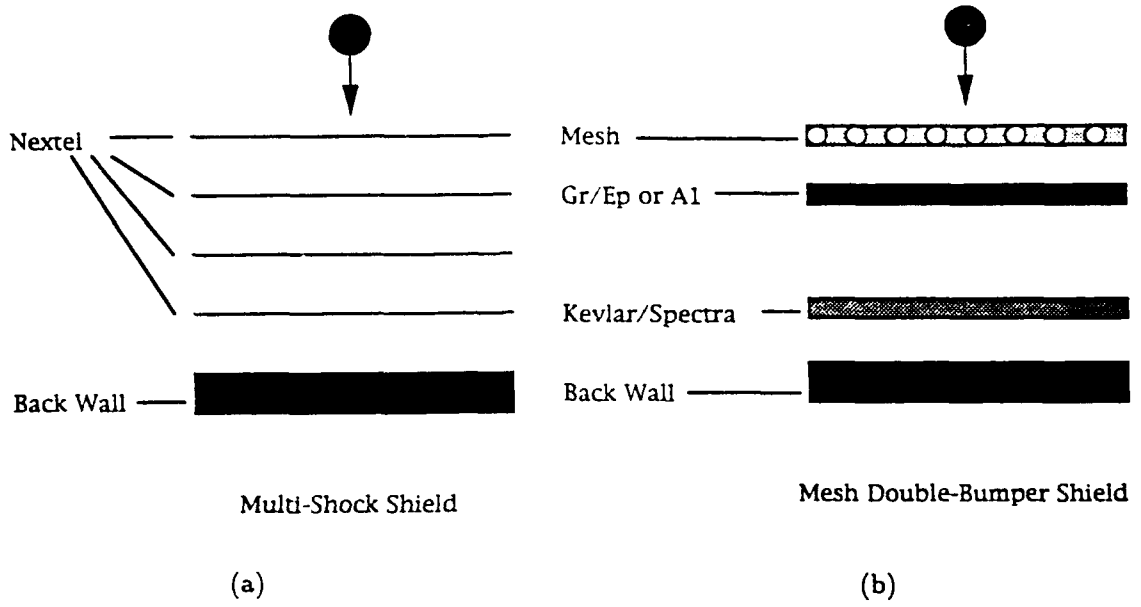


Fig. 2. The Multi-Shock Shield (a) and the Mesh Double-Bumper (b) both provide significant weight savings over a single Whipple bumper.

Mesh Double-Bumper

The Mesh Double-Bumper (MDB) is another configuration that has shown more than a 40% weight savings over a standard Whipple bumper (Crews and Christiansen, 1992). A schematic of this shield is shown in Fig. 2b. The first layer is an aluminum wire mesh which again serves to break up the projectile, and spread and heat its fragments (Christiansen, 1990). The second bumper reshocks the fragments as in the MS concept. The third layer is a sheet of Spectra or Kevlar fabric that slows the debris and stops a portion of the cloud so that the back wall can survive the remaining load.

TOPOGRAPHICALLY MODIFIED BUMPERS

A Topographically Modified Bumper (TMB) is a single layer, ridged, continuous sheet bumper that is capable of providing more protection than an equal weight flat plate bumper. Its effectiveness as a shield is based on the principle of superposition of shock waves that are initiated in the projectile at the location of each impacted rib. Figure 3a illustrates this principle using square ribbing and a spherical projectile. The waves propagate across the sphere as before, but superposition amplifies the pressure as the waves overlap. The result is an increase in temperature and a greater chance of multiple spalling at the rear surface.

Another advantage of TMB's over flat plate bumpers is that, like the mesh layer of the MDB, it can be rolled for storage and deployed as a shield augmentation layer. Unlike the mesh, however, a TMB with ribs in only one direction can provide structural support in the direction of the ribs.

Finally, by having a continuous backing sheet, the TMB can protect subsequent shielding or insulating layers that might be sensitive to the incidence of atomic oxygen, dust, or radiation. For example, LDEF demonstrated that graphite epoxy, a material which has demonstrated improved MDB performance when used in place of aluminum as the second sheet, could be substantially eroded by atomic oxygen (See *et al.*, 1990). Thus, TMB bumpers are designed to enhance the performance of single flat sheet bumper shields, or can be used as the first layer in a Multi-Shock or MDB-type design to increase debris dispersion.

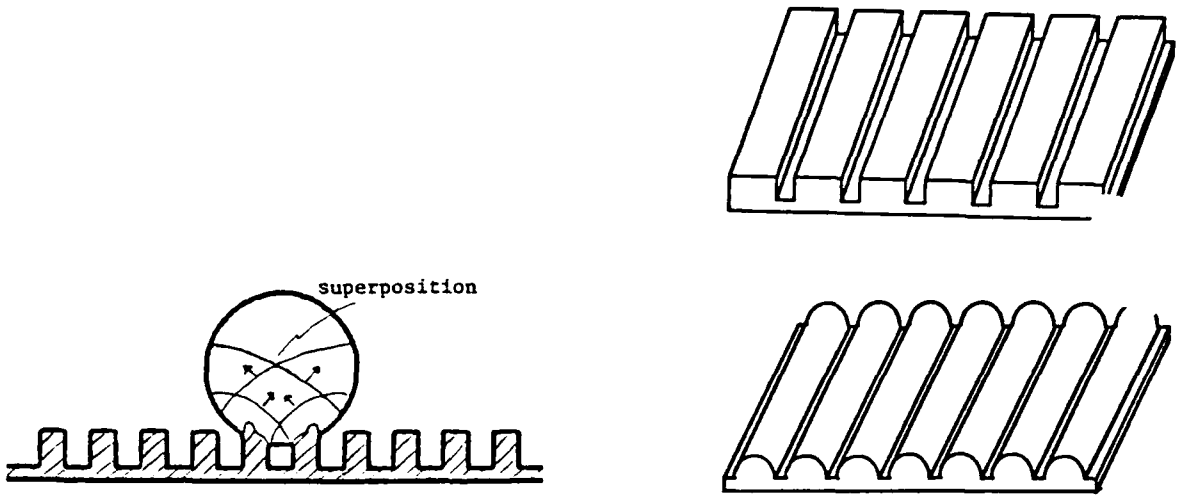


Fig. 3. (a) The TMB designs use superposition to amplify the shock strength. (b) The performance of square and hemispherically grooved TMB's are compared with that of a flat plate of equal weight.

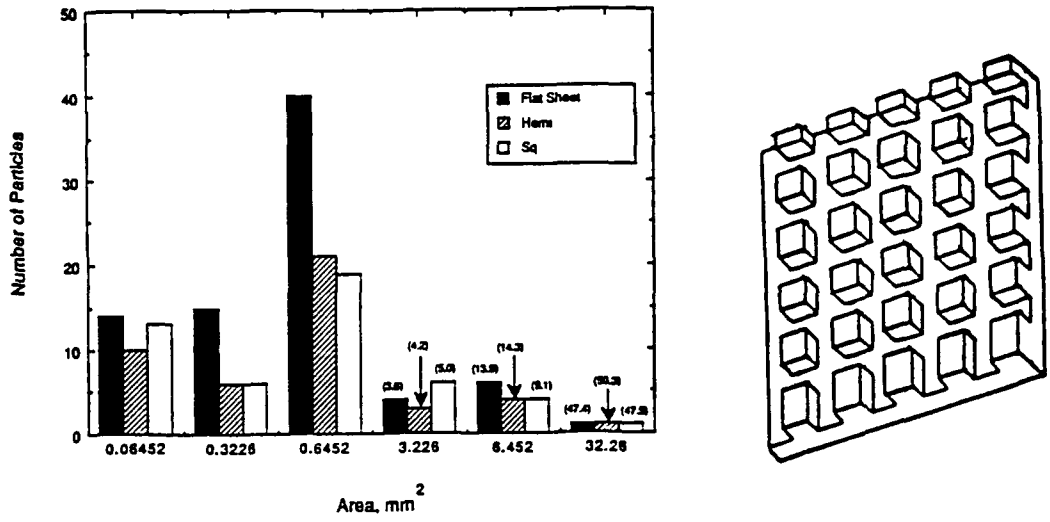
LOW VELOCITY IMPACTS

TMB's using different geometric shapes were evaluated experimentally at low velocities of several kilometers per second as part of Martin Marietta's DSD program. The plates were milled in one direction (from here on called a 1-D TMB) with square and hemispherical features, and their performances were compared to that of a flat plate. Figure 3b shows the designs considered. In each case, the projectile was a $\frac{1}{4}$ inch tantalum sphere traveling between 1.66 and 1.71 $\frac{km}{sec}$. The plates were also tantalum, and had equal areal densities of 1.27 $\frac{gm}{cm^2}$, a value determined by the .030" thickness of the flat plate tested.

The figure of merit used in evaluating these designs was the size of the largest few fragments, since they pose the greatest threat to the protected structure. The smaller these major particles are, the better the performance of the shield. Using a technique developed under the DSD program, the debris clouds were scanned into a computer from X-ray photographs, and fragment cross sectional areas were recorded. Figure 4a shows this data as a histogram of the number of debris particles versus cross sectional area. Abscissa values represent lower limits of the bins, and numbers in parentheses indicate average areas within that bin.

The histogram shows that the bumper with square ribs outperformed the other two. In the largest two bins, the square design has the fewest pieces and the lowest average cross sectional areas. In fact, the hemisphere design and the flat plate resulted in 28% and 56% more total area, respectively, in fragments with cross sections larger than 6.452 mm^2. This result, combined with the fact that square-ribbed plates are easier to fabricate, makes this design the most promising.

Several other TMB designs were tested in this series as well, including ones with triangular ribs, and flat plate bumpers with circular, oblong, and slotted perforations machined into them. These configurations were not as effective, however, and were not considered further. The square-ribbed TMB (from here on simply called the TMB) was also compared to an equal areal density set of wires running in one direction (1-D wire mesh). The results were comparable, and as in the case of the 2-D wire mesh, a cross grooved TMB (2-D TMB) like that shown in Fig. 4b yielded improved results over an equal weight 1-D TMB.



(a) (b)

Fig. 4. (a) The square ribbed TMB is the most effective at reducing the size and number of the largest fragments. (b) Milling grooves in two directions increases the efficiency of the TMB.

MID-RANGE VELOCITY IMPACTS

Only a few shots have been performed on TMB's thus far at velocities higher than several kilometers per second. Two shots were performed by *JSC/HIRL* with a 1-*D* aluminum TMB in place of the wire mesh in a full Mesh Double-Bumper shield. The projectile was a $\frac{1}{8}$ inch aluminum sphere which impacted at $6.2\frac{km}{sec}$. The original mesh's $.051\frac{gm}{cm^2}$ areal density was maintained for the TMB, although the height and width of the ribs differed for the two tests. The rib frequency was set to three ribs per projectile diameter for both shots.

The post-shot inspection revealed back plate penetrations in both TMB shots, while the original wire mesh MDB survived the impact. This difference is thought to be at least in part due to the fact that the TMB had not yet been optimized, and that it was only milled in one direction. Additional tests currently are being planned to help identify optimizing trends and evaluate the effectiveness of a cross-grooved TMB in this configuration. The 1-D TMB and 1-D wire mesh were compared again in shots made at these mid-range velocities, and, as at the lower velocities, were found to behave similarly. A significant advantage to the 1-D TMB determined by the tests was that it sustained much less damage (e.g. smaller hole size) than its wire mesh counterpart, thereby better maintaining its protective capability for subsequent debris encounters.

HIGH VELOCITY IMPACTS

Experimental testing at velocities more typical of orbital encounters was not possible, so numerical simulation with the CTH hydrocode is relied on for a high velocity study. Because of computer limitations, only single plate simulations could be run, and the evaluation of shield performances is based on debris cloud characteristics behind the bumper. Using CTH, the effect of varying the rib height (H), width (D), and spacing (L), as well as the backing plate thickness (T), is investigated. In all cases, the threat is taken to be a 6.35 mm ($\frac{1}{4}$ in) diameter (d) aluminum sphere traveling at 10 $\frac{km}{sec}$. All shields are assumed to be aluminum, and the point of impact is centered between two ribs in each simulation. The baseline flat plate used for performance comparison is 1.27 mm (.050 in) thick, so all bumpers have an areal density of $.34\frac{gm}{cm^2}$.

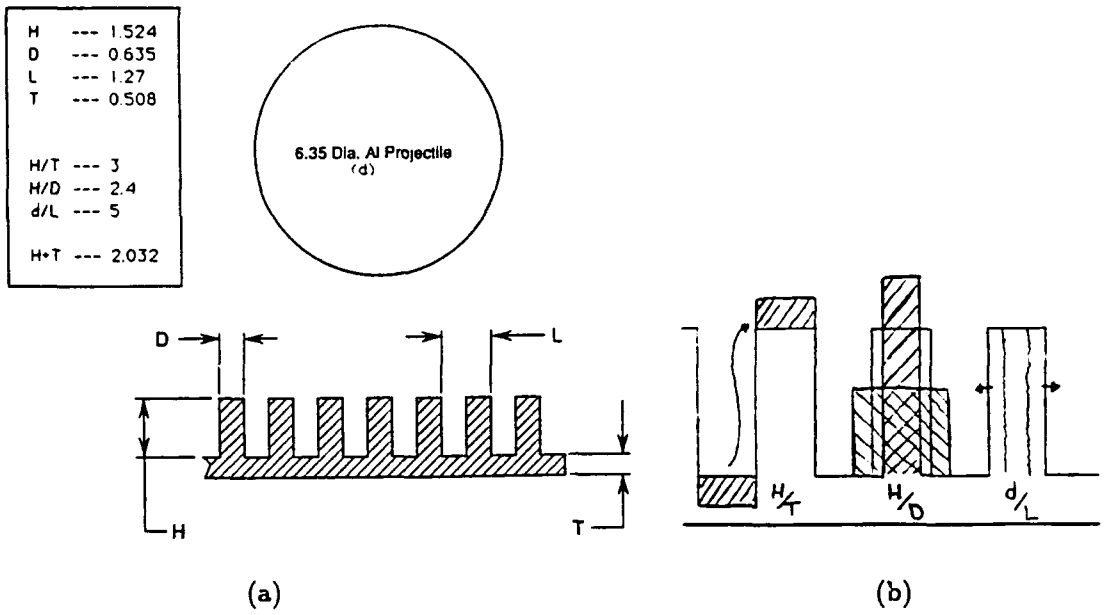


Fig. 5. (a) Rib height, width, spacing, and backing thickness are defined for the nominal configuration. (b) The effect of varying $\frac{H}{T}$, $\frac{H}{T}$, and $\frac{H}{T}$, are investigated for optimization.

Figure 5a defines the various dimensions mentioned above, and gives their values for the nominal TMB configuration. Also given are the initial values of the three variables being considered for the parametric study: $\frac{H}{T}$, $\frac{H}{D}$, and $\frac{d}{L}$. Each ratio is varied twice, once higher and once lower than the nominal value, while holding the uninvolved dimensions constant. (Unfortunately, the ratios are coupled, so changing one changes another.) Thus, eight CTH runs are needed for the study. Runs one and two are the flat plate and nominal TMB, respectively, and dimensions for runs three through eight are given in Table 1. Figure 5b qualitatively shows how the parameter variations affect the TMB.

Table 1: Parameter Variation Matrix For CTH Runs

Run	$\frac{H}{T}$	$\frac{H}{D}$	$\frac{d}{L}$	H	D	L	T
1	N/A	N/A	N/A	0	0	0	1.27
2	3.0	2.4	5.0	1.52	0.63	1.27	0.51
3	1.0	1.3	5.0	0.85	0.63	1.27	0.85
4	5.0	2.9	5.0	1.81	0.63	1.27	0.36
5	1.9	1.0	5.0	0.98	0.98	1.27	0.51
6	4.2	4.8	5.0	2.15	0.45	1.27	0.51
7	3.0	1.4	3.0	1.52	1.06	2.12	0.51
8	3.0	3.4	7.0	1.52	0.45	0.91	0.51

All of the simulations are run in the two dimensional, axis-symmetric formulation. The authors are aware that slight elongation and other minor non-physical irregularities can occur along the symmetry axis using this formulation because of the imposition of artificial boundary conditions, but no serious problems are encountered in this study.

The flat plate simulation at three microseconds after impact is pictured in Fig. 6. The shape of the debris cloud is not surprising, and a spall on the verge of detaching from the back of the

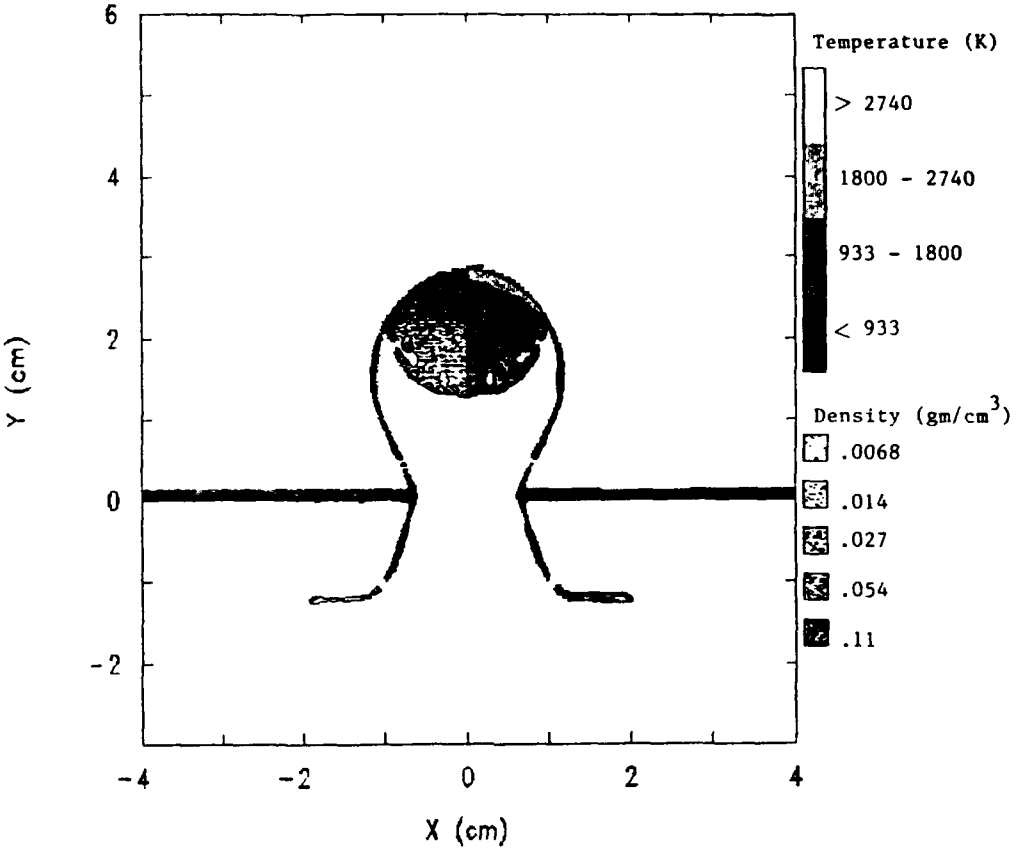


Fig. 6. A CTH simulation of a sphere striking a flat plate at $10\frac{km}{sec}$ shows the typical debris cloud shape three microseconds after impact. Temperature is indicated on the right, and density is on the left.

projectile is evident. Note also that the debris velocity remains virtually unchanged. Temperature is plotted on the right half of the image. On the legend, note aluminum's melting and boiling temperatures of 933.5 deg Kelvin and 2,740 deg Kelvin, respectively. By three microseconds, the primary shock has passed through the material and the temperature of the cloud has become reasonably stable (Hertel, 1992). The image shows that the entire cloud is liquid, and no vapor is apparent. The material density is shown on the left half of the image with dot shading.

The nominal TMB simulation at the same time after impact appears in Fig. 7. Several observations can be made from this image. Firstly, the superposition of shock waves from multiple impact points has amplified the shock's net magnitude. This is evidenced by the multiple spalling at the back of the projectile and the increase in temperature compared to Fig. 6. The vapor appearing on the centerline, however, is most likely a manifestation of the artificial boundary conditions mentioned earlier. Secondly, the spalled fragments are comparatively dense and have not melted, suggesting that at least a portion of the residual internal energy usually seen as heat has gone into the fracturing process. Thirdly, the debris spread angle has been increased slightly, helping to reduce the impulse on downstream objects. Lastly, the volume of the cloud is larger, indicating a lower average cloud density. Moreover, the spalled particles are small and have been slowed to about half of their initial velocity by the spalling process, making them a much lesser threat to the remaining structure.

Similar analyses were performed on each of the remaining six runs, and the following conclusions were drawn. First, a high $\frac{H}{T}$ (Run 4) appears to provide better protection than a low $\frac{H}{T}$ (Run 3). This result makes sense since in the limit as this ratio approaches zero, one arrives back at the flat plate. Second, tall, skinny ribs (Run 6) seem to outperform short, fat ribs (Run 5). This is

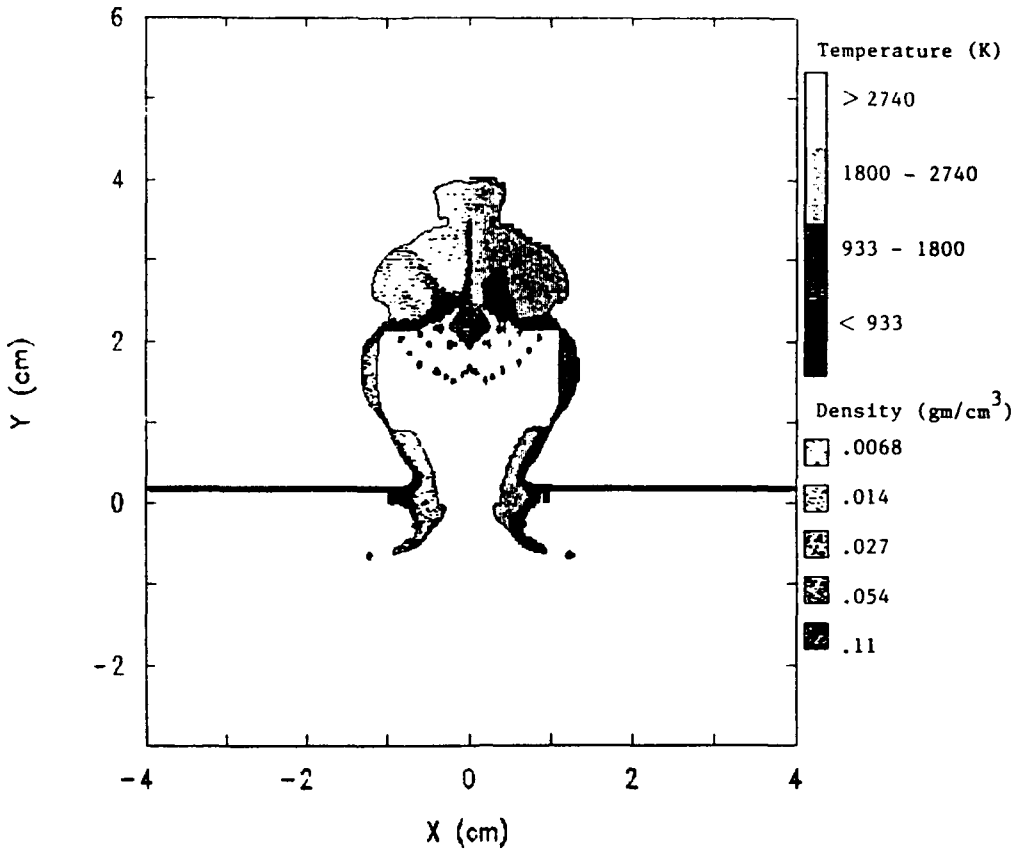


Fig. 7. At three microseconds, a CTH simulation of a sphere striking the nominal TMB at $10\frac{km}{sec}$ shows multiple spalling and increased temperatures due to the superposition of shock waves. Temperature is indicated on the right, and density is on the left.

also not surprising, for the same reason. Last, fewer ribs per projectile diameter (Run 7) appear better than more (Run 8). This is a little less obvious, but again can be explained by considering limiting cases. As the rib width approaches the projectile diameter, the impacting object sees a plate of thickness $H + T$ (assuming it is unlucky enough to have hit the rib!). At the other extreme, as rib width approaches zero, the projectile sees a plate with two different densities. The backing plate remains at the original density but only has thickness T. The ribs, on the other hand, are nothing more than tightly spaced filaments which are seen by the projectile as a solid, but less dense layer of thickness H. Hence, the shock is reduced in this latter case, as are debris spread and temperature.

The most effective of the eight runs is Run 7. The image of its debris cloud is given in Fig. 8. Of primary interest and importance is the debris spread. At three microseconds, the cloud from Run 7 is nearly 50% wider than the cloud from Run 1, and almost 28% wider than the cloud from Run 2. Additionally, there is more spalled material, and more debris mass at higher temperatures (not obvious from the images).

It should be noted that these evaluations are based on single plate simulations, and are subject to some interpretation. For example, some evidence of debris chanelling between the ribs exists, and this may temper or even override the advantages outlined above. To verify that the conclusions drawn here are accurate, simulations should be run with a witness plate so the actual damage to a secondary structure could be directly observed. Unfortunately, these runs are quite CPU intensive, and only a limited number can be made. Runs 1 and 2 were rerun as two-plate problems by inserting a 5 mm witness plate 6.5 cm behind the bumper. Neither witness plate failed, but

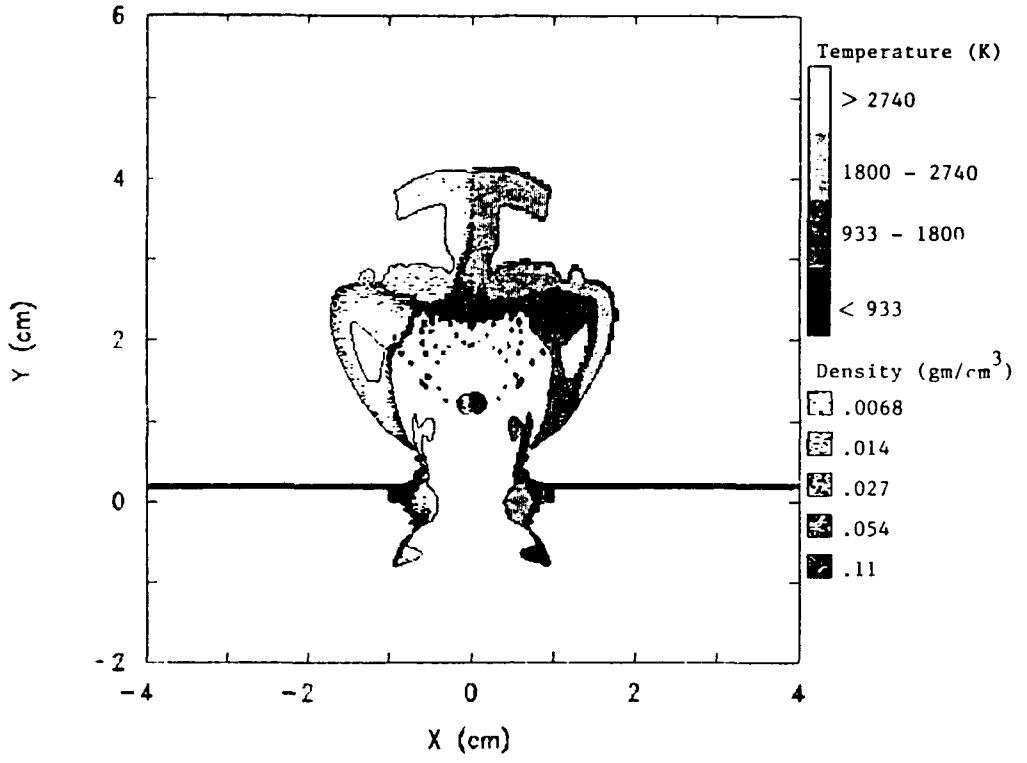


Fig. 8. At three microseconds, an image of Run 7 shows multiple spalling, increased temperatures, and the largest lateral spread found in any of the runs. Temperature is indicated on the right, and density is on the left.

the dent in the plate in Run 1 was larger than in Run 2. While not much information was revealed by these particular two-plate simulations, additional runs and experimental testing at higher velocities can provide the needed data.

CONCLUSIONS

It has been shown that, throughout the entire velocity range expected during on-orbit debris interactions, a bumper plate with geometric patterns milled into its front surface affords more protection than a flat plate of equal weight. Through experiment, the 1-D TMB has proven to be comparable to a 1-D row of wires of equal weight, and the 2-D TMB of equal weight has shown additional improvement. In comparing the 1-D TMB to the wire mesh, it was found that smaller hole sizes resulted in the TMB, offering better protection against local second strikes. It has been demonstrated through numerical simulation that for a given threat, the TMB can be optimized by varying its configuration. It appears that increasing $\frac{H}{T}$ and $\frac{H}{D}$, and decreasing $\frac{d}{L}$ from the nominal values results in a more effective design.

In addition to shielding against impact, TMB's can contribute as a structural member of a wall and offer atomic oxygen, dust, and radiation protection for vulnerable materials.

Additional testing and numerical simulation would be useful to help better quantify the results presented here. This would also aid in the identification of performance trends as a function of threat variations such as debris size, shape, obliquity, and density.

ACKNOWLEDGEMENTS

The authors would like to thank Eugene Hertel from Sandia National Laboratories for supplying the CTH computer code and corresponding technical support, Kelly Leutkemeyer from the University of Colorado for his technical and graphics support regarding CTH, and Dr. Pete Snow from Kaman Sciences and John Gassner from Foster Miller for assistance with TMB design development. The authors are also indebted to Andrew Piekutowski from the University of Dayton Research Institute and Eric Christiansen from the Johnson Space Center for their experimental contributions.

This research is supported in part by the Strategic Defense Initiative Organization, (SDIO/TN) under Martin Marietta's DSD program, by the United States Space Command, Center for Aerospace Analysis under IPA agreements, by the Air Force Armament Laboratory, Eglin AFB, under Award No. F 08635-89-K-0227, by the Martin Marietta Corporation under Contract No.'s 9-040021 and GS0-660111, and by the NASA Johnson Space Center under NASA Grant NAG 9-407 Basic. The research is conducted in part using the facilities of the Colorado Center for Astrodynamics Research and the Department of Aerospace Engineering Sciences at the University of Colorado, Boulder.

REFERENCES

Anderson Jr., C.E., Trucano, T.G., and Mullin, S.A. (1990). Debris Cloud Dynamics. *Int. Journal of Impact Engineering,* Vol. 9, No. 1, pp. 89-113.

Chhabildas, L.C., and Hertel, E.S. (1991). Experimental and Numerical Simulations of Orbital Debris Impact on a Simple Whipple Bumper Shield. Workshop on Hypervelocity Impacts in Space, University of Canterbury at Kent.

Christiansen, E.L. (1990). Advanced Meteoroid and Debris Shielding Concepts. Paper AIAA 90-1336, AIAA/NASA/DOD Orbital Debris Conference: Technical Issues and Future Directions, Baltimore, MD.

Cour-Palais, B.G., and Crews, J.L. (1990). A Multi-Shock Concept for Spacecraft Shielding. *Int. Journal of Impact Engineering,* Vol. 10, pp. 135-146.

Crews, J.L., and Christiansen, E.L. (1992). The NASA JSC Hypervelocity Impact Test Facility (HIT-F). Paper AIAA 92-1640, AIAA Space Programs and Technologies Conference, Huntsville, AL.

Hertel, E.S., Chhabildas, L.C., and Yarrington, L. (1991). Computational Determination of Ballistic Limits for a Simple Whipple Bumper Shield. Workshop on Hypervelocity Impacts in Space, University of Canterbury at Kent.

Hertel, E.S. (1992). Personal communication.

Maclay, T.D., Madler, R.A., McNamara, R., and Culp, R.D. (1991). Orbital Debris Hazard Analysis for Long-Term Space Assets. Workshop on Hypervelocity Impacts in Space, University of Canterbury at Kent.

McKnight, D. (1991). Space Shuttle Performs Maneuver to Avoid Debris. *Orbital Debris Monitor,* Vol. 4, No. 4, p. 3.

Morrison, R.H. (1972). A Preliminary Investigation of Projectile Shape Effects in Hypervelocity Impact of a Double-Sheet Structure. NASA TN D-6944, Ames Research Center, Moffett Field, CA.

Piekutowski, A.J. (1987). Debris Clouds Generated by Hypervelocity Impact of Cylindrical Projectiles with Thin Aluminum Plates. *Int. Journal of Impact Engineering,* Vol. 5, No. 1, pp. 509-518.

See, T., Allbrooks, M., Atkinson, D., Simon, C., and Zolensky, M. (1990). Meteoroid and Debris Impact Features Documented On The Long Duration Exposure Facility: A Preliminary Report. NASA Pub. No. 84, JSC No. 24608.

Whipple, F.L. (1947). Meteorites and Space Travel. *The Astronomical Journal,* Vol. 52, No. 1161, p. 131.

Int. J. Impact Engng Vol 14, pp 491–502, 1993
Printed in Great Britain

0734-743X/93 $6.00 + 0.00
Pergamon Press Ltd

CERAMICS MODELS IN THE MESA CODES

David A. Mandell and Rudolph Henninger

Hydrodynamic Applications Group
Los Alamos National Laboratory
Los Alamos, NM 87545

ABSTRACT

We have implemented two ceramics models into the MESA Eulerian finite difference hydrocodes and evaluated them by comparing code predictions of the free surface velocity as a function of time to data for one-dimensional flyer plate impacts and to free surface velocity data for the penetration of subscale tungsten rods into ceramic plates. Results were obtained for silicon carbide, boron carbide, alumina, titanium diboride, and for a base calculation using a steel plate

INTRODUCTION

The ability to predict the response of ceramics to impacts is important in the design of armor/anti-armor devices, aerospace structures, and other modern applications of advanced ceramic materials. A large number of material models exist for ceramic materials. Gordon Johnson has compiled a list that includes eleven models (Johnson, 1991). In this paper we discuss the implementation and evaluation of two ceramic material strength models into the MESA 2-D and 3-D Eulerian codes (Holian *et al.*, 1991). In the future we plan to use the MESA codes as testbeds for the examination of other models.

We have implemented the Steinberg ceramic model (Steinberg, 1990) into both 2-D and 3-D MESA, and we have implemented the Johnson-Holmquist brittle model (Johnson *et al.*, 1990) into 2-D MESA. In order to evaluate the models, we have compared code calculations to free surface velocity data for 1-D plate impacts and to tungsten impacts into ceramic disks. These data were obtained from Sandia National Laboratories (Kipp *et al.*, 1989, Wise *et al.*, 1990). Materials calculated include silicon carbide, boron carbide, alumina, titanium diboride, and a base case calculation of steel. Model and mesh sensitivity studies were performed in order to determine their effects on the calculated free surface velocities, which could be compared to experimental measurements, and to guide users in developing their calculational models.

The basic hydrodynamics, material strength, equation-of-state (EOS), and fracture models implemented in the MESA 2-D and 3-D codes have been previously described (Holian *et al.*, 1991). Several points are worth noting about the material strength and fracture models in the codes. In general they are semi-empirical models. That is they were obtained by fitting data to equations that give the correct physical trends, but they are not derived from basic physical principles. Second, in Eulerian codes, such as MESA, the material moves through a fixed mesh. This movement requires the use of mixed cells; that is, cells

with more than one material. This mixture presents a complication regarding the treatment of stress and damage in these mixed cells and the advection of these quantities into adjacent cells.

Steinberg Ceramic Model

Steinberg and his co-workers have developed a number of material models for ductile materials (Steinberg 1990, Steinberg *et al.*, 1988) and more recently he has developed a similar model for ceramics materials, based on the 1-D plate impact experiments performed at Sandia. This model includes strain, strain rate, pressure and temperature effects. Equations are provided for both the yield strength and the shear modulus. A number of material constants are needed. Due to the limited range of available experiments, some constants had to be estimated.

Johnson-Holmquist Model

The Johnson-Holmquist brittle model is also based on a series of ceramic experiments, but has the advantage over the Steinberg model that a fracture model is incorporated into the model. Essentially the model is based on two sets of curves of equivalent stress vs. pressure. Each set depends on plastic strain rate, with one set being used prior to fracture (damage < 1.0) and the other set being used after fracture has occurred in the cell (damage > = 1.0). The damage is calculated in a similar fashion to the well-known Johnson-Cook (Johnson et al., 1985) fracture model in which fractional strain to failure is accumulated for each cycle until the value exceeds one. The damage variable, D, presents a problem in Eulerian codes since material is advected between cells, and thus fractured material may enter a cell where it is mixed with undamaged material resulting in a cell with no fractured material and thus creating an artificial healing process. The shear modulus is a constant in this model.

Fracture Models

It appears from the results obtained, which are presented and discussed below, that the model used to represent ceramic fracture is very critical in predicting the behavior of the experiments. Fracture is built into the Johnson-Holmquist model. There are two pressure-dependent flow stress curves, one for intact material and one for failed material (damage greater than one). In contrast, the Steinberg model does not provide a fracture component, and thus a separate fracture model must be provided in the code. Two options have been provided in MESA for fracture in a brittle material when using the Steinberg model. First the Johnson-Cook ductile fracture model constants can be input such that fracture occurs (damage = 1.0) as soon as a small amount of strain occurs. Second a simple maximum principal stress criteria is available. In this model the maximum principal stress is calculated for each cell during each code time cycle. When the principal stress exceeds an input value, the cell is considered fractured. In a fractured cell the strength is set to zero in tension.

Material Constants Available

The constants needed for the Steinberg ceramics model and the Johnson-Holmquist brittle model are derived from a range of ceramics experiments. An extensive amount of work is needed to obtain the needed constants for a given material, and therefore, constants are currently available for a only a few materials for each of the models. The following table indicates the materials, the experiments used for each material in this study and the model for which constants are available for each ceramic. It should be noted that the constants may vary between ceramics produced by different manufactures and between different samples. In general, sets of constants for these variations are not available.

Table 1. Available material constants and experiments.

MATERIAL	1-D PLATE	TUNGSTEN IMPACT	MODEL CONSTANTS AVAILABLE SC = Steinberg JH = Johnson-Holmquist
SiC	X		SC, JH
A B			JH
AD 85	X	X	JH
AD 995			SC
PYROCERAM			JH
PSZ (ZrO_2)	X		SC
B_4C	X	X	SC
TiB_2	X	X	SC
AIN	X		SC, JH

COMPARISON WITH TUNGSTEN ROD IMPACTS

Wise and Kipp performed a number of experiments in which small tungsten penetrators impacted steel and also a number of ceramics. A copper buffer was attached to the back of the target, and the free surface velocity was measured as a function of time at the back of the copper. A schematic of the experimental setup is shown in Fig. 1.

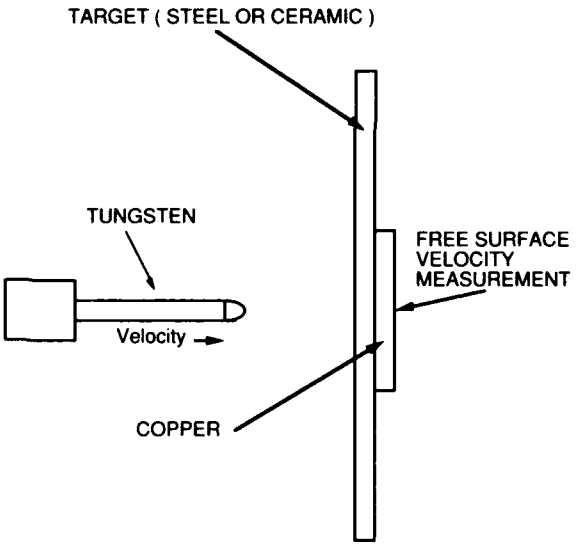


Fig. 1. MESA Schematic for the Wise Kipp Experiments.

We have predicted these experiments using the MESA 2-D code containing the Steinberg and Johnson-Holmquist models. In order to verify that we had the correct geometrical model and code input constants, the steel experiment was first predicted. A model and mesh sensitivity study was also performed. The results are presented in the following sections. The computational mesh consisted of square cells. Unless otherwise noted in the figures, these cells were 0.25 mm on each side. The tungsten penetrator was 2 mm in diameter so a mesh cell of length 0.25 mm on each side results in 8 cells across the rod. The targets were 9.08 mm to 10.19 mm in thickness, and the copper buffer behind the target was 1.94 to 2.0 mm in thickness. Frequently a mesh of variable size is used in order to reduce computer run times, but this additional variable was not studied in the current work.

The ceramic material strength was modeled using either the Steinberg ceramic model or the Johnson-Holmquist model. The other materials were assumed to be elastic-perfectly plastic; that is the yield strength and shear modulus were constant for the non-ceramic materials.

Steel

The steel target experiment was first calculated as a test of our geometrical setup and also to be sure that our equation of state(EOS) and material constants were correct. The U_S-U_p EOS was used for all

materials in this experiment. No fracture model was used in the steel calculations, but a minimum tensile pressure criterion was used. The mesh size study shown in Fig. 2 indicates that a 0.50-mm mesh is not converged. A 0.10-mm mesh is slightly different from the 0.25-mm mesh and a little further from the data. The 0.25-mesh results are in excellent agreement with the data except for a small disagreement in the initial peak. A gap existed between the tungsten and the target in the TIESA setup and thus times are relative. Therefore, times were shifted to bring the initial velocity rises into agreement. Based on these runs, a 0.25-mm mesh was chosen as the basis for the ceramic runs.

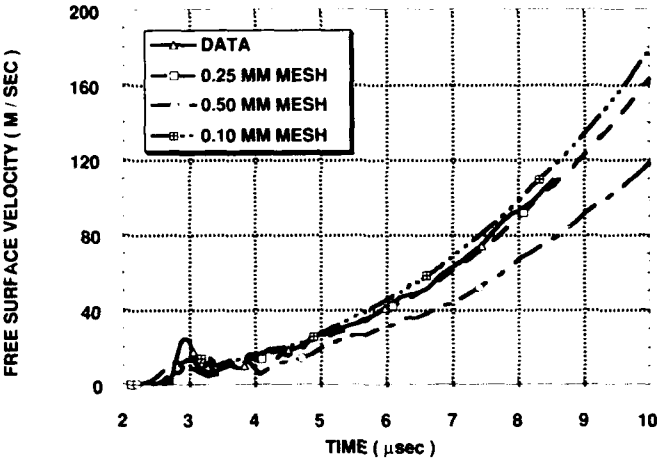


Fig. 2 Tungsten Impacting Steel - Mesh Sensitivity.

Boron Carbide (B_4C)

The B_4C 0.10 mm mesh cell comparison shown in Fig. 3 is in very good agreement with the data. This calculation was done with the Steinberg ceramic model and the simple maximum tensile fracture criterion. The effect of the maximum principal stress fracture value, σ_{max}, is shown in Fig. 4. This figure indicates that the results are fairly sensitive to the tensile stress value chosen for fracture. The results in Fig. 3 were obtained using a 1-kbar value of σ_{max}.

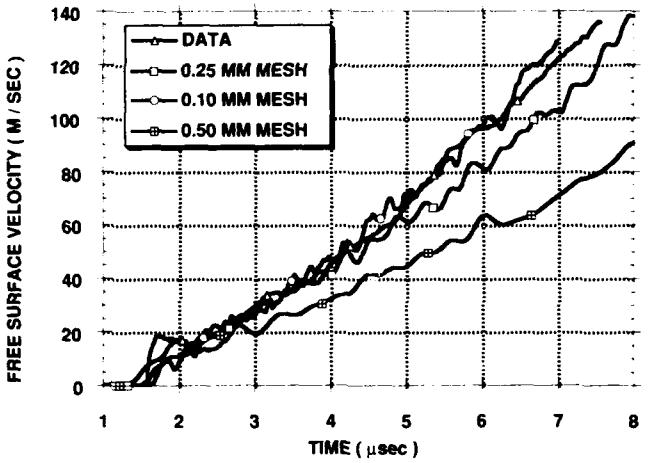


Fig. 3. Prediction of Tungsten Impacting Boron Carbide - Mesh Sensitivity.

When examining new material strength models, it is useful to compare them to the simple elastic-plastic model in which the yield strength and shear modulus are a constant. This comparison for boron carbide is shown in Figure 5. The elastic plastic model results in the correct shape for the velocity/time curve, but the magnitude is too low. A different value of the yield stress may improve the agreement, but it was not felt worthwhile to make a large number of elastic plastic calculations. A no-strength (hydro only) run was also made in order to see the effect of

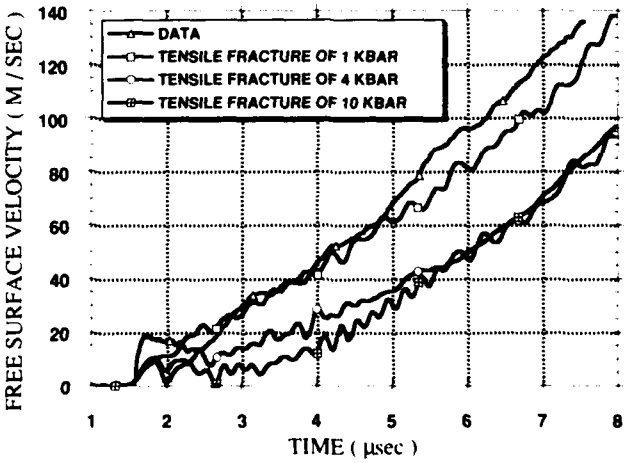


Fig. 4. Prediction of Tungsten Impacting Boron Carbide - Effect of Tensile Fracture Value.

hydro-only run initially is in good agreement with the data but has the wrong slope at the end of the run. This difference may be due to the lack of material fracture in this calculation.

Alumina(Al_2O_3)

For alumina we initially had only model constants for the Johnson Holmquist model, and therefore this model was used for the majority of the study. Preliminary constants for alumina (AD 995) for the Steinberg ceramics model became available recently, and one calculation with this model is also included. The base results are shown in Fig.6. The agreement between the calculations and the data is very good during the initial portion of the predictions but becomes worse during the latter parts of the experiment. More work is needed to determine if better model constants would improve the agreement, if there is an aspect of the alumina that is not being considered, or if basic model improvements are required.

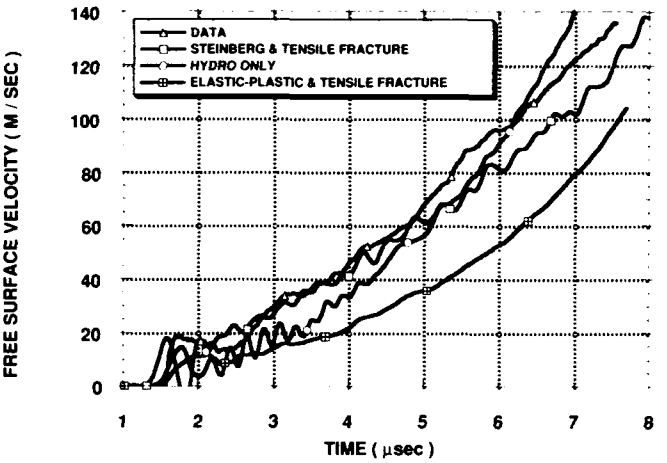


Fig. 5. Prediction of Tungsten Impacting Boron Carbide Using the Elastic Plastic and Tensile Fracture Models.

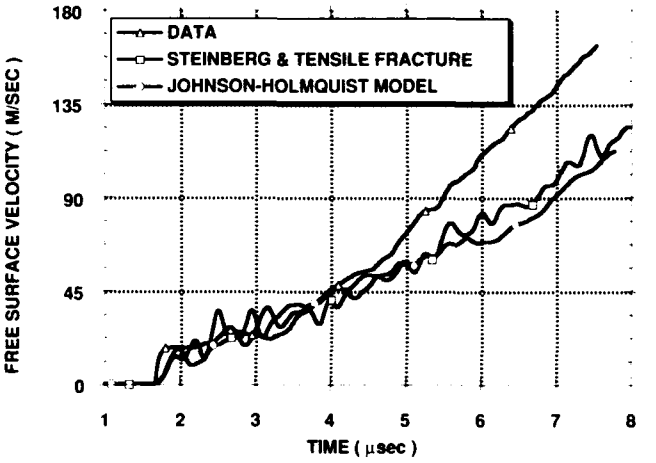


Fig. 6. Prediction of Tungsten Impacting Alumina.

The alumina used in this experiment, as well as in the 1-D plate impact discussed later, was believed to be very porous and nonuniform. (Grady, 1991). These characteristics may account for the difficulty in obtaining calculations that match the data. In order to see the effect of porosity, MESA calculations were performed for porosities of 2, 5, and 11 percent in addition to the base case at zero porosity (Unless otherwise indicated, all results in this paper are at zero porosity). Porosity enters these calculations only through a modification to the equation of state. The results are shown in Fig. 7 for the Johnson-Holmquist model. A two percent porosity calculation is in much better agreement with the data than the other calculations, but this level of porosity resulted in a worse comparison between the data and the calculation for the 1-D impact (Mandell and Henninger, 1992). The effect of porosity on the intact and fractured material strength, which was not taken into account, may also be important.

The 0.10-and 0.25-mm mesh results are in fairly close agreement, as seen in Fig. 8. The three mesh size calculations are converging as would be expected, but the 0.5-mm mesh is clearly bad.

When examining new material strength models, it is instructive to compare the calculated results to results using a simple elastic-plastic model. These results are shown in Fig. 9. The elastic-plastic model without a fracture model agrees very poorly with the data. Thus, one can conclude that the fracture model is critical to accurately predicting these types of experiments. As noted previously, the Johnson-Holmquist model incorporates a fracture model, but the Steinberg ceramic model requires a separate fracture model.

It is interesting to examine the computer resources needed to run these MESA 2D calculations, which were run on a Cray Y-MP computer. Table 2 shows the computer time and memory needed for the calculations at the three mesh spacings using the Johnson-Holmquist model.

Table 2. Required MESA2D Computer Resources

MESH CELL LENGTH (mm)	CPU (min.)	MEMORY (Million Words)	TOTAL NUMBER OF CELLS
0.10	150.4	7.19	160,000
0.25	12.0	1.75	25,600
0.50	2.0	0.98	6400

As shown in theTable 2, it is desirable to do parameter studies with the fewest number of cells possible and then do a confirmatory calculation with the number of cells needed for mesh convergence. From the above results it appears that sufficient cells are not practical in 3-D calculations, but it has been found that a mesh of square cells is not required. Typically a variable mesh with a ratio of 1.1 between adjacent cells can be used. This ratio significantly reduces the number of cells required. Variable meshes were not studied in this work.

Titanium Diboride (TiB_2)

The titanium diboride predictions shown in Fig. 10 are clearly in poor agreement with the data. The mesh sensitivity results are not converging to the data as occurred with the alumina and somewhat with the steel target. Steinberg (Steinberg, 1990) discusses the fact that TiB_2 has a number of unusual properties including a possible phase transition. In addition, Steinberg uses a nonlinear U_S-U_P equation of state for TiB_2, and MESA only includes a linear U_S-U_P. Thus we did not use the same EOS model in MESA as Steinberg used in his calculations for TiB_2. The results Steinberg presents are in worse agreement with the data than the results for the other materials that he looked at. The 1-D TiB_2 results presented later in this paper are in agreement with Steinberg's results, considering differences in his code and the MESA codes. Thus we cannot expect better agreement in the results of Fig. 10.

Figures 11-12 show the mesh and model sensitivities for the TiB_2 calculations. The tensile fracture value, Fig. 11, shows again considerable sensitivity to the selected value. Perhaps a more sophisticated fracture model is needed.

The elastic-plastic predictions are compared to the data and the calculations using the

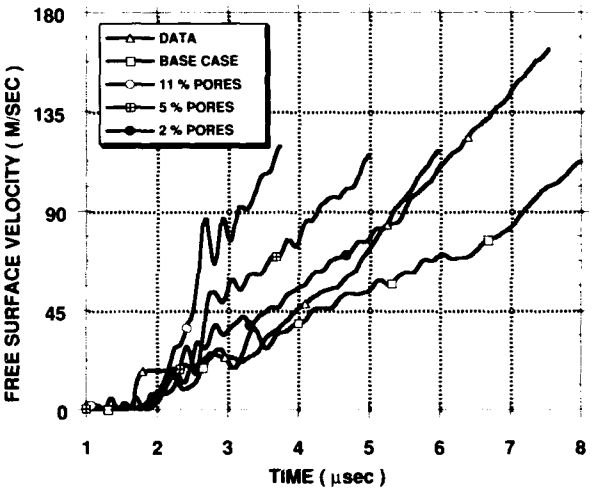


Fig. 7. Prediction of Tungsten Impacting Alumina - Effect of Porosity.

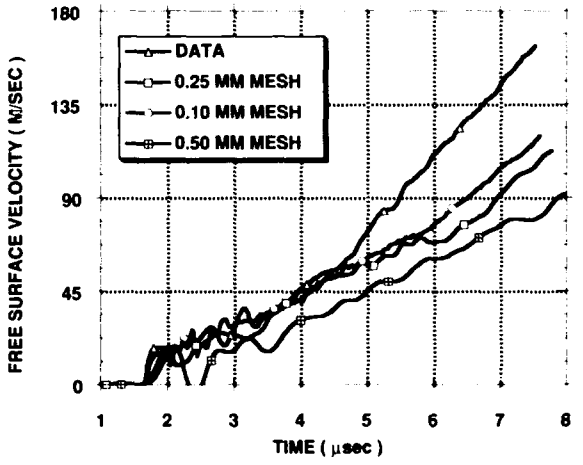


Fig. 8. Prediction of Tungsten Impacting Alumina - Mesh Sensitivity.

Steinberg model in Fig. 12. The elastic-plastic results are a little worse than the results obtained by using a variable yield stress and shear modulus.

COMPARISON WITH 1-D PLATE IMPACTS

The 1-D plate impact experiments involve an impactor of the same material as the target ceramic, shot into the target by a single stage powder gun. The target was backed by a lithium floride window.

Interface velocity measurements as a function of time were made at the target window interface. Experiments were performed at two nominal impactor velocities - one near 1.5 km/sec and one near 2.0 km/sec - for each ceramic. We predicted a number of these experiments, and the results are presented in the following sections. The schematic for the MESA geometrical model for the 1-D flyer plate experiments is shown in Figure 13.

Silicon Carbide (SiC)

Silicon carbide interface velocities as a function of time are presented for both models and for velocities of 1.542 km/sec and 2.1 km/sec. In addition EPIC calculations were available for these experiments. The results are presented in Figs 14-17.

If we have implemented the Johnson-Holmquist model correctly in MESA, then the MESA and EPIC results in Figs. 14 and 16 should agree except for differences between a Lagrangian code (EPIC) and an Eulerian code (MESA) and differences in the problem model. There are some differences, and we believe they are due primarily to differences in the problem setup, such as the gap and closure effects.

The calculated results using the Steinberg ceramic model are in good agreement with the data. It should be noted that the Sandia 1-D flyer plate

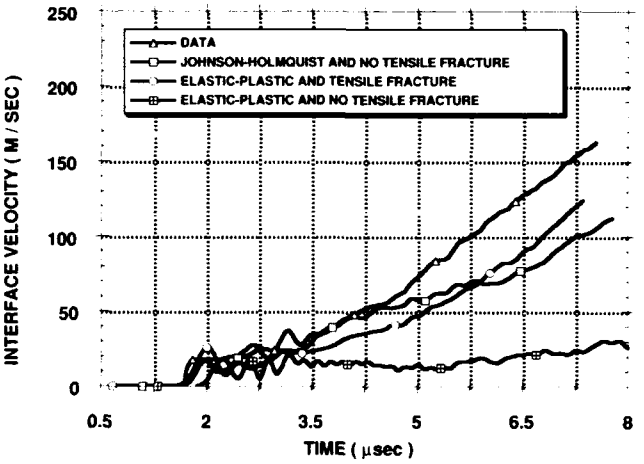


Fig. 9. Prediction of Tungsten Impacting Alumina Using The Elastic Plastic Strength Model and Tensile Fracture.

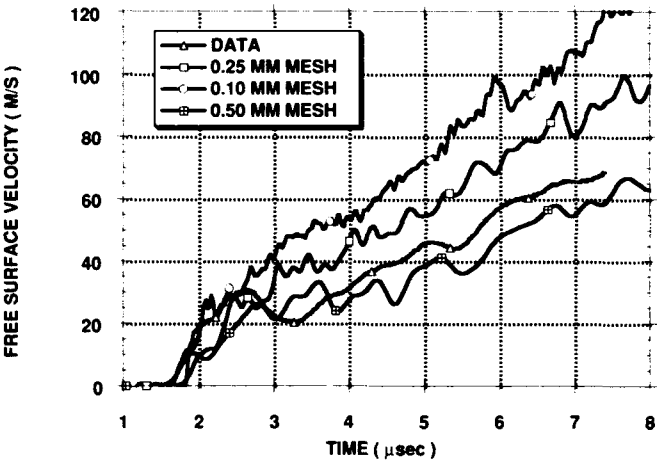


Fig. 10. Prediction of Tungsten Impacting Titanium Diboride - Mesh Sensitivity.

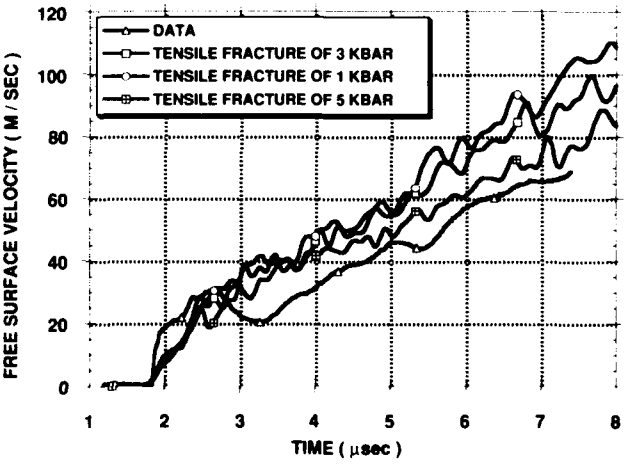


Fig. 11. Prediction of Tungsten Impacting Titanium Diboride - Tensile Fracture Sensitivity.

data were used in developing Steinberg's model, and therefore one would expect good agreement. These experiments were not used in obtaining the constants for the Johnson-Holmquist model. A change in the constants may give better agreement between the calculations and the data.

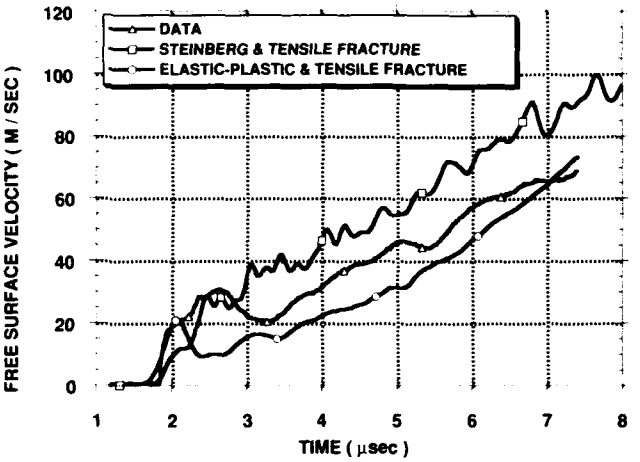


Fig. 12. Prediction of Tungsten Impacting Titanium Diboride Using The Elastic-Plastic And Tensile Fracture Models.

Boron Carbide (B_4C)

The boron carbide one-dimensional flyer plate predicted interface velocity results as a function of time are compared to the data obtained from Sandia National Laboratories in Figs.18 and 19. The low velocity (1.546 km/s) calculated results have the correct shape but are displaced a small amount from the data. The high velocity (2.21 km/s) results are in much better agreement with the data. Small changes in the strength or fracture model constants might improve the low velocity results but this change has not been

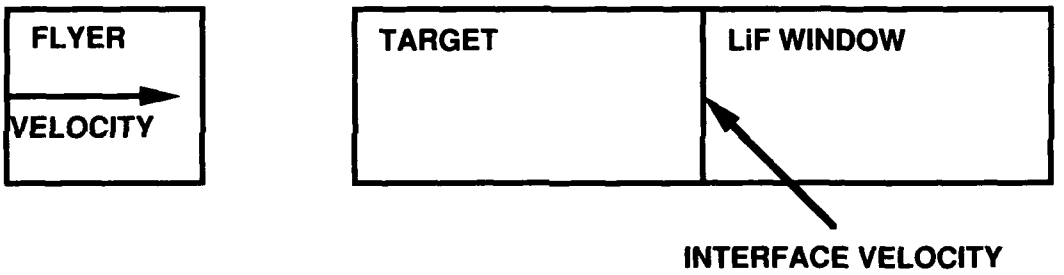


Fig. 13. Schematic For 1-D Flyer Plate Impacts.

investigated in the current study.

Titanium Diboride (TiB_2)

The titanium diboride results using the Steinberg ceramic model and the maximum principal tensile stress fracture criteria are compared to the data in Figs. 20 and 21. The predictions are in poor agreement with the data as were the tungsten impact into TiB_2 results discussed previously. These trends are similar to those obtained by Steinberg using a 1-D Lagrangian code. Clearly further work is required on TiB_2.

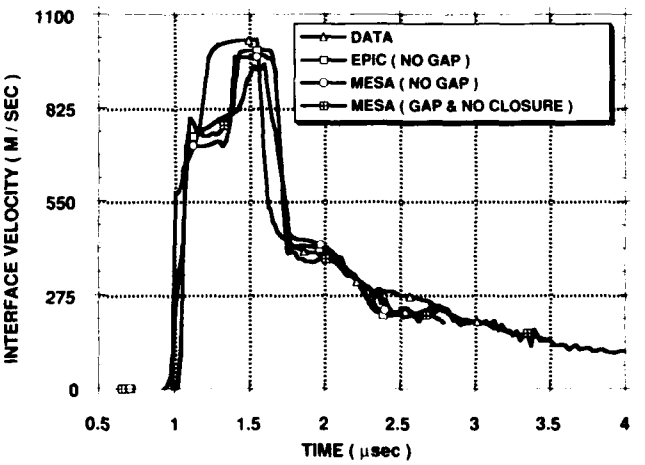


Fig. 14. Prediction of Silicon Carbide Flyer at 1542 m/s - Johnson-Holmquist Model.

Alumina (Al_2O_3)

Alumina 1-D flyer impact data was predicted using the Johnson Holmquist model, and the results are shown in Fig. 22 for a flyer velocity of 1.55 km/s and in Fig. 23 for 2.201 km/s. As seen previously with other materials, the lower velocity predictions are considerably worse than the higher velocity results. It should be noted that an EPIC calculation was available at 2100 m/s, and the MESA calculation was done at the same velocity. A MESA calculation at the experimental velocity of 2201 was only slightly different from the 2100 m/s calculation. The excellent agreement between the EPIC and MESA results indicates that the model was implemented into MESA correctly. Further work is needed in understanding the behavior of alumina including the influence of different samples on the model constants.

CONCLUSIONS AND RECOMMENDATIONS

We have implemented the Johnson-Holmquist brittle model, which includes material strength and fracture features, and the Steinberg ceramic model, which requires a separate fracture model, into the MESA2D code. The Steinberg model has also been implemented into MESA3D. A simple maximum principal tensile stress fracture criterion was implemented for use with the Steinberg model. Comparisons of results predicted by the EPIC and MESA hydrocodes implies that the Johnson-Holmquist model was implemented correctly in MESA.

One-dimensional flyer plate impact experiments and two-dimensional penetration experiments conducted at Sandia National Laboratories were predicted using the above models.

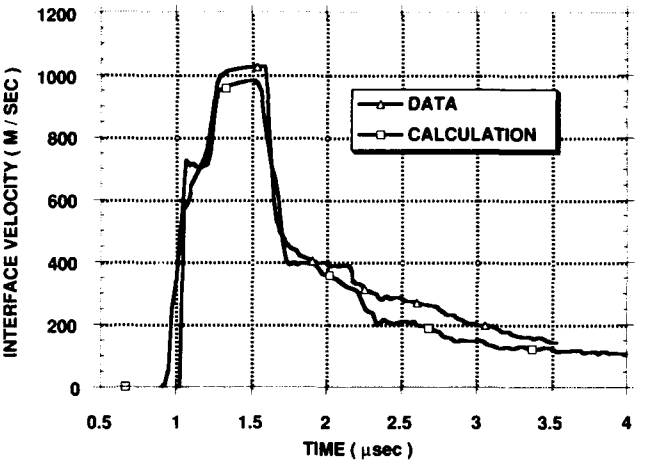


Fig. 15. Prediction of Silicon Carbide Flyer at 1542 ms Using the Steinberg Model.

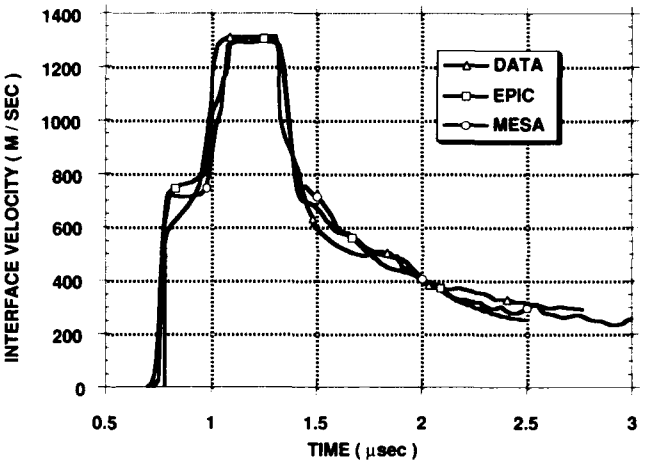


Fig. 16. Prediction of Sillicon Carbide Flyer at 2100 m/s Using the Johnson-Holmquist Model.

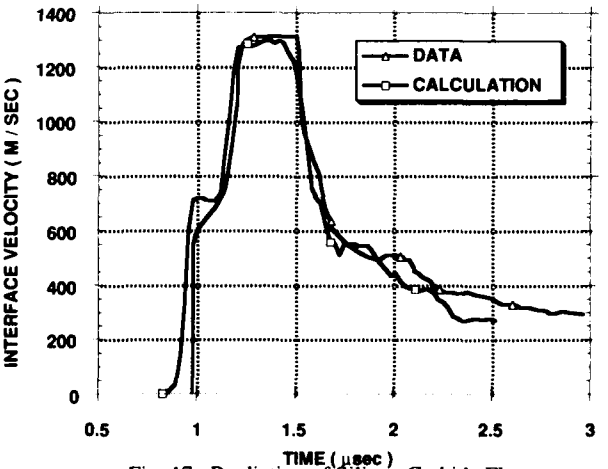


Fig. 17. Prediction of Silicon Carbide Flyer at 2100 m/s Using the Steinberg Model.

These results were obtained for a number of ceramics - silicon carbide, boron carbide, titanium diboride, and alumina. Good agreement between the predictions and the experiments was obtained for some of the materials, but poor agreement was obtained in other cases. In particular the silicon carbide and boron carbide results were good, and the alumina and titanium diboride results were poor. A better understanding of the material properties that influence the calculations is needed in order to determine what improvements, if any, are needed in the material models.

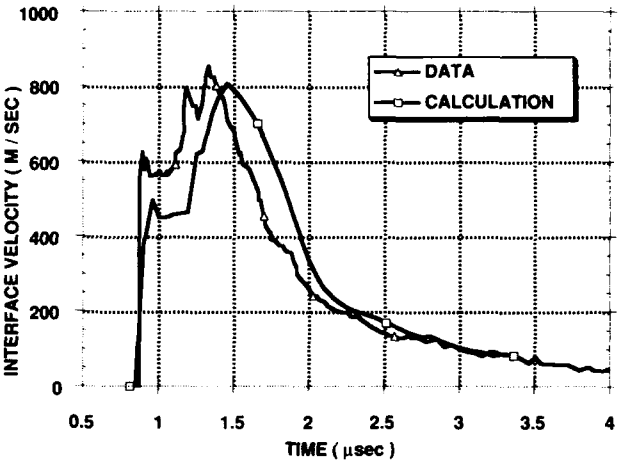


Fig. 18. Prediction of Boron Carbide Flyer at 1546 m/s Using the Steinberg Model.

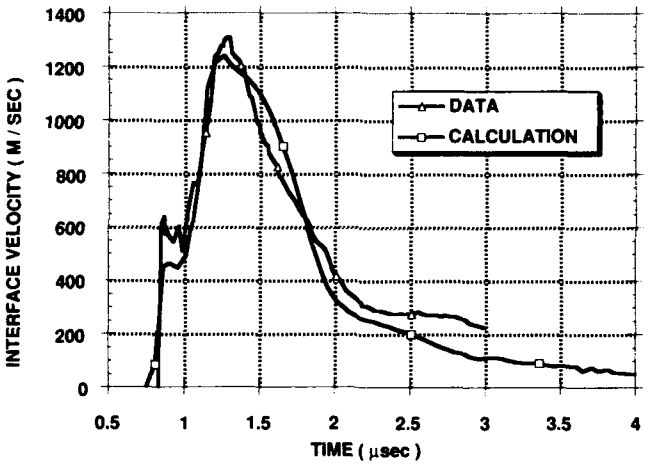


Fig. 19. Prediction of Boron Carbide Flyer at 2210 m/s Using the Steinberg Model.

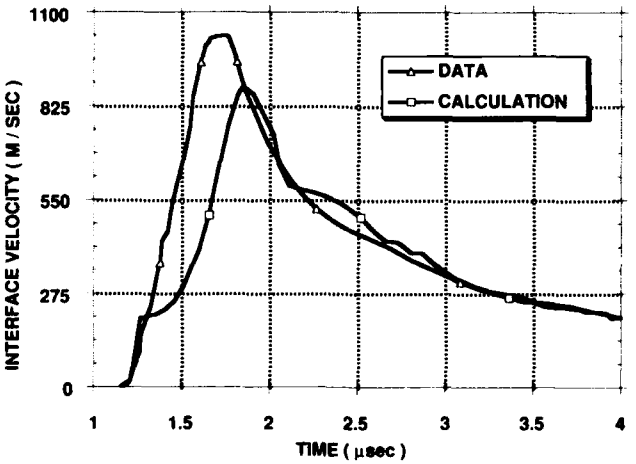


Fig. 20. Prediction of Titanium Diboride Flyer at 1515 m/s Using the Steinberg Model.

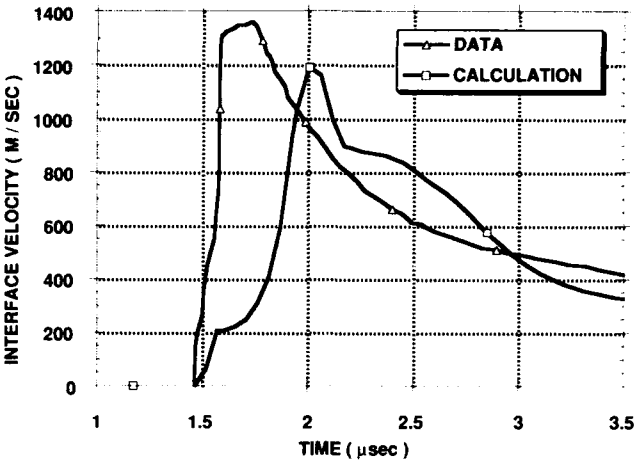


Fig. 21. Prediction of Titanium Diboride Flyer at 2113 m/s Using the Steinberg Model.

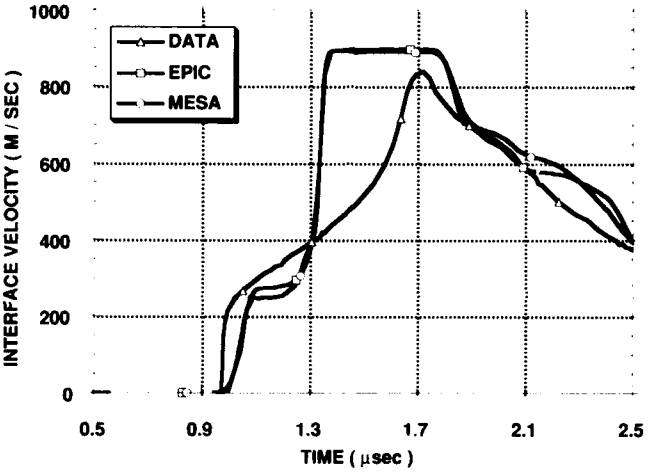


Fig. 22 Predection of Alumina Flyer At 1550 m/s Using The Johnson-Holmquist Model.

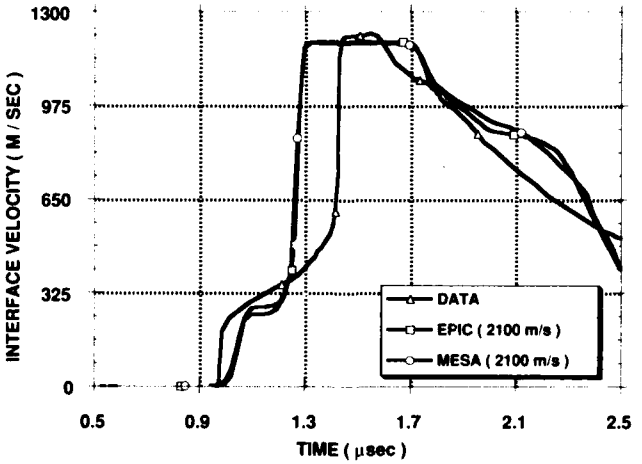


Fig. 23. Prediction of alumina Flyer at 2201 m/s Using The Johnson-Holmquist Model.

A number of additional ceramic material models have been or are being developed. We hope to implement other models into MESA so that these models can be compared to the two models discussed herein. In particular the ISO-SCM model (Addessio, *et al.* 1990) is a candidate for implementation in the future. Predictions need to be made for a better characterized alumina in order to determine if the poor alumina results are due to the material. Additional ceramic model work is needed before a reliable design tool is achieved.

ACKNOWLEDGEMENTS

The authors would like to thank Marlin Kipp and Dennis Grady, Sandia National Labratories, Albuquerque, for providing data; Gordon Johnson and Tim Holmquist, Alliant Techsystems, for help in understanding their model and providing advice that helped in finding an error in our implementation of their model, and Dan Steinberg, Lawrence Livermore National Laboratory, for providing preliminary alumina model constants and for a number of helpful discussions concerning his ceramic model.

REFERENCES

Addessio, Frank L. and Johnson, James N. (1990)A Constitutive Model for the Dynamic Response of Brittle Materials, *J. Appl. Phy.*, pp 3275-3286.

Grady, Dennis, (1991) Sandia National Laboratories, private communication

Holian, K. S. ,Mosso, S. J., Mandell, D. A. and Henninger, R. (1991) MESA: A 3-D Computer Code For Armor/Anti-Armor Applications, Los Alamos National Laboratory LA-UR-91-569 .

Johnson, Gordon (1991) Alliant Techsystems, private communication.

Johnson, G. R. and Cook, W. H. (1985) Fracture Characteristics of Three Metals Subjected To Various Strains, Strain Rates, Temperatures and Pressures, *Engineering Fracture Mechanics* 21, Part 1, pp 31-48.

Johnson, G. R. and Holmquist, T. J., (1990) A Computational Model For Brittle Materials Subjected to Large Strains, High Strain Rates, and High Pressures, EXPLOMET, San Diego, CA.

Kipp, Marlin E. and Grady, Dennis E. (1989) Shock Compression and Release in High-Strength Ceramics, Sandia National Laboratories Report SAND89-1461.

Mandell, David A. and Henninger, Rudolph (1992) Evaluation of Two Ceramic Models in the MESA Codes, Los Alamos National Laboratory Report LA-12267.

Steinberg, Daniel (1990) Computer Studies of the Dynamic Strength of Ceramics, Lawrence Livermore National Laboratory Report UCRL-ID-106004 .

Steinberg, D. J., Cochran, S. G., and Guinan, M. W., (1980) A Constitutive Model for Metals Applicable at High Strain Rate, *J. Appl. Phy.*, 51 (3), pp 1498-1504.

Steinberg, D. J. and Lund, C. M., (1988)A Constitutive Model For Strain Rates From 10^{-4} to 10^{6} s^{-1}, *Journal de Physique, Colloque C3*, Supplement au n°9, Tome 49.

Wise, Jack L. , and Kipp, Marlin E., (1990) Time-Resolved Response of Ceramics and Steel Plates, in *Shock Compression of Condensed Matter* - 1989, S. C. Schmidt, J. N. Johnson, and L. W. Davidson editors, Elsevier Science Publishers B. V.

Int. J. Impact Engng Vol. 14, pp. 503-508, 1993
Printed in Great Britain

0734-743X/93 $6.00 + 0.00
1993 Pergamon Press Ltd

VOID FORMATION IN OFE COPPER

JESSICA L. MAYES, STEVEN L. HATFIELD and PETER P. GILLIS

Department of Materials Science & Engineering, University of Kentucky
Lexington, Kentucky 40506

JOEL W. HOUSE

Wright Laboratory Armament Directorate - MNMW
Eglin AFB, Florida 32542

ABSTRACT

This paper reports results from the study of dynamic plastic deformation produced in OFE copper specimens by symmetric rod impact (rod-on-rod) tests. The study was performed by post-test sectioning of the specimens and examination of their microstructure using relatively low magnification optical microscopy. Particular emphasis was placed on porosity as a microstructural feature that relates directly to damage theories of constitutive behavior.

INTRODUCTION

Following World War II, Taylor (1947) and Whiffin (1947) published the technique of impacting a cylindrical specimen against a massive anvil and the concomitant elementary analysis that estimates the specimen flow stress from its post-test deformation. Since then, this test has remained a means of primary importance in determining dynamic mechanical properties of ductile materials. As high-speed, large capacity computers came into general use, highly sophisticated numerical analyses were applied to this test. Uncertainties concerning friction, compliance, and impedance, at the specimen-anvil interface eventually led Erlich *et al.*, (1981) to modify this test by impacting a pair of identical rods, one against the other. This form of the test is generally referred to as a symmetric rod impact test or a rod-on-rod (ROR) test, whereas the original rod against anvil experiment is often called a Taylor test. This paper reports results from the study of deformation damage produced in ROR impact testing.

The study was performed by post-test sectioning of the specimens and examination of their microstructures using relatively low magnification optical microscopy. Particular emphasis was placed on porosity, or the lack thereof.

Metallographic analysis of impact specimens subject to high strain rates provides insight into continuum processes, such as plasticity and damage. The objective of this paper is to describe and compare the observed microstructure of Oxygen Free Electronic (OFE) Copper ROR specimens tested at different impact velocities.

EXPERIMENTAL

The material used in these ROR impact tests was OFE copper. However, two different initial grain sizes were used, 75 and 40 μm. Specimens were cut to length from cylindrical rod stock of an initial diameter of 7.94 mm and then turned to a final diameter of 7.62 mm to match the bore of the mann barrel. Material to be tested was annealed at 600°C for one hour in a vacuum and the final average grain size of the specimens tested was 75 and 40 μm, as shown in Fig. 1. The large grain material was impacted at 392 m/s and

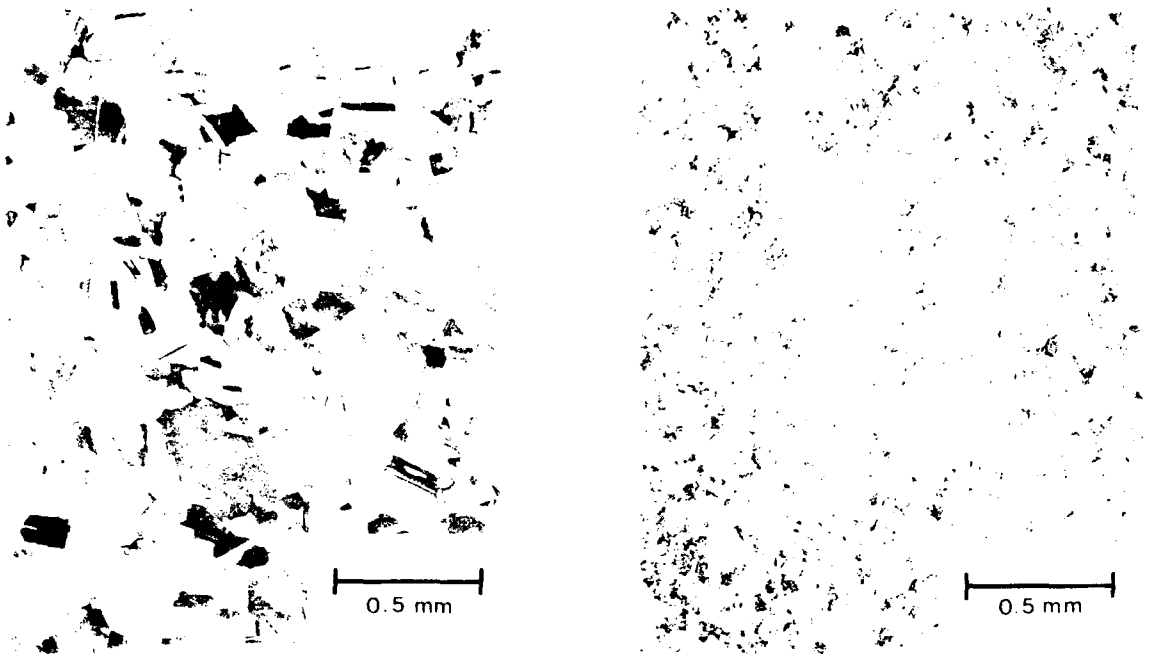


Fig. 1. Initial microstructure of OFE copper material. a) 5 micron average grain size. b) 40 micron average grain size.

300 m/s. The fine grain material was impacted at 233 m/s. Complete details of the experimental apparatus, data acquisition techniques, and interpretation are presented elsewhere (House *et al.*, 1992).

Recovered ROR specimens were sectioned along the axis of the rod. Sectioning of the rods was accomplished using a diamond abrasive cutting wheel. After mounting in cold mount epoxy, the specimens were ground and polished using standard methods for preparing copper materials. Final polishing was completed using 0.05 μm alumina abrasive. Dichromate etch was applied to reveal grain structure. The specimens were then viewed under an optical microscope at 50X magnification for microstructural analysis.

RESULTS AND DISCUSSION

Figure 2 is a montage created from photomicrographs originally taken at 50X magnification. The test specimens had been impacted together at 392 m/s. The montage details a midplane of the impactor and receptor rods, from the impact interface back to near the undeformed regions of each. By enlarging this area of interest under the microscope, microstructural features in the plastically deformed region are clearly observed.

As expected, grains near the impact interface and near the specimen axis had collapsed under the large compressive load. The post-impact structure has flat, pancake-shaped grains parallel to the impact face as shown in location a of Fig. 2. Similar deformation is observed to different degrees throughout the mushroomed region However, it is most severe nearest the impact face and nearest the axis.

Of particular interest, however, are voids observed along the axis near the impact face in both the impactor and receptor, location b. Typically, these cavities are non-symmetric. In order to assess whether the observed porosity resulted from metallographic polishing, the mating surfaces to those shown in Fig. 2 were polished using a different technique. The voids observed in these mating surfaces matched those in the figure. Thus, we believe the observed damage was produced during the impact event

The void porosity, or damage, results from strong tensile release waves that propagate from the lateral free surface of the rods after the initial compressive wave. These tensile release waves focus on the rod axis

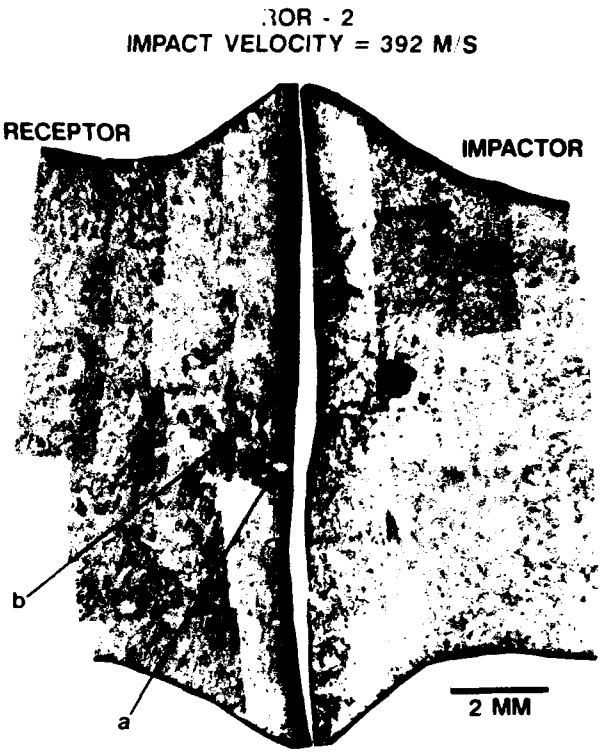


Fig. 2. Deformed microst ɔcture of 75 μm copper impacted at 392 m/s.

to create a very high, radial tensile stress. This stress causes microvoids to nucleate and grow. Close inspection reveals that the nucleation sites are along grain boundaries with void growth, or link up, occurring along grain boundaries as well.

Christy *et al.*, (1986) reported on microstructural features of similar OFE copper shock loaded in flyer plate experiments. They reported that in large grain copper, 250 μm and 90 μm material, void nucleation and growth occurred at grain boundaries. The average grain size of the material in Fig. 1a is 75 ±12 μm as determined by the linear intercept method.

Figure 3 shows results from a test conducted at 300 m/s with the 75 μm copper. Comparison between Figs. 2 and 3 shows similar grain deformation has occurred at the impact interface nearest the rod axis. Void nucleation has occurred and appears to be associated with the grain boundaries of the material. In general, Fig. 3 reveals a smaller void size which is consistent with a lower impact velocity. The amplitude of the initial compressive and tensile release waves are impact velocity dependent.

Figure 4 shows results from a test conducted at 233 m/s with the 40 μm copper. Comparison with the 75 μm material shows similar types of grain deformation. However, the void porosity on the rod axis nearest the interface has now increased, and the geometric shape of the voids is spherical. The increased void porosity, for a lower impact velocity experiment, indicates a relationship between the stress state in the material and the grain size.

Christy *et al.*, also experimented with finer grain, 20 μm, copper and with cold worked copper. These materials revealed a change in phenomenology associated with void nucleation and growth. In these materials, Christy *et al.*, observed that the nucleation sites for voids were occurring as often in the matrix

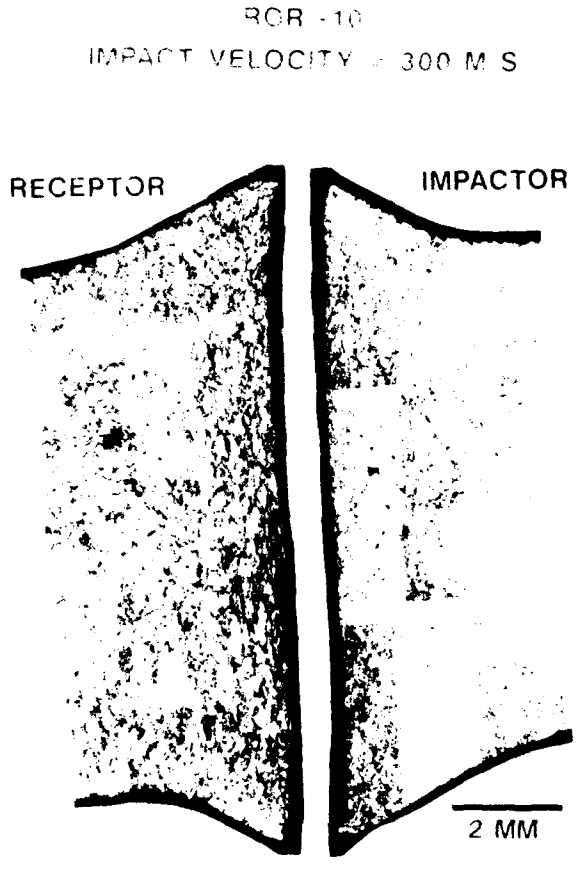


Fig. 3. Deformed microstructure of 75 μm copper impacted at 300 m/s.

as they did at the grain boundary. Propagation of the voids in fine grain and cold worked copper was occurring by transgranular growth. These observations are consistent with the results seen in Fig. 4.

Grain size studies show that a small grain material will harden faster at low levels of strain than does a larger grain material. This phenomena is related to the grain boundary surface area per unit volume and to the strain compatibility requirements between neighboring grains. Under an applied load, grain boundaries act to create dislocation pile-ups and can be sinks for dislocation annihilation. Because of a high volume fraction of grain boundary, a fine grain material tends to harden rapidly at low strain levels and to have a relatively homogeneous distribution of dislocations.

Copper with a large grain size has a lower volume fraction of grain boundary, it tends to harden more slowly and to have, initially, a more heterogeneous distribution of dislocations. In larger grain material, regions adjacent to grain boundaries have a high dislocation density, whereas in the inner matrix material the dislocation density remains relatively low. Consequently, under the stress state created by tensile release waves, the large grain material hardens along the grain boundaries where eventually the stress state will cause void nucleation to occur. Once nucleated, voids in the material will propagate along the grain boundaries where the energy requirement for crack growth will be lowest.

Under the same stress state, fine grain materials will uniformly harden both at the grain boundary and in the matrix. This condition makes the probability of void nucleation at the grain boundary versus the matrix

approximately equal. Once nucleated, voids grow in accordance with the local stress condition, given that uniform hardness exists in the surrounding regions. This pattern of void growth is consistent with that observed in Fig. 4.

There is a highly important relationship of these observations to hypervelocity impact phenomena. In recent years, various damage models of material behavior have been incorporated into the constitutive relations that are used to calculate — or predict — the deformation response of materials under hypervelocity impact. The postulated damage is usually in the form of porosity. Often, an evolutionary equation is used that associates a porosity growth rate with a tensile hydrostatic stress, and no change when the hydrostatic stress is compressive. Accumulation of porosity has two effects on the material: it increases true stress because the internal load is transmitted through less material, and it facilitates fracture. These material models, therefore, can be very important in describing such hypervelocity impact phenomena as, for example, spallation.

Damage models of material behavior have been motivated by observations of porosity in the necked regions of ductile metal tension test specimens. However, the mechanical behavior of materials is generally affected by deformation rate. Hence, observations of damage under pseudo-static test conditions need not describe what occurs during hypervelocity impact. The present tests and observations are a small step on the long road to producing a quantified damage theory applicable at high rates of deformation.

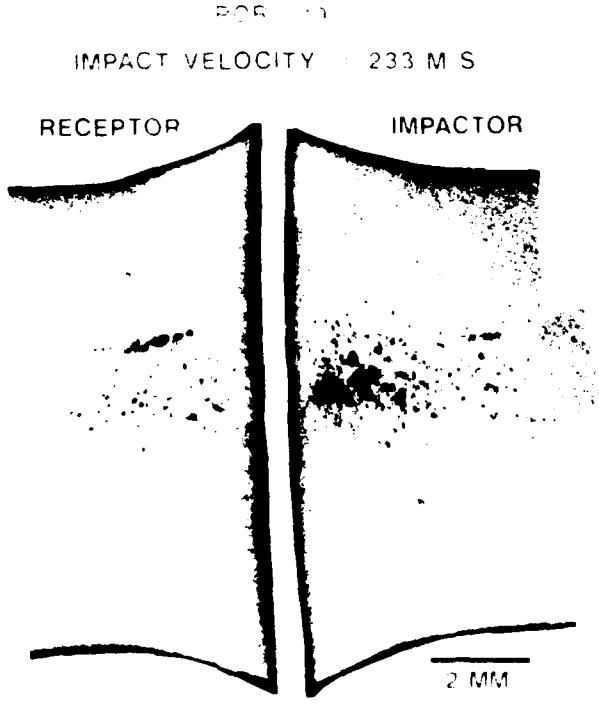


Fig. 4. Deformed microstructure of 40 μm copper impacted at 233 m s

One significant difference arises in the quantitative interpretation of porosity between high-speed ROR tests and pseudo-static tension tests. In the latter, the hydrostatic stress is somewhat uniform over any cross-section of the specimen, even after severe necking. Consequently, the area fraction of porosity on any cross-section can be easily calculated and from it the volume fraction (that appears in most theories) can be readily found. By contrast, the stress state in an ROR specimen is much more variable. There are axial and time variations as in the tension specimen, but, unlike the tension specimen, there are large radial variations in stress. In fact, except near transverse free surfaces, the only region of the specimen in which the hydrostatic stress can become tensile is the longitudinal axis. Radial waves from the lateral surface propagate tensile (release) stresses towards the specimen axis. As they converge on the axis, they amplify and produce extremely high hydrostatic tensions in this region even though the axial stress component remains compressive. This description is consistent with the observations of porosity near the specimen axis and complete absence thereof near the lateral surface (Worswick *et al.*, 1991). This leads to the conclusion that there is a radial variation in fractional porosity from center to surface, which raises the question of what total area should be used to calculate an area fraction.

CONCLUSIONS

Microstructural features such as grain deformation and porosity have been examined in specimens recovered from ROR impact tests. These experiments revealed that grain size played a major role in determining the hardening and void growth characteristics of OFE copper. Experiments with 75 μm material at 392 m/s and 300 m/s showed a smaller void size at the lower velocity. An experiment conducted with 40 μm material at 233 m/s showed a striking increase in void porosity and a general change in void geometry. This demonstrates the influence of the grain boundary causing more rapid hardening of the fine grain material than in the larger grain material. The ROR impact test has proven to be a useful experiment for studying high strain-rate deformation when combined with an analysis of internal material damage.

REFERENCES

Christy, S., H. Pak, and M.A. Meyers (1986). In: *Metallurgical Applications of Shock-Wave and High-Strain-Rate Phenomena* (L.E. Murr, K.P. Staudhammmer, M.A. Meyers, eds.), pp. 835-863. Marcel Dekker, Inc., New York.

Erlich, D., D.A. Shockey and L. Seaman (1981). In: *AIP Conference Proceedings, No. 78, Second Topical Conference on Shock Waves in Condensed Matter,* pp. 402-406. Menlo Park, California.

House, J.W., L.L. Wilson, T. Wallace, P. Maudlin (1992). Experimental Results of Symmetric Taylor Tests Using OFE Copper, In preparation.

Taylor, G.I. (1947). The Use of Flat-Ended Projectiles for Determining Dynamic Yield Stress, I. Theoretical Considerations, *Proc. Roy. Soc. London, Series A,* **194,** 289-299.

Whiffin, A.C (1947). The Use of Flat-Ended Projectiles for Determining Dynamic Yield Stress. II. Tests on Various Metallic Materials, *Proc. Roy. Soc. London, Series A,* **194,** 300-322.

Worswick, M.J., B. Wang and R.J. Pick (1991). Void Growth During High-Velocity Impact: Experiment and Model. *Journal de Physique,* **4,** 605-612.

Int. J. Impact Engng Vol.14, pp.509–518, 1993
Printed in Great Britain

0734-743X/93 $6.00+0.00
© 1993 Pergamon Press Ltd

A COMPARISON OF HOLE SIZE FORMATION CAUSED BY A HYPERVELOCITY IMPACT WITH A THIN FILM USING MOLECULAR DYNAMICS AND CTH

*Robert A. McDonald, *William G. Tanner and * W. M. Alexander

*Baylor University Space Science Laboratory Department of Physics
Waco, Texas 76798-7303

ABSTRACT

The relationship of the mass, velocity, and density of an impacting projectile to the hole formed as a consequence of a hypervelocity penetration is a subject of great importance in the study of Interplanetary Dust Particles and Orbital Debris. During the past twenty years extensive efforts have been made in developing computational procedures that model hypervelocity impacts. The vast majority of these projects have used hydrodynamic equations with either a Lagrangian or Eulerian grid or some hybrid of the two forms. Another numerical procedure that can be applied to the study of hypervelocity penetrations is molecular dynamics (MD). The appeal of MD to the problem of hypervelocity impacts lies in the fact that the thermodynamic variables of pressure, temperature, and density are found independently of each other without requiring an equation of state. The primary disadvantage of MD is the size of the system that can be effectively modeled. In this paper six different hypervelocity impacts are considered using MD and the hydrocode CTH developed at Sandia National Laboratories. The six impacts consist of a cube impacting a thin film at 7, 9, and 11 km/s with an aspect ratio of one to one and two to one. The time evolution of the density, pressure, and temperature are compared for each of the methods. Finally the hole size created by the impacts are calculated for each method, and the results compared. Conclusions about the effectiveness of MD are offered with suggestions for future work.

INTRODUCTION

The scientific community interested in hypervelocity impact phenomena has utilized hydrocodes for over twenty years to study subjects as penetrations, crater formations, debris clouds, and ejecta spray. Considerable effort has been devoted to the development of numerical techniques such as molecular dynamics and the Metropolis Monte Carlo to model liquids on the molecular level. For a good overview of the use of computers to study liquids see Allen and Tildesley (1987). Several years ago Holian (1987) used MD to study debris cloud formation in the case of a hypervelocity impact of a lead ball on a lead plate. More recently Hoover (1992) has used MD to study plastics deformation in an amorphous solid comparing the results to those obtained using a two dimensional Lagrangian code and suggested the development of a hybrid code. In this paper the techniques of MD are applied to several cases of an aluminum cube hitting an aluminum film. The Eulerian hydrocode CTH is used to model the impact of a cube hitting a 500 Å thin film with an aspect ratio of one to one and two to one. A Lennard-Jones potential is used in a MD simulation to model an impact with the same aspect ratios with a film whose thickness is 16.2 Å. A scaling factor is employed to examine the impacts at times that correspond to the same stage in the hypervelocity impact. The results for the hole created by the penetration are compared in an effort to arrive at an understanding of the effectiveness of MD in

studying long time macroscopic phenomena.

MOLECULAR DYNAMICS AND HYDRODYNAMICS

Since the determination in the last century that all matter is composed of atoms, scientists have attempted to determine how macroscopic phenomena arises from interatomic or intermolecular interactions. It is not possible or necessary here to consider the details involved in the study of kinetic theory and molecular hydrodynamics. It is only necessary for the purposes of this paper to note that for any quantity χ that is conserved in a molecular collision then it is possible to arrive at a general conservation law (Huang 1987),

$$\frac{\partial}{\partial t} n\langle\chi\rangle + \sum_{i=1}^{3} \frac{\partial}{\partial x_i} n\langle\chi v_i\rangle - \sum_{i=1}^{3} n\left\langle v_i \frac{\partial \chi}{\partial x_i}\right\rangle - \sum_{i=1}^{3} \frac{n}{m}\left\langle F_i \frac{\partial \chi}{\partial v_i}\right\rangle = 0 \tag{1}$$

where n is the number distribution, χ is the physical quantity of interest such as mass, momentum, and energy, v_i is the velocity of the ith particle, and F_i is the ith component of the external force such as gravity. By considering a system with no external forces that possesses a local Maxwell-Boltzmann distribution with a correction term one finds the conservation equations that form the basis of hydrodynamics (Huang 1987). To stay consistent with the assumptions employed in finding these relationships it is necessary to choose an intermolecular potential whose interacting length is on the order of Angstroms. One such potential commonly used in MD is the Lennard-Jones potential.

$$\Phi(r) = 4\varepsilon\left[\left(\frac{\sigma}{r}\right)^{12} - \left(\frac{\sigma}{r}\right)^{6}\right] \tag{2}$$

The values for the two parameters in the Lennard-Jones potential are determined by using the relationship that the cohesive energy is $E_{coh} = -8.6\varepsilon$ and the nearest neighbor distance in equilibrium is given by $r_0 = 1.09\sigma$ (Ashcroft and Mermin 1976). Using the experimentally determined values for the cohesive energy and the nearest neighbor distance for aluminum, one finds the values for the Lennard-Jones parameters: ε and σ.

The temperature is found using the expression (Plischke and Bergson 1989)

$$T(t) = \frac{1}{3k_B N}\sum_{i=1}^{N} m v_i(t)^2 \tag{3}$$

where T(t) is the instantaneous temperature, N is the number of molecules, m is the mass of the molecules (here assumed to be the same), and $v_i(t)$ is the instantaneous velocity of the ith particles. The pressure is found using the equation (Plischke and Bergson 1989)

$$P(t) = \frac{N}{V} k_B T(t) + \frac{1}{6V}\sum_{i \neq j}\left[\vec{r_i}(t) - \vec{r_j}(t)\right]\cdot\vec{F_{ij}}(t) \tag{4}$$

where P(t) is the pressure at a given time t, V is the volume r_i is the position of the ith particle and F_{ij} is the force between the ith and jth particles which should not be confused with the external force contained in equation (1).

CTH AND MOLECULAR DYNAMICS PROCEDURES

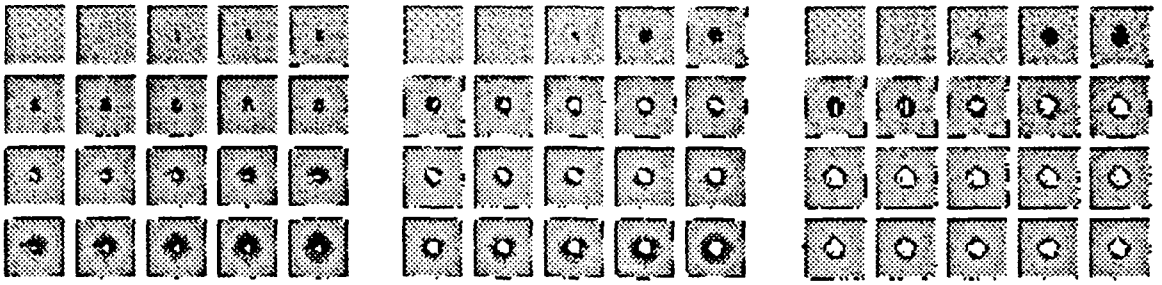
The hydrocode CTH developed at Sandia National Laboratories has been used at the Baylor University Space Science Laboratory (BUSSL) for several years to conduct theoretical investigations of thin film penetrations. This work was motivated by the flying of several experiments using thin films on several shuttle missions and an experiment currently being flown as part of the European Retrievable Carrier 1 mission. The impacting particles studied are spheres traveling at orbital and interplanetary velocities hitting a thin film. The size of the film selected for investigation using CTH corresponds to the surface area and thickness of

the film used in the in-situ experiment. For comparison with results obtained by MD the geometry of the particle was altered to a cube with all the other parameters kept the same. The computational calculations that were completed for CTH used 200 x 400 cells covering an area of 160 x 200 microns squared with each zone being 50 Å on a side. The minimum time step employed for the runs was $5x10^{-15}$ seconds with an average of $3x10^{-13}$ seconds. The thickness of the film (T_f) was 500 Å and possessed a width of 10,000 Å. The width and cell size were chosen to allow the system a sufficient space to allow the creation of a penetration hole, and to compare with experimental results reported in a companion paper (Tanner 1992). The equation of state employed was Mie-Grüneisen for aluminum, and the velocities of the impacting projectile (v_p) were the same as those used in the MD simulations discussed below.

In addition to hydrocode calculations BUSSL has been using MD to study hypervelocity penetrations of thin films for different velocities under a given potential (McDonald 1991). Once a potential has been selected, MD consists in numerically solving the Newtonian equations of motion for the system of N particles. In the MD simulations considered here the potential was truncated at 1.78σ. The net cube approximation (Arnold and Mauser 1990) was used as a bookkeeping procedure to eliminate calculating most of the forces between particles whose distance exceed the truncation distance. A film consisting of 9216 particles, whose thickness was 16.2 Å with a surface area 36 times the thickness, was equilibrated at room temperature. The face of the film was laid in the XZ plane so that the velocity component normal to the film's face is in the y direction. Two projectiles, one of which had a dimension of 16.2 x 16.2 x 16.2 $Å^3$ was composed of 256 particles and the second with one dimension twice as long as the first with double the number of particles, were also equilibrated at room temperature. Three velocities: (7, 9 and 11 km/seconds in the y direction) were considered for both projectiles. Since the thickness of the film used in the MD computer simulations is significantly smaller than that employed in the hydrocode, a scaling element was used to make comparison possible between the two systems. In order to compare the size of the hole generated by the hypervelocity penetration, a time scaling element (TSE) was used. A TSE is the time for a projectile to travel the thickness of the film, i.e. T_f/v_p. Two sets of runs using MD were made. The first saved the positions and velocities of all the particles in the system every TSE, and this information is used to study the thermodynamic behavior of the system and the formation of the hole growth which is presented below. The definitions for temperature and pressure given in eqns. (3) and (4) were used to calculate the thermodynamic values inside a predefined fixed volume of space that the particles were free to move through. Two fixed Eulerian Grids were used to show the time evolution of the system during the six impacts. The first was an XZ view of the volume originally occupied by the thin film. The second is a YZ plot which is the impact as if viewed from a distance. After examination of the thermodynamic data it became clear that saving the data every TSE provided too coarse of a sampling rate to watch the thermodynamic response at the earliest stages of the impact. Therefore a second group of computer runs using MD, covering a shorter time period ($t < 6$ TSE's), saved the positions and velocities of the particles in the system at a higher sampling rate. This data was used to calculate the thermodynamic variables at the earliest stages of the impact which is considered below.

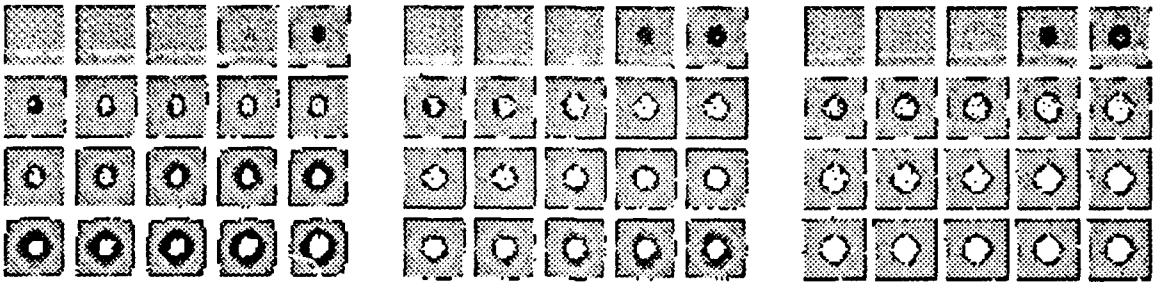
MD RESULTS AND CTH RESULTS

As mentioned above the T_f/v_p normalization factor was used to provide points of comparison between each of the impacts in the behavior of the pressure, temperature, and density. Figures 1 through 4 show the time evolution of the density in two views: one of the XZ plane whose dimensions correspond to the original volume of the film and the second which is viewing the impact from far away in the YZ plane. The XZ plots of the density show that for the 7 km/s impact there exist three distinct regions of density. These are the original density of the film, an area of smaller density corresponding to approximately 1.3 to 1.7 gm/cm^3, and the final region is an area of zero density that is used to determine the hole size. This three tiered distribution of the density is also apparent in the 9 km/s impact, but the size of the second region has decreased while the area of zero density has increased. In the 11 km/s impact the middle density values form a very thin ring around the zero density region. A possible explanation for these results lies in the mixture of penetration and cratering phenomena at the lower velocities. An examination of the YZ plots of the density supports this possibility. Note that for the impact at 7 km/s with an aspect ratio of one to one a bowing of the film appears to be occurring with very little spall coming off the back edges of the film. A debris cloud is also not in evidence for the one to one 7 km/s impact. Such a debris cloud and spall is evident for the 9 and 11 km/s runs. Note the complete absence of bowing of the film at 11 km/s. This suggests that the energy



v = 7 km/s v = 9 km/s v = 11 km/

Fig. 1. XZ plots of the time evolution of the density during the normal impacts with an aspect ratio of one to one. Each frame is a Time Scaling Element (TSE).



v = 7 km/s v = 9 km/s v = 11 km/

Fig. 2. XZ plots of the time evolution of the density during the normal impacts with an aspect ratio of one to one. Each frame is a Time Scaling Element (TSE).



v = 7 km/s v = 9 km/s v = 11 km/

Fig. 3. YZ plots of the time evolution of the density during the normal impacts with an aspect ratio of one to one. Each frame is a Time Scaling Element (TSE).



v = 7 km/s v = 9 km/s v = 11 km/

Fig. 4. YZ plots of the time evolution of the density during the normal impacts with an aspect ratio of one to one. Each frame is a Time Scaling Element (TSE).

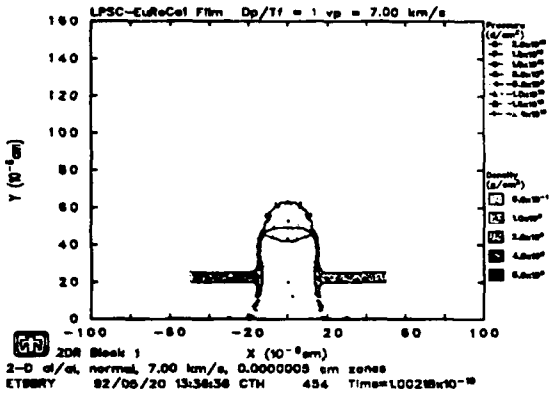
level at this velocity is sufficient to allow a penetration with almost none of the features of a cratering event. These basic features are retained in the impacts with a two to one aspect ratio with the expected exception that the penetration has improved for the long rod.

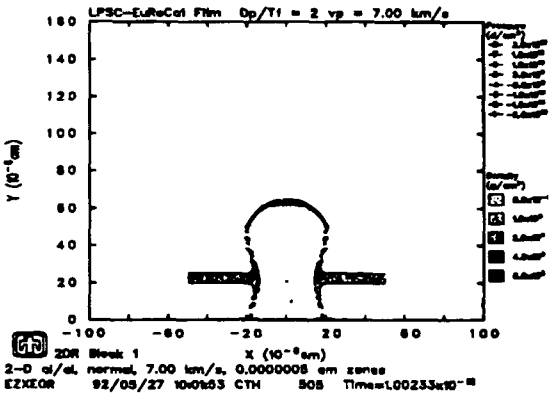
The stopping point for the computer experiments, conducted using the hydrocode CTH varied with the impact. The criteria used for determining when the hypervelocity event had finished was that the pressure has reduced to the level of background. The stopping point for the impact at 7 km/s for both aspect ratios was 14 TSE's. Sixteen and 18 TSE's were the end points for the one to one and two to one 9 km/s impacts respectively. The stopping points for the 11 km/s impacts were 17 and 22 TSE's. Figures 5 and 6 show the two dimensional density and pressure distribution in the thin film and the debris cloud at the final time. Comparing these results with the Figs. 1 through 4 one immediate difference is the length of the film in the CTH runs was 20 times larger than its thickness, while the MD simulations used a film whose dimensions normal to the thickness was six times larger than that used for the T_f. The other fact that is apparent when comparing the two results is that for the impacts at 7 and 9 km/s the hole formation has not stabilized at 14 TSE's. Only in the 11 km/s impact does the event appear to be over. The reasons for this difference are not known at the present time.

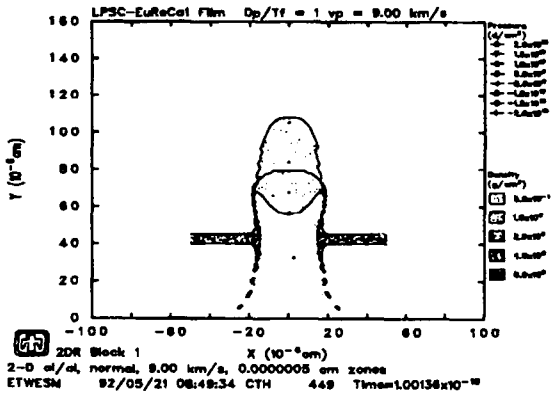
Before direct comparisons between the hole sizes generated by the two methods are made the behavior of the pressure and temperature will be considered. A Lagrange point was chosen in CTH that was originally located at the center of the impact site between the projectile and thin film. In order to compare the results for the macroscopic thermodynamic variables a volume element ,whose dimensions were equal to those of the projectile at the beginning of the simulation, was located at the center of the film directly in the line of the velocity vector. This volume element was used to calculate the density, pressure, and temperature of the grid point. The macroscopic velocity was found for the volume element which was free to move with the calculated velocities. Figures. 7 through 10 show the history of the pressure and temperature for both computer experiments. The MD graphs are plotted in TSE units while the CTH graphs are plotted in absolute time. For comparison between MD and CTH note that the conversion between the two time scales is given by: 7.14 ps for the 7 km/s impacts, 5.56 ps for the 9 km/s, and 4.55 ps for the 11 km/s. Using these scaling factors for comparison purposes it is apparent through the study of the plots that the values for the temperature calculated using MD were consistently smaller than those found by CTH. Another immediate difference is that the temperature in the MD run returned close to the initial or background value for the Lagrangian volume element while the temperature found by CTH retains a value that is significantly larger than the background values. The estimates for the pressure show that MD has values for the peak pressure that are slightly smaller than those generated by the hydrocode. Using the thermodynamic variables calculated for the Lagrangian volume element in MD it is possible to plot the relationship between pressure and temperature for a constant density. If one plots the pressure versus temperature for densities of 2.4 and 2.7 gm/cm^3 as done in Fig. 11, one finds that a linear relationship between pressure and temperature is a good approximation of the EOS for constant densities. The Mie-Grüneisen EOS used by CTH postulates a linear relationship between pressure and temperature for a volume held at constant density. This preliminary discussion of the EOS that was found using MD, suggests that this method holds promise for future study of hypervelocity impacts. The interesting behavior of the thermodynamic variables is in the earliest stages of the impact ($t < 6$ TSE's), while other macroscopic phenomena such as the formation of the hole resulting from penetration take significantly longer. A comparison of hole size will now be done for MD and CTH.

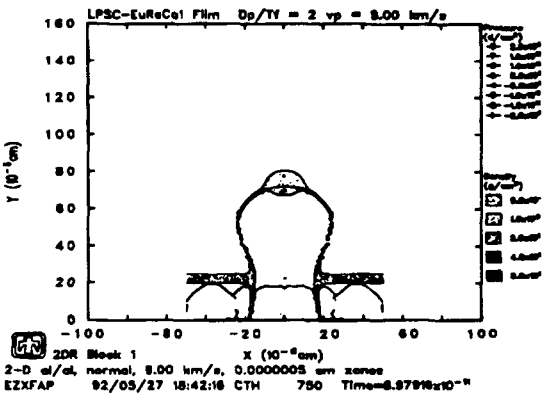
As noted above in the analysis of the XZ density graphs the computer experiments show three distinct values of density with the area of the second region decreasing with impact velocity. At this point it is necessary to determine the ratio of the diameter of the penetration hole (D_h) to the dimension of the projectile parallel to the film (D_p) in order to undertake a comparison with those values found by using CTH. This was done by examining a slice through the center of the film and counting those grid points where there was one or less particles. In an effort to minimize the error in diameter, only those values that occur concurrently were considered. Figure 12 shows the history of hole growth in the one to one aspect ratio for the MD computer experiments. The hole growth for the two to one impacts is shown in Fig. 13.

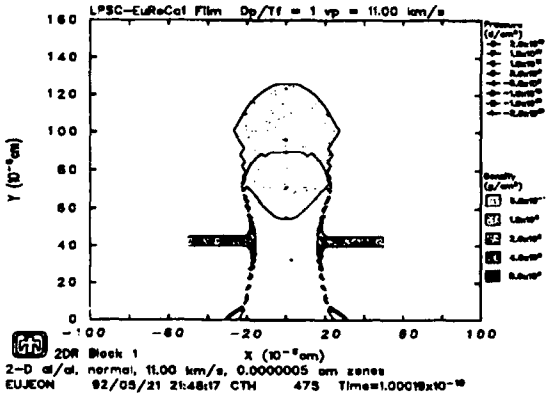
To determine the hole size as shown by the hydrocode calculation the smallest distance between the two sides of the film as seen in Figs. 5 and 6 was measured at the appropriate TSE. The results from the CTH runs are











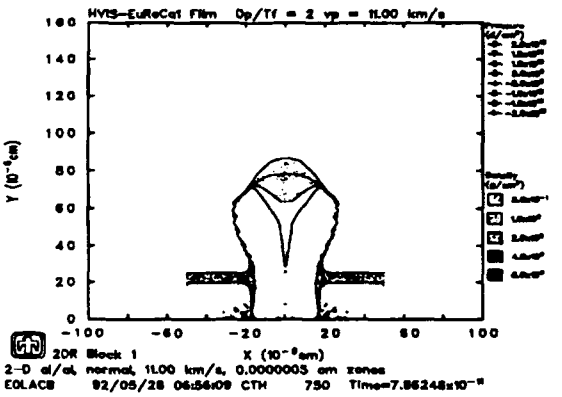
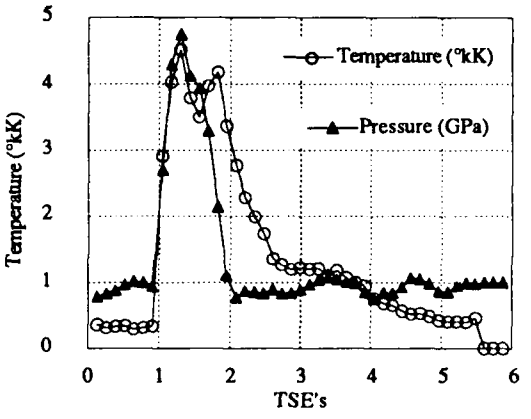


Fig. 5. Plots of the density and pressure generated by CTH at the stopping point for the one to one normal impacts.

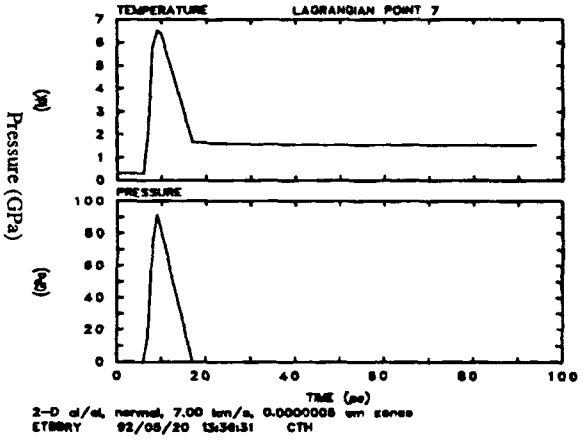
Fig. 6. Plots of the density and pressure generated by CTH at the stopping point for the two to one normal impacts.

shown in Table 1 which shows the final hole size determined by the two different methods. The MD calculations are consistently smaller than those obtained using CTH. Since the CTH values lie in good agreement with experimental calibrations of penetration hole sizes (Tanner 1992), the disagreement is a subject that needs future study.

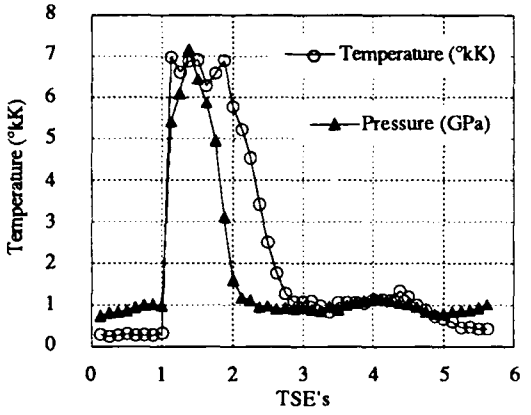
Several possibilities exist to explain the small values obtained by MD. The first is that the size of the system used is too small. As seen in Table 1 the ratio Dh/Dp exceeds five for all of the impacts. Since the width of the film is only six times larger than the diameter of the projectile then those values that lie near six are



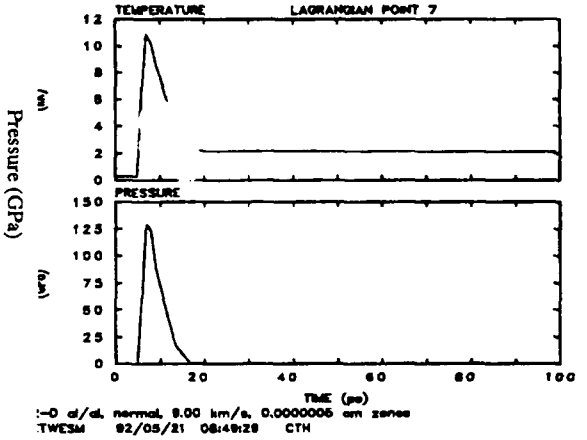
v = 7 km/s



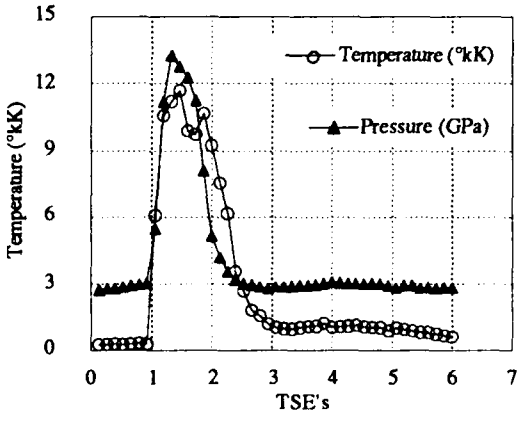
v = 7 km/s



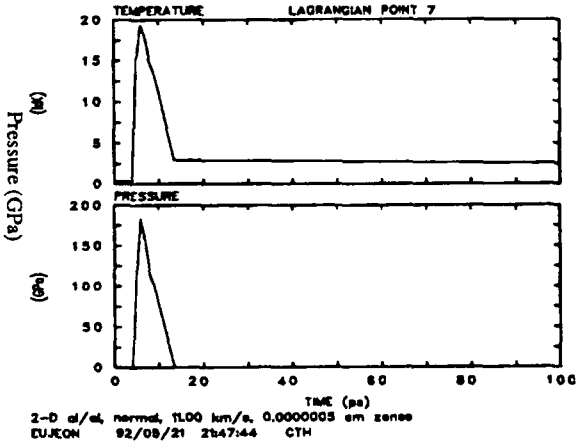
v = 9 km/s



v = 9 km/s



v = 11 km/s



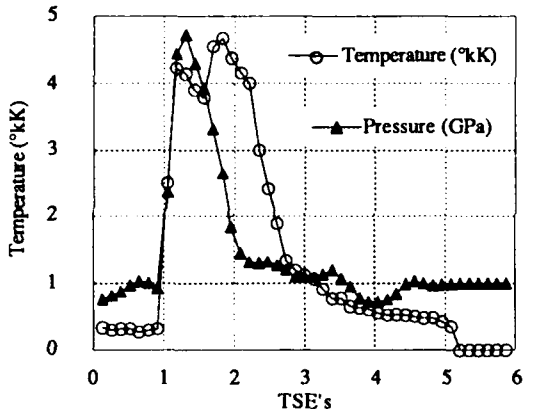
v = 11 km/s

One to One Impact

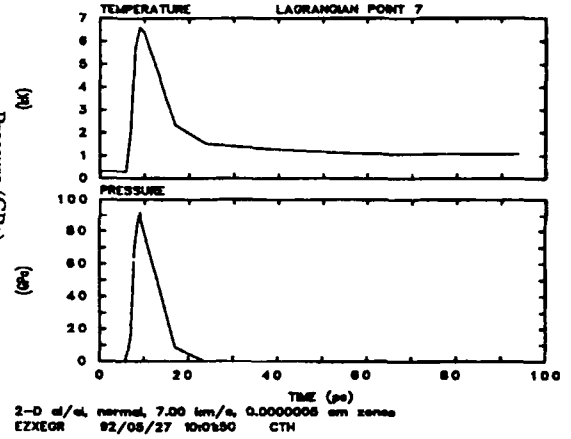
Fig. 7. Plots of the time evolution of temperature and pressure vs. the Time Scaling Elements defined in the text for the one to one impacts as found in the MD computer experiments.

One to One Impact

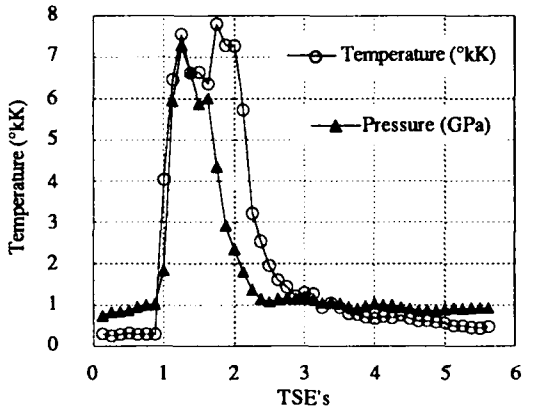
Fig. 8. History Plots generated by CTH of the pressure and temperature during the one to one normal impacts.



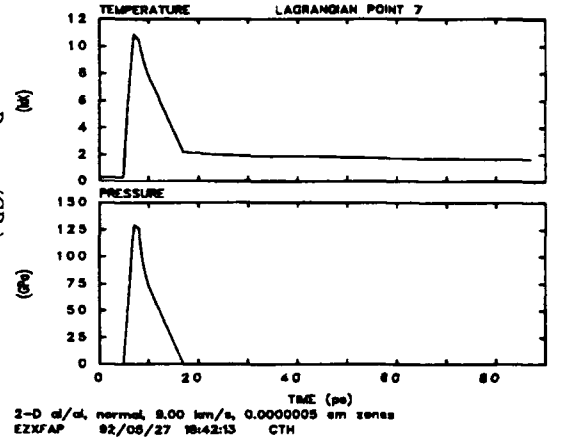
v = 7 km/s



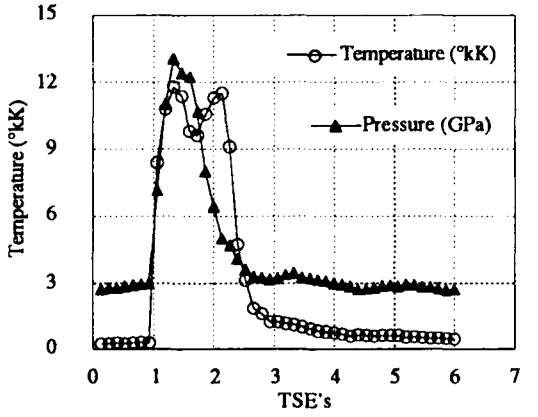
v = 7 km/s



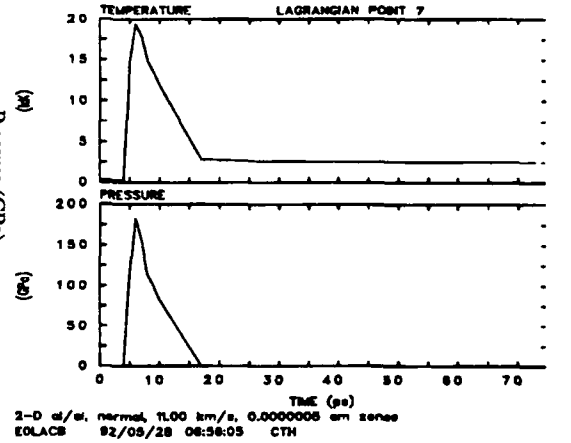
v = 9 km/s



v = 9 km/s



v = 11 km/s



v = 11 km/s

Two to One Impact

Fig. 9. Plots of the time evolution of temperature and pressure vs. the Time Scaling Elements defined in the text for the two to one impacts as found in the MD computer experiments.

Two to One Impact

Fig. 10. History Plots generated by CTH of the pressure and temperature during the one to one normal impacts.

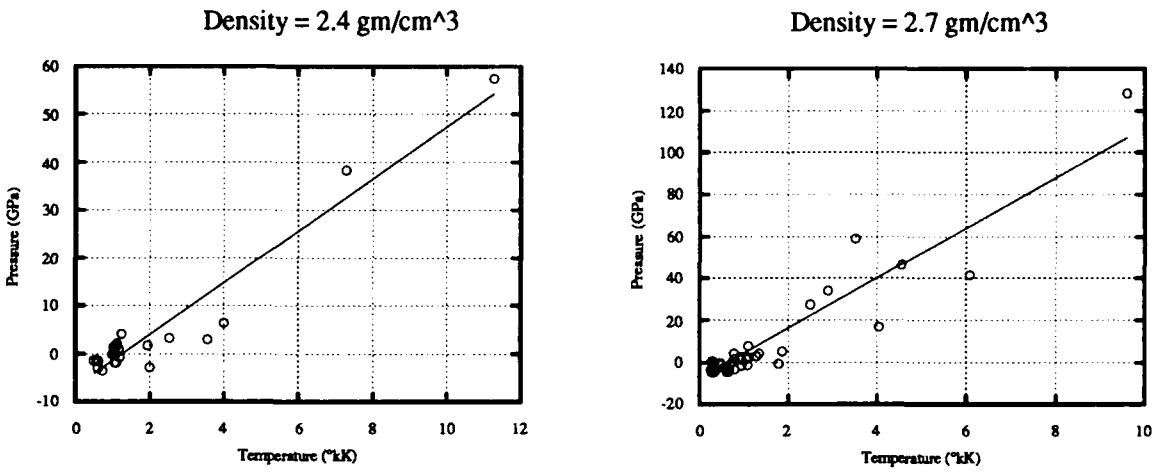


Fig. 11. Plots of Pressure vs. Temperature for two different densities found from the Lagrangian volume element discussed in the text.

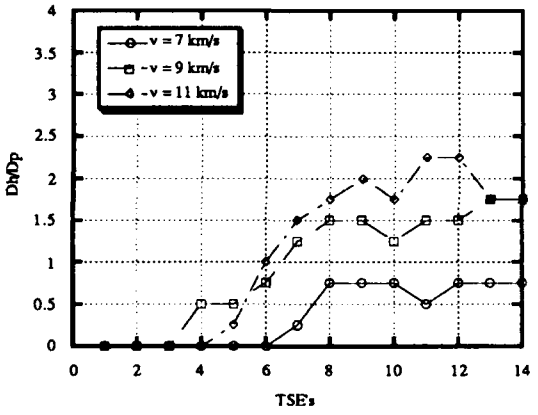


Fig. 12. Hole growth as modeled using MD for normal impacts with aspect ratios of one to one.

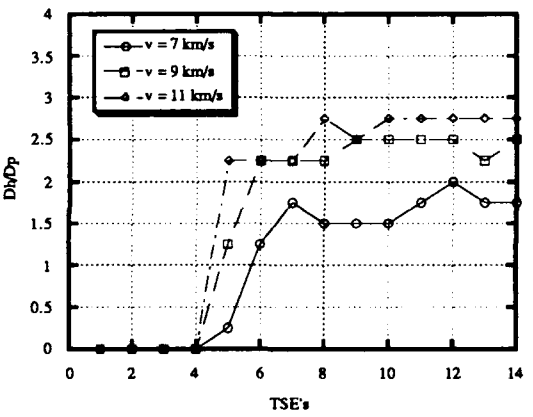


Fig. 13. Hole growth as modeled using MD for normal impacts with aspect ratios of two to one.

Table 1: Dh/Dp Measurements

Velocity (km/s)	v = 7	v = 9	v = 11	v = 7	v = 9	v = 11
Aspect Ratio	1 to 1	1 to 1	1 to 1	2 to 1	2 to 1	2 to 1
MD Simulations	0.75	1.75	1.75	1.75	2.5	2.75
CTH Simulations	5.45	5.8	6.1	5.16	5.75	6.28

not capable of being modeled with a system composed of this few particles. This could be remedied by the use of larger systems which is being made more practical by the development of massively parallel computers, although a complete simulation of the system used in the hydrocode simulation would require more than a billion particles. Another possibility is the fact the the film used in the MD simulations is only 16.2 Å thick. Experimental investigations have shown that the ratio Dh/Dp decreases as the film and particle decrease in absolute size (Schneider 1979). The results reached in the MD calculations could then be a lower limit on the penetration hole sizes. Physically this could arise since the film used in the simulations was a perfect FCC crystal. The lack of dislocations and flaws in the film could explain why the damage was smaller than that seen in the hydrocode calculations which use equations of state which are based on macroscopic investigations where all crystals contain flaws. Both of these explanations can be tested with future computer experiments as larger systems can be used, and dislocations introduced into the system to investigate what effect the presence of dislocations have on hole size formations.

CONCLUSIONS

The comparison of the results obtained by using molecular dynamics and hydrodynamics shows that. with the exception of the calculation of the pressure, MD consistently underestimates the values obtained by CTH. Since the results obtained by CTH are in good agreement with experimental curves reported, it would appear that the disagreement suggests the need for the use of larger systems in MD to model hypervelocity events. In considering the behavior of the temperature and pressure the major difference is the long time behavior of the temperature in the two methods. The reasons for this discrepancy need to be explored in future studies. The hole sizes predicted by MD are significantly smaller than those found using CTH, and future work needs to be done in order to determine if the smaller sizes found using MD have a physical basis or are a feature of the size of the system employed. It will also be of interest to utilize potentials that have been developed to describe metals (Pettifor and Ward 1984) to examine what significance the selection of the potential has on macroscopic phenomena. Both MD and hydrocodes have a significant role to play in the continuing studies of hypervelocity impact phenomena. The use of larger systems, which are becoming more feasible as computational power continues to increase, offers a chance for MD to become far more effective in modeling hypervelocity impacts than its present capability.

REFERENCES

Allen, M. P. and D. J. Tildesley (1987). Computer Simulation of Liquids. New York, Oxford University Press.

Arnold, A. and N. Mauser (1990). "An Efficient Method of Bookkeeping Next Neighbors in Molecular Dynamics." Computer Physics Communications 59, 267-275.

Ashcroft, N. W. and N. D. Mermin (1976). Solid State Physics. Philadelphia, Holt, Rinehart and Winston.

Holian, B. L. (1987). "Hypervelocity-impact phenomena via molecular dynamics." Physical Review A 36(8), 3943-3946.

Hoover, W. G., A. J. DeGroot, et al. (1992). "Massively parallel computer simulation of plane-strain elastic-plastic flow via nonequilibrium molecular dynamics and Lagrangian continuum mechanics." Computers in Physics 6(2), 155-167.

Huang, K. (1987). Statistical Mechanics. New York, John Wiley & Sons.

McDonald, R. A. (1991). "A Study of Hypervelocity Impacts using Molecular Dynamics". Ph. D. Dissertation Baylor University.

Pettifor, D. G. and M. A. Ward (1984). "An Analytic Pair Potential for Simple Metals." Solid State Communications 49(3), 291-294.

Plischke, M. and B. Bergson (1989). Equilibrium Statistical Physics. Englewoods Cliff, New Jersey, Prentice Hall.

Schneider, E. (1979). "Velocity Dependencies of Some Impact Phenomena". The Comet Halley Micrometeriod Hazard, Workshop held at ESTEC Noordwijk, the Netherlands, ESA SP-153.

Tanner, W. G., R. A. McDonald, et al. (1992). "An Examination of Hypervelocity Particle Penetration Parameters for Thin Films Flown in Space." submitted to the 1992 HVIS Conference.

Int. J. Impact Engng Vol.14, pp.519 - 530, 1993
Printed in Great Britain

0734-743X/93 $6.00+0.00
Pergamon Press Ltd

DEVELOPMENT AND OPTIMIZATION OF A MULTIBUMPER DESIGN MODEL FOR SPACECRAFT PROTECTIVE STRUCTURES

R. A. MOG,* M. J. HELBA,♣ and J. H. ROBINSON•

*Science Applications International Corp., Huntsville, AL 35806
♣Science Applications International Corp., Huntsville, AL 35806
•NASA Marshall Space Flight Center/ED52, Huntsville, AL 35812

ABSTRACT

The development and optimization of a design model for multibumper spacecraft protective structures to defeat orbital space debris is presented. The Marshall Space Flight Center (MSFC) Materials and Processes (M&P) Laboratory Hypervelocity Impact Database is first filtered to experiments comprising metallic configurations without multilayered insulation present and for projectile velocities exceeding 2.5 km/sec. This filtering results in 337 single, double, and triple bumper hypervelocity impact experiments. Regression variables of interest include projectile diameter, density, velocity, and impact angle, bumper standoff distances, bumper densities and thicknesses, wall density and thickness, and number of bumpers. The dependent regression variable is the total number of plate penetrations, beginning with the wall and continuing through the witness plates. A unique intrinsically linear regression form, which accounts for the number of bumpers employed and invokes a posynomial (polynomial with positive coefficients, positive valued independent variables, and real valued exponents) form, is chosen based on a comparison of various regression forms using correlation coefficient and F-statistic as measures of effectiveness. The least squares regression is performed followed by an ANOVA, tests of the correlation coefficient and F value, and graphical examination of residuals. Regression results indicate that statistically significant least squares is possible using the chosen form on the MSFC M&P database with small residual effects. Generic nonlinear regression forms are also investigated.

The resulting regression model is next used in the formulation of a nonlinear optimization program. This program is devised to minimize the protective structures areal density subject to a limitation on total standoff distance between the first bumper and the wall. The decision variables of interest are the optimal values of the areal densities of the bumpers and wall, as well as the optimal individual standoff distances. The problem is solved using the dual transformation of geometric programming. The optimal independent variables and minimum system areal density are solved for analytically in terms of the systemic parameters. A sensitivity analysis to these parameters is then performed. Additionally, the optimal number of bumpers is evaluated in this sensitivity study. The most significant results from a hypervelocity impact standpoint are that additional hypervelocity impact tests and analyses should be performed to support understanding of multiple bumper, large particle diameter, large separation, large particle mass density, various particle impact angles, and spallation phenomenologies. Additionally, more emphasis should be placed on understanding the transition regions between particle shatter, melt, and vaporization, while less emphasis should be placed on small velocity differences within these regions. Major protective structures design results indicate that for Space Station Freedom impact scenarios of interest, and within the limitations of the regressed hypervelocity impact database, at most four metallic bumpers are optimal. In particular, a transition region from optimal number of bumpers of 2 to 3 (and 3 to 4) has been identified for particle diameters in the 0.25-0.5 cm (and 1 to 1.25 cm) range. An interesting transition region from 3 to 4 optimal

*Systems Survivability Engineer, SAIC.
Associate Graduate Faculty Member, UAH.
Principal Consultant, Huntsville Research Consortium, Inc.
♣Physicist, SAIC.
•Aerospace Engineer, Structures and Dynamics Lab, MSFC.

number of bumpers has been discovered for standoff distances between 10 and 15 cm. Furthermore, the optimal protective structures design sensitivity to impact angle is very low. Finally, the results of this investigation indicate that this combination of regression form and resulting optimization approach is useful in identifying protective structures design trends for spacecraft subject to hypervelocity impact environments.

LIST OF SYMBOLS

a_i = estimated parameters for regression
d, D = projectile diameter (cm)
L_n = wall material parameter
n = number of plates (bumpers and wall)
N = number of "walls" penetrated (walls + witness plates)
S_i = separation between bumper i and bumper i+1 (cm)
S_{ToT} = total allowable separation from 1st bumper to wall (cm)
t_i = bumper thickness, i=1,2,...,n-1 (cm)
t_n = wall thickness (cm)
V = projectile impact velocity (km/sec)
W = structure mass per unit area or weight (gm/cm^3)
θ = impact angle from surface normal (deg)
ρ_i = bumper density, i=1,2,...,n-1 (gm/cm^3)
ρ_n = wall density (gm/cm^3)
ρ_p = projectile mass density (gm/cm^3)
A 0 subscript denotes optimal value for a primal variable.

INTRODUCTION

Since the 1960's, the effects of meteoroid impacts on spacecraft function and safety have been a concern to systems design engineers. With the recent increase in man's activity in low Earth orbit, this concern has expanded to include the man-made orbital debris environment. Unlike the meteoroid environment, the number of debris particles continues to grow as more vehicles are launched into Earth's orbit. This increasing hazard requires that spacecraft designers become more innovative and efficient in designing the shield systems necessary to protect the spacecraft being launched today. In addition to the more numerous debris particles, future space missions (e.g., Space Station *Freedom*) pose other critical design problems. Unlike the short-term missions of the past, future vehicles will have longer exposure periods to both the meteoroid and debris environments. These vehicles will also be more complex and much larger than earlier spacecraft. The larger area-time product of exposure places these vehicles at increased risk of impact of critically damaging particles. The traditional measure of protective structures design effectiveness is the probability of no penetration of the primary spacecraft wall. This measure is the risk associated with the occurrence of the impacting particle size, impact velocity, and impact angle. Finally, the inherent uncertainties in the meteoroid and debris projectile mass, velocity, density, shape, and impact angle further complicate the design problem, making the traditional deterministic design approach impractical.

The traditional design solution to this problem has generally been to place a "bumper" outboard from the spacecraft wall to disrupt the incoming projectiles. The existing spacecraft wall is often better able to withstand the impacts of the resulting dust than that of the single larger particle. This passive measure has resulted in significant weight savings relative to a single wall concept with the same protective capability. The problem, then, is to efficiently design these protective structures so that the bumper breaks up the projectile while minimizing its lethality to the primary wall, the crew, and the onboard equipment.

Existing design and analysis techniques which are commonly used to aid in the design of shielding include hypervelocity impact testing, empirical penetration equations, and hydrodynamic codes. The most widely accepted of these is impact testing, which has the advantage of providing actual spacecraft hardware design verification. However, in existing test facilities, test velocities are limited to about 25% of the expected impact velocity distribution of man-made debris, and even less for meteoroids. An additional detriment to relying on impact tests alone is the extensive number of tests required to characterize the effects of each of the large number of design parameters to statistically significant trends. Hydrodynamic code analysis can help overcome the velocity limitations, but this method is

very computer time intensive, and there is a fair amount of controversy involved in the selection of appropriate equations-of-state and code-specific parameters. Empirical penetration equations generally provide the best quick-look of a shield design's protective capability. However, special care must be taken to be sure they are used only within the same parametric limitations from which they were experimentally or theoretically derived, and with a clear understanding of the regression analysis used in their statistical formation. If the problem to be solved falls within the experimental parameter limitations, the equations can provide more information about the design than a limited number of experimental results.

Through nonlinear optimization techniques, the characteristics of the empirical penetration predictor equation can be determined with sensitivities anchored around a given design for the shield system. Analytic or numerical solutions result, depending on the nature of the predictor, the problem formulation, and the technique used. In this paper, nonlinear optimization techniques are used to first develop a preliminary design predictor for the shielding that might be required to defeat the meteoroid and debris impacts that futuristic spacecraft might encounter. Mission parameters and design environments are chosen to best represent those we believe to be most realistic for Space Station missions, based on today's information. Optimal design sensitivity trades are then shown to determine operating points for system and design engineers.

PAPER GOALS

The goals of this paper are to:
1. Develop a nonlinear regression predictor for multiple bumper systems.
2. Optimize the predictor in a protective structures design context.
3. Provide a sensitivity analysis to various hypervelocity impact systemic parameters.
4. Provide a sensitivity analysis to Space Station mission parameters.

EARTH ORBITAL SPACE DEBRIS ENVIRONMENT

The space debris and meteoroid environment models chosen for this paper are based on the environment given in Reference 10. This debris environment is a perturbation of a previous environment definition due to Kessler (1989). The major inputs for this definition include space debris growth rate, spacecraft operational period, mission altitude and inclination, spacecraft debris area, orientation, and probability of no penetration. The previous Kessler environment is first used to obtain a ballpark estimate of critical diameter for two numerical search techniques. The Newton's method and a random search technique are then employed to numerically hone in on a relationship between the actual particle diameter and the other parameters for the orbital debris and meteoroid environments, as specified by Reference 10.

ADVANCED SHIELDING FOR PROJECTILE SHATTER (MULTIBUMPERS)

The database used for regression is the MSFC Hypervelocity Impact Test Database Developed by the Materials & Processes Lab. Database filtering was performed to include only metallic configurations with velocities greater than 2.5 km/sec and no MLI present. The database filtering resulted in 234 single bumper tests, 94 double bumper tests, and 9 triple bumper tests.
A preliminary investigation using various posynomial regression forms was performed. The fact that many spacecraft, including Space Station *Freedom*, has sufficiently low curvature in primary areas needing protection allows for the assumption of minimizing system mass per unit area. The "best" intrinsically linear posynomial form resulting from this preliminary investigation is given by:

$$N+1 = K d^{a_1} \rho_p^{a_2} V^{a_3} \left[\cos\left(\frac{\theta}{g(n-1)} \right) \right]^{a_4} \left(\prod_{i=1}^{n-1} S_i \right)^{\frac{a_5}{h(n-1)}} \left(\prod_{i=1}^{n-1} \rho_i t_i \right)^{\frac{a_6}{h(n-1)}} (\rho_n t_n)^{a_7} (n-1)^{a_8} \qquad [1]$$

A linear least squares analysis results in:

$$K = 3.2586, \quad a_1 = 1.0471, \quad a_2 = 0.3837, \quad a_3 = 0.1780,$$

$$a_4 = 0.2979, \quad a_5 = -0.3397, \quad a_6 = -0.3249, a_7 = -0.4003, \quad a_8 = -1.0158 \qquad [2]$$

with optimal bumper scaling functions (found through search) of

$$g(n-1) = n-1, \quad h(n-1) = (n-1)^{0.65} \qquad [3]$$

From an analysis of variance, F tests, and correlation coefficient tests, the regressed model is found to be both physically (from the filtering of model forms) and statistically significant. The designer problem statement is given by: Minimize system mass per unit area:

$$\min W = \sum_{i=1}^{n-1} m_i + \frac{K}{\left(\prod_{i=1}^{n-1} S_i^{\frac{0.5486}{(n-1)^{0.65}}}\right)\left(\prod_{i=1}^{n-1} m_i^{\frac{0.8116}{(n-1)^{0.65}}}\right)} \quad [4]$$

where

$$K = \frac{19.1257 d^{2.6158} \rho_p^{0.9585} V^{0.4447} \left[\cos\left(\frac{\theta}{n-1}\right)\right]^{0.7442}}{(N+1)^{2.4981}(n-1)^{2.5376}} \quad [5]$$

subject to the following constraint: The total separation (first bumper to wall) is limited to a prespecified value

$$s.t. \sum_{i=1}^{n-1} S_i = S_{ToT}$$

$$where \quad m_i = \rho_i t_i \quad [6]$$

We must determine the optimal values of the mass per unit area for the bumper(s) and wall, the optimal individual separations, and the minimum system mass per unit area. (S_{ToT} is the total separation between the first bumper and the wall, and n-1 is the total number of bumpers (n is the total number of plates).) Using 0 degree of difficulty dual geometric programming, the minimum weight and globally optimal areal densities are given by

$$W_0 = \left(\frac{0.6786(n-1)+(n-1)^{0.65}}{0.6786}\right)^{\frac{0.6786(n-1)}{0.6786(n-1)+(n-1)^{0.65}}} [K(0.6786(n-1)^{0.35}+1)]^{\frac{1}{0.6786(n-1)^{0.35}+1}}$$

$$\cdot\left(\frac{1.0911(n-1)}{0.6786(n-1)+(n-1)^{0.65}}\right)^{\frac{1.0911(n-1)}{0.6786(n-1)+(n-1)^{0.65}}} \left(\frac{0.6786(n-1)+(n-1)^{0.65}}{1.0911 S_{ToT}}\right)^{\frac{1.0911(n-1)}{0.6786(n-1)+(n-1)^{0.65}}} \quad [7]$$

$$m_{i_0} = \delta_i W_0 \quad [8]$$

$$m_{n_0} = [1-(n-1)\delta_i] W_0 \quad [9]$$

The optimal individual separations are given by

$$S_{j_0} = \frac{S_{ToT}}{n-1}, \qquad j = 1, 2, \ldots, n-1 \quad [10]$$

BASELINE PARAMETERS

The baseline parameters for an impact systemic parameter sensitivity study are given in **Table 1.**

Table 1. Baseline Systemic Impact Parameters

* Particle Diameter = 1 cm
* Particle Density = 2.8 gm/cm^3
* Particle Velocity = 5 km/sec
* Total Bumper/Wall Separation = 10 cm
* Normal Impact
* Ballistic Limit (N = 1)

Figure 1 shows the sensitivity of optimal protective structures design variables (including optimal number of bumpers) to particle diameter. Two transition regions are found, one between 0.25 and 0.5 cm and one between 1 and 1.25 cm. In these regions, the optimal number of bumpers changes from 2 to 3 followed by 3 to 4 due to increases in diameter penetrability. Thus, given sufficient separation, as the threat grows in terms of particle diameter, there is a large incentive for adding bumpers. A sensitivity of optimal protective structures design to particle velocity shows a relative lack of sensitivity of the design over a fairly wide velocity range (3-7.5 km/sec). Although this sensitivity is more pronounced than for the vaporization region, particle velocity uncertainties do not significantly drive the system designer. **Figure 2** shows the sensitivity of optimal protective structures design variables (including optimal number of bumpers) to total bumper/wall separation. One transition region is found in this sensitivity, between 10 and 15 cm. The optimal number of bumpers changes from 3 to 4 over this range. Thus, the greater the standoff distance, the more incentive to increase the number of bumpers in the design. There is roughly a 25% weight reduction achieved by increasing the separation from 10 to 15

cm. A sensitivity of optimal protective structures design to particle impact angle from normal found no transition region to optimal number of bumpers. In fact, this sensitivity is remarkably flat. Impact angle, thus, does not affect the system design for three bumpers. **Figure 3** shows the sensitivity of optimal protective structures design variables (including optimal number of bumpers) to particle density. One transition region is found in this sensitivity, between 3.5 and 4 gm/cm^3. The optimal number of bumpers changes from 3 to 4 over this range, due to increased particle lethality. **Figure 4** shows the sensitivity of optimal protective structures design variables (including optimal number of bumpers) to wall penetration factor (1 being ballistic limit). One transition region is found in this sensitivity, between 70 and 80% penetration. The optimal number of bumpers decreases from 4 to 3 due to decreasing lethality.

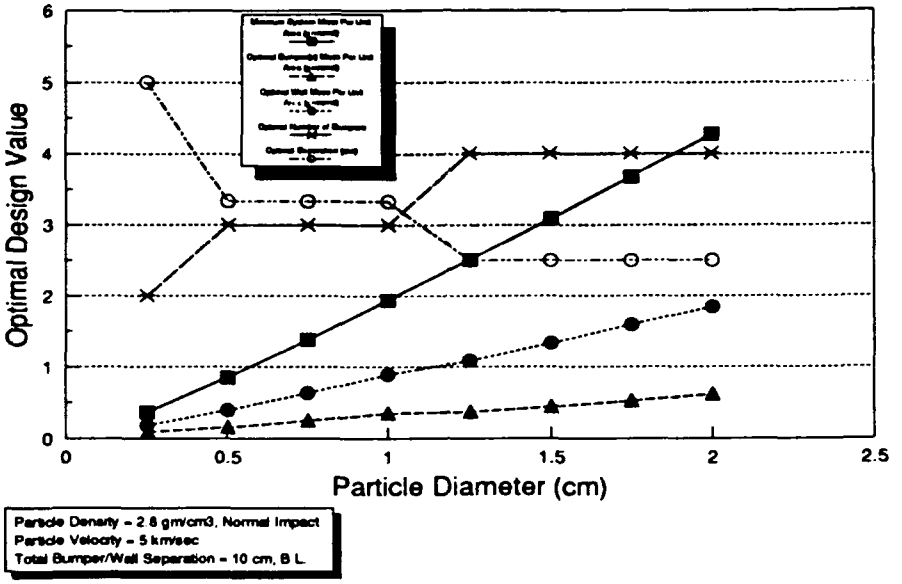


Fig. 1. Optimal Protective Structures Design Values vs. Particle Diameter (Shatter Region). Larger Threats Result in Additional Bumpers.

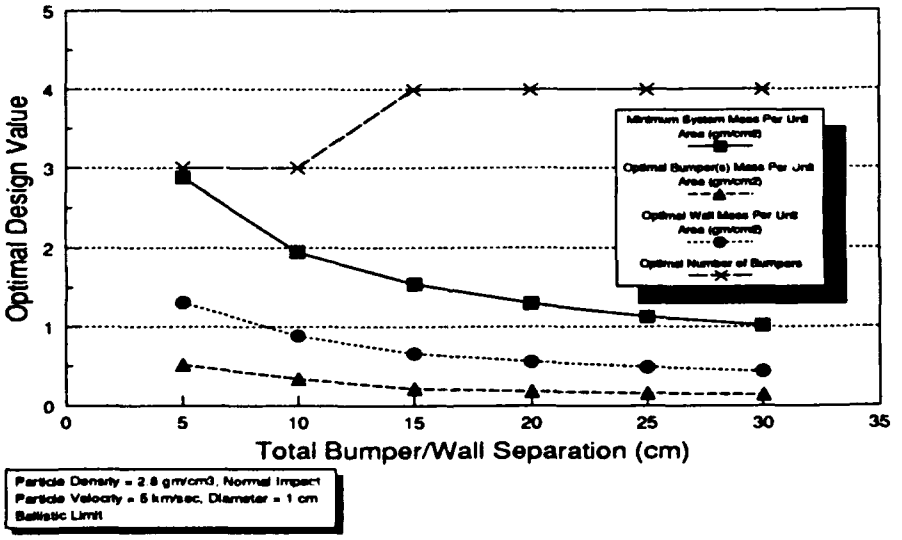


Fig. 2. Optimal Protective Structures Design Values vs. Total Bumper/Wall Separation (Shatter Region). Greater Separation Allows for Multiple Bumpers.

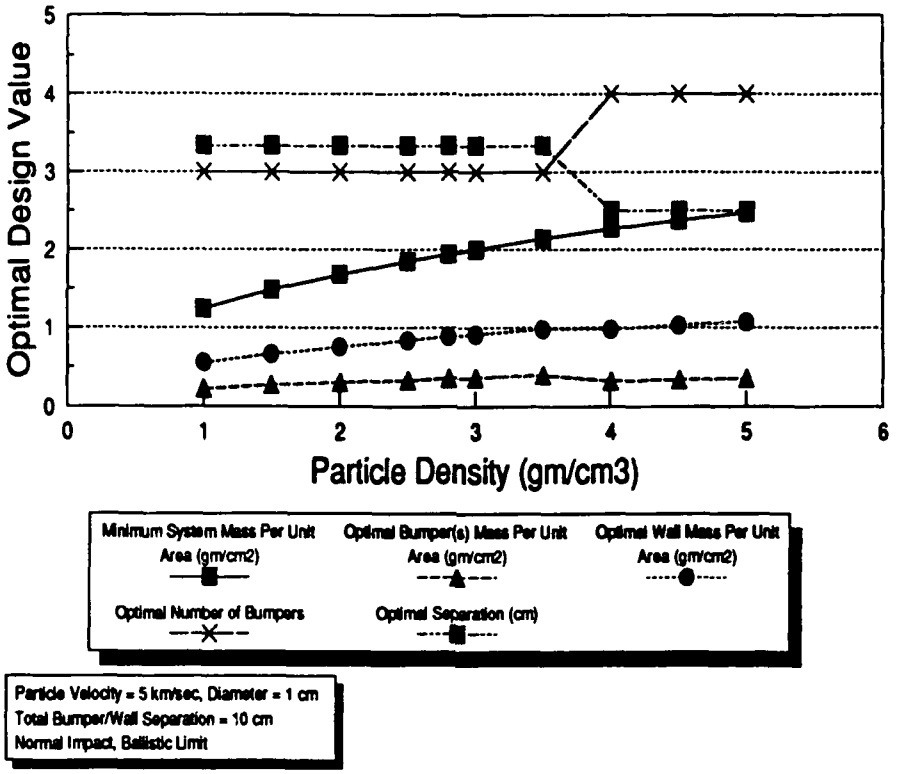


Fig. 3. Optimal Protective Structures Design Values vs. Particle Density (Shatter Region). Higher Densities Require Additional Bumpers.

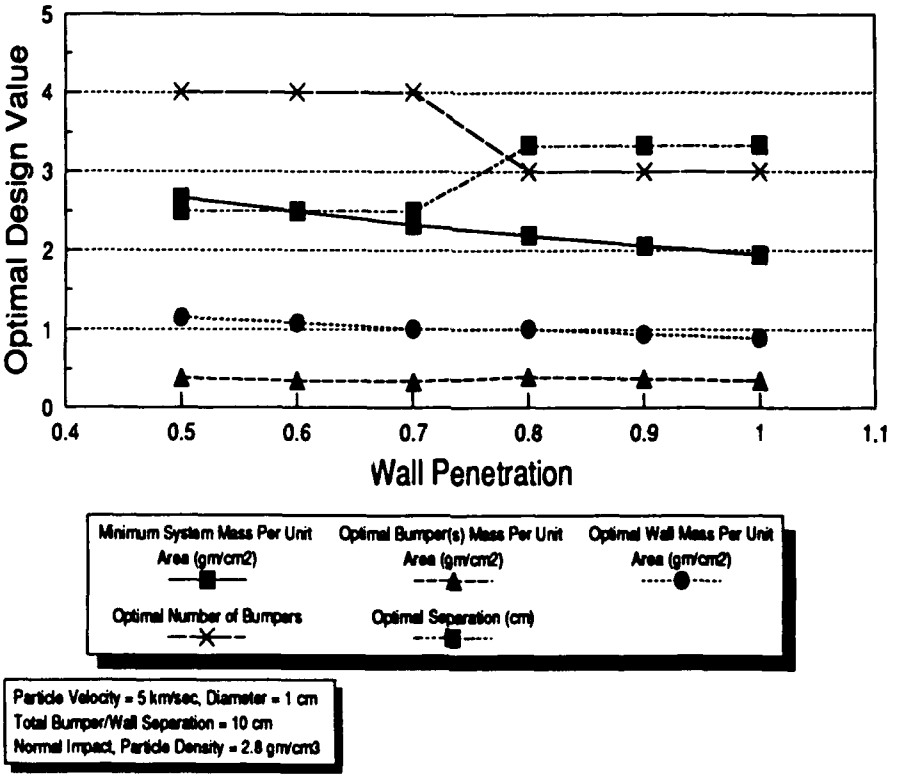


Fig. 4. Optimal Protective Structures Design Values vs. Wall Penetration (Shatter Region). Spallation May Be a Design Driver.

MULTIBUMPER PROTECTIVE STRUCTURES DESIGN TRADES

The baseline parameters and assumptions for an orbital debris analysis of multibumper systems is shown in **Table 2.** The parametric sensitivities investigated are also shown in **Table 3.**

Table 2. Baseline Parameters and Assumptions

* Reference 10 Debris Environment Except Particle Density = 2.8 gm/cm^3
* 1997-2007 Mission Timeline
* Altitude = 398 km
* Inclination = 28.5 deg.
* Total Mission PNP = 0.9733 (Lab.,Hab.,Node,Node with Cupola,2 LOX Cryo,2 N_2 Cryo,0.9955/element)
* Total Debris Area = 603 m^2
* "0.8" Multibumper Wilkinson/Shatter Regression (Integrated)
* Total Bumper/Wall Separation = 10 cm
* Ballistic Limit

Table 3. Parametric Sensitivities

* Mission Start Year: 1997-2005
* Mission Duration: 5-30 years
* Average Mission Altitude: 200-1000km
* Total Mission PNP: 0.8-0.99
* Total Debris Area: 100-1000 m^2
* Total Bumper/Wall Separation: 5-30 cm

Figure 5 shows the sensitivity of optimal protective structures design variables (including optimal number of bumpers) to mission start date. Note the strong sensitivity to start date over the years from 2000 to 2003. The optimal number of bumpers remains constant at one for mission start dates through 2005. **Figure 6** shows the sensitivity of optimal protective structures design variables (including optimal number of bumpers) to design life. A transition region from one bumper to two (and then from two to three) is found in the 10-15 year (25 to 30 year) duration range. The shape of this curve is partly reflective of the space debris growth rate model and partly reflective of the solar flux effect. **Figure 7** shows the sensitivity of optimal protective structures design variables (including optimal number of bumpers) to average mission altitude. Two transition regions are found, one between 400 and 500 km altitude and one between 600 and 700 km. In these regions, the optimal number of bumpers changes from 1 to 2 (and then 2 to 3) due to increased particle threat. **Figure 8** shows the sensitivity of optimal protective structures design variables (including optimal number of bumpers) to total mission probability of no penetration. A transition from 1 bumper to 2 is found in the region between 0.98 and 0.99 PNP. This corresponds to element PNP's between 0.9966 and 0.9983. **Figure 9** shows the sensitivity of optimal protective structures design variables (including optimal number of bumpers) to total mission debris area. A transition region is found between 800 and 900 m^2. In this region, the optimal number of bumpers changes from 1 to 2 due to increases in particle threat size. **Figure 10** shows the sensitivity of optimal protective structures design variables (including optimal number of bumpers) to total bumper/wall separation. No transition region is found from 5 to 30 cm total separation. An increase in total separation from 10 to 15 cm results in a 30% reduction in weight.

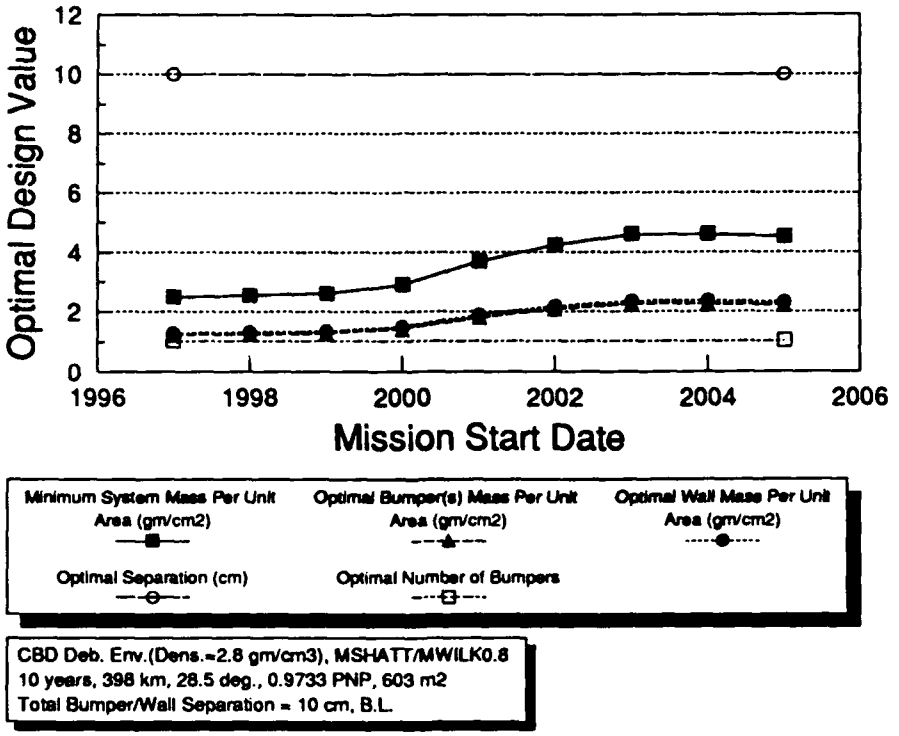


Fig. 5. Optimal Protective Structures Design Values vs. Mission Start Date. There is a Large Penalty to Pay for Schedule Delays in the 2000 to 2003 Timeframe.

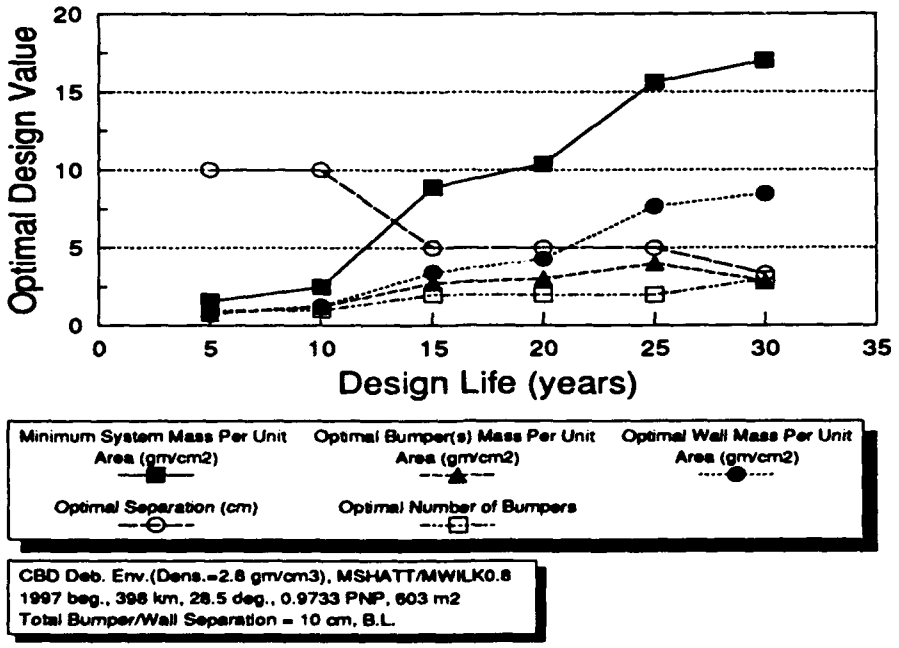


Fig. 6. Optimal Protective Structures Design Values vs. Design Life. Long Duration Design Lives Require Additional Bumpers.

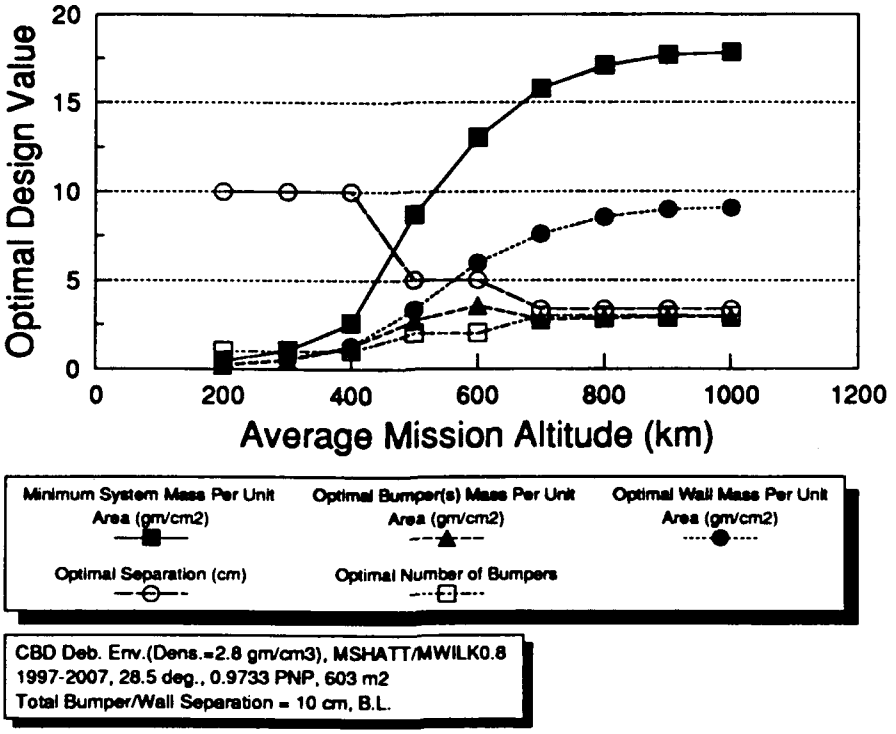


Fig. 7. Optimal Protective Structures Design Values vs. Average Mission Altitude. Altitude Increases Above 400 km Require Additional Bumpers.

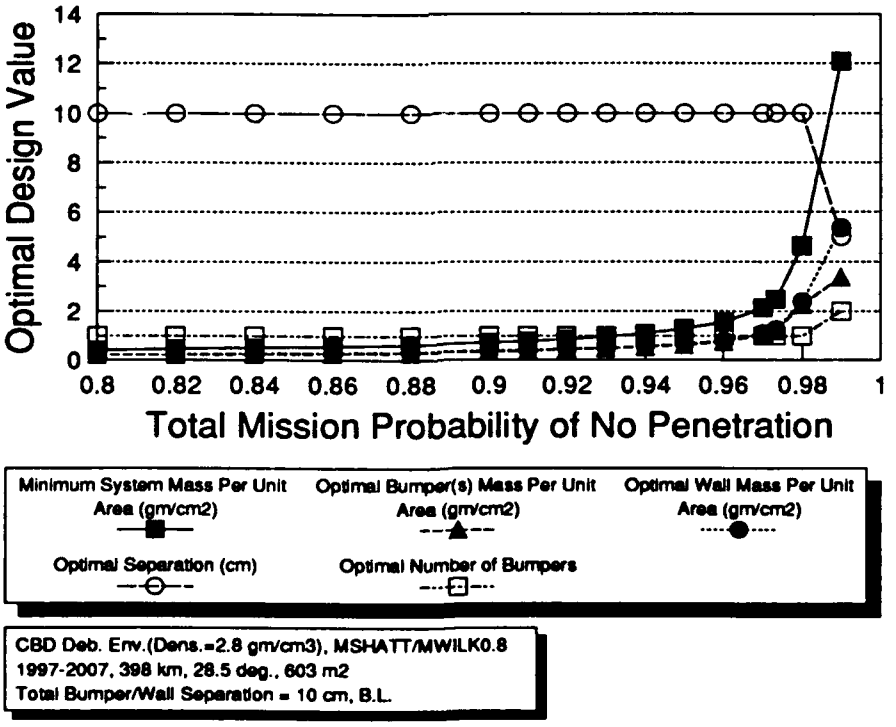


Fig. 8. Optimal Protective Structures Design Values vs. Total Mission PNP. Increases in Required PNP's Result in Need for Additional Bumpers.

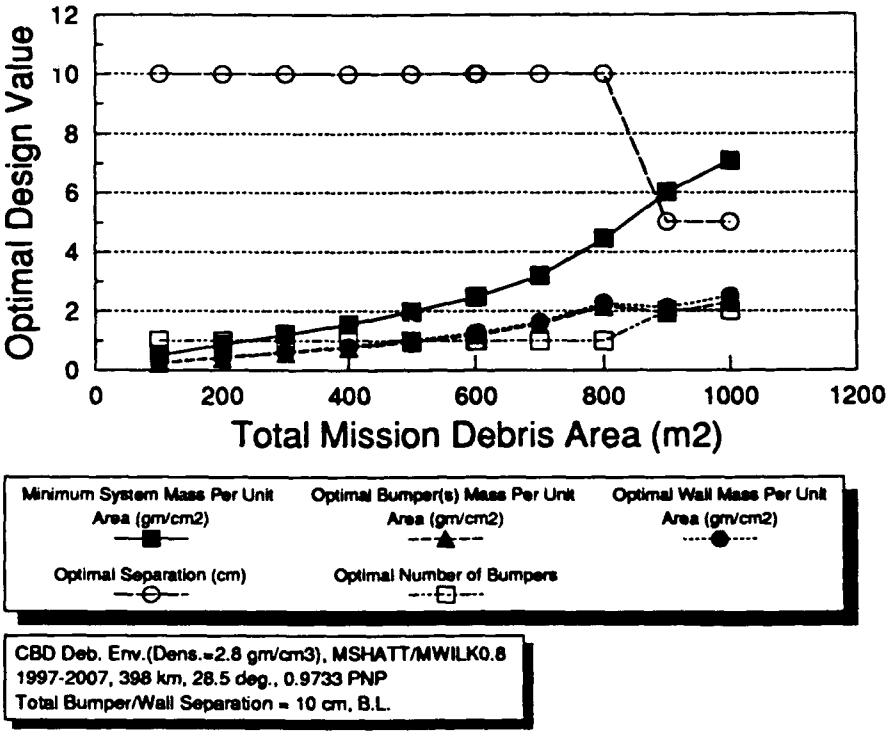


Fig. 9. Optimal Protective Structures Design Values vs. Total Mission Debris Area. Design Growth Requires Additional Bumpers.

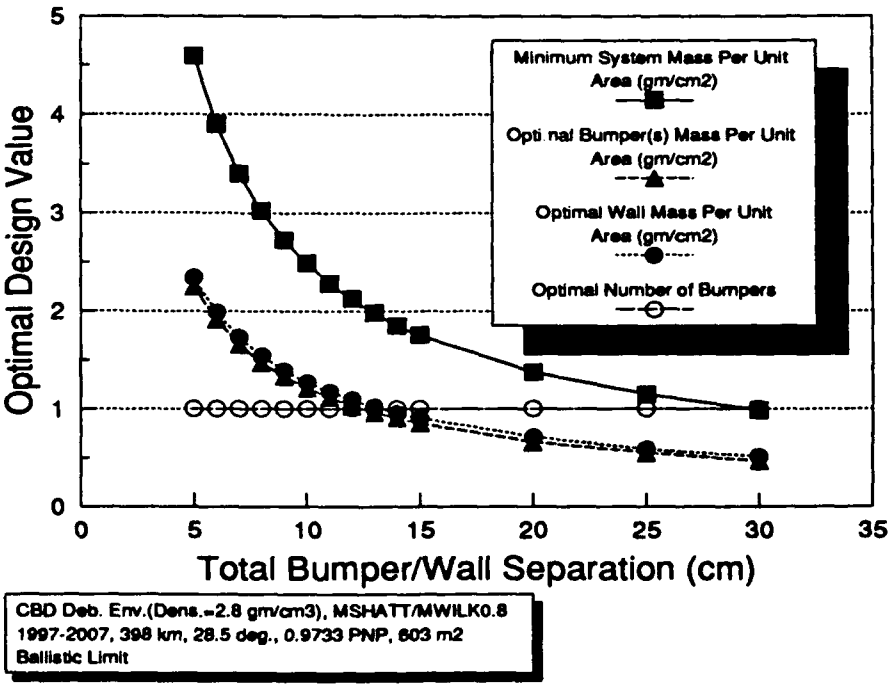


Fig. 10. Optimal Protective Structures Design Values vs. Total Bumper/Wall Separation. Increased Separation to 15 cm Eases Design Requirements Significantly.

INTRINSICALLY NONLINEAR REGRESSION FOR MULTIBUMPER PROJECTILE SHATTER

An intrinsically nonlinear regression form to predict reactions to hypervelocity impacts of multiplate structures has been developed and is given by

$$N = \sum_{i=1}^{T} K_i d^{a_{1_i}} \rho_p^{a_{2_i}} V^{a_{3_i}} \left[\cos\left(\frac{\theta}{(n-1)^{a_{5_i}}} \right) \right]^{a_{4_i}} \left(\prod_{j=1}^{n-1} S_j \right)^{\frac{a_{5_i}}{(n-1)^{a_{10_i}}}} \left(\prod_{j=1}^{n-1} \rho_j t_j \right)^{\frac{a_{6_i}}{(n-1)^{a_{11_i}}}} (\rho_n t_n)^{a_{7_i}} (n-1)^{a_{8_i}} \qquad [11]$$

Models for T=1,2,3 have been generated. Residual plots, extra sum of squares analyses, and ballistic limit curves have been generated. The T=2 model has been selected as best representing the physical phenomenology, while maintaining significant statistical improvements over the intrinsically linear model. Optimization and system trades are currently under development.

CONCLUSIONS

HYPERVELOCITY IMPACT IMPLICATIONS

1. Because the optimal number of bumpers increases with increasing particle diameter, more emphasis should be placed on performing hypervelocity impact testing and analyses for larger particles impacting multiple bumper systems. (Note transition regions between d=0.25 cm and d=0.5 cm (and 1 to 1.25 cm) particle sizes.)
2. Since the protective structures design sensitivity to velocity is relatively flat with constant optimal number of bumpers = 3, less concern should be placed on hypervelocity impact analyses and testing to determine the effects of small velocity differences, and more emphasis should be placed on understanding transition regions from projectile shatter to melt and vaporization.
3. Because the optimal number of bumpers as a function of total separation varies from 3 to 4, more hypervelocity impact tests and analyses should be performed for larger separations and more bumpers.
4. Because of the small sensitivity of optimal number of bumpers to impact angle, fewer hypervelocity impact analyses and tests should be conducted for multiple bumper configurations.
5. Because the optimal number of bumpers for large ranges of particle density varies from 3 to 4, additional hypervelocity impact tests and analyses should be performed for these particle mass densities and more bumpers.
6. Due to the fact that the minimum system mass per unit area is fairly sensitive to wall penetration factor, additional hypervelocity impact analyses and tests should be performed to provide a better understanding of spallation.

SPACE STATION FREEDOM IMPLICATIONS

1. Optimal areal densities are equal for bumper(s).
2. Optimal bumper(s) and wall areal densities are generally not equal.
3. Wall areal density generally dominates bumper areal densities.
4. Optimal individual separations are equal.
5. Optimal protective structures design is very sensitive to design life.
6. Transition region from 1 to 2 (and 2 to 3) bumpers is between 10 and 15 (25 and 30) year design lives.
7. Optimal protective structures design is very sensitive to average mission altitude above 400 km.
8. Transition region from 1 to 2 (2 to 3) bumpers is between 400 and 500 (600 and 700) km altitudes.
9. Optimal protective structures design is very sensitive to mission PNP above 0.97.
10. Knee of the PNP curve is compatible with baseline requirement of 0.9733.
11. Transition region from 1 to 2 bumpers is between 0.98 and 0.99 PNP. (0.9966 and 0.9983/element).
12. Optimal protective structures design is very sensitive to total debris area.
13. Transition region from 1 to 2 bumpers is between 800 and 900 m^2.
14. Optimal protective structures design is sensitive to total bumper/wall separation between 5 and 20 cm.
15. Knee of the separation curve appears to be between 10 and 15 cm.
16. Shift to 15 cm separation results in about 30% reduction in protective weight.

STATISTICAL REGRESSION IMPLICATIONS

1. Intrinsically linear posynomial regression can be performed to statistically significant levels for multiple bumper hypervelocity impact reactions.
2. Residual plots appear to be normal.

RECOMMENDATIONS

1. Perform second order sensitivities.
2. Perform PNP requirements balancing among critical elements.
3. Investigate configuration build-up timelines/augmentation.
4. Continue exploration of intrinsically nonlinear regression.

ACKNOWLEDGMENT

The authors wish to thank Mr. Bill Jolly of Kaman for his help in providing MSFC database filtering for use in the regression.

REFERENCES

[1]Coronado, A. R., Gibbins, M. N., Wright, M. A., and Stern, P. H., "Space Station Integrated Wall Design and Penetration Damage Control," Boeing Aerospace Company Final Report, Contract NAS8-36426, July 1987.
[2]Cour-Palais, B., "Meteoroid Environment Model - 1969 (Near-Earth to Lunar Surface)," NASA SP-8013, March 1969.
[3]Cour-Palais, B. G., et Al., "Meteoroid Environment Model - 1970, (Interplanetary and Planetary)," NASA SP-8038, October 1970.
[4]Duffin, R. J., Peterson, E. L., and Zener, *Geometric Programming*, John Wiley and Sons, Inc., 1967.
[5]Kessler, D., "Orbital Debris Environment for Spacecraft Designed to Operate in Low Earth Orbit," NASA TM-100471, April 1989.
[6]Mog, R. A., Spacecraft Protective Structures Design Optimization, *AIAA Journal of Spacecraft and Rockets*, Vol. 28, No. 1, Jan.-Feb. 1991.
[7]Mog, R. A., Lovett, J. N., and Avans, S. L., "Global Nonlinear Optimization of Spacecraft Protective Structures Design," NASA TM-100387, January 1990.
[8]Mog, R. A., and Price, D. M., "Optimization Techniques Applied to Passive Measures for In-Orbit Spacecraft Survivability - Final Report," SAIC HV410-12, Contract NAS8-37378, Nov. 1987.
[9]NASA, "Space and Planetary Environment Criteria Guidelines for Use in Space Vehicle Development: 1971 Revision," NASA TM-64627, November 1971.
[10]NASA, "Update of Meteoroid and Orbital Debris Environment Definition," Change Directive to SSP 30425, July 3, 1991.
[11]Wilkinson, J. P. D., "A Penetration Criterion for Double-Walled Structures Subject to Meteoroid Impact," AIAA Journal, Vol. 7, No. 10, October 1969.

Int. J. Impact Engng Vol.14, pp.531 - 539, 1993
Printed in Great Britain

0734-743X/93 $6.00+0.00
Pergamon Press Ltd

RECOVERY OF MATERIALS IMPACTED AT HIGH VELOCITY*

W. J. NELLIS and A. J. GRATZ

Lawrence Livermore National Laboratory, University of California
Livermore, California 94550

ABSTRACT

Hypervelocity impact can produce unique effects in materials, including crystal structures, microstructures, and properties. Examples include impact-driven shock waves to synthesize novel materials 1 mm and 1 μm thin shocked to pressures up to 100 GPa (1 Mbar), preferential crystallographic alignment achieved by taking into account the shape and size of powder particles, and high-pressure phase transitions quenched in geological materials. Thin specimens are used to achieve the highest quench rates. Methods are described which show that the experiments can be performed by precooling or preheating specimens in the range -170° to +1000° C. Calculational results for the quartz experiments show the importance of computational simulations to determine the pressure history in the specimen.

INTRODUCTION

Hypervelocity impact produces high dynamic pressures and temperatures. The rates of both the application and of the release of pressure and temperature are very large for bulk materials. Maximum shock pressures typically range from 1-100 GPa (0.01 to 1 Mbar) and temperatures can reach up to a few 1000 K for times of about a μsec. During application of pressure, strain rates can exceed 10^8/s (Chhabildas and Asay, 1979). Calculated quench rates from extreme conditions reach up to 10^{12} bar/s and 10^9 K/s (Nellis et al., 1986; Nellis et al., 1988). These quench rates are the physical limits in macroscopic bodies because they occur at the speed of sound. Shock pressures of 100 GPa can be achieved in specimens embedded in Cu by planar impact of Cu onto Cu at velocities near 3.4 km/s. This velocity is easily reached with a two-stage light-gas gun using He driving gas. The extreme conditions reached can achieve unique effects in terms of microstructure, crystal structure, and resulting properties. The purpose of this paper is to describe a variety of techniques used at high dynamic pressure to induce and investigate changes in the structure and properties of recovered materials.

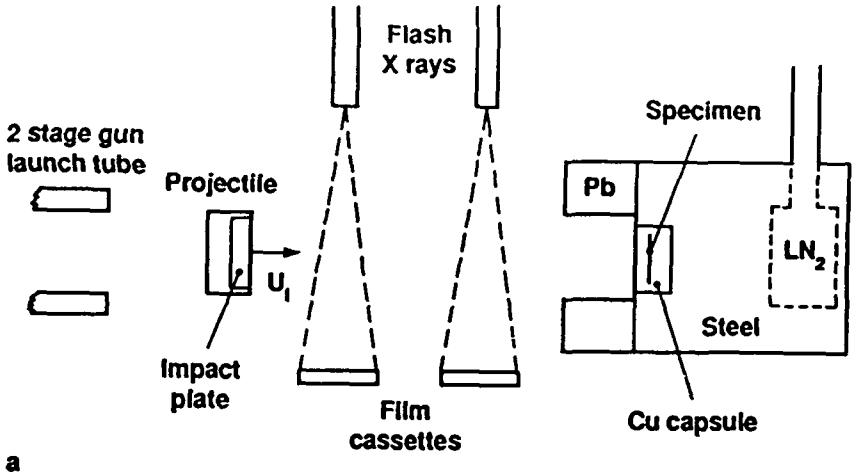
Advantages of gas gun experiments include the fact that thin specimens can be used to obtain very high quench rates into surrounding metal, for example, and that specimens weighing a gram or less can be used. Thus, the high-rate quenching limits of the shock technique can be investigated Also, because of the small masses, many materials available only in research quantities can be subjected to high dynamic pressures and the structures and properties of the recovered materials can be characterized.

Gas gun experiments will be described below in which mm and μm thin specimens, usually 10 mm in diameter in our experiments, are recovered from pressures up to 100 GPa and characterized. Preferential crystallographic alignment and associated changes in physical properties are achieved by taking into account particle shape and size. High pressure phase transitions can be quenched by choosing relatively thin specimens with highest quench rates. Natural phenomena, such as explosive volcanism, can be simulated in the laboratory. Recovered microstructures can be compared with those in nature to obtain information about possible mechanisms of naturally occurring microstructures. Conditions achieved in recovery experiments and their time histories are obtained generally by computational simulations, illustrating the importance of calculations for characterizing dynamic histories of specimens. Initial

specimen temperature can be precooled to about -170° C or preheated up to about +1000° C. By varying initial temperature the phase and microstructure of the recovered material might also be effected.

SYNTHESIS AT 100 GPa (1 MBAR) PRESSURES

The first example is chosen to illustrate that metastable phases can be synthesized by application of pressures as large as 100 GPa (Neumeier et al., 1989). The high pressures and temperatures can drive some materials into a metastable high pressure phase and the fast quench offers the possibility of retaining the metastable phase on release. The example is the synthesis of metastable cubic A15-phase Nb_3Si from the nonsuperconducting tetragonal Ti_3P phase by application of 100 GPa pressures. The research size experiment is shown in Fig. 1, which uses a 6.5 mm-long 20 mm-bore two-stage gun. The muzzle of the gun and the recovery fixture are contained in an evacuated target chamber to minimize the generation of sound and the effect of friction. The specimen was 12 mm in diameter and 1.5 mm thick



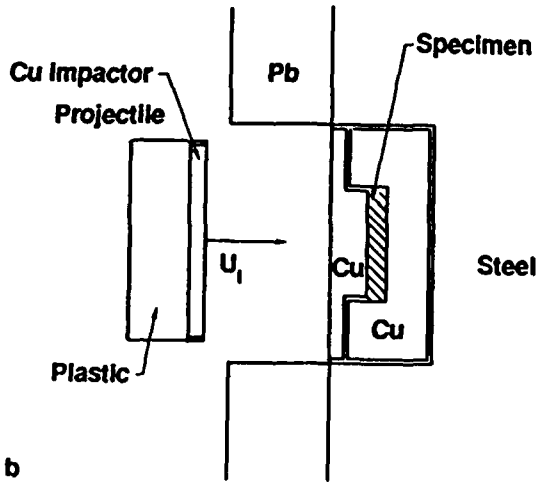


Fig. 1. (a) Cross-sectional schematic of system for subjecting specimens to 100 GPa (1 Mbar) shock pressures. Liquid N_2 chamber is used for precooling. Flash x rays measure impact velocity, which is used to calculate impact pressure. Evacuated target chamber is not shown. (b) Expanded view of one type of specimen capsule in recovery fixture.

and weighed about a gram, which is sufficiently large for several characterizations. The Cu recovery capsule was chosen for its ductility to avoid fracture, for its high thermal conductivity for quenching, and for its good shock impedance match to the specimen and to the surrounding steel fixture. The Pb ring is a heavy tamper to maintain the integrity of the steel fixture when a high pressure shock wave diverges from the impact point out along the steel surface. Without the Pb ring a crater is formed rather than a relatively simple recovery. For small residual temperatures and large thermal quench rates, the recovery fixture was precooled to near liquid N_2 temperature, about -170° C (100 K). A Cu impactor plate 2 mm thick was used to generate pressure. Total thickness of the impactor was 7.8 mm with a 20 mm diameter; total projectile mass was 8.7 g.

An advantage of this gun technique is that an impactor weighing less than 10 g interacts with the fixture. The much heavier gunpowder and driving gas are decoupled from the impactor and target when the impactor enters the evacuated target chamber. The relatively small impactor minimizes the momentum and kinetic energy which must be dissipated in the fixture and causes the high dynamic pressures and temperatures to be localized in the immediate vicinity of the specimen. This means that most of the steel backing material can maintain its strength for effective containment, because most of it is essentially unheated by the strong shock wave generated by impact.

The synthesized cubic A15 phase is superconducting and so superconducting properties can be used to characterize the shocked specimen. Characterizations with x rays, optical microscopy, electrical resistance, magnetic susceptibilty, specific heat, upper critical magnetic field, pressure dependence of superconducting critical temperature T_c, and annealing studies were reported previously. Basically, 82 GPa induces a partial phase change, as seen by the electrical restistance. 100 GPa shock pressure induces a single superconducting transition at 18 K, as seen by the electrical resistance. Analysis of the bulk specific-heat data indicates that about 67 % of the specimen converted to the A15 phase. Greater conversion efficiencies might be achieved by using starting specimens with a higher fraction of the tetragonal phase and using thinner specimens for faster effective quench rates to retain the high pressure phase.

THIN FILMS AT 100 GPa PRESSURES

In order to test whether thin specimens could be recovered intact from very high pressures and very high quench rates, we embedded ductile films in a ductile metal matrix with high thermal conductivity and shocked the specimen capsule to 70 and 100 GPa (Koch et al., 1990). The recovered films were examined by scanning and transmission electron microscopy, SEM and TEM, respectively. Four Nb dots 3.2 mm in diameter and 1, 2.5, 5, and 10 μm thin were sputter-deposited on a machined Cu substrate 3 mm thick and 19 mm in diameter. A Cu film about 5 μm thin was sputter-deposited over the substrate, providing a protective coating on the Nb dots. A Cu layer 3 mm thick was then electroplated over the sputtered Cu layer. The Cu piece was machined to a thickness of 6 mm, with 3 mm of machined Cu, 3 mm of electoplated Cu, and the Nb films embedded in between. The Cu piece was then used as the specimen capsule in Fig. 1 and maraging steel was used for the steel recovery fixture. The latter was chosen for its high strength to inhibit deformation of the Cu capsule. The fact that maraging steel is brittle does not matter significantly, because it fractures after high pressures are released, leaving the Cu specimen capsule separated from the steel recovery fixture. Cu impactors were accelerated to velocities of 2.7 and 3.4 km/s by the 6.5-m-long two-stage gun; the impact pressures produced were 72 and 97 GPa.

Specimens were characterized by optical and electron microscopy, as reported previously. The three thinner films shocked to 100 GPa essentially retained continuity. The Nb film originally 10 μm thin was penetrated by Cu in many places with the widths of the perturbed region being about twice the thickness of the starting film. The film shocked to 70 GPa was also essentially intact but it separated nearly completely at the interface of the machined Cu substrate and the vapor-deposited Cu, indicating that most of the Nb films adhered more strongly to the vapor-deposited Cu film. These results show that Nb films can be recovered nearly intact from dynamic high pressures. However, specific results for other materials are probably material and preparation dependent.

This method was used successfully with C_{60} fullerenes. For relatively thick 100-μm powder layers, Raman spectroscopy showed that C_{60} is stable up to about 17 GPa shock pressure, where a continuous transformation to graphite begins. Above 50 GPa nanocrystalline or amorphous C is observed (Yoo and Nellis, 1991). For a relatively thin 2 μm C_{60} film layer, a diamond like phase, and other C phases, are found with TEM after a shock pressure of 69 GPa (Yoo et al., 1992). Thus, specimen pressure,

temperature, morphology, and quench rates via specimen thickness could be investigated systemmatically to investigate the synthesis of various C and other metastable phases.

PARTICLE SHAPE AND SIZE

The shape and size of particles can sometimes be used to determine the microstructure and physical properties of a shock compact (Weir et al., 1991). A representative example is the superconducting compound $Bi_2Sr_2CaCu_2O_8$, often referred to as BSSCO. This compound can be made in powder form with particles having a platelet shape; that is, particles can be made with a cross sectional area and thickness such that the cross sectional dimensions in the plane of the platelet are large compared to the thickness of the platelet. In this case the **a** and **b** directions of the crystal structure are in the plane of the platelet particle and the **c**-axis crystallographic direction is normal to the plane. The **ab** plane is also the high current plane in BSSCO. The observed particle shape suggests using particles of relatively uniform size and tapping them into the specimen fixture, so that the platelets lie flat in the fixture. In this way the high-current **ab** plane can be arranged to lie in the plane of a compact. By restricting particle size to be relatively uniform, all particles experience each other on settling and tend to align crystallographically. If, for example, a wide range of particle sizes were used, it would be possible for relatively small particles to misalign themselves between relatively large particles. It also happens that BSSCO is quite ductile, so that this material tends to flow under shock loading, rather than fracture. As a result shock compaction tends to bond BSSCO particles together into a compact with aligned grains. In this case the dominant effect of the shock appears to be oxygen disordering rather than microcracking. The compacts still need to be annealed in oxygen at sufficiently high temperature to order the oxygen atoms, while keeping the temperature sufficiently low to prevent atomic disorder in the compound. This temperature is about 800 C° from annealing studies.

Our shock compression experiments on BSSCO were performed using the fixture of Fig. 1, with the exception that the Pb ring of Fig. 1 was replaced with steel to produce a one-piece steel recovery fixture. Also, since the goal was to compact powder with shock induced defects, pressures were in the range for bonding particles dynamically rather than synthesizing new phases, 3.5 to 13.5 GPa. The powder was sifted into various sizes using commercial sieves and specimens were 0.5 mm thick and 10 mm in diameter.. Specimen characterization was performed using optical microscopy, x-ray diffraction, SQUID magnetometer, TEM, and electrical resistance.

A shock compact made this way has a substantial amount of preferential crystallographic alignment. As a result, the magnetic properties are expected to vary substantially depending on whether the applied magnetic field is perpendicular or parallel to the plane of the preferentially aligned specimen. Measurements showed that this anisotropy can range up to a factor of about 7. Based on the x-ray and magnetic data, a 10 GPa shock produced a relatively well aligned compact with particle sizes of 5 to 10 μm, while the poorest x-ray alignment and magnetic anisotropy were obtained with particle sizes less than 5 μm. Thus, particle size, shape, and alignment can have a significant influence on properties of shocked materials.

QUARTZ

Shock-loading of quartz produces microstructures and phase transformations which geologists use to identify and analyze sites of meteorite impact. These phenomena are interpreted using shock-wave data and shock recovery experiments. Experiments are typically performed on single crystals, and the goal is to characterize the type of deformation associated with each set of shock loading conditions. Because meteorite impacts often occur on hot or cold planetary surfaces, we use preheated and precooled targets to explore the role of target temperature in shock deformation and transformation of quartz (Gratz et al., 1988, Gratz et al., 1992) The experiments also provide fundamental information on the kinetics of shock-induced amorphization. Transmission electron microscopy (TEM) is the fundamental tool for studying the submicron features induced by loading. Computer simulation of loading history is crucial for estimating pressure-time history.

To achieve initial temperatures from room temperature up to as high as +1000° C, specimens are placed in metal holders, which in turn are placed in the recovery fixture illustrated in Fig. 2. Room temperature experiments omit use of the furnace in Fig. 2. To achieve high initial temperatures, the recovery fixture is placed inside a ceramic furnace, as shown. Friedrich Hörz at the NASA-Johnson Space Center provided the design for the furnace heater. For both precooled (Fig. 1) and preheated experiments (Fig. 2), initial temperatures are monitored with thermocouples on the recovery fixture until a few seconds before firing the gas gun. Equilibrated temperature of the fixture is maintained for

several minutes or longer prior to each shot. Quartz single crystals were shocked in this fashion to pressures of 12, 22, and 27 GPa (see below); initial temperatures were -170, 20, 500, 800 and 1000°C. Following each shot, the specimen remains for several minutes in the target chamber. For initial temperatures of 500°C and greater, the shocked fixtures were placed in an oven at 200°C and the fixture was allowed to cool over several hours to minimize thermal shock and to simulate cooling of an ejecta layer. Specimens preheated to 800°C and 1000°C are in the β-quartz and tridymite stability fields, respectively. There is no evidence that β-quartz deformed differently than α-quartz nor that tridymite was formed.

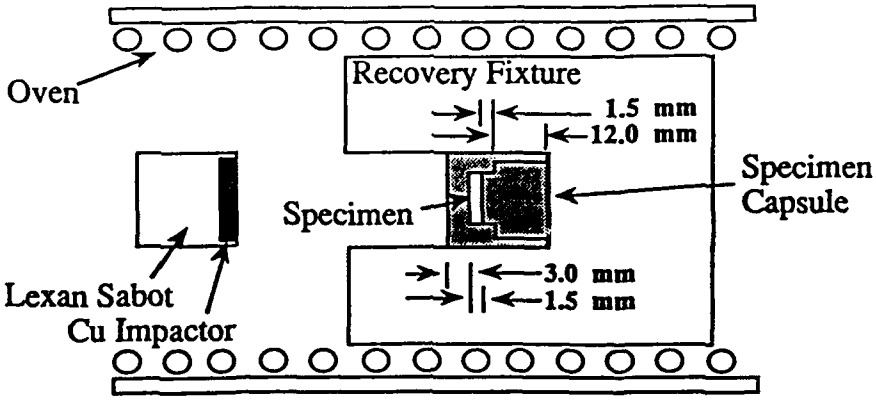


Fig. 2. Schematic of recovery fixture for experiments initially at room temperature or at high temperatures. The oven is used to achieve high temperatures; it is not used for room temperature experiments. The screw-in plug of the specimen capsule fixes the specimen in place, so that it is surrounded by a metal capsule, supported and surrounded by a recovery fixture.

Quartz specimens were taken from the same Brazilian single crystal used in previous shock experiments (Gratz et al., 1988). All specimens were highly-polished, initially-transparent disks 11 mm in diameter and 1.5 mm thick. The crystals were x-cut, i.e. the normal to each disk was parallel to the a <1120> crystal direction. Planar surfaces are polished flat to <0.5 μm. Specimen thickness varied by <10 μm in most cases and <20 μm in all cases. TEM of the starting material reveals no dislocations, implying dislocation densities of $<10^6/cm^2$.

The shock experiments initially at room temperature were simulated using the Lagrangian finite-difference wavecode Toody, which incorporates a two-phase model capable of describing arbitrary transformation kinetics (Swegle, 1990). The model is calibrated for x-cut quartz based on Hugoniot data. It includes a two-wave structure when the elastic wave is not overdriven, a mixed-phase regime in which both quartz and a high-pressure phase are present, and allows for residual strength in the compressed mixture. Shock-transformed quartz is assumed to have physical properties close to stishovite, and the high-pressure phase mixture remains frozen until the equilibrium phase boundary is crossed, at which time reversion occurs.

Peak stress and temperature were attained by a series of 3-5 reverberations (Fig. 3). This loading is quasi-isentropic, in contrast to single-shock loading attained in Hugoniot experiments. The calculated peak stresses (14, 22, 27 GPa) are distinctly different from impact shock pressures obtained by impedance match calculations (12, 24, and 32 GPa). The peak stress duration is short for 22 and 27 GPa experiments, lasting for ~0.1 μs. The stress history is slightly different for the low-stress experiment, which used a simple lexan impactor. The fact that peak pressure is achieved by a multi-shock reverberation process means that the mean bulk temperature of the specimen is lower than that achieved by a single shock to the same pressure. Preheating the specimen permits the achievement of final pressures and temperatures representative of single-shock Hugoniot states of quartz initially at room temperature or hotter. Temperatures are estimated by adding the initial temperatures to the calculated ones. Post-shock temperatures are taken from Raikes and Ahrens (1979), and provide for 100, 160 and 200 C heating at the three shock pressures. It should be noted that calculated post-shock temperatures are mean bulk temperatures. The microstructures described below are due primarily to

heterogeneous deformation. The calculated pressures and temperatures achieved were overlaid on the equilibrium silica phase diagram of Frondel (1962) and Akaogi and Navrotsky (1984), in which stishovite is the equilibrium high pressure phase. Microstructural investigations showed that essentially none of the equilibrium stishovite phase was recovered.

Two-dimensional calculations reveal a nonuniform pressure distribution across the sample (Fig. 4). However, the local differences in stress history are primarily minor variations in unloading. The peak stress achieved at any point in the sample is very close to that estimated from a simple 1-D model, and peak deviatoric stresses reach ~5 GPa. Early lateral release should have occurred in the low-pressure

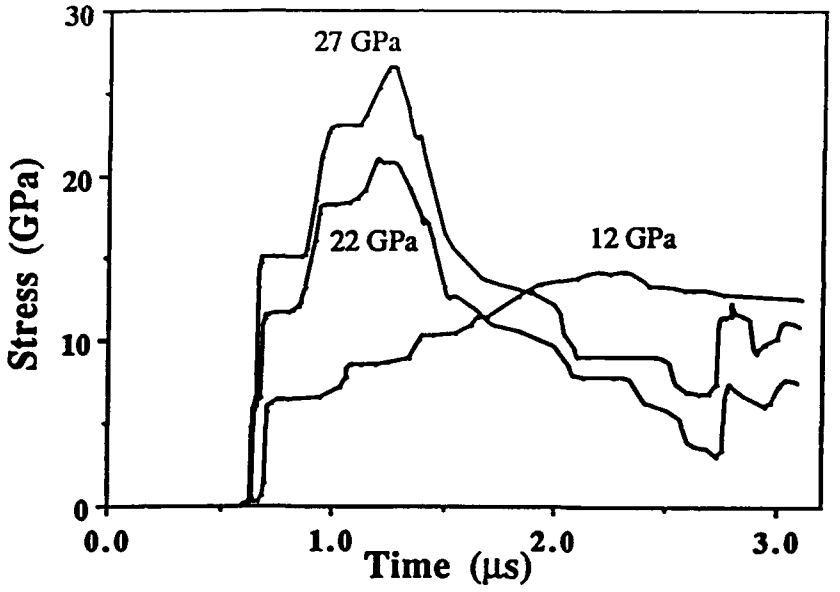


Fig. 3. Calculated stress histories in α-quartz specimens calculated with a one-dimensional hydrodynamic computer code.

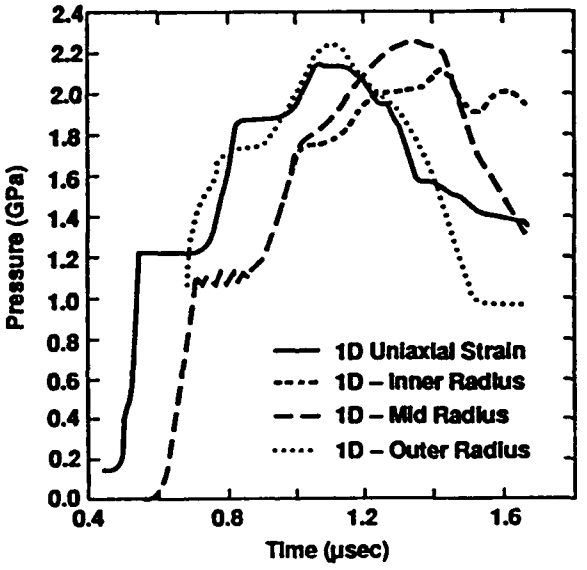


Fig. 4. Stress profiles for three locations in the α-quartz specimen at 22 GPa using a two-dimensional computer model. All three locations have similar stress histories and peak pressures.

experiment only. This results in a slightly lower peak stress, 12 instead of 14 GPa. All TEM foils were taken from the mid-radius of the sample.

At low stresses (7-10 GPa), shock produced abundant fractures (sometimes in narrow, planar sets), Dauphiné twins, and microfault zones. The last are shear fractures on which frictional melting occurs, leading to a zone of melt mixed with crystallites. Such melting, which is analagous to intergranular melting in shock compacted powders, is important. These melts are later injected throughout the specimen and serve to cement it together.

Higher shock stresses (>10 GPa) induce additional features: transformation lamellae (layers of glass, highly-fractured material, and/or stishovite up to 100s of nms wide), and unresolved contrast lamellae (layers whose defect density is too high to resolve individual features). Transformation lamellae in particular are unique to shock metamorphism, and their nature and genesis remain uncertain. They commonly occur in planes of zero shear stress, and possess complex substructures. That is, narrow, (0001) transformation lamellae are seen at pressures below 15 GPa, whereas wide (>20 nm), (101n) transformation lamellae, often with oblique sublamellae, are produced at pressures of ~18 GPa and above. We interpret these as the loci of lattice collapse, with no evidence for significant production of either crystalline phases or melt.

At the highest shock pressures, transformation lamellae dominate the sample which becomes completely amorphous. Our experiments show the pressure required for complete amorphization is sensitive to initial temperature, ranging from 35-40 GPa at T_0=20°C and ~22 GPa at T_0=1000°C. Thus, for example, significantly increased amorphization is expected on hot planetary surfaces compared to cold ones; cold surfaces are expected to produce highly disrupted ejecta. Because the extent of amorphization is often used to estimate the pressure experienced by natural impactites, these results emphasize the importance of allowing for pre-shock temperature.

With increasing shock pressure, the quartz Hugoniot moves gradually from the quartz hydrostat to that of a denser phase in the range 10-40 GPa as quartz progressively transforms to a dense, disordered phase. The extent of the phase transformation corresponds to the abundance of transformation lamellae induced by shock. Our TEM observations show that there is very limited or no production of high-pressure crystalline phases due to kinetic limitations. However, the detailed structure of the dense Hugoniot phase is not known but it has an equation-of-state very close to that of stishovite. The term "mixed-phase region" (Grady et al., 1974) is used to describe shock loading conditions which result in P-V states intermediate between that of crystalline quartz and of shock-transformed quartz. Measurements on thick samples (Podurets et al., 1977) implied that this assemblage is formed close to the shock front. Thus, the lamellae are expected to form by propagation of linear collapse zones at or near the shock front. During release, the densified, amorphous quartz expands to form diaplectic glass with no signs of melting or flow, in contrast to fusion glass. Recently, quasi-static compression experiments in the diamond-anvil cell above ~10 GPa have also produced gradual amorphization which becomes complete by ~35 GPa (Hemley et al., 1988), and molecular dynamics (MD) simulations have essentially reproduced the amorphization process (Tse and Klug, 1991). Indeed, the process of pressure amorphization is now recognized in a wide range of silicates, as well as other oxides and iodides. The process of pressure amorphization, first recognized in shock experiments, is thus proving to be a general phenomenon associated with kinetically-frustrated phase transformations. Our results indicate the importance of varying initial temperature in future experiments on pressure-amorphization.

CRISTOBALITE

Whereas shock of brittle single crystals often causes disaggregation, shock-loading of oxide powders can induce the opposite effect, cementing the particles into tough aggregates. We conducted a series of shock compaction experiments on cristobalite, the high-temperature and low-pressure polymorph of SiO_2, found in volcanic rocks and devitrified glasses. This provides an opportunity to study, for the first time, phase transformations of this form of silica while exploring shock compaction of silica powders.

Like quartz, we find that shock caused amorphization, although the shock pressure was considerably lower (between 22 and 27 GPa) than in quartz (~35 GPa). Unlike quartz, the transformation does not proceed along lamellae; also unlike quartz, the "mixed-phase" regime is quite narrow, <5 GPa wide and possibly much smaller. Despite these differences in transformation kinetics, physical properties of the diaplectic glass made from cristobalite are very close to those of diaplectic glass made from quartz, suggesting that both forms of silica transform to the same, disordered, high-pressure phase.

In contrast to the microfaulting, which broke quartz single crystals into small islands, the cristobalite grains remain intact both above and below the amorphization pressure. Melting is extensive but confined to the grain boundaries, where it created a bubbly glass which cements the grains into a tough composite with porosity <2%. The assemblage produced is unique, consisting of a pressure glass cemented by a fusion glass. Work on other systems show that yet higher pressures result in total melting. Thus, shock-loading presents a range of alternatives for converting powders into consolidated aggregates with novel properties.

LABORATORY SIMULATION OF EXPLOSIVE VOLCANIC LOADING

The discovery of an Ir-rich clay layer at Cretaceous/Tertiary (K/T) boundary layer sites (Alvarez et al., 1980) has been used as evidence that the boundary and accompanying mass extinctions were caused by hypervelocity meteorite impact. Detection of certain deformation features in boundary layer quartz and feldspars (Bohor et al., 1984) strongly supports an impact origin. An alternative hypothesis states that deformation observed in the K/T boundary was caused by intense volcanism (Officer and Drake, 1985). This issue has been investigated extensively and references were reported previously (Gratz et al., 1992a). We have simulated explosive volcanism in the laboratory in order to compare microstructures of material recovered in the laboratory with material from the K/T boundary to learn if explosive volcanism could be responsible for the observed effect.

The purpose of the experiment is to preheat a rock specimen to about 600° C, impact it with a low-velocity projectile to obtain pressures comparable to explosive volcanism, recover the rock specimen, and determine the microstructure of the recovered pressurized minerals. The experiment is illustrated in Fig. 5. The granite specimen is preheated in a furnace to 600° C, a temperature representative of rock around a volcanic intrusion, and impacted by plastic at a few 100 m/s to obtain pressures up to 1.3 GPa. This is a high pressure to contain brittle rock and the process is expected to be representative of strong explosive volcanism. Granite was chosen because it contains quartz and other silicate rocks found in the K/T boundary. The impact ejecta is trapped in the foam and is found in the form of small particles, which are examined by optical microscopy and TEM.

The dynamic pulse reduced the rock to sand-sized and larger particles ranging from about 100 μm up to about 5 mm. Most fracturing was intergranular and individual fragments were essentially undamaged. No evidence was found of other deformation features. Thus, deformation features commonly observed in the K/T boundary and associated with shock metamorphism were not found in these specimens. Our conclusion is that meteorite impact is the only hypthesis capable of explaining the microstructures characteristic of shocked quartz and feldspars found in the K/T boundary layer.

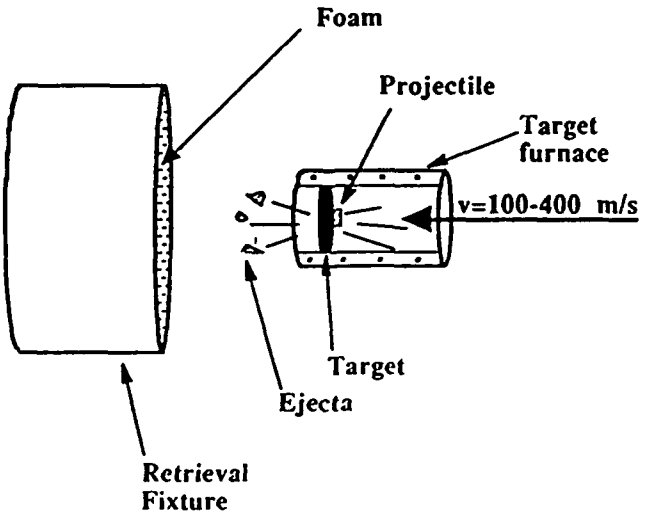


Fig. 5. Schematic of experimental setup to simulate volcanism in the laboratory. A plastic projectile at a few 100 m/s impacts a preheated granite disk, producing ejecta which is caught in foam.

CONCLUSION

This paper describes techniques for subjecting a variety of materials to dynamic high pressures and recovering them for characterization of material structure and proprereties.

*This work was performed under the auspices of the U.S. Department of Energy under Contract No. W-7405-ENG-48. The gas gun was operated by N. A. Hinsey who performed most of these experiments. This work was supported by the LLNL Branch of the University of California Institute of Geophysics and Planetary Physics and by H Division.

REFERENCES

Alvarez, L. W., W. Alvarez, F. Asaro, and H. V. Michel (1980). Extraterrestial cause for the Cretaceous/Tertiary extinction. Science, 208, 1095-1108.

Akaogi, M. and A. Novrotsky (1984). The quartz-coesite-stishovite transformation: new calorimetric measurements and calculation of phase diagrams. Phys. Earth Planet. Inter., 36, 124-134.

Bohor, B. F., E. E. Foord, P. J. Modreski, D. M. Triplehorn (1984). Minerologic evidence for an impact event at the Cretaceous/Tertiary boundary. Science, 224, 867-868.

Chhabildas, L. C. and J. R. Asay (1979). Rise time measurements of shock transitions in aluminum, copper, and steel. J. Appl. Phys., 50, 2749-2756.

Frondel, C. (1962). The System of Minerology III. Silica Minerals. Wiley, New York.

Grady, D. E., W. J. Murri, and G. R. Fowles (1974). Quartz to stishovite: wave propagation in the mixed phase region. J. Geophys. Res., 79, 332-338.

Gratz, A. J., W. J. Nellis, J. M. Christie, W. Brocious, J. Swegle, and P. Cordier (1992). Shock metamorphism of quartz with initial temperatures -170° to +1000°C. Phys. Chem Min. (in press).

Gratz A. J., J. Tyburczy, J. Christie, T. Ahrens, and P. Pongratz (1988). Shock metamorphism of deformed quartz. Phys. Chem Min., 16, 221-233.

Gratz, A. J., W. J. Nellis, and N. A. Hinsey (1992a). Laboratory simulation of explosive volcanic loading and implications for the cause of the K/T boundary. Geophys. Res. Lett., 19, 1391-1394.

Hemley, R. J., A. P. Jephcoat, H. K. Mao, L. C. Ming, and M. H. Manghnani (1988). Pressure-induced amorphization of crystalline silica. Nature, 334, 52-54.

Koch, R., W. J. Nellis, J. W. Hunter, H. Davidson, and T. H. Geballe (1990). Microstructures of Nb films recovered from megabar dynamic pressures. Pract. Met., 27, 391-405.

Nellis, W. J., W. H. Gourdin, and M. B. Maple (1988). Shock-induced melting and rapid solidification. In: Shock Waves in Condensed Matter 1987 (S. C. Schmidt and N. C. Holmes, Eds.), pp. 407-410.

Nellis, W. J., H. B. Radousky, T. H. Geballe, R. H. Hammond, R. Koch, and G. W. Hull, Jr. (1986). Superconductivity of Nb films recovered from megabar dynamic pressures. Appl. Phys. Lett., 49, 413-415.

Neumeier, J. J., W. J. Nellis, M. B. Maple, M. S. Torikachvili, K. N. Yang, J. M. Ferreira, L. T. Summers, J. I. Miller, and B. C. Sales (1989). Metastable A15 phase Nb_3Si synthesized by high dynamic pressure. High Pressure Res., 1, 267-289.

Officer, C. B. and C. L. Drake (1985). Terminal Cretaceous environmental events. Science, 227, 1161-1167.

Podurets, M. A., L. V. Popov, A. G. Sevastyanova, G. V. Simakov, and R. F. Trunin (1977). On the relation between the size of studied specimens and the position of the silica shock adiabat. Phys. Solid Earth, 12, 727-728.

Raikes, S. A. and T. J. Ahrens (1979). Post-shock temperatures in minerals. Geophys. J. R. Astron. Soc., 58, 717-747.

Swegle, J. W. (1990). Irreversible phase transitions and wave propagation in silicate geologic materials. J. Appl. Phys., 68, 1563-1579.

Tse, J. S. and D. D. Klug (1991). Mechanical stability of a-quartz: a Molecular-Dynamics study. Phys. Rev. Lett., 67, 3559-3562.

Weir, S. T., W. J. Nellis, C. L. Seaman, E. A. Early, M. B. Maple, M. Kikuchi, and Y. Syono (1991). Shock consolidation of crystallographically aligned $Bi_2Sr_2CaCu_2O_8$ powders. Physica C, 184, 1-12.

Yoo, C. S. and W. J. Nellis (1991). Phase transformations in carbon fullerenes at high shock pressures. Science, 254, 1489-1491.

Yoo, C. S., W. J. Nellis, M. L. Sattler, and R. G. Musket (1992). Diamondlike metastable carbon phases from shock-compressed C_{60} films. Appl. Phys. Lett., 61, 273-275.

Int. J. Impact Engng Vol. 14, pp. 541 – 549, 1993
Printed in Great Britain

0734-743X/93 $6.00 + 0.00
Pergamon Press Ltd

ADVANCED SHIELD DESIGN FOR SPACE STATION *FREEDOM*

G. D. OLSEN and A. M. NOLEN

National Aeronautics and Space Administration
George C. Marshall Space Flight Center, AL 35812

ABSTRACT

Due to the predicted increase in the severity of the orbital debris environment in low-Earth orbit, the baseline meteoroid/debris protection system for Space Station *Freedom* (S.S. *Freedom*) must be augmented on orbit. In response to this need, an advanced shield design effort is underway at NASA's Marshall Space Flight Center (MSFC). The results to date of this program are presented.

A series of 18 hypervelocity impact tests were conducted at MSFC's Space Debris Simulation Facility. These tests consisted of launching aluminum projectiles at velocities up to 7 km/s to evaluate various design solutions. Parameters investigated include shield material and geometric configuration (thickness, spacing, orientation, and arrangement) in relation to the baseline aluminum "Whipple" bumper.

The results of the hypervelocity impact tests are presented. Comparison with protection offered by the baseline protection system is made. Evaluation of protection offered by candidate augmented systems and hydrocode simulations is performed. An assessment of the often-overlooked structural design considerations such as launch loads, on-orbit loads, extravehicular activity requirements, maintainability, etc., is presented. These analyses lead to the identification of a candidate system to augment the baseline meteoroid/debris protection system for the habitable modules of S.S. *Freedom*.

INTRODUCTION

The evolution of the standard dual-sheet aluminum Whipple shield for providing protection for spacecraft from meteoroids and orbital debris is well documented (Whipple, 1947; Cour-Palais, 1969; Swift and Hopkins, 1970). The baseline protection system for the habitable modules for S.S. *Freedom* consists of a dual-sheet structure for its initial 10 years of operation.

With the adoption of the revised orbital debris environment model (SSP 30425, 1992), it is evident that additional shielding will be required to provide the level of protection specified by program requirements. The "new" environment raised the orbital debris flux (number of particles at a given size and velocity per square meter per year) by an order of magnitude over the original model adopted by the S.S. *Freedom* program. Tests and analyses show that additional protection will be required to meet the initial requirement of 0.9955 probability of no failure per element per 10 years, as well as the 30-year life of the station.

In this effort, shield configurations were evaluated in terms of design and operational simplicity as well as penetration resistance. All too often, shield protection systems are designed based on protection afforded and shield weight alone. The often-significant support structure mass is neglected. With the advent of long duration spacecraft such as S.S. *Freedom*, on-orbit loads, extravehicular

activity, and maintainability become design drivers. Candidate configurations are evaluated in terms of all of these factors.

S.S. *FREEDOM* BASELINE PROTECTION SYSTEM

To meet the prescribed probability of no failure, the baseline protection system for the habitable modules consists of a single aluminum shield spaced a finite distance from the pressure wall as shown in Fig. 1. The shields cover the Habitation, Laboratory, and Pressurized Logistics Elements as well as the Resource Nodes. Kahl and Stokes (1992) provide a thorough overview of the meteoroid/debris protection system.

The means by which the Whipple bumper system protects the spacecraft is illustrated in Fig. 2 (Elfer and Kovacevic, 1985). The bumper is designed to fragment, melt, or vaporize the projectile and disperse its energy over a wider area on the rear wall. If the bumper is too thin, the projectile will not be shocked sufficiently to disperse the energy. Conversely, if the bumper is too thick, the system weight increases and bumper fragments can be projected onto the rear wall. The pressure wall must be designed to withstand the blast loading and fragments present in the debris cloud generated at the impact site.

For S.S. *Freedom*, the pressure wall thickness is set at 0.3175 cm of 2219-T87 aluminum. With the adoption of the new environment, the present system will not adequately defeat the increase in projectile mass. National Space Transportation System launch weight restrictions prohibit the addition of more shielding, and envelope constraints deny increased standoff distance prior to launch.

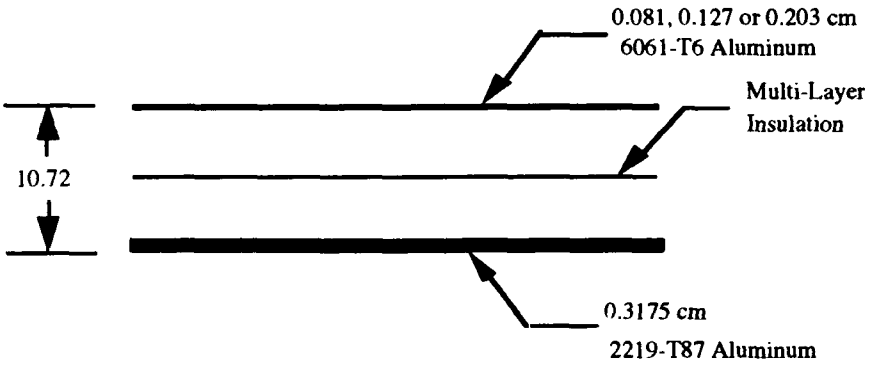
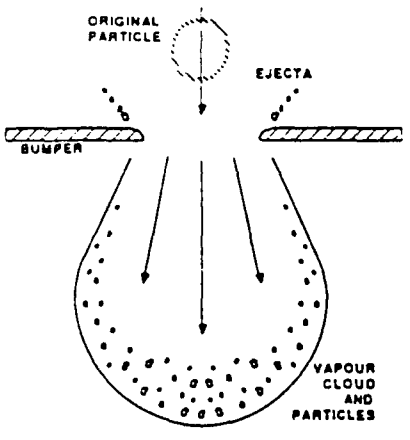
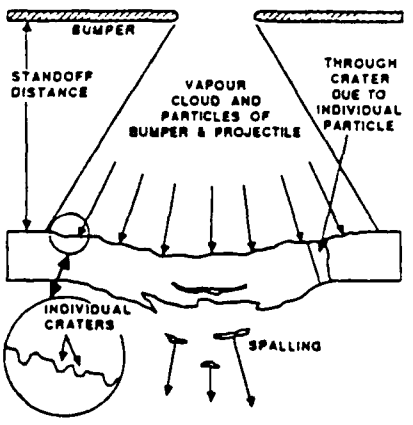


Fig. 1. S.S. *Freedom* Baseline Meteoroid/Debris Shield



Hypervelocity impact will fragment/melt/ vaporize the projectile and bumper.



The rear wall must then survive the fragments and blast loading.

Fig. 2. Whipple Bumper System (Elfer and Kovacevic, 1985)

EXPERIMENTAL PROCEDURE

This program examined two different approaches to augment the existing S.S. *Freedom* meteoroid/debris protection system. The first approach consisted of placing an additional shield between the existing bumper and pressure wall. The second approach placed the augmentation in front of the existing baseline configuration.

Each test was performed at MSFC in the Space Debris Impact Facility (Taylor, 1987). The facility consists of an instrumented two-stage light gas gun capable of launching projectiles 0.3175 to 1.27 cm in diameter at velocities from 3 to 7 km/s. A schematic of the facility is shown in Fig. 3. Projectile velocity measurements are accomplished by a pulsed x-ray system and a Hall photographic station. A description of the test article for each shot is listed in Table 1. Some factors were held constant for each test. An 1100-O aluminum spherical projectile was used for each test along with a 0.3175 cm 2219-T87 aluminum panel to simulate the pressure wall. Each test also had a 20-layer multilayer insulation (MLI) blanket located halfway between the baseline shield and the rear wall. Impact parameters for each shot are listed in Table 2 along with the impact damage to the rear wall.

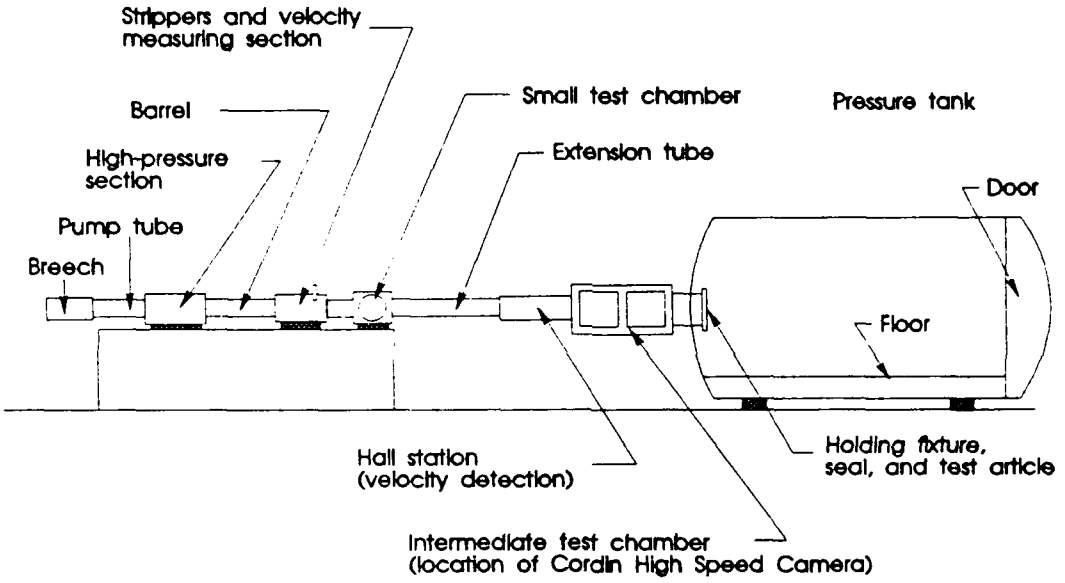


Fig. 3. MSFC Space Debris Impact Facility

TEST MATRIX AND RESULTS

Two different approaches were taken to investigate means of augmenting the existing protection system. The first consisted of placing an additional shield between the existing bumper and pressure wall. The function of an intermediate shield is to reduce the debris cloud's largest fragment size and velocity which, in turn, alters the pressure loading on the rear wall (Piekutowski, 1991). Although studies of more sophisticated intermediate shields are underway (Zwiener, et al., 1992), style 710 Kevlar® cloth (8 ounces per square yard) was chosen for shots 1323, 1325, and 1333 based on previous work by Elfer (1988).

Test 1323 consisted of placing four layers of Kevlar® immediately in front of the MLI and replacing the 0.127-cm bumper with a 0.102-cm bumper. The total areal density of this configuration is approximately 11.5-percent greater than that of the baseline system. The projectile impacted the bumper at 45° obliquity. From an interpolated ballistic limit curve for the baseline system (Bjorkman, 1991), the ballistic limit velocity for a 0.635-cm projectile is 7.1 km/s. No perforation resulted.

Table 1. Test Article Data

Test No.	Config	Total S/O cm	Bumper 1-a t cm	Bumper 1-a Areal Den g/cm^2	Bumper 2 t cm	Bumper 2 Areal Den g/cm^2	Bumper 3 t cm	Bumper 3 Areal Den g/cm^2	Bumper 4 t cm	Bumper 4 Areal Den g/cm^2	Total Areal Den g/cm^2
1323	IB	10.16	0.102	0.276	4 Layers-b	0.109					0.384
1325	Corr IB	10.16	0.102	0.276	4 Layers-b	0.109					0.384
1333	IB	10.16	0.102	0.276	3 Layers-b	0.081					0.357
1334	Corr IB	10.16	0.102	0.276	0.051	0.138					0.413
1353	DB	30.48	0.127	0.345	0.127	0.345					0.689
1354	DB	30.48	0.127	0.345	0.127	0.345					0.689
1369	DB	30.48	0.127	0.345	0.127	0.345					0.689
1370	Hyb MS	40.64	0.081	0.221	2 Layers-c	0.088	2 Layers-c	0.088	0.127	0.345	0.741
1371	Hyb MS	40.64	0.081	0.221	2 Layers-c	0.088	2 Layers-c	0.088	0.127	0.345	0.741
1372	Hyb MS	40.64	0.081	0.221	2 Layers-c	0.088	2 Layers-c	0.088	0.127	0.345	0.741
1373	DB	40.64	0.127	0.345	0.127	0.345					0.689
1374	Al MS	40.64	0.051	0.138	0.051-d	0.138	0.051-d	0.138	0.127	0.345	0.758
1375	Al MS	40.64	0.051	0.138	0.051-d	0.138	0.051-d	0.138	0.127	0.345	0.758
1376	DB	40.64	0.160	0.434	0.127	0.345					0.779
1377	DB	30.48	0.160	0.434	0.127	0.345					0.779
1378	DB	40.64	0.160	0.434	0.127	0.345					0.779
1379	DB	30.48	0.160	0.434	0.127	0.345					0.779
1383	DB	40.64	0.127	0.345	0.127	0.345					0.689

IB - Intermediate Bumper
Corr IB - Corrugated with Intermediate Bumper
DB - Double Bumper
Hyb MS - Hybrid Multi-Shock
Al MS - Aluminum Multi-Shock

a - All bumpers are 6061-T6 Al unless stated
b - Kevlar® Style 710 blanket
c - AF26 Nextel blanket
d - 2024-T4 Aluminum

Table 2. Hypervelocity Impact Data

Test No.	Config	Projectile Dia cm	Projectile Vel km/s	Rear Sheet Damage Perf	Hole Size cm	Damage Area	Comments
1323	IB	0.635	7.1	No		3.8 x 7.6	No crtrs
1325	Corr IB	0.635	7.0	No		5.1 dia	No crtrs
1333	IB	0.795	7.0	Yes	1.2 dia	7.1 dia	Petalled hole w/ cracks
1334	Corr IB	0.635	7.0	No		8.9 x 10.2	No crtrs
1353	DB	0.953	6.6	No		12.7 dia	No crtrs
1354	DB	0.953	3.6	Yes	0.84 x 0.46	10.2 dia	4 crtrs w/ rear surf dmpls
1369	DB	0.953	6.2	No		16.5 dia	No crtrs
1370	Hyb MS	0.953	6.6	No		None	No damage
1371	Hyb MS	0.953	6.2	No		None	No damage
1372	Hyb MS	0.953	3.6	Yes	0.89 x 0.66	6.4 dia	2 crtrs w/ rear surf dmpls
1373	DB	0.953	6.6	No		6.4 dia	No crtrs
1374	Al MS	0.953	6.6	No		None	No damage
1375	Al MS	0.953	3.6	Yes	0.38 & 0.66 dia	12.7 dia	8 crtrs w/ rear surf dmpls
1376	DB	0.953	3.6	No		11.4 dia	6 crtrs w/ rear surf dmpls, 1 w/ crcks
1377	DB	0.953	3.6	No		11.4 dia	9 crtrs w/ rear surf dmpls, 2 w/ crcks
1378	DB	0.953	6.6	No		2.5 dia	No crtrs
1379	DB	0.953	6.6	No		6.4 dia	No crtrs
1383	DB	0.953	3.6	Yes	0.58,0.58,0.43	7.6 dia	10 crtrs w/ rear surf dmpls

Shot 1333 had three layers of Kevlar® versus four layers in shot 1323 to more closely replicate the areal density of the baseline system (+3.6 percent). A larger projectile (0.795 cm) impacted normally, resulting in a petalled hole. At 7 km/s, the interpolated critical diameter is 0.72 cm. No appreciable increase in penetration resistance is noted.

Shots 1325 and 1334 sought to combine the benefits of intermediate shields with corrugated bumpers. Schonberg (1990) reported an increase in penetration resistance by using equal weight corrugated bumpers versus monolithic bumpers. An additional benefit would be an inherent stiffness to more aptly handle significant launch loads.

Test 1325 utilized a 30° corrugation angle as shown in Fig. 4. In test 1334, the Kevlar® was replaced with a 0.051-cm sheet of 2024-T4 aluminum. Both resulted in no penetration as predicted by the ballistic limit curve.

From a structural design viewpoint, it would be difficult to install an intermediate shield on-orbit using extravehicular activity (EVA). The amount of penetration resistance gained would not be worth the many hours of EVA time. The Kevlar® intermediate shields also generated an extraordinary amount of broken and loose fibers as shown in Fig. 4. This could pose a contamination threat to S.S. *Freedom* components. The promise of corrugated shields should be investigated further.

Based upon these findings, an investigation into augmented shielding external to the existing protection was initiated. It has been shown that increasing the total standoff distance from the bumper to the rear wall will increase the penetration resistance of the structure (Lundeburg, Stern and Bristow, 1967; Cour-Palais, 1969; Richardson, 1969). Even so, there appears to be a point of diminishing return at a specific distance. In general, there is ample room outside the baseline shield to add material without diminishing S.S. *Freedom* operations.

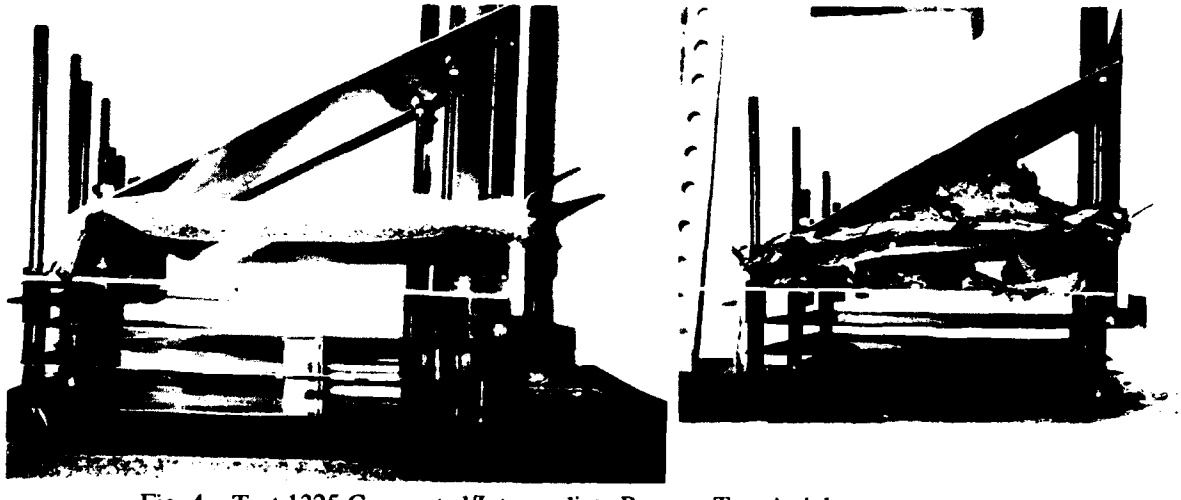


Fig. 4. Test 1325 Corrugated/Intermediate Bumper Test Article

Tests 1370, 1371, and 1372 were performed to investigate a concept proposed by Boeing Defense and Space Group to deal with the increasing severity of the environment. A derivative of the multishock concept (Cour-Palais and Crews, 1990), it employs two Nextel shields and one 0.081-cm 6061-T6 aluminum bumper in a 30.48-cm standoff package as shown in Fig. 5. Although Christensen (1990) has derived a set of equations for sizing a hybrid multishock system, he does not incorporate a leading aluminum bumper. MSFC and Boeing shield designers interpret the design requirements to specify a hard surface to resist a crew member's kick-off load, thus the need for an aluminum outer shield. Also, one of the advantages of multishock shielding is the reduction in thickness of the rear surface. The pressure vessel wall thickness for S.S. *Freedom*'s habitable elements is set at 0.3175 cm due, in part, to loads and manufacturing concerns and cannot be changed at this stage in the design cycle.

As shown in Table 2, the 0.953-cm projectile perforated the rear wall at 3.6 km/s, but not at 6.2 or 6.6 km/s. Additionally, at both the higher velocities, the baseline shield was not perforated; it suffered a 15-cm diameter by 2.5-cm deep bulge. The Nextel layers were severely damaged as shown in Fig. 5. They experienced the same type of failure as the intermediate Kevlar® layers and pose the same type of threat to S.S. *Freedom*.

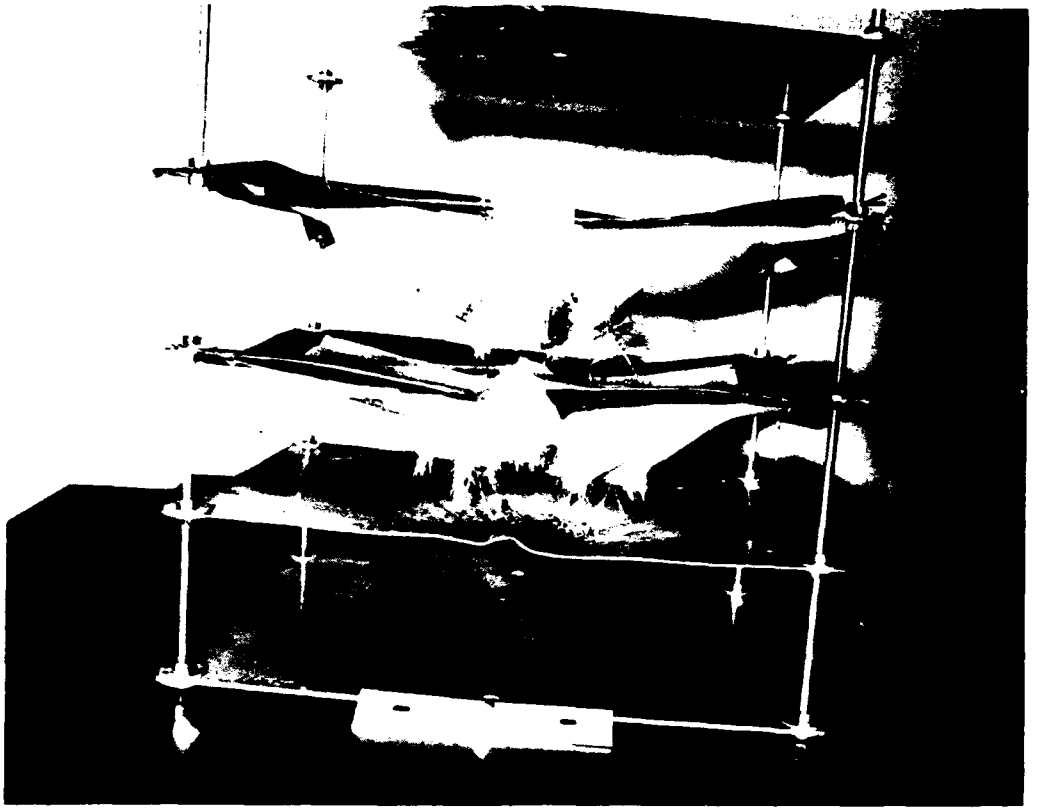


Fig. 5. Test 1370 Hybrid Multishock Test Article

Tests 1374 and 1375 examined a derivative of the aluminum multishock configuration proposed by Cour-Palais and Crews (1990). Three 0.051-cm 2024-T4 aluminum shields were spaced at 10.16-cm intervals in front of the baseline configuration. Although they failed at 3.6 km/s, at 6.6 km/s they produced no rear wall damage.

The remaining tests investigated the use of double aluminum shields. Richardson and Sanders (1972) conducted impact tests of double aluminum bumpers and found them to be over twice as efficient as single bumpers in resisting perforation in the fragmentation regime. Although the majority of the orbital debris impacts will be in the molten and vaporization regimes, it is still thought that double bumpers can provide the required protection. The two shield thicknesses tested were 0.127 and 0.160 cm located at both 20.32 and 30.48 cm in front of the baseline shield.

Tests 1353, 1354, and 1369 had a 0.127-cm bumper located 20.32 cm in front of the baseline shield. Again, perforation occurred at 3.6 km/s, but not at the higher velocities as shown in Fig. 6. Tests 1377 and 1379 examined a 0.160-cm shield at 20.32-cm additional standoff. This configuration survived both the 3.6 and 6.6 km/s impacts with no perforations.

Moving each of these shield thicknesses out an additional 10.16 cm reduced the rear wall damage further as shown in the results of Tests 1373, 1376, 1378 and 1383.

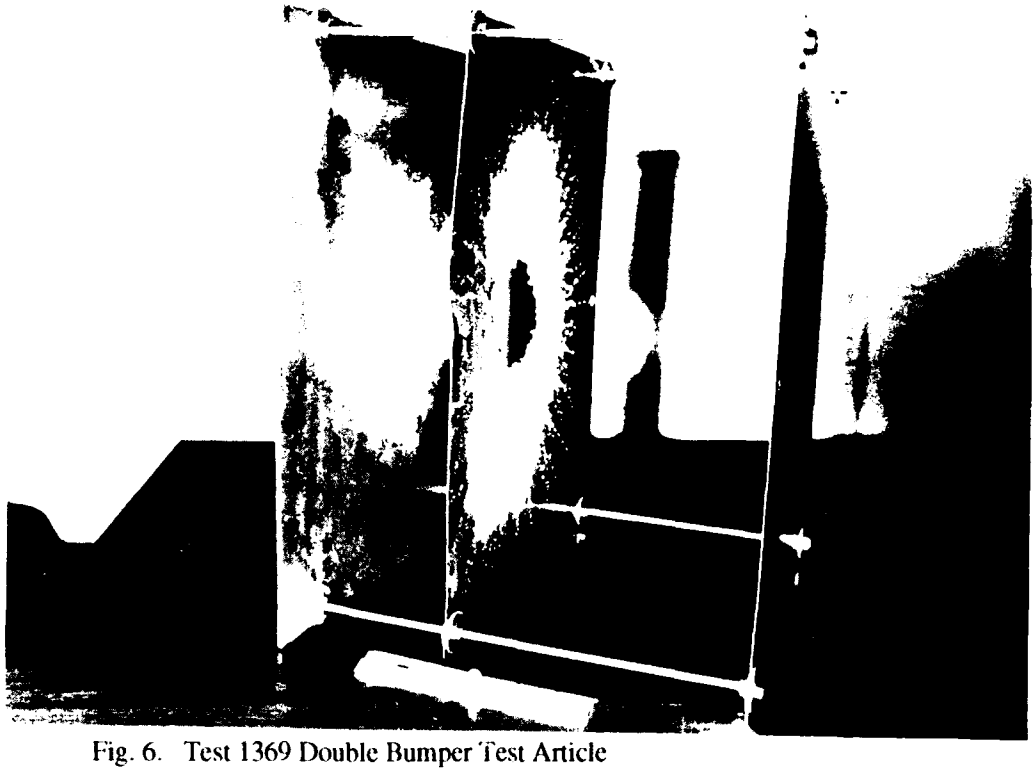


Fig. 6. Test 1369 Double Bumper Test Article

DESIGN CONSIDERATIONS

As previously stated, all too often meteoroid/debris protection systems are designed in terms of penetration resistance and shield weight alone. Other considerations, such as support structure and launch loads, are considered after the design is accepted. Also, with the advent of long duration spacecraft, such as S.S. *Freedom*, maintainability (repair and replacement), EVA operations, and residual effects become important considerations.

Although launch loads are not a consideration for on-orbit installed shields, the support structure is a factor. Not only does it support the baseline and augmented protection, but it must react loads induced by a crew member in an EVA suit. While EVA requirements are still being formulated, a good guide to start with is the requirements for intravehicular activity (IVA). The current IVA requirement for handholds is the ability to withstand 1,113 Newtons of force in all directions (NASA-STD-3000, 1991). As standoff distance increases, the moment arm at which the load is applied increases. This, in turn, leads to a massive fitting to react these loads. It is anticipated that the EVA loads will be even greater. Compound this with the requirement that handholds be spaced no greater than 90 cm apart. This leads to approximately 110 fittings for one S.S. *Freedom* element.

Another structural consideration is to be able to withstand the "kick load" from accidental impact by a crew member. This load has been estimated to be 556 Newtons. Based on this, a rigid surface is preferred to a fabric as an outer shield.

The benefits of multiple thin shields to reduce weight also have a penalty. The requirement to support and separate several layers and meet EVA load requirements could lead to substantial support structure. Before a decision is made to use multiple bumpers (more than two), a trade must be performed to consider the total mass of the system versus penetration resistance.

Since the augmented protection is to be assembled/installed on-orbit, design simplicity is a must. With EVA crew time at a premium (as evidenced by the May 1992 space shuttle retrieval of the INTELSAT), even a small difference in installation time can make a difference. Manual dexterity of the EVA gloved crew member must be considered.

In addition there are several other structural details that must be addressed. Means of attaching shields must be EVA compatible. Protection systems must provide access (122 cm diameter cylinder) for a crew member to inspect the rear wall. The shield must remain within the temperature ranges for EVA touch temperatures as well as meet thermal/optical levels. Hardware must be transportable to installation points.

Maintainability of the protection system is also a prime concern. Given the size of the habitable modules of S.S. *Freedom* (approximately 720 m^2 of surface area), maintenance can only be performed periodically and must be simple to perform. The shields must be repairable and/or replaceable in situ with a minimal level of effort. Following a noncritical impact (e.g., nonperforation of the rear wall), the protection system must still provide protection from the total environment as much as possible.

HYDROCODE ANALYSIS

John Tipton of the U.S. Army Corps of Engineers performed a hydrocode analysis of the double aluminum bumper concept. Using the HULL code, a simulation of test 1369 was conducted. Prior to impacting the second bumper, the problem is rezoned to allow more efficient use of computer resources. Also, to alleviate premature loss of mass, the strength model is not active until just before the debris cloud strikes the rear wall.

This two-dimensional axisymmetric computer simulation shows agreement with the test data. More simulations at other test points could prove HULL to be applicable in the testable regime.

CONCLUSIONS

Based on the aforementioned arguments and the very limited testing performed in this effort, the most promising advanced shield design appears to be a double aluminum bumper system with a 0.160-cm outer shield. The perforation resistance is comparable to the hybrid multishock system tested in shots 1370, 1371, and 1372 with only a 5-percent increase in areal density. This weight difference should be overcome due to the minimal support structure required. Hill (1992) has devised a simple means of attaching an additional rigid shield to the baseline bumper with no extra support structure other than fasteners. The concept is shown in Fig. 7, both schematically and applied to a cylinder.

Plans call for more hypervelocity impact testing to evaluate both double bumper and multishock protection systems. Concurrent with this effort will be design trades to develop efficient means of supporting and assembling the systems as well as meeting the other design criteria.

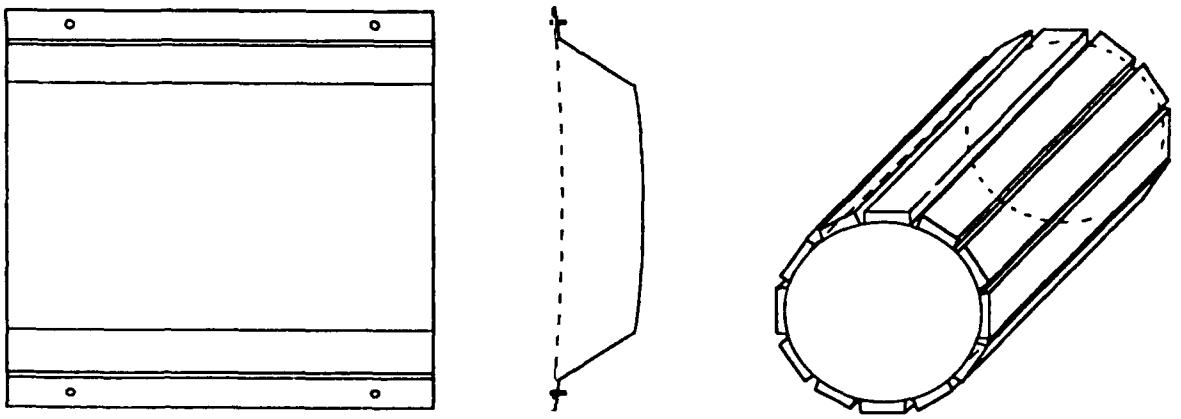


Fig. 7. Double Bumper "Hat Section" Design Concept

ACKNOWLEDGEMENTS

The authors would like to thank Ken Herren and Melanie McClain of NASA-MSFC and Charles Semmel and John Sims of Sverdrup Technology, Inc./MSFC Group for performing the hypervelocity impact tests and Scott Hill of NASA-MSFC for his review.

REFERENCES

Bjorkman, M.D. and Williams, D.R. (1992). Results of the ballistic limit testing of aluminum meteoroid/debris shields. D683-10578-1, The Boeing Company.

Christensen, E.L. (1990). Advanced meteoroid and debris shielding concepts. AIAA 90-1336, AIAA/NASA/DOD Orbital Debris Conference.

Christensen, E.L. (1991). Hybrid multishock shield ballistic limit equations. NASA-JSC Memo SN3-92-35.

Cour-Palais, B.G. (1969). Meteoroid protection by multiwall structures. AIAA 69-372, AIAA Hypervelocity Impact Conference.

Cour-Palais, B.G. and Crews, J.L. (1990). A multishock concept for spacecraft shielding. *Int. J. Impact Engng.*, 10, No. 1-4, 135–146.

Elfer, N. and Kovacevic, G., (1985). Design for space debris protection. Third AIAA Aerospace Technology Symposium.

Elfer, N., (1988). IR&D Report S87-47501-001. Martin Marietta Corporation.

Kahl, M.S. and Stokes, J. (1992). Operability of Space Station *Freedom*'s meteoroid/debris protection system. AIAA 92-1524, AIAA Space Programs and Technologies Conference.

Hill, S.A. (1992). Unpublished work, NASA-MSFC.

Lundeberg, J.F., Stern, P.H. and Bristow, R.J. (1965). Meteoroid protection for spacecraft structures. D2-24056, The Boeing Company,.

NASA-STD-3000, Rev. A, (1989).

Piekutowski, A.J. (1991). Debris cloud modeling and design of shields with intermediate layers. NASA Contract NAS8-38856 Quarterly Review.

Richardson, A.J. (1969). Theoretical penetration mechanics of multisheet structures based on discrete debris particle modeling. AIAA 69-371, AIAA Hypervelocity Impact Conference.

Richardson, A.J. and Sanders, J.P. (1972). Development of dual bumper wall construction for advanced spacecraft. *J. of Spacecraft and Rockets*, 9, No. 6, 448-451.

Schonberg, W.P., Bean, A.J. and Darzi, K. (1991). Hypervelocity Impact Physics. NASA Contractor Report 4343.

Swift, H.F. and Hopkins, A.K. (1970). Effects of bumper material properties on the operation of spaced meteoroid shields. *J. of Spacecraft*, 7, No. 1, 73-77.

Taylor, R.A. (1987). A space debris simulation facility for spacecraft materials evaluation. *SAMPE Quarterly*, 18, No. 2.

Whipple, F.L. (1947). Meteorites and space travel. *Astronomical Journal*, 52, 137.

Zwiener, J., Mount, A., Herren, K., Nettles, A., Semmel, C. and Sims, J. (1992). An enhanced Whipple bumper system: Impact resistance of composite materials. AIAA 92-1589, AIAA Space Programs and Technologies Conference.

Int. J. Impact Engng Vol.14, pp.551–560, 1993
Printed in Great Britain

0734-743X/93 $6.00+0.00
Pergamon Press Ltd

IMPACT AND PENETRATION BY L/D ≤ 1 PROJECTILES

D.L. ORPHAL*
C.E. ANDERSON, JR.**
R.R. FRANZEN*
J.D. WALKER**
P.N. SCHNEIDEWIND*
M.E. MAJERUS*

*California Research & Technology Division, The Titan Corporation
5117 Johnson Drive, Pleasanton, CA 94588
**Southwest Research Institute
6220 Culebra Road, San Antonio, TX 78288

ABSTRACT

Calculations of steel target penetration by L/D ≤ 1 tungsten and tungsten alloy projectiles have been extended to L/D = 1/32 over the velocity range 1.5 to 5 km/s. The ratio of crater to projectile diameter tends to 1 as L/D decreases over this entire velocity range. For impact velocities of 1.5 and 3 km/s, penetration depth normalized by projectile length, P/L, increases with decreasing projectile L/D up to a maximum value and then decreases for still lower L/D. Experiments at impact velocities of 2 and 3 km/s confirm these results. For 5 km/s impact velocity, the calculations show P/L increasing with decreasing projectile L/D over the entire range 1/32 ≤ L/D ≤ 1. The projectile L/D for which the maximum P/L occurs appears to depend on the impact velocity. P/L generally scales with impact velocity as $P/L \sim v^{f(L/D)}$ where f(L/D) ranges from 0 for a long rod to, we believe, 2 in the limit as projectile L/D approaches zero. The calculations show for 1/8 ≤ L/D ≤ 1/2, $P/L \sim v^{0.9}$; for L/D = 1/16, $P/L \sim v^{1.5}$; and for L/D = 1/32, the new results give $P/L \sim v^{1.9}$.

NOTATION

α	$(\rho_p/\rho_t)^{1/2}$	D_c	crater diameter	u	axial velocity along projectile/ target centerline
β	D_c/D	K	constant	v	impact velocity
ϕ,ϕ'	proportionality constant	L	projectile length	Y_o	flow stress
ρ_p	projectile density	m	curve fitting exponent	Z	shock impedance ratio: $Z_p/(Z_p + Z_t)$
ρ_t	target density	n	curve fitting exponent	Z_p	projectile shock impedance: $\rho_p(u_s)_p$
ζ	axial coordinate	P	depth of penetration	Z_t	target shock impedance: $\rho_t(u_s)_t$
c_1, c_2, c_3	curve fitting constants	q	curve fitting exponent		
c_p	projectile sound speed	u_p	penetration velocity		
c_t	target sound speed	u_s	shock velocity		
D	projectile diameter				

INTRODUCTION

Earlier results from this ongoing study of the penetration mechanics and performance of L/D ≤ 1 projectiles are given in Orphal *et al.*, (1992) and Orphal *et al.* (1990). This paper extends these earlier results to projectile L/D = 1/32. Also, the calculational results are now compared with experimental data at 2 km/s reported by Bjerke, *et al.* (1992) and the results of our recent experiments at 2 and 3 km/s.

The penetration physics of L/D < 1 projectiles has not been studied extensively, and among the many questions of interest are the scaling of penetration depth and crater dimensions with velocity and projectile L/D. It is now well established that the penetration depth, P, for long rods at high velocity becomes essentially independent of velocity, e.g., Tate (1969) and Hohler and Stilp (1987). That is, $P \sim v^0$. For this case, crater or target hole volume is essentially proportional to kinetic energy (Murphy, 1987), and therefore, crater or hole diameter, D_c, is proportional to v.

For the case of an L/D = 1 projectile at high velocity, craters are approximately hemispherical in shape and crater volume is proportional to the kinetic energy of impact. Therefore, for L/D = 1 projectiles $P \sim v^{2/3}$ and $D_c \sim v^{2/3}$. Although $v^{2/3}$ scaling is often assumed for L/D = 1 projectiles, e.g., Murphy (1987), detailed analyses of experimental data and calculational results suggest that penetration may scale more closely to $v^{0.6}$ (Walsh and Johnson, 1965; Sedgwick 1980).

Research on penetration by projectiles with L/D < 1 suggests that the scaling of penetration depth with velocity may be $P \sim v^n$ with n > 2/3 (Orphal *et al.*, 1992, Orphal *et al.*, 1990; Orphal and Franzen, 1990; Herbette, 1989). It is hoped that this research will also extend understanding of the variation of target crater volume and shape with projectile L/D and impact velocity.

HYDROCODE CALCULATIONS

Computations were performed assuming axial symmetry. The calculations were performed over a period of time using two different finite difference Eulerian "hydrocodes": the 3-D code CTH (McGlaun *et al.*, 1988) and the 2-D code CSQIII (Thompson and McGlaun, 1988). In many cases, the same computation was performed using both codes. Generally it was found that the two codes gave very similar results.

The matrix of computer calculations performed is given in Table 1. In Table 1 CSQ calculations are denoted with a dot (•) and CTH calculations with a cross (+).

Table 1. Matrix of Computer Calculations.

	Impact Velocity (km/s)		
L/D	1.5	3.0	5.0
1/1	+	•+	+
1/2	+	•+	•
1/4	•+	•+	•
1/8	•+	•+	•+
1/16	+	•+	+
1/32	+	+	+

In the CSQ calculations the materials were assumed to behave as elastic-perfectly plastic with a flow stress Y_o. The constitutive parameters for the CSQ calculations are given in Orphal, *et al.* (1990). In the CTH calculations for $1/16 \leq L/D \leq 1$, the steel target was modeled using the Johnson-Cook 4340-steel model which included strain hardening. The constitutive parameters for the Johnson-Cook model used in these CTH calculations are given in Johnson and Cook (1985). For the most recent CTH calculations for L/D = 1/32, the tungsten and steel were modeled as elastic-perfectly plastic with the same constitutive parameters as Orphal, *et al.* (1990).

The diameter for the penetrator was 1.0 cm. Typical zoning was 0.5-mm square zones for the L/D = 1 and L/D = 1/2 penetrator problems. For penetrators with $L/D \leq 1/4$, 10 zones were used through the penetrator length (thickness). Computing times on a CRAY Y-MP ranged from approximately 10 minutes to more than 2 hours, depending on the L/D and impact velocity.

COMPUTATIONAL RESULTS

Results for penetration P are presented in terms of the normalized penetration depth $P/\alpha L$, where $\alpha = (\rho_p/\rho_t)^{1/2}$ and $\rho_p$and ρ_t are the projectile and target material densities, respectively. This allows combining the results for calculations using pure tungsten (ρ_p = 19.2 g/cm^3) with those using a tungsten-alloy penetrator (ρ_t = 17.4 g/cm^3). The use of the square root of the ratio of densities to perform this normalization is an assumption, but it is consistent with both theory and experimental results for high-velocity long rods (Tate, 1969; Hohler and Stilp, 1987). The square root of the density ratio is also suggested by the results reported by Sedgwick (1980). On the other hand, some researchers have suggested that penetration should scale as $(\rho_p/\rho_t)^{1/3}$ or $(\rho_p/\rho_t)^{2/3}$ for L/D = 1 projectiles (Herrmann and Wilbeck, 1987). For this paper we choose $\alpha = (\rho_p/\rho_t)^{1/2}$ for normalization. This assumption has no effect on the essential results presented here; however, this scaling for high velocity projectiles with L/D < 1 deserves further examination.

Penetration Versus Projectile L/D

Figure 1 shows the calculated normalized penetration, $P/\alpha L$, versus projectile L/D for impact velocities of 1.5, 3 and 5 km/s. For all three impact velocities, $P/\alpha L$ increases with decreasing projectile L/D over the range $1/8 \leq L/D \leq 1$. For an impact velocity of 1.5 km/s, $P/\alpha L$ reaches a maximum at a projectile L/D ~ 1/8 and for L/D < 1/8 penetration decreases with decreasing L/D. The 3 km/s calculations show the same phenomena with the maximum in $P/\alpha L$ occurring for L/D ~ 1/16. The results for an impact of 5 km/s exhibit no maximum in the $P/\alpha L$ versus L/D curve for the range of L/D studied.

These results combined suggest that $P/\alpha L$ achieves a maximum as L/D is decreased. The L/D for which this maximum occurs appears to depend on the impact velocity. This is consistent with the results reported in Orphal, *et al.* (1992) and both the experimental and computational results reported by Bjerke, *et al.* (1992).

The variation in $P/\alpha L$ with L/D (before the maximum in the $P/\alpha L$ versus L/D curve) can be approximated by a power law

$$P/\alpha L = c_1 (L/D)^m \tag{1}$$

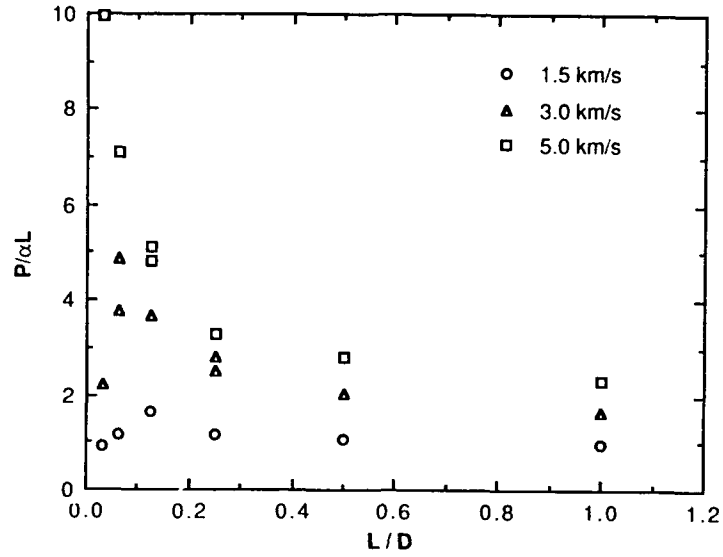


Fig. 1. P/aL versus projectile L/D.

The computational results give the following values for the exponent m (and the correlation coefficient r^2) over the range of projectile L/D indicated.

v (km/s)	m	Range of Projectile L/D
1.5	-0.29 (r^2 = 0.97)	1/8 ≤ L/D ≤ 1
3.0	-0.36 (r^2 = 0.96)	1/16 ≤ L/D ≤ 1
5.0	-0.43 (r^2 = 0.99)	1/32 ≤ L/D ≤ 1

P/αL Versus Impact Velocity

The computational results for P/αL versus impact velocity are plotted in log-log space in Fig. 2. The data, of course, are limited but the results do seem relatively linear in log-log space. If the variation of P/αL with velocity is assumed to be a power law of the form

$$P/\alpha L = c_2 v^n \tag{2}$$

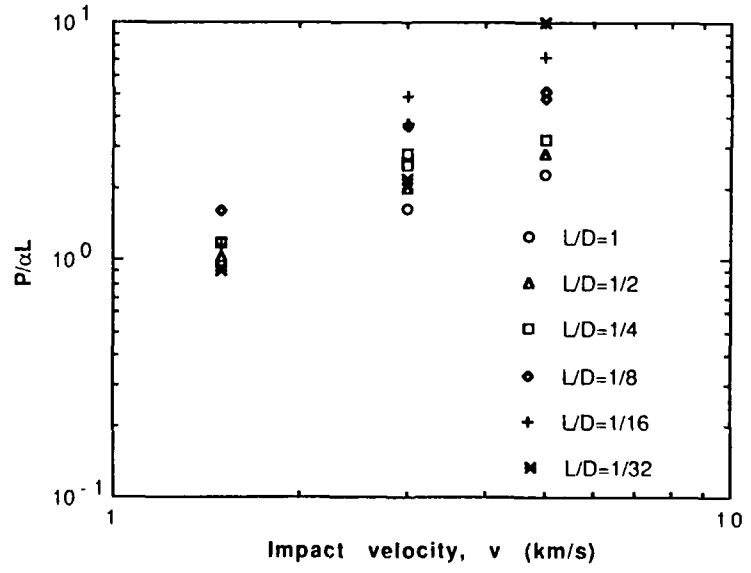


Fig. 2. Normalized penetration versus impact velocity.

the computational results give the following values for the exponent n:

Projectile L/D	n in v^n	r^2
1/1	0.72	0.99
1/2	0.84	0.98
1/4	0.87	0.90
1/8	0.91	0.97
1/16	1.54	0.94
1/32	1.95	0.97

Figure 3 shows the exponent n (in $P/\alpha L = c_2 v^n$) versus 1/(L/D). These results suggest that n is greater than 1 and varies rapidly for $1/8 \lesssim L/D \leq 1/32$. The obvious question of the limiting value for n as L/D approaches zero is discussed below.

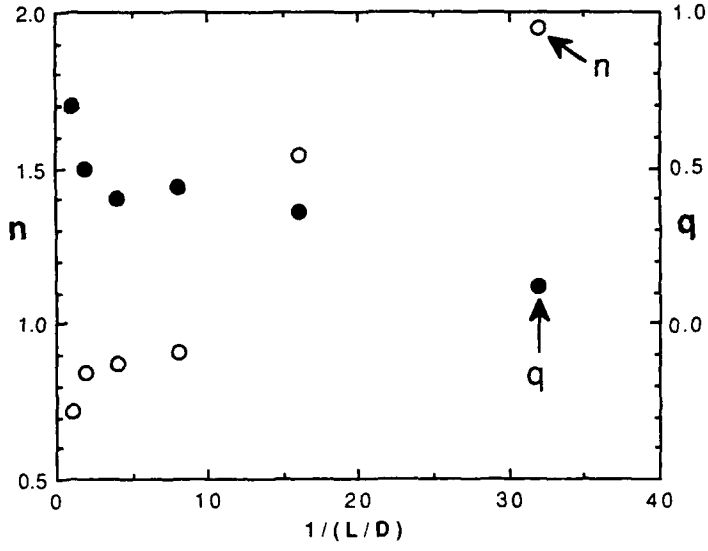


Fig. 3. n in $(P/\alpha L) = c_2 v^n$ and q in $Dc/D = c_3 v^q$ versus 1/(L/D).

Crater Diameter Versus Impact Velocity and Projectile L/D

Figure 4 shows the computed crater diameter, D_c, normalized by the projectile diameter, D, versus impact velocity. Again, the linearity in log-log space suggests a power law of the form

$$(D_c/D) = c_3 v^q \tag{3}$$

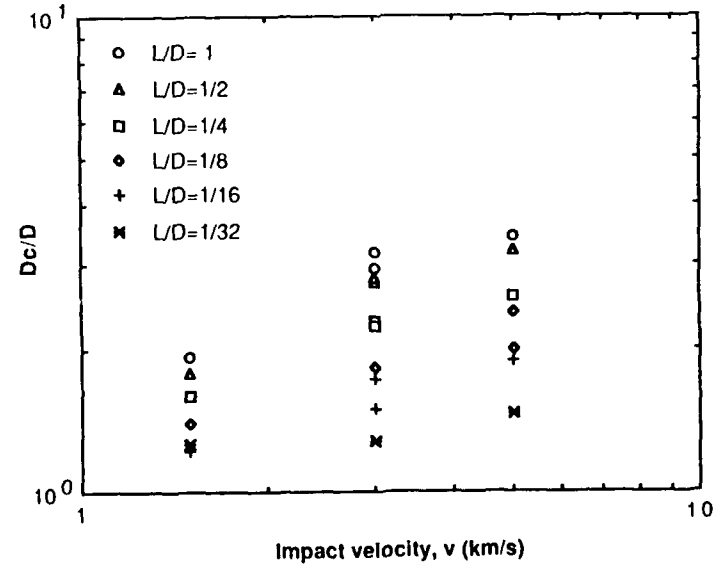


Fig. 4. D_c/D versus v.

A least squares fit of the computational results gives the following values for the exponent q:

Projectile L/D	q	r^2
1/1	0.70	0.99
1/2	0.50	0.97
1/4	0.40	0.98
1/8	0.44	0.99
1/16	0.36	0.95
1/32	0.12	0.87

The exponent q in $(D_c/D) = c_3 v^q$ versus $1/(L/D)$ is also plotted in Fig. 3. The calculational results suggest that (D_c/D) is becoming independent of impact velocity as projectile L/D approaches zero.

Figure 5 shows the computed normalized crater diameter, D_c/D, versus projectile L/D for impact velocities of 1.5, 3 and 5 km/s. For this range of impact velocities, D_c/D appears to be approaching a value of about 1 as projectile L/D approaches zero.

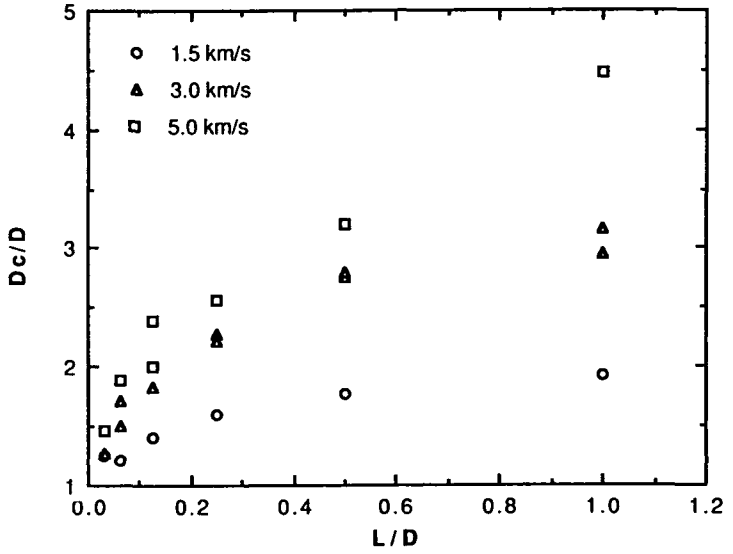


Fig. 5. D_c/D versus L/D for calculations.

Penetration Velocity

The particle (penetration) velocities versus time along the projectile/target centerline are shown as a function of projectile L/D in Fig. 6 for the 3.0 km/s impact velocity. The other two impact velocities studied showed similar behavior. The penetration velocity-time profile changes dramatically as the L/D of the projectile goes from 1/1 and 1/2 to 1/4 and smaller. For all cases, the initial penetration velocity is given by the Hugoniot jump conditions. For the L/D = 1/1 and 1/2 cases, the penetration velocity initially increases as the state of stress changes from one of uniaxial strain to a more complicated state of stress resulting from rarefaction waves propagating from the sides of the projectile. Then the penetration velocity decreases with time as the projectile encounters resistance from the target.

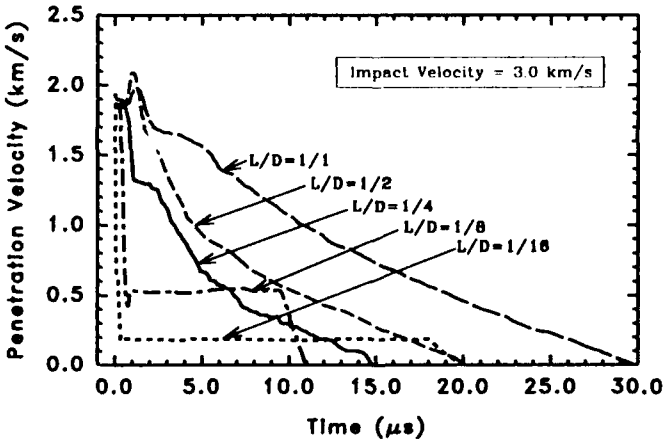


Fig. 6. Computed centerline penetration velocity for L/D = 1, 1/2, 1/4, 1/8 and 1/16 projectiles at 3 km/s impact velocity.

For the L/D = 1/4 projectile, rarefaction waves from the sides of the projectile arrive at nominally the same time as the rarefaction wave resulting from the interaction of the impact shock and the rear of the projectile. For smaller L/D projectiles, several axial unloading waves (between the rear of the projectile and the projectile/target interface) occur before the side rarefaction wave arrives at the centerline.

The interface velocity can be approximated (Walker, *et al.*, 1993) for small L/c_p, by:

$$u_p = Zv \exp\left\{-\frac{c_p}{L}(1-Z)t\right\} \tag{4}$$

Equation (4) can be used to infer a velocity profile along the target centerline by noting that the particle velocity waves travel from the interface at the sound speed of the target:

$$u(\zeta) = Zv \exp\left\{-\frac{c_p}{c_t L}(1-Z)(c_t t - \zeta)\right\} \tag{5}$$

where $\zeta = 0$ is the original projectile/target interface. The rarefaction from the corner of the projectile reaches a point ζ on the centerline at roughly

$$t = \frac{\sqrt{\zeta^2 + (D/2)^2}}{c_t} \tag{6}$$

and the release essentially "freezes" the current axial velocity of the materials. An expression for this velocity is given by:

$$u^{release}(\zeta) = Zv \exp\left\{-\frac{c_p}{c_t L}(1-Z)\left[\left(\zeta^2+(D/2)^2\right)^{1/2} - \zeta\right]\right\} \tag{7}$$

This velocity is an increasing function of the initial coordinate ζ and therefore slowest at the projectile/target interface of $\zeta = 0$. The projectile "coasts" into the target at a comparatively low velocity given by:

$$u_p = Zv \exp\left\{-\frac{Dc_p}{2Lc_t}(1-Z)\right\} \tag{8}$$

Target motion is stopped by strength and inertial effects and rebounds elastically; when this occurs, projectiled penetration is very quickly terminated.

EXPERIMENTAL RESULTS

Bjerke, *et al.* (1992) performed a series of experiments in which tungsten alloy (X-27, $\rho_p = 17.27$ g/cm^3) projectiles impacted steel (RHA) targets at nominally 2 km/s. The L/D for the projectiles used in these experiments ranged from 1/2 down to 1/32. These experiments were performed in the direct ballistic mode. With one exception, projectile diameter was 25.4 mm. The projectiles were launched in a one-piece nylon 6/6 sabot by a 50-mm diameter, 6-meter long smooth bore powder gun. The sabot was "stripped" by passage through a thin break screen which was also used to trigger two down-range orthogonal X-rays to obtain penetrator velocity and attitude prior to impact. Impacts were nominally zero degrees obliquity and zero degrees yaw, although non-zero yaw was experienced, particularly for the L/D = 1/16 and 1/32 projectiles. Targets were recovered post-test for measuring penetration depth and crater geometry. Further details of the experiments are given in Bjerke, *et al.* (1992).

For the present study, we performed a series of experiments to compliment and extend to higher impact velocities the experiments by Bjerke, *et al.* (1992). Our experiments were also performed in the direct ballistic mode using a 38-mm launch tube/115-mm pump tube two-stage light-gas gun. Experiments for L/D = 1/2, 1/4, 1/8, 1/16 and 1/32 projectiles were planned at nominal impact velocities of 2, 3, and 4 km/s. Unfortunately, not all these experiments are completed. In particular we have not yet been successful in launching these projectiles and stripping the sabot at 4 km/s. For these experiments the projectiles were made of 91% by weight tungsten alloy (X-27) and were 25.4 mm in diameter. The targets were RHA. Flash X-rays were used to determine the velocity, integrity and attitude of the projectile prior to impact. The targets were recovered, and post-test analyses of the targets were performed to determine penetration depth and crater geometry.

Figure 7 shows the experimental values for $P/\alpha L$ versus projectile L/D reported by Bjerke, *et al.* (1992) for v = 2 km/s along with our recent experimental results and the calculational results reported here for v = 1.5 km/s. In Figure 7 and other figures below, data from Bjerke, *et al.* (1992) are denoted BRL and data and calculational results from this research are denoted CRT. Both sets of experiments and the calculational results generally agree well with the shape of the $P/\alpha L$ versus L/D curve. All show $P/\alpha L$ increasing with decreasing L/D until a maximum is reached for L/D ~ 1/8. For L/D < 1/8 the results show $P/\alpha L$ rapidly decreasing with decreasing L/D. The agreement between the CRT calculations and experiments is also considered quite good. The Bjerke, *et al.* (1992) data are consistantly higher than those from our experiments. The reason for this difference is not known at this time but there is some reason to believe that the hardness of the targets used in the two sets of experiments differed.

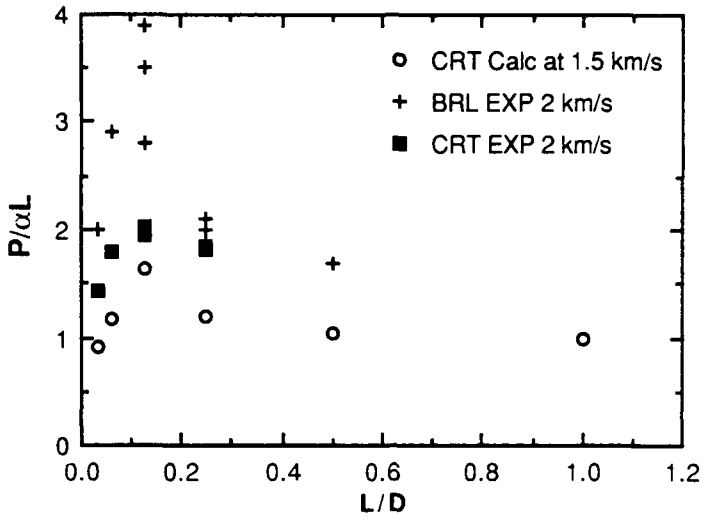


Fig. 7. Comparison of experimental results for P/aL versus L/D at 2 km/s by Bjerke, *et al.* (1992) (BRL) and Orphal, *et al.* (1993) (CRT) with computational results for 1.5 km/s.

Figure 8 compares the P/αL versus L/D data from our recent experiments at 2 and 3 km/s. The shapes of the P/αL versus L/D curves are similar but the maximum in the curves appears to be impact velocity dependent. This is consistent with the computational results. For 2 km/s impact, P/αL appears to reach a maximum at L/D ~ 1/8. Increasing the impact velocity to 3 km/s appears to shift the curve so that the maximum P/αL now occurs for L/D ~ 1/16.

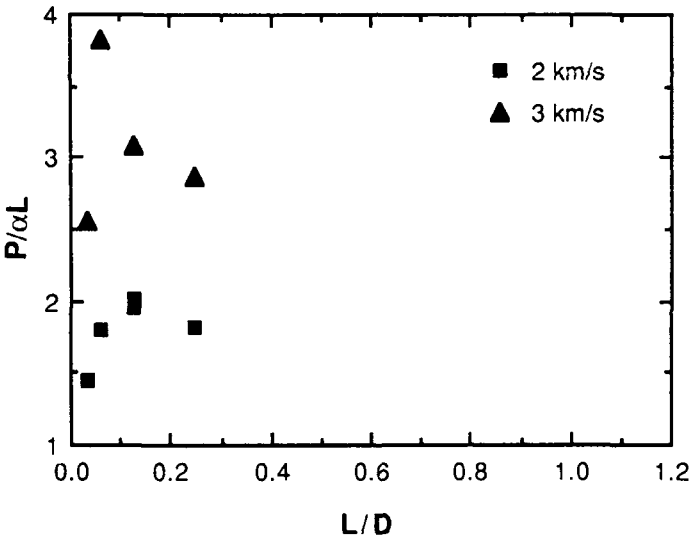


Fig. 8. Experimental results for P/αL versus L/D for impact velocities of 2 and 3 km/s.

Figure 9 compares the experimental data for crater diameter, D_c/D, versus L/D for the 2 km/s experiments by Bjerke, *et al.* (1992) and the calculations reported here. The agreement between the experimental data and computational results is considered good. The experimental data at 2 km/s also suggest that (D_c/D) is approaching a value of 1 as projectile L/D decreases.

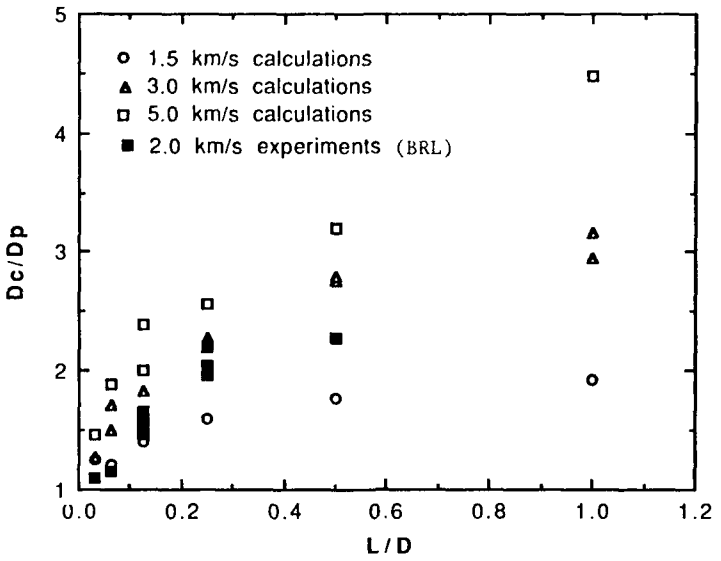


Fig. 9. D_c/D versus L/D for both calculations and experiments.

DISCUSSION

The penetration mechanics of these low L/D projectiles is governed by a unique mixture of one and two-dimensional processes. The "steady-state" (plateau) penetration velocity is the result of the side rarefaction wave (a 2-D effect) freezing the one-dimensional unloading from the rear surface of the projectile. Penetration itself is a 2-D manifestation since target material must flow radially from below the penetrator. The ability to flow target material radially is velocity dependent; however, as $L/D \rightarrow 0$, the impact problem approaches a true one-dimensional idealization. If Eq. 4 is integrated from t = 0 to infinity, the one-dimensional penetration depth can be estimated:

$$\left(\frac{P}{L}\right)_{1-D} = \frac{Zv}{(1-Z)c_p} \tag{9}$$

This expression agrees quite well with the one-dimensional depths of penetration calculated using CTH (0.58, 0.95, and 1.28 for the impact velocities of 1.5, 3.0, and 5.0 km/s, respectively). These 1-D P/L values, however, are significantly less than either the calculated or experimentally measured values as shown in Figs. 1 or 2, and indicate that as L/D becomes smaller and smaller, P/L performance should reach a maximum and then decrease as the impact physics becomes a one-dimensional problem. Both the calculations and the experiments indicate the P/L reaches a maximum value and then decreases as $L/D \rightarrow 0$. The discussion here provides a semi-quantitative description of the physics of penetration of low L/D projectiles; the reader is referred to Walker, *et al.* (1993), for a more detailed analysis of P/L as a function of L/D and impact velocity.

It is usually assumed for high velocity impact that the crater volume is proportional to the kinetic energy of the projectile. Our calculations suggest that this is at least approximately true for L/D < 1 projectiles. Assume, then, that the volume of the impact crater is proportional to the projectile kinetic energy. Let the crater volume be $\phi D_c^2 P$ where ϕ is a proportionality constant which includes a geometric factor describing the shape of the crater. The mass of the projectile is of course given by $\pi \rho_p D_p^2 L / 4$. Equating the crater volume and projectile kinetic energy gives:

$$\frac{P}{L} = \frac{\rho_p v^2}{\beta^2 \phi'} \tag{10}$$

where β is D_c/D an ϕ' incorporates the other constants.

Figure 10 shows P/L versus the parameter $(\rho_p v^2/\beta^2)$. The parameter $(\rho_p v^2/\beta^2)$ accounts for much (but certainly not all) of the computed variation in $P/\alpha L$ as projectile L/D is varied from 1 to 1/32 and impact velocity is varied from 1.5 to 5 km/s and, consequently $(\rho_p v^2/\beta^2)$ varies over an order of magnitude. Of course the parameter is quite sensitive to errors in determining D_c. D_c was measured as the crater diameter at the original target surface, but this is sensitive to the tensile strength of the target. Bjerke, *et al.* (1992) report impact crater diameters for their experiments so the parameter $(\rho_p v^2/\beta^2)$ may be calculated for each of these tests. This data is also shown in Fig. 10. The parameter $(\rho_p v^2/\beta^2)$ reasonably collapses the experimental data as well as the computational results. The agreement evident between the computational results and experiments seems quite good when it's recalled that in the experiments the velocity was essentially constant at 2 km/s. Thus, for the experimental data, the variation of the parameter $(\rho_p v^2/\beta^2)$ is essentially only the variation of $\beta = D_c/D$ with projectile L/D.

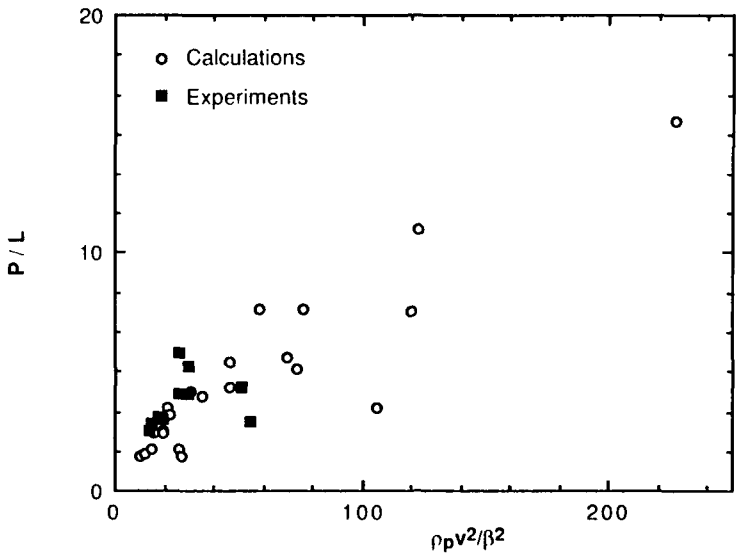


Fig. 10. Comparison of P/L versus $\rho_p v^2/\beta^2$ for calculations and experiments.

Substituting $(D_c/D)^2$ for β^2, equation (10) becomes

$$P/L = \rho_p v^2/(D_c/D)^2 \tag{11}$$

Since D_c/D can at least be approximated by the power law in Eq. (3)

$$P/L = K\, \rho_p\, v^{2(1-q)} \tag{12}$$

where all the various constants are lumped into the constant K.

From Fig. 3 and as discussed in relation to Eq. (3), q appears to be a function of projectile L/D. Furthermore, q appears to be approaching zero as projectile L/D approaches zero. That is, (D_c/D) is becoming independent of impact velocity as projectile $L/D \rightarrow 0$. Indeed from the results shown in Fig. 5, at least for the 1.5 - 5 km/s velocity range studied, (D_c/D) appears to be approaching a constant value of 1 as projectile $L/D \rightarrow 0$.

From Eq. (12), if $q \rightarrow 0$ as projectile $L/D \rightarrow 0$, then the scaling of P/L with impact velocity approaches v^2, i.e.,

$$P/L \rightarrow K\, \rho_p\, v^2 \text{ as projectile } L/D \rightarrow 0 \tag{13}$$

This is consistent with the computational and experimental results.

There is much interest recently in the concept of segmented rods, e.g., Orphal and Franzen (1990); Charters, *et al.* (1990); Kivity, *et al.* (1989); Naz and Lehr (1990); Scheffler and Zukas (1990). If indeed penetration scales with velocity as $v^{>2/3}$ for $L/D \leq 1/2$, and $v^{>1}$ for $L/D \leq 1/8$, the implication for penetration by segmented rods is obvious. The need for more research on $L/D < 1$ projectile penetration mechanics, as well as the potential benefits, seems compelling.

ACKNOWLEDGMENTS

Some of the work reported here was performed as part of the Joint DARPA, Army and Marine Corps Armor/Anti-Armor Program under the direction of Dr. Peter Kemmey (DARPA) and initially Dr. Tom Kiehne (now at the Institute for Advanced Technology). The interest and assistance of Dr. Kemmey and Dr. Kiehne is greatly appreciated, as is that of Dr. Crowson, Army Research Office; Billy Hogan of the LANL/ATAC; and René Larriva of Interferometrics. We would like to particularly acknowledge the assistance and cooperation of Todd Bjerke, BRL, in understanding his experiments and planning our experiments. We thank Ms. Bentley for her care and assistance in preparation of this manuscript.

REFERENCES

Bjerke, T.W., J.A. Zukas and K.D. Kinsey (1992). Penetration Performance of Disk Shaped Penetrators. *Int. J. Impact Engng.*, 12(2), 263-280.

Charters, A.C., T.L. Menna, and A.J. Piekutowski (1990). Penetration Dynamics of Rods from Direct Ballistic Tests of Advanced Armor Components at 2-3 km/s. *Int. J. Impact Engng.*, 10 (1-4), 93-106.

Herbette, G. (1989). The Influence of Projectile Shape on Penetration Power. *Proceedings of the 11th International Symposium on Ballistics, Vol. II*, Paper TB-35/1, Brussels, Belgium.

Herrmann, W. and J.S. Wilbeck (1987). Review of Hypervelocity Penetration Theories. *Int. J. Impact Engng.*, 5 (1-4), 307-322.

Hohler, V., and A.J. Stilp (1987). Hypervelocity Impact of Rod Projectiles with L/D from 1 to 32. *Int. J. Impact Engng.*, 5 (1-4), 323-331.

Johnson G.R., and W.H. Cook (1985). Fracture Characteristics of Three Metals Subjected to Various Strains, Strain Rates, Temperatures and Pressures. *Engng. Fracture Mech.*, 21 (1), 31-48.

Kivity, Y., E. Yitzhak, E. Hirsch, and R. Hasharon (1989). Penetration of Segmented Rods into Homogeneous Targets. *Proceedings of the 11th International Symposium on Ballistics, Vol. II*, Paper TB-25/1, Brussels, Belgium.

McGlaun, J.M., F.L. Zeigler, S.L. Thompson, M.G. Elrick (1990). CTH: A Three-Dimensional Shock Wave Physics Code. *Int. J. Impact Engng.*, 10, 351-360.

Murphy, M.J. (1987). Survey of the Influence of Velocity and Material on the Projectile Energy/Target Hole Volume Relationship. *Proceedings of the 10th International Symposium on Ballistics, Vol. II*, San Diego, CA.

Naz, P., and H.F. Lehr (1990). The Crater Formation Due to Segmented Rod Penetrators. *Int. J. Impact Engng.*, 10 (1-4), 413-425.

Orphal, D.L., C.E. Anderson, Jr., and R.R. Franzen (1990). Impact Calculations of L/D $\leq$ 1 Penetrators. *Proceedings of the 12th International Symposium on Ballistics*, San Antonio, TX.

Orphal, D.L., C.E. Anderson, Jr., R.R. Franzen, J.D. Walker, and P.N. Schneidewind (1992). Penetration by L/D < 1 Projectiles. *Proceedings of the 13th International Symposium on Ballistics*, Stockholm, Sweden.

Orphal, D.L. and R.R. Franzen (1990). Penetration Mechanics and Performance of Segmented Rods Against Metal Targets. *Int. J. Impact Engng.*, 10 (1-4), 427-438.

Scheffler, D.R. and J.A. Zukas (1990). Numerical Simulation of Segmented Penetrator Impact. *Int. J. Impact Engng.*, 10 (1-4), 487-497.

Sedgwick, R.T. (1980). Numerical Techniques for Modeling High Velocity Penetration and Perforation Processes. in *Ballistic Materials and Penetration Mechanics*, R.C. Laible (ed), Elsevier.

Tate, A. (1969). Further Results in the Theory of Long Rod Penetration. *J. Mech. Phys. Solids*, 17, 141-150.

Thompson, S.L. and J.M. McGlaun (1988). CSQIII, An Eulerian Finite Difference Program for Two-Dimensional Material Response: User Manual. SAND87-2763, Sandia National Laboratories, Albuquerque, NM.

Walker, J.D., C.E. Anderson, Jr., and D.L. Orphal (1993). A Model for Penetration by Very Low Aspect Ratio Projectiles. To be published.

Walsh, J.M. and W.E. Johnson (1965). On the Theory of Hypervelocity Impact. *Proceedings of the Seventh Symposium on Hypervelocity Impact, Vol. II.*

Int. J. Impact Engng Vol 14, pp.561–571, 1993
Printed in Great Britain

0734-743X/93 $6.00+0.00
Pergamon Press Ltd

TUMBLING OF HYPERVELOCITY RODS INDUCED BY IMPACT WITH OBLIQUE PLATE TARGETS

M. A. Persechino* and A. E. Williams

Naval Research Laboratory
Washington, DC

*Potomac Research, Inc.
6121 Lincolnia Rd., Alexandria, VA 22312
Potomac Research, Inc.

ABSTRACT

We investigated the cause of tumbling by hypervelocity rods after impact with oblique plate targets. The projectiles were strong rods, length to diameter ratio of 6 to 10, prepared from aluminum (10 tests) or steel (5 tests), launched at velocities of 4.2 to 4.8 km/s, and impacted into like material targets. The rods had little or no initial yaw (the average yaw was 1.8°). The residual projectile properties of length, tumbling rate and radial velocity were measured and evaluated in a simple model for rod tumbling. The model is based on the observation that plastic shear continues at the nose of the rod for a finite time after target perforation. Based on the observed tumbling rate, duration of plastic flow and the inertia of the residual rod an implicit determination of the shear strength of the rod was obtained. The calculated shear strength was in fair agreement with static shear values.

THE MODEL

The hypervelocity impact of a rod projectile into an oblique plate target will cause the residual projectile to rotate towards the plate normal. The impulse inducing the rotation appears to be the result of asymmetrical flow at the tip of the rod as the rod emerges from contact with the back surface of the plate. Such an impact is illustrated in Figure 1. The calculations (Figure 1) show that by relating the angular momentum to the angular impulse, one can estimate the shear stress, σ_s, acting for a time, Δt, over a cross-section, A, which produces the angular impulse. The shear stress should be similar to the static shear strength of the rod material (only elastic stresses can be transmitted into the remaining, undamaged rod). The duration of the shear flow after target perforation is difficult to specify. Based on flash x-ray measurements, we observed from limited tests with strong rod projectiles that length loss to the rod was completed after about 3 projectile diameters of travel beyond the rear of the plate. However, in a hydrocode model of a strong aluminum rod impacting a thick aluminum plate the rod length loss continued for about 6 projectile diameters of travel. For the calculations in this paper, we chose an in between value, 4.5 diameters of projectile travel. The Δt based on a 4.5 km/s velocity and a 0.32 cm rod diameter is 3.2 μsec. As illustrated

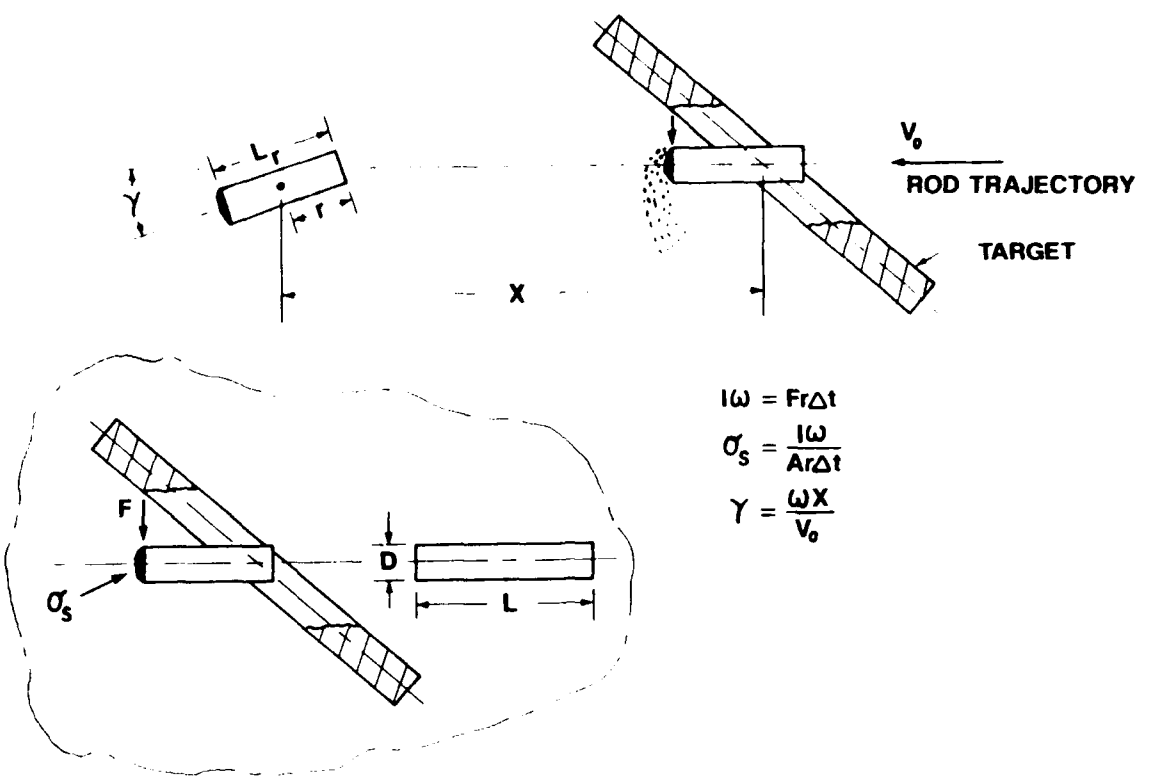


Fig. 1. Schematic illustrating a model for determining the shear and residual rod rotation from angular impulse.

in Figure 1, a radiograph of the projectile after target perforation allows a measurement of residual rod length and orientation. This data plus the known time after impact allows a calculation of tumbling rate, ω, and moment of inertia, I. The angular momentum is then equated to the angular impulse,

$$I\omega = Fr\Delta t \tag{1}$$

where

$$F = \sigma_s A$$

The components of the angular impulse are the radial force, F (shear strength X the cross section of the rod), the distance to the center of mass, r (one half the length of the rod, ℓ_r) and the duration of the impulse, Δt (3.2 μsec). The shear strength required to produce the observed tumbling rate is therefore

$$\sigma_s = I\omega/(Ar\Delta t) \tag{2}$$

TEST CONDITIONS AND RESULTS

The test conditions are summarized in Table 1. The projectiles were 0.32 cm diameter rods, either 2024-T86 aluminum or 4340 steel, heat treated to Rockwell "C" 50. The static shear strength for these materials would be:

2024-T86 aluminum: σ_s = 283 MPa
4340 steel, R_c 50: σ_s = 828 MPa

Table 1: Summary of Rod Impact Conditions for Oblique Target Data

Shot Number	Proj. Material	Target Material	ℓ_o/D^*	T/D*	V_o km/sec	α_o	ℓ_r/D^*
1-2-159	2024-T86 Aluminum	2024-T3 Aluminum	9.78	0.50	4.24	30	7.0
1-2-160			9.72	0.50	4.44	30	6.9
1-1-233			9.01	1.95	4.50	60	5.0
1-1-234			9.04	1.95	4.63	30	1.8
1-1-268			9.43	0.50	4.47	10	1.8
1-1-269			9.63	0.50	4.59	20	5.3
1-1-273			9.41	1.00	4.44	30	4.1
1-1-289			9.25	1.00	4.20	30	4.9
1-1-293			9.35	0.25	4.36	30	7.4
1-1-295			9.21	0.25	4.40	10	4.1
1-1-343	4340 Steel	4340 Steel	5.78	1.00	4.58	30	1.7
1-1-344		Cold-Rolled	7.29	0.22	4.65	10	2.8
1-1-369		RC	7.20	0.22	4.42	10	1.9
1-1-371		30-35	7.62	0.22	4.79	20	5.4
1-1-372			7.63	0.22	4.64	15	4.2

*Rod Diameter = 0.3175 cm

The initial length of the rods varied from 5.8 projectile diameters (1.84 cm) to 9.8 diameters (3.1 cm). The target plates were nearly like materials, 2024-T3 aluminum and 4340 steel at R_c 30-35. Plate thickness varied from 0.22 projectile diameters (0.07 cm) to 1.95 diameters (0.62 cm) and the impact angle varied from 10 to 60°. This variation in target thickness and orientation produced a wide variation in rod length loss which, in turn, had a large effect on moment of inertia and tumbling rate.

$$I = m_r (D^2/4 + \ell_r^2/3)/4$$

$$\omega = Fr\Delta t/I = \frac{2\sigma_s \Delta t}{\rho (D^2/4 + \ell_r^2/3)} \tag{3}$$

For equal value of angular momentum an $\ell_r/D = 2$ projectile would have 3.5 times the tumbling rate of an $\ell_r/D = 4$ projectile. The amount of measured projectile rotation varied from a low of 1° to a maximum of 183°, for an average of 63°.

The test results are summarized in Table 2. The last column presents the calculated values of shear stress corresponding to the observed values of angular momentum. The average shear strength for the aluminum rods was 283 MPa and for the steel rods was 973 MPa. However, the variation about these averages was considerable.

Table 2: Summary of Rod Rotation Rate, Angular Momentum, and Shear Stress Calculations

Shot Number	ω deg x 10^3	m_r g	I g cm^2	Iω g cm^2/sec	σ_s MPa
Al → Al					
1-2-159	257	0.473	0.196	880	314
1-2-160	183	0.466	0.188	602	215
2-1-233	115	0.337	0.072	143	72
1-1-234	2,591	0.125	0.004	181	253
1-1-268	3,149	0.119	0.004	220	313
1-1-269	845	0.357	0.085	1267	616
1-1-273	639	0.280	0.042	509	305
1-1-289	576	0.331	0.068	684	329
1-1-293	17	0.503	0.234	69	23
1-1-295	915	0.276	0.040	639	387
St → St					
1-1-343	1,433	0.325	0.010	250	384
*1-1-344	3,452	0.553	0.040	2410	2172
*1-1-369	3,749	0.377	0.014	916	1169
1-1-371	175	1.061	0.268	819	404
1-1-372	545	0.819	0.125	1188	737

*Residual rod is bent, mass and I are uncertain

A SECOND MODEL

An even simpler model for evaluating projectile motion can be obtained by relating linear radial momentum to radial impulse:

$$m_r \Delta V = F\Delta t = \sigma_s A \Delta t \tag{4}$$

The right side of the equation is the same as before; the radial momentum is the product of the residual projectile mass (calculated from the observed residual rod length, ℓ_r) times the measured radial velocity. The model is illustrated in Figure 2. The shear stress is simple:

$$\sigma_s = m_r \Delta V / (A \Delta t) \tag{5}$$

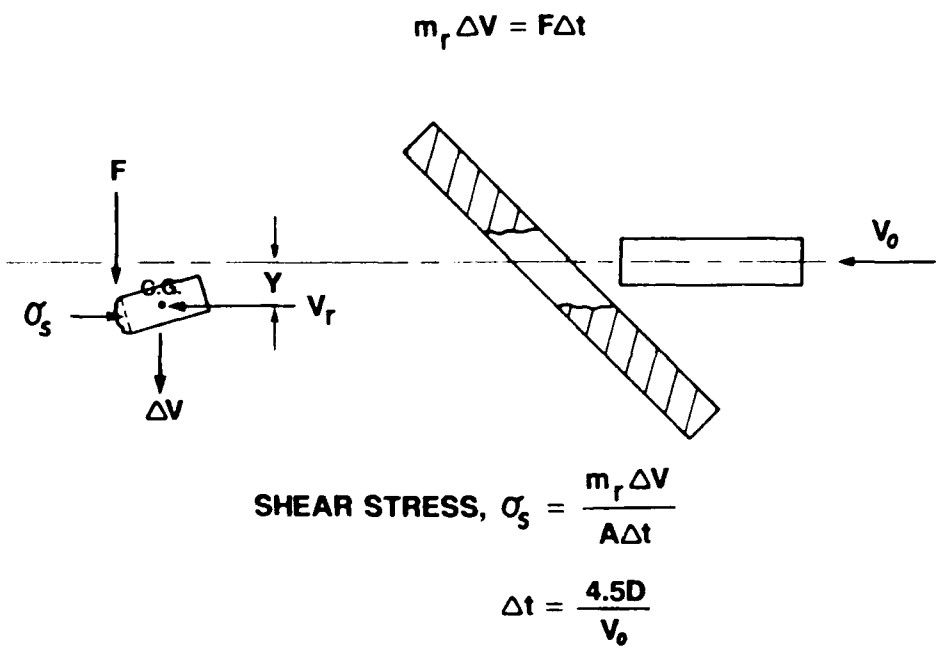


Fig. 2. Schematic diagram illustrating the slight deviation from trajectory caused by the linear impulse.

The results for 11 tests are summarized in Table 3. The average shear stress for the six aluminum tests was 293 MPa; the average for the five steel tests was 1855 MPa. The scatter in the calculated values is quite large which is partially attributable to the accuracy of the radial displacement measurements, approximately ± 1mm.

DISCUSSION

The projectile rotation model does not account for the effects of target orientation or target thickness except as a consequence of change in residual length. The observed effects of orientation and thickness on rotation rate for aluminum rod impacts are shown in Figures 3 and 4. Both decreasing impact angle and increasing target thickness decrease the residual rod length and increase the rotation rate. The effect of target thickness on angular momentum is demonstrated in Figure 5. The results

Table 3: Summary of Data for Determining Shear Stress from the Linear Impulse

Shot Number	y mm	t μs	km/sec ΔV	m_r g	σ_s MPa
1-1-268	+1.7	49.9	+0.03	0.12	141
1-1-269	0	59.7	0	0.36	0
1-1-273	-3.9	59.9	-0.07	0.28	769
1-1-289	-1.7	59.0	-0.03	0.33	369
1-1-293	+0.1	59.2	+0.002	0.50	39
1-1-295	-2.6	57.9	-0.04	0.28	443
1-1-343	-6.0	69.8	-0.09	0.33	1190
1-1-344	-5.9	41.4	-0.14	0.53	3000
1-1-369	-33.0	144.7	-0.23	0.34	3388
1-1-371	-1.6	165.5	-0.01	1.06	450
1-1-372	-6.1	165.5	0.037	0.82	1247

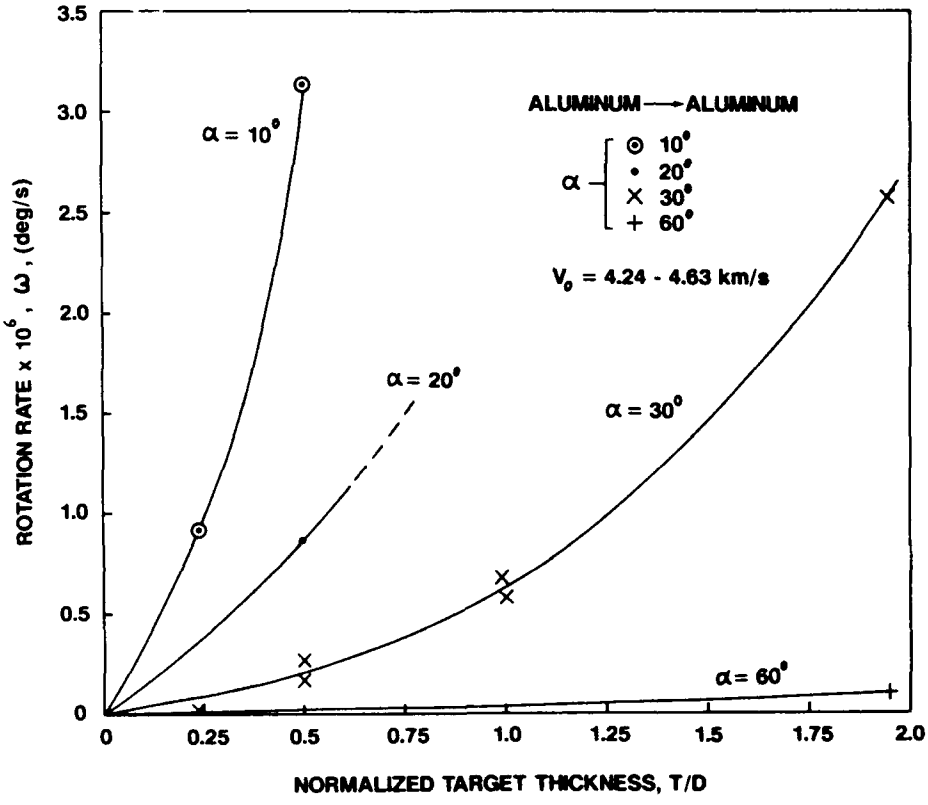


Fig. 3. Effect of target thickness on angular velocity.

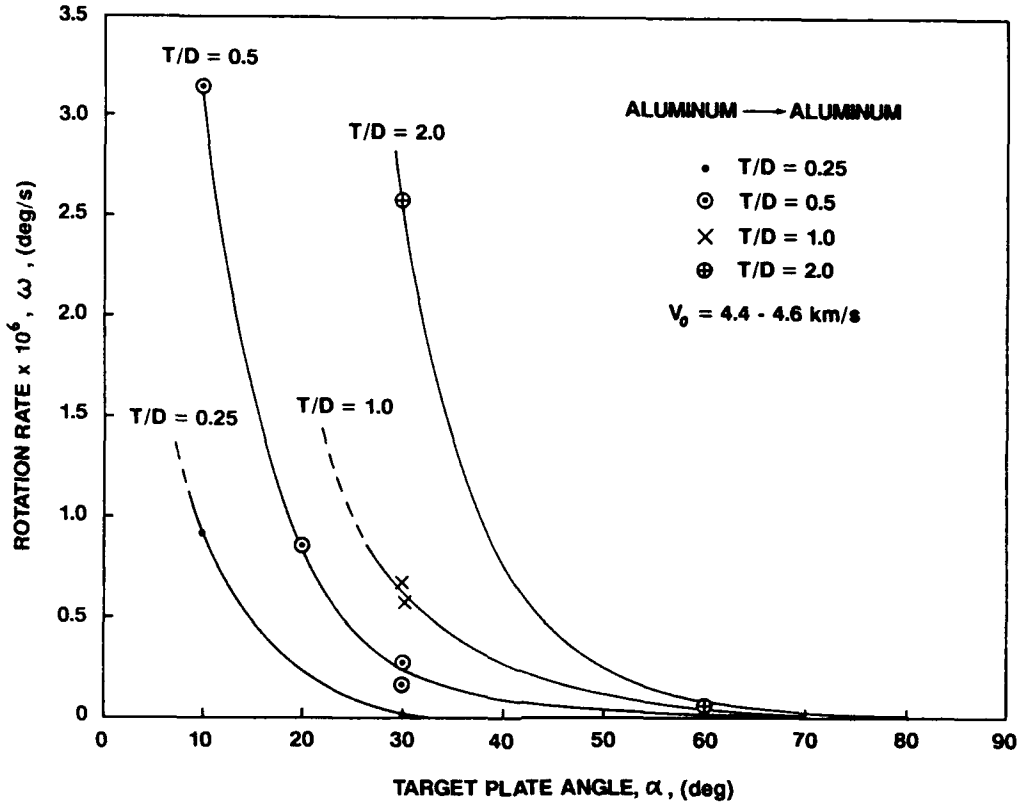


Fig. 4. Effect of target plate obliquity on angular velocity.

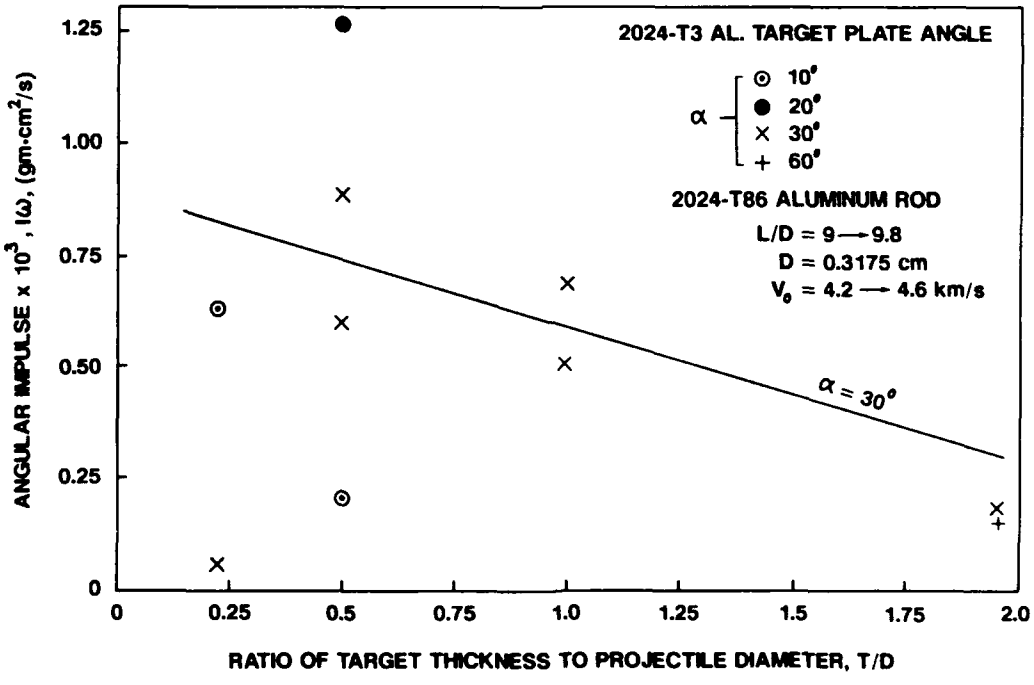


Fig. 5. Angular impulse due to rod impact with oblique plate targets.

for 30° impacts show that angular momentum decreases with increasing target thickness but this result is primarily the consequence of decreasing moment arm length due to greater rod length loss. From Baker we have rod length loss for like-like impact:

$$\frac{\Delta \ell}{D} = \frac{T}{D} + \frac{\Delta T}{D} + \frac{V\tau}{D}\left(1-\exp\left(-\frac{\Delta \ell/D + T/D + \Delta T/D}{fV\tau/D}\right)\right) \tag{6}$$

where ΔT, τ and F are empirical constants and V is the impact velocity. $\Delta T/D$ is a small number, approximately equal to 0.15. For oblique impact the target thickness, T, is replaced by an effective thickness:

$$T_e = T/\sin\alpha + D/2\tan\alpha \tag{7}$$

The $T/\sin\alpha$ term represents the path length through the target; the $D/2\tan\alpha$ term represents a length of continued contact between the target and the rod due to the projectile diameter.

The residual rod length is therefore:

$$\ell_r = \ell_o - \Delta\ell = \ell_o - \left(T_e + \Delta T + V\tau\left(1-\exp\left(-\frac{\Delta \ell/D + T_e/D + \Delta T/D}{fV\tau/D}\right)\right)\right) \tag{8}$$

The rod length loss during target penetration is simply $\Delta\ell = T_e$; the length loss after target perforation is given by:

$$\Delta\ell' = \Delta T + V\tau\left(1-\exp\left(-\frac{\Delta \ell/D + Te/D + \Delta T/D}{fV\tau/D}\right)\right) \tag{9}$$

The time duration of continued plastic deformation is therefore dependent upon both impact velocity and target thickness rather than a constant as defined previously. The duration of the shear flow should also be dependent upon the impact angle. Impacts near 90° incidence should not produce significant rod tumbling, independent of the duration of plastic flow after target perforation. The duration of shear flow would therefore be expressible as:

$$\Delta t = f(\Delta\ell')\ X\ g(\alpha) \tag{10}$$

Consider

$$f(\Delta\ell') = k\,\Delta\ell'/V = 1.46\,\Delta\ell'/V \tag{11}$$

$$g(\alpha) = (\tan\alpha)^{-1} \tag{12}$$

$$\Delta t = 1.46\,\Delta\ell'/(V\tan\alpha) \tag{13}$$

The value k = 1.46 Eqn (11) is arbitrary, allowing the same mean value for σ_s as obtained for the aluminum rod tests, Δt = 3.2 μsec. The values of Δt from Eqn (13) were used to calculate new values of σ_s in Eqn (2). The results are summarized in Table 4.

Table 4: Summary of Calculated Stress Values

Test #	Initial Conditions				Results			Eqn (2)			Eqns (2, 13)		Eqns (2, 14)	
	T/D	α (deg)	V (km/s)	ω (Rad/s)	ℓ_r (cm)	Iω (g•cm²/s)	Δt (μsec)	σ_x (MPa)	Δℓ (cm)	Δℓ' (cm)	Δt (μsec)	σ_x (MPa)	Δt (μsec)	σ_x (MPa)
Al → Al														
1-2-159	0.50	30	4.24	4489	2.21	880	3.2	314	0.90	0.31	1.85	544	2.05	516
1-2-160	0.50	30	4.44	3203	2.18	602		214	0.90	0.31	1.77	396	1.96	353
1-1-233	1.95	60	4.50	2011	1.58	143		72	1.29	0.48	0.90	253	1.73	133
1-1-234	1.95	30	4.63	45221	0.59	181		253	2.29	0.77	4.21	185	4.66	167
1-1-268	0.50	10	4.47	54960	0.56	220		313	2.44	0.62	11.5	86	7.04	142
1-1-269	0.50	20	4.59	14753	1.67	1267		616	1.39	0.49	4.28	447	3.77	511
1-1-273	1.00	30	4.44	11168	1.31	509		305	1.68	0.77	4.39	224	4.87	202
1-1-289	1.00	30	4.20	10060	1.55	684		329	1.39	0.48	2.89	386	3.21	350
1-1-293	0.25	30	4.36	295	2.35	69		23	0.62	0.18	1.04	70	1.16	64
1-1-295	0.25	10	4.40	15978	1.29	639		387	1.63	0.28	5.28	238	3.23	389
MEAN								283				283		283
σ_x								156				148		154
σ_x/MEAN								0.55				0.52		0.54
St → St														
1-1-343	1.00	30	4.58	25010	0.53	250	3.2	384	1.31	0.99	5.47	219	6.06	197
1-1-344	0.22	10	4.65	60249	0.90	2410		2172	1.42	1.01	18.0	371	11.0	605
1-1-369	0.22	10	4.42	65432	0.61	916		1169	1.68	1.27	23.8	160	14.5	360
1-1-371	0.22	20	4.79	3054	1.72	819		404	0.70	0.49	4.11	292	3.61	334
1-1-372	0.22	15	4.64	9512	1.33	1188		737	1.10	0.83	9.78	233	7.36	308
MEAN								973				255		361
σ_x								664				72		134
σ_x/MEAN								0.68				0.28		0.37

A different form for Eqn (12) was considered:

$$g(\alpha) = (\tan\alpha)^{-0.5}$$

$$\Delta t = 2.13\,\Delta \ell'/(V(\tan\alpha)^{0.5}) \tag{14}$$

The value 2.13 in Eqn (14) again forces the mean result for σ_s, aluminum rod impact, to be 283 MPa. Values of Δt and σ_s calculated from Eqns (14) and (2) are also presented in Table 2.

CONCLUSIONS

The quality of the model for representing the data is demonstrated by the ratio of the standard deviation of the data set (n data points) to the average value for the data set. On this basis, none of the three models obtained from rod rotation data, Eqns. 2, 13, and 14, provide a good fit to the aluminum rod data set. The second model, based on Eqns (2) and (13) provides a substantial improvement over the constant Δt model for the steel rod data set.

Another indication of the variation in results is a comparison of tests for which the initial conditions are nearly identical and the values of Δt are therefore the same.

Test Condition	Test #	σ_s (Constant Δt)	$\frac{\text{DIFFERENCE}}{\text{AVERAGE}} \times 100\%$
Al→Al	1-2-159	314	19%
	1-2-160	214	
Al→Al	1-1-273	305	4%
	1-1-289	329	
St→St	1-1-344	2172	30%
	1-1-369	1169	

Even for matched sets of tests the variation in results can be grossly different. The overall results suggest that other factors contributed to angular rotation. For example, recent NRL studies of impact by "chunky" projectiles into oblique plate targets have shown that hole growth is minimal in the direction corresoponding to the "uprange" end of the plate (the down direction in Figs. 1 and 2). Even small values of initial upward pitch (Figs. 1 and 2) could result in contact between the back of the rod and the plate, thereby inducing a CCW rotation.

REFERENCES

Baker, J. and Williams, A., "Hypervelocity Penetration of Plate Targets by Rod and Rod-like Projectiles", Int. J. Impact Eng., Vol. 5, pp. 101-110, 1987.

Int. J. Impact Engng Vol. 14, pp. 573 - 586, 1993
Printed in Great Britain

0734-743X/93 $6.00+0.00
1993 Pergamon Press Ltd

CHARACTERISTICS OF DEBRIS CLOUDS PRODUCED BY HYPERVELOCITY IMPACT OF ALUMINUM SPHERES WITH THIN ALUMINUM PLATES

ANDREW J. PIEKUTOWSKI

University of Dayton Research Institute
Dayton, Ohio 45469

ABSTRACT

Debris clouds produced by the normal impact of aluminum spheres with aluminum bumper plates are shown to consist of an ejecta veil, an external bubble of debris, and a significant internal structure composed of three distinct elements. Effects of variations in bumper-plate thickness, sphere diameter, and impact velocity on the shape and velocity of the elements of the internal structure are described and compared. Three alloys of bumper material and several diameters of 2017-T4 aluminum spheres, ranging from 6.35 mm to 12.70 mm, were used in the tests described in this paper. Test results were sorted into two sets. In the first set, impact velocity was held constant at 6.7 km/s and the bumper-thickness-to-projectile-diameter ratio, t/D, varied from 0.026 to 0.424. In the second set, t/D ratio was held constant at 0.049 and the impact velocity varied from 3.77 km/s to 7.23 km/s. In both sets of test results, debris-cloud properties are shown to scale with projectile diameter. Characteristics of the front element of the debris-cloud internal structure are shown to be sensitive to changes in t/D ratio and impact velocity. A model for the formation of this front element is presented and used to develop a description of a debris cloud consisting of material in the solid-liquid and/or liquid-vapor phases.

INTRODUCTION

From earliest interest in the development of spacecraft shield systems, investigators have used a variety of materials to simulate micrometeoroids. A significant fraction of the work has employed aluminum spheres impacting aluminum sheets or plates (Maiden, 1963; Maiden et al., 1965; Backman and Stronge, 1967; Swift and Hopkins, 1968; and Nysmith and Denardo, 1969; and others). Aluminum spheres continue to be used in shield studies as simulants of orbital-debris fragments. Determination of the ballistic limit of a shield, optimization of a shield against a specific threat, and/or development of design criteria are the usual purposes for most test programs. Occasionally, radiographs or high-speed photographs of "typical" debris clouds are presented with test results. However, quantitative descriptions of the debris clouds are rarely given and when descriptions are provided, they are not systematic (i.e., do not describe changes in the debris-cloud morphology as a result of changes in impact velocity, bumper thickness, etc.)

This paper examines the formation of debris clouds produced by the impact of aluminum spheres with thin aluminum plates and presents results of tests used to quantitatively evaluate debris-cloud

morphology as a function of bumper-thickness-to-projectile-diameter ratio, t/D, and impact velocity. The evaluation was limited to: (1) t/D ratios from 0.026 to 0.424 for an impact velocity of 6.7 km/s and (2) impact velocities from 3.77 km/s to 7.23 km/s for a t/D ratio of 0.049. All impacts were normal to the bumper or front sheet. A model for the interaction and effect of shock-wave processes initiated by the impact event is presented. Finally, a description of debris clouds containing liquid and vapor is presented for the case in which the t/D ratio is near optimum.

EXPERIMENTAL DESIGN

Data presented in this paper were obtained from tests performed for Martin Marietta Manned Space Systems, McDonnell Douglas Space Systems Company, and from equipment and/or range performance tests conducted by the University of Dayton Research Institute (UDRI). All tests were performed in the UDRI Impact Physics Laboratory using a 50/20 mm, two-stage, light-gas gun.

The tests were performed with the bumper plate normal to the range center line. Various thicknesses of 1100-O, 2024-T3, and 6061-T6 aluminum plates, ranging from 0.25 mm to 4 mm, were used as bumpers. Most tests used 9.53-mm-diameter 2017-T4 aluminum spheres as their projectiles. Several tests used 6.35-mm or 12.70-mm-diameter 2017-T4 aluminum spheres. The specific plate alloy, thickness, and sphere diameter used for each test are included in figures presented later in this paper. Impact velocity for the tests ranged from 3.77 km/s to 7.23 km/s and was determined using time-of-flight measurements between four laser-photodetector stations located along the range center line. Accuracy of the impact velocity determination was better than $\pm$ 0.5 percent. Finally, an aluminum witness plate was placed 38 cm downrange of the bumper, for each test, to record the damage pattern produced by the debris cloud.

Three or four pairs of fine-source, soft, flash x-rays were used to observe the projectile and debris clouds. The x-ray heads were accurately positioned on the target chamber to provide simultaneous orthogonal views of the debris clouds. Although individual test setups varied slightly, a typical test setup for one view is shown in Fig. 1. The first pair of x-rays was used to view and record the position of the projectile a few microseconds before impact. This view served to verify projectile integrity and to permit accurate determination of the time after impact for the two or three views taken of the debris cloud after its formation. Normally, views were taken when the cloud was about 4 cm and 12 cm downrange (approximately 6 μs and 19 μs, respectively, after impact). The fourth pair of x-rays, if used, were usually not fired until the debris cloud was about 30 cm downrange of the bumper. The delay in firing the x-rays allowed the cloud to expand and permitted a more detailed

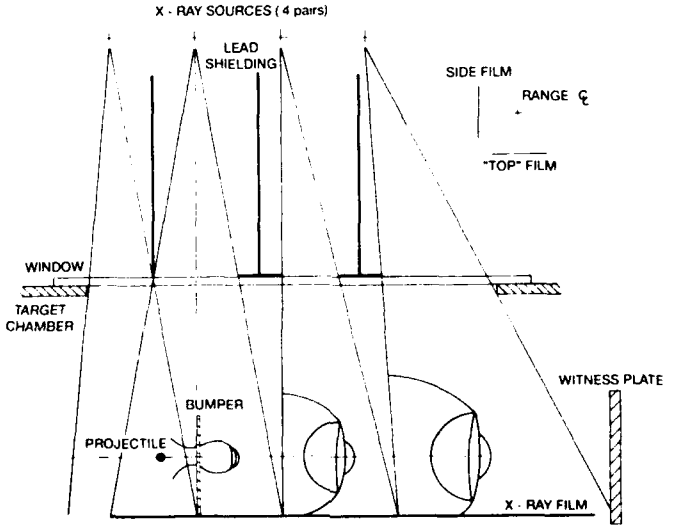


Fig. 1. Setup used to obtain multiple-exposure, orthogonal-pair, flash radiographs of debris clouds.

examination of the cloud structure. The fourth pair of heads was usually positioned as shown in Fig. 1 to obtain an oblique (~ 13 degrees from normal) view of the cloud; in some tests these heads were positioned 31.5 cm downrange of the bumper to provide a normal view of the cloud.

Post test documentation consisted of measurement of bumper-hole diameters and witness-plate damage patterns. Debris-cloud measurements taken from the radiographs and the late-time views were analyzed, when possible, to determine the largest fragment dimensions and the size and number of fragments forming the debris cloud. Results of these additional measurements may be found in Piekutowski (1992a and 1992b).

DESCRIPTION OF DEBRIS CLOUDS

Two views of a debris cloud are presented in Fig. 2 to illustrate three major features of the cloud. First, an ejecta veil, consisting almost entirely of bumper fragments, is ejected from the impact or front side of the bumper. Second, an expanding bubble of bumper debris forms on the rear side of the bumper. Finally, there is a significant structure composed of projectile debris located inside and at the front of the external bubble of bumper debris. This internal structure is composed of a front, center, and rear element. For a 6.70 km/s impact, the front element consists of finely divided,

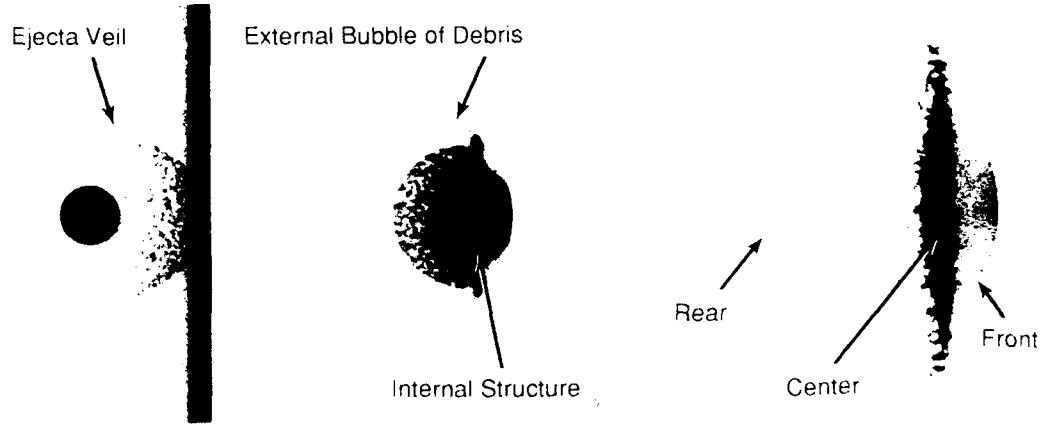


Fig. 2. Morphological features and elements of a debris cloud. Note that the ejecta veil and projectile are a double exposure in this figure and in all radiographs presented in this paper.

molten droplets of bumper and projectile. The disc-like center element is composed of numerous splintery projectile fragments. This element also contains a single large chunky projectile fragment that is located at the center of the disc and on the debris-cloud center line. A central fragment was observed in all debris clouds where the t/D ratio was less than 0.2, and was most clearly observed in the late-time view of the debris cloud. This central fragment represented the most severe threat to rear wall integrity (Piekutowski, 1992a). The rear element of the structure is a hemispherical shell of fragments spalled from the rear surface of the sphere. The internal structure of the debris cloud, shown in Fig. 2 and subsequent figures, is the most significant feature of the debris cloud in terms of potential for rear wall damage. In the remainder of this paper, the term "debris cloud" will be considered synonymous with "internal structure."

The effect of a change in the t/D ratio on the debris-cloud morphology is shown in Fig. 3 for eight t/D ratios. All debris clouds shown in this figure were produced by the impact of a 9.53-mm-diameter 2017-T4 aluminum sphere with a 6061-T6 aluminum bumper at an impact velocity of 6.70 km/s $\pm$ 0.08 km/s. Use of other bumper materials, 1100-O and 2024-T3 aluminum, did not measurably affect debris-cloud shape or characteristics. As shown in Fig. 3, t/D ratios for the tests ranged from 0.026 to 0.424. As the t/D ratio increased from the minimum value, significant expansion of the internal structure of the debris cloud was observed. The following changes in internal-structure morphology occurred as t/D ratio increased: (1) the diameter of the disc-like

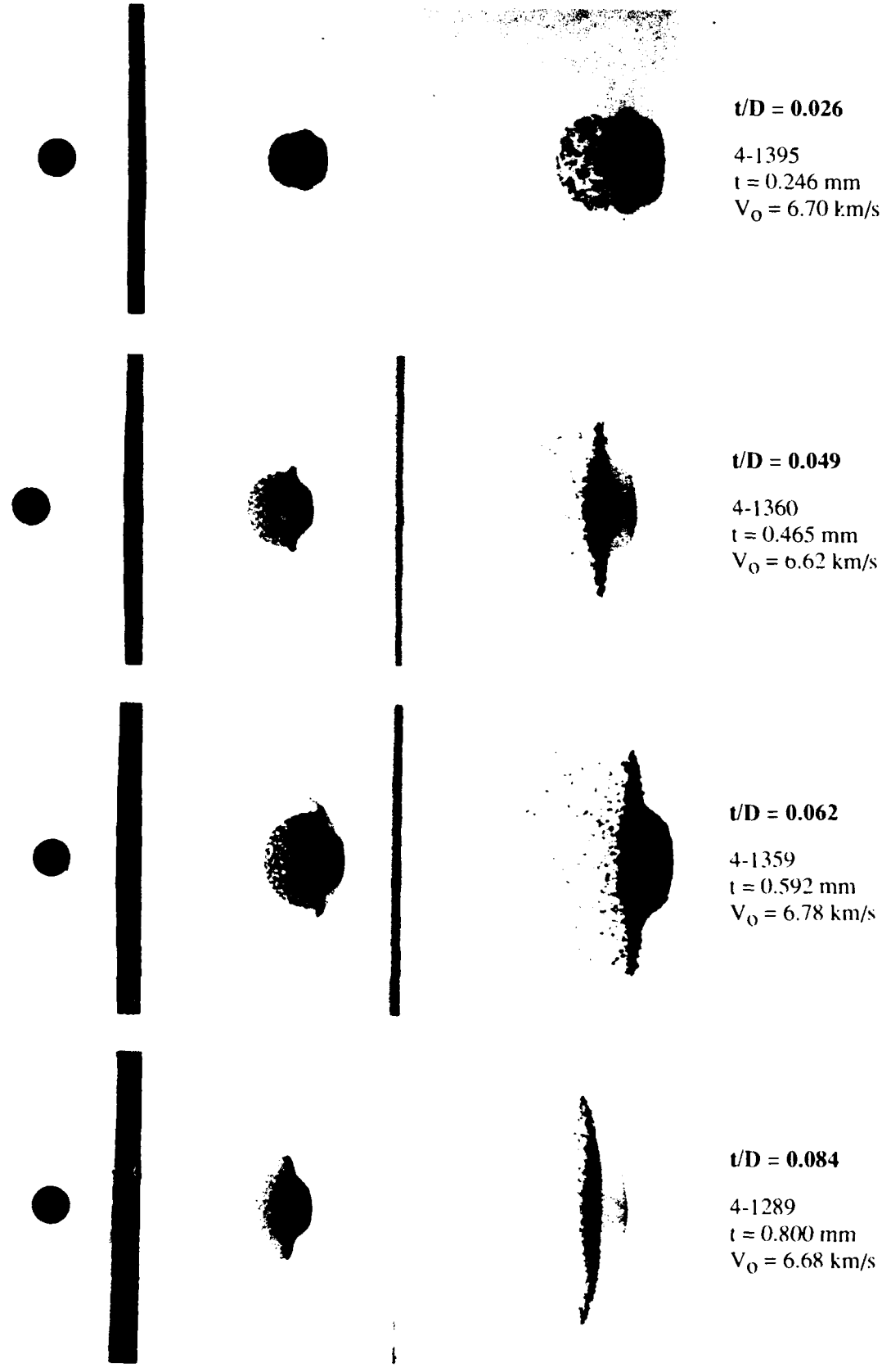


Fig. 3. Views of debris clouds produced by impact of 9.53-mm-diameter, 1.275-g, 2017-T4 aluminum spheres with various thicknesses of 6061-T6 aluminum plates. Impact velocity constant.

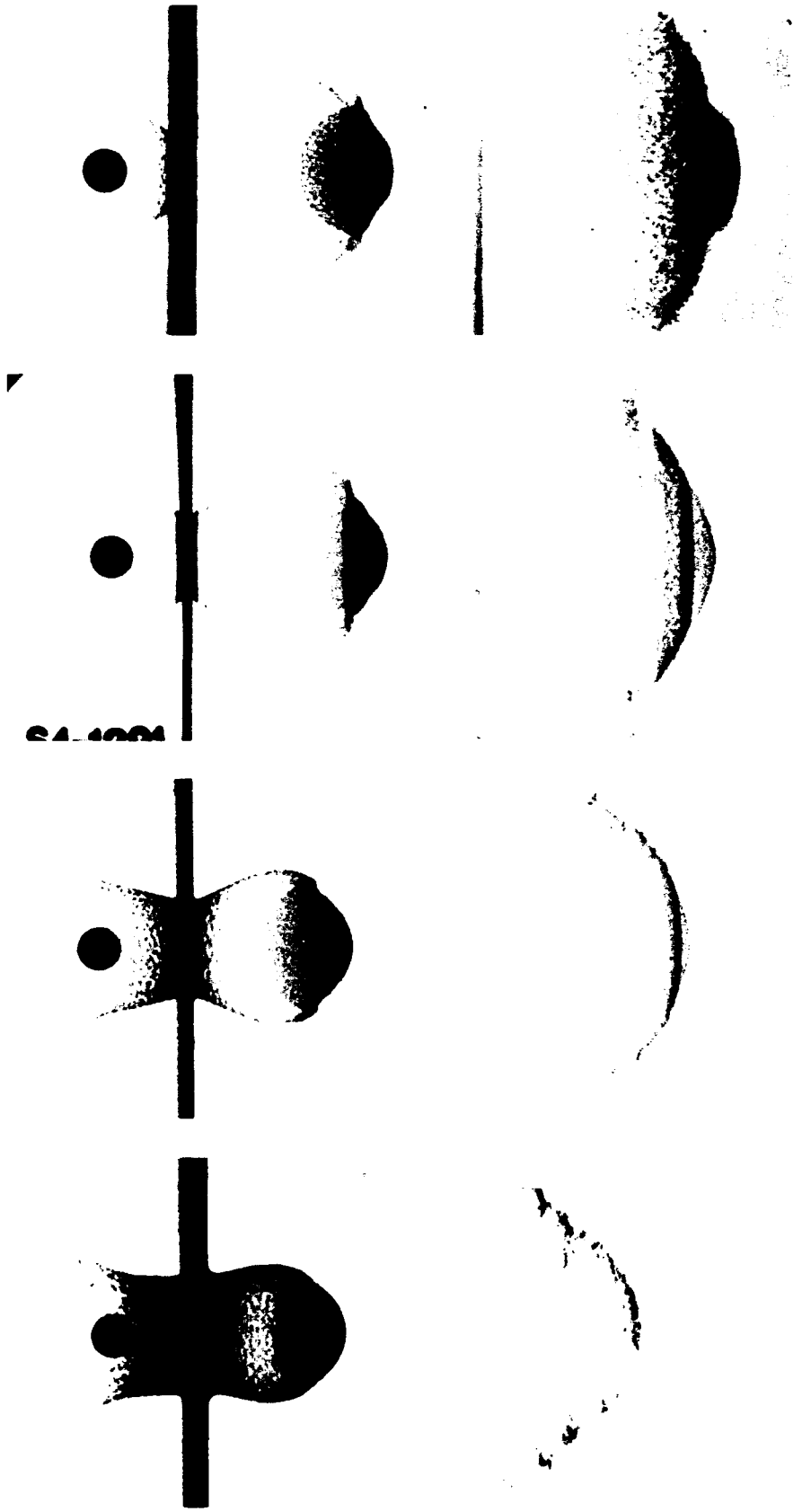


Fig. 3. (Concluded). Views of debris clouds produced by impact of 9.53-mm-diameter, 1.275-g, 2017-T4 aluminum spheres with various thicknesses of 6061-T6 aluminum plate. Impact velocity constant.

center element increased, began to "bend over" at a t/D of 0.084, and formed a flat-bottomed bowl at t/D = 0.163; (2) radial expansion of the hemispherical shell of spall fragments at the rear of the internal structure increased; and (3) the size of fragments in the center and rear element decreased. In contrast to the growth of the center and rear element, the front element of the cloud did not vary significantly in size, shape (a truncated cone), or radiographic density until the t/D ratio was greater than 0.102. At t/D ratios of 0.163 and 0.234 this element was a spherical sector and did not exist when the t/D ratio was 0.424. The relatively constant radiographic density of the front element for the lower t/D ratios was noteworthy when compared to the varying density of the external bubble of debris and the ejecta veil for these same tests.

The effects of a change in impact velocity on debris-cloud morphology are shown in Fig. 4 for tests with a constant t/D ratio. For the four lower velocity tests, 9.53-mm-diameter 2017-T4 aluminum spheres and 0.465-mm-thick (t/D = 0.049) 6061-T6 aluminum bumpers were used. A 6.35-mm-diameter 2017-T4 aluminum sphere and a 0.318-mm-thick (t/D = 0.050) 6061-T6 aluminum bumper were used for the 7.23 km/s test. Although not visible in the photographic reproduction of the radiograph for the test at 3.77 km/s, the post impact views for this test show a narrow region of reduced density just inside the rear surface of the sphere. Apparently, a spalled region developed inside the projectile, forming a shell that was loosely attached to the rear of the sphere. A slight flattening of the front of the sphere and a small piece of bumper that moved downrange of the front of the flattened sphere was also observed for this test. As impact velocity increased, fragmentation of the projectile and an increase in the axial and diametral expansion of the internal structure was observed. A small front element was clearly evident when the impact velocity reached 5.45 km/s. Further development of the front element occurred as impact velocity was increased to 6.62 km/s and 7.23 km/s.

Growth of the internal structure of a debris cloud was sensitive to both t/D ratio and impact velocity, and increased as both parameters increased--at least to the optimum t/D ratio (estimated to be between 0.18 and 0.20). Development and growth of the front element was most sensitive to impact velocity. Further quantitative comparisons of these debris-clouds follow.

RESULTS AND DISCUSSION

Readily identifiable points or locations in the debris clouds were assigned positions as shown by the circled numbers in Fig. 5. Axial and radial positions and velocities of each of these points, with respect to the cloud center line, and the radial expansion velocity of the hemispherical shell of projectile spall fragments was determined. Use of the fine-source, soft x-rays and a direct-exposure film produced radiographs in which fragments as small as 0.25 mm could be seen and measured. Accurate positioning of the heads and use of a common reference point, for all measurements taken from the radiographs, permitted specific debris-cloud positions to be determined to within $\pm$0.25 mm or better. Rotation of individual fragments at critical measurement points produced most of the error encountered when determining the location of these points. The time between firing of the pairs of flash x-rays was determined within $\pm$0.1 μs. Accordingly, velocities of material at measurement points could be determined to within $\pm$0.1 km/s or better. For those cases in which test results for two nearly identical test conditions were available, agreement between measured values was excellent.

Before examination of test results begins, several comments regarding notation in the following figures are in order. Six points in Fig. 5, ⑤ through ⑩ inclusive, are points for which two sets of measurements were taken: (1) axial distance from the bumper and (2) distance between points, measured normal to the debris-cloud center line. These measurements were used, with appropriate timing information, to determine axial and diametral velocities of these points or pairs of points, respectively. Axial velocities are denoted when the points are separated by a comma. Diametral velocities are denoted when the points are separated by a dash. All velocity data have been normalized by dividing specific measured velocities by the impact velocity used for the test.

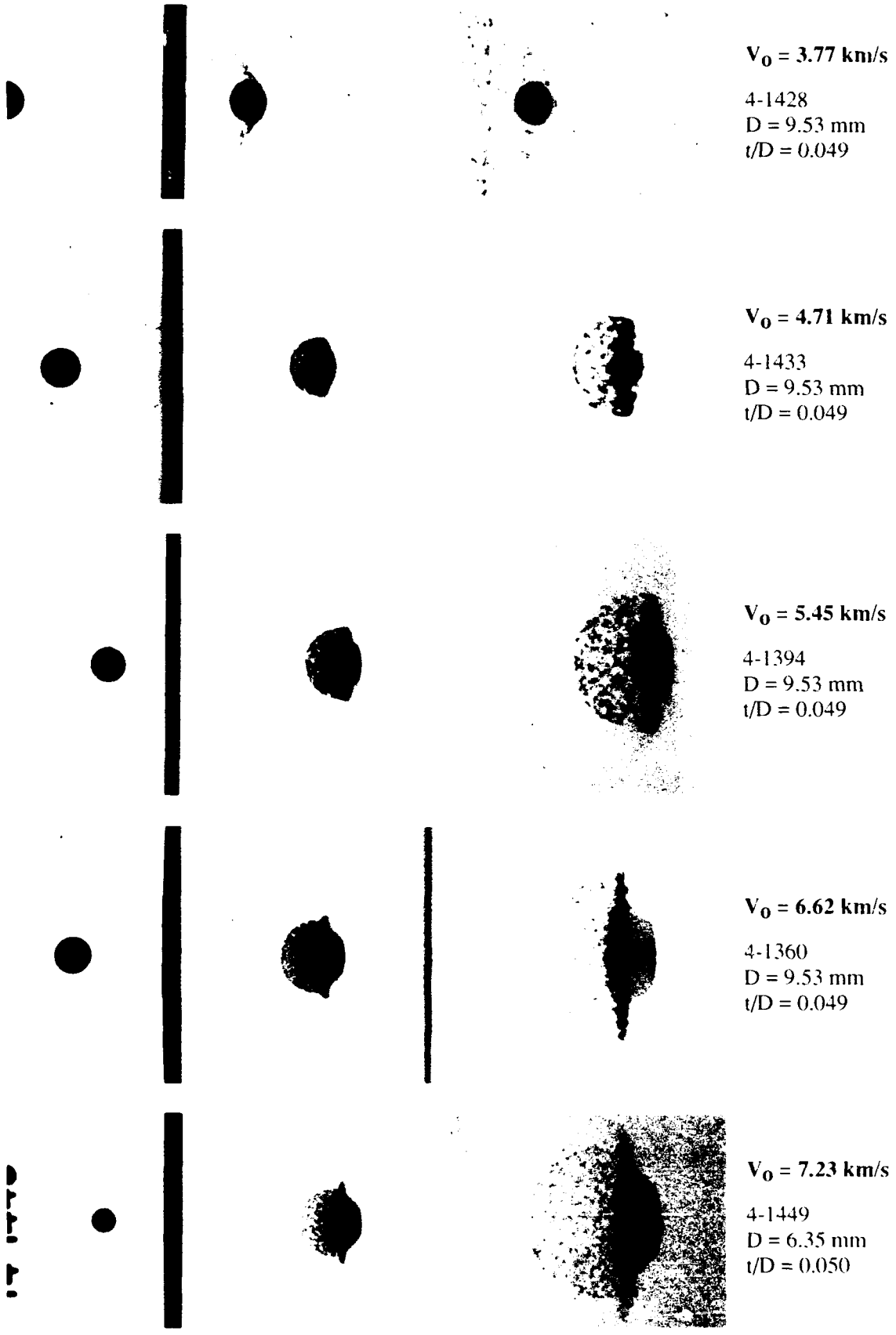


Fig. 4. Views of debris clouds produced by impact of 9.53-mm and 6.35-mm-diameter 2017-T4 aluminum spheres with 6061-T6 aluminum plates. Impact velocity varied and t/D ratio held constant.

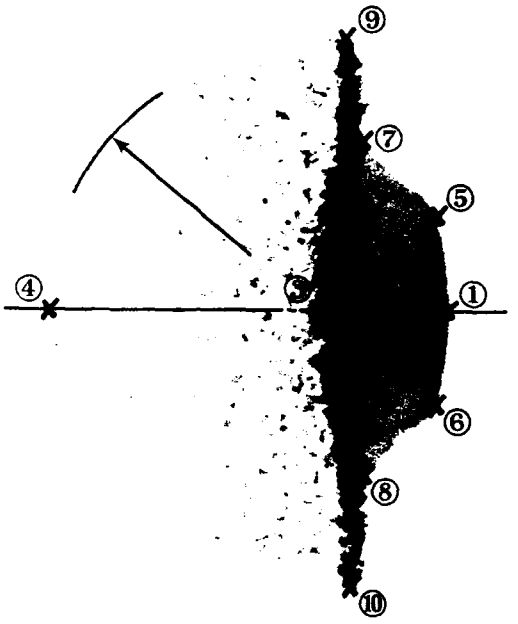


Fig 5. Points used when making measurements of debris-cloud features.

Effect of t/D Ratio and Impact Velocity on Debris-Cloud Velocities

In this section, the effects of a change in t/D ratio and/or impact velocity on the velocity of the axial measurement points of the debris cloud, the axial and diametral velocity of the disc-like center element, and the axial and diametral velocity of the front element are presented, in that order.

In Fig. 6a, normalized axial debris-cloud velocities decrease as t/D ratio increases. Overall, an increase in the axial dispersion of the cloud is observed. The velocity of point ② is probably very close to or may be the velocity of the center of mass of the debris cloud. The observed decrease in velocity of this point is not surprising since conservation of momentum would predict this behavior as the t/D ratio increases and the mass of bumper involved in the collision increases. The velocity

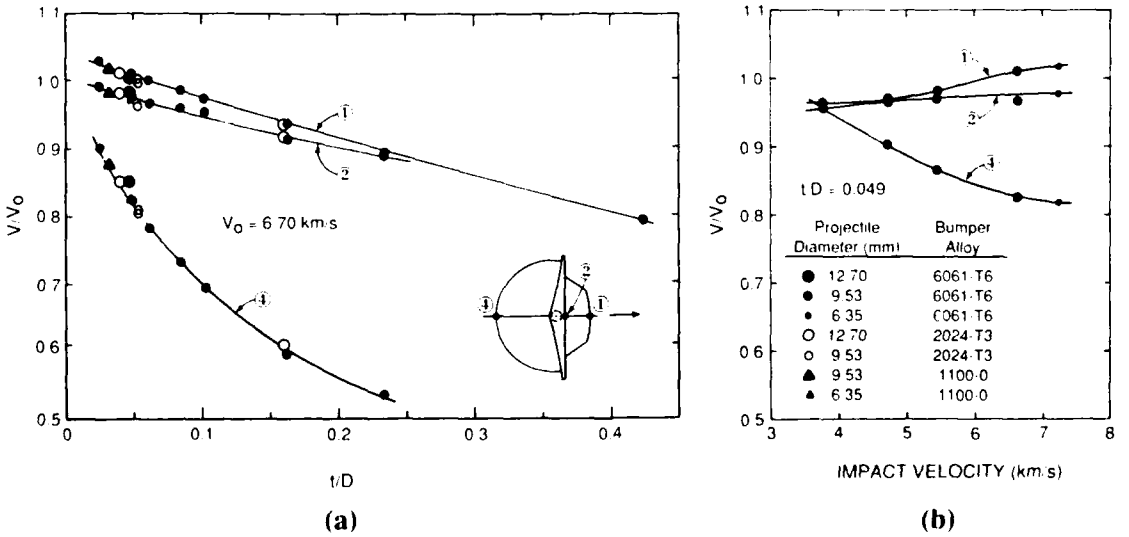


Fig. 6. Normalized velocity of selected on-axis measurement points in debris cloud versus t/D ratio and impact velocity.

of point ② in Fig. 6b is nearly constant, as would be expected since the t/D ratio is constant. However, the sudden increase in velocity of point ① in Fig. 6b is noteworthy and will be discussed in more detail later in this section. The velocity of point ④, in Fig. 6b, appears to be approaching the value shown for a t/D of 0.049 in Fig. 6a.

Normalized axial and diametral velocities of points ⑨ and ⑩ are shown in Fig. 7. A decrease in axial velocity and an increase in the diametral velocity of these points occurs as the t/D ratio increases. These points cease to be distinct in the cloud when the t/D ratio is between 0.10 and 0.16 because of rearward flow at the periphery of the center element. As impact velocity increases, little change in the axial velocity of this region is observed; however, a moderate increase of the diametral velocity of these points occurs.

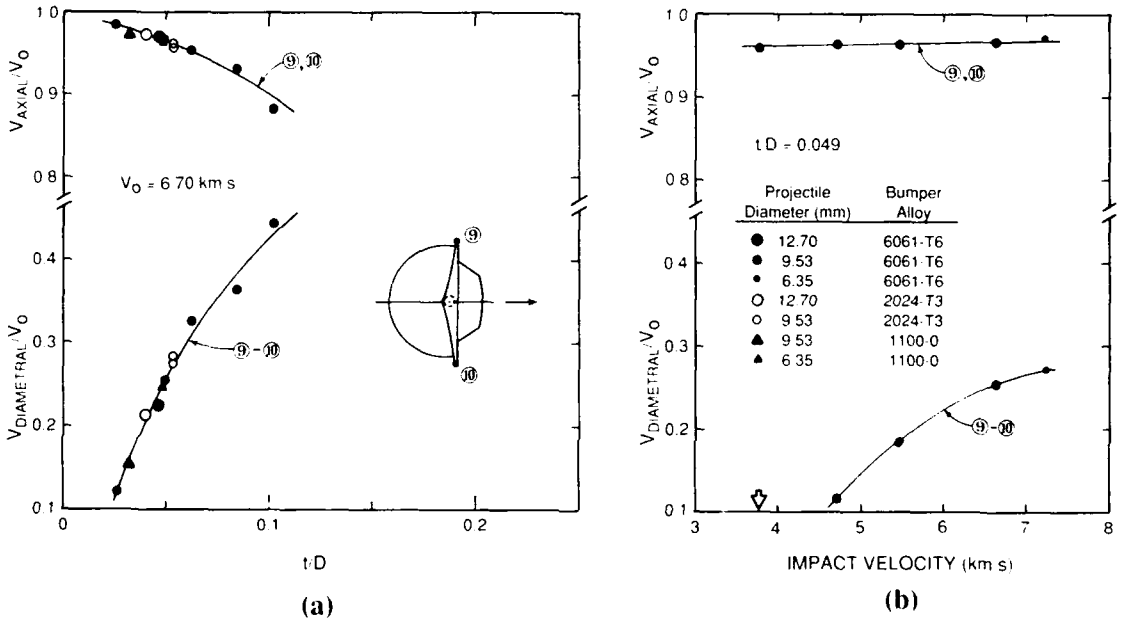


Fig. 7. Normalized axial and diametral velocities of center element of debris cloud versus t/D ratio and impact velocity.

Normalized axial and diametral velocities of points ⑤, ⑥, ⑦, and ⑧ are presented in Fig. 8. As t/D ratio increases, in Fig. 8a, the axial velocity of all four points decreases. Points ⑤ and ⑥ cease to be distinct when this element changes from a truncated-cone shape to a spherical sector at a t/D ratio between 0.10 and 0.16. The diametral velocity of these pairs of points increases slightly to a maximum at t/D = 0.16, then decreases rapidly until this feature disappears (t/D > 0.23). The opposite behavior of these points is observed when impact velocity increases. The axial velocity of points ⑤ and ⑥ increases considerably; however, little or no change in the axial velocity of points ⑦ and ⑧ is observed. Significant increases in the diametral velocity of both pairs of points, particularly ⑦ and ⑧, are the most noteable feature of Fig. 8b.

Growth of the debris-cloud internal structure occurs as t/D ratio and impact velocity increase. Comparison of normalized debris-cloud velocities, as a function of t/D ratio, indicates that the velocities of points used to evaluate this growth agree (within measurement limits) despite a factor of two variation in projectile diameter and a factor of eight in projectile mass. The limited data (one point) would indicate that similar agreement of normalized velocities occurs as impact velocity is varied. Caution is urged in extending these observations to all combinations of t/D ratio and impact velocity, however. The development and growth (or minimal growth) of the front element was the most interesting and significant aspect of comparison of debris-cloud features.

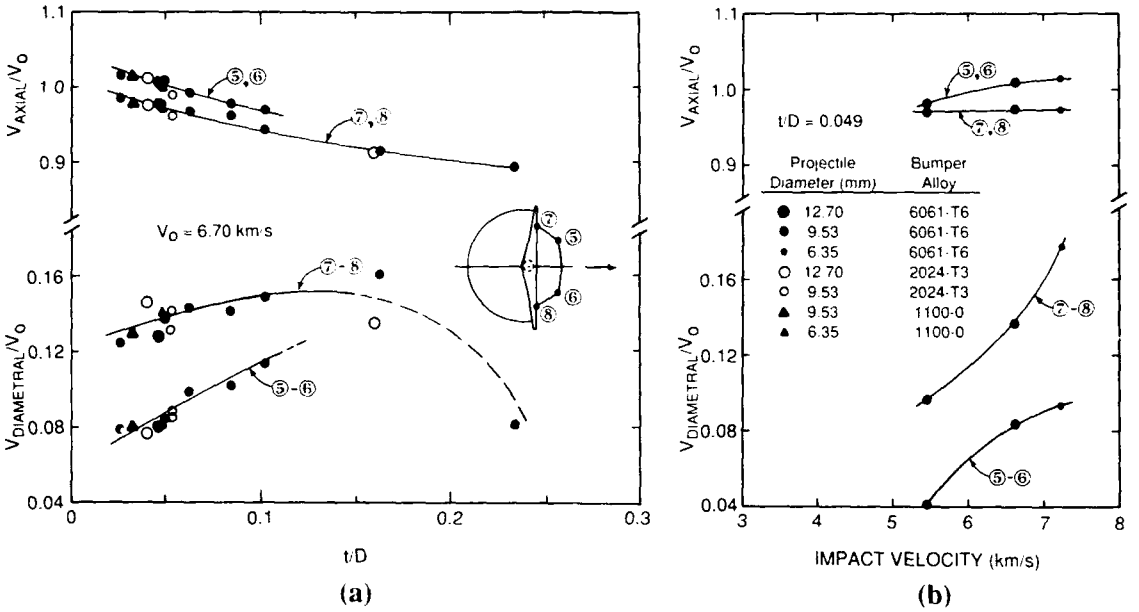


Fig. 8. Normalized axial and diametral velocities of front element of debris cloud versus t/D ratio and impact velocity.

Model for Early-Time Interactions at Impact Site

Late-time views of the debris clouds presented in Fig. 4 are shown in Fig. 9. These late-time views clearly show the development and growth of the front element of the debris-cloud internal structure as impact velocity increases. The front element of each view in Fig. 9 consists of the following: (9a) and (9b) a single fragment and several solid fragments, respectively; (9c) a small cloud of solid fragments; (9d) and (9e) a large cloud of finely divided droplets of molten aluminum.

A model for the formation of the front element is presented in this subsection. The essential features of the model are shown in Fig. 10. The model draws heavily on a description of the kinematics of the impact process given by Ang (1990) and used to determine the source of material



Fig. 9. Late-time views of debris clouds showing development of front element of internal structure as a function of increase in impact velocity. Views (a) through (d) used 9.53-mm-diameter, 2017-T4 aluminum spheres. View (e) used a 6.35 mm-diameter, 2017-T4 aluminum sphere. All tests used 6061-T6 aluminum bumpers (t/D = 0.049). See Fig. 4 for earlier views of these clouds.

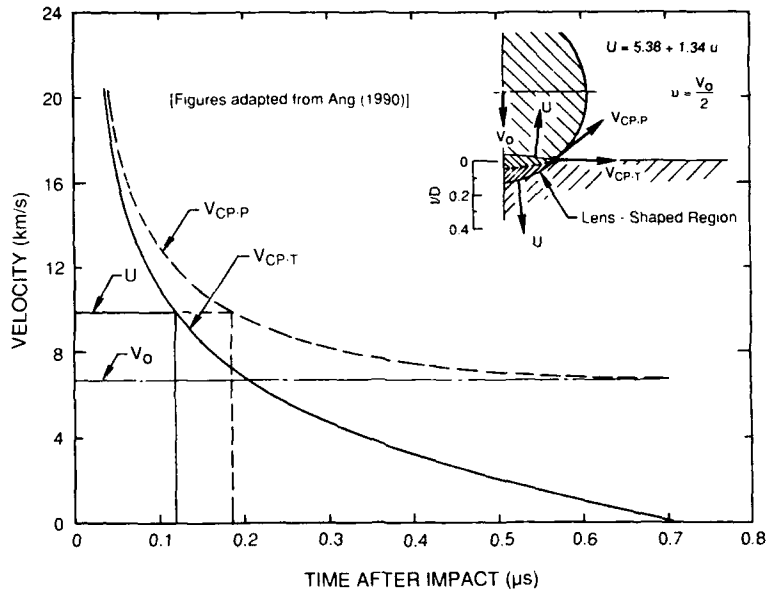


Fig. 10. Illustration of interactions at impact site. Collision-point velocities versus time after impact, for a 9.53-mm-diameter sphere traveling at 6.70 km/s, are shown in this figure. In the inset, the impacting sphere and impacted plate are shown with appropriate notation for the velocities referenced in the paper.

dominating an impact flash signature. In Fig. 10, U is the shock-wave front velocity, u is the particle velocity behind the shock-wave front, V_0 is the sphere impact velocity, $V_{CP,P}$ is the velocity of the collision point between the surfaces of the sphere and target in the reference frame of the projectile, and $V_{CP,T}$ is the velocity of the collision point in the reference frame of the target. *Half of a sphere impacting half a semi-infinite plate is shown in the inset in this figure.*

As shown in Fig. 10, $V_{CP,\,T}$ is greater than U for the first 0.12 μs after impact. Consequently, loading of the lens-shaped region shown in the inset is quasi one-dimensional during this time interval. Formation of release waves at the boundaries of the lens-shaped region is not possible as long as $V_{CP,\,T}$ is greater than U. When $V_{CP,\,T}$ is less than U, release waves are generated in the target prior to contact by the oncoming sphere. As the impact process continues, formation of release waves in the sphere begins and a decrease in U occurs, due to spherical divergence of the wave front. These later-time events quickly complicate description of the shock-wave interactions taking place during the remainder of the impact event. In the inset in Fig. 10, the lens-shaped region of compressed material is shown to scale at the time $V_{CP,\,T}$ equals U (0.12 μs after impact). The diameter of the compressed region is approximately 56 percent of the diameter of the sphere. Also shown is a t/D scale that allows the reader to determine the fraction of bumper-plate thickness that experiences quasi one-dimensional loading during impact.

The nearly constant radiographic density and shape of the front element, for the low t/D ratio tests, would indicate that the materials involved in the formation of the front elements experienced similar shock loadings. At greater t/D ratios, increasingly larger volumes of material are involved in formation of the front elements. However, this material is derived from regions where the shock wave interactions are complicated and where shock-wave velocities and pressures are lower. These factors contribute to processes that alter the prominence and shape of the front element.

Growth of the lens-shaped region, shown in Fig. 10, into the darker portion of the front element is illustrated in Fig. 11a. The diameter of the heavily shaded region in this figure was determined from the radiograph of the debris cloud shown in Fig. 11b. This diameter and the measured diametral velocity of this portion of the debris cloud were used to compute the diameter of the lens-shaped region at 0.12 μs after impact. The computed diameter and the nominal diameter of this region (56 percent of the sphere diameter) agreed exactly. The darker region in the front element was also observed in radiographs of tests with t/D ratios of 0.026 and 0.049.

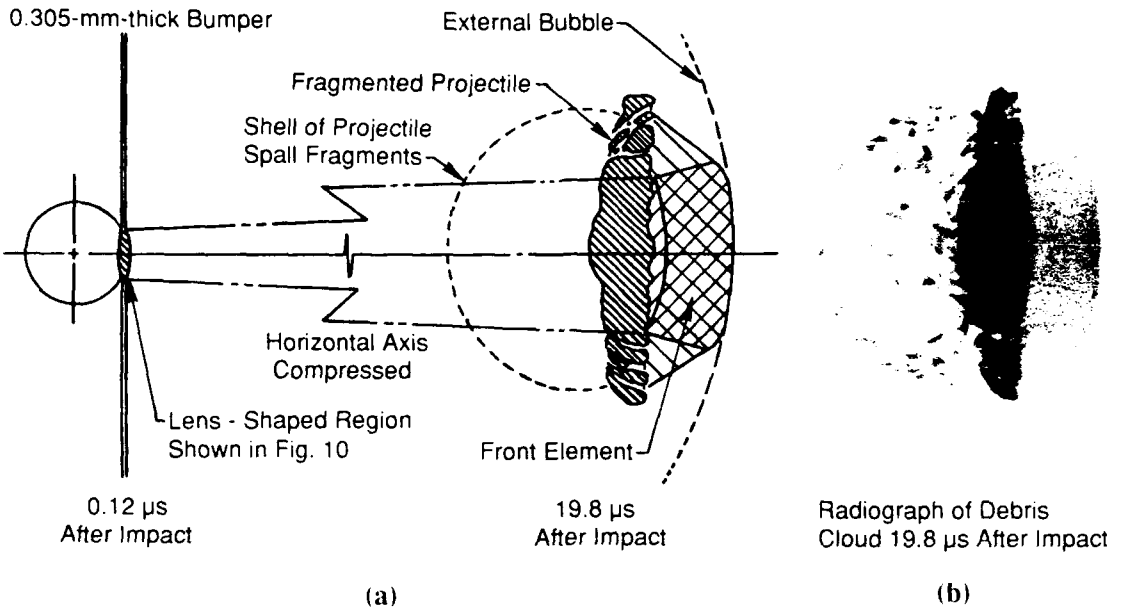


Fig. 11. Development of features in front element of internal structure of debris cloud. (a) Expansion of region in which collision-point velocity in target exceeds shock-wave front velocity (see Fig. 10). (b) View of debris cloud produced by impact of a 9.53-mm-diameter 2017-T4 aluminum sphere with an 1100-O aluminum sheet at 6.67 km/s (Shot 4-1290, t/D = 0.032).

Effect of Change of State on Debris-Cloud Velocities and Morphology.

Projectile and bumper-plate material that form the front element are the most intensely shocked material in the debris cloud. It has been shown (see Anderson et al., 1990, for example) that release from a shocked state is a nearly isentropic process and that a significant amount of energy remains in the previously shocked material after release. This residual energy is converted to heat and, depending on the amount of heat available, melting and/or vaporization of the previously shocked material may occur. Anderson et al. have estimated the residual temperatures, as a function of particle velocity of the shocked material, for four metals: aluminum, cadmium, lead, and molybdenum. An adaptation of a figure taken from their work is presented in Fig. 12 and shows the results of their computations for aluminum. The lens-shaped region of Fig. 10 can be

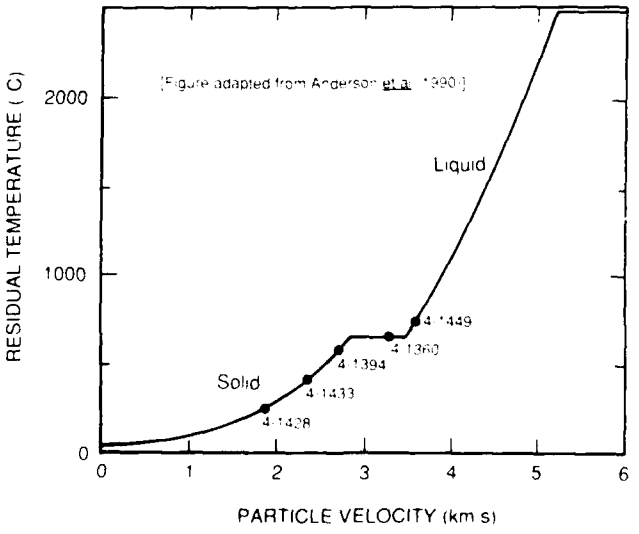


Fig. 12. Estimated residual temperature versus particle velocity using Tillotson EOS. Shot numbers noted in this figure are for tests shown in Figs. 4 and 9.

treated as experiencing a nearly one-dimensional shock. Following release from the shocked state, material in this region should attain temperatures and phases indicated in Fig. 12. As the t/D ratio increases, material outside this region would not be as highly shocked and increasingly larger portions of the bumper and projectile would remain as solid but heated fragments.

Studies performed at UDRI, by Schmidt et al. (1993), have provided radiographs of tests in which cadmium spheres were fired at cadmium plates (t/D ratios ~ 0.16). Impact velocities for these tests were high enough to cause vaporization of projectile and bumper material. Results of an analysis of these tests and the tests with aluminum spheres and plates were used to develop the sequence of debris-cloud cross sections illustrated in Fig. 13. In this figure, effects of change of state due to increased impact velocity are first manifested in the lens-shaped region shown in Figs. 10 and 11. When impact velocity is low, the cloud is composed of solid fragments. As impact velocity increases, a small region of liquid develops but may have a thin zone of solid-liquid phase bumper material at the front and a thick zone of solid-liquid phase projectile material at the rear. The entire zone liquefies as impact velocity and residual temperature increases. Further increases in impact velocity produce regions of liquid-vapor phase and vapor. Low-density vaporous material at the front of the cloud is driven outward due to the expansion of regions of higher density vapor below. This outward expansion produces a fuller and more rounded debris-cloud profile. As expansion continues, the regions of high-density vapor are exhausted and disappear. The increase in the velocity of point ①, in Fig. 6b, is indicative of a significant decrease in material strength resulting from complete liquefaction of material in the front element.

Similarities between the cadmium and aluminum debris cloud were striking when the comparisons were made on the basis of t/D ratio. In Schmidt et al., issues related to scaling of impact velocity, thermodynamic properties of the materials involved in the impact, etc., are discussed. Test results presented by Schmidt et.al. show that properly scaled aluminum and cadmium experiments produced similar damage to or failure of the rear wall of a Whipple-type shield. Similarity of cloud structure and properties has been observed in the other UDRI tests involving impacts of like materials. The structural features of the aluminum tests described in this paper conform to the features shown for the low and moderate impact velocity debris clouds in Fig. 13. All evidence indicates that impacts of aluminum spheres with aluminum plates at velocities high enough to produce vaporization would produce debris clouds that look like the vaporous cloud shown in Fig. 13.

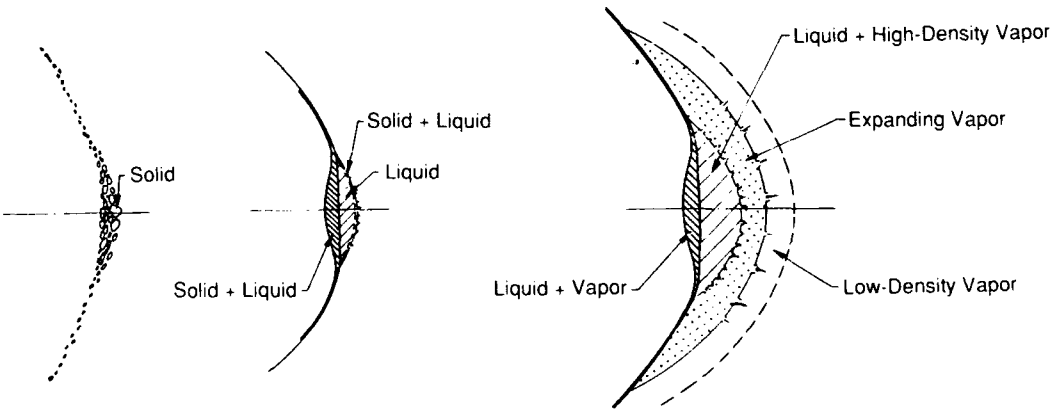


Fig. 13. Illustration of various debris-cloud structural features resulting from change of phase of material in cloud elements. Cloud development typical for t/D ratio near or just below optimum.

SUMMARY

Debris clouds produced by the impact of aluminum spheres with thin aluminum plates were shown to consist of three structural features: (1) an ejecta veil, (2) an external bubble of debris, and (3) a significant structure inside the external bubble of debris. The internal structure consisted of a front,

center, and rear element. The prominence and size of the three internal structural elements was shown to vary with t/D ratio and impact velocity. Changes in impact velocity produced the more significant changes in the front element.

A model for the development of the front element of the internal structure was presented. This model and the appropriate thermodynamic descriptions of the metals used for the bumper and projectile can be used to determine the state of material in this region of the debris cloud. A description of a debris cloud containing solid, solid-liquid, and/or liquid-vapor phases was presented.

ACKNOWLEDGMENT

A major portion of the analytical effort and several of the tests were performed under Prime Contract NAS 8-38856 on Subcontract A71447 with Martin Marietta Manned Space Systems (MMMSS). The author wishes to gratefully acknowledge Mr. Joel Williamsen, NASA MSFC and Dr. Norman Elfer (MMMSS) for their support of this work. He also wishes to express his appreciation to Mr. Burton Cour-Palais of McDonnell Douglas Space Systems Company and Dr. Robert Schmidt of Boeing Defense & Space Group for the use of their data and to Dr. Schmidt for providing several of the thinner 6061-T6 bumper-sheet materials used in the tests.

The author would also like to express his appreciation to the following associates at UDRI: The Office of the Director, for support provided for the range and equipment tests; Kevin Poormon and Donald Jurick, for their many helpful discussions; Robert Gooding and Chuck Blair, for performing the test firings; Richard Tocci and Brian Oeschger, for their careful handling and printing of the radiographs; and Gloria Hardy and Kristy Johnson, for their patience and care in preparing the manuscript.

REFERENCES

Anderson, C.E., T.J. Trucano, and S.A. Mullin (1990). Debris Cloud Dynamics. Int. J. Impact Engng, **9**, No. 1, pp. 89-113.

Ang, J.A. (1990). Impact Flash Jet Initiation Phenomenology. Int. J. Impact Engng, **10**, pp. 23-33.

Backman, M.E. and W.J. Stronge (1967). Penetration Mechanics and Post-Perforation Effects in an Aluminum-Aluminum System. NWC TP 4414.

Maiden, C.J. (1963). Experimental and Theoretical Results Concerning the Protective Ability of a Thin Shield Against Hypervelocity Projectiles. Proc. 6th Symp. on Hypervelocity Impact. Cleveland, OH, Vol. 3, 69.

Maiden, C.J., A. R. McMillan, and R.E. Sennett (1965). Thin Sheet Impact, NASA CR-295.

Nysmith, C.R. and B.P. Denardo (1969). Experimental Investigation of the Momentum Transfer Associated with Impact into Thin Aluminum Targets. NASA TN D-5492.

Piekutowski, A.J. (1992a). Properties of Largest Fragment Produced by Hypervelocity Impact of Aluminum Spheres with Thin Aluminum Sheets. Proc. AIAA Space Programs and Technologies Conference. Huntsville, AL, Paper No. 92-1588.

Piekutowski, A.J. (1992b). Formation and Description of Debris Clouds and Related Damage to Shield Structures Resulting from Hypervelocity Impact. UDR-TR-92-128, to be published as a NASA contractors report. Marshall Space Flight Center, AL.

Schmidt, R.M., K.R. Housen, A.J. Piekutowski, and K.L. Poormon (1993). Cadmium Simulations of Orbital Debris Shield Performance to 18 km/s. Int. J. Impact Engng, **14**.

Swift, H.F. and A.K. Hopkins (1968). The Effects of Bumper Material Properties on the Operation of Spaced Hypervelocity Particle Shields, AFML-TR-68-257.

Int. J. Impact Engng Vol.14, pp.587–596, 1993
Printed in Great Britain

0734-743X/93 $6.00+0.00
© 1993 Pergamon Press Ltd

EXPERIMENTS ON THE HYPERVELOCITY PENETRATION OF THIN ALUMINIUM SHEETS

W. RESCHAUER and E. IGENBERGS

Lehrstuhl für Raumfahrttechnik (LRT), Technische Universität München (TUM)
D-8000 München 2, Arcisstraße 21, FRG

ABSTRACT

Penetration experiments were conducted at the plasma accelerator test facility of the LRT/TUM. Thin aluminium sheets (8 to 125 μm thick) were impacted and penetrated by glass spheres with diameters of 20 to 60 μm at velocities between 10 and 15 km/s. In earlier experiments similar impacts on semi-infinite targets were analyzed and a method was developed to quantitatively measure the electrical charge contained in the impact plasma. This method has been extended to impacts on thin targets which were perforated. The electrical charges were measured on both sides of the target together with the velocity and the diameter of the projectile. Sensors behind the target detected the light from the penetration itself as well as from the debris plume. These experiments were conducted with a modular target system, which was designed to assure a constant accuracy, while significant parameters were varied. These experiments offer a new method for the determination of the projectile diameter.

INTRODUCTION

One of the main objectives of the experiments in the laboratory of the Lehrstuhl für Raumfahrttechnik (LRT) is the simulation of micrometeoroids and space debris. Small particles are accelerated in a plasma accelerator (Igenbergs and Shriver, 1973; Hüdepohl et al., 1989).

Helium gas is injected between two coaxial electrodes. This gas is used to generate a helium plasma by the discharge of a capacitor bank (365 μF, 20 kV). The current flowing through the plasma and the magnetic field around the center electrode cause Lorentz-forces accelerating the plasma piston out of the electrodes into a conical coil. There, the plasma is compressed to several kilobars and passes the nozzle of the coil with a velocity on the order of 80 km/s. In front of the coil, small glass spheres are exposed to the plasma flow and hence are drag-accelerated. Glass is the most appropriate material to withstand the high temperatures and the shock conditions during the acceleration phase. After a flight path of almost 4m the particles will impact a target mounted in a detector within the high vacuum section of the range.

Impacts of sufficiently high kinetic energy will evaporate and partly ionize material of both the projectile and the target and then eject the material out of the penetration zone. Within this ejecta cloud the electrical charges are transported to collector plates placed on both sides to the flight path of the projectile. The collectors are biased to opposite voltages to separate negative and positive charges. The mass and the velocity of the impacting projectile can be calculated of these electrical charges. This principle is presently used in a space experiment called Munich Dust Counter (MDC) on board of the Japanese satellite Hiten (Igenbergs et al., 1990). The micrometeoroid impacts measured between the Earth and the Moon provided new data of the micrometeoroid flux in space.

EXPERIMENTAL SETUP

The detector (Fig. 1) is designed to determine the mass and the velocity of the impacting projectile, as well as the positive and negative charges carried by the ionized ejecta clouds in front of and behind the target. On the rear side of the target, the light emission generated by the penetration is detected.
Three axially displacable frames are mounted perpendicular to the flight path. The components of the setup are designed as slides which are inserted into the frames providing a target area of 60 x 60 mm. The upper frame holds a submicron nitrocellulosis film (NC-foil) for the

determination of the projectile size. The middle frame carries the target and the front and rear charge collector plates. The lower frame holds the light detector. In order to minimize the length of the wires from the detectors to the amplifiers, the electronics are situated within the vacuum chamber. A cylindrical box below the light detector contains four high-speed operational amplifiers for the charge signals and four high impedance sensing amplifiers for the light signals. The experimental setup is shielded by a housing to reduce the interference of the photosensors with the plasma light within the accelerator. The entire detector is surrounded by a metallic cylinder for protection against electromagnetic radiation.

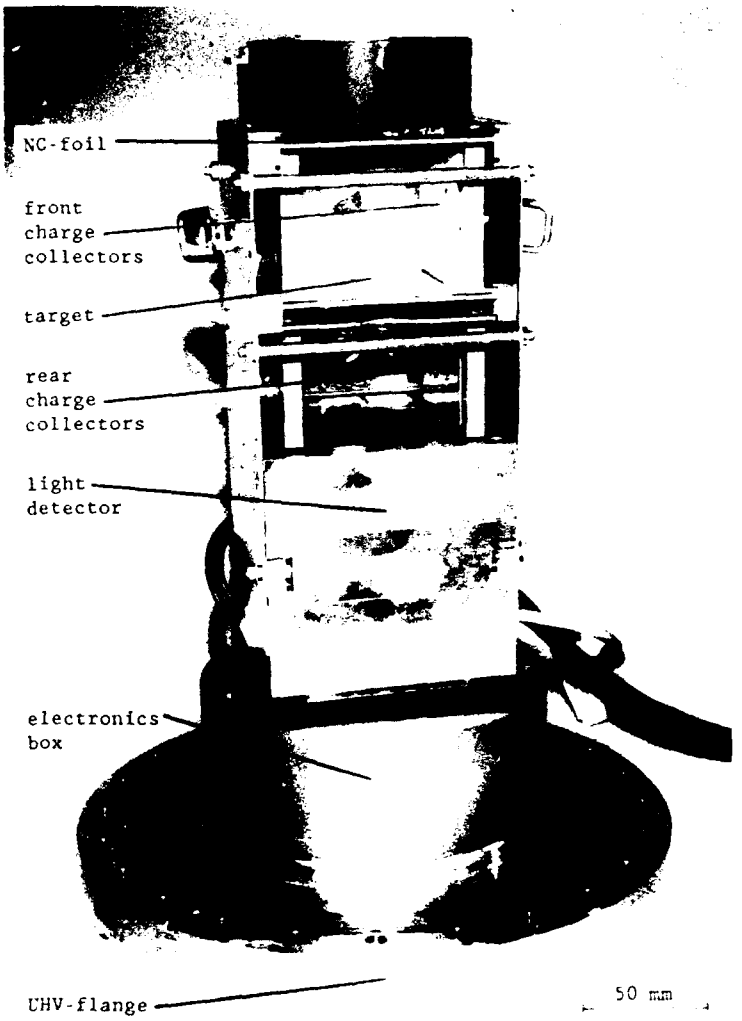


Fig. 1. The impact detector is mounted on the back end flange of the high vacuum section. The cylindrical shielding and the front cover of the housing are removed. Above the cylindrical electronics box three frames hold the light detector, the target slide and the four charge collectors, the NC-foil slide and the lower half of a vacuum labyrinth ensuring electromagnetic shielding.

EXPERIMENTS

The projectile parameters must be determined immediately prior to the impact because ablation during the acceleration process reduces the initial size of the projectile.

A submicron nitrocellulosis film (NC-foil) is used to determine the projectile mass. The thickness of the NC-foil is at least two orders of magnitude smaller than the projectile diameter. The penetrating projectile will generate a hole which corresponds very closely in size and shape to the cross-section of the projectile. Spherical shape for every projectile in this experiment series is assumed, because all impacts which did not show circular holes in the NC-foil were excluded from further evaluation. The mass is computed using the known density of the projectile.

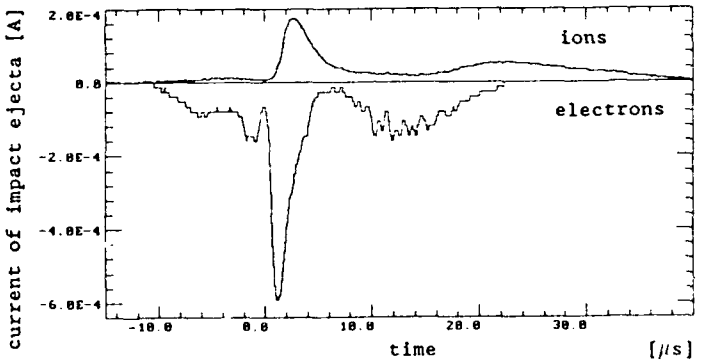
The velocity of the impacting projectile is determined by a time of flight measurement. The projectiles leave 20 μs after the initiation of the capacitor bank discharge (Igenbergs et al., 1987). The acceleration of the projectiles is only effective throughout a short distance compared to the flight path of the projectile because of the divergent plasma flow behind the compressor coil. Thus, for the calculation the velocity is assumed to be constant.

Electromagnetic radiation from the plasma accelerator strongly influences the detector system for about 250 μs after initiation of the experiment. Then the resistance of the ignitron switches increases by several orders of magnitude and disconnects the capacitor bank of the accelerator. Thus, a flight path of 3969 mm allows enough delay to record signals of projectiles whith velocities less than 17 km/s without electromagnetic noise from the capacitor bank.

The collector plates are biased to +30 V and -30 V, respectively and separate the positive and negative charges of the impact plasma. The electrical currents detected by the collectors are on the order of 100 μA and cannot be measured directly with a transient recorder. High slew rate operational amplifiers convert the currents into signals of several volts.

The currents detected in front of the target (Fig.2a) typically show the three features of a hypervelocity impact signal explained by Iglseder and Igenbergs (1987): the NC-foil penetration, the actual impact and secondary ejecta impacts. The charge collectors behind the target (Fig. 2b) cannot detect the NC-foil perforation, but do record the target perforation and secondary effects caused by ejecta impacts.

a.



b.

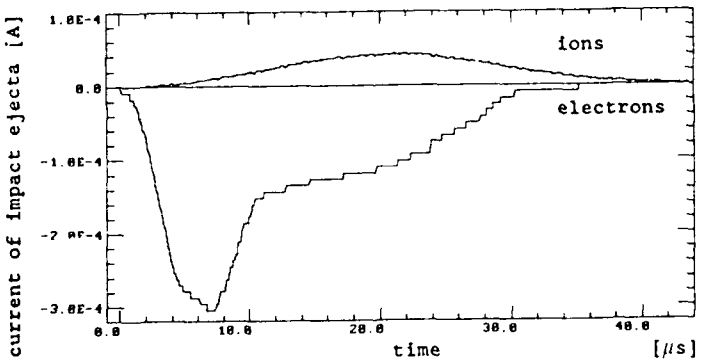
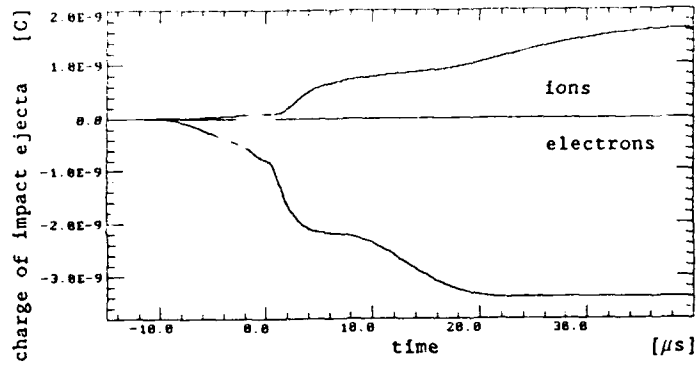


Fig. 2. The charge current signals are generated by ions (positive) and electrons (negative).
(aluminium sheet, thickness: 110 μm)
a. The signals measured in front of the target show three events: the NC-foil penetration, the impact on the target and impacts of the ejecta from the target.
(projectile diameter: 45 μm, impact velocity: 8.5 km/s)
b. The signals measuread behind the target show a main peak and subsequent secondary impacts.
(projectile diameter: 44 μm, impact velocity: 11.9 km/s)

Integrating the current over time yields the electrical charge (Fig. 3). Both the time between the peaks of the main and the secondary impacts and their amplitudes vary with the distance of the collectors from the impact location. Hence, the main impact and the secondary effects may merge and then are hardly distinguished in the charge signal.

a.



b.

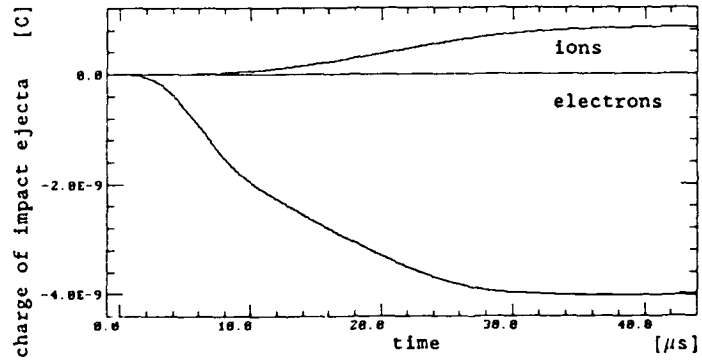


Fig. 3. The charges of ions (positive) and electrons (negative) are obtained by integrating the charge current signals.
a. The front charges correspond to Fig. 2a.
b. The rear charges correspond to Fig. 2b.

The impact light emissions on the rear side of the target and of the debris plume are detected by Avalanche Photo Diodes (APDs). The APDs are operated in an inverse direction circuit, biased to -220 V and are similar to photomultipier tubes. The spectral responsivity is higher than 30 A/W within a wavelength band from 520 nm to 970 nm (maximum responsivity: 77 A/W at 830 nm). Hence, heated matter of the impact event may be the main source of the detected radiation. The sensors can be used uncalibrated to provide some information on the location of the perforation. The space behind the target is divided into four chambers. Each APD surveys one quarter of the rear target surface. The light emitted in one quadrant is focussed by a lens onto the corresponding APD. A honeycomb structure in front of the lenses avoids stray light from the neighbouring chambers and from the outside.

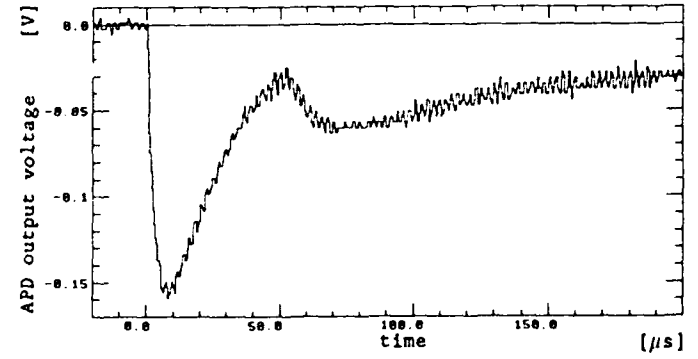


Fig. 4. The light signal of a single APD shows the optical features behind a target perforated by a hypervelocity projectile: emission from the penetration location itself and the radiation from the expanding debris plume.
(copper sheet, thickness: 40 μm,
projectile diameter: 58 μm, impact velocity: 7.1 km/s)
Note: Using copper as target material shows the two sources of the light signal. The light detected from the penetration location is superposed on the stronger radiation of the debris plume if aluminium targets are impacted.

An APD signal (Fig. 4) shows a steep slope caused by light emitted from the location of the perforation. This peak is superposed on the radiation of the debris plume which causes a slower rise of the light signal, but, in the case of an aluminium target, a higher amplitude. The expanding ejecta cloud is also detected by the other three APDs with a time delay and a lower amplitude. It is a specific feature of the plasma accelerator that generally more than one projectile is accelerated. All light signals together (Fig. 5) are used to relate an impact event to its charge signals. With this light detector even two impacts in the same quadrant can be distinguished.

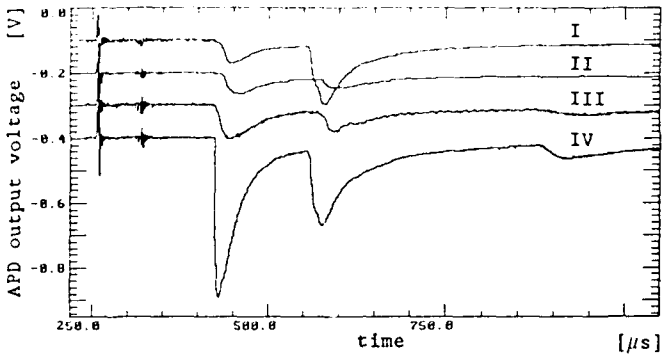


Fig. 5. The four quadrants of the rear target side are surveyed by one APD each (signals from above: quadrants I-IV). This light detector record shows target penetrations at different locations within the fourth quadrant. The fastest impact occurred in the middle, the second one close to the first and the slowest one close to the third quadrant.
(sheet material: aluminium, thickness 10 μm,
projectile diameter: 29 μm, impact velocity: 9.8 km/s
29 μm, 7.4 km/s
13 μm, 4.6 km/s)

TARGETS AND PROJECTILES

Sheets of pure aluminium with thicknesses between 8 and 125 μm and a smooth surface on both sides are used as targets.

The projectile parameters are varied by changing the size of the glass spheres loaded prior to the test. The projectile mass varies statistically due to plasma flow effects. In these experiments the mass ranged from 10^{-10} to 10^{-6} g, the impact velocity from 1.9 to 18.4 km/s.

EVALUATION OF THE EXPERIMENTS

The target and, close above, the NC-foil slide are mounted in a frame with a transparent grid and then are investigated with a microscope. This frame preserves the relative position of the aluminium sheet and the NC-foil.

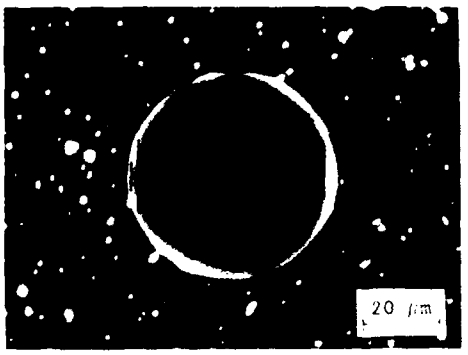


Fig. 6. A penetration hole in the NC-foil with 56 μm in diameter.

The perforation holes in the NC-foil (Fig. 6) have a smooth rim and are surrounded by a halo of deposited vapour which accompanied and swept up the projectile. Holes generated by ejecta

perforation look different: These have irregular rims and no halo. Sometimes the hole of the projectile is removed subsequently by ejecta perforation and the mass of the projectile cannot be estimated.

In the experiments described here, the impact velocity is higher than the sound velocity in the target and the impacts show the typical features of a hypervelocity event. Both, the front and the rear side of the hole are rimmed by a steep, overturned lip (Fig.7). The target material next to the impact remains in the original state.

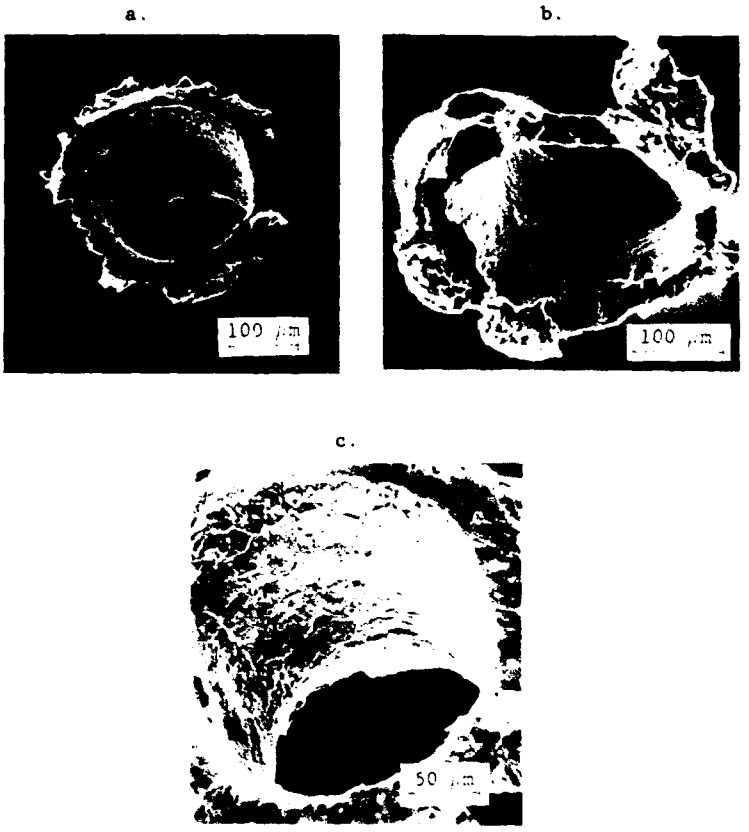


Fig. 7. A penetration hole was scanned with an electron microscope.
(aluminium sheet, thickness: 125 µm,
hole diameter: 220 µm,
projectile diameter: 56 µm, impact velocity: 10.6 km/s)
a. Front view
b. Rear side view (several rows of crater lips are visible)
c. View inside the hole

A glass plate is located behind the target during the experiments. A fine deposit of spray is found there as opposed to the expected secondary impacts. This indicates a high degree of ejecta vaporization during the penetration of the target. No projectile material remains inside the penetration hole. The surface there is smooth or shows patterns similar to fish scales due to cracks caused by the release from the shocked state (Fig. 7c).

Sometimes the rear side shows two or more rows of lips inside of the outer steep lip (Fig. 7b). In this case the surface between the lips is rough and looks crumbly. This feature ("scabbing") is caused by spallation and also was observed on sheets penetrated in low earth orbit (Carey et al., 1985a). The impacts probably occurred close to the ballistic limit if the spallation features remained intact. Generally, these features are subsequently removed by the penetrating projectile at higher impact energies.

Hypervelocity impacts of spheres into semi-infinite targets generate craters of ellipsoidal shape (Iglseder and Igenbergs, 1990). Penetration holes through targets which are thin compared to the projectile diameter are of cylindrical, or hyperboloidal, shape. The target penetrated in these experiments are neither semi-infinte nor thin compared to the diameter of the impacting projectile. Hence, the transition from the crater to the hole generation process is visible if impacts close to the ballistic limit are examined (Fig.8).

a. b.

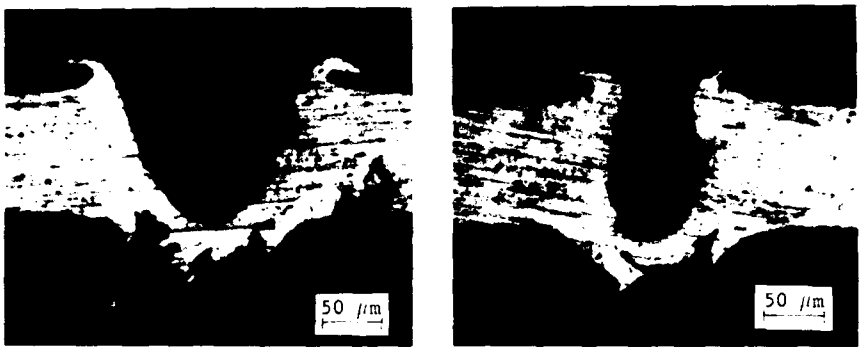


Fig. 8. Two cross-sections of impact craters close to the ballistic limit are compared:
(aluminium sheet, thickness: 110 µm)
a. The impact features are similar to a crater in a semi-infinite target. The rear surface of the target, however, is already bent outward and disrupted by spallation.
(crater diameter: 183 µm,
projectile diameter: 47 µm, impact velocity: 7.3 km/s)
b. The projectile almost disrupted the rear surface to generate a penetration hole with a cylindrical shape.
(crater diameter: 160 µm,
projectile diameter: 40 µm, velocity: 8.5 km/s)
Note: The cross-sections do not show the maximum diameters.

The further beyond the ballistic limit an impact occurs (e.g. a reduction of the target thickness), the more cylindrical the penetration hole is and the smaller the crater lips are, compared to the hole size (Fig. 9).

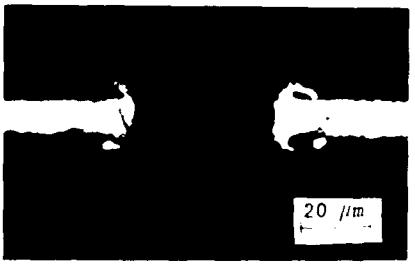


Fig. 9. A penetration hole further beyond the ballistic limit.
(aluminium sheet, thickness: 10 µm,
hole diameter: 37 µm,
projectile diameter: 13 µm, impact velocity: 8.5 km/s)
Note: This cross-section does not show the maximum diameter.

The impact velocity influences the shape of a penetration hole if the projectile diameter and the target thickness are of the same order of magnitude. The faster the impact occurs, the more conical are the penetration holes; i.e. the ratio of the entry-to-exit-side hole diameter increases (Carey et al., 1985b). This may correspond to an increasing ratio of front-to-rear-side ejecta mass, as indicated by the ejecta charge measurements (Fig. 10, see also Fig. 13).

Most of the empirical equations of crater sizes and impact parameters are more or less based on a direct dependence of the crater volume to the impact energy if material properties are not varied (e.g. Frisch et al., 1986; Iglseder and Igenbergs, 1990). Hence, the mass of the target material removed from its original location is proportional to the impact energy as well. The experiments discussed here indicate a lower amount of extracted target material per unit energy compared to the empirical equations above. The kinetic energy of the debris plume is increased by the excess energy. (Fig. 11)

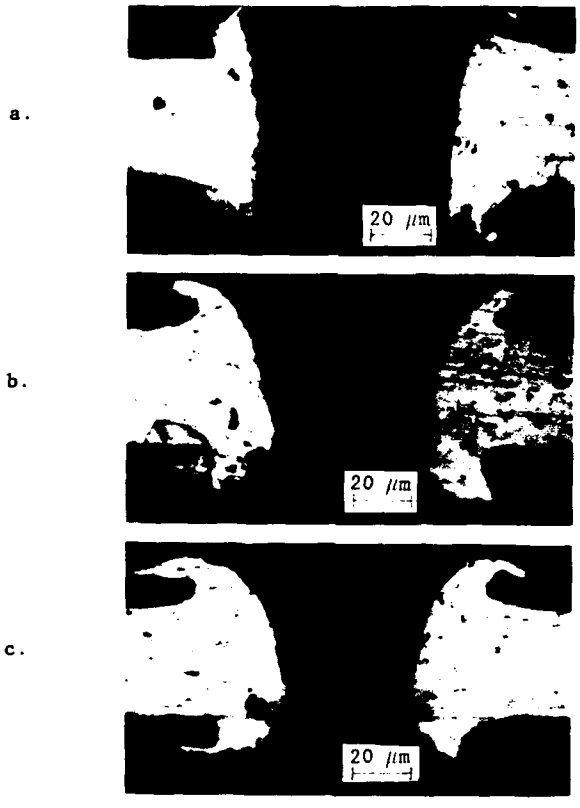


Fig. 10. A series of impacts on the same target with increasing velocity and constant projectile diameter shows a variation of the hole shape.
(aluminium sheet, thickness: 40 μm)
a. hole diameter: 79 μm,
projectile diameter: 24 μm, impact velocity: 6.8 km/s,
b. hole diameter: 100 μm,
projectile diameter: 24 μm, impact velocity: 9.5 km/s,
c. hole diameter: 107 μm,
projectile diameter: 23 μm, impact velocity: 11.5 km/s
Note: The cross-sections do not show the maximum diameters.

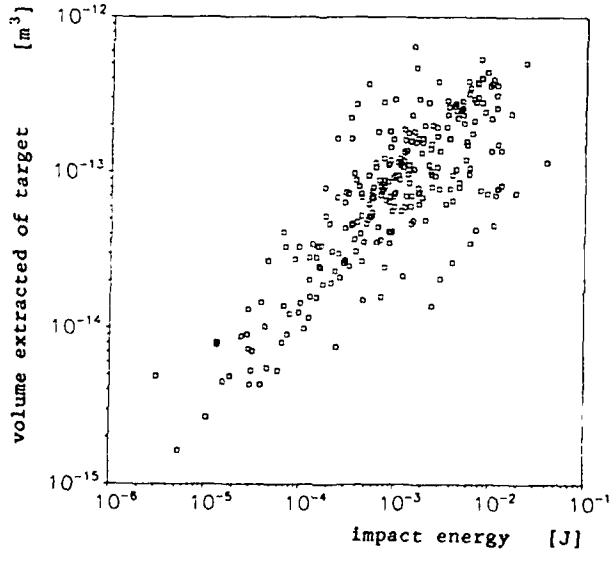


Fig. 11. A relation between the impact energy and the hole volume (similar to impacts on semi-infinite targets) is still visible for the perforation if the target thickness and the projectile diameter are of the same order of magnitude.

For impacts of glass beads on semi-infinite targets the ejecta charge per unit mass satisfies a power function of the impact velocity (Iglseder and Igenbergs, 1987). If the targets are perforated, the amount of ionized ejecta collected with an identical setup is smaller compared to an impact on a semi-infinite target (Fig. 12).

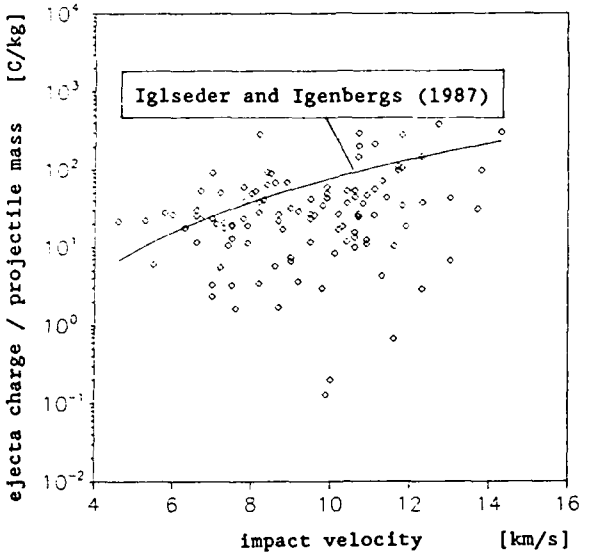


Fig. 12. The average of the total electron charges (both from the front and the rear) divided by the projectile mass is less than the charge generated by an eqivalent impact on a semi-infinite target (indicated by the line).

Spallation occurs within a small range rather than at a certain impact velocity referring to the momentum transfer model of Nysmith and Denardo (1969). However, the impact velocity determines the Hugoniot state and the material compression by the shock wave propagating through the target. Hence, the spallation generated by the shock wave occurs closer to the rear target surface with an increasing shock wave amplitude. The projectile penetrates deeper into the target until the rear target surface is disrupted and more material is ejected to the front side of the target (Fig.13).

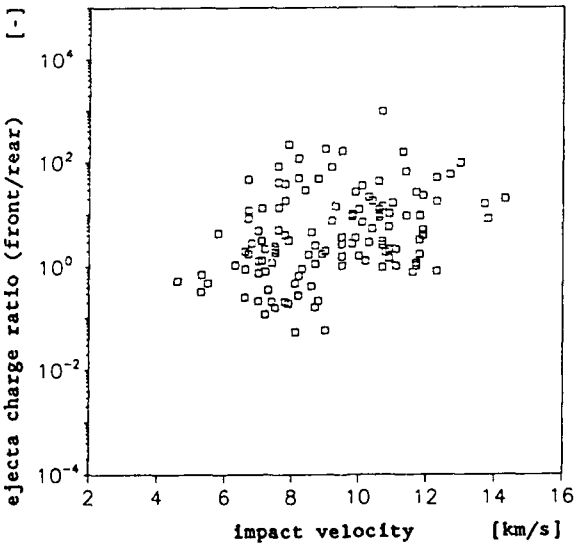


Fig. 13. The penetration experiments indicate an increase of the ratio of front-to-rear-side ejecta charges with the impact velocity.

The detector seperately measures the ejecta charges on both sides of the target. The charge ratio measured in front of and behind the target correlates to the ratio of the ejecta mass. Therefore, the debris clouds on both sides have to be in a similar state. This fact could not be verified by the data from these experiments, but the average ratio of the measured charges tends to increase with the impact velocity independently of the projectile mass.

UNCERTAINTIES OF THE EXPERIMENTS

The impact velocity can be determined quite accurately due to the long distance from the accelerator to the target. The projectile mass is derived from the hole size of the NC-foil perforation. Hence, this measuring error depends on the third power.

The location of the charge collectors determined by Iglseder (1987) guarantees a maximum charge profit if two polarities are required. A variation of the bias voltages does not show different amounts of the collected charges, whereas the distance or the angle of the collectors with respect to the target has a significant influence to the charge collection. A higher accuracy of the electron charge signal compared to the ion charge signal supports the assumption that the forces of the electrical field between the collectors are dominated by the momentum of the ejecta cloud itself.

CONCLUDING REMARKS

A new setup for the hypervelocity penetration of thin sheets was used in the plasma accelerator facility of the Lehrstuhl für Raumfahrtechnik (LRT) to measure the charge currents of the ejecta clouds on both sides of the target and to detect light emissions from the rear of the perforation and the debris plume.

The impact charge measurement will be improved if the collector plates are replaced by wire grids mounted parallel to both sides of the target. This will simplify the setup to a unipolar detector providing a constant distance from the impact location to the grids. The collection of electrons will increase the measurement accuracy.

Appropriate targets and collector grids will allow a determination of the impact parameters by electron charge measurements. The total ejecta charge is related to both the impact velocity and the projectile mass due to an energy transfer to ionize the material of the penetration zone. The ratio of the charges measured on both sides of the target varies with the impact velocity due to shock wave effects and, hence, is not depending on the projectile mass. Light signals allow to redundantly determine the impact velocity and relate the charge signals to the penetration holes if several impact events per test occur.

The new data indicate that empirical equations similar to existing equations for the semi-infinite impact show a correlation of the the target mass removed during the penetration process and the impact energy. The total ejecta charge increases with the projectile mass as well as with the impact velocity. If the projectile size and the sheet thickness are of the same order of magnitude, the ratio of ejecta charges of the front and rear side of the target increases with the impact velocity.

The transition phase of beginning to complete spallation is to be investigated in more detail to explain phenomena such as follow-on spallation which was observed as additional rows of crater lips on the rear side of the penetration hole.

REFERENCES

Carey, W.C., D.G. Dixon, and J.A.M. McDonnell (1985a). Space Shuttle microabrasion foil experiment (MFE): Implications for aluminium oxide sphere contamination at near earth space. Adv. Space Res., Vol. 5, Chap. 2, 87-90.

Carey, W.C., J.A.M. McDonnell and D.G. Dixon (1985b). Capture cells: decoding the impacting projectile parameters. Lunar Planet. Sci., 16, 111-112.

Frisch, W., S. Aigner and E. Igenbergs (1986). Hypervelocity impact calibration of SOLAR MAX thermal blankets. Adv. Space Res., Vol. 10, Chap. 3, 413-416.

Hüdepohl, A., M. Rott and E. Igenbergs (1989). Coaxial plasma accelerator with compressor coil and radial gas injection. IEEE Trans. Mag., Vol. 25, Chap. 1, 232-237.

Igenbergs, E. and E.L. Shriver (1973). Magnetogasdynamic compression of a coaxial plasma accelerator flow for micrometeoroid simulation. J. Appl. Phys., Vol. 44, Chap. 5, 2177-2187.

Igenbergs, E., S. Aigner, A. Hüdepohl, H. Iglseder, H. Kuczera, M. Rott and U. Weishaupt (1987). Launcher technology, inflight measurement and impact diagnostics at the TUM/LRT. Int. J. Impact Engng., 5, 371-380.

Igenbergs, E., A. Hüdepohl, K. Uesugi, T. Hayashi, H. Svedhem, H. Iglseder, G. Koller, A. Glasmachers, E. Grün, G. Schwehm, H. Mizutani, T. Yamamoto, A. Fujimura, N. Ishii, H. Araki, K. Yamakoshi and K. Nogami (1991). The Munich Dust Counter: a cosmic dust experiment on board of the MUSES-A mission of Japan. In: Origin and Evolution of Interplanetary Dust (A.C. Levassseur-Regourd and H. Hasegawa, eds.), 45-48. Kluwer Academic Publishers, London.

Iglseder, H. and E. Igenbergs (1987). Measured charge generation by small mass impacts at velocities between 1 and 45km/s. Int. J. Impact Engng., 5, 381-388.

Iglseder H. and E. Igenbergs (1990). Crater morphology at impact velocities between 8 and 17km/s. Int. J. Impact Engng., 10, 271-280.

Nysmith, C.R. and B.P. Denardo (1969). Experimental investigation of the momentum transfer associated with impact into thin aluminum targets. NASA Techn. Note, D-5492.

Int. J. Impact Engng Vol.14, pp.597–606, 1993
Printed in Great Britain

0734-743X/93 $6.00+0.00
© 1993 Pergamon Press Ltd

EXPLOSIVE SIMULATION TO INVESTIGATE ENHANCED ABLATOR REMOVAL

Mohsen Sanai and James D. Colton

SRI International
Menlo Park, CA 94025

ABSTRACT

We have developed a method to simulate with explosives the impact and penetration of a reentry vehicle (RV) shell by a high-density hypervelocity fragment. Using a two-dimensional Lagrangian hydrocode, we modeled various hypervelocity fragment impact conditions and innovative explosive configurations that simulate the impact effects. The method is based on matching the damage inflicted on the heatshield by the impact and penetration of the fragment. Specifically, we set a simulation objective of matching the hole size, the time history of the stress environment, and the final effective plastic strain field for both the silica phenolic heatshield and aluminum layers while keeping the momentum imparted to the target the same. The calculations showed that the explosive jet from an explosive charge placed inside a short disposable steel barrel produced a hole that matched the simulation criteria reasonably well except that the aluminum substrate stretched excessively before failing. A much improved simulation was obtained when the target was penetrated with a fragment projected by an explosive charge. All the simulation criteria listed above were matched very well, indicating that explosive simulation can be used to simulate the impact of hypervelocity fragments with a high degree of fidelity.

INTRODUCTION

Investigation of dense fragments impacting and penetrating a space target or reentry vehicle requires advanced gun facilities capable of accelerating such fragments to hypervelocity speed. As an alternative to using such guns, we developed a cost-efficient explosive simulation technique that duplicates the important impact phenomena with a high degree of fidelity. The simulation criteria we set were to match in both the heatshield and substrate materials the following parameters while keeping the momentum imparted to the target the same:

(1) Hole size.

(2) Time history of the stress environment produced around the hole during penetration.

(3) Final effective plastic strain (EPS) field produced around the hole after penetration.

Our approach to satisfying the above simulation criteria is to develop shaped explosive charges that replicate the desired impact as closely as possible, either directly or through projection of a shaped fragment.

RESULTS OF CALCULATIONS

As a reference case, we chose the configuration shown in Figure 1, for which experimental data and a KAPP* code prediction for hole size are available. This reference case consists of a 2-g tungsten sphere impacting at 4.9 km/s a 0.25-in.-thick (6.35-mm) silica phenolic layer placed over a 0.125-in.-thick (3.175-mm) aluminum substrate. A two-dimensional finite-difference Lagrangian computer code called SRI L2D was used to model the penetration numerically. This code has the capability of accepting triangular cells and has the option of automatic rezoning, thus, making it suitable for performing penetration calculations that involve large deformation of the initial computation zones. The calculation reported here used roughly 5000 zones initially comprising at least 5 zones through the thickness of each material included in the calculation. The equation of state for the common materials used in the calculations (tungsten, steel, aluminum, and explosives) are the standard ones found in the literature. For the silica phenolic, we developed a Mie-Gruneisen equation of state based on the limited information available in the literature. The silica phenolic was assumed to be isotropic with the shock Hugoniot chosen as the reference line. A von Mises elastic-plastic strength model was used to describe the material state undergoing large strains. The initial density is 1.72 g/cm ^{3} and the shear modulus and yield stress are assumed to be 0.03 and 0.004 Mbar, respectively. Our previous experience with the SRI L2D code has indicated good agreement with experimental data provided that reliable data are available for developing the material models. For example, comparison with experimental data for a tailored explosive charge that simulated hypervelocity impact has been reported in the previous Hypervelocity Impact Symposium (Ref. 2).

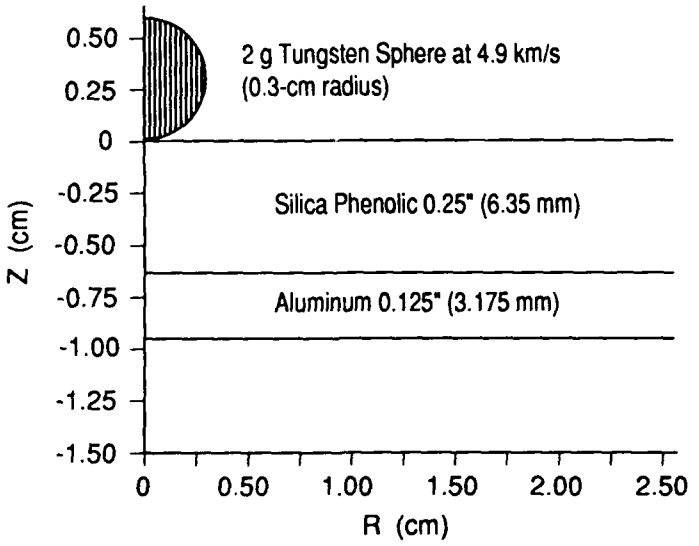


Fig. 1. Computer modeling of a 2-g tungsten sphere impacting a silica phenolic/aluminum target plate at 4.9 km/s.

The sequence of penetration of the target plate by the tungsten sphere is shown in Figure 2. As shown in Figure 3, calculations were continued until the penetration process was complete so that the final hole size could be compared with the prediction of the KAPP code. Because the KAPP code is based on

* The Kaman Analytical Penetration Program (KAPP), discussed in detail in Ref. 1, is a fast-running semi-empirical code designed to predict penetration depth and hole size in reentry vehicles targets impacted by a chunky projectile. The penetration depth is calculated by using an integrated form of a simple differential equation that equates the forces acting on the projectile to the combined resistive forces due to target hardness and inertia. The hole size is calculated based on the projected area of the projectile and is modified according to the thickness and properties of the target plate. As stated in Ref. 1, KAPP has been calibrated and benchmarked against an extensive experimental data base covering a wide range of impact conditions.

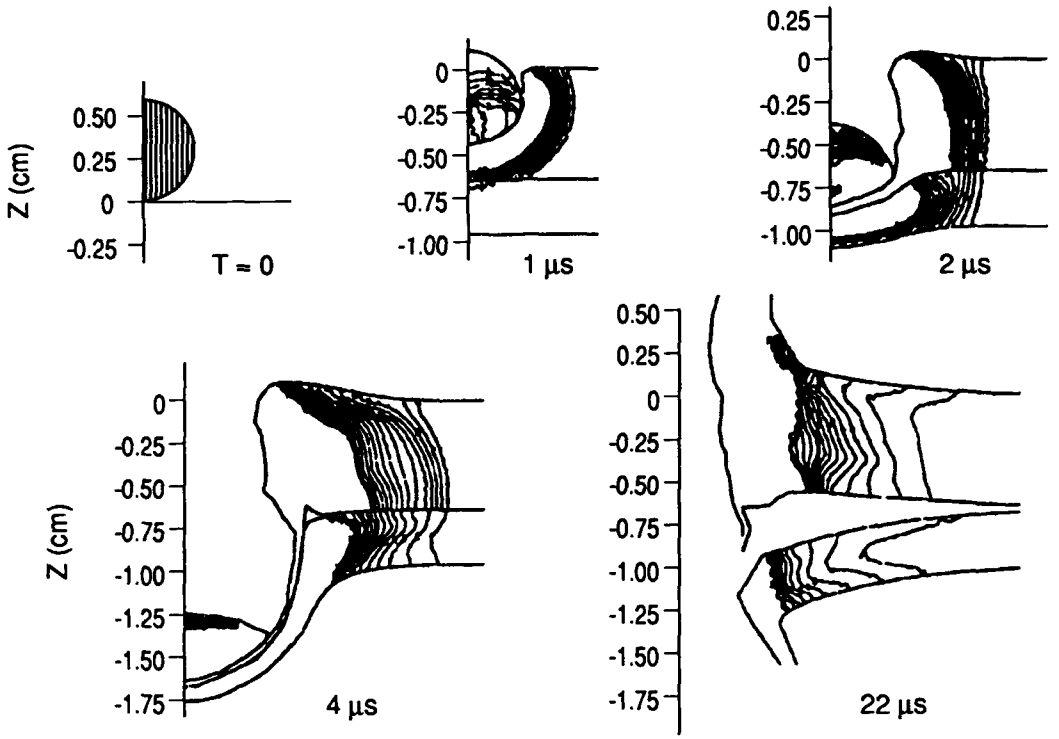


Fig. 2. Penetration of a tungsten sphere through a silica phenolic/aluminum target.

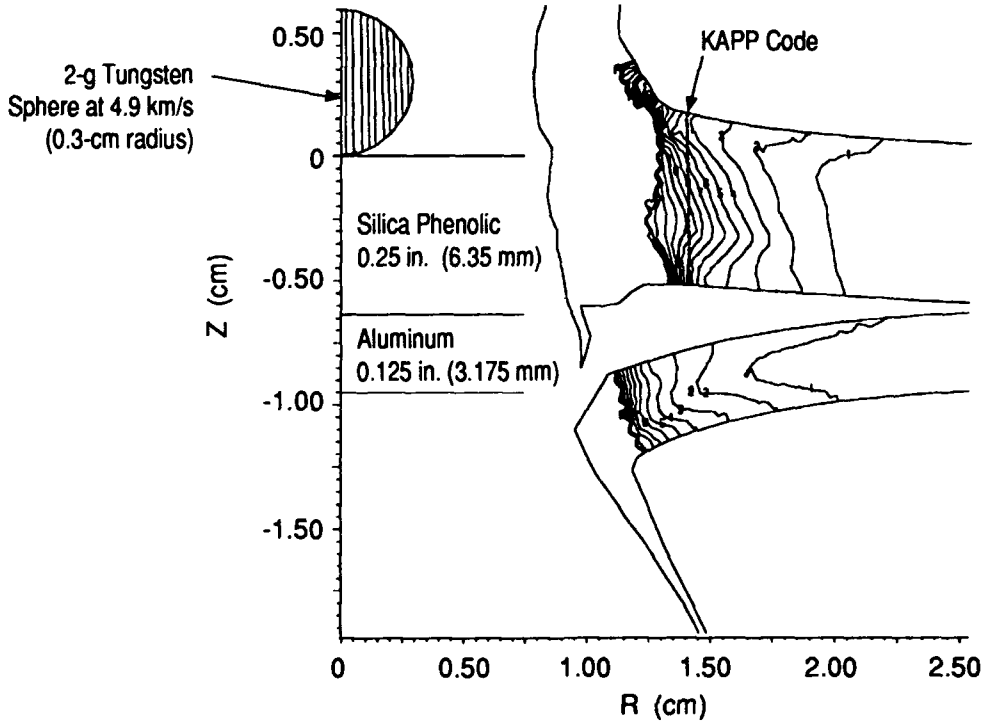


Fig. 3. Final equivalent plastic strain (EPS) contours for a tungsten sphere impact. The contours indicate 2% intervals in EPS.

correlation with an extensive experimental data base, [1] comparisons made with the hole size "predicted" by the KAPP code is essentially equivalent to direct comparison with the actual experimental data, justifying the use of the KAPP code to benchmark the numerical simulations discussed here. As shown in Figure 3, comparison of the equivalent plastic strain (EPS) contour plots with the hole size predicted by KAPP indicates that all the silica phenolic material which undergoes an EPS of about 16% (contour number 8) is removed as a result of the fragment impact and penetration.

The histories of peak stress inside the silica phenolic (Location 7 in Figure 4) and aluminum (Location 13 in Figure 4) are shown in Figure 5 for this reference impact case.

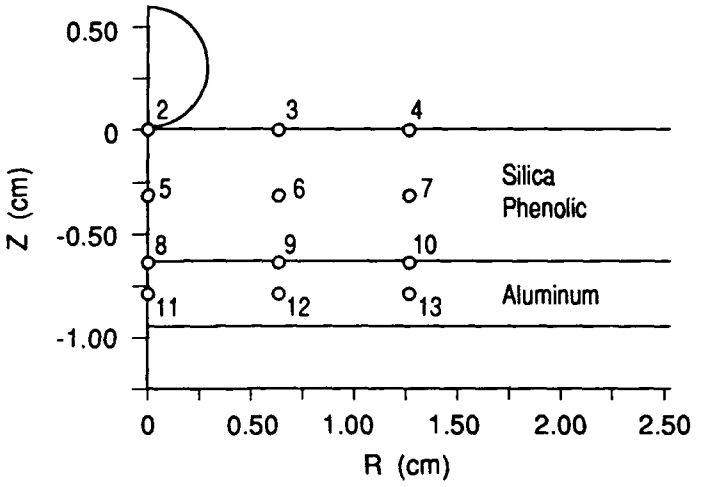


Fig. 4. Lagrangian locations for pressure history calculation.

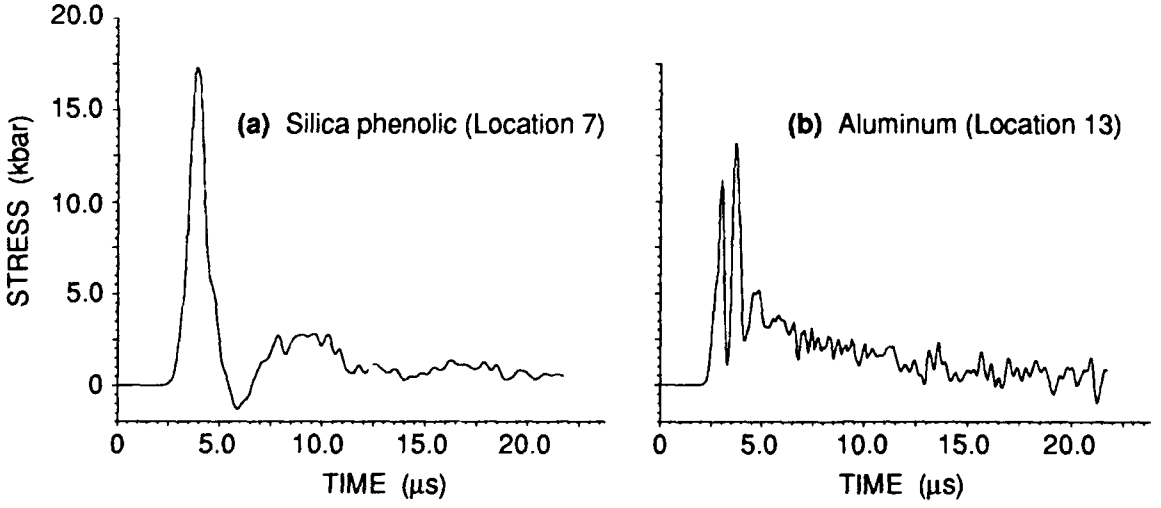


Fig. 5. Stress time histories in silica phenolic and aluminum (tungsten sphere impact).

SIMULATION WITH EXPLOSIVE JET

To simulate the fragment impact with an explosive charge, we performed calculations for the three configurations shown in Figure 6, in which an explosive column encased in a steel closure is used to dir-

ect and penetrate the target with a high pressure jet. * Figure 6(a) models a thick-walled steel closure design, whereas Figure 6(b) and (c) use a more practical closure design with one-third the wall thickness. The explosive charge in Figure 6(c) is stood off from the loaded surface to determine if the hole size can be controlled by adjusting the standoff distance.

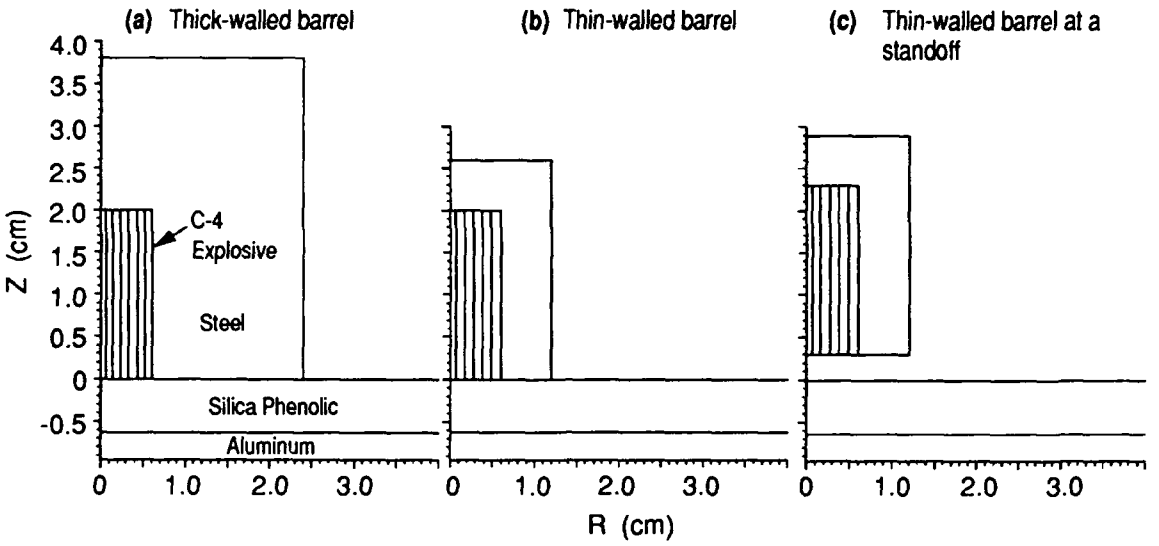


Figure 6. High explosive configurations to simulate a tungsten sphere impact.

Figure 7 shows the sequence of penetration of the target plate for the configuration of Figure 6(a). A clean hole is made in the silica phenolic, but the aluminum substrate seems to be stretched more than for the reference case shown in Figure 2. Also, the stresses calculated for this case (shown in Figure 8) have roughly the same peak as in the reference case (shown in Figure 5), but the pulse width and details of the waveforms are not identical.

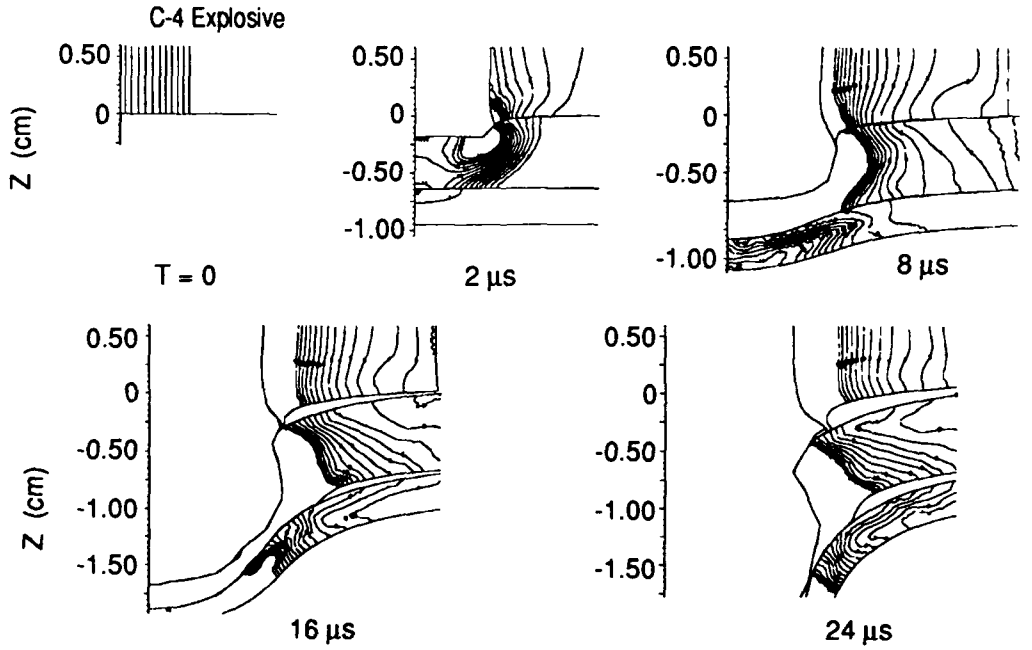


Fig. 7. Penetration of a high explosive jet through a silica phenolic/aluminum target. [Initial configuration of Figure 6(a).]

* This configuration was first proposed and tested by Curt Romander (Ref. 3).

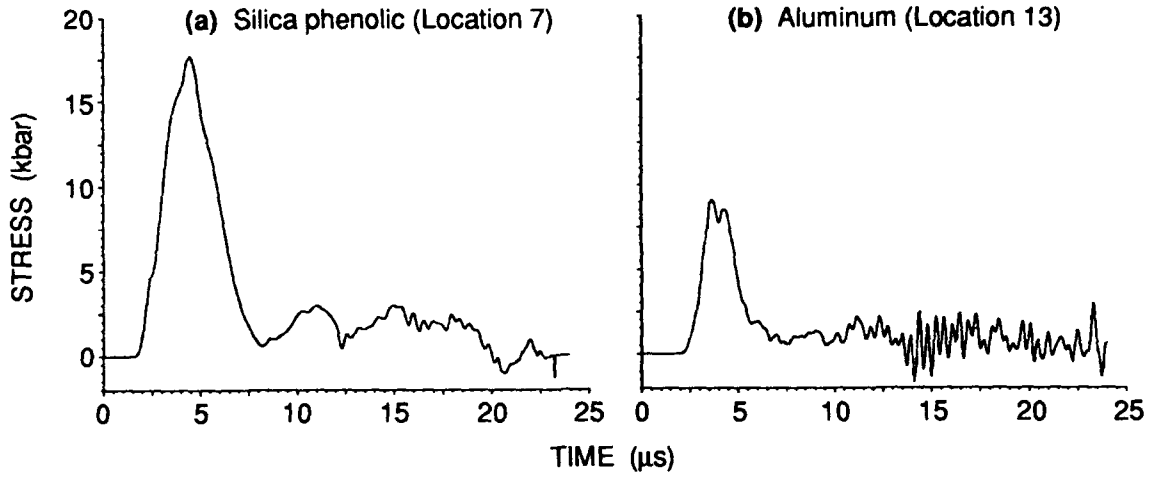


Fig. 8. Stress time histories in silica phenolic and aluminum for the high explosive configuration shown in Figure 6(a).

The calculated shapes of the final configurations corresponding to the three cases shown in Figure 6 are shown in Figure 9. Hole sizes and contour plots comparable to the reference case are obtained in all three cases. However, the aluminum substrate in all cases shows excessive stretching, indicating that sufficient control of substrate response to fragment penetration may not be possible for this target configuration when simple explosive jets are used to directly load and penetrate the target plate.

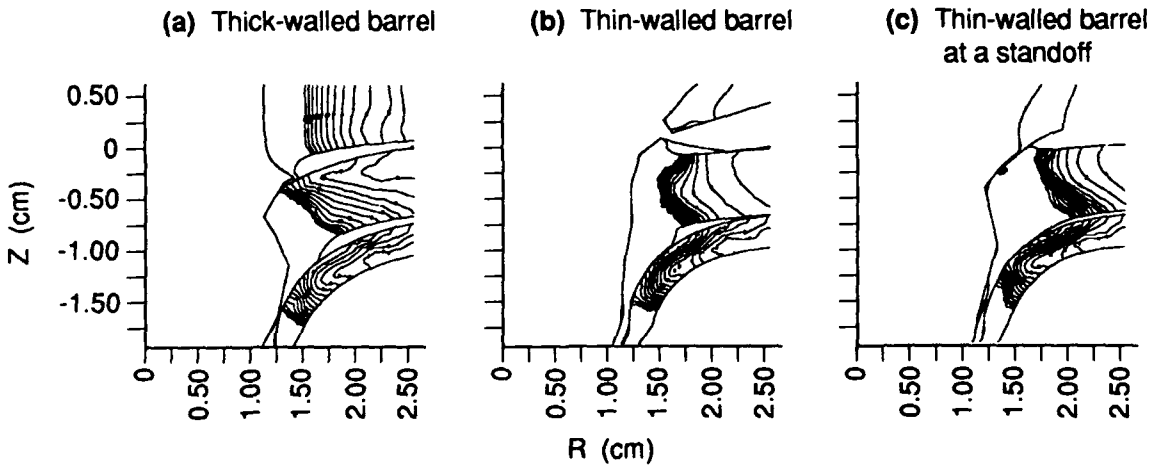


Fig. 9. Final effective plastic strain contours for the three high explosive configurations shown in Figure 6.

SIMULATION WITH SHAPED FRAGMENTS

We investigated projection of fragments made with a different material and shape to simulate the impact of hypervelocity fragments. Figure 10 shows four axisymmetric steel projectile configurations designed to simulate the impact of the tungsten sphere in the reference case. The impact velocity is reduced to 2 km/s, a value that is readily attainable with conventional high explosive. Figures 11 and 12 show the impact and penetration sequence for the disk projectile shown in Figure 10(a) and for the hollow plug projectile shown in Figure 10(d), respectively, and Figure 13 shows the final configurations for all four cases shown in Figure 10. The contour plots in Figure 13 show a striking resemblance to the reference calculations shown in Figures 2 and 3. In particular, Figure 13(a) shows an equal hole size and virtually identical distribution of EPS contour around the hole made in silica phenolic. The stress histories in silica phenolic and aluminum further confirm this similarity. For example, the peak stress histories for the flat disk impact (shown in Figure 14) indicate a stress field virtually identical to that produced in the reference case (shown in Figure 5).

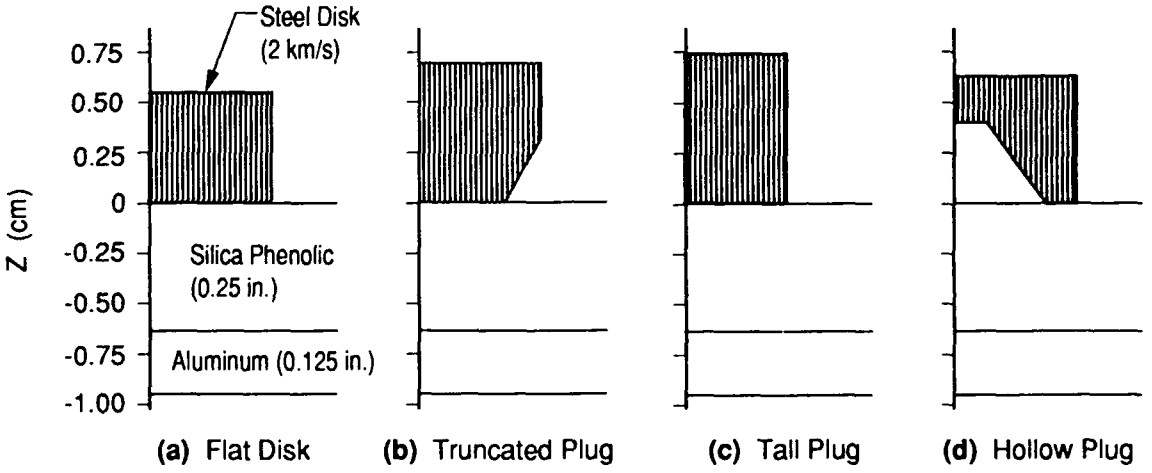


Fig. 10. Steel projectile configurations to simulate a tungsten sphere impact.

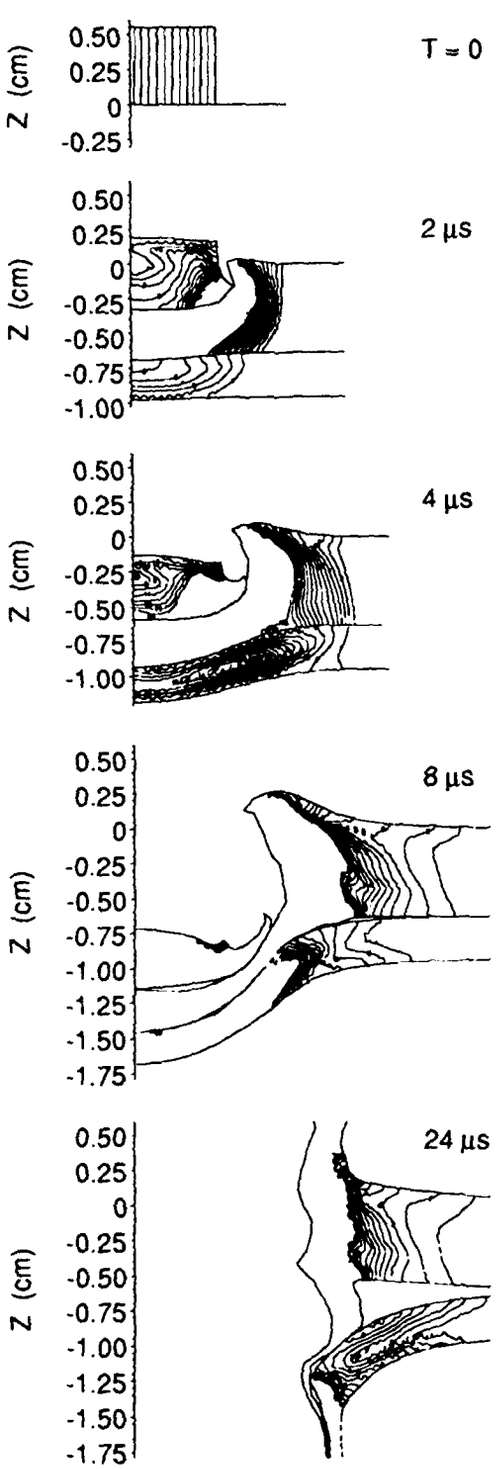


Fig. 11. Penetration of the flat steel disk shown in Figure 10(a) through a silica phenolic/aluminum target.

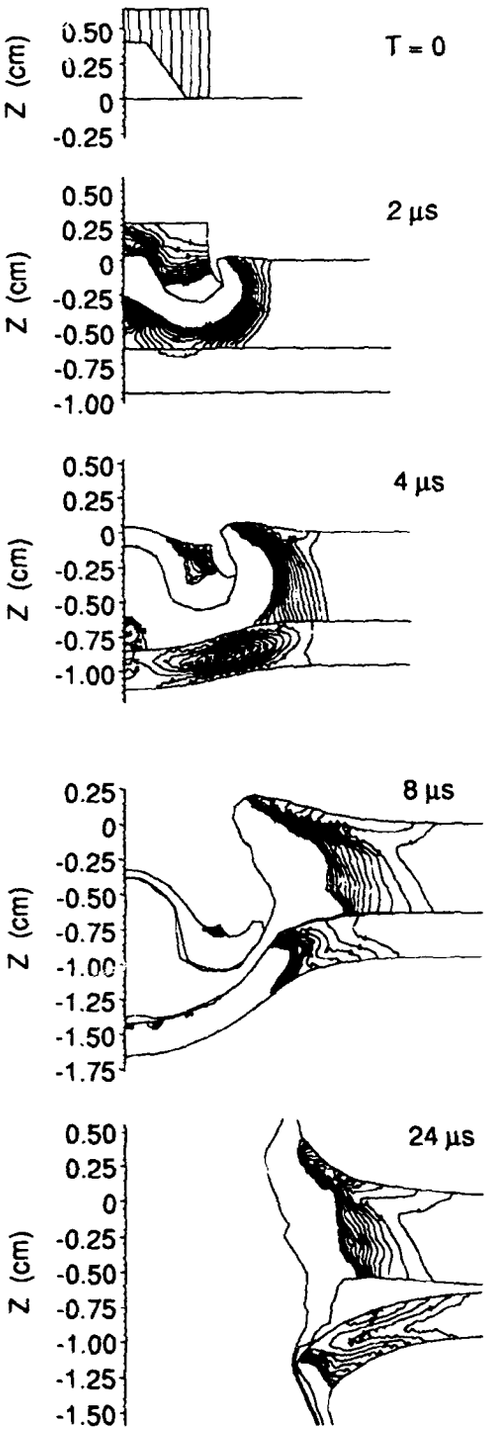


Fig. 12. Penetration of the hollow steel plug shown in Figure 10(d) through a silica phenolic/aluminum target.

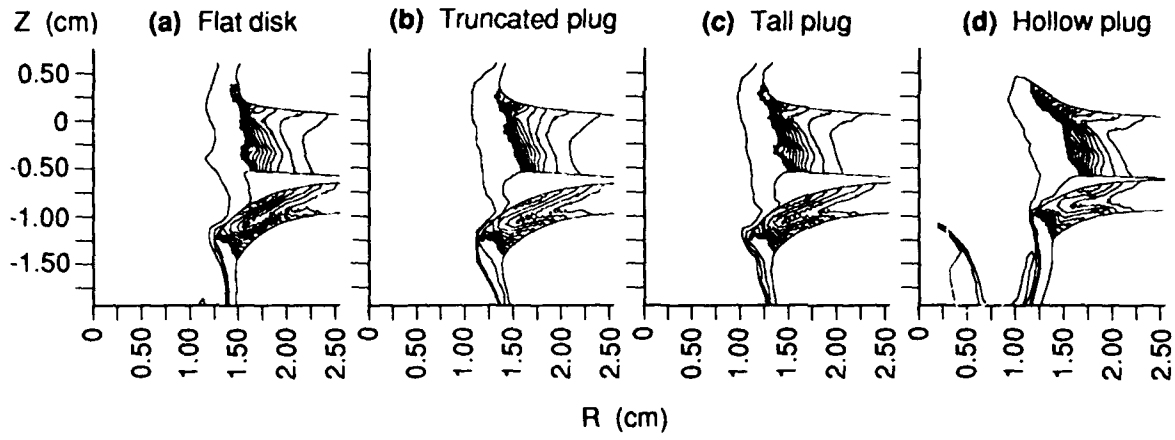


Fig. 13. Final effective plastic strain contours for the four configurations shown in Figure 10.

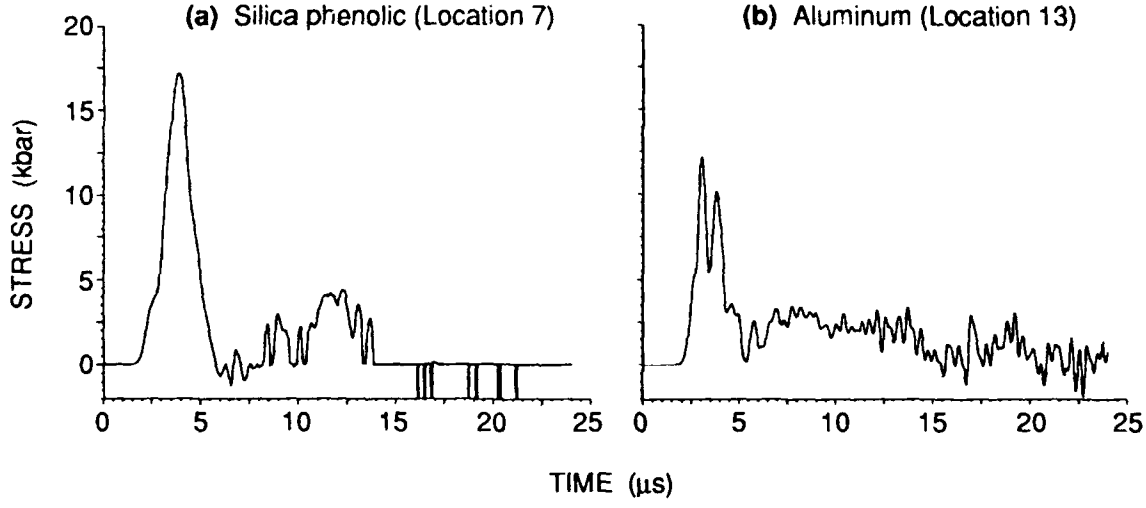


Fig. 14. Stress-time histories in silica phenolic and aluminum [flat steel disk shown in Figure 10(a)].

SUMMARY

We have investigated the potential use of conventional high explosives for simulating the impact and subsequent penetration of silica phenolic/aluminum panels by hypervelocity fragments. When a shaped explosive charge encased in a steel closure was used, the hole size, stress field, and EPS contours produced around the impact point were matched quite well. However, the aluminum substrate seemed to stretch more than that in the reference case before puncturing. Using a steel disk projected at moderate speeds (2 km/s) replicated the reference case very well and fully satisfied the simulation criteria of matching the hole size, stress field, and EPS contours for both the silica phenolic and aluminum layers.

In summary, results of the impact calculations tend to indicate that high explosives can be used to obtain a high fidelity simulation of impact and subsequent penetration of layered aluminum and silica phenolic panels by a fragment moving at hypersonic speed. This simulation technique is expected to be more cost-effective than similar experiments with conventional hypervelocity guns. Moreover, fragment mass and speed not achievable with the existing hypervelocity guns can be simulated using the high explosive technique reported here.

ACKNOWLEDGMENT

The work reported here was performed for U.S. Army Strategic Defense Command. The technical monitor was Dr. Milan Dutta. The calculations were performed by Mr. Thomas Cooper of SRI using the L2D computer code he has developed at SRI.

REFERENCE

Rodger Greer and Tom Simmerman, "KAPP User's Manual," Kaman Sciences Corporation Report K90-27U(R) on Contract DASG60-86-0071 (July 1990).

M. Sanai and J. D. Colton, "Development of a Tailored Explosive Charge to Simulate the Loads from a Hypervelocity Projectile Impacting a Liquid Tank," presented at the 1989 Hypervelocity Impact Symposium, San Antonio, Texas (December 12-14, 1989).

C. M. Romander, M. Sanai, and J. D. Colton, "Explosive Simulation to Investigate Enhanced Ablator Removal (U)," Final Report prepared for U.S. Army Strategic Defense Command, Contract DASG60-90-C-0005 (February 1991). (UNCLASSIFIED)

Int. J. Impact Engng Vol.14, pp.607–618, 1993
Printed in Great Britain

0734-743X/93 $6.00+0.00
Pergamon Press Ltd

THE SIZE, VELOCITY AND TRAJECTORY OF DEBRIS FRAGMENTS PRODUCED BY IMPACT WITH PLATE TARGETS

I. SARAVANE* and A. E. WILLIAMS

Naval Research Laboratory
Washington D.C.

*Potomac Research, Inc.
6121 Lincolnia Rd., Alexandria, VA 22312

ABSTRACT

The paper presents a general, summarized description of the debris cloud properties resulting from the hypervelocity impact of a compact projectile with a plate. The experimental study involved the impacts of three compact projectiles, L/d = 1, of two materials (*Graphite epoxy, and aluminum*) at 3 and 6 km/s with three thicknesses of aluminum plate. The test matrix was tailored to explore the effects of such impact variables as plate thickness, impact speed and projectile properties on characteristics of the debris cloud. A few tests were dedicated to scaling. While most of the results were expected, some were interesting and unexpected.

INTRODUCTION

The hypervelocity impact of a compact projectile with a plate target will shatter the projectile and produce a divergent cloud of debris. If a second plate is placed a short distance behind the first plate then this second plate will be cratered, holed, spalled or bent by the combined effect of many closely spaced impacts. However, if the second plate is placed a very large distance behind the first plate, the debris can spread out sufficiently so that the debris fragments produce independent craters. This configuration was used to measure the size and trajectory of the debris fragments.

DEBRIS CHARACTERIZATION STUDY

For the study presented here the second plate (1100-F aluminum witness plate) was 72 projectile diameters from the first (2024-T3 aluminum shatter plate). The soft aluminum witness plate assembly consisted of a rigid outer "window frame" and a central plate which was free to move as a pendulum, allowing a measurement of plate velocity and momentum (see Fig. 1). The projectile was an L/d = 1 cylinder, made of solid 2024-T3 aluminum (2.77 g/cc), solid graphite epoxy (1.55 g/cc) or 2024-T3 aluminum with multiple holes to reduce the average density to match the graphite epoxy (see Fig. 2).

By measuring the fragment cloud velocity, V_x, and the volume of each crater, V_c, the approximate mass of each fragment, m_k, was determined from the known relationship of crater volume to fragment energy

at that particular velocity (see Fig. 3). The crater location was also measured (see Fig. 4). The impact tests therefore yielded the measurements of fragment size, velocity and trajectory for tens to hundreds of fragments. The fragment sizes included particles as small as 0.1% of the original projectile mass. The appearance of the debris cloud and the independent craters on the witness plates are shown in Figs. 5 and 6.

The experiments were conducted at the Naval Research Laboratory using a two stage light gas gun. The test conditions are summarized in Table 1. The test matrix included three thicknesses of shatter plate (0.1 mm, 1.0 mm, and 9.9 mm) and two impact velocities (low velocity is about 3 km/s and high is around 6 km/s). Three of the 10 small-scale tests were repeated at 2.5 times the scale and are included in Table 1 as shots 3-16-89 thru 3-18-89. All tests were at normal incidence except tests 2-539 and 2-541 for which shatter plate was placed at an impact angle of 30°. The ratios of target to projectile momentum are also presented in Table 1. The ratio is approximately 1 for most cases. However, for the few tests with a thick shatter plate, the values of the ratio are less than those of the other tests, probably the result of increased debris dispersion such that a smaller fraction of debris was intercepted by the central plate.

Projectile Fragmentation

Figures 7-14 show the projectile fragmentation resulting from the small scale tests. The fragments were sorted decreasingly by mass and are presented in a log-log plot so that the large fragments are emphasized. The steep drop-off toward the end of the plots may reflect the inherent errors of the measuring process in which some measurable craters were discarded. A power law fit gave the best representation of size distribution. For high speed impact (6 km/s) the multi-hole (complex) aluminum projectile produced the largest fragments and the graphite epoxy the smallest fragments (see Fig. 7). The appearance of the debris cloud from the complex projectile test suggests that the fragments are long shards that are characteristic of the projectile structure (see Fig. 8). The empty spaces in the complex projectile have attenuated the impact shock so that the large pieces of projectile could survive impact with the shatter plate. The significance of the large fragments is displayed in Fig. 9. For instance, the mass of the four largest fragments consists of 56% of the total fragment mass accounted for, and is equivalent to the mass of the largest 43 fragments of the solid aluminum projectile. In comparison, the solid aluminum projectile shattered into fragments of more uniform size than those of the complex projectile, as indicated by the gradual rise in the cumulative mass. In general, the uniform fragments of the solid aluminum projectile will create larger craters per unit mass than the shards produced by the complex projectile. The values of fragment mass in Fig. 7 for the complex projectile are likely to be low estimates because the calculation of fragment mass from Fig. 3 assumed the fragments were spheres. The cumulative mass curve for the complex projectile in Fig. 9 should therefore be higher and should not cross the solid aluminum projectile curve.

As the impact speed decreases, the degree of projectile shatter decreases. Figure 10 shows that the low velocity projectiles generally shattered into larger fragments than those at high speed. In this case the solid aluminum generated the largest fragment instead of the complex aluminum as was the case for high speed impact. In Fig. 11, the cumulative mass of both aluminum designs exceeds the original projectile mass (6 g). The additional mass may: 1) be generated from the shatter plate material; 2) represent the effect of local bulging in the thick central witness plate which results in a larger crater volume than for a semi-infinite target.

Figure 12 demonstrates the effects of impact speed on the fragment recovery. The amount of projectile mass identified increases as the impact speed decreases. Only 25% of the aluminum projectile mass was accounted for at 6 km/s but nearly all the mass was found at 3 km/s. The measured graphite epoxy mass was much smaller: 6 and 33% respectively at the two velocities. Therefore, regardless of impact speed, the graphite epoxy is still most sensitive to the pulverization effects among the three projectiles. Despite the gross differences in measured residual fragment mass, the ratio of target momentum to initial projectile momentum was approximately the same for graphite expoxy and aluminum projectiles.

Large variations in the shatter plate thickness produced large variations in the characteristics of the debris cloud. Figures 13 and 14 compare the projectile fragmentation resulting from the high velocity impacts of the graphite epoxy projectile into shatter plates of the three thicknesses. The impact with the thin shatter plate placed at an impact angle of 30° was sufficient to shatter the projectile but did not disperse the debris (see Fig. 15). As a consequence, the projectile debris produced a large crater in the central witness plate. The projectile mass attributable to this crater was 88% of initial projectile mass. The remaining 51 measured craters were produced by the fragments which made up 4% of projectile mass. In contrast to the thin plate impact, the impact with the thick plate appeared to consume the projectile and produced a cloud of highly dispersed aluminum plate fragments. Figure 5 shows the amount of dispersion by comparing the total size of the debris cloud with the fraction of the cloud subtended by the 31° and 60° angles representing the approximate portions of the debris cloud intercepted by the central witness plate and total witness plate areas respectively. The dispersion reduced the impulse delivered to the central witness plate to about 1/3 the value observed for the medium thickness shatter plate test. As shown in Fig. 14, the total cumulative fragment mass for the thick plate test is substantially greater than that for the medium thickness plate impact because the debris cloud for the thick plate impact was mostly plate fragments.

Projectile Skew Angle and Debris Pattern

Table 1 reports the projectile skew angle (the angle between the trajectory and the projectile axis) and the projectile polar angle, P_1 , (the angle between the horizontal line on the witness plate and the projection of the projectile axis onto the witness plate). A similar orthogonal polar angle, P_2 , was observed for the distribution of craters on the witness plates. Most of the tests produced an impact pattern which exhibits an axis of symmetry. It was further observed that this axis of symmetry was nearly orthogonal to the projectile polar direction. That is, the largest debris fragments spread out in a direction normal to the projectile axis. An example of the polar angles is illustrated in Fig. 16. The differences between these angles, $|P_1 - P_2|$, are also included in Table 1. A cursory examination of the witness plates suggests that the line of craters defining the polar angle, P_2, on the witness plate is displaced from the trajectory in the direction of the projectile axis. Apparently the impact of the skewed projectile with the shatter plate is generating an asymmetrical radial impulse on the debris and pushing the debris in the direction of the projectile polar angle.

Dispersion of Debris

The spatial distribution of the debris on the witness plates is described in Figs. 17 - 24. For high speed impact, the fragments from the graphite epoxy impact dispersed by the largest amount among the three projectiles (see Fig. 17). For instance, 70% of the identified fragment mass from the graphite epoxy impact is spread over an area 15 times the area occupied by the complex aluminum fragments, and 3 times the area occupied by the solid aluminum. However, as the impact speed decreases, the dispersion also decreases as shown in Fig. 18. In this case, the same amount of the identified mass from the graphite epoxy impact is concentrated in an area of only 1/8 the area occupied by the fragments from high speed impact. The big steps at the steep portion of the curves reflect the concentration of the large fragments around the center of the witness plate.

Along with projectile design and impact speed, the shatter plate thickness also influences the dispersion of the debris cloud. Figure 19 indicates that debris cloud dispersion increases as the thickness of shatter plate increases. For a thick-plate impact, the type of projectile does not have much effect on the dispersion characteristics of the debris clouds, as demonstrated in Fig. 20.

Figures 21-24 show the distribution of the fragments in terms of population density (mass per unit area) as a function of the dispersion angle. The sampling technique involved the division of the entire witness plate area into 15 equal circular areas (see Fig. 3). A large number of rings would increase the fluctuations of the data (as the ring area becomes small, the number of craters also becomes small). The

lack of a data point for some sampling areas indicates that there no craters exist within that particular sampling area. For most cases, the test results exhibit a higher level of fragment concentration toward the center of the witness plate, with the exception of the thick plate impacts in which the concentration is relatively low at the center and near the edge of the witness plate. Thus, the thick plate results are smoothest. Part of the reason for the chaos is the asymmetry in the fragment distribution due to the projectile yaw.

Scaling

Figures 25-27 show the scaling effects on the projectile fragmentation by comparing the results of the small scale impact with those of the large scale impact (2.5 times small scale test). The comparisons indicate that the tests scale fairly well, especially the multi-hole aluminum projectile tests. However, there exists some disagreement in scaling, which may be due to the differences in projectile yaw.

CONCLUSIONS

The debris cloud observations obtained from the 13 impact tests lead to a number of conclusions, some expected based on data from other hypervelocity impact tests, but some results lead to unexpected conclusions.

1. As expected, increased impact velocity causes increased debris dispersion. The sharp reduction of identified fragment mass from 100% (aluminum projectiles) to 25% due to a doubling of the velocity is more than we expected. The normalized impulse to the central witness plate was about the same at the two velocities, suggesting that most of the mass does strike the central witness plate at both low and high velocity. An extrapolation of the population distribution plots of Fig. 7 would seem unlikely to yield the missing mass. The most probable explanation is that the very small fragments (< 1 mg) were decelerated by the 4 - 9 torr residual atmosphere and therefore did not have sufficient energy to produce craters. The observed motion of the witness plate may be due to the motion of the air between the shatter plate and central witness plate (this volume would contain about 3 g of air).

2. The effect of plate thickness on debris dispersion was generally expected. The amount of indicated fragment mass observed for the two thick target tests, 2 g, seems low, given the amount of plate and projectile debris generated, 60 g. However, some of the debris is ejected uprange and, as indicated by Fig. 5, much of the debris mass is dispersed by such a large amount that it misses the witness plate. Still, the indicated fragment mass is only 3% of the initial 60 g.

The results obtained with the thin shatter plate are interesting. Despite the fact that the projectile was completely shattered (see Fig. 15), the debris was not dispersed and the debris produced a single crater that corresponded to the impact of a solid projectile into a semi-infinite target. Although the description of the data presented here identifies one fragment mass for each crater, it is likely that most of the large craters are produced by several debris particles. However, since the end use of an impact model will be predictions of target damage, the ascribing of the damage effect of several particles to a single large particle would appear to be meaningful for most impact model applications.

3. The effect of projectile design on debris cloud properties was also expected. Previous tests with sub-scale models of space based interceptors (complex projectiles) have demonstrated that thin plate impact produces large debris particles. Further, tests with sintered projectiles have demonstrated that plate impact produces dust size particles, similar to the result observed with the graphite epoxy projectile.

The effect of projectile orientation on debris distributions was unexpected. Projectiles that had large skew angles generated debris clouds for which the largest fragments were distributed in a direction normal to the projectile axis. This results in a string of craters on the witness plate. Further, this string of craters does not contain the intersection of the original trajectory with the witness plate. Instead, the string lies

a short distance from this intersection, in the direction of the nose of the projectile.

Table 1. Impact conditions for debris characterization tests.

TEST #	TARGET	PROJECTILE					RESULTS			
	Shatter plate thick. (mm)	Mat.	Density (g/cc)	Mass (g)	Initial vel. (km/s)	Skew angle (deg)	Polar angle P_1 (deg)	Polar angle P_2 (deg)	$\lvert P_1-P_2 \rvert$ (deg)	Mom. ratio M_t/M_p
2-539	0.1	Gr/Ep	1.55	5.8	5.70	36	41	---	---	---
2-534	1.0	Gr/Ep	1.55	6.0	6.14	86	91	---	---	0.84
2-535	1.0	Al	1.55	5.8	5.84	51	157	63	94	0.99
2-533	1.0	Al	2.77	5.9	5.75	17	---	---	---	---
2-537	1.0	Gr/Ep	1.55	5.9	2.84	69	87	177	90	0.94
2-543	1.0	Al	1.55	5.9	2.82	41	152	65	87	1.02
2-545	1.0	Al	2.77	5.9	2.85	52	104	---	---	1.15
2-541	1.0	Al	1.55	5.9	5.94	38	115	55	60	0.76
2-536	9.9	Gr/Ep	1.55	5.9	5.80	33	13	---	---	0.30
2-542	9.9	Al	1.55	6.0	5.9	---	---	---	---	0.43
3-16-83	2.5	Al	2.77	95.8	5.84	31	6	110	104	---
3-17-89	2.5	Gr/Ep	1.55	72.9	5.89	18	51	135	84	---
3-18-89	2.5	Al	1.55	93.0	6.05	40	164	71	93	---

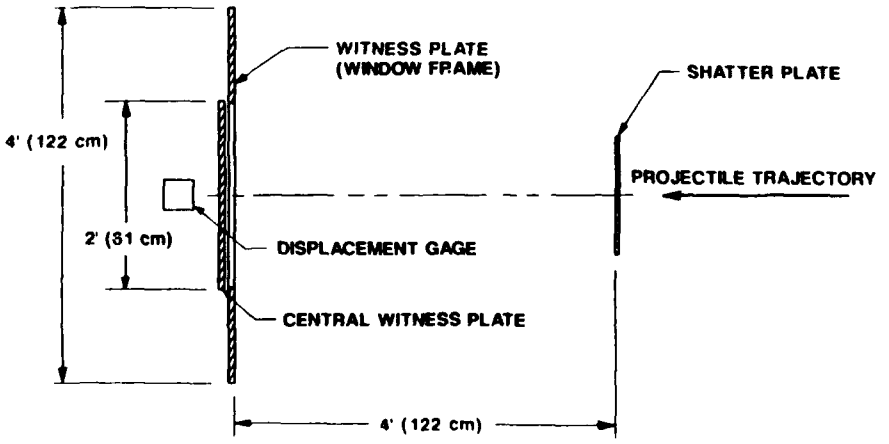


Fig. 1. Target layout for small scale tests (side view)

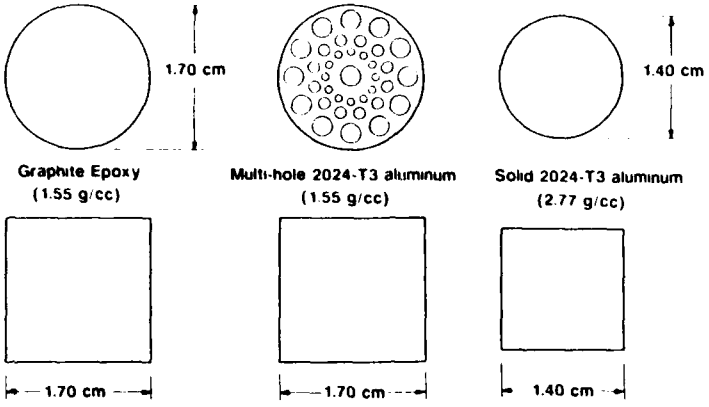


Fig. 2. Projectile designs (small scale dimensions)

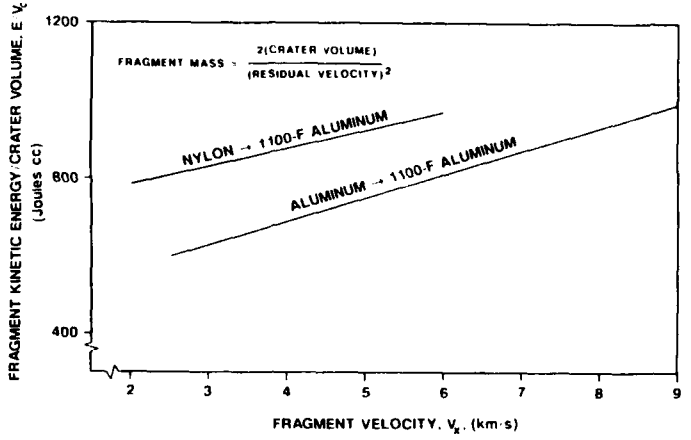


Fig. 3. Sphere impact into semi-infinite target.

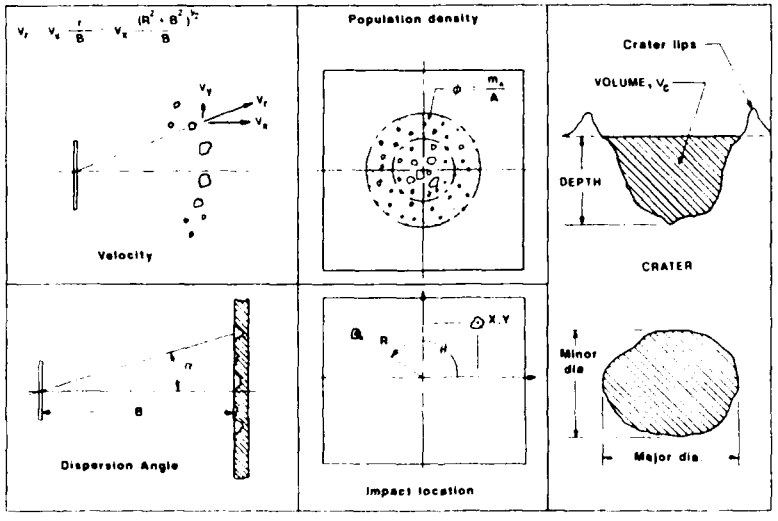


Fig. 4. Data reduction technique.

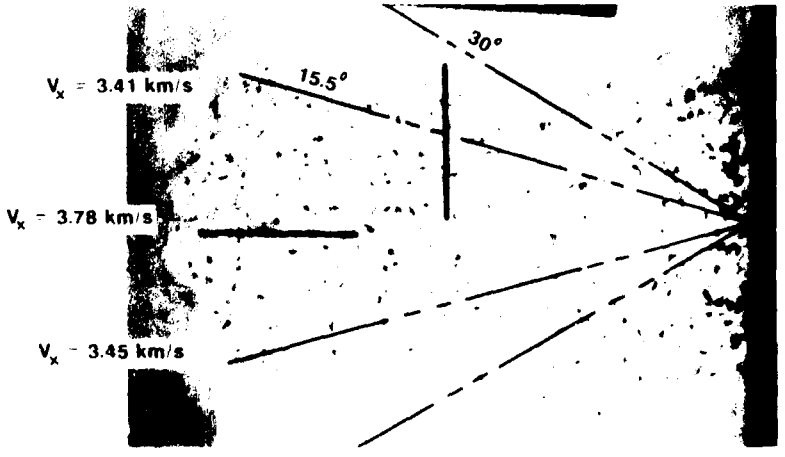


Fig. 5. Shell debris cloud (Gr/Ep into al. target)

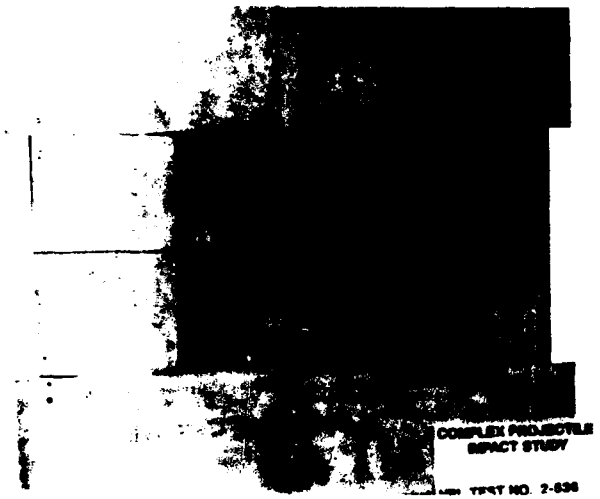


Fig. 6. Independent craters on soft aluminum witness plate.

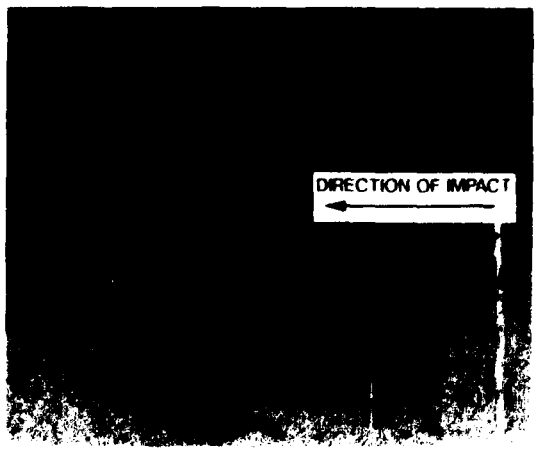


Fig. 8. Debris cloud from the impact (6 km/s) of complex aluminum projectile with a 1.0 mm thick al. plate.

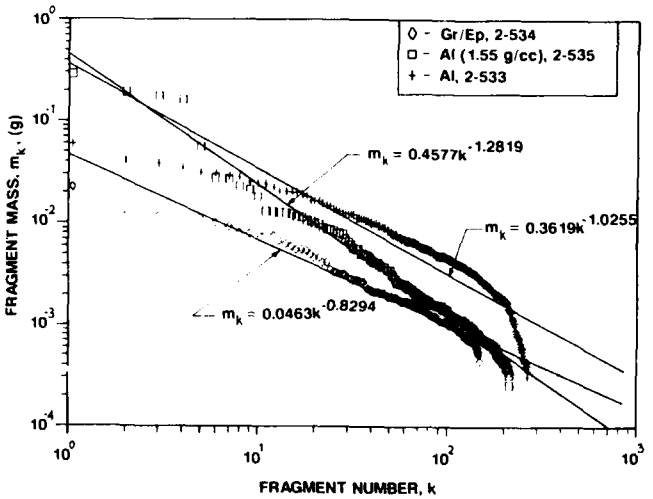


Fig. 7. Projectile fragmentation (impact at 6 km/s into a 1.0 mm 2024-T3 al. plate.).

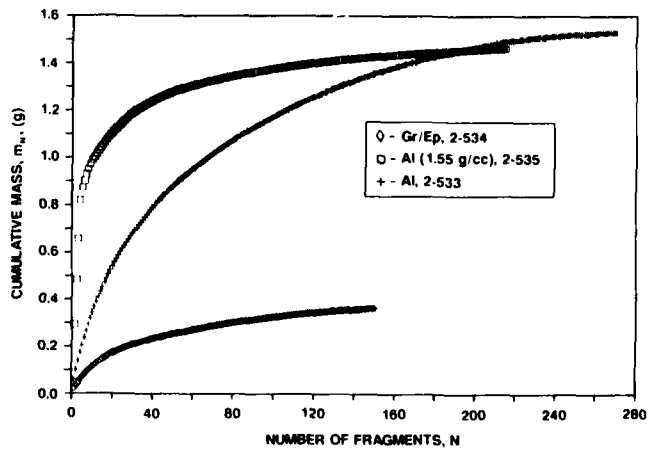


Fig. 9. Fragment mass determined from the high speed impact into a 1.0 mm thick aluminum plate.

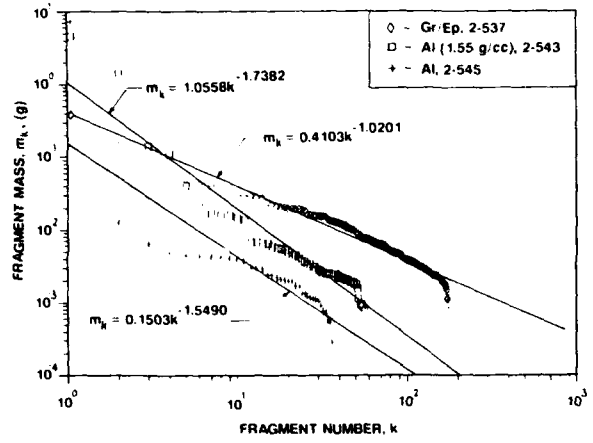


Fig. 10. Projectile fragmentation from low speed impact (3 km/s) into a 1.0 mm aluminum plate.

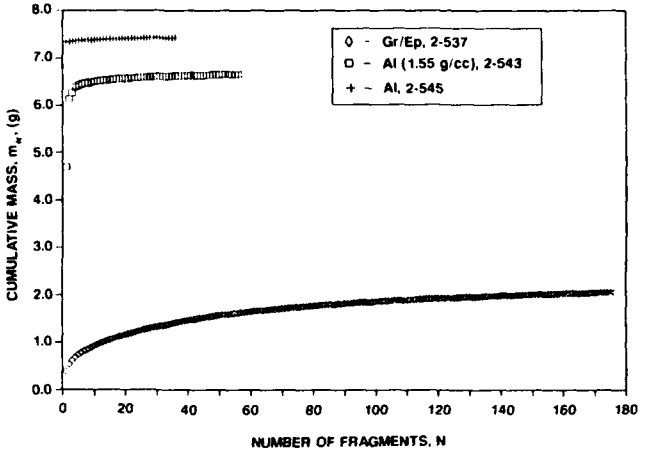


Fig. 11. Fragment mass determined from low speed impact (3 km/s) into a 1.0 mm thick aluminum plate.

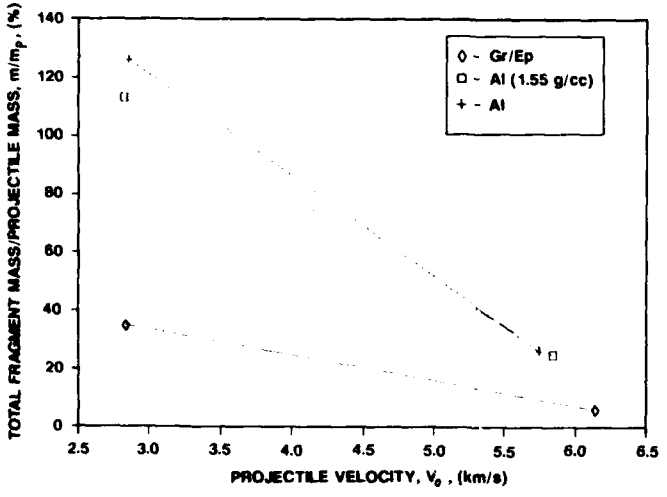


Fig. 12. Effects of impact speed on total fragment mass determined. Shatter plate: 1.0 mm thick aluminum.

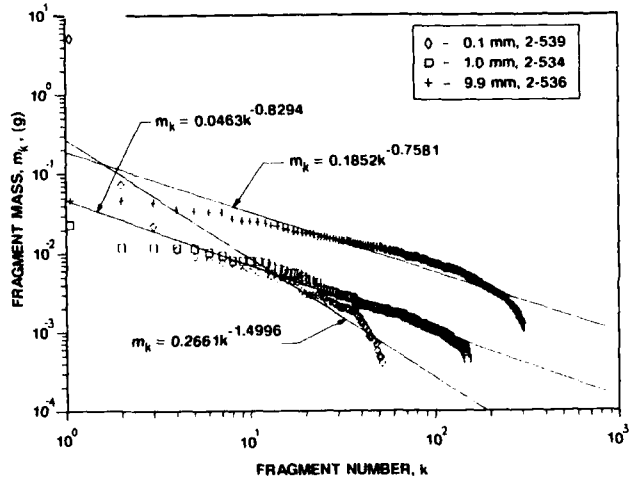


Fig. 13. Effects of plate thickness on projectile fragmentation (Gr/Ep projectile at 6 km/s).

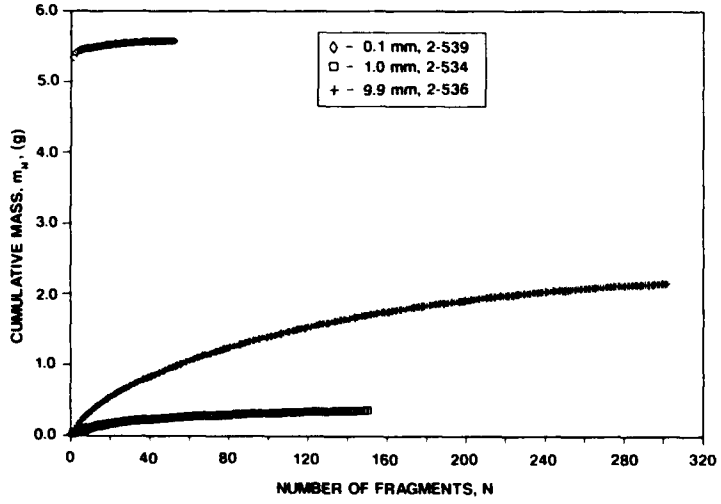


Fig. 14. Effects of plate thickness on total fragment mass determined. (Gr/Ep projectile at 6 km/s).

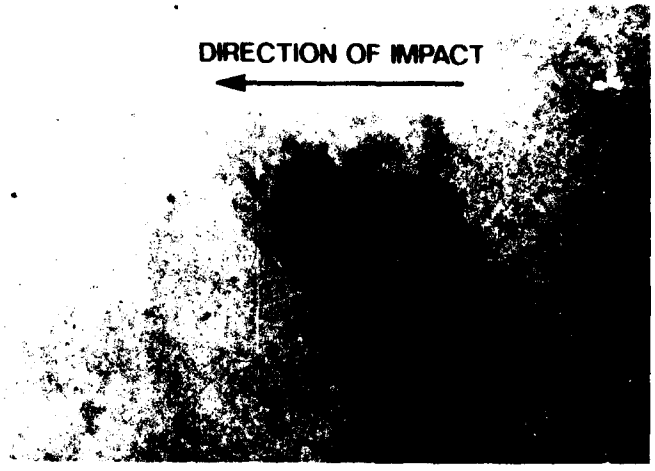


Fig. 15. Fragments of Gr/Ep projectile after impact at 6 km/s into a 0.1 mm thick al. plate (test 2-539).

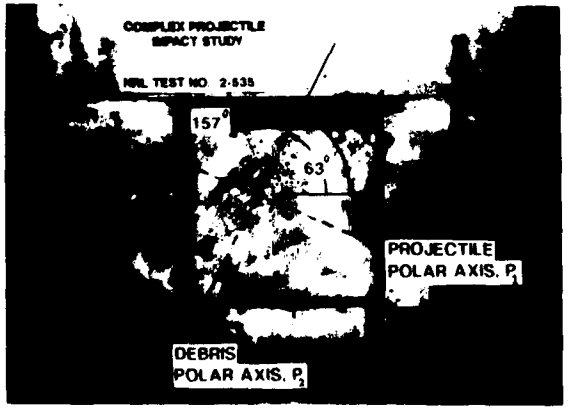


Fig. 16. The relationship of debris cloud distribution with the projectile skew angle.

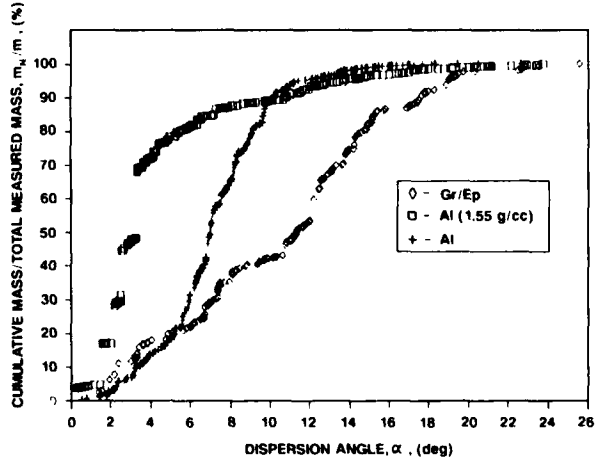


Fig.17. Distribution of debris from high speed impact (6 km/s) into a 1.0 mm thick aluminum plate.

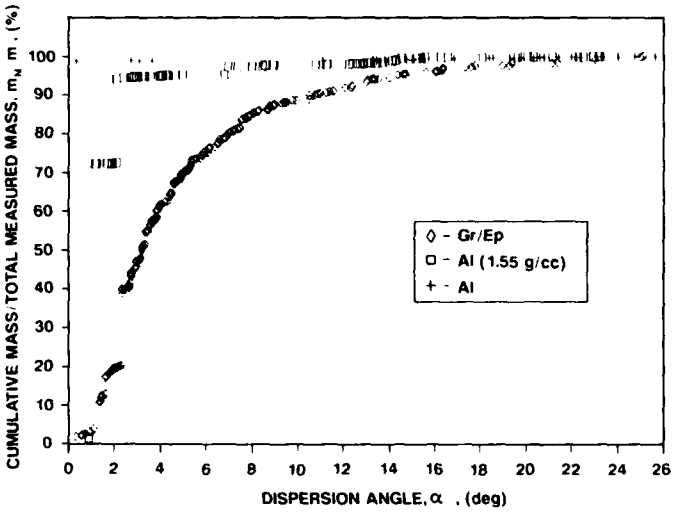


Fig. 18. Dispersion of debris from low speed impact (3 km/s) into a 1.0 mm thick aluminum plate.

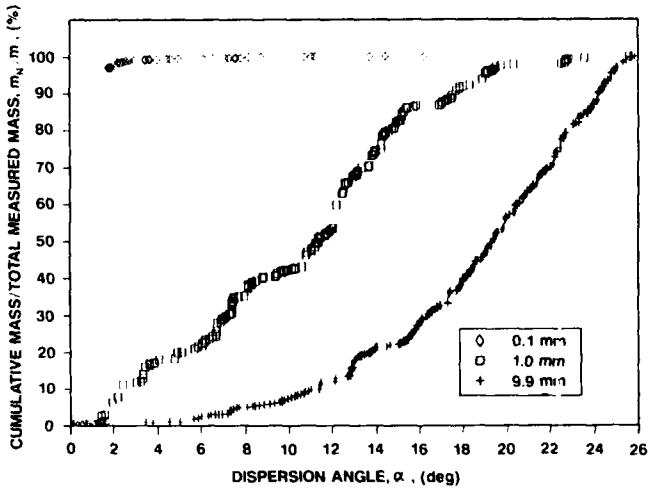


Fig. 19. Effects of shatter plate thickness on the dispersion of the debris cloud (Gr/Ep projectile at ó km/s).

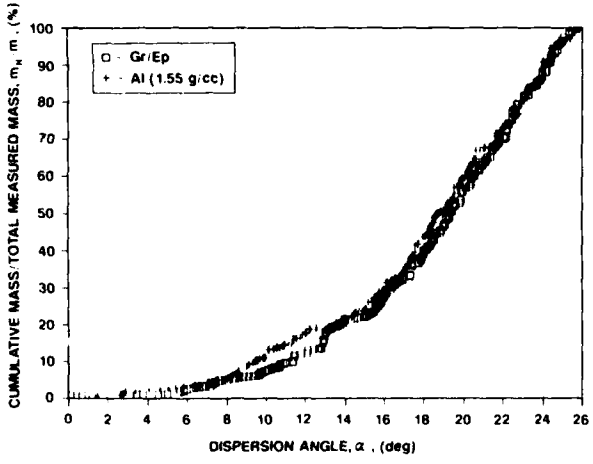


Fig. 20. Dispersion of debris from the thick plate impact (10.0 mm thick aluminum, V = 6 km/s).

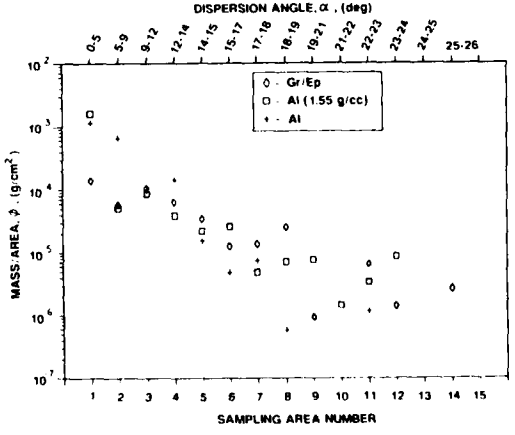


Fig. 21. Spatial concentration of debris from high speed impact into a 1.0 mm thick aluminum plate.

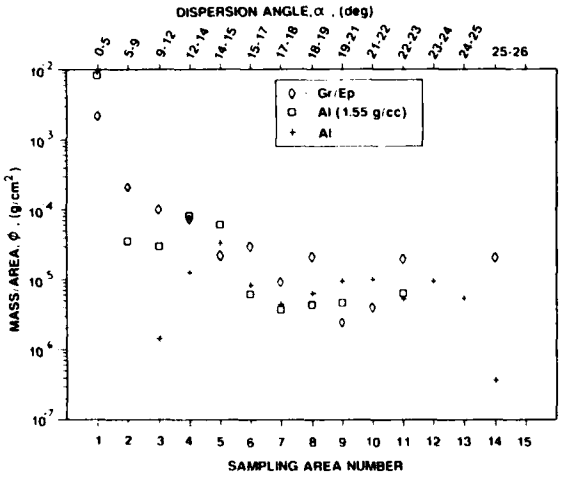


Fig. 22. Spatial concentration of debris from low speed impact (3 km/s) into a 1.0 mm thick al. plate.

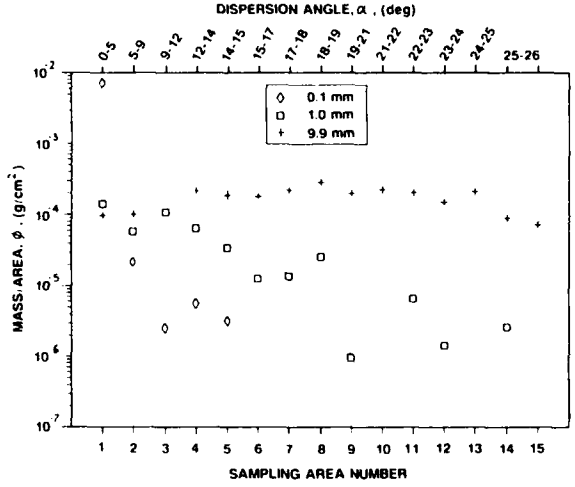


Fig. 23. Effects of plate thickness on the spatial concentration of debris (Gr/Ep projectile at 6 km/s).

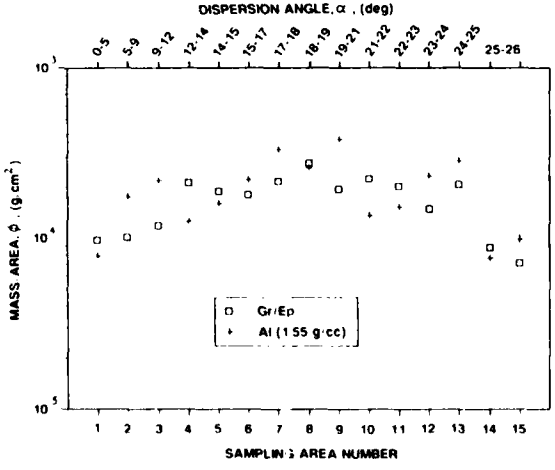


Fig. 24. Spatial concentration of debris from thick plate impact (10.0 mm thick, V = 6 km/s).

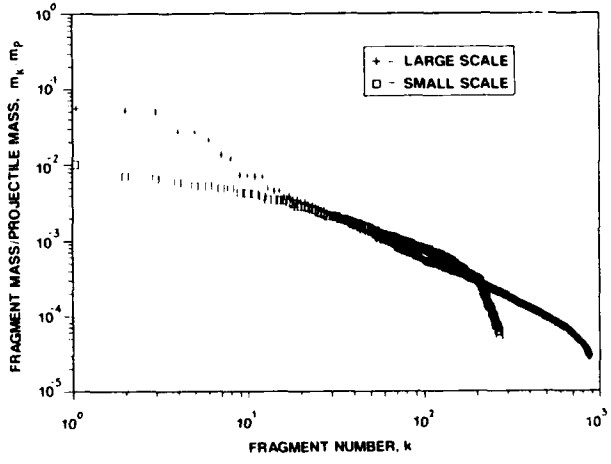


Fig. 25. Effects of scaling on the fragmentation of the solid aluminum projectile.

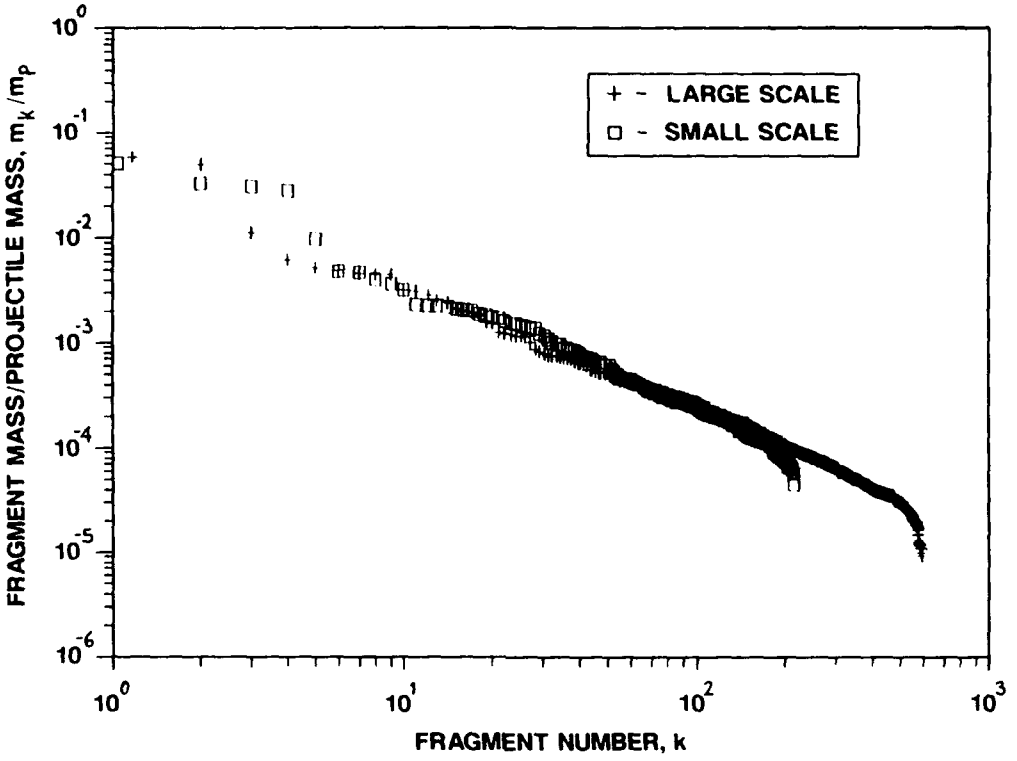


Fig. 26. Effects of scaling on the fragmentation of the complex aluminum projectile.

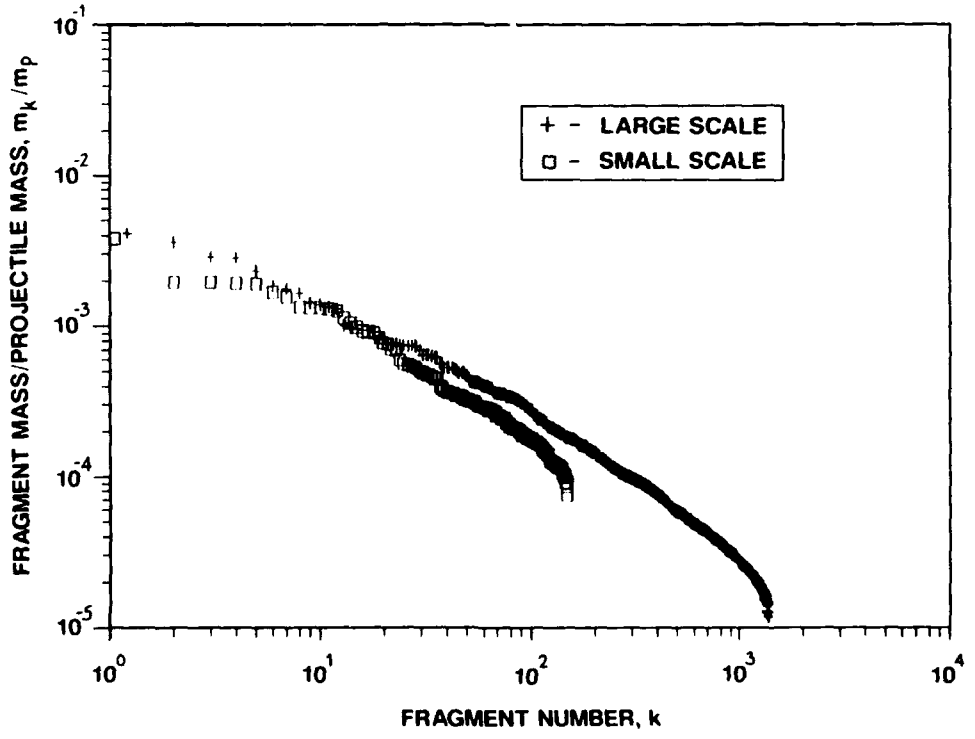


Fig. 27. Effects of scaling on the fragmentation of the Gr/Ep projectile.

Int. J. Impact Engng Vol.14, pp.619–630, 1993
Printed in Great Britain

0734-743X/93 $6.00+0.00
Pergamon Press Ltd

HYPERVELOCITY LAUNCH DYNAMICS

E. M. SCHMIDT, B. J. HELD, and D. S. SAVICK

Weapons Technology Directorate, U.S. Army Research Laboratory
Aberdeen Proving Ground, MD 21005-5066

ABSTRACT

The launch dynamics from a generic hypervelocity cannon are considered over the velocity range from 1500 through 3500 m/s. Both fin and flare stabilized projectiles are examined for the influence of in-bore dynamics, muzzle blast, sabot discard, and free flight aerodynamics upon their trajectory. Computations are performed using codes developed and validated for conventional cannon with ordnance muzzle velocities (approximately 1700 m/s). While the extension into the hypervelocity regime is not supported by experimental data, this initial study is intended to aid in defining potential problem areas.

INTRODUCTION

Hypervelocity offers the promise of improved terminal performance and reduced time of flight to the target. However, there is an associated burden of achieving adequate launch conditions both in terms of projectile integrity and dynamics. The latter are of particular interest in defining overall system accuracy. Considerable effort has been expended to describe the launch dynamics of conventional cannon. The present paper will apply some of these techniques to hypervelocity launchers.

Launch consists of a sequence of coupled mechanical and gasdynamic interactions leading up to free flight of the projectile. Since the launch tube provides a guide for the projectile, both its static and dynamic characteristics are of interest. Even statically, the tube is not perfectly straight. It has curvature associated with manufacturing, gravity, and thermal gradients. Dynamically, the tube responds to the chemical or electromagnetic forcing function, the moving projectile, and its own recoil/attachment fixtures. As the projectile accelerates along the distorting gun tube, it is subject to lateral loads that produce not only rigid body motion (balloting) but also excite internal vibration of the round. At the muzzle, the

projectile disengages from the gun tube and passes the muzzle region which for a conventional cannon consists of the reverse flow of the muzzle blast while for an electromagnetic cannon includes the processes associated with the interruption of the current path. Subsequently, kinetic energy projectiles must discard their sabots. During this process, both mechanical and aerodynamic interactions are experienced. Finally in free flight, the trajectory is still subject to perturbations associated with yawing motion (aerodynamic jump) and asymmetry.

A two-dimensional, finite difference model developed by Erline and Kregel (1990) is used to predict projectile/gun dynamics. The muzzle blast interaction is estimated using the analytic approach of Schmidt et al. (1977), while sabot discard is calculated using the semi-empirical treatment of Siegelman et al. (1983) Finally, free flight perturbations are handled with methods of Murphy and Bradley (1959) and Murphy (1963). It was necessary to place restrictions on the scope of the study. No attempt is made to perform a realistic system analysis; rather, the intent is to ascertain the nature of changes to the predicted launch perturbations as velocity increases into the hypervelocity regime. For this reason the gun tube, projectile, and sabot designs are fixed across the velocity range considered (1500 through 3500 m/s). The gun tube is 7.0m long and has a 120mm bore diameter. The tube length was selected as a compromise between maximum acceleration and practicality. The round is a saboted, steel rod which can be either fin or flare stabilized, Fig. (1), and represents two versions of a training projectile considered for use with the U.S. 120mm tank cannon. The round is not designed to survive the increased pressure or acceleration of the high velocity cases; however, structural integrity is neglected in favor of obtaining a straightforward comparison of transverse perturbations. Obviously, an improved simulation would require better definition of the lethal mechanism, its target, and the launch system available.

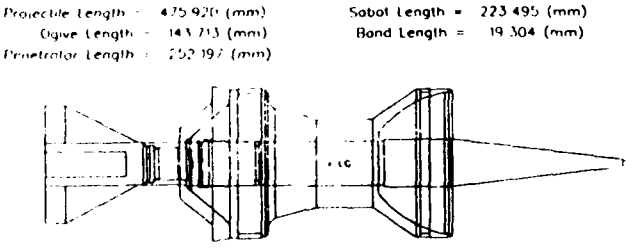


Fig. 1a. Fin Stabilized Training Projectile

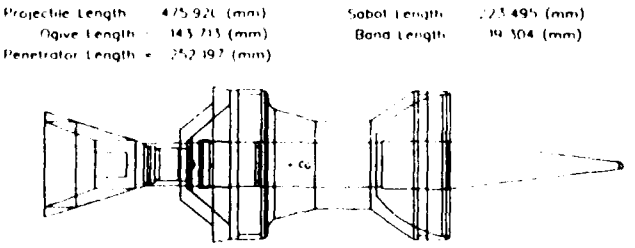


Fig. 1b. Flare Stabilized Training Projectile

IN-BORE DYNAMICS

In-bore dynamics are calculated in the vertical plane using the 'Little Rascal' code (Erline and Kregel, 1990) which is a two-dimensional finite element model employing a direct transient analysis approach. Both the barrel and projectile are modeled utilizing a series of equally spaced cylindrical elements, nodes of which are assigned equivalent mass and spring stiffness values. Inertial forces as well as barrel flexure forces can then be calculated using this simplified description. Flexure at each node is approximated by a second order difference method permitting bending forces to be computed. In addition to forces produced by flexure of the barrel, there are those from pressure effects, mounting characteristics and projectile/barrel interactions. The projectile is assumed supported in the tube by two elastic springs representing the sabots. The stiffness of the springs are determined experimentally (Lyon, 1992). All forces are integrated by a predictor-corrector technique stabilized by a numerically stiff ordinary differential equation solver.

In its application to hypervelocity launch, the code may have certain deficiencies. First, the projectile and sabots are treated as a solid body; thus, discontinuous interfaces between various components are not considered. Under severe acceleration loads, large deformations may occur and this approximation will no longer be valid. In addition, the code assumes linearly elastic behavior. As will be seen from the output, this assumption is not unreasonable as far as lateral deformations are concerned. High longitudinal velocity does not necessarily translate into large lateral deformation; although, the associated longitudinal accelerations may be sufficient to move the bodies into the plastic regime.

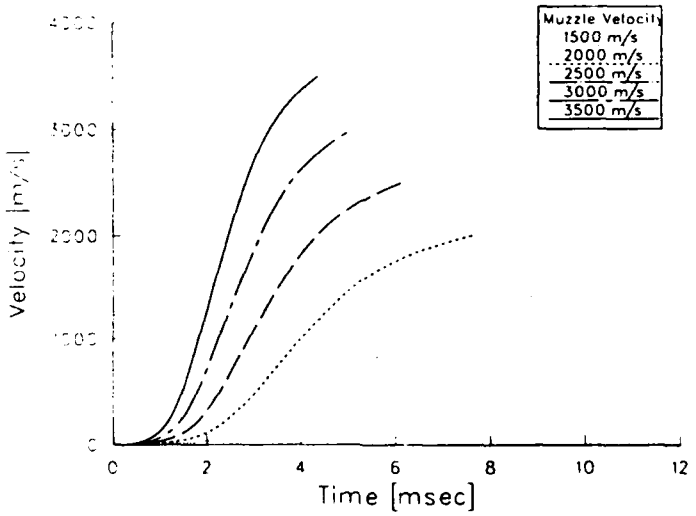


Fig. 2. Interior Ballistics Velocity Profiles

'Little Rascal' requires as input the projectile in-bore velocity profile which is used to define position along the tube and breech pressure histories. The position information is compared with a description of the tube centerline profile to define variation in

lateral constraint, while the breech pressure is used to calculate the weapon recoil. For the present purposes, the pressure can be assumed to result from gas generation or electromotive forces. It is recognized that at 3500 m/s the system is approaching the limit velocity for conventional gas expansion systems other than traveling charge concepts. A similarity approach was selected to describe the velocity profiles over the range of interest. The known interior ballistics of the training projectile is used to define the function, $v/V_m = f(x/L)$, and expanded for different muzzle velocities, Fig. (2). Even with a 7.0m long tube, peak breech pressure levels for V_m = 3500 m/s reached 11,500 bar while the maximum projectile acceleration was 165,000 g. The code also requires a centerline profile of the gun tube. A profile was created for the current tube by repeating the pattern of manufacturing irregularities of a production 120mm tank cannon over a length of 7.0m. The gun tube was supported near the breech with two bearings separated by 2.0m. The mass and stiffnesses of the gun tube nodes, as well as gun tube droop due to gravity, are calculated by Rascal from a user defined geometry. For the 7.0m tube, the wall thickness was defined to be the same for all cases and equal to that required to survive the highest velocity launch. This means that the droop under gravity is constant for all cases.

Calculations were made at 500 m/s intervals over the velocity range of interest. For comparison purposes, the dynamic response of the forward portion of the projectile, where the sabot is most flexible, is selected. In Fig. (3), the lateral motion of the projectile tip is presented. The data extend from shot start through exit of the projectile from the tube. Clearly, for higher velocities the in-bore residence time is shorter. Initially, the tip is quiescent; however this is followed by a build up of displacement as the projectile accelerates. Surprisingly, the frequency and amplitude of the tip motion as the projectile approaches exit does not vary dramatically as velocity increases. There are more cycles and the growth of the oscillation is more gradual for the lower velocity cases, but the final states are remarkably similar.

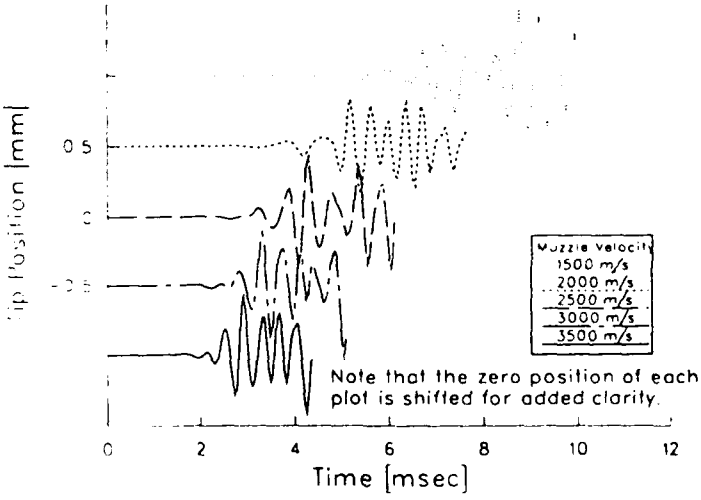


Fig. 3. Projectile Tip Motion

The angular orientation of the projectile, defined as the angle between the center of the projectile at the front and rear bore riding surfaces, is presented in Fig. (4). The angular orientation is dominated by the gravity droop of the tank cannon. The Rascal code rotates the gun tube so that the muzzle of the cannon has zero slope initially. This means that the cannon is rotated up to account for gravity droop. The plot of projectile angle reflects this rotation in that the projectile starts with an angle of 1.25 milliradians and moves toward zero. Superimposed upon this large scale variation are oscillations of a significantly higher frequency.

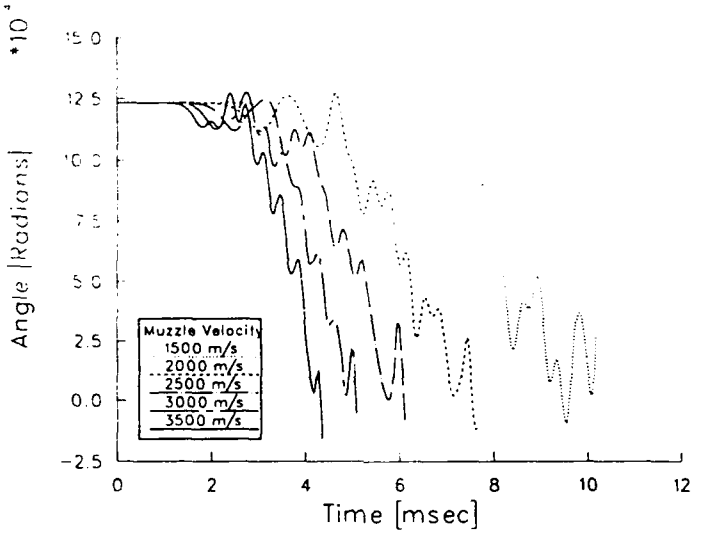


Fig. 4. Projectile In-Bore Angular Orientation

These are better observed in the projectile angular velocity variations, Fig. (5). In all cases, the angular velocity of the projectile varies at approximately 1.7 kHz by shot exit. Again, the amplitude is similar across velocities. For the highest velocity cases, a negative trend for the mean angular velocity is observed reflecting the gravitational curvature of the gun tube.

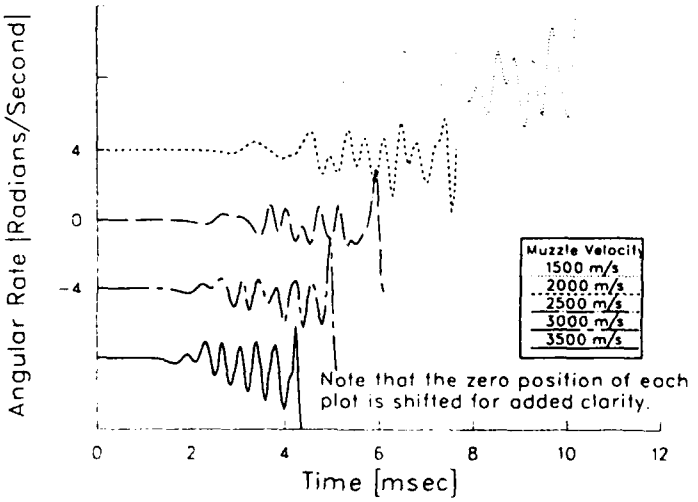


Fig. 5. Projectile In-Bore Angular Velocity

In summary, while there are differences in the transverse response of the projectile with velocity, none appear catastrophic to the structural integrity of the projectile or in the launch conditions at shot exit. This must be caveated with the fact that while the model has been validated in terms of its ability to predict gun dynamics, no data were available describing projectile response.

MUZZLE BLAST

Weapons using chemical propulsion such as traveling charge or electrothermal chemical systems will undoubtedly generate a muzzle blast flow. On the other hand, the discharge at the muzzle of electromagnetic guns will vary depending upon whether it is a rail gun with arc or armature current path or a coil gun. Within the scope of the present study, the analysis is limited to the chemical systems.

Two distinct flows form at the muzzle of a gun (Schmidt and Shear, 1975). The precursor consists of air and leakage propellant gases ejected from the tube ahead of the projectile, while the propellant gas flow begins when the obturator clears the muzzle and releases the high pressure propellant gases. The relative strength of the two is dependent upon the design of the gun and the interior ballistics of the round. Typically, the propellant gas flow is dominant. As these gases expand, they accelerate to velocities greater than that of the projectile so that the round initially sees a relative flow from the rear rather than from the front. As the gases decelerate through a series of shock waves, the projectile passes into normal forward flow of undisturbed air.

Methodology has been developed to treat the muzzle blast loads to fin stabilized projectiles fired at ordnance velocities (Schmidt et al., 1977). Essentially thin airfoil theory is coupled to a description of the propellant gas exhaust flow as an underexpanded supersonic jet plume to arrive at the following expression for trajectory deflection due to muzzle blast:

$$\frac{\Theta_{mb}}{p^* \alpha} = \left[1 + \left(\frac{C_{L_\alpha}}{C_{M_\alpha}}\right)\left(\frac{\Delta_{mb}}{l}\right)\right](\gamma + 1)\pi AD \frac{\bar{P}}{2mV_m^2} \qquad [1]$$

which again is valid only for fin stabilized projectiles.

Since flare stabilized projectiles present a bluff base to the reverse flow, the perturbation due to muzzle blast should be significantly less than that for finners. Exit pressure and angle of attack are taken to the left hand side of Eq. (1) to increase the general applicability of the relationship. The terms on the right hand side are all properties of the projectile and its launch velocity or Mach number. It is worth noting that the velocity squared appears in the denominator. The value of the expression in Eq. (1) is plotted over the range of velocities of interest in Fig. (6).

At low velocities, the perturbation can be quite large because there is both an in-bore and out of bore contribution to the exit process. As velocity increases, the magnitude of the disturbance decreases because the projectile rapidly moves through this region. A broad minimum occurs at between 800 and 1500 m/s after which the disturbance to the trajectory begins to grow. This increase is mainly due to the diminishing effectiveness of the fins with increased velocity, a subject that will be treated in more detail in a subsequent section. A peak occurs at around 2000 m/s followed by continued decrease with increasing velocity. For existing tank cannon, the dispersion in point of impact due to muzzle blast has been shown (Schmidt et al., 1977) to be an order of magnitude lower than the measured system dispersion. It is to be expected that for hypervelocity launch, assuming reasonable levels of launch angle of attack and muzzle pressure, that the factor of two growth in the trajectory perturbation factor seen in Fig. (6) will not dramatically alter this conclusion.

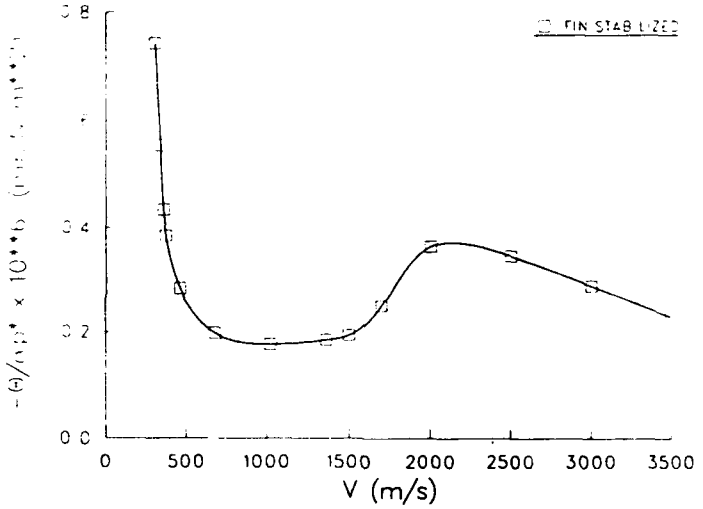


Fig. 6. Muzzle Blast Induced Jump

SABOT DISCARD

A semi-empirical model of the sabot discard process has been developed by Siegelman, et al. (1983). It estimates both the dynamics of the sabots and the resultant mechanical and gasdynamic impulse imparted to the projectile by the discard process. To start the program, initial conditions for each of the components is required. Kietzman, et al (1992), present predictions of the linear and angular velocity of sabot components following launch from a 120mm cannon. The angular velocity varies from 0 through 40 rad/s depending upon the weapon considered and the relative orientation of the sabot component. For purposes of the present exercise, it is assumed for all velocities considered that one sabot component has a nose up pitch rate of 20 rad/s while the other two components have a zero rate.

The resulting sabot induced impulse to the projectile is shown in Fig. (7) for the fin stabilized case. The code is not currently configured to treat a flare, but it will be assumed that the impulse is roughly equal to that of the finner. The impulse is seen to increase by more than a factor of two with velocity from 1500 to 2000 m/s, after which it continuously decreases.

Both the linear and angular velocity of the projectile are influenced by sabot discard. The magnitude of these disturbances to the trajectory of the round are shown in Fig. (8). For a fin stabilized round, the effect is quite significant reaching a maximum deflection of nearly 0.9 mrad at around 2200 m/s. Again this reflects the decreasing effectiveness of the fins at hypersonic conditions. On the other hand, the flare stabilized design shows relatively low sensitivity to sabot discard, reaching a maximum deviation of 0.15 mrad and steadily decaying with velocity until it is negligible by 3500 m/s.

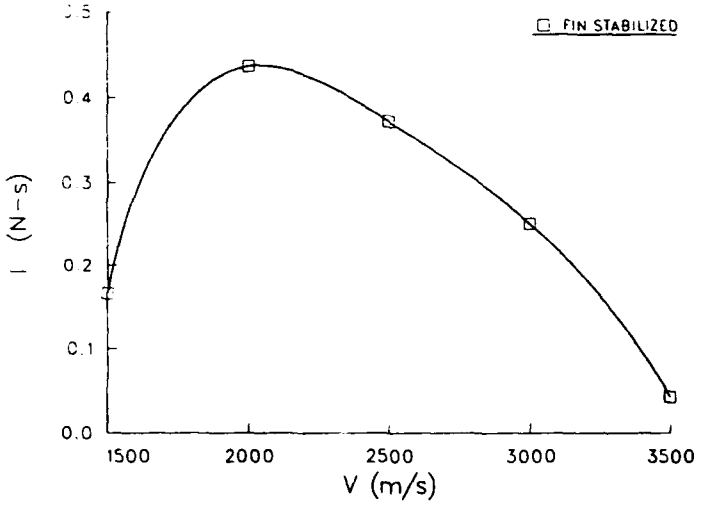


Fig. 7. Sabot Induced Asymetric Impulse

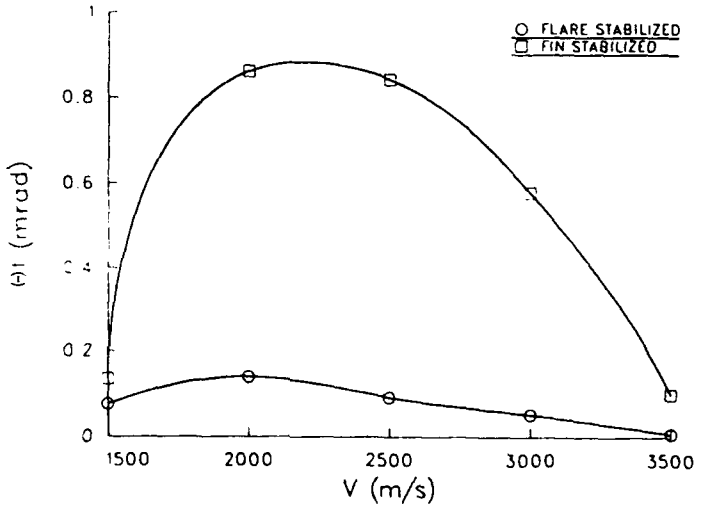


Fig. 8. Total Sabot Impulse Trajectory Deflection

FREE FLIGHT AERODYNAMICS

Two free flight effects are considered, first, the aerodynamic jump (Murphy, 1963) or trajectory deflection associated with projectile yawing motion and, second, the jump due to an initial asymmetry (Murphy and Bradley, 1959). In order to evaluate these terms, it is necessary to establish the aerodynamic characteristics of the projectiles. The PRODAS code (Whyte and Hathaway, 1991) is used for this purpose. Based on a combination of aerodynamic theory and experimental data for projectiles in the flight regime just beginning to approach hypervelocity, the present applications at velocities up to 3500 m/s may be stretching its capabilities somewhat. It is the intent of the authors to test the code against a series of firings scheduled to be conducted in the BRL Aerodynamics Range.

The aerodynamics of both the fin and flare stabilized designs have been computed and are tabulated below:

Aerodynamic Coefficients

Velocity	Flare Stabilized			Fin Stabilized		
M	C_D	C_{L_α}	C_{M_α}	C_D	C_{L_α}	C_{M_α}
1.0	2.91	5.96	-14.3	0.60	13.47	-49.0
2.0	2.05	7.68	-14.3	0.49	11.84	-38.2
3.0	1.47	8.42	-14.9	0.35	9.44	-22.0
4.0	1.11	8.74	-15.6	0.29	7.41	-11.7
5.0	0.88	8.93	-16.2	0.24	6.14	-5.4
6.0	0.77	9.05	-16.7	0.22	5.50	-2.3
8.0	0.67	9.18	-17.0	0.20	5.33	-1.6
10.0	0.57	9.83	-17.1	0.19	5.28	-1.4

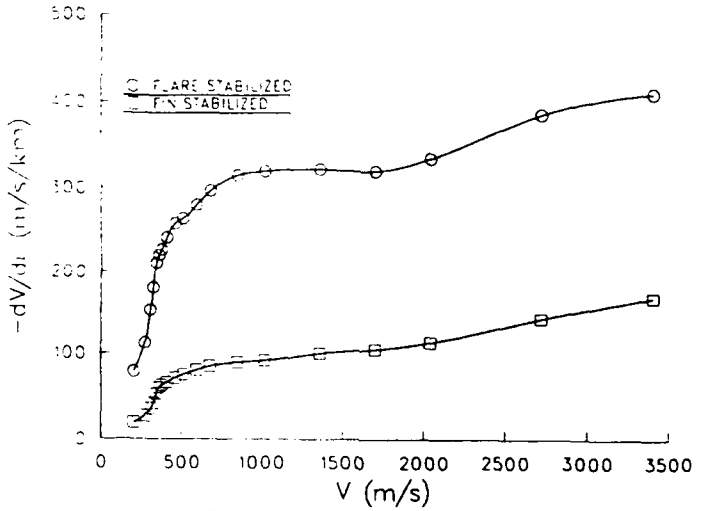


Fig. 9. Predicted Retardation

A few points should be made regarding this table. First, the drag coefficient of the finner is significantly lower than for the flare. This behavior is reflected in a more practical parameter, the retardation, Fig. (9). Evaluated as the decrease in velocity in m/s per kilometer of range, it is seen that as velocity increases the

flare has roughly three times the retardation of the finner. Obviously, the designer has the option of altering the flare angle to control the magnitude of retardation in accordance with the mission requirements imposed on the round. For the present study, there was no defined mission so no changes were made.

A second point is the behavior of the moment coefficient C_m. While the flare shows little variation in this coefficient, there is a strong decrease in its value with Mach number for the finner. As the rounds are statically stable, large negative values of the moment coefficient are desirable. For fins, as the Mach number increases there effectiveness decreases nearly linearly; whereas, the flare retains constant behavior (normal force coefficient of a cone approaches 2.0 as Mach number increases). This loss of static margin for the fin stabilized design has been reflected in the sensitivity to muzzle blast and sabot discard impulses described previously and will be seen again in this section.

The aerodynamic jump of a projectile represents the response of the trajectory to yawing motion. Essentially the coupling between yaw motion and linear motion is associated with the lift force generated as the projectile yaws. The expression (Murphy, 1963) for the trajectory deflection is:

$$\Theta_{aj} = \left[\frac{I_t}{m\ l\ V_m} \right] \left[\frac{C_{L_\alpha}}{C_{M_\alpha}} \right] \dot{\alpha} \qquad [2]$$

the behavior of the terms multiplying the angular rate on the left hand side of Eq. (2) is shown in Fig. (10). As velocity increases, the fin stabilized design becomes more sensitive; whereas, the flare sensitivity continually decays.

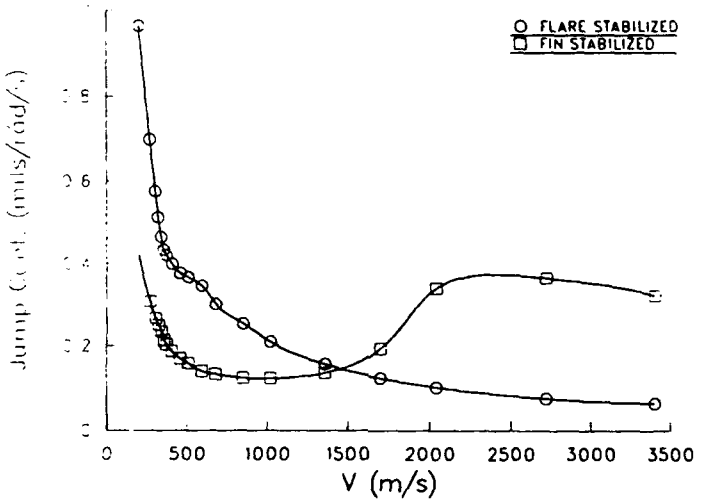


Fig. 10. Predicted Aerodynamic Jump Coefficient

Aerodynamic or inertial asymmetry can also cause deviation from the desired trajectory. Murphy and Bradley (1959) give the jump due to aerodynamic asymmetry which, for the case of a round launched at a spin rate equal to its steady state spin, can be expressed as:

$$\theta_{asy} = \left[C_{N_\epsilon} - \frac{C_{L_\alpha} C_{M_\epsilon}}{C_{M_\alpha}}\right]\left[\frac{\rho S l}{2m}\right]\epsilon\, e^{i\phi_\epsilon} \qquad [3]$$

The terms on the right hand side that vary with velocity are contained within the brackets. These are taken to be the asymmetric jump coefficient, J_a, and are plotted in Fig. (11). Again it is seen that the behavior of the flare is quite benign remaining essentially unchanged with increasing velocity. In contrast, the fin stabilized design shows increasing sensitivity past a velocity of 1700 m/s.

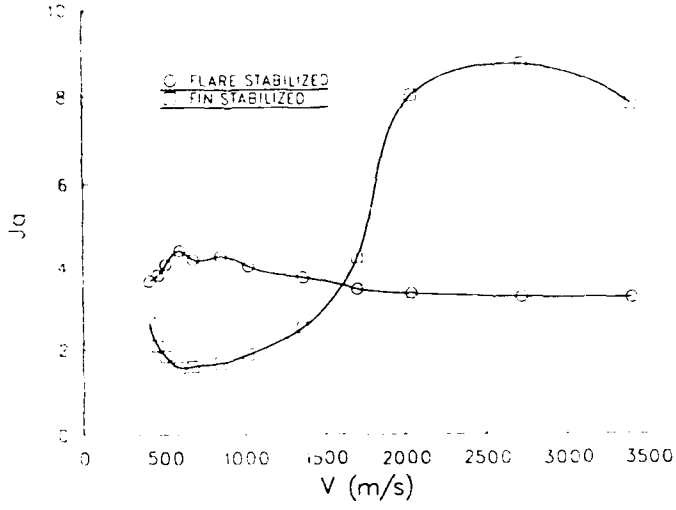


Fig. 11. Asymmetry Induced Jump

SUMMARY AND CONCLUSIONS

While it was expected that increasing launch velocity would produce substantial growth in launch disturbances, available analytic techniques did not predict such an occurrence. Lateral in-bore dynamics were computed to be remarkably unchanged as velocity grew. The influence of muzzle blast (for those launchers where muzzle blast is generated) was greater at higher velocities, but not enough to make it a major contributor to overall dispersion. Both fin and flare stabilization were considered, and it was shown that fin effectiveness degraded as velocity increased. This resulted in enhanced sensitivity to sabot discard, aerodynamic jump, and asymmetry for the finners. However, the flare stabilized design had stable aerodynamic properties as velocity increased and did not show marked sensitivity to any of the aforementioned perturbations. The flare did have higher retardation than the finner making consideration of a balance between stability and drag something the designer must consider.

References

Erline, T. F., M. Kregel, and M. Pantano (1990) Gun and Projectile Flexural Dynamics Modeled by Little Rascal. BRL TR 3122, US Army Ballistic Research Laboratory, Aberdeen Proving Ground, MD.

Kietzman, J., J. Bornstein, D. S. Savick, D. H. Lyon, and E. M. Schmidt (1992) Improved Simulation of the Launch Dynamics of Tank Cannon. 1992 International Summer Computer Simulation Conference, Reno, NV.

Lyon, D. H. (To Be Published) Measurement of the Flexural Stiffness of Sabot Components. US Army Ballistic Research Laboratory, Aberdeen Proving Ground, MD.

Murphy, C. H. and J. W. Bradley (1959) Jump due to Aerodynamic Asymmetry of a Projectile with Varying Roll Rate. BRL R 1077, US Army Ballistic Research Laboratory, Aberdeen Proving Ground, MD.

Murphy, C. H. (1963) Free Flight Motion of Symmetric Missiles. BRL R 1216, US Army Ballistic Research Laboratory, Aberdeen Proving Ground, MD.

Siegelman, D., J. Wang, and P. Crimi (1983) Computation of Sabot Discard. BRL CR 00505, Ballistic Research Laboratory, Aberdeen Proving Ground, MD.

Schmidt, E.M., K. S. Fansler, and D. D. Shear (1977) Trajectory Perturbations of Fin-Stabilized Projectiles due to Muzzle Blast. *AIAA J. Spacecraft and Rockets*, Vol. 14, No 6, pp. 339-344.

Schmidt, E. M. and D. D. Shear (1975) Optical Measurements of Muzzle Blast. *AIAA J.*, Vol. 13, No 7, pp. 1048-1055.

Whyte, R. and W. Hathaway (1991) PC PRODAS Version 3.6 User Manual. Arrow Tech Associates, South Burlington, VT.

List of Symbols

A	Planform Area of a Single Fin
C_D	Coefficient of Drag
C_{L_α}	Projectile Lift Coefficient Derivative With Respect To α
C_{M_α}	Projectile Static Moment Coefficient
C_{M_ϵ}	Moment Coefficient Due To Fin Deflection
C_{N_ϵ}	Normal Force Coefficient Due To Fin Deflection
D	Diameter of Gun Bore
I_t	Transverse Moment of Inertia
l	Reference Length = Diameter of Projectile
L	Gun Tube Length
m	Projectile Mass
M	Mach Number
n	Number of Fins
p^*	Pressure At Muzzle For Critical Conditions
$\bar{P}$	Dimensionless Moment Function
S	Reference Area of Projectile $\frac{\pi l^2}{4}$
v	Projectile Velocity
V_m	Muzzle Velocity
x	Projectile Position
α	Angle of Attack
$\dot{\alpha}$	Angle of Attack Angular Rate
Δ_{mb}	c.p. - c.g. Separation During Reverse Flow
ϵ	Magnitude of Asymmetric Fin Cant Angle
ϕ_ϵ	Initial, Free Flight Orientation of Asymmetric Fin Force
γ	Ratio of Specific Heats
ρ	Density
θ_{aj}	Aerodynamic Jump
θ_{asy}	Jump Due To Aerodynamic Asymmetry
θ_{mb}	Angular Deflection of Projectile Due To Muzzle Blast

Int. J. Impact Engng Vol.14, pp.631 - 636, 1993
Printed in Great Britain

0734-743X/93 $6.00 + 0.00
1993 Pergamon Press Ltd

HYPERVELOCITY IMPACT SIMULATION EXPERIMENTS ON LDEF°-FOILS

E. SCHNEIDER and A. STILP

Fraunhofer-Institut für Kurzzeitdynamik - Ernst-Mach-Institut -
Eckerstr. 4, 7800 Freiburg/Br., Germany

M. ROTT

Lehrstuhl für Raumfahrttechnik, TU München, Germany

F. LEVADOU and G. SCHWEHM

European Space Research and Technology Centre
- ESTEC - Noordwijk, The Netherlands

ABSTRACT

A variety of space environmental effects can be studied on many experiments having been exposed on the LDEF-satellite.

Among others the thermal blankets of the Ultra-Heavy Cosmic Ray Nuclei Experiment ("UHCRE", Exp. A0178) displayed many micrometeoroid / space debris impact features.

In an effort to understand their nature and characteristics, an experimental impact simulation program has been carried out.
UHCRE-spare foils have been impacted by glass, aluminium, and iron projectiles with masses ranging from about 30 nanograms up to several milligrams. Impact velocities range between about 3 km/s and 13 km/s.

Characteristic impact craters and perforation holes have been produced. Their sizes and morphologies have been related with respective projectile impact parameters.

"Halo zones" around perforation holes, as they had been observed in the exposed LDEF-foils, have also been obtained experimentally. They were found to be delamination effects within the foil layers caused by the propagation of impact shock waves.

° LDEF = Long Duration Exposure Facility

INTRODUCTION

Most of the experiments having been exposed to the space environment for about 68 months during the LDEF-mission, offer the opportunity to study micrometeoroid and orbital debris impact features.

Sixteen LDEF-trays had been devoted to an Ultra Heavy Cosmic Ray Nuclei Experiment (UHCRE) run by ESA/ESTEC, Noordwijk, Netherlands, in cooperation with the Dublin Institute for Advanced Studies, Dublin, Ireland. Impact crater statistics are presently performed on the thermal blankets, which had covered the trays. A variety of impact features (e.g. secondary impacts, oblique impacts, perforation holes, "halo-zones" around impact sites etc.) has been detected on such exposure areas.

In a cooperation between the Lehrstuhl für Raumfahrttechnik of the Technical University, Munich, and the Ernst-Mach-Institut, Freiburg/Br. an experimental simulation program has been established under an ESA-contract, in order to study such impact phenomena in thermal blanket spare foils, and to relate the morphology of impact features with projectile parameters.

EXPERIMENTS AND RESULTS

The experiments have been performed using the electromagnetic plasma accelerator of the Technical University Munich (TUM) and the light gas guns of the Ernst-Mach-Institut (EMI). Facility descriptions and operation principles are given by Hüdepohl et al. (1989) and for example by Stilp (1987), respectively.

The two accelerator facilities have different projectile mass and velocity ranges The TUM plasma gun accelerates effectively glass particles with masses between 10^{-10} g and 10^{-5} g with a velocity range of 2 km/s $< v <$ 18 km/s. The projectile mass range of the light gas guns used was from μg to g, with velocities of up to 10 km/s. In both facilities individual particles can be accelerated and their velocities can be determined with high accuracy (error $<1\%$).

The foil targets (UHCRE thermal blanket spare samples) are laminates consisting of a substrate of black paint (Chemglaze Z306), layers of inconel and silver, covered by a layer of Teflon (FEP). The respective thicknesses are given in the sample cross section of Fig.1. The total thickness varied locally between 180μm and 200 μm since the thickness of the paint substrate was not sufficiently constant.

Former foil penetration experiments using plastic and aluminum foil targets have already been performed by Pailer and Grün (1979). Their foils, however, have been very thin (order of several μm) compared to the UHCRE thermal blanket foil.

Impact calibration experiments of the SOLAR MAX thermal blanket have been reported by Frisch et al. (1990). The configuration of this blanket is also completely different from the UHCRE foil samples.

The experiments performed during the first phase of this program were direct (primary) impacts at normal incidence.

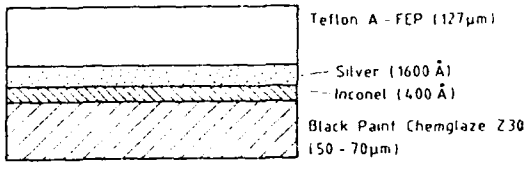


Fig. 1. Cross section of UHCRE thermal blanket.

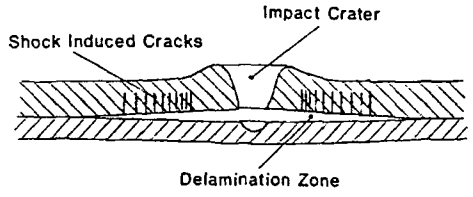


Fig. 2. Characteristic impact features observed in UHCRE-foils.

The principal characteristics observed at the impact features produced are indicated in the sketch of Fig.2. (applicable for perforation holes as well): A central crater pit, or a perforation hole with a bulged crater rim, typical for hypervelocity impact, is formed. Starting from the crater rim, a shock induced system of radial and concentric cracks is produced within the Teflon layer. In nearly all cases also relatively large concentric

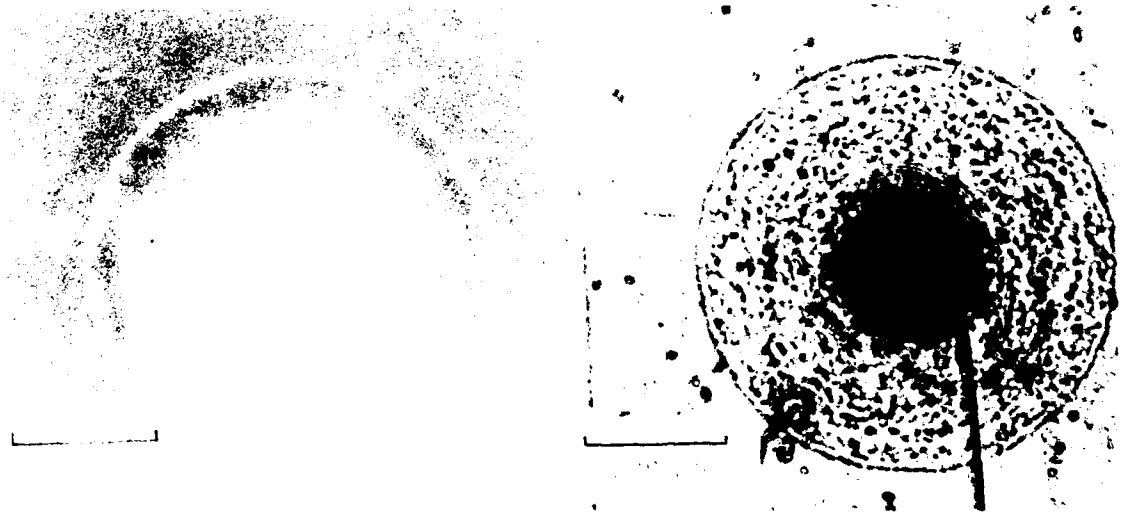


Fig. 3. Impact crater with "halo" (delamination zone). Projectile: 48 μm glass sphere at 6.0 km/s. (TUM Experiment)

"halo" zones are observed around the craters or perforation holes, which are due to delamination of the silver and Teflon layers. This delamination is very probably caused by a circular shock wave propagating into the target foil. The borderline of this delamination zone is marked by a very sharp and very regular ring. Sometimes this ring is only weakly visible, sometimes it is developed as a whole system of concentric rings. Figs. 3,4,and 5 present photos of craters and perforation holes which demonstrate these effects very nicely. Respective impact parameters are given in the figure captions.

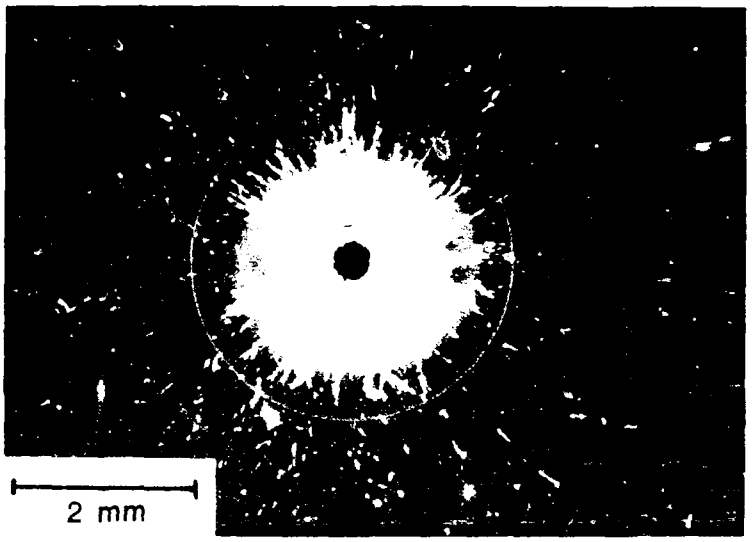


Fig. 4. Perforation hole with "halo" (delamination zone). Projecti · 350 μm steel sphere at 3.2 km/s. (EMI E. eriment)

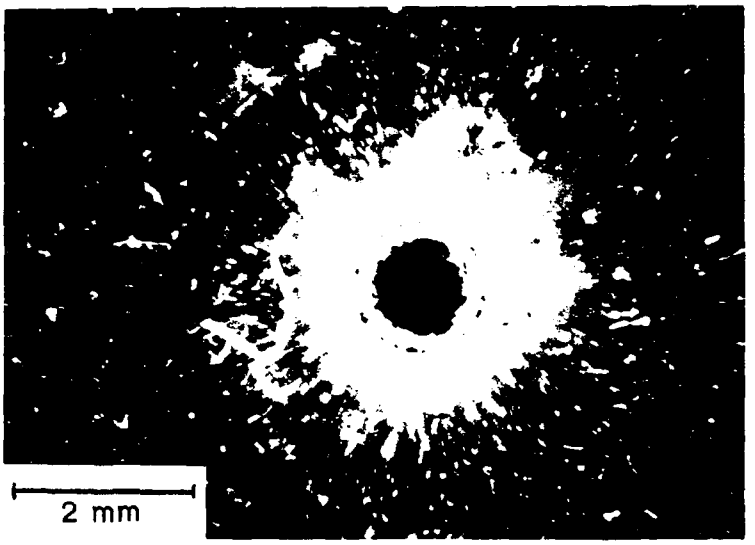


Fig. 5. Perforation hole with "multi-ring halo". Projectile: 1 mm glass sphere at 7.8 km/s. (EMI Experiment)

Table 1 summarizes the impact experiments and results performed at the TUM plasma accelerator. The projectiles were glass spheres with a material density of 2.5 g/cm^3. Their masses and velocities were well defined. With one exception the impacts did not perforate the target foil and the respective craters can be considered as being formed in a semi-infinite laminated target. Only the impact with a velocity of 12.6 km/s just perforated the foil. From the morphology, however, it ranges very close to the ballistic limit parameters.

Mat.	Projectile Diam. [μm]	Mass [10^{-8}g]	Speed [km/s]	Hole diam. [μm]	Halo diam. [mm]
	58	25.5	6.35	152	1.34
	34	5.1	8.84	125	0.64
G	46	12.7	7.27	162	1.15
	61	29.7	5.45	192	1.86
l	48	14.5	5.97	102	0.56
	80	67.0	4.61	195	2.21
a	97	119.4	2.33	136	1.33
	80	67.0	5.00	210	~1.8
s	32	4.3	6.39	86	0.51
	69	43.0	2.24	85	-
s	64	34.3	9.54	140	0.65
	180	763.4	1.94	201	~1.6
	71	46.8	12.65	335	0.69
	35	5.6	7.50	102	0.47

Table 1: Experiments performed at TUM.

In Fig.6 the hole diameter D normalized by the particle diameter d is plotted versus the impact velocity v. A best fit approximation of the data yields (Levadou et al., 1991):

$$D/d = 0.78\ v^{0.667}$$

Despite the considerable scatter of the data, which is mainly due to target foil inhomogeinities and thickness variations of individual layers, the fit is in accordance with the fact that the crater volume is proportional to the kinetic projectile energy, which implies a $D/d \approx v^{2/3}$ - dependence.

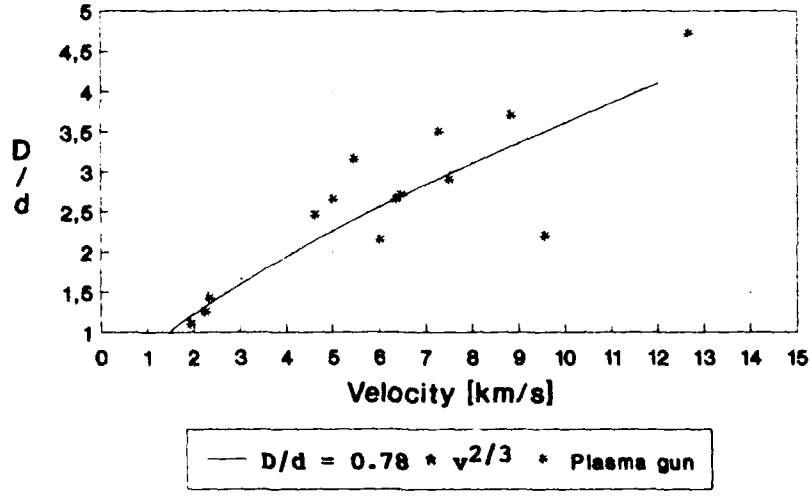


Fig. 6. Normalized crater diameter vs. impact velocity for the TUM experiments.

In table 2 the experiments and results obtained at EMI are listed in a similar way. Glass spheres (density 2.5 g/cm^3), Al-spheres (density 2.7 g/cm^3), and Fe-spheres (density 7.85 g/cm^3) have been used as projectiles. Due to the higher projectile mass range, all impacts resulted in perforations of the target foil. Fig.7 shows a D/d-vs.-v-diagram of all impacts performed. In the diagram of Fig.8 the D/d-values of glass and Al-projectiles which are comperable in density are plotted together with the best fit curve of the TUM semi-infinite results. All D/d-values range below the curve for semi-infinite penetration, where the total kinetic projectile energy is dissipated in the cratering process. In the case of perforation the energy partition within the target foil depends on the projectile parameters. The further the impact parameters range beyond the ballistic limit conditions, the smaller is the portion of energy which is used for the penetration and hole formation process, and the higher remains the residual energy of the projectile. Similar results are reported by Hörz et al. (1992) for Aluminum foil perforations. Thus the deviation of the D/d-values from the semi-infinite curve represents a measure of how far the impact parameters range below the ballistic limit. In the diagram of Fig.9 this behavior is also

Projectile				Hole diam.	Halo diam.
Mat.	Diam. [μm]	Mass [mg]	Speed [km/s]	[μm]	[mm]
Steel	500	0.514	5.2	915	4.5
Steel	350	0.176	4.9	724	3.9
Steel	1000	4.11	5.4	1510	5.9
Steel	500	0.514	3.3	836	4.2
Steel	1000	4.11	2.9	1335	5.2
Steel	350	0.176	3.2	541	3.6
Steel	1000	4.11	5.5	1614	6.2
Steel	350	0.176	7.9	660	1.4
Al	900	1.03	5.4	1743	6.3
Al	900	1.03	2.8	1400	5.3
Al	900	1.03	8.5	1940	6.5
Glass	1000	1.36	5.1	1560	6.1
Glass	500	0.170	4.6	984	4.7
Glass	1000	1.36	2.9	1250	5.2
Glass	500	0.170	2.9	748	4.0
Glass	350	0.054	2.9	376	2.3
Glass	1000	1.36	7.8	1600	4.2
Glass	500	0.170	7.0	1300	3.8

Table 2: Experiments performed at EMI.

demonstrated by plotting the area of the perforation hole F versus the kinetic projectile energy E. Despite of the considerable scatter of the data, it becomes obvious, that only for low energies, close to the ballistic limit conditions, the hole area which represents also the perforated volume, increases linearly with the kinetic energy.

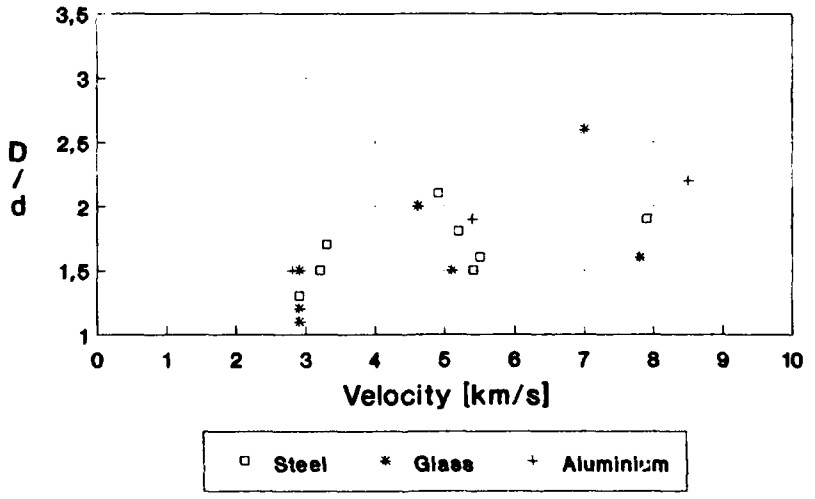


Fig. 7. Normalized perforation hole diameter vs. impact velocity of all EMI experiments.

DISCUSSION

The results obtained show that impact features on LDEF-samples can be well simulated experimentally.

For impact craters, quantitative relations between crater and projectile parameters can be established, whereas for perforation holes unambiguous relations are only possible in favourable cases. To a certain extent, conclusions on the impact velocity can be drawn from morphological evidence.

No systematic dependencies between dimensions of the so-called "halo-zones" and other impact parameters have been found. The occurence and nature of these delamination zones, especially the development of multi-ring systems is not yet understood. Additional experiments are necessary to study these effects in a more systematic way.

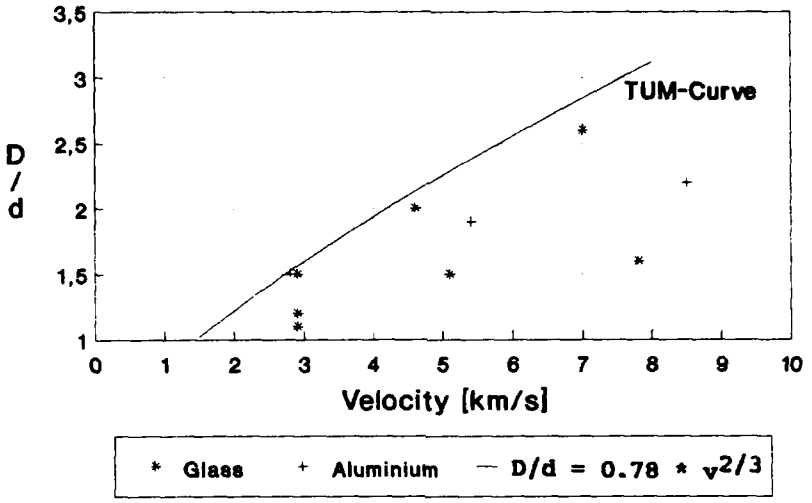


Fig. 8. Normalized perforation hole diameter vs. impact velocity for glass and Al-projectiles.

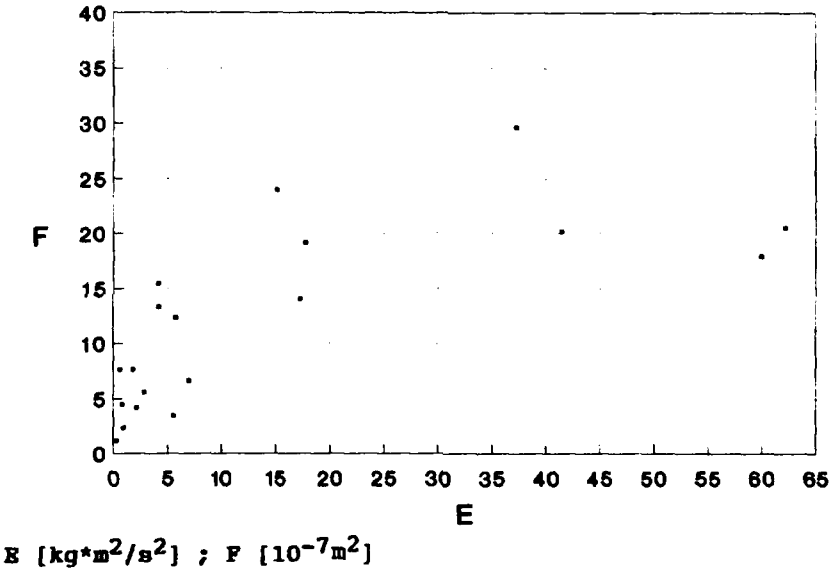


Fig. 9. Perforation hole area plotted vs. kinetic projectile energy.

There might be degradation effects (e.g. radiation, atomic oxygen etc.) causing changes in the material behaviour of space-exposed thermal blanket foils, which could result in different crater/hole characteristics. Therefore, it would be interesting to perform some comparative experiments on exposed foils.

Also oblique and secondary impacts should be simulated.

REFERENCES

Hüdepohl, A., M. Rott and E. Igenbergs (1989). Coaxial Plasma Accelerator with Compressor Coil and Radial Gas Injection. *IEEE Transactions on Magnetics*, 25, No. 1, pp. 232-237.

Stilp, A. (1987). Review of Modern Hypervelocity Impact Facilities. *Int. J. Impact Engng.*, 5, pp. 613 - 621.

Pailer, N. and E. Grün (1979). The Penetration Limit of Thin Films. Rep. MPI H-1979-V16, Max-Planck-Inst. f. Kernphysik, Heidelberg, F.R.G.

Frisch, W., S. Aigner and E. Igenbergs (1990). Hypervelocity Impact Calibration of SOLAR MAX Thermal Blankets. *Adv. Space Res.*, 10, pp. 413-416.

Levadou, F., M. Froggatt, M. Rott and E. Schneider (1991). Preliminary Investigations into UHCRE Thermal Control Materials. First LDEF Post-Retrieval Symposium, Kissemmee, Florida (1991), NASA Conference Publication 3134, Part II, pp. 875.

Hörz, F., M. Cintala, R.P. Bernhard and T.H. See (1992). Dimensionally Scaled Penetration Experiments: Aluminum Targets and Glass Projectiles 50 μm to 3.2 mm in Diameter. This Conference.

Int. J. Impact Engng Vol.14, pp.637-646, 1993
Printed in Great Britain

0734-743X/93 $6.00+0.00
© 1993 Pergamon Press Ltd

EFFECT OF INTERNAL STRESS FIELDS ON THE PERFORATION RESPONSE OF DUAL-WALL STRUCTURES UNDER HYPERVELOCITY IMPACT

William P. Schonberg

Mechanical Engineering Department
University of Alabama in Huntsville
Huntsville, Alabama 35899

ABSTRACT

Traditional perforation-resistant wall design for long-duration spacecraft consists of a 'bumper' that is placed at a small distance away from the main 'pressure wall' of a spacecraft compartment or module. This concept has been studied extensively in the last four decades as a means of reducing the perforation threat of hypervelocity projectiles such as meteoroids and orbital debris. If a dual-wall system is employed on an earth-orbiting spacecraft, then a bi-axial stress field will be induced within the pressure wall of the dual-wall system due to the pressurization of the spacecraft. Unfortunately, little or no attempt has been made to include the effects of this low-level internal stress field in the study of the perforation resistance of dual-wall structural systems. This paper presents the results of an experimental study in which aluminum dual-wall structures were tested under a variety of high-speed impact conditions in an attempt to quantify the effect of an internal pressure wall stress field on perforation resistance. A test-by-test comparative analysis of the damage sustained by similar dual-wall systems with stressed and unstressed pressure wall plates under similar impact loading conditions revealed that the internal pressure wall stress field had a negligible effect on the ballistic limit of the dual-wall structures considered. However, the internal stress field did have a significant effect on the extent of the damage sustained by the pressure wall.

INTRODUCTION

The design of a spacecraft for a long-duration earth-orbiting mission must take into account the possibility of high-speed orbital debris particle impacts and their effects on the spacecraft and on all of its exposed subsystem components. To prevent mission failure and possibly loss of life, protection against perforation by such high-speed impacts must be included. Traditional perforation-resistant wall design for long-duration spacecraft consists of a 'bumper' that is placed at a small distance away from the main 'pressure wall' of the spacecraft compartment or module. This concept was first proposed by Whipple (1947) and has been studied extensively in the last four decades as a means of reducing the perforation threat of hypervelocity projectiles such as meteoroids and orbital debris particles (see, e.g., Wallace et.al., 1962; Maiden and McMillan, 1964; Lundeberg et.al., 1966; Riney and Halda, 1968; Sawle, 1970; Coronado et.al., 1987; Schonberg et.al., 1991). Dual-wall configurations were repeatedly shown to provide significant increases in protection against perforation by high-speed projectiles over equivalent single-wall structures.

If a dual-wall system is used on a habitable earth-orbiting spacecraft or module, then a low-level bi-axial stress field will exist within the pressure wall of the dual-wall system due to the internal spacecraft or module pressure. Unfortunately, little or no attempt has been made to study the effect of this pressure wall stress field, whether beneficial, negligible, or detrimental, on the perforation resistance of dual-wall structures. It is unclear, therefore, as to whether or not the high-speed impact test results obtained using dual-wall structures with unstressed pressure walls can be used to predict the response of actual dual-wall structures in which such internal stress fields are certain to exist.

This paper presents the results of an experimental study in which aluminum dual-wall structures were tested under a variety of high-speed impact conditions. The objectives of this study were to 1) quantify the effect of an internal pressure wall stress field on perforation resistance, and 2) determine the extent, if any, that high-speed impact response characteristics of dual-wall systems with unstressed pressure wall plates could be used to predict the impact response of dual-wall systems in which internal pressure wall stress fields would develop. These objectives were realized through a comparative analysis of the damage sustained by geometrically similar dual-wall systems with stressed and unstressed pressure wall plates caused by projectiles with similar impact energies. The analysis focused on a test-by-test comparison of dual-wall system response and a comparison of the ballistic limit curves of the dual-wall systems.

HYPERVELOCITY IMPACT RESPONSE OF DUAL-WALL STRUCTURES

Consider the hypervelocity impact of a dual-wall structure by a spherical projectile of diameter d traveling at velocity V. Figure 1 shows an oblique impact of such a system. The projectile initially collides with the protective bumper (thickness t_s), which is usually a relatively thin layer of material placed at a small distance S in front of the pressure wall (thickness t_w) of the stuctural system. The bumper plate protects the pressure wall plate against perforation by disintegrating the impacting particle and by creating one or more diffuse debris clouds. These debris clouds, which consist of projectile and bumper plate fragments, travel towards and eventually impact the pressure wall plate. However, the impacts of these debris clouds impart a significantly lower impulsive loading to the pressure wall than would an intact projectile. The area over which the impulsive loading of the debris clouds is distributed is governed by the manner in which the projectile and bumper plate fragment, melt, or vaporize, and by the spacing between the bumper plate and the pressure wall plate. Occasionally, the impact of the debris clouds result in rarefaction stresses near the rear surface of the pressure wall plate that exceed the dynamic tensile fracture strength of the pressure wall material. In these cases, spall fragments are ejected at high velocities from the rear side of the pressure wall plate.

In an oblique impact, the hole in the bumper plate is elliptical, with the elongation in the direction of the original projectile trajectory. In such impacts, two distinct debris clouds are often formed: the 'normal' and 'in-line' debris clouds. It is hypothesized that the 'normal' debris cloud contains mainly bumper plate fragments while the 'in-line' debris cloud contains mainly projectile fragments (Burch, 1967). The impact of these debris clouds on the pressure wall creates 'normal' and 'in-line' damage areas A_{d1} and A_{d2}, respectively (Figure 1). Analogously, A_{s1} and A_{s2} in Figure 1 refer to 'normal' and 'in-line' areas of rear-side spallation. In a normal impact, the bumper plate hole is circular, and only one debris cloud containing both projectile and bumper plate fragments is evident. The collision of this debris cloud with the pressure wall creates a single area of crater damage A_d, and, occasionally, an area of rear surface spall A_s.

HYPERVELOCITY IMPACT TEST PARAMETERS

The high-speed impact tests that generated the data for this study were performed at the Space Debris Simulation Facility at the NASA/Marshall Space Flight Center (Taylor, 1987). The facility consists of an instrumented two-stage light gas gun capable of launching 2.5 mm to 12.7 mm projectiles at velocities of 2 to 8 km/sec. Projectile velocity measurements were accomplished via pulsed X-ray, laser diode detectors, and a Hall photographic station.

The conditions of impact in the experimental tests were chosen to simulate orbital debris impact of light-weight space structures as closely as possible, and still remain within the realm of experimental feasibility. Kessler et.al. (1988) state that the average mass density for pieces of orbital debris less than 10 mm in diameter is approximately 2.8 gm/cm^3, which is similar to that of aluminum. Therefore, the projectiles used in the test program were aluminum 1100-0 spheres with diameters ranging from 0.475 cm to 0.953 cm. Although the shape of an impacting projectile will affect the formation and spread of the debris cloud(s) formed in a high-speed impact (Morrison, 1972; Schonberg, 1992), spherical projectiles were used in the test program to maintain repeatability and consistency. The projectiles were launched at velocities ranging from 2.02 km/sec to 7.29 km/sec. To determine whether or not the effects of internal pressure wall stress fields were dependent on projectile trajectory obliquity, the tests were performed at two different trajectory obliquities: 0^0 and 45^0. The bumper plates in the dual-wall systems were all made from aluminum 6061-T6 and were all 1.6 mm thick; the pressure wall plates in all of the systems were made from aluminum 2219-T87, were 3.175 mm thick, and were separated from the bumper plates by a constant distance of 10.16 cm. Detailed test parameters for systems with unstressed and stressed pressure wall plates may be found in Tables 1 and 2, respectively.

To simulate the presence of thermal insulation within the structural systems, the tests were performed with MLI (multi-layer insulation) resting on the pressure wall plate. The MLI consisted of 30 layers of 0.5 mil Kapton aluminized on one side and 29 layers of Dacron mesh, one layer between each Kapton layer. Additionally, 1 layer of beta-cloth (coated s-glass) was added to the side nearest the bumper plate for durability. The areal density of this combination was calculated to be approximately 0.107 gm/cm^2 (Coronado et.al., 1987). It is noted that the MLI was taped on to the pressure wall plate without being pulled taut. This enabled the layers within the MLI to act individually and not as a single layer. In an actual design application, this method of MLI installation would allow the MLI to deliver maximum thermal and ballistic protection.

To study the effect of an internal pressure wall stress field on the perforation resistance of a dual-wall system under hypervelocity impact, two pressure wall stress states were considered: unstressed and bi-axially stressed. The testing performed using unstressed pressure wall plates provided baseline response characteristics. The bi-axial stress state was induced

in the pressure walls of the stressed systems by applying distributed tensile loads to the pressure wall plates. The magnitudes of the tensile loads were calculated using the equations for the bi-axial stress distribution in a thin cylindrical shell:

$$\sigma_1 = pr/t \quad \ldots \quad \text{hoop stress} \tag{1}$$

$$\sigma_2 = pr/2t \quad \ldots \quad \text{longitudinal stress} \tag{2}$$

where r is the cylindrical shell radius, t is the shell wall thickness, and p is the outwardly-directed internal pressure (Ugural, 1981). For the purposes of this study, r=2.13 m, t=3.175 mm, and p=1 atm (approx. 101.4 Pa). In this manner, the bi-axial stress state considered in this study was an approximation of the state of stress that can be expected to exist within the module walls of the Space Station Freedom. In the remainder of this paper, the phrases 'stressed system' and 'unstressed system' refer to dual-wall systems with bi-axially stressed and unstressed pressure wall plates.

A total of 32 high-speed impact tests were performed during the course of this investigation. The results of the normal and oblique impact tests are presented in Tables 3 and 4, respectively. In Tables 3 and 4, impact tests are grouped in pairs according to similar impact energy and geometry. An entry of '----' in these Tables indicates that a certain event, such as perforation, petalling, or spallation, did not occur. Additionally, in Table 3 (ie. for normal impacts), D and d_h are the diameter of the hole in the bumper plate and the equivalent single hole diameter of all the holes in a perforated pressure wall plate, respectively. For oblique impacts (Table 4), D_{min}, D_{max} and d_{h1}, d_{h2} are the minimum, maximum bumper plate hole dimensions and the equivalent single hole diameters for the 'normal', 'in-line' pressure wall plate damage areas, respectively. When an impact test resulted in a pressure wall perforation that was accompanied by petalling of the pressure wall material, the equivalent pressure wall hole diameter was calculated using the equation

$$d_h = [(4/\pi)A_h]^{1/2} \tag{3}$$

where A_h is the area of the smallest ellipse (or circle) that could have been placed over the perforated region of the pressure wall and enclose all of the petals. In Tables 3 and 4, L_p is the length of the longest pressure wall plate petal in the event that petal formation accompanied pressure wall perforation.

Figures 2 and 5 present ballistic limit curves for the stressed and unstressed systems considered in this investigation for normal and 45^0 trajectory obliquities, respectively. It is noted that in Figures 2 and 5, the lines shown are merely lines of demarcation between projectile velocity-diameter combinations that did (below) or did not (above) result in pressure wall perforation. Finally, Figures 3 and 4 depict typical damaged pressure wall plates under normal hypervelocity impact. These figures highlight some of the similarities and differences between stressed and unstressed pressure wall response.

A comparison of the impact test results presented in Table 3,4 and visual inspection of the damaged pressure wall plates revealed many interesting hypervelocity impact response similarities and differences for stressed and unstressed dual-wall systems. These results are discussed in detail in the next section, first for normal impacts and then for oblique impacts.

EXPERIMENTAL RESULTS AND DISCUSSION

Normal Impact

In all but one pair of tests, the presence of the internal bi-axial stress state did not affect whether or not the pressure wall was perforated: if the pressure wall of an unstressed system was perforated, so was that of a stressed system, and vice versa (Table 3). This similarity in response is further borne out in Figure 2, which shows the ballistic limit curves for the stressed and unstressed dual-wall systems under normal impact. The curve for the stressed system was virtually identical from that for the unstressed system; hence, only one line is given in Figure 2. The difference in response between tests FP12 (stressed, not perforated) and MD-TA (unstressed, perforated) is probably due to the fact that the bumper plate hole in the unstressed test was nearly 30% larger than that in the stressed test. Hence, the mass content of the debris cloud in the unstressed system test was considerably higher than that of the debris cloud in the test of the stressed system. As a result, the debris cloud in test MD-TA was able to inflict more damage to the pressure wall plate than the less massive debris cloud in test FP12.

Interestingly enough, when pressure wall perforation occurred in corresponding stressed and unstressed systems, the equivalent diameters of the holes in the stressed pressure wall plates were very similar to those in the unstressed plates (Table 3). On average, the equivalent single hole diameters in perforated stressed and unstressed pressure wall plates were within 5% of each other, with a standard deviation of 16%. However, the similarity of the equivalent hole diameters is deceptive, especially at high impact energies. When the impact energy was

less than 10,000 joules, the holes in both types of pressure wall plates (stressed and unstressed) were similar in size and approximately circular. As the impact energy was increased above 10,000 joules, pressure wall perforation began to be accompanied by petal formation. For impact energies above 10,000 joules but less than 25,000 joules, the unstressed pressure wall plates typically sustained a central bulge with two co-linear cracks (see, e.g. Figure 3a). However, at the same impact energy levels, the bi-axially stressed pressure wall plates sustained a cruciform petal formation (Figure 3b). When the impact energy was increased past 25,000 joules, both pressure wall types again experienced a similar mode of pressure wall perforation -- both had large holes with approximately six long petals (see Figures 4a,b).

Thus, it would appear that the presence of a bi-axial stress field within a pressure wall plate of a dual-wall system did not significantly affect the mode of pressure wall perforation in low and high energy impacts ie. below 10,000 joules and above 25,000 joules, respectively). Its effect was mainly felt in the intermediate impact energy regime, that is, between 10,000 and 25,000 joules. In this impact energy regime, the bi-axial tensile stress state altered the type and number of petals formed by creating additional petals and cracks in a direction normal to that of the cracks in the unstressed plates. This also explains why the petal lengths in the unstressed pressure walls exceeded those in the stressed pressure walls (Table 3). On average, the maximum petal length in the stressed pressure wall plates was approximately 14% less than the maximum petal length in the unstressed plates, with a standard deviation of approximately 27%. The creation of additional petals in the bi-axially stressed pressure wall plates absorbed a portion of the energy of the impacting debris cloud that in the case of the unstressed plates went into the extension of the colinear cracks.

Rear-side pressure wall spallation occurred in only two stressed-unstressed test pairs. In both cases, the bi-axially stressed pressure wall plates faired better than the corresponding unstressed pressure wall plates. In one instance, the stressed pressure wall experienced an area of rear-side spallation that was less than half as large as that experienced by the unstressed plate. In the other instance, the rear-side spall area of the unstressed plate was ten times as large as the rear-side spall area of the stressed plate (Table 3). This tendency of the stressed pressure wall plates to experience less spallation than corresponding unstressed plates is due to an increase in the apparent stiffness of the stressed plates caused by the applied tensile stress field. This increase in stiffness naturally acted against spall formation in those plates.

Oblique Impact

In a manner similar to the normal impact tests, the presence of the internal bi-axial stress state did not affect whether or not the pressure wall was perforated (Table 4). This similarity in perforation response is also borne out in Figure 5, which shows the ballistic limit curves for dual-wall systems under 45° impact with stressed and unstressed pressure wall plates. Once again, the curve for the stressed system was virtually identical to that for the unstressed system; hence, only one line is given in Figure 5.

Although the 'in-line' pressure wall damage areas were typically smaller than the 'normal' damage areas (note the values of A_{d2} as compared to A_{d1} in Table 4), this was due to the fact that the 'in-line' debris clouds were more concentrated, and not because they contained fewer particles than the 'normal' debris clouds. In fact, more serious pressure wall damage and/or failure was caused by the impact of the 'in-line' debris cloud rather than the 'normal' debris cloud: pressure wall plate perforation occurred only in the 'in-line' damage area, while not even a single pinhole was found in a 'normal' damage area (Table 4). Apparently, for the parameters considered in this study, the MLI on the pressure wall plate was able to absorb most (or all) of the energy of the slower moving, more disperse 'normal' debris clouds, but was not able to stop the larger, less fragmented particles of the more condensed 'in-line' debris clouds.

When a perforation did occur in corresponding stressed and unstressed systems, with the exception of tests FP18 (stressed) and 205C (unstressed), the equivalent diameters of the pressure wall plate holes in the stressed systems were in general larger than those in the unstressed systems (Table 4). This difference in hole diameter was especially pronounced in the lower energy tests and decreased monotonically as the impact energy increased. At an impact energy level of approximately 9,000, 16,000, and 18,000 joules, the holes in the stressed plates were approximately 5, 3.67, and 1.38 times larger than the holes in corresponding unstressed plates. In tests FP18 and 205C, although the hole in the stressed plate was smaller than that in the unstressed plate, the stressed plate also contained a 0.7 cm diameter crater at the bottom of which was a 0.6 cm long through-crack. While this crater with a through-crack does not constitute a hole, an additional perforation in the stressed plate is evident nonetheless. As a result, the difference between the results for tests FP18 and 205C was determined not to be as dramatic as originally supposed.

The reason for the larger hole diameters in the stressed systems is that in an oblique impact, the individual 'in-line' pressure wall craters and holes were elliptical and therefore highly sensitive to the in-plane pressure wall stress field. Under the action of the in-plane stress distribution, the stress concentrations at the sharp tips of the pressure wall craters and

holes invariably led to material rupture and hole growth. These stress concentrations also led to an increased maximum petal length in the stressed pressure wall of one of the tests as compared to that of an unstressed pressure wall plate in a corresponding system under similar impact conditions (note the relative values of L_{max} for tests FP25 and 3028A in Table 4). It was also found that as the impact energy increased, the effect of the in-plane stress field decreased and the holes in the stressed plates began to resemble those in the unstressed plates. This increased consistency in perforation response with increased impact energy is also similar to that which was observed under normal high-speed impact.

Finally, pressure wall plate petalling under oblique impact did not begin to appear until the kinetic energy of the impacting projectile exceeded approximately 17,500 joules. This appears to be in great contrast with the fact that under normal impact, petalling appeared in pressure walls of dual-wall systems impacted at energies as low as 9,500 joules. However, the two apparent threshold energy levels for petal formation are consistent if one considers that the amount of normally directed impact energy is proportional to the total impact energy in an oblique impact multiplied by the square of the cosine of the impact angle. In the case of a 45^0 impact, the normally directed impact energy at the apparent threshold energy level for petal formation is therefore equal to 8,750 joules, a mere 8% below the apparent threshold energy level for petal formation under normal high-speed impacts.

CONCLUSIONS

A study was performed to assess the effects of an internal pressure wall stress field on the response of a dual-wall structure under normal and oblique hypervelocity projectile impact. The study focused on a test-by-test comparison of hypervelocity impact response characteristics, including whether or not the pressure wall was perforated, the diameter of the hole in a perforated pressure wall, maximum petal length, and the occurrence of rear-side spallation. It was found that the internal pressure wall stress distribution had a negligible effect on whether or not the pressure wall plate of the dual-wall system was perforated. However, pressure wall hole diameter, maximum petal length, and extent of rear-side spallation did show some dependence on the presence of the pressure wall stress field.

Based on the results obtained in this study, it is concluded that for the stress levels and the impact, material, and geometric parameters considered, the results of high-speed impact tests of similar dual-wall systems with unstressed pressure wall plates can be used fairly accurately to predict the ballistic limit of actual dual-wall systems of similar construction in which internal pressure wall stress fields are expected to exist. However, the exact nature of the impact response can vary significantly between stressed and unstressed systems. Details that can be expected to vary between stressed and unstressed system response include the hole diameter in a perforated pressure wall plate, the extent of rear-side spallation, and the number and length of pressure wall petals created by debris cloud impact. To obtain reliable information for these response characteristics, it is necessary to perform high-speed impact tests and include an internal pressure wall stress field to account for the effects of the stress field that would exist in the actual dual-wall system.

ACKNOWLEDGMENTS

The author is grateful for support from a NASA/Marshall Space Flight Center contract (NAS8-36955/D.O.74) with Miria Finckenor serving as Technical Monitor. The author would also like to express his appreciation to Jim Zwiener and Joe Lambert of the Laboratory Support Branch of the NASA/Marshall Space Flight Center Materials and Processes Laboratory, and to Hubert Smith, Ben Ramsey, and Mike Bjorkman of the Boeing Aerospace Corporation for conducting the impact testing that made this investigation possible. Finally, the author also wishes to acknowledge the assistance of Kent Darzi in the data collection phase of this investigation.

REFERENCES

Burch, G.T. (1967). Multi-Plate Damage Study, AFATL-TR-67-116, Air Force Armament Laboratory, Eglin Air Force Base, Florida.

Coronado, A.R., M.N. Gibbins, M.A. Wright and P.H. Stern (1987). Space Station Integrated Wall Design and Penetration Damage Control, Boeing Aerospace Company, Seattle, Washington, Rept. D180-30550-1.

Kessler, D.J., R.C. Reynolds and P.P. Anz-Meador (1988). Orbital Debris Environment for Spacecraft Designed to Operate in Low Earth Orbit, NASA TM-100471, Houston, Texas.

Lundeberg, J.F., D.H. Lee and G.T. Burch (1966). "Impact Penetration of Manned Spacecraft", Journal of Spacecraft, 3, 182-187.

Maiden, C.J. and A.R. McMillan (1964). "An Investigation of the Protection Afforded a Spacecraft by a Thin Shield", AIAA Journal, 2, 1992-1998.

Morrison, R.H. (1972). A Preliminary Investigation of Projectile Shape Effects in Hypervelocity Impact of a Double-Sheet Structure, NASA TN D-6944, Washington, D.C.

Riney, T.D. and E.J. Halda (1968). "Effectiveness of Meteroid Bumpers Composed of Two Layers of Distinct Materials", AIAA Journal, 6, 338-344.

Sawle, D.R. (1970). "Hypervelocity Impact on Thin Sheets and Semi-Infinite Targets at 15 km/sec," AIAA Journal, 8, 1240-1244.

Schonberg, W.P., A.B. Bean and K. Darzi (1991). Hypervelocity Impact Physics, NASA CR-4343, Washington, D.C.

Schonberg, W.P. and K. Darzi (1992). "Projectile Shape and Material Effects in Hypervelocity Impact Response of Dual-Wall Structures", Journal of Aerospace Engineering, 5, 405-424.

Taylor, R.A. (1987). "A Space Debris Simulation Facility for Spacecraft Materials Evaluation", SAMPE Quarterly, 18, 28-34.

Ugural, A.C. (1981). Stresses in Plates and Shells, McGraw-Hill, New York.

Wallace, R.R., J.R. Vinson and M. Kornhauser (1962). "Effects of Hypervelocity Particles on Shielded Structures", ARS Journal, 32, 1231-1237.

Whipple, F.L. (1947). "Meteorites and Space Travel", Astronomical Journal, 52, 137.

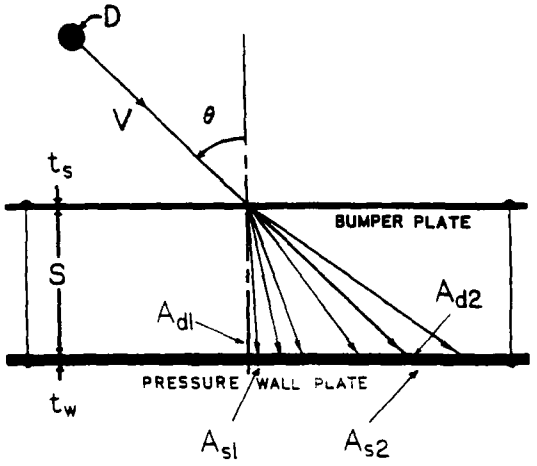


Figure 1. High-Speed Impact of a Dual-Wall Structure

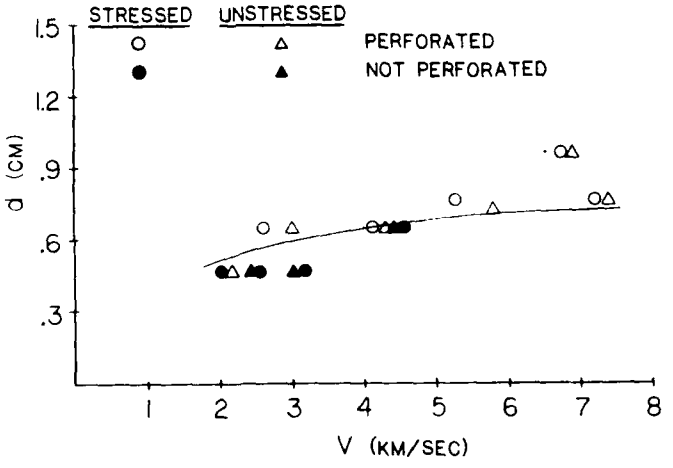


Figure 2. Ballistic Limit Curve, 0° Trajectory Obliquity, Stressed and Unstressed Systems, t_s=1.6 mm, t_w=3.175 mm, S=10.16 cm

TABLE 1 Hypervelocity Impact Test Parameters, Unstressed Pressure Wall Plates (t_s=1.6 mm, t_w=3.175 mm, S=10.16 cm)

Test No.	d (cm)	V (km/sec)	θ (deg)	MLI
FP02	0.953	6.92	0	Y
MD-TA	0.475	2.15	0	Y
MD-TB	0.475	2.45	0	Y
P08	0.635	2.96	0	Y
P12C	0.635	4.33	0	Y
P21D	0.762	5.85	0	Y
P27D	0.475	3.08	0	Y
T2-4	0.635	4.28	0	Y
002B	0.795	6.51	45	Y
205C	0.635	5.30	45	Y
205D	0.635	6.42	45	Y
230A	0.475	4.41	45	Y
230B	0.475	3.23	45	Y
3020B	0.795	7.05	0	Y
3027A	0.635	6.90	45	Y
3028A	0.795	7.01	45	Y

TABLE 2 Hypervelocity Impact Tests Parameters, Stressed Pressure Wall Plates (t_s=1.6 mm, t_w=3,175 mm, S=10.16 cm)

Test No.	d (cm)	V (km/sec)	θ (deg)	MLI	σ_1 (MPa)	σ_2 (MPa)
FP01	0.953	6.88	0	Y	68	34
FP10	0.475	2.47	0	Y	68	34
FP11	0.475	3.07	0	Y	68	34
FP12	0.475	2.02	0	Y	68	34
FP13	0.635	4.14	0	Y	68	34
FP14	0.475	3.26	45	Y	68	34
FP15	0.475	4.34	45	Y	68	34
FP16	0.635	2.60	0	Y	68	34
FP17	0.635	4.35	0	Y	68	34
FP18	0.635	5.32	45	Y	68	34
FP19	0.635	6.50	45	Y	68	34
FP20	0.635	7.05	45	Y	68	34
FP21	0.795	5.19	0	Y	68	34
FP23	0.795	7.21	0	Y	68	34
FP24	0.795	6.90	45	Y	68	34
FP25	0.795	7.29	45	Y	68	34

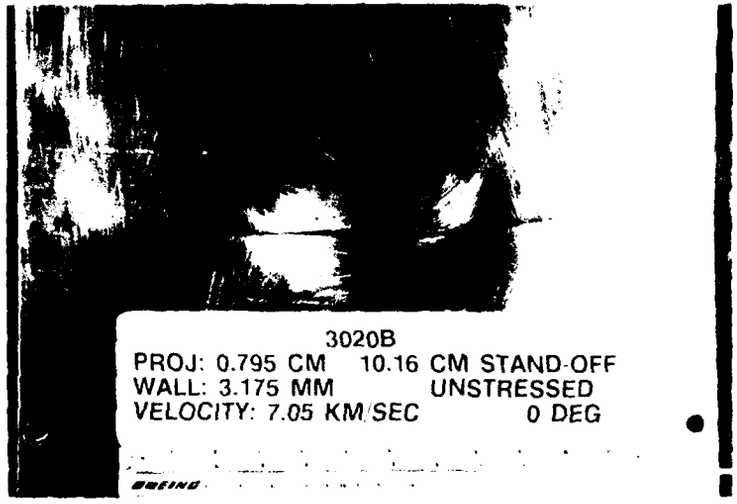


Figure 3a. Pressure Wall Plate, Unstressed System Test No. 3020B
d=0.795 cm, V=7.05 km/sec, θ=0°

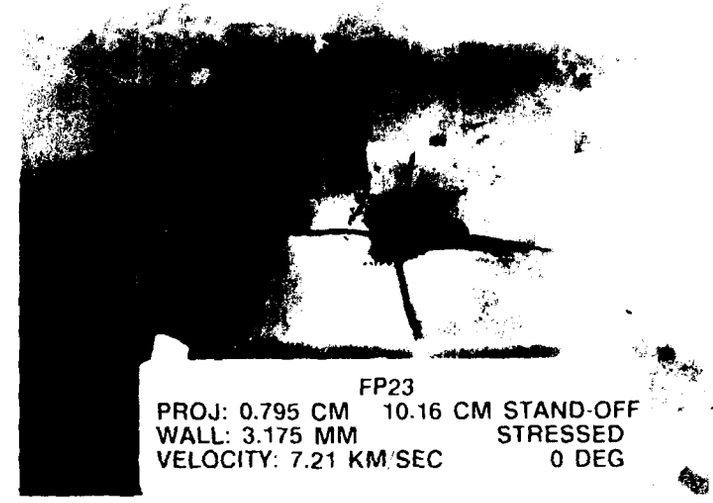


Figure 3b. Pressure Wall Plate, Stressed System Test No. FP23
d=0.795 cm, V=7.21 km/sec, θ=0°

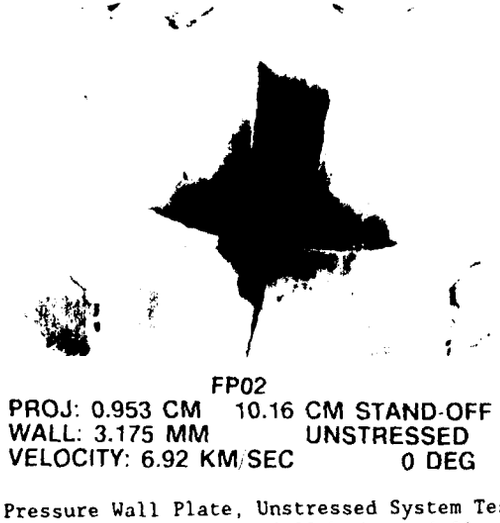


Figure 4a. Pressure Wall Plate, Unstressed System Test No. FP02
d=0.953 cm, V=6.92 km/sec, θ=0°

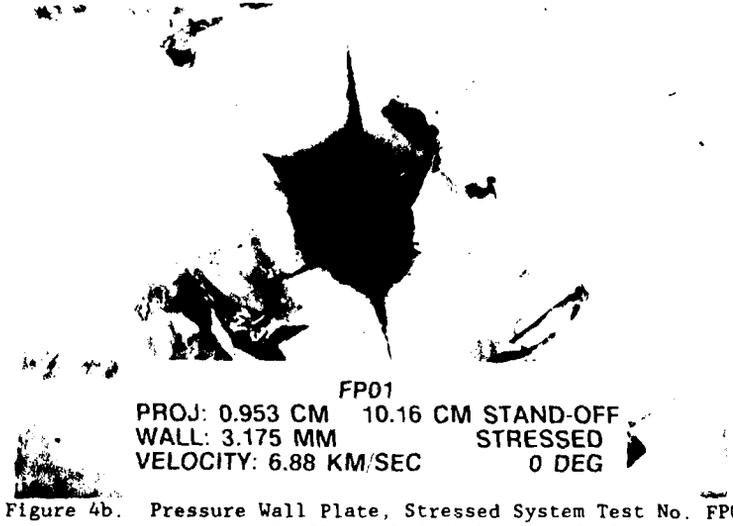


Figure 4b. Pressure Wall Plate, Stressed System Test No. FP01
d=0.953 cm, V=6.88 km/sec, θ=0°

TABLE 3 Comparison of Stressed and Unstressed Pressure Wall Plates Normal (0^0) Impact

Test No.	Impact Energy (J)	σ_1 (MPa)	σ_2 (MPa)	D (cm)	d_h (cm)	A_d (cm^2)	L_b (cm)	A_s (cm^2)
FP12	310	68	34	0.64	----	5.10	----	----
MD-TA	352	0	0	0.82	0.81[1]	2.85	----	----
FP10	464	68	34	0.80	----	20.26	----	----
MD-TB	457	0	0	0.81	----	25.68	----	----
FP11	717	68	34	0.87	----	11.35	----	----
P27D	722	0	0	0.88	----	10.90	----	----
FP16	1,229	68	34	0.95	1.11[1]	31.68	----	1.03
P08	1,593	0	0	1.09	0.99[1]	20.26	----	2.13
FP13	3,117	68	34	1.11	1.11[1]	38.32	----	0.35
T2-4	3,331	0	0	1.11	1.34[2]	49.48	----	3.58
FP17	3,441	68	34	1.19	----	20.29	----	----
P12C	3,409	0	0	1.19	----	20.26	----	----
FP21	9,613	68	34	1.43	7.13	45.61	5.72	----
P21D	10,753	0	0	1.49	9.53	38.90	9.12	----
FP23	18,551	68	34	1.60	19.15	292.64	11.43	----
3020B	17,737	0	0	1.62	18.07	256.52	14.22	----
FP01	29,049	68	34	1.74	24.89	457.29	17.78	----
FP02	29,388	0	0	1.75	25.27	457.29	15.24	----

[1]One distinct hole
[2]Multiple holes

TABLE 4 Comparison of Stressed and Unstressed Pressure Wall Plates Oblique (45°) Impact

Test No.	Impact Energy (J)	σ_1 (MPa)	σ_2 (MPa)	D_{min} (cm)	D_{max} (cm)	d_{h1} (cm)	d_{h2} (cm)	A_{d1} (cm^2)	A_{d2} (cm^2)	L_p (cm)
FP14	809	68	34	0.87	1.11	----	----	----	62.06	----
230B	794	0	0	0.90	1.18	----	----	----	76.06	----
FP15	1,433	68	34	0.95	1.11	----	----	----	81.03	----
230A	1,480	0	0	0.98	1.18	----	----	----	81.03	----
FP18	5,146	68	34	1.27	1.67	----	0.25[1]	20.26	15.55	----
205C	5,109	0	0	1.24	1.51	----	0.97[2]	11.35	11.35	----
FP19	7,683	68	34	1.67	1.74	----	0.43[1]	46.61	2.90	----
205D	7,217	0	0	1.28	1.62	----	crack	20.26	5.09	----
FP20	9,037	68	34	1.43	1.75	----	0.45[1]	16.39	24.52	----
3027A	9,089	0	0	1.41	1.76	----	0.09[1]	31.68	20.26	----
FP24	16,990	68	34	1.65	1.98	----	1.80[2]	28.45	13.38	----
002B	15,123	0	0	1.53	2.01	----	0.49[1]	20.26	9.55	----
FP25	18,965	68	34	1.66	2.18	----	4.21	45.61	25.68	4.45
3028A	17,536	0	0	1.70	2.11	----	3.05	66.39	41.47	1.91

[1]One distinct hole
[2]Multiple holes

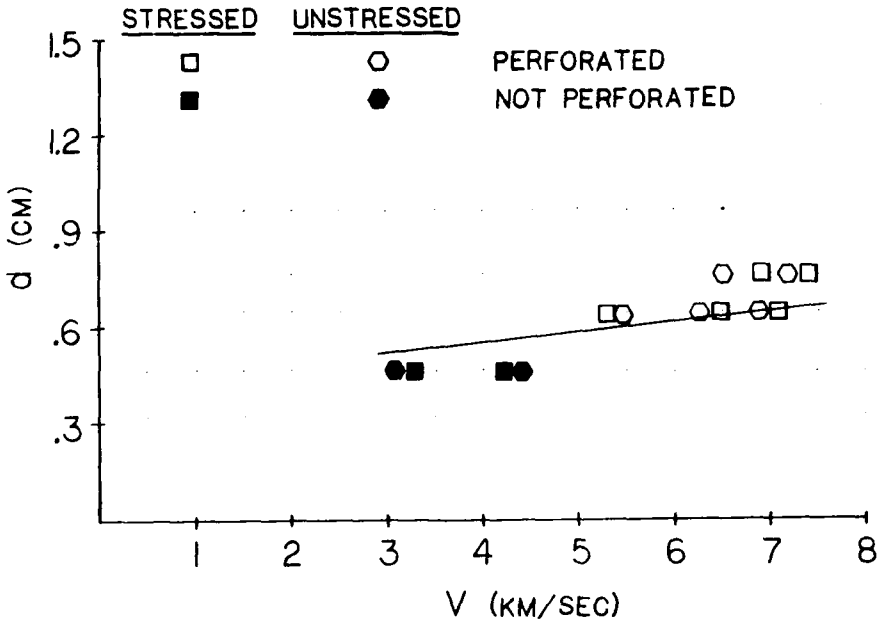


Figure 5. Ballistic Limit Curve, 45° Trajectory Obliquity, Stressed and Unstressed Systems, t_s=1.6 mm, t_w=3.175 mm, S=10.16 cm

Int. J. Impact Engng Vol.14, pp.647–658, 1993
Printed in Great Britain

0734-743X/93 $6.00+0.00
© 1993 Pergamon Press Ltd

RESPONSE OF SPACE STRUCTURES TO ORBITAL DEBRIS PARTICLE IMPACT

William P. Schonberg and Fengwei Yang

Mechanical Engineering Department
University of Alabama in Huntsville
Huntsville, AL 35899

ABSTRACT

All long-duration space and aerospace support and transportation systems, such as the Space Station Freedom and the Space Shuttle, are susceptible to impacts by pieces of orbital debris. These impacts occur at high speeds and can damage the flight-critical systems of such spacecraft. Therefore, the design of a structure that will be exposed to a hazardous orbital debris environment must address the possibility of such hypervelocity impacts and their effect on the integrity of the entire structural system. A technique is developed for analyzing the response of dual-wall structures to oblique hypervelocity projectile impact. Ballistic limit curves that predict the potential of an impacting projectile to perforate the main wall of a dual-wall structural system are obtained using the technique and are compared against experimentally derived curves. Comparisons are performed for a variety of impact velocities, trajectory obliquities and projectile masses. It is shown that the results obtained using the technique developed herein compare very well with experimental results.

INTRODUCTION

All earth-orbiting spacecraft, especially those with a mission duration of more than a few days, are susceptible to high-speed impacts by pieces of orbiting debris. These orbital debris particles range in size from microscopic solid propellant particles to spent rocket boosters still in low earth orbit. The impacts of these particles, which can occur at speeds as high as 12 to 14 km/sec (Kessler, 1982), can damage flight-critical systems and lead to catastrophic failure of the spacecraft (Kessler and Cour-Palais, 1978; Kessler, 1981; Reynolds *et al*, 1983). Therefore, the design of a long duration spacecraft in earth orbit must take into account the effects of such impacts and must contain protective systems to insure its integrity and the safety of its occupants.

The design of protective systems for earth-orbiting structures largely depends on the ability to predict the response of a variety of structural components to hypervelocity impact. Forty-five years ago it was suggested that a 'bumper' could be used to minimize the damage caused by meteoroid impact (Whipple, 1947). Since then, numerous investigations have been performed to study the effectiveness of multi-sheet structures in reducing the damage threat of hypervelocity projectiles (Wallace *et al*, 1962; Maiden and McMillan, 1964; Lundeberg *et al*, 1966; Wilkinson, 1969; Swift *et al*, 1983). Dual-wall configurations were repeatedly shown to provide significant increases in protection against perforation by hypervelocity projectiles over equivalent single-wall structures.

Recent experimental investigations of oblique hypervelocity impact phenomena have shown that the response of a dual-wall structure to oblique hypervelocity projectile impact is significantly different from its response to normal hypervelocity impact (Coronado *et al*, 1987; Schonberg and Taylor, 1989). Unlike normal high-speed impacts, oblique impacts can produce a tremendous volume of ricochet debris particles which can severely damage panels of instrumentation units located on the exterior of a structure (Schonberg, 1989). Obliquity effects, therefore, must be considered in the design of a space structure that will be exposed to the orbital debris environment.

A wide variety of analytical models exist that predict the response of thin plates to normal impact loadings. On the other hand, only a relatively small number of models have been developed for oblique impact. Many early analytical perforation studies were performed in an attempt to model the response of armor to impacts by bullets and bullet-like projectiles at impact speeds less than 2 km/sec (see e.g., Taylor; 1948, Thomson; 1955, Zaid and Paul, 1957; Paul and Zaid, 1958). Although the importance of trajectory obliquity was occasionally studied (Zaid and Paul, 1959; Recht and Ipson, 1963), the problem of normal impact was usually solved because the assumption of axisymmetric response made it much more tractable mathematically. More recent attempts at modelling thin plate perforation by normally impacting projectiles have included elastic/plastic and visco-plastic analyses (Goldsmith *et al*, 1965; Calder and Goldsmith, 1971; Levy and Goldsmith, 1984) and comprehensive mechanics-of- materials approaches (Ravid and Bodner, 1983; Awerbuch, 1970; Awerbuch and Bodner, 1974).

The objective of the work presented herein was to develop and validate a technique that could be used to predict the response of dual-wall structure to oblique hypervelocity impact. This technique was developed in three phases. In the first phase, a general theory of thin plate response to an impulsive asymmetric velocity distribution was developed. In the second stage, this theory was applied to the analysis of the response of the inner plate in a dual-wall structure. In the final stage, a series of ballisstic limit curves were derived for a variety of impact parameters. The validity of these curves was demonstrated by comparing them with existing ballistic limit curves that were experimentally obtained in a previous investigation of (Schonberg *et al*, 1991).

METHOD OVERVIEW AND ASSUMPTIONS

Consider a dual-wall structure that is impacted by a spherical projectile of diameter D_t (mass M_t) traveling at a velocity V_t at an angle θ_t with respect to the outward normal of the outer wall (Figure 1). The 'bumper' (thickness t_b) is separated from the 'pressure wall' (thickness t_w) by a distance S called the 'stand-off distance'. The fragments created during the impact of the projectile on the bumper are sprayed on the pressure wall in the form of asymmetric debris clouds while some fragments ricochet away from the dual-wall structure. A spherical projectile is assumed in the analysis in order that forthcoming results may be compared directly against experimental data obtained using spherical projectiles. The analysis of the response of this structure to an oblique hypervelocity impact is based in part on a technique that predicts the ballistic limit of dual-wall structures under normal hypervelocity projectile impact (Madden, 1967; Madden, 1969).

The impact of the debris clouds on the pressure wall typically creates two elliptical areas of damage. The extent of the areas over which the asymmetric impulsive loadings of the debris clouds are distributed on the pressure wall is governed by the manner in which the projectile and bumper plate fragment, melt, and vaporize. In Figure 1, the angles θ_1 and θ_2 denote the trajectories of the centers-of-mass of the 'normal' and 'in-line' debris clouds, respectively; the angles Φ_1 and Φ_2 represent the spread of these fragments. The 'normal' and 'in-line' damage areas are denoted Σ_1 and Σ_2, respectively, on the front surface of the pressure wall; θ_r and θ_{99} characterize the trajectory of the center-of-mass and the spread of the ricochet debris fragments, respectively.

In the first phase of the analysis, a general theory of thin plate response to an impulsive asymmetric velocity distribution is developed. It is assumed that the plate is circular and that Kirchhoff plate theory assumptions are valid. In the second phase, this theory is applied to the analysis of the response of a pressure wall plate in a dual-wall structure under the impacts of the asymmetric debris clouds. In the final phase, a series of ballistic limit curves that indicate the likehood of pressure wall perforation due to an oblique hypervelocity impact are developed and verified for a variety of impact parameters. The assumptions used in the second phase of the analysis are discussed in more detail in the following paragraphs.

In applying the general theory developed in the first phase of the analysis, it is assumed that the projection of the projectile trajectory on the bumper surface is coincident with the line on the bumper defined by $\theta=\pi$, $0\le r<\infty$. This implies that the response of the bumper plate to the impact will be symmetric with respect to the line defined by the union of the lines $\theta=0$, $0\le r<\infty$ and $\theta=\pi$, $0\le r<\infty$. The symmetry of the bumper response allows us to assume further that the debris clouds generated and the subsequent response of the pressure wall to their impact will also be symmetric with respect to the projection of that line on the pressure wall.

The initial impact on the bumper is assumed to occur fast enough so that the debris clouds consist primarily vaporous material, and that all particles of a debris cloud impact the pressure wall at the same time. In this manner, the loads transmitted by the debris clouds to the pressure wall can be assumed to be in the form of initial velocity distributions which are assumed to be directed perpendicularly onto the pressure wall. Thus, for the purposes of this study, the tangential component of the debris cloud loading is neglected.

Because of the obliquity of the initial impact and the oblique trajectories of the debris clouds, the initial velocity distribution corresponding to each debris cloud is applied over an elliptical area of the pressure wall and is asymmetric with the peak occurring over the 'nearer' focus of the ellipse. This focus also defines the point on the pressure wall to which the line defining the trajectory of a particular debris cloud is drawn. A sketch of a generic asymmetric velocity distribution with an elliptical horizontial cross-section is shown in Figure 2. In Figure 2, the origin of the polar coordinate system coincides with a focus of the ellipse. This allows the equation defining the ellipse to be written as:

$$a(1-\epsilon^2) = r(1-\epsilon\cos\theta) \qquad (1)$$

where $\epsilon=\sqrt{(a^2-b^2)}/a$ is the eccentricity of the ellipse, and a and b are lengths of the semi-major and semi-minor axes of the ellipse, respectively.

Because of the high speeds at which the debris clouds travel, it is assumed that the impacts

of the 'normal' and 'in-line' debris clouds on the pressure wall occur simultaneously so that the response of the pressure wall to one is not affected by the impact of the other. The pressure wall is assumed to be circular and the damage areas created by the debris clouds are assumed to be much smaller than the area of the plate. This assumption, together with that of zero interaction between the debris cloud loadings, allows the focus of the ellipse at the base of each debris cloud to be placed at the origin of the pressure wall and subsequent response analysis to be performed independently for the 'normal' and 'in-line' debris cloud loadings. Furthermore, because the damage areas are local effects, the effects of the debris cloud impacts are confined to relatively small areas surrounding the damage areas. This allows the edges of the plate to be modelled as clamped, rather than simply-supported. Additional assumptions are discussed as they arise in the analysis.

PHASE ONE: DYNAMIC THIN PLATE ANALYSIS

In this section, a general theory of thin plate response to an asymmetric impulsive velocity distribution is developed. From linear plate theory for isotropic, homogeneous materials, the governing differential equation for dynamic plate deflection $u(r,\theta,t)$ in polar coordinates can be written as follows:

$$\nabla^2\nabla^2 u + k^4 \frac{\partial^2 u}{\partial t^2} = 0 \tag{2}$$

where $k = \{2[3(1-\nu^2)]^{1/2}/ct_w\}^{1/2}$, c is the speed of sound in the plate material, ν is Poisson's ratio, t_w is the plate thickness, and

$$\nabla^2 = \frac{\partial^2}{\partial r^2} + \frac{\partial}{r\partial r} + \frac{\partial^2}{r^2\partial\theta^2} \tag{3}$$

If the plate is clamped along its boundary, then we have the boundary conditions

$$u|_{\partial\Sigma} = 0; \qquad \left.\frac{\partial u}{\partial r}\right|_{\partial\Sigma} = 0 \tag{4}$$

where $\partial\Sigma$ is the boundary of the plate. If the plate is subjected to an initial velocity $V_0(r,\theta)$, then $u(r,\theta,t)$ must also satisfy the initial conditions

$$u|_{t=0} = 0; \qquad \left.\frac{\partial u}{\partial t}\right|_{t=0} = V_0(r,\theta) \tag{5}$$

This initial and boundary value problem is solved by using separation of variables, that is, we let

$$u(r,\theta,t) = X(r)\,Y(\theta)\,G(t) \tag{6}$$

Upon insertion of equation (6) into equation (2) and application of the method, we find that the functions X(r), Y(θ), and G(t) are given by

$$X_{nm}(r) = \alpha_{nm}J_n(\eta_{nm}kr) + \beta_{nm}I_n(\eta_{nm}kr) + \zeta_{nm}N_n(\eta_{nm}kr) + \xi_{nm}K_n(\eta_{nm}kr) \tag{7}$$

$$Y_n(\theta) = D_1\cos(n\theta) + D_2\sin(n\theta) \tag{8}$$

$$G_{nm}(t) = P_1\cos(\eta_{nm}^2 t) + P_2\sin(\eta_{nm}^2 t) \tag{9}$$

where n^2 is a constant of separation and I_n, J_n, and N_n, K_n are n-th order Bessel Functions of the first and second kind, respectively. The periodicity of Y(θ) implies that for Y(θ) to be a single-valued function, we must have $Y(\theta+2\pi)=Y(\theta)$. This in turn implies that n must be an positive integer or zero. Additionally, since the plate and the loading both possess symmetry with respect to $\theta=0$, $Y_n(\theta)$ must also be symmetric with respect to $\theta=0$. Hence, $D_2=0$ in equation (8). To avoid infinite deflections at the center of the plate, the functions $X_{nm}(r)$ must be bounded at r=0. This implies that $\zeta_n=0$ and $\xi_n=0$ in equation (7). The η_{nm} are the roots of the equation

$$J_n(\eta_n kR)\,I_n'(\eta_n kR) - I_n(\eta_n kR)\,J_n'(\eta_n kR) = 0 \tag{10}$$

which is obtained by substituting $X_{nm}(r)$ according to equation (7) into the boundary conditions given by equation (4). Combining equations (7-9) yields

$$u_{nm}(r,\theta,t) = X_{nm}(r)\cos(n\theta)\,[P_1\cos(\eta_{nm}^2 t) + P_2\sin(\eta_{nm}^2 t)] \tag{11}$$

where the constant D_1 has been combined into α_{nm} and β_{nm}. The initial condition $u(r,\theta,0)=0$

implies that P_1=0. Combination of P_2 into α_{nm} and β_{nm} yields the following expression for $u(r,\theta,t)$:

$$u(r,\theta,t) = \sum_{n=0}^{\infty}\sum_{m=1}^{\infty} X_{nm}(r)\cos(n\theta)\sin(\eta_{nm}^2 t) \tag{12}$$

where

$$X_{nm}(r) = \alpha_{nm}J_n(\eta_{nm}kr) + \beta_{nm}I_n(\eta_{nm}kr) \tag{13}$$

All that remains is to evaluate the constants α_{nm} and β_{nm}. Differentiating equation (12) with respect to t, evaluating the result at t=0, and applying the initial condition given in equation (5), we obtain

$$\left.\frac{\partial u}{\partial t}\right|_{t=0} = \sum_{n=0}^{\infty}\sum_{m=1}^{\infty} \eta_{nm}^2 X_{nm}(r)\cos(n\theta) = V_0(r,\theta) \tag{14}$$

Multiplying both sides of equation (14) by $\cos(n\theta)$, and integrating from 0 to 2π, we obtain

$$\sum_{m=1}^{\infty} \pi\eta_{nm}^2 X_{nm}(r) = \int_0^{2\pi} V_0(r,\theta)\cos(n\theta)\,d\theta \tag{15}$$

Similarly, multiplying both sides of equation (15) by $rX_{nm}(r)$ and integrating from 0 to R, we find

$$\pi\eta_{nm}^2\int_0^R rX_{nm}^2(r)\,dr = \int_0^R\int_0^{2\pi} rX_{nm}(r)\,V_0(r,\theta)\cos(n\theta)\,d\theta\,dr \tag{16}$$

If we substitute $X_{nm}(r)$ according to equation (13) into the first of the boundary conditions given by equation (4), we find that β_{nm} can be written as

$$\beta_{nm} = -\alpha_{nm}\frac{J_n(\eta_{nm}kR)}{I_n(\eta_{nm}kR)} \tag{17}$$

Substitution of β_{nm} into equation (13) yields

$$X_{nm}(r) = \alpha_{nm}\left[J_n(\eta_{nm}kr) - \frac{J_n(\eta_{nm}kR)}{I_n(\eta_{nm}kR)}J_n(\eta_{nm}kr)\right] \tag{18}$$

Substitution of equation (18) for $X_{nm}(r)$ into equation (16) yields the following for α_{nm}

$$\alpha_{nm} = \frac{\int_0^R\int_0^{2\pi} r\left[J_n(\eta_{nm}kr) - \frac{J_n(\eta_{nm}kR)}{I_n(\eta_{nm}kR)}I_n(\eta_{nm}kr)\right]V_0(r,\theta)\cos(n\theta)\,d\theta\,dr}{\pi\eta_{nm}^2\int_0^R r\left[J_n(\eta_{nm}kr) - \frac{J_n(\eta_{nm}kR)}{I_n(\eta_{nm}kR)}I_n(\eta_{nm}kr)\right]^2 dr} \tag{19}$$

The solution process is now complete. Stresses within the plate can be calculated using the standard expressions for σ_r, σ_θ and $\sigma_{r\theta}$ in terms of transverse displacement (Ugural, 1981).

PHASE TWO: DEBRIS CLOUD LOADING OF A PRESSURE WALL PLATE

The first step in applying the general theory developed in the previous section to the analysis of pressure wall response is to determine a functional form of the normal initial velocity distribution $V_{0i}(r,\theta)$ for each debris cloud. In order to be able to do this, the total mass M_i, the axial and radial expansion velocities, trajectory angles θ_i and debris cloud spread angles Φ_i must be known for the 'normal' (i=1) and 'in-line' (i=2) debris clouds. While the axial velocities of the 'normal' and 'in-line' debris clouds, V_1 and V_2, respectively, are assumed not to be equal, it is assumed for the purposes of this study that the average radial expansion velocities of the debris clouds are equal and denoted by V_e. These quantities are found by applying conservation of mass, momentum and energy before and after the initial impact of the projectile on the bumper plate. This calculation is presented in the Appendix. Once these quantities are known, the actual form of $V_{0i}(r,\theta)$ for each debris cloud is determined as follows. The mass per unit area impacting on the pressure wall is assumed to be of the form

$$m_i(r,\theta) = A_i e^{-\left(\frac{1-e_i\cos\theta}{\Delta_i}r\right)^2} \tag{20}$$

This form of the mass distribution is motivated by the assumed shape of the velocity distribution. In equation (20), there are three parameters to be determined for each debris cloud: ϵ_i, A_i, and Δ_i. The parameter ϵ_i is determined from geometrical considerations at the elliptical base of the initial velocity distribution (Figure 3) and given by

$$\epsilon_i = \sqrt{1-\frac{2\tan(\Phi_i/2)}{\cos\Theta_i[\tan(\Theta_i+\Phi_i/2)-\tan(\Theta_i-\Phi_i/2)]}} \tag{21}$$

To obtain Δ_i, we consider the total kinetic energy of each debris cloud

$$E_i = \frac{1}{2}M_i(V_e^2+V_i^2) \tag{22}$$

The kinetic energy of a debris cloud can also be obtained by considering the vertical and horizontal velocity components of a particle with mass $dm = m_i(r,\theta)rdrd\theta$ that impacts the pressure wall at a point (r,θ). These velocity components of the particle are given by $V_i\cos\Theta_i$ and $R_i(r,\theta)/\delta t_i$, respectively the quantity $\delta t_i = S/(V_i\cos\Theta_i)$ is the time required for the leading edge of a debris cloud to travel the distance from bumper to the pressure wall (see Figure 3) while $R_i(r,\theta)$ is the horizontal displacement of the particle and given as

$$R_i(r,\theta) = \sqrt{(S\tan\Theta_i)^2-2rS\tan\Theta_i\cos(\pi-\theta)+r^2} \tag{23}$$

Thus, the kinetic energy of a debris cloud can also be expressed as

$$E_i = \frac{1}{2}\int_0^{2\pi}\int_0^{f_i(\theta)} m_i(r,\theta)\left(V_i^2\cos^2\Theta_i+\frac{R_i^2(r,\theta)}{\delta t_i^2}\right)rdrd\theta \tag{24}$$

where

$$f_i(\theta) = \frac{S[\tan(\Theta_i+\Phi_i/2)-\tan(\Theta_i-\Phi_i/2)](1-\epsilon_i^2)}{2(1-\epsilon_i\cos\theta)} \tag{25}$$

Substituting for $m_i(r,\theta)$ into equation (24), performing the integrations and equating the result to equation (22) we obtain the following quadratic equation for Δ_i:

$$\frac{V_i^2\cos^2\Theta_i}{2S^2}\frac{(2+3\epsilon_i^2)}{(1-\epsilon_i^2)^2}\Delta_i^2+\frac{3\epsilon_i\sqrt{\pi}V_i^2\sin\Theta_i\cos\Theta_i}{2S(1-\epsilon_i^2)}\Delta_i-V_e^2 = 0 \tag{26}$$

Once a value for Δ_i is obtained, A_i can be determined by integrating the assumed mass distribution for a debris cloud over the elliptical damage region Σ_i of the pressure wall and then equating the result to the debris cloud mass M_i , that is,

$$M_i = \int_0^{2\pi}\int_0^{f_i(\theta)} m_i(r,\theta)\,rdrd\theta \tag{27}$$

The equation for A_i is then given by

$$M_i = \frac{\pi A_i\Delta_i^2}{(1-\epsilon_i^2)^{3/2}} \tag{28}$$

Once the constants ϵ_i, A_i and Δ_i are determined, the mass distribution of each debris cloud is completely defined. We are now ready to determine the expression for the initial velocity distribution due to the impact of a debris cloud on a pressure wall. By balancing the momentum of a debris cloud before its impact with the pressure wall, and the momentum of the debris cloud material and the pressure wall after the impact, we find

$$m_i(r,\theta)\,V_i\cos\Theta_i = [m_i(r,\theta)+m^*]\,V_{0i}(r,\theta) \tag{29}$$

where $V_{0i}(r,\theta)$ is the initial velocity distribution imparted to the pressure wall by a debris cloud "i", $m^*=\rho_w t_w$ is the mass per unit area of the pressure wall and ρ_w is the density of the pressure wall material. Substitution of $m_i(r,\theta)$ according to equation (20) and solution of equation (29) for $V_{0i}(r,\theta)$ gives

$$V_{0i}(r,\theta) = \frac{V_i\cos\Theta_i}{1+\frac{m^*}{A_i}e^{\left(\frac{1-\epsilon_i\cos\theta}{\Delta_i}r\right)^2}} \tag{30}$$

Substitution of equation (30) into equation (19) defines α_{nm}, and subsequently $u(r,\theta,t)$, for each debris cloud loading.

PHASE THREE: PERFORATION CURVE DEVELOPMENT

Because the peak of the impulsive velocity distribution occurs over the origin of the pressure wall, a critical stress at the origin will be used in developing the criterion for perforation of the pressure wall plate. At the origin, shear stress vanishes and the radial and circumferential stresses are equal. Therefore, either stress may be considered and yields the following expression for stress at r=0 on the surface of the plate:

$$\sigma_r|_{r=0} = -\frac{Et_w}{4}\left[\frac{k}{1-\nu}\sum_{m=1}^{\infty}(-\alpha_{0m}+\beta_{0m})\eta_{0m}\sin\eta_{0m}t\right.$$

$$\left.+\frac{k\cos(2\theta)}{2(1+\nu)}\sum_{m=1}^{\infty}(-\alpha_{2m}+\beta_{2m})\eta_{2m}\sin\eta_{2m}t\right] \tag{31}$$

All other terms involving α_{nm} and β_{nm} vanish because the corresponding Bessel Functions vanish at r=0. It is noted that the stress calculated by equation (31) is the result of elastic plate theory calculations. However, in the event of a perforation, the stress levels in the pressure wall plate will exceed the elastic limit of the plate material by several orders of magnitude. This apparent inconsistency can be resolved as follows.

Let the actual stress at r=0 be related to the elastic stress at that point according to

$$\sigma_{act} = \omega\sigma_r|_{r=0} \tag{32}$$

where ω is a function of geometrical and mechanical properties of the plate only (i.e., ω is independent of initial impact parameters). This expression is motivated by the fact that the portions of the pressure wall plate that are impacted by the debris clouds will respond hydrodynamically to the debris cloud loadings. Consider a generic one-dimensional stress-strain curve and a generic hydrostatic curve superimposed on a single set of axes as shown in Figure 4. Let ϵ_1 and ϵ_2 be the strains that exist in the pressure wall plate due to loading conditions "1" and "2". A purely elastic analysis of plate response would result in corresponding stress states $\sigma_{el,1}$ and $\sigma_{el,2}$, respectively. However, if the response is hydrodynamic in nature, then the actual stress states would be $\sigma_{act,1}$ and $\sigma_{act,2}$ as shown. Because $\sigma_{el,1}$ and $\sigma_{el,2}$ are obtained from a linear, elastic analysis, we have

$$\frac{\sigma_{el,1}}{\sigma_{el,2}} = \frac{\epsilon_1}{\epsilon_2} \tag{33}$$

If the hydrostat is assumed to be nearly linear, then it also follows that

$$\frac{\sigma_{act,1}}{\sigma_{act,2}} \approx \frac{\epsilon_1}{\epsilon_2} \tag{34}$$

Combining equations (33) and (34) yields

$$\frac{\sigma_{act,1}}{\sigma_{act,2}} \approx \frac{\sigma_{el,1}}{\sigma_{el,2}} \tag{35}$$

which leads directly to equation (32).

If the actual stress at the origin exceeds some critical value, then the plate is assumed to be perforated. If the critical value is assumed to be some multiple of the ultimate strength of the plate material, then if

$$\sigma_{act} \geq \gamma\sigma_{ult} \tag{36}$$

the plate will be perforated. Substituting for σ_{act} according to equation (32) into equation (36), we obtain the following condition for plate perforation:

$$\sigma_r|_{r=0} \geq \chi\sigma_{ult} \tag{37}$$

where $\chi=\gamma/\omega$ is a constant for a given system configuration and pressure wall material. Computations of the stresses at the origin were made by adapting the analytical model to a FORTRAN 77 program and running the program on the Alabama Supercomputer Network CRAY X-MP/24.

In all cases, the materials of the pressure wall, the projectile, and the bumper were aluminum. In the numerical calculations, $E=0.7X10^{11}$ N/m^2, $\nu=0.35$, $\rho_p=\rho_w=2768.0$ kg/m^3, $\sigma_{ult}=0.31X10^9$ N/m^2, S=10.16 cm, $t_w=0.318$ cm, and R=50 cm. The diameters of the projectile were chosen to be 0.475, 0.635, 0.795, and 0.953 cm; the impact velocities of the projectile were 4.0, 5.5, and 7.0 km/sec. Results were obtained for trajectory obliquity angles of 30°, 45°, 60°, and 65° and are presented in Figures 5-8.

COMPARISON WITH EXPERIMENTAL DATA

Figures 5-8 show the results obtained using the analytical model developed herein for the various impact parameters considered. The results are presented in terms of whether or not pressure wall perforation had occurred. A hollow circle represents a perforation; a solid circle represents an unperforated pressure wall. Superimposed on the analytical results are experimentally obtained ballistic limit curves (Coronado *et al*, 1987; Schonberg *et al*, 1991). It is noted that these curves are merely lines of demarcation between regions of parameter combinations leading to perforation (above) or no perforation (below). Whether or not the pressure wall was perforated was determined using the criterion given by equation (37). In order to be able to use equation (37), a value of χ had to be chosen. After performing the required calculations, it was determined that if a value of $\chi=0.25$ was used in equation (37), then the analytical predictions lined up very well with the experimental results.

For impact obliquities 30° and 45° (Figures 5 and 6, respectively), a comparison of the results obtained by the analytical model with the ballistic limit curves obtained from the experiments shows very good agreement. All of the projectile diameter and impact velocity combinations that result in pressure wall perforation lay above the experimental ballistic curve while all those that do not lay on or below it. For an impact obliquity of 65° (Figure 8), the results of the analytical model also compare very well with ballistic limit curve obtained by the Boeing Aerospace Company (Coronado *et al*, 1987) for the same trajectory obliquity. In the case of a 60° impact (Figure 7), there is very little experiment data available. However, the results predicted by the analytical model show no contradiction with the available experimental data. In fact, the analytical results provide information that complements the existing data.

CONCLUSIONS

An analytical model was developed to predict the response of dual-wall structures to orbital debris particle impact. The analysis was performed in three stages. In the first stage, a general theory of thin plate response to an impulsive asymmetric velocity distribution was developed. In the second stage, this theory was applied to the analysis of the response of a pressure wall plate in a dual-wall structure under the impacts of the asymmetric projectile and bumper plate secondary debris clouds. In the final stage, a series of ballistic limit curves that indicate the likehood of pressure wall perforation due to an oblique hypervelocity impact was developed and verified for a variety of impact parameters. Based on the results obtained and the subsequent comparison with experimental results, the model that has been developed appears quite capable of predicting the ballistic limit curves of an aluminium dual-wall system for a variety of trajectory obliquities.

ACKNOWLEDGEMENTS

The authors would like to acknowledge the support of the Engineering Foundation through an Engineering Research Initiation Grant (Grant No. RI-A-89-6).

REFERENCES

Awerbuch, J. (1970). A Mechanics Approach to Projectile Penetration. Isr. J. Tech., 8, 375-383.

Awerbuch, J., and S.R. Bodner (1974). Analysis of the Mechanics of Perforation of Projecitles in Metallic Plates. Int. J. Solids Structures, 10, 671-684.

Burch, G.T. (1967). Multi-plate Damage Study. Air Force Armament Laboratory, Report No. AFATL-TR-67-116, Eglin AFB, Florida.

Calder, C.A., and W. Goldsmith (1971). Plastic Deformation and Perforation of Thin Plates Resulting From Projectile Impacts. Int. J. Solids Structures, 7, 863-881.

Coronado, A.R., M.N. Gibbins, M.A. Wright, and P.H. Stern (1987). Space Station Integrated Wall Design and Penetration Damage Control, Final Report, NAS8-36426, Boeing Aerospace Company, Report No. D180-30550-1, Seattle, Washington.

Goldsmith, W., T.W.Liu, and S. Chulay (1965). Plate Impact and Perforation by Projectiles. Exp. Mech., 5, 385-404.

Kessler, D.J. (1981). Sources of Orbital Debris and the Projected Environment for Future Spacecraft. J. Spacecraft, 18, 357-360.

Kessler, D.J. and B.G. Cour-Palais (1978). Collision Frequency of Artificial Satellites: The Creation of a Debris Belt. J. Geophys. Res., 83, 2637-2646.

Kessler, D.J., and S.Y. Su (1982). eds., Orbital Debris, NASA CP 2360, Washington, D.C.
Levy, N., and W. Goldsmith (1984). Normal Impact and Perforation of Thin Plates by Hemispherically-Tipped Projectiles-I. Analyitical Considerations. Int. J. Impact Engng., 2, 209-229.
Lundeberg, J.F., D.H. Lee, and G.T. Burch (1966). Impact Penetration of Manned Spacecraft. J. Spacecraft, 3, 182-187.
Madden, R. (1967). Ballistic Limit of Double-Walled Meteoroid Bumper Systems. NASA TN D-3916, Washington, D.C.
Madden, R. (1969). Equations for the Comparison of the Ballistic Limit of Single and Double Wall Structures. Proc. AIAA Hypervelocity Impact Conference, Cincinatti, Ohio, Paper No. 69-370.
Maiden, C.J., and A.R. McMillan (1964). An Investigation of the Protection Afforded a Spacecraft by a Thin Shield. AIAA Journal, 2, 1992-1998.
Paul, B., and M. Zaid (1958). Normal Perforation of a Thin Plate by Truncated Projectiles. J. Frank. Inst., 265, 317-335.
Ravid, M., and S.R. Bodner (1983). Dynamic Perforation of Viscoplastic Platesby Rigid Projectiles. Int. J. Engng. Sci., 21, 577-591.
Recht, R.F., and T.W. Ipson (1963). Ballistic Perforation Dynamics. J. Appl. Mech., 384-390.
Reynolds, R.C., N.H. Fisher, and E.E. Rice (1983). Man-Made Debris in Low Earth Orbit - A Threat to Future Space Operations. J. Spacecraft, 20, 279-285.
Schonberg, W.P. (1989). Characterizing the Damage Potential of Ricochet Debris Due to an Oblique Hypervelocity Impact. Proc. Thirtieth AIAA/ASME/ASCE/AHS/ACS Structures, Structural Dynamics, and Materials Conference, Mobile, Alabama, Paper No. 89-1410.
Schonberg, W.P., A.J. Bean, and K. Darzi (1991). Hypervelocity Impact Physics, NASA CR-4343.
Schonberg, W.P., and R.A. Taylor (1989). Penetration and Ricochet Phenomena in Oblique Hypervelocity Impact. AIAA Journal, 29, 639- 656.
Swift, H.F, R. Bamford, and R. Chen (1983). Designing Space Vehicle Shields for Meteoroid Protection: A New Analysis. Adv. Space Res., 2, 219-234.
Taylor, G.L. (1948). The Formation and Enlargement of a Circular Hole in a Thin Plastic Sheet. Quart. J. of Mech. and Appl. Mat., 1, 103-124.
Thomson, W.T. (1955). An Approximate Theory of Armor Penetration. J. Appl. Phys., 26, 80-83.
Ugural, A.C. (1981). Stresses in Plates and Shells. McGraw-Hill, New York.
Wallace, R.R, J.R. Vinson, J.R., and M. Kornhauser (1962). Effects of Hypervelocity Particles on Shielded Structures. ARS Journal, 1231-1237.
Whipple, E.L. (1947). Meteorites and Space Travel. Astron. Journal, 52, 5.
Wilkinson, J.P.D. (1969). A Penetration Criterion for Double-Walled Structures Subject to Meteoroid Impact. AIAA Journal, 7, 1937-1943.
Zaid, M., and B. Paul (1957). Mechanics of High Speed Projectile Perforation. J. Frank. Inst., 264, 117-126.
Zaid, M., and B. Paul (1959). Oblique Perforation of a Thin Plate by a Truncated Conical Projectile. J. Frank. Inst., 266, 24-4 .

APPENDIX: CALCULATION OF SECONDARY DEBRIS CLOUD CHARACTERISTICS IN AN OBLIQUE HYPERVELOCITY IMPACT

Conservation Equations

Recall the dual-wall structure shown in Figure 1. The quantities V_1, V_2 and V_r are the axial velocities of the various debris clouds travel; the parameter V_e characterizes the average radial expansion velocity of the three debris clouds. The following sections describe a method that allows us to calculate M_i, θ_i and V_i (i=1,2 and r), as functions of the initial impact parameters M_p, V_p, and θ_p.

Applying conservation of momentum before and after the initial impact of the projectile on the bumper plate in the vertical and horizontal directions, we arrive at the following equations:

$$M_p V_p \cos\theta_p = M_1 V_1 \cos\theta_1 + M_2 V_2 \cos\theta_2 + M_r V_r \sin\theta_r \qquad (A.1)$$

$$M_p V_p \sin\theta_p = M_1 V_1 \sin\theta_1 + M_2 V_2 \sin\theta_2 - M_r V_r \cos\theta_r \qquad (A.2)$$

Assuming that no mass is lost in the initial impact, the principle of mass conservation yields

$$M_p + M_f = M_1 + M_2 + M_r \qquad (A.3)$$

where M_f is the mass of the material that is punched out in the creation of the hole in the bumper plate, and is calculated by noting that for the trajectory obliquities considered, the bumper plate hole is elliptical (Schonberg *et al*, 1991):

$$M_f = \pi \rho D_{min} D_{max} t_w / 4 \qquad (A.4)$$

The quantities D_{min} and D_{max} are the lengths of the minor and major axes of the bumper plate hole and were calculated using the empirical equations Schonberg *et al* (1991). It is noted that these equations were derived from hypervelocity impact tests in which spherical aluminum

projectiles impacted thin aluminum plates. Hence, while the general methodology described herein may be valid for other materials besides aluminum, the use of empirical equations based on tests employing aluminum plates renders this specific analysis valid only for spherical aluminum projectiles impacting aluminum dual-wall structures.

Equations (A.1)-(A.3) constitute a system of 3 equations in 9 unknowns which must be solved for: 3 debris cloud masses, 3 axial velocities, 3 center-of-mass trajectories. An additional unknown exists in the form of the average radial expansion velocity of the debris clouds V_e, which must also be solved for. The solution process is facilitated by utilizing experimental observations from high-speed impact tests of aluminum dual-wall structures to determine several of the unknowns in equations (A.1)-(A.3). The remaining unknowns can then be determined in closed form. Once this is accomplished, an additional equation can be introduced to solve for V_e. The process by which this is done is described in the following sections.

Trajectory Angles

The angles θ_1 and θ_2 initially increase as θ_p is increased (Schonberg *et al*, 1991). This continues until a critical value of θ_p is reached beyond which θ_1 and θ_2 decrease with continued increases in θ_p. This kind of behavior is very difficult to predict analytically without resorting to an advanced shock physics analysis. As a result, the analytical prediction of this behavior is beyond the scope of the present work and empirical equations are used to calculate values of θ_1 and θ_2 as functions of the intial impact parameters. These equations are given in Schonberg *et al* (1991). The trajectory of the center-of-mass of the ricochet debris cloud has been observed to decrease monotonically with increasing values of trajectory obliquity. The following empirical equations can be used to calculate the value of θ_r for a given value of θ_p:

$$\theta_r = -3.333\theta_p + 160.0^\circ \qquad if\ 30^\circ \le \theta_p \le 45^\circ \tag{A.5a}$$

$$\theta_r = -0.333\theta_p + 25.0^\circ \qquad if\ 45^\circ \le \theta_p \le 60^\circ \tag{A.5b}$$

$$\theta_r = -0.166\theta_p + 15.0^\circ \qquad if\ 60^\circ \le \theta_p \le 90^\circ \tag{A.5c}$$

This allows θ_1, θ_2, and θ_r to be treated as known quantities which reduces the number of unknowns in equations (A.1)-(A.3) to six.

Debris Cloud Masses

The three unknown debris cloud masses are calculated by systematically distributing the mass of the projectile and the mass of the bumper plate material that is punched out by the initial impact among the three debris clouds and then invoking the conservation of mass equation, equation (A.3). This distribution process is accomplished as follows.

First, it is noted that as r_t increases, the amount of material in the normal and in-line debris clouds monotonically decreases while that in the ricochet debris cloud steadily increases (Schonberg *et al*, 1991). Furthermore, it has been hypothesized that the material in the normal debris cloud is primarily bumper plate material, while the material in the in-line debris cloud is primarily projectile material (Burch, 1967). The obliquity of the initial impact on the bumper plate also madates that the in-line and ricochet debris clouds contain a portion of the bumper plate material. Based on these observations, we postulate the following functional forms of M_1 and M_2:

$$M_1 = \overline{M_f}\cos^n\theta_p \tag{A.6}$$

$$M_2 = \alpha_2(M_f - \overline{M_f})\cos^n\theta_p + M_p\cos^n\theta_p \tag{A.7}$$

where $\overline{M}_f$ is the mass of bumper plate material that would be ejected in a normal impact at a reduced velocity $V'<V_p$, ie., $M_f=M_f(\theta_t=0^\circ, V_p=V')$, and α_2 is that fraction of the ejected bumper plate material in the in-line debris cloud. These forms satisfy the requirement that the debris cloud masses decrease as θ_t increases and do not violate the hypotheses regarding the origins of the material in the respective debris clouds. The values of the exponent n and the coefficient α_2 are adjusted so that the final preditions for the debris cloud spread angles based on this analysis procedure compare well with those obtained using empirical predictor equations for debris cloud spread angles (Schonberg *et al*, 1991). Thus, the solution process proposed herein becomes an iterative one, requiring initial estimates for n and a_2 which are then modified based on subsequent comparisons with empirical information.

The reduced velocity V' used to calculate the mass of bumper plate material in the 'normal' debris cloud is taken to be the normal component of the original impact velocity. Any material

in excess of that which such a normal impact would produce is allocted to the 'in-line' and ricochet debris clouds. Therefore, the reduced velocity V' is given by

$$V' = \eta V_p \cos\theta_p \qquad (A.8)$$

where η is a correction factor that is also adjusted so that the final predictions for debris cloud spread angles based on the analysis procedure presented herein compare well with those obtained using empirical predictor equations. Substitution of equations (A.6) and (A.7) into equation (A.3) results in the following expression for the mass of the ricochet debris cloud:

$$M_r = (1-\alpha_2)(M_f-\overline{M_f})\cos^n\theta_p + (M_f+M_p)(1-\cos^n\theta_p) \qquad (A.9)$$

These calculations and assumptions allow M_1, M_2, and M_r to be treated as known quantities which reduces the number of unknowns to three. Since one of the equations was used in the preceding analysis, we now have a system of two equations in three unknowns (V_1,V_2, and V_r).

Debris Cloud Axial Velocities

Since the 'normal' debris cloud is assumed to contain only bumper plate material and the mass of that material is calculated assuming a normal impact, the method for calculating its velocity is based on a procedure currently utilized for calculating debris cloud velocities in normal impacts of thin plates. This procedure is summarized in the following paragraph.

The initial normal impact of a projectile on a thin plate produces a shock wave that undergoes reflection at the rear surface of the plate. An elementary shock wave propagation analysis indicates that the velocity of the rear surface at the moment of reflection is equal to twice the particle velocity of the plate material as the shock wave passes through the plate. For a normal impact of an aluminum projectile on an aluminum plate, particle velocity is equal to one-half of the impact velocity. Hence, a simple substitution shows that for the particular projectile and bumper plate materials under consideration, under normal impact, the velocity of the rear surface of the plate is equal to the initial normal impact velocity. Since the reflection of the shock wave from the rear surface causes the plate material to fragment and thereby creates the debris cloud, the presumption is made that the axial velocity of the debris cloud created by the normal impact is equal to the velocity of the rear surface of the plate.

Applying this to the problem at hand, since the normal velocity assumed to create the 'normal' debris cloud is given by V', then the axial velocity of the 'normal' debris cloud is also given by V', that is,

$$V_1 = \eta V_p \cos\theta_p \qquad (A.10)$$

We are now left with a system of two equations in two unknowns, V_2 and V_r. This system is solved explicitly with the following results:

$$V_2 = [M_p V_p \cos(\theta_p-\theta_r) - M_1 V_1 \cos(\theta_1-\theta_r)] \,/\, M_2 \cos(\theta_2-\theta_r) \qquad (A.11)$$

$$V_r = [M_p V_p \sin\theta_p - M_1 V_1 \sin\theta_1 - M_2 V_2 \sin\theta_2] \,/\, M_r \cos\theta_r \qquad (A.12)$$

Thus, all of the unknowns in equations (A.1)-(A.3) are now determined. The final unknown to be determined is V_e. The procedure by which it is found is discussed in the next Section.

Debris Cloud Radial Expansion Velocity

If we apply the principle of energy conservation before and after the initial impact of the projectile on the bumper plate, we have the following symbolic equation:

$$K.E._{initial} = K.E._{debris} + K.E._{lost} \qquad (A.13)$$

where the initial kinetic energy is that of the incoming projectile, the kinetic energy of the debris clouds is that due to their axial motion and expansion, and the kinetic energy that is lost is due to the irreversible processes that occur during the initial impact such as material heating, light flash, etc. If the energy that is lost is written as some fraction ξ of the initial impact energy, then writing the kinetic energy of the projectile and the debris clouds in standard form yields the following:

$$(1-\xi) M_p V_p^2/2 = (M_1+M_2+M_r) V_e^2/2 + (M_1 V_1^2 + M_2 V_2^2 + M_r V_r^2)/2 \qquad (A.14)$$

The term on the left hand side of equation (A.13) may be regarded as the energy available for debris cloud motion and expansion. The parameter ξ is adjusted so that the final predictions for debris cloud spread angles based on the analysis procedure presented herein compare well with those obtained using empirical predictor equations. Since the only unknown in equation

(A.18) is V_e, the solution for the final unknown is immediate:

$$V_e = \frac{(1-\xi)M_p V_p^2 - (M_1 V_1^2 + M_2 V_2^2 + M_r V_r^2)}{\sqrt{M_1 + M_2 + M_r}} \qquad (A.15)$$

Validation of Analysis

The validity of the proposed method of solution for the ten unknowns that characterize the debris clouds created as a result of an oblique hypervelocity impact of a thin plate (as well as all the attendent assumptions) is assessed by comparing the predictions of debris cloud spread angles with experimental results. Once the various debris cloud velocities have been obtained using the method proposed herein, the spread angles of the 'normal' and 'in-line' debris clouds can be found using simple trigonomentry as

$$\Phi_i = 2\tan^{-1}(V_e/V_i) \qquad i = 1, 2 \qquad (A.16)$$

The empirical values of the debris cloud spread angles are found using the empirical relationships in Schonberg *et al* (1991).

Table A-1 presents an error summary showing average percent differences between prediction and experiment for the various impact trajectories and obliquities considered. For each spread angle, the first column shows the average difference between prediction and experiment; the second column shows the standard deviations of the averages. As can be seen from this Table, the values of the spread angles that result from the calculations described herein are very close to the experimental values. Naturally, the values of the parameters α_2, η, ξ, and n have been adjusted to ensure that the predictions and empirical results are closely matched. A summary of the empirical parameter values used is presented in Tables A-2 to A-4.

V_p km/sec	θ_p	Normal Debris Cloud		In-Line Debris Cloud	
		% ε	σ %	% ε	σ %
4.0	30°	-3.7	6.9	3.6	7.2
	45°	-5.1	1.4	4.4	7.2
	60°	12.3	1.9	-14.9	4.6
5.5	30°	-4.7	5.3	2.2	7.8
	45°	-1.1	4.9	2.1	8.6
	60°	10.8	2.7	-7.5	0.8
7.0	30°	-8.0	4.7	1.2	8.1
	45°	-9.3	2.7	5.8	3.9
	60°	3.2	4.3	-1.6	1.3

Table A-1. Error Summary for Debris Cloud Angles

V_p (km/sec)	d_p (cm)	η	n	α_2	$1-\alpha_2$	ε
4.0	0.475	0.55	3.60	1.00	0.00	0.25
	0.635	0.65	2.00	1.00	0.00	0.25
	0.795	0.75	1.40	1.00	0.00	0.22
	0.953	0.85	1.30	1.00	0.00	0.18
5.5	0.475	0.50	3.70	1.00	0.00	0.30
	0.635	0.60	2.40	1.00	0.00	0.25
	0.795	0.75	1.70	1.00	0.00	0.19
	0.953	0.85	1.60	1.00	0.00	0.12
7.0	0.475	0.45	3.75	1.00	0.00	0.35
	0.635	0.60	2.50	0.95	0.05	0.25
	0.795	0.75	2.00	0.93	0.07	0.15
	0.953	0.85	1.80	0.91	0.09	0.05

Table A-2. Empirical Parameters for θ_p=30°

V_p (km/sec)	d_p (cm)	η	n	α_2	$1-\alpha_2$	ε
4.0	0.475	0.85	3.05	1.00	0.00	0.25
	0.635	0.90	2.00	1.00	0.00	0.25
	0.795	0.95	1.38	1.00	0.00	0.23
	0.953	0.98	1.00	1.00	0.00	0.19
5.5	0.475	0.65	3.05	1.00	0.00	0.30
	0.635	0.80	2.15	1.00	0.00	0.27
	0.795	0.90	1.45	0.97	0.03	0.24
	0.953	0.95	1.10	0.90	0.10	0.19
7.0	0.475	0.65	3.00	1.00	0.00	0.35
	0.635	0.80	2.05	0.90	0.10	0.30
	0.795	0.90	1.50	0.87	0.13	0.25
	0.953	0.95	1.10	0.84	0.16	0.20

Table A-3. Empirical Parameters for θ_p=45°

V_p (km/sec)	d_p (cm)	η	n	α_2	$1-\alpha_2$	ε
4.0	0.475	1.00	2.35	1.00	0.00	0.25
	0.635	1.00	1.73	1.00	0.00	0.25
	0.795	1.00	1.30	0.98	0.02	0.23
	0.953	1.00	0.99	0.97	0.03	0.20
5.5	0.475	0.97	2.35	1.00	0.00	0.30
	0.635	0.99	1.80	1.00	0.00	0.28
	0.795	1.00	1.33	0.93	0.07	0.27
	0.953	1.00	0.95	0.82	0.18	0.26
7.0	0.475	0.90	2.30	1.00	0.00	0.35
	0.635	0.92	1.67	0.90	0.10	0.35
	0.795	0.95	1.20	0.85	0.15	0.35
	0.953	0.98	0.80	0.82	0.18	0.35

Table A-4. Empirical Parameters for θ_p=60°

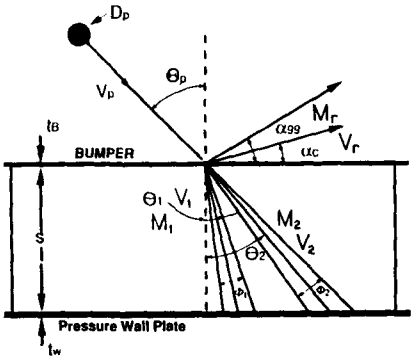


Figure 1. Oblique Hypervelocity Impact of a Dual-Wall Structure

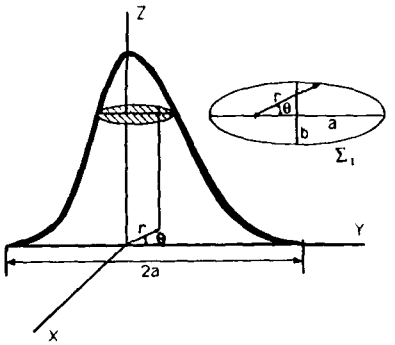


Figure 2 . Generic Initial Velocity Distribution

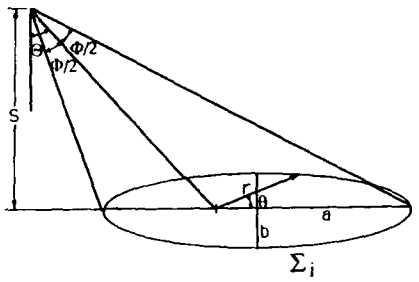


Figure 3 . Geometric Considerations for Debris Cloud Impacts

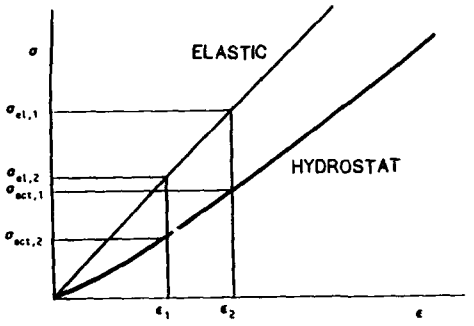


Figure 4. Generic Uniaxial Stress-Strain and Hydrostat Curves

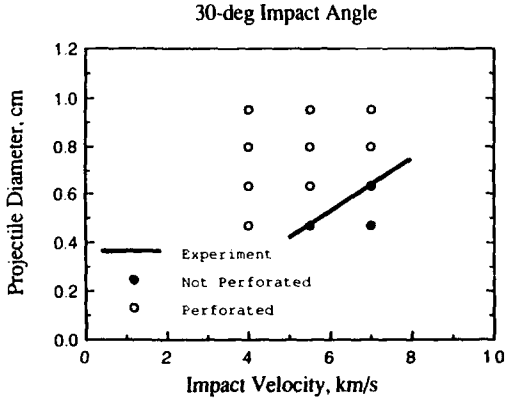


Figure 5. Comparison of Analytical Predictions With Experimental Results, 30-deg Impact Angle

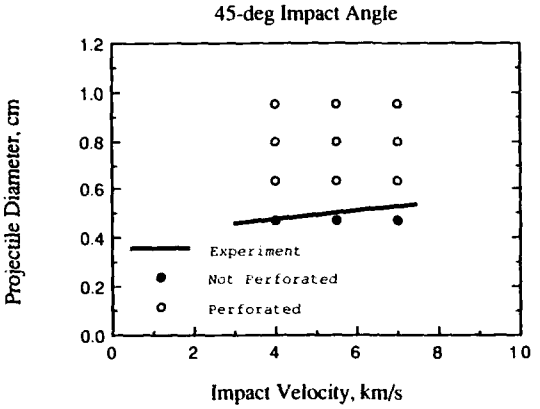


Figure 6. Comparison of Analytical Predictions With Experimental Results, 45-deg Impact Angle

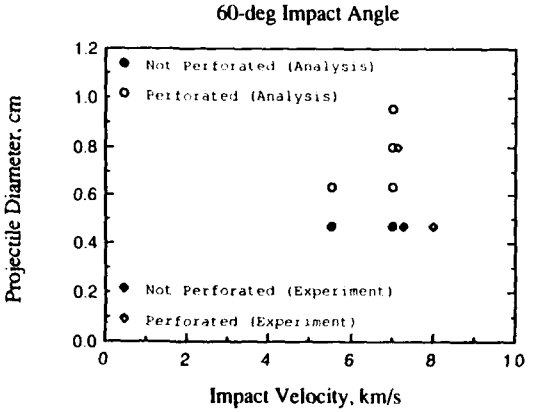


Figure 7. Comparison of Analytical Predictions With Experimental Results, 60-deg Impact Angle

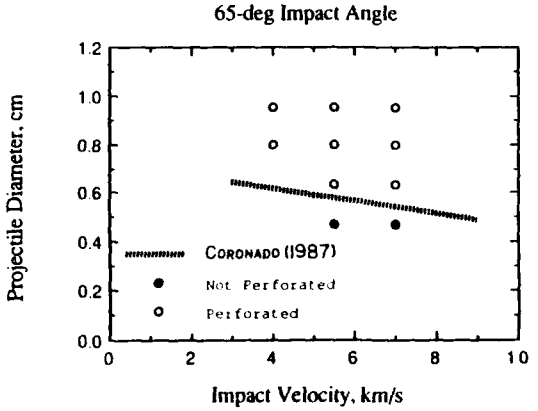


Figure 8. Comparison of Analytical Predictions With Experimental Results, 65-deg Impact Angle

Int. J. Impact Engng Vol.14, pp.659–670, 1993
Printed in Great Britain

0734-743X/93 $6.00+0.00
Pergamon Press Ltd

IMPACT CRATER GROWTH IN AN ATMOSPHERE

PETER H. SCHULTZ

Brown University, Department of Geological Sciences, Providence, RI 02912

ABSTRACT

Laboratory impact experiments demonstrate that the presence of an atmosphere can significantly retard late-stage crater growth due to the combined roles of static (ambient) and dynamic (aerodynamic) forces acting on the ballistic flow field. Drag forces limit growth by decelerating ejecta particles and by retarding the outward advance of the ballistic ejecta curtain. Because craters first grow downward then outward, arresting crater growth prematurely not only reduces cratering efficiency but also reduces the diameter-depth ratio. Under high atmospheric pressures and densities, the resulting oversteepened crater profile in low-cohesion, fine-grained targets collapses after maximum growth. Observed reductions in cratering efficiency and crater diameter can be accommodated by replacing gravity with the drag force in gravity-controlled scaling relations. Such scaling relations suggest that the atmosphere should play a significant role in reducing crater size under the dense atmosphere of Venus.

INTRODUCTION

The wide range of impact conditions on different planetary surfaces create mega-laboratories for testing concepts of the cratering process. Such "experiments", however, only preserve the outcome without specific information on impactor properties or processes. Since the extreme range in environmental variables (gravity, atmospheric pressure) greatly exceed the range in possible impactor properties, at least first-order conclusions can be reached by recognizing key signatures. For example, the high atmospheric density (0.1 g/cm^3) and gravity (870 cm/s^2) on Venus result in distinctive crater morphologies that can be explained by energy partitioning processes with the atmosphere from before the moment of impact to long-lived disturbances well after crater formation (Phillips *et al.*, 1991; Schultz, 1992a). Figure 1 underscores this contrast by comparing a 100 km-diameter crater on the Moon (vacuum, low gravity of 162 cm/s^2) with a 50 km-diameter crater on Venus. The factor of two difference in size has been selected in order to compare the consequences of similar ejecta impact velocities at the same crater-scaled range in the different gravitational fields.

Laboratory experiments cannot be used to directly simulate all aspects of the formation of a 50 km-diameter crater, regardless of the planetary environment. Experiments instead can reveal controlling processes and their signatures at different stages of formation. Early studies of explosion cratering (Chabai, 1965, 1977; Johnson *et al.*, 1969) viewed the effect of an atmosphere as a static pressure term added to the lithostatic overburden. Subsequent studies (Herr, 1971; Holsapple, 1980) concluded that atmospheric pressure plays a relatively minor role, particularly as scale increases. More recent studies (Schultz, 1992b and c), however, revealed that atmospheric density and target particle properties (size and

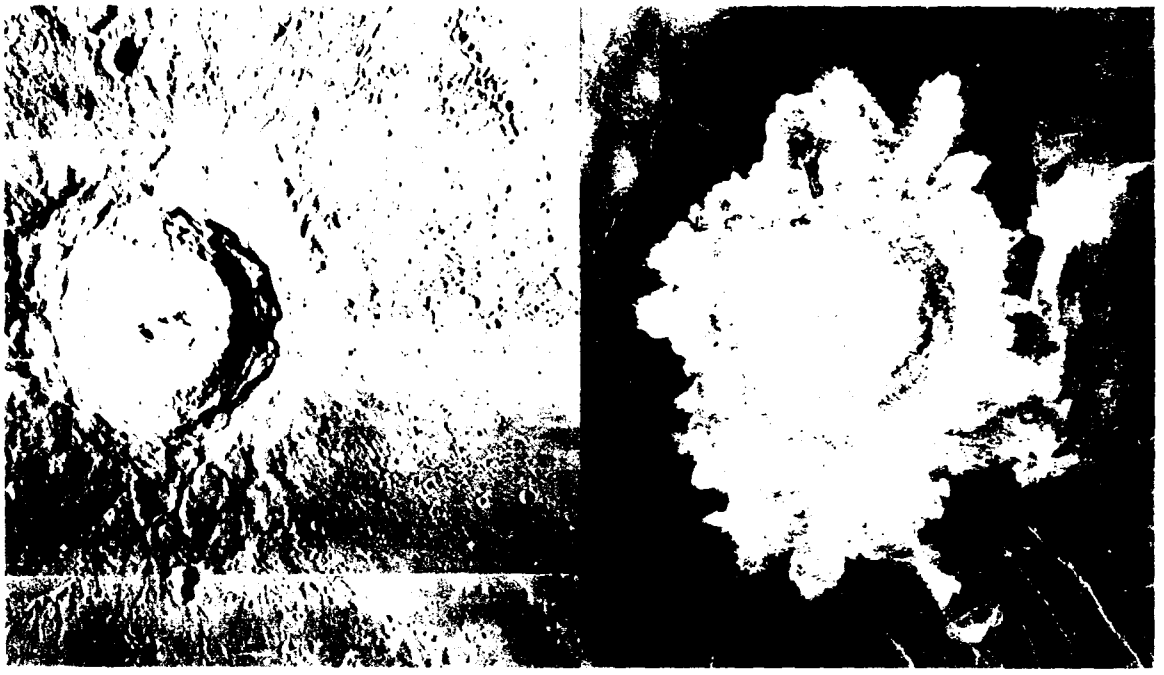


Fig. 1. Comparison of the 100 km-diameter crater Copernicus (left) on the Moon and a 60 km crater on Venus (right). The atmosphere on Venus prevents ballistic ejecta from traveling beyond a crater radius from the rim.

density) can reduce cratering efficiency by as much as an order of magnitude as dramatized in Fig. 2. Consequently, use of dimensionless scaling ratios without recognition of the controlling processes may fail to characterize fully the role of the atmosphere at laboratory scales and may miss the importance at larger scales.

Table 1 summarizes the competing forces between the cratering flow field and the atmosphere. The cratering flow field can be characterized by either an Euler number (ratio of pressure to inertial forces) for crater excavation limited by target strength or an inverse Froude number (ratio of gravity to inertial

TABLE 1. Summary of Processes Affecting Crater Growth in an Atmosphere

Controlling Forces	Process	Dimensionless Scaling Ratio	Scaling Law
Target Strength	Material properties limits crater growth	$Y/\delta_t v_i^2$	Euler Number
Gravity	Ballistic flow field limits growth	gr/v_i^2	Inverse Froude Number
Atmospheric Pressure	Adds to lithostatic overburden	$P/\delta_t v_i^2$	Euler Number
Gas Dynamic Pressure (particle scale)	Dynamic forces acting on ejecta particles	$C_D\rho v_e^2/\delta_e ga$	Froude Number, Reynolds Number (C_D) and density ratio
Gas Dynamic Pressure (curtain scale)	Dynamic forces acting on outward-moving ejecta wall	$C_D\rho v_e^2/\delta_c gw$	Froude Number, Reynolds Number (C_D) and density ratio

Y = target strength, g = gravitational acceleration; P = atmospheric pressure; ρ = atmospheric density; δ = target (t), ejecta particle (e) or ejecta curtain (c) density; v = projectile impact (i), ejecta (e), or curtain (c) velocity; r = projectile radius; a = ejecta particle diameter; w = curtain width; C_D = drag coefficient.

forces) for excavation limited by "strengthless" ballistic flow. The presence of an atmosphere introduces a different set of resisting forces to the cratering flow field. If static ambient pressure simply adds to the lithostatic overburden (Chabai, 1965), then it resembles a strength term (i.e., an Euler number depicting atmospheric interactions). During crater growth, however, the ejecta curtain represents an extension of the material flow field in the target. As the ejecta curtain moves outward as an extension of the growing cavity lip, dynamic forces act on both the ensemble of ejecta and individual ejecta particles; consequently, two Froude-scaling relations for dynamic forces need to be considered. The Reynolds number (ratio of inertial to viscous forces) also enters through the drag coefficient at the particle-interaction scale. At the

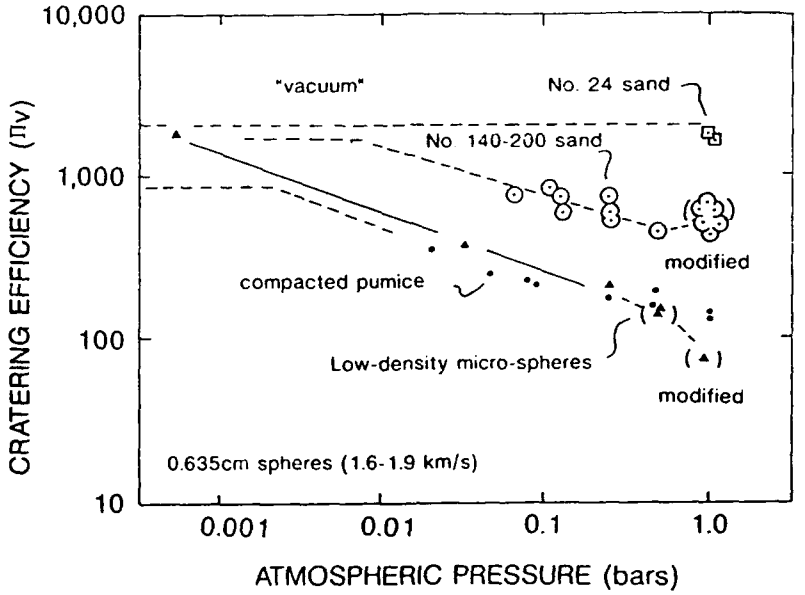


Fig. 2. Comparison of atmospheric effects on cratering efficiency (displaced target mass divided by impactor mass) for different particulate targets distinguished principally by grain size and density (see Table 2). Different atmospheric densities are represented (i.e., different atmospheric gases). "Modified" data (in parentheses) indicate craters that have undergone clear rim-wall collapse. From Schultz (1992b).

scale of the advancing ejecta curtain, however, the Reynolds number is high enough (≥ 1000) that the drag coefficient can be approximated by the value for a flat plate (i.e., $C_D \approx 2$). Scaling of a laboratory model is then possible provided that the density ratio between the flow and resisting atmosphere is introduced (Mellor, 1978).

The following discussion reviews the various processes observed in laboratory experiments including evolution of the ejecta curtain, crater shape, wake-blast effects, and total cratering efficiency. These observations are then placed in context of scaling formulations presented in Table 1. Lastly, possible signatures of atmospheric effects at much larger planetary scales are briefly considered.

ATMOSPHERIC EFFECTS ON CRATER EXCAVATION

The presence of an atmosphere may modify energy transfer between impactor and target through complex shock interactions (Gault and Sonett, 1982) or effects of accompanying ionized gas in the leading aircap or trailing ionized wake (Schultz, 1992b). Energy partitioned to such gas dynamic effects, however, represents a relatively small fraction of the total impactor kinetic energy transferred to the target. Consequently, emphasis here focuses on late-time atmospheric effects that modify or arrest the ballistic cratering flow field established at much earlier times. Four different target types have been used with contrasting constituent grain sizes, densities, and cohesion (internal angle of friction) as summarized in Table 2. This range in target properties allows recognizing the controlling processes associated with crater growth in an atmosphere.

Table 2. Target Properties

Type	Grain Sizes*, μm			Bulk Density,** g/cm^3	Internal Angle of Friction†
	20%	50%	80%		
Pumice (compacted)	120	81	26	1.52	>80°
Microspheres	130	97	65	0.4	~20°
No. 140-200 Sand	145	125	89	1.55	~30°
No. 24	620	457	320	1.70	~30°

*Size of ejecta where cumulative fraction (by weight) is coarser than percentage given. For example, 20% (by weight) of the grains comprising pumice are larger than 120 μm with most (80%) larger than 26 μm.

**Bulk density for pumice refers to compacted pumice used in this study. Uncompacted pumice exhibits a density of 1.3 g/cm^3 and results in clumping of ejecta.

†Internal angle of friction refers to the maximum slope that is stable against collapse and reflects the cohesion (a measure of strength) for particulate targets.

Experimental Conditions:

The experiments were performed at the NASA-Ames Vertical Gun Range, a national facility supported by the Planetary Geology and Geophysics Program and managed jointly through NASA Ames Research Center and the Lunar and Planetary Institute. The large impact chamber (2.5 m x 2.5 m) and variable impact angle (from horizontal to vertical in 15° increments) allows unique experiments exploring processes where gravity is important (e.g., gravity-limited crater growth and low strength target materials such as sand and water) or where a large chamber is essential (e.g., impact vapor cloud expansion and impact-induced magnetic fields).

Three launch capabilities provide impact velocities from 0.03 to 7 km/s for a variety of projectile types. A two-stage light gas gun launches 0.159 cm to 0.635 cm spheres or cylinders and their polyethylene sabots from 3 km/s to 7 km/s, whereas a powder gun covers the velocity range from 0.5 to 2.5 km/s. Because of the relatively short launch distance, rifling in the launch tube induces a spin that separates the split sabot from the projectile by centrifugal force. Projectile velocity and integrity are determined electronically and photographically from three velocity stations downrange from a sabot separation and capture chamber. In addition, an air gun capable of launching 1.5 cm objects allows exploring the very low velocity range (below 300 m/s).

The impact chamber is slowly evacuated to about 0.5 Torr and then refilled with the desired non-reactive (helium, argon, carbon dioxide, nitrogen) gases in order to avoid combustible mixing with hydrogen from the two-stage light gas gun. Spectra of ionized gases above the impact reveal that little (if any) residual air was retained within the target. The powder gun, however, is operated with air as well as other gases in the impact chamber. A thin mylar diaphragm is placed at the end of the launch tube for light-gas and powder gun experiments in order to allow a clean launch and to assess diagnostics under vacuum conditions. This procedure limits projectiles to ductile materials with high tensile strength, such as aluminum, steel, or polyethylene since pyrex projectiles shatter during passage through the diaphragm (see Schultz and Gault, 1985). Comparisons between craters formed under vacuum conditions with and without an atmosphere confirm the minimal effect of the mylar diaphragm on projectile velocity and integrity for the selected projectiles. Impact velocity at the target surface is calculated using the standard drag formula as further confirmed through the use of high-frame-rate cameras (35,000 frames per second).

Target buckets 60 cm in diameter and 15 cm deep contain the particulate target materials. Shaking and compacting such targets prior to each shot minimize the pore space. All targets undergo vacuum purging

prior to each series of experiments. Pumice targets, however, are further compressed by standing on a flat plate on the surface. With such procedures, the calculated porosity of the various targets approached similar values (see Table 2). Uncompacted pumice was found to have a density of 1.28 g/cm^3 and resulted in large ejecta clumps that minimized aerodynamic drag effects. Nevertheless, impacts under vacuum conditions revealed no effects of any residual gases still trapped in the pore spaces. Removal of shocked and comminuted ejecta from within the crater and from the exterior surface after each experiment maintained a relatively "fresh" target. Consistency of the data over a long time period (years) validates this approach.

Ejecta Curtain Evolution:

During late-stage gravity-controlled crater growth, ballistic ejecta form a thin wall (or "curtain") of debris tied to the lip of the widening cavity (see Gault *et al.*, 1968). The contrasting effects of an atmosphere on the ejecta curtain profile is illustrated in Fig. 3. Each shade of grey represents crater growth after 7.5 ms, 15 ms, 30 ms, 60 ms, 120 ms, and 240 ms. Images were created by computer digitizing the film record and digitally subtracting selected frames. Consequently each image provides a condensed summary of the film record. During crater growth, the curtain angle increases with increasing atmospheric pressure. After crater formation, the ballistic curtain bulges at its base and actually appears to advance more rapidly than the curtain under vacuum conditions. Since this distinctive response is observed for impact angles as low as 10 m/s, it does not reflect the effects of atmospheric heating. Rather, the bulging reflects in part the response of the atmosphere to the advancing curtain (see Schultz, 1992c).

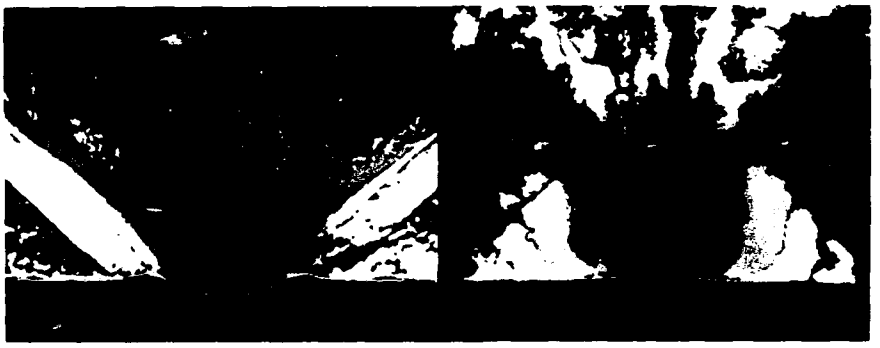


Fig. 3. Comparison of time history of 1.5 km/s impacts by 0.635 cm-diameter aluminum spheres into pumice under vacuum (Fig. 3a) and a 1 bar atmosphere of air (Fig. 3b).

Evolution of the ejecta curtain angle (with respect to the target surface) depends on target type and different atmospheric densities. Use of helium allows differentiating between the effects of pressure and density, as well as sound speed. Under high atmospheric densities (at 1 bar of air) the ejecta curtain is more vertical (>60°) and increases in angle with time (Schultz, 1992c). As an extension of the growing cavity wall, such ejection angles (corresponding to the curtain angle) greatly exceed the angle of repose once motion has ceased. Under the identical pressure of helium, however, curtain angles (<45°) resemble air at the same density (air at reduced pressure). Curtain angle is affected to a greater degree for pumice and microsphere targets, which contains significantly smaller grain sizes relative to the 140-200 sand.

The effect of atmospheric pressure on the growth of the ejecta curtain with time is shown in Fig. 4. The base diameter of the ejecta curtain (Fig. 4a) was measured above the inflection point at the same height in each image of a high frame-rate NOVA camera, whereas the overall curtain diameter was measured at a common height of 10 cm above the surface. Figure 4a reveals that the diameter of the curtain near the surface grows more rapidly at higher pressures. The basal bulge is believed to reflect turbulence generated by the outward-moving ballistic curtain. Above the surface, the curtain under high chamber pressure also moves outward ahead of the curtain relative to low chamber pressure, but ceases to advance after only 60 milliseconds, well before the time required for crater formation in a vacuum (~ 150 ms).

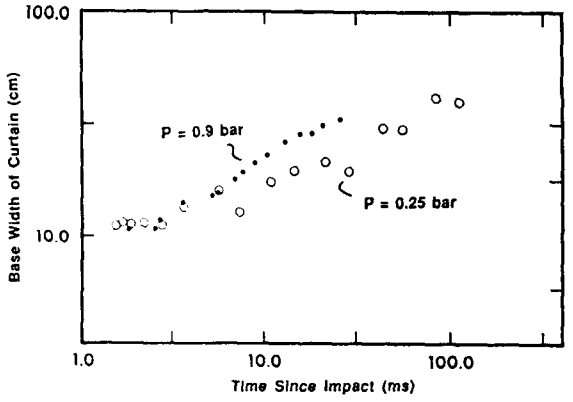


Fig. 4a. Evolution of the base of the ejecta curtain for 5.5 km/s impacts into pumice targets by 0.635 cm-diameter aluminum spheres under different density atmospheres (argon).

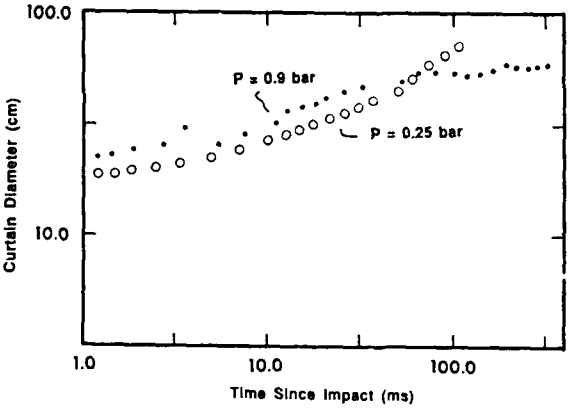


Fig. 4b. Ejecta curtain diameter measured 10 cm above the surface. Gas dynamic forces stop advance of ejecta curtain before crater completion expected for vacuum conditions.

Figures 3 and 4 demonstrate that atmospheric density rather than pressure controls ejecta curtain evolution. Moreover, the greater effect on craters produced in pumice and microspheres having the smallest particles indicates that dynamic pressure acting on the ejecta and ejecta curtain plays a controlling role.

Crater Profile:

The observed systematic changes in ejecta curtain evolution with atmospheric density and target type can be correlated with changes in crater profile (Fig. 5a). The aspect ratio for craters in sand increases (craters become shallower) with increasing density, whereas it decreases for craters in pumice. Lower density atmosphere (helium atmosphere) reduces this effect for sand. The steepening ejection angles with increasing atmospheric density (Fig. 3b), however, indicate that the excavation cavity may be transient since interior wall slopes greatly exceed the angle of repose for targets with low cohesion. This process can be tested by comparing the reduction in crater diameter and depth for impacts into targets with different internal angles of friction and by performing quarter-space experiments.

Figure 5b contrasts the reduction in crater diameter and depth with density for impact craters produced in pumice and sand. Under vacuum conditions, crater diameter and depth increase proportionally with

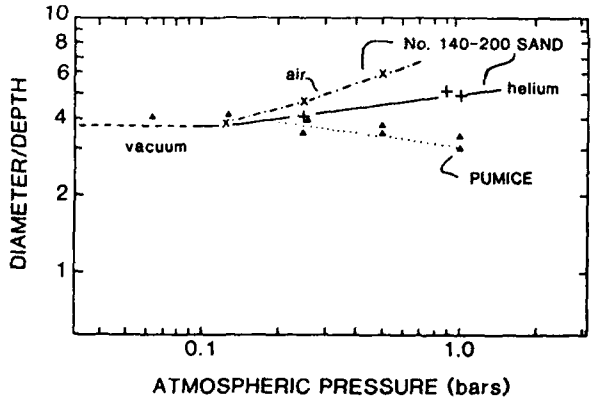


Fig. 5a. Effect of atmospheric pressure on the crater aspect ratio (diameter/depth) for sand and pumice targets. All data shown in Fig. 6a are for 1.5-2 km/s impact velocities by 0.635 cm aluminum spheres.

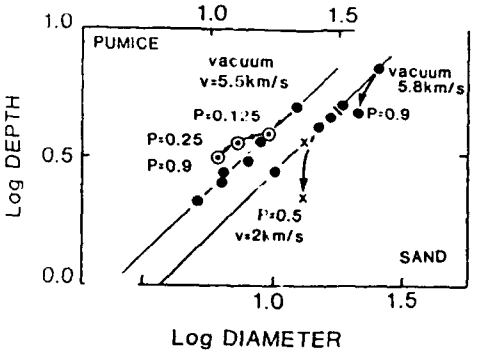


Fig. 5b. Contrasting effects of atmospheric pressure (air) on final crater diameter and depth for pumice and sand targets. Lower velocity impacts (2 km/s) are indicated by crosses; all projectiles were 0.635 cm aluminum.

impactor velocity and size. For given impactor conditions into pumice, both depth and diameter at first decrease proportionally along the vacuum line (solid circles) as atmospheric pressure (density for given gas) increases. From 0.125 to 0.25 bars, however, diameter decreases more rapidly than depth but becomes more parallel with the vacuum line at higher pressures. In contrast, impacts into sand result in decreasing depths as well as decreasing diameters.

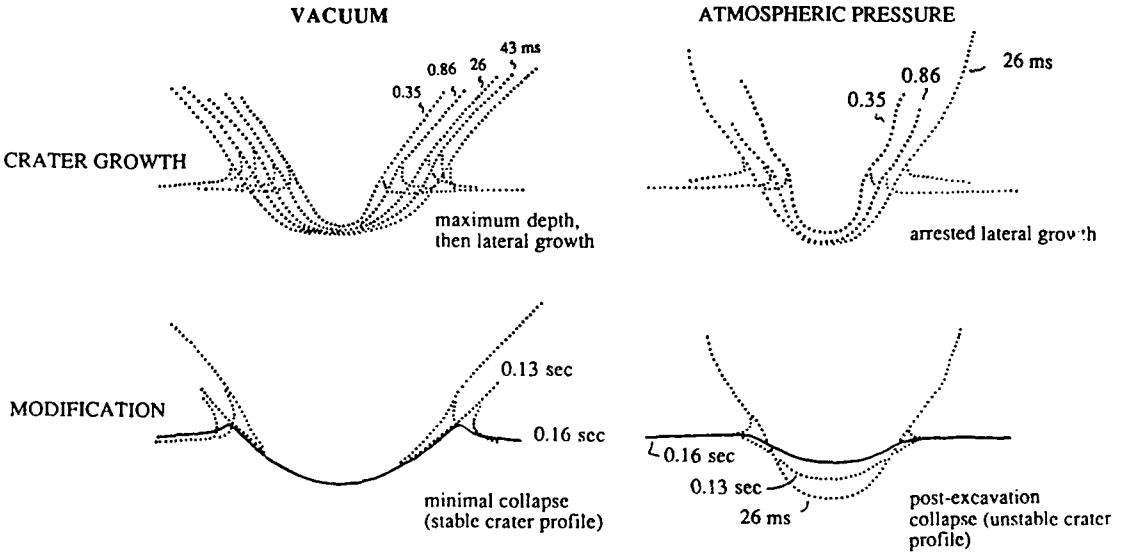


Fig. 6. Crater growth and ejecta curtain evolution revealed by quarter-space experiments for 1.5 km/s impacts into No. 140-200 sand. Under vacuum (left) crater widens with time and preserves final profile. Under a 1 bar (air) atmosphere (right), lateral growth ceases after 26 ms and crater collapses.

High-speed film and video further reveal that the contrasting diameter and depths of the measured craters with atmospheric density reflect collapse of a transient excavation cavity. Quarter-space experiments further confirm that craters in pumice, sand, and microspheres grow initially as if they had formed in a vacuum. As crater growth ceases, the final excavation profile is preserved in compacted pumice but collapses in sand (and microspheres) as shown in Fig. 6. Reduction in preserved rim height further documents this modification process.

In summary, the observed increase in ejecta curtain angle is reflected in a decrease in the crater aspect ratio (diameter:depth) that is preserved in pumice but is "transient" in sand and microsphere targets. Although the very low strength (cohesion) of sand makes it a preferred target for examining gravity-limited crater growth, this property can limit its use under atmospheric conditions.

Cratering Efficiency:

Total cratering efficiency is defined as the total displaced target mass M divided by the initial impactor mass m_p. Holsapple and Schmidt (1982, 1987) proposed scaling laws based on dimensional analysis and late-stage equivalence, i.e., late-stage crater growth has little memory of the energy-transfer process as documented by Dienes and Walsh (1968). This formalism can be viewed as Froude scaling for gravity-controlled growth (maintaining the same ratio of gravitational to inertial forces) or Euler scaling for strength-controlled growth (maintaining the same resisting pressure or stress to inertial forces) and can be expressed as π groups:

$$\pi_V = k'_g \, \pi_2^{-\alpha} \qquad (1a)$$

$$= k'_g \, (gr/v_i^2)^{-\alpha}$$

for gravity scaling, or

$$\pi_V = k'_Y \pi_Y^{-\beta'} \qquad (1b)$$
$$= k'_Y (Y/\delta_t v_i^2)^{-\beta'}$$

for gravitational acceleration g, impactor radius r and velocity v_i, and target strength Y and density δ_t.

The exponents in equation (1) were found by Holsapple and Schmidt (1987) to be simply expressed by $\alpha = 3\mu/(2 + \mu)$ and $\beta' = 3\mu/2$ for a coupling parameter μ representing the energy/momentum transfer process from impactor to target with $\mu = 2/3$ for energy scaling and $\mu = 1/3$ for momentum scaling. For most particulate targets, they found $\mu \cong 0.4$, whereas solid, strength controlled targets generally exhibit $\mu \sim 0.55$. Under vacuum conditions, the targets in the present study displayed gravity-limited growth with the constants and exponents given in Schultz (1992b). Compacted pumice targets exhibited gravity-controlled growth only for sufficiently high values of π_2 which exceeded the transition from gravity to strength controlled regimes.

If the observed cratering efficiency under atmospheric conditions is referenced to gravity-limited excavation under vacuum conditions, then equation (1a) can be rewritten as:

$$\pi_{VA}/\pi_{vv} = k\pi_2^{\alpha}\pi_{VA} \qquad (2)$$

where the subscripts V and A refer to vacuum and atmospheric conditions, respectively, and $k = (1/k'_g)$. Figure 7 contrasts the observed reduction in cratering efficiency for the various target types as a function of the pressure-scaling parameter (see Table 1). Reduction in cratering efficiency follows very similar dependences on the pressure parameter with the exception of sand and micro-spheres at higher atmospheric pressures. These departures reflect crater collapse in part, but also may be related to offsetting effects created by the impinging wake blast (discussed below).

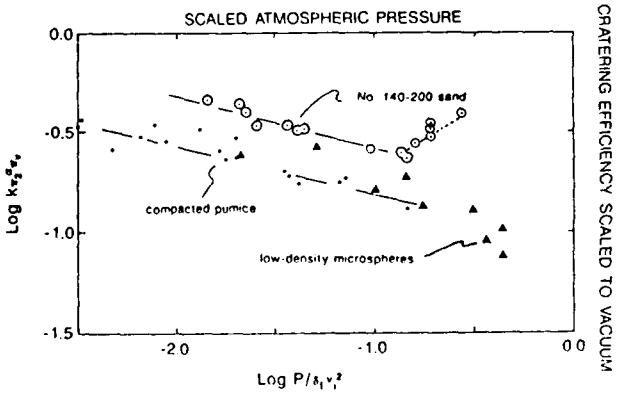


Fig. 7. Reduction in cratering efficiency relative to vacuum conditions as a function of a dimensionless pressure ratio (Euler number). Pumice and sand targets used 0.635 cm Al spheres at 1.5-2.0 km/s, whereas microsphere targets used 0.635 cm polyethylene spheres. From Schultz (1992b).

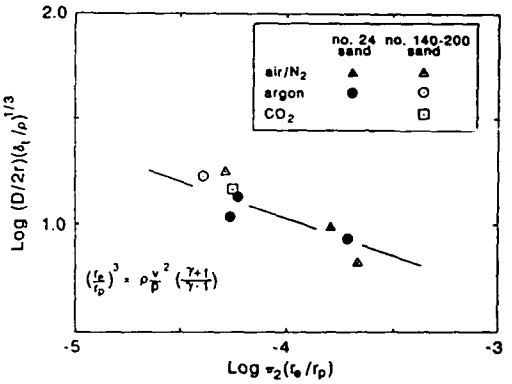


Fig. 8. Wake-induced cratering in sand. Wake gases trailing the projectile as it transits an atmosphere were isolated from the impactors by allowing the projectile to pass through a tube in the target. Wake blast alone produces craters as large as 10% of observed craters from solid impactors.

Even though compacted pumice exhibits material properties which are very different from micro-spheres, Fig. 7 reveals that they exhibit very similar reductions in cratering efficiency. The principal controlling variable offsetting these data sets appears to be related to target particle density and size, consistent with unaccounted effects of dynamic pressure (Table 2). The role of gas dynamic pressure in limiting crater growth will be considered more fully in a later section.

Wake-Blast Effects:

Quarter-space experiments and high-frame-rate imaging reveal that the disturbed atmosphere accompanying the impactor is injected into the early-time crater cavity (Schultz and Gault, 1982). The low internal strength of sand and microspheres could result in augmenting excavation when atmospheric densities (gas-dynamic back pressures) become high enough, perhaps accounting for the trend reversal exhibited by sand in Fig. 7. This process can be assessed by projectile-less collisions where the projectile is isolated from the wake by allowing it to pass through a hole or tube (Schultz, 1992b). The effective volume r_e^3 of the impinging disturbed air mass scaled to projectile volume r_p^3 can be expressed as $(\rho v_i^2/P)(\gamma + 1)/(\gamma - 1)$ for an atmospheric density ρ and pressure P with ratio of specific heats γ impinging at a velocity v_i (assumed to be the impactor velocity). The diameter D of the excavated crater formed by the air-mass should exhibit approximately the same dependence on the gravity-scaling parameter:

$$(D/2r)(\delta_t/\rho)^{1/3} \sim [\pi_2 (r_e/r_p)]^{-\alpha} \quad (3)$$

where δ_p has now been replaced by the ambient density of the gas ρ. Figure 8 compares the results for No. 140-200 sand and coarser No. 24 sand under a range of atmospheric gases. Consequently, the isolated wake blast has sufficient energy density to contribute to crater excavation. Wake-blast effects coupled with the impactor, however, appear to be important only at high atmospheric densities, $\rho/\rho_o > 0.5$ (Schultz, 1992b).

DISCUSSION

Dynamic Pressure Effects:

The role of atmospheric density and target grain size in altering both the ejecta-curtain angle and the transient crater shape indicates that crater growth is literally being choked off by the atmosphere. Impact craters are observed in both laboratory (Gault *et al.*, 1968; also see Fig. 6, left)) and computational (Orphal *et al.*, 1980; Schultz *et al.*, 1981) experiments to grow to a maximum depth and then expand laterally. Arresting growth prematurely would result in a smaller aspect ratio (D/d), provided this transient shape is stable. As a working hypothesis, it is proposed that crater growth in particulate targets in an atmosphere is limited by dynamic forces retarding advance of the ejecta curtain.

If the cratering flow field represents an incompressible, inviscid flow, then forces acting on its extension above the surface (transient crater lip) should be transmitted hydrostatically. Consequently, the overall effect of dynamic forces will resemble gravitational forces retarding the ballistic flow field. When increased gravitational forces are applied to a computed cratering flow field resulting from a 30 m iron projectile impacting an anorthosite target at 15 km/s, the crater aspect ratio also was reduced (see Schultz *et al.*, 1981). Dynamic forces retard advance of the curtain at two scales (Table 1): deceleration of individual ejecta and deceleration of the ejecta ensemble comprising the outward-moving curtain. These two processes are not independent but for purposes of illustration they are treated separately.

In the laboratory experiments, the Reynolds number (R_e) for late-stage ejecta under a low density atmosphere ($\rho/\rho_o < 0.2$ where ρ_o = density of air at STP) approaches unity; consequently, the drag coefficient can be expressed by $24/R_e$. The dimensionless ratio of acrodynamic drag d to gravitational forces g as given in Table 1 provides a meaningful scaling parameter (Schultz and Gault, 1979). When the drag coefficient varies inversely with the Reynolds number, d/g simply depends on particle size (a), particle density (δ_e), ejection velocity (v_e), and viscosity of the atmosphere (μ):

$$d/g \sim \mu v_e^2/\delta_e g a^2 \quad (4a)$$

or

$$d/g \sim \mu R_v/\delta_e a^2 \quad (4b)$$

where ejection velocity for gravity-controlled flow under vacuum conditions has been replaced by $(gR_v)^{1/2}$ with R_v representing the crater radius had it formed in a vacuum (see Post, 1974; Schultz and Gault, 1979; Housen *et al.*, 1983). Figure 9a applies this formulation for the data in Fig. 7 and reveals that this approach largely accommodates the diverse target types. Figure 9b illustrates a wider range of conditions but with two specific values of the Reynolds number resulting in a constant drag coefficient for each set. The dimensionless scaling ratio d/g again is given in Table 1 with $R_v = v_e^2$.

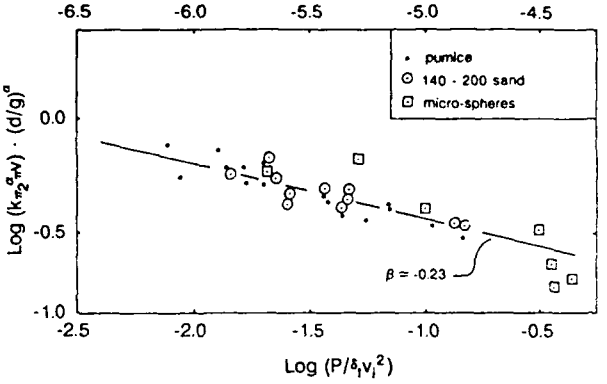


Fig. 9a. Comparison of gas dynamic forces acting on various targets (inset) under different atmospheric conditions with gravitational forces g replaced by drag forces g in the π_2 scaling parameter. Data are for impacts under lower atmospheric densities resulting in a drag coefficient equal to $24/R_e$ for a Reynolds number R_e. The pressure parameter is shown on the lower axis with pressure P in bars, velocity v in km/s, and density δ_t in g/cm^3 but in dimensionless form along the upper axis. From Schultz (1992b).

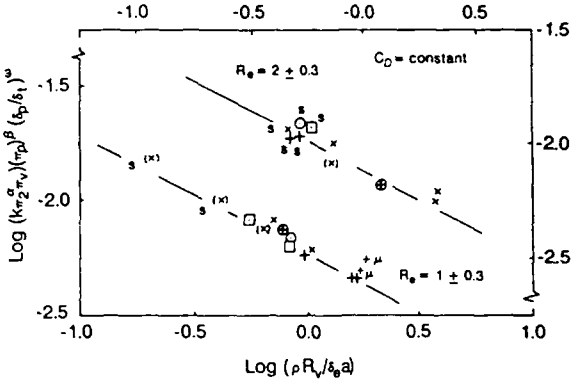


Fig. 9b. Data corrected for atmospheric pressure effects as a function of dimensionless drag for two constant values of the drag coefficient (same Reynolds number). Atmospheric density ρ is referenced to air while particle size and density have been referenced to values for pumice. Symbols represent different gas compositions (x = air, + = low-velocity helium, ⊕ = high-velocity helium, ⊙ = argon, ⊡ = carbon dioxide; parentheses indicate 0.318 cm Al spheres with all others being 0.635 cm in diameter). Labels "μ" and "s" distinguish microspheres and sand, respectively, from unlabeled pumice targets. From Schultz (1992b).

Alternatively, dynamic forces act on the ejecta curtain as if it were a thin, coherent plate. Deceleration of such a plate from an initial velocity v_o to v' over a distance X can be expressed analytically by the following:

$$\ln (v'/v_o) = -1/2 C_D \rho X A_c/M_c \quad (5a)$$

where A_c and M_c represent the area and mass of the curtain at a given stage of growth, which simplifies to the following since $M_c = \delta_c A_c w$ for an ejecta curtain thickness w:

$$\ln (v'/v_o) = -1/2 C_D (\rho/\delta_c)(X/w) \quad (5b)$$

This approach is clearly an oversimplification since the outward velocity of the curtain continuously decreases and since curtain thickness continuously increases with time (stage of growth). Nevertheless, it is easy to show that the velocity of the curtain decreases by only 80% during the last half (by mass) of crater growth. A characteristic velocity should depend on the square root of both scale (crater radius R_v had it formed in a vacuum) and gravity. Moreover, adopting a constant value for w should underestimate the deceleration of the curtain. Equation (5b) now can be rewritten in terms of a smaller equivalent gravity-controlled crater of radius R_v' corresponding to the terminal velocity of v'.

$$\ln (R_v'/R_v) = - C_D (\rho/\delta_c)(R_v/w) \quad (6)$$

where X has been replaced by R_v with the assumption that the ratio of transient crater size to ejecta curtain width is approximately constant. For an ejecta curtain with a constant ratio of $R_v/w = 300$ (equivalent to the maximum thickness of 0.05 cm for a 30 cm-diameter crater), equation (6) predicts that a one bar atmosphere of argon would reduce crater size by a factor of about 0.55 corresponding to a 5-fold decrease in cratering efficiency, approximating values shown in Fig. 7. A comparable numerical model of an outward-moving wall of ejecta of constant height and thickness where the curtain velocity decreases as $v(X/R) = v_o(X/R)^{-2.5}$ results in cessation of growth (v_o = 30 cm/s) at 0.7 R. This corresponds to a 3-fold decrease in cratering efficiency.

An ejecta curtain with $R_v/w = 300$ corresponds to a curtain only about 10 grains in width. Consequently, effects of gas dynamic forces on both the particle and curtain scale can be understood intuitively. The significance of viewing arrested crater growth in terms of gas dynamic forces acting on a coherent (impermeable) sheet, however, is that even non-particulate targets such as water should display significant atmospheric effects as observed by Gault and Sonett, 1982.

CONCLUDING REMARKS

The experiments cannot yet establish a firm quantitative basis for assessing the degree of crater size reduction on planets with atmospheres. If crater growth is limited simply by drag acting on constituent ejecta, then atmospheric effects should increase with both increasing atmospheric density and crater size (ejection velocity at a given stage of crater growth) but decreasing ejecta size. If it is limited by forces acting on the outward advance of the ejecta curtain (crater lip), then atmospheric effects may increase as $R_v^{1/2}$ although considerable uncertainty remains. A more critical assessment of dynamic forces acting on the ejecta curtain requires assessing the air flow and boundary conditions impinging on the curtain during growth (Barnouin and Schultz, 1992).

The experiments nevertheless provide a different perspective for interpreting the unusual ejecta morphologies and crater profiles in different planetary environments, as well as a starting point for considering more suitable models and scaling relations. A first-order prediction for Venus is that crater excavation will occur ballistically but the inclined ejecta curtain should evolve into a near-vertical wall that collapses into a non-ballistic style of emplacement. The example in Fig. 1 reveals that the ejecta deposits are completely confined to within a crater radius of the rim without secondary craters. Other examples (Schultz, 1992a) establish that low-relief domes (300 m) as close as 0.25 R from the crater rim are not overrun by ejecta. Instead such relief act as barriers for surface flow of ejecta. Both observations are consistent with the atmosphere restricting the outward advance of ejecta.

Craters on Mars also allow testing the role of gas dynamic drag. The wide range of geologic processes has resulted in a range of lithologies from competent bedrock to fine-grained airfall deposits (<100 m). The dimensionless drag ratio predicts that aerodynamic forces in laboratory-scale experiments will be comparable to a 10 km-diameter crater on Mars provided that a significant fraction of the ejecta is smaller than a centimeter. The low atmospheric pressure (6 mb) on Mars, however, should result in minimal static pressure effects. If gas dynamic forces limit crater growth, then the crater aspect ratio should be different for different lithologies. In fact, crater depths in wind-sensitive substrates (that is, eolian materials with a<50 μ) are consistently and significantly deeper than crater depths in competent substrates (lava plains) as shown in Schultz (1990). Such a result is consistent with the trends illustrated in Fig. 5b where the fine-grained eolian deposits exhibit a high angle of repose. The high crater rims and deeper than expected floors on Venus (Phillips *et al.*, 1991; Schultz, 1992a) are also consistent with the expected effects from a dense atmosphere.

Acknowledgements: The continued contributions of the technical crew at the NASA-Ames Vertical Gun Range is gratefully acknowledged (John Vongrey, Ben Langedyk, and Wayne Logsdon). Also gratefully recognized is the numerical modeling of the advancing curtain by O. Barnouin. This research was performed under NASA grant NAGW-705.

REFERENCES

Barnouin, O. and P.H. Schultz (1992). A continuum m odel for atmospheric response to an advancing ejecta curtain. *Lunar and Planet. Sci. XXIII*, 65-66.

Chabai, A.J. (1965). On scaling of craters produced by buried explosives. *J. Geophys. Res.*, 70, 5075-5098.

Chabai, A.J. (1977). Influence of gravitational field and atmospheric pressures on scaling of explosion craters. In: *Impact and Explosion Cratering* (D.J. Roddy, R.O. Pepin, and R.B. Merrill, eds.) pp. 1191-1214. Pergamon, New York.

Dienes, J.K. and J.M. Walsh (1970). Theory of impact: Some general principals and the method of Eulerian codes. In: *High-Velocity Impact Phenomena* (R. Kinslow, ed.), pp. 46-104. Academic, San Diego, CA.

Gault, D.E., and C.P. Sonett (1982). Laboratory simulation of pelagic asteroidal impact: Atmospheric injection, benthic topography, and the surface wave radiation field. *Spec. Pap. Geol. Soc. Am.*, 190, 69-92.

Gault, D.E., W.L. Quaide, and V.R. Oberbeck (1968). Impact cratering mechanics and structure, *Shock Metamorphism of Natural Materials* (B.M. French and N.M. Short, eds.), pp. 87-100. Mono Books, Baltimore, Md.

Herr, R.W. (1971). Effects of atmospheric-lithostatic pressure ratio on explosive craters in dry soil. *NASA TRR-366*.

Holsapple, K.A. (1980) The equivalent depth of burst for impact cratering. *Proc. Lunar Planet. Sci., 11th*, 2379-2401.

Holsapple, K.A., and R.M. Schmidt (1982). On the scaling of crater dimensions, 2, Impact processes. *J. Geophys. Res.*, 87, 1949-1970.

Holsapple, K.A., and R.M. Schmidt (1987) Point source solutions and coupling parameters in cratering mechanics. *J. Geophys. Res.*, 92, 6350-6376.

Housen, K.R., R.M. Schmidt, and K.A. Holsapple (1983). Crater ejecta scaling laws: Fundamental forms based on dimensional analysis. *J. Geophys. Res.*, 88, 2485-2499.

Johnson, S.W., J.A. Smith, E.G. Franklin, L.K. Moraski, and D.J. Teal (1969). Gravity and atmospheric pressure effects on crater formation in sand. *J. Geophys. Res.*, 74, 4838-4850.

Mellor, M. (1978). Dynamics of snow avalanches. In: *Rockslides and Avalanches, I, Natural Phenomena* (B. Voigt, ed.), pp. 752-792. Elsevier-Holland, Inc., New York.

Orphal, D.L., W.F. Borden, S.A. Larson, and P.H. Schultz (1980). Impact melt generation and transport. *Proc. Lunar Planet. Sci. Conf.,11th*, 2309-2323.

Phillips, R.J., R.E. Arvidson, J.M. Boyce, D.B. Campbell, J.E. Guest, G.G. Schaber, and L.A. Soderblom (1991). Impact craters on Venus: Initial analysis from Magellan. *Science*, 252, 288-296.

Post, R.L. (1974). Ejecta distributions from near-surface nuclear and HE bursts. *Rep. AFWL-TR-74-51*, Air Force Weapons Lab, Kirtland, AFB, N.M.

Schultz, P.H. (1982). Atmospheric effects on impact cratering efficiency. *Lunar Planet. Sci., XIII*, 694-695.

Schultz, P.H.(1990). Evidence for atmospheric effects on Martian crater shape. *Lunar Planet. Sci., XXI*, 1097-1098.

Schultz, P.H. (1992a). Atmospheric effects on ejecta emplacement and crater growth on Venus from Magellan. *J. Geophys. Res.*, 97, No. E10, 16,183-16,248.

Schultz, P.H. (1992b). Atmospheric effects on cratering efficiency. *J. Geophys. Res.*, 97, 975-1005.

Schultz, P.H. (1992c). Atmospheric effects on ejecta emplacement. *J. Geophys. Res.*, 97, 11,623-11,662.

Schultz, P.H., and D.E. Gault (1979). Atmospheric effects on Martian ejecta emplacement. *J. Geophys. Res.*, 84, 7669-7687.

Schultz, P.H., and D.E. Gault (1982). Impact ejecta dynamics in an atmosphere: Experimental results and extrapolations. *Spec. Pap. Geol. Soc. Am.*, 190, 153-174.

Schultz, P.H., and D.E. Gault (1985). Clustered impacts: Experiments and implications. *J. Geophys. Res.*, 90, 3701-3732.

Schultz, P.H., D.L. Orphal, B. Miller, W.F. Borden, and S.A. Larsen (1981). Multi-ring basin formation: Possible clues from impact cratering calculations. In: *Multi-ring Basins* (P. Schultz and R.B. Merrill, eds.), pp. 197-205. Pergamon, New York.

Int. J. Impact Engng Vol.14, pp.671–682, 1993
Printed in Great Britain

0734-743X/93 $6.00+0.00
© 1993 Pergamon Press Ltd

SECONDARY DEBRIS IMPACT DAMAGE AND ENVIRONMENT STUDY

GILLIAN L. Y. SHEPHARD and STEVEN A. SCHEER

Lockheed Engineering & Sciences Company[1]
2400 NASA Rd. 1, Houston, TX 77058

ABSTRACT

All long-duration spacecraft, such as Space Station *Freedom* (SSF), are subject to impacts by micrometeoroid and orbital debris (MM/OD) particles in low Earth orbit. The secondary effects of such impacts on SSF was the subject of the Secondary Debris Impact Damage and Environment Study. The primary objective was the assessment of possible damage to SSF hardware in the vicinity of large surface areas impacted by typical MM/OD particles. Several SSF components were evaluated that showed varying degrees of damage due to secondary ejecta. A comparison of the results from 45° and 60° MM/OD impacts revealed that penetration ejecta had greater damage potential at 45° and ricochet ejecta had greater damage potential at 60°. The significant ricochet damage was concentrated within an angle of 15° with respect to the primary target. The impact distribution data was evaluated further using a previous math model. The comparison was inconclusive due to insufficient data within the bounds of the model. Preliminary results of the study showed that secondary debris has the potential to penetrate and induce some damage to SSF hardware. The failure of hardware due to the damage is unknown. Further testing with larger MM/OD particle sizes and varying impact angles is recommended.

INTRODUCTION

In the modern space environment, MM/OD particles pose a serious threat to the survival of long-duration spacecraft in low Earth orbit, such as SSF. The space station, as a design goal, is projected to remain in orbit a minimum of 30 years, which means it is likely to see damaging MM/OD impacts in the course of its orbital lifetime. Up to this point, shielding design evaluations have been based solely on the threat of primary MM/OD impacts. With shielding designed to protect against initial impacts only, a secondary debris impact theory has not been sufficiently developed for a design evaluation of SSF hardware. The ongoing Secondary Debris Impact Damage and Environment Study (also known as the Secondary Debris Study) is an attempt to further understand the damage capability of secondary debris.

---

[1]Under Contract NAS 9-17900 with the National Aeronautics and Space Administration, Lyndon B. Johnson Space Center (JSC).

The main objective of the initial phase of the Secondary Debris Study was to assess the secondary debris threat due to impacts on SSF hardware with large surface areas. The primary targets for this study were therefore selected by size. Each secondary target was chosen with respect to its proximity to a primary target site, as well as its vulnerability to impacts.

The primary targets were simulated by flat plates of corresponding thicknesses to hardware design. Actual hardware (test hardware, vendor samples, etc.) was used whenever available for secondary targets. Flat plates of corresponding thickness and material were substituted when hardware was unavailable.

TESTING DESCRIPTION AND PLANS

The hypervelocity impact (HVI) testing for this study was conducted in the Hypervelocity Impact Research Laboratory (HIRL) at JSC. The .17 caliber and .50 caliber light gas guns were made available for this test program. Therefore, the test articles were designed considering the limits of the vacuum chamber for each gun.

The general setup consisted of a plate simulating the surface for the initial debris impact (referred to as the primary target), with secondary targets simulating the secondary impact surfaces on SSF. The basic test setup for this study is depicted in Fig. 1. The primary and secondary target materials and setup were as representative of SSF hardware as constraints allowed. Particles were shot at the primary target at an angle Θ measured from the normal to the target. For this test matrix, Θ was limited to angles of 45° and 60°. Previous studies concluded that an angle Θ less than 60° yielded more penetration debris and an angle Θ greater than 60° was more critical with respect to the amount of ricochet debris generated (Schonberg and Taylor, 1988, 1989a, b).

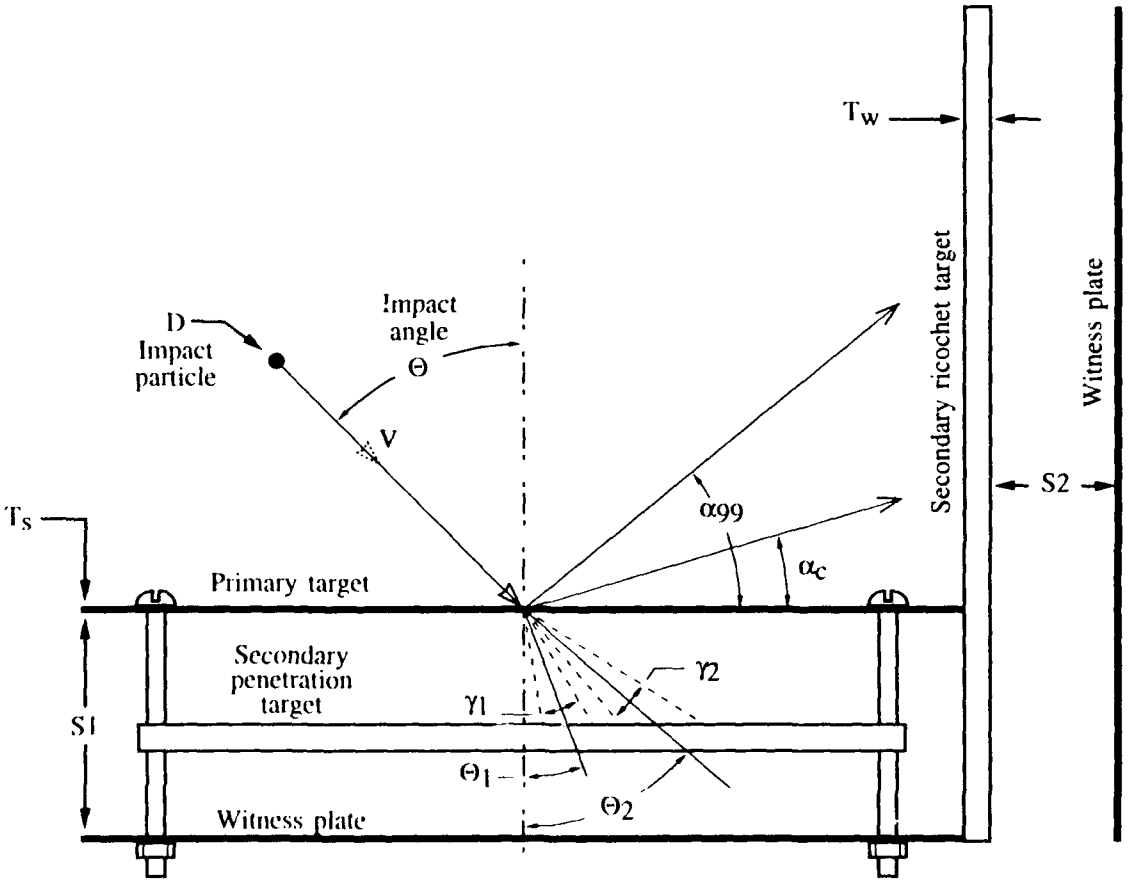


Fig. 1. Test setup.

Also shown in Fig.1 are the ricochet angles and angles of penetration, α_c, α_{99}, γ_1, γ_2, Θ_1, and Θ_2 . The ricochet angles, α_c and α_{99}, are symbols for the trajectory angle of the center of mass of the ricochet fragments and the angle below which lies 99 percent of the ricochet fragments, respectively. The penetration angles, γ_1 and γ_2, are the angular spread of the fragments which result from the primary target plate and the impacting particle, respectively. Angles Θ_1 and Θ_2 denote the trajectory of the center of mass of the primary target plate particles and the center of mass of the MM/OD particles after impact, respectively.

The materials for the projectiles were chosen to best simulate OD and MM particles. An Al 2017-T3 ball was chosen to represent an OD particle of constant density equal to 2.796 g/cc. The MM particle with a density of 0.5 g/cc was simulated with a nylon ball. Test particle sizes were derived using Bumper, which is a Fortran 77 code that simulates the MM/OD environment. The particle sizes from Bumper were energy scaled to account for the lower velocities during testing. The energy scaled critical particle size, which represents 10 OD impacts per year in a 10-year period, is approximately 0.3175 cm (1/8 in.). The critical particle size, which represents 10 MM impacts per year in a 10-year period, is 1.89 cm (3/4 in.). Due to the size of the MM particle being greater than current available testing capabilities, the decision was made to start both OD and MM testing with the 1/8-in.-diameter particle.

Table 1 illustrates the primary target hardware chosen for the Secondary Debris Study. The truss structure, habitable modules with shielding, and the radiator panels are the largest metallic components on SSF. The primary target data describes how each of the components was simulated in the test setup. It should be noted that these targets were representative with respect to dimensions and materials for SSF. For instance, the SSF truss structure varies in thickness and geometry throughout the design, but a thickness of 0.635 cm (0.25 in.) was chosen as a typical representation.

Table 1. Primary target materials and dimensions data

Primary target hardware	Primary target data
Truss member	Al 2219-T851 plate, 0.25 in. thick, 6×12 in^2
Module bumper	Al 6061-T6 sheet, 0.05 in. thick, 6×10 in^2
Radiator panel	Hexcel honeycomb (CR-III-1/8-3.1-5052-0007), 0.01 in. Al 6061-T6 skin, 0.005 in. Z93 thermal coat, 5×5 in^2

Table 2 lists the secondary target materials that were included in this study. The electrical power system (EPS) orbital replaceable unit (ORU) box wall was simulated using the honeycomb sheet with the specifications provided by work package 4. The fluid umbilical line was simulated with flexible aluminum conduit provided by a vendor, as suggested by McDonnell Douglas-Huntington Beach. The aluminum conduit consists of aluminum rings formed into a hose-type covering. The electrical umbilical cabling was simulated using individual cables provided by JSC, banded in bundles of seven cables and double wrapped with 10 mil Teflon® overwrap. The Ku-band waveguide was simulated using actual copper waveguide material provided by JSC and aluminum waveguide material purchased from a recommended vendor. The aluminum waveguide material was acquired with the necessary hardware for properties measurement.

Table 3 displays the test matrix for the study based upon the primary and secondary test articles. Before final secondary target selection, each component was researched to determine probable secondary ejecta threats and a final decision was made for each test setup.

The secondary targets were positioned behind and parallel to the primary target for perforation debris and perpendicular at the end of the primary target for ricochet debris. Oblique impacts result in ricochet debris, which spray onto the secondary target normal to the primary target. In addition, some of the SSF hardware will encounter debris from the perforation of a primary target. The truss/fluid umbilicals setup

was an example of a situation where the secondary target may see ricochet and/or perforation debris from an impact on the primary target. Witness plates were placed behind all of the secondary targets to catch any debris that penetrated or missed the secondary targets.

The data collection procedure included (1) before and after weight measurements to assess the amount of ejecta collected in the test chamber that did not remain attached to the test article, (2) high-speed photographic evaluation of primary debris particle velocity information, and (3) classification of damage to secondary targets.

Table 2. Secondary target materials data

Secondary target hardware	Secondary target data
ORU boxes	Al 7075-T73 face and back sheets (16 mils), Al honeycomb (5056-H39, 3/16 hexagonal cell), ORU contents simulated with thin Al sheet (ORUs not pressurized, but units may contain pressurized hardware (batteries).)
Fluid umbilicals	Cover material: Al flex hose Al 5052-H34 (6.0 in. inner diameter, 0.06 in. thickness)
Electrical umbilicals	Cover material: Teflon® overwrap, 0.022 in. (0.56 mm) thickness (used 2 layers of 0.01 in.), cables: #18 AWG 2 conductor unshielded plenum cable non-conduit, 0.007 in. (0.18 mm) Fep Teflon® insulation, 0.01 in. (0.25 mm) Fep Teflon® jacket, 0.143 in. (3.632 cm) outer diameter
SGS antenna waveguide (aluminum)	Rectangular tubing, Al 6061-T4 or T6, 0.04 in. (1.0 mm) with irodite and epoxy coatings
SGS antenna waveguide (copper)	Rectangular copper tubing, 0.04 in. thick

Table 3. Secondary Debris Study test matrix

	Shot number								
Impact angle (deg)									
45	1	3	5	7	9	11	13		
60	2	4	6	8	10	12	14	15	16
Particle size (in.)									
1/8 in. nylon							X		
1/8 in. Al	X	X	X	X	X	X		X	X
Test article									
Truss/EPS ORU boxes	X								
Truss/fluid umbilicals		X							
Truss/electrical umbilicals			X						
Module/EPS ORU boxes				X					
Module/fluid umbilicals					X				
Module/electrical umbilicals						X			
Radiator/EPS ORU boxes							X		
Truss/waveguide (aluminum)								X	
Truss/waveguide (copper)									X

STUDY RESULTS

Both qualitative and quantitative results were documented for this study. For simplicity, the quantitative data is tabulated in Tables 4, 5, and 6 and will be used for the qualitative discussion, as well as a comparison with data collected in previous studies. These tables also present the results of the shots completed and display the impact parameters for each shot, as well as the resultant damage measurements (entry hole dimensions, trajectory angles, etc.).

Overall, the dimensions of the primary target entry holes (Dmax by Dmin) were much larger than the projected area of particles on the target. This result indicates that some of the primary target plate broke away in the form of ricochet and penetration debris. The entry holes were elliptical in shape where the elongation of the hole was in line with the particle trajectory.

Ricochet debris was found to impact secondary targets in the form of columns. At $\Theta = 45°$, these columns are typically very definite and easy to observe. As Θ increases, the columns of debris spread and become obscured with more evenly distributed debris. Also, more ricochet debris is concentrated at the intersection of the primary target plate and the secondary target plate. As a result, the greater portion of the damage in the 60° tests was near the intersection of the targets, compared to the 45° tests.

Fluid Umbilicals

The flexible aluminum fluid umbilicals for SSF are positioned within the truss structure in the vicinity of the module pattern, running from the utility trays to the modules. The fluid umbilicals may be subjected to secondary ricochet debris from the module bumpers, as well as secondary ricochet and penetration debris from the truss members.

Tests A1534 and A1537 impacted the module bumper at $\Theta = 45°$ and $\Theta = 60°$, respectively. The 45° test produced a penetration of the module bumper. The ricochet particles produced some small perforations of the aluminum conduit with no noticeable impacts on the witness sheet inside the conduit. The 60° test produced a penetration of the module bumper with greater damage to the aluminum conduit. Perforations were noted in the first eight rings of the conduit, of which the largest perforation was 2.0 mm in diameter. The witness sheet inside the conduit showed several small impact craters ranging up to 1 mm in diameter.

Table 4. Projectile and primary test data

HRL shot number	Projectile type	Projectile diameter (cm)	Projectile mass (g)	Projectile velocity (km/s)	Impact angle (deg)	Primary material	Primary thickness (mm)	tp/d	Entry hole (mm)
A1534	Al 2017-T3	0.318	0.047	6.42	45	Al 6061-T6	0.127	0.4	7.6×9.0
A1537	Al 2017-T3	0.318	0.047	6.4	60	Al 6061-T6	0.127	0.4	7.5×10.1
A1544	Nylon	0.318	0.0198	6	60	Radiator	1.27	4.0	7.7×11.7
A1577	Al 2017-T3	0.318	0.047	6.44	45	Al 2219	0.635	2.0	8.3×8.8
A1579	Al 2017-T3	0.318	0.047	6.5	60	Al 2219	0.635	2.0	2.6×2.9
A1597	Al 2017-T3	0.318	0.047	6.16	60	Al 2219	0.635	2.0	2.3×4.1
A1617	Al 2017-T3	0.318	0.047	6.29	60	Al 2219	0.635	2.0	3.1×3.6
A1621	Al 2017-T3	0.318	0.047	6.15	60	Al 6061-T6	0.127	0.4	7.4×10.1
A1624	Al 2017-T3	0.318	0.047	6.34	45	Al 2219	0.635	2.0	7.9×8.3
A1625	Al 2017-T3	0.318	0.047	6.35	45	Al 6061-T6	0.127	0.4	8.0×9.5
A1633	Al 2017-T3	0.318	0.047	6.21	45	Radiator	1.27	4.0	5.3×7.4
A1634	Al 2017-T3	0.318	0.047	6.37	60	Radiator	1.27	4.0	4.8×8.8
A1638	Al 2017-T3	0.318	0.047	6.15	60	Al 2219	0.635	2.0	2.1×2.6
A1639	Al 2017-T3	0.318	0.047	6.14	60	Al 6061-T6	0.127	0.4	1.0×1.6
A1641	Al 2017-T3	0.318	0.047	6.27	45	Al 2219	0.635	2.0	7.4×10.2
A1642	Al 2017-T3	0.318	0.047	6.24	45	Al 6061-T6	0.127	0.4	7.9×9.1

Table 5. Penetration (back wall) target test data

HIRL shot number	Spacing (cm)	S/d	Back wall material	Back wall thickness (cm)	Number of holes	Maximum hole size (mm)	Damage class
A1534	6.35	20	FL. UMB.	0.064	80	2.7	F5/F1
A1537	6.35	20	FL. UMB.	0.064	55	2.5	F5/F1
A1544	2.54	8	Al 6061-T6	0.064	2	0.4	C4
A1577	2.54	8	FL. UMB.	0.161	1	6.8×10.5	F5
A1579	2.54	8	FL. UMB.	0.181	1	2.2×5.5	F5
A1597	2.54	8	Al 6061-T6	0.084	0	0	F2
A1617	5.08	16	H/C panel	0.635	FS:1 BS:0	FS:6.7×9.2 BS:0.0	C4/C0
A1621	5.08	16	Al 6061-T6	0.064	47	1.8×3.3	C5
A1624	5.08	16	H/C panel	0.635	FS:6 BS:1	FS:5.5×6.5 BS:< 0.01	C5/F4
A1625	5.08	16	Al 6061-T6	0.160	6	2.0×3.5	C5
A1633	6.35	20	Al 6061-T6	0.064	5	1.0×1.1	C4
A1634	5.08	16	Al 6061-T6	0.064	0	0	C2
A1638	5.08	16	EL. UMB.	0.064	0	0	C0
A1639	5.08	16	Al 6061-T6	0.064	46	2.4×3.5	C5
A1641	10.16	16	EL. UMB./ Al 6061-T6	0.064	UMB. = 0 WS = 0	EL. UMB. = 0 WS = 0	F3
A1642	10.16	32	Al 6061-T6	0.064	90	3.8×6.4	C5/F3

NOTE: FL. UMB. = fluid umbilical, H/C - honeycomb, F/S = H/C face sheet, B/S = H/C back sheet, EL. UMB. = electrical umbilical, and WS = witness sheet.

Table 6. Ricochet target test data

HIRL shot number	Spacing (cm)	Target material	Target thickness (cm)	Number of holes	Maximum hole size (mm)	Damage class
A1534	13.3	FL. UMB.	0.1613	56	0.7	C4
A1537	15.7	FL. UMB.	0.1613	115	1.8	C5
A1544	13.9	Cu waveguide	0.127	50	1.4	C2
A1577	12.6	FL. UMB.	0.1613	52	1.8×2.5	C5
A1579	13.3	FL. UMB.	0.1613	56	0.7	C4
A1597	14.9	Al waveguide	0.127	200	0.19	C2
A1617	13.4	H/C panel	0.635	FS:340+ BS:0	FS:1.4 BS:0	C4
A1621	18.0	H/C panel	0.635	FS:300+ BS:0	FS:1.5 BS:0	C4
A1624	13.8	H/C panel	0.635	FS:50+ BS:0	FS:0.6 BS:0	C4
A1625	13.5	H/C panel	0.635	FS:10 BS:0	FS:0.5 BS:0	C4
A1633	7.3	H/C panel	0.635	FS:5 BS:0	FS:0.4 BS:0	C4
A1634	8.05	H/C panel	0.635	FS:125 BS:0	FS:1.2 BS:0	C4
A1638	15.3	EL. UMB./ Al 6061-T6	0.064	Multiple	1.9	C4
A1639	11.5	EL. UMB./ Al 6061-T6	0.064	7	1.9	C4
A1641	14.6	EL. UMB./ Al 6061-T6	0.064	7	0.5	C4
A1642	13.4	EL. UMB./ Al 6061-T6	0.064	6	0.6	C5

The truss primary target plates ejected more debris than did the thinner module bumper plates. In truss tests A1577 and A1579 (Θ = 45° and Θ = 60°, respectively), the truss member was penetrated, producing penetration products and spall off the back of the plate. The ricochet debris from the tests produced numerous perforations of the conduit, up to 2.5 mm in diameter. The 60° test again showed the impacts concentrated near the base of the secondary target. Negligible damage was done to the witness sheets inside the conduit. The secondary penetration targets were completely penetrated in several places. In the 45° test, nine large perforations within a 10.5- by 6.8-mm area were seen on the penetration umbilical, which peeled inward five rings of the conduit. The witness sheet showed several dimples, but no penetrations. The underside of the truss plate in this test had a large ring of detached spall with dimensions 1.8 by 1.6 cm (hole size equal to 1.4 by 1.3 cm). This size is much larger than the dimensions of the entry hole, so it can be deduced that the primary target plate contributed a large amount of debris to the damage. The 60° test showed one perforation of the penetration target (6.0 by 2.3 mm across) that peeled the surrounding area inward. The underside of the truss plate showed partially detached spall, which contributed to the secondary debris. Witness sheet damage was limited to some small impact craters.

In summary, the witness sheets received damage in the form of dimples or craters. This is not conclusive evidence of failure of the fluid lines.

Electrical Umbilicals

The electrical umbilicals for SSF are positioned similar to the fluid umbilicals and are subject to similar threats from secondary debris. The electrical umbilicals may be subjected to secondary ricochet debris from the module bumpers, as well as secondary ricochet and penetration debris from the truss members. The wire bundles for this study, simulating the electrical umbilicals, were positioned parallel and perpendicular to the bumper plate for ricochet debris and parallel and along the line of the particle trajectory for the penetration debris.

Tests A1641 and A1638 impacted the truss plates at Θ = 45°and Θ = 60°, respectively. Test A1641 produced a penetration of the truss plate and showed several large perforations of the Teflon® tape for the penetration bundle. Resistance tests before and after showed no change in the condition of the wires. The ricochet bundle in this test showed some impacts on the Teflon® tape, but no penetrations and no change in resistance. Test A1638 showed more damage to the ricochet bundle than did test A1641. The Teflon® tape separated from the electrical cables in the middle of the bundle, where the insulation broke in three places. Resistance tests again showed no change. The penetration bundle in test A1638 was missed by the penetration debris; therefore, no data was obtained.

Tests A1642 and A1639 impacted and penetrated the module bumper at Θ = 45° and Θ = 60°, respectively. The 45° test showed impacts on the Teflon® tape, but no penetrations were noted. The 60° test produced damage to the Teflon® tape, causing it to break loose from the bundle. Insulation breaks occurred in two wires, but there was no change in the resistance.

The breaks in the insulation showed no effect with respect to the resistance measurements of the cables. However, the breaks in the insulation could result in a short circuit if the damage were extensive enough. The cables were not live when tested, which would be required to test for this type of damage to the cables.

EPS ORU Boxes

The EPS ORU boxes are positioned at numerous points within the truss structure along the length of the space station. They are unpressurized, but the boxes may contain pressurized hardware such as batteries. The ORUs will be subjected to possible secondary ricochet debris from the truss members, the module bumpers, and the radiators, as well as penetration debris from the truss members.

In test A1624, impacted at Θ = 45°, the truss plate had a neat ring of detached spall (16.0 by 16.1 mm across) surrounding the penetration hole, which was 7.9 by 8.3 mm across. The damage to the penetration ORU plate consisted of six separate perforations of the face sheet (maximum size was 2.0 by

3.5 mm across) and a large dent in the back face, which emitted light through the crack. This was not considered a failure since the ORU box was not pressurized. The ricochet ORU damage was limited, compared to the penetration damage, with about 50 perforations ranging from 0.1 to 0.6 mm in diameter on the face sheet of the ORU panel.

In test A1617, the truss plate was impacted at $\Theta = 60°$, creating a penetration hole 3.1 by 3.6 mm across. The spall on the back side of the plate was partially detached and broke off in one large chunk, which lodged in the ORU panel. No damage was done to the back face of the ORU. The ricochet plate in this test saw much more damage than in test A1624, with much larger perforations (0.1 to 1.4 mm across).

Test A1625 impacted the module bumper at $\Theta = 45°$, creating a 9.6- by 10.9-mm hole in the bumper material. The ricochet debris resulted in 10 perforations (up to 0.5 mm across) of the ORU face sheet.

Test A1621 impacted the module bumper at $\Theta = 60°$ with a penetration hole 7.4 by 10.1 mm across. The ORU face sheet showed over 300 perforations from ricochet debris, with the diameter ranging from 0.1 to 1.5 mm. As in the truss 60° shot, there were a few dents on the back side of the ricochet ORU panel.

Tests A1633 and A1634 impacted the radiator panels at $\Theta = 45°$ and $\Theta = 60°$, respectively. Test A1633 showed very little ricochet damage, with five perforations of the ORU face sheet less than 0.4 mm across. No damage was done to the ORU back face. In test A1634, the ricochet panel sustained over 125 perforations, with one penetration of the ORU face sheet (0.5 mm across).

Overall the ORU panels showed only surface damage to the face sheets and minimal damage to the back face. No evidence of failure due to secondary debris was found in this study.

Waveguide

The Ku-band waveguide for SSF is positioned on the Ku-band antenna boom on the top, front of the truss structure. The waveguide may be subjected to secondary ricochet debris from the truss structure or the radiators. The antenna boom in the test was modeled to show any further secondary debris effects. Two tests were completed for the waveguide at $\Theta = 60°$. A section of copper waveguide was paired with a radiator panel, impacted by a nylon particle, in test A1544. An aluminum waveguide with flanges was coupled with a truss plate, impacted by an aluminum particle, in test A1597. The aluminum waveguide was measured for wave properties before and after the impact testing. In both tests, the waveguide was placed in the ricochet target position at a standoff of 6 in. from the impact site.

In test A1544, the copper waveguide showed no perforations but many small craters (0.1 to 0.8 mm across) within an impact area 2.5 by 7.0 cm on and around the waveguide. The damage was considered negligible based upon the results of test A1597. There are two possible reasons for the small amount of damage on the copper waveguide. First, a nylon particle disintegrates on impact. Second, the radiator panels produce small ricochet particles since they have fairly thin face sheets, 0.0254 cm (0.01 in.) thick, and most of the ricochet debris is from the face sheet.

In test A1597, the waveguide was found to be perforated in 12 places (0.1 to 2.0 mm across) within an impact area of 11.5 by 11.8 cm on and around the waveguide. There were many craters, which made dimples on the inner surface of the waveguide, ranging in diameter from 0.1 to 1.7 mm. The damage was more severe than in test A1544 due to the aluminum versus nylon particle, as well as the primary target. The radiator panels produced less ricochet debris than did the truss plates due to the thin face sheets. Most of the debris from the radiator panels traveled out the back of the panel. Although the waveguide sustained concentrated perforations, antenna performance was not seriously affected in comparison to before the HVI test.

THEORETICAL COMPARISON

A review of the available results from previous studies provided some insight into the expected study results, as well as equations for deriving the penetration and impact angles described earlier in this paper.

First, a review of the available sources gave a set of conclusions that were compared with the test results from this study. The previous findings are as follows:

(1) There is a critical angle of obliquity for ricochet debris ($60° < \Theta < 65°$). Projectiles with Θ less than the critical angle produce greater damage to the interior walls behind the primary plate. Projectiles with Θ greater than the critical angle generate more ricochet debris, resulting in greater damage to ricochet targets.

(2) The most serious ricochet damage was found to occur within an angle of $\alpha = 15$. pect to the plane of the primary plate.

(3) The damage potential of ricochet debris is difficult to extrapolate from existing data due to coupling effects of ricochet particle size and velocity.

The objectives of this study did not provide enough data to investigate the first statement completely. However, as Θ increased from 45° to 60°, the amount of ricochet damage increased. The results of this study showed agreement with statement 2. At the higher angle of $\Theta = 60°$, the worst ricochet damage was concentrated at a low angle of $\alpha < 15°$. For $\Theta = 45°$, the results were inconclusive since the damage due to ricochet debris is reduced. The third statement is obvious based upon the complexity of the MM/OD problem and the variables involved.

The available literature provided three sets of related equations for predicting the penetration and ricochet angles of secondary debris from aluminum impacts on aluminum plates. The three sets were derived during sequential studies conducted at Marshall Space Flight Center (MSFC). The third set is considered the best for use in this comparison. All of the equations had roughly the same qualifying parameters, with respect to primary plate thickness (t_s), impact velocity (V), and obliquity (Θ). This set of parameters eliminated all but shots A1534, A1537, A1621, A1625, A1639, and A1642 for the module bumper. The set of equations for predicting Dmin, Dmax, α_c, α_{99}, γ_1, γ_2, Θ_1, and Θ_2, which were used for comparison with the study data, came from Schonberg and Taylor (1989b).

$$\text{Dmin/d} = 2.825\ (\text{V/C})^{1.043}\ (\cos\Theta)^{0.283}\ (t_s/d)^{0.782} + 1.01 \qquad 0° < \Theta < 75° \qquad (1)$$

$$\text{Dmax/d} = 1.25\ (\text{V/C})^{0.851}\ e^{1.064\,\Theta}\ (t_s/d)^{0.672} + 1.4 \qquad 0° < \Theta < 75° \qquad (2)$$

$$\Theta_1/\Theta = 0.184\ (\text{V/C})^{0.29}\ (\cos\Theta)^{1.372}\ (t_s/d)^{-0.488} \qquad 45° < \Theta < 75° \qquad (3)$$

$$\Theta_2/\Theta = 0.49\ (\text{V/C})^{-0.056}\ (\cos\Theta)^{0.909}\ (t_s/d)^{-0.626} \qquad 30° < \Theta < 75° \qquad (4)$$

$$\alpha_c/\Theta = 0.033\ (\text{V/C})^{0.982}\ (\sin\Theta)^{-3.215}\ (t_s/d)^{-0.531} \qquad 45° < \Theta < 75° \qquad (5)$$

$$\alpha_{99}/\Theta = 0.194\ (\text{V/C})^{0.39}\ (\sin\Theta)^{-1.874}\ (t_s/d)^{-0.235} \qquad 45° < \Theta < 75° \qquad (6)$$

$$\gamma_1/\Theta = 0.417\ (\text{V/C})^{0.228}\ (\cos\Theta)^{0.225}\ (t_s/d)^{-0.491} \qquad 45° < \Theta < 75° \qquad (7)$$

$$\gamma_2/\Theta = 2.539\ (\text{V/C})^{1.217}\ (\cos\Theta)^{2.972}\ (t_s/d)^{0.296} \qquad 30° < \Theta < 65° \qquad (8)$$

Where:
d = impacting particle diameter
C = speed of sound in primary target material
V = impacting particle velocity
t_s = thickness of primary target plate

The equations above are valid for $0.0853 < ts/d < 0.4278$ and $5 < V < 8$ km/s.

Table 7 shows the results of the equations along with the test data. The percentage difference calculations show that the correlation with previous theory is not very good. However, this could be due to several factors. First, the measurements can be affected by who is recording the data and the methodology used. This was especially apparent with the angle α_c, which varied depending on the data analyst and the measurement approach. The correct assessment for α_c would be to measure each crater

Table 7a. Dmin and Dmax comparison

Shot number	Θ (deg)	Dmin (cm)			Dmax (cm)		
		Test	MSFC equation	Difference (%)	Test	MSFC equation	Difference (%)
A1534	45	0.76	0.86	-11.63	.9	1.038	-13.8
A1537	60	0.75	0.777	-3.47	1.01	1.234	-22.4
A1621	60	0.74	0.758	-2.37	1.01	1.208	-19.8
A1625	45	0.8	0.820	-2.0	.95	1.033	-8.3
A1639	60	0.74	0.758	-1.8	1.02	1.206	-18.6
A1642	45	0.79	0.811	-2.1	.91	1.024	-11.4

Table 7b. α_c and α_{99} comparison

Shot number	Θ (deg)	α_c (deg)			α_{99} (deg)		
		Test	MSFC equation	Difference (%)	Test	MSFC equation	Difference (%)
A1534	45	23.5	9.23	154.6	41	22.68	80.7
A1537	60	11.0	6.39	72.4	38	20.65	84.02
A1621	60	12.0	6.15	95.12	32	20.34	57.32
A1625	45	18.5	9.13	102.6	42	22.58	86.1
A1639	60	14.0	6.14	128.01	41	20.32	101.7
A1642	45	20.0	8.97	122.9	46	22.43	105.08

Table 7c. γ_1 and γ_2 comparison

Shot number	Θ (deg)	γ_1 (deg)			γ_2 (deg)		
		Test	MSFC equation	Difference (%)	Test	MSFC equation	Difference (%)
A1534	45	31	28.69	8.05	16	41.15	-61.12
A1537	60	21	35.35	-40.59	29	19.52	48.56
A1621	60	76	35.03	116.9	2	18.59	-89.24
A1625	45	69	28.61	141.17	31	40.61	-23.66
A1639	60	70	35.02	99.88	14	18.55	-24.53
A1642	45	63	28.5	121.05	29	39.75	-27.04

Table 7d. Θ_1 and Θ_2 comparison

Shot number	Θ (deg)	Θ_1 (deg)			Θ_2 (deg)		
		Test	MSFC equation	Difference (%)	Test	MSFC equation	Difference (%)
A1534	45	9	8.6	4.65	38	28.18	34.8
A1537	60	10	7.12	40.45	35	27.43	27.59
A1621	60	59	7.04	738.1	77	27.5	180
A1625	45	35	8.58	307.9	62	28.21	119.78
A1639	60	41	7.04	482.4	58	27.5	110.9
A1642	45	29	8.53	239.97	52	28.24	84.13

dimension and location to find the center of mass. However, due to time and measurement capabilities, α_c was estimated as the angle for half the distance from the lowest point of damage on the secondary target to the location of maximum damage. Another possible reason for differences between theory and test is the positioning and shape of the test articles. The test program was meant to simulate actual SSF hardware. Hardly any of these objects were simple, flat plates as in the previous studies. For instance, the fluid umbilicals were 6-in. cylinders. This complicates the data somewhat, which may contribute to the lack of correlation between the theory and test data.

CONCLUSIONS AND RECOMMENDATIONS

Thus far, no catastrophic or complete failures, due to secondary debris impacts, have been seen for any of the hardware evaluated in this study. Based upon the preliminary test parameter analysis, larger particles will be seen on-orbit than were used in the latest tests. Therefore, further testing with larger particles is recommended, especially for the umbilicals and ORU boxes, which did show possible impacts to the internal hardware (fluid lines, cables, and batteries). This study also looked at the minimum critical angle for ricochet debris. Further evaluation of higher impact angles, such as 70°, may be beneficial.

As far as the comparison with previous theory, this study did not provide enough usable data for an effective comparison. The data that was available did not correlate very well. Several possible reasons for the lack of correlation were discussed. Some additional work in this area may be beneficial, especially if it expands the theory to include thicknesses that cover the range of the truss members.

FUTURE WORK

Continuing work for the Secondary Debris Impact Damage and Environment Study will include:

(1) Additional testing at higher obliquities and with larger particles

(2) Continued testing with further SSF hardware

(3) A test program to evaluate and quantify secondary debris flux around the truss structure, module pattern, and radiators.

ACKNOWLEDGMENTS

We would like to express our appreciation to the technicians at the HIRL and JSC Technical Services for their effort and support throughout this study, the Technical Publications support personnel at Lockheed for their assistance with the documentation, and our co-workers at JSC for their guidance throughout the study.

REFERENCES

Christiansen, E. L. (1990). Advanced meteoroid and debris shielding concepts. Presented at AIAA/NASA/DOD Orbital Debris Conf.: Technical Issues & Future Directions, Apr. 16-19, Baltimore, Paper No. 90-1336.

Cour-Palais, B. G. (1982). Hypervelocity impact investigations and meteoroid shielding experience related to Apollo and Skylab. In: *Orbital Debris*, NASA CP-2360, pp. 247-275.

Eagle Engineering (1986). Secondary impact hazard assessment final report. Report No. 86-128.

Elfer, N. and G. Kovacevic (1985). Design for space debris protection. Presented at Third AIAA Aerospace Technol. Symp., Nov. 7-8, New Orleans.

Fraas, A. P. (1988). Protection of spacecraft from meteoroids and orbital debris. Report Nos. ORNL/TM--9904 and DE86 009996, Oakridge National Laboratory for U.S. Dept. of Energy.

Schonberg, W. P. and R. A. Taylor (1988). Analysis of oblique hypervelocity impact phenomena for meteoroid/space debris protection system design. In: *Proc. of AIAA SDM Issues of the Intl. Space Station Symp.*, Paper No. 88-2463.

Schonberg, W. P. and R. A. Taylor (1989a). Oblique hypervelocity impact response of dual-sheet structures. NASA TM-100358. Washington, D.C.

Schonberg, W. P. and R. A. Taylor (1989b). Penetration and ricochet phenomena in oblique hypervelocity impact. *AIAA J.*, 27:5, 639-646.

Int. J. Impact Engng Vol 14, pp 683 694, 1993
Printed in Great Britain

0734-743X/93 $6.00+0.00
1993 Pergamon Press Ltd

HYPERVELOCITY IMPACT TESTING OF MICROMETEORITE CAPTURE CELLS IN CONJUNCTION WITH A PVDF THIN-FILM VELOCITY/TRAJECTORY SENSOR AND A SIMPLE PLASMA VELOCITY DETECTOR

C. G. Simon

McDonnell Center for the Space Sciences, Washington University, St. Louis, Mo 63130, USA
current address: *Institute for Space Science and Technology, 1810 NW 6th Street, Gainesville, Florida 32609, USA*

ABSTRACT

Five different small particle capture cell designs were evaluated for their ability to capture fragments and residue from 10-200 μm diameter glass projectiles and oblong olivine crystals impacting at 1-15 km/s in sufficient quantity for chemical and isotopic analyses. Aluminum multi-foils (0.1-100 μm thick with ~10, 100 and 1800 μm spacing), foil covered germanium crystals, and 0.50 and 0.120 g/cm^3 Aerogels, were positioned behind either multi-film (1.4-6.0 μm thick) polyvinylidene fluoride (PVDF) velocity/trajectory sensor devices or a simple wire-grid plasma velocity detector. All capture cells collected significant amounts of impactor debris behind the PVDF sensors from nominal 100 μm diameter glass projectiles and olivine crystals which struck the sensor at velocities up to 6.4 km/s. At velocities >8 km/s little or no debris penetrated the second PVDF film. Results were inconclusive for velocities between 6.5 and 8 km/s. Plasma detector results showed identifiable impactor residue on Al foils for velocities up to 8.7 km/s and impact tracks with apparent debris imbedded in the Aerogels for velocities up to 12.7 km/s. Maximum foil penetration of glass spheres and olivine crystals were the same, but more particulate debris was associated with olivine crystal ipacts versus glass impacts. Foil spacing beyond one particle diameter had no effect on total penetration. Aerogels are identified as a capture cell media that warrants further investigation. The Al multi-foil capture cell with 100 μm net spacers is identified as the most effective of the other designs and offers the advantages of compact structure, low secondary ejecta from impacts, and easy recovery of impactor debris for analysis.

INTRODUCTION

As part of a continuing effort to develop cosmic dust detectors/collectors for use in space, we performed a set of hypervelocity impact experiments on combined sensor/capture-cell assemblies using 10-200 μm diameter glass projectiles and olivine crystals at velocities of 0.9-14.4 km/s. The design objective of the space-flight instrument is to measure the trajectories of individual particles with sufficient accuracy to permit identification of their parent bodies and to capture enough impactor material to allow chemical and isotopic analyses of samples returned to earth. In this study we report on the morphology of impacts in various types of capture cells after passage through two PVDF sensor films. We identified impactor fragments in selected capture cells from impacts at velocities up to 6.4 km/s using scanning electron microscopy with energy dispersive spectroscopy (SEM/EDS) and report qualitatively on chemical fractionation of selected soda-lime glass impactor fragments.

EXPERIMENTAL

Dust Accelerators

Two hypervelocity launchers were used in this study. The plasma gun facility at the Technical University of Munich is fully described by Igenbergs *et al.*, (1987) and Hudepohl *et al.*, (1989). Nominal 100 μm diameter soda-lime glass projectiles used in this study were highly eroded, partially melted, and sometimes fused by the 100 km/s high temperature He plasma that drag accelerated them. We recorded a maximum velocity of 14.4 km/s for an ~175 μm glass projectile using this gun. Impactor size was determined by measuring the penetration hole above an impact site in an ultra-thin (~500Å) organic polymer film (trade named "VYNS") that was mounted 0.64 cm ahead of the first detector film. Projectile sizes could also be estimated from the detector signals and/or the penetration hole in the first PVDF sensor film. This study and past studies have established the relationship between particle mass/velocity and the signal generated by its impact into the detectors (Simpson *et al.*, 1989a; Tuzzolino, 1991, 1992). These same studies, along with more recent work by Horz *et al.*, (1991) on teflon films, have also shown that a penetration hole to impactor diameter ratio (D_h/D_p) of <1.2 is expected for systems with an impactor/film-thickness ratio (D_p/T_f) >20:1, and a D_h/D_p of ~1.0 is expected for penetrations in the 500Å polymer film where D_p/T_f>200 for projectiles >10 μm in diameter. Thus, post experimental analysis of detector signals and/or penetration holes provided moderately accurate projectile sizes for many impactors.

The second launcher used in this study was a two stage light gas gun at the Johnson Space Center (JSC) is described by Horz (1989). A "shotgun" technique was used to launch 100 μm diameter glass beads and rectangular olivine crystals (maximum dimensions 105 to 125 μm) at 6-7 km/s. Particles were placed in a precision bored hole in the end of an assembled 4-piece sabot and held in place with bits of styrofoam. Out of ~100 particles launched, 1 to 7 struck the target at essentially the same velocity (measured by detection of impact flash and/or sabot velocity).

All reported velocities are for impacts into the first PVDF film. A velocity reduction of 0-20% for most impactors that penetrated the first film was observed by measuring the time-of-flight of the particle (or fragments) between the first and second PVDF films. In a few cases, greater velocity reductions (and even velocity increases) were observed for some impactor fragments. Several shots were made into three film sensors in order to observe the effect of the second sensor film on impactor velocity. Target assemblies were positioned normal to the beam line in all experiments except two, where olivine crystals were shot into targets positioned 45° from normal.

Sensor/Capture-Cell Assemblies

The five types of capture cells evaluated are shown in Figs. 1a-e. All cells used the same type of 2.3 x (10 x 10) cm aluminum cassette holder to mount the target assemblies. Four of the five capture cell designs were based on flight hardware onboard the Solar Maximum satellite or the Long Duration Exposure Facility (LDEF). The successful recovery of impactor residue in the multi-layer thermal blankets retrieved from Solar Max (Schramm *et al.*, 1986; Laurance and Brownlee, 1986; Bradley *et al.*, 1986; Warren *et al.*, 1989) led to the choice of aluminum foil multi-layer "blanket" type capture cells with either 100 μm thick dacron net spacers, or no spacers, between thin (3-8 μm) Al foils mounted on a 25 μm thick Al foil. Another multi-foil design incorporating Al films from 0.1 to 100 μm thick with an interfoil spacing of 1.8 mm was based on the capture cell design flown by McDonnell *et al.*, (1984; 1990). Typical foil stacks had a 0.1 or 0.3 μm foil on top for event registration, followed by one to four 1.0 and/or 3.0 μm foils, which were then followed by several 8 μm foils and one or two 25 μm and 100 μm foils. The effect of foil thickness order was investigated by varying the number and order of the 3 and 8 μm foils. Foils ≤ 3μm thickness were made by physical vapor deposition of Al on Ni support grids. Other foils were high purity cold rolled Al.

Mounted foils were scanned on a light box and any background pin holes were marked on the foil surface for 8-100 μm thick foils, or on a plastic mm reference grid overlay for the thinner, 0.1-3.0 μm, foils. Average pinhole (>~5 μm) counts for all foils were less than 2/cm^2. After exposure to the hypervelocity particle beam, the foils were again viewed on the light box and all new holes were noted in color codes on plastic grid overlays. This system was capable of easily identifying and recording locations of 10 μm diameter holes in the opaque Al films with the unaided eye. It was also used to view the PVDF sensor films.

A fourth capture cell design was based on our own foil-covered (200 μm spacing) germanium crystal wafer capture cell that also flew on the LDEF (Jessberger *et al.*, 1985; Fechtig *et al.*, 1987; Amari *et al.*, 1991). A metal coated, 2 μm thick Mylar film used in the original design to cover 0.5 mm thick Ge crystals was replaced by either a 0.1 or 1.0 μm thick aluminum foil in this series of experiments. All of the capture cell surfaces in these four designs could be accessed easily and inserted directly into analytical instruments such as optical and scanning electron microscopes (SEM) and secondary ion mass spectrometers (SIMS) without pre-treatment of the impacted area.

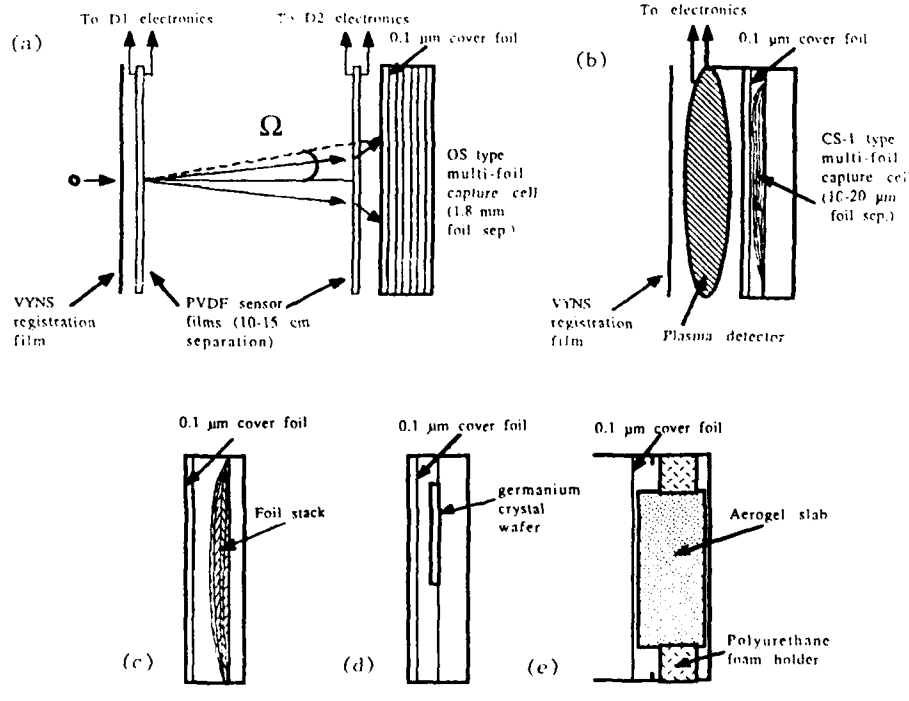


Fig. 1. Five capture cell designs. (a) "OS" multi-foil capture cell, 1.8 mm foil spacing, showing position of 2-film PVDF trajectory/velocity sensor, VYNS registration film, and effective debris dispersion angle [Ω]. (b) "CS-1" multi-foil capture cell, 10-20 μm foil spacing, showing position of wire grid plasma detector. (c) "CS-2" multi-foil capture cell with 100 μm thick dacron net spacers. (d) "Ge" capture cell with cover foil. (e) Aerogel capture cell with Al cover foil.

A fifth capture cell design consisted of either a 12 or a 25 mm thick slab of Aerogel (50 and 120 mg/cm^3, respectively) preceded by one thin (≤1 μm) Al foil (1-2 mm separation) for hole registration and plasma generation. Impact damage was photo-documented using optical microscopy. Only four shots were made with these capture cells mated to PVDF detectors, and the results were inconclusive. However, fourteen correlated impact events with Aerogel capture cells behind the plasma detector were recorded. After photographic documentation, the Aerogel-120 samples were returned to JSC, and the Aerogel-50 samples were returned to the Jet Propulsion Laboratory (JPL), where selected particle fragments were extracted and analyzed. The results were included in larger studies reported by Zolensky *et al.*, (1990) and Tsou *et al.*, (1990), respectively, and agreed well with other studies that showed retention of some crystalline structure and most impactor mass at velocities up to ~7 km/s (Tsou *et al.*, 1989a, b; Zolenski *et al.*, 1989; Bunch *et al.*, 1990; Barret and Zolenski, 1991) Apparent (optical microscopy) retention of impactor debris in Aerogel at velocities up to 12.7 km/s was observed in this study, but not confirmed.

A two stage thin film PVDF particle trajectory/velocity sensor developed and tested by our co-investigators at the University of Chicago was evaluated with the five types of capture cells. (A single film version of this dust-detector/mass-analyzer has successfully flown on the two USSR Vega spacecraft which encountered comet Halley in March, 1986 [see Perkins *et al.*, 1985; Simpson *et al.*, 1987a, b, 1989b].) Tuzzolino (1991, 1992) has reported results of the trajectory/velocity detector portion of the current study. The sensors function by detecting penetrations of electrically active thin PVDF or PVDF-copolymer films. The experimental devices consisted of 2 or 3 frame mounted (10x10 cm with 8x8 cm active area) PVDF films with 10-15 cm spacing. The final PVDF film was 5 mm above the capture cell surface. Some of the PVDF films had 1 mm wide, electronically distinguishable strip electrodes deposited at 90° angles on opposite sides. This allowed accurate assessment (1-3 mm) of the x,y coordinates of an impact and represented a true velocity-trajectory sensor arrangement. The sensor films varied in thickness from 1.4 to 6.0 μm and the effects of their thickness on particle fragmentation and total film penetration were observed. The initial shock loads resulted in varying degrees of impactor fragmentation. An attempt was made to minimize the shock load on fragments that survived penetration of the two PVDF films by placing several very thin Al foils (0.1-1.0 μm) ahead of thicker (3-25 μm) foils in the capture cells. In two experiments a 0.3 μm thick Al film was placed 1.7 cm behind the first PVDF film to register initial particle fragmentation and capture impactor debris.

A simple wire grid plasma-type velocity detector (Iglseder and Igenbergs, 1987) constructed and operated by the Munich plasma-gun staff, and a flash detector operated by the JSC gun staff were used in several tests in order to observe the performance of capture cells on unfragmented projectiles. Impactor sizes in plasma gun shots were determined by measuring the penetration hole sizes in a ~500Å thick polymer film positioned in front of the detector grid, or estimated using the associated penetration holes in the first capture cell foil and the plasma detector signals. Impactor sizes in the JSC light gas gun shots were assumed to be the same as launched particles.

Impact Analyses

All impact sites were examined with an optical microscope. Representative impacts that had well correlated electronic test data from the PVDF sensors were selected for SEM/EDS analysis using a JEOL JSM-840A SEM equipped with a Tracor/Northern EDS with two dimensional, 8-element x-ray mapping capability. The effects of intermixing of capture cell and impactor materials were minimized by using high purity Al and Ge target materials. Impact areas on Al foils were cut out using a 2.5 cm dia. ring mount for SEM analysis. Ge crystal wafers were inserted directly into the instrument. This is a significant advantage since samples are available for immediate analyses upon return from orbit. The major disadvantage to these types of capture cells is the high specific shock imparted to the small particles, especially into the Ge target, which results in the loss of most structural information and may cause chemical, and possibly isotopic, fractionation, as well as intermixing of capture cell materials with projectile material. X-ray maps of Na, Mg, Si, and Ca concentrations were recorded at 300X magnification over selected impact areas around penetration holes and craters. This allowed identification of ~2 μm size particles that had higher than background concentrations of any or all of these elements. Processing of the x-ray maps allowed identification of glass and olivine projectile debris and relative element abundances. This technique was extremely useful in identifying debris deposits and segregating them from target debris and artifacts. ***It was apparent throughout the SEM/EDS analyses that debris morphology alone could not be used to accurately distinguish impactor debris from target debris.*** Several examples of this point are presented in the next section. Elemental line intensity ratios were used to verify the presence or absence of edge effects in the x-ray spectra that may have led to misidentification of debris liners. The automated mapping was augmented by extensive viewing and x-ray spot and area analyses at higher magnifications and lower beam voltages. However, very thin deposits o. material (<100 nm), such as light vapor condensates, would not be identified by these techniques. Our past experience has shown that when sufficient material exists to allow identification with EDS, there is ample material for isotopic analyses using SIMS.

The extent of chemical fractionation of impactors is addressed qualitatively in this study, a limitation due to the inherent heterogeneity of the glass projectiles used in most experiments. Results from quantitative EDS analyses of five nominal 100 μm diameter soda lime glass beads randomly selected from the batch used as projectiles, and for a melt residue of a projectile found in an Al foil stack after a 2.74 km/s impact, are shown in Table 1. Quantitative analyses of olivine crystals and residues have not been performed at this time. (Major elements in the olivine crystals were O, Mg and Si.) NBS standard glasses 107 and 108 (basalts), 202 (labradorite), 217 (Sr feldspar), 218 (celsian), 242 (uvite), and 620 (soda lime glass) were used for instrument calibration.

Penetration hole diameters (D_h) and foil thicknesses (T_f) were used to estimate the apparent diameters (D_p) of major impactor fragments that penetrated various capture-cell foils using the D_h/T_f versus D_p/T_f relations developed by Carey et al. (1987), and empirically quantified by Horz et al. (1991) for glass/Al and glass/teflon impactor/target systems. Mean diameters for oval holes were calculated using the relation: $D_h = [(d_a)(d_b)]^{1/2}$ where d_a and d_b are the major and minor axes. Masses were calculated from D_p values using a density value of 2.6 g/cm^3 for the glass.

Table 1. Quantitative EDS analyses of five nominal 100 μm soda-lime glass projectiles before launch and an impactor melt residue after a 2.74 km/sec impact.

	T_b	% concentration in unlaunched projectiles						% conc. in melt residue
Compound	(K)	1	2	3	4	5	Average	from 2.74 km/sec impac
SiO_2	2590	79.6	69.7	76.4	76.4	75.5	75.5 ±3.60	78.9
AL_2O_3	3250	1.12	4.96	0.67	0.97	1.27	1.80±1.78	7.27
MgO	3870	4.04	4.09	3.82	4.47	4.24	4.13±0.24	2.70
CaO	3120	7.57	7.78	8.56	8.69	8.45	8.21±0.50	7.37
Na_2O	1550 (sub)	6.76	10.7	9.50	9.03	9.78	9.15±1.47	2.91
Total		99.1	97.2	98.9	99.6	99.2	98.8	99.2

RESULTS

Impact sites whose geographic locations were matched to impactor velocity/size data with high confidence were considered correlated events. A total of 93 shots produced a total of 75 correlated impacts at velocities of 0.9 to 14.4 km/s. Individual experimental conditions and capture cell results for correlated impactors are listed in Table 2 in order of increasing impactor velocity under each sensor/capture-cell category. Analytical results are described below for four representative impact events: two impacts of nominal 100 μm glass particles in OS type capture cells (1.8 mm foil spacing) positioned behind two-film PVDF sensors at velocities of 2.7 and 4.8 km/s, and one similar impact behind a three-film PVDF sensor at 6.4 km/s; and one set of olivine crystal impacts into a CS-2 type capture cell (100 μm foil spacing) positioned behind a simulated two-film PVDF sensor (1.5 μm thick Mylar films were substituted for active PVDF films) at 6.2 km/s and a 45° angle.

All impactors fragmented during the multiple shock impact events experienced in multi-film sensor/capture-cell assemblies. Significant amounts of impactor debris in the form of melted and embedded globs and spatters and partial melt rims around holes and craters in most foils, were observed for impacts at velocities ≤6.4 km/s. The only verified intact capture of impactors was observed in A-120 and A-50 cells behind the plasma detector at velocities ≤3.5 km/s. Intact capture of similar size particles and/or large fragments at velocities up to 7 km/s has been reported by Tsou *et al.*, (1988, 1989, 1990) and Zolenski *et al.*, (1989, 1990), and indeed there appeared to be well defined particles at the end of Aerogel tracks at velocities up to 12.7 km/s in our experiments. Six shots were performed on PVDF/Aerogel assemblies in this study, but results were inconclusive due to the difficulty in identifying small glass and olivine fragments in the Aerogel matrix. Colored projectiles could mitigate this problem in future studies.

Two major criteria were of interest in evaluating multi-foil capture cell performance as it related to the survival and subsequent identification of impactor debris: [1] the effective debris dispersion angle, Ω, and [2] the total (cumulative) foil penetration, $F_t = \Sigma F_i$ (where F_i is Al or PVDF foil thickness). Ω for the mixture of target/impactor fragments exiting the second PVDF film was determined using the formula $\tan\Omega = ¥/2ß$ where ¥ equals the maximum dimension of the impact affected area on the first Al foil in the capture cell and ß equals the distance from the first PVDF film to the first capture cell foil (see Ω illustrated in Fig. 1a). This angle describes the dispersion of surviving impactor fragments and vaporized material and is directly related to the practical ability to locate these materials for analysis.

Ω values are not directly comparable to dispersion angles determined in one film penetration studies since two PVDF films were penetrated and the large standoff distance between the first and second sensor films (10-15 cm compared to the 0.01 cm diameter projectiles) precluded observation of impact induced damage from the spray of very fine particles associated with fragmented hypervelocity projectiles. Ω values for debris clouds ranged from 0.6° to 5.0°, with a mean of 2.5° ± 1.4° for normal impacts in the 0.9 to 7.7 km/s range (Table 2, Fig. 2). Four olivine particle impacts at 45° (shot 454) had Ω values of 0.6° to 3.5°, with a mean of 1.7° ± 1.3°. At velocities >8 km/s, very little impactor debris reached the capture cells after penetrating two PVDF sensor films.

Multi-Foil Capture Cell Penetration Results

Impactor fragments that survived penetration of the two PVDF films fragmented further during subsequent foil penetrations. Among the critical design criteria for multi-foil capture cells are the selections of the thickness, number, ordering and spacing of the foils required to stop the most penetrating micrometeorites. These parameters are listed in Table 2 for the experiments in this study along with associated impactor sizes and velocities. A penetration refers to a hole through a film, even if it is the result of back side spallation. A plot of F_t, total (cumulative) film penetration versus velocity for the different multi-foil detector/capture-cell combinations is presented in Fig. 3. In some cases a debris fragment imbedded into or cratered the final film, but in most instances the debris was deposited on top of the final film. In some impacts over 8 km/s the final PVDF sensor film was not penetrated. Impactor diameters for the plotted data ranged from ~10-175 μm (see Table 2). The plotted data were not corrected for impactor mass differences, nor were corrections made for differences in physical properties of the polymeric PVDF films and the Al films. (Numerical simulation has shown that the peak compressive stresses experienced by 100 μm impactors into 2, 5 and 10 μm thick Mylar and Al films are in the 10^{10} to 10^{11} Pa range, and are within a factor of two of each other for velocities >8 km/s, and within a factor of five for a 5 km/s impact [Cour-Palais et al., 1989].)

The data show a clear trend of decreasing cumulative film penetration with increasing velocity for all sensor/multi-foil capture cell assemblies. F_t values for assemblies that employed three films in the sensor portion, either three PVDF or two PVDF and one 0.3 μm Al foil, along with OS or CS-2 capture cells showed more scatter than the 2-film-sensor/OS data but were in the same general range or lower. F_t values for normal incidence glass and olivine impacts

Table 2. Summary of impact test results for sensor/capture-cell assemblies using glass and olivine (shots 447, 450 and 454) projectiles. Targets were normal to the flightpath except where noted. OS=Al foils, 1.8 mm spacing; CS-1=Al foils, no spacers, 10-20 μm separation; CS-2=Al foils, 100 μm dacron net spacers; Ge= Ge wafer, Al cover foil; A-120=120mg/cm^3 Aerogel, Al cover foil.

Shot No.	Velocity (km/s)	Proj. size (μm)	μm of PVDF penetrated	Capture Cell Results Type	μm Al foil penetrated	F_t, total film penetrated (μm)	Area on 1st. cell foil (mm)	Debris angle, Ω
Targets with 2-film PVDF sensors								
34	0.9	~70	4.5+4.9=9.4	OS	0.3+1+3+8+8=20.3	29.7	2 x 3	0.6
31	2.1	~80	4.5+4.9=9.4	"	0.3+1+3+8+8+25=45.3	54.7	10 x 14	2.7
17	2.1	73 x 85	6+6=12	"	0.1+1+8+8=17.1	29.1	7 x 11	2.1
* 17	2.7	96	6+6=12	"	0.1+1+8+8=17.1	29.1	8 x 12	2.3
43	2.9	147	1.6+2.2=3.8	"	0.3+3+3+3+3+8=20.3	24.1	7 x 14	2.7
45	4.4	~80	1.6+2.2=3.8	"	0.3+3+3+3+3+8=20.3	24.1	14 x 16	3.1
* 23	4.8	~100	6+6=12	"	0.1+3+8=11.1	23.1	13 x 26	5.0
45	4.9	~100-150	1.6+2.2=3.8	"	0.3+3+3+3+3+8=20.3	24.1	-	-
23	5.6	~100	6+6=12	"	0.1+3=3.1	15.1	15 x 20	3.9
10	7.7	24	3.3+2.5=5.8	"	0.1+1+3=4.1	9.9	8 x 9	1.7
12	8.0	31 x93	2.0+1.5=3.5	"	1.0	4.5	-	-
41	8.1	cluster	1.6+(2.2)≤3.8	"	0	≤3.8	0	-
35	1.8	~100	4.5+4.9=9.4	CS-1	0.1+3+(4x8)+25=60.1	69.5	4 x 7	1.4
35	2.1	~100	4.5+4.9=9.4	"	0.1+3+(4x8)+(~12)=~47	~56	14 x 15	2.9
30	2.7	~50	4.5+4.9=9.4	"	0.1+3+(4x8)=35.1	44.5	12 x 14	2.7
26	4.7	85	4.5+4.9=9.4	"	0.1+3+(4x8)=35.1	44.5	25 x 25	4.8
30	5.0	~60	4.5+4.9=9.4	"	0.1+3+(4x8)=35.1	44.5	17 x 20	3.9
451	6.0	~115	1.5+5.4=6.9	CS-2	2.5+(3x4)=14.5	21.1	(not rec.)	
406	6.1	~100	1.6+2.2=3.8	"	3+(4x8)=35	38.8	6x6	1.2
"	"	"	"	"	"	"	7x9	1.7
450	6.2	~115	5.4+4=9.4	"	2.5+(3x4)=14.5	23.9	(not rec.)	
"	"	"	"	"	"	"	"	
"	"	"	"	"	"	"	"	
"	"	"	"	"	"	"	"	
"	"	"	"	"	"	"	"	
*454	6.2	~115	1.5+1.5=3.0	"	2.5+4+4=10.5	13.5	4x10	1.9
(45°)	"	"	"	"	"	"	4x18	3.5
"	"	"	"	"	2.5+(3x4)=14.5	17.5	2x4	0.8
"	"	"	"	"	"		2x3	0.6
48	2.7	97	1.6+2.2=3.8	Ge	(1.0)	4.8+crater	7 x 12	2.3
29	4.7	24 x 27	4.5+4.9=9.4	"	(1.0)	7.7+crater	-	-
20	5.5	65 x 80	6+6=12	"	(1.0)	13.0+crater	-	-
40	10.2	~70	2.0+(1.5)≤3.5	"	0	≤3.5	-	-
40	13.8	~70	2.0+(1.5)≤3.5	"	0	≤3.5	-	-
63	8.4	(>100)	2.2+2.9=5.1	A-120	(0.1)	no visible tracks		-
64	12.0	(<30)	2.2+2.9=5.1	"	(0.1)	no visible tracks		-
Targets with 3-film PVDF sensors								
49	5.2	~30-40	1.6+2.2+2.5=6.3	OS	0.3	6.6	-	-
* 55	6.4	~85	2.2+2.9+3.5=8.6	"	0.3+3+3+8=14.3	22.9	-	-
58	7.7	120	2.2+2.9+3.5=8.6	"	0.3	8.9	-	-
52	12.0	63 x 92	1.6+(2.2)+0≤3.8	"	0	≤3.8	-	-
54	13.1	<10	1.6+0+0≤1.6	"	0	≤1.6	-	-
53	14.1	48	1.6+(2.2)+0≤3.8	"	0	≤3.8	-	-
56	14.4	~175	2.2+2.9+3.5=8.6	"	0.3	8.9	-	-
62	5.0	95	2.2+(0.3 Al)+2.9=5.4	CS-2	0.3+3=3.3	8.7	-	-
59	10.2	52	2.2+(0.3 Al)+2.9=5.4	"	0.3	5.7	-	-
Targets with flash detector								
403	6.2	~100	-	CS-2	1+3+3+8+8=23	23	-	-
"	"	"	-	"	"	"	-	-
"	"	"	-	"	"	"	-	-
"	"	"	-	"	"	"	-	-
"	"	"	-	"	"	"	-	-
447	6.2	~115	-	CS-2	3+(6x4)=27	27	-	-
"	"	"	-	"	"	"	-	-
"	"	"	-	"	3+(5x4)=23	23	-	-
"	"	"	-	"	"	"	-	-
"	"	"	-	"	"	"	-	-
Targets with plasma detector								
M	6.8	50	-	OS	0.1+1+3+8=12.1	12.1	-	-
M	8.7	15 x 30	-	OS	0.1+1+3+8=12.1	12.1	-	-
A	2.6	71 x 83	-	CS-1	0.1+3+(4x8)+25=60.1		-	-

Table 2. (cont.) A-50 and A-120 = 50 and 120 mg/cm^3, respectively, Aerogel targets.

Aerogel targets with plasma detector

Shot No.	Velocity (km/s)	†Impactor size (μm)	Capture cell type	Entrance hole dia.	Impact track dimensions (μm) length	max. width	fracture zone width	"Projectile" debris dia.
G	<1.9	61 x 76	A-120	56	1500	310	630	125
S	2.1	100+90	A-120	105	~1200	220	890	97+89 (fused)
R	2.9	(medium)	A-120	95	1950	280	620	70
G	3.1	91 x 129	A-120	160	3060	440	940	110
J	4.3	(medium)	A-120	(hit grid wire)	~1500	~3mm spray area		frag
B	3.9	(70)	A-120	(frag, 1630)	~1500	(1630)	-	frag
B	5.4	(60)	A-120	126	2890	270	760	250
J	7.1	(medium)	A-120	(hit grid wire)	~1500	~3mm spray area		frag
S	12.3	(medium)	A-120	190	3940	440	570	89
F	12.7	30 x 45	A-120	~60	830	130	580	37
E	2.2	68	A-50	160	5810	280	940	63
E	3.5	46 x 91	A-50	130	2880	310	810	frag
H	6.9	~80	A-50	(frag, 340)	1250	410	940	frag
H	10.5	~100	A-50	110	2940	440	2250	frag

*Detailed SEM/EDS analyses of these impact events are presented in the text.

†Values in ( ) were estimated using plasma detector response calibration curves derived from Al plate impacts.

at 6 km/s into CS-2 capture cells behind two-film PVDF sensors also showed more scatter than similar impacts into OS capture cells, ranging from 23 to 39 μm. The lower values are associated with thicker PVDF films, larger debris dispersion angles, and thinner capture cell foils. In both cases, either 6 or 7 films were penetrated. This result led to replacement of 8 μm Al capture cell foils with 4 μm foils in subsequent shots. A subsequent shot at 6.2 km/s at a 45° angle through simulated sensor films (1.5 μm thick Mylar) into 4 μm Al foils yielded F_t values of 11 and 15 μm.

Four correlated high speed impacts (>12 km/s) were recorded with 3-film (2.2, 2.9, and 3.5 μm) sensors/OS-capture-cell assemblies. A 63 x 92 μm projectile impacting at 12.7 km/s in shot 52 fragmented after passing through the first sensor film into one large (30 x 71 μm) and several smaller fragments which then struck the second sensor at 12.1 km/s. A spray of very fine fragments exited the second film and struck the third sensor film with an onset velocity of 34 km/s. This was the greatest velocity enhancement noted during the study and was verified by post-test analysis of the detector signal trace. An ~10 μm projectile impacting at 13.1 km/s in shot 54 only penetrated one sensor film. This result indicated that small, high speed projectiles may not be effectively recovered using the baseline 2-film sensor with any capture cell. An ~60 μm projectile impacting the first sensor film at 14.1 km/s in shot 53 lost ~90% of its mass before striking the second sensor film at 9.4 km/s. No signal was detected on the third sensor film. An ~175 μm projectile (estimated from sensor response) in shot 56 impacted the first PVDF sensor at 14.4 km/s. A small (~25 μm) fragment emerged and struck the second sensor at 11.0 km/s, and a very small fragment (~ 14 μm, or ~0.05% of the original impactor mass) struck the third sensor film at 1.8 km/s and then penetrated the first capture cell foil. This event showed the velocity and mass loss that could be expected when a large, fast impactor penetrates the multi-film sensor. It also showed that impactor fragments from this event would have penetrated several capture cell foils behind a 2-film sensor.

Another notable observation was the presence of impactor/target debris on the backsides of the foils in CS-1 and CS-2 capture cells, and the lack of debris on the backsides of foils in OS capture cells. This indicates an important advantage of the CS-2 cells, which have similar penetration performance as the OS cells, but are much more compact, occupying <1 mm in depth compared to ~1 cm for the OS cells.

Multi-Foil Capture Cell Impactor Debris Analysis

Experimental conditions for the four impact events discussed below are marked with an asterisk in Table 2. The events are discussed in order of increasing velocity.

Shot 17, 2.7 km/s, two 6 μm thick x,y position sensing PVDF detector films, OS capture cell (1.8 mm foil spacing). A 96 μm diameter (1.2 μg, estimated from detector signal) glass projectile impacted the first PVDF film at 2.7 km/s and penetrated with no apparent fragmentation. The particle struck the second PVDF film at 2.4 km/s and broke into two major fragments. Impactor fragments then penetrated a 0.1, a 1.0 and two 8 μm thick Al foils (Figs. 4a-d). The foils were littered with 1-10 μm size impactor fragments. X-ray maps of the largest hole in the first 8 μm foil and surrounding area (Figs. 4e and 4f) show a thick glass liner covering ~1/3 of the rim, two 15 μm droplets of glass extending in a ray from the rim, and two smaller rays of glass ~2 μm wide and ~30 μm long also extending from the rim. Impactor melt liners were also found on penetration hole exit side rims. These images also demonstrate the difficulty in identifying impactor debris from morphology by showing that only a small fraction of the debris particles visible in Fig. 4e are identified as impactor material in the x-ray image (Fig. 4f) despite their similar appearance. Figure 5a shows a 15 μm diameter impactor fragment imbedded in the third Al foil, and Fig. 5b shows a 70 μm long fragment of the glass impactor resting on top of the fourth foil. A semi-quantitative x-ray analysis of the 15 μm impactor fragment indicated a depletion of the volatile Na_2O constituent of the glass matrix and was representative of the degree of chemical fractionation observed in these events. The Na_2O concentration of 2.9% measured in this impactor fragment was ~1/3 of the 8.2 ± 0.5% average concentration found in unlaunched projectiles.

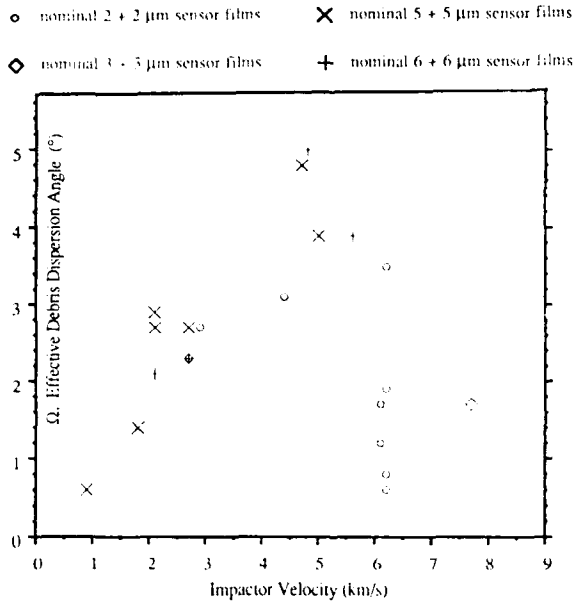


Fig. 2. (above) Plot of impactor debris dispersion angle, Ω, versus velocity.

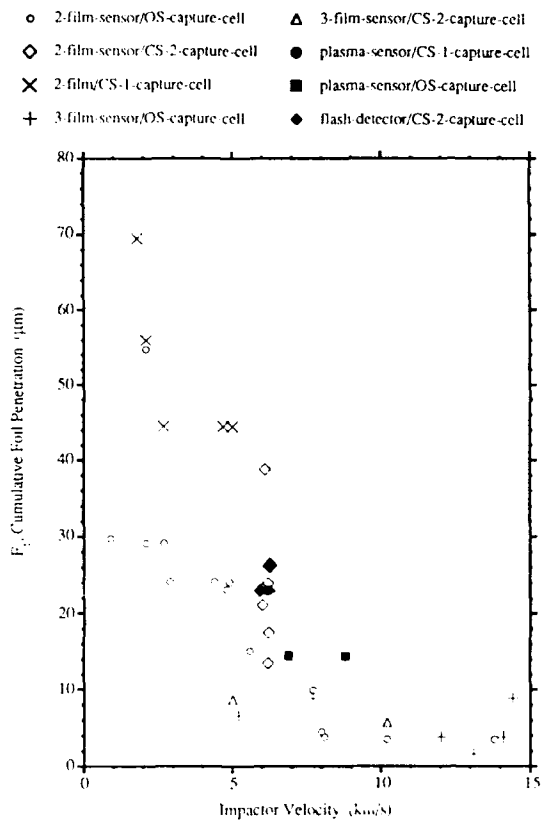


Fig. 3. (right) Plot of cumulative foil penetration, F_t, versus velocity. Impactors ranged in size from 10-200 μm.

The fifth Al foil in the capture cell, 25 μm thick, had a large blob of glass, 110 μm long and ~30 μm in diameter, partially embedded in the foil (Fig. 5c) and one other area with significant impactor debris (Fig. 5d). These two images are another example of the difficulty in using morphology to distinguish impactor debris. In Fig. 5d a spatter of Al is resting on top of a large (70 x 150 μm by ~5 μm thick) spatter of glass that has apparently fractured on cooling. Thus, the glass has a more "metallic" appearance than the Al and both materials charge under high beam currents since the Al spatter is insulated from the grounded substrate by the glass spatter. The dozen smaller spatters (10-40 μm) and numerous small bits and filaments of debris are all glass. The "debris" pictured in Fig. 5e is actually an embedded silicaceous contaminate, probably pressed into the film during the rolling process. The presence of Fe and the morphology of the feature showed that it was not an impactor fragment.

Shot 23, 4.8 km/s, two 6 μm thick x,y position sensing PVDF detector films, OS capture cell (1.8 mm foil spacing). A 65 x 96 μm glass particle (determined from VYNS film penetration hole) impacted a 2-film-sensor/OS-capture-cell assembly at 4.8 km/s. The particle suffered severe fragmentation on penetrating the first PVDF film. Fragments struck the second PVDF film at 4.5 km/s. Fragments then penetrated a 0.1, a 3.0, and an 8 μm thick Al foil. Figures 6a-f show SEM micrographs and associated x-ray maps of selected glass fragment and filament impacts on the second and third capture cell foils. Impactor residue is present in portions of the trough-like craters formed by filaments, and partially around the rims of some holes. Some individual 2 μm size bits of impactor debris are also identified.

Shot 454, 6.2 km/s, two 1.5 μm Mylar foils (simulating PVDF sensors for particle fragmentation purposes), CS-2 capture cell (100 μm foil spacing). Four 105-125 μm size olivine crystals penetrated the Mylar films and struck the capture cell, penetrating a 2.5 and either two or three 4.0 μm thick Al foils. Figure 7a-g show selected areas of impact damage on the second and third capture cell foils and associated impactor debris with EDS spectra. Impactor debris was found on both the front and back sides of the foils. While some olivine fragments had obviously undergone melting, other fragments retained some crystalline structure. In general, more particulate debris was associated with these olivine impacts than with the glass impactors at the same velocity, as would be expected from the higher melting point of olivine compared to soda-lime glass. No impactor material was found in the pile of Al foil debris found on top of the fourth foil (Fig. 7h).

Shot 55, 6.4 km/s, three PVDF detector films (2.2, 2.9, 3.5 μm thick), OS capture cell (1.8 mm foil spacing). A 77 x 90 μm (0.79 μg, determined from VYNS film penetration hole) glass particle accompanied by ~50 very small particles (<<10 μm dia.) impacted the first PVDF film at 6.4 km/s. The large particle fragmented significantly on penetrating the first film and a shower of fragments struck the second PVDF film with an onset velocity of 6.4 km/s. Fragments that penetrated the second sensor film struck the third PVDF film with an onset velocity of 5.9 km/s. Figures 8a-d show selected views of the subsequent penetrations in a 0.3, two 3.0 and one 8 μm thick Al capture cell foils. The high degree of impactor/target material intermixing is evident from these micrographs. Figures 8e-i show two details of the impact area on the second foil and corresponding Si x-ray maps. Impactor debris is present in the form of small particles (2-4 μm) around the large penetration hole shown in Fig. 8a.

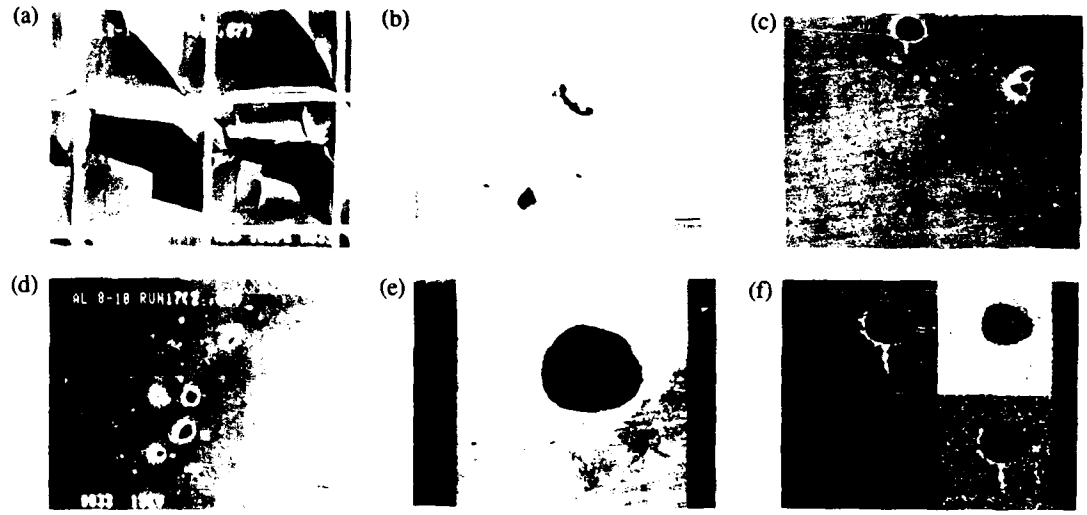


Fig. 4. [Shot 17, 96 μm diameter glass projectile, 2.7 km/s, 2-film PVDF sensor, OS capture cell {1.8 mm foil spacing}] (a-d) Secondary electron (SE) images of impact areas on the first four Al foils [0.1, 0.3, 8, and 8 μm thick]. (e) Largest hole in the 3rd foil. (f) X-ray maps of (e) showing Si [up ltl, Na [up rtl and Ca.

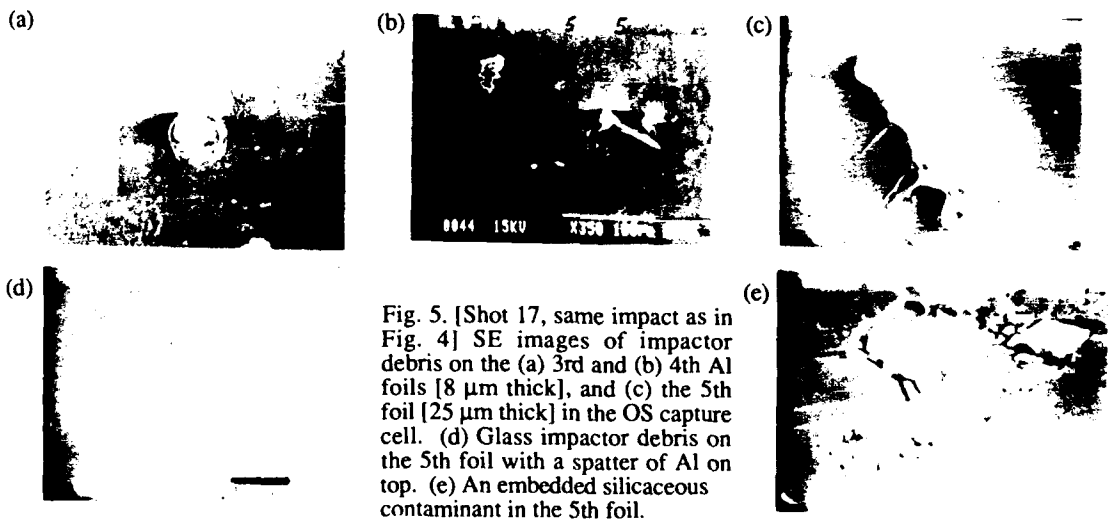


Fig. 5. [Shot 17, same impact as in Fig. 4] SE images of impactor debris on the (a) 3rd and (b) 4th Al foils [8 μm thick], and (c) the 5th foil [25 μm thick] in the OS capture cell. (d) Glass impactor debris on the 5th foil with a spatter of Al on top. (e) An embedded silicaceous contaminant in the 5th foil.

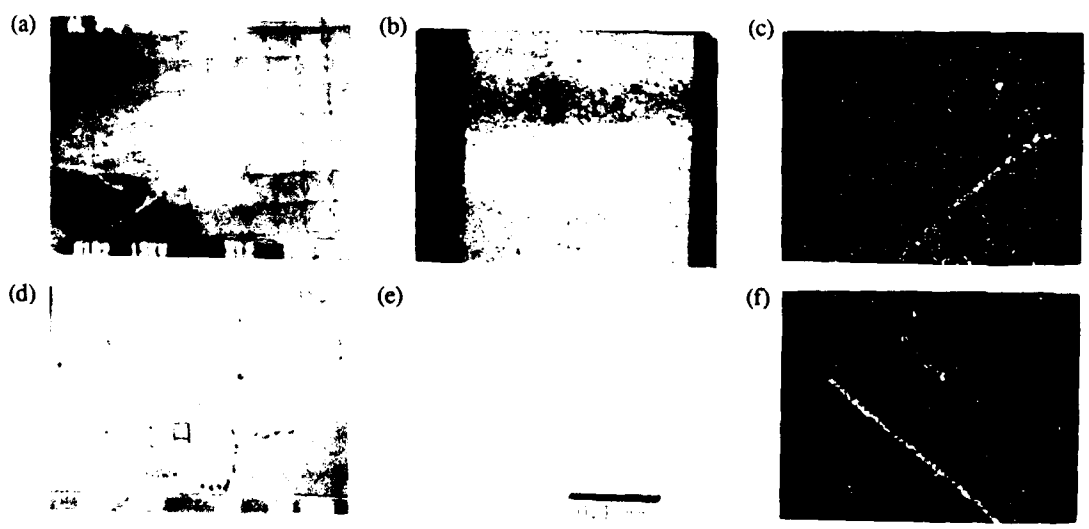


Fig. 6. [Shot 23, 65 x 96 μm glass projectile, 4.8 km/s, 2-film PVDF sensor, OS capture cell] SE images of (a) impact area on the 2nd foil, (b) a glass filament impact on the 2nd foil. (c) Si x-ray map of (b). (d) Impact area on the 3rd foil. (e) Closeup of a filament impact on the 3rd foil. (f) Si x-ray map of (e).

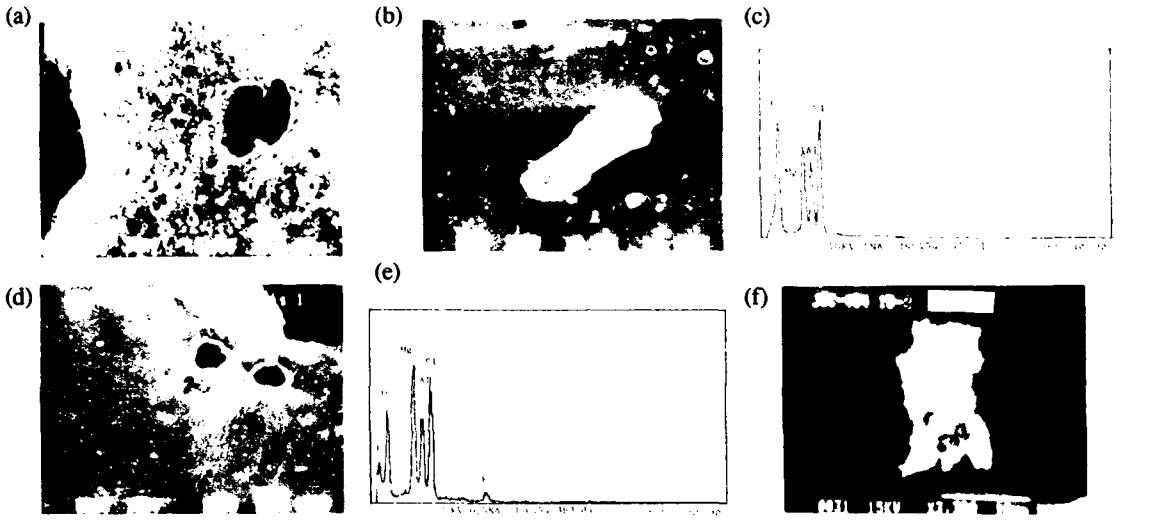


Fig. 7. [Shot 454, ~115 μm olivine crystal projectile, 6.2 km/s, simulated 2-film PVDF detector {1.5 μm thick Mylar foils}, CS-2 capture cell at *45°*]. SE images of (a) front side of the 3rd, and final, Al foil penetrated, and (b) a particle found in (a) and its (c) EDS spectrum. (d) Back side of 2nd foil directly above (a) showing 4 particles of olivine that had undergone melting. (e) EDS spectrum of particle 4 shown in (d). (f) Large impactor fragment found on the front side of the 3rd foil and (g) its EDS spectrum. (h) Debris pile 4th foil was nearly all Al.

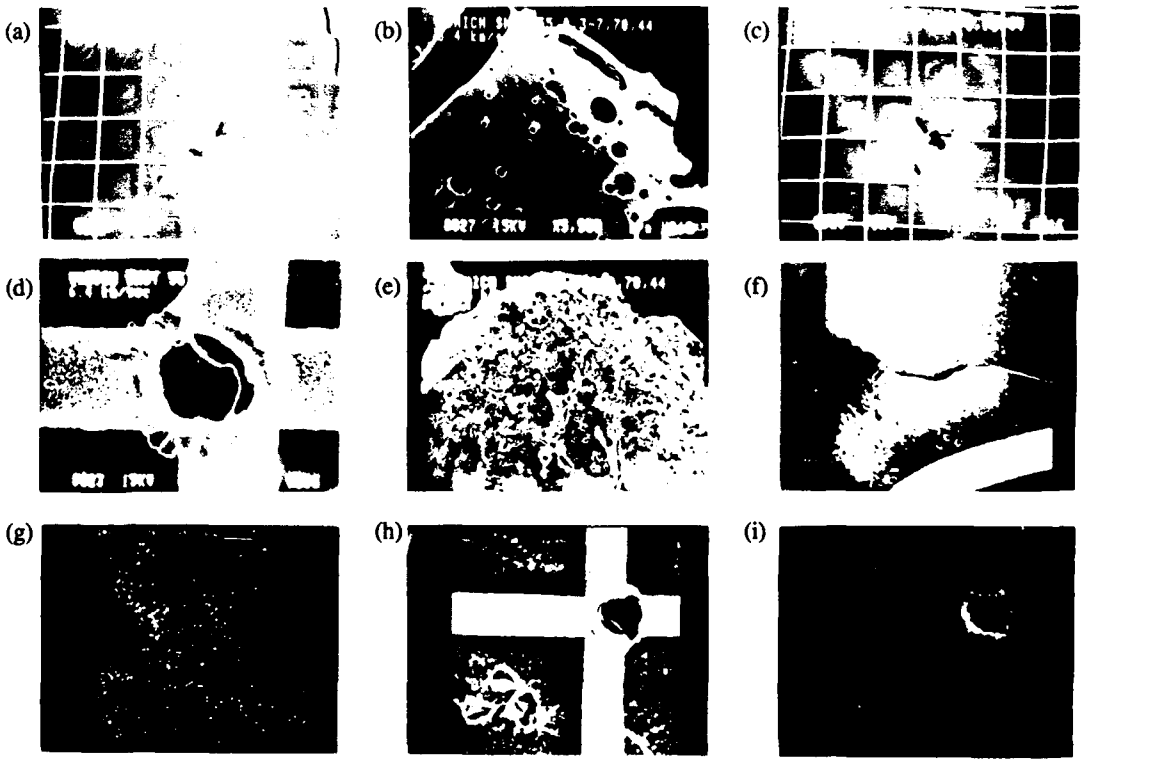


Fig. 8. [Shot 55, 77 x 90 μm glass projectile, 6.4 km/s, 3-film PVDF sensor, OS capture cell] SE images. (a) Impact area on the 1st capture cell foil. (b) Detail from (a). (c) Impact area on the 2nd foil. (d) Detail from (c) showing penetration of a 50 μm thick Ni grid wire. (e) Intermixed impactor and target debris. (f) broken grid wire on the 2nd foil and surrounding impactor debris. (g) Si x-ray map of (f). (h and i) Digitized SE image and corresponding Si x-ray map of the grid wire penetration shown in (c) and surrounding area.

A substantial glass liner is present on the Ni grid wire crater rim shown in Fig. 8h, but very little impactor debris is associated with the small penetration holes adjacent to the grid wire. This is another example of the difficulty in identifying impactor debris solely from morphology. Impactor debris was only found on the front sides of foils in this capture cell.

Germanium Crystal Wafer (Ge) Capture Cell Impact Results

Three correlated impact events (2.7-5.5 km/s) in 2-film PVDF-(2.2 + 2.9 μm)-sensor/Ge-capture-cell assemblies produced craters in Ge crystals. Two other impacts of ~70 μm particles at 10.2 and 13.8 km/s did not penetrate the cover foil in the capture cell, pointing to the limitation of the widely spaced, two-film PVDF sensor.

Impact sites were examined optically and showed the same general morphology as seen in earlier tests of the capture cells without the PVDF detectors, which included detailed chemical and isotopic analyses of impactor residues Jessberger et al., (1985) Fechtig et al., (1987), identified impactor debris imbedded in craters in the Ge and deposited on the back side of the cover foils in the earlier studies. One problem identified with the Ge capture cell in the current study was cover foil blow out from impact rebound. The 0.1 μm thick Al cover foil used in the first Ge capture cell tests was replaced with a 1.0 μm foil and no further massive disruption from rebound was observed.

Aerogel (A-120 and A-50) Capture Cell Impact Results

Results for the shots into Aerogel targets are listed in Table 2. Two impacts into A-120 targets behind a 2-film PVDF sensor were recorded (Table 2). In shot 63 a large particle (>100 μm) impacted the sensor at 8.4 km/s, and in shot 64 a small projectile (<30 μm) impacted the sensor at 12.0 km/s. In both cases the projectiles fragmented severely and some fragments penetrated both sensor films and a 0.1 μm Al cover foil over the Aerogel target. No tracks were found in the Aerogel target under optical microscopic examination. However, it was impossible to identify small bits of the glass impactor debris that were located near the top of the Aerogel slab. The use of colored glass or metallic projectiles would mitigate this problem in future experiments. These results were inconclusive, but they serve to illustrate the high degree of difficulty in locating small pieces of debris in the 3-dimensional Aerogel matrix.

The plasma velocity detector used in these experiments did not interact with the projectiles before they struck the capture cells. Therefore, these impact results represent a best case scenario for Aerogel capture cell performance. Impact tracks are described in Table 2 in terms of their entrance hole diameter, their maximum length and width, the fracture zone width, and the diameter of the apparent debris particle at the end of the track. In general, track length was not a good indicator of velocity. In two cases (shot J, 4.3 and 7.1 km/s) projectiles hit grid wires in the Al cover foil and fragmented severely, spraying debris over ~3 mm wide areas. Small fragments could be seen at the ends of most of the multiple small tracks. The presence of particles at the ends of impact tracks in A-120 targets for velocities up to 12.7 km/s illustrates the apparent effectiveness of the media for debris containment. Other investigators (cited above) have reported that for velocities >~6 km/s, these residue particles are composed of brecciated projectile/Aerogel conglomerates with compressed Aerogel rims.

Examples of impact events recorded in Aerogels in the present study are presented in Figs. 9a-e. The photographs are back lighted images taken through several cm of the Aerogel matrix and emphasize the optical clarity of the material. Figure 9a shows an impact track from a low velocity impact, <1.9 km/s (shot G), into an A-120 capture cell with the intact, unaltered 61 x 76 μm glass projectile at the end. An intact impactor consisting of two nominal 100 μm glass spheres fused into a dumbbell shape was recovered from a 2.1 km/s impact into an A-120 capture cell (shot S) and is

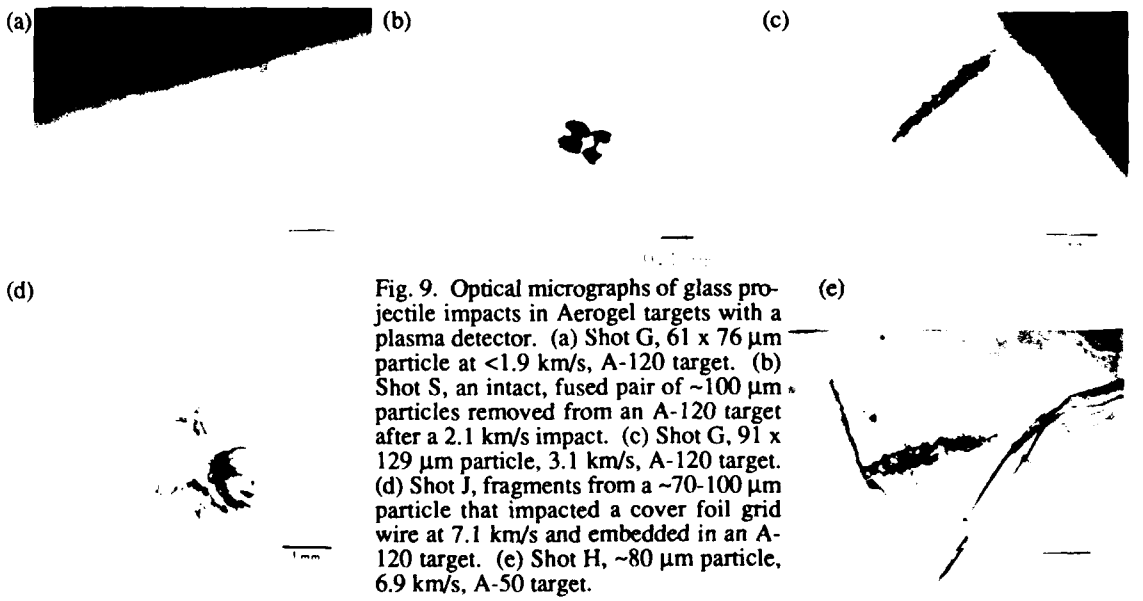


Fig. 9. Optical micrographs of glass projectile impacts in Aerogel targets with a plasma detector. (a) Shot G, 61 x 76 μm particle at <1.9 km/s, A-120 target. (b) Shot S, an intact, fused pair of ~100 μm particles removed from an A-120 target after a 2.1 km/s impact. (c) Shot G, 91 x 129 μm particle, 3.1 km/s, A-120 target. (d) Shot J, fragments from a ~70-100 μm particle that impacted a cover foil grid wire at 7.1 km/s and embedded in an A-120 target. (e) Shot H, ~80 μm particle, 6.9 km/s, A-50 target.

shown in Fig. 9b. A 3.1 km/s impact event in another A-120 capture cell (shot G) is shown in Fig. 9c. Again, an apparently intact 110 μm glass projectile is seen at the end of the track. These events illustrate the ability of the Aerogel to capture nominal 100 μm glass particles at low velocities (<~3 km/s) with little or no alteration. These results differ significantly from impact results in the multi-foil capture cells at the same velocities in that the projectiles did not melt or fragment in the Aerogel capture cells. The impactors' relatively large sizes made recovery a simple matter of physically breaking down the surrounding matrix and picking the particles out.

The severe fragmentation experienced by a 70-100 μm projectile that struck an Al foil grid wire in an A-120 cell at 7.1 km/s (shot J) is shown in Fig. 9d. Small fragment particles can be seen at the ends of many of the secondary tracks in this overhead view. The fragments may be brecciated conglomerates of target/impactor material and are probably rimmed with melted Aerogel. Figure 9e shows an example of impactor fragmentation within the Aerogel matrix in a 6.9 km/s impact of an ~80 μm glass projectile into an A-50 capture cell (shot H). These two examples illustrate the degree of difficulty of recovering small projectile fragments from the Aerogel matrix. The current method (Zolenski et al., 1990) is to saturate the matrix with an organic epoxy and thin section the impact area using ultramicrotomy.

The overall results of this series of hypervelocity impacts into Aerogel targets are consistent with the experiences of other investigators and illustrate the effectiveness of the media in preserving impactor material. They also illustrate the complexity of microimpactor sample recovery from the matrix and the need for better handling and sample location techniques for the Aerogel materials.

SUMMARY

The 2-film PVDF velocity/trajectory sensors caused increasing fragmentation of particles at increasing velocities, but only dispersed the major fragments a maximum of ~5° between the initial point of impact on the first sensor film and the points of impact on the first capture cell foil. The thinnest sensor films (~ 2 μm) caused somewhat less disruption and spread of impactor material than the two thicker types of sensor films (4.5 and 6 μm). For glass particles <100 μm in diameter impacting at velocities >8 km/s severe fragmentation occurred and little or no impactor debris was found in the capture cells.

Sufficient impactor debris for chemical and isotopic analyses was found in all multi-foil cells positioned behind multi-film PVDF sensors for nominal 100 μm diameter glass projectiles and olivine crystals impacting at velocities up to 6.4 km/s. The maximum cumulative foil penetration was not significantly different for foils spaced 1800 or 100 μm apart, but was approximately twice as great for foils spaced 10-20 μm apart. Of the five capture cell designs tested in conjunction with 2-film PVDF velocity/trajectory sensors, the multi-foil cell with 100 μm dacron net spacers appears to be the best. The dacron net spacers confined the spread of the impactor debris cloud without increasing total foil penetration and resulted in both front and back side deposition of debris. Analysis of samples was straight forward since impact features on capture cell foils could be easily mounted in metal rings for instrumental analyses of both surfaces. The use of Al foils and dacron nets in a flight instrument would limit the ability to detect Al and C in manmade debris particles and in natural particles, and would likely be replaced by a rare metal such as Au.

Foil covered Ge wafer targets behind PVDF sensors also retained significant impactor debris at tested velocities up to 5.5 km/s, but offered no advantages over multi-foil cells and are appreciably more expensive to produce and somewhat more difficult to package. Also, the advantage of having a pure Ge matrix for debris analysis is countered to some extent in this design by the presence of the sensor films and Al registration film ahead of the Ge surface.

Evaluation of 50 and 120 mg/cm^3 Aerogel targets behind PVDF sensors was inconclusive due to the limited number of tests, but initial results indicated that small impactor fragments would be difficult to locate and recover. Packaging of the friable material also needs further development. The Aerogels performed well behind a simple plasma detector, and intact nominal 100 μm glass projectiles were recovered from low velocity impacts (<3 km/s). There were visual indications that significant impactor debris may have survived impacts into Aerogels at velocities up to 12.7 km/s, but these tentative results were not verified. The superior capture characteristics of the Aerogels justifies further testing of these capture cell candidates in conjunction with the PVDF sensors. A standard method of containment and mounting, and better microparticle location techniques, need to be developed for the friable Aerogel materials.

ACKNOWLEDGEMENTS

The author would like to thank the many collaborators involved in this study: A. Tuzzolino, E. LaRue and G. Drag from the Laboratory for Astrophysics and Space Research at the Enrico Fermi Institute, University of Chicago for making this combined dust calibration series possible, and for their efforts in correlating impact events; J. Williams and R. Cordi at the Los Alamos National Laboratories for the production of the custom series of frame mounted high-purity Al foils; M. Zolensky of the Johnson Space Center and P. Tsou of the Jet Propulsion Laboratory for supplying Aerogel targets; E. Igenbergs and his staff of plasma gun operators, M. Rott, W. Reschauer, W. Frisch, A. Jean-Jacques and K. Graf at the Technical University of Munich for the many successful hypervelocity shots and their technical assistance in providing and operating the plasma detector system; F. Horz and his light gas gun staff, F. Cardenas, W. Davidson and G. Haynes at the Johnson Space Center, also for many successful hypervelocity shots and velocity detector operation; Z. Wang and W. Cantrell at the McDonnell Center for the Space Sciences, Washington University, for SEM/EDS analyses and for assistance with the preparation of this manuscript, respectively; and to R. M. Walker for the original concept of combining the PVDF detectors and meteoroid capture cells and for his valued assistance in experimental design, execution and interpretation of data. Funding for this study was provided under NASA grant NAGW-1603.

REFERENCES

Amari, S., J. Foote, E. K. Jessberger, C. G. Simon, F. J. Stadermann, P. Swan, R. Walker and E. Zinner (1991). SIMS analysis of extended impact features on LDEF experiment A0187-2. *NASA CP-3134*, 503-516.

Barrett, R. A., and M. E. Zolenski (1991). Analytical studies of impact experiments simulating capture of cosmic dust in silica Aerogel. *22nd Lunar and Planet. Sci. Conf. (Abstracts)*, 53-54.

Bradley, J., W. Carey and R. M. Walker (1986). Solar Max impact particles: perturbation of captured material. *17th Lunar and Planet. Sci. Conf. (Abstracts)*, 80-81.

Bunch, T. E., P. Schultz, D. Brownlee, M. Podolak, R. Reynolds, P. Cassen and S. Chang (1990). Hypervelocity impact penetration experiments -- A guide to the origin of rims on chondrules. *21st Lunar and Planet. Sci. Conf. (Abstracts)*, 143-144.

Carey, W. C., J. A. M. McDonnell and D. G. Dixon (1987). An empirical penetration equation for thin metallic films used in capture cell techniques, in *Properties and Interaction of Interplanetary Dust* (edited by R.H. Giese and P. Lamy) 131-136, D. Reidel Publishing Co., Boston.

Fechtig, H., F. Horz, E. Igenbergs, E. Jessberger, H. Kuczera, G. Lange, N. Pailer, S. Sutton, P. Swan, R. Walker and E. Zinner (1987). Measurement of the elemental and isotopic composition of interplanetary dust collected on LDEF, in *Properties and Interaction of Interplanetary Dust* (R. Giese and P. Lamy, eds.) 121-126, D. Reidel Publishing Co., Boston.

Gafney, E. S., D. A. Hyndman and C. M. Breen (1989). Numerical simulation of hypervelocity impact by micrometeorites on thin films. *Annual Report, Job No. 147,* Ktech Corp., Albuquerque, New Mexico.

Horz , F. (1989). A small caliber light gas gun for the simulation of cosmic dust impacts. *ARA Report* , 26 pp available from author, Solar System Exploration Division, JSC, Houston TX 77058.

Horz , F., S. Messenger , R. Bernhard, T. H. See and G. Haynes (1991). Penetration phenomena in teflon and aluminum films using 50-3200 μm glass projectiles. *22nd Lunar and Planet. Sci. Conf. (Abstracts)*, 591-592.

Hudelpohl, A., M. Rott and E. Igenbergs (1989). Coaxial plasma accelerator with compressor coil and radial gas injection. *IEEE Transactions on Magnetics* 25, 232-237.

Igenbergs, E., S. Aigner, A. Hudelpohl, H. Iglseder, H. Kuczera, M. Rott and U. Weishaupt (1987). Launcher technology, in-flight velocity measurement and impact diagnostics at the TUM/LRT. *Int. J. Impact Engng* 5, 371-380.

Iglseder, H., and E. Igenbergs (1987). Measured charge generation by small mass impact at velocities between 1 and 45 km/s. *Int. J. Impact Engng* 5, 381-388.

Jessberger, E., H. Kuczera, G. Lange, S. Sutton and E. Zinner (1985). Ion microprobe analyses of simulated LDEF impact residues. *16th Lunar and Planet. Sci. Conf. (Abstracts)*, 400-401.

Laurance, M. R., and D. E. Brownlee (1986). The flux of meteoroids and orbital space debris striking satellites in low Earth orbit. *Nature* 323, 136-138.

McDonnell, J. A. M., W. C. Carey and D. G. Dixon (1984). Cosmic dust collection by the capture cell technique on the Space Shuttle. *Nature* 309, 237-240.

McDonnell, J. A. M., S. P. Deshpande, S. F. Green, P. J. Newman, M. T. Paley, P. R. Ratcliff, T. J. Stevenson and K. Sullivan (1990). First results of particulate impacts and foil perforations on LDEF. Presented at the *28th COSPAR meeting*, The Hague.

Perkins, M. A., J. A. Simpson and A. J. Tuzzolino (1985). A cometary and interplanetary dust experiment on the Vega spacecraft missions to Halley's comet. *Nucl. Instr. and Meth.* A239, 310-323.

Schramm, L. S., R. A. Barrett, M. L. Lieurance, D. S. McKay and S. J. Wentworth (1986). Particles associated with impact features in the main electronics box (MEB) thermal blanket from the Solar Max satellite. *17th Lunar and Planet. Sci. Conf. (Abstracts)*, 769-770.

Simpson, J. A., D. Rabinowitz, A. J. Tuzzolino, L. V. Ksanfomality and R. Z. Sagdeev (1987a). Dust coma of comet Halley: measurements on the Vega-1 and Vega-2 spacecraft. *Astron. and Astrophys.* 187, 742-752.

Simpson, J. A., D. Rabinowitz, A. J. Tuzzolino, L. V. Ksanfomality and R. Z. Sagdeev (1987b). The origin of low mass particles within and beyond the dust coma envelopes of comet Halley. *ESA SP-278, Symp. on the Diversity and Similarity of Comets,* 391-397.

Simpson, J. A., D. Rabinowitz and A. J. Tuzzolino (1989a). Cosmic dust investigations I. PVDF detector signal dependence on mass and velocity for penetrating particles. *Nucl. Instr. and Meth.* A279, 611-624.

Simpson, J. A., D. Rabinowitz, A. J. Tuzzolino, L. V. Ksanfomality, R. Z. Sagdeev and O. L. Vaisberg (1989b). Confirmation of dust clusters in the coma of Comet Halley. *Advances in Space Research* 9, 359-362.

Tsou, P., D. E. Brownlee, M. R. Laurance, L. Hrubesh and A. L. Albee (1988). Intact capture of hypervelocity micrometeoroid analogs. *19th Lunar and Planet. Sci. Conf. (Abstracts)*, 1205-1206.

Tsou, P., J. Aubert, D. Brownlee, L. Hrubesh, J. Williams and A. Albee (1989). Effectiveness of intact capture media. *20th Lunar and Planet. Sci. Conf. (Abstracts)*, 1132-1133.

Tsou, P., J. Bradley, D. E. Brownlee, H. Fechtig, L. W. Hrubesh, P. W. Keaton, M. R. Laurance, C. G. Simon, G. L. Stradling, A. Teetsov and A. L. Albee (1990). Intact capture of cosmic dust analogs in Aerogel. *21st Lunar and Planet. Sci. Conf. (Abstracts)*, 1264-1265.

Tuzzolino, A. J. (1991). Two-dimensional position-sensing PVDF dust detectors for measurement of dust particle trajectory velocity, and mass. *Nucl. Instr. and Meth.* A301, 558-567.

Tuzzolino, A. J. (1992). PVDF copolymer dust detectors: particle response and penetration characteristics *Nucl. Instr. and Meth.* A316, 223-237.

Warren, J. L., H. A. Zook, J. H. Alton, U. S. Clanton, C. B. Dardano, J. A. Holder, R. R. Marlow, R. A. Schultz, L. A. Watts and S. J. Wentworth (1989). The detection and observation of meteoroid and space debris impact features on the Solar Maximum satellite. *Proc. of the 19th Lunar and Planet. Sci. Conf.*, 641-657.

Zolenski, M. E., R. A Barrett, F. Horz, F. Cardenas, W. Davidson, G. Haynes, W. Carswell and S. L. Koontz (1989). The utility of silica Aerogel as a cosmic dust capture medium on the Space Station. *20th Lunar and Planet. Sci. Conf (Abstracts)*, 1251-1252.

Zolenski, M. E., R. A. Barrett, L. Hrubesh, F. Horz and D. Lindstrom (1990). Cosmic dust capture simulation experiments using silica Aerogels. *21st Lunar and Planet. Sci. Conf. (Abstracts)*, 1381-1382.

Int. J. Impact Engng Vol.14, pp.695–706, 1993
Printed in Great Britain

0734-743X/93 $6.00+0.00
© 1993 Pergamon Press Ltd

DEVELOPMENT OF A SCRAMACCELERATOR BASED HYPERVELOCITY LAUNCHER

Thomas H. Sobota, Ph.D.
Advanced Projects Research Incorporated
147 Ward Street, Hightstown, NJ 08520

Susan M. Babcock, Ph.D.
TITAN/CRT Impact Research Laboratory
520b Wheeler Ave., SE, Albuquerque, NM 87102

Joseph W. Humphrey, Ph.D.
Advanced Projects Research Incorporated
5301 N. Commerce Ave, Ste A, Moorpark, CA 93021

ABSTRACT

The Scramaccelerator, a novel type of supersonic-combustion, tube-based launcher has been developed that can accelerate projectiles to velocities of 3 to over 7 km/sec. Extremely flexible in application, the Scramaccelerator could launch impact specimens, wind tunnel specimens, projectiles, satellites, or spacecraft. This paper describes the technology demonstration of the concept by firing 120 gram projectiles into a 38 mm barrel at 2.8 to 3.2 km/sec at the Titan/CRT Impact Research Laboratory in Albuquerque. This technology promises an upward scalability beyond that of any conventional ballistic guns and electromagnetic launchers for high mass hypervelocity applications. It is the objective of this program to demonstrate the practical application of detonation physics to hypervelocity launchers. Critical test issues discussed include sabot separation, venting requirements, Scramaccelerator tube requirements, and test performance. The current data indicate projectile accelerations were achieved in excess of 5,000 g's. Hence, these tests finally demonstrate that oblique detonation/supersonic combustion can be harnessed as a useful mechanism for hypervelocity propulsion. In addition, these tests demonstrate hypersonic propulsion at Mach numbers above 9, acceleration at greater than 3 kilometers per second, and system integration technology sufficient to accomplish this success. Scalability of the device allows for the hypervelocity launch of large masses.

INTRODUCTION

The demonstration Scramaccelerator system consists of a two stage light gas gun which fires the projectile at velocities above 2.5 km/sec into a tube filled with a mixture of fuel and oxidizer, hydrogen and air in these tests. After the initial launch to reach the insertion velocity required by the Scramaccelerator mode, the projectile sabot launch package then enters a sabot separator assembly which vents the base pressure on the sabot, strips the sabot from the projectile, and vents the precursor gas which is in front of the projectile prior to Scramaccelerator tube insertion. The Scramaccelerator tubes are the barrel sections where the Scramaccelerator mode of acceleration occurs. The projectile punctures a diaphragm and enters the Scramaccelerator tubes filled with the fuel and oxidizer mixture.

BACKGROUND

There exists a long-standing interest in harnessing detonation waves for propulsion of hypersonic aircraft [1] [2] [3] [4] and hyper-velocity projectile launchers [5] [6]. Approximate performance calculations show that normal (as opposed to oblique) detonations are unsuitable for propulsion, due to the difficulty of wave stabilization and to exceedingly high loss of total pressure. Standing oblique detonation waves (ODW's) appear to be satisfactory from a total pressure loss standpoint, but historical attempts to stabilize ODW's in combustion tunnels [7] were inconclusive, due in part to limited approach Mach numbers, as well as a fundamental lack of understanding of detonation wave mechanics. However, recent theoretical work [8] [9] clarified under what conditions standing ODW's can be stabilized with acceptable propulsive efficiency. Specifically, reference [10] shows that only overdriven weak ODW's are suitable for propulsion, and that, for any given approach Mach number and reactant gas thermodynamic state, there are minimum and maximum flow deflection angles outside of which an ODW cannot be stabilized.

Based on analytical studies, it is possible to design an ODW Scramaccelerator which, through staging and appropriate choice of the initial launcher, can accelerate projectiles of any practical size and weight to earth escape velocity and beyond. This study describes the experimental demonstration of the technology. Applications include strategic and tactical kinetic energy weapons, and low-cost transport of structural materials to low earth orbit. The oblique detonation wave Scramaccelerator, as with conventional thermal propulsion cycles, has the three aero-thermodynamic processes of compression, heat release and expansion.

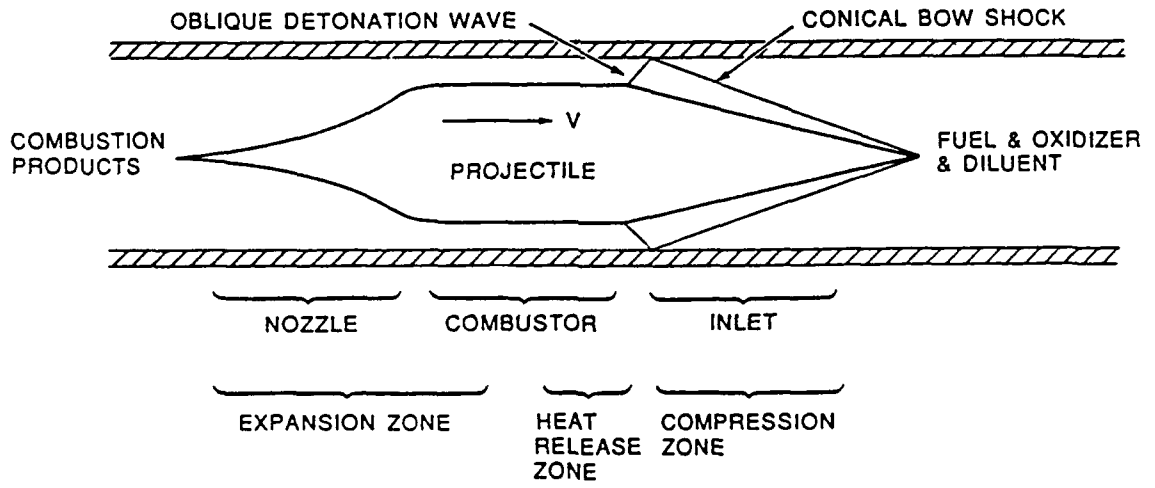


Figure 1: Oblique Detonation Wave Scramaccelerator.

In the Scramaccelerator, represented schematically in Figure 1, the launch tube is initially filled with premixed fuel, oxidizer, and optional diluent (nitrogen in this case). The projectile is designed so the forebody forms the inlet compression region, the land forms the combustor region, and the tail of the projectile forms the supersonic exhaust nozzle. The inert projectile (no onboard propellants), whose diameter is approximately ninety percent of the launch tube internal diameter is injected axially into the launch tube at high initial velocity. Ram compression of the reactant gases is accomplished by a suitable sequence of weak oblique shocks set up by a supersonic inlet center body. The reflected wave off the tube wall is of sufficient strength to stabilize an over-driven oblique detonation [8] that occurs in the compressed reactant gas flowing through the annular area between the projectile body and the tube wall. Expansion from the annulus to the full tube area in the projectile wake occurs through a supersonic nozzle zone defined by the projectile afterbody geometry. The static pressure on the projectile afterbody is considerably greater than on the conical forebody with a resultant net thrust.

During compression of the reactant mixture, care must be taken not to ignite or detonate the reactant gas mixture prematurely. This can be controlled in one or both of two ways: by insuring that the residence time in the inlet/diffuser region is less than the chemical induction time [11], and/or by insuring that the flow turning angle through the conical bow shock is less than the minimum flow turning angle required for an ODW to stabilize [10]. Hertzberg et al. [6] claim that a ballistic efficiency (defined as the rate of kinetic energy increase of the projectile divided by the rate of chemical heat release) of thirty percent is achievable. Preliminary calculations for projectiles with a simple conical forebody, confirm that Hertzberg's claim is realistic. With a properly designed supersonic centerbody diffuser in place of the cone, even higher ballistic efficiencies should be realizable. Thrust on the projectile is predicted to be relatively constant over a wide range of Mach numbers, and is directly proportional to the product of the heat released per unit mass of propellant the propellant fill mass density, the tube cross-sectional area, and the ballistic efficiency. The length of launch tube required for a given velocity increment is directly proportional to the corresponding increment of projectile kinetic energy, divided by the thrust. More detailed performance discussions can be found in References [12] [13] [14].

SYSTEM CONFIGURATION

The tests required a launcher that could accelerate the specially designed projectiles to supersonic velocities prior to the projectile entering the Scramaccelerator barrels. The two-stage light-gas gun at the IRL was chosen for this task. The launch tube diameter of 38mm allows the projectile model to be large enough to minimize some secondary effects during the Scramaccelerator process. The Scramaccelerator is a hypervelocity acceleration device that requires a minimum insertion velocity or "takeover velocity". The minimum is determined by the geometry and the Chapman-Jouguet Mach Number of the fuel and oxidizer to by used. For these tests, the insertion velocities required were above 2.5 km/sec. For most of the tests, 3.1 km/sec was the target insertion velocity. The insertion velocity impacts the required base pressure to be delivered by the light gas gun. The demonstration Scramaccelerator system consists of a two-stage Light Gas Gun (LGG) and sabot separator assembly which first accelerates the projectile up to velocities of 3.1 km/sec and then strips the obturating sabot (needed for the light gas gun launch but not acceptable in the Scramaccelerator mode of acceleration). The system must do so without propagating a normal shock downstream into the Scramaccelerator tube filled with a mixture of fuel and oxidizer.

Description of Venting Problem.

In order for the Scramaccelerator to function properly an oblique conical shock must be generated on the forebody of the projectile. To do this, the projectile must pass through the gasdynamic shock which is driven ahead of the projectile in bore. In the terminology of the aircraft propulsion field, this process is known as "shock swallowing" or "inlet starting". There are at least two ways to start (initiate supersonic flow around the projectile) the Scramaccelerator process [15]. The one used successfully in these experiments is described here. The sabot was removed by gas dynamic stripping. The gas in front of the projectile as a result of the sabot stripping must be vented sufficiently to allow the projectile inlet to start in the vent tube prior to reaching the diaphragm which contains the Scramaccelerator fuel and oxidizer gases. If this condition is not met, the gas in front of the projectile will break the diaphragm and initiate a normal driven detonation in front of the projectile preventing the system from starting.

An internal ballistics code was used in the determination of venting requirements in the Scramaccelerator technology demonstration program. (A complete description is given by Humphrey et al. [15]. Detailed analysis was required to determine venting requirements for inlet starting of a Scramaccelerator projectile moving at hypersonic velocities in a tube. The results provided needed design detail.

Since launching into a complete vacuum is impossible, it is important, in fact necessary, to understand the contribution of transmitted, reflected, and convected waves in the solution of a Mach 9 and higher shock wave propagating down a tube, crossing interfaces of different gases, pressure, temperature, and retaining diaphragms between tube sections that contain venting. The essential goal is to be able to start a projectile of fixed geometry as it traverses the launch tubes prior to reaching the fuel and oxidizer filled Scramaccelerator tubes. The results aptly demonstrate the hypersonic nature of this problem and illustrate Mach number effects when considering a problem of high Mach number – in excess of Mach 9.

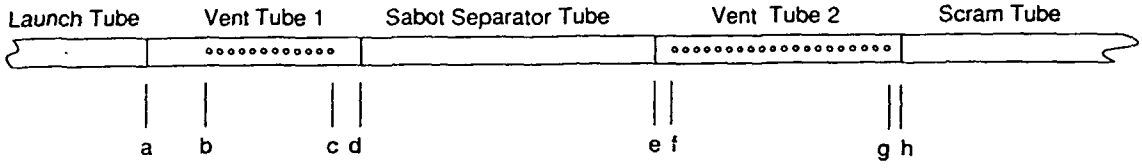


Figure 2: Barrel Venting Configuration.

Results of Barrel Venting Calculations. The geometry of the actual configuration of interest is given in Figure 2. The system consists of a 30 foot launch tube (the second stage of a two-stage light gas gun), a vent tube (vent tube 1), a sabot separator tube, a second vent tube (vent tube 2), and the entrance to the Scramaccelerator tubes. The venting in the first vent tube is to be designed to adequately vent the base pressure on the launch package shown in Figure 3. Adequate base pressure venting is determined by the sabot separation phase. Sabot separation

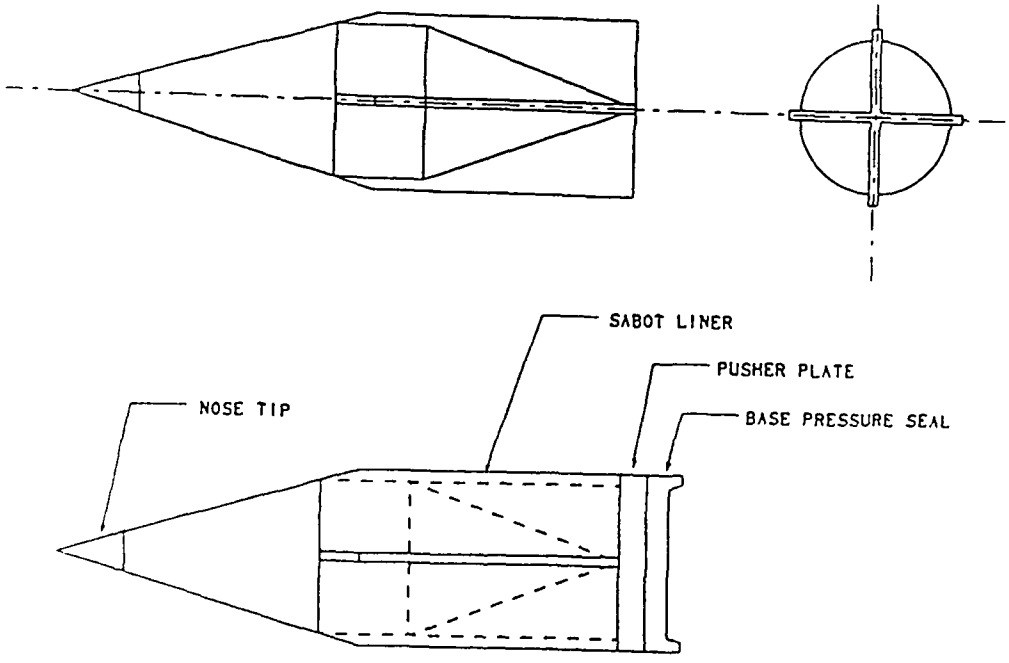


Figure 3: Projectile and Sabot Geometry.

is accomplished by gas dynamic stripping of the sabot in the sabot separator tube. The sabot separator is filled with gas that is retained by diaphragms at both ends. The gas pressure in the sabot separator is higher than the pressure in the two vent tubes. While the sabot and obturator

are in launch position against the projectile, the launch package can be treated as a piston driving a gas column in the tube. When the piston enters the sabot separator, the piston driven normal shock in front of the projectile raises the pressure on the face of the projectile. The first vent tube, meanwhile, has vented the high pressure LGG launch gases from the base of the obturator. The large pressure differential across the launch package will strip the sabot/obturator off of the projectile. This is possible because the flow of the gas relative to the projectile (behind the normal shock) is subsonic. The pressure is relatively constant behind the shock wave all the way to the face of the sabot and hence the sabot supports the pressure difference between the vented base pressure and the leading shock. (The pressure difference across the sabot is reduced by the drag on the projectile as a result of the flow past the projectile to fill the void between the projectile and sabot as the sabot decelerates relative to the projectile due to the pressure differential.)

The separation distance between the projectile and sabot is determined by the time of flight in the sabot separator, the pressure difference across the sabot, and the mass of the sabot. Simultaneously, the leading piston driven shock is reduced in strength by the mass leakage past the projectile as the sabot and projectile separate. Given the launch conditions, all of these effects can be accounted for. The second vent tube can be operated in two modes in order to start the projectile inlet. Mode 1 inlet starting is accomplished by first venting the sabot separator gas in front of the projectile and then reaching a steady state standoff distance of sufficiently short length that the leading shock is swallowed in the converging inlet. (Stability of shocks in converging inlets with venting is not considered here, but, is an area where further study is required to determine the stability criteria for shock swallowing.) Mode 2 inlet starting is to design the diaphragm at the inlet of the Scramaccelerator tube to act as a wall to the transient shock propagation through the tube and to stop the flow by reflecting a shock back toward the projectile. In this case, the projectile Mach number must be sufficient relative to the gas conditions in front of the diaphragm (which has undergone two shocks and is at high temperature) to assure inlet starting when the projectile meets with the reflected shock. Only mode 1 inlet starting is discussed here. In the Mode 1 method of inlet starting, the second vent tube *must perform two functions*: 1) to vent the transmitted shock and gas that is pushed in front of the projectile as a result of the sabot stripping process, and 2) to start the projectile inlet prior to the projectile entering the Scramaccelerator tube so that the projectile tip breaks the Scramaccelerator tube diaphragm rather than a normal shock which would propagate through the Scramaccelerator tube as a Chapman-Jouguet detonation ahead of the projectile. The starting sequence is depicted schematically in figure 4.

The first function in Mode 1 operation of the second vent tube is to vent the gas in front of the projectile, the precursor gas, as the projectile leaves the sabot separator and prior to inlet starting. This process was numerically calculated for several cases. The second function of the second vent tube is inlet starting. Since there is venting in the second vent tube, there exists a steady state stand-off distance of the projectile driven shock for a sufficiently long vent tube. The important factors that determine this standoff distance are the velocity of the projectile, the temperature of the initial gas in the tube and the ratio of the venting area to vented tube volume. This can be solved analytically and compared with the results of the computations.

In order to start the projectile inlet, it is necessary for the standoff distance to be less than the length of the inlet (detailed calculations are shown in [15]). This can be used to determine the venting ratio required to accomplish the starting of the inlet. The insertion velocities required of the Scramaccelerator in the demonstration testing resulted in Mach numbers in excess of Mach 9. The important processes evaluated were sabot separation and inlet starting. These studies were used to design the Scramaccelerator test hardware and to develop the test conditions and proved essential to starting the inlet in the test hardware.

Facility Layout and Configuration

Eighteen tests firings related to the development of Scramaccelerator technology were completed

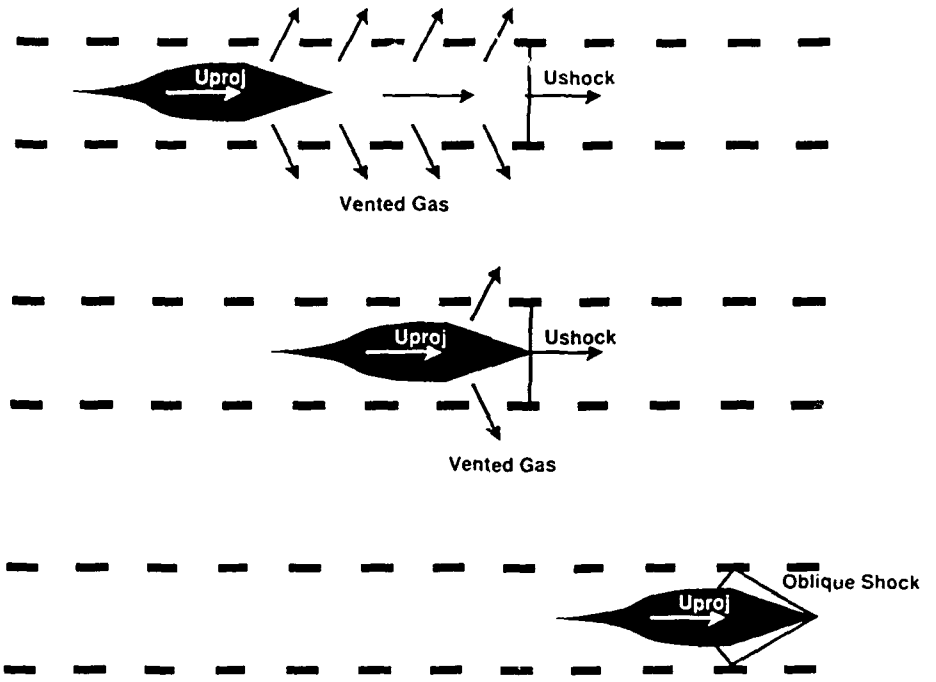


Figure 4: Mode 1 Starting Process.

by Advanced Projects Research Incorporated (APRI) at the Titan Corporation Impact Research Laboratory (IRL).

Two Stage Light Gas Gun. The launcher consists of a two-stage light-gas gun with a 115 mm pump tube and a 38 mm launch tube. The pump tube is pressurized to a few MPa with a light gas (hydrogen was used for all of these tests). Smokeless powder is burned in a powder breech, generating sufficiently high pressures to propel a compression piston down the pump tube. The piston further compresses the hydrogen in the pump tube, which then ruptures a petal valve located just uprange of the launch package, accelerating the launch package down the launch tube.

Large Target Tank. The range tankage consists of several tanks, each with a specific purpose. The extra barrels required for the Scramaccelerator were designed to couple directly to the existing barrels and to fit into the existing tankage. The muzzle of the launch tube (LT) of the Light-Gas Gun (LGG) enters the range tankage and is coupled to a 1.06m (42in) vent tube (VT). The blast tank is sized to ensure that pressures due to the hydrogen that is dumped into the tank during a test remain significantly below one atmosphere when a vacuum of a few Torr is pulled pretest. This criterion guarantees that hydrogen will not seep out of the tank post-test should any leaks develop in the range during a test. The two small tanks downrange of the blast tank are referred to as the sabot separator tank and the small target tank. These tanks provided access to various barrels for cleaning, maintenance, and installation of instrumentation.

Operation. Once the desired injection velocity was obtained by the Light Gas Gun (LGG), sabot separation was required as described earlier. The effort to achieve this condition was more difficult than was originally planned and involved several barrel reconfigurations and modifications. All of the shots included the basic LGG launcher and a 1.07m (3.5ft) vent tube. Shots 1 through 4 coupled a 3.05m (10ft) sabot separator tube (SST) to the vent tube. The .91m (3ft) Scramaccelerator tube (ST) was installed as the final stage. Two different methods were used to separate

the sabot. Shot 1 used one atmosphere of air in the SST to slow down the sabot, causing it to separate from the projectile. This method created a shock wave in front of the projectile which if unvented would initiate combustion of the fuel in the Scramaccelerator tube before the projectile arrived.

Due to the difficulties with starting, a barrel modification was made. The SST was machined int two separate tubes; a 1.83m (72in) long SST and a 1.12m (44in) long vent tube. This new vent tube was designed with slots, rather than holes, to maximize the venting capability. Shots 5 through 11 used this slotted vent tube (SVT). It was finally abandoned for the final seven tests because of the damage to the tube, projectile, and sabot. The 0.91m (3ft) ST was slightly modified to allow it to be coupled to the 1.83m (72in) barrel that had been used as an SST. In Shots 12 through 18, the 0.91m (3ft) ST did the job of the SST, while the 1.83m (72in) barrel acted just as a connection tube joining the LGG and its VT with the downrange barrels.

Shots 5, 6 and 7 used one 3.05m (10ft) ST coupled directly downrange to the SVT. Shot 8 used two 3.05m (10ft) ST sections; the first section was evacuated with the range and the second section was pressurized to be used as the Scramaccelerator. Starting was not evident in these tests.

To help vent the pressure that developed from the sabot separation process, another barrel modification was made. One of the 3.05m (10ft) STs was machined (see drawing) with almost 300 vent holes. This barrel was located downrange of the slotted vent tube in Shots 9, 10, and 11. In Shots 12 through 18, when the slotted vent tube was replaced with the 0.91m (3ft) SST, the 3.05m (10ft) VT was coupled to the downrange end of the 0.91m (3ft) SST.

The ST was the last barrel in all 18 tests. Shots 1 through 4 used the 0.91m (3ft) ST, while Shots 5 through 18 used a 3.05m (10ft) ST. Shots 2 and 3 did not have any pressure in the ST. All of the other tests did have pressure in the ST.

One large tank makes up the remaining tankage used for these tests. This final tank is a large target tank, which has a 2.44m (8ft) diameter and is about 3.66m (12ft) long. The muzzle of the Scramaccelerator was located in the uprange end of this tank. Distance between the muzzle and the terminator plates was allowed to take flash radiography after the projectile left the muzzle and was in free flight. The downrange end of the tank contained the sand, wood and steel used to stop the projectile. Figure 5 is a schematic of the range tankage with a generic barrel setup inside the tanks.

RANGE INSTRUMENTATION

Essential to the test program is the instrumentation which required extremely fast time response. Since the velocities of interest are 3 to 5 km/sec, the projectile will traverse 3 to 5 mm per microsecond. The determination of position, time of arrival, velocity, and acceleration is dependent upon the time response of the measurements. The performance of the Scramaccelerator process is measured using a DC X-ray intervalometer, pressure transducers, optical detectors, magnetic detectors, and flash radiographs. The velocity of the projectile is recorded at the muzzle of the two-stage light gas gun using a DC X-ray intervalometer. This velocity can then be compared to the exit velocity from the Scramaccelerator barrel. The exit velocity and the condition of the projectile are recorded with flash X-ray. Passive optical detectors record the passage of the projectile by utilizing the light emitted during the hypersonic shock and combustion process. Pressure histories from transducers placed along the Scramaccelerator barrels aid in the evaluation and analysis process.

DC X-ray Intervalometer. The IRL XR-202-W/100-10 X-ray Interruptor System was used in all of the tests to measure the velocity at the muzzle of the launch tube of the LGG. The system is based on a continuous X-ray source that can produce energy levels up to 100KV. The X-rays

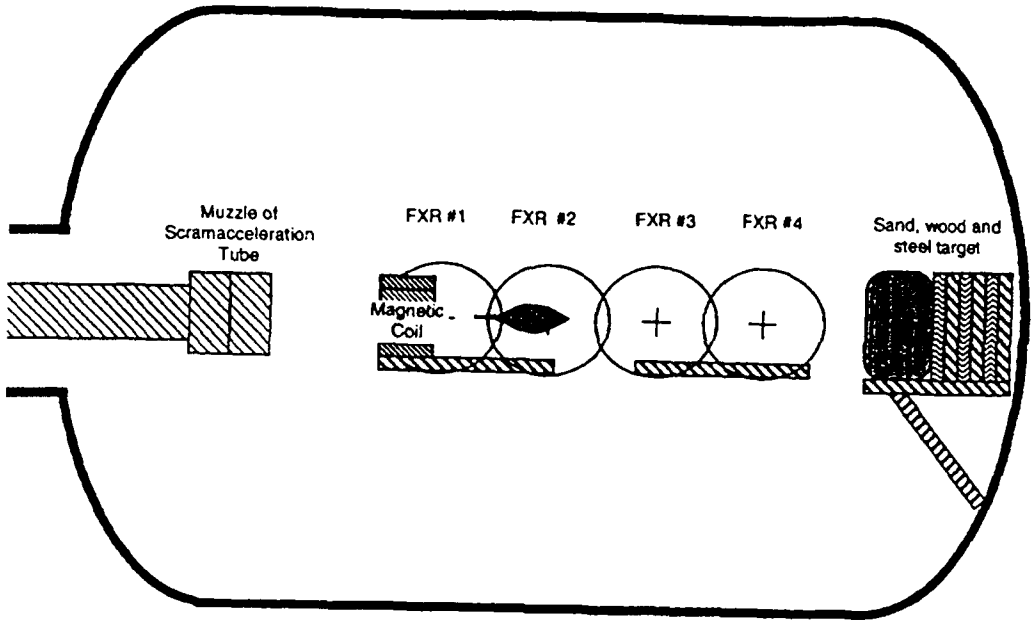


Figure 5: Typical Large Target Tank Setup.

are converted into visible light by a scintilation crystal. The triggering pulses based on the X-ray source interruption technique is very effective in hostile gun range environments. The emitter and crystal are place on opposite sides of the launch tube, looking through special ports machined in each side of the barrel. Unlike the conventional predecessors, however, this system utilizes fiber optics technology in order to isolate the triggering sensor electronics from the EMI/RFI fields that are commonly in existence in most large gun range facilities.

Flash X-ray Radiography. Four channels of flash X-rays were utilized during the tests. These were configured to observe velocity, condition, yaw and pitch of the projectile during free flight. The X-rays were taken with a Scandiflash 450 System. The specifications of this system are as follows:

Output Voltage	150 - 450 keV
Output Peak Current	10 kA
Pulse Width	20 ns
Max Dose per pulse at 1 m	20 mR
Focal Spot Size	1 mm
Penetration of Steel at 2.5m	18 mm

Table 1: Flash X-ray Conditions.

The film used in all of the shots was Dupont NDT 57. Spectroline regular scintilation screens were used both in front of and behind the film. The object to source and object to film distances for shots 1 through 4 were 1.52m (5ft) and 0.15m (6in), respectively. These respective distances for shots 5 through 8 were 2.59m (8.5ft) and 0.15m (6in), and for shots 9 through 18 were 2.90m (9.5ft) and 0.15m (6in). The various methods used to trigger the flash X-rays are discussed in the sections below. The digital delay generator built into the Scandiflash System allows the X-ray pulse to be synchronized with the event. The system is triggered by short circuiting the input of the delay generator or by providing a positive pulse input. The output from the delay generator starts the trigger amplifier that is mounted on the pulser. The pulser is an "electrical energy storage and voltage multiplier assembly." It stores a selected voltage in oil filled capacitors and delivers the stored energy in series at high voltage and current levels in an extremely short

elapsed time.

Streak Camera. Because of extremely hostile environment and the difficulties with making a triggering system for the flash X-ray survive, a streak camera was added to several tests. The Fastax II, Model 46-0008, streak camera is a high speed 16mm camera. Streak photography involves recording the actual motion of a real article. The streak photography produced a shadowgraph of the projectile in free flight past a slit aperture that is placed at the film plane to limit the camera's view to a narrow band. The camera was positioned with the slit aperture parallel to the subject motion and the film travel at 90 degrees to the path of motion. The film record contained a resultant line image with time measured along the length of the film and object displacement across the film width.

Pressure. All 18 tests included the use of piezo-electric ballistic pressure transducers. These transducers were used to measure the transient pressures in the sabot separation and venting tubes and in the Scramaccelerator tubes. Several models from two different vendors were used; all with less than satisfactory results. The transducers used initially provided no useful pressure data other than time-of-flight information because they each failed during their first use. The transducers used in the latest shots generally provided good pressure data for only the first use and time-of-flight data on subsequent shots.

Optical. Optical ports were provided through the Scramaccelerator tube wall in order to detect the luminosity of the gas during the launch sequence. Multimode plastic optical fibers were inserted into the each optical port. The luminosity of the gas was detected at the opposite end of the fiber with a photodiode detector circuit.

Break Screens. In the first 6 tests, a make screen was used to provide the trigger for the flash X-rays. The make screens varied from two layers aluminum foil insulated by a thin layer of paper to two layers of 3.1mm (1/8in) thick aluminum plate insulated from each other by about a half inch airspace. The only attempts that succeeded were with the 3.1mm (1/8in) thick plates on tests that did not have a mix of fuel and air in the ST (Shots 2 and 3). Make screens were abandoned for this test series due to the high probability of a blast front occurring in front of the projectile. The blast caused the make screen either to trigger the flash X-ray before the projectile arrived or caused the make screen to be completely blown away without any contact occurring, therefore providing no trigger to the flash X-rays.

Magnetic Coil. In shots 9 through 18, a magnetic coil was used to provide a trigger for the flash X-ray. The coil was one of a pair that make up the IRL Magnetic Intervalometer System, Model No. SS-100N. The Large-Aperture Magnetic Coil is a rugged, flexible instrument designed for detecting oncoming projectiles in the presence of hostile environments. Output from the control/display may be used to trigger auxiliary instrumentation. The detector head is a classic passive magnetic projectile sensor. The outer portion of the aluminum-encased toroid is filled with magnetic material, which produces a strong solenoidal magnetic field within the aperture. A search coil is wound on the outer diameter of the massive fiberglass tube that surrounds the aperture. This coil is maintained in a rigidly fixed position with respect to a permanent magnetic field. A projectile approaching the detector head experiences a time-varying magnetic field as it moves along the axis of the permanent magnet's field. If the projectile is made from electrically conducting material, eddy currents are induced in its outer surface which produce a counter field that effectively prevents penetration of the external fields into the projectile interior. The magnetic field produced by the eddy current extends well beyond the projectile and is sensed by the search coil which produces a voltage excursion at its output terminals.

Pretest LGG Configuration Calculations.

The desired injection velocity for the Scramaccelerator was obtained with the LGG. Calculations

to correctly configure the powder charge and light gas in the LGG were performed using a computer program documented by Charters and Sangster in 1973 [16]. The main variables required for these calculations include piston mass, petal valve rupture pressure, gun geometry, launch package mass, has type and pressure in the pump tube and the powder charge type and weight. For all the tests, only three of these parameters were varied, the projectile mass, the hydrogen pressure and the amount of powder used. The type of powder used was Hodgden 5010. Only three different shot configurations were used during the testing. Tests 1 through 12 used 1900 gm H5010 and 350 psi H2 for a launch package that nominally weighed 215 gm. Tests 13 through 17 used 1800 gm H5010 and 350 psi H2. Finally, Test 18 used 2000 gm H5010 and 400 psi H2. The launch package weight for both these configurations was 196 gm.

LAUNCH PACKAGES

The design of the launch package, projectile, sabot, obturator, and pusher plate combination, required consideration of several issues. Some of the more important requirements are listed here.

1. Integration of the projectile with the sabot.
2. Low speed launcher physical constraints.
3. Scramaccelerator launcher constraints.
4. Acceleration loading of launch package in the low speed launch phase.
5. Acceleration loading of projectile in the Scramaccelerator launch phase.
6. Sabot stripping between the low speed and Scramaccelerator phases.
7. Heat transfer at the nose tip.
8. Heat transfer along the annulus in the hot flow after the detonation.
9. Ease of manufacture for several parametric shapes.
10. Optimum gas dynamic performance.
11. Flight dynamics.
12. Structural integrity.
13. Scramaccelerator diaphragm interaction with the projectile nosetip.

The studies thus far have generated a projectile design that has a simple conical forebody, an ideal expansion nozzle afterbody, and a constant area center body. Each of the cone sections will be threaded onto the center body for interchangeability of various angle cones and reduced manufacturing costs. There are four equi-spaced fins that will run from the forward edge of the centerbody back to the end of the expansion nozzle. The trailing edge of the fins were perpendicular to the projectile axis. The forebody cone had a separate nosetip which was press fit into the projectile, so that the tip material could be chosen for its thermal characteristics.

In addition to the projectile body itself, the launch package consisted of an obturator, pusher plate, and a sabot.

RESULTS

A summary of the 18 shots is provided in table 2. All shots were fired at or near 3.1 km/sec. The first four shots were preliminary shots performed without all of the barrel sections in place. The objectives of the first four shots were to verify the launch package design, to shakedown the instrumentation, to verify sabot separation and to locate unanticipated problems. Several changes were made before proceeding to the second round of four shots. In the second shot, through the flash X-ray radiographs and the streak camera photos, it was discovered that the projectile tips were breaking free from the projectile during the light gas gun launch phase. The tip was redesigned to provide a stronger connection to the projectile body. It was also discovered that the ballistic pressure transducers initially chosen could not withstand the dynamic

Shot Number	Objective/Result
1-4	Projectile Integrity, Sabot Separation Instrumentation Shakedown
5-8	Instrumentation Shakedown, Venting and Starting
9-12	Venting and Starting
13,14	SUCCESSFUL, Starting and Positive Acceleration
15-17	Projectile Failure
18	SUCCESSFUL, Starting and Positive Acceleration

Table 2: Experimental Results - 18 Shots

loading to which they were subjected. Each transducer would fail, catastrophically, during its first use. Subsequently, shock hardened transducers from another vendor were supplied. Finally, modifications to the sabot separation system were dictated by data from the first four shots.

During shots 5 through 8 it was discovered that the projectile was not starting because venting was not adequate with the slotted vent under the pressure conditions used. In shots 9 through 12 modifications to the vent tube set up and fill pressures were made until the projectile was successfully started in shot 13. In both shots 13 and 14, the Scramaccelerator started and the projectile exhibited acceleration in the Scramaccelerator tube.

In shots 15 through 17 excessive damage to the projectile prevented the Scramaccelerator process from starting. This damage was attributed to very high launch loads in the light gas gun which were likely the result of excessive piston distortion in the AR section (secondary breech). The light gas gun parameters were varied for shot 18 to produce a softer launch for the same muzzle velocity. This required more hydrogen in the pump tube and a higher LGG muzzle pressure possibly affecting the sabot separation process. Shot 18 performed much like shots 13 and 14.

CONCLUSIONS AND DISCUSSION

Experimentally, the Scramaccelerator tests proved to be challenging. Even though the range has a great deal of flexibility designed into it, constrictions limited some tests configurations. The joints between barrels had to be located in specific locations throughout the tankage to allow for access. Instrumentation port locations were restricted due to limited access. Options to place parts of the gun under vacuum while other parts were placed under pressure were limited by the range configuration. These limitations could not have been identified prior to beginning the experimental program because the technical difficulties of accomplishing a start condition under supersonic conditions could not be fully identified. Barrel modifications and changes in the barrel configurations had to be made as more was learned about the process. The difficulty of obtaining a start condition affected other factors involved in the testing also. The selection and installation procedure of pressure transducers were driven by the ability to survive the high pressures, shock and mechanical vibrations present during combustion in the Scramacclerator barrels. A lack of a start condition also meant that combustion occurred in front of the projectile, creating a blast condition. This blast preceded the projectile during free flight, causing problems for some triggering systems for the flash X-rays. The blast obscured the optical image of the projectile in streak camera photography.

The Oblique Detonation Wave Scramaccelerator system was demonstrated to start and provide positive acceleration in the 3 to 3.2 km/sec range. A detailed understanding of the starting process was developed. Substantial progress was made in the instrumentation area for this type of effort. Subsequent tests should concentrate on mapping out the performance envelope of Scramaccelerator systems as a function of the wide multi-variate parameter space.

References

[1] C.J. O'Brien and A.C. Kobayashi. Advanced earth to orbit propulsion concepts. *AIAA/SAE/ASME/ASEE 22nd Joint Propulsion Conference*, (AIAA-86-1386), June 1986.

[2] T.C. Adamson and R.B. Morrison. On the classification of normal detonation waves. *Jet Propulsion*, August 1955.

[3] R. A. Strehlow. *Fundamentals of Combustion*. International Textbook Company, 1968.

[4] C.L. Mader. *Numerical Modeling of Detonation*. University of California Press, 1979.

[5] H.F. Lehr. Experiments of shock-induced combustion. *Astronautica Acta.*, 17(4 and 5), 1972.

[6] A. Hertzberg, A.P. Bruckner, and D.W. Bogdanoff. The ram accelerator: a new chemical method of achieving ultrahigh velocities. *37th Meeting of the Aeroballistic Range Association*, September 1986.

[7] R.A. Gross and W. Chinitz. A study of supersonic combustion. *Journal of the Aerospace Sciences*, July 1960.

[8] David T. Pratt and Joseph W. Humphrey. Morphology of a standing oblique detonation wave. *Journal of Propulsion and Power*, 7(1), January 1991.

[9] David T. Pratt and D.E. Glenn. Numerical simulation of a standing oblique hydrogen-air detonation wave. *SIAM Conference on Numerical Combustion*, March 1987.

[10] David T. Pratt, Joseph W. Humphrey, and D.E. Glenn. Morphology of a standing oblique detonation wave. *AIAA/SAE/ASME/ASEE 23rd Joint Propulsion Conference*, June 1987. AIAA 87-1785.

[11] E.S. Oran, J.P. Boris, T. Young, M. Flanigan, T. Burks, and M. Picone. Numerical simulations of detonations in hydrogen-air and methane- air mixtures. *Eighteenth International Symposium on Combustion*, 1981.

[12] Joseph W. Humphrey. Study of an oblique detonation wave ramaccelerator driven hypersonic test facility, final report. Technical report, ADVANCED PROJECTS RESEARCH INCORPORATED, Moorpark, California, August 1989. Prepared for NASA Langley Research Center under contract NAS1-18802.

[13] Joseph W. Humphrey. Parametric study of an ODW Scramaccelerator for hypersonic test facilities. *AIAA/SAE/ASME/ASEE 26th Joint Propulsion Conference*, July 1990. AIAA 90-2470.

[14] Kaveh Ghorbanian, David T. Pratt, and Joseph W. Humphrey. Supersonic flow of reactive gases over sphere-cone bodies. *AIAA 30th Aerospace Sciences Meeting*, January 1992. AIAA 92-0091.

[15] J.W. Humphrey, F.P. Brueckner, T.H. Sobota, and Darrell W. Pepper. Internal ballistics and inlet starting of projectiles in Ram- and Scramaccelerator launch tubes with venting. *AIAA 31st Aerospace Sciences Meeting*, January 1992. to be presented.

[16] A.C. Charters and David K. Sangster. Manual: Fortran computer program for the interior ballistic analysis of light-gas guns. Technical report, July 1973.

ACKNOWLEDGMENTS

Portions of APRI's efforts in this work have been funded by APRI, NASA Langley Research Center, SDIO, and the New Jersey Commission on Science and Technology.

Int. J. Impact Engng Vol.14, pp.707–718, 1993
Printed in Great Britain

0734-743X/93 $6.00+0.00
1993 Pergamon Press Ltd

IMPACT MODELING WITH SMOOTH PARTICLE HYDRODYNAMICS

R. F. STELLINGWERF and C. A. WINGATE

Los Alamos National Laboratory, MS F645, Los Alamos, NM 87545

ABSTRACT

Smooth Particle Hydrodynamics (SPH) is a new computational technique well suited to computation of hypervelocity impact phenomena. This paper reviews the characteristics, philosophy, and a bit of the derivation of the method. As illustrations of the technique, several test case computations and several application computations are shown.

PHILOSOPHY OF SPH

SPH is a gridless Lagrangian hydrodynamic computational technique. With some care, it can be written in a fully conservative form. The form of the SPH equations is extremely simple, even in 3 dimensions. These characteristics, together with the physical "feeling" for the problem that is embodied in a fully Lagrangian code makes SPH an attractive approach for problems with complicated geometry, large void areas, fracture, or chaotic flow fields.

SPH was first derived by Lucy (1977) as a Monte-Carlo approach to solving the hydrodynamic time evolution equations. Subsequently, Monaghan and co-workers (Monaghan 1982, 1985, 1988, Gingold and Monaghan 1977, 1982) reformulated the derivation in terms of an interpolation theory, which was shown to better estimate the error scaling of the technique. According to the interpolation derivation, each SPH "particle" represents a mathematical interpolation point at which the fluid properties are known. The complete solution is obtained at all points in space by application of an interpolation function. This function is required to be continuous and differentiable. Gradients that appear in the flow equations are obtained via analytic differentiation of the smooth, interpolated functions. Monaghan showed that other well known techniques, such as PIC, finite element, and finite volume methods could also be derived in this way through appropriate choice of interpolation technique. SPH is distinguished by the simplicity of its approach: interpolation is done by summing over "kernels" associated with each particle. Each kernel is a spherically symmetric function centered at the particle location and generally resembling a Gaussian in shape. The order of accuracy of the interpolation (and thus of the difference equations) is determined by the smoothness of the kernel. The kernel is required to approach a delta function in the limit of small extent. The interpolation is accomplished by summing each equation or variable at any location over nearby known values at particle locations, each weighted by its own kernel weighting function. Each kernel function is required to integrate over all space to exactly unity, thus normalizing the interpolation sums. By appropriately modifying the normalization condition, the same code can easily switch between 1D, 2D, 3D, spherical or cylindrical geometric configurations. This feature allows code development in 1D or 2D, with confidence that the same coding will work for all cases if implemented carefully.

There are two SPH codes currently under development at Los Alamos National Laboratory (LANL). The first is SPHC, which was originally written by Stellingwerf. SPHC is a research tool written in C that runs on a variety of platforms. The second code is SPHINX, which is a fully vectorized CRAY version with a more convenient user interface and an integrated X-Windows graphic runtime display. SPHINX will be the production code used for high resolution 2D and 3D modeling. SPHINX is currently being developed by Wingate at LANL. The code description and applications discussed below were all run on SPHC, but the coding and results from SPHINX are similar. See the paper by Wingate *et al.* in this symposium for further code details.

Applications that have been tested on these codes include blast wave stability, laser-plasma interaction, Rayleigh-Taylor instability, strong shocks, and hypervelocity impact. In the following sections we briefly discuss the equations solved in SPH, and show several hypervelocity test cases.

FLUID EQUATIONS

SPHC solves the general fluid dynamics equations. The first of these is the continuity equation

$$\frac{d\rho}{dt} + \rho \frac{\partial}{\partial x^\alpha} U^\alpha = 0 \tag{1}$$

where ρ is the material density and U is the material velocity. We use Greek superscripts to indicate coordinate directions with implied summation on repeated indices. Roman subscripts will be used to label particles. Summation is not implied on repeated subscripts (the summation sign must appear directly).

The second equation is the momentum equation

$$\frac{d}{dt} U^\alpha = \frac{1}{\rho} \frac{\partial}{\partial x^\beta} \sigma^{\alpha\beta} \tag{2}$$

where $\sigma^{\alpha\beta}$ is the stress tensor. This is divided into an isotropic part which is the pressure P and a traceless deviatoric stress tensor $S^{\alpha\beta}$ and is given by:

$$\sigma^{\alpha\beta} = -P\delta^{\alpha\beta} + S^{\alpha\beta}. \tag{3}$$

The final equation is the energy equation:

$$\frac{de}{dt} = \frac{1}{\rho} \sigma^{\alpha\beta} \dot{\epsilon}^{\alpha\beta} \tag{4}$$

where e is the specific internal energy and $\dot{\epsilon}$ is the strain rate tensor given by

$$\dot{\epsilon}^{\alpha\beta} = \frac{1}{2} \left(\frac{\partial}{\partial x^\beta} U^\alpha + \frac{\partial}{\partial x^\alpha} U^\beta \right) \tag{5}$$

Using the definition of the stress tensor (equation 3) and that the trace of the strain rate tensor is the divergence of the velocity, the energy equation can be rewritten (in perhaps the more familiar form) as:

$$\frac{de}{dt} = -\frac{P}{\rho} \frac{\partial}{\partial x^\alpha} U^\alpha + \frac{1}{\rho} S^{\alpha\beta} \dot{\epsilon}^{\alpha\beta}. \tag{6}$$

The procedure for converting the analytic equations into interpolated SPH equations is described in many places, for example see Monaghan (1988) or Benz (1989). Here we list the results. The continuity equation is usually solved in integral form as:

$$\rho_i = \sum_j m_j W_{ij} \tag{7}$$

where m_j is the mass of particle j and W_{ij} is the smoothing kernel. The kernel could be written as $W_{ij}(|r_i - r_j|, h)$ to indicate its dependence on the distance between particles i and j and its dependence on the smoothing length h. For simplicity, however, we will write it simply as W_{ij}. The smoothing length is a measure of the width of the kernel, and may vary from particle to particle. The kernel in SPHC used in these calculations is a cubic B-spline designated as W4 in Gingold and Monaghan (1982).

The momentum equation in the SPH approximation becomes:

$$\frac{d}{dt}U_i^\alpha = \sum_j m_j \left(\frac{\sigma_i^{\alpha\beta}}{\rho_i^2} + \frac{\sigma_j^{\alpha\beta}}{\rho_j^2} \right) \frac{\partial W_{ij}}{\partial x^\beta}. \tag{8}$$

If this equation is multiplied by m_i we see that the time derivative of the momentum is exactly symmetric in i and j thus ensuring exact conservation of both linear and angular momentum.

The energy equation in the SPH approximation is:

$$\frac{de_i}{dt} = \frac{1}{2}\sum_j m_j (U_j^\alpha - U_i^\alpha) \left(\frac{\sigma_i^{\alpha\beta}}{\rho_i^2} + \frac{\sigma_j^{\alpha\beta}}{\rho_j^2} \right) \frac{\partial W_{ij}}{\partial x_i^\beta}. \tag{9}$$

Multiplying this equation by m_i, summing over i, and using equation 8, we can prove exact energy conservation for the full system of particles. A rearragement of terms in the energy sum formed from equation (9) produces a slightly more physical and more stable form of the energy equation, which is the form used in SPHC, and is also exactly conservative:

$$\frac{de_i}{dt} = \sum_j m_j (U_j^\alpha - U_i^\alpha) \left(\frac{\sigma_i^{\alpha\beta}}{\rho_i^2} \right) \frac{\partial W_{ij}}{\partial x_i^\beta}. \tag{10}$$

To obtain the particle approximation for the strain rate tensor we follow Libersky and Petschek (1990) to get

$$\dot{\varepsilon}_i^{\alpha\beta} = \frac{1}{2}\sum_j \frac{m_j}{\rho_j} \left((U_j^\alpha - U_i^\alpha) \frac{\partial W_{ij}}{\partial x_i^\beta} + (U_j^\beta - U_i^\beta) \frac{\partial W_{ij}}{\partial x_i^\alpha} \right). \tag{11}$$

ELASTIC PERFECTLY PLASTIC STRENGTH MODEL

The strength model installed in SPHC is a basic Hooke's law model where the stress deviator rate is proportional to the strain rate. This type of model was first used in a smooth particle hydrodynamic code by Libersky and Petschek (1990). The elastic constitutive equation which relates the deviatoric stress rate to the strain rate can be found in various places, and is given by

$$\frac{d}{dt}S^{\alpha\beta} = 2\mu(\dot{\varepsilon}^{\alpha\beta} - \frac{1}{3}\delta^{\alpha\beta}\dot{\varepsilon}^{\gamma\gamma}) + S^{\alpha\gamma}R^{\beta\gamma} + S^{\gamma\beta}R^{\alpha\gamma} \tag{12}$$

where μ is the shear modulus, and R is the rotation rate tensor defined by

$$R^{\alpha\beta} = \frac{1}{2}\left(\frac{\partial}{\partial x^\beta}U^\alpha - \frac{\partial}{\partial x^\alpha}U^\beta\right). \tag{13}$$

The SPH approximation to the rotation rate tensor is identical to the SPH approximation for the strain rate tensor with the plus sign is replaced by a minus sign

$$R_i^{\alpha\beta} = \frac{1}{2}\sum_j \frac{m_j}{\rho_j}\left((U_j^\alpha - U_i^\alpha)\frac{\partial W_{ij}}{\partial x_i^\beta} - (U_j^\beta - U_i^\beta)\frac{\partial W_{ij}}{\partial x_i^\alpha}\right). \tag{14}$$

The von Mises yield criterion is used for plastic flow. This criterion limits the deviatoric stress in the following way. Define a quantity f by

$$f = min\left(\left(\frac{Y_0^2}{3J}\right)^{1/2}, 1\right) \tag{15}$$

where Y_0 is the yield stress and J is the second invariant of the deviatoric stress tensor

$$J = \frac{1}{2}S^{\alpha\beta}S^{\alpha\beta}. \tag{16}$$

The deviatoric stress tensor is then limited by

$$S^{\alpha\beta} = \quad ^{\beta}. \tag{17}$$

PHYSICS AND MATERIAL PROPERTIES

Installation and testing of material property routines and data bases is currently one of the primary areas of code development for the SPH codes. Current models use a Grüneisen equation of state with a custom temperature/energy relation incorporating solid/liquid/vapor/ion phases. In addition, the codes can access the LANL SESAME material property library for all available materials. Additional equation of state options are planned.

Strength models currently implemented are: elastic-perfectly plastic, Johnson-Cook, and Steinberg-Guinan. Each model accesses its own data base of material properties. Fracture models are discussed in the following section.

Other physics installed in the SPHC code includes thermal diffusion, radiation diffusion, laser deposition, laser ablation, ideal magnetohydrodynamics, and neutron production. These capabilities are not used in the impact tests discussed below.

Numerical techniques in the SPHC code include variable smoothing length and particle division to model low density regions, arbitrary dimensionality and geometry, ghost particle boundary conditions, and interactive run-time graphics (Stellingwerf, 1990).

FRACTURE AND FRAGMENTATION MODELS

The treatment of fracture and fragmentation in a hydrocode continues to be a challenge. We distinguish here between the two concepts on a purely numerical level:

A ***fracture model*** refers to the way that an object "comes apart" during a numerical computation. It may involve generating new void regions, inserting new interfaces, or other procedures depending on the code characteristics. These new voids may or may not be capable of rejoining later in the calculation. The criteria for fracture may depend on stress level, stress history, strain level, strain rate, etc.

In SPH there is no need to artificially insert void regions, since the physical process of stretching a solid object will naturally produce cracks, spall, and other void regions in the course of the computation. Material properties that affect this process are 1) the yield condition for plastic flow, 2) a specified "spall strength" for each material that acts as a limit to the tensile stress that a material can support, and 3) a specified maximum "void fraction" that the material can support prior to failure. The exact functional form of each of these criteria depends on the strength model and the implementation of the fracture model. The simplest and most promising approach in SPH is simply to set the yield stress and the spall strength criteria according to an appropriate model for the material and allow the object to respond naturally to the body stresses at each point. The degree of brittleness or ductility of the material can be varied via the recipe for the variable smoothing length (less allowed variation implies more brittle material), or by decreasing the tensile forces at some level of void fraction, as measured by the local density (smaller allowed void fraction implies more brittle material). The preferred model is likely to be different for different materials. Tests of these ideas are currently in progress and will be presented in future publications.

In contrast to the numerical treatment of fracture, a ***fragmentation model*** is a phenomenological model of the characteristics of the debris formed from a certain type of impact. The approach of Grady and Kipp (1987) is an example of this type of model. A fragmentation model can predict the degree of damage at each point in an object for use by a fracture model, and predict the distribution of masses, shapes, etc. of debris fragments over a much wider range than the hydrocode alone. Such a model has been tested in SPH by Benz and Melosh (1992) and is currently implemented in the LANL SPH codes.

BASIC CODE TESTS

The SPH technique has been validated for a variety of simple test cases including rarefaction expansion, spherical blast wave, shock tube, and the Noh problem (infinite strength converging shock). As an illustration of the code results on such a test, we show in figure 1 the SPH solution for a Riemann shock tube with an initial density jump of a factor of 4 at a specific time for three different cases of particle resolution. An artificial viscosity is added to the pressure to handle the shock, resulting in the shock front being spread over 3-5 particles, but the solution is very close to the plotted analytic result, and is clearly converging as the resolution is increased.

As a test of the strength models, the Taylor Anvil test of an iron rod colliding at 197 m/s with an unyielding surface has been computed. Figure 2 shows the results with the simple elastic-plastic as well as the more detailed Johnson-Cook strength models. The experimental data are taken from Johnson and Holmquist (1988), and are shown as an outline in solid lines. Although both cases represent the data very reasonably, the Johnson-Cook model does a better job reproducing the spreading at the surface and the small shoulder above the spreading region. Sections of rods taken following experiments show incipient fracturing and small void regions near the bottom of the rods. Although the simulation is rather coarse resolution, the rearrangement of particles near the surface/rod interface represents this effect.

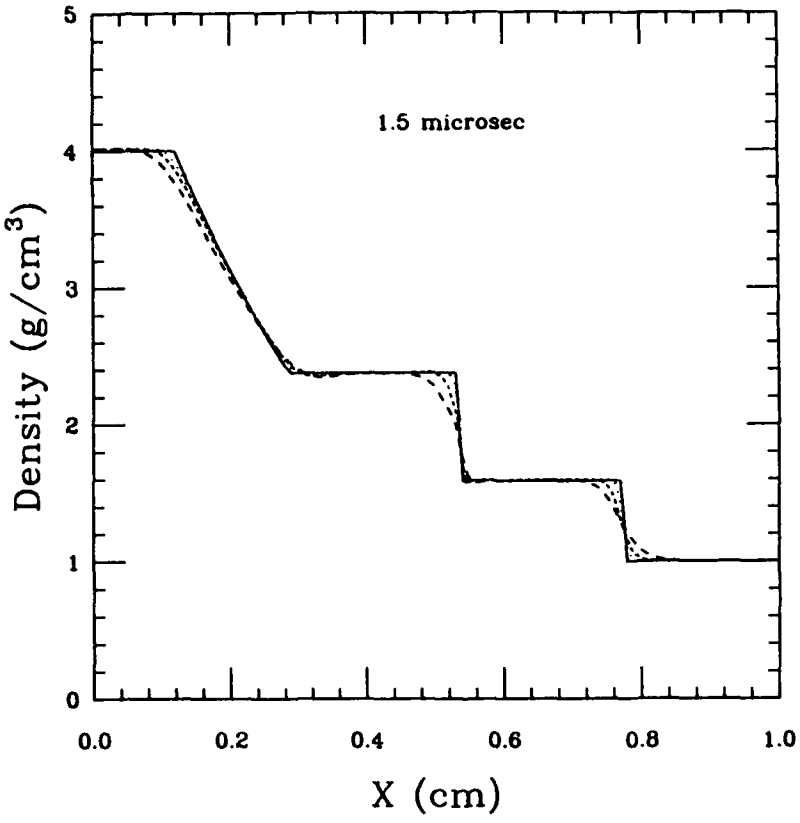


Fig. 1. Comparison of SPH results for 90, 180, and 360 particles to the exact analytic solution for the Riemann shock tube test case with $\gamma = 1.4$, initial density jump = factor of 4

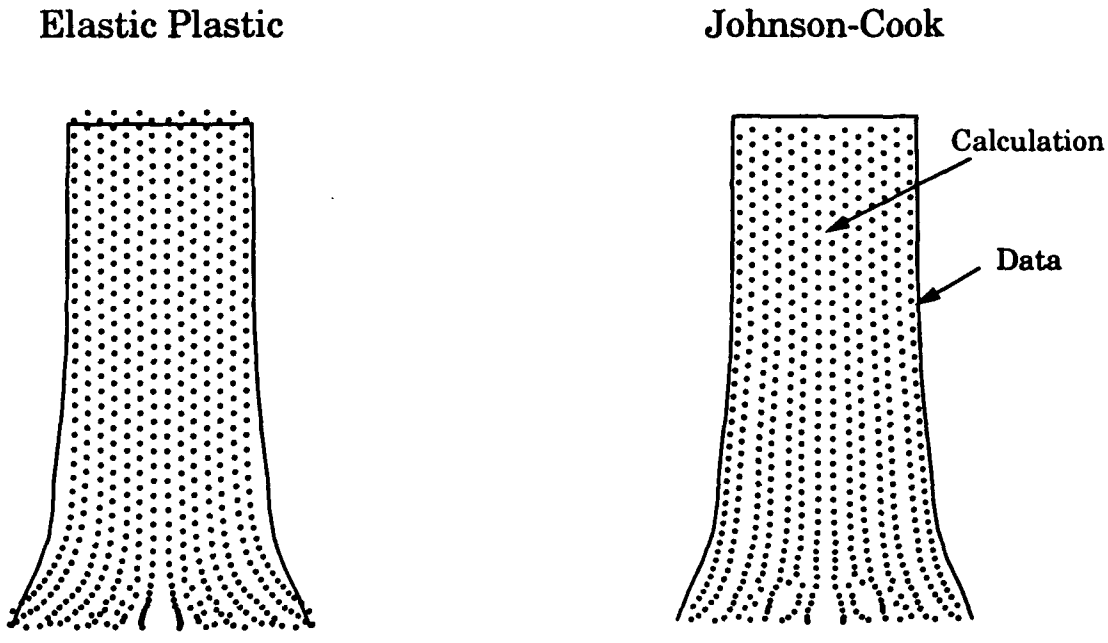


Fig. 2. Taylor anvil tests: final configuration of an Armco Iron rod after collision with a rigid surface at 197 m/s. Left: elastic-plastic strength model, right: Johnson-Cook model. Solid line: data

THIN BUMPER SHIELD COLLISION AT 6.75 KM/S

This section describes a simulation of a spherical aluminum projectile with radius 0.475 cm colliding with a thin aluminum sheet with thickness 0.0381 cm at a velocity of 6.75 km/s. This test is similar to a very well documented series of experiments done recently by Piekutowski (1992a,b) at University of Dayton Research Institute.

This simulation was run using SPHC with about 2500 particles in 2D cylindrical mode. The EOS is Grüneisen, and the strength model is elastic/plastic. The spall strength was set to 6 kbar. Figure 3 shows the initial conditions as well as the material configuration at 5 and 10 μs. This is a particle plot, which indicates the location of the material, with a gray scale to show values of the local density. We see that the projectile has broken into many fragments with a conspicuous spall "bubble" at the rear surface, and numerous cracks along the direction of motion that have developed as a result of later expansion of the projectile. The bulk of the material lies in a flattened disk, with what appears to be an intact core. The halo of low density material in front of and to the sides of the fractured projectile is liquid/vapor material formed from the impacted bumper and a thin shell of the projectile. All of these features are consistent with experimental radiographs, although details, such as the structure in the liquid/vapor phases, do not correspond exactly. We expect that these details will improve with the planned upgrading of the equation of state.

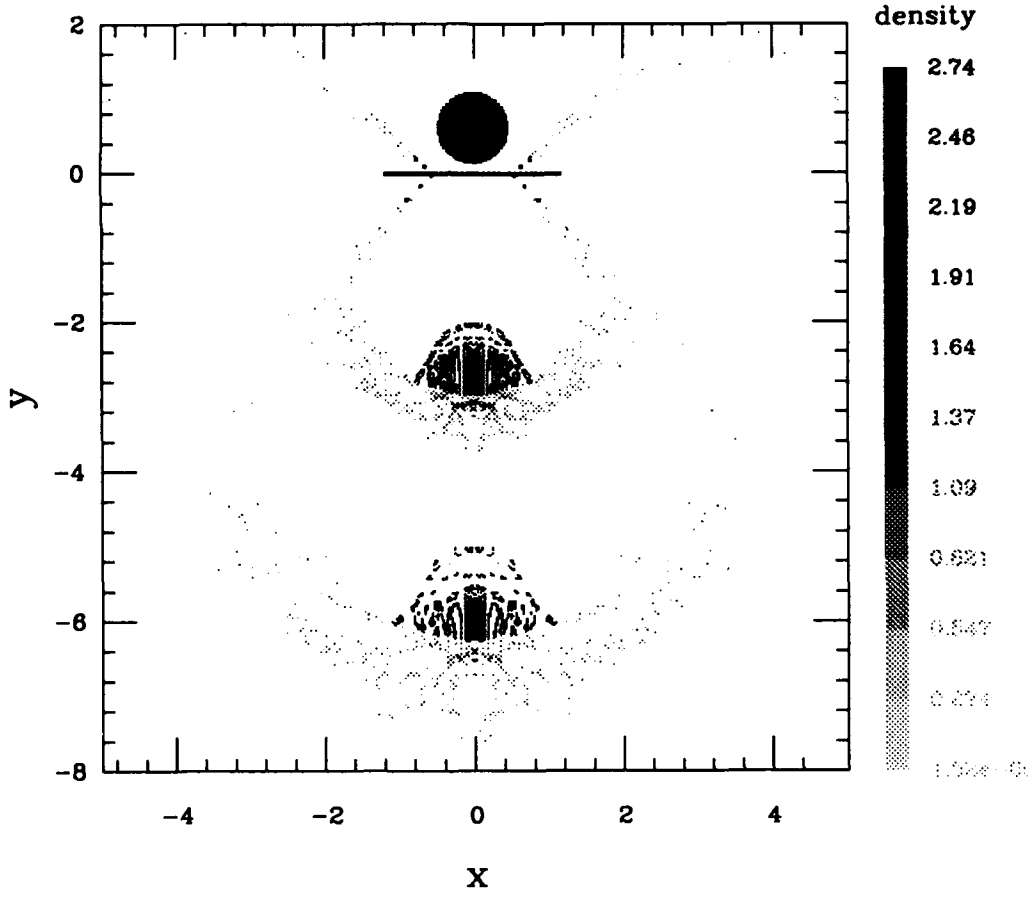


Fig. 3. Snapshots of the spherical projectile/ bumper collision at time = 0, 5, and 10 μs.

This simulation will be used as the primary test of the fracture/fragmentation scheme as the codes develop.

SHIELD / HULL COLLISIONS AT 10 KM/S.

As another example of an SPH impact application, we show models of several aluminum disk impact experiments carried out at Sandia by Chhabildas, et al. (1991).

The first model is of the experiment designated WS-12, or NASA-12. The initial setup for the run is shown in figure 4 (left). The model was run with 10,000 particles in 2D cylindrical geometry with SPHC. The EOS is Grüneisen, and the strength model is elastic/plastic. The spall strength was set to 6 kbar. The projectile is a disk of radius 0.95 cm, thickness 0.0868 cm, and velocity 10.0 km/s. The shield is a plate of thickness 0.127 cm. Both projectile and shield are made of 6061-T6 aluminum. The "hull" or witness plate was placed 11.43 cm beyond the shield, has thickness 0.32 cm, and was made of 2219-T87 aluminum. On the right of figure 4 we show the material configuration at 16 μs, just as the debris reaches the hull plate. In this case the entire cloud of debris is liquid at the vaporization temperature, indicating a mixed phase region. A dense column extends downward from the shield to the hull with nearly constant density of about 0.1 g/cc and a linear velocity profile. This column is about 1/2 projectile material and 1/2 shield material, as expected. The central core is surrounded by a halo of lower density material, extending to a shell of extruded shield at the outer edge. The maximum velocity of the debris is found to be nearly equal to the impact velocity of 10.1 km/s. This result agrees very well with UDRI experiments (Schmidt, et al. 1992, fig. 13a). A low density shell of material travelling at 14 km/s was observed in the Sandia experiment, but does not appear in this simulation.

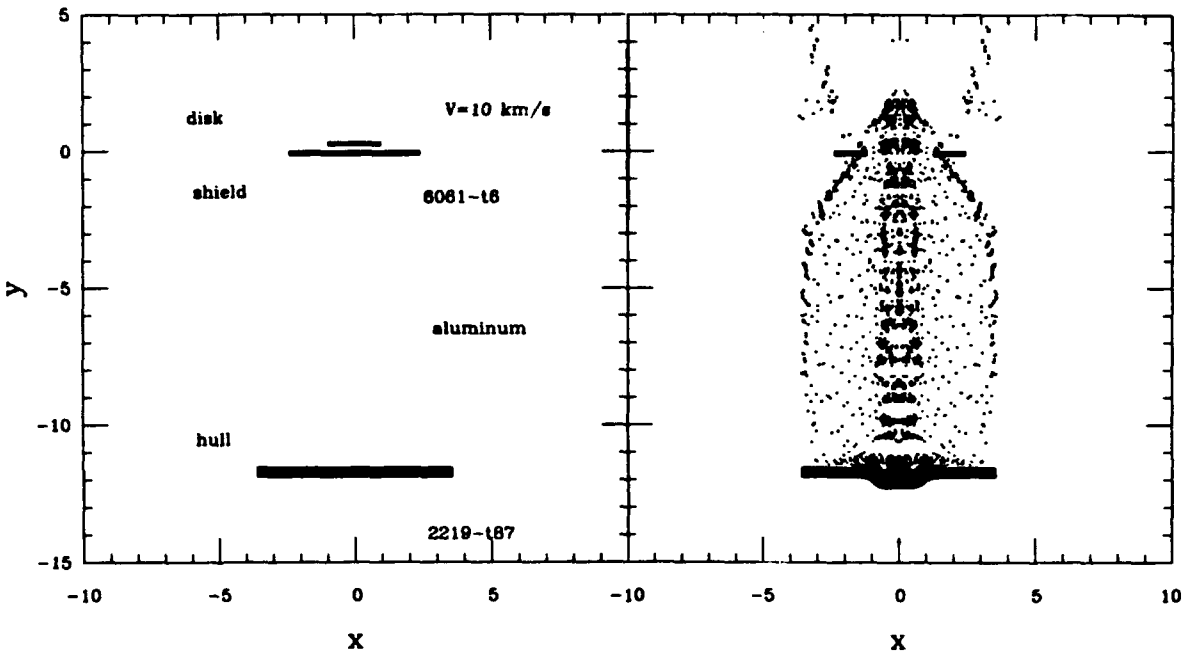


Fig. 4. Left: initial configuration for the simulation of WS-12. Right: configuration at secondary impact at 16 μs.

Figure 5 shows a details of the hull at 16 and 28 μs. At 16 μs the impacting liquid material has fully vaporized, a liquid layer has formed at the surface of the hull material, and strong hydrodynamic instability has developed at the interface. At 28 μs the hull is fully ruptured and hot vapor has begun to flow to the rear of the impact point. The times of hull deformation and rupture agree well with experiment, and both show a hole diameter of about 2 cm.

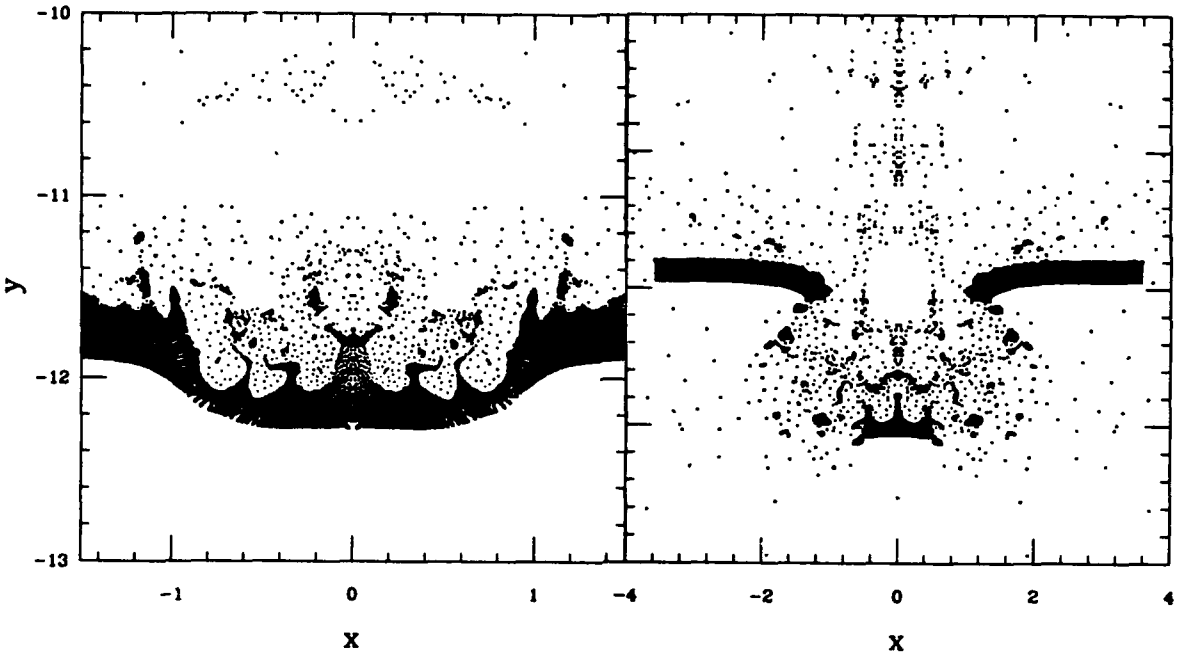


Fig. 5. Detail of the hull showing development of the hole and surface instabilities. Left: at 16 μs, right: at 28 μs. Note change of scale.

Another experiment, designated WS-11, or NASA-11, was also modeled. This experiment was similar to WS-12 except that the projectile radius was 0.60 cm, thickness 0.0953, and velocity 10.5 km/s. This implies about half the mass of WS-12. Shot WS-11 did not penetrate the hull, although some hull damage was observed. A model similar to the above WS-12 simulation was run with WS-11 parameters, and produced a ruptured hull similar to that observed in figure 5. Chhabildas, et al. comment that the projectile may have been distorted in some or all of the experimental shots, and this may have been the case for shot WS-11. The model was therefore re-run with a slightly "cupped" projectile, achieved by replacing the disk with a shallow cone with slope 0.25. Figure 6 shows the configuration for this simulation, again at 16 μs. In this case the hull has not ruptured, since the debris is considerably dispersed at its leading edge. The exact symmetry of the simulation, however, has formed virtually all of the projectile material into an arrow of dense material that is arrayed along the axis of the simulation, and does produce a small hole in the hull at later time. Asymmetries present in the experiment probably break up this "arrow", resulting in the several scattered damaged regions actually observed. A 3-dimensional simulation of this case is planned to test this hypothesis. The SPH results shown here are in general agreement with the CTH code results shown in Chhabildas et al. (1991).

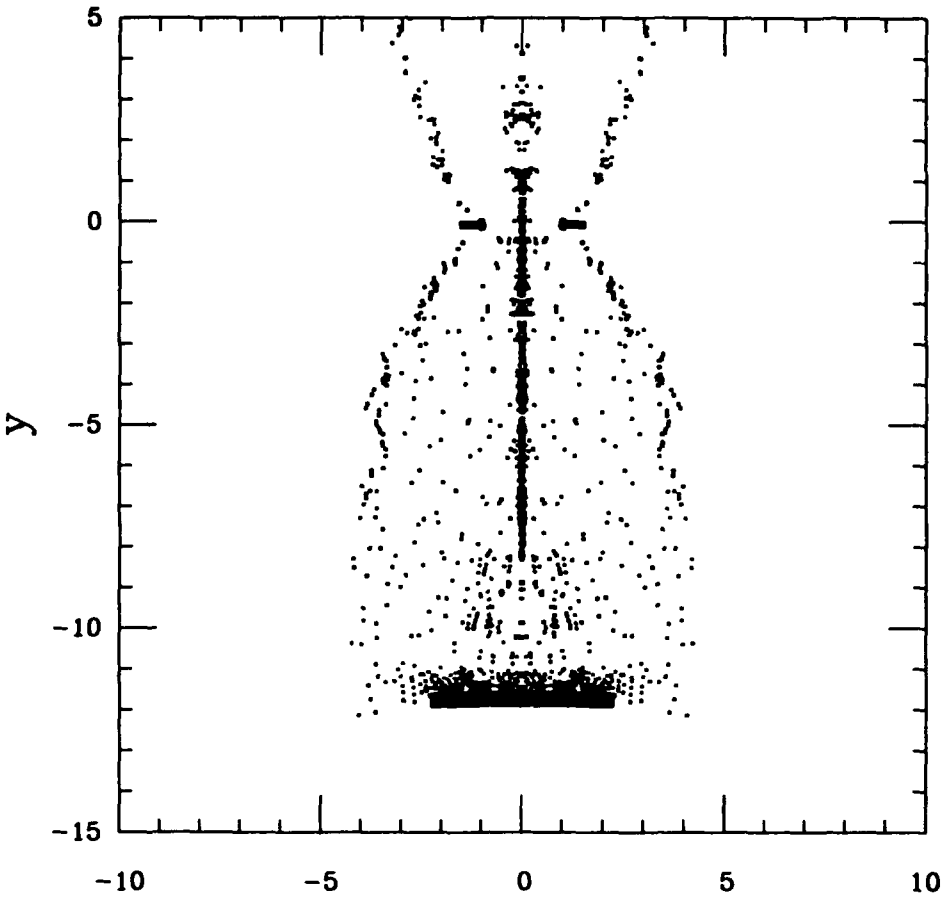


Fig. 6. The WS-11 simulation at 16 μs, showing intact hull and projectile "arrow".

OBLIQUE IMPACTS

The calculations of a sphere obliquely impacting a bumper modeled a NASA impact experiment similar to EH1C (Schonberg. et al. 1988). The sphere was made of 1100 Aluminum with a radius of 0.476 cm, a velocity of 7.0 km/s and a 60 degree angle from the normal. The bumper was 6061-T6 Aluminum with a thickness of 0.16 cm. The calculation was done in 3 dimensions using 60,000 particles. The equation of state used was Grüneisen. The strength model was elastic perfectly plastic with a shear modulus of 265 kbar and a yield strength of 0.345 kbar for the 1100 Al and 2.75 kbar for the 6061-T6 Al. The configuration after 20 microseconds is shown in Figure 4, side projection. Some projectile material scraped from the top of the projectile upon impact has slid along the plate and continued to the left, followed by ejected target material above the plane of impact. The long feature so formed is travelling ballistically to the left - there is no boundary beyond that shown in the figure. Below the plane, the projectile material is located at the left edge of the debris cloud, while target material forms the bulk of the rest of the cloud. This configuration is matched almost identically in unpublished experimental results obtained by Piekutowski at UDRI (experiment 4-1439).

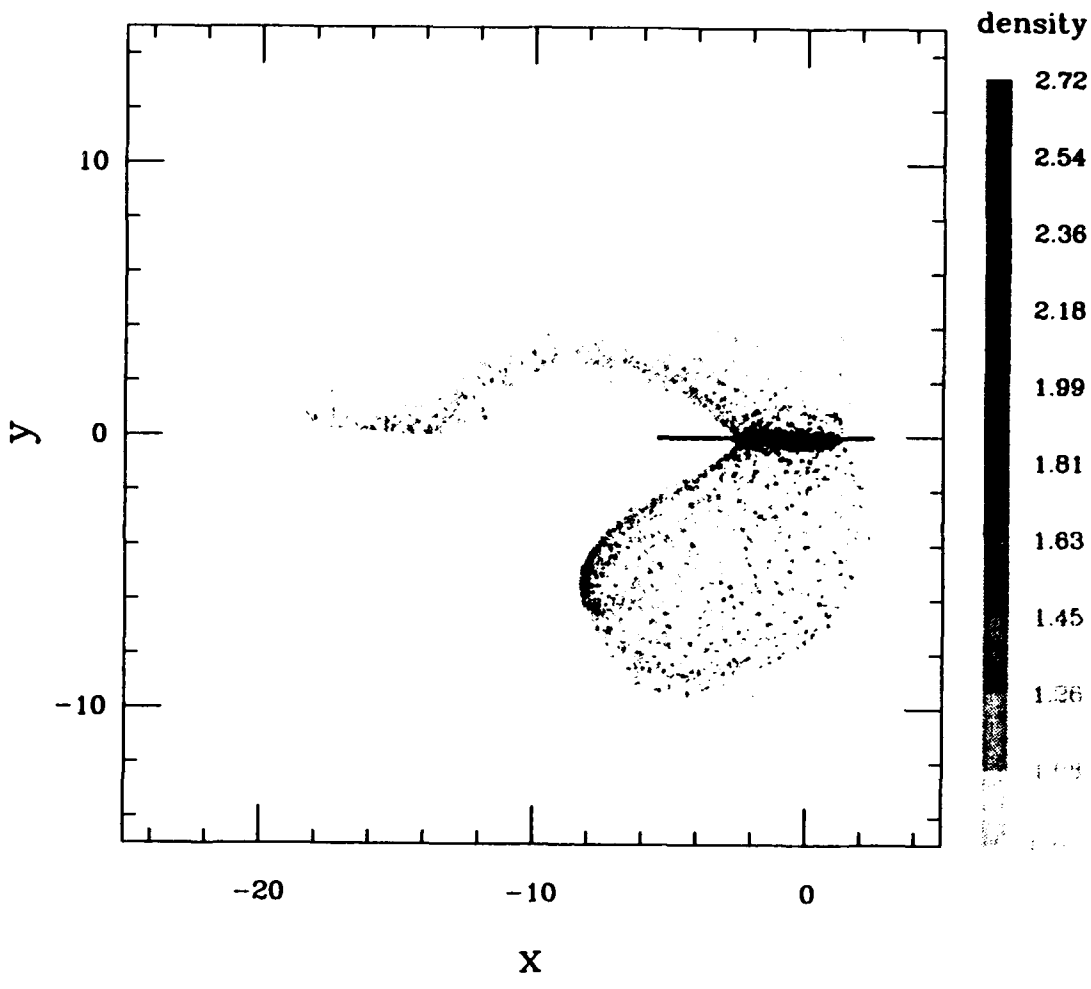


Fig. 7. Oblique impact model, projectile is a sphere entering at an angle of 60 degrees from the normal moving from top right to bottom left. See text for details.

SUMMARY.

The technique of Smooth Particle Hydrodynamics shows considerable promise for simulations of hypervelocity impacts. Of special interest is its ability to produce and track debris fragments, allowing computation of secondary impacts over unlimited distances.

The SPH codes at LANL are currently undergoing tests on a variety of applications, and are in the developmental stage of code and material properties upgrades. The results so far are encouraging, and further improvements should produce a useful and unique tool

ACKNOWLEDGMENTS.

This research is supported in part by the Department of Energy and the Defense Nuclear Agency.

REFERENCES

Benz, W. (1989). Smooth Particle Hydrodynamics: A Review, Harvard-Smithsonian Center for Astrophysics Preprint No. 2884.

Benz W.,and H. J. Melosh, (1992) private communication.

Chhabildas, L. C., E. S. Hertel, W. D. Reinhart and J. M. Miller, (1991). Whipple Bumper Shield Results And CTH Simulations At Velocities In Excess Of 10 km/s, Sandia Technical Report SAND-91-2683.

Gingold, R. A. and J. J. Monaghan (1977). Smoothed Particle Hydrodynamics: Theory And Application To Non Spherical Stars, Mon. Not. Roy. Astron. Soc. **181**, 375-389.

Gingold R. A. and J. J. Monaghan (1982). Kernel Estimates as a Basis for General Particle Methods in Hydrodynamics, J. Comput. Phys. **46**, 429-453.

Grady D. E. and M. E. Kipp, (1987). Dynamic Rock Fragmentation, *Fracture Mechanics of Rock*, Academic Press, 429-475.

Johnson, G. R. and T. J. Holmquist (1988). Evaluation of Cylinder-impact Test Data for Constitutive Model Constants, J. Appl. Phys. **64**, 3901-3910.

Libersky L. D., and A. G. Petschek, (1990). Smooth Particle Hydrodynamics with Strength of Materials, *Advances in the Free-Lagrange Method*, (Trease, Fritts, and Crowley, eds.), Springer Verlag, 248

Lucy, L. (1977). A Numerical Approach To Testing the Fission Hypothesis, Astron. J., 82, 1013-1024.

Monaghan, J. J. (1988). An Introduction to SPH, Comput. Phys. Comm. **48**, 89-96.

Monaghan, J. J. (1982). Why Particle Methods Work, SIAM J. Sci. Stat. Comput. **3**, 422-433.

Monaghan, J. J. (1985). Particle Methods for Hydrodynamics, Comp. Phy. Rep. **3**, 71-124.

Piekutowski, A. (1992a). Properties of Largest Fragment Produced by Hypervelocity Impact of Aluminum Spheres with Thin Aluminum Sheets, AIAA 92-1588, Space Programs and Technologies Conference.

Piekutowski, A. (1992b). Characteristics Of Debris Clouds Produced by Hypervelocity Impact of Aluminum Spheres with Thin Aluminum Plates, this volume.

Schmidt, R. M., Housen, K. R., Piekutowski, A. J. and Poormon, K. L. (1992). Cadmium Simulations of Orbital Debris Shield Performance to 18 km/s, this volume.

Schonberg, W. P., R. A. Taylor, and J. R. Horn, (1988). An Analysis of Penetration and Ricochet Phenomena in Oblique Hypervelocity Impact, NASA TM-100319.

Stellingwerf, R. (1989). The SPH_C Manual, User's Guide, Programmer's Guide, Technical Guide, Function Reference, Test Cases, Mission Research Corporation report AMRC-N-384.1-384.5.

Stellingwerf, R. F (1989). Boundary Condition Tests Using Smooth Particle Hydrodynamics, Mission Research Corporation report MRC/ABQ-N-426.

Stellingwerf, R. F (1990). Blast Wave Stability in Nuclear Explosions I, Mission Research Corporation report MRC/ABQ-R-1254.

Stellingwerf, R. F. and R. E. Peterkin, (1990). Smooth Particle Magnetohydrodynamics, Mission Research Corporation report MRC/ABQ-R-1248.

Stellingwerf, R. F. (1990). Smooth Particle Hydrodynamics, *Advances in the Free-Lagrange Method*, (Trease, Fritts, and Crowley, eds.), Springer Verlag, 239.

Stellingwerf, R. F. (1992). Shock Tests for Smooth Particle Hydrodynamics, LANL memo X-1(1/92)29.

Wilkins, M. L. (1969). Calculation of Elastic-Plastic Flow, Lawrence Livermore National Laboratory report UCRL-7322 Rev. 1.

Wingate, C. A. and H. N. Fisher, (1992). Strength Modeling in SPHC, in preparation.

Int. J. Impact Engng Vol.14, pp.719–727, 1993
Printed in Great Britain

0734-743X/93 $6.00+0.00
Pergamon Press Ltd

ULTRA-HIGH VELOCITY IMPACTS: CRATERING STUDIES OF MICROSCOPIC IMPACTS FROM 3 KM/S TO 30 KM/S

G. L. STRADLING, G. C. IDZOREK, B. P. SHAFER
Los Alamos National Laboratory
Los Alamos, NM 87545

H. L. CURLING, JR. AND M. T. COLLOPY
Science Applications International Corporation
Division 212, 2109 Air Park Rd.
Albuquerque, NM 87106

A. A. HOPKINS BLOSSOM
EG&G Energy Measurements Inc.
P.O. Box 809
Los Alamos, NM 87544

S. FUERSTENAU
Yale University, Dept. of Mechanical Engineering
P. O. Box 2159 Yale Station
New Haven, Conn. 06520-2159

ABSTRACT

Cratering experiments performed under carefully controlled conditions at impact velocities ranging from 3 km/s to 30 km/s into a wide variety of target materials are presented. These impact experiments use the 6 MV vertical Van de Graaff accelerator of the Ion Beam Facility at the Los Alamos National Laboratory to electrostatically accelerate highly charged iron micro-spheres. The sub-micron spheres, from a random size distribution, are shocklessly accelerated along an 8 m flight path. Ultra-sensitive charge detectors monitor the passage of the projectiles at a rate of up to 100 projectiles/second. An online computer records and displays in real time the charge, velocity and mass of the projectiles and provides cross correlation between the events observed by the several in-flight charge detectors and impact detectors. Real-time logic controls an electrostatic kicker which deflects projectiles of selected charge and velocity onto the target. Thus each experiment consists of an ensemble of 10 to 40 impacts onto a single target within a narrow window of the projectile parameter space, providing excellent statistical resolution of each data point.

The target materials used include single crystal copper and single crystal aluminum, gold, and quartz as well as pyrolytic graphic and epoxy used in composite materials of interest to space applications. We also conducted impact experiments onto thin Mylar and nickel foils. This paper presents these experiments and summarizes the cratering characterization performed to date. Emphasis is placed on cratering results in several materials over a range of impact velocities.

INTRODUCTION

The work presented here has been funded in support of space applications for which the physics of impact under exceedingly high closing velocities constrain the technical development of space systems. In these cases, where the upper velocity range of interest is not accessible with existing macroscopic ballistic

ranges, we have used microscopic projectiles accelerated electrostatically to explore this ultra-high velocity region of impact phenomenology. We have employed Van de Graaff accelerator technology (Keaton, 1990, Stradling 1990, Idzorek, 1990) developed under the space program (Friichtenicht, 1962, 1962, Lewis, 1970) to accelerate spherical iron projectiles, which though microscopic, are bodies consisting of millions of atoms and so are relevant to continuum impact experiments. The Hypervelocity Microparticle Impact (HMI) project has had the objective of obtaining quantitative cratering data over a span of velocities and in materials relevant to space applications.

As part of the task, we have necessarily needed to address the relevance of microscopic experiments to macroscopic impacts. In so doing, we examined a number of potential processes which might interfere with size scaling between micro and macro size impacts. These processes may depend on the size, temperature, or shock front thickness of the impact at the micro-scales of the HMI experiments. However, only two of these appear to affect the scaling.

The first obstacle to size scaling is target inhomogeneities of the same scale as the crater size. Target materials with inhomogeneities of this scale were avoided where possible. Targets were prepared to be homogeneous and without bulk or surface non-uniformities on the scale of the impact craters. Special single crystal copper and aluminum targets were used to avoid effects of pre-existent crystal domain boundaries. Target surfaces were lapped and chemically etched to avoid a depth dependent strength variation from surface work hardening which might result from mechanical finishing processes like diamond turning.

A second, more subtle, process appears to modify simple size scaling from macro to micro impacts. This is the increase of material strength at the very high strain rates which are characteristic of very small impacts. The analysis of this effect is presented in a companion paper (Walsh, 1992).

The existence of cratering data over the range of impact velocities and cratering strain rates presented here has proved to be a stimulus to the further development of impact models, material strength models and hydrodynamic code treatments of impact processes. In particular, there is work presented in these proceedings where the HMI data is modeled using the hydrodynamics codes; SPH, MESA, EPIC and CALE (Wingate, 1992).

DESCRIPTION OF EXPERIMENT CONFIGURATION

The hyper-velocity microparticle impact experiments discussed here are a refinement of the experiments presented at the 1989 HVIS by Keaton, 1990.. Particular emphasis has been placed on insuring that the projectiles which impact the target are of known mass and velocity. All of the impacts discussed here are made at normal incidence to the target surface. All are made in a vacuum of approximately 10^{-6} torr. In all cases the impacting projectile was iron, obtained from a carbonyl iron powder (Japka, 1988) of spherically shaped, solid (99.9%) iron particles of random size as shown in Fig. 1.

The particles are charged by passing them across the point of a high voltage tungsten needle, where a high field strips electrons out of the conductive sphere. The positively charged spheres are then injected into the acceleration tube of a 6 MV Van de Graaff accelerator, where they are shocklessly accelerated along an 8 m path to their final velocities. Particles coming into the accelerator are random in size, with diameters ranging between a micron and 10 nanometers as shown in Fig. 1. The final velocities of the projectiles are determined by the acceleration voltage and by the charge and the mass of the projectile, both of which latter parameters vary with the projectile radius as detailed in Keaton, 1990. The smaller projectiles can be accelerated to much higher velocities than the larger projectiles.

As the projectile stream exits the acceleration region of the accelerator, it drifts through a redundant set of shielded cylindrical, highly sensitive charge detectors.

Projectile Selection for Mass and Velocity

In the previous experiments, mass and velocity selection was attempted by first deflecting the projectile stream away from the target location by passing the stream through a pair of high-voltage deflection plates which served as a "kicker." When a projectile of interest was identified to have the desired combination of mass and velocity, the deflection plates would be quickly shorted to ground potential, letting the projectile pass through to the target. The mass of the projectile is inferred from the charge measured by the charge detectors.

While simple to execute and align, this technique relied on the deflection system being able to deflect all unwanted particles from the target. In practice it did not discriminate effectively against all projectiles coming through the system, including uncharged particles and scattered debris from collisions with walls and baffles. To eliminate the uncertainty in which particles were allowed onto the targets for the present impact experiments, we modified the selection apparatus from that reported in Keaton, 1990.

The current projectile selection technique places the target in a location offset from the beam path by 1 cm and then deflects selected projectiles onto the target. The "kicking" pulse on the deflection plates can be quite short, insuring that the projectiles of interest may be deflected without also affecting much

slower projectiles, which take longer times to transit the deflection portion of the drift tube. Unwanted projectiles drift into a beam stop without active interference from the "kicker."



Fig. 1. Impacting projectiles are 99.9% iron, obtained from a carbonyl iron powder of spherically shaped, solid iron particles of random size

The effectiveness of this selection technique is evaluated by allowing an ensemble of projectiles of a given charge and velocity to collect on a single target disk and by examining the spread in the diameter of the craters which are formed. We have found that the data ensembles collected in this manner have very little spread in the crater size. With this evidence of positive discrimination, we can confidently assign projectile velocities and masses to the craters formed on the targets.

Calculated Particle Trajectories

To accelerate and control particles that are massive by Van de Graaff accelerator standards without risking severe damage to the accelerating structure, it was necessary to calculate the behavior of the particles in the Van De Graaff accelerator and associated systems. The Van de Graaff system consisted of a series of electrostatic and magnetic deflectors and lenses with beam profiling sensors interspersed between them. The Van de Graaff operator tunes the beam by adjusting the deflectors and lenses and then observing the beam image on the sensors. While the iron particles were more highly charged than the ions normally used, there were many fewer particles than ions resulting in integrated beam currents below the detection threshold of the beam profiling sensors, rendering the sensors useless for our experiments. A quick calculation also showed that the magnetic systems were ineffective with iron particles due to the extremely poor charge to mass ratio of the particles which required magnetic field strengths beyond the capability of the system. Fortunately a purely electrostatic system can accelerate and focus particles independent of the charge, mass, or velocity of the particles. By using the electrostatic beam optics code OPTIC II we were able to calculate the trajectories of the iron particles and set the electrostatic lens potentials before accelerating particles. This avoided the possibility of high velocity particles striking and damaging the Van de Graaff accelerator beam tube electrodes. The trajectory calculations allowed the optimal placement of collimating slits and shields to insure only the well-behaved particles (i.e. not debris) reached the target.

SELECTION OF MATERIALS AND VELOCITY RANGE

The objective of this series of HMI impact experiments was to obtain crater size data from a range of impact velocities, from 3 km/s to 30 km/s, in a variety of materials relevant to the evaluation of computational deformation models and codes as well as materials relevant to applications in space. Gold had been suggested as a material which is straight forward to model computationally because of its malleability and inert nature. Although gold was later determined to not be as ideal for computational modeling as initially supposed, we did complete a data set in solid gold targets which were micro machined and then chemically lapped to eliminate work hardening of the impact surface. The metals, copper and aluminum, are both represented in a wealth of impact data obtained in macroscopic impacts at velocities up to 6 km/s at conventional ballistic ranges. Single-crystal samples of both of these common experimental metals were impacted over a wide range of velocities. We chose to experiment with single crystals of metals because of concerns that small scale crystalline structure in the material might affect the crater size reached at stagnation. As with the gold targets, the impact surfaces were diamond turned and chemically lapped.

Because of the importance of quartz to space optics and windows, we impacted quartz samples. These samples were prepared with annealed surfaces. Likewise, we examined the craters resulting from impacts in an epoxy formulation used in composites common to space vehicles as well as pyrolytic graphic crystals used in space composites. Another material common to space applications which we impacted was thin Mylar foil.

Targets

The targets were in general disks 3/4" and 1/2" in diameter and between one and several mm thick (infinitely thick for the purposes of the microparticle impacts). The thin foil targets of Mylar and nickel are the only exceptions. The targets were positioned on a carousel wheel with 18 positions in a small (12" x 10" x 8") vacuum chamber at the bottom of the free flight path. Targets adjacent to the beam focus were shielded from any debris or stray particles from above. A charge-collecting Faraday cup (with an axial hole for the projectiles to pass through) was positioned above the target to detect impact plasma for impact verification.

EXPERIMENTAL RESULTS

Extensive crater data were collected in the form of ensembles of craters created within a narrow projectile parameter window of mass and velocity The velocity was generally constrained to a range of 1/2 km/s around the velocity of interest. This velocity acceptance region was expanded to 1 km/s in cases when the projectile fluence in the parameter window of interest was particularly slow. The range of projectile mass was constrained by the projectile flux and by the time required to obtain a satisfactory ensemble of impacts, generally between 10 and 30 impacts. Accumulation times for a given parameter set could extend to several hours.

Figure 2 shows graphically the array of data obtained as crater ensembles on all of the target materials. A subset of these targets was examined with a scanning electron microscope (SEM) and crater diameters were determined. Stereoscopic data was recorded in the form of a pair of Polaroid photographs taken at ± 4° from normal for each target examined with the SEM. Ideally we would prefer to measure crater volumes by determining the crater depth as well as the diameter. Computer modeling of these impacts indicate that the elongation from hemisphericity may be expected in these target materials (Wingate, 1992). Funding shortfalls have prevented us from measuring the craters on all of the targets and also from analyzing the stereoscopic data in detail to determine crater depths.

Detailed data of the projectile size and velocity distribution are obtained with each experimental run. These data are used to validate the measurements and are archived for later reference. Table 1 is a summary of the data obtained to date from the HMI project.

Qualitative SEM crater images are shown in Fig.'s 3 through 10. In general the crater shapes are circular with a lip formed above the edge of the crater. Copper, gold and aluminum crater morphology was typical with some characteristics unique to each material. The lips of aluminum are much finer than those in copper and gold and even appear transparent to the electron beam used in the SEM. Copper exhibits a uniform texture of what appear to be micro-spallation features inside the craters. Quartz forms a definite melt region around the crater in the middle of a larger spallation zone (Fig. 7).

Exceptions to the typical crater characteristics were seen. One example of non circular craters is in single crystal copper samples for which the target surface was oriented in the 110 plane of the single crystalline sample. In this case the material strength is anisotropic and the craters formed in the material are elliptical (Fig. 6). Single crystal copper samples oriented in the symmetric 100 plane form circular craters on impact (Fig. 5) as would be expected from the symmetry of the strength tensor.

Table 1. A compilation of the crater data. The data is tabulated by run number and date with target material, projectile velocity range, projectile mass range, number of measured impacts, average crater diameter, and the standard deviation of the crater diameter data.

Target ID	Velocity km/s	Window km/s	Craters Found	Avg Dia µm	Std Dev µm	Mass femto gm	Std Dev fgm	Mass %	Notes
AL SC	6.5	1	24	2.84	0.2	2359.0	251.0	11%	
AL SC	8.5	1	28	2.19	0.11	671.0	80.6	12%	
AL SC	11.0	2	13	4.18	0.11	2952.0	205.2	7%	1
AL SC	12.5	1	19	2.90	0.09	1017.0	79.0	8%	
AL SC	14.5	1	11	2.53	0.18	557.0	79.2	14%	
AL SC	16.5	1	40	2.01	0.18	244.8	52.0	21%	
AL SC	18.5	1	29	2.48	0.06	276.0	13.8	5%	
AL SC	20.5	1	33	1.70	0.12	92.2	15.7	17%	
AL SC	22.5	1	21	1.77	0.23	99.9	25.3	25%	
AL SC	24.5	1	11	1.82	0.18	79.7	19.8	25%	
AL SC	27.0	2	38	1.86	0.31	57.7	21.1	36%	
AL SC D	6.0	1	8	2.94	0.10	2415.5	253.6	10%	2
AL SC D	10.0	1	10	1.74	0.06	230.7	18.5	8%	2
AL SC D	12.0	1	5	2.33	0.12	389.3	28.7	7%	2
AL SC D	14.0	1	24	2.06	0.10	289.5	21.3	7%	2
CU SC	5.5	1	27	2.58	0.09	1522.6	105.8	7%	3
CU SC	7.5	1	22	1.51	0.09	240.9	30.4	13%	3
CU SC	10.5	1	22	2.02	0.21	350.5	96.5	28%	3
CU SC	12.5	1	15	3.98	0.35	1888.5	447.0	24%	3
CU SC	14.5	1	8	3.39	0.16	848.4	114.5	13%	3
CU SC	16.5	1	26	2.75	0.09	517.1	23.2	4%	3
CU SC	18.5	1	22	2.52	0.12	355.0	22.1	6%	3
CU SC	20.5	1	24	2.38	0.13	233.8	42.8	18%	4
CU SC	22.5	1	25	1.84	0.05	111.1	7.7	7%	4
CU SC	24.5	1	24	1.67	0.10	85.8	11.9	14%	4
E10	12.5	1	23	1.12	0.11	1707.1	341.6	20%	
Q14	24.5	1	21	0.69	0.09	88.3	13.4	15%	

1. Craters are larger due to the large kicker window set for the run.
2. These single-crystal targets were diamond turned but not chemically polished.
3. Single crystal Cu target cut for 100 face.
4. Single crystal Cu target, 110 face, Dia. is AVERAGE of minor and major diameters.

Epoxy (Fig. 8) and Mylar (Fig. 9) are much more volatile than the other target samples impacted and, perhaps for that reason, did not form lips around the edge of the craters. In the Mylar foils, the strength tensor is anisotropic due to the directional stretching of the plastic which takes place in forming of the foil. An elliptical hole is formed by impact (Fig. 9). Other interesting crater pathology is noted in the epoxy samples. From the stereoscopic images it is apparent that instead of the semi-hemispherical craters formed in the metals and glass, the craters in epoxy are cavity shaped with the opening at the surface smaller than the largest diameter. Typically a roughly hexagonal fracture structure in seen in epoxy (Fig. 8). The 5 µm thick nickel foil is substantially thicker than the crater depth and so formed craters similar to the other metals.

Quantitative trends in cratering effectiveness as a function of impact velocity may be seen if the crater data are plotted as a ratio of crater volume to projectile volume, V/V_0 as is typical in the impact literature. Because of the difficulty of extracting crater volume from SEM images, we normalize a volume-like quantity, crater diameter cubed, to projectile mass (which is also proportional to the projectile volume) and plot the ratio against projectile velocity in Fig. 11. This alternative to crater

volume is not completely satisfactory because craters are known to deviate from hemisphericity; nonetheless, this analysis can give some comparison of the range of data.

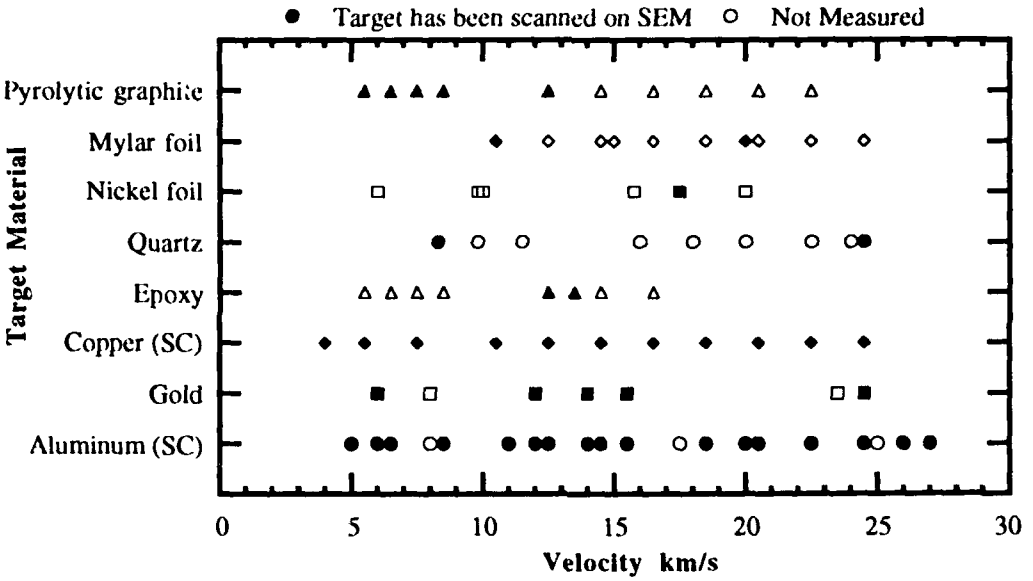


Fig. 2. This represents the array of target materials and impact velocities for which cratering samples collected. Only one velocity value was permitted per target. The solid symbols represent cratering samples which have been measured under the SEM. The targets which have not been examined are indicated by open data points.



Fig. 3. A SEM micro-photograph of a 1.86 μm diameter impact crater in single-crystal **aluminum** target from a 58 femto-gm iron projectile traveling 27 km/s. The lips of the aluminum craters are finer than those formed in denser materials.

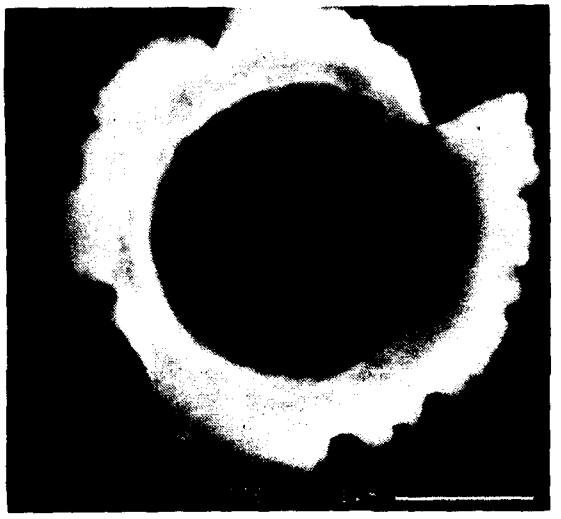


Fig. 4. A SEM micro-photograph of a 2.2 μm diameter impact crater in a **gold** target from an iron projectile traveling 15.5 km/s.

Figure 11 shows the crater data in both single crystal copper and single crystal aluminum targets. In addition to the microscopic impact data, several macroscopic impact data points of copper impacting copper and of aluminum impacting aluminum are shown. The impact parameters of the macroscopic data are shown in Table 2. Macroscopic impacts data are not available at significantly higher velocities for

direct comparison. The difference in the D^3/m between the macroscopic and microscopic data at the same impact velocity indicates that although size scales with moderate fidelity over four orders of magnitude in linear dimensions, the scaling relationship is imperfect without some factor which corrects for the size of the impact. As mentioned above, the strain rate of the cratering deformation is linearly dependent on the projectile size and at very high strain rates, the material strength increases with strain rate. A detailed discussion of this difference and a means for compensating for strain-rate induced strength changes is presented in the companion paper (Walsh, 1992).

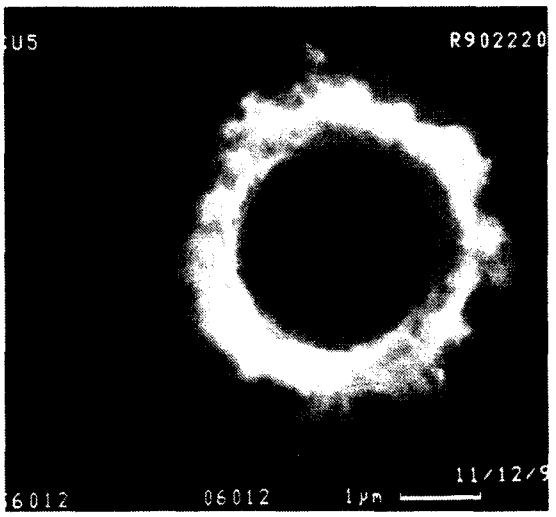


Fig. 5. A SEM micro-photograph of a 2.5 μm diameter impact crater in a **single-crystal copper** target from a 355 femto-gm iron projectile traveling 18.5 km/s. The target face is cut parallel to the **100 crystal plane**. Copper typically exhibits small scale spallation features in the craters.

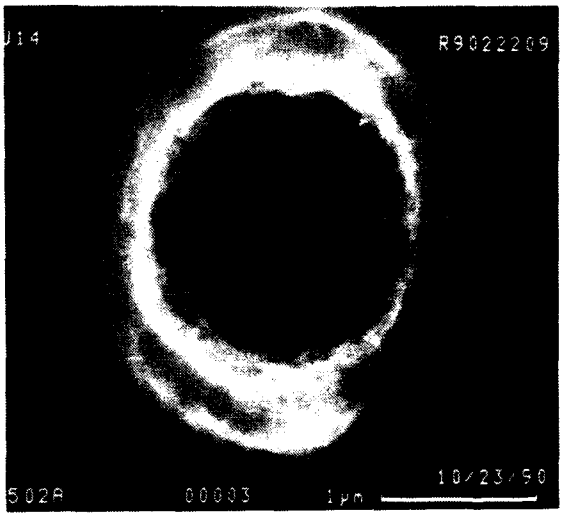


Fig. 6. A SEM micro-photograph of a 1.84 μm average diameter impact crater in a **single-crystal copper** target from a 111 femto-gm iron projectile traveling 22.5 km/s. This face is cut parallel to the **110 crystal plane**. This crystal plane produces elliptical craters characteristic of anisotropic stress values in the material.



Fig. 7. A SEM micro-photograph of a 0.6 μm diameter impact crater in a **quartz** target from a 88 femto-gm iron projectile traveling 24.5 km/s. Craters in quartz typically exhibit a melted crater lip surrounded by a larger spallation zone.

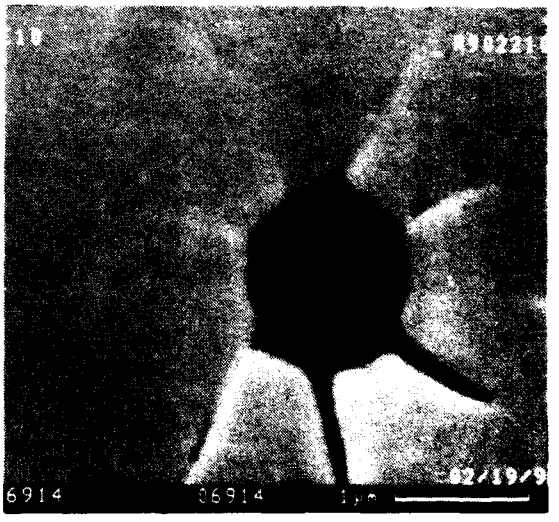


Fig. 8. A SEM micro-photograph of a 1.7 pico-gm iron impact in an **epoxy** target at 12.5 km/s. The hexagonal fracture structure is typical and the cavity of the crater appears to be larger than the crater opening.

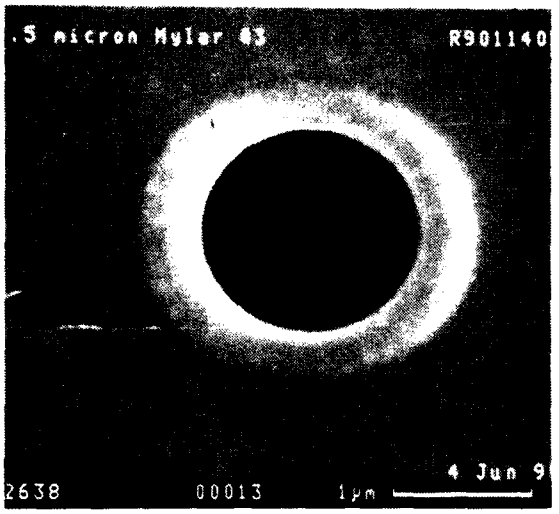


Fig. 9. A SEM micro-photograph of a 1.3 μm diameter impact crater in a 1.5 μm thick **Mylar film** target from an iron projectile traveling 15 km/s. Mylar films are stretched in production and so produce elliptical craters characteristic of anisotropic stress values in the material.

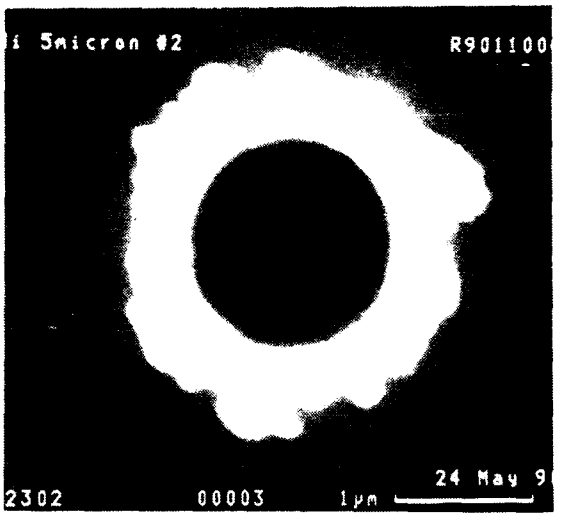


Fig. 10. A SEM micro-photograph of a 1.6 μm diameter impact crater in a 5 μm thick **nickel foil** target from an iron projectile traveling 17.5 km/s. Spallation bubbles were formed on the back side of these foils when the crater size approached the foil thickness.

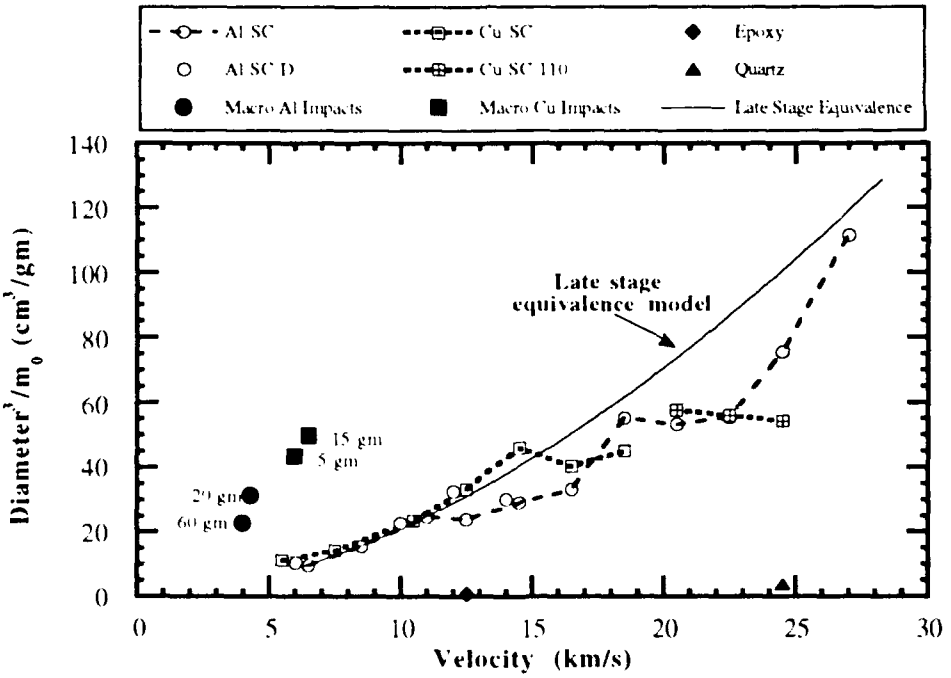


Fig. 11. Crater data from the several materials impacted. The data are plotted as (crater diameter^3)/ projectile mass) versus impact velocity. Plotted with the microscopic data are sets of macroscopic impact data both in aluminum and in copper. The microscopic data of impacts in both copper and in aluminum exhibit interesting plateaus as they deviate from the empirical late stage equivalence model. Phase changes in the target material with increasing impact velocity may be responsible for these plateaus. The microscopic impact craters are somewhat smaller than might be expected from simple size scaling, as discussed in the companion paper (Walsh, 1992). The impacts in quartz and in epoxy deviate strongly from the metal data. This difference may be attributed to non-hemispherical craters, which are not taken into account by a crater-lip diameter parameter.

Table 2. The parameters corresponding to the macroscopic data presented in Fig. 11.

Material	Mass (gm)	Diameter (cm)	Impact velocity (km/s)	Crater diameter (cm)
Aluminum	20	2.4	4.28	8.57
Aluminum	60	3.5	4.0	11.1
Copper	0.15	0.48	6.5	1.9
Copper	0.50	0.32	6.0	2.8

Without detailed knowledge of the impact process, late stage equivalence indicates that the quantity D^3/m should increase with $v^{1.74}$. A curve showing that trend is plotted with the microscopic data. A second observation of interest is that while the microscopic data follow the late stage equivalence curve, they tend to fall below it and also there are two definite plateaus in both the copper and the aluminum data.

CONCLUSIONS

We have performed impact cratering experiments over a wide range of impact velocities, above those normally accessible with standard ballistic range. We have impacted a variety of materials which are interesting both for practical engineering applications and for the simplicity of their deformation characteristics for computational modeling. These experiments represent a region of extremely high strain rates and compel the examination of the scaling relationship between micro and macro impacts. The results of these experiments have challenged the limits of both theoretical and computational modeling of deformation physics. We have obtained a wealth of impact data in the form of cratered targets, many still awaiting analysis. However, in the measured data we see considerable phenomenology which is not easily explained.

REFERENCES

Friichtenicht, J. F. (1962), Two million volt electrostatic accelerator for hypervelocity research, *Rev. Sci. Inst.*, **33**, 209.

Friichtenicht, J. F. (1964), Micrometeroid simulation using nuclear accelerator techniques, *Nucl. Inst. Meth.* **28**, 70.

Idzorek, G. C., P. W. Keaton, G. L. Stradling, M. T. Collopy, H. L. Curling Jr., and D. B. McColl (1989). Data acquisition system for a hypervelocity-microparticle-impacts laboratory, *International Journal of Impact Engineering*, **10**, 261-270.

Keaton, P. W. *et. al.* (1990) A hypervelocity-microparticle-impacts laboratory with 100 km/s projectiles, *Int. J. Impact Engng.* **10**, 295-308.

Japka, J. E. (1988). Microstructure and properties of carbonyl iron powder. Journal of Metals, August, 18-21.

Lewis, A. R. and R. A. Walter (1970) Electrostatic acceleration system for hypervelocity microparticles with selected kinematic properties. NASA TN D-5780, Electronics Research Center, Cambridge, MA.

Stradling, G. L. *et. al.* (1990) Searching for momentum enhancement in hypervelocity impacts, *Int. J. Impact Engng.* **10**, 555-570.

Walsh, J. M., G. L. Stradling, G. C. Idzorek, B. P. Shafer, H. L. Curling, Jr., Microparticle impacts at ultrahigh velocities and their relation to macroparticle impacts, this proceedings.

Wingate, C. A., R. F. Stellingwerf, R. F. Davidson, M. W. Burkett, "Models of high-velocity impact phenomena", this proceedings.

Int. J. Impact Engng Vol.14, pp.729–737, 1993
Printed in Great Britain

0734-743X/93 $6.00+0.00
Pergamon Press Ltd

AN EXAMINATION OF HYPERVELOCITY PARTICLE PENETRATION PARAMETERS FOR THIN FILMS FLOWN IN SPACE

W. G. TANNER, JR., R. A. MCDONALD, and W. M. ALEXANDER

Baylor University Space Science Laboratory
Department of Physics, Waco, Texas 76798 USA

C. R. MAAG

Science Applications International Corporation
Glendora, California 91740 USA

ABSTRACT

Many materials and techniques have been developed by the authors to sample the flux of particles in Low Earth Orbit (LEO); and through regular *in situ* sampling of the flux in LEO, the materials and techniques have produced data which compliment the data now being amassed by Long Duration Exposure Facility (LDEF) research activities. A comparison of the data provided by LDEF studies with data derived from the analysis of other materials which have been exposed to the space environment has been ongoing. In order to augment the amount of material returned in a form which can be analyzed on Earth, the survivability of the experiment as well as the captured particles has been assessed. Using Sandia National Laboratory's hydrodynamic computer code CTH, hypervelocity impacts on the materials which comprise the experiments have been investigated. The progress of these studies will be reported

INTRODUCTION

Space-based systems exposed to the extreme environment of Low-Earth Orbit (LEO) will avoid catastrophic failures only if the materials which compose them can provide a "shield" against the effects of continuous hypervelocity impacts. Extensive research has been conducted to characterize the effects on materials subjected to hypervelocity impacts by large masses. Even though the large mass impactors carry the highest probability of precipitating a catastrophic event, the number of large mass objects which might be encountered by an exposed surface in LEO is believed to be quite small. However, the size distribution of objects a surface will encounter in LEO has not been adequately characterized, especially for that portion of the distribution which contains the largest number of objects, i.e., the smallest. In order to provide *in situ* data depicting the size distribution of the most numerous objects in LEO, an experiment has been designed and successfully flown in the Science Applications International Corporation (SAIC) Interim Operational Contamination Monitor (IOCM) aboard the US Space Shuttle (STS-32, STS-44), and the Particle Impact Experiment (PIE) aboard STS-46, and STS-52. Each of these shuttle secondary experiments have been scheduled for flight on STS-56 (PIE) and STS-63 (IOCM). As a result of the experimental activities

associated with Carl Maag's IOCM missions, an opportunity to participate in the European Space Agency's European Retrievable Carrier (EuReCa 1) on the Timeband Capture Cell Experiment (TICCE) has been provided for a nine-month exposure at 525 km for a large surface area thin film experiment.

EXPERIMENTAL DESIGN

Characterization of the orbital debris and micrometeoroid complex which any surface will encounter in LEO implies an implementation of several concurrent processes. Foremost, there should be a means to sample *in situ* the flux with a frequency which can establish good statistics for multiple samples. There also should be access to that environment for an extended period, e.g., LDEF, and EuReCa, so that the existence of any temporal fluctuations in that flux can be identified. The experiments flown can be passive sensors if the materials can be easily returned to Earth. In fact, the complete analysis of the LEO environment cannot be adequately conducted without repeated examinations of materials which have been exposed to the extremes of space. Hence the experimental design which can provide a much needed investigation of small grains, D_p 10 cm, would be a passive sensor which could both detect and capture constituents of the orbital debris and micrometeoroid complex.

Passive Sensor Development

In an effort to develop such a system of sensors, the authors have designed and tested several prototypes on STS missions. The primary means to test these devices has been in the IOCM created by Carl R. Maag of SAIC. The IOCM contains an array of passive and active sensors which continuously sample three orthogonal directions in the STS cargo bay. Fig. 1. depicts the position of the IOCM during the LDEF retrieval mission, STS-32.

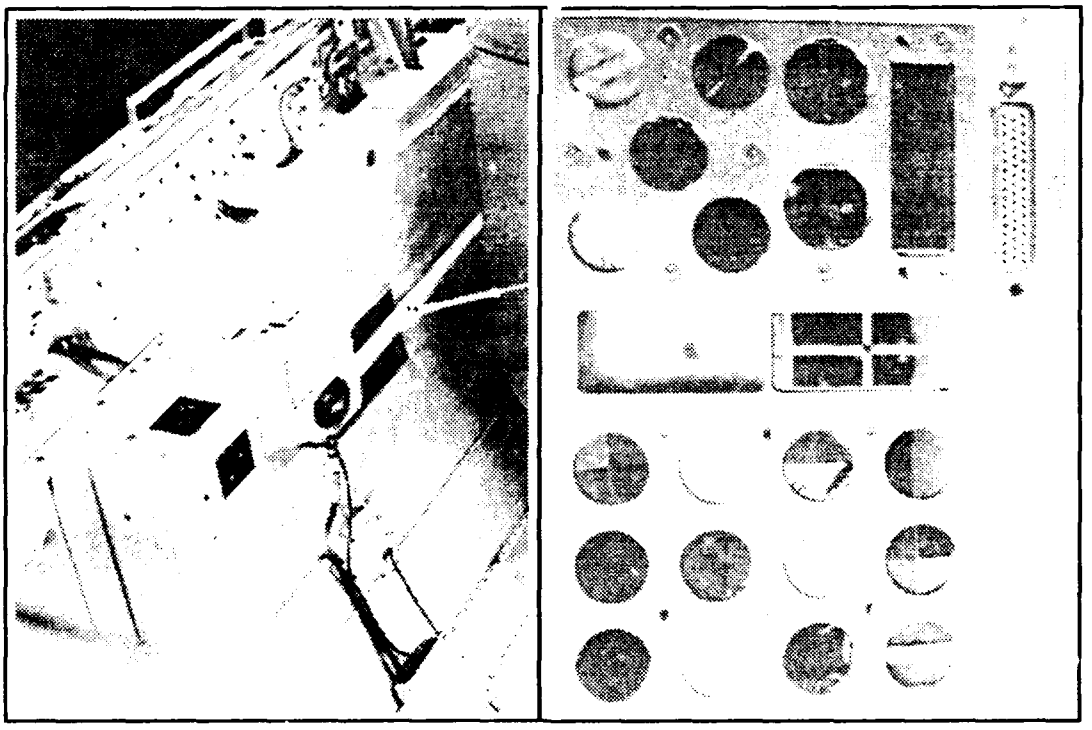


Fig. 1. Position of IOCM in STS-32 cargo bay during LDEF retrieval mission.

STS-32 Flown Films

The primary objectives of the STS-32 Experiment were to sample the LEO orbital debris and micrometeoroid complex and to conduct a prototype test-flight of the BUSSL thin films and holders. An initial design goal of the STS-32 Experiment was to test a thin film with a thickness of less than 1 μm and with a combined density of less than 3.0 g/cm^3. The basic design of the STS-32 Experiment suspended a thin film above an

impact plate. Fig. 2. shows an exploded diagram of the design which was flown. The thin film holders, machined by BUSSL workers, were made of 1100 aluminum (99% pure). Situated 1.8 mm below the thin film, each unit possessed a highly polished impact surface on which was sputtered 2000 Å gold. The manufacture of the ultra-thin metallic films required expertise not immediately available at BUSSL. Consequently, a contract was let to Arizona Carbon Foils (ACF) to deposit 0.68 μm of aluminum onto a 440 Å carbon foil over a 30-line-per-inch, 90% transmissive grid (Buckbee Mears). Each film was then mounted onto a steel ring with 25.40 mm O.D. x 20.32 mm I.D. x 1.143 mm thickness using Y-966 adhesive provided to ACF by Carl Maag of SAIC. Of the three units which were shipped directly to SAIC, two were placed into the IOCM, leaving one for control.

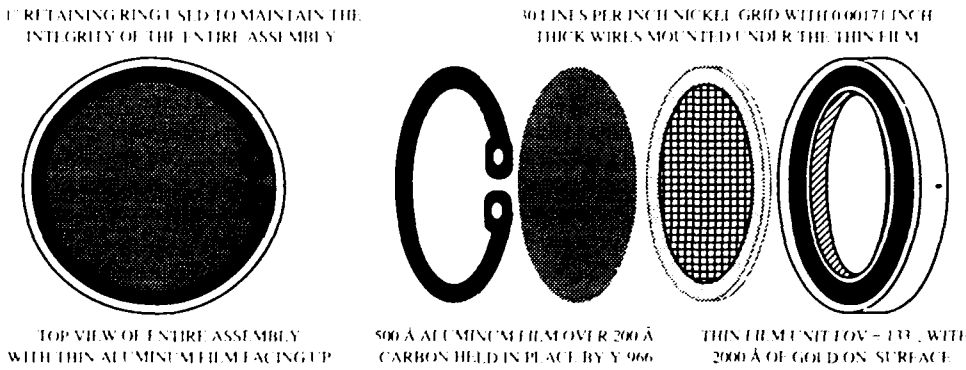


Fig. 2. Exploded View of the BUSSL Impact Uinit Flown on STS missions.

STS-44, STS-46 and other STS Films

Once the durability of the thin films and the integrity of the mounting structure had been established by the STS-32 flight, the next STS experiments suspended ultra-thin films (thickness, T_f 0.1 μm) above an impact plate on which was sputtered 2000 Å of gold. Six identical units, fabricated at BUSSL, possess films of 500 Å aluminum deposited onto 200 Å carbon. One unit flown on STS-44 has been returned for analysis, while three units have been flown on the STS-46 mission earlier this year. The analyses on these films and impact plates have been undertaken at BUSSL and at SAIC once each of the STS missions has been completed. Although the primary objective of the STS experiments was to sample the LEO orbital debris and micrometeoroid complex, an additional design goal for these experiments was to test the survivability of an ultra-thin film with a thickness of less than 750 Å which possessed a density of less than 3.0 g/cm^3. When the ratio of the particle diameter, D_p, to the film thickness, T_f, viz., D_p/T_f, is large and the density of the material composing the film is comparable to the impacting grain ($\rho_p = \rho_f$), the fragmentation of the penetrating grain will be reduced. Consequently, large fragments of the incident grain will impact the gold-coated aluminum impact plate below the ultra-thin film.

EuReCa Experiment Films

As a consequence of the experimental experience derived during STS missions, the authors have produced and delivered experiments for the European Space Agency's European Retrievable Carrier (EuReCa 1) which will provide a nine-month exposure at 525 km for similar thin film experiments. The data to be returned by the EuReCa 1 experiment will be produced through an examination of the morphology of primary and secondary hypervelocity impact craters. Primary attention will be paid to craters caused by ejecta produced during hypervelocity impacts on different substrates, e.g., gold, aluminum, palladium, and at different angles of incidence, viz., 45°, 35°, 25°, 0°. From these data one can determine the size distribution of ejecta by means of witness plates and collect fragments of ejecta from craters by means of momentum sensitive micro-pore foam. With an established ejecta size distribution and with the determination of total momenta of each ejected particle, a velocity distribution by angle will be derived, given that the ejecta number density is a strong function of the angle taken w.r.t. the surface normal of the impact target.

EuReCa I Experimental Design

Each 100 mm x 100 mm x 8 mm unit possesses an ultra-thin aluminum film (nominal $T_f < 500$ Å) stacked above a coated substrate (Fig. 3.). The plane of each film contains 100 cm^2 of impact surface under which a Buckbee Mears (90% transmissive) grid is placed to support the ultra-thin film. Each mesh has been covered with an aluminum-coated epoxy layer nominally 5 μm thick to inhibit production of X-rays by 20keV electrons during laboratory analyses. An estimate of the trajectory of grains within the experiment can be derived from analysis of penetrations made in the thin film and impact sights. Beneath the thin film and above the substrate a network of collimating plates have been constructed. Each highly polished 0.525 mm thick 3300 aluminum plate is 100 mm long with a height of 8 mm, and possess slots so that itcan interlock with perpendicular plates. These divisions insure that grains whose velocity vectors make a large angle with respect to the surface normal of the 500 Å film will not impinge on another cell but will impact the witness plates of a specific cell or be stopped by a thin film. The 3300 aluminum witness plates will also record the demise of "barely" penetrating grains. The underside of each thin film will be investigated to assess the constituents of debris clouds deposited on each thin film. The primary function of the 3300 aluminum witness plates near the substrate will be to record the ejecta produced when a hypervelocity grain encounters a semi-infinite stopping plate, viz., the substrate, which has been coated with 2000 Å of gold. Each portion of the substrate surface need not be normal to the particle's incident direction. In fact, since the grains which penetrate the film will be directional, the effects of oblique hypervelocity impacts can be examined using the orbital debris and micrometeoroid complex. A maxmium angle of 45° with respect to the substrate surface normal has been accommodated in the design of several of the cells.

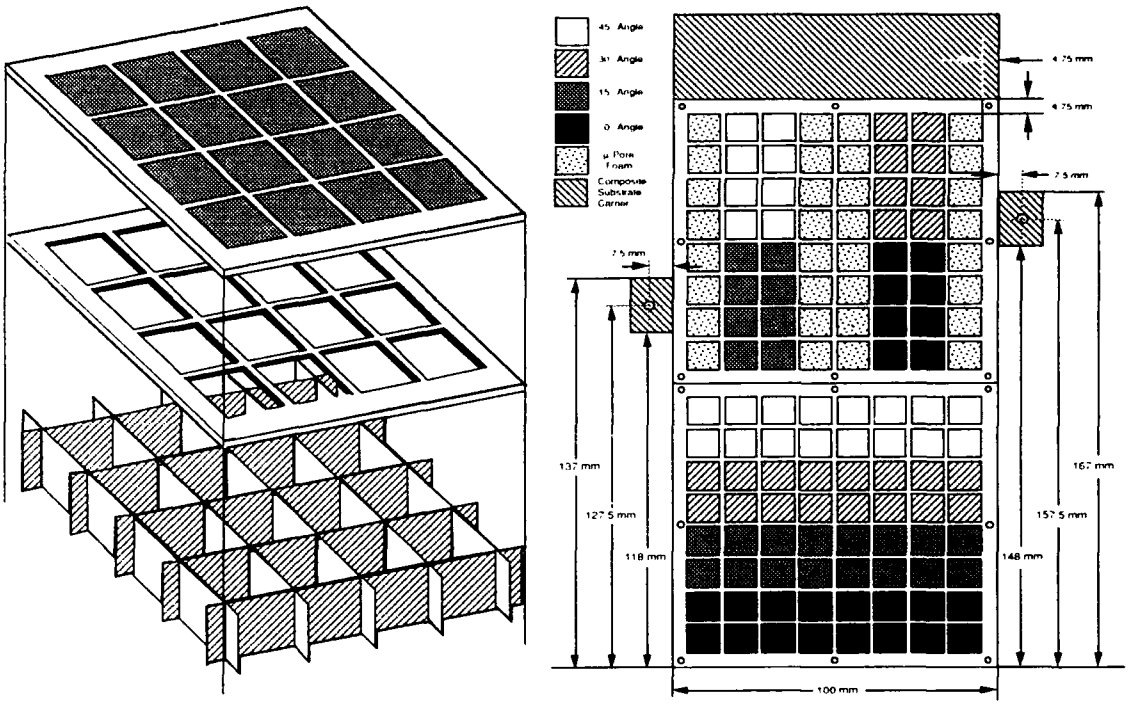


Fig. 3. BUSSL hypervelocity impact experiment flown on EuReCa 1 - TiCCE.

EuReCa I Scientific Objectives

Few laboratory hypervelocity impact experiments have investigated the mechanisms of ejecta creation. Consequently, a significant uncertainty attends predictions of what effects high-speed ejecta can have on surfaces lying near the site of a hypervelocity impact. For this reason, the effect on materials which will be incorporated into the design of future Earth-orbiting vehicles needs to be investigated by exposure to long-duration space flight conditions. This experiment has been devised to afford opportunities to assess a wide range of the dynamics of ejecta created by hypervelocity impacts on various substrates. Experimental data suggest that an oblique angle hypervelocity impact can create much more ejecta particles than normal

incidence impacts, and that the velocity distribution of these ejecta particles will be skewed toward higher values. Therefore, ejecta created in oblique impacts will transfer a significant portion of the impactor's kinetic energy to the surrounding structures. The effects of this energy transfer can be examined through a characterization of the morphological properties of impact craters on witness plates using a Scanning Electron Microscope (SEM) and a digital image processing system. In order to examine this phenomenon further, there is a need for an experiment which can capture hypervelocity ejecta so that an ejecta size and velocity distribution may be derived from a non-destructive study. The effects which a variation in the density of the substrate might have on ejecta production must also be investigated. Hydrodynamic and molecular dynamics computer programs developed by BUSSL will assist in theoretical establishment of relevant hypervelocity impact parameters for the full regime of impact events from ultra-thin film penetrations to semi-infinite targets composed of mixed material systems, viz., metallic surface evaporated onto a substrate.

COMPUTER SIMULATIONS OF THIN FILM PENETRATION

During the decades ahead a significant amount of material which has been exposed to the LEO environment will be returned for analysis. Interpretation of the evidence presented by these materials will require extensive knowledge concerning the failure modes of similar materials subjected to hypervelocity impacts. An accurate assessment of the properties of objects which might have created the features evident on the returned materials will insure that an exact "picture" of the orbital debris and micrometeoroid population can be developed. To this end, extensive experimental investigations have measured the penetration parameters of several types of metallic substances in the velocity and size regimes commensurate with that of Interplanetary Dust Particles (IDPs) and Orbital Debris. Through numerous hypervelocity impact investigations, Baylor University Space Science Laboratory (BUSSL) researchers have accumulated experience which has been applied to hydrodynamic computer program development and the utilization the multi-dimensional hydrodynamics code CTH (McGlaun, S.L. Thompson, and M.G. Elrick, 1990; Thompson and Lauson, 1984) produced by Sandia National Laboratory. Primarily, CTH will be used to investigate the relationship between the particle diameter, D_p, and the diameter, D_h, of the hole created in an aluminum thin film 500 Å thick (T_f) for relevant particle sizes, densities and velocities. The results of these CTH runs will be employed to analyze the penetration parameters of the thin films flown on STS and EuReCa.

EMPIRICAL ESTIMATIONS OF PENETRATION PARAMETERS

Extensive experimental work has established several empirical relationships (McDonnell, Carey, and Dixon, 1984; Carey, McDonnell, and Dixon, 1985) which describe the hypervelocity impact event of thin film penetration. Interpretations of the solutions derived by use of CTH must be substantiated by a clear connection with parameters derived by experiment. Through by no means an exhaustive list of penetration equations, the four listed below are representative equations of the empirically derived penetration limits for thin films. One important aspect about these equations to notice is the apparent continuity between early work dating back to 1965 and even the most recent empirical equations.

$$\frac{T_f}{D_p} = 0.57 \; D_p^{0.056} \; \varepsilon^{-0.056} \left(\frac{\rho_p}{\rho_T}\right)^{0.5} \; V_p^{0.875} \; ; \qquad \text{Fish \& Summers (1965)}$$

$$\frac{T_f}{D_p} = 0.635 \; D_p^{0.056} \; \rho_p^{-0.056} \; V_p^{0.67} \; : \qquad \text{Cour-Palais (1979)}$$

$$\frac{T_f}{D_p} = 0.772 \; D_p^{0.2} \; \varepsilon^{-0.06} \; \rho_p^{0.73} \; \rho_T^{-0.5} \left(V_p \cos\alpha\right)^{0.88} \; ; \qquad \text{Pailer \& Grün (1980)}$$

$$\frac{T_f}{D_p} = 0.833 \; D_p^{0.056} \left(\frac{\rho_p}{\rho_T}\right)^{0.476} \left(\frac{\sigma_{Al}}{\sigma_T}\right)^{0.134} \; V_p^{0.738} \; ; \qquad \text{McDonnell \& Sullivan (1992)}$$

Each of these four penetration equations have been plotted versus velocity in Fig. 4. where the material being penetrated possesses the properties of the BUSSL thin film experiment.

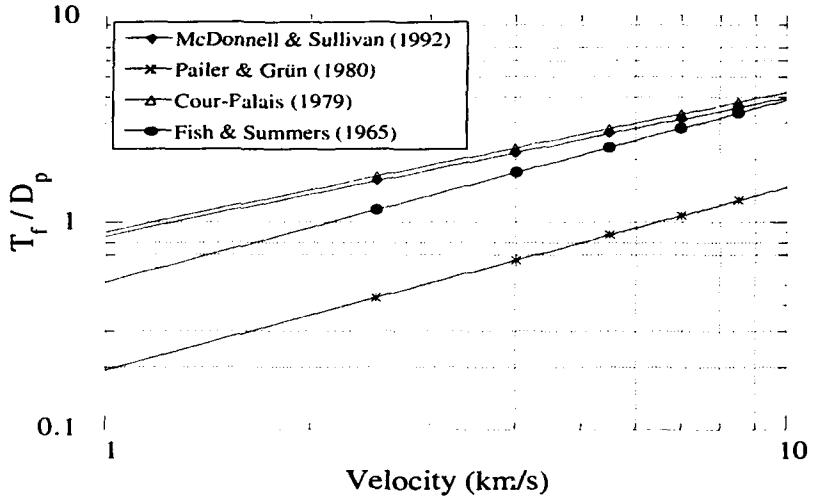


Fig. 4. Plots of thin film penetration equations for the velocity of 7 km/s.

In order to analyze by empirical means the penetration parameters of thin films like those flown on STS and EuReCa, one may utilize the Fish-Summers (Fish and Summers, 1965) penetration formula. Given that the thickness of the metallic foil is 5.00×10^{-6} cm, density of 2.7 g/cm^3, and velocity of 7 km/s, then the minimum mass which could penetrate the thin film would be:

$$T_f = K\ r_p^{0.148}\ M_p^{0.352}\ V_p^{0.667} \text{ or } M_p = \left[\frac{T_f}{K\ r_f^{0.148}\ v_p^{0.667}}\right]^{2.84} = 2.2 \times 10^{-15}\,\text{g},$$

where $K = 3.56 \times 10^{-4}$ *for aluminum. A recent empirical equation reported by* McDonnell (McDonnell and Sullivan, 1992) which gives a measure of the penetration limits for metallic films exposed to the LEO orbital debris and micrometeoroid complex can be used to derive the following penetration mass limit. These mass calculations suggest that the thin films can be penetrated by a grain which possesses a mass greater than a one-hundredth of a picogram. Using the aforementioned equation one finds that:

$$D_p = \frac{T_f}{0.833}\left[\frac{\rho_T}{\rho_P}\right]^{0.476}\left[\frac{\sigma_t}{\sigma_0}\right]^{0.134} v_p^{-0.738} = 3.82 \times 10^{-7}\text{m};\ M_p = 7.91 \times 10^{-14}\text{g}.$$

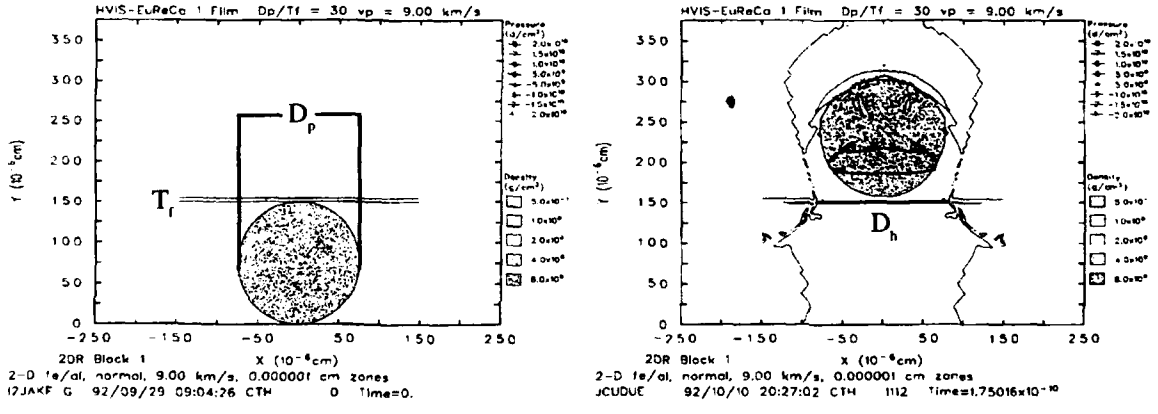


Fig. 5. CTH output to depict the measurement of a film thickness, T_f, a particle diameter, D_p, and a hole diameter, D_h for a thin film penetration at a velocity of 9 km/s.

Of particular interest in these investigations is a specific empirical form which relates penetration hole size with the diameter of the penetration hole. This experimentally derived equation for the description of the

penetration relationship for Iron projectiles impacting aluminum films of various thicknesses was developed by Carey, McDonnell, and Dixon equation (CMD) (Carey, McDonnell, and Dixon, 1985). The Carey, McDonnell & Dixon (CMD) empirical equation has been compared with the results of computer simulation of hypervelocity impacts and has been plotted in the following graphs for various velocities of interest for surfaces flown in LEO.

$$\frac{D_h}{D_p} = 1 + 1.5 \left(\frac{T_f}{D_p}\right) v_p^{0.3} \left(\frac{1}{1 + \left(\frac{T_f}{D_p}\right)^2 v_p^{-n}}\right) ; \text{Where } n = 1.02 - 4 \exp\left(-0.9\, v_p^{0.9}\right) - 0.003\,(20 - v_p)$$

Table 1. Summary of Computer Generated Hypervelocity Impacts§

	Aluminum on Aluminum			Alumina on Aluminum			Iron on Aluminum		
Dp / Tf	Dh (Å)	Dh / Tf	Dh / Dp	Dh (Å)	Dh / Tf	Dh / Dp	Dh (Å	Dh / Tf	Dh / Dp
30	15672	31.34	1.045	15772	31.54	1.052	15900	31.80	1.060
25	13570	27.14	1.085	13657	27.31	1.093	13806	27.62	1.105
20	11493	22.98	1.149	11567	23.13	1.157	11418	22.84	1.142
15	9911	19.82	1.322	9732	19.46	1.298	9234	18.47	1.231
10	7687	15.37	1.537	7500	15.00	1.500	7027	14.05	1.405
7.5	5970	11.94	1.592	5807	11.61	1.549	5689	11.38	1.517
5.0	5040	10.08	2.016	4896	9.79	1.958	4239	8.48	1.696
4.0	3970	7.94	1.985	4148	8.30	2.074	———	—.—	—.——
3.0	3230	6.46	2.153	3304	6.61	2.203	3526	7.05	2.351
2.0	2300	4.62	2.300	2234	4.68	2.234	2435	4.87	2.435
1.0	1674	3.35	3.348	1689	3.38	3.378	1704	3.41	3.408
0.75‡	360	.72	.960	———	—.—	—.——	———	—.—	—.——

§ Summary of the CTH computer simulations of normal incidence 7 km/s hypervelocity impacts,
‡ Only for Aluminum on aluminum are there data for the marginal pentrating event.

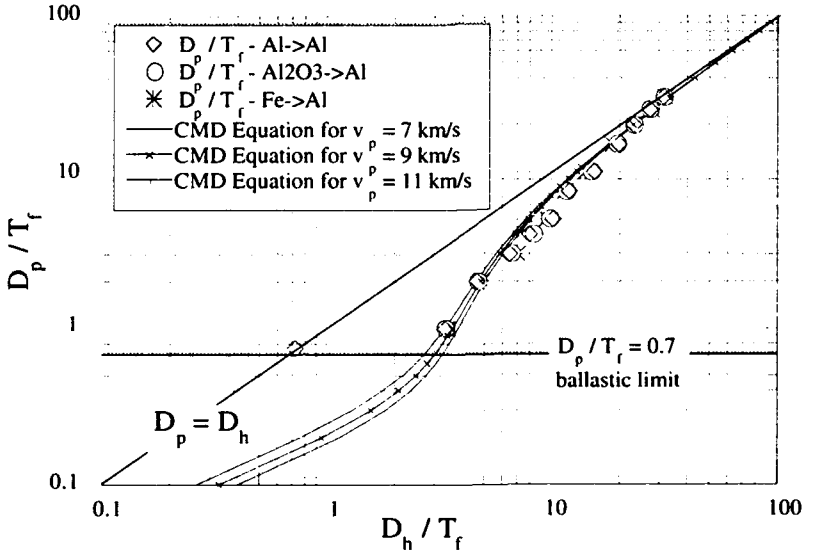


Fig. 6. Plots of values from Table 2. which illustrate the CTH solutions for various sizes and densities of particles. To compare the CTH calculations with the CMD equation for velocities of 7, 9, and 11 km/s, the equations are also plotted.

Table 2. Summary of Computer Generated Hypervelocity Impacts§

	Alumium on Aluminum			Alumina on Aluminum			Iron on Aluminum		
Dp / Tf	Dh (Å)	Dh / Tf	Dh / Dp	Dh (Å)	Dh / Tf	Dh / Dp	Dh (Å	Dh / Tf	Dh / Dp
30	16165	32.33	1.078	16275	32.55	1.085	15918	31.84	1.061
25	14135	28.74	1.130	14215	28.43	1.137	13910	27.82	1.113
20	11955	23.91	1.196	12060	24.12	1.206	11729	23.46	1.173
15	9896	19.79	1.319	———	—.—	—.——	9708	19.42	1.294
10	8000	16.00	1.600	———	—.—	—.——	7506	15.01	1.501
7.5	6150	12.30	1.640	6300	12.60	1.680	5895	11.79	1.570
5.0	5074	10.15	2.030	5373	10.75	2.149	4511	9.02	1.805
4.0	4632	9.26	2.320	4812	9.62	2.410	4300	8.60	2.150
3.0	4030	8.06	2.686	4271	8.54	2.850	3790	7.58	2.530
2.0	3450	6.90	3.450	3609	7.22	3.610	3338	6.68	3.340
1.0	2520	5.040	5.040	2647	5.29	5.290	2692	5.383	5.383

§ Summary of the CTH computer simulations of normal incidence 9 km/s hypervelocity impacts.

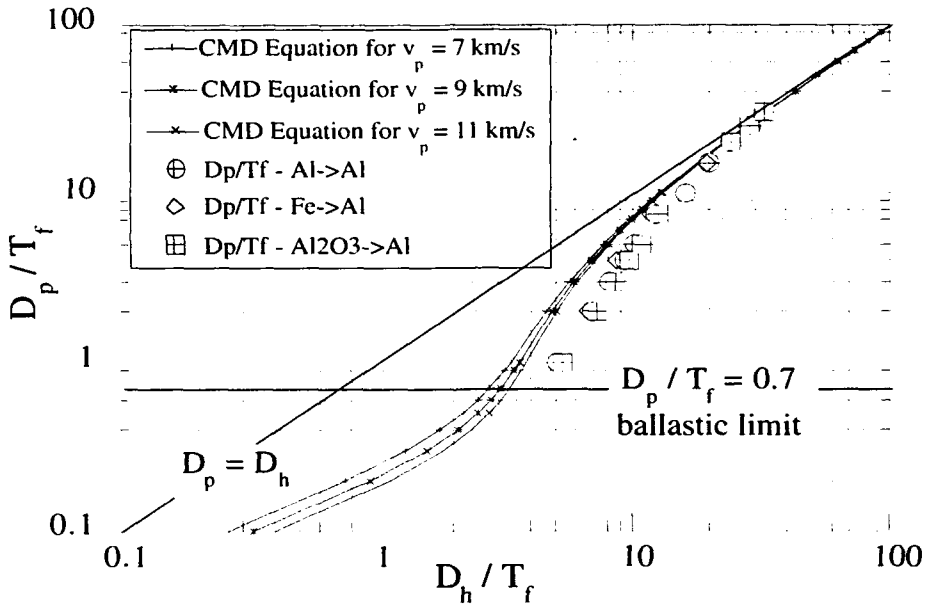


Fig. 7. Plots of values from Table 2. which illustrate the CTH solutions for various sizes and densities of particles. To compare the CTH calculations with the CMD equation for velocities of 7, 9, and 11 km/s, the equations are also plotted.

CONCLUSIONS

A primary goal remains to establish by theoretical and experimental means the limit for the hole-growth in an ultra-thin film which has been penetrated by a hypervelocity impact. To ascertain that the maximum hole-growth has occurred, the computer run-time limit has been scaled to film thickness, projectile velocity and diameter so that the experiment length will be comparable to three times the particle penetration time. Complete penetration by the particle will have been achieved when the pressure and density parameters indicate the full attenuation of the shock wave in the target and when the physical dimensions of the hole in the theoretical calculation no longer increase (Lagrangian tracer points will no longer be in motion relative to the normal impact components). Data from two-dimensional (2D) computer simulations of the hypervelocity impact events (Table 1 and Fig. 6; Table 2 and Fig. 7) which penetrate the STS and the EuReCa

l thin films conform to a high degree with CMD equation for all densities tested. The CMD relationship between the particle diameter, D_p, and the diameter, D_h, of the hole created in a 500 Å aluminum thin film (T_f) for relevant particle and film parameters when compared with other thin film penetration data, is found to agree. The CMD relationship will be compared with experimentally derived penetration data as well as with further CTH computer simulations at higher velocities, i.e., 11, 15, 19, and 23 km/s, where with higher velocity a divergennce between CTH calculations and the CMD equation is suspected for the low D_p/T_f ratio cases. The extension of CTH hypervelocity impact simulations is warranted by the success of the CMD equation in the preliminary analyses. The good agreement of the CMD relationship for low hypervelocity suggests that the CMD equation mayu be may be used to analyze *in situ* data produced by thin film experiments flown in LEO and to determine the size distribution of particles which penetrate the thin films.

REFERENCES

Carey, W. C., J.A.M. McDonnell, and D.G. Dixon (1985). An empirical penetration equation for thin metallic films used in capture cell techniques. Properties and Interactions of Interplanetary Dust , 85th Proceedings of IAU.

Cour-Palais, B. G. (1979). Space vehicle meteoroid shielding design. The Comet Halley Micrometeoroid Hazard, ESA S-153.

Fish, R.H., and J.L. Summers (1965). The effect of material properties on threshold perforation. Proc. Seventh Hypervelocity Impact Symposium, Vol. 6.

McDonnell, J.A.M., W. C. Carey, and D.G. Dixon (1984). Cosmic dust collection by the capture cell technique on the Shuttle Pathfinder mission, Nature 309.

McDonnell, J.A.M., S.P. Deshpande, S.F. Green, P.J. Newman, M.T. Paley, T.J. Stevenson, and K. Sullivan (1990). First results of particulate impacts and foil perforations of LDEF, In Proceedings of the XXI Lunar and Planetary Science Conference.

McDonnell, J.A.M., and K. Sullivan (1992). Hypervelocity impacts on space detectors: decoding the projectile parameters, In Proceedings of the Hypervelocity Impacts in Space Symposium.

McGlaun, J. M., S.L. Thompson, M.G. Elrick (1990). CTH: A Three-Dimensional Shock Wave Physics Code, Int. J.of Impact Engng, Vol. 10.

Pailer, N., and E. Grün (1980). The penetration limit of thin films, Planetary Space Science, Volume 28.

Thompson, S. L., H.S. Lauson (1984). Improvements in the Chart D radiation-hydrodynamic CODE V: 1972/1973 modifications, Sandia National Laboratory Report, SC-RR-71 0714.

Int. J. Impact Engng Vol.14, pp.739–749, 1993
Printed in Great Britain

0734-743X/93 $6.00+0.00
© 1993 Pergamon Press Ltd

RESPONSE OF WOVEN CERAMIC BUMPERS TO HYPERVELOCITY IMPACTS

L.E. Thompson and M.S. Johnson
McDonnell Douglas, Huntington Beach, CA

ABSTRACT

The multi-shock shield concept devised by Crews and Cour-Palais,[1] composed of multiple ceramic cloth bumper layers and an aluminum back sheet, was used to investigate the response of woven ceramic bumpers to a hypervelocity impact. Observations made on past hypervelocity impact test data show that areal density is the most important bumper characteristic for initially breaking up solid particles. Our research has shown that once the solid particle has been shocked into a cloud of liquid and vapor, the weave pattern of the cloth bumper can influence the ability of the shield to absorb and contain the energy of the debris cloud.

To design a weave that will absorb particle energy more efficiently, we need to understand the micromechanics of the interaction between the debris cloud and the cloth bumper. In this paper we discuss our observations on the response of a ceramic cloth bumper to a hypervelocity impact and the failure mode occurring at the individual strand level.

SYMBOLS

Δs	spacing between bumper layers
t	thickness of each bumper layer
v	velocity of incoming projectile
R_f	weave ratio, number of strands per inch in the warp direction divided by the number of strands per inch in the fill direction
$R_{h_{ave}}$	average ratio of the length of the hole in the fill strand direction divided by the length of the hole in the warp strand direction
a	distance between cross-over points, unsupported strand length
A_d	areal density with units of g/cm^2

11/10/92

INTRODUCTION

The conventional approach to shielding against micrometeorites has been to use a Whipple shield.[2] This shield is made of two aluminum sheets placed a distance apart. The first sheet is referred to as the "bumper." Its function is to intercept the incoming projectile, shocking the particle and causing it to vaporize, melt, and/or fracture, forming a debris cloud made up of one or more of these states. The resulting debris cloud then expands and impacts the second sheet. The second sheet is designed to resist the impulse created by the impact of the debris cloud. This two-layer shield concept is lighter in weight than a single-wall shield that provides an equivalent measure of protection.

A new shield called the multi-shock shield,[1] devised by Jeanne Crews of NASA-JSC and Burt Cour-Palais of McDonnell Douglas Corporation (MDC)-Houston, offers 30% to 50% weight savings over the conventional Whipple

shield. The multi-shock shield is a lightweight shield consisting of multiple layers of thin bumper elements spaced a small distance apart (Δs), to repeatedly shock the incoming projectile to a higher energy state (see Fig. 1).

In our research, we investigate the interaction of the liquefied or vaporized particle debris cloud with woven ceramic bumpers at the individual strand level. We have modified conventional fabrics to improve their ability to withstand the impact of the debris cloud.

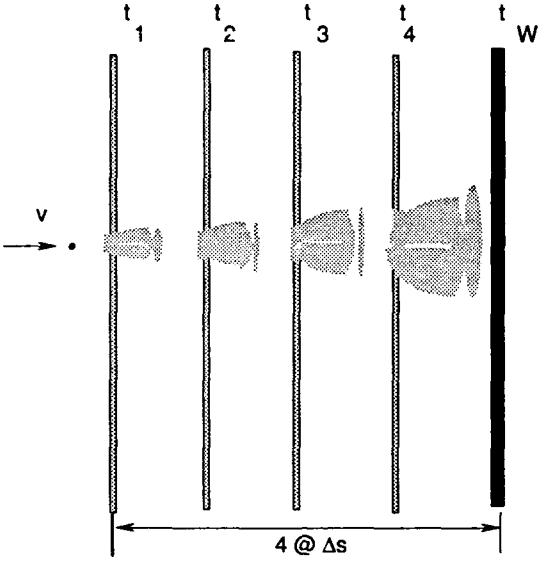


Fig. 1. Multi-shock shield concept.

OBSERVATIONS OF PREVIOUS HYPERVELOCITY IMPACT TESTS

We reviewed past tests performed on multi-shock shields at the Hypervelocity Impact Test Facility (HIT-F) at NASA-JSC. These shields used Nextel and Astroquartz ceramic cloths for the bumper layers. We observed that the hole produced in the ceramic cloth bumper layers of the shield was either square or rectangular in shape. Further investigation of the bumpers revealed that fabrics with nearly equal numbers of strands in the warp and fill direction produced a square hole (Nextel AF-26) and that fabrics with an unequal number of strands in the warp and fill directions produced a rectangular hole (Nextel BF-22, BF-40, and Astroquartz II). The hole size produced in these tests was measured to be the length of the damaged area, up to the first unbroken strand in both warp and fill directions. We found these observations to be unique to cloth bumpers. Tests run on rigid, isotropic bumpers (aluminum, tantalum, etc.) produce uniform circular damage patterns in the bumper layers.

The cloth bumpers tested at HIT-F all had a five-harness satin weave (the weave pattern follows the form: over four strands and under one) but had different numbers of strands per inch in the warp and fill strand directions. Table 1

Table 1. Characteristics of cloth bumpers

Fabric Name	Type	Areal Density (gm/cm^2)	Weave Pattern	R_f	$R_{h_{max}}$	Hole Shape
Nextel AF-26	5-H Satin	0.0435	29 strands/in. warp 26 strands/in. fill	1.11	1.07	Square
Nextel BF-22	5-H Satin	0.0474	33 strands/in. warp 21 strands/in. fill	1.57	1.40	Rectangular
Nextel BF-40	5-H Satin	0.090	32 strands/in. warp 20 strands/in. fill	1.60	1.40	Rectangular
Astroquartz II	5-H Satin	0.0663	38 strands/in. warp 24 strands/in. fill	1.58	1.41	Rectangular

prof-paper 92h0600 11 1 11 10/92

shows the characteristic weave pattern, weave ratio, areal density, average hole dimension ratio (length of the hole in the fill direction divided by its length in the warp direction), and hole shape of these ceramic cloth bumpers. The weave ratio, R_f, and the average hole dimension ratio, $R_{h_{avg}}$, are approximately the same for each type of cloth bumper tested, possibly showing that the weave of the bumper affects the shape of the hole created.

Nextel BF-22, BF-40, and Astroquartz II fabrics have weaves with more strands per inch in the warp direction than in the fill direction, and the holes produced in all these fabric bumper layers was always rectangular in shape. Further investigation of the rectangular hole found the longer side of the hole always to be in the warp strand direction. This is illustrated in Fig. 2. We feel that these observations imply that the orientation of the rectangular hole created in the bumper is dependent on the orientation of the fabric.

These observations also lead us to believe that the debris cloud is causing the bumpers to fail at the individual strand locations. The strands are failing in the area of their highest bending stress, the location where the strand bends over and under a transverse strand (Fig. 3). In a typical five-harness satin weave, a strand crosses over four strands and under one. The term "a" refers to the distance between these cross-over points, or the unsupported length of a strand. The "a" distance is greater in the warp strand direction than in the fill strand direction for fabrics BF-22 and Astroquartz, due to the weave pattern. If the strands are breaking at these cross-over points, then this could be the reason why these bumpers exhibit a rectangular damage hole. The AF-26 fabric has approximately the same "a" distance in both the fill and warp direction, therefore producing a square damage hole.

By investigating each bumper layer, one can identify the unsupported strand length "a" occurring around the damaged hole. Fig. 2 shows the front and back face of the Astroquartz II bumper No. 2, test A1004. The rectangular hole is evident. This bumper shows that each broken strand has multiple fiber failures at the same location. The fibers in the bundles are approximately of length "a" and can be seen around the hole's perimeter. In all these tests, the longer side of the rectangular hole is oriented in the warp strand direction. Again, we feel that these tests imply that the orientation of the hole created in the bumper layer is dependent on the orientation of the fabric.

The area of the hole created in each bumper layer for all the Nextel BF series and Astroquartz shots tested under McDonnell Douglas Independent Research and Development are shown in Fig. 4. The shot configurations consist of four layers of Nextel BF-22 (each bumper A_d = 0.0474 g/cm^2), three layers of Astroquartz (each bumper A_d = 0.0663 g/cm^2), and a three-layer Nextel configuration consisting of two layers of BF-22 and a layer of BF-40 (A_d = 0.090 g/cm^2). All shots were made with a 0.125-in.-diameter aluminum sphere at a velocity of approximately 6.4 km/sec. The horizontal axis shows the total cumulative bumper areal density of the shield. This plot shows a linear relationship between the area of the hole created in each bumper layer and the cumulative bumper areal density. Therefore, as you go from one bumper layer to the next, the damage hole area increases linearly. We feel that the size of the hole created in each bumper is related to the energy level of the particles and the size of the expanding debris cloud. In Fig. 4, the size of the debris cloud increases with each bumper layer, showing that the debris cloud is still expanding after four layers. Damage done to each witness plate (aluminum back plate) consisted of an indentation but no penetration.

For breaking up solid particles, the bumper's areal density and material type are important bumper characteristics, but for containing the trailing debris cloud, the weave pattern of the fabric bumper is important. Review of previous multi-shock shield test results has led us to believe that the weave of the ceramic cloth bumper affects the shape of the hole produced by a hypervelocity impact. We also believe that the size of the hole is determined by the size of the debris cloud. By modifying the weave and therefore the dimensions of the hole, we can produce a bumper that more closely matches the expanding debris cloud. This modification will allow for the design of a bumper that reacts more efficiently to the shape and size of the resulting debris cloud.

The strength of a strand plays a great role in absorbing the impact energy of the projectile. The weak points in a strand are where it crosses over or under the transverse strand, the area of the highest bending stress. It is at these locations that the strands are breaking prematurely in bending (see Fig. 3).

TEST CONFIGURATION

The weaves of BF-22 and AF-40 Nextel fabric were modified for testing at HIT-F, and the bumpers were modified by manually removing every other strand in the fill direction. This doubled the "a" distance and reduced the bending stress concentrations (see Fig. 3). Reducing the bending stress and increasing the unsupported length of the strand allow increased tensile loads prior to strand failure. This loading takes advantage of the relatively high tensile strength of the strand as opposed to its lower bending strength. The increased tensile loads in the strand allow dissipation of energy along its length, not just at the debris cloud impact location, and also allow a larger area of the fabric to react to the impact, increasing the size of the hole formed by the debris cloud. Each subsequent bumper layer then absorbs more particle energy through shield displacement.

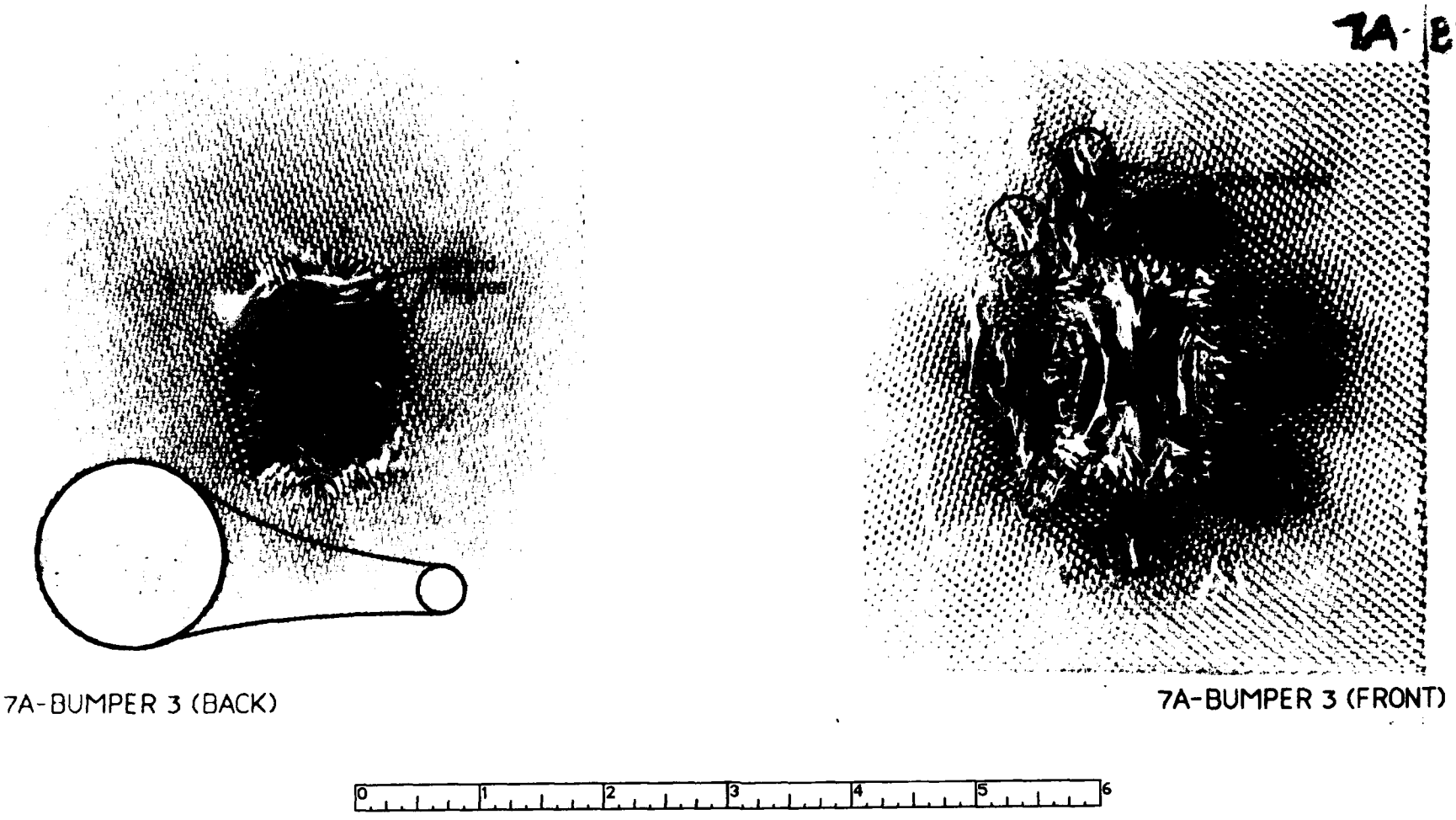


Fig. 2. Front and back face of Astroquartz II bumper layer No. 2.

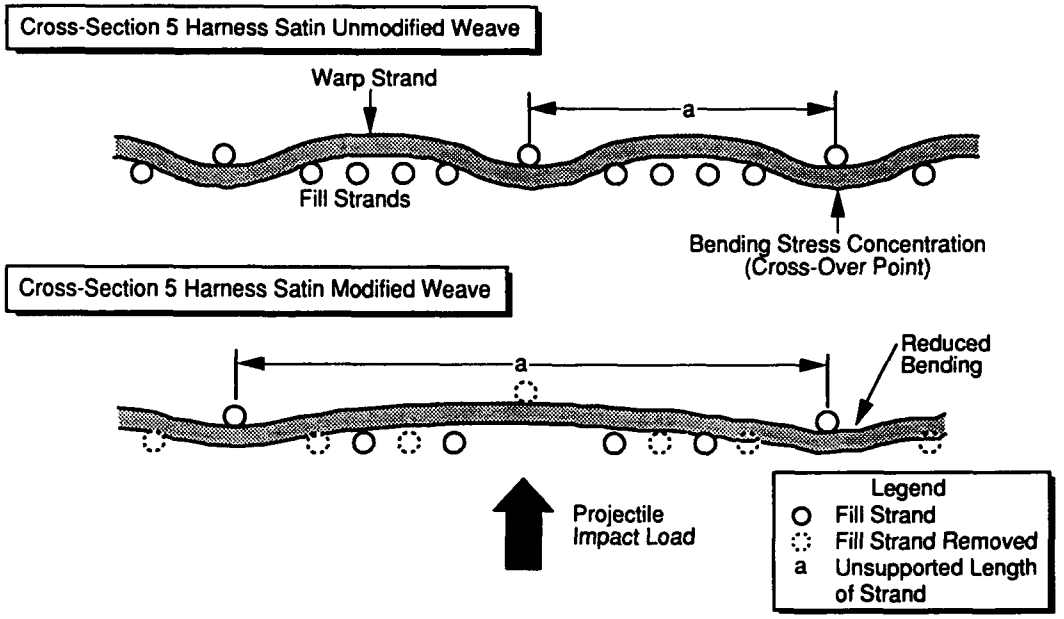


Fig. 3. Cross-section of individual strands in an unmodified and modified five-harness satin weave.

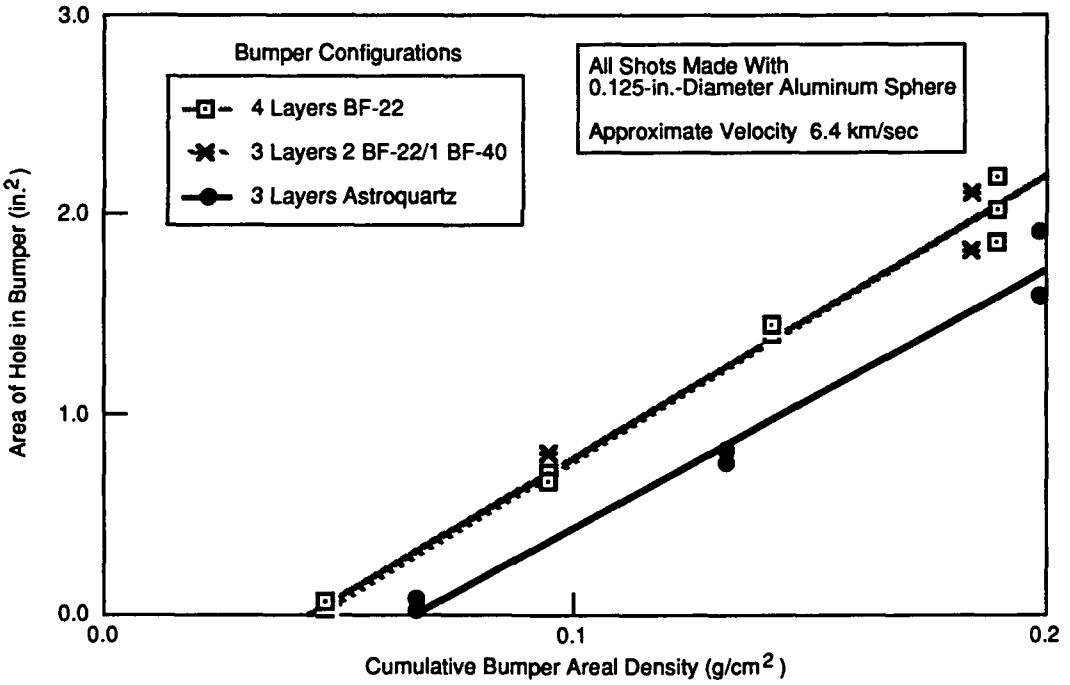
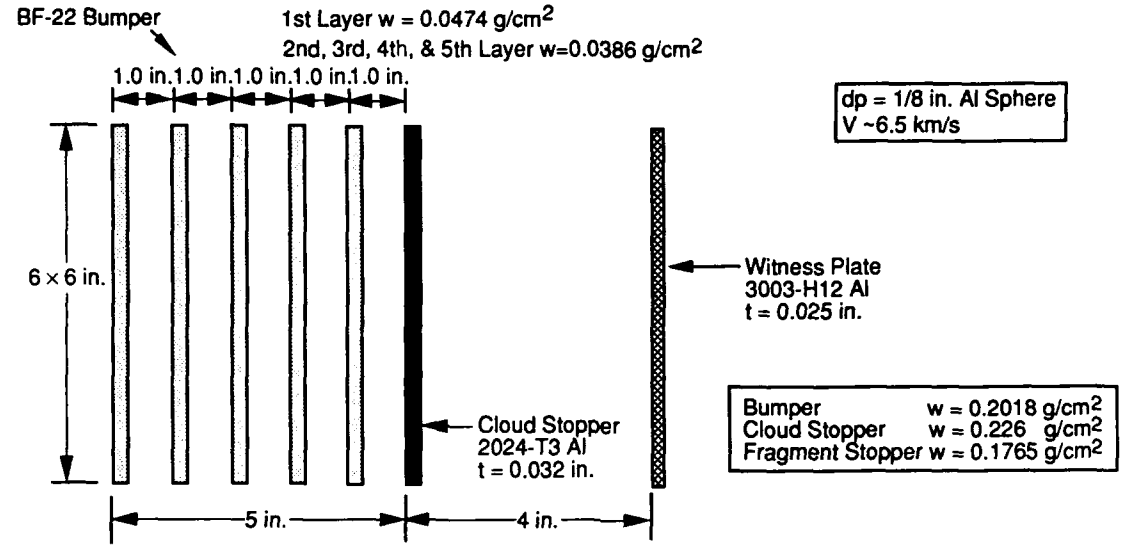


Fig. 4. Linear relationship between the cumulative bumper areal density hole and the area of the hole created in each bumper layer.

The perimeter of each 6- by 6-in. bumper layer was taped in order to stop the fabric from unraveling during handling. Each test consisted of five bumper layers placed 1 in. apart, followed by an aluminum 2024-T3 (t = 0.032 in.) back plate (see Fig. 5 and Fig. 6 for the test configuration). The back plate material and thickness were chosen in order to make a direct comparison to tests performed previously.

The removal of fill strands reduced the areal density of the bumpers. The density of the modified BF-22 fabric is 0.2018 gm/cm^2, and the density of the modified AF-40 is 0.3619 gm/cm^2.

We manually removed every other fill strand and rotated every other bumper layer in order to have the maximum number of strands interact with the impinging rectangular debris cloud.



Orientation of Bumper Layers

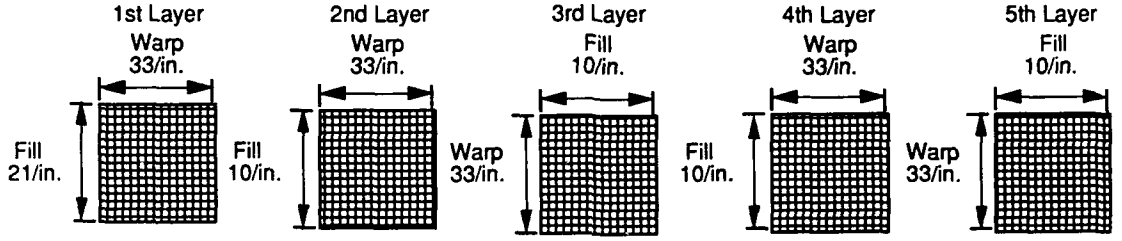
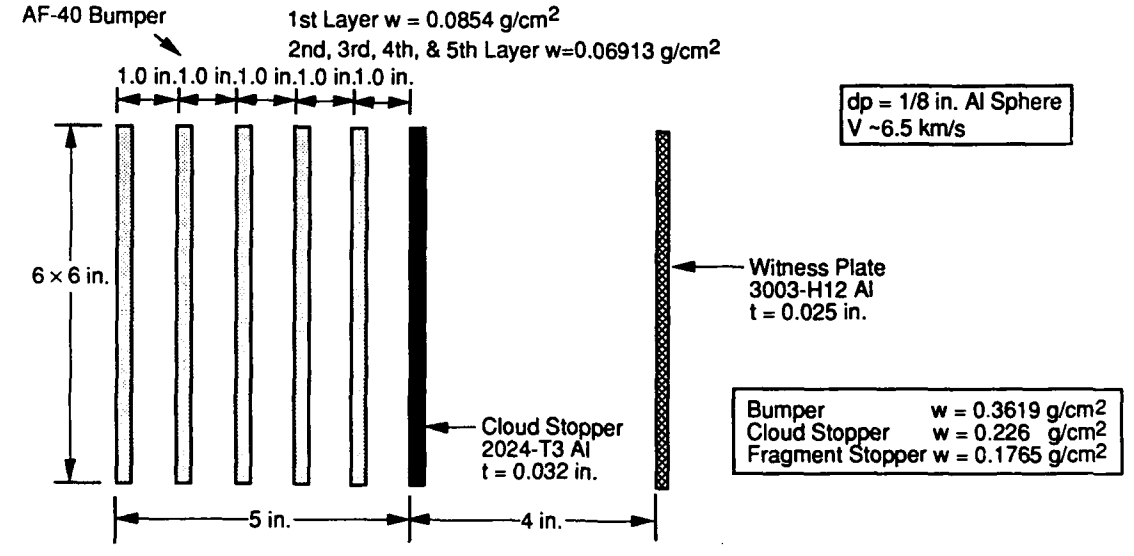


Fig. 5 Five-layer BF-22 modified bumper multi-shock shield configuration.



Orientation of Bumper Layers

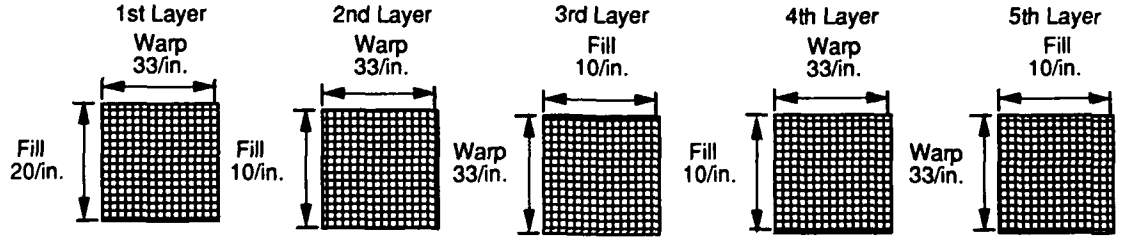


Fig. 6. Five-layer AF-40 modified bumper multi-shock shield configuration.

TEST RESULTS AND ANALYSIS OF MODIFIED SHOTS

A plot showing the area of the hole versus the bumper layer for these tests is shown in Fig. 7. A linear relationship is shown for the unmodified BF-22 test samples tested in PD 12-100, and a nonlinear relationship for the modified BF-22 shots tested.

We feel that the area under each of these curves (modified and unmodified) is a function of the amount of energy the shield needs to absorb in order to stop the incoming projectile. Earlier, we stated that the size and shape of the bumper hole was related to the size and shape of the debris cloud. We feel that the size of the hole is also a function of the energy absorbed by the strands. In the modified bumper shields tested, the first bumper layer was not modified, so that the same shocking of the particle demonstrated in the first layer of the unmodified shots would be produced.

The modified curve shows that the size of the hole in the second, third, and fourth bumpers is larger than that of the unmodified curve. It reveals that the size of the hole increases earlier than in the unmodified bumpers, possibly indicating that the debris cloud is being created earlier for a modified layer. The modified bumper is also 20% lighter than the unmodified bumper. The modified curve levels off, or plateaus, at the fourth and fifth bumper layers, showing that the debris cloud is no longer increasing in size but remaining constant. In the unmodified bumper shields, the debris cloud is still increasing at an equivalent cumulative bumper density. If the modified shield had one more bumper (a sixth layer), we feel that the size of the hole in this layer would be smaller, and eventually no hole would be formed in subsequent bumper layers because all the particle energy would be absorbed by the previous bumper layers.

The AF-40 test shots produced the same results as the BF-22 shots but also showed that the fifth (last) bumper layer produced no hole and therefore absorbed all the remaining energy of the debris cloud. A plot of the area of the hole versus bumper layer is shown in Fig. 8. We tested the AF-40 Nextel fabric because of its heavier areal density as compared to BF-22 (0.0854 gm/cm^2 as compared to 0.0474 gm/cm^2). We felt that the heavier areal density fabric would dramatically show that our hypothesis was correct: that by increasing the unsupported length of the strands, the energy of the projectile is absorbed by shield displacement (or strand displacement).

Again, Fig. 8 shows that the area of the hole created in each bumper increases with increasing layers and peaks at the third bumper layer. The area of the hole in the fourth bumper is smaller, and no hole is produced in the fifth layer. This curve shows that the debris cloud stopped growing, or peaked, at the third layer, then continued to decrease in size. No hole was created in the last bumper of the shield, but the bumper was indented or cupped (see Fig. 9). Also, the warp strands were pulled out of the taped boundary, showing strand displacement in the warp direction and

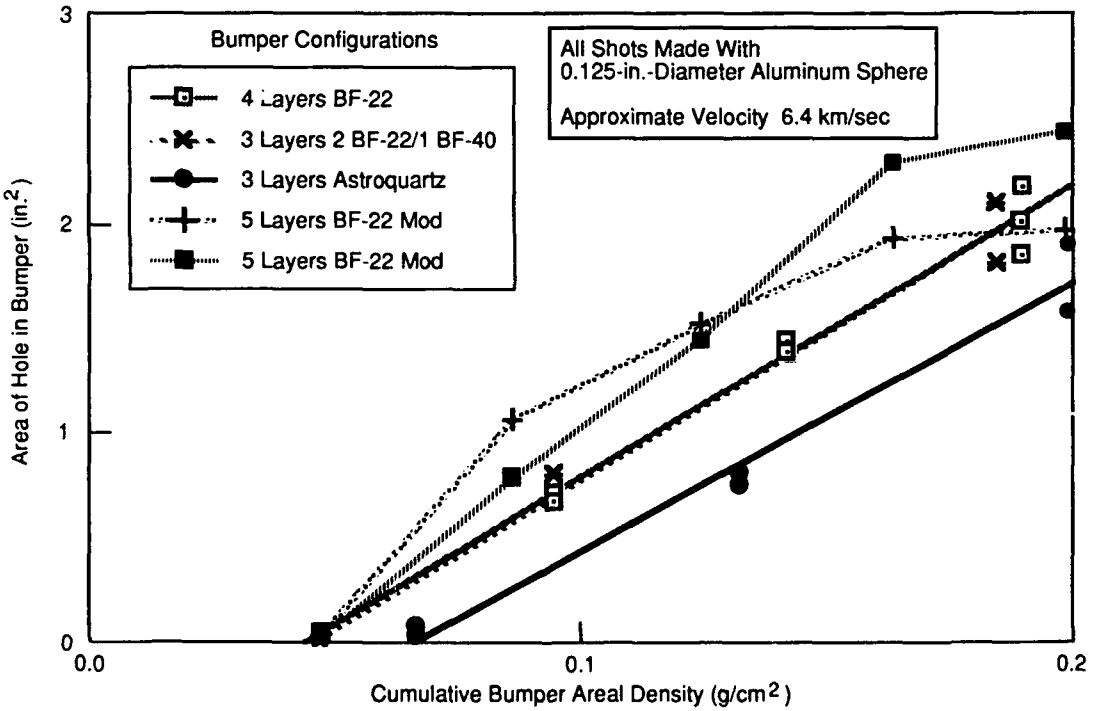


Fig. 7. Modified bumpers show a nonlinear relationship between the cumulative bumper areal density and the area of the hole created in each bumper layer.

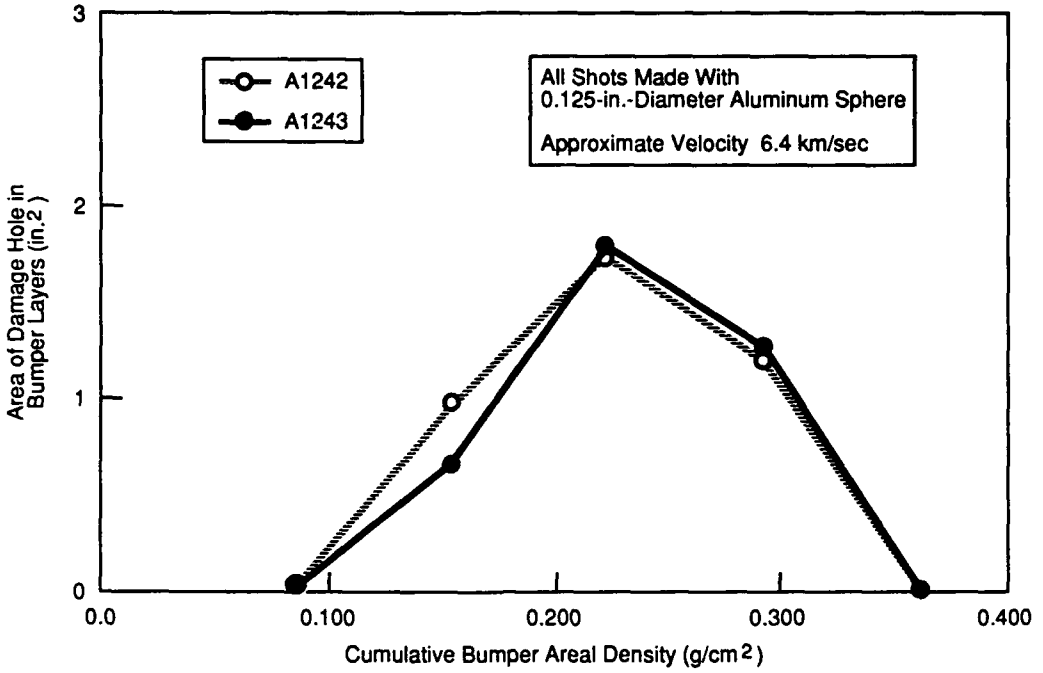
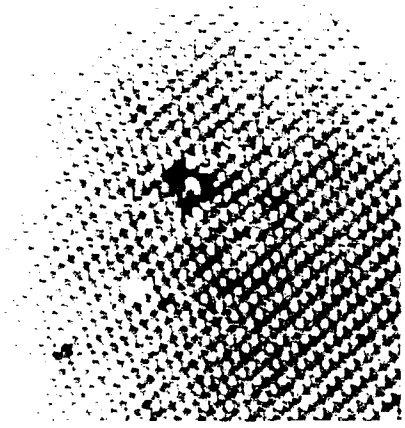
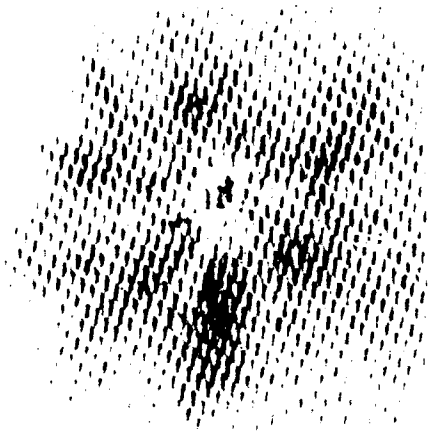


Fig. 8. AF-40 multi-shock shield absorbed all the particle energy of the debris cloud, *therefore producing no hone in the last* bumper layer.

cupping of the test sample. Strands pulled out of the tape in the warp strand direction show that the entire strand length reacted to the load and that particle energy was absorbed by loading the strands in tension.



Front

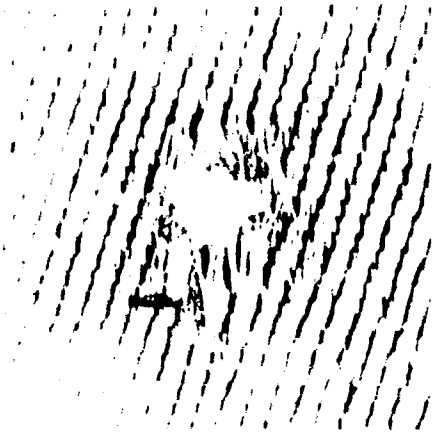


Back

Bumper Layer 1

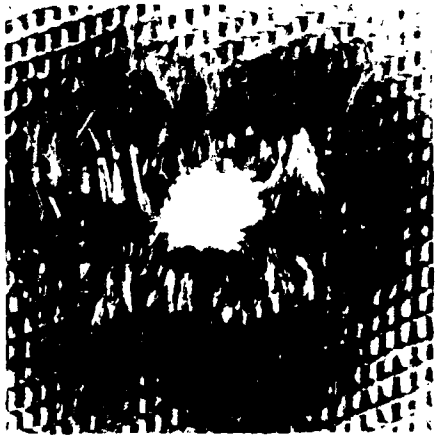


Front

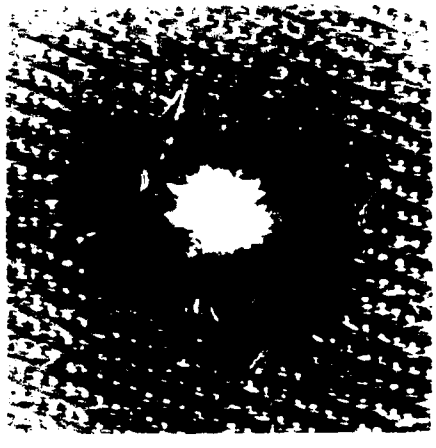


Back

Bumper Layer 2



Front



Back

Bumper Layer 3

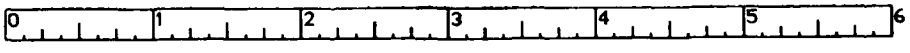
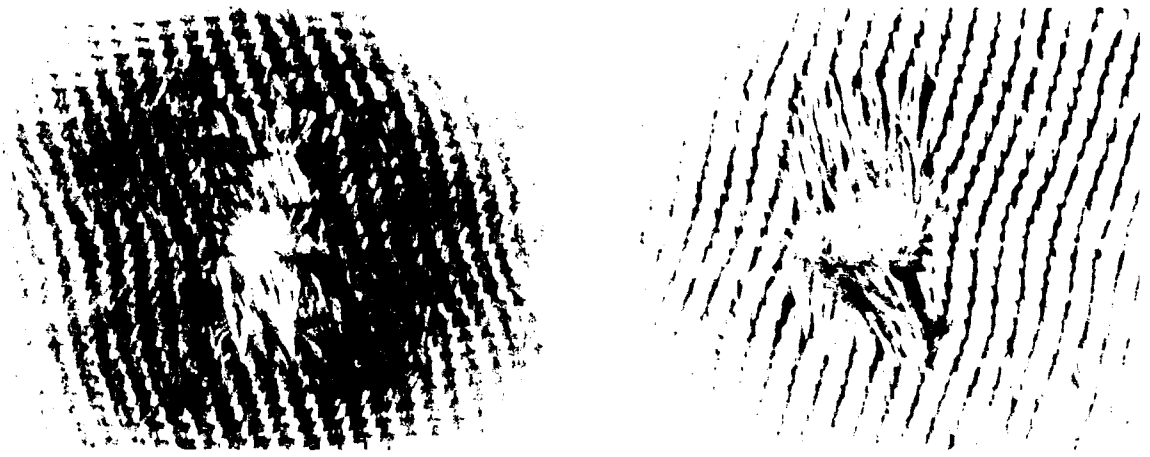


Fig. 9. Results of modified AF-40 bumper tests.



Front Back

Bumper Layer 4

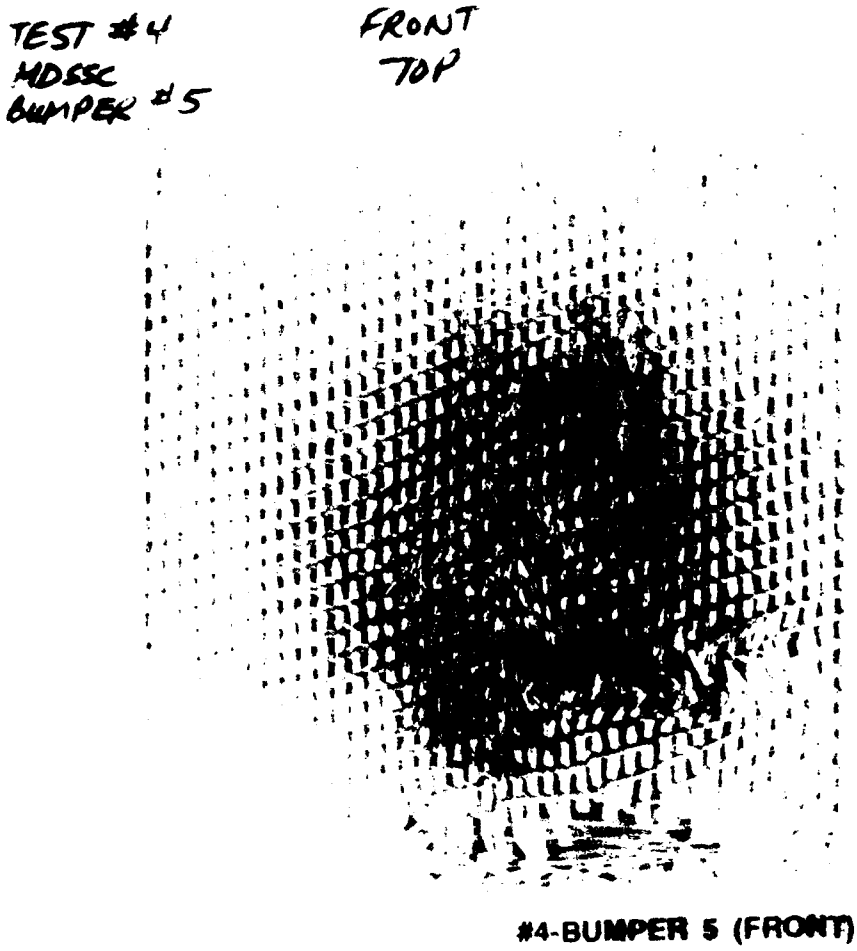


Fig. 9. Results of modified AF-40 bumper tests (continued).

CONCLUSIONS

We feel that our BF-22 shield results demonstrated that we can increase the rate at which the energy of the debris cloud is absorbed by modifying the weaves of the bumpers to reduce bending stresses in the strands.

The AF-40 tests showed that an increase in the tensile loading of the strands (Fig. 9) causes the debris cloud energy to be absorbed through displacement of the bumpers.

Woven ceramic shields tend to move when subjected to hypervelocity impacts; metal shields do not. This means that methods of ensuring shield spacing will be required to maintain proper spacing for subsequent impacts. It is also important to recognize that tension in the bumpers generated by mounting or deployment hardware will probably degrade the ability of the bumper to shield against hypervelocity impacts. Any tension preload in the strands contributes to bending stress concentrations and restricts the ability of the bumper to move with the debris cloud impact.

Larger test specimens might be required to better simulate the response of multi-shock bumpers to hypervelocity impacts. Our testing of a modified AF-40 Nextel fabric showed that the impact loads were transmitted along the length of the strands to where the ends were taped. It is easy to visualize different test results for strands that are securely fixed and for strands that are free floating.

ACKNOWLEDGMENTS

All testing done for this program was performed at NASA's Johnson Space Center Hypervelocity Impact Test Facility. We appreciate NASA's interest in this program and thank them for their work. Coordination of the testing at NASA-JSC HIT-F was done by Kim Dahl of MDC-Houston. Some of the Nextel test samples were supplied by Jack Dillon of 3M at no cost to this program. We would also like to thank Ken McClymonds of the Space Station Division of McDonnell Douglas. Observations of his 1989 test samples helped create the idea for this study.

REFERENCES

1. Cour-Palais, B. G., and Crews, J. L., "A Multi-Shock Concept for Spacecraft Shielding." Journal of Impact Engineering, Vol 10, 1990.
2. Whipple, E. L., "Meteorites and Space Travel." Astronomical Journal, Vol 52, March 1947, p 137.

Int. J. Impact Engng Vol.14, pp.751 – 761, 1993
Printed in Great Britain

0734-743X/93 $6.00+0.00
© 1993 Pergamon Press Ltd

EXPLORATORY INVESTIGATIONS OF HYPERVELOCITY INTACT CAPTURE SPECTROSCOPY

Peter Tsou* **and David J. Griffiths****

*Jet Propulsion Laboratory, California Institute of Technology
Pasadena, CA 91109
**Department of Physics, Oregon State University, Corvallis, OR 97331

ABSTRACT

The ability to capture hypervelocity projectiles intact opens a new technique available for hypervelocity research. A determination of the reactions taking place between the projectile and the capture medium during the process of intact capture is extremely important to an understanding of the intact capture phenomenon, to improving the capture technique, and to developing a theory describing the phenomenon. The intact capture of hypervelocity projectiles by underdense media generates spectra, characteristic of the material species of projectile and capture medium involved. Initial exploratory results into real-time characterization of hypervelocity intact capture techniques by spectroscopy include ultra-violet and visible spectra obtained by use of reflecting gratings, transmitting gratings, and prisms, and recorded by photographic and electronic means. Spectrometry proved to be a valuable real-time diagnostic tool for hypervelocity intact capture events, offering understanding of the interactions of the projectile and the capture medium during the initial period and providing information not obtainable by other characterizations. Preliminary results and analyses of spectra produced by the intact capture of hypervelocity aluminum spheres in polyethylene (PE), polystyrene (PS), and polyurethane (PU) foams are presented. Included are tentative emission species identifications, as well as gray body temperatures produced in the intact capture process.

INTRODUCTION

The ability to capture hypervelocity projectiles intact opened new applications in space science [Tsou et al., 1984] and hypervelocity research [Tsou, 1991]. Intact capture refers to capturing a portion of the projectile unmelted and with its original structure retained. For space science, planetary and cosmic particles at hypervelocities can be captured intact in space, in situ, and returned for detailed laboratory analyses without rendezvousing which is very costly to accomplish. Sample return offers science not possible by remote observations or in situ measurements. Being able to achieve the intact capture of fragments generated during a hypervelocity impact would offer important verification and characterization of the event. For this reason, fragment intact capture offers a new tool for hypervelocity research.

The real-time action and reaction between the projectile and the capture medium is immensely important to understanding the intact capture phenomenon, to improving the capture technique, and to developing a theory describing the phenomenon. Since a hypervelocity intact capture event is completed in less than a fraction of a millisecond, means to provide a temporal expansion of the event are desired. The pursuit of an in-depth understanding of key factors of this new intact capture

technique via spectrometry becomes a logical and needed sequence of development technology. This paper presents the exploratory results of such a temporal expansion characterization of a hypervelocity intact capture by spectrometry. A wide range of wave lengths and means of spectra acquisition were examined to determine the effectiveness of different approaches; thus, spectra in the ultra-violet, as well as the visible, have been acquired with prisms, reflection and transmission gratings, and recorded by photographic and electronic media. Qualitative understanding gained by such a spectrometry study on the intact capture process and the effectiveness of different spectra acquisition techniques are discussed.

Real-time Characterization

A hypervelocity intact capture event begins at the instant a projectile makes contact with the capture medium, and ends with the projectile resting at the end of a pointed carrot track, Fig. 1. Since the bulk of the energy dissipation occurs before the peak of the track expansion and both the projectile and the capture medium sustain the greatest physical change during this time interval, characterizing the interactions between the projectile and the capture medium material during this initial intact capture phenomenon would contribute the greatest understanding. The interactions of interest include the physical and chemical reactions of the two materials with respect to time from entry, and spatial distribution both radially and along the direction of penetration. Questions of interest are: does the projectile material react with the capture medium? how does dissipation occur? what is the instantaneous temperature of the event? are there transition species generated?

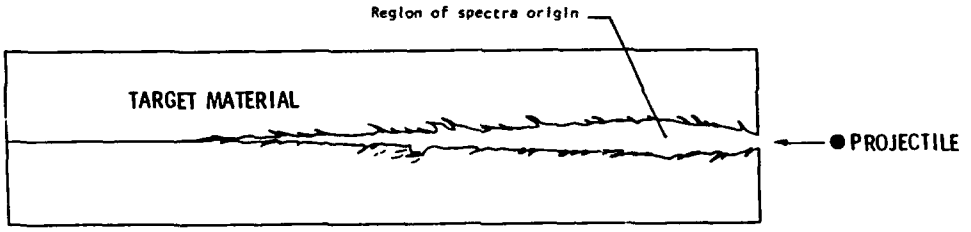


Fig. 1. Schematic illustrating typical capture track and indicating region of spectra origin.

Many real-time measurement tools have been used for hypervelocity events such as various forms of imaging; optical imaging tends to be obscured by impact flash and debris; X-ray imaging provides positional information but is restricted to discrete frames, and the number of X-ray stations is limited. Spectroscopy, can provide a spectral image representative of both temporal and spatial domains at the same time, given an understanding of opacity factors. In this regard, Jongeward and Wilson [1991] have recently shown that the acquisition of optical emission signals from hypervelocity impact can provide useful diagnostics of structured targets. Both physical and chemical reactions can be deduced from the spectroscopic images. Consequently, in order to explore the potential of spectrometry for intact capture research, a wide range of spectrum acquisition techniques and media were evaluated.

While morphological features of capture media reflect the residual effects that have taken place within the retarding medium [Tsou, 1990] they do not inform us directly of what went on during the time of capture. In order to freeze real-time response closely associated with the intact capture process, some type of temporal expansion of the event is required [Griffiths, 1989]. Visible and ultra-violet spectroscopy are capable of providing such a frozen time window, allowing acquisition of data generated during the intact capture process, itself.

Experimental Arrangements

A wide range of spectrometric arrangements were utilized to explore the best approach to acquire optical and ultraviolet of the intact capture process [Buettner, 1991]. The various methods used to gather spectral data are summarized in Table I. All of the spectral acquisition experiments were performed at the NASA Ames' Vertical Gun Range whose hypervelocity accelerator can launch projectiles from the horizontal to the vertical in six positions. Hydrogen gas is used for the second stage compression medium. Our experiments were performed in the vertical position with the target chamber typically evacuated to a pressure of 5 Torr, and the entire facility darkened to eliminate stray light. The intact capture medium is placed vertically on the base of the intact chamber. For our initial experiments, light was reflected to the spectrometer through a large rectangular camera port on the side of the chamber by means of front surface mirrors. Photographic camera shutters were left open before the experiment and shut manually in the dark, after the capture event. Electronic triggering for the diode array is taken from the last stage of the high-voltage spark gap, used for incident speed determination. In order to avoid mirrors and the camera port window, optic fibers were next used for light conduit. Since light transmission efficiency and size of the optic fibers limited the amount of light that could be directed to the spectrometer, the spectrometer was subsequently set up inside the chamber with the entrance slit positioned so that essentially the entire entry solid angle opened on to the plasma discharge path.

SPECTROMETERS

The reflection grating spectrograph, a f/1.5 stigmatic spectrograph, was developed at NASA Ames Research Center and uses a 35 mm Nikon camera as recorder [Borucki 1970]. The optics limited these spectra to the visible range of wavelengths. The spectrometer light path is shown in Fig. 2(a). The Oriel spectrographic system, multi-spec model number 77400, made use of a 1024 element diode array detector with its light path shown in Fig. 2(b). Spectra are digitized and recorded on the hard disk of the controlling computer. Transmission grating spectrometry was produced with a customed 52 mm grating mounted as a filter on a 35 mm camera. The Hilger E584, was a small ultra-violet spectrograph, using 4" x 4" film packs, and its light path is shown in Fig. 2(c).

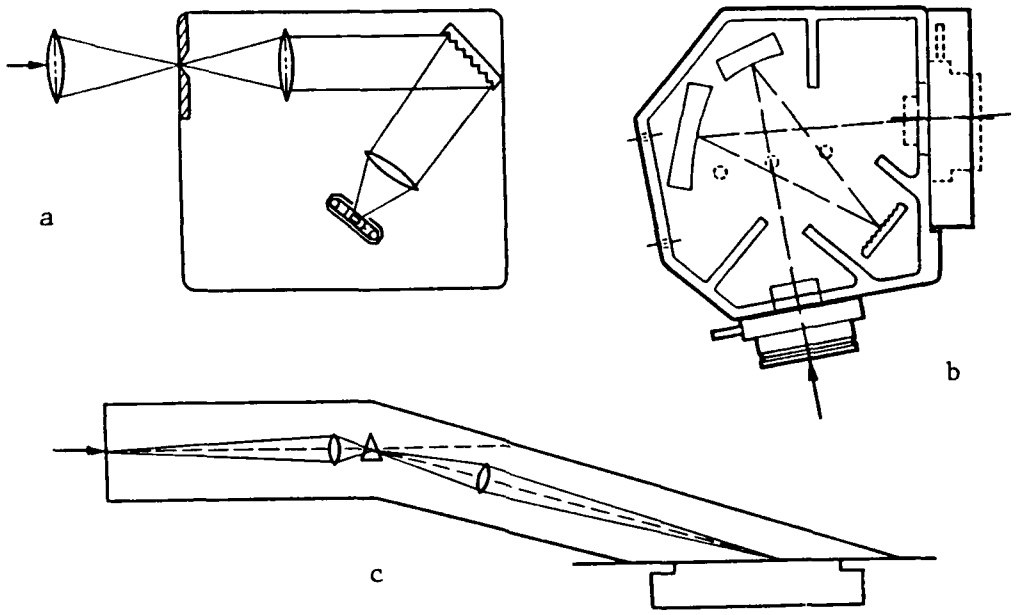


Fig. 2. Experimental arrangements of the major spectrometers used in this research. (a) Reflection grating, (b) Oriel Multi-Spec 77400, (c) Hilger E584.

TABLE I. Summary of Experimental Arrangements

SPECTROMETER	DISPERSING ELEMENT	ACQUISITION MODE	DETECTOR/ RECORDING MEDIUM	DATA ANALYSIS MODE
NASA AMES	Reflection Grating	External via Window	TX 50635 film ASA 1600 film	Densitometer
NASA AMES	Reflection Grating	External Fiber Optics	Tri-X Pan film TMZ-P3200 film	Densitometer
HILGER UV E584	Quartz Prism	In Chamber Direct	TMZ-P3200 film	Densitometer
BAUSCH AND LOMB	Transmission Grating	External via Window	ASA 1600 film	Visual and Densitometer
ORIEL MULTI-SPEC 77400	Reflection Grating	In Chamber Direct	1024 Element Diode Array	Digital

NASA Ames Spectrometer

The first spectrum of an intact capture event is shown in Fig. 3 [Tsou et al., 1987], and was obtained from a 3.2 mm diameter aluminum sphere impacting multilayers of 10 μm thick mylar (PET) films with the NASA Ames reflection grating spectrograph. The spectrograph was first positioned outside the target chamber of the NASA Ames Vertical Gun Range, and the light generated by impact was reflected to it by means four first surface mirrors. Subsequently, the spectrometer was successfully moved to the inside of the chamber. The spectra were recorded on film and the intensities determined as a function of wavelength by means of a microdensitometer.

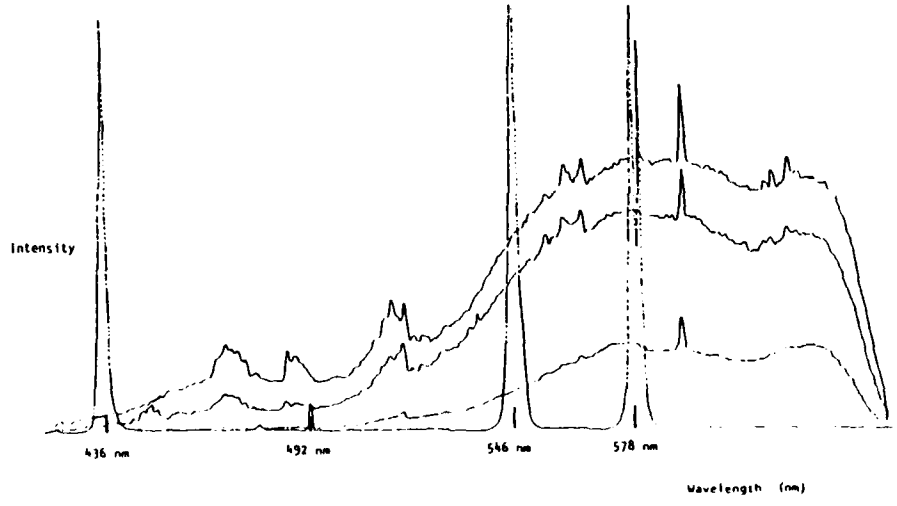


Fig. 3. First spectrum generated by intact capture. Al into polystyrene (PS) film stack. Shown are three spectral traces taken at different locations along the emission path. Also shown is a portion of the Mercury calibration spectrum.

The features of this arrangement were: (1) sufficient light intensity to produce a spectrum on film, (2) good sensitivity, revealing many of the structural details of the spectrum in the form of molecular bands, and (3) the spectrometer and camera accepted light from a portion of the impact area and, thus, allowed, limited spatial distribution. In order to achieve true spatial resolution in which a spectrum is essentially recorded at each point along the emission path, it is necessary that the spectrometer and its associated optics operate in the stigmatic mode.

Characteristically, the amount of radiation generated in a foam medium capture is reduced considerably from that of multiple film media. Multiple scattering of light within foams causes much lower emitted light intensity than multiple film medium, made from the same polymeric target material. To avoid having to use mirrors and thick 1" camera port window, efforts were made initially to "pipe" the light out of the evacuated target chamber to the spectrometer by means of fiber optics. However, the uncertainty in precisely locating the impacting point and its associated emission path through the foams precluded any guarantee of getting significant illumination into the optical fibers. The low radiation situation was solved only when the spectrometers were physically placed directly inside the impact chamber next to the target. Even in this case, foam target spectra were successfully acquired **only** by using a diode array detector.

Transmission Grating Spectrometer

If one could obtain a spectrum at each point along the discharge path, it would then be possible, in principle, to determine temperature and emission species profiles in the capture track direction. The conventional slit spreading does provide some spatial spread of a limited range. A simple approach was able to acquire spectra along the entire path of the intact capture event along with a corresponding visible image of the event by placing a transmission grating in front of a 35 mm camera. The transmission grating has 600 lines per mm, and is shaped and mounted in a 52 mm filter frame which can be placed on a 35 mm camera lens, much as a color filter. Due to the shift of light by the transmission grating, the aim of the target in the view finder has to be off set. The grating causes various orders of spectral images to be placed on the film. An example of intact capture of a 3.2 mm diameter aluminum projectile by 10 μm thick multiple polystyrene films, through a transmission grating is shown in Fig. 4. The spectra are displayed along with the actual integrated light image of the capture medium. Note that the left side spectral image indicates clearly the a variation of temperature along the length of the path associated with the capture process. This manner of spectra acquisition clearly provides the opportunity of determining the temperature profile along the discharge path. Such output from the transmission grating - camera system, therefore, allows its use as a valuable diagnostic tool in the highly non-linear response of the target medium to hypervelocity intact capture.



Fig. 4. Spectrum (color) produced by transmission grating and 35 mm camera, illustrating spatial, as well as wavelength spreading of the image. Spectrum is at left.

Although the transmission grating provides a wide spatial spread, densitometer readings are difficult to obtain due to overlapping of the multiple higher orders of the spectrum. Improved orientation may provide the desired information with minimal noise.

Hilger UV Spectrometer

While the Swan bands of C_2 are well known molecular bands appearing in the visible, most of the distinguishing bands associated with organic molecules lie outside the visible. Those associated with electronic reconfiguration lie in the ultraviolet, while those associated with transitions between various vibrational/rotational levels of a given electronic configuration lie in the infrared. Additionally, since the Hilger uses a quartz prism, rather than a grating, the problem of multiple orders does not arise.

The Hilger E584 is designed so that its film plane is set at such an angle to the direction of refracted radiation that the ultraviolet portion of it receives an enhancement in the spatial spreading of its wavelengths. In this manner, the Hilger E584 is able to give an excellent representation of molecular emission bands in the ultraviolet.

Multi-Spec Diode Array Spectrometer

Spectrometers that make use of film as a detector and recording medium are restricted in wave length sensitivity and require a high threshold of light. For a given film, spectral sensitivity is restricted. Although solid state devices are limited in active detector area, they do have very low light thresholds and allow instant data for study and experimental adjustments. Films require at least a day for processing. For our study, a 1024 element diode array spectrometer from Oriel was used.

The first successful acquisition of a visible/uv spectrum generated by an intact capture event in a foam target was obtained from polystyrene (PS) foam, and is shown in Fig. 5. This spectrum was captured by the Oriel Multi-Spec Spectrometer, Model 77400, which recorded the spectrum from about 200 nm to 700 nm. The spectrum was produced by the polystyrene (PS) foam capturing a 3.2 mm diameter aluminum sphere, incident upon the foam at a speed of 5.4 km/s.

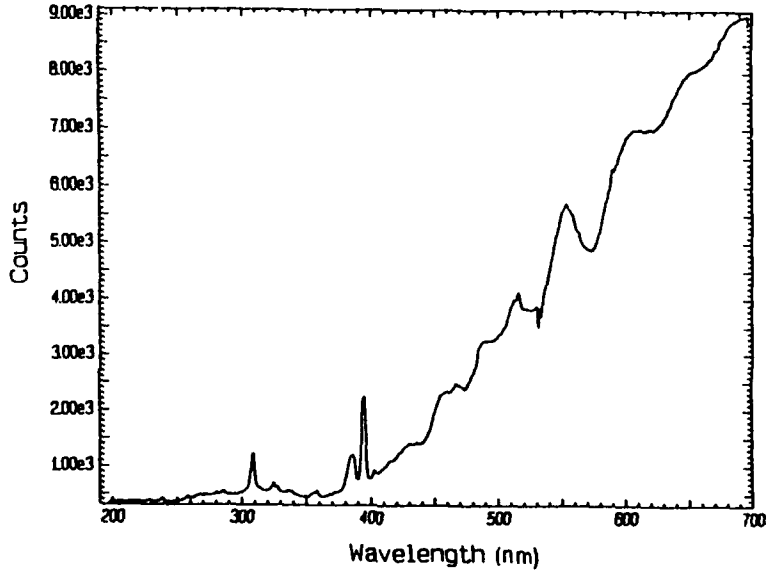


Fig. 5. First spectrum generated by intact capture taking place in a foam taken with Oriel Multi-Spec Spectrometer, Model 77400. 3.2 mm diameter aluminum sphere, incident at 5.4 km/s into polystyrene (PS) foam.

ANALYSIS

Using these spectrometers, spectra for various hypervelocity capture events were obtained with 3.2 mm diameter aluminum projectiles launched into multiple films or foam capture media at speed around 6 km/s. The spectra were studied to address the objectives of this effort. Aluminum into aluminum spectra were obtained to resolve the source of some bands.

Spectra Intensity Comparison

A statistical analysis, based on the assumption of a normal distribution, was conducted on data taken from the "flat" response region of the spectra generated by 3.2 mm aluminum spheres incident into polyethylene (PE) foam, and a polyethylene (PE) film stack, at speeds of 5.5 km/s and 5.8 km/s, respectively, Fig. 6. In this study, 612 and 5556 counts were recorded in 100 channels in the foam and film stack spectra, respectively. The result for the case of the foam spectrum was a mean value of 6.1 counts and a standard deviation of 4.2, while the film stack spectrum yielded a mean value of 55.6 counts and a standard deviation of 4.1.

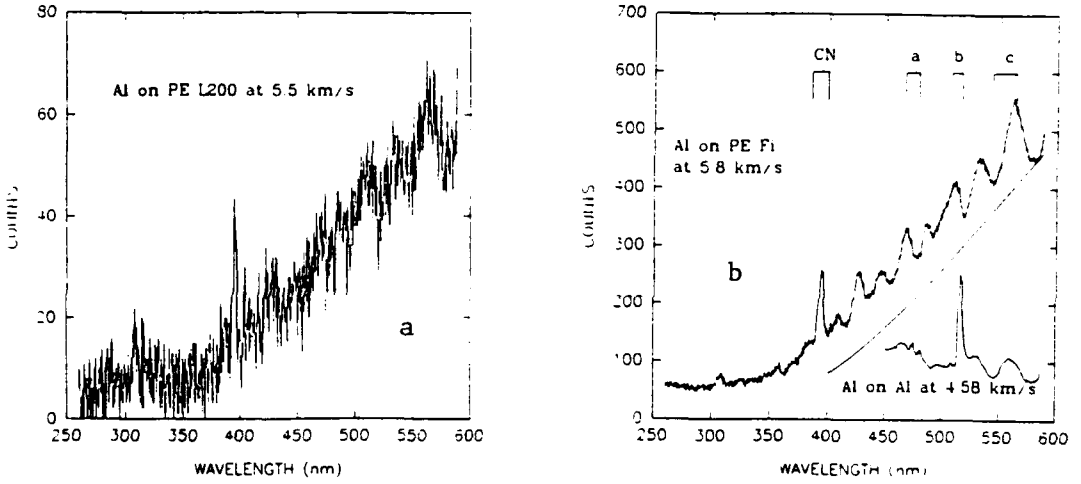


Fig. 6. (a) Spectrum from polyethylene (PE L200) foam taken with Oriel Multi-Spec Spectrometer, Model 77400. 3.2 mm diameter aluminum sphere, incident at 5.5 km/s. Indicated are the locations of CN (0-0) band, and three Swan bands of C_2; a: (1-0), b: (0-0), c: (0-1). (b) Spectrum from polyethylene (PE) film stack taken with Oriel Multi-Spec Spectrometer, Model 77400. 3.2 mm diameter aluminum sphere, incident at 5.8 km/s. Indicated are the locations of CN; (0-0) band, and three Swan bands of C_2; a: (1-0), b: (0-0), c: (0-1). Also indicated is a portion of the Planck curve for T = 3100 K, and a portion of the Al-Al spectrum.

The total sample count in the PE film was 9.1 times greater than that for the PE foam. On this basis, one would expect the spread of readings in the PE film to be increased by $(9.1)^{1/2} \approx 3.0$ with respect to that in the PE foam, with the result that the **relative precision** of values, $\Delta N/N$, would vary as $1/\sqrt{N} = 0.33$, leading to an expected value of 0.23 for the relative precision in the PE film. This is expected solely on the basis of the "law of large numbers". What is found, however, is a significantly lower value of 0.07 for the relative spread in the PE film. This means that it would require getting almost 100 times more counts in the foam spectrum than was done in order to get the same value of relative precision achieved in the corresponding film stack - a circumstance not very likely to happen.

Spectra Interpretation

The basic qualitative nature of the emission spectra generated by the intact capture of hypervelocity particles in underdense media: polyethylene (PE), polystyrene (PS), and polyurethane (PU), targets can be seen in Figs. 6 & 7. It is one of **overlapping** emission bands superposed on a gray body spectrum. In each of these spectra, the shortest wavelength at which the intensity rises from the noise, λ_0, is readily identified. This initial onset of intensity with wavelength is often too rapid to be due to thermal emission alone, a fact which might serve to indicate the species present in any unknown underdense capture medium. This observation also allows a determination that the thermal emission intensity must be negligible at any wavelengths shorter than λ_0.

Swan bands of diatomic carbon (C_2) occur whenever this molecule de-excites. Since C_2 is a homopolar molecule, the transition **must be** accompanied by an electronic re-configuration, and it is this which puts the wavelengths of its spectrum into the visible. If fragments of the polymeric target media are being produced by bond breaking, then it is quite likely that most will be more complex than simply C_2. Nevertheless, one might still expect some emission bands to lie close to those of true Swan bands for cases where the fragments are not too massive. It might even be that for such cases, a chromophoric response would still produce bands not too far removed in wavelength. The location of the Swan band sequences; (1-0) from 466.9 nm to 478.2 nm; (0-0) from 507.1 nm to 516.5 nm; and (0-1) from 544.8 nm to 563.6 nm are indicated in most of the spectra shown in this article.

Recent experiments in which aluminum spheres have been launched into aluminum foil targets have yielded preliminary data indicating evidence for the production of the (0-0) band of AlO at 484.2 nm. Some evidence of this band can be seen in the spectrum of PE multiple films, where it can be seen as a distinct peak in Fig. 6a, and in that of PU foam, Fig. 7b, where it appears in the form of a shoulder between successive Swan-like bands. It is possible that some of the additional structure seen in these spectra is associated with molecular bands of AlH, centered at 424.1 nm and 531.5 nm. However, there does not appear to be any evidence of the formation of AlC during the interaction of projectile with target medium.

Both the PE foam spectrum, Fig. 6a, and the PE film stack spectrum, Fig. 6b, as well as the earlier PS foam, Fig. 5, reveal a sharp molecular band contained between 388 nm and 400 nm. Ethylene flames are known to exhibit a strong band at 390 nm, identified with emission from CH. Since this feature does not turn up in either the polystyrene ringlet (PSR) or polyurethane (PU) spectra, Figs. 7a and 7b, it is tempting to assign its origin to CH emission. However, this band is seen in the original polystyrene (PS) film stack spectrum of Fig. 3, and this raises the possibility that it may be the (0-0) band of CN at 388.3 nm, produced in the target chamber. This points out the need for a number of additional control experiments to be conducted, which will, in turn, allow definitive elimination of a number of possible sources.

Aluminum Spectrum

An 3.2 mm diameter aluminum projectile was launched into a multiple layer aluminum foil capture medium at a speed of 4.6 km/s, in order to determine whether some of the band structure observed in the impacted foams might be due to residual hydrocarbon vapors in the impact chamber [Nicol et al., 1988]. We have taken steps to avoid the acquisition of Swan-like emission bands arising from any possible extraneous hydrocarbon sources within the target chamber. The portion of this Al on Al spectrum, not to scale, covering the range of wavelengths from 450 nm to 550 nm is shown as an inset to Fig. 6b.

While the resulting Al on Al, or more likely Al_xO_y on Al_xO_y, spectrum reveals a complexity of structure, it is important to note that the (0-0) and (1-0) Swan-like band sequences, seen in the

impacted foams, are missing from the spectrum of impacted aluminum. This supports the idea that the Swan-like bands, generated in our experiments on foams, are due to the de-excitation of molecular fragments produced by hypervelocity dissociation of the polymer material comprising the foam, itself. Some process of possible emission source elimination has to be pursued at present, given emission spectra so "cluttered" with bands and, possessing such a wide selection of possible organic molecular sources.

Temperature Estimation

Any accurate assignment of a gray-body temperature to the shocked foam will require spectral detection through the visible and into the near infrared. The wavelength scale for the spectra presented in this article was calibrated by means of a standard mercury arc source. No absolute intensity scale was calibrated for these measurements. It was possible, however, to determine relative intensities by conducting a normalization of the spectral readings, knowing both the wavelength dependence of the relative efficiency of the diffraction grating used in the Multi-Spec 77400 spectrometer, and that of its associated photodiode spectral response curve.

For the experiments shown in Figs. 7a and 7b, the incident kinetic energy of the hypervelocity projectile (KE_0) did not vary substantially with regard to the total energy deposited in the target. Black-body temperatures of the shocked foams have been estimated and their associated Planck curves have been added to the three figures. These curves were determined on the basis of a number of relative measurements taken from each spectrum. These intensities are proportional to

$$N(\lambda,T) = \frac{C_1}{\lambda^5}\frac{1}{\exp(C_2/\lambda T)-1} \qquad (1)$$

where T is the absolute temperature of the radiating region of the foam target, λ is the wavelength, and the constants in the expression have the values $C_1 = 1.191x10^{-16} W \cdot m^2/sterad$, and $C_2 = 0.0144\ m \cdot K$.

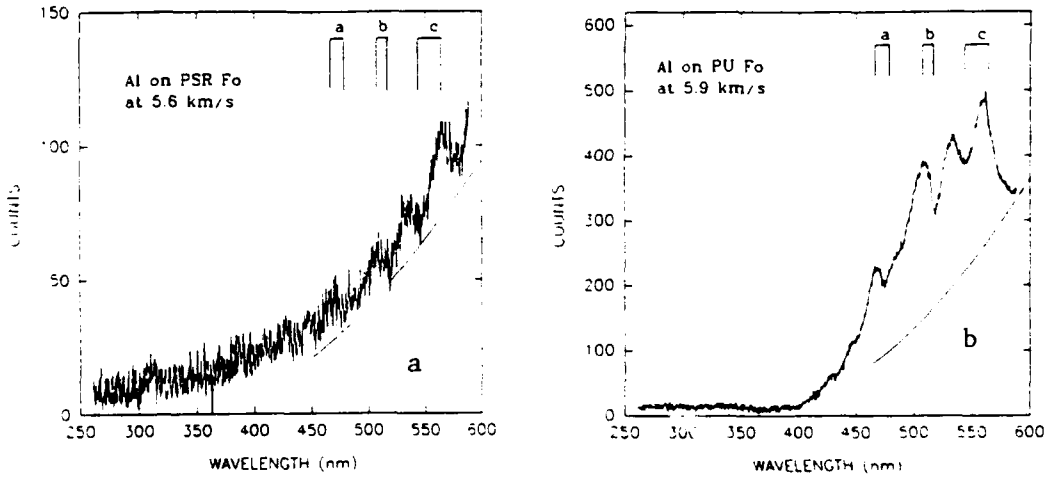


Fig. 7. (a) Spectrum from polystyrene ringlet (PSR) foam taken with Oriel Multi-Spec Spectrometer, Model 77400. 3.2 mm diameter aluminum sphere, incident at 5.6 km/s. Indicated are the locations of three Swan bands of C_2; a: (1-0), b: (0-0), c: (0-1), and a portion of the Planck curve for T = 2700 K. (b) Spectrum from polyurethane (PU) foam taken with Oriel Multi-Spec Spectrometer, Model 77400. 3.2 mm diameter aluminum sphere, incident at 5.9 km/s. Indicated are the locations of three Swan bands of C_2; a: (1-0), b: (0-0), c: (0-1), and a portion of the Planck curve for T = 2500 K.

In the case of the PSR foam, Fig. 7a, the temperature is estimated to be between 2500 K and 2700 K. This range of temperatures arises due to the undetermined nature of the spectral intensity at the lowest wavelengths. In the event that the small wavelength intensity is truly non-zero, independent of its source, the portion of the Planck curve shown in Fig. 7a is that associated with a thermal radiator at 2700 K. Consideration of the shortest wavelength intensity as some type of background reduces the black body temperature of the PSR foam to 2500 K. These relatively high temperatures appear to be representative of those produced by shock heating of porous materials. As seen in Fig. 7b, the associated black-body Planck curve for PU foam corresponds to a temperature of 2500 K, essentially the same as for the case of PSR foam. Finally, it is to be noted that the black-body temperature estimated for the PE films, and by comparison of spectra, the PE foam, is the highest of all capture media, being well approximated by a Planck curve at 3100 K.

Earlier measurements taken on shocked polystyrene films and foam were able to give only an indication of the temperature to which the targets had been raised upon impacting. Even there, however, those estimates were in the region of 3000 K. It also appeared that the difference in temperature between the shocked foam and shocked film stacks was not significant. Table II lists the black-body temperatures determined for the underdense media studied in this work.

TABLE II. Summary of Estimated Temperatures

MEDIUM	PSR	PE	PU
TEMPERATURE (K)	2500 - 2700	3100	2500

CONCLUSIONS

It has been demonstrated that it is possible to collect visible and ultra-violet spectra generated by intact capture of hypervelocity particles with a very high level of confidence in obtaining viable data. Bond breaking is one mode of energy dissipation and gives rise to the formation of sub-polymeric molecular fragments. Experimental confirmation of this has been provided by the spectra, all of which display molecular bands similar in location and character to the Swan bands of diatomic carbon, but arising from species of the form $C_2 \cdot X$, where X is some additional sub-complex associated with the parent monomer.

Additional bands associated with AlO, and possibly AlH, but not AlC, give evidence of standard chemical reactivity taking place between the projectile and target medium during the intact capture event. The requirement to distinguish between what appears to be either the (0-0) band of CN or a CH band emphasizes the need to examine spectra generated by different polymeric capture media, under a variety of environments. It is only by such an approach that various possible sources of molecular bands can be conclusively eliminated.

These experiments have also shown that it is possible to assign a gray body temperature to the source region by spectrometric means. Moreover, the transmission grating - camera arrangement has the potential to serve as a valuable diagnostic tool, since it is able to determine a spatial profile of the temperature within the emitting region. Visible and ultra-violet spectroscopy of intact capture provides insight ultimately leading to improvement in the design of capture media, since it provides a means of determining: (1) the number and type of polymeric bonds (single, double, ring) being broken under impact; (2) the reactivity of projectile and target; and, (3) the temperature to which the capture medium and projectile have been elevated. It is an understanding of the playoff between the rate of bond breaking and the amount of temperature elevation that will determine the optimum underdense medium for use in future intact work.

Finally, it is concluded, on the basis of the success of these initial experiments, that it should be feasible, and certainly helpful, to conduct time-resolved spectroscopy on the intact capture process. These arrangements would take a form similar to those used by Boslough and Ahrens [1989], and Radousky and Mitchell [1989], who have measured time-dependent shock temperatures in other media under different conditions. Such experiments could identify the reactions taking place in the contact zone at the time they occurred, as well as the dynamics governing the rate at which energy is transported out of the impact region.

ACKNOWLEDGMENTS

The help of Chul Park, of the NASA Ames Research Center, in loaning the reflection grating spectrometer, getting us started with spectrometry, and interpreting initial data is gratefully appreciated. Robert J. Miller's able assistance in obtaining spectra with the Ames reflection grating spectrometer was indispensable in acquiring those spectra. Douglas Buettner designed the fiber optics system, performed most of the spectrometry experiments, and conducted most of the data reduction efforts, all of which are deeply appreciated. We are grateful to Oriel for helping, loaning their spectrometer, and taking a genuine interest in our experiment. The crew at the NASA Ames Vertical Gun Range was always helpful and is appreciated. This work was carried out, in part, at JPL, Caltech, under NASA contract.

REFERENCES

Borucki, W. J. (1970). Applied Optics, 9, 260.

Boslough, M. B. and T. J. Ahrens (1989). Rev. Sci. Instrum. 60, 3711.

Buettner, D. J. (1991). Hypervelocity Spectroscopy from Impacts in Polymeric Materials. Thesis, Master of Science degree, Oregon State University, April 30, 1991.

Griffiths, D. J. (1989). Theoretical Considerations of Capture Medium Response for Hypervelocity Intact Capture. JPL D-6237.

Jongeward, K. A. and W. Wilson (1991). Technical Report; AFATL-TR-90-88.

Nicol, M., S. W. Johnson and N. C. Holmes (1988). Shock-Chemistry of Benzene Studied by Spectra from and behind the Shock Front. Shock Waves in Condensed Matter 1987, 471-476.

Radousky, H. B. and A. C. Mitchell (1989). Rev. Sci. Instrum. 60, 3707.

Tsou, P. (1990). Intact Capture of Hypervelocity Projectiles. Int. J. Impact Engng, Vol.10, 615-627.

Tsou, P., S. T. J. Peng and A. L. Albee (1987). 18th Lunar and Planetary Sciences Conference, pp. 1026-1027.

Tsou, P., D. Brownlee and A. Albee (1984). Experiments on Contact Capture of Hypervelocity Particles. 15th Lunar and Planetary Science Conference, pp. 866-867.

Tsou, P. (1991). Fragment Ballistics Determination. JPL-D8278.

Int. J. Impact Engng Vol 14, pp 763–774, 1993
Printed in Great Britain

0734-743X/93 $6.00 + 0.00
1993 Pergamon Press Ltd

A HYPERVELOCITY FRAGMENT LAUNCHER BASED ON AN INHIBITED SHAPED CHARGE

JAMES D. WALKER, DONALD J. GROSCH, and SCOTT A. MULLIN

Southwest Research Institute
San Antonio, Texas 78228-0510

ABSTRACT

A hypervelocity fragment launcher based on an inhibited shaped charge was developed, which launches a 0.5-1.0 g aluminum fragment at 11.2±0.2 km/s. Experimental and computational work performed during its development are presented. The launched fragment is characterized by in-flight flash radiography and impact crater examination.

INTRODUCTION

Impacts on spacecraft and satellites from orbiting debris in space are a growing concern, due to the amount of debris and the potentially high impact velocities. Low Earth orbital velocity ranges from 7.3 to 7.8 km/s. Space Station Freedom will have an orbital velocity near 7.7 km/s (NASA, 1991). Debris in orbits with differing inclination angles, but similar heights, have similar velocities. If α is the difference in inclination angle between two intersecting orbits, then the impact velocity is given by

$$v_{impact} = \sqrt{2 - 2\cos\alpha}\, v_{orbit} \tag{1}$$

A collision between a spacecraft and debris in polar and equatorial orbits ($\alpha = 90°$) would occur at a velocity of 10.9 km/s for $v_{orbit} = 7.7$ km/s, while a collision between a spacecraft and debris in standard and retrograde orbits ($\alpha = 180°$) would occur at 15.4 km/s. Thus, to test shielding concepts for spacecraft, it is necessary to perform laboratory impact tests in the 11 to 15 km/s regime. Two-stage light gas guns are able to launch projectiles at speeds up to 9 km/s. To launch projectiles at higher velocities, we began examining explosive launching techniques.

Metal lined shaped charges are able to produce metal jets with tip speeds over 10 km/s. In the 1960's, the concept of using a shaped charge and severing the high velocity jet to isolate the jet tip as a fragment was investigated (Kronman and Merendino, 1963, Merendino, *et al.*, 1963, Wenzel and Gehring, 1965, Wenzel, 1986). However, a series of recent tests revealed limitations of the previous work (Tullos, *et al.*, 1988). An experimental and computational modeling program was initiated to re-examine the concept and attempt to design a hypervelocity fragment launcher based on an inhibited shaped charge.

This paper first presents a brief overview of shaped charge jets to suggest the possible applicability and performance of an explosive fragment launching device. Experimental and computational results are then presented to provide information on the liner collapse process; this information was used in the design of the charge. The simulations were not sufficiently accurate to perform the complete design on the computer, due as much to a lack of material response information at the extreme pressures and strain rates involved as to numerical inaccuracies. Also, the simulations were two dimensional, and the final charge design was three dimensional, having asymmetric components. During the design process, there was a strong interplay between the experimental work and computational work, both of which led to a conceptual understanding of the collapse and subsequent jet-inhibitor interaction. Numerous experimental tests and the synergism between the experiments and the computations led to an understanding of the device and a working hypervelocity fragment launcher.

The launched aluminum fragment has a length to diameter ratio (L/D) between 3 and 4, with a nominal diameter of 5 mm. Its mass ranges from 0.5 to 1.0 gram. Occasionally, the fragment rotates in flight, which led to a confirmation that the fragment is hollow. The velocity of the fragment is 11.2±0.2 km/s. At the end of the article, flash radiographs of the fragment and a photograph of a crater produced in a large aluminum target are presented.

THE SHAPED CHARGE APPROACH

Shaped Charges

The explosively driven collapse of a metal lined cavity produces a high velocity metal jet of relatively great length (for an overview of shaped charges, see Walters and Zukas, 1989). For shielding analysis, a high velocity fragment with an L/D = 1 would be ideal. To take advantage of the high velocities produced by shaped charges, it is necessary to isolate a fragment at the leading tip of the jet.

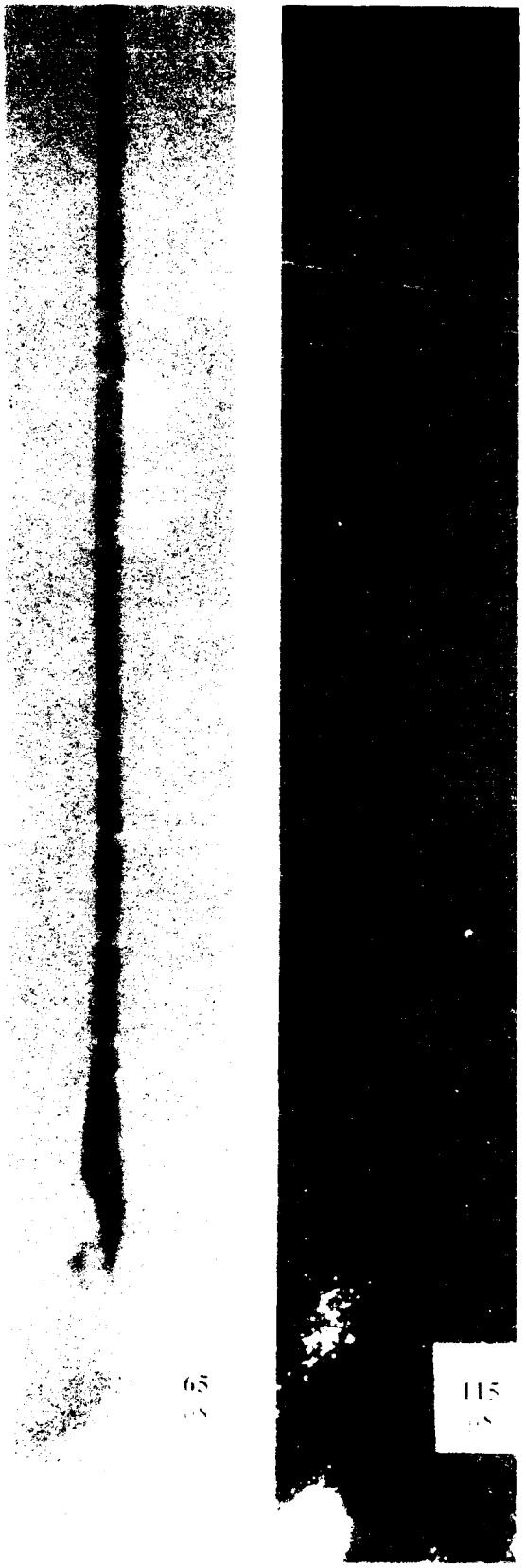


Fig. 1. X-ray views from an aluminum 30° liner angle charge. The left figure at 65 μs after detonation of the charge shows the intact jet, and the right figure at 115 μs shows the fragmenting jet.

The long jet formed by the shaped charge has a large velocity gradient. This gradient eventually causes the jet to break into small fragments. Figure 1 shows a portion of an aluminum jet from a 30° conical shaped charge whose explosive component was Octol 70/30. The jet tip is travelling at 11.1 km/s. The left frame, at 65 μs after initiation, shows the long stretching jet and the second frame, at 115 μs, shows the jet shortly after breaking into fragments. The fragments have an L/D ranging from 1 to 5. The large jet tip is evident.

The high speed leading fragment of the jet would be an excellent projectile for hypervelocity impact testing. To remove the unwanted trailing fragments, material is placed within the cavity of the shaped charge. This material inhibits the formation of the majority of the jet, and hence will be referred to as an "inhibitor." The inhibitor allows the jet tip to form, but removes most of following jet material. Only the leading fragment is allowed to travel down the flight line.

Jet Incoherence and Expected Velocities

It has been observed that in some shaped charge jets there is a large radial component to the jet velocity, resulting in a radial expansion of the jet material as it travels down range. This is referred to as incoherence of the jet. For example, Fig. 2 shows the tip of an aluminum jet for a 20° liner angle with Octol 70/30 explosive. The jet tip is travelling at 12.0 km/s, but is undergoing radial expansion (this result for aluminum agrees with that of Kronman and Merendino, 1963). An incoherent jet will not produce a desirable fragment for space debris simulation, since it is breaking into many pieces.

A large amount of research has been performed on jet incoherence. In general, there seems to be a jet tip velocity below which the jet is coherent, and above which it is not (Walters and Zukas, 1989, Chanteret, 1992). This velocity depends on the liner material and the shape of the cavity (for example, the liner angle for a conical charge). Different jet tip velocities for a given material can be achieved by using different cavity geometries and explosives with different detonation velocities.

A starting place for the design of a hypervelocity launcher is the charge with the highest jet tip velocity for a coherent jet. An exact analytical expression for the maximum coherent jet tip velocity has not been found, and so charge designers use empirical expressions to estimate this quantity. Most of these expressions compare the velocity at which the liner material is moving into the collapse region with the sound speed of the material. One such expression is

$$V_l \leq 1.23 c_0 \tag{2}$$

In this equation V_l is the velocity at which the liner material is moving into the collapse region and c_0 is usually taken to be the bulk sound speed of the liner material. A heuristic interpretation of this equation is that the flow must be subsonic: the collapse velocity V_l must be less than the sound speed of the highly compressed material in the vicinity of the collapse point (hence, the 1.23 factor). This expression seems to hold for a number of materials, where V_l is obtained from an analytic shaped charge model or a hydrocode calculation. The calculation which provides V_l also provides the jet tip velocity, thus allowing the determination of the maximum coherent jet tip velocity.

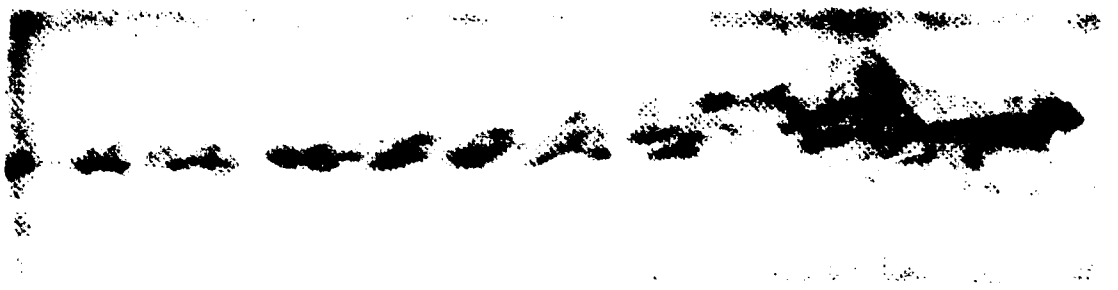


Fig. 2. X-ray view of the jet from an aluminum 20° liner angle charge.

More direct, however, is another expression used for jet coherency:

$$V_{tip} > 2.41c \tag{3}$$

This expression (Walters and Zukas, 1989) more simply states that the maximum jet tip velocity is 2.41 times the bulk sound speed of the liner material, and thus combines effects of high pressure and charge geometry into one constant. (Chanteret, 1992, suggests 2.46 rather than 2.41, and that even higher jet tip velocities are possible depending on the actual geometry and explosive of the charge.) Although further removed from physical meaning, Eq. (3) is also based on empirical results, and in Table I it is used to estimate the maximum tip velocity for various materials. The last column lists coherent jet tip velocities observed for the materials; the aluminum value is from this research, and all other values are from Chanteret (1992).

Table I. Coherent Jet Tip Velocities

Material	Bulk Sound Speed (km/s)	Maximum Coherent Jet Tip Velocity (From Eq. 3) (km/s)	Observed Coherent Jet Tip Velocity (km/s)
Aluminum	5.35	12.9	11.5
Copper	3.94	9.50	9.7
Molybdenum	5.12	12.3	12.3
Nickel	4.60	11.1	11.4
Steel	4.57	11.0	10.7 (Iron)

Aluminum is the most common structural material for satellites. Although density estimates for space debris are debris size dependent (NASA, 1991), estimates usually place it near that of aluminum. According to Eq. (3), it should be possible to design a charge which would produce a coherent aluminum jet tip travelling at 12.9 km/s. For a conical charge with an aluminum liner, it is possible to plot the jet tip velocity versus liner angle. This is done for the Octol 70/30 explosive in Fig. 3, using the SC1d model (Buckley, 1990). In our experiments using an Octol 70/30 explosive and conical aluminum liners, a 30° liner angle produced a coherent jet travelling at 11.2 km/s, while a 20° liner angle produced an incoherent jet travelling at 12.0 km/s. The fact that aluminum does not seem to follow Eq. (3) has been noted by other researchers (Chanteret, 1992), and experimentally it appears that the fastest coherent jet possible with aluminum has a jet tip velocity less than 11.6 km/s. Equation (3) does appear to hold for other materials, and the corresponding coherent jet tip velocities for many other materials have been achieved. Thus, the technique described in this report should be applicable to the hypervelocity launching of fragments of other materials.

EXPERIMENTAL PROGRAM

The hypervelocity fragment launcher design was based on an aluminum lined conical shaped charge, shown in Fig. 4. As discussed above, initial experiments showed that a 20° liner angle did not produce a coherent jet. Therefore, 30° liner angle charges were examined in tests and computations (Grosch, *et al.*, 1991, and this research). Early tests used the cup shaped apex depicted in Fig. 4. The cup shaped apex was initially adopted since Kronman and Merendino (1963) has used such a design. It was thought that a larger jet tip might be produced by such an apex. More recent tests utilize a hemispherical apex, which produces a more repeatable jet tip. The liner was made of 1100-O aluminum. The explosive was Octol 70/30, and was initiated by an RDX booster pellet at the top of the charge. The charge height was 15.75 cm, and the charge diameter was 6.5 cm.

Tests were performed both in atmosphere and in an evacuated chamber. In the tests, the dimensions of the inhibitor were varied. Two pair of orthogonal flash X-rays were used to image the jet in flight. These radiographs were used to determine the influence of changes in the inhibitor on the jet tip. The craters resulting from the impact of the jet with aluminum targets were also studied. For the tests in atmosphere, the standoff from the target was 130 cm, and X-ray heads were centered at 41 cm and 92 cm from the base of the charge along the flight line. For the tests in the evacuated chamber, the standoff from the target was 2.1 cm, and X-ray heads were centered at 203 cm and 251 cm from the base of the charge along the flight line. Tests in the evacuated chamber were performed at a pressure of 3 torr. Jet tip velocities were obtained from location measurements on the X-ray radiographs. The jet tip velocities were very repeatable, with a jet tip velocity of 11.2±0.2 km/s.

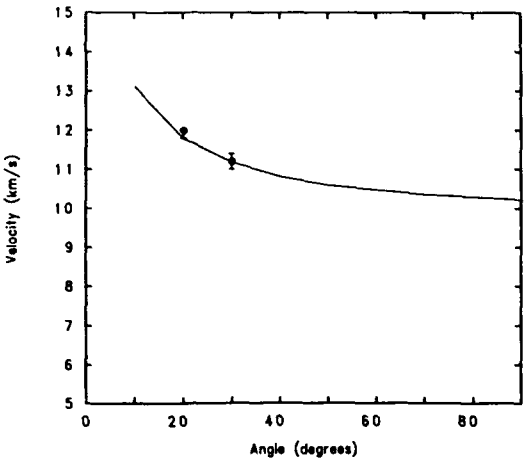


Fig. 3. Jet tip velocity versus liner angle, based on a one-dimensional shaped charge model. The dots are experimental values.

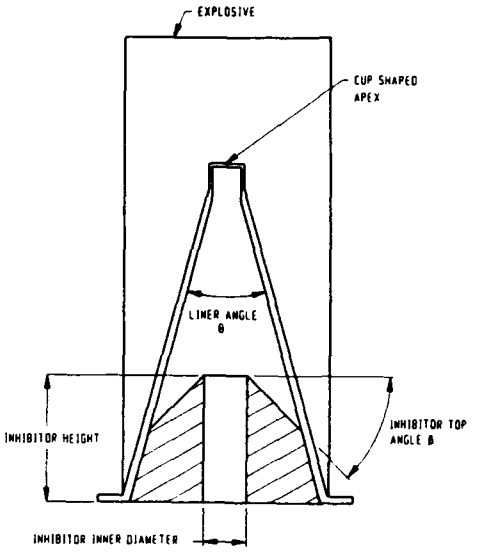


Fig. 4. The shaped charge and inhibitor set-up and terminology.

In early testing, flash radiographs revealed that when a fragment exited the charge, it was followed by trailing debris. This debris was unlike the fragments following the jet tip seen in Fig. 1, in that the particles were smaller and were spread over a larger region. The inhibitor removed most of the jet, but additional trailing debris exited the charge. The computational results were therefore carefully examined to gain a greater understanding of jet formation and inhibitor interaction to suggest an approach for removing this trailing debris.

COMPUTATIONS

A series of computations modeled the shaped charge jet formation (Walker, 1991). These were done concurrently with experiments, and were used to aid in the interpretation of experiments and suggest further refinements in the inhibitor design. Interestingly, the experimental results also aided in the interpretation of the computations. Lagrangian calculations were performed with the hydrocode EPIC (Johnson and Stryk, 1986) and Arbitrary Lagrangian-Eulerian calculations were performed with the hydrocode CALE (Tipton, 1990). The liner and inhibitor were modeled as elastic-perfectly plastic, with relatively low flow stresses, and with a Mie-Grueneisen equation of state. The explosive was modeled with the JWL equation of state, with a detonation velocity of 8.48 km/s. The collapse process was modeled in detail, as was the inhibitor response. There were three primary results of the computations:

1) It was determined that the inhibitor should be made of a dense material, instead of the low density plastic used previously (Kronman and Merendino, 1963). Subsequently, copper was used in testing.

2) It was revealed that the inhibitor collapse was not actually cutting the jet. Rather, the inhibitor was pinching down on the jet, causing the portion of the jet already formed to stretch and fragment. This isolated the jet tip as a large fragment, but also created the debris immediately following it. This understanding of the origin of the debris suggested techniques for its removal.

3) The computations provided information on jet material's original location in the liner, as well as the path this material was traversing as it travelled from the liner to the collapse region, and into the jet. The material's path (location versus time) was helpful in determining the geometric arrangement of the inhibitor and the asymmetric insert placed within the charge cavity. The computations identified which material in the liner needed to be given an off-axis velocity component, and where the insert should be located to provide it.

Each of these results would have been very difficult to obtain experimentally, as it would have taken extensive testing and the use of X-ray techniques for looking inside the liner and inhibitor during the collapse. Each will be discussed in more detail below. Also, calculations were performed with both cup and hemispherical apexes to verify that inhibitor geometry did not need to be altered due to the change in apex design.

Lagrangian Calculations

The intent of early calculations was to determine the appropriate size and shape for the inhibitor. Different heights and materials for the inhibitor were examined. The major result of the Lagrangian computations was that a more dense material should be used for the inhibitor. In the early work (Kronman and Merendino, 1963) a plastic had been used. However, in the computations this material was ineffectual in cutting the jet. Calculations with inhibitors made of various materials convinced us that material inertia is more important than strength in cutting the jet. In the present design, the inhibitor is made of copper, a relatively dense material.

Calculations were also done to investigate inhibitor heights and shapes. Three different top designs were examined: these included a flat top ($\beta = 0$) and tops with angles $\beta = \pm 45°$ (see Fig. 4). In the EPIC computations, the resulting jet after pinching was the most narrow for the +45° slope. This design was adopted.

Due to the way jet collapse occurs, it was not possible to sever the jet computationally. Based on observed collisions between and jet and inhibitor, and the subsequent narrowing of the jet, it was possible to infer where cutting would probably occur. This is an underlying difficulty in the Lagrangian calculations, since the cutting of the jet to produce a single fragment was the program objective. To learn more from computations, it was necessary to transition to an Eulerian formulation. It was thought such an approach would allow the examination of the separation of the jet material to form a fragment. However, the jet tip separation process is quite complicated, and even Eulerian formulations were not be able to treat the fragmentation which occurs. Thus, inferences regarding the formation of the fragment were still necessary.

Arbitrary Lagrangian-Eulerian Calculations

Arbitrary Lagrangian-Eulerian (ALE) codes allow the grid motion to be independent of the material motion. If the grid is fixed, the calculation is purely Eulerian. If the grid moves with the material, the calculation is purely Lagrangian. ALE is between these two extremes. The grid has its own equations of motion, and the grid can move independently of the material motion or be linked to the material motion in some fashion.

In the ALE calculations, the zoning roughly moved with the jet material, making it possible to maintain fine zoning in the jet even though it was impractical to cover the entire region of interest with fine zoning. In this sense, the ALE approach was very beneficial. The ability of the material to move independent of the mesh (Eulerian) avoided very small zones due to the large deformations in the jet collapse. The ability of the mesh to loosely follow the material (Lagrangian) kept relatively fine zoning in the area of interest as the jet travelled along the flight line.

Severing of the Jet

The ALE calculations led to a (presumably) fairly accurate picture of what was happening during the liner collapse, and how the jet was being severed.

It was learned that the inhibitor was not cleanly cutting the jet. Rather, the jet was being "cut" in three steps. First, the initial part of the jet forms. The jet tip begins traveling down the axis of symmetry, through the hollow inner diameter of the inhibitor. Second, when the detonation front reaches the inhibitor, the inhibitor begins an inward radial collapse which clamps down on the jet. As the inhibitor is quite dense, this greatly decelerates the portion of the jet which comes in contact with the collapsing inhibitor. Third, a large velocity gradient in the jet results, where the jet tip, with a velocity of roughly 11 km/s, is traveling much faster than the portion of the jet trapped by the inhibitor. A region of the jet between the jet tip and the top of the inhibitor then stretches and fragments. The jet tip survives as a large fragment, and numerous small trailing fragments are created.

This sequence of events can be seen in Figs. 5, 6, and 7. Figure 5 shows the initial geometry comprised of an aluminum liner and a copper inhibitor with 5.08 cm height and 1.19 cm inner diameter, an aluminum base plate on which the charge rests with a 1.27 cm hole, as well as a steel supporting structure. The cavity is filled with air. Figure 6 is a sequence of material boundary plots from the collapse, from 8 μs to 19 μs. By 10 μs, the jet tip is formed. The "wing-tip" shape of the jet tip is due to the cup shaped apex of the liner — it does not occur for a hemispherical or conical apex. During this early collapse, the aluminum's trip from its original liner location (measured from the time of arrival of the detonation front) to the jet takes roughly 4 μs. By the time it reaches the jet, the aluminum has been plastically strained nearly 400%. This corresponds to plastic strain rates on the order of $10^6\ s^{-1}$ ($4/4\ \mu s = 10^6\ s^{-1}$). At 15 μs, a section of the collapsing liner collides with the top of the inhibitor ($\beta = +45°$), almost simultaneously along the whole top of the inhibitor. This collision behavior is part of the reason the slanted $\beta = +45°$ top was chosen. The explosive now begins driving the inhibitor closed, and liner material touching the inhibitor nearly comes to a stop due to the density and volume of the inhibitor. At 16 μs, the top of the inhibitor begins to collapse, and by 19 μs it is clamping down on the jet.

Between 16 μs and 19 μs, the jet tip travels 3.4 cm, which gives it a velocity of 11.3 km/s. The front 3 cm of the jet has passed by the top of the inhibitor before the collision between the inhibitor and the liner, and now appears to travel without alteration in shape. The jet material between the jet tip and the inhibitor is undergoing large tensile deformations. Plastic strain rates in this region of the jet are between $10^5\ s^{-1}$ and $10^6\ s^{-1}$. This large stretching tears the jet apart. To see this, consider the upper half of the sequence in Fig. 7, which is a density plot for a different computation (the lower half of the figure will be discussed in the next section). At 15 μs (Fig. 7d) the collision with the inhibitor has just occurred and the jet has not yet begun to stretch. The density throughout the jet is uniform. At 16.5 μs (Fig. 7e) the jet has begun to stretch, and in the density plot the decrease in density is the darker region within the jet. At 20 μs (Fig. 7f) the region of the jet between the inhibitor and the intact jet tip has a low density, implying material separation.

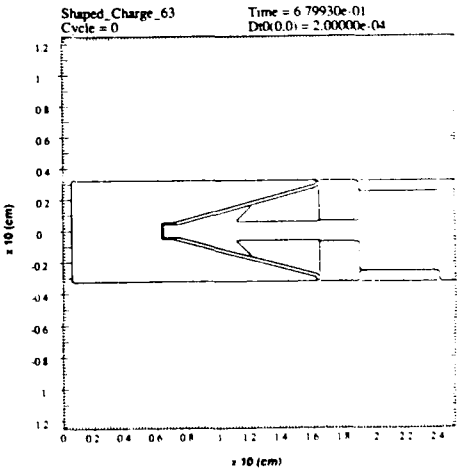


Fig. 5. Initial geometry showing liner, copper inhibitor, aluminum plate, and steel support.

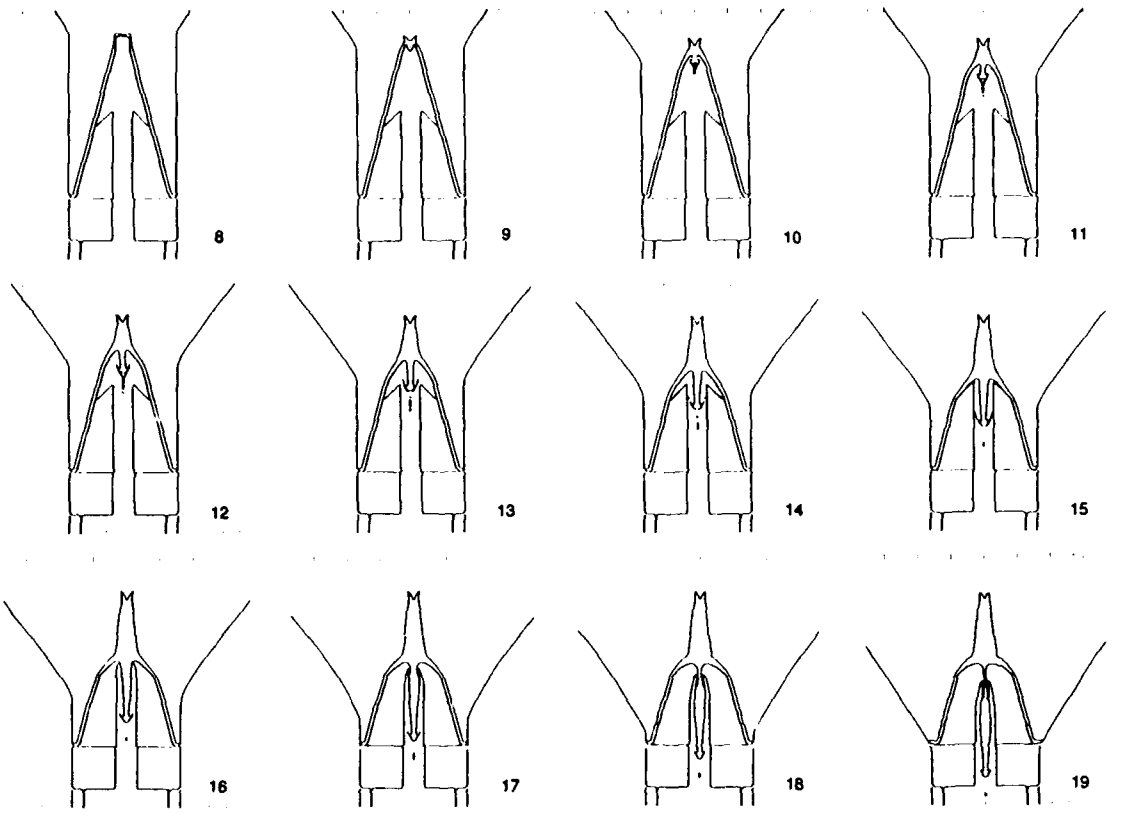


Fig. 6. Sequence of frames showing the collapse of liner and interaction with inhibitor at 8 μs to 19 μs.

In the calculations, this region continues to stretch, as there is no mechanism in the computer code for fracture of the material. However, in the actual physical event, the large tensile stresses cause the jet material to fracture and fragment. The front region of the jet is nearly unaffected by this fragmentation, forming the desired large fragment, but the region with the large tensile gradient breaks into pieces. These pieces form a debris cloud, which follows the main fragment. For a clean fragment, this debris must be removed.

The Sliced Liner Calculations

To overcome some of the difficulties in eliminating trailing debris in the tests, a better understanding of the jet material's original location in the liner was needed. Following Walters and Golaski (1987), the aluminum liner was sliced into pieces of width 0.5 cm. Each slice was identified in the code as a differenct region, making it possible to follow each slice of the liner separately throughout the calculation.

Six different times from the calculation with a sliced 30° liner are shown in Fig. 7. The upper half of each figure is a density plot, with the grey scale to the right indicating density. The initial densities of aluminum (2.70 g/cm^3) and copper (8.93 g/cm^3) have been identified. At the center of collapse, where pressures are slightly above 0.5 Mbar, the aluminum has been compressed to a density of 3.6 g/cm^3. This region is often referred to as a stagnation point, because material remains there on the dividing line between flow into the jet and flow in the opposite direction into the slug. The lower half of each figure shows the region shading. In the original work, each slice was colored, but in this paper the figures have been reproduced in black and white. The aluminum liner is represented by five shades for each of five different regions.

In Fig. 7b (10 μs) the detonation front in the explosive is marked, and is discernable in the density plot by a slight compression. The pointed tip of the jet is being formed by the top of the cup shaped apex. The cavity in the jet tip and the subsequent wing tip front on the jet are due to the cup shape of the apex, not the slicing of the liner. Figure 7c (12.5 μs) shows that most of the liner material is going into the slug; one-tenth to one-fifth of the liner material goes into the jet. Figure 7d (15 μs) shows the collision of the liner and inhibitor. Almost all the material from the cup apex has been left behind. The jet tip is comprised of material from the liner near the intersection of the cup and the cone. The first 3 cm of the jet comes from inner surface material of the first 7 slices of the liner (not counting the two at the apex), or about 3.5 cm of liner material. If the liner were conical all the way to the apex, this would be 4.6 cm of liner material. Thus, the liner material which makes up the jet tip has been identified.

The copper inhibitor is pressing into the collapse point in Fig. 7e (16.5 μs). Material in the 8th slice of the liner ends up in the tail end of the jet. The density plot reveals that the jet density near the inhibitor is beginning to decrease, indicating that the material is stretching. At this stage, fragmentation probably begins. Figure 7f (20 μs) shows that a large length of the jet has low density, implying that it has undergone large tensile stretching. However, the tip of the jet is moving with little deformation. The jet tip is composed of material from the first four or five slices of the

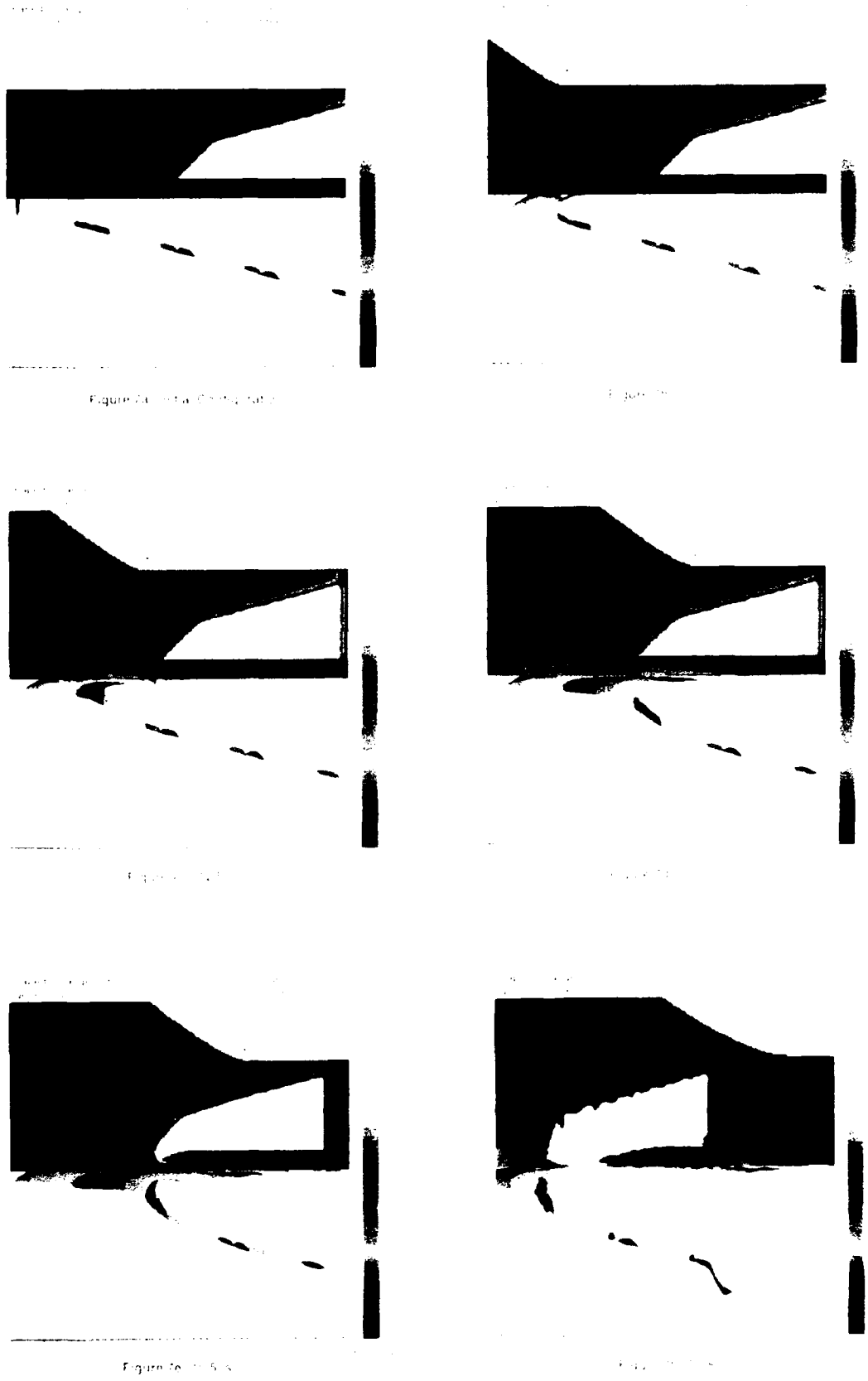


Fig. 7. Sequence of frames showing the interaction of the jet and the inhibitor.

liner, or 2 to 2.5 cm of liner material as measured from the intersection of the conical liner and the cup apex. A geometrical calculation provides an estimate of the fragment mass: if 2 cm of material of the liner is involved and one-tenth of the material goes into the jet, then a fragment mass of 0.96 g results; if 2.5 cm of liner is involved and one-fifth of the material goes into the jet, then a fragment mass of 2.52 g results.

Finally, Fig. 8 (40 μs) is a late time picture from this calculation compared with an X-ray radiograph from one of the tests at a later time (65 μs), where the length scales differ. There is a qualitative agreement between the fragment and the debris in both the calculation and experiment. The formation of a "fragment" in the numerical calculation is due to the way the interface tracker preferentially moves material and the slicing of the liner providing many different regions to be moved: fracture is not being modeled. In the computation, the mass of the fragment is 1 g, and the velocity is 11.2 km/s. However, fragment masses from the experiments were usually lower. This could be due to two possibilities. First, a larger region of the jet could fragment during the stretching and breaking of the jet, so that less material remains in the main fragment. Fracture is not being modeled, and it is unlikely that the extent of the region undergoing large tensile strains directly corresponds to the extent of the region of the jet which fragments. Second, we do not expect the computation to exactly predict the event. There are inaccuracies in the equations of state of the aluminum and explosives in the computations, as well as possible lack of symmetry in the detonation wave and the liner fabrication in the experiments. Finally, the computational fragment has a higher L/D than those seen in the experiments, correlating with its larger mass. Again, this may be attributable to the lack of fracture modeling within the computer program. The late time velocity, though, is surprisingly close to that seen in tests. The probable reason for this agreement is that the jet tip is unaffected by the fragmentation of jet material behind it, and so the jet tip velocity does not depend on the mechanics of fracture of the jet. In computations without the inhibitor, the jet tip looks exactly the same as those computations which include an inhibitor. A copper jet is also seen in the calculations. Such a jet was not observed in the tests, although small amounts of copper did impact some of the targets.

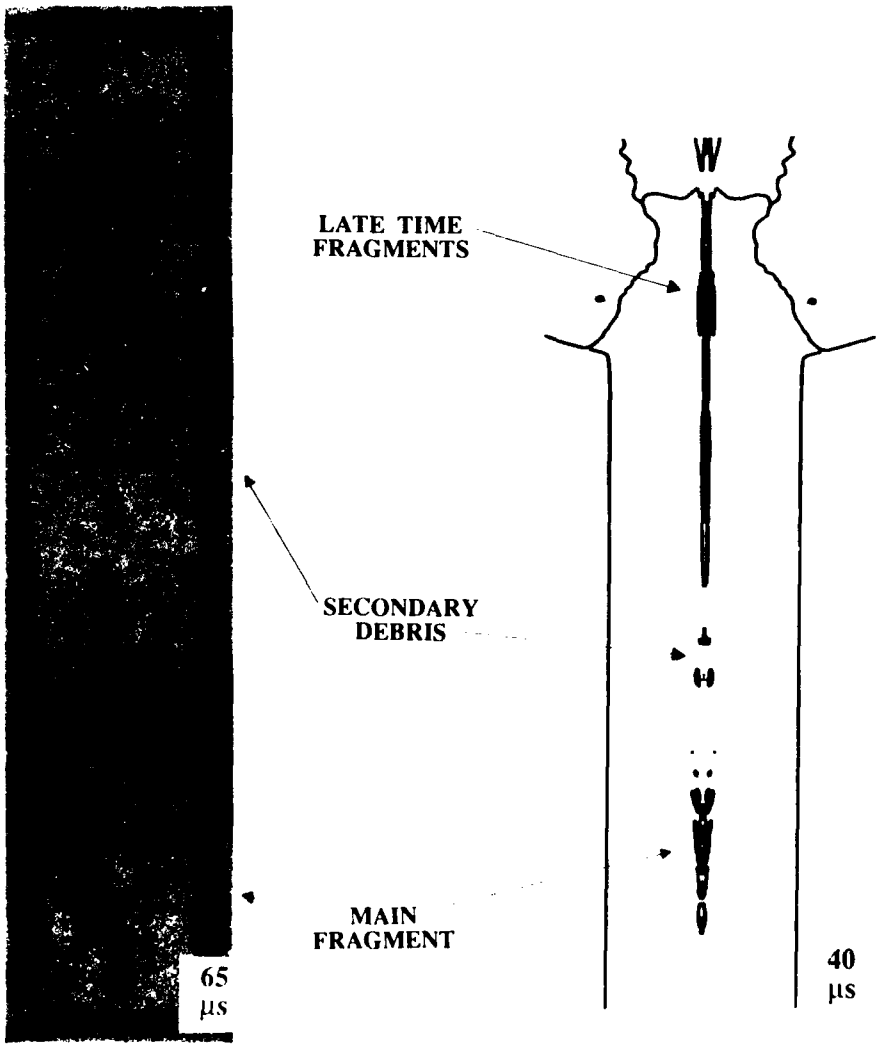


Fig. 8. Products produced by an inhibited shaped charge.

Removing the Trailing Debris

The jet severing interpretation provided by the computations and experiments showed that the trailing debris, which was coming from the stretching and breaking of the jet, could not be removed by altering the height or inner diameter of an axially symmetric inhibitor. To avoid active systems, such as explosive flyer plates, an asymmetry was needed in the collapse to push the debris off the flight line.

If the liner material which formed the debris was given an off-axis velocity component before it entered the collapse region, it would go through the jet formation and subsequent fragmentation process and still have an off-axis velocity component. Based on wave transit times, it appeared it would not be possible to produce the desired asymmetric behavior by applying a partial exterior confinement to the explosive. Rather, the asymmetric behavior would need to be caused by an insert within the cavity. The calculations were 2-D axisymmetric, but they could still be used to see if the location of the asymmetric insert allowed interaction with the liner material at the proper times and locations.

If the liner material that became the part of the jet which stretched and broke could be given an off-axis velocity, that debris would not impact the target. The sliced simulations identified the liner material that needed to be affected. Figure 7 shows that the region of liner material that goes into the stretching region of the jet begins in the 4th and 5th slices. Thus, only the first 2 cm of liner material should be allowed to collapse without being affected by the insert.

An asymmetric triangle insert was placed on top of the inhibitor. To check the timing of the design, a calculation was done with an aluminum tube inside the inhibitor, the tube having the same height as the triangle insert. Figure 9 shows the initial geometry, as well as two later times. At 12 μs, the liner is just impacting the insert. This material would be the first part of the liner to have an asymmetric collapse, and thus an off-axis velocity component. The next frame, at 13 μs, shows the progression of the interaction. Due to the symmetry of the calculation, a continuation of this calculation is not relevant to the jet behavior. However, this calculation does show that the insert allows the jet tip material to collapse unaffected to form the fragment.

Figure 10 is comprised of two radiographs. The one on the left is from a test without the asymmetric insert, while the one on the right has the insert. Otherwise, the two tests are identical. It appears the insert is removing the late time debris, and examination of the targets confirmed this conclusion.

EFFECTS OF THE ATMOSPHERE

In addition to tests in air, tests in vacuum were desired to more realistically test spacecraft shielding components. The transition from air to a vacuum resulted in some dimension changes for the inhibitor and insert. The figures so far presented have been from tests in air; the rest of the figures will be from tests in vacuum.

Air seemed to affect the fragment. Erosion of the jet tip was clearly visible in an uninhibited test where there was substantial rotation of the leading fragment. In another uninhibited test, the large particle at the jet tip was seen to decrease in length between radiographs, from 3.0 cm to 2.3 cm in 50 μs (over a distance of 57 cm). This could be due to a number of effects: a negative velocity gradient in the particle, which would contract the particle; mechanical erosion of one material travelling through another; and ablation, where a phase change aids in the erosion. As to a negative velocity gradient in the jet tip, no change in the jet tip diameter was detectable from the radiographs, and a negative velocity gradient in the jet tip was not observed in the computations. The second two possibilities are difficult to quantitatively discuss. If the materials were incompressible perfect (nonviscous) fluids, Bernoulli's law could be used to estimate the erosion rate:

$$\frac{1}{2}\rho_{Al}(v-u)^2 = \frac{1}{2}\rho_{air}u^2 \qquad (5)$$

where v - u is the erosion rate. With ρ_{Al} = 2.7 g/cm^3 and ρ_{air} = 1.3 g/l one obtains an erosion rate of 250 m/s. In the above test, 1.25 cm would have eroded based on this approach. This is much larger than what actually occurred, but then air and aluminum are not incompressible perfect fluids, especially air at these velocities. However, certainly some decrease in length is due to erosion.

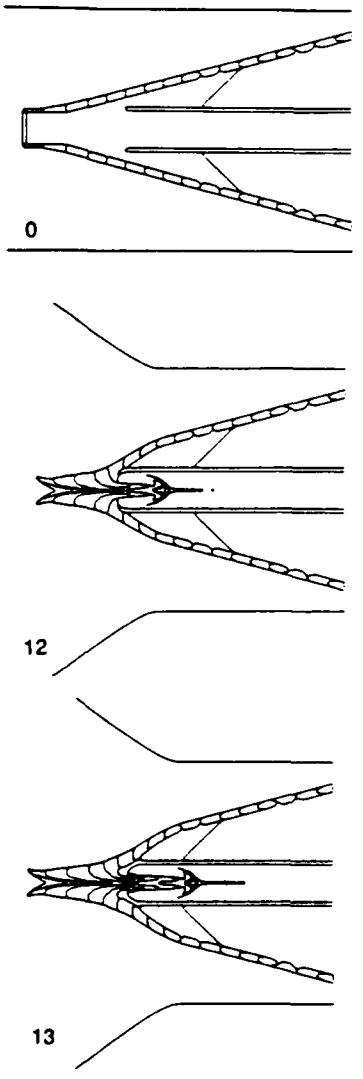


Fig. 9. Three times from the calculation with a tubular insert, at 0, 12, and 13 μs.



Fig. 10. X-ray views of tests without (left) and with (right) the aluminum insert. Note the absence of trailing debris in the right view.

Once in the vacuum chamber, the inhibitor and insert dimensions which were being used for the atmospheric tests produced an incohesive fragment over the greater flight distance. This was resolved by decreasing the height of the inhibitor, and lowering the height of the insert. This gave rise to a cohesive fragment with a larger mass. However, the fragment now seemed to be surrounded by a small amount of debris. It is possible that the air was helping retard this debris in the atmospheric tests.

EXAMPLES

The current design of the hypervelocity fragment launcher uses a copper inhibitor of height 4.47 cm and an inner diameter 1.19 cm, and a 0.76 cm tall triangular aluminum asymmetric insert placed within the cavity of the charge, shown in Fig. 11. These dimensions were determined through both experiments and computations. In the following X-ray views, the direction of motion is from top to bottom.

As a first example, Fig. 12 shows orthogonal views from the test which had the highest rotation rate encountered during the test program, rotating 90° in 240 μs. This rotation rate was constant based on measurements from the two sets of radiographs, with 0° extrapolating back to the vicinity of the original charge location. The fragment velocity was 11.1 km/s. These views showed that the fragment was hollow. Careful examination of Fig. 7 shows that the computations were also showing a decreased material density along the axial centerline.

Next, Fig. 13 shows orthogonal views of a fragment in flight. The fragment had an approximate length of 1.4 cm and a diameter of 0.53 cm to give an L/D of 2.6. Using a diameter for the hollow region of 0.18 cm, a fragment mass of 0.74 g was calculated. The fragment velocity was 11.2 km/s. The resulting crater in a 6061-T6 aluminum block is shown in Fig. 14. The target block was 15.3 cm in diameter, and 7.8 cm thick. The crater depth, measured from the top plane of the target, is 3.0 cm and its diameter is 4.1 cm. A spall plane is located 0.6 cm from the bottom of the target. The two very small craters visible on the top surface (to the right of the main crater) are due to trailing debris.

Although the charge is being used for the testing of shielding concepts at this time, it is still undergoing refinement.

CONCLUSION

The primary achievement of this program was the design of a hypervelocity fragment launcher. Experimental tests were performed to evaluate and refine the design. Numerical simulations were able to provide a qualitative picture of how the inhibitor was interacting with the jet, as well as quantitative times for these interactions. These computations provided considerable guidance in the design of the insert and inhibitor. The hypervelocity fragment launcher is being used to test various spacecraft shielding concepts. Further work would be to remove the remaining debris which seems to be travelling along with the fragment in the vacuum tests.

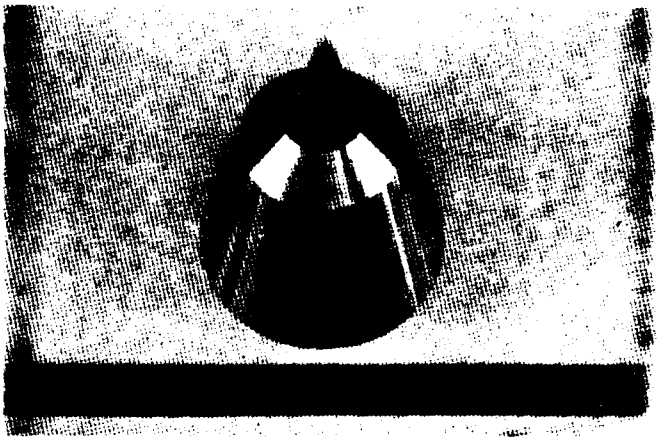


Fig. 11. Inhibitor design, with insert.

ACKNOWLEDGEMENTS

We would like to thank Jeanne Crews NASA-JSC for primary support and encouragement for this work. Support for calculations was also supplied by Southwest Research Institute under their Internal Research program. Robert Tipton and Chris Simonson, of Lawrence Livermore National Laboratories, were helpful in answering questions about CALE. The authors would like to thank Randy Tullos for his considerable help in all phases of the project.

REFERENCES

Buckley, P. (1990). Shaped Charge One-Dimensional (SC1d) computer code (evaluation copy), PMC, Inc.

Chanteret, P. Y. (1992). "Studies of Maximum Velocities for Coherent Shaped Charge Jets," *13th International Ballistics Symposium*, Stockholm, Sweden.

Grosch, D., J. Walker, S. Mullin and R. Tullos (1991). "Development of an Inhibited Explosive Hypervelocity Launcher," Southwest Research Institute Final Report 06-3513, San Antonio, Texas.

Johnson, G. R. and R. A. Stryk (1986). "User Instructions for the EPIC-2 Code," AFATL-TR-86-51.

Kronman, S. and A. Merendino (1963). "Inhibited Jet Charge," *Proceedings of the Sixth Symposium on Hypervelocity Impact*, Cleveland, Ohio.

Merendino, A., J. M. Regan and S. Kronman (1963). "A Method of Obtaining a Massive Hypervelocity Pellet From a Shaped Charge Jet," Ballistic Research Laboratories Memorandum Report No. 1508, Aberdeen Proving Ground, Maryland.

NASA (1991). "Space Station Program Natural Environment Definition for Design," Change Notice A1, SSP 30425 Revision A July 1991.

Tipton, R. (1990). "CALE Users Manual, Version 901101," Lawrence Livermore National Laboratory, Livermore, California.

Tullos, R., W. Gray and S. Mullin (1988). "Test and Evaluation of an Explosive Hypervelocity Launcher," Southwest Research Institute Final Report 06-1967, San Antonio, Texas.

Tullos, R., D. Grosch and J. Walker (1990). "An Explosive Hypervelocity Launcher for Orbital Debris Impact Simulations at 11.4—11.9 km/s," Southwest Research Institute Final Report 06-2880, San Antonio, Texas.

Walker, J. D. (1991). "Computational Modeling of an Explosive Hypervelocity Launcher," Southwest Research Institute Internal Research Report 06-9571, San Antonio, Texas.

Walters, W. P. and S. K. Golaski (1987). "Hemispherical and Conical Shaped-Charge Liner Collapse and Jet Formation," US Army Ballistic Research Laboratory Technical Report BRL-TR-2781, Aberdeen Proving Ground, Maryland.

Walters, W. P. and J. A. Zukas (1989). *Fundamentals of Shaped Charges*, New York, Wiley-Interscience.

Wenzel, A. B. (1987). "A Review of Explosive Accelerators for Hypervelocity Impact," Int. J. Impact Engng. 5, 681-692.

Wenzel, A. B. and J. W. Gehring (1965). "Techniques for Launching 0.01- to 25-Gram Discrete Projectiles at Velocities Up to 54,100 Ft/Sec," *Fourth Hypervelocity Techniques Symposium*, Arnold Air Force Station.

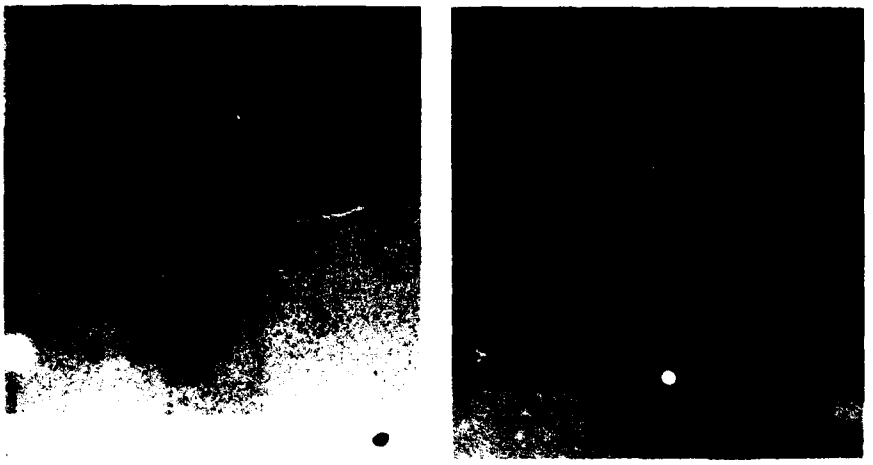


Fig. 12. Orthogonal radiographs of rotating fragment, travelling at 11.1 km/s.



Fig. 13. Orthogonal radiographs of fragment travelling at 11.2 km/s.

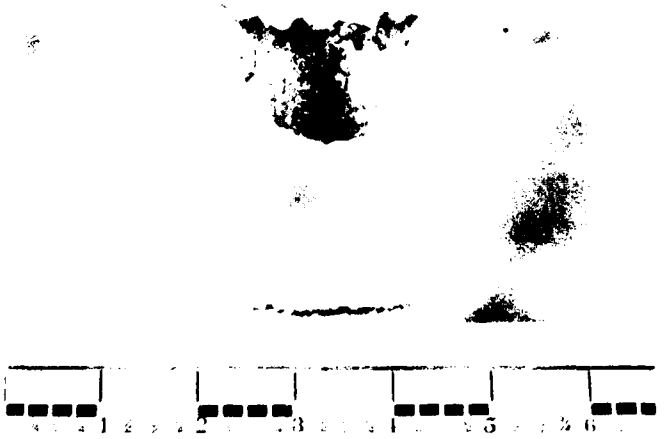


Fig. 14. Photograph of crater resulting from impact of Al 6061-T6 target and fragment shown in Fig. 13.

Int. J. Impact Engng Vol.14, pp 775 - 784, 1993
Printed in Great Britain

0734-743X/93 $6.00+0.00
Pergamon Press Ltd

MICROPARTICLE IMPACTS AT ULTRA-HIGH VELOCITIES: THEIR RELATION TO MACROPARTICLE IMPACTS

J. M. WALSH, G. L. STRADLING, G. C. IDZOREK, P-14
B. P. SHAFER, WX-DO,
Los Alamos National Laboratory
P.O. Box 1663, MS-D410
Los Alamos, New Mexico 87545

H. L. CURLING, JR.
Science Applications International Corporation
2301 Yale S. E. Suite E, Albuquerque, NM 87106

ABSTRACT

In recent years the Hypervelocity Microparticle Impact (HMI) project at Los Alamos has utilized electrostatically accelerated iron spheres of microscopic dimensions to generate ultra-high velocity impact experiments to about 100 km/sec, about an order of magnitude beyond the data range for precisely controlled impact tests with ordinary macroscopic projectiles. But the extreme smallness of the micro impact events brings into question whether the usual shock-hydrodynamic size scaling can be assumed. It is to this question of the validity of size scaling (and its refinement) that the present study is directed.

Impact experiments are compared in which two comparable impact events at a given velocity, a microscopic impact and a macroscopic impact, are essentially identical except that the projectile masses and crater volumes differ by nearly 12 orders of magnitude---linear dimensions and times differing by 4 orders of magnitude. Strain rates at corresponding points in the deforming crater increase 4 orders of magnitude with the size reduction. Departures from exact scaling, by a factor of 3.7 in crater volume, are observed for copper targets--with the micro craters being smaller than scaling would predict. This is attributed to a factor 4.7 higher effective yield stress occurring in the micro cratering flow. This, in turn, is because the strain rate there is about 10^8/sec as compared to a strain rate of only 10^4/sec in the macro impact.

The measurement of impact craters for very small impact events leads to the determination of metal yield stresses at strain rates an order of magnitude greater than have been obtained by other methods. The determination of material strengths at these exceedingly high strain rates is of obvious fundamental importance. Results are compared to recent theoretical models by Follansbee, Kochs and Rollett.

Finally, the problem is addressed of predicting crater sizes in a target material with strain rate effects. First some basic results are recalled pertaining to the late stage equivalence of hypervelocity impacts. It is then seen, for a strain rate dependent material, that the curve of dimensionless crater volume versus impact velocity is replaced by a family of curves, each member of which is for one final crater size. The spacing of the curves is determined by the stress versus strain properties of the material.

I. INTRODUCTION

The Hypervelocity Microparticle Impact (HMI) project, (Keaton, *et. al.*, 1990 Stradling, *et. al.* 1990) has obtained impact data from microscopic iron spheres impacting targets at impact velocities from 1×10^5 cm/sec to 100×10^5 cm/sec. The iron spheres are charged and accelerated electrostatically (Friichtenicht, 1962, Friichtenicht, 1964, Lewis, *et.al.*, 1970) in a 6 MV Van de Graaff accelerator. Each impact is characterized by simultaneous measurement of projectile charge and velocity using careful cross-correlation techniques (Idzorek, *et. al.*, 1990). Measurement of impact crater characteristics is performed

using a scanning electron microscope. A typical crater in copper is shown in Fig. 1. Impact studies have been performed on a variety of materials relevant both to practical impacts in space and to the study of impact physics. In this discussion we focus on impacts in copper and aluminum in order to compare with existing libraries of data from macroscopic impact physics research.

II. DEPARTURE FROM STRICT SIZE SCALING FOR IMPACT CRATERS IN SOFT COPPER TARGETS

Micro impacts, when compared to the same impacts at ordinary sizes, make it possible to put classical shock-hydrodynamic size scaling to severe tests in which corresponding masses (and other extensive variables) are scaled down nearly 12 orders of magnitude---linear dimensions and times being scaled down 4 orders of magnitude. Strain rates increase four orders of magnitude in the size reduction.

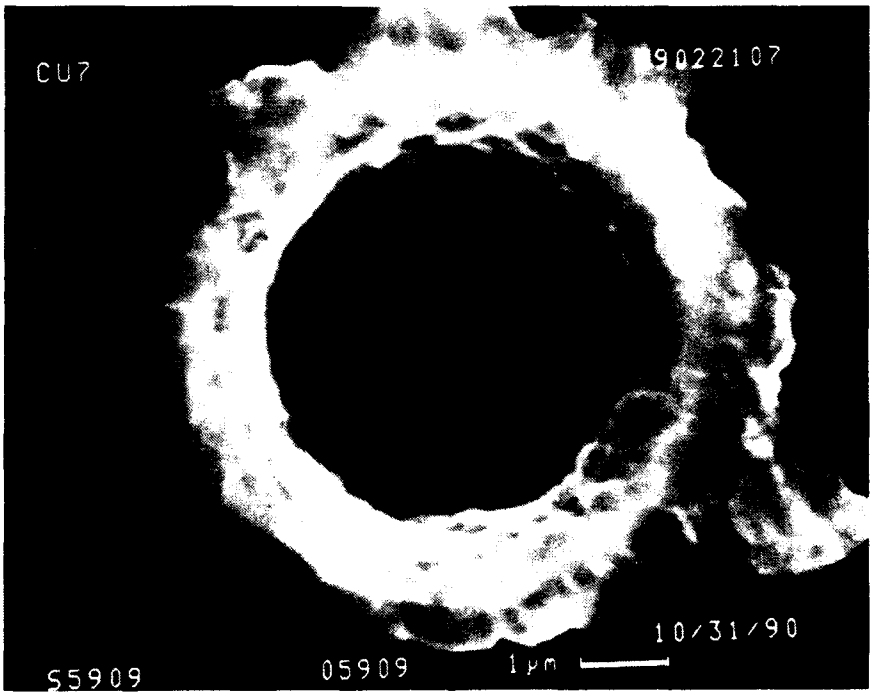


Fig. 1. A typical hypervelocity impact crater in a single-crystal sample of copper cut in the 100 crystalline plane. The projectile was a microscopic iron sphere of mass 1.89×10^{-12} gm impacting at 12.5×10^5 cm/s. The craters produced by microscopic impacts in homogeneous materials are axisymmeteric and appear to be geometrically similar to the craters produced by macroscopic impacts. In this case the crater diameter is 4.0 μm. Crater depth is not easily obtained with the scanning electron microscopy technique used to characterize the craters.

As Fig. 2 we reproduce the pertinent data for copper, to call attention to the fact that the normalized target crater volume is a factor of 3.7 smaller for the HMI micro-impacts (projectile masses 0.25×10^{-12} gm and 1.5×10^{-12} gm) than for the large scale impacts (projectile masses 0.15 gm and 0.50 gm) at the same impact velocity (6×10^5 cm/sec). Exact size scaling would, of course, require that these normalized crater volumes be equal. Thus, the size reduction, by a factor[1] of about 0.3×10^{12} in the projectile mass (or, equivalently, by a factor of 0.7×10^4 in projectile diameter) has not only reduced the crater volume by a factor of 0.3×10^{12}, as it should in accord with strict scaling, but also by an additional factor of 3.7.

[1] The average mass of the bigger impacts is $(0.5 + 0.15)/2 = 0.3$ gm. The average mass of the HMI impacts is $(0.25 + 1.5) \times 10^{-12}/2 = 0.9 \times 10^{-12}$ gm. Thus the reduction is by a factor of about 0.3×10^{12} on mass, or 0.7×10^4 on linear dimensions and times.

III. STRAIN-RATE EFFECT AS A REASON FOR SCALING FAILURE

We believe that this failure to scale exactly is due to strain-rate effect within the copper. More fully, we develop here the notion that the higher strain rates in the smaller flows[2] cause a higher effective flow stress in the smaller flows and a correspondingly smaller crater.

In Fig. 3 we reproduce (in addition to impact data for copper) a well-known correlation formula due to Sorensen (Sorensen, 1965) for hypervelocity impact data. It shows, in particular, that crater volume V varies with target shear yield strength s as $s^{-0.845}$. This dependence of V on s is shown by Sorensen to fit a wide range of impact data for metal targets, encompassing a variation of s from 0.13 kilobars for lead to nearly 10 kilobars for a steel. See Sorensen, 1965 for a detailed discussion. Similar dependences of V on s have been established in hydrocode studies. (An early example is the calculation of cratering for hard and soft aluminum, reported in Dienes and Walsh, 1969 and 1970 and described in section IV below. Very recently Rich Davidson and Michael Burkett at Los Alamos have each independently performed cratering calculations for copper, in support of the present effort, and find crater volumes in good agreement with Sorenson.) Thus, adopting Sorensen's correlation, we find that the observed 3.7-fold reduction in crater volume could be attributed to a yield stress increase of a factor of 4.7.

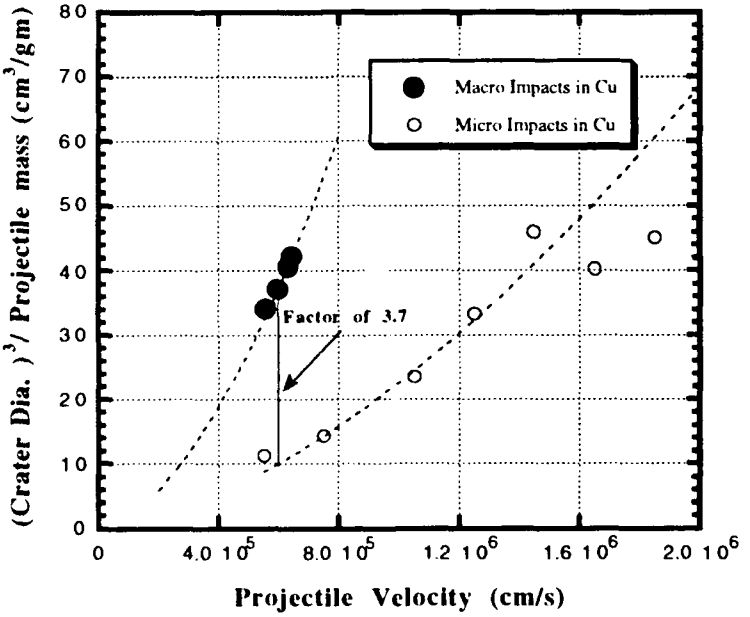


Fig. 2. Hypervelocity impact cratering data for copper. The upper curve, with four representative data points, is from Sorensen's empirical correlation of (macro) impact data for copper. See also Fig. 3 and Sorensen, 1965, for further information on Sorensen's work. The lower curve shows the (micro) impact data on copper. Of importance to the present discussion is the fact that the normalized crater volumes in the micro impacts are smaller by a factor of 3.7. The two curves would coincide if size scaling were exact.

IV. STRAIN RATES IN HYPERVELOCITY IMPACT

Next, we need a reasonably good estimate of the strain rates occurring in the cratering process. Specifically, it will suffice to estimate the average strain rate during the crater formation for the 0.3 gm (macro) impact at 6×10^5 cm/sec since we already know the ratio of the strain rates in the micro and macro events. Making this estimate is the object of the present Section.

[2] By the above factor of 0.7×10^4 if the flows scaled exactly, and by an additional factor of $3.7^{0.333} = 1.5$ because of the smaller-than-expected craters--combining for a factor of 10^4.

In a hypervelocity impact, the initial shock pressure is given by:

$$P = \rho U_S U_p = 1.9 \times 10^{12} \text{ dynes/cm}^2 = 1.9 \text{ megabars}, \quad (1)$$

since the shock particle velocity U_p is 3×10^5 cm/sec from symmetry, the density ρ is 8.9 gm/cc and the shock wave velocity U_S associated with the given particle velocity is 7×10^5 cm/sec. This is more than three orders of magnitude greater than material strength, implying that the early phases of the impact are hydrodynamic with strength playing a negligible role. This shock front and the attached pressure pulse propagate almost hemispherically into the thick copper target, and serve to set the engulfed copper into nearly hemispherical motion. Were it not for the finite yield strength of the copper the (nearly hemispherical) crater would grow without limit. Instead, the 1.385 kilobar copper yield strength limits the crater volume to about 83 times the volume of the impacting projectile, in accord with Sorensen's correlation formula as applied to this impact.

Two-dimensional finite difference hydrocode calculations (axisymmetric and time dependent, incorporating material compressibility and strength effects by utilizing available material property formulations) can provide us with a very detailed description of the impact process, and such calculations have been provided by a number of investigators over the past 30 years.

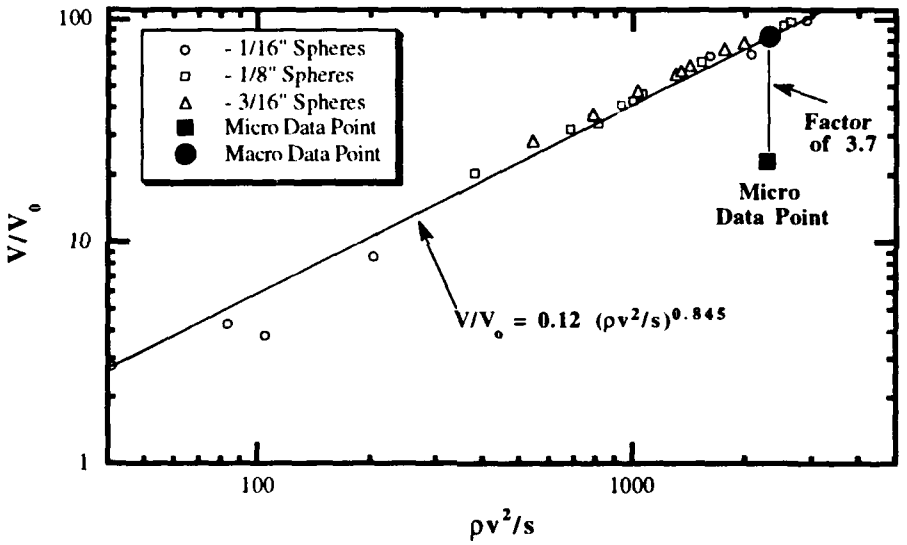


Fig. 3. Sorensen's data correlation for copper, from Sorensen, 1965. The data extend to about 7.5×10^5 cm/sec. The analytical correlation is for several metals and therefore does not fit copper exactly, although quite well. It may be noted that the factor 3 variation in projectile diameters (27 in masses) does **not** cause an apparent size effect in the macro data points. The point at $v = 6 \times 10^5$ cm/sec on the micro curve (Fig. 2) has been transformed to this plot and is seen to be substantially below the macro data. (To transform this point the values $\rho = 8.9$ gm/cm^3 and $s = 1.385 \times 10^9$ dynes/cm^2 were used for the density and shear yield strength of annealed copper.) The projectile mass ratio between the micro and macro experiments is nearly twelve orders of magnitude, as explained in the fourth footnote.

While a specific computation has not yet been performed for our 0.3 gm, 6×10^5 cm/sec impact into copper, suitable computed results from other impacts have been reported in the literature and can be used to deduce (using only Sorensen's correlation formula and dimensional analysis) useful estimates of the effective strain rate in our impact. Dienes has reported calculations (Dienes and Walsh, 1969 and 1970) for a spherical aluminum projectile (diameter 0.476 cm) impacting a hard aluminum target (shear yield strength 2.39 kilobars) of density 2.7 gm/cc at a velocity of 7.3×10^5 cm/sec. He finds for times of 2, 4, 8 and 16 microseconds that the crater depth is 0.4, 0.8, 0.9, and 1.0 of its final value. Hence for present purposes we can take this aluminum crater formation time to be 15 microseconds. Next we note that Sorensen's correlation formula:

$$V/V_0 = C_1(\rho v^2/s)^{.845} \tag{2}$$

is entirely equivalent to

$$T/T_0 = C_2(\rho v^2/s)^{\frac{.845}{3}} = C_2\,(\rho v^2/s)^{.282} \tag{3}$$

when re-expressed to give the time T for crater formation, Here C_1 and C_2 are dimensionless constants and T_0 is any suitable measure of the impacting projectile size (such as the time it takes the free flying projectile to move one diameter) that must, of course, be the same measure for the two impacts under consideration. Thus T_0 would be:

$$T_0 = 0.476 \text{ cm}/(7.3 \times 10^5 \text{ cm/sec}) = .65 \text{ microseconds} \tag{4}$$

for the aluminum problem and

$$T_0 = 0.400 \text{ cm}/(6.0 \times 10^5 \text{ cm/sec}) = .67 \text{ microseconds} \tag{5}$$

for our copper impact. Next for the two cases of aluminum and copper impacts, the quantities $(\rho v^2/s)$ and $(\rho v^2/s)^{.282}$ would be:

$$(\rho v^2/s) = 602; \qquad (\rho v^2/s)^{.282} = 6.08 \tag{6}$$

and for the copper impact;

$$(\rho v^2/s) = 2313, \qquad (\rho v^2/s)^{.282} = 8.88. \tag{7}$$

Hence the 15 microsecond crater formation time for aluminum scales to

$$T=(\,8.88/6.08)(.67/.65)15 \text{ microseconds} = 23 \text{ microseconds} \tag{8}$$

for our copper impact.

In another problem from (Dienes and Walsh, 1969 and 1970) a soft aluminum target (shear yield 0.75 kilobars) was used and total plastic work was reported instead of crater depth. (Other problem parameters were the same as in the hard aluminum impact.) At 4, 8 and 16 microseconds the total plastic work was 20%, 50%, and 95% of the final value when the flow was completely arrested. This again suggests a time of about 15 microseconds for flow arrest. Scaling this over to our copper impact, by a calculation similar to that detailed for the hard aluminum, gives a time of 16 microseconds for the copper impact.

We need also to know the average strain occurring in the plastically deforming material when the crater is formed. Here both computational and experimental evidence (where targets thicker than about two crater depths react much the same as semi-infinite targets subjected to the same projectile impact) suggest that the target material within about one crater radius of the crater is effective in arresting the flow. For this material the strain field is a maximum, about 0.6 at the crater surface, dropping to essentially zero a crater depth into the material. A suitable average strain for this plastically deforming material is about 0.2. (This value may be reliable only to about a factor of two.) Dividing it by the above crater formation times of 23 microseconds and 16 microseconds implies average strain rates of 0.86×10^4/sec and 1.25×10^4/sec. Hence we adopt a value of 1.0×10^4/sec as an average strain rate in our 0.3 gm copper impact, recognizing that this value is uncertain by a factor of two. Surprisingly, perhaps, this uncertainty is tolerable in present considerations because of the weak dependence of yield stress on strain rate.

It may be noted that a more accurate determination of this average strain rate could be made as part of a hydrocode computation of our copper impact. For this purpose we suggest

$$\bar{\dot{\varepsilon}}_p = \frac{\sum_N \sum_K W_p(K,N)\,\dot{\varepsilon}_p(K,N)}{\sum_N \sum_K W_p(K,N)} \tag{9}$$

where K is the cell number and N is the time step number. The formula gives an average strain rate, averaged over all (Eulerian) cells and all time steps, with each $\varepsilon_p(K,N)$ weighted in proportion to the amount of plastic work $W_p(K,N)$ occurring in the cell during the time step.

V. COMPARISON OF RESULTS WITH RECENT THEORETICAL EXPECTATIONS

In Section II we saw that when the projectile mass was reduced by a factor 0.3×10^{12}, the crater volume was reduced not only by this factor, as expected from size scaling, but by an additional factor of 3.7.

In Section III we found, using a well-established empirical correlation, that the factor 3.7 crater volume reduction would be caused by a yield stress increase by a factor of 4.7.

In Section IV we used published computational results for the crater formation process, together with the Sorensen correlation formula, to establish that the average strain rate in the macro impact was about 1.0×10^4/sec. This means that the average strain rate in our micro impact [which must be greater by a factor of $(0.3 \times 10^{12} \times 3.7)^{.333} = 1.03 \times 10^4$] is about 1.0×10^8/sec. So it remains to ask whether it is indeed reasonable to expect a factor 4.7 increase in the flow stress over this strain rate regime.

Experimental work by Clifton and co-workers (see Clifton, R. J. 1990, Klopp, R. W. *et. al.* 1985, Tong, W. *et. al.* 1992) at Brown University, using a well-known oblique impact technique developed by them, has been performed for copper, aluminum and iron specimens and has provided some flow stress data in the 10^4 to 10^7 sec^{-1} strain rate regime. The technique is quite different from the one described here; in particular, the specimen is simultaneously subjected to high impact pressure during deformation whereas in the present effort the deformation occurs during the crater formation flow at essentially zero pressure. The Brown University work suggests a substantial strain rate effect in copper at high strain rates, in qualitative agreement with the present study. Ultimately, it would clearly be desirable to combine the two types of data into a comprehensive model including both the strain rate effect and pressure hardening.

Fortunately, the properties of copper at exceedingly high strain rates has been the subject of theoretical modelling investigations by Follansbee, Kocks, Rollett and others (Follansbee, 1988, 1991). In Fig. 4 the theoretical stress *versus* strain rate curve is reproduced (from Fig. 2 of Follansbee, 1991) for a constant strain of 0.1. This strain is taken to be an average strain <u>during</u> the cratering flow, corresponding to the estimate made in Section III that the average <u>total</u> strain is about 0.2. (Also the theoretical stresses were reduced by a factor of $\sqrt{3}$, , in accord with the von Mises yield condition, because longitudinal yield stresses were used, whereas shear yield stresses are used throughout the present paper.)

Plotted also in Fig. 4 are our two experimental points $\sigma = 1.385$ kilobars at $\dot{\varepsilon}_p = 10^4$ /sec and $\sigma = 6.5$ kilobars at $\dot{\varepsilon}_p = 10^8$ /sec.

The most important conclusion to be drawn from the present comparison is that both the theory (Follansbee, 1988, 1991) and experiment are indicating a very substantial strain rate effect in copper in the 10^4/sec to 10^8/sec strain rate regime. The experimental effect is somewhat the larger, the yield stress increasing by a factor of 4.7 as compared to 2.8 for the theoretical curve. In the theoretical modelling[9] this strain rate effect has been attributed to a gradual transition, as the strain rate is increased, from thermally-activated to viscous-drag controlled deformation.

The experimental factor of 4.7 depends upon only the experimental volume ratio of 3.7 (Fig. 2) and the Sorensen correlation formula, and is estimated here to be reliable to 10% or less. Other aspects of the comparison are discussed in the next section.

VI. COMMENTS ON SOURCES OF ERROR

It was remarked in Section IV that the estimate of the average strain rate in the macro impact was uncertain by a factor of about two. In the Fig. 4 data plot the experimental points are represented as circles with diameters spanning a factor of four in the strain rate. It is readily apparent that a lateral shift of the macro data point to either of the extreme positions (causing an equal lateral shift of the micro point) would have only a very small effect on the comparison.

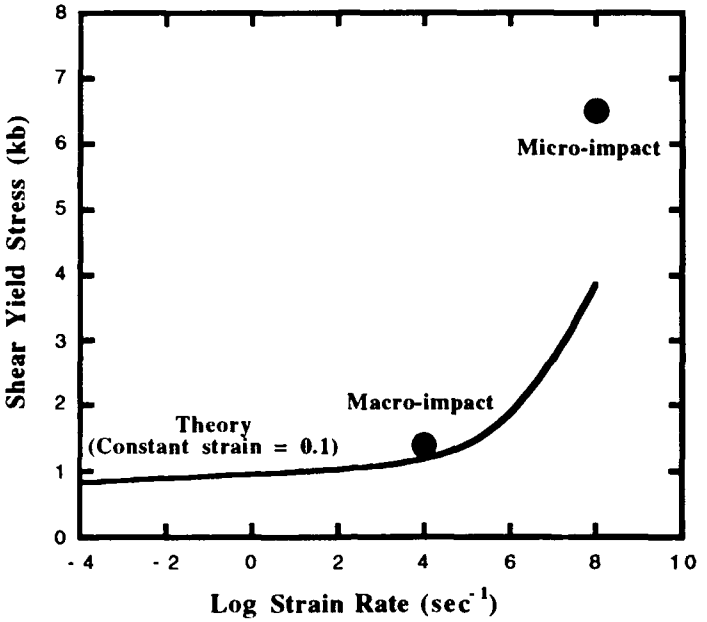


Fig. 4. Shear yield stress σ versus strain rate for copper strained to 0.1. The theoretical curve is from Follansbee, 1991, the results from Fig. 2 of the reference being re-presented here in terms of shear yield stress at a constant strain of 0.1.

In Section V we estimated an average strain in the cratering flow to be 0.1. This strain was used to select the appropriate constant-strain theoretical curve from (Follansbee, 1991). Had one used 0.05 or 0.2 instead of 0.1, the corresponding average-strain theoretical curve, in the two cases, would be below or above the macro experimental point and in somewhat poorer agreement with that point. Here, however, an alternative interpretation is useful: The properties of copper at strain rates around 10^4/sec and below, where test data and theoretical understanding have been in accord for years, can be assumed known. One then selects that particular constant-strain curve from (Follansbee, 1991) that causes agreement with the macro data point. This constant-strain curve is the one for an average strain in the cratering flow of about 0.13, instead of our estimated value of 0.1 given above. (This might, in the present situation, be a better way to estimate the average strain in the cratering flow). In any event, the theoretical strain rate enhancement factor (taken to be 2.8 in Sec. V) is a weak function of which constant-strain curve one uses and would not be substantially affected.

Finally, we recall that the impacting spheres in the micro experiments are actually iron instead of copper. In our comparison of the micro- and macro-events these iron projectiles are assumed to be equivalent to copper projectiles of equal mass. This equal-mass assumption has been investigated extensively in test work and in computer studies and is found to be accurate for sufficiently high velocities and/or density ratios sufficiently close to unity. For the present application at 6×10^5 cm/sec, with iron and copper projectiles, the cratering effects on thick copper targets are expected to be essentially identical.

VII. EXTENSION TO ALUMINUM

The HMI data for aluminum target impacts exhibits essentially the same behavior as copper, i. e. the micro crater volumes are small by about a factor of 4, corresponding to a strain rate enhancement of yield stress by a factor of 5.

Attention here has been focussed on copper because its constitutive modelling appears to be more advanced, but it seems likely that aluminum (another FCC metal) will exhibit similar behavior to copper at high strain rates. (Private communications with A. D. Rollett and P. S. Follansbee.)

VIII. CRATER SIZE PREDICTION FOR TARGET MATERIALS WITH STRAIN RATE EFFECTS

From a knowledge of the stress versus strain rate curve for a material, such as the one for copper in Fig. 4, and certain results pertaining to the late stage equivalence of hypervelocity impacts, one can arrive at a complete capability for crater size prediction in a rate dependent material.

First, we recall a basic result about the hypervelocity impacts of chunky projectiles on thick targets: Two interactions differing only in regard to the impact velocity, while qualitatively different in their early stages (quite different pressures, flow velocities, and so forth) become more similar as the interactions progress until they are essentially identical at late times, except for a simple size scale factor. The linear scale size factor between the flows is found, computationally, to be equal to the .58-power of the factor by which the impact velocity is increased. Thus the craters, which are formed after the flows become similar, differ in crater linear dimensions by a factor equal to the .58-power of the velocity increase factor, or in volume by a factor equal to the impact velocity ratio to the 1.74-power (since 3 x 0.58 = 1.74). The exponent 1.74±.01 is found to be remarkably independent of the target material (though only plastically deforming metal targets have been studied). Also this late stage equivalence is observed only for sufficiently high impact velocities (greater than about target sound speed) and is apparently intimately associated with the highly non-linear nature of the early stage of hypervelocity impact. The primary usefullness of the result is that it forms a sound theoretical basis for extending experimental impact results (a single impact crater determination at, say, 6×10^5 cm/sec for a specified projectile and a given target material) to the highest velocities of interest in meteroid and space applications.

The late stage equivalence of hypervelocity impacts is best documented in the comprehensive review article by Dienes, (Dienes and Walsh, 1970), where results from many impact calculations are discussed. Dienes also provided a satisfying purely analytical treatment of the relatively simple case of slab impact of ideal gases, thus demonstrating the principle of late stage equivalence in impact dynamics, without having to rely on hydrocode computations inaccesible to the reader.

In these earlier works attention was restricted to strain-rate independent materials. For such materials, the effective yield stress is independent of the size of the cratering flow. For strain rate dependant materials this is no longer true. Since the strain rate is inversely proportional to the linear scale size, the smaller of two flows will have higher strain rates at corresponding points and thus associated higher yield stresses. For two cratering flows of the same size, however, the effective yield stress is the same, so that we can assume that V/V_0 again varies as the impact velocity, $v^{1.74}$. These curves of constant crater size are plotted for copper as Fig. 5. On a given curve there exists some effective average strain rate and an associated average yield stress, both of which can sensibly be taken to be constant within a single crater formation flow. However, differences in these values must be accounted for in comparing micro and macro impacts such as those discussed in earlier sections for copper. On each curve the crater size (volume V or crater diameter d) is constant, but the projectile size ($V_0 = m_0/\rho_0$) is understood to vary. For the copper data discussed earlier the 1 micron curve lies below the (macro) 1 centimeter curve by a factor of 3.7 in V/V_0 and the intermediate curves are at positions determined by the stress versus strain rate curve for copper.

For many applications it is desirable to have the projectile size constant on each curve, so that the crater size increases. Such a replot of the information in Fig. 5 is presented in Fig. 6. Along these curves the crater volume V increases more rapidly than $V^{1.74}$. This is because strain rate and yield strength are decreasing, causing larger craters.

XI. CONCLUSIONS

The classical laws of size scaling, as applied to the shock hydrodynamics of condensed media, have been put to severe test. The size reduction spans four orders of magnitude in length or time dimensions, or 12 orders of magnitude in extensive variables, such as corresponding masses or volumes. The observed departure from exact scaling is by a factor of 3.7 in extensive variables, or by 1.5 in corresponding lengths or times.

The departure is attributed to strain rate enhancement of the flow stress in the copper targets. This dramatic rise in flow stress at very high strain rates had already been anticipated in the theoretical literature.

Work in this area is of interest for several reasons:

1. It validates and/or refines classical shock-hydrodynamic size scaling, and thus pertains directly to the important engineering area of scale model experimentation.

2. Strain rates attainable in microparticle impacts extend the present-day test range by more than an order of magnitude. The determination of material strengths at these exceedingly high strain rates is of obvious fundamental importance.

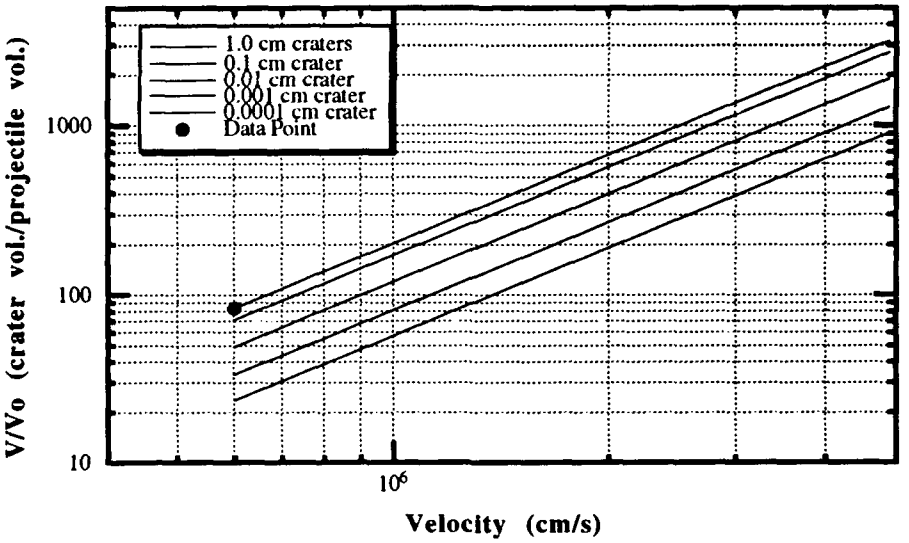


Fig. 5. Relative crater volume V/V_0 versus impact velocity for copper targets. The data point is the experimental macro point discussed in the text ($v = 6 \times 10^5$ cm/sec, $V/V_0 = 83.5$, crater diameter 1 cm, average strain rate $\dot{\varepsilon} = 10^4$ /sec). Each curve of constant crater size has slope 1.74. Curve spacings are determined from: $\dot{\varepsilon} d = 10^4$ cm/sec assumed constant (size scaling), $s = [1.385 + 0.3(\log\dot{\varepsilon} - 4)^2] \times 10^9$ dynes/cm^2 (a fit to the stress versus strain rate curve of Fig. 4, for $\dot{\varepsilon} \geq 10^4$ /sec), and the $s^{-0.845}$ dependence of relative crater volume upon yield strength for constant impact velocity (from the Sorensen correlation seen as Fig. 2).

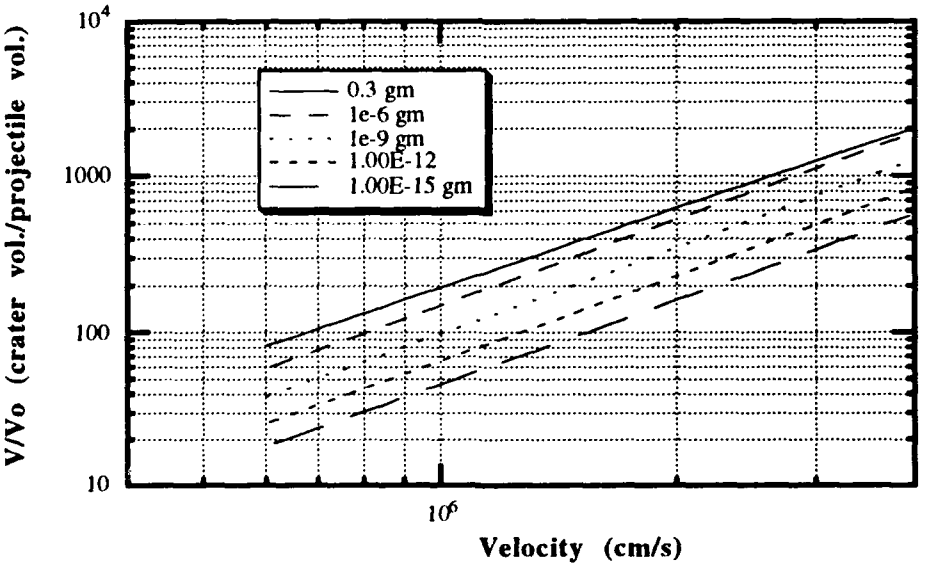


Fig. 6. Relative crater volume V/V_0 versus impact velocity for copper targets. Projectile mass is constant for each curve.

3. For velocities above about 15×10^5 cm/sec, the only precisely controlled hypervelocity experiments have been performed, at Los Alamos and elsewhere, with electrostatically accelerated microparticles. Experimental data are available for velocities throughout the meteoroid velocity range (to

about 70 x 10^5 cm/sec) and beyond. To understand this valuable data source, and to be able to scale it with confidence to larger impact events we need, as done here for copper, to quantify the departures from exact size scaling and attribute such departures to appropriate material properties.

ACKNOWLEDGEMENTS

We wish to acknowledge the excellent support of the other members of the HMI team whose contributions to the impact experiments over many long shifts produced the data discussed above. These include Roger Persons, Anna Blossom, Mike Collopy, Steven Fuerstenau and the LANL Ion Beam Facility operating crew. We also acknowledge many helpful interactions with M. Scharff and J. Kamm of SAIC, La Jolla.

REFERENCES

Clifton, R. J. (1990) High strain rate behavior of metals, *Appl Mech Rev*, **43**, no 5, Part 2 S9-S22.

Dienes, J. K. and J. M. Walsh (1969) Theory of Hypervelocity Impact, S-Cubed Report 3SIR-676.

Dienes, J. K. and J. M. Walsh (1970) Theory of Impact: Some general principles and the method of Eulerian codes, In: *Hyper Velocity Impact Phenomena*, Edited by Ray Kinslow, Academic Press.

Follansbee, P. S. (1988) The rate dependence of structural evolution in copper and its influence on the stress-strain behavior at very high strain rates. In: *Impact Loading and Dynamic Behavior of Materials*, Edited by, C. Y. Chiem, H. D. Kunze, and L. W. Myer, Vol. 1, Informationsgesellschaft, Verlag.

Follansbee, P. S. (1991) Shear prediction in shock loaded copper," In: *Proceedings of 1991 APS Topical Conference on Shock Compression of Condensed Matter*. Also available as Los Alamos document, LA-UR 91-1994.

Friichtenicht, J. F. (1962), Two million volt electrostatic accelerator for hypervelocity research, *Rev. Sci. Inst.*, **33**, 209.

Friichtenicht, J. F. (1964), Micrometeroid simulation using nuclear accelerator techniques, *Nucl. Inst. Meth.* **28**, 70.

Idzorek, G. C., P. W. Keaton, G. L. Stradling, M. T. Collopy, H. L. Curling Jr., and D. B. McColl (1989). Data acquisition system for a hypervelocity-microparticle-impacts laboratory, *International Journal of Impact Engineering*, **10**, 261-270.

Keaton, P. W. *et. al.* (1990) A hypervelocity-microparticle-impacts laboratory with 100 km/s projectiles, *Int. J. Impact Engng.* **10**, 295-308.

Klopp, R. W. , R. J. Clifton, and T. G. Shawki (1985) Pressure-shear impact and the dynamic vistoplastic response of metals, In: *Mechanics of Materials*, North-Holland **4** 375-385.

Lewis, A. R. and R. A. Walter (1970) Electrostatic acceleration system for hypervelocity microparticles with selected kinematic properties. NASA TN D-5780, Electronics Research Center, Cambridge, MA.

Sorensen, N. R. (1965) Systematic investigation of crater formation in metals, In: *Proceedings of Seventh Hypervelocity Impact Symposium*. Martin Company, Orlando.

Stradling, G. I *et. al.* (1990) Searching for momentum enhancement in hypervelocity impacts, *Int. J. Impact Engng.* **10**, 555-570.

Tong, W., R. J. Clifton, and S. Huang (1992) Pressure-shear Impact Investigation of strain rate history effects in oxygen-free high-conductivity copper, *J. Mech. Phys. Solids*, **40** no 6 1251-1294.

Int. J. Impact Engng Vol.14, pp.785 – 796, 1993
Printed in Great Britain

0734-743X/93 $6.00+0.00
Pergamon Press Ltd

CHARACTERIZATION OF A SMALL-SCALE EXPLODING BRIDGE FOIL FLYER GENERATOR

J.A.Waschl and D.J.Hatt

DSTO, Materials Research Laboratory,
PO Box 50, Ascot Vale, Victoria, 3032,
Australia

ABSTRACT

Empirical relationships between the velocity of small plastic flyer plates and capacitor charge voltage and energy have been developed for small exploding bridge foil (EBF) assemblies used in an electric gun arrangement. Of particular interest was the effect of capacitance, inductance, flyer plate thickness and barrel dimension. Three different switch types were used. Velocity measurements were performed over the range 0.5 mm/μs to 7 mm/μs using a VISAR velocity interferometer.

Electrical Gurney parameters were calculated from flyer velocity and burst current density data. The Gurney parameters were found to be different for each capacitance value. For fixed capacitance, but different EBF configurations, the parameters were found to be similar.

The peak flyer velocity as a function of charge voltage was found to be non-linear; this was also the case for the peak flyer velocity versus firing energy and energy-up-to-burst versus firing energy data. The non-linear relationship indicates that the EBF flyer generator becomes less efficient as the firing energy increases.

INTRODUCTION

The exploding bridge foil (EBF) comprises an " hour-glass " shaped thin metal foil intimately bonded to a thin plastic sheet (typically Mylar or Kapton). The waist area of the foil defines the bridge. When a high current rapidly flows through the foil, the bridge explodes and accelerates a section of the plastic sheet to high velocity (often in excess of 5 mm/μs). This flying section, commonly referred to as a flyer plate, can be used to tailor the impact pressure and shock duration in shock impact experiments (Chau *et al.*, 1990). For improved efficiency, the EBF assembly usually includes a tamper and a barrel (Fig.1). The complete EBF flyer generator includes a storage capacitor, a fast acting switch, a transmission line, and the EBF assembly.

The performance of an exploding bridge foil generator, defined in terms of the velocity of the flyer plate, is governed by the EBF configuration and by the firing unit circuit parameters, viz. capacitance, inductance, resistance, and capacitor charge voltage (or energy). To understand the individual effect of these parameters the velocity of the flyer plate can either be measured continuously or over discrete intervals. For the former, optical techniques such as the VISAR (Velocity Interferometer System for Any Reflector) (Barker and Hollenbach, 1972) or the Fabry-Perot interferometer (McMillan *et al.*,

1988) are usually used. For the latter, a TOAD (Time of Arrival Detector) technique (Waschl, 1988) provides an average velocity.

In the present paper, VISAR data were employed to determine the effect of circuit parameters on the peak velocity of small-scale flyer plates (< 1 mm square bridge). In addition, the effect on peak velocity of different EBF designs and of three different spark gap switches are presented. Empirical relationships between the electrical characteristics of the bursting bridge and the peak velocity are also examined.

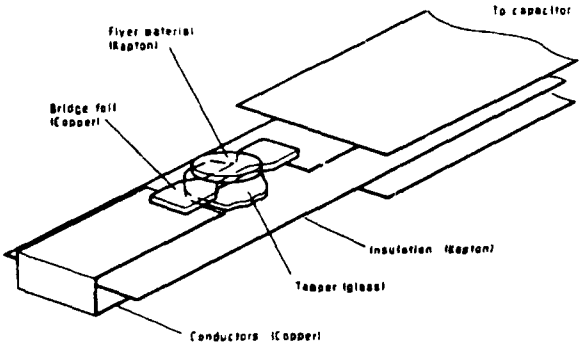


Fig. 1. Exploding bridge foil (EBF) flyer generator.

EXPERIMENTAL

The EBF flyer generator employed flyer plates (Kapton) of 13 μm, 25 μm, and 50 μm thickness. The barrel diameters were 0.25 mm, 1.0 mm or infinite (i.e., no barrel). A copper stripline connected the selected firing capacitor to the bridge foil. The capacitor values were 0.05 μF, 0.10 μF, and 0.22 μF; to facilitate operations, two capacitors of each value were used. A glass tamper was used underneath the foil. For some of the tests performed, the standard circuit inductance of ≈10 nH was increased to 35 nH and 73 nH.

Two of the three switches used were triggered vacuum spark gap switches (Reynolds IVARC 251-1001 and EEV TVG-5) while the third was an MRL experimental planar triggered spark gap switch operated at ambient air pressure. The planar switch consisted of three electrodes etched from the stripline material (Fig. 2). For the triggered vacuum spark gap switches, an alternative stripline design employed a rectangular gap across which a switch was attached.

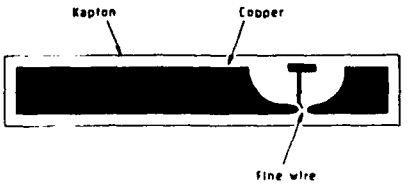


Fig. 2. Planar spark gap switch.

The firing capacitor was charged from MRL designed and constructed high voltage power supplies. The supplies operated in a simple transformer mode using a quadrupler. The high voltage output was monitored via a high impedance voltage probe and a digital voltmeter.

The EBF current and voltage were monitored via a current viewing resistor (CVR) and a two pin voltage probe, respectively. The probe comprised a 50 Ω resistor in series with a current transformer (Tektronix CT-2). A data reduction program (Waschl, 1988) was employed to determine various electrical characteristics of the EBF. Parameters such as dynamic foil resistance, current density and energy-up-to-burst were calculated for later comparison with the velocity data.

Once the capacitor was charged, a delay pulse generator was triggered to provide sequential triggering of, in order, an electro-optical shutter, the VISAR photomultipliers, an avalanche transistor pulse generator, and finally the spark gap switch. The avalanche pulser provided a fiducial signal so that records from different oscilloscopes could be correlated.

Laser output powers were in the range 0.1 W to 0.3 W and exposure of the target to the laser beam, controlled by the electro-optic shutter, commenced a few microseconds before bridge foil functioning.

RESULTS

System Characterization

The intrinsic circuit inductance and resistance are influenced by the choice of capacitor and the design of the stripline. In addition, the dynamic circuit resistance is dependent on the spark gap switch (Loeb, 1939) and the charge voltage (Richardson, 1987). In these experiments, the stripline design was essentially kept constant.

For each circuit parameter or EBF configuration investigated, the circuit inductance and resistance was estimated from ringdowns (Waschl, 1988). The approximate mean calculated values for inductance and resistance are shown in Table I. For the six different switch and capacitor arrangements the inductance values were in the range 9-14 nH while the resistance values were in the range 40-230 mΩ. The resistance for each arrangement tends to increase as the voltage decreases. For the MRL switch/0.05 μF arrangement the trend was less clearly defined due to the scatter in the data. The MRL switch was more resistive than the vacuum spark gap switches.

Table I. Circuit Inductance and Resistance

Switch	Capacitance (μF)	Inductance (nH)	Resistance (mΩ)	Firing Voltage (kV)
MRL	0.05	9	230	3.7-2.0
	0.10	10	90-170	2.2-0.6
	0.22	11	90-150	2.0-0.6
Reynolds	0.05	11	70-90	3.2-1.5
	0.22	14	40-80	3.0-0.5
EEV	0.22	14	50-90	1.8-0.5

The measured peak current as a function of firing voltage is shown for each of the three switch arrangements in Fig. 3. The peak current-voltage relationships appear to be linear.

Variation of Peak Velocity with Firing Voltage/Energy

The peak flyer velocities were measured from the velocity-time histories. The signal-to-noise ratio of the raw VISAR data signals was usually low at the moment the flyer reached its maximum velocity.

Consequently, many of the velocity-time histories were correspondingly noisy near the peak; the peak values were thus determined by smoothing the curve by eye. In general, the noise level increased with increased firing voltage. The uncertainty of the VISAR measurements was estimated to have ranged from $\pm 2\%$ to $\pm 5\%$.

By the method of least squares (Asystant GPIB, 1988), the velocity-voltage data were fitted to the following equations:

$$U_f = \ln(aV_C + b) + cV_C \tag{1}$$

$$U_f = \ln(aE_C + b) + cE_C \tag{2}$$

where U_f = peak flyer plate velocity in mm/μs, V_C = capacitor firing voltage in kV, and E_C = capacitor firing energy in mJ.

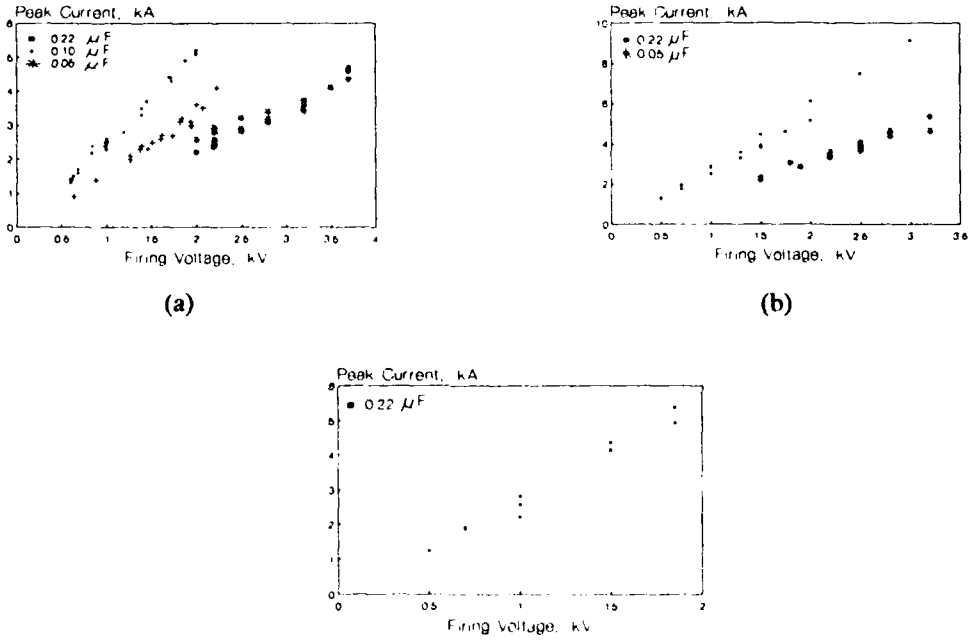


Fig. 3. Peak current versus firing voltage for: (a) MRL switch, (b) Reynolds switch, and (c) EEV switch.

In fitting the data, no attempt at distinguishing between capacitors of the same nominal capacitance was made. The form of the equation was chosen on the basis that the variance was less than that for a polynomial (quadratic) fit. The fitted equations are given in Tables II and III for flyer velocity as a function of voltage and energy, respectively. The velocity/voltage observations and the fitted curves for the various capacitance, inductance, switch, flyer thickness, and barrel diameter arrangements evaluated are shown in Fig. 4. The velocity/ energy data are shown in Fig. 5.

A number of velocity measurements were conducted at voltages near the onset of flyer formation (e.g., for the MRL switch this occurred around 0.6 kV for the 0.22 μF capacitor). For some of these firings, the thin plastic sheet covering the bridge foil remained intact. Post burst inspections revealed a small bubble above the burst bridge.

The time of the initial motion of the flyer plate was also investigated with respect to the burst voltage time. For all of the capacitance, inductance, switch, flyer thickness, and barrel diameter arrangements

tested, the data show that for firing voltages above ≈1.5 kV that the initial motion of the flyer plate and the burst voltage time was coincident to within about ±10 ns (the error bar for each data point was about ±5 ns). Below this voltage the initial flyer motion began to occur before the burst voltage time. Near the lowest firing voltage of ≈0.5 kV, the time difference was in some cases >50 ns.

Table II. Fitted Voltage Equations

Capacitance		Switches	
MRL Switch:		*0.22 μF:*	
0.22 μF	$U_f = ln(13.1V_c - 7.36) + 0.878V_c$	MRL	$U_f = ln(13.1V_c - 7.36) + 0.878V_c$
0.10 μF	$U_f = ln(10.2V_c - 9.92) + 0.506V_c$	Reynolds	$U_f = ln(13.7V_c - 6.33) + 0.918V_c$
0.05 μF	$U_f = ln(5.68V_c - 10.3) + 0.554V_c$	EEV	$U_f = ln(31.7V_c - 16.4) + 0.429V_c$
Reynolds:		Flyer Thickness	
0.22 μF	$U_f = ln(13.7V_c - 6.33) + 0.918V_c$	*0.22 μF/Reynolds:*	
0.05μF	$U_f = ln(7.14V_c - 7.89) + 0.531V_c$	13 μm	$U_f = ln(36.0V_c - 17.8) + 0.533V_c$
		25 μm	$U_f = ln(13.7V_c - 6.33) + 0.918V_c$
		50 μm	$U_f = ln(13.8V_c - 6.97) + 0.307V_c$
Inductance		Barrel Diameter	
0.22 μF/Reynolds:		*0.22 μF/Reynolds:*	
14 nH	$U_f = ln(13.7V_c - 6.33) + 0.918V_c$	infinite	$U_f = ln(13.7V_c - 6.33) + 0.918V_c$
35 nH	$U_f = ln(31.4V_c - 19.6) + 0.466V_c$	0.25 mm	$U_f = ln(36.2V_c - 22.8) + 0.499V_c$
73 nH	$U_f = ln(102V_c - 68.1) - 0.496V_c$	1.0 mm	$U_f = ln(15.6V_c - 8.32) + 1.02V_c$

Table III. Fitted Energy Equations

Capacitance		Switches	
MRL Switch:		*0.22 μF:*	
0.22 μF	$U_f = ln(0.165E_c - 5.67) + 0.00109E_c$	MRL	$U_f = ln(0.165E_c - 5.67) + 0.00109E_c$
0.10 μF	$U_f = ln(0.154E_c - 7.15) + 0.00109E_c$	Reynolds	$U_f = ln(0.193E_c - 4.48) + 0.00108E_c$
0.05 μF	$U_f = ln(0.147E_c - 12.1) + 0.00227E_c$	EEV	$U_f = ln(0.302E_c - 8.68) - 0.000218E_c$
Reynolds:		Flyer Thickness	
0.22 μF	$U_f = ln(0.193E_c - 4.48) + 0.00108E_c$	*0.22 μF/Reynolds:*	
0.05 μF	$U_f = ln(0.234E_c - 7.27) + 0.00154E_c$	13 μm	$U_f = ln(0.366E_c - 9.61) + 0.000157E_c$
		25 μm	$U_f = ln(0.193E_c - 4.48) + 0.00108E_c$
		50 μm	$U_f = ln(0.117E_c - 2.98) - 0.000488E_c$
Inductance		Barrel Diameter	
0.22 μF/Reynolds:		*0.22 μF/Reynolds:*	
14 nH	$U_f = ln(0.193E_c - 4.48) + 0.00108E_c$	infinite	$U_f = ln(0.193E_c - 4.48) + 0.00108E_c$
35 nH	$U_f = ln(0.291E_c - 12.4) - 0.000262E_c$	0.25 mm	$U_f = ln(0.337E_c - 14.6) - 0.000115E_c$
73 nH	$U_f = ln(0.458E_c - 22.1) - 0.00304E_c$	1.0 mm	$U_f = ln(0.219E_c - 6.97) + 0.00155E_c$

Electrical Characterization of the EBF

From the EBF current and corrected voltage measurements (Podlesak *et al.*, 1992) the current density, dynamic resistance and energy deposited-up-to-burst were calculated. Over the voltage range investigated, only the resistance at burst was found to be nearly constant and independent of the other parameters employed. The value was typically between 0.6 Ω and 0.7 Ω, falling to 0.2 Ω only for the lowest firing voltages.

The energy deposited-up-to-burst, E_b, is plotted in Fig. 6 as a function of firing energy for the capacitance, inductance, switch, flyer thickness, and barrel diameter arrangements evaluated. The data begin steeply and then tend to flatten out at the higher firing energies.

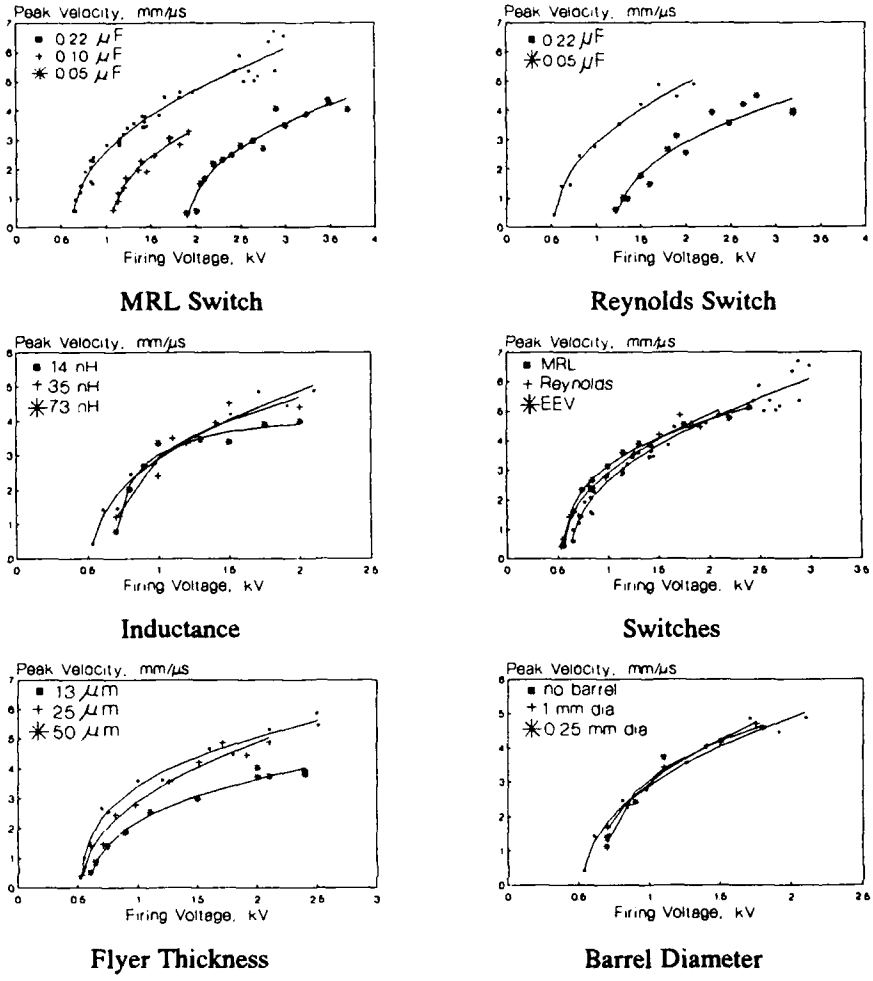


Fig. 4. Peak flyer velocity versus firing voltage for the capacitance, inductance, switch, flyer thickness, and barrel diameter arrangements evaluated.

Figure 7 shows the relationship between the burst current density, J_b, and the peak flyer velocity as a function of capacitance. Theoretical curves based on the electrical Gurney model (Tucker and Stanton, 1975) are also shown. The values for the electrical Gurney parameters, K and n, were found by using a least squares fit (Press *et al.*, 1987) on the burst current density data and are shown in Table IV. Switch type did not affect the determination of K and n and therefore K and n values for the particular switches are not shown explicitly. Too few data points were available to provide K and n values for the inductance and barrel diameter investigations.

DISCUSSION

Table I shows that for both the MRL and Reynolds switches, the calculated circuit inductance was approximately constant over the range of capacitance values employed. Within each of these switch-capacitance sets the calculated resistance ranges are also similar, except for the MRL switch/0.05 μF arrangement where the resistance is significantly higher. The MRL-, Reynolds-, and EEV/0.22 μF arrangements had approximately the same circuit inductance and resistance values.

It was found that at low voltages (≈0.6 kV) for the MRL switch/0.22 μF and 0.10 μF arrangements there appeared to be a decrease in inductance but this is believed to be the result of an unreliable calculation. The signal-to-noise ratio was low causing the time-interval measurement to be of dubious

precision. No apparent decrease in inductance occurred for the Reynolds and EEV switches.

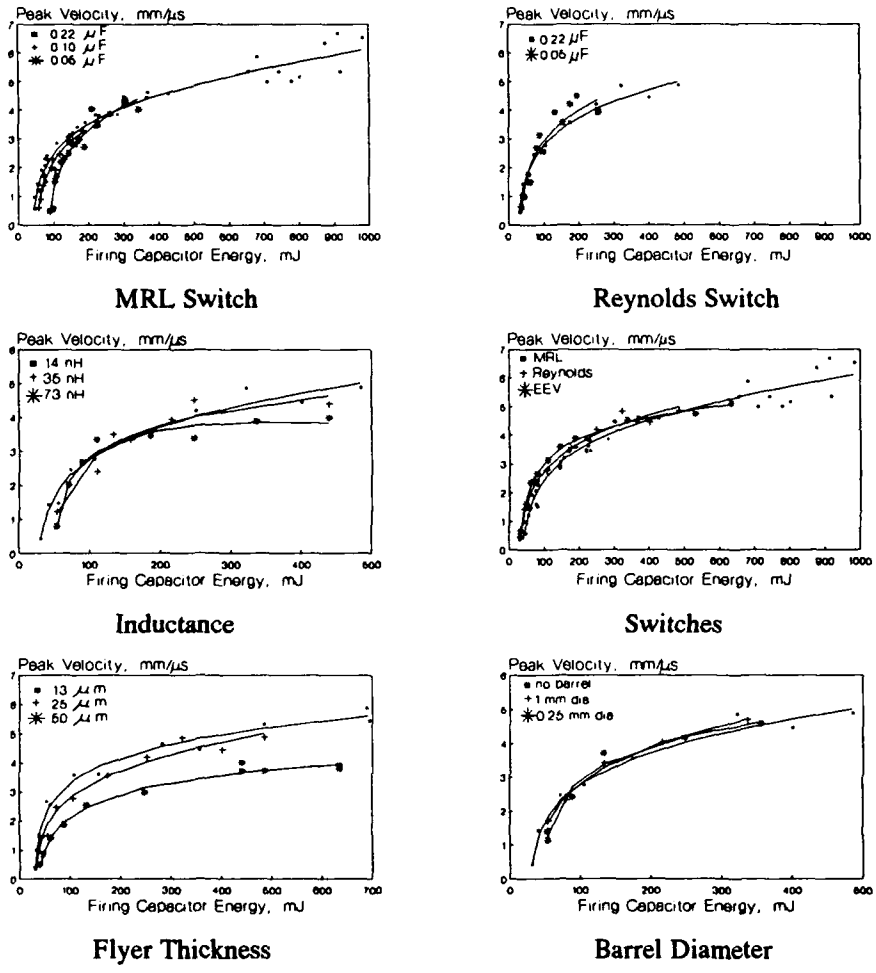


Fig. 5. Peak flyer velocity versus firing capacitor energy for the capacitance, inductance, switch, flyer thickness, and barrel diameter arrangements evaluated.

Based on the measured peak currents (Fig. 3), the two capacitors employed at each capacitance value are electrically equivalent.

For a ringdown, the first current peak is approximately given by

$$I_p = V_c\sqrt{\frac{C}{L}}e^{-\frac{\pi R}{4}\sqrt{\frac{C}{L}}} \tag{3}$$

where I_P = peak current, R = circuit resistance, C=capacitance, and L = circuit inductance.

Assuming constant C and L, equation (3) shows that if changes of R with changing V_c are small, the peak current would be approximately directly proportional to V_c, which is the form of the data shown in Fig. 3. Fitting a straight line to the data and using equation (3) provides an alternative method for estimating R. Values obtained for R in this way were higher (by up to 200% in some cases) than those obtained from ringdowns.

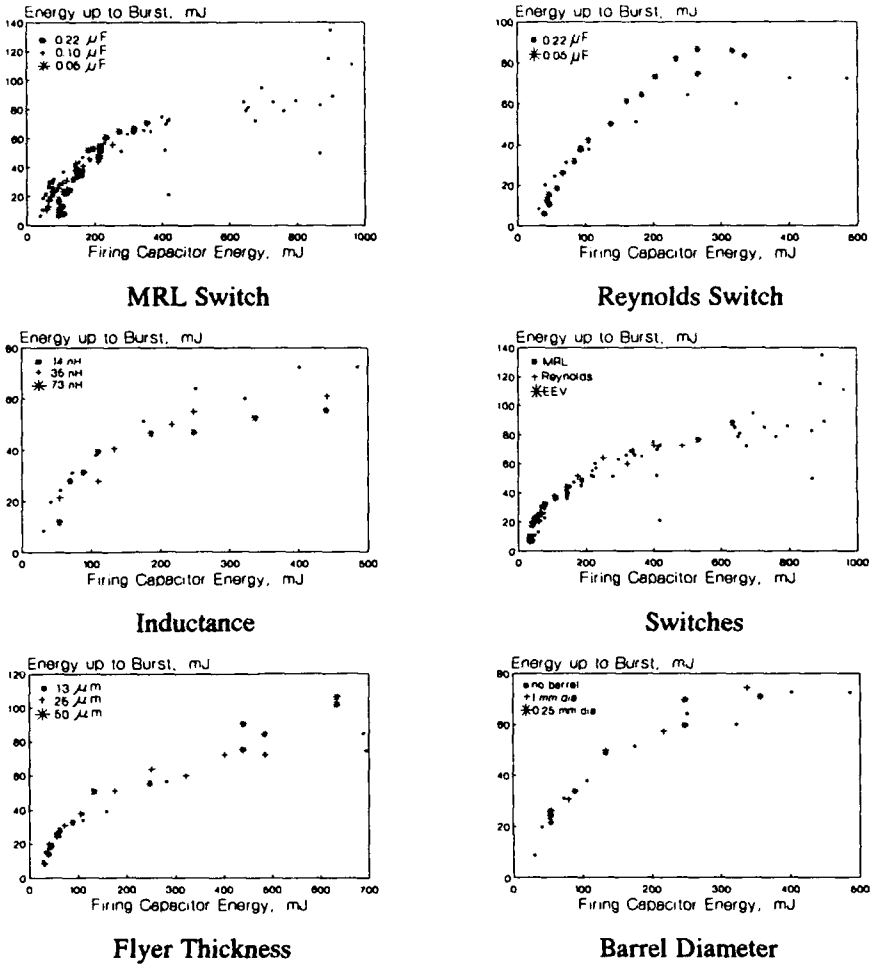


Fig. 6. Energy-up-to-burst versus firing capacitor energy for the capacitance, inductance, switch, flyer thickness, and barrel diameter arrangements evaluated.

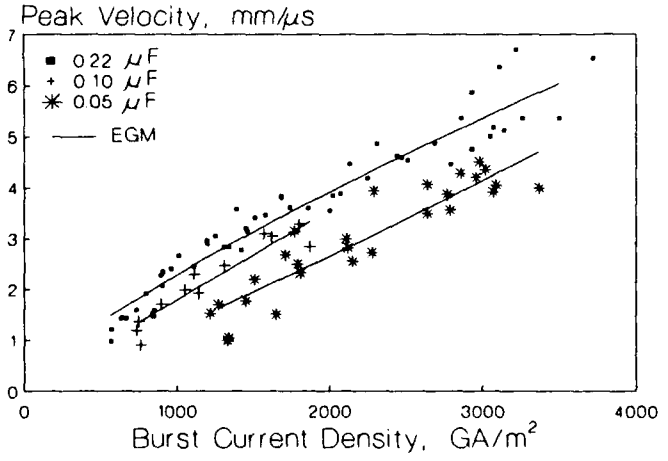


Fig. 7. Peak flyer plate velocity as a function of burst current density for EBF flyer generators employing 0.05, 0.10 and 0.22 μF capacitors. For each set of data the electrical Gurney model (EGM) is also shown.

Table IV. Electrical Gurney Energy Parameters

K	n	EBF(Cu) C (μF)	EBF(Cu) *Flyer Plate* Thickness (μm)	EBF(Cu) L (nH)
3.08×10^{-7}	2.176	0.05	25	10
2.70×10^{-6}	1.968	0.10	25	10
8.67×10^{-5}	1.536	0.22	25	12
5.60×10^{-5}	1.544	0.22	13	14
5.80×10^{-5}	1.564	0.22	50	14

As mentioned above, within switch-capacitance sets the EBF flyer generators have about the same circuit inductance and resistance. Thus it seems valid that a comparison of the performance of the EBF generators within the MRL and Reynolds switch sets would show the effect of using different circuit capacitances. Based on firing capacitor energies, Fig. 5 shows that for the MRL switch there appears to be an insignificant difference between the 0.22 μF and 0.10 μF capacitors but a significant difference between these capacitors and the 0.05 μF capacitor. On the other hand, for the Reynolds switch there is an insignificant difference between the 0.22 μF and 0.05 μF capacitors up to an E_c of approximately 100 mJ. Above this energy, a small difference occurs.

Similar features are evident in the E_b versus E_c curves (Fig. 6). The different performance of the MRL/0.05 μF arrangement at low firing energy is considered to be related to the higher switch resistance rather than a capacitance effect. The switching is less efficient and therefore a higher minimum E_c is required before the flyer plate can be launched.

The crossover in the energy and velocity curves (Figs 5 and 6) is believed to occur because (at a given energy level) the smaller valued capacitor is charged to a higher voltage thereby producing a higher dI/dt on discharge. Hence it can deliver energy to the bridge at a faster rate. The different rates at which different capacitors can deposit energy results in the smaller capacitor ultimately depositing more energy into the bridge and thus achieving a higher flyer plate velocity.

The Reynolds switch/0.22 μF arrangement with and without added circuit inductance shows that gross inductance changes are needed to cause significant changes to EBF flyer generator performance. This supports the assumption that the small inductance differences shown in Table 1 do not invalidate the investigation of capacitance effects.

For optimum transfer of electrical energy to kinetic energy of the flyer plate, the bridge should burst near the peak of the ringdown cycle (at this point no energy is stored on the capacitor). The time at which the bridge bursts is dependent on the firing energy and can also be modified by changing the circuit inductance. Therefore by adding inductance the burst point can be brought closer to the peak of the ringdown cycle thereby compensating for the effects of reduced dI/dt and i. Hence it is possible to achieve equality in performance over a small E_c range for different circuits as shown in Figs 4, 5 and 6.

Only minor differences were found for the performance of the MRL-, Reynolds-, and EEV/0.22 μF arrangements (Figs 4 and 5). This result would be expected because of the similar circuit inductance and resistance of the switches (Table 1).

The performance of the Reynolds switch/0.22 μF arrangement with different flyer thicknesses (Figs 4 and 5) follows the expected trend for the 25 μm and 50 μm flyers based on the expression

$$v_2 = v_1\sqrt{\frac{m_1}{m_2}} \tag{4}$$

where v_1, v_2, m_1, and m_2 are the velocity and mass of the two different flyers. Equation (4) is derived on the assumption that the same kinetic energy is imparted to the two different flyers. For the 13 μm thick flyer the trend is different, the velocity increase being at least 20% less than that predicted by equation (4).

An interesting feature of the effect of the flyer plate thickness on E_b can be seen in Fig. 6. Up to an E_c of 300-400 mJ, E_b is found to be independent of flyer plate thickness. This suggests that over this range of E_c the kinetic energy of the flyer plates should be essentially independent of flyer plate thickness. Thereafter the bridge attached to the thicker flyer plate, which is able to remain intact for longest, achieves the highest E_b values. The reduced ability of the thinner flyer plate to confine the foil after burst may be one reason for the lower than expected velocity for that flyer plate; confinement by the flyer plate has been found to affect the resistivity of the foil (Stanton, 1976).

The performance of the Reynolds switch/0.22 μF arrangement with different barrel diameters (Figs 4 and 5) are essentially the same although the 0.25 mm diameter barrel shows a small difference at E_c less than about 75 mJ. As shown in Fig. 8 velocity-distance data for the three different barrel arrangements also appear to be the same. McDaniel (1990) suggests that an EBF flyer generator without a barrel could require 20% more firing energy to achieve the same velocity as that with one.

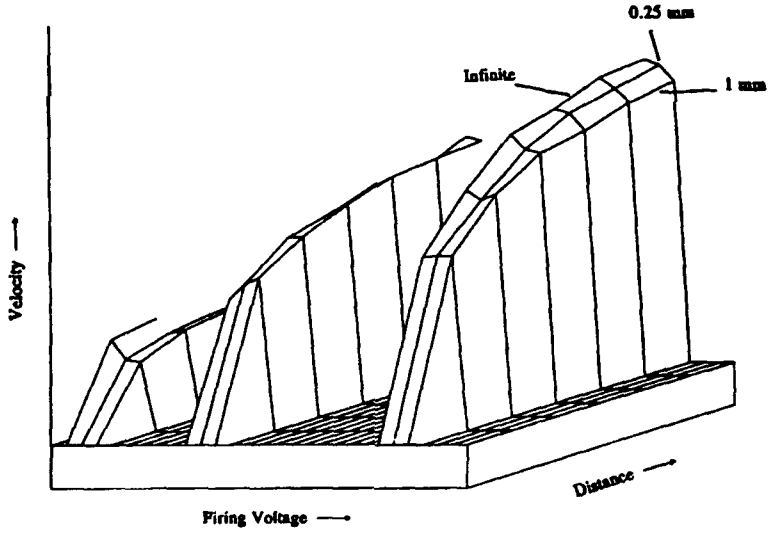


Fig. 8. Velocity-distance data at nominal firing voltages of 0.7 kV, 1.0 kV, and 1.75 kV for EBF flyer generators with barrel diameters of infinite (i.e. no barrel), 0.25 mm, and 1.0 mm.

Several investigators (Harlan *et al.*, 1981, Kleinhanss *et al.*, 1989, Schwarz, 1977, Vorek and Velicky, 1981) have considered the shape of the flyer velocity versus voltage curve. For large bridges (measured in mm) an almost linear relationship over a narrow voltage range has been reported (Harlan *et al.*, 1981, Schwarz, 1977, Vorek and Velicky, 1981). Schwarz (1977) has found a non-linear relationship for bridges similar to those studied here. Barrels were employed in all those investigations and only Schwarz (1977) considered voltages down to the onset of flyer formation.

Figure 6 shows that there is also a non-linear relationship between E_b and E_c. In fact Figs 6 and 5 show similar trends as might be expected. The gradient changes in the E_b curves are reflected in the gradient changes in the peak velocity curves. This suggests that the peak velocity might be proportional to E_b. The exact relationship between E_b and U_f, and the contribution to U_f due to energy deposited into the bridge following burst, has not been addressed in this paper.

The reason for the non-linear relationship is not clear. One factor may be the degree of ionization that is achieved after the bridge is vaporized. This is important because as the gas ionizes, the resistivity begins to drop (Chen, 1974) making it more difficult to deposit energy. Therefore, while operating the EBF flyer generator at a higher firing energy certainly results in a greater E_b, this is achieved with a reduced efficiency.

It is interesting to note that such a non-linear relationship between flyer velocity and voltage implies that a simple energy balance consideration such as:

$$E_{kf} = E_c - E_o \tag{5}$$

where E_{kf} = the kinetic energy of the flyer plate, and E_o = a constant, cannot provide accurate estimates of the flyer velocity over a wide voltage range because, in general, E_o is not constant. Such expressions, however, may be valid over small voltage ranges as proposed by Harlan *et al.* (1981). In these cases E_o is a constant and

$$U_f \propto V_c \tag{6}$$

The electrical Gurney parameters shown in Table IV indicate that K and n are not independent of the circuit capacitance. For increasing capacitance, K increases while n decreases. This dependence is possibly related to the unaccounted for rate dependencies of the l and m parameters employed in the original electrical Gurney model development (Tucker and Stanton, 1975). A relationship between circuit inductance and the Gurney parameters may also exist, although insufficient data are presently available to determine this.

Table IV shows that similar values for K and n for various flyer plate thicknesses were obtained for the 0.22 μF EBF flyer generators. This shows that the configuration factor adequately accounts for flyer plate construction, as expected.

CONCLUSIONS

The functional dependence between the flyer plate velocity and the firing voltage or energy has been established for different EBF flyer generators. The relationship was found to be non-linear over a wide voltage range. The same non-linearity can be seen in the relationship between E_b and E_c suggesting that the energy deposited into the post-burst plasma may only have a minor effect on the final velocity. The non-linearity is due to the decreasing efficiency of the energy transfer from the charged capacitor into the bridge as the charge voltage increases.

This study has shown that circuit inductance, capacitance and resistance (including switch resistance) can affect the performance of these small-scale EBF flyer generators. It is possible, however, to achieve essentially equivalent performance over a range of E_c by appropriately adjusting the circuit parameters. Altering the flyer plate thickness also affected performance, although this appears to reduce as the thickness decreases. Barrel dimension seems to have an insignificant effect on final flyer plate velocity.

The electrical Gurney model parameters for the various EBF flyer generators investigated were found to depend on circuit capacitance. Switch type and flyer plate construction did not affect these parameters.

ACKNOWLEDGEMENTS

The authors acknowledge the technical assistance of R. Klar and B. Jones. Useful discussions with D.D. Richardson, W.F. Hemsing (LANL) and D.E. Mitchell (SNL) are also acknowledged.

REFERENCES

Asystant GPIB (1988). Asyst Software Technologies, Inc. NY, USA.

Barker, L. M. and Hollenbach, R. E. (1972). Laser interferometer for measuring high velocities of any reflecting surface. *J. Applied Physics*, 43, 4669-4675.

Chau, H. H., Dittbenner, G., Hofer, W. W., Honodel, C. A., Steinberg, D. J., Stroud, J. R. Weingart, R. C. and Lee, R.S. (1980). Electric gun: A versatile tool for high-pressure shock-wave research. *Review of Scientific Instruments*, 51 (12), 1676-1681.

Chen, F. F. (1974). *Introduction to Plasma Physics*, Plenum Press, New York.

Harlan, J. G., Rice, J. K., and Rogers, J. W. Jr. (1981). The role of air and other gases in flyer plate initiation of explosives. In: *Proc. 7th Symp.(Int.) on Detonation*, pp. 930-939.

Kleinhanss, H. R., Lungenstrass, F. and Zollner, H. (1989). Initiation threshold of high explosives in small flyer plate experiments. In: *Proc. 9th Symp.(Int.) on Detonation*, Vol 1. pp. 66-76.

Loeb, L. B. (1939). *Fundamental processes of electrical discharge in gases*. John Wiley & Sons, New York.

McDaniel, O. K. (1990). Exploding foil initiators - an overview. In: *Proc.14th Symp. on Explosives and Pyrotechnics*. pp. 11.1-11.58.

McMillan, C. F., Goosman, D. R., Parker, N. L., Steinmetz, L. L., Chau, H. H., Huen, T., Whipkey, R. K. and Perry, S. J. (1988). Velocity of fast surfaces using Fabry-Perot interferometry. *Review of Scientific Instruments*, 59 (1), 1-20.

Podlesak, M., Richardson, D. D., and Olsson, C. (1992). An Exploding Foil Flying Plate Generator for Shock Wave Studies-Calibrations. Materials Research Laboratory Report *MRL-RR-1-92*.

Press, W. H., Flannery, B. P., Teukolsky, S. A. and Vetterling, W. T. (1987). *Numerical recipes: The art of scientific computing*. Cambridge University Press, Cambridge, UK.

Richardson, D. D. (1987). Private communication.

Schwarz, A. C. (1977). A new technique for characterizing an explosive for shock initiation sensitivity. In:*Proc. Conf. on Standardisation of Safety and Performance Tests for Energetic Materials.* (L. Avrami, H.J. Matsugama and R.F. Walker, eds.), Vol 1. pp. 527-550.

Stanton, P. L. (1976). The Acceleration of Flyer Plates by Electrically Exploded Foils. Sandia National Laboratories Report *SAND-75-0221*.

Tucker, T. C. and Stanton, P. L. (1975). Electrical Gurney energy: A new concept in modelling of energy transfer from electrically exploded conductors. Sandia National Laboratories Report *SAND-75-0244*.

Vorek, W. E. and Velicky, R. W. (1981). Exploding foil shock sensitivity test. In: *Proc. of the 7th Symp. (Int.) on Detonation*, pp. 924-929.

Waschl, J. (1988).Performance measurement of slapper detonation systems. In: *ADPA Conf. Pyrotechnics and Explosives Applications Section*.

Int. J. Impact Engng Vol.14, pp.797 - 808, 1993
Printed in Great Britain

0734-743X/93 $6.00+0.00
1993 Pergamon Press Ltd

IMPACT FLASH AND DEBRIS CLOUD EXPANSION OF HIGH-PURE METAL FOILS

K. WEBER, V. HOHLER, A. J. STILP

Fraunhofer-Institut für Kurzzeitdynamik
- Ernst-Mach-Institut -
Terminal Ballistics and Impact Physics Division
Eckerstraße 4, D-7800 Freiburg, FRG

ABSTRACT

Results of 2 mm aluminum spheres perforating Al, Cu, Mo, Ag, Au, Sn, and Zn metal foils of a purity > 99.9 % with thicknesses between 0.1 mm and 2.0 mm, densities of up to 20 g/cm^3, melting temperatures of 500 - 3000 K and specific heats of fusion of 20 - 350 kJ/kg at impact velocities between v_p =4.5 km/s and v_p = 9 km/s are presented. The influence of target thickness, target material properties and impact velocity on the perforation hole diameter, impact flash duration and expansion velocity, fragmentation and debris cloud formation at nearly constant areal density is demonstrated. The dependence of impact crater pattern at witness plates on target material density, thickness, impact velocity and areal density ratio between projectile and target material is discussed. For tin and lead evidence is given for the ability of digital scanning electron microscope analysis as an effective tool for indicating change of aggregation from solid into liquid and for the determination of relative projectile and target material quantities.

INTRODUCTION

Space objects, e.g. satellites and manned space vehicles, are hit by micrometeoroids from comets and asteroids or space debris fragments. These natural and man-made particles in low (LEO) and geostationary (GEO) earth orbit have average velocities in the order of several km/s to 20 km/s. Projectile and target interaction results in an impact flash and a fragmentation process with different states of aggregation of the involved materials. These impact phenomena can be simulated by means of a two-stage light gas gun for impact velocities of up to 10 km/s. The tests have been carried out at velocities of 4.5 km/s, 6 km/s and 9 km/s with 2 mm diameter aluminum spheres against thin metal targets with a purity of > 99.9 %, melting temperatures between 500 K and 3000 K, heats of fusion from 20 kJ/kg to 350 kJ/kg and areal densities of $\rho \cdot t$ = 2.2 - 2.7 kg/m^2 for the investigation of (1) the duration and expansion of the impact flash, (2) the influence on the perforation process and (3) the fragmentation behaviour and debris cloud formation. According to the high shock wave amplitude at these impact velocities, the fragmentation process is accompanied by melting and vaporization of both projectile and target material. For examination of the fragmentation behaviour and the state of aggregation the debris cloud formation has been observed with an IMACON-790 high-speed camera and polished copper and aluminum witness plates have been additionally positioned behind the target. Perforation hole lips as well as impact crater patterns on witness plates were analyzed by scanning electron microscope technique for (1) identification of solid and molten material and (2) for determination of relative projectile and target material quantities.

EXPERIMENTAL SET-UP AND TEST PARAMETERS

The impact experiments have been performed at the EMI 15/5 mm two-stage light gas gun for impact velocities of $v_p \leq 6$ km/s and at the 40/10 mm LGG for $v_p > 6$ km/s. A high vacuum pump system allows target chamber pressures of up to 10^{-3} Pa. An adapted IMACON-790 high-speed camera with a time resolution from microseconds to nanoseconds is triggered by the projectile shortly before the projectile impacts the target (Fig. 1) and initiates plasma, debris cloud and backsplash formation. Polished copper and aluminum witness plates, 100 x 100 mm in size have been positioned 75 mm behind the target to evaluate the state of aggregation of both projectile and target material.

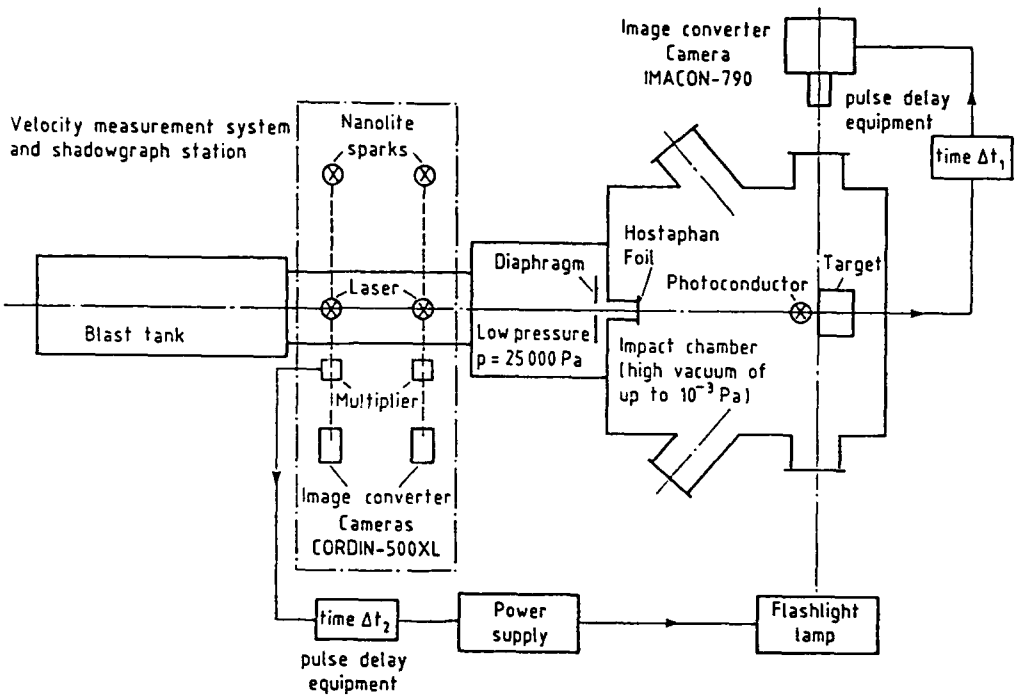


Fig. 1. Experimental set-up

In all tests 2 mm diameter aluminum spheres were used. The foil thicknesses were varied from 0.125 mm for gold (Au) to 1.0 mm for aluminum (Al) and densities between 20 g/cm^3 (Au) and 2.7 g/cm^3 (Al) due to roughly constant areal densities of $\rho \cdot t = 2.2 - 2.7$ kg/m^2. Especially for investigation of phase changes 2.0 mm thick tin (Sn) and zinc (Zn) targets with high areal densities of $\rho \cdot t \approx 14.5$ g/cm^3 and low melting temperatures of $T_m \approx 500$ K (Sn) and $T_m \approx 700$ K (Zn), respectively, have been tested. As can be seen from Table 1, the melting temperature of all other investigated materials - besides lead (Pb) - are distinctly higher and achieve a maximum of $T_m \approx 3000$ K for molybdenum (Mo). Further physical and thermodynamic properties, given in Table 1, are sound velocity c_s, material density ρ, vaporization temperature T_v, specific heat of fusion q_m, specific heat of vaporization q_v, target thickness t and areal density $\rho \cdot t$.

Table 1. Physical and thermodynamic properties of metal foils

Mat.	purity [g/cm^3]	ρ	T_m [K]	T_v [K]	q_m [kJ/kg]	q_v [kJ/kg]	t [mm]	ρ*t [kg/m^2]	c_s [m/s]
Mg	99.9	1.74	923	1373	209.3	5652	1.0	1.74	5070
Al	99.999	2.7	933	2543	355.9	11723	1.0	2.7	5110
Ni	-	8.90	1728	3273	293.1	6197	0.3	2.7	4970
Cu	99.99	8.96	1356	2603	209.3	4647	0.25	2.2	3800
Mo	99.9	10.2	2898	5833	292.4	7188	0.25	2.6	5600
Ag	99.95	10.45	1234	2223	104.7	2177	0.25	2.6	2790
Au	99.99	19.3	1336	2973	67.0	1758	0.125	2.4	2000
Zn	99.95	7.1	692	1180	112.2	1800	2.0	14.2	3600
Sn	99.99	7.3	505	2573	58.6	2596	2.0	14.6	2690
Pb	-	11.34	601	2003	23.9	921	1.5	17.0	1200

THIN TARGET PERFORATION

By definition thin targets are plates with thicknesses t less than or equal to the projectile diameter d. Dependent on t/d, material properties, and impact velocity, the projectile and target material can be strongly disrupted into solid fragments, and at higher velocities melting and vaporization can additionally occur. The hole diameter increases with increasing velocity from values nearly identical to the projectile diameter d for very thin targets with $t/d << 1$ to maximum diameters for semi-infinite targets with $t/d >> 1$. Fig. 2 shows the target hole diameter D normalized by the projectile diameter d as a function of the impact velocity v_p and the t/d ratio as a parameter.

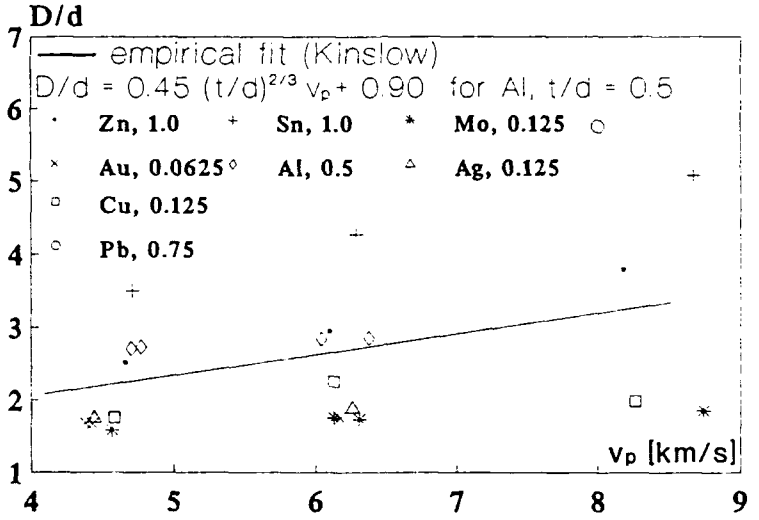


Fig. 2 Perforation hole diameter D normalized by projectile diameter d versus impact velocity v_p for 2 mm diameter aluminum spheres and t/d = 0.0625, 0.125, 0.5, 0.75, 1.0

In the diagram the foil thickness to projectile diameter ratio has been varied from t/d = 0.0625 for gold (Au) to t/d = 0.125 for molybdenum (Mo), copper (Cu) and silver (Ag), which are materials with a relatively high density and melting temperature. For these t/d ratios the D/d dependence on v_p is very weak. For greater t/d ratios the normalized perforation hole diameter D/d increases with increasing v_p, as shown in Fig. 2 for the aluminum and tin/zinc foils with t/d ratios of 0.5 and 1.0/1.0. For comparison reasons the relationship

$$\frac{D}{d} = 0.45 \cdot v_p \cdot \left(\frac{t}{d}\right)^{2/3} + 0.90 \quad \text{for } v_p \text{ [km/s] and } 0.040 \leq \frac{t}{d} \leq 0.504$$

derived from experimental data for aluminum spheres and 2024-T3 Al shields given by Kinslow (1970) demonstrates an underestimation of the experimental data found for the aluminum foils of high purity, tested in this work. Further, the underestimation is much stronger for the metal foils with thicknesses of t/d = 0.0625, 0.125 and 1.0, which consist of Au, Ag, Mo, Cu, Sn and Zn. For the tested tin foils the D/d values are about 50% greater than for the zinc targets, although identical target thicknesses were chosen (see also Fig. 4). With ρ = 7.1 g/cm^3 for tin and ρ = 7.3 g/cm^3 for zinc the material densities are nearly identical and both materials have low melting temperatures of T_m = 505 K and T_m = 692 K but the specific heat of fusion q_m of tin is half the value of q_m of zinc. For melting 1 kg tin a heat of fusion of only Q_m = 58.6 kJ is necessary, whereas the liquefaction of the same mass of zinc needs twice this amount (see Table 1).

Assuming that during the perforation process of the tin as well as the zinc foil, the impact-induced shock wave causes identical amounts of the kinetic energy to melt target material, in the case of tin twice the mass of zinc will be molten. Indeed, a comparison of target mass losses during perforation, determined from the perforation hole diameters, gives evidence for this assumption. The corresponding mass loss values for the velocities around 4.5 km/s, 6 km/s and 9 km/s are listed in Table 2:

Table 2. Heat of fusion Q_m and molten target masses Δm_T

target material	v_p [m/s]	E_{kin} [J]	Δm_T [g]	Q_m [J]	Q_m/E_{kin} [%]	$\frac{\Delta m_{T/Sn}}{\Delta m_{T/Zn}}$
Zn	4660	122.8	0.283	31.8	25.9	1.99
Sn	4710	125.4	0.562	32.9	26.2	
Zn	6100	210.4	0.388	43.5	20.7	2.16
Sn	6290	223.7	0.836	49.0	21.9	
Zn	8180	378.4	0.644	72.3	19.1	1.84
Sn	8670	425.1	1.184	69.4	16.3	

The projectile mass of $m_p = 1.13 \cdot 10^{-5}$ kg was determined due to an aluminum sphere diameter of d = 2 mm and a material density of $\rho = 2.7$ g/cm^3. The heat of fusion was normalized by the kinetic energy $E_{kin} = \frac{1}{2} m_p \cdot v_p^2$.

Additionally to the tests with tin and zinc foils, one experiment has been performed with a lead foil of t = 1.5 mm due to an areal density of $\rho \cdot t = 17.0$ kg/m^2, similar to the $\rho \cdot t$ values of Sn and Zn. The melting temperature of $T_m = 601$ K of lead is between T_m (Sn) and T_m (Zn), but its specific heat of fusion q_m is about half the q_m of Sn and one fifth the q_m of Zn (Table 1). Fig. 2 demonstrates that lead has the highest D/d ratio of all tested foils. From this, an additional hint is given for the perforation hole formation dependence on thermodynamic material properties, e.g. Q_m.

From Figs. 3 and 5 it can be seen that D/d converges asymptotically against D/d = 1 for infinitely thin foils with $d/t \rightarrow \infty$, independent of the material properties and impact velocity.

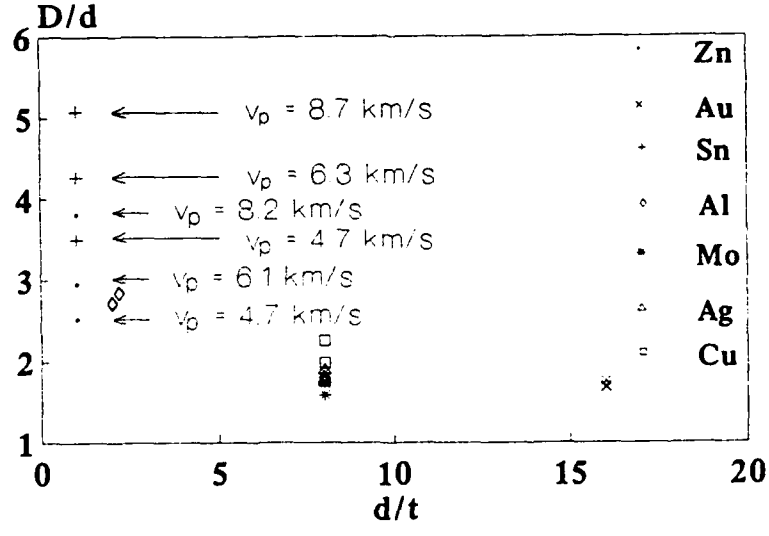
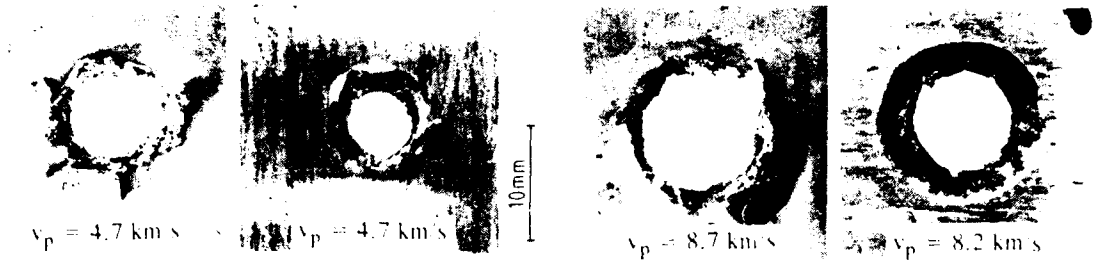
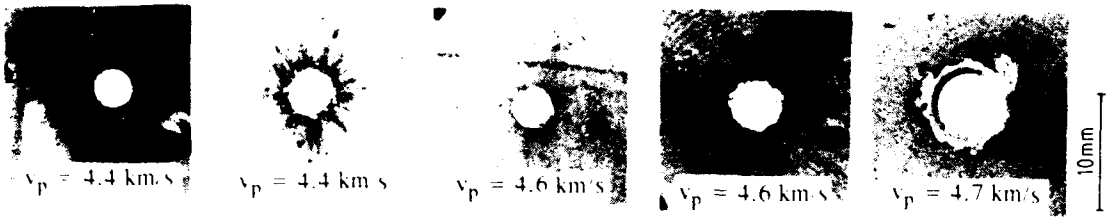


Fig. 3 Perforation hole diameter D normalized by projectile diameter d versus projectile diameter to foil thickness ratio d/t for 2 mm diameter aluminum spheres at impact velocities between $v_p = 4.4$ km/s and $v_p = 8.7$ km/s



a) Sn 2.0 mm; b) Zn 2.0 mm; c) Sn 2.0 mm; d) Zn 2.0 mm;

Fig. 4 Rear sides of perforation holes in 2 mm thick tin and zinc targets perforated by a 2 mm diameter aluminum sphere with impact velocities between 4.7 km/s and 8.7 km/s



a) Au 0.125 mm; b) Ag 0.25 mm; c) Mo 0.25 mm; d) Cu 0.25 mm; e) Al 1.0 mm;

Fig. 5 Front sides of perforation holes in gold (Au), silver (Ag), molybdenum (Mo), copper (Cu) and aluminum (Al) targets with thicknesses of t = 0.125 mm, 0.25 mm and 1.0 mm perforated by a 2 mm diameter aluminum sphere at an impact velocity around v_p = 4.5 km/s

IMPACT FLASH AND BACKSPLASH FORMATION

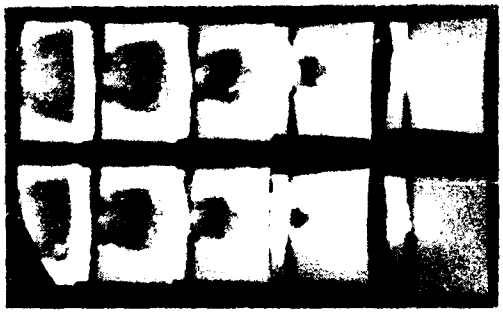
The impact of a projectile against a target is accompanied by an impact flash and ionization of the involved materials. Impact flash as well as ionization are, besides crater parameters such as diameter, depth and volume, an effective tool for the detection and identification of the material, mass and velocity of micrometeoroids. The impact flash is caused by emissions from a jet of shocked material, similar to the processes in shaped charges. Impact flash intensity measurements delivered the presence of two plasma pulses (Jean and Rollins, 1970). The first pulse, on the order of 1 μs, is emitted from a hot, high pressure plasma at the projectile target contact point. The beginning of the second, less intense pulse of several μs, comes from the expanding, low pressure cloud, can be defined as the instant that the impact angle ranging between 0° and 90° equals a critical angle α_{crit}. At this angle, which is dependent on the impact velocity and material shock properties, a jet formed by projectile as well as target material is emitted as a quasi steady flow. From experiments with magnesium, aluminum, steel and silver particles and aluminum targets, it was concluded that the flash intensity is only determined by the target material properties (Gehring and Warnica, 1963).

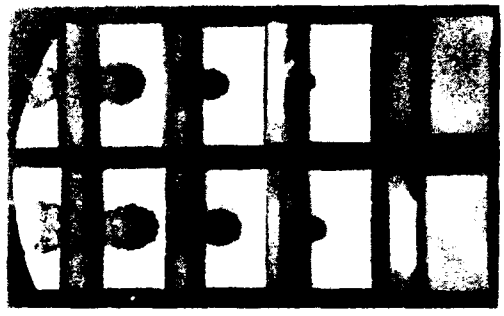
From parametric studies with copper spheres impacting cadmium targets (Jean and Rollins, 1970) and carbon, aluminum, iron and tungsten particles impacting gold targets (Eichhorn, 1976) it has been found that the impact flash intensity I correlates linear with the particle mass m_p and with the exponent n of the impact velocity v_p, according to,

$$I = m_p \cdot v_p^n \qquad 4 \leq n \leq 8$$

In a recent work, it was proven by a theoretical model that the jet is initiated from either the target or the projectile material, dependent on the target projectile material combinations (Ang, 1990).

In this work the duration and expansion velocity of the impact flash for different target materials and impact velocities of 2 mm diameter Al spheres has been investigated. The impact flash duration seems to be strongly dependent on the impact velocity (Table 3, Figs. 6 + 7). At $v_p \approx 4.5$ km/s the impact flash duration time is in the order of $\Delta t_{ff} = 1 - 2$ μs (Fig. 7). For higher values of $v_p > 6$ km/s and $v_p \approx 8.5$ km/s, the flash lifetime increases to $\Delta t_{ff} = 3 - 4$ μs and $\Delta t_{ff} > 4$ μs, respectively. Impact flash can be additionally influenced by physical properties other than the densities of the projectile and target materials. For a 0.25 mm copper foil which was penetrated by a 2 mm diameter aluminum sphere at $v_p = 8.3$ km/s, Fig. 6 and Table 3 indicate an impact flash duration time of $\Delta t_{ff} > 8$ μs. On the other hand, the impact flash duration time of nickel is in the order of only $\Delta t_{ff} = 3$ μs, although nickel and copper have nearly identical densities of ρ_{Ni} = 8.90 g/cm^3 and ρ_{Cu} = 8.96 g/cm^3, and very similar Hugoniot data characteristics (Kinslow, 1970).





DEBRIS CLOUD FORMATION

Projectile and target materials fragmentation

During the perforation of a target by a hypervelocity projectile, fragmentation of projectile as well as target material can occur if the tensile stress exceeds the fracture stress. Additionally, at each free surface the shock waves will be reflected as rarefaction waves and can cause further fragmentation. The shape, dimensions and material distribution of the debris cloud as well as the fragment size of projectile and target materials is a function of the material densities, thermodynamic properties such as melting temperature T_m, specific heat of fusion q_m, projectile-diameter-to-target-thickness ratio d/t, and the impact velocity v_p.

In Fig. 8 a 0.1 mm thick brass foil with a material density of 8.6 g/cm^3 ($\rho \cdot t = 0.86$ kg/m^2) was perforated by a 2 mm diameter aluminum sphere (d/t = 20) at v_p = 3.1 km/s, 4.2 km/s and 4.5 km/s. For the lower velocity of v_p = 3.1 km/s the projectile remains nearly intact only surrounded by small projectile particles. With increasing velocity the impactor material is more and more distributed backward of the ellipsoid-shaped cloud due to the higher degree of fragmentation. At v_p = 4.2 km/s the shock and reflection waves are strong enough to disrupt the projectile into particles of uniform size distributed on a concentric ring. A small increase of v_p causes a distinctly smaller fragment size located on a larger ring diameter D_r (Table 4). At an impact velocity around 6 km/s the crater ring pattern has been replaced by a roughly homogeneous crater size frequency distribution.

Table 4. Crater ring diameters and half space angles; spacing 75 mm

Target material	thick-ness [mm]	v_p [km/s]	D_{r1} [mm]	D_{r2} [mm]	Θ_1 [degree]	Θ_2 [degree]	Fig. No.
Ms	0.1	4.2	16.5	-	6.3	-	8b
Ms	0.1	4.5	21	-	8.0	-	8c
Au	0.125	4.4	28	-	10.6	-	9a
Ag	0.25	4.4	24.75	39.5	9.4	14.8	-
Mo	0.25	4.6	24.5	38	9.3	14.2	9c
Cu	0.25	4.6	25	-	9.5	-	9d
Al	1.0	4.7	26.5	-	10.0	-	10a
Al	0.914	6.0	31	40.5	11.7	15.1	10b

The occurrence of the crater ring pattern seems to be not very sensitive in a variation of the foil thickness t and the projectile diameter to foil thickness ratio d/t, respectively, as long as the areal density $\rho \cdot t$ will not be changed dramatically. Figs. 8 - 10 depict the witness plates of Ms, Au, Mo, Cu and Al foils for areal densities of $\rho \cdot t$ = 0.9 - 2.7 kg/m^2 and d/t values between 2 and 20 due to foil thicknesses of 0.1 - 1.0 mm (Table 1) perforated by 2 mm diameter aluminum spheres at v_p around 4.5 km/s. A comparison of Fig. 8c, Figs. 9 - 10b and Table 4 shows distinctly larger impact craters on a smaller crater ring diameter D_{r1} for the 0.1 mm Ms foil than for the thicker Ag, Mo, Cu, Au and Al targets. In addition, maximum half space angles of Θ_1 = 10.0 degrees and 10.6 degrees were measured for the low dense aluminum (ρ = 2.7 g/cm^3, t = 1.0 mm) and high dense gold foils (ρ = 19.3 g/cm^3, t = 0.125 mm). For the 0.25 mm Ag, Mo and Cu bumpers nearly identical Θ_1 values of 9.4, 9.3 and 9.5 degrees have been determined. Additionally, for the Ag and Mo sheets of equal densities ρ = 10.45 g/cm^3 and ρ = 10.2 g/cm^3, second crater rings of Θ_2 = 14.8 degrees (Θ_1 = 9.4 degrees) and Θ_2 = 14.2 degrees (Θ_1 = 9.3 degrees) have been observed.

At higher velocities of v_p around 6 km/s crater ring patterns could only be identified for 1 mm aluminum targets (Figs. 10a + 10b).

In nearly all experiments the impact crater ring pattern on witness plates is indicated by the shape of a truncated cone of the front part of the cloud with particle concentration at front and rear lines.

Crater ring pattern has also been found for 10 mm hard metal spheres of ρ = 14.7 g/cm^3 impacting 2 mm steel targets of an areal density of $\rho \cdot t$ = 15.7 kg/m^2 at impact velocities between 3.5 km/s and 4 km/s (Stilp et al., 1990) and for 1 mm soda-lime glass spheres against 0.25 mm teflon foils at v_p = 6 km/s (Hörz, 1990). From this and the results presented here, a necessary condition for the appearance of impact crater ring pattern seems to be that the areal density of projectile material $\rho_p \cdot d$ is greater than the areal density $\rho \cdot t$ of target material.

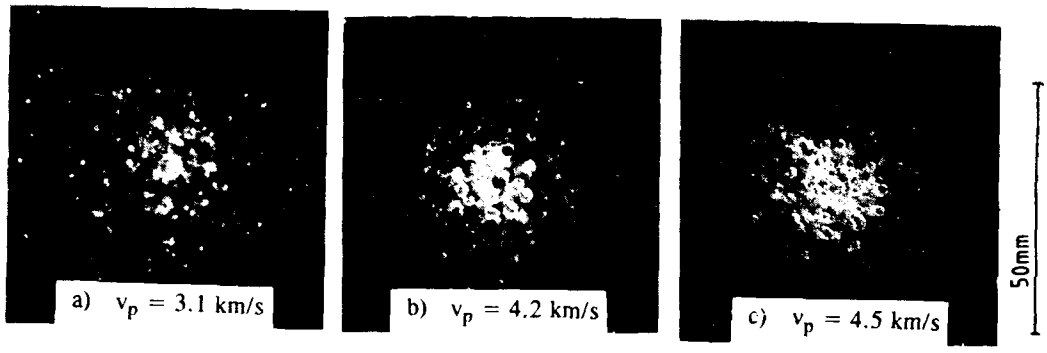


Fig. 8 Impact crater pattern of 2 mm diameter aluminum spheres against 0.1 mm brass foils; aluminum witness plates with a spacing of 75 mm

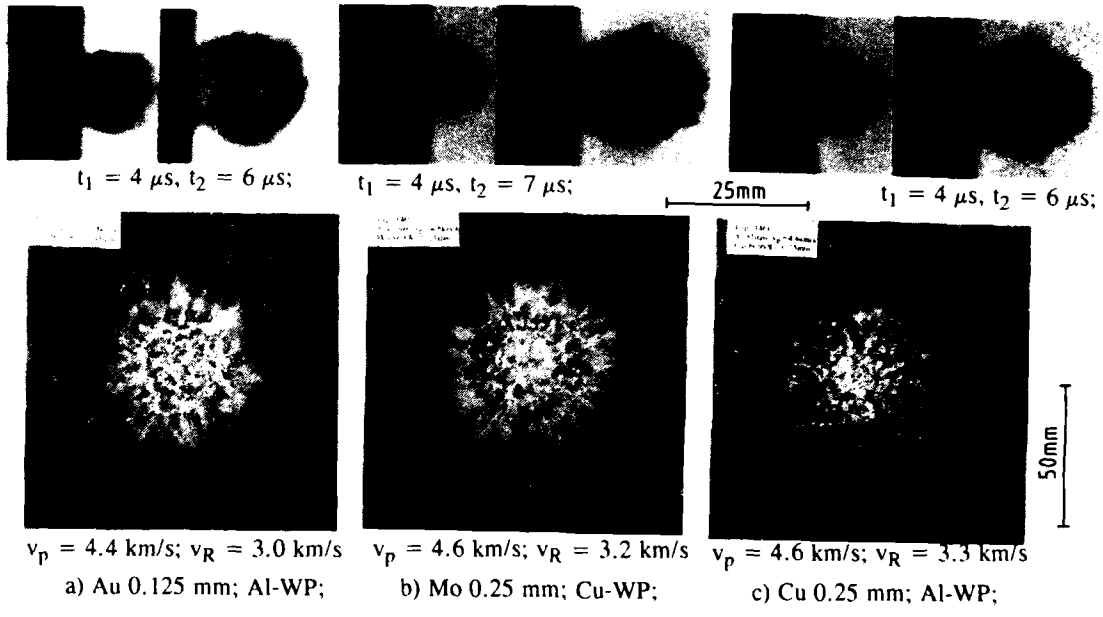


Fig. 9 Debris clouds at times t_1 and t_2 after impact and impact crater pattern of 2 mm diameter aluminum spheres against gold (Au), molybdenum (Mo) and copper (Cu) foils; aluminum (Al-WP) and copper (Cu-WP) witness plates with a spacing of 75 mm

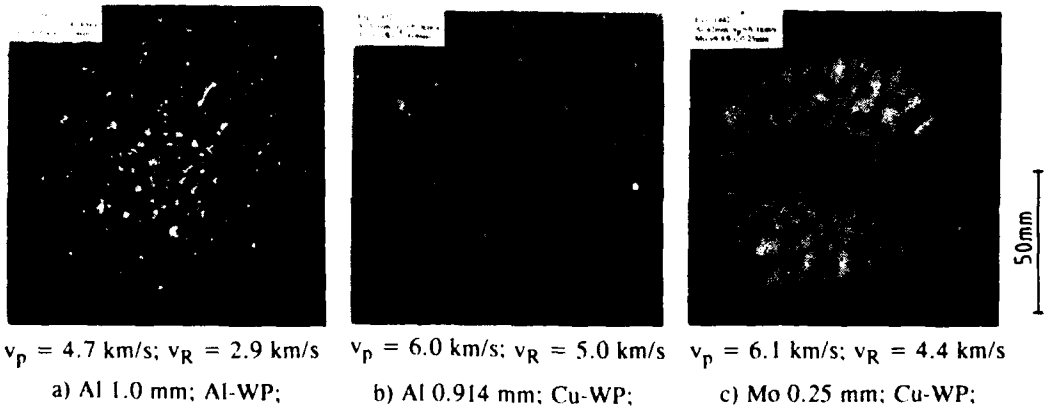
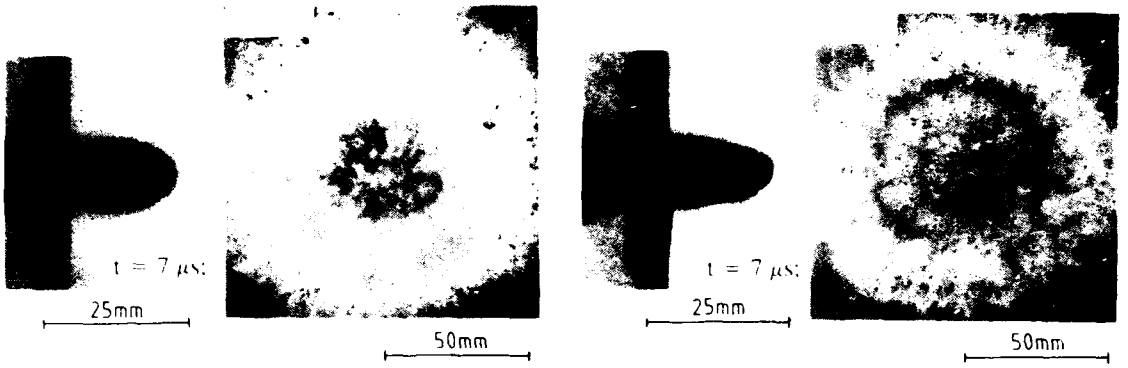


Fig. 10 Impact crater pattern of 2 mm diameter aluminum spheres against aluminum (Al) and molybdenum (Mo) foils; aluminum (Al-WP) and copper (Cu-WP) witness plates with a spacing of 75 mm



a) Sn 2.0 mm; v_p = 8.7 km/s; v_R = 3.2 km/s b) Zn 2.0 mm; v_p = 8.2 km/s; v_R = 2.9 km/s

Fig. 11 Debris clouds at time t after impact and impact crater pattern of 2 mm diameter aluminum spheres at impact velocities around v_p = 8.5 km/s against 2 mm thick tin (Sn) and zinc (Zn) foils; copper witness plates with a spacing of 75 mm.

Fig. 11 exhibits the results of 2 mm thick tin and zinc foils with densities of ρ = 7.3 g/cm³ and ρ = 7.1 g/cm³, due to areal densities of $\rho \cdot t$ = 14.6 kg/m² and $\rho \cdot t$ = 14.2 kg/m², perforated by 2 mm diameter aluminum spheres ($\rho_p \cdot d$ = 5.4 kg/m²) at velocities around v_p = 8.5 km/s. As pointed out and indicated by geometrical shapes of debris clouds, no crater ring pattern appears. The degree of fragmentation of tin is much higher than for zinc due to the lower specific heat of fusion q_m of tin (Fig. 15).

Changes of state of aggregation

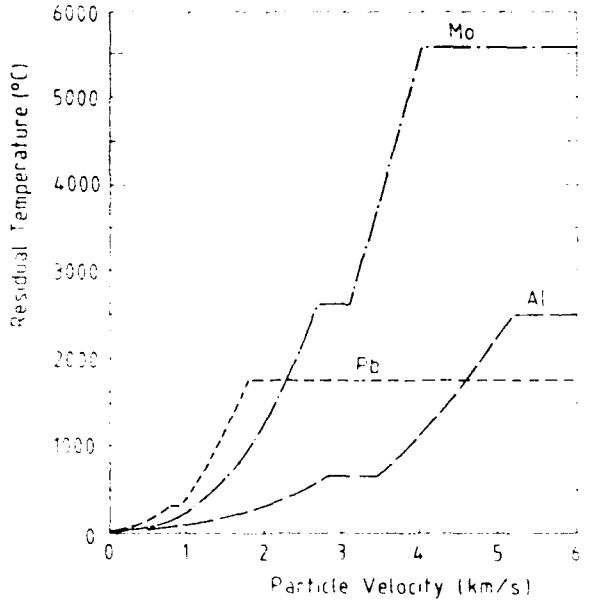
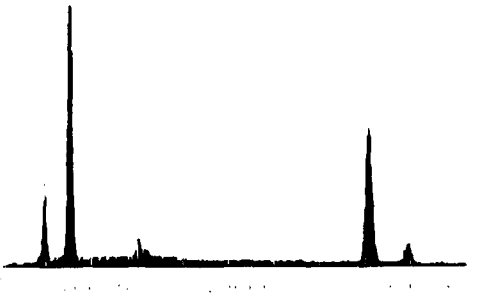


Fig. 12 Estimates of residual temperature versus particle velocity using Ahrens EOS



a) Enlarged sector of a crater



b) Material compound analysis of the rectangular area, marked in a)

Fig. 13 Typical material distribution inside craters of a crater ring pattern at v_p = 4.4 km/s (2 mm Al sphere against a 0.25 mm Ag foil)

The material compression by the shock waves along the Hugoniot curve is a nonisentropic process, whereas the release to ambient pressure is a near isentropic one, thus the impact-involved material will be heated in its final (decompressed) state. Dependent on the impact velocity, the state of material can be changed from solid into the liquid and/or vaporized condition. Table 5 depicts the Hugoniot pressures for melting and vaporization of some metals tested in this work (Kinslow, 1970; Zukas, 1982; Anderson, Jr., et al., 1990). For the Al, Cu and Pb targets where the projectile consisted of Al the impact velocities for the state change are given. Fig. 12 shows the estimated residual temperature versus particle velocity (one-half of the impact velocity) for Al → Al, Pb → Pb and Mo → Mo (Anderson, Jr., et al., 1990). A comparison of Table 5 and Fig. 12 delivers that the given impact velocities of Table 5 for incipient/complete melting and vaporization are twice the value of the particle velocities if impactor and target consist of the same material.

Table 5: Impact pressures and velocities for melting and vaporization

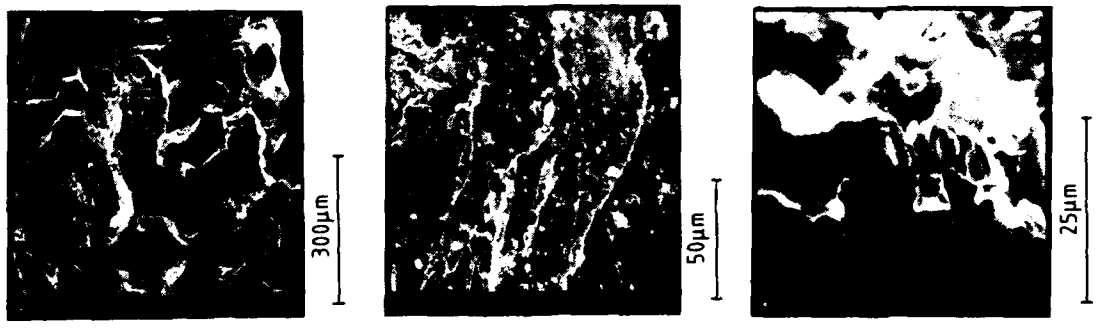
Target mat.	Proj. mat.	Incipient Melting pressure [GPa]	v_p [km/s]	Complete Melting pressure [GPa]	v_p [km/s]	Incipient Vaporization pressure [GPa]	v_p [km/s]	Complete Vaporization pressure [GPa]	v_p [km/s]
Al #	Al	67	5.50	88	6.6	167	10.2	470	-
Cu #	Al	140	6.60	184	8.00	340	12.6	3400	-
Pb #	Al	27	2.1	34	2.5	84	4.8	230	9.1
Au *	-	150	-	160	-	-	- -	-	
Mo +	Mo	238	5.5	289	6.3	409	8.00	-	-

[Zukas], * [Kinslow], + [Anderson, Jr.]

The digital scanning electron microscope photographs of Fig. 13 present a typical impact crater of an Al/Ag crater ring pattern at v_p = 4.4 km/s. According to Table 5, for an Al/Al impact incipient melting can be achieved at v_p = 5.5 km/s. Because of $\rho_{Ag} > 3 \cdot \rho_{Al}$ the Al/Ag impact yields melting at a lower v_p, proven by the pasty look of the crater surface material (Fig. 13a), mainly consisting of aluminum from the projectile (Fig. 13b). It has been found that the target material, here indicated by silver, is homogeneously distributed inside as well as outside the craters, evident with the assumption of a uniform target material distribution over debris cloud surface (Zukas, 1982; Piekutowski, 1990).

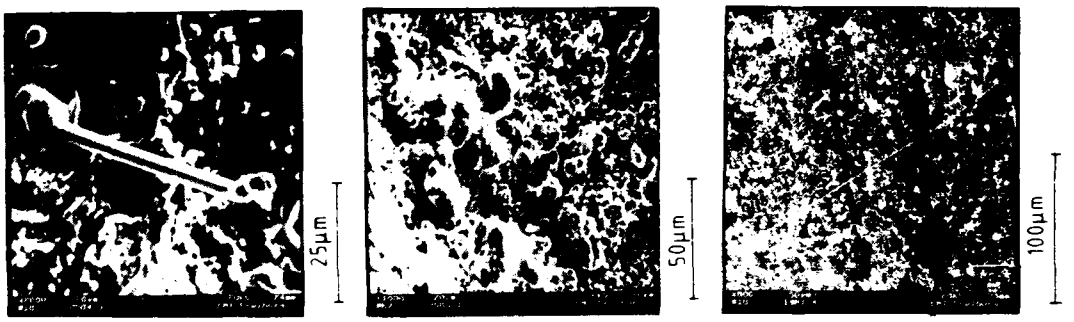
For incipient melting of Pb by an Al projectile a v_p = 2.1 km/s is necessary, which is distinctly lower than the impact velocity for melting of tin due to the different shock wave data (van Thiel, 1966) and thermodynamic properties.

In the case of tin and zinc foils (d/t = 1.0) the residual velocity of debris cloud particles $v_R \leq 1/3\ v_p$ (Fig. 11) is sufficiently low not to cause changes of aggregation of copper witness plate material by Sn and Zn particle impact.



a) Sn 2.0 mm; v_p = 4.7 km/s b) Sn 2.0 mm; v_p = 8.7 km/s c) Zn 2.0 mm; v_p = 8.2 km/s

Fig. 14 Digital scanning electron micrographs of the front part of the perforation hole lips of 2.0 mm thick tin (Sn) and zinc (Zn) foils perforated by 2 mm diameter aluminum spheres at impact velocities between v_p = 4.7 km/s and 8.7 km/s, corresponding to Fig. 4.



a) Sn 2.0 mm; v_p = 8.7 km/s b) Zn 2.0 mm; v_p = 8.2 km/s c) Pb 1.5 mm; v_p = 8.0 km/s

Fig. 15 Digital scanning electron micrographs of the projectile and target material distribution of 2 mm diameter aluminum spheres and tin (Sn), zinc (Zn) and lead (Pb) foils at impact velocities around 8.5 km/s on copper witness plates.

By comparison of Figs. 14 and 15 melting of tin obviously occurs at a lower v_p than melting of zinc, because of different thermodynamic properties but equal Hugoniot data (von Thiel, 1966). The molten condition of tin as well as lead is reliably indicated by filaments of liquid material streaming out of cracks on the surface of solidified droplets at the instance of impact. The higher the temperature and impact velocity of molten material, the longer the filaments.

CONCLUSIONS

Perforation processes of 2 mm diameter aluminum spheres and thin, high-pure metal foils with comparable areal densities accompanied by impact phenomena such as impact flash and changes of aggregation at impact velocities of up to 9 km/s have been discussed. It has been found that, for infinitely thin foils, the perforation hole diameter converges to the projectile diameter, independent of the material properties and impact velocity. For thicker foils the influence of the impact velocity on the hole size increases. In the case of metals with low melting temperatures and specific heats of fusion, such as tin, zinc and lead the perforation process was additionally effected by changes of aggregation. For 2 mm thick tin and zinc targets, it was shown that perforation of materials with comparable densities and melting temperatures but lower specific heats of fusion causes larger perforation hole diameters.

The duration of the impact flash was found to be dependent on impact velocity and target material. At velocities around 4 km/s and 8.5 km/s the flash duration time was in the order of 1 μs and 4 μs, respectively, in the case of copper foils even more than 8 μs. A comparison of outcomes found in literature and results presented in this paper depicted that, at impact velocities between 4 km/s and 9 km/s the expansion velocity of the impact flash does not exceed 10 - 15 km/s.

The occurrence of crater ring pattern of thin foils with areal densities between 0.9 - 2.7 kg/m^2 due to projectile diameter to foil thickness ratios of 2 - 20 has been observed at an impact velocity around 4.5 km/s. This pattern is indicated by the shape of a truncated cone of the front part of the debris cloud, identified in high speed photographs. The formation of these crater rings seem to be not very sensitive in a variation of the foil thickness, if the areal density is not changed dramatically. It has been exhibited that in all experiments where this ring pattern has appeared, the areal density of the projectile was greater than that of the target.

Digital scanning electron microscope analysis was pointed out as a successful tool to distinguish between solid and liquid states of aggregation of debris cloud material trapped by witness plates.

REFERENCES

Anderson, Ch. E., Jr. et al. (1990). Debris Cloud Dynamics. Int. J. Impact Engng., Vol. 9, No. 1, pp. 89 - 113.

Ang, J. A. (1990). Impact Flash Jet Initiation Phenomenology. Int. J. Impact Engng., Vol. 10, pp. 23 - 33.

Eichhorn, G. (1976). Analysis of the Hypervelocity Impact Process from Impact Flash Measurements. Planet. Space Sci., No. 24, pp. 771 - 781.

Gehring, J. W., and R. L. Warnica (1963). An Investigation of the Phenomena of Impact Flash and Its Potential Use as a Hit Detection and Target Discrimination Technique. Int. J. Impact Engng., Vol. 2, No. 2, pp. 627 - 681.

Gotting, G. (1977), private communication at EMI Freiburg, FRG.

Horz, F. (1990). A Small Caliber Light Gas Gun to Simulate Cosmic Dust Impacts, ARA, San Diego, USA.

Jean, B., and T. L. Rollins (1969). Radiation from Hypervelocity Impact Generated Plasma. AIAA, Vol. of Techn. Papers, No. 69 - 364.

Jean, B., and T. L. Rollins (1970). Radiation from Hypervelocity Impact Generated Plasma. AIAA J., No. 8, pp. 1742 - 1748.
Kinslow, R. (1970). High-Velocity Impact Phenomena, Chap. IV, pp. 113 - 117. Academic Press New York and London.
Piekutowski, A. J. (1990). A Simple Dynamic Model for the Formation of Debris Clouds. Int. J. Impact Engng., Vol. 10, pp. 453 - 471.
Stilp, A. J., et al. (1990). Debris Cloud Expansion Studies. Int. J. Impact Engng., Vol. 10, pp. 543 - 553.
Zukas, J. A. (1982). Impact Dynamics, Chap. 6, pp. 223 - 230. John Wiley & Sons, New York.

Int. J. Impact Engng Vol.14, pp.809–818, 1993
Printed in Great Britain

0734-743X/93 $6.00+0.00
Pergamon Press Ltd

PENETRATION OF EXPLOSIVELY FORMED PROJECTILES

C.A. WEICKERT and P.J. GALLAGHER

Defence Research Establishment Suffield
Box 4000, Medicine Hat, Alberta, Canada, T1A 8K6

ABSTRACT

Results of an experimental and computational investigation on the effects of the shape of an explosively formed projectile on the penetration into various targets are presented. Seven different shapes of Armco iron EFPs with a velocity range of 1666 - 1862 m/s were fired into stacked targets consisting of mild steel, RHA, aluminum armour, and OFHC copper plates. Numerical simulations were performed with the ZeuS two-dimensional hydro-code. It was found that a range of projectile profiles and velocities produced differing levels of penetration into the various targets.

INTRODUCTION

The design of explosively formed projectile (EFP) warheads involves many parameters which effect the projectile shape. Physical properties and responses of the explosive, liner and casing materials represent some of these parameters. Other parameters are geometric, such as liner contours, casing dimensions, charge diameter, etc.. Successful EFP design will arrive at parameters which lead to an EFP able to defeat a specific target.

Presented in this paper are comparisons of experimental results of 19 firings (sectioned target profiles) and two-dimensional finite element calculations of EFP penetration. Correlations between the EFP profiles and velocities and the penetration depths were established.

EXPERIMENTAL SET-UP

The EFP charge design is described previously (Weickert and Gallagher, 1992). Through variation of the charge confinement parameters, seven EFP shapes were produced from a single liner/case design. Characterization of the EFPs was derived from flash X-radiographs of the projectiles in flight and through examination of soft-recovered projectiles.

A series of targets, made up of stacked thicknesses of plate, were assembled and fired against with an array of the seven iron EFP shapes generated (shown in Fig. 1.); 1-7 against mild steel, and 1, 3, 5, and 7 against each of RHA, Al, and Cu. Each target was composed as described in Table I below.

Targets were shot at close range (~1.4 m), but at a sufficient distance to allow the EFPs to form completely. Flash X-radiographs were taken for each EFP prior to impact to establish velocity and profile.

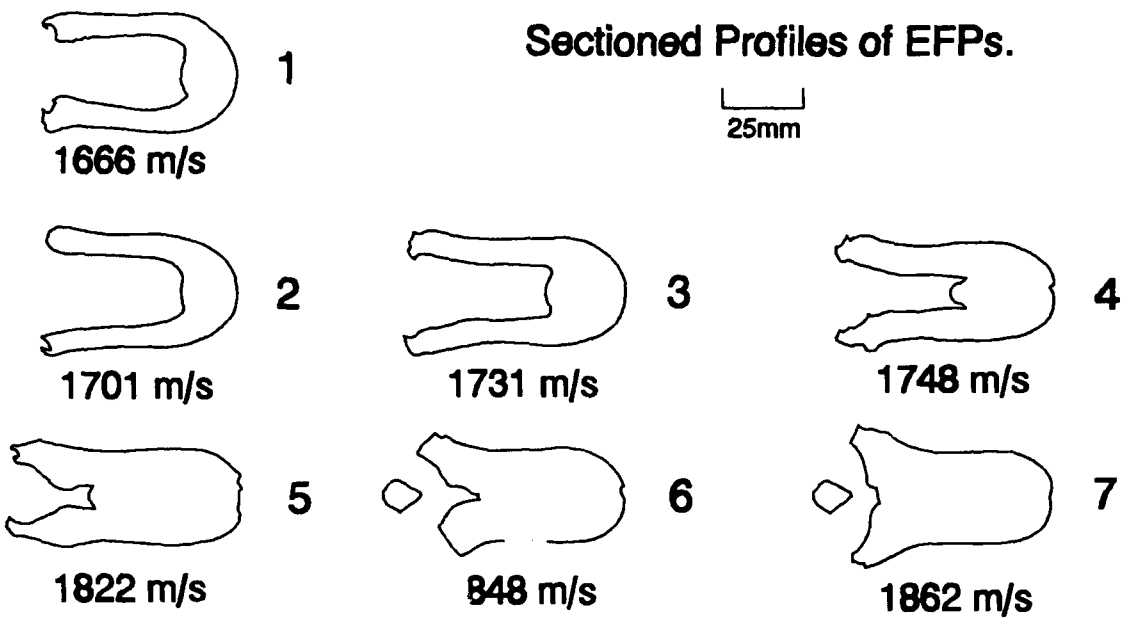


Fig. 1 Experimental EFP profiles.

Table I. Target material description.

T1	2 - 300 mm squares of 50.8 mm thick mild steel plate.
T2	2 - 300 mm squares of 50.8 mm thick RHA steel plate.
T3	4 - 300 mm squares of 38.1 mm thick 7039 aluminum armour plate.
T4	4 - 250 mm squares of 25.4 mm thick OFHC copper plate.

*All backed with 4 - 300 mm squares of 25.4 mm thick mild steel and a 600 mm square of 100 mm thick armour plate.

NUMERICAL SET-UP

Numerical simulations of the EFPs impacting and penetrating the various targets were run on an 80486 based micro computer using ZeuS (Zukas and Segletes, 1987) a two-dimensional, Lagrangian hydro-code. The penetrator and target properties used for the code's material models, are shown in Table II. This was the latest release of the ZeuS code, and there is not yet an extensive library of material properties. Furthermore, the failure and erosion criteria, in the code have been re-worked. Thus parameters controlling these events have not been developed fully for the materials studied here. They are also code dependent numerical parameters and not completely linked to a physical property. Also, strain rate and temperature dependent properties were not used, since the specific materials used here have not yet been characterized to this extent.

RESULTS

The purpose of the present study was to determine the effect of an EFP profile on the penetration into a variety of target materials.

In Fig. 1 are shown the seven EFP profiles produced, P1 through P7, and their velocities (Weickert and Gallagher, 1992). A timed sequence (Δt = 25 μs) of an EFP, P5, going into a target (T1) is shown in Fig. 2. The final (t=150μs) frame and experimental profile are shown in Fig. 7.

The full sequence of penetrator shapes (P1-P7) were fired against mild steel targets (T1). The computed and experimental profiles of this series are shown in Figs. 3-9.

For the RHA, Al, and Cu targets (T2, T3, T4), only penetrators P1, P3 ,P5, and P7 were used. The simulations and experiments for these targets are shown in Figs. 10-13 (RHA), Figs. 14-17 (Al), and Figs. 18-21 (Cu).

Reasonable agreement can be seen between the predicted and experimental penetrations, especially considering the range covered by the series. The EFP profiles were characterized by: velocity, projectile length, solid length over projectile length ratio, and percent solid volume (Table III). Plots of penetration depth versus each of these parameters are shown in Figs. 22-25. There is a knee in most of the plots indicating minimal penetration performance enhancement above a limit. Although, penetration depth is only one parameter, and closer examination of the post-impact target profiles, reveals changes to the hole size, shape and deformation of non-penetrated plates with each shot.

Table II. Model material properties.

	σ_{yield} (MPa)	σ_{uts} (MPa)	ε_{uts}	P_{min} (MPa)
Armco Iron (EFP)	400	500	0.20	1230
Mild Steel (Target 1)	820	820	0.0001	1230
RHA steel (Target 2)	900	1100	0.20	3030
7039 Al (Target 3)	400	500	0.20	1000
OFHC Cu (Target 4)	450	450	0.20	5000

Table III. Projectile characterization data.

Projectile	Velocity (m/s)	Length (mm)	Solid Length/ Length	%Solid Volume
P1	1666	59.7	0.29	75.2
P2	1701	60.7	0.29	68.3
P3	1731	69.7	0.36	76.8
P4	1748	67.3	0.48	86.5
P5	1822	70.9	0.67	90.6
P6	1848	65.3	0.71	91.3
P7	1862	62.1	0.86	93.4

CONCLUSION

The shape of an EFP significantly effects the depth and profile of the penetration into a target materials. Each EFP profile carried a specific set of velocity, length, and degree of solidness (wrt length and volume), and as such no single parameter could be singled out.

More work is required in properly characterizing the materials to bring the simulation into closer agreement with the experiments. The ZeuS code allows for externally defined material models, which could, in time, generate an improved matching to the experimental results. With better agreement established, then single parameter variation, computational studies could be carried out, relatively inexpensively, to further optimize EFPs.

REFERENCES

Weickert, C.A. and Gallagher, P.J. (1992). Parametric Study of the Effect of a Confinement Ring on the Shape of an Explosively Formed Projectile, *13th International Symposium on Ballistics*, Sweden, vol.2 413-420.

Zukas, J. and Segletes, S. (1987). *ZeuS, Technical Description and Users Manual*, Computational Mechanics Consultants, Towson, MD.

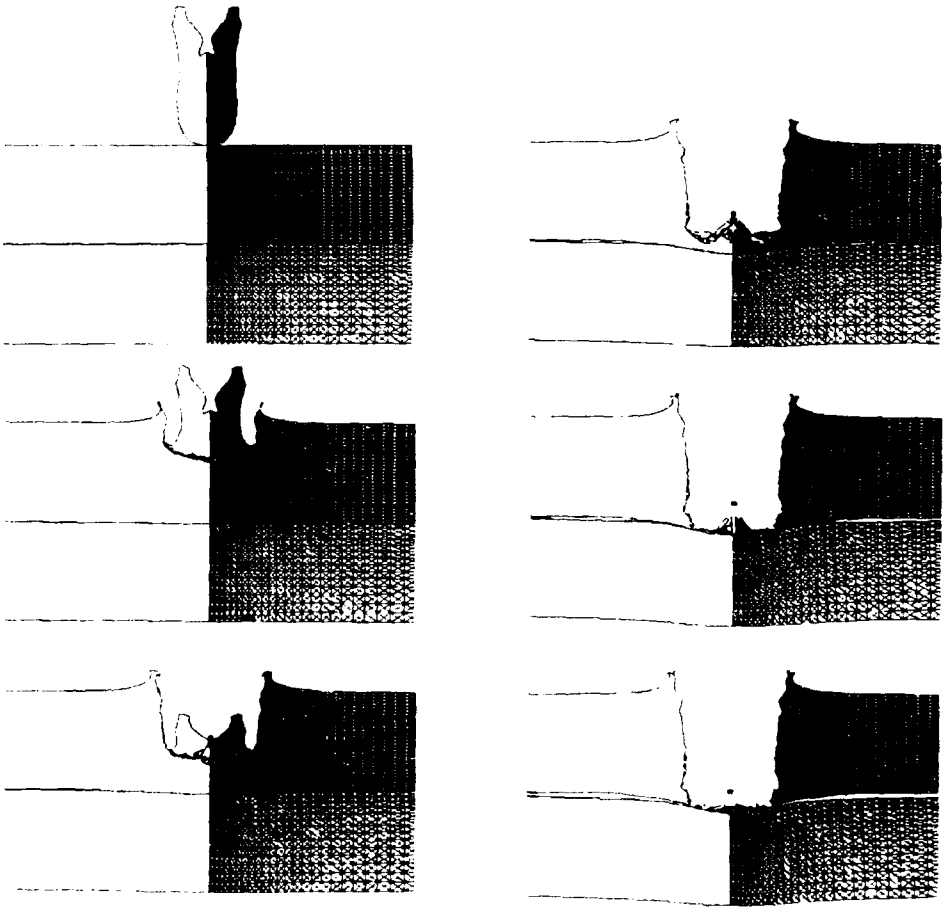


Fig. 2 Computational sequence of an EFP (P5) entering a target (T1), Δt = 25 μs, times 0 to 125 μs.

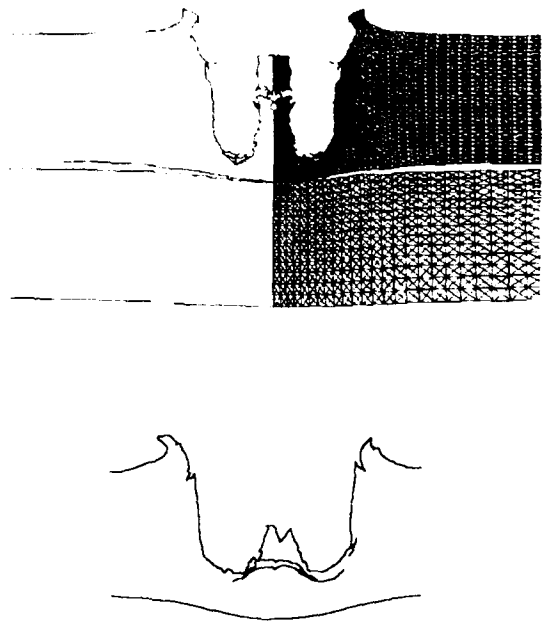


Fig. 3 Projectile (P1) into Target (T1), simulation @ 150 μs (top) and experiment.

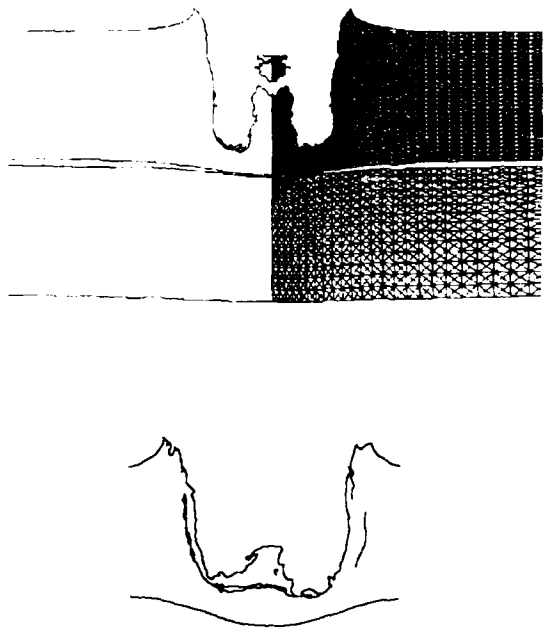


Fig. 4 Projectile (P2) into target (T1), simulation @ 150 μs (top) and experiment.

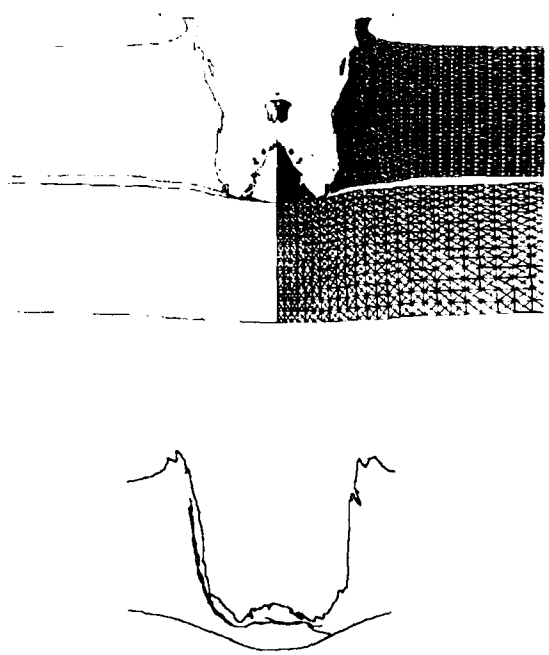


Fig. 5 Projectile (P3) into Target (T1), simulation @ 150 μs (top) and experiment.

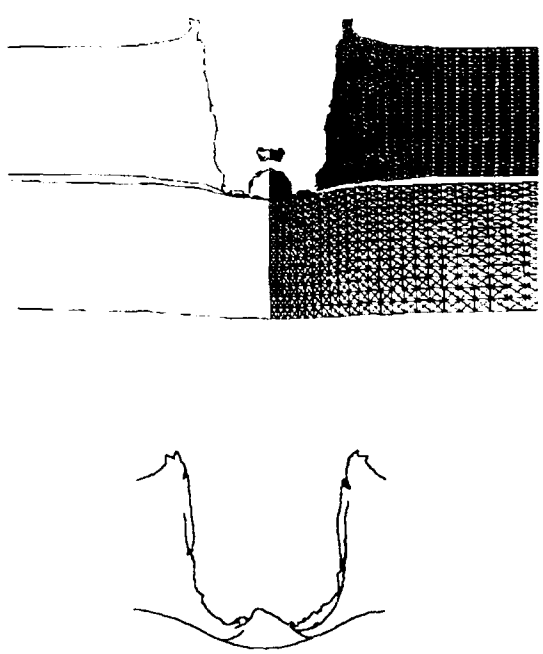


Fig. 6 Projectile (P4) into target (T1), simulation @ 150 μs (top) and experiment.

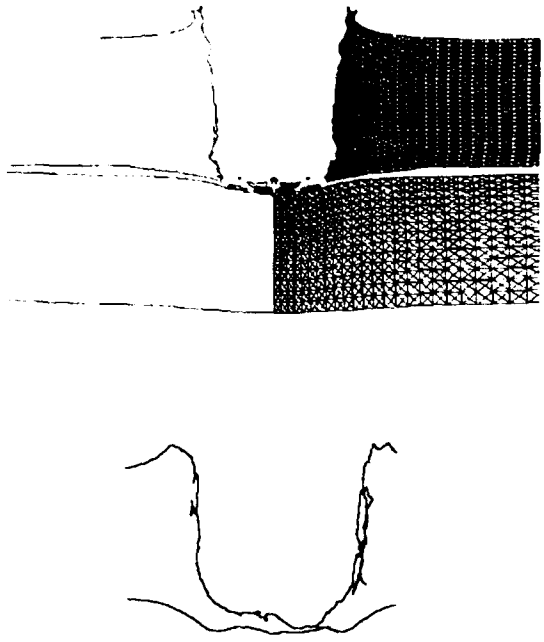


Fig. 7 Projectile (P5) into target (T1), simulation @ 150 μs (top) and experiment.

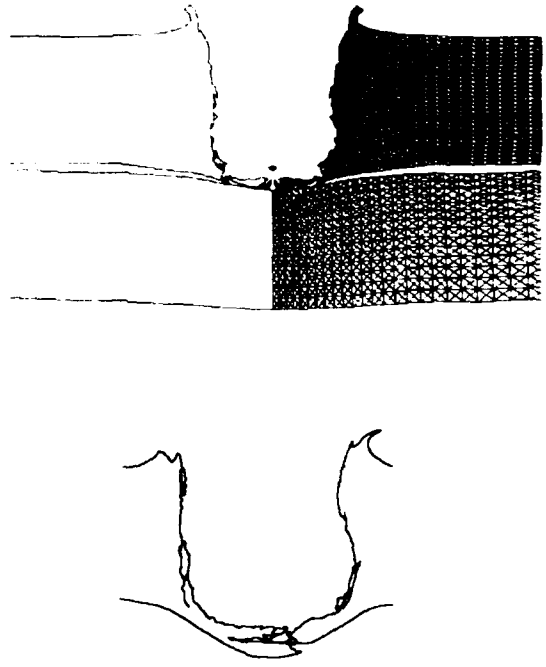


Fig. 8 Projectile (P6) into target (T1), simulation @ 150 μs (top) and experiment.

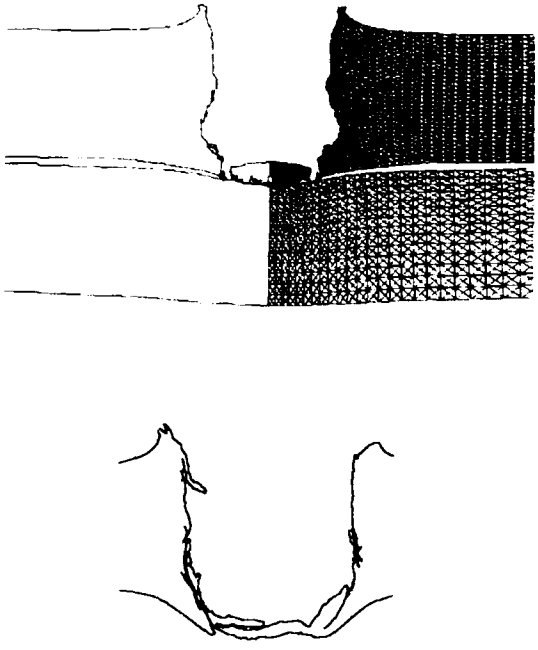


Fig. 9 Projectile (P7) into target (T1), simulation @ 150 μs (top) and experiment.

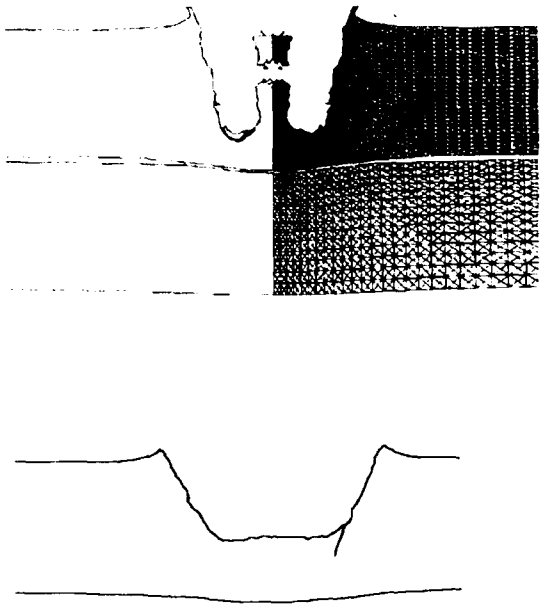


Fig. 10 Projectile (P1) into Target (T2), simulation @ 150 μs (top) and experiment.

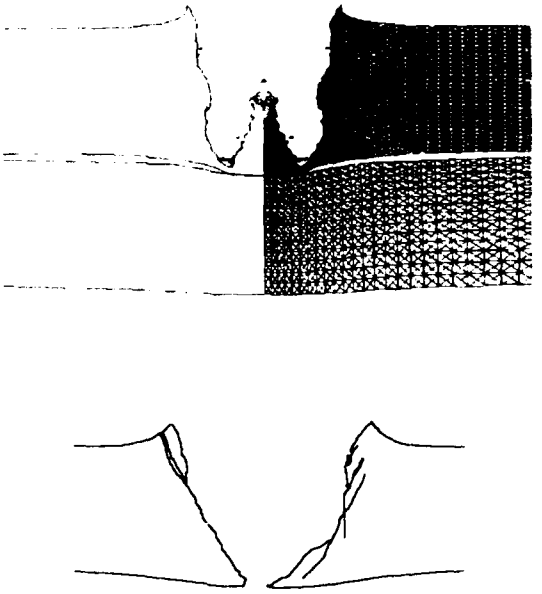


Fig. 11 Projectile (P3) into target (T2), simulation @ 150 μs (top) and experiment.

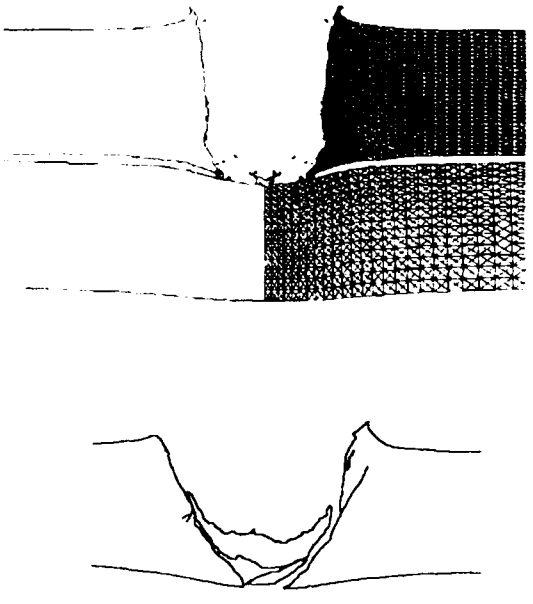


Fig. 12 Projectile (P5) into Target (T2), simulation @ 150 μs (top) and experiment.

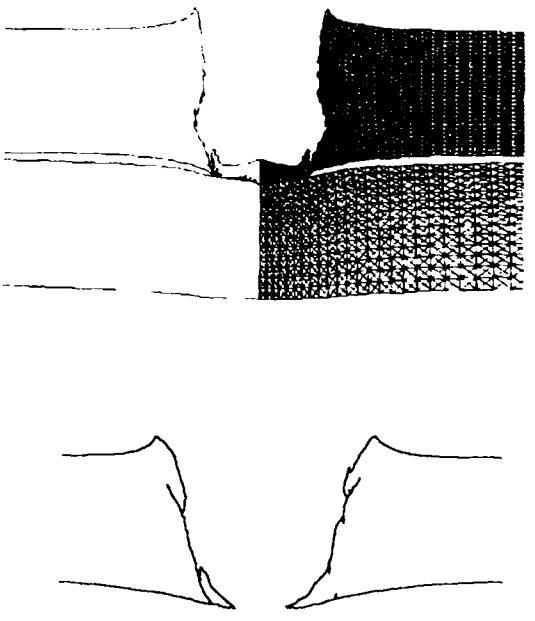


Fig. 13 Projectile (P7) into target (T2), simulation @ 150 μs (top) and experiment.

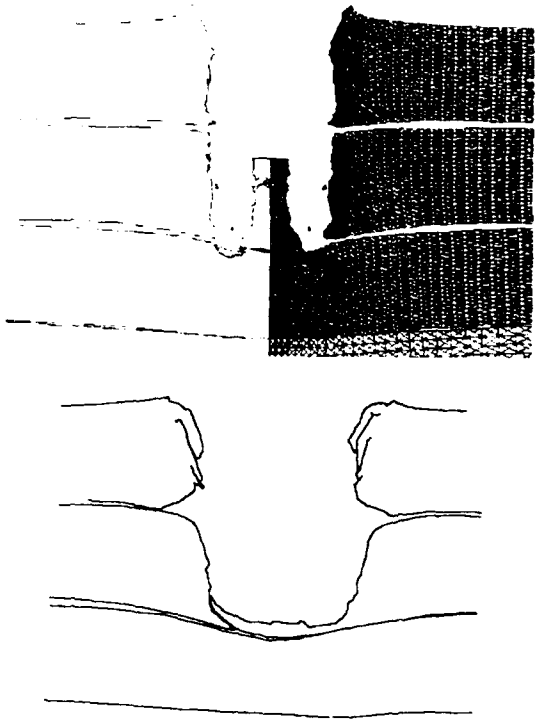


Fig. 14 Projectile (P1) into Target (T3), simulation @ 150 μs (top) and experiment.

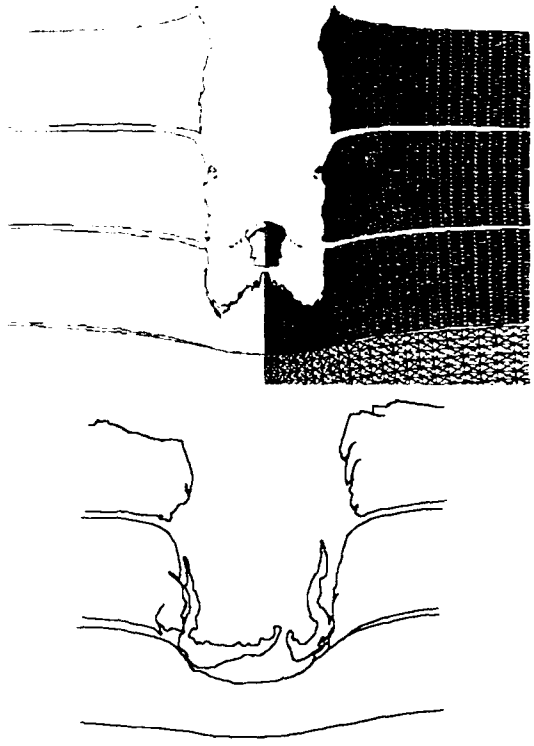


Fig. 15 Projectile (P3) into target (T3), simulation @ 150 μs (top) and experiment.

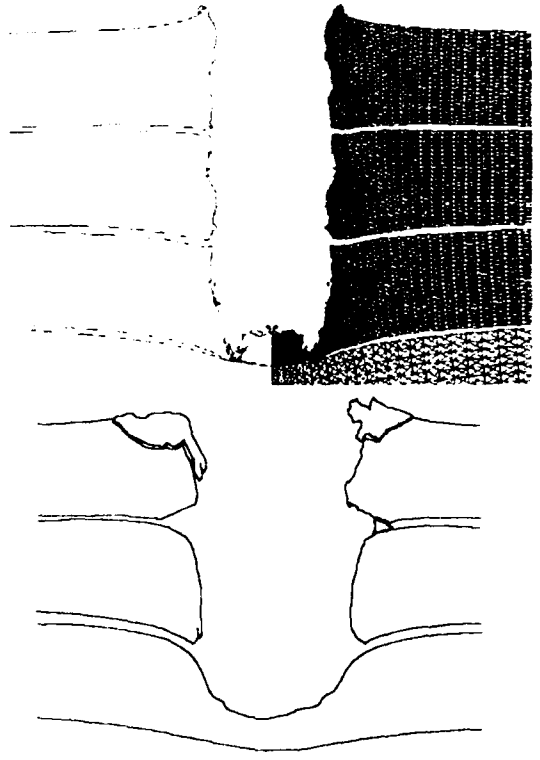


Fig. 16 Projectile (P5) into Target (T3), simulation @ 150 μs (top) and experiment.

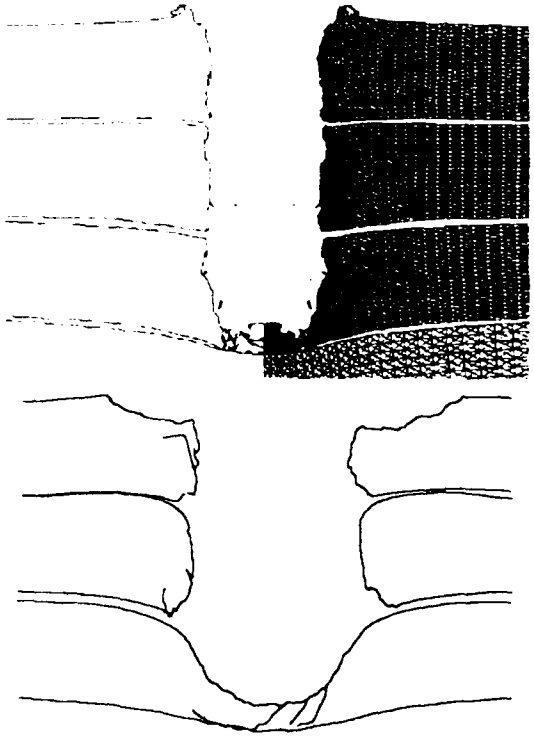


Fig. 17 Projectile (P7) into target (T3), simulation @ 150 μs (top) and experiment.

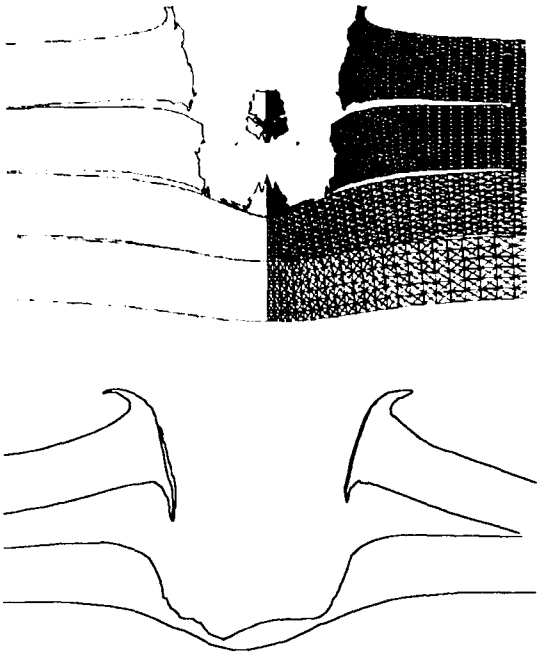


Fig. 18 Projectile (P1) into Target (T4), simulation @ 150 μs (top) and experiment.

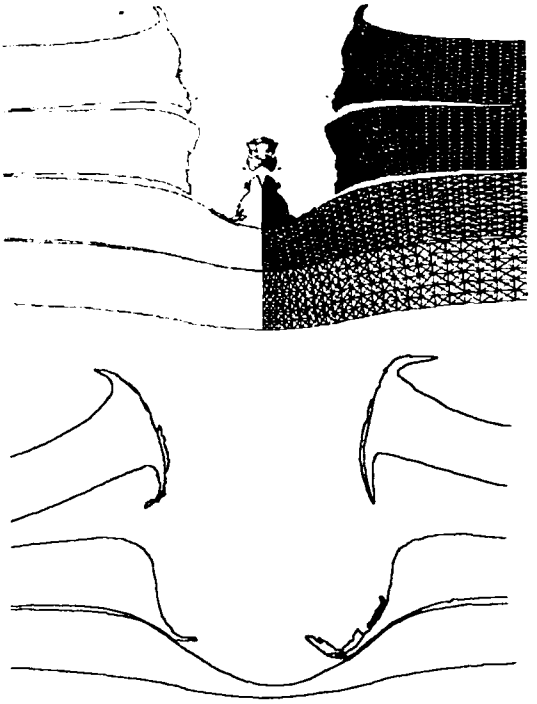


Fig. 19 Projectile (P3) into target (T4), simulation @ 150 μs (top) and experiment.

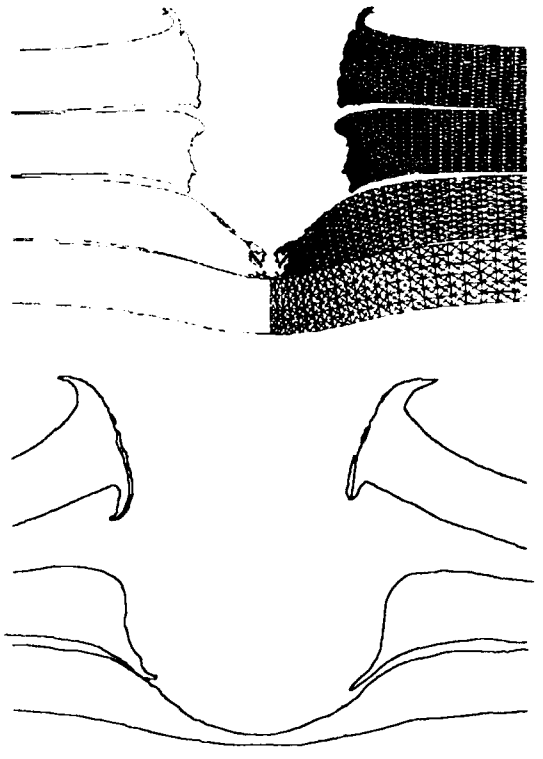


Fig. 20 Projectile (P5) into Target (T4), simulation @ 150 μs (top) and experiment.

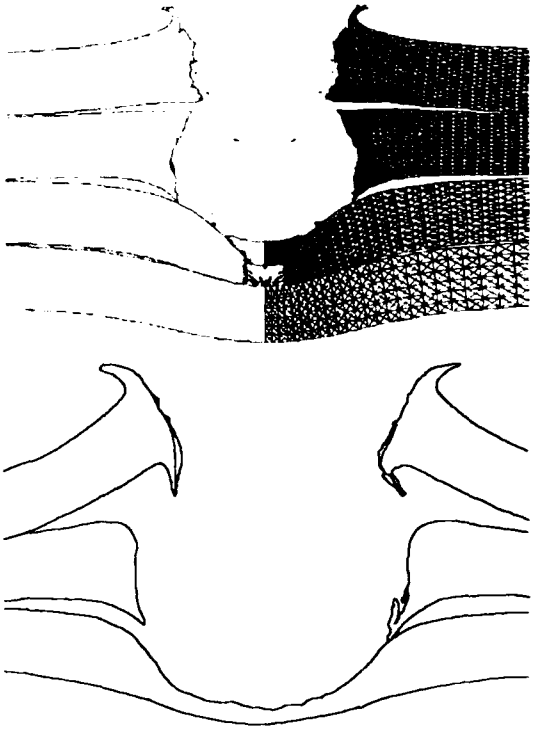


Fig. 21 Projectile (P7) into target (T4), simulation @ 150 μs (top) and experiment.

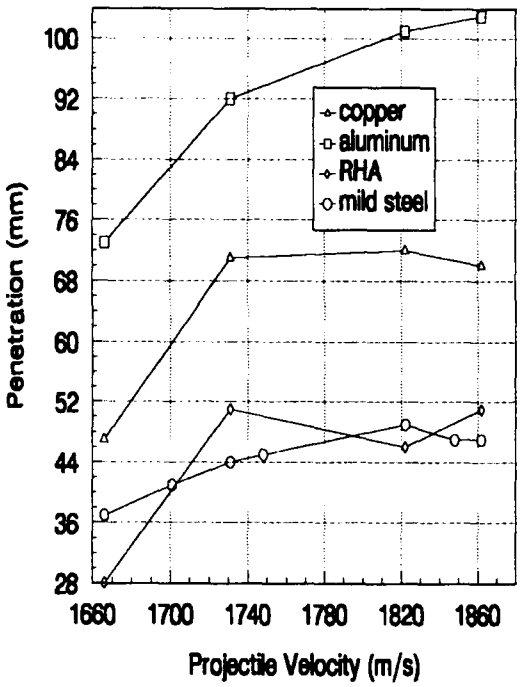


Fig. 22. Penetration vs EFP Velocity.

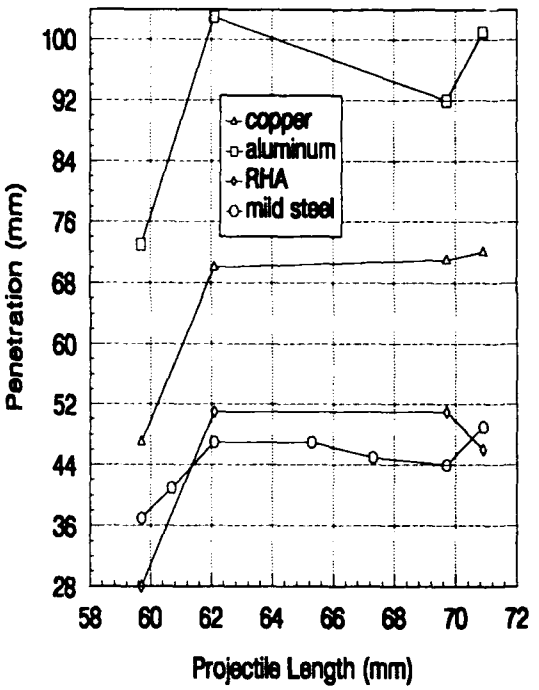


Fig. 23. Penetration vs EFP Length.

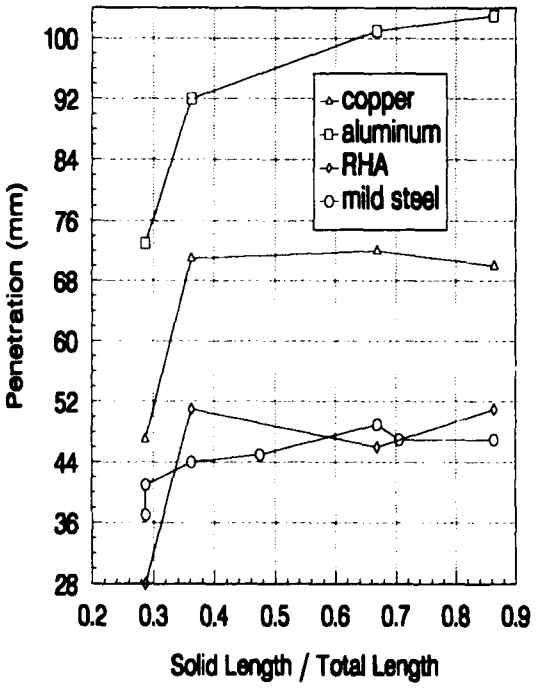


Fig. 24. Penetration vs Solid Length/EFP Length.

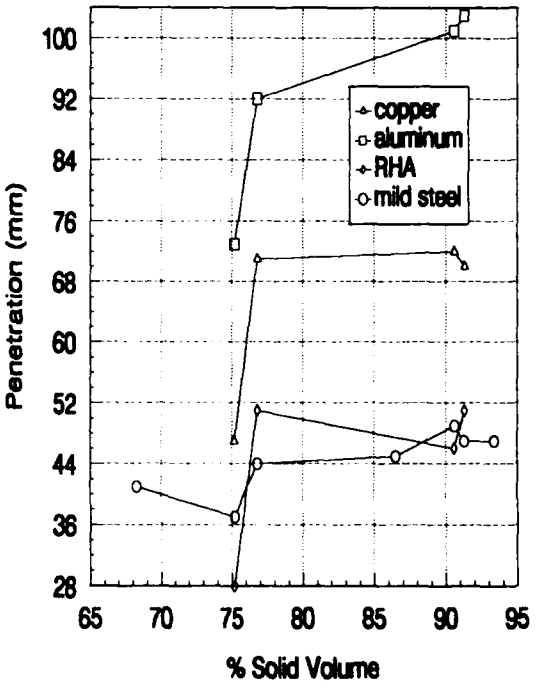


Fig. 25. Penetration vs EFP %Solid.

Int. J. Impact Engng Vol.14, pp.819–830, 1993
Printed in Great Britain

0734-743X/93 $6.00+0.00
© 1993 Pergamon Press Ltd

MODELS OF HIGH VELOCITY IMPACT PHENOMENA

C. A. Wingate, R. F. Stellingwerf, R. F. Davidson and M. W. Burkett

Los Alamos National Laboratory, Los Alamos, NM 87545

ABSTRACT

Models of craters formed by impacts at velocities of up to 24.5 km/sec have been computed using the Smooth Particle Hydrodynamics, MESA, EPIC and CALE codes. These modeling efforts are compared to data obtained from the Hypervelocity Microparticle Impact project at Los Alamos using the van de Graaff accelerator. A factor of 5 increase in yield strength was needed to account for high strain rate effects and to match the data. Structure in the data is addressed by using crater volume instead of crater diameter cubed. Detailed code comparisons were made between the four codes with good agreement found.

INTRODUCTION

The Hypervelocity Microparticle Impact (HMI) project (Keaton *et. al.*, 1990; Stradling *et. al.*, 1990) has obtained impact data from microscopic iron spheres at velocities of 1 km/sec to 100 km/sec impacting a variety of targets. The iron sphere projectiles are charged and accelerated electrostatically in a 6 MV Van de Graaff accelerator. Each impact is characterized by simultaneous measurement of projectile charge and velocity using careful cross-correlation techniques. A scanning electron microscope is used to measure the crater characteristics with the crater diameter being the pertinent piece of data for this work. For the work reported here ve have concentrated on the copper and aluminum targets.

Figure 1 shows a plot of the Cu and Al data for the velocity range of about 5 - 30 km/sec. The quantity plotted is the crater diameter cubed divided by the projectile mass and is plotted versus the projectile velocity. This particular quantity is plotted in order to show the scaling features. In addition to the HMI data there are a few macroscopic impact data points plotted. There are two interesting features to this data. The first is that the HMI microparticle impact crater volume divided by projectile mass in the range of 5-10 km/sec is about a factor of 4 below the macroscopic impacts. If the scaling were obeyed by the microscopic impacts they should lie on top of the macroscopic data. The other interesting feature of the HMI data is the structure in the data in the range of 10-30 km/sec. There are two plateaus in the data.

Another way of seeing the crater volume difference between the macroscopic and microscopic data is with the Sorensen data correlation shown in Fig. 2 (taken from Walsh *et. al.*, 1991). This figure plots the volume ratio, V divided by V_0, versus the scaling quantity

$$\frac{\rho v^2}{s} \qquad (1)$$

where ρ is the target density, v is the impact velocity and s is the shear yield strength for the target material. The data plotted are all copper-copper impacts of various sizes and include one HMI data point. The line is a data correlation due to Sorensen (1965) and fits the macroscopic data quite well. The formula for the correlation is

$$\frac{V}{V_0} = 0.12\left(\frac{\rho v^2}{s}\right)^{0.845} \tag{2}$$

The HMI data point falls well below the macroscopic data points and the correlation.

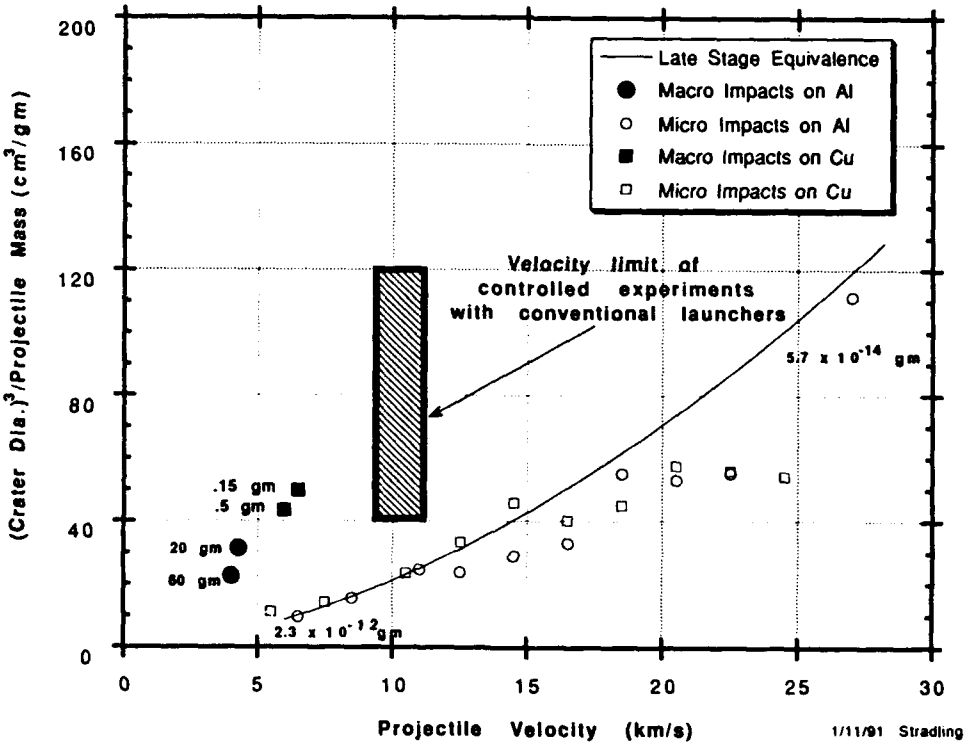


Fig. 1. Plot of the Cu and Al data for the velocity range of about 5 - 30 km/sec. The quantity plotted is the crater diameter cubed divided by the projectile mass and is plotted versus the projectile velocity. In addition to the HMI data there are a few macroscopic impact data points plotted. The two interesting features to this data is that the HMI microparticle impacts in the range of 5-10 km/sec are about a factor of 4 below the macroscopic impacts contrary to scaling and that there is plateau structures in the data in the range of 10-30 km/sec.

The reason for this scaling failure, put forward by Walsh *et. al.* (1991) is that this is due to strain-rate effects in the target material (copper in this case). They argue that the smaller flows in the HMI data imply much higher strain rates than in the macroscopic data and cause a higher effective flow stress which leads to a smaller crater. The increase in the flow stress required to match the HMI data can be found by increasing s in the Sorensen correlation until it matches the HMI copper data. This results in a factor of 4.7 increase in shear yield strength to match the HMI data.

The focus of the work reported in this paper is to understand the volume difference between the macroscopic data and the HMI data from a computational standpoint. Some initial work will also be reported on trying to understand the structure in the HMI data in the higher velocity region.

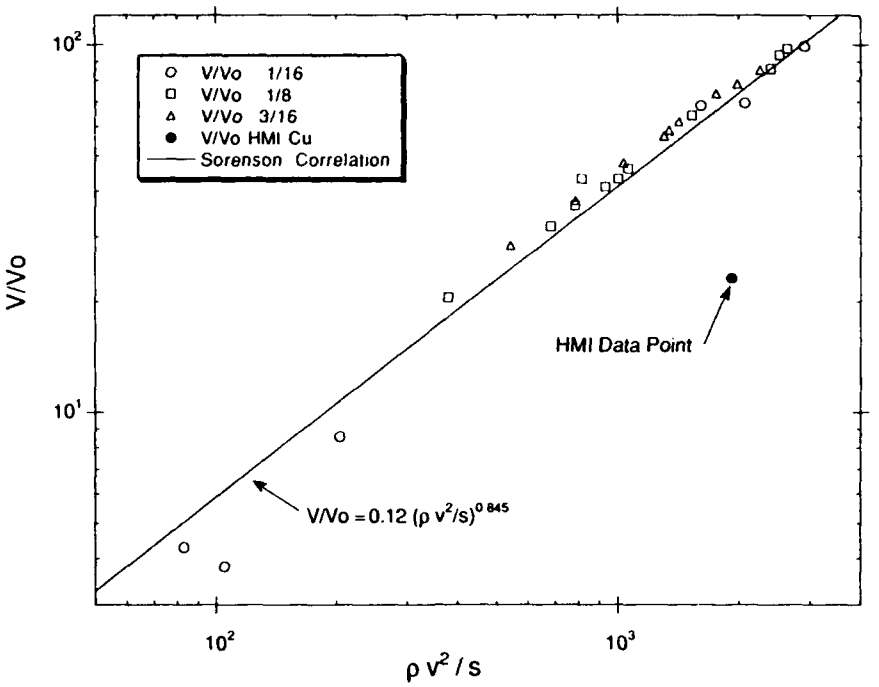


Fig. 2. Sorensen data correlation showing the volume difference between the macroscopic and microscopic data.

DESCRIPTION OF CODES

The four hydro codes used in this work were EPIC, MESA, SPH and CALE. This section gives a brief description of each code and references to more detailed reports.

Smooth Particle Hydrodynamics (SPH) is a relatively new technique for hydrodynamic calculations. It is a gridless Lagrangian method using a pseudo-particle interpolation method to compute smooth hydrodynamic variables. Each pseudo-particle has a mass, Lagrangian velocity, and internal energy, whereas other quantities are derived by interpolation or from constitutive relations. This technique has now been extended to include an elastic-plastic strength model, and a fragmentation model is being worked on. The code has been applied to a variety of kinetic energy impact problems including crater formation and target penetration and breakup. The current version of the code uses perfect gas, Gruneissen and SESAME eos, includes thermal diffusion, works in 1d, 2d, 3d cartesian coordinates, 2d cylindrically symmetric and 1d spherically symmetric. Besides the elastic-plastic strength model the code also has the Johnson-Cook and Steinberg-Guinan (being tested) strength models. HE burn is being worked on. The code is used primarily on Unix workstations and Cray machines where it is fully vectorized. There are also versions for PC's and McIntoshes. Details of SPH are given by Monaghan (1982, 1985, 1988), Benz (1989), Stellingwerf (1989, 1990), Libersky and Petschek (1990) Wingate and Fisher (1992) and Stellingwerf and Wingate (1992).

EPIC (Elastic Plastic Impact Computations, Sept. 90 version) (Johnson, 1977, 1978) is a multi-material, explicit, Lagrangian hydrodynamics code used primarily for analysis of ballistic and hypervelocity impacts and jet/fragment formations. Cartesian, cylindrical and spherical geometry are available in 1D, while plane stress, plane strain, and axisymmetric geometry is available in 2D. The 2D version employs triangular elements (standard and crossed), quadrilateral and one-dimensional elements. Shell elements and the variable conductivity (NABOR) nodes are also available. The 3D version uses tetrahedral elements. EPIC utilizes an explicit time integration coupled with a lumped mass formulation. Five different

material types are available to the user: solids, explosives, crushable solids, liquids and brittle solids. An elastic-plastic formulation, the Johnson-Cook strength model (Johnson and Cook, 1983) and the Zerilli-Armstrong FCC and BCC models (Zerilli and Armstrong, 1987) are options for solids. Also, a Mie-Gruneissen equation of state (EOS) and a cumulative damage failure/fracture model (Johnson and Cook, 1985) can be employed. When fracture occurs, the solid can develop hydrostatic stresses but can no longer support deviatoric or tensile stresses. Also, erosion or total failure is permitted by removing the element volume from the mesh while retaining the element mass. The erosion algorithm allows EPIC to perform penetration calculations without mesh distortion problems. Explosives require a Jones-Wilkins-Lee (JWL) or gamma law EOS. The explosive reaction is simulated with the programmed burn option. Response of brittle solids can be simulated with the brittle strength and fracture model (Johnson and Holmquist (1990). A master-slave sliding interface logic is used to model sliding surfaces, voids and failure via erosion. Finally, the code can accommodate a variety of geometric shapes and has the standard hydrocode boundary condition options. The code sponsor for EPIC is the Air Force Armament Laboratory (AFATL/MNW), Elgin Air Force Base and Honeywell Inc. was the major developer.

MESA (Bolstad and Mandell, 1992; Holian *et. al.*, 1991) is a multi-material, explicit Eulerian hydrocode used primarily for armor/anti-armor applications. The code employs a second order accurate finite difference scheme with a staggered grid for two and three dimensional problems. Cartesian and cylindrical geometry options are available. An "operator splitting" technique (Youngs, 1982) is utilized to obtain a time dependent solution of the problem. During the calculation, each cycle consists of two phases: a Lagrangian phase (updates material densities, velocities and internal energies) and an advection phase (the transport of mass, internal energy and momentum is performed). Also, a Van Leer (Van Leer, 1979) limiter is used to minimize oscillations associated with large gradients. Interface positions are resolved to determine material volume fractions within a cell (Youngs, date unknown). The MESA EOS options include: ideal gas, Mie-Gruneissen, modified Osborne, JWL and SESAME (Holian, 1984). An elastic-perfectly plastic, modified Steinberg-Cochran-Guinan (Steinberg, 1980, 1991) and Johnson-Cook strength models are available. The Johnson-Cook damage fracture model has been implemented. A standard programmed burn and a dynamic burn technique are available. MESA can accommodate a variety of geometric shapes and has standard hydrocode boundary condition options.

CALE (Tipton, 1991) is a 2D ALE (Arbitrary Lagrangian Eulerian) hydrodynamics computer program written in the "C" programming language. The "C" language was chosen to give both portability over a wide range of computers and high flexibility in defining complex data structures. The Hybrid "C" vectorizing compiler developed at LLNL is used on CRAY computers to produce highly optimized coding. CALE has been ported to a variety of machines including VAX, MIPS, STELLAR, SUN SPARC, CONVEX, DEC Work Station, SGI Work Station and IBM RISC 6000. The name CALE was chosen because it was referred to as the "C" ALE code. CALE is capable of multi-material Eulerian flow using a volume fraction method to keep track of the interfaces. The strength models in CALE include: no strength, constant shear and yield moduli, Steinberg-Guinan model, Cagnoux-Glenn model for ceramic material, tabulated yield versus pressure and constant shear and yield moduli with constant melt temperature for the temperature mode. CALE has a slide line treatment, can do axisymmetric problems in addition to Cartesian problems and has an MHD package.

CODE CALCULATIONS FOR THE CU MACROSCOPIC PROBLEM

The purpose of these calculations was to determine the variation in crater volume caused by a 5-fold increase in yield stress. Should the volume change be similar to that observed between the HMI and macroscopic data it would be an indication that the strain rate effect hypothesis is correct. In addition to this major purpose we were also interested in doing a detailed code comparison in several areas.

There were many possible experiments that could have been modeled for this work including the HMI data itself. The problem selected for comparing the codes was a macroscopic Cu on Cu impact. The reason for selecting a macroscopic experiment was that there are more detailed data for the experiment in-

cluding crater depth and volume that is not available for the HMI data. The Cu target was selected since we are focusing on the Cu and Al HMI data. Table 1 gives the details of the Cu-Cu impact experiment parameters.

The procedure was simply to do a base calculation using nominal yield stress and a second identical calculation with the yield stress increased by a factor of 5. For Cu the nominal yield stress used was 2.4 kbar and the increased yield stress was 12.0 kbar. The setup for the code models is also given in Table 1. All four codes were used to model the nominal problem. Three of the codes (EPIC, MESA and SPH) were also used to model the increased yield stress problem. Even though the codes are all quite different we made sure that they all ran the same problem as outlined in Table 1 and thus have a very good benchmark on how the codes compare.

The initial and final plots of the crater as calculated with SPH is shown in Fig. 3. Figure 4 shows the final crater shape for the EPIC and MESA calculations for the nominal yield case.

Table 1. Macro Hydrocode Calculations Input Specifications

Category	Quantity	Value
Initial Conditions	Projectile and Target Material	Copper
	Impact Velocity	6.0 km/sec
	Projectile Mass	0.5 g
	Target Dimensions	4.0 cm radius, 4.0 cm thick for low strength calculation
	Target Dimensions	3.0 cm radius, 3.0 cm thick for high strength calculation
EOS Parameters	Density	8.93 g/cm^3
	Sound Speed	3.94 km/sec
	"s" Parameter	1.49
	Gamma	1.96
Strength Parameters	Type	elastic perfectly plastic
	Yield Strength	2.4e-3 Mbar, 1.2e-2 Mbar
	Shear Modulus	4.6e-1 Mbar
Discretization	Geometry	axisymmetric
	Cell Size	dr = dz = 0.04 cm
Boundary Conditions	Symmetry Axis	reflective
	Target Surfaces	free surface

The results for the crater volume is given in Table 2. The nominal yield strength calculations compared well with the experimental data for crater shape and dimensions. Table 2 compares several scaling parameters between the calculations and experiment. The high yield strength calculation showed that a factor of 5 increase resulted in factors of 3.3 to 4.4 decrease in the selected scaling parameters. Reference 3 reported that an increase in crater diameter^3/projectile mass ratio by a factor of 3.7 corresponds to an enhancement in yield strength by a factor of 4.7 when contrasting macro and micro impact experimental data using Sorensen's scaling law[4]. Thus the code calculations bracket this factor of 3.7 and provide evidence for the strain rate hypothesis described in reference 3. Table 2 shows that the MESA and EPIC

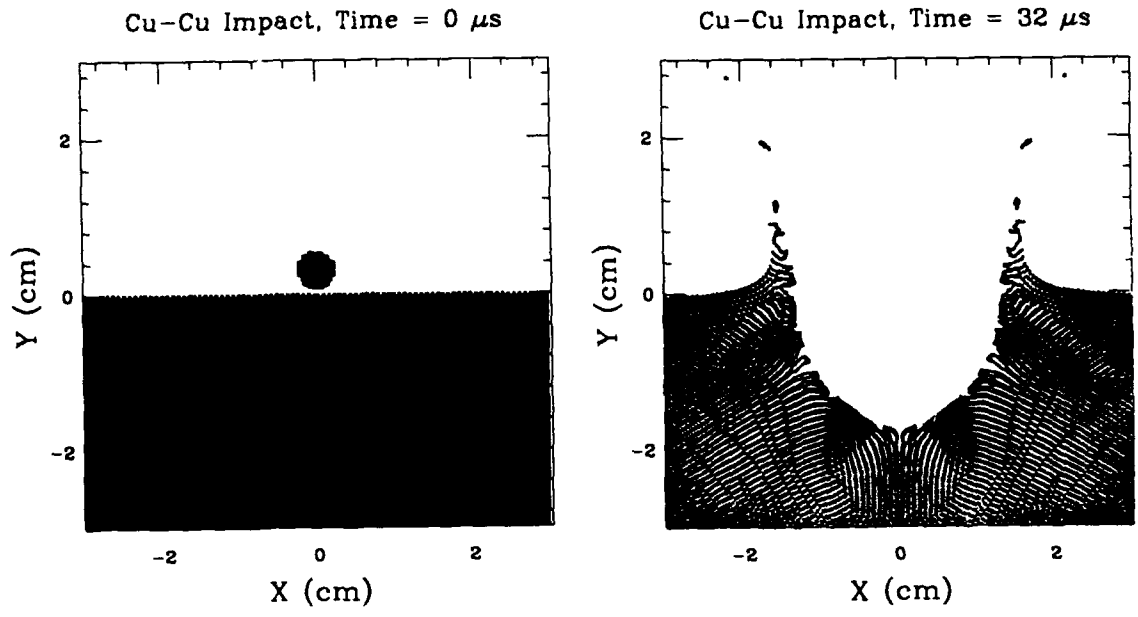


Fig. 3. Initial and final plots of the Cu-Cu macroscopic impact experiment as calculated by SPH.

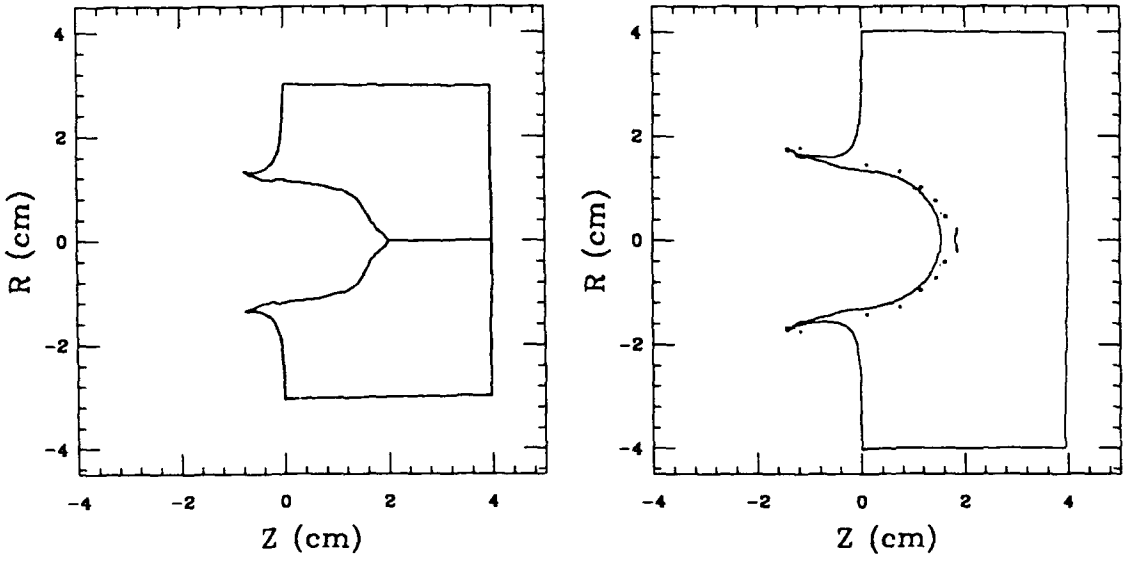


Fig. 4. The final crater shape for the EPIC and MESA calculations. Both plots are for the nominal yield strength case.

calculated crater volume decreased by factors of 4.4 and 4.1 when the yield strength was increased by a factor of 5. SPH predicted a factor of 3.3 decrease.

Table 2. Comparison of code results for crater volume. The two calculations done were with nominal yield stress (2.4 kbar) and with the stress increased by 5.

Quantity	Experiment	EPIC	MESA	SPH	CALE
Crater Volume (cm^3) at 32 μs	4.82	5.52	6.17	6.16	5.16
Crater Volume (cm^3) at 16 μs (Yield Stress times 5)		1.35	1.41	1.89	
Ratio		4.1	4.4	3.3	

The results for other crater quantities are given in Table 3. An average plastic strain rate and strain were calculated and are provided in Table 3. At each time step (cycle), the incremental plastic work for a cell (DPW_i) containing target material was used to weight the current strain and strain rate in that cell. At the end of the cycle, instantaneous average strain rate and strain values were calculated from the plastic work weighted strain and strain rate contributions from all the target cells divided by the total plastic work for the target material $\sum_i DPW_i$ during that cycle. For each time step n, the instantaneous average strain rate $\langle \dot{e}_n \rangle$ is,

$$\langle \dot{e}_n \rangle = \frac{\sum_i (DPW_i)\,\dot{e}_i}{\sum_i DPW_i} \tag{3}$$

where i denotes the target cell number. The average or characteristic strain rate $\langle \dot{e} \rangle$ for the calculation was determined by performing the following summation for all time steps:

$$\langle \dot{e} \rangle = \frac{\sum_n \sum_i (DPW_i)\,\dot{e}_i}{\sum_n \sum_i DPW_i} \tag{4}$$

where n denotes the time step. The instantaneous plastic strain $\langle e_n \rangle$ and the average or characteristic plastic strain $\langle e \rangle$ for the calculation were calculated in a similar manner:

$$\langle e_n \rangle = \frac{\sum_i (DPW_i)\,e_i}{\sum_i DPW_i} \text{ and } \langle e \rangle = \frac{\sum_n \sum_i (DPW_i)\,e_i}{\sum_n \sum_i DPW_i}. \tag{5}$$

The crater depth and volume predicted by all codes were larger than the experimental value (Tables 2 and 3). The MESA and SPH crater diameters were larger than observed while EPIC and CALE were a bit smaller. Qualitatively the crater shape predicted by all the codes was similar to the experimental crater with EPIC having a small notch at the bottom of the crater. The codes predicted and the experiment showed that the impact crater was deeper than what a hemispherical crater would have been.

When the yield strength was increased by a factor of 5, the crater was found to be smaller in diameter and depth and had a reduced volume. Also, the flow around the crater bottom had been fully arrested by about 16 μs. As was the case for the lower yield strength calculation, the crater was somewhat hemispherical.

Table 3. Comparison of code results for various crater quantities. (For nominal, 2.4 kbar, yield strength)

Quantity	Experiment	EPIC	MESA	SPH	CALE
Crater Depth(cm)	1.4	1.8	1.59	1.73	1.51
Crater Diameter(cm)	2.54	2.4	2.8	2.6	2.44
Depth / Diameter	0.55	0.75	0.57	0.67	0.62
Characteristic Strain		0.3	0.37		
Characteristic Strain Rate (sec^{-1})		$7.5x10^4$	$5.5x10^4$		

An important point to make here is that these calculations used the simple elastic perfectly plastic strength model (except for CALE which used the Steinberg-Guinan model). By going to a better strength model, like Johnson-Cook or Steinberg-Guinan, it is expected that better agreement with the data would result.

In Fig. 5 a comparison of the crater diameter and depth between the MESA, EPIC and SPH calculations for the nominal yield stress is made. The agreement between the three codes is quite good.

Comparisons of the run time quantities are shown in Table 4. These comparisons were made for the nominal strength problem run to 32 μs. The problem generation time is not included in the run times.

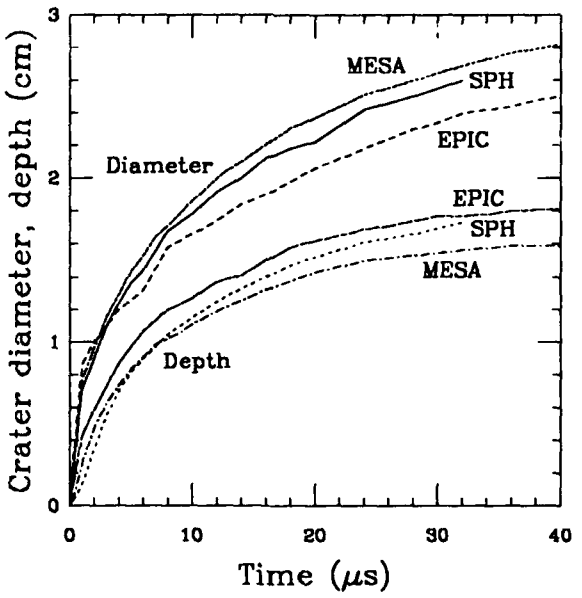


Fig. 5. Comparison of the crater diameter and depth between the MESA, EPIC and SPH calculations for the nominal yield stress is made. The agreement between the three codes is quite good.

Table 4. Comparison of run quantities for three codes (all run on a Cray YMP).

Quantity	EPIC	MESA	SPH
Number of cycles	1806	308	201
Problem size elements, cells or particles)	11350	14280	6595
Run time (min) (not including setup time)	6.49	7.53	4.4
Grind time (sec/cycle/node)	0.19×10^{-4}	1.03×10^{-4}	2.0×10^{-4}

CALCULATIONS OF THE HMI DATA

SPH and MESA calculations were made of the HMI Aluminum single crystal data points in the range of 6.5 to 24.5 km/sec. The data is shown in Fig. 1 as the open circles. Each SPH calculation used about 1500 points, was axisymmetric and took about 3-4 hours to run on a SUN SPARCstation 2. The only quantities varied between the calculations was the projectile mass and velocity both of which were obtained from the HMI data. Table 5 gives the input velocities, input masses, calculated crater diameters d, and the quantity $d^3/mass$.

Table 5. Input and results for the SPH and MESA HMI calculations

Velocity km/sec	Mass (fg)	Diameter d (μ)		d^3/m (cm^3/g)	
		SPH	MESA	SPH	MESA
6.5	2359	3.6	3.8	19.8	24
11.0	2950	5.6		59.5	
12.5	1017	4.4		83.8	
14.5	557	3.7	3.7	90.9	91
16.5	244.8	3.3	3.0	146.8	110
18.5	276	3.7	3.2	183.5	124
20.5	92.2	3.1		323.1	
22.5	99.9	3.2		328.0	
24.5	79.7	3.2		411.1	

These results are shown in Fig. 6 where the crater diameter^3/projectile mass is plotted versus the projectile velocity. Also shown on this plot is the Aluminum single crystal HMI data. The SPH results are about 2 to 8 times greater than the data and show a structure similar to that seen in the data. The SPH and MESA results agree well at low velocity but begin to disagree at intermediate velocities.

To explain the structure in the calculations, the SPH runs were redone using a constant projectile mass in order to eliminate any mass effects. The mass chosen was 244.8 fg from the 16.5 km/sec data point. This gave similar structure as before as seen in Fig. 6. It was noticed, however, that points forming the plateaus having the same crater diameters had different crater volumes because of different crater shapes. When the crater volumes are plotted, Fig. 7, much of the structure disappears. Thus it may be that the plateaus in the HMI data would smooth out if the crater volumes (which have not been extracted from the data yet) could be determined and plotted instead of the diameter cubed. A possible explanation for the changes in

crater shape is the melt and vaporization phase changes. This is supported by the fact that SPH includes phase change effects whereas MESA and EPIC (where the plateaus are not seen) do not include phase change effects.

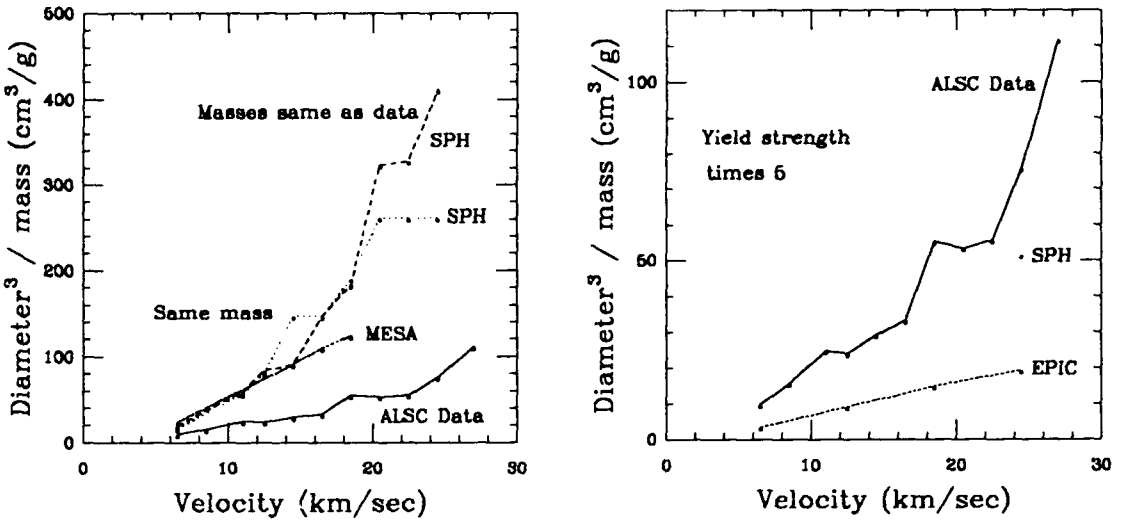


Fig. 6. SPH, EPIC and MESA calculations of the HMI Aluminum single crystal data plotting crater diameter^3/projectile mass versus the projectile velocity along with the HMI data. The SPH results are about 2 to 8 times greater than the data and show a structure similar to that seen in the data. The SPH and MESA results agree well at low velocity but begin to disagree at intermediate velocities. Also plotted are SPH calculations which use a constant projectile mass. This curve shows the same plateau structure as in the other SPH calculations. SPH and EPIC calculations using a factor of 5 increase in yield strength are shown and agree much better with the data.

The fact that the SPH calculations are higher than the data is explained by the strain rate theory, Walsh, *et. al.* (1991), described in the introduction. These microparticle calculations are in a very high strain rate regime (10^9 /s) and the yield strength, which was calibrated in a much lower strain rate region, is too low. Increasing the yield strength by a factor of 4.7 should bring the calculation in agreement. This has been done for some SPH and EPIC calculations where the yield strength was increased by a factor of 5. These high yield strength calculated points are plotted in Fig. 6 and are much closer to the data. SPH calculations using the standard Johnson-Cook and Steinberg-Guinan models have also been done for the 24.5 km/s case. The results show much larger crater diameters than the elastic plastic nominal yield strength case and thus further from the data.

CONCLUSIONS

A Cu-Cu macroscopic impact problem was calculated with EPIC, MESA, SPH and CALE to investigate the effect of a change in the yield strength. Strain-rate theory suggests that a change of 4.7 in the yield strength should yield a change in volume of about 3.7. The codes used a yield strength factor of 5.0 and yielded volume changes between 3.3 and 4.4, in agreement with the strain-rate theory.

Code comparisons have been made between EPIC, MESA, SPH and CALE for the Cu-Cu macroscopic problem. Good agreement was found between the codes.

SPH, EPIC and MESA calculations were made of the HMI Aluminum single crystal data points in the range of 6.5 to 24.5 km/sec. The SPH results are about 2 to 8 times greater than the data and show a structure similar to that seen in the data. This structure seems to be due to plotting diameter cubed instead of volume and may be the reason for the structure in the HMI data. This must wait for verification until the crater volumes are extracted from the data. The SPH and MESA results agree well at low velocity but begin to disagree at intermediate velocities. The strain rate theory was corroborated with the high yield SPH and EPIC calculated points falling much closer to the data.

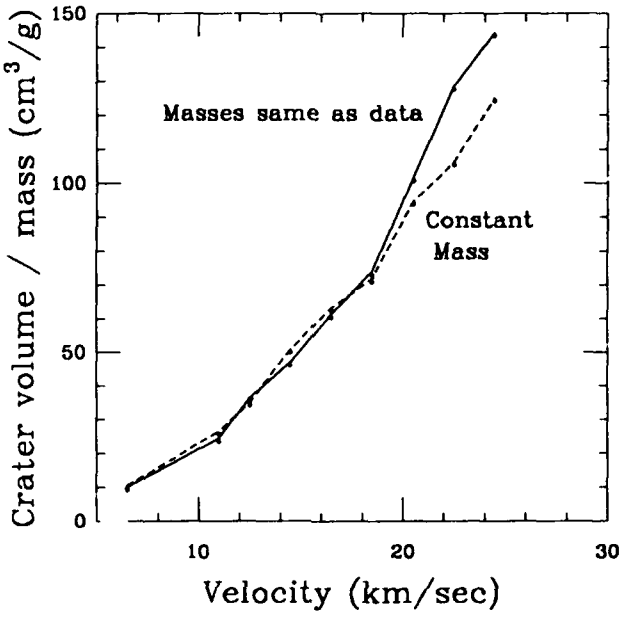


Fig. 7. Plot of crater volume instead of crater diameter cubed. Much of the structure has disappeared.

ACKNOWLEDGMENTS

The authors would like to acknowledge Gary Stradling for providing us with the data and for many discussions of this work. We would also like to acknowledge many fruitful discussions with Barry Shafer and Mac Walsh. We acknowledge Marv Alme of Alme and Associates for doing the CALE calculations reported in this work. This research is supported by the Department of Energy.

REFERENCES

Benz, W. (1989). Smooth Particle Hydrodynamics: A Review. Harvard-Smithsonian Center for Astrophysics Preprint No. 2884

Bolstad, J. and D. Mandell (1992). Calculation of a Shaped Charge Jet Using MESA-2D and MESA-3D Hydrodynamic Computer Codes. Los Alamos National Laboratory report LA-12274

Holian, K. S. ed. (1984). T-4 Handbook of Material Properties Data Bases. Los Alamos National Laboratory report LA-10160-MS

Holian, K. S., S. J. Mosso, D. A. Mandell, and R. Henninger (1991). MESA: A 3-D computer Code for Armor/Anti-armor Applications. Los Alamos National Laboratory report LA-UR-91-569

Johnson, G. R. (1978). EPIC-2, A computer Program for Elastic-Plastic Impact Computations in 2 dimension plus Spin. Honeywell Inc., Hopkins, Minnesota, Contract Report ARBRL-CR-00373

Johnson, G. R. (1977). EPIC-3, A Computer Program for Elastic-Plastic Impact Calculations in 3 Dimensions. Honeywell Inc., Hopkins, Minnesota, Contract Report ARBRL-CR-343

Johnson, G. R. and W. H. Cook (1983). A constitutive Model and Data for Metals Subjected to Large Strains, High Strain Rates, and High Temperatures. Proceedings of Seventh International Symposium on Ballistics, The Hague, The Netherlands

Johnson, G. R. and W. H. Cook (1985). Fracture Characteristics of Three Metals Subjected to Various Strains, Strain Rates, Temperatures, and Pressures. Engineering Fracture Mechanics, 21

Johnson, G. R. and T. J. Holmquist (1990). A Computational Constitutive Model for Brittle Materials Subjected to Large Strains, High Strain Rates and High Pressures. to be published in Proceedings of EXPLOMET Symposium

Keaton, P. W. *et. al.* (1990). A hypervelocity-microparticle-impacts laboratory with 100 km/s projectiles. Int. J. Impact Engng. **10**, pp. 295-308

Libersky L. D., and A. G. Petschek, (1990). Smooth Particle Hydrodynamics with Strength of Materials, *Advances in the Free-Lagrange Method*, (Trease, Fritts, and Crowley, eds.), Springer Verlag, 248

Monaghan, J. J. (1988). An Introduction to SPH. Comput. Phys. Comm. **48**, 89-96

Monaghan, J. J. (1982). Why Particle Methods Work. SIAM J. Sci. Stat. Comput. **3**, 422-433

Monaghan, J. J. (1985). Particle Methods for Hydrodynamics. Comp. Phy. Rep. **3**, 71-124

Sorensen, N. R. (1965). Systematic investigation of crater formation in metals. in Proceedings of Seventh Hypervelocity Impact Symposium, Martin Company, Orlando

Steinberg, D. J. (1991). Equation of State and Strength Properties of Selected Materials. Lawrence Livermore National Laboratory report UCRL-MA-106439

Steinberg, D. J. (1980). A constitutive Model for Metals at High-Strain Rates. J. Appl. Phys. 51(3)

Stellingwerf, R. F. (1989). The SPH_C Manual, User's Guide, Programmer's Guide, Technical Guide, Function Reference, Test Cases. Mission Research Corporation report AMRC-N-384.1-384.5

Stellingwerf, R. F. (1990). Smooth Particle Hydrodynamics, *Advances in the Free-Lagrange Method*, (Trease, Fritts, and Crowley, eds.), Springer Verlag, 239.

Stellingwerf, R. F. and C. A. Wingate (1992). Impact Modeling with Smooth Particle Hydrodynamics. Hypervelocity Impact Symposium 1992 conference proceedings.

Stradling, G. L. *et. al.* (1990). Searching for momentum enhancement in hypervelocity impacts. Int. J. Impact Engng. **10**, pp. 555-570

Tipton, R. (1991). CALE Users Manual, version 910701. Lawrence Livermore National Laboratory

Van Leer, B. (1979). Towards the Ultimate Conservative Difference Scheme. V. A Second-Order Sequel to Gudunov's Method. J. of Comp. Phy., 32, pp. 101-136

Walsh, J. M., G. L. Stradling, G. C. Idzorek, B. P. Shafer, and H. L. Curling, Jr. (1991). On Size Scaling in Shock Hydrodynamics and the Stress-Strain Behavior of Copper at Exceedingly High Strain Rates. Los Alamos National Laboratory informal report

Wingate, C. A. and H. N. Fisher (1992). Strength Modeling in SPHC. in preparation

Youngs, D. L. (1982). Time Dependent Multi-Material Flow with Large Fluid Distortion. Morton, K. W. and Baines, J. H., ed., Numerical Methods for Fluid Dynamics, Associated Press

Youngs, D. L. (date unknown). An Interface Tracking Method for a 3D Eulerian Hydrodynamics Code. Atomic Weapons Research Establishment report AWRE/44/92/35

Zerilli, F. J. and R. W. Armstrong (1987). Dislocation-Mechanics-Based Constitutive Relations for Material Dynamics Calculation. Journal of Applied Physics, 61 (1987).

Int. J. Impact Engng Vol.14, pp.831–842, 1993
Printed in Great Britain

0734-743X/93 $6.00+0.00
© 1993 Pergamon Press Ltd

AN ENGINEERING MODEL TO PREDICT PERFORATION DAMAGE TO PLATES IMPACTED BY HIGH VELOCITY DEBRIS CLOUDS

Jerome D. Yatteau* and David L. Dickinson**

*Applied Research Associates, Inc.
7114 West Jefferson Ave., Lakewood, Colorado 80235

**Naval Surface Warfare Center
Dahlgren, Virginia 22448

ABSTRACT

This paper describes experiments and the development of a model to predict damage to metallic plates impacted by high velocity, multi-particle debris clouds. The experiments involved single steel spheres fired at a steel shatter plate at speeds near 1.5 and 2.0 km/sec to generate the debris clouds. In each series of tests, the impact velocity was controlled, and a witness plate was placed at increasing distances behind the shatter plate to observe the effects of debris particle dispersion on plate damage. This paper focuses on the variations, with plate spacing, in the size of the central region removed from the witness plates. The central hole size model compares the post impact kinetic energy distribution in a witness plate impacted by a debris cloud to the free impact residual kinetic energy in an equivalent plate impacted by an L/D=1 steel cylinder, at the ballistic limit velocity. This approach permits extension of the model to other plate materials through utilization of existing ballistic limit velocity data.

INTRODUCTION

Modern air-to-air combat involves warhead fragment impact velocities well above the threshold velocity for shattering both the fragment and the plate material in its path. As a result, incident warhead fragments are transformed into expanding clouds of high velocity fragment and plate particles after perforating the outer skin of an air target. Weapons effectiveness estimates require fast running, engineering type models to predict damage to interior target structures and vital components impacted by these high velocity debris clouds. Of particular importance are predictions of the material removed from target elements.

The photographs in Fig. 1 illustrate the debris cloud behind the first plate and the damage to the second plate for a typical high velocity fragment penetration event. Witness plate damage usually includes a circular or elliptical pattern of individual craters and/or holes with an areal density that decreases with increasing radius from the center of the pattern. There is generally an enlarged central hole where the plate material is completely removed as shown in Fig. 1. Hypervelocity impact debris clouds can also cause material to be spalled from the rear surface of the plate. Finally, the plate will be plastically deformed (dished) to an extent dependent on the magnitude and distribution of the impulse transmitted to the plate by the impacting particles and by the stiffness of the plate.

This paper describes the development of a model to predict the kind of high velocity debris cloud perforation damage shown in Fig. 1. Specifically, experiments and a model are described to determine the size of the enlarged central hole as a function of the debris cloud characteristics, and witness plate material, thickness, and spacing from the shatter plate.

EXPERIMENTS

Because of debris particle radial dispersion, the impulsive loading distribution on a witness plate, for a fixed set of debris cloud characteristics, will vary with the spacing from the shatter plate. For plate spacings approaching zero, the particle impacts will overlap and the debris cloud will penetrate or crater the witness plate like a single intact fragment. For large spacings, the particle impacts will be far apart, the particles will perforate individually, and a blast like dishing response will be observed in the perforated and/or cratered witness plate. The size of the witness plate central hole will therefore first increase and then decrease with increased spacing behind the shatter plate.

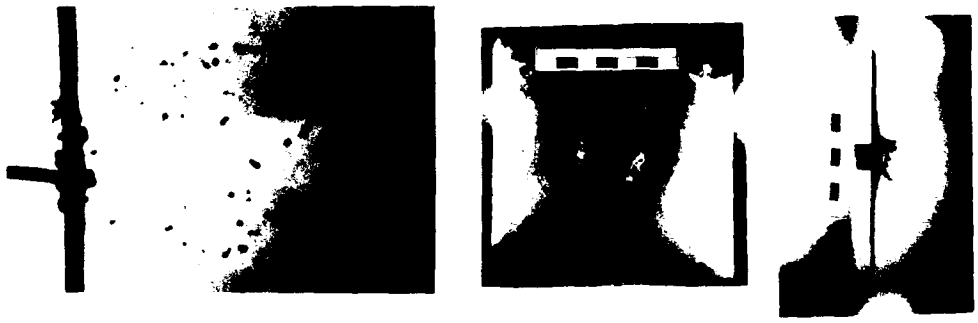


Fig 1 High Velocity Debris Cloud Radiograph and Witness Plate Damage (Steel Sphere vs. Steel Plates, V = 2 km/sec)

The test arrangement is shown schematically in Fig. 2. A 6.9 gram hardened steel ball bearing was fired at a mild steel shatter plate to generate the debris clouds. A witness plate was positioned normal to the shotline at a distance, S, behind the shatter plate. A single series of 6-12 tests entailed holding the impact velocity, witness plate material and thickness constant, and varying the plate spacing, S. Measurements of the resulting central hole diameter, D_h, were thereby obtained as a function of plate spacing S. For the larger plate spacings, a hardened steel stripper plate was placed behind the shatter plate to prevent the outer portion of the debris cloud from striking X-ray heads near the witness plate. The stripper plate was positioned so that the impact pattern diameter on the witness plate was always much larger than the central hole diameter and outside region of plastic plate response. The test conditions and central hole diameter measurements are summarized in Table 1. Figure 3 contains plate photographs confirming the expected effects of increased plate spacing on debris dispersion and the resulting decrease in the size of the central hole. The stripper plate was in use for these tests and therefore the pattern diameters are nearly the same for the two spacings. Note that the particles perforated the relatively thin plate individually. The radiographs in Fig. 4 reveal typical dynamic response of a plate impacted (from top to bottom) by a high velocity debris cloud. The radiograph on the left was taken during the penetration by a debris cloud like the one shown in Fig. 1. The radiograph on the right was taken after the test and shows that the larger plate petals ultimately were separated from the plate by a bending failure.

Additional experiments with multiple flash radiographs and debris particle collection in micro-crystalline wax were conducted to determine the numbers and sizes of debris particles, the dispersion angles for the sphere and plate particles, and the shape of the debris clouds. The cylindrical container of wax was positioned directly behind the shatter plate. The debris particles were separated from the wax by first melting and pouring off the wax and then washing the particles in a solvent. The wax collection technique netted 80-90% recovery of the total possible weight (sphere + weight of material removed from the plate) including practically uncountable dustlike particles. The missing mass is presumed to have been lost on the front side of the shatter plate. Figure 5 contains a sample of the debris cloud radiographs and the wax debris recovery results for the two test velocities. The radiographs in Fig. 5 provide additional examples of ellipsoidal debris clouds and confirm the relative dispersions for the sphere and plate particles.

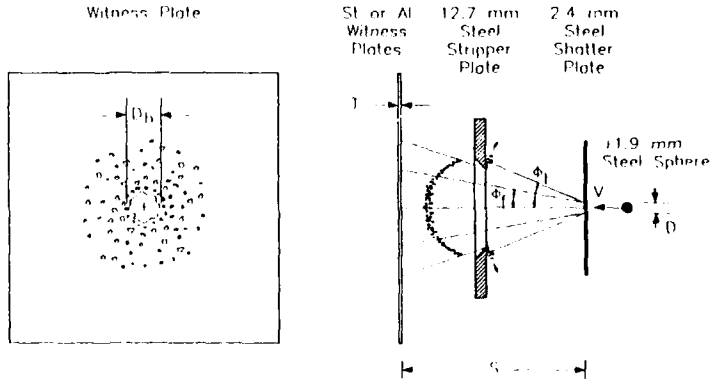


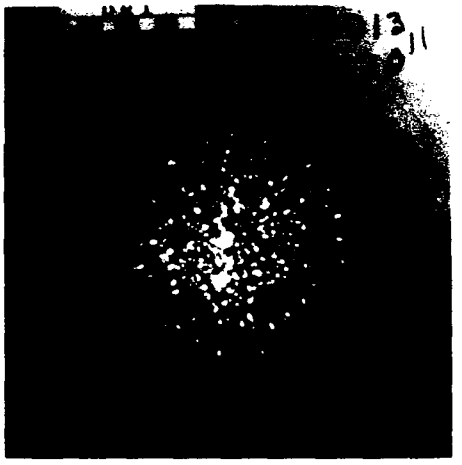
Fig. 2 Test Arrangement

Table 1 Witness Plate Central Hole Diameters for 11.9 mm Steel Spheres Impacting 2.4 mm Mild Steel Shatter Plates Located a Distance, S, in Front of the Witness Plates

Witness Plate Thickness (mm)	Material	Spacing S (mm)	Impact Velocity (m/s)	Central Hole Diam. D_h (mm)
0.81	Mild Steel	25.4	1650	24.13
0.81	Mild Steel	76.2	1593	30.48
0.81	Mild Steel	127.0	1584	27.94
0.81	Mild Steel	127.0	1604	31.75
0.81	Mild Steel	254.0	1519	33.53
0.81	Mild Steel	355.6	1429	30.48
0.81	Mild Steel	25.4	2056	35.56
0.81	Mild Steel	76.2	2102	43.18
0.81	Mild Steel	101.6	2296	65.53
0.81	Mild Steel	152.4	2068	64.52
0.81	Mild Steel	203.2	2138	76.20
0.81	Mild Steel	254.0	1972	70.87
0.81	Mild Steel	381.0	2268	54.61
0.81	Mild Steel	381.0	2269	19.56
0.81	Mild Steel	406.4	2092	38.10
0.81	Mild Steel	508.0	2088	11.43
2.39	Mild Steel	152.4	2262	51.82
2.39	Mild Steel	203.2	2243	60.20
2.39	Mild Steel	254.0	2044	67.56
2.39	Mild Steel	254.0	2300	56.64
2.39	Mild Steel	304.8	2272	23.88
2.39	Mild Steel	381.0	2035	13.21
1.60	2024-T3 Al	203.2	1785	50.55
1.60	2024-T3 Al	304.8	1447	35.05
1.60	2024-T3 Al	304.8	1654	3.81
1.60	2024-T3 Al	304.8	1818	39.37
1.60	2024-T3 Al	330.2	1799	39.37
1.60	2024-T3 Al	368.3	1502	24.13
1.60	2024-T3 Al	381.0	1559	29.46
1.60	2024-T3 Al	381.0	1831	13.97
1.60	2024-T3 Al	254.0	2289	44.45
1.60	2024-T3 Al	355.6	2249	33.27
1.60	2024-T3 Al	368.3	2095	33.53
1.60	2024-T3 Al	381.0	2225	7.87
1.60	2024-T3 Al	381.0	2395	62.99
1.60	2024-T3 Al	406.4	2219	13.97
1.60	2024-T3 Al	508.0	2237	9.91
4.82	2024-T3 Al	25.4	2268	27.94
4.82	2024-T3 Al	76.2	2361	35.56
4.82	2024-T3 Al	152.4	2305	51.05
4.82	2024-T3 Al	203.2	2268	56.64
4.82	2024-T3 Al	304.8	2272	58.93
4.82	2024-T3 Al	355.6	2389	10.92
4.82	2024-T3 Al	381.0	2331	11.68
4.82	2024-T3 Al	406.4	2267	15.24



V = 2.3 km/sec, S = 381 mm



V = 2.1 km/sec, S = 508 mm

Fig 3 Effect of Plate Spacing on 0.81 mm St Witness Plate Damage

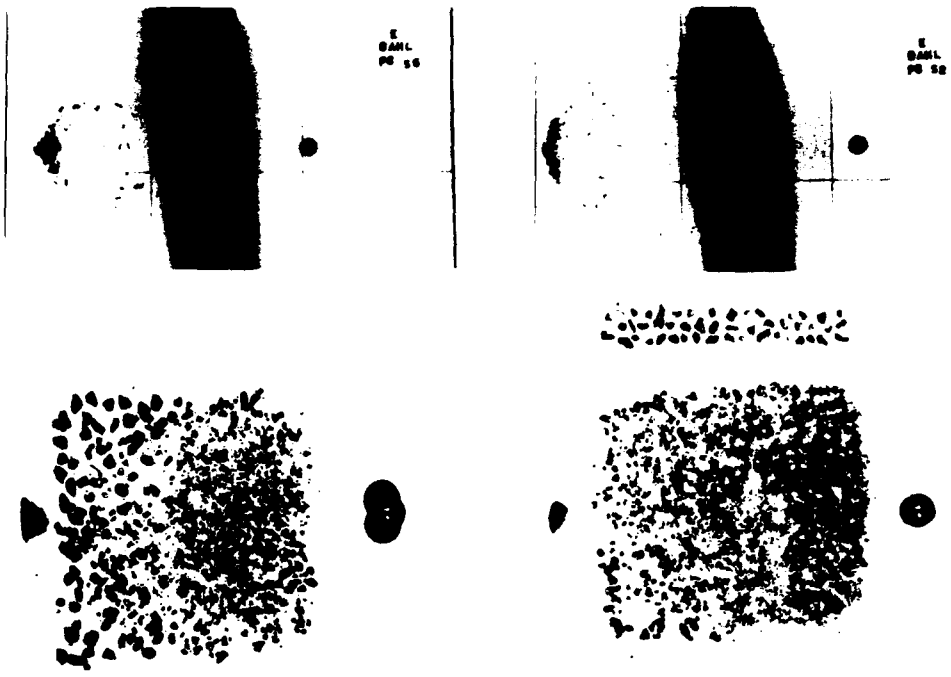


During Impact



After Test

Fig 4 Radiographs of 3.2 mm Al Plate Impacted by Debris Cloud (V = 2.8 km/sec)



V = 1.6 km/sec V = 2.4 km/sec

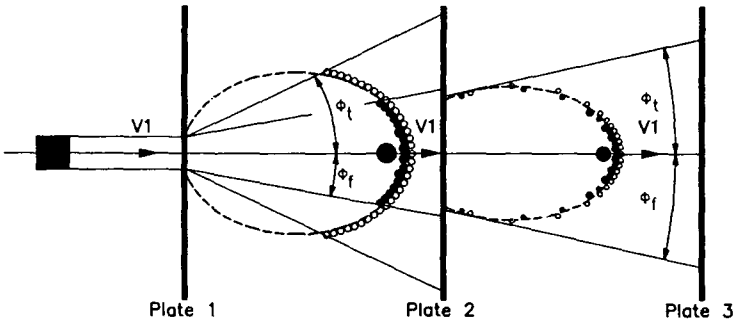
Fig 5. Debris Cloud Characteristics at Two Impact Velocities

MODEL DEVELOPMENT

The models presented below for the central hole size in witness plates were developed for inclusion in the FATEPEN computer code. The FATEPEN computer code has been developed for the Naval Surface Warfare Center, Dahlgren Laboratory as a fast running, engineering type analytical/empirical penetration model for use in air target vulnerability assessments. FATEPEN was originally developed for application to high velocity (up to 5 km/s) fragment penetration of thin aluminum plates by compact steel fragments (Yatteau, 1982). Several additional experimental and analytical efforts have been conducted since its original release to extend the range of model applications to impact speeds below the fracture threshold, to additional fragment and target materials, and to a variety of fragment shapes (Yatteau *et al.*, 1991a, b). The original version of the model calculated the size of the central hole based on the accumulated area removal by individual perforating debris particles. The current version of FATEPEN includes a new central hole model based on impulsive loading and response of the plate. Both models are presented below following an overview of the FATEPEN debris cloud specifications which are the essential input for the plate damage models. Predictions from the two models are then compared with the test results.

Debris Cloud Description

Debris Particle Numbers and Sizes. The numbers of fragment and target particles can be very large, and the sizes of debris particles can range continuously over several orders of magnitude relative to the mean particle size (Yatteau *et al.*, 1991a). To avoid making individual computations for each and every debris particle, it is necessary to select a subset of particle sizes when describing the debris cloud. The current FATEPEN debris cloud model is shown in Fig. 6. Three penetrator particle sizes are used along with a single average size for the target particles. The size of the primary, or largest, fragment particle, M_{f1}, and the total number of secondary particles are determined by empirical functions of the encounter conditions at the shatter plate. The representative numbers and sizes of larger and smaller secondary fragment particles, N_{f2}, M_{f2}, N_{f3}, and M_{f3}, respectively, are then computed from the total number of particles using experimentally determined size distribution functions for steel cubes. The larger particles represent the mean size and total mass of all particles above the mean particle size of the entire population, and the smaller particles represent the mean size and total mass of all particles below the population mean. The number, N_t, and average size, M_t, of the target particles are determined from the total mass of plate



	NUMBER	WEIGHT	DIAM
Primary Penetrator Particle		M_{f1}	D_{f1}
Larger Secondary Penetrator Particles	N_{f2}	M_{f2}	D_{f2}
Smaller Secondary Penetrator Particles	N_{f3}	M_{f3}	D_{f3}
Plate Particles	N_t	M_t	D_t

Fig 6. FATEPEN Debris Cloud Model

material driven out the rear of the plate and an empirically determined function of the encounter conditions for the number of plate particles. The current wax collection debris data for the steel spheres were used to determine appropriate modifications to the total particle number and size distribution functions for steel cubes. The predicted numbers and sizes of debris particles used to obtain model predictions of plate damage are listed in each of the comparison graphs presented below.

Debris Particle Velocity Distribution Based on observations of debris cloud radiographs for steel fragments impacting steel plates at speeds up to 3000 m/s, the debris particles are presumed to reside on the surface of an expanding, hollow, ellipsoid of revolution with a major-to-minor axis ratio of 1.5 (Rolens *et al.*, 1976). For normal shatter plates, the axis of the debris ellipsoid will be aligned with the shotline. Assuming that all debris particles emanate from a point on the axis at the upstream end of the ellipsoid, the distribution of particle velocities can be closely approximated by the following simple function

$$V_x(\varphi) = V_l \cos(q\varphi) \tag{1}$$

where $V_x(\varphi)$ is the component of the particle velocity parallel to the shotline, φ is the trajectory inclination angle relative to the shotline, V_l is the debris cloud leading edge velocity, and q is a constant depending on the shape of the ellipsoid. The leading edge velocity is determined using single particle penetration equations contained in FATEPEN. A value of q given by

$$q = 1.92 \tag{2}$$

has been found to provide agreement with the exact velocity distribution for the 1.5 ratio ellipsoid to within 1% for trajectory inclination angles up to 25°. The function defined by Eqs. 1 and 2 was selected in part because its suitability to describing velocity distributions behind subsequent plates.

Debris Particle Trajectory Distribution Experiments involving steel cubes perforating steel plates with collection of debris particles in Celotex have shown that the number of debris particle trajectory intersections on planes normal to the debris cloud axis within a radius r of the debris cloud axis increases nearly linearly with increasing r out to the edge of the pattern (Recht *et al.*, 1969). In other words,

$$N(r) = (r/r_m)\, N_m \tag{3}$$

where N(r) is the number of particle trajectories impacting a plate normal to the debris cloud axis within a radius, r, about the center of the impact pattern, r_m is the maximum pattern radius, and N_m is the total number of debris particles striking the plate. The maximum pattern radii for penetrator and plate particles are determined by their respective maximum trajectory inclination angles, φ_f and φ_t and the plate spacing as illustrated in Fig. 6. The sphere debris cloud radiographs such as shown in Fig. 5 were used to determine the following maximum trajectory inclination angles for the sphere generated debris clouds

$$\varphi_f = 10° \quad \text{and} \quad \varphi_t = 20° \tag{4}$$

The trajectory distribution given by Eq. 3 is presumed to apply to the current debris clouds. It follows that the number of debris particles, dN, intercepted by ring elements of width, dr, about the center of the pattern is a constant given by

$$dN = (N_m/r_m)\, dr \tag{5}$$

It also follows from Eq. 3 that the areal density of trajectory interceptions varies inversely with the radius. The impact patterns illustrated in Figs. 3 and 10 were created using the trajectory distribution function given by Eqs. 3 and 5 and can be seen to provide a reasonably good representation of the crater and hole patterns in the plates of Figs. 1, 3 and 5.

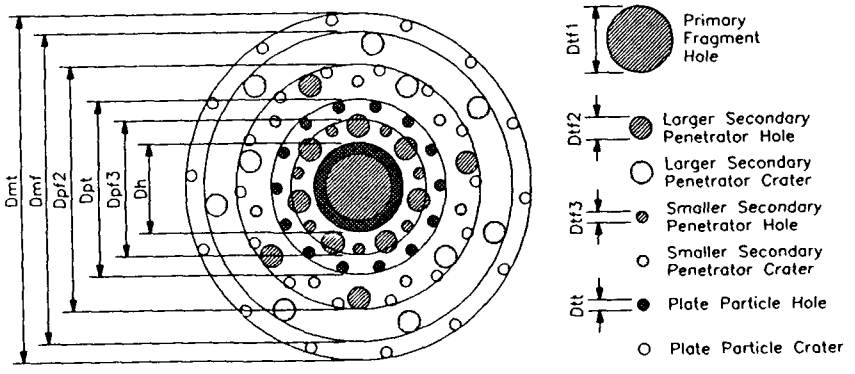
Plate Damage Models

Area Removal Model. Plate damage characteristics predicted by the FATEPEN code are illustrated in Fig. 7. The pattern diameters, D_{mf} and D_{mt} for the two sets of debris particles are determined by the dispersion angles and the plate spacing. The sizes of individual holes are predicted as a function of debris particle density, size, and impact velocity and plate material and thickness. Hole size is predicted to increase above the diameter of the fragment with increasing impact speed and with increasing plate thickness. This model incorporates empirical relationships for hypervelocity impact crater sizes in semi-infinite plates (Yatteau, 1982). Prior to inclusion of the impulse model, the determination of the diameter, D_h, of the enlarged central hole was based strictly on area removal geometry. That is, if the sum of the areas of the holes produced in a ring increment about the center of the pattern exceeds the area of the ring, then that ring is deemed to be removed. The FATEPEN trajectory distribution function (Eq. 3) and the area removal model are illustrated in Fig. 8. Each of the ring increments in Fig. 8 (including the central circle) contain the same number of impacts. It can be shown that for ring elements impacted by all three secondary particle sizes, the central hole diameter based on area removal is given by

$$D_h = 0.5\, [(N_{f2}\, D_{tf2}^2 + N_{f3}\, D_{tf3}^2)/D_{mf} + N_t\, D_{tt}^2/D_{mt}] \tag{6}$$

where D_{tf2}, D_{tf3}, and D_{tt} are the individual particle hole sizes calculated using the average impact velocity for the perforating particles of each kind.

The area removal model does not take into account material removal between holes due to the effects of the impulse transmitted to the plates by individual perforating and nonperforating particles. Observed impulsive loading effects include the blow-out of material between holes, the shearing out of large plate plugs in moderately thick plates by nonperforating particles, and membrane type tensile failures in thin perforated and nonperforated plates. The area removal is therefore conservative with respect to fragment lethality and generally underpredicts the diameter of the central hole.



Dh:	Enlarged central hole diameter due to combined effects of penetrator and plate particles
Dpf2, Dpf3:	Diameter enclosing perforations due to penetrator particles of weight Mf2 and Mf3, respectively
Dpt:	Diameter enclosing perforations due to plate particles
Dmf:	Diameter enclosing impacting penetrator particles
Dmt:	Diameter enclosing impacting plate particles

Fig. 7 FATEPEN Plate Damage Characteristics

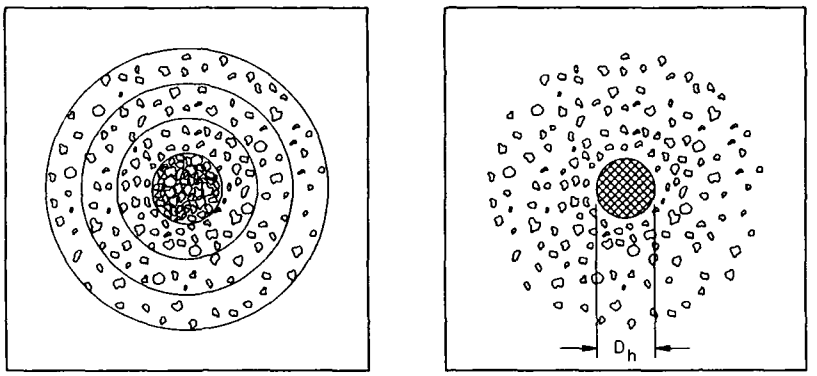


Fig. 8. Illustration of FATEPEN Debris Cloud Trajectory Distribution and Area Removal Model for Central Hole Size

Impulsive Loading and Response Model. The new impulsive loading and response model is an attempt to improve upon the impulse-punch model developed by Recht (Rolens, *et al.*, 1976). The Recht model examines the velocity and areal density of particles impacting the plate within some radial ring increment located a distance, r, from the center of the pattern. An equivalent cylinder of radius, r, is defined as having the same areal density as the particles impacting the ring increment in question. If the velocity of the debris particles at r exceeds the ballistic limit velocity for the equivalent cylinder and plate in question, then that ring increment is deemed to be removed from the plate. The Recht model was applied to current test conditions and found to greatly over-predict the capacity for the debris particles to enlarge the central hole. The probable reason for this is that, by comparing the debris particle velocity to the ballistic limit velocity of the equivalent cylinder, the model implicitly assumes that all of the debris particles incident momentum is available to remove material from the plate. Since perforating particles transmit only a fraction of their impulse to the plate, the Recht model can be expected to overpredict central hole size in plates which are perforated by individual debris particles.

The new model retains the Recht concept of using available ballistic limit velocity data to supply the required failure criterion for an impulsively loaded plate. Prediction of the required response and failure characteristics from first principles would otherwise be extremely difficult and complex. The new model focuses on the post-impact kinetic energy imparted to the remaining plate material by both perforating and nonperforating debris particles and compares it with the post-impact kinetic energy of the penetrator and plate plug for the equivalent cylinder impact at the ballistic limit velocity. In this way, only the impulse actually delivered to the plate by perforating particles is accounted for. The equivalent cylinder impact definition in the new model involves only steel cylinders with a slenderness ratio, L/D, of unity. This modification was introduced to enable direct use of steel Fragment Simulating Projectile (FSP) data for a variety of plate materials and to avoid the need to extrapolate this data to wafer-like cylinders which otherwise results when the debris particle areal density is used to define the equivalent cylinder. Finally, the new model attempts to account for the effects of the holes in a perforated plate on its subsequent response and failure.

The impulsive loading and response model is illustrated in Fig. 9. The model is based on the idealization that the impacting debris particles load the plate impulsively. That is, perforating and nonperforating particles instantaneously impart a velocity distribution in the plate across the impact pattern before significant plate deformation occurs. A typical initial post-impact velocity distribution across a plate is shown in the upper right of Fig. 9. The material near the center of the impact pattern will generally achieve a higher velocity than material near the edge of the pattern. The break in the velocity distribution in Fig. 9 coincides with the edge of the tighter beam of penetrator particles defined by φ_f.

If the initial radial velocity gradient normal to the plate near the center of the plate is too large to be accommodated by shear strain behind the radially propagating plastic shear wave, a shear failure will occur early, and material at the center of the impact pattern will be punched from the plate. This type of failure can be observed in closely spaced plates before significant dispersion of the debris cloud occurs and in thicker plates which experience larger impulsive loading by nonperforating particles. If the initial post-impact velocity gradient is not too large, the plate will initially deform in shear, but failure can still occur later under combined shear, membrane, and bending stresses. This type of failure usually is seen in thinner plates impacted by well-dispersed debris particles. Petalling of the plate commonly accompanies later time response failures.

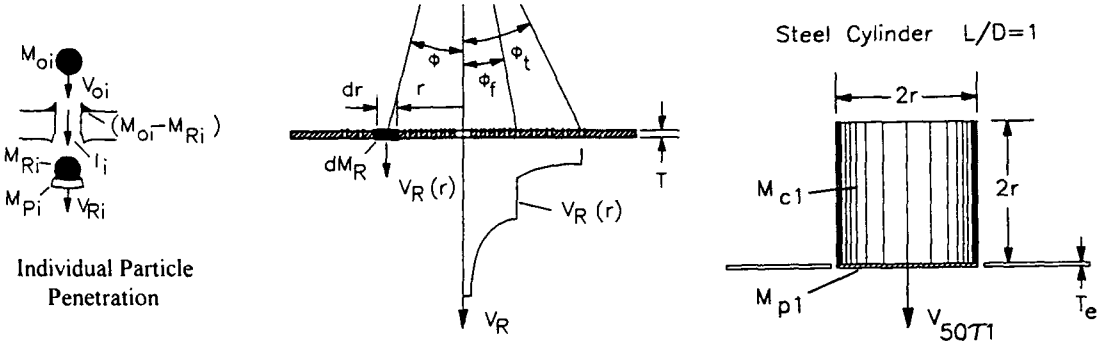


Fig 9. FATEPEN Impulsive Loading Model for Central Hole Size

No attempt is made to analytically model these plate response and failure mechanisms. Instead, we compare the post-impact kinetic energy distribution in the perforated and cratered plate impacted by the debris cloud to the post-impact kinetic energy for equivalent plate impacted by a steel cylinder as described above and as illustrated by the lower sketch in Fig. 9. In FATEPEN, the comparison between the actual and equivalent impact is accomplished incrementally by examining the impact and response of differential ring elements of increasing radius. The plate for the equivalent cylinder impact is defined as having the areal density of the current ring element less any material removed by perforating particles. Thus we assume that the perforated plate is set in motion by the debris cloud and a uniform plate of the same material and areal density impacted by a steel cylinder will deform similarly and have similar capacities to convert kinetic energy to plastic work. The free impact residual kinetic energy for the equivalent plate impacted by the steel cylinder at the appropriate ballistic limit velocity then determines maximum kinetic energy that can be converted to plastic work without failure. The essential calculations are as follows (see Fig. 9).

The radius, area and initial mass of the current ring element of width dr are

$$r = r + dr \tag{7}$$

$$dA = \pi[r^2-(r-dr)^2] \tag{8}$$

$$dM_t = \rho_t \, dA \, T \tag{9}$$

where ρ_t is the density of the plate material, and T is the thickness of the plate.

The trajectory inclination angle and particle impact velocity for the current ring are (Eqs. 1 and 2)

$$\varphi = \mathrm{Tan}^{-1}\,[(r-D_s/2)/S] \tag{10}$$

$$V_{oi} = V_1 \,\mathrm{Cos}\,(q\varphi) \tag{11}$$

where D_s is the fragment hole diameter in the shatter plate, and S is the spacing between this plate and the shatter plate.

The number of ith type particles (i = f1,f2 or t, see Fig. 8) impacting the current ring element is (Eq. 5)

$$dN_i = N_i \,(dr/r_m) \tag{12}$$

Each of the debris particles are presumed to penetrate individually without any influence from neighboring particles (Fig. 11). Single particle residual mass and velocity models in FATEPEN are applied to each type of particle to compute particle residual mass, M_{Ri}, and velocity, V_{Ri}, at the current ring element as functions of the impact velocity, particle material and mass, M_{oi}, and plate material and thickness, T. The debris particles are presumed to be spheres for these calculations. Each particle is assumed to remove a plug of plate material, and the plug diameter is assumed to be equal to the particle diameter. An individual particle plug mass is

$$M_{pi} = \pi D_i^2 \, \rho_t \, T/4 \tag{13}$$

where D_i is the ith type particle diameter.

The impulse delivered by all of the ith particles to the ring is

$$dI_i = [M_{oi} \, V_{oi} - (M_{Ri} + M_{pi}) \, V_{Ri}]dN_i \tag{14}$$

which presumes the mass lost by the debris particle is deposited in the plate and V_{Ri} is the residual velocity of residual particle and plate plug combined mass center. Also, the small retarding impulse from plate material outside the ring element during the impact has been neglected.

The mass deposited in the ring element by all the ith particles

$$dMD_i = (M_{oi} - M_{Ri})\, dN_i \tag{15}$$

and the total mass removed by the perforating ith particles is

$$dML_i = M_{pi}\, dN_i \tag{16}$$

The residual mass of plate material within the current radius r is

$$dM_{tR} = dMR_t + dM_t - \sum_i dML_i \tag{17}$$

where dMR_t is the plate mass of any interior ring elements not yet removed (calculated below). It is noted that if dM_{tR} is less than zero, the ring is deemed removed by overlapping perforations as in the area removal model described above. The total residual mass of plate material and penetrator material in the current ring is

$$dM_R = dMR + dMt + \sum_i (dMD_i - dML_i) \tag{18}$$

where dMR is the retained total residual mass not yet removed at lesser radii.

The total impulse delivered to the current and any retained interior rings from all particles is

$$dI = dIR + \sum_i dIi \tag{19}$$

where dIR is the impulse delivered to retained interior rings. The average residual velocity of the perforated plate and deposited debris particle mass remaining within r is

$$V_R = dI/dM_R \tag{20}$$

The potential for the actual nonuniform debris cloud to remove the current ring element is presumed to be the same as that for a debris cloud with a uniform trajectory areal density within r equal to the actual debris particle trajectory areal density at r. This assumption provides an approximation for the contribution of debris particles striking the plate interior to r to removal of plate material at r. Any contribution to the removal of the current ring by particles impacting outside r is neglected in this analysis. Thus, the post-impact kinetic energy in the plate impacted by the uniform debris cloud that is to be compared with the equivalent cylinder impact is

$$KE_R = [0.5\, dMR\, V_R^2]\, r^2/A_r \tag{21}$$

where A_r is the total area of remaining ring elements within the radius r

$$A_r = AR_n + dA \tag{22}$$

where AR_r is the retained area of unremoved ring elements at lesser radii

Only the remaining plate material undergoes plastic work during the plate response (i.e., the deposited debris mass will be carried without further deformation). The uniform plate thickness representing the same energy absorbing capacity per unit area as the perforated ring element is therefore

$$T_c = dM_{tR}/(A_r \rho_t) \tag{23}$$

A rigid steel cylinder with mass, M_{c1}, impacting the equivalent plate at the ballistic limit velocity, V_{50}, will first exchange momentum with the plate plug of mass, M_{t1}, in the path of the cylinder. The initial momentum exchange is assumed to occur as a free impact without influence of the surrounding plate material. The free impact decelerates the cylinder and accelerates the plate plug to an initial post-impact velocity of

$$V_{Rc1} = M_{c1}\, V_{50}/(M_{c1} + M_{t1}) \tag{24}$$

prior to any deformation of the plate. The mass of the steel cylinder with L/D = 1 is

$$M_{c1} = 2\pi r^3 \rho_{st} \tag{25}$$

and the plate plug mass is

$$M_{tl} = \pi r^2 \rho_t T_c \tag{26}$$

The free impact residual kinetic energy for the equivalent impact is

$$KE_{Rcl} = 0.5 M_{cl} V_{50}^2/(1 + M_{tcl}/M_{cl}) \tag{27}$$

Since the equivalent impact occurs at the ballistic limit velocity, KE_{Rcl} should provide a good estimate for the maximum free impact residual kinetic energy that can be removed by plastic work in the plate without rupturing. Thus the criterion for removal of the current ring element by the debris cloud is

$$\text{IF } KE_R > KE_{Rcl} \quad \text{The ring element is removed and} \tag{28}$$

$$dMR_t = dMR = dIR = AR_r = 0 \tag{29}$$

$$\text{OTHERWISE} \quad \text{The ring element is retained and}$$

$$dMR_t = dM_{tR},\ dMR = dM_R,\ dIR = dI,\ AR_r = Ar \tag{30}$$

An important question remains as to what ballistic limit velocity expression is most appropriate for the model. An initial attempt to use a ballistic limit velocity equation for deforming steel cylinders with an upwards correction term for thin plates to account for membrane type response produced central hole predictions that were too low. The second attempt was to use the ballistic limit velocity expression for very efficient plugging type perforations by nondeforming steel cylinders, namely (Ipson and Recht, 1977)

$$V_{50} = V_{50\tau} = C_\tau (T/D)^{0.75}/(L/D)^{0.5} \tag{31}$$

where C_τ is an empirically determined constant depending on plate material. For an L/D = 1 cylinder perforating the equivalent plate, Eq. 31 reduces to

$$V_{50} = V_{50\tau 1} = C_\tau (T_c/2r)^{0.75} \tag{32}$$

Values of C_τ for steel plates are given by (Ipson and Recht, 1977)

$$C_\tau = -0.0062 (BHN_t)2 + 3.28 (BHN_t) + 184 \quad \text{(m/s)} \tag{33}$$

and for aluminum plates by (Ipson and Recht, 1977)

$$C_\tau = -.00166 (BHN_t)2 + 0.75 (BHN_t) + 300 \quad \text{(m/s)} \tag{34}$$

where BHN_t is the Brinell hardness of the plate material. The values used for the mild steel plates (BHN_t = 185) and the 2024 aluminum plates (BHN_t = 120) for the model and test data comparisons below were

$$C_\tau = 578 \text{ m/s} \quad \text{(Mild Steel Plates)}, \qquad C_\tau = 366 \text{ m/s} \quad \text{(2024 Aluminum Plates)}$$

The plug-shear limit velocity expressions above provided much better agreement between model predictions and the test results. A closer look at the calculations revealed predicted post-impact ring velocities on the order of 1000 m/s which is too high for the plate response component of the limit velocity to be actuated. It would thus appear that the high velocity gradient, early-time plugging type failures were predominant in the test results.

COMPARISONS BETWEEN MODEL PREDICTIONS AND TEST RESULTS

The area removal and impulse-response models for the central hole diameter, D_h, are compared with the test results in Figs. 10 and 11. The test conditions and FATEPEN debris characteristics (see *Debris Particle Numbers and Sizes*) are listed above each graph. Also shown in each graph are the maximum impact pattern diameters, D_{mf} and D_{mt}, for the penetrator and plate particles based on their respective maximum dispersion angles of 10° and 20°, respectively. It can be seen that the impulse model predicts that the faster dispersing plate particles enlarge the central hole beyond the pattern of penetrator particles only for plate spacings on the order of a few sphere diameters. It can be seen that the impulse-response model provides improved predictions over the simple area removal model in all cases, and that this model predicts that hole enlargement is determined mostly by the denser pattern of penetrator particles. The new model applies particularly well to the thinner plates (Fig. 10) but underpredicts the central hole diameters in the thicker plates at larger plate spacings (Fig. 11). The low predictions probably reflect the need to better account for the impulse transmitted to the current ring increment by plate material removed at inner radii.

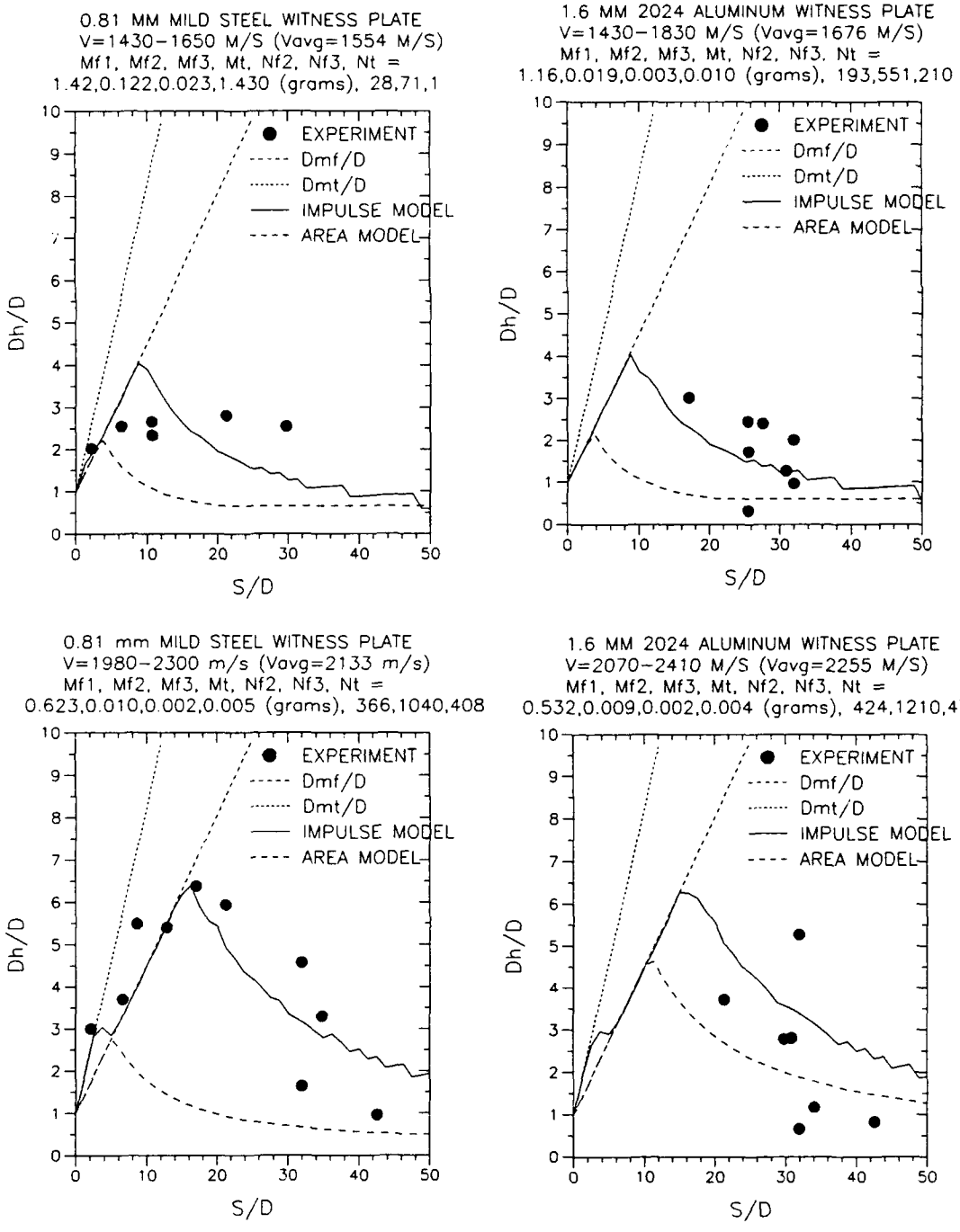


Fig 10 Comparisons Between Model Predictions and Test Results for Thinner Steel and Aluminum Plates

SUMMARY AND CONCLUSIONS

A relatively simple engineering model has been developed to predict the size of the central hole in plates impacted by high velocity multi-particle debris clouds The model is based on straightforward momentum conservation and utilizes well established individual particle penetration equations applied to each of the generic particles in the debris cloud The multi-particle effects are determined by simple summation of the individual particle effects The model employs empirical ballistic limit velocity data for L/D= 1 steel cylinders as an expedient substitute for first principle modeling of plate response and failure

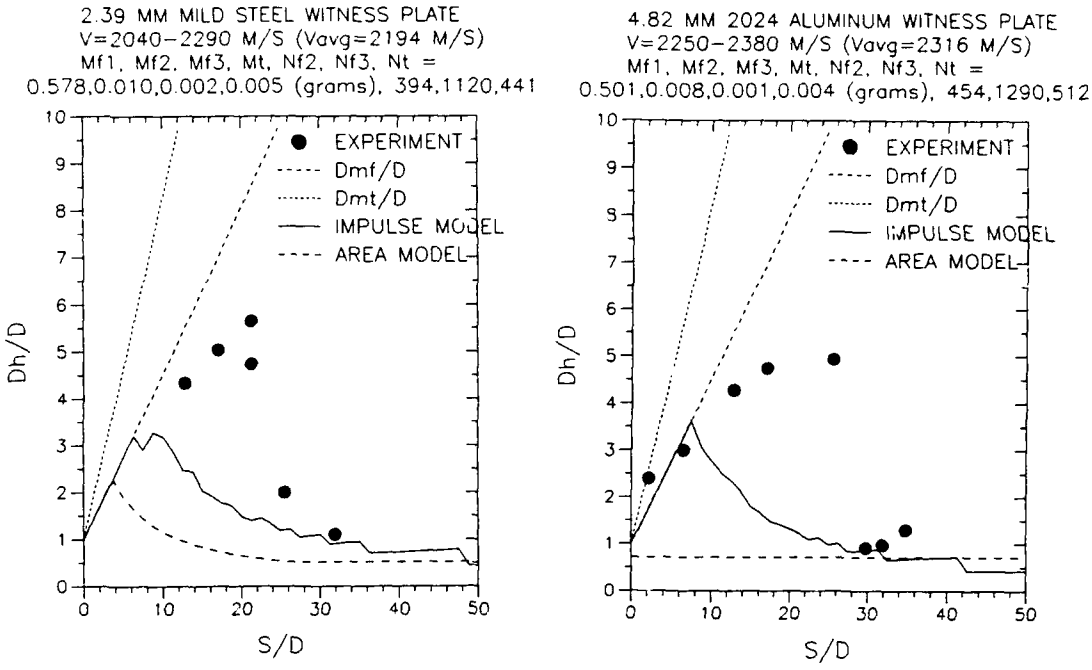


Fig. 11. Comparison Between Model Predictions and Test Results for Thicker Steel and Aluminum Plates

The impulsive loading and response model provides much improved agreement with test data over predictions from an earlier model base on simple area removal. The new model currently predicts damage to thinner plates more accurately than thicker plates. The comparisons between model predictions and test results suggest that early time shear failure is the likely predominant failure mechanism for central hole enlargement. Future model improvement efforts should include an improved accounting of impact load transmission between the plate ring elements.

ACKNOWLEDGMENTS

The plate damage experiments described in this paper were performed by Jim Dunn, Steve Lightsey, and Steve Ford of the Denver Research Institute. Richard Zernow of Applied Research Associates assisted in preparation of the photographs and line drawings. This work was funded by the Naval Surface Warfare Center, Dahlgren, Virginia.

REFERENCES

Ipson, T. W. and R. F. Recht (1977) *Ballistic Perforation by Fragments of Arbitrary Shape*, NWC TP 5927, Denver Research Institute, Denver, CO.

Recht, R. F., T. W. Ipson, and E. P. Wittrock (1969) *Transformation of Terminal Ballistic Threat Definitions into Vital Component Malfunction Predictions*, NWC TP 4871, Denver Research Institute, Denver, CO.

Rolens, D. K., R. F. Recht, and E. S. Grubin (1976) *Effects of "G" Loading on Aircraft Vulnerability - A User's Guide to Structural Residual Determinations*, BRL Contractor Report No. 293, Denver Research Institute, Denver, CO.

Yatteau, J. D. (1982) *High Velocity Multiple Plate Penetration Model*, NSWC TR 82-123, Denver Research Institute, Denver, CO.

Yatteau, J. D., J. A. Dunn, and D. L. Dickinson (1991a) *Terminal Ballistic Impact Fracture of Steel Cubes*, NAVSWC TR 91-397, Applied Research Associates, Inc., Lakewood, CO.

Yatteau, J. D., R. H. Zernow, and R. F. Recht (1991b) *Compact Fragment Multiple Plate Penetration Model (FATEPEN2), Vol. I - Model Description, Vol. II - Computer Code User's Manual*, NAVSWC TR 21-399, Applied Research Associates, Inc., Lakewood, CO.

Int. J. Impact Engng Vol.14, pp.843–850, 1993
Printed in Great Britain

0734-743X/93 $6.00+0.00
© 1993 Pergamon Press Ltd

THE APPLICATION OF THE INTEGRAL THEORY OF IMPACT TO MODEL PENETRATION OF HYPERVELOCITY IMPACT

D. Yaziv and J. P. Riegel

Southwest Research Institute
6220 Culebra Road, San Antonio, TX 78238

ABSTRACT

The Integral Theory of Impact (ITI) (Swanson and Donaldson, 1978) is a unique formulation of the equations of motions of projectiles to describe the penetration process. The model requires only basic material properties, no empirical data is needed. The original model was modified to divide the penetration process into three consecutive phases. The new model has successfully modeled impacts over a wide range of velocities, at normal or oblique impact, for infinite or finite targets. In order to better match the experimental observations of impacts in the hypervelocity range, it was necessary to include a thermal softening effect on flow stress. For finite targets, the back-face effect is proposed to be a function of both penetration velocity and the speed of sound, extending the model's applicability to hypervelocity penetration.

INTRODUCTION

The Integral Theory of Impact (ITI) was applied by Swanson and Donaldson (1978) to the problems of modeling long rod penetration performance. The penetrator is modeled as a right circular cylinder shaft with a cylindrical head. Schematically, this is shown in Fig. 1 for the actual case and the model. At impact, the head is allowed to expand radially and contract axially. The target material starts to flow from the shaft into the head and is assumed to be sheared off the radial surface of the head by the target material. This simulates the spreading of the head as it is eroded during penetration.

Equations of motion are derived based on the global conservation of mass, momentum and energy. Strength terms of the target and rod materials are governed by the adiabatic hardness and the adiabatic yield strength respectively. The model requires only basic mechanical and thermal properties to complete the problem description.

The ITI model was rederived, modified and applied for a wide range of impact velocities. The Modified Integral Theory of Impact (MITI) model was implemented into the Computer Aided Armor Design/Analysis (CAAD) system (Riegel, et al., 1990).

THE ITI MODEL

The original ITI model is based on E*, the energy per unit mass dissipated in the form of plastic work as the target flows around the penetrator. (Swanson and Donaldson, 1978) gives an expression for E* in terms of the heat capacity, Cp, melting temperature, T_m, and flow stress σ_f:

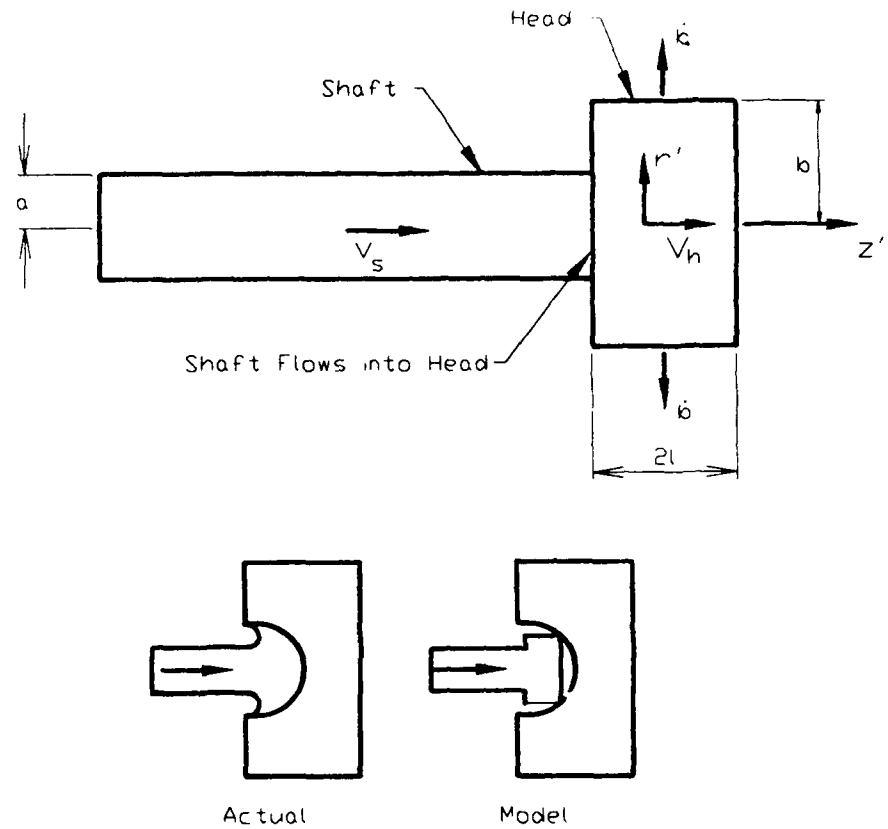


Fig. 1. Long Rod Model.

$$E^* = 0.55 C_p T_m ln\left[\frac{\sigma_f(T,\dot{\varepsilon})}{.08\rho C_p T_m} + 1\right] \tag{1}$$

The flow stress is defined as a function of temperature and strain rate; however, Swanson and Donaldson (1978) state that E* is insensitive to strain rate for most materials. In our extension of the model for the hypervelocity range it was necessary to include a thermal softening effect on flow stress.

Strength terms for the rod and the target materials are defined as follows (respectively):

$$\begin{aligned} \text{Adiabatic Yield Strength} &= \rho_p E_p^* \\ \text{Adiabatic Hardness} &= \rho_t E_t^* \end{aligned} \tag{2}$$

where ρ is the material density and subscripts p and t are related to penetrator and target respectively. The pressure at the head/target interface is governed by fluid drag, C_d, and the adiabatic hardness:

$$P_h = \rho_t\left(\frac{C_d}{2} V_h^2 + E_t^*\right) \tag{3}$$

where V_h is the head velocity.

Having defined the geometry, velocities and the adiabatic terms, the equations of motion of the system are derived using conservation laws.

Model Modifications

Several modifications to the original model were made to better match experimental observations:

a. The penetration process was divided into three phases.

b. A modified axial force was applied for oblique impact was presented by Yaziv, Cox, and Riegel (1991).

c. Modeling of yawed penetration in the 0 to 90 degrees range was presented by Yaziv, Walker, and Riegel, (1992).

d. Thermal softening effect was applied for hypervelocity impacts.

e. The back-face effect was extended for perforations in the hypervelocity range.

The Penetration Process. The penetration process is divided into three phases:

Phase I:	Head Formation
Phase II:	Steady State Penetration
Phase III:	Final Penetration

The initial penetration velocity is determined from the shock conditions generated upon impact at the head/target interface. The linear Hugoniot relationship between the shock velocity, U, and the particle velocity, V, is assumed:

$$U = C_o + SV \tag{4}$$

where C_o is the bulk sound speed and S is the slope.

At the head/shaft interface, the dynamic pressure is given by:

$$P_o = \rho_p[(V_s - V_h)^2 + E_p^*] \tag{5}$$

where V_s is the shaft velocity.

The volume of the head is assumed to be constant and its initial length equals the shaft diameter. The constant mass requires that the rate of mass inflow, $\dot{m}_i$, equals the rate of mass outflow, $\dot{m}_o$.

The terms for the head radius and the mass flow (and their derivatives) together with the global conservation laws of momentum and energy are used to establish the head formation and its equation of motion. The forces acting on both sides of the head are determined from Equations (3), (5) and the instantaneous areas.

The termination of Phase I and the transition to Phase II, the steady state penetration, occurs when one of the following two conditions is met:

a. The decreasing head velocity reaches steady state velocity.

b. The shock condition at the center of the head/target interface is distorted by release waves.

The head final relative radius is:

$$\dot{\varepsilon}_o = b_{max}/a \tag{6}$$

where a and b are the shaft and the head radii, shown in Fig. 1.

Steady state penetration is obtained when the forces acting on both sides of the moving head are balanced while the penetrator keeps eroding. Solving Equations (3), (5) and (8) yields V_h as a function of V_s:

$$\rho_p[(V_s - V_h)^2 + E_p^* = \rho_t E_o^2 \left(\frac{C_d}{2} V_h^2 + E_t^* \right) \tag{7}$$

The deceleration of the shaft is caused by its adiabatic yield strength (Tate, 1978):

$$\Delta V_s = \frac{E_p^*}{l_s} \Delta t \tag{8}$$

where l_s is the instantaneous shaft length and Δt is the time interval.

There are three main differences between the current steady state and the Tate (1978) model:

(1) The specific energy, E_t^*, replaces R_t and Y_p for the target resistance and the rod strength.

(2) A head is formed instead of constant cross section.

(3) Forces on both sides of the moving head are balanced instead of pressures.

Item (1) gives the advantage of determining material strength based on material properties only. Items (2) and (3) permit a more realistic modeling of oblique impact. The relations between the forces and the pressures for steady state penetration have been discussed by Write and Frank (1988). They showed that Tate's modified Bernoulli equation follows as a consequence of the global conservation of mass, momentum and energy in a steady flow.

In Phase III of the penetration process, we enabled four options by which penetration terminated:

a. The rod is consumed if the shaft velocity is sufficiently high to completely erode the rod.

b. The penetration ceases if the shaft velocity falls below a critical velocity at which the head reaches zero velocity. This occurs when the target adiabatic hardness is higher than the rod adiabatic yield strength and impact velocity is low.

c. Rigid penetration occurs if the shaft velocity reaches head velocity and the rod ceases to deform. This may occur when the rod adiabatic yield strength is higher than the target adiabatic hardness and the impact velocity is low.

d. The target is perforated if the target thickness is less than the penetrating ability of the rod.

Penetration at Hypervelocity Impact

The MITI model predictions match experimental results at ordnance velocities (up to 2 km/s), as demonstrated by Yaziv, et al., (1991, 1992). However, for higher impact velocities, the model starts to underestimate the measured values. In order to better match the experimental observations at the hypervelocity range, it was necessary to use a flow stress expression that is a function of temperature (see Equation 1).

At high velocities, the temperature may soften the target material and cause both E* and the adiabatic hardness of the target material to decrease. The effect of the strain rate sensitivity on the material flow stress (Equation 1) is negligibly small.

The temperature rise caused by the shock wave generated at the rod/target interface vicinity is on the order of 0.1° K/GPa (McQueen, et al., 1963) while the temperature rise (T - T_o) caused by plastic flow of the target material is:

$$T - T_o = \frac{E^* \varepsilon_p}{C_p} \tag{9}$$

where ε_p is the plastic strain in the target material.

The constitutive response of the target material is presented in Equation 1 by the Johnson-Cook model (1985) neglecting the strain rate effect:

$$\sigma = \sigma_o [1 + B\varepsilon_p^n] [1 + T^{*m}] \tag{10}$$

where T* is the homologous temperature $(T - T_o) / (T_m - T_o)$, while B, n and m are material constants. Anderson and Walker (1991) used numerical simulations of a tungsten long rod projectile penetrating into semi-infinite 4340 (Rc30) steel to calculate the normalized depth of penetration P/L (P is the penetration depth and L is the rod initial length). For impact velocities 1.2 to 1.7 km/s they used: $B = 0.644$; $n = 0.26$. When they increased the temperature exponent m from 0 to 1.03, P/L was increased from 0.785 to 0.850 at 1.5 km/s. That considerable rise of 8.3% can grow for higher impact velocities.

Modification of Back Face Effect for High Velocities

Back face effects are treated (Swanson and Donaldson, 1978) by reducing E_t^* as the penetrator approaches the back face of the target. An analytic function was derived by performing indentation hardness tests on aluminum and lexan at different depths of penetration. Based on these results, the following function was developed for E_t^*, which reduces its magnitude linearly as the penetrator approaches the back face:

$$\begin{aligned} E_t^* &= E^* \qquad for \qquad t - p > \beta b \\ E_t^* &= E^* \frac{t-p}{\beta b} \qquad for \qquad t - p \le \beta b \end{aligned} \tag{11}$$

where t is the target thickness and b is the instantaneous head radius. We found that this model, derived from static experiments, overestimates the back face effect for high impact velocity.

For high velocities, the effect of the back face is weaker and the free face information approaches the head/target interface at a distance associated with the speed of sound, C_t, in the target material. Thus, we modified the model as follows:

$$\beta = \beta_o \left(1 - \frac{V_h}{C_t} \right) \tag{12}$$

Equation (12) is substituted into Eq. (11) with $\beta_o = 4$.

Back face effect for oblique impacts are treated in the same way as for normal impact. They are based on the distance from the penetrator to the back surface, measured along a normal to the back surface and not along the penetrator axis in the direction of penetration, as the penetrator approaches the back face.

COMPARISON WITH EXPERIMENTS

Results of the MITI calculations versus experimental data are presented. Material properties are given in Table 1, and the model constants as defined by Swanson and Donaldson (1978) are: $C_d = 0.5$ and $\beta_o = 4$.

Table 1. Materials Properties

Material	ρ (kg/m³)	σ (Kbar)	C_p	Tmelt (°K)	C_o (m/s)	S	E* (x10⁶)
RHA	7850	8	454	2100	4670	1.440	0.4493
HH Steel	7850	9	454	2100	4670	1.440	0.5150
Tungsten	17500	14	116	2640	4029	1.237	0.2443
DU	18600	14.82	118	1473	3030	1.270	0.1823

MITI calculations compared with Tate, et al., (1978) experiments, with tungsten rods against semi-infinite targets, are shown in Fig. 2. Calculations compared with Hohler and Stilp (1977) experiments in a wide range of impact velocities are shown in Fig. 3. Here normalized penetration versus impact velocity (C is the sound speed) for both tungsten and steel rods are presented. Table 2 presents BRL long DU rod tests (Mullin, 1991) against 269 BHN steel. The experimental results compared favorably with the MITI calculations. The deviation of the calculated values are 5% or less below the experimental data.

Figure 4 represents CSTA tungsten long rod tests at 45° obliquity against 3/4"-thick RHA target plates (Keele, et al., 1990). Calculations of residual rod velocity and residual rod length, made with the MITI model, show reasonable agreement with the experimental results (data for finite targets at higher velocities were not available).

Additional calculations of the MITI model are given by Yaziv, et al., (1991, 1992).

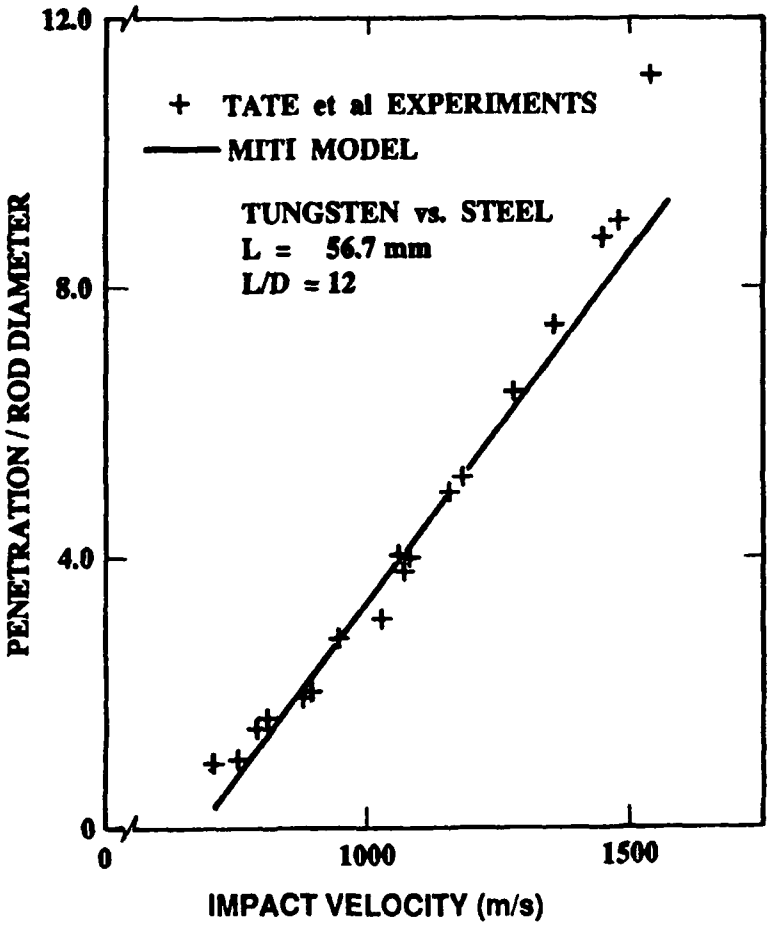


Fig. 2. Penetration versus Impact Velocity—Tate, et al., (1978) Experiments.

Table 2. DU Tests (Keele, et al., 1990)

	Velocity	Penetration (mm)		
Shot	(m/sec)	Experiment	MITI	Deviation
1240	1979	334.0	325	2.7%
1241	2344	377.5	364	3.6%
1242	2074	347.0	336	3.2%
1243	2391	388.0	369	4.9%
1244	1927	326.0	319	2.1%
2045	1725	302.0	287	5.0%

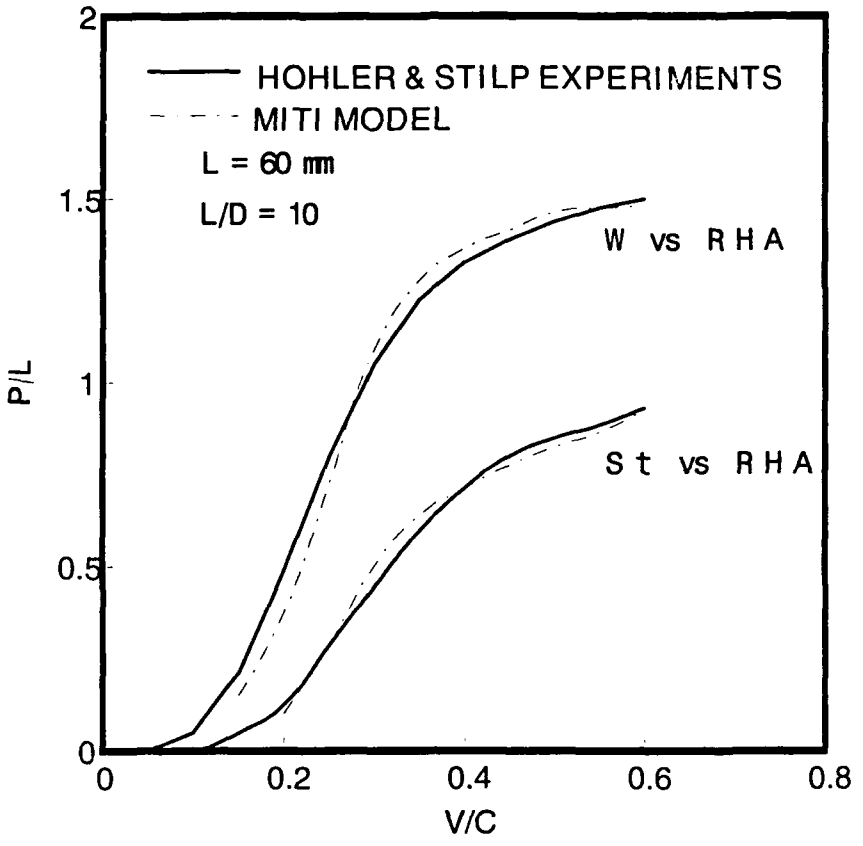
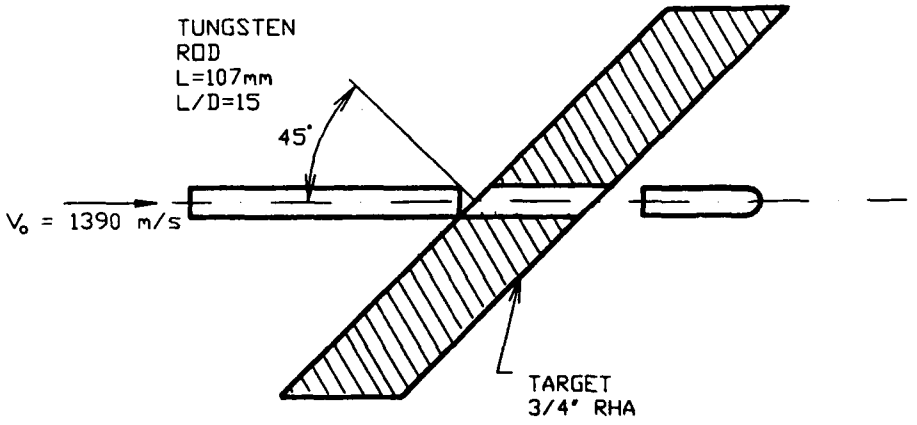


Fig. 3. Penetration versus Impact Velocity—Hohler and Stilp (1977) Experiments.



	Measured	Calculated
Residual Velocity (m/s)	1307 ± 50	1319
Residual Length (mm)	66 ± 10	72

Fig. 4. CSTA Tests—Oblique Impact Against Thin Targets.

CONCLUSIONS

Several modifications were incorporated to make the original ITI model applicable over a wide range of impact velocities. In order to better match the experimental observations at the hypervelocity range, it was necessary to use a flow stress expression that is a function of temperature. At high velocities, the temperature may soften the target material and as a consequence, to decrease both E* and the adiabatic hardness of the target material. The back face effect also was extended for perforations at the hypervelocity range. For high velocities, the back face effect is weaker and the free face information approaches the head/target interface at a distance associated with speed of sound in the target material.

REFERENCES

Anderson, C. E. and J. D. Walker, (1991). *Int. J. Impact Engng.*, **11**(4), 481.

Hohler, V. and A. J. Stilp, 3rd Int. Symp. Ballistics, (1977).

Johnson, G. R. and W. H. Cook, (1985). *Engng. Fracture Mech.* **21**(1), 31.

Keele, M., E. Rapacki and W. Bruchey, (1990). 12th Int. Symp. Ballistics.

McQueen, R. G., (1963). *Marsh, Taylor, Fritz and Carter in High Velocity Impact Phenomena*, (ed. R. Kinslow), Academic Press.

Mullin, S. A., (1991). Tests for the CAAD program, CSTA.

Riegel, J. P., S. A. Mullin and D. Tenenbaum, (1990). *Combat Vehicle Survivability Symp.*, U. S. A..

Swanson, C. V. and C. D. Donaldson, (1978). ARAP Report 333, Princeton.

Tate, A., (1978). *J. Mech. Phys. Solids*, **15**, 387.

Tate, A., K. A. B. Green, P. G. Chamberlain and R. G. Baker, 4th Int. Symp. Ballistics, (1978).

Write, T. W. and K. Frank, (1988). BRL Report BRL-TR-2957.

Yaziv, D., P. A. Cox and J. P. Riegel, (1991). *APS Topical Conf. Shock Compression of Condensed Matter*, Williamsburg, VA.

Yaziv, D., J. D. Walker and J. P. Riegel, (1992). 13th Int. Symp. Ballistics, Stockholm, Sweden.

Int. J. Impact Engng Vol.14, pp.851–862, 1993
Printed in Great Britain

0734-743X/93 $6.00+0.00
Pergamon Press Ltd

A SIMPLE MODEL FOR DEBRIS CLOUDS PRODUCED BY HYPERVELOCITY PARTICLE IMPACT

C. H. YEW[1], D. E. GRADY[2], and R. J. LAWRENCE[2]

[1]The University of Texas at Austin, Austin, TX 78712
[2]Sandia National Laboratories, Albuquerque, NM 87185

ABSTRACT

A simple debris cloud model is developed by considering the one dimensional shock wave motion in the material together with the catastrophic fragmentation theory by Grady. The model provides a simple method for calculating the velocities at the outer perimeter of the cloud and the average particle size in the cloud.

INTRODUCTION

The debris cloud produced by hypervelocity particle impact has received considerable interest in the impact engineering community. Recent experimental and analytical studies on this subject are documented in the Hypervelocity Impact Symposia edited by Anderson (1987, 1990). In these symposium volumes, excellent x-ray photographs portraying the behavior of debris clouds produced by both normal and oblique impact were presented by Piekutowski (1987, 1990). However, there is a lack of rigorous analysis on these observed phenomena. The major difficulty has been that the material, upon hypervelocity impact, will be broken into a debris cloud; yet in the analytical treatment, the material has been treated as a continuum that breaks down when the tensile stress in the medium has reached a critical value. This approach, although proper for the process of dynamic fracturings, does not appear suitable for the formation of a debris cloud resulting from catastrophic failure of the material. Upon hypervelocity impact, shock waves are generated at the contact surface, propagate outward, and set the media into a state of compression. It is intuitively clear that the fragmentation process will not take place until the stress in the media is changed to tensile by the reflected waves from the boundary or by the scattered waves from the internal flaws. Until then, a large amount of tensile energy is imparted to the material in a very short time. When the tensile stresses exceed the fracture limits, a catastrophic break-down of the material occurs and a debris cloud is formed.

In a series of papers, a fragmentation theory based on energy balance was developed by Grady (1982, 1987a, b) for explaining the catastrophic failure process. In this paper, we will demonstrate that the formation of a debris cloud produced by a hypervelocity impact can be understood by following the wave motions in the medium together with Grady's catastrophic fragmentation theory. In the following sections, a brief recount of wave motions in the media produced by impact will be presented. A discussion of Grady's catastrophic fragmentation theory then follows in section III. Since a different interpretation is required for the application of theory to the formation of a debris cloud, a brief review of the theory and its interpretation will be presented in this section. A simple debris cloud model, based on one-dimensional wave motion in the media and Grady's catastrophic fragmentation theory, is presented in section IV. The analytical predictions are compared with Piekutowski's experimental results in section

V. The model provides a reasonable prediction on the velocity vectors at the outer perimeter of the cloud and the average size of particles in the cloud.

WAVE MOTIONS PRODUCED BY IMPACT

Consider a flat plate of thickness "h" to be impacted by a cylinder (LxD) with a velocity V_I as shown in Fig. 1. Following Maiden (1963), upon hypervelocity impact, the projectile and target materials are shocked into the fluid-like state. Shock waves S_1 and S_2 (the latter is not shown in the figure) are generated at the contact surface propagating outward and set the media into a state of compression. At the same time, the rarefaction wave R_1 from the free boundaries begin to propagate into the compressed zone changing the state of stress into tensile. Some fragments are therefore immediately ejected from the tension zone as shown in Fig. 1. In this study, we shall focus our attention on the debris cloud that will emerge from the back surface of the target plate.

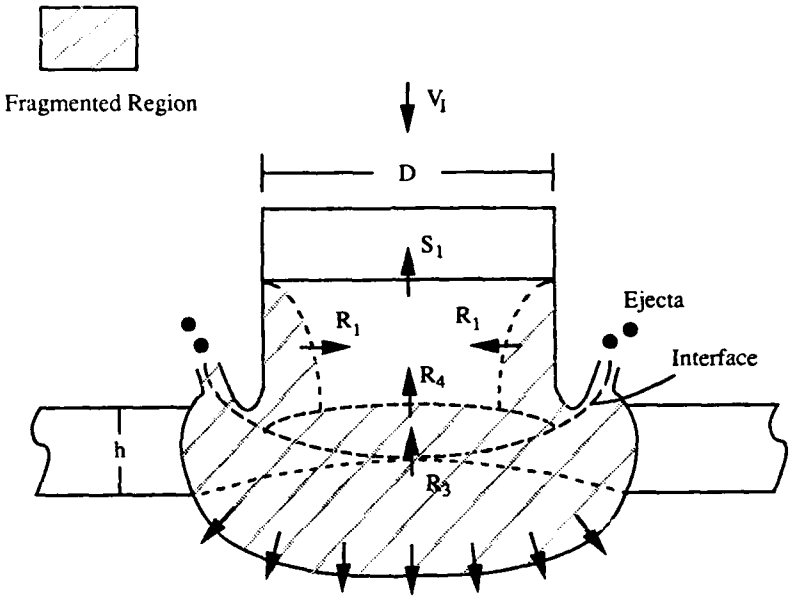


Fig. 1. Wave Motions and Fragmentation. (After Maiden)

Assuming the target plate is thin relative to the diameter and length of the projectile, the shock wave S_2 (not shown in the figure) is reflected as a rarefaction wave R_3 from the back surface of the plate. When the R_3 reaches interface (I) between the projectile and target plate, a reflection and transmission of the wave takes place. Let R_4 be the wave transmitted into the projectile. The material in the region swept by rarefaction waves R_1, and R_3 (or R_4) are now in the state of tension. Since a large amount of tensile energy is imparted into the material, catastrophic fragmentation of material can take place in these regions. As the rarefaction wave R_4 continues to propagate into the projectile, depending upon the dimension of projectile and its material properties, one of the following three situations as portrayed in Fig. 2 may occur:

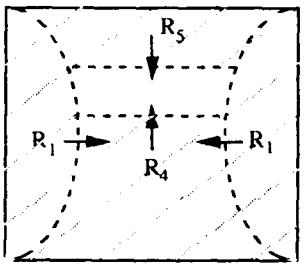
1) Shock wave S_1 is reflected as R_5 from the free boundary of the projectile. Rarefaction wave R_5 interacts with R_4 and sets the entire region into a state of tension. In this case, the projectile together with a portion of the target plate are shattered into fragments forming a debris cloud.

2) Rarefaction wave R_4 catches up with S_1 creating an attenuating wave. The diminishing strength of this wave may reduce the fragmentation of the remaining portion of the projectile, or produce fragments of larger size.

3) The rarefaction waves R_1 from the free boundary meet at the axis of symmetry of the projectile as shown in case 3 of Fig. 2. This would unload the remaining portion of the projectile. The unloaded portion of the projectile would continue its motion as a rigid body.

The wave motions described in the above paragraphs were qualitatively analyzed by Maiden (1963) using one-dimensional wave theory. Since the deformation of the projectile and target plate are axi-symmetric, the problem can be rigorously analyzed by applying the two dimensional characteristic method. The method was developed by Butler (1960) and Elliott (1962), and was applied to the related dynamic penetration problems by Madden (1967). The same fragmentation problem was also analyzed by Trucano, Grady, and McGlaun (1990) by applying the CTH Hydrocode. In this paper, we will demonstrate that the characteristics of the debris cloud produced by hypervelocity impact can be qualitatively described by analyzing the one dimensional shock wave motion in the media together with Grady's catastrophic fragmentation theory.

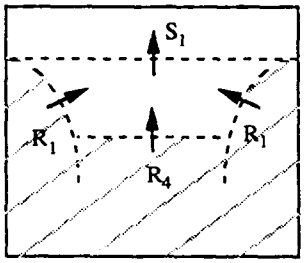
Case1: The entire region is fragmented.





Fragmented Region

Case 2: R_4 catches up S_1, and greatly reduces the strength of both waves



Case 3: R_1 merges at the center of projectile, and completely unload the remaining portion of the projectile.

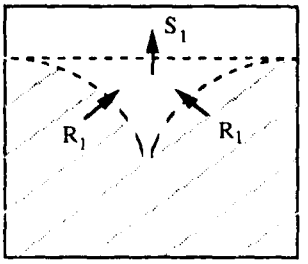


Fig. 2. Possible Modes of Fragmentation

GRADY'S CATASTROPHIC FRAGMENTATION THEORY

By regarding the dynamic fragmentation process as a macroscopic failure through internal spalls, the following three criteria for catastrophic fragmentation were postulated by Grady (1982, 1985, 1988):

The Spalling Strength -- A Material Property

As the material is loaded in tension, an elastic energy is stored in the medium. A theoretical spall strength (P_{th}) can be obtained by setting the elastic energy equal to the cohesive energy of the material. Note that the spalling strength of the material (P_{th}), in a rigorous manner, is not necessarily a constant; it can be a function of the local strain rate and temperature. In the following development, P_{th} will be regarded as a constant material parameter, and spallation will occur when the tensile stress in the region exceeds the theoretical spallation strength (P_{th}) of the material.

Following Grady, consider an element of mass δM within an expanding elastic body as shown in Fig. 3. Although the strain rate may vary from point to point throughout the body, δM is assumed sufficiently small such that the dilatational strain rate, $\dot{\varepsilon}$, within the element (modelled as a sphere)

$$\dot{\varepsilon} = \frac{\dot{\rho}}{3\rho}, \tag{1}$$

is nominally a constant.

The time dependency of the mean tension (P) in the expanding body is

$$P = \rho c_o^2 \dot{\varepsilon} t. \tag{2}$$

In the above equations, ρ is the current density, and c_0 is the speed of sound in the medium. Equation (2) implies that a time "t" is required for the tension in the material to reach the magnitude "P".

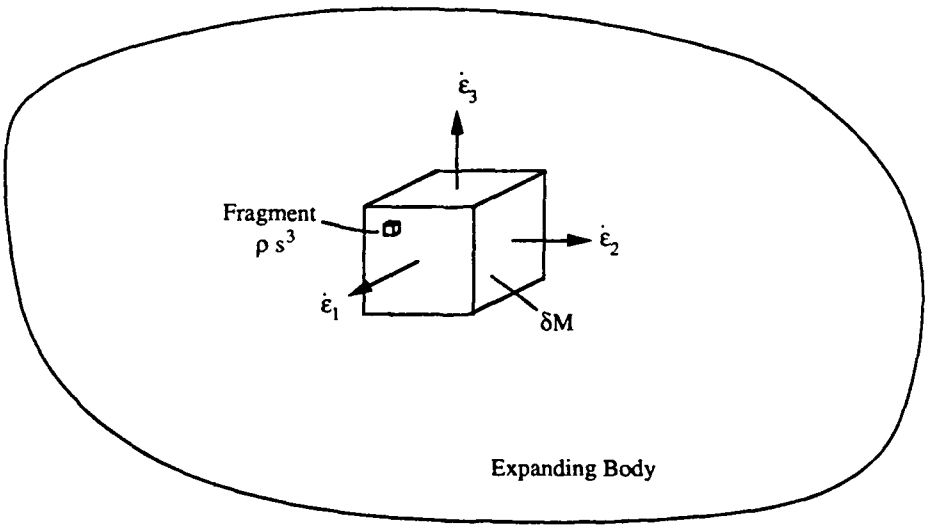


Fig. 3. Formation of Fragments. (After Grady)

The Horizon Condition

For a body undergoing catastrophic macroscopic failure through internal spalls, it is necessary for each and every volume of size approximately $(c_o t)^3$ to fail independently. Since, at time t, the communication horizon can not be greater than $c_o t$, the nominal fragment size (s) should satisfy the inequality,

$$s < 2c_o t. \tag{3}$$

A physical interpretation of this condition can be made by observing that the wave length (λ) is related to the frequency (ω) and the speed (c_o) of the wave by equation

$$\lambda\omega = c_o. \tag{4}$$

By replacing λ by s/2 and ω by 1/t, the above equation becomes

$$(\frac{s}{2})(\frac{1}{t}) = c_o. \tag{5}$$

In view of Eq. (5), the horizontal condition (Eq. 3) implies that the fragment size distribution is controlled by the frequency spectrum of the pressure pulse produced by the impact.

The Energy Condition

If the body is catastrophically fragmented into particles of a nominal size "s", the following energy inequality must be satisfied for the local mass δM:

$$T_L + E_L > E_F. \tag{6}$$

In the above equation, T_L is the local kinetic energy in δM available for fragmentation. By assuming that the fragments are spheres of diameter "s", T_L can be expressed as (Grady, 1982):

$$T_L = \frac{1}{120}\rho\dot{\epsilon}^2 s^2. \tag{7}$$

The term E_L is the total strain energy in δM as the element is carried into tension, and E_L can be expressed as:

$$E_L = \frac{1}{2}\frac{P^2}{\rho c_o^2}. \tag{8}$$

If the body is broken into spherical fragments of size s, a fracture surface area per unit volume equal to 6/s is created. Consequently, the local fracture surface energy E_F can be written as:

$$E_F = \frac{3K_c^2}{\rho c_o^2 s}. \tag{9}$$

where, K_C is the mode I critical stress intensity factor of the material.

Grady postulated that, for brittle spall to be energetically permissible within the element δM, inequality (6) must be satisfied. A minimum time requirement among Eqs. (2), (3), and (6) gives the expression for the brittle spalling strength (P_S), the fracture time (t_S), and the fragments size (s) as follows:

$$P_s = (3\rho c_o K_c^2 \dot{\varepsilon})^{1/3}, \tag{10}$$

$$t_s = \frac{1}{c_o}\left(\frac{\sqrt{3}K_c}{\rho c_o \dot{\varepsilon}}\right)^{2/3}, \tag{11}$$

$$s = 2\left(\frac{\sqrt{3}K_c}{\rho c_o \dot{\varepsilon}}\right)^{2/3}. \tag{12}$$

The above equations may be interpreted as follows: For an element δM to be catastrophically broken down into fragments of an average size "s", the required spalling strength is P_S, the strain rate in the material at the instant of spalling is $\dot{\varepsilon}$, and the time for the material to reach the state of spalling into fragments of size "s" is "t_S".

The hypervelocity impact produces a large stress and a high strain rate in the material in a very short time. Also, the magnitude of the impact-produced tensile stress P_m is expected to be much higher than the theoretical spalling strength P_{th} of the material (a much lower value of P_{th} can be expected if the material has internal flaws). Since the time for reaching the maximum stress P_m in the material is short, it seems reasonable to expect that the size of fragments is affected only by the strength of the maximum stress P_m ($>>P_S$) produced by the impact. Replacing P_S in Eq. (10) by P_m and substituting Eq. (10) into Eqs. (11) and (12) in favor of P_m, the following equations are obtained:

$$s = 6\left(\frac{K_c}{P_m}\right)^2, \tag{13}$$

$$t_s = \frac{3}{c_o}\left(\frac{K_c}{P_m}\right)^2. \tag{14}$$

The above equations imply that, if the rise time (t_r) for reaching stress P_m is less than or equal to t_S, the material would be broken into fragments of an average size "s" as expressed by Eq. (13).

It is interesting to note that the critical stress intensity factor K_C in Eq. (13) is equivalent to the strain energy release rate during the fracturing process. During catastrophic fragmentations, the plastic zone in front of fracture tips is expected to be very small. This conjecture suggests that Eq. (13) may be applicable to ductile materials as well.

Now consider the material to be shocked into a fluid-like state by the intensive pressure and temperature produced by impact. Applying the same reasoning as outlined in the previous paragraphs, the average size of the fragments and the corresponding rise time of the pressure pulse are, respectively

$$s = 12\left(\frac{\rho c_o^2 \gamma}{P_m^2}\right), \tag{15}$$

$$t_s = 6\left(\frac{\rho c_o \gamma}{P_m^2}\right), \tag{16}$$

where, γ, a function of the current temperature, is the surface energy of the liquid.

The above equations, Eqs. (13) through (16), are based on the premise that due to non-equilibrium characteristics of the fragmentation process, all or most of the shock energy goes into the fracture surface energy. Experiments may show, in fact, that this over predicts the intensity of the catastrophic

fragmentation process. If so, it will be necessary to alter the theory by introducing an effective break-down stress $P_{eff} < P_m$ based on other fracture considerations. One possibility would be that

$$P_{eff} = \left(\frac{3K_c^2 P_m}{R}\right)^{1/3}, \tag{17}$$

where R is a characteristic dimension of material achieving shock state of P_m .

Equation (13) or Eq. (15) is a convenient equation for calculating the size of fragments because the maximum stress P_m is directly related to the impact velocity and the relative material properties and geometry of the projectile and the target plate.

A SIMPLE DEBRIS CLOUD MODEL

As demonstrated in section II, the fragmentation of material can only occur in the tension regions swept by rarefaction waves. Knowing the distribution of tensile stresses and particle velocity vectors in these regions, the break-down of the material and the formation of a debris cloud can be analyzed by applying Grady's catastrophic fragmentation theory.

The objective of this study is to develop a simple debris cloud model that is capable of capturing the main features in the cloud. Consider a plate of thickness "h" to be impacted by a cylindrical projectile (D x L) with a velocity V_I as shown in Fig. 4. For a thin plate and a high impact velocity, it is reasonable to assume that the area of the plate directly underneath the projectile is punched out as shown in the figure. Let m_p be the mass of projectile and m_t be the mass of the punched-out portion of the plate. The conservation of linear momentum gives the velocity at the mass center (C) of the system as:

$$V_c = \frac{m_p V_I}{m_p + m_t}. \tag{18}$$

The wave motions in the punched-out portion is similar to that described in Fig. 2. Let ρ and q be the density of projectile and target plate, and subscript "o" denote to the state of material ahead of the shock and subscript "1" behind shock, respectively. The pressure, particle velocity, and the shock wave speed in the compressed region can be calculated by applying the one-dimensional shock wave theory (Maiden, 1962) to give:

$$p = \frac{\rho_o V_I^2}{1 - \frac{\rho_o}{\rho_1}} \left\{1 + \left[\frac{\rho_o\left(1 - \frac{q_o}{q_1}\right)}{q_o\left(1 - \frac{\rho_o}{\rho_1}\right)}\right]^{-1/2}\right\}^{-2}, \tag{19}$$

$$v = V_I \left\{1 + \left[\frac{q_o\left(1 - \frac{\rho_o}{\rho_1}\right)}{\rho_o\left(1 - \frac{q_o}{q_1}\right)}\right]^{1/2}\right\}^{-1}. \tag{20}$$

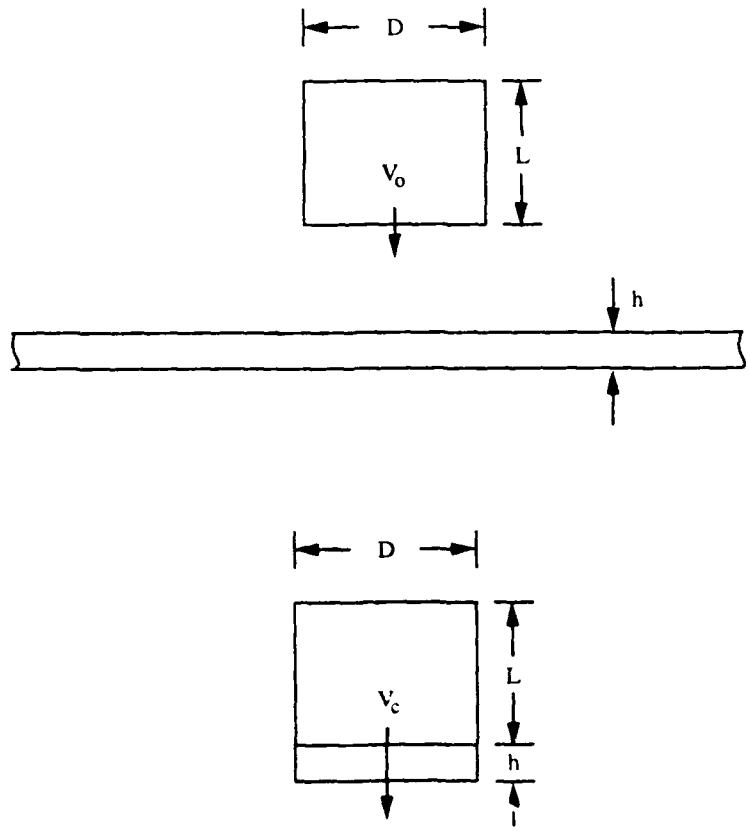
The shock wave speed in the projectile is

$$U_1 = \frac{V_1 - \frac{\rho_1}{\rho_o} v}{\frac{\rho_1}{\rho_o} - 1}, \tag{21}$$

and in the target plate is

$$U_2 = \frac{v \frac{q_1}{q_o}}{\frac{q_1}{q_o} - 1}. \tag{22}$$

The above equations, Eqs. (19) through (22), governs the state of the shock-compressed region. The corresponding density-pressure relationship of the materials are described by the Hugoniot equations.



After impact, a portion of plate is sheared out by the projectile

Fig. 4. Impact of a Short Cylinder on a Thin Plate

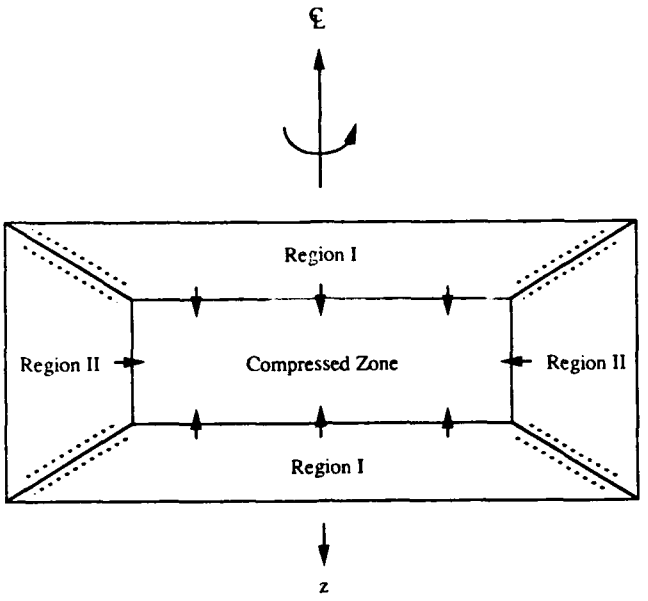


Fig. 5. Regions (I and II) Swept by the Unloading Waves from Boundary

Assume that the length (L) of projectile is short as is shown in case 1 of Fig. 2. As the shock waves reach the corresponding free boundary of the projectile and target plate, reflection of the waves takes place and they propagate into the medium as the unloading (or rarefaction) waves. Referring to Fig. 5, the unloading process is divided into the following two regions: region I is the region swept by the unloading waves from the top and bottom free surfaces of the projectile and target plate, while region II is the region swept by the unloading wave from the circumference of the projectile and target plate.

In region I, after reflection of waves, the particle velocity at the center of the free surface of the target is $v_A = 2v$; and similarly $v_B = 2v - V_I$ at the free surface of the projectile. The magnitude of velocity "v" can be calculated directly from Eq. (20) together with the Hugoniot equation of the materials. The shock wave is reflected as a simple wave by the free boundary. Note that the break-down of material in region I can not occur until the arrival of unloading waves from the free circumference of the projectile and target plate.

The unloading waves from the free circumference provide a radial particle velocity "v_{rad}" to the material. By assuming that the vertical particle velocity "v" is constant throughout region I and the unloading shock front in region II is perpendicular to the r-axis, the radial particle velocity component "v_{rad}" at the edge of target plate can be calculated from the Rankine-Hugoniot relation (Elliott, 1962) across the shock to give:

$$v_{rad} = \left[\frac{p}{\rho_o}\left(\frac{\rho_1}{\rho_o} - 1\right)\right]^{1/2} \tag{23}$$

Also, the corresponding velocity at the edge of the projectile can be obtained by replacing ρ_0 and ρ_1 by the corresponding q_0 and q_1.

The passage of rarefaction waves sets the material in the region in a state of tension. Since the Hugoniot equation is limited to the material in a state of compression, there is a lack of equations of state for the calculation of tensile stress distributions in the region swept by the rarefaction waves. Assume that the tensile pressure in the region swept by the rarefaction wave is "- p" . For a thin projectile and target plate, this assumption appears to be reasonable. The material in the region thus breaks down catastrophically according to Grady's theory, and the average particle size in the cloud can be estimated from Eq. (13) or Eq. (15).

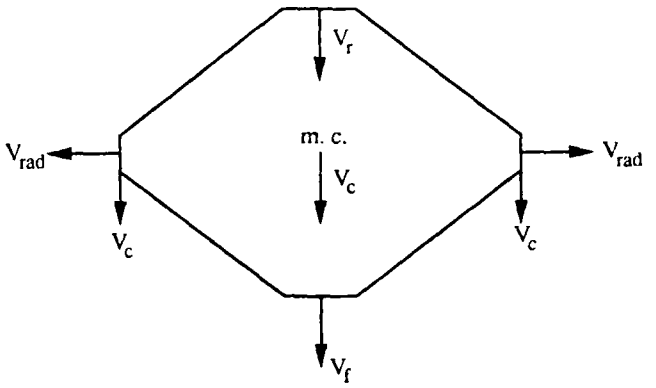


Fig. 6. Piekutowski's Debris Cloud Model (1990)

PLATE IMPACT EXPERIMENTS

Piekutowski (1990) carried out an experimental study of debris clouds produced by impacting a copper disk against an aluminum plate. Based on x-ray pictures, he modelled the debris as a rhombus shaped cloud as sketched in Fig. 6. He also measured the velocities at the front (V_f), rear (V_r), and edges (V_c, V_{rad}) of the cloud. Using the Hugoniot curves of aluminum and copper given in Fig. 13 of Maiden (1963), the corresponding velocities can be calculated from the above equations. A comparison with Piekutowski's measured results are presented in Table 1. In the calculated results, the projectile inclination angles were assumed to be zero. It is seen that the agreement between the velocities at the front (V_f), rear (V_r) and center (V_c) of the cloud is indeed reasonable. We attribute the discrepancies to the material properties (Hugoniot curves) used in the calculations. The predicted radial velocity at the edge of cloud is much larger than that measured by Piekutowski. Our model predicts that, at the edge of cloud, the projectile (copper) and target plate (aluminum) have different radial velocities. For the aluminum cloud, our model predicts an approximate 40-degree cloud spread angle (at $V_0 = 6.53$ km/s), which is close to the experimental observation (45 degrees at $V_0 > 10$ km/s) by Chhabildas (1992). It is interesting to note that the debris cloud from the target plate (aluminum) is separated from the cloud from the projectile (copper), and the copper cloud has a much smaller spread angle (22 degrees).

Assume that the aluminum target breaks down in a brittle manner, and that the stress intensity factor (K_I) for aluminum is 30 MN-m$^{-3/2}$. Also, assume that the copper was melted by the intense heat generated by impact, and the surface energy (γ) of liquid copper is 1.36 J-m^{-2} (at 1100 C) (Allen, 1972). Using this information, the average particle size in the cloud can be calculated by substituting Eq. (19) into Eq. (13) and Eq. (15). The calculated values are tabulated in Table 1. It is interesting to note that the copper cloud has much finer particles than the aluminum cloud.

The exact shape of the cloud and the size of particles in the cloud depend upon the shape of the shock-compressed material and the position of the rarefaction waves from the boundaries. These can only be modelled precisely from at least a two-dimensional shock wave analysis together with the equations of state for materials both in compression and in tension. The model presented in this study provides a simple means for estimating the velocity and the average particle size in the cloud. Knowing the average particle size in the cloud, the linear momentum and the expansion of the cloud can be estimated from the velocities at the front (V_f), rear (V_r), and edge (V_c, V_{rad}) of the cloud as demonstrated by Piekutowski (1990).

Table 1. Debris Cloud Velocities at Various Impact Velocities
Aluminum Bumpers Impacted by 1 g Copper Disk (L/D=0.3)
Based on Piekutowski's Data (1990)

Bumper Thickness (mm)	Impact Velocity V_0 (Km/sec)	Inclination Degree	Measured Velocities				Calculated Results						
										V_{rad}/V_0		Average Particle Size (mm)	
			V_f/V_0	V_c/V_0	V_r/V_0	V_{rad}/V_0	V_f/V_0	V_c/V_0	V_r/V_0	Al	Cu	Al 10^{-3}	Cu 10^{-6}
1.0	6.39	4.6	1.44	0.91	0.36	0.24	1.324	0.885	0.324	0.838	0.411	0.328	0.271
1.5	6.36	7.8	1.44	0.88	0.36	0.24	1.324	0.837	0.324	0.838	0.411	0.333	0.275
2.0	6.38	10.7	1.42	0.83	0.35	0.27	1.324	0.794	0.324	0.838	0.411	0.329	0.273
2.5	6.53	2.5	1.46	0.79	0.35	0.27	1.324	0.756	0.324	0.841	0.411	0.305	0.254
1.5	3.45	2.5	1.37	0.86	0.43	0.23	1.334	0.837	0.334	0.784	0.378	1.992	1.439
1.5	4.85	4.7	1.43	0.87	0.39	0.23	1.326	0.837	0.326	0.812	0.399	0.771	0.602

CONCLUDING REMARKS

The debris cloud model presented in this study was developed by considering the one-dimensional wave motions in the medium together with Grady's catastrophic fragmentation theory. Since the material properties of both the projectile and target plate, as well as their fragmentation characteristics, are taken into consideration, the model may be regarded as an improvement over the spherical expansion model that has been used by many authors (Richardson, 1969; Swift, Bamford, and Chen, 1982; and Lawrence, 1987, 1989) in their studies of the protective shield (i.e. bumper plate) and the survivability of the underlying structure. In the design of a hypervelocity particle shield, the time duration and the spacial distribution of the impulsive force impinged on the underlying structure are of main concern. Since the particle velocity at the outer perimeter of the cloud and the average particle size in the cloud can be calculated from the equations presented in this study, the model can be used to calculate the momentum and spread of the debris cloud produced by a hypervelocity impact.

ACKNOWLEDGEMENT

This research has been supported in part by a grant, NAG 114, from the Johnson Space Center of NASA to the first author (CHY). The reported study was carried out when the first author was with the Sandia National Laboratories as a summer (1991) faculty member. The hospitality of SNL is gratefully acknowledged.

REFERENCES

Allen, B. C. (1972). *Liquid Metals* (Beer, S. V.Beer, ed.), Dekker Publications, New York, N. Y.

Anderson, C. E. Jr. (1987). Symposium on Hypervelocity Impact, held at San Antonio, Texas, *Int. J. of Impact Eng.*, Vol. 5, No. 1-4.

Anderson, C. E. Jr. (1990). Symposium on Hypervelocity Impact, held at San Antonio, Texas, *Int. J. of Impact Eng.*, Vol. 10, No. 1-4

Butler, D. S. (1960). The Numerical Solution of Hyperbolic Systems of Partial Differential Equations in Three Independent Variables. Proceedings of the Royal Society, Series A, Vol. 255, pp.232-252.

Chhabildas, L. C. (1992): private communication.

Elliot, L. A. (1962). Shock Fronts in Two-dimensional Flow. Proceedings of Royal Society, Series A, Vol. 269, pp.558-565.

Grady, D. E. (1987a). Spall Strength of Condensed Matter. *J. of Mechanics and Physics of Solids*, Vol. 36, no. 3, pp. 353-384.

Grady, D. E. (1987b). Fragmentation of Rapidly Expanding Jets and Sheets. *Int. J. of Impact Eng.*, Vol. 5, the 1986 Hypervelocity Impact Symposium, pp.285-292.

Grady, D. E. (1982). Local Inertia Effects in Dynamic Fragmentation. *J. of Appld Physics*, 53(1), pp. 322-325.

Lawrence, R. J. (1987). A Simple Model for the Optimization of Stand-off Hypervelocity Particle Shields. *Int. J. of Impact Eng.*, Vol. 5. the 1986 Hypervelocity Impact Symposium, pp. 451-461.

Lawrence, R. J. (1989). Stand-off Hypervelocity Particle Shields for Fixed Structures. Sandia Report, SAND 89-0442, Sandia National Laboratories, Albuquerque, N.M.

Madden, R. (1967). The Application of the Method of Characteristics in Three Independent Variables to the Hypervelocity Impact Problem. Ph.D. dissertation, Dept. of Engineering Mechanics, Virginia Polytechnic Institute.

Maiden, C. L. (1963). Experimental and Theoretical Results Concerning the Protective Ability of a Thin Shield Against Hypervelocity Projectile. Sixth Symposium on Hypervelocity Impact, Vol. III, pp. 70-156.

Piekutowski, A. J. (1987). Debris Clouds Generated by Hypervelocity Impact of Cylindrical Projectile with Thin Aluminum Plates. *Int. J. of Impact Eng.*, Vol. 5, the 1986 Hypervelocity Impact Symposium, pp. 509-518.

Piekutowski, A. J. (1990). A Simple Dynamic Model for the Formation of Debris Cloud. *Int. J. of Impact Eng.*, Vol. 10, the 1989 Hypervelocity Impact Symposium, pp. 453-471.

Richardson, A. J. (1969). Theoretical Penetration Mechanics of Multisheet Structures Based on Discrete Debris Particle Modelling. Paper no. 69-371, Hypervelocity Impact Conference, Cincinnati, Ohio.

Swift, H. F., R. Bamford, and R.Chen (1982). Designing Dual-Plate Meteoroid Shields -- A New Analysis. JPL publication no. 82-39, Jet Propulsion Laboratory, Pasadena, California.

Trucano, T., D. E. Grady, and J. M.McGlaun (1990). Fragmentation Statistics from Eulerian Hydrocode Calculations. *Int. J. of Impact Eng.*, Vol. 10, the 1989 Hypervelocity Impact Symposium, pp. 587-600.

Int. J. Impact Engng Vol.14, pp.863 - 875, 1993
Printed in Great Britain

0734-743X/93 $6.00+0.00
© 1993 Pergamon Press Ltd

EXPERIMENTAL AND ANALYTICAL STUDY OF EARLY TIME MATERIAL PROCESSING, IN A COLLAPSING SHAPED - CHARGE LINER, USING "SOFTLY - RECOVERED" PARTIALLY - COLLAPSED COPPER LINERS

Dr. L. Zernow (1)*, Dr. E. J. Chapyak (2)

(1) Zernow Technical Services Inc., San Dimas, CA
(2) Los Alamos National Laboratory, Los Alamos, NM

ABSTRACT

It is not yet clear what detailed deformation mechanisms enable copper shaped charge jets to exhibit the extraordinarily high ductility, which characterizes their dynamic behavior. The study described in this paper seeks to find some of these answers, by stopping the liner collapse process at various intermediate stages, and examining the grain structures in the partially collapsed liners.

Well characterized OFE copper shaped-charge liners, assembled into a cylindrical polycarbonate case, of constant length and volume, were partially collapsed, with reduced-weight cylindrical explosive charges. A series of increasing explosive charge weights were used to obtain progressively greater partial deformations on individual copper liners. The shock waves from the varying length explosive charges were coupled to the copper liners through intermediate water fill, which was in direct contact with the rear of the liners.

The series of partially collapsed copper liners was captured by "soft recovery" in low density polystyrene. Flash radiography prior to liner recovery, confirmed that the unexpected shapes of the recovered partially collapsed liners, actually existed prior to their entering the recovery medium and were not the result of the recovery process itself. This was an early concern when the unusual shapes of the recovered liners were first seen.

These shapes were also independently confirmed by a series of computations at Los Alamos National Laboratory, using MESA 2D.

A comparison of the photomicrographs of undeformed virgin copper liners and the series of partially collapsed liners, shows regions on the inner apex near the liner axis where plastic flow has occurred, with very substantial modifications (refinement and elongation) in grain structure even for the small deformations which barely change the overall liner shape.

Time dependent strain and strain rate computations, using LaGrangean tracer markers, indicate very large strain rates, between 3×10^7/sec. and 4.7×10^7/sec. in those regions with plastic flow where grain refinement and elongation are seen, even with very small overall deformation.

It is believed likely that this early time material processing and grain refinement, arising from the localized plastic deformation of the liner, plays a key role in preparing the liner material structure, so that it can exhibit the high dynamic ductility, characteristic of copper shaped-charge jets.

INTRODUCTION

Although it has been known for well over fifty years that the copper in a shaped charge jet exhibits extraordinarily high dynamic ductility, the detailed physical mechanisms, based on sound fundamental physical models, which can quantitatively account for this phenomenon are not presently well understood, despite the fact that specific aspects of the problem have been extensively studied. The possible role of material strength and work hardening as well as the existence of a critical preferred disturbance wave length, which "grows faster than all others" thereby determining the average jet particle length after jet particulation, has been studied by Chou, et al (Ref. 1, 2). Scaling analysis has been studied by Walsh (Ref. 3). Instability criteria have been analyzed by Curtis (Ref. 4) and Pack (Ref. 5). Romero (Ref. 6a, 6b) has developed a stability parameter (L) which involves the ratio of inertial and plastic forces in the stretching jet. Very recently, Brown, Curtis and Cook (Ref. 7) have reexamined the role of asymmetry, which can also affect the particulation process by accelerating it.

The copper jet which is formed when a typical uniform walled copper liner is collapsed by an explosive charge (e.g. in a VIPER warhead), displays an approximately linear velocity gradient, with the front end of the jet moving at a velocity in excess of 9 km/sec and the rear of the jet moving at a velocity of about 2-3 km/sec. Under the action of this linear velocity gradient, the jet which remains in the solid plastic state, stretches like taffy, until it eventually particulates. The particulation process, which is preceded by quasi periodic ductile necking along the length of the stretching jet, defines the ductility limit by defining the maximum strain prior to fracture. Experimental observations of this stretching and particulation process, obtained by means of flash x-ray observations, indicate that a conservative estimate of the approximate average strain, at the time of fracture, can be higher than 10. This corresponds to 1000% strain. The approximate average strain is defined here as:

$$\frac{\Delta L}{L_0} = \frac{L - L_0}{L_0}$$

where $\frac{\Delta L}{L_0}$ = approximate average strain

L = length of the continuous jet at the start of particulation

L_0 = length of the cone element (slant height of the cone) from which the jet was formed

ΔL = change in length = $(L - L_0)$ of the cone element from which the jet was formed

The observed dynamic ductility of the copper in the jet is therefore clearly in the superplastic range.

OVERVIEW OF SIGNIFICANT FACTORS

There are several factors, both physical and geometrical, which can be immediately recognized as playing a potentially significant role in supporting and stabilizing such a high dynamic ductility. The elevated jet temperature and its effect upon the yield strength is clearly one of the physical factors that can affect the ductility (Ref. 8). The precision and uniformity of the liner wall thickness, as well as the coaxial symmetry of the liner, the explosive charge and the charge case, are typical of the geometrical factors which can separately affect the stability of the stretching process (Ref. 7).

There are many other more subtle factors which can also be seen as potential contributors (positive and negative) to the ductility limits. These would include the strain-hardening and strain-rate hardening properties of the copper which interact with the thermal softening properties (Ref. 9).

It is also suspected that the incidence of deformation induced porosity in the stretching jet (Ref. 10) especially in the necking regions, can also play a role in affecting how long the ductile stretching is maintained before fracture (particulation). The effect of dynamically introduced porosity on the particulation process is currently being examined computationally in another separate study (Ref. 11).

Finally, there has been continued wide ranging speculation regarding the physical source of the perturbations which result in the quasi periodic localized necking process. These perturbations and their growth ultimately define the stability and particulation of the stretching jet, and therefore the observed ductility limit, even in the absence of geometrical asymmetries. Compressibility effects and surface imperfections (e.g. machining marks) on the liner have been among the factors mentioned.

There have been preliminary attempts (Ref. 12) to account for the superplastic behavior of the copper jet by invoking the process known as dynamic recrystallization This is a strain rate sensitive process, which at sufficiently high strain rates, results in dynamic grain refinement, which may lead to the fine grain sizes normally associated with superplastic behavior. However, the attempts at the quantitative application of this mechanism to the analysis of the ductility of copper jets has so far not adequately accounted for the ductile behavior of these jets. Nevertheless, the concept itself is very attractive and warrants additional study. Part of the problem in evaluating such a model, is the previously unsuspected complexity of the material flow from the liner to the jet, which has recently been shown to exhibit large time dependent radial gradients of strain and strain rate (Ref. 13) as well as time dependent radial gradients of temperature (Ref. 8).

It is therefore evident that the current state of knowledge still does not provide a quantitative basis for a thorough understanding of the interacting combination of physical and geometrical mechanisms that permit the copper to undergo such large stable superplastic strains, in a shaped charge jet, before particulation. Qualitatively, the geometrical contribution of charge and liner symmetry to the jet stability is easiest to understand. The more difficult problem resides in the details involving the other physical mechanisms.

MOTIVATION FOR THE PRESENT STUDY

It is very difficult to experimentally obtain time resolved dynamic information regarding the changing grain structure of the liner, as it is accelerated and deformed by the explosive charge, and ultimately flows into and out of the collision zone (stagnation region). It is even more difficult to experimentally obtain the time-dependent grain structure information as the flow leaves the stagnation region, dividing itself between the jet and the slug. These diverging flows are moving in directions 180^{o} apart, in the moving collision point coordinate system.

Some details of this complex flow (such as mass motion and temperature) can be accessed computationally (Ref. 13) but the 2D axially symmetric computational analysis presently provides no information regarding the transient time-dependent grain structure.; It

should be noted however that work at Los Alamos (Ref. 14) holds out the hope that at some future time, it might be possible to model some aspects of that part of the problem, related to the plastic deformation of a polycrystalline structure, in which the individual grain orientations are considered in order to provide information on the texture, before and after deformation.

In view of these difficulties, it appeared that any attempt to obtain even partial and approximate time-dependent grain structure information, could be beneficial. In thinking about this problem, the writer recalled some very early work he had done in the 1940's with S. Kronman, at the BRL (Ref. 15) in which copper shaped charge liners were partially collapsed by means of reduced mass explosive charges whose shock waves were attenuated and coupled to the liner through a water medium. The deformed liners were subsequently recovered in water. Increasing the mass of the explosive charge, permitted the partial collapse process to go progressively further until a set of liners was collected, displaying a wide range of deformations, which included the early collapse as well as the jetting and slug formation process.

These recovered liners were cut in half along the cone axis and mounted on a display board, which still exists today at BRL,(now ARL) as a matter of historical record. They were regarded for many years as interesting trophies which illustrated the nature of the shaped charge collapse process (Ref. 16) but, to the knowledge of the authors, partially collapsed liners were never studied quantitatively.

The partially collapsed liners could reasonably be regarded as approximate snapshots of the geometry of the progressive collapse process. It would however, not be reasonable to assume that the microstructure of the copper grains in those liners, truly reflected the instantaneous grain structure in the collapsed liner, at the time corresponding to the state of partial deformation in the recovered liner. However, despite this caveat, it was natural to contemplate what the deformed microstructure might show, especially in comparison with the original microstructure in the virgin unfired liner. It was this line of thinking that led to the experiments which are described in this paper.

SUCCESSIVE STEPS IN THE DEFORMATION PROCESSING OF THE LINER MATERIAL DURING LINER COLLAPSE AND JET AND SLUG FORMATION

In order to help understand how and why the initial material properties of the shaped charge liner can influence the jet formation process, it is illuminating to consider a simplified view of how the liner material is being processed by shocks and by the severe plastic deformation during the liner collapse and jet formation process. The simplification involves ignoring the known radial variations in strain and strain rate discussed in Ref. 13. We will use the collision point coordinate system shown in Fig. 1A for this discussion. We will discuss primarily the processes pertinent to the partial collapse situation and will omit the details of the jet stretching and particulation process.

(1) As the explosive detonation proceeds, the liner is impacted obliquely by a detonation wave of 300-400 Kb amplitude. This initial interaction immediately results in shock heating of the liner and probably in the generation of numerous new dislocation sources and other structural defects, including twinning, stacking faults and possibly reduction of the initial grain size. The shocks induced in the liner material cause the heated liner material to bend toward the axis, and they can continue to generate high speed intersecting dislocations, leaving behind vacancies and other crystal lattice defects, as a consequence of the material deformation.

(2) The initial shock wave compression and shear stress causes shock heating of the liner material, and can drive it momentarily to temperatures higher than 600°C. As the shock pressure in the liner material decays, the material temperature falls to a lower residual temperature, which for copper, may be several hundred degrees lower than the initial shocked temperature, when the pressure has fallen to ambient atmospheric pressure.

(3) Under the impulsive loading provided by the detonating explosive, at pressure levels well beyond the yield strength of the liner material, it flows radially inward in a nearly hydrodynamic mode (see Ref. 17), undergoing increasing compression and shear deformation as it approaches the symmetry axis. This plastic deformation work causes the temperature of the liner material to increase again. In work hardening liner materials, like copper, this deformation can also induce work hardening, but the temperature increases also encourage thermal annealing of the induced lattice defects. Both processes can occur competitively.

(4) When the flowing liner material enters the collision zone, it undergoes further compression as well as a very drastic additional change of flow direction and very severe additional plastic deformation resulting in still more heating. It is believed that here, on the axis in the collision zone, is where the liner material attains its maximum temperature, which may be in the range of 800°C for a copper liner like the one in the VIPER charge. Most of the liner material originating in approximately the outer 75% of the liner thickness, goes into the slug and the remaining liner material coming from the inner thickness region of the liner, goes into the jet. This drastic divergence of the flow occurs close to the collision point and will be shown later in this paper to result in enormous localized strains and strain rates.

One might also imagine that for some liner materials, the temperature rise in the collision zone might be high enough to momentarily melt the liner material which might quickly resolidify as it left the collision zone. However, this seems relatively unlikely, on the basis of homogeneous heating computations, (Ref. 8) since the pressure in the collision zone is also very high. This would inhibit the melting process by substantially increasing the melting point by several hundred degrees C. There is both direct and indirect evidence that for materials like copper, the jet itself is essentially a plastically deforming crystalline solid. There has been no convincing evidence obtained so far to suggest even momentary melting in the collision zone (Ref.8) on the basis of homogeneous plastic deformation, although this conclusion awaits a more detailed examination of the microcrystalline region and central hole often found at the center of recovered copper jet particles (Ref.18) and a reexamination of the SESAME table for copper at lower temperatures and pressures, since this table was used in the computational analysis of the temperature distribution in the jet. There is also the possibility of attaining higher localized temperatures on slip bands, if the deformation energy is distributed inhomogeneously (Ref.19).

(5) The nature of the flow of liner material into the jet from a conical liner with a uniform wall thickness imparts a roughly linear average velocity gradient along the jet, with the forward portion of the jet moving faster than the rearward portion. The jet therefore continues to stretch plastically, like taffy, with its local diameter decreasing as the jet length increases. The plastic deformation work continues to be put into the stretching jet until just before the particulation process is completed. It is known that there are radial thermal gradients across the jet diameter, as well as along the jet length (Ref.8). There is also reason to believe that a large amount of microscopic porosity is being generated in the dynamically stretching jet material. Such a mechanism is needed to explain at least a part of the reduced material densities seen in flash x-rays of the jet prior to particulation (Ref.20,21,22). The temperature rise is clearly far too small to

explain the 15%-50% density reductions which are observed radiographically in the stretching continuous jet and in certain EFP observations.

The purpose of this relatively detailed review of the early thermal and deformation history during the formation of the jet and slug, is to indicate the overall nature of the changing environment to which the liner material has been exposed during jet formation. It provides an initial physical basis for interpretation of any information that can be extracted from a sophisticated and microstructural examination of jet particles captured by soft recovery, (Ref. 8) for comparison with the original liner material from which the jet was formed. Similarly, it is useful for interpretation of the microstructural examination of recovered partially collapsed liners, and their comparison with the virgin liner material in the unfired liner.

THE OVERALL PROGRAM PLAN

General

Experimental The program plan consisted of an experimental phase and an analytical phase. In the experimental phase, the initial virgin liners were carefully characterized in order to provide a baseline for comparison. The partially collapsed liners were "softly recovered" in low density polystyrene (1-2 PCF), sectioned and compared with the virgin liners.

Analytical In the analytical phase, the partial collapse experiments were examined computationally, using the MESA 2D Eulerian Code. The liner deformations which were predicted by the computations were compared with the observed deformations on the recovered liners. It should be noted that the computation did not attempt to resolve the time-dependent shock reverberation history within the liner walls.

Specific Experimental Details

The shaped charge design selected for this partial collapse study is shown in Fig.2 and used a copper liner (OFE C10100). It was selected for numerous reasons, including the fact that this was the charge design used in the jet particle recovery experiments and the MESA 2D computation for the fully loaded charge had already been carried out in connection with the ongoing work on jet particle recovery (Ref.8). This simplified the set up for the computation of the reduced charge experiments, since all of the charge description parameters were already available and only the variable explosive charge description needed to be added. In addition, the characterization of the structure of the virgin unfired liners was also being carried out in connection with the jet particle recovery program (Ref.23). It was also helpful that the charge was of the proper size (33.3mm cone diameter) to make the flash x-ray observation and the "soft recovery" process easy to carry out, without modifying existing experimental set-ups. Finally, the requirements for metallurgical specimen preparation and examination were essentially identical and complementary to those being applied to the remainder of the jet particle recovery work.

The experimental set-up is shown in Fig. 3. The recovery medium was 24" in front of the charge. Flash x-ray was used to ascertain the configurations of the partially collapsed liner, prior to the time that it entered the recovery medium, which was a stack of low density polystyrene sheets(1-2 PCF), 12" x 12" x 1/2" thick.

The flash x-ray observations turned out to be a very significant experimental addition, since the shapes of the recovered partially collapsed liners were completely unexpected and were initially considered to be possibly deformed by interactions with the low density recovery medium. The availability of the flash radio-graphs however, clearly indicated that the recovered partially collapsed liner shapes were essentially identical to those seen in the flash radiographs, prior to their entry into the recovery medium. This conclusion was independently supported by the computational analysis, which will be discussed in more detail later.

Computational Approach

The computational approach involved the use of MESA 2D, an Eulerian Code which has already been used quite successfully at LANL (Ref.24) for shaped-charge studies and in earlier portions of this program for jet temperature studies (Ref.8). The copper was treated as an elastic perfectly plastic solid with a 4.5 Kb yield stress. The Los Alamos tabular equation of state SESAME, was used for the copper and the standard JWL equation of state for the H.E. The computations were carried out until plastic deformation ceased and the residual motion of the partially collapsed liner consisted essentially of translation of the center of mass.

THE EXPERIMENTAL DETAILS

The series of progressively increasing explosive charges, which were used to generate increasingly larger degrees of partial cone collapse, are described in Table I. These charges were placed at the rear of the interior body volume, as shown in Fig.2. The remaining volume, between the charge and the liner, was filled with water. By carefully inserting the detonator holder with the attached charge into the plastic body, excess water could be squeezed out around the rim of the detonator holder leaving a bubble free water fill, in contact with the liner, most of the time. Occasionally, a few small bubbles would form near the base of the liner as a result of chemical reaction of the water with the epoxy cement used to seal the liner in the body. Most of the modest asymmetry seen in some of the partially collapsed liners with the larger explosive charges, can be attributed to these bubbles in the water, since the charges were all fired horizontally and the bubbles therefore floated to the upper side of the charge.

EXPERIMENTAL RESULTS

General

The experimental results are divided into three parts. The first part contains the data which characterizes the initial virgin liners, which were fabricated by a forging process. The second part contains the data describing the geometrical configurations of the series of partially collapsed liners. The third part contains the data comparing the structure in the partially collapsed liners, with the original structure in the virgin unfired liners.

Characterization of the Original Virgin Liners

The original liners were fabricated by a cold forging operation, using conical dies and a cylindrical work piece, beveled at the front. As a consequence, the portion of the liner which ultimately formed the apex of the liner, was less severely cold worked than the portion forming the remainder of the cone. Subsequent heat treatment of the forged liners,

was nominally designed to provide both fine grain liners and coarse grain liners. All liners were machined to final dimension after heat treatment.

The large variations in the degree of cold work between the apex and the remainder of the liner which are characteristic of this particular fabrication process, tended to obscure the effects of the heat treatment. As a result, it can be seen in Figs. 4 and 5 that while differences in grain size between the nominal fine and coarse grain liners are evident, they were much smaller than had been expected. In addition, the variation from apex to base on both the fine and coarse liners was quite large, with the lower portions near the base showing a small grain size and the upper portions nearer the apex showing a larger grain size, in both cases. However, the grain sizes in the upper regions of the "coarse" liners are only very slightly larger than in the corresponding locations on the "fine" liners, as can be seen from Fig. 4. In specific cases, however, where these observations concentrated at the apex, were repeated on new liners from the same batch, the average grain sizes through the apex region were indistinguishable between the "fine" and the "coarse" liners, as shown in Fig.4a. For the purpose of this paper, they will be considered to be indistinguishable through the apex region.

This particular characteristic of the large grains in the structure near the apex of both the "fine" and "coarse" liners provided an unexpected advantage, in assisting in the interpretation of the partially collapsed liner structures, because it provided a basis for separating the contribution of the shock wave from the contributions of the plastic deformation in causing visible changes in the grain structure. This will be discussed later, in more detail.

Experimental Details and Recovered Liner Identification

There were eight partial collapse experiments. Table II summarizes the individual identification numbers assigned to each of the eight recovered liners and the conditions of the experiment.

Structure Observed in the Partially Collapsed Liners

Macroscopic Examination In macroscopically examining the first two partially collapsed liners shown in Fig. 6, at 3x, the overall degree of deformation is seen to be relatively small in both cases. Liner 1F, collapsed with the 3.3 gram charge of Detasheet, as expected, showed a smaller degree of deformation than liner 2F, which was subjected to a 7.5 gram charge. Both showed observable thickening deformation and optical reflectivity changes on the polished section, in the apex region. They showed minor deformation along the sides. The polished cross sections of these two recovered liners which are shown in Fig. 6, reveal the reflectivity changes in the deformed region near the inner apex. Liner 8C, shown in Fig. 7, was also collapsed with 7.5 grams of Detasheet, in the same way as liner 2F. 8C clearly shows the start of a jet at the inner apex. Fig. 8 shows interior views of the inner apex region of recovered liners 2F and 8C at about 12x magnification, prior to sectioning. Both show evidence of significant apex thickening and the start-up of the jetting process. Liner 2F, the "finer" grained liner shows a smoother interior deformation surface than liner 8C, the "coarser" grained liner. Both show radial structures in the jetting start-up region, which are believed to be caused by compression folding instabilities which might occur more readily at the lower strain rates characteristic of a partial collapse process. Both also show circumferential circular structures which appear to be related to the machining marks on the liner.

Microscopic Examination of Liner 8C which was Collapsed with the Same 7.5 Gram Charge as Liner 2F When the apex region on collapsed liner 8C is examined at 50x magnification as shown in Fig. 9, an extremely interesting observation can be made, which reveals a transition in grain structure from the initially undisturbed grains in the outer rear of the apex region, to the deformed interior grains of the lower apex region, at the bottom of which the jetting process has started, and an emerging jet can be seen. The significance of this observation can be found in the fact that outwardly, the shock wave does not appear to have affected the appearance of the original grain structure, except in those regions in which plastic deformation and flow has occurred, as shown by the reflectivity change. In those deformed apex regions, below the outer apex and near the inner apex, the grains have clearly been elongated and severely distorted, as the plastic flow converged toward the axis, eventually generating the jet, seen in Fig. 9.

The unchanged outward appearance of the larger rear grains, which do not appear to have been disturbed by the shock wave passage, only means that at this shock pressure level, there are no optically visible effects of the shock wave, but there may very well have been dislocations, vacancies and other defects introduced, which would require special TEM techniques to be identified.

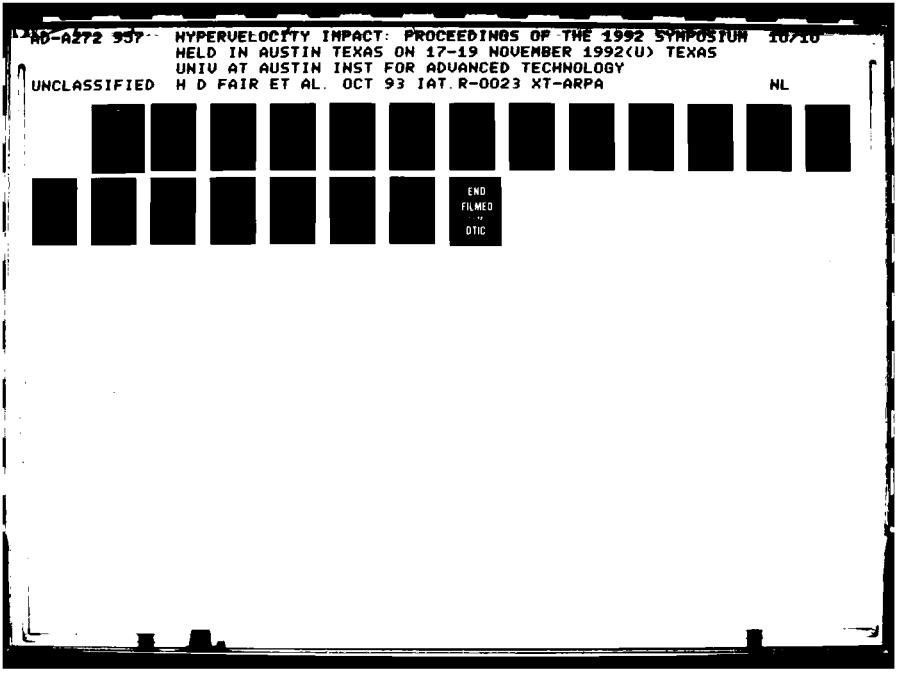
Microscopic Examination of Liner 1F In view of the observations in liner 8C, discussed above, the photo-micrographs for liner 1F were reexamined to determine if a similar grain structure modification and transition had occurred with the reduced 3.3 gram charge. Fig.10 shows that there was indeed a similar transition, but because the degree of plastic flow was smaller in liner 1F, the changes in the smaller deformed inner apex region were primarily in grain size. The plastic flow contours are just beginning to become visible near the inner apex region. The macrophotographs shown in Fig. 6 also show only small regions near the inner apex on liner 1F, in which there were noticeable reflectivity changes which define the plastic flow region. The corresponding reflectivity changes on liner 8C, in the inner apex region, were much larger and more pronounced.

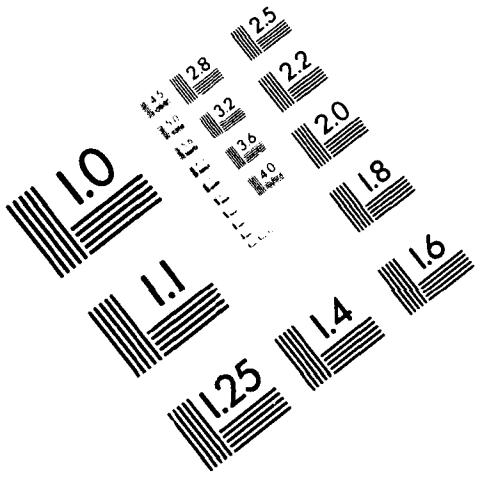
Macroscopic and Microscopic Examination of More Heavily Deformed Partially Collapsed Liners It was now useful to examine the partially collapsed liners deformed with still larger explosive charges (14.4 grams and 21.4 grams of C-4 respectively). The first is almost twice as large as the charge used on liners 2C and 8C. The second is almost three times as large.

Fig.11 shows the macroscopic longitudinal cross sections of such partially collapsed liners after cutting, polishing and etching. Liner 3C (14.4 gram charge) shows the unusual "sombrero" configuration and liners 4C and 5F (21.4 gram charge) show the liner folded back toward the slug. As noted earlier, it was verified by flash x-ray that these unexpected odd shapes existed prior to soft recovery in the polystyrene.

The severely deformed region on the axis of the slug in liner 3C (Fig.11) again shows the typical reflectivity changes characterizing the new grain structure that exists in the region of severe plastic flow. The forward end (marked JET) shows what remained of the rear portion of the jet that was still attached to the slug after recovery. This will be discussed in the computational analysis.

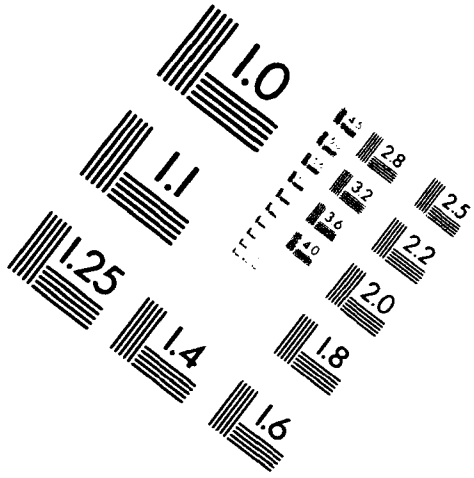
The cross section of liner 6F (Fig.11) which was collapsed with the largest charge used (27.6 grams) shows an almost conventional slug, with the remainder of the liner which did not participate in the jetting process, folded back and still attached to the slug. The reflectivity changes have now extended to the forward jetting end, in the region that is

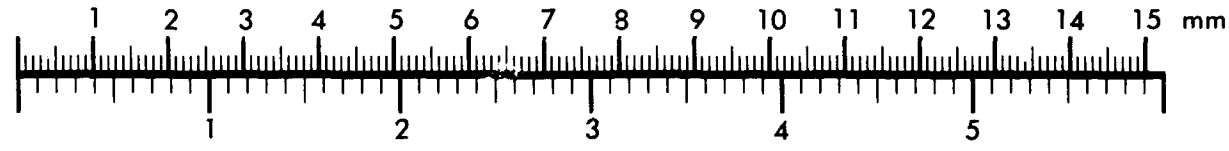

AD-A272 937
HYPERVELOCITY IMPACT: PROCEEDINGS OF THE 1992 SYMPOSIUM
HELD IN AUSTIN TEXAS ON 17-19 NOVEMBER 1992(U) TEXAS
UNIV AT AUSTIN INST FOR ADVANCED TECHNOLOGY
UNCLASSIFIED
H D FAIR ET AL. OCT 93 IAT.R-0023 XT-ARPA
NL
END
FILMED
DTIC

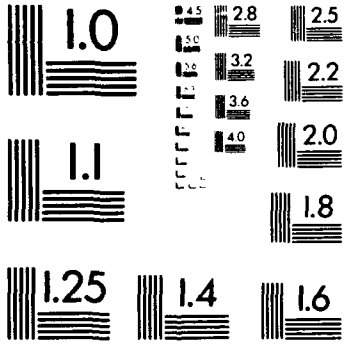


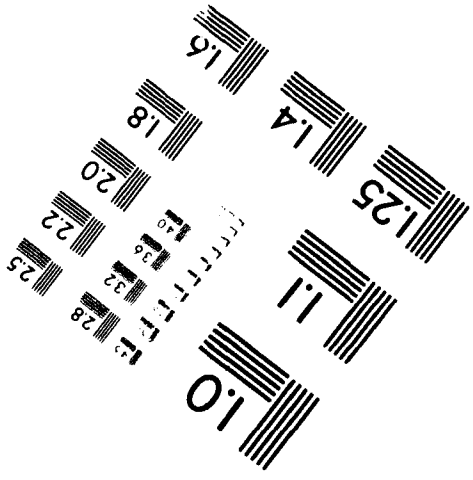


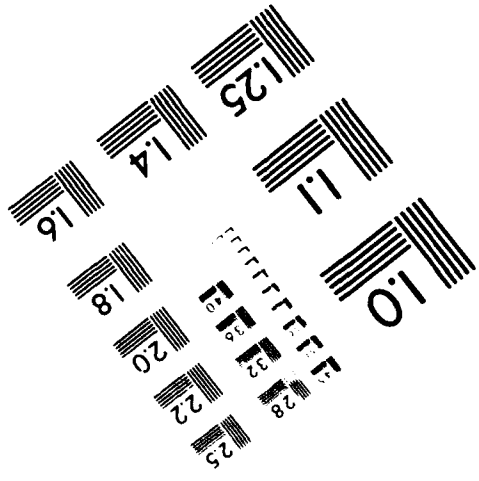
Association for Information and Image Management
1100 Wayne Avenue, Suite 1100
Silver Spring, Maryland 20910
301/587-8202











MANUFACTURED TO AIIM STANDARDS
BY APPLIED IMAGE, INC.

normally fully detached from the slug, when the liner undergoes cone collapse driven by a full explosive charge.

The microscopic examination of the rear of the liner 3C, in the region where the outer apex was originally located, is shown in Fig.12. This again showed a region at the upper outer apex, which retained the large grain structure seen in that region in the virgin unfired liners. This again indicates that the major optically observed grain structure modification occurs primarily in the regions where plastic flow has occurred. The passage of the shock wave through the outer apex has now, however, begun to leave the larger grains at the rear with the first evidence of slip bands and twinning.

The forward region containing the residual rear of the jet still left attached to the slug, is shown in Fig.13. Interestingly, this photomicrograph shows a fine grained structure in the tip with only a few of the elongated grains characteristic of the plastic flow region seen elsewhere to the rear on the liner axis. However, not far behind the residual jet tip, the elongated grain structure associated with plastic flow is again clearly visible and can be seen in the photomicrograph of the adjacent region behind the tip.

The same observations were made on recovered liners 4C, 5F, 6F and 7C. Fig.14 shows the interior view of liner 4C with the radial and circumferential markings. In addition, the tip of the residual jet shows the orthogonal shear traces, previously observed on many of the captured jet particles (Ref.8). The general observational result was essentially the same on the remaining liners. There was however, a trend for the length of the region of the larger grains to become smaller as the charge weight increased. In addition, as the charge weight increased, the slip markings and twinning in the larger rear grains became more severe. This indicates the increasingly severe effects of the shock wave passage. Fig.15 shows a 200x photomicrograph of the rear of the apex of liner 5F graphically illustrating the intragranular slip bands and the twinning at the outer rear apex, in the region of large grains. Finally, as the slug became longer, the region of convergent plastic flow became longer. However, in all cases, the front interior of the recovered liner, from which the jet emanated, clearly showed a very fine grain structure with very little of the interior flow process showing at the very tip where the rear of the jet separated from the slug. However, the orthogonal shear traces shown in Fig.14 were almost always present.

INITIAL OUTPUT OF THE COMPUTATIONAL STUDY

The initial computational analysis of the partial collapse experiments which was carried out at the Los Alamos National Laboratory, using the MESA 2D Code, shows a good agreement of the predicted final partially collapsed liner configurations with the actual shapes of the recovered liners. Figs.16 to 18 inclusive, show the computed partially collapsed configurations predicted for the first four charges and can be compared with the actual cross sections of the recovered liners. The 27.5 gram charge has not yet been computed.

One of the surprises coming from the computations was the prediction of the actual jet formation process in all of the partial collapse experiments except the one with the smallest charge (3.3 grams). The recovered liners were weighed before firing, but, through an oversight, were unfortunately not reweighed after cleaning and before being sectioned for microscopic optical examination. Consequently, the amount of weight loss attributable to jetting could not be determined on these experimental runs, for comparison with the computational prediction. Needless to say, this omission will be corrected on future experiments.

The delay settings required to catch the slow moving final collapsed liners were so long (in the millisecond range) that the much higher velocity jet particles were no longer in the same field of view of the radiographs as the collapsed liners. Thus Fig.18 shows that the jetting, which is clearly visible in the computational output at 40, 80 and 120 microseconds is no longer seen near the collapsed liner at 160 microseconds and would be long gone from the field of view after a millisecond.

The analysis of the computations will continue in the future, with a more detailed study of the stress-time and pressure time histories to which various portions of the partially collapsed liners have been subjected. This will provide further quantitative insights regarding the observed response of the various portions of the collapsing liners.

SUMMARY AND CONCLUSIONS

This work reported in this paper, represents a start at the problem of understanding, in phenomenological terms, the superplastic behavior of copper in a shaped charge jet.

An important preliminary conclusion is that very early in the collapse process, portions of the grain structure of the liner are being refined by the plastic flow processes, that start to move the liner material into the jet and the slug. These highly localized flows and the grain structure modifications that they cause, can be identified on both longitudinal and transversely sectioned samples of the partially collapsed liners, by a distinct change in reflectivity. In these regions, initially equiaxed grains in the inner apex region have been forced to undergo elongation and substantial diameter reductions, as a result of the material flow and the associated plastic deformation. The drastically reduced grain diameters essentially provide an early preconditioning which leads to the attainment of the fine grain structure, leading to increased dynamic ductility and ultimately leading to superplastic deformation of the stretching jet. The mechanism involved is primarily the plastic flow process which is effectively extruding the liner material into the jet.

A second observation is that the passage of the shock wave itself, through the liner material (e.g. at the apex) causes other types of modifications that depend on the shock amplitude. The behavior of the rearmost apex grains provide a convenient location for observing these effects. At the lowest shock amplitudes studied, the large, roughly equiaxed grains at the outer apex of the liners, (seen in Fig.4a in the virgin unfired liners) show little or not change in external appearance, whereas the grains at the inner apex of the same liner (e.g. 1F in Fig. 10 and 2F in Fig. 9) show very noticeable changes including grain deformation and grain refinement. The grains at the inner apex are of course, the ones which have undergone some plastic deformation as they start to converge and flow into the jet, to form the jet tip. The passage of the shock wave would still be expected to introduce various lattice defects into the material traversed, but these changes would not be readily visible in optical photomicrographs, when the shock amplitudes are low.

As the shock amplitude increases, one can begin to see in the nominally undeformed grains at the outer apex, the appearance of twinning and increasingly severe intragranular slip lines, as well as other evidence of the effect of the transient shock wave, although the grains at the rear do not appear to have undergone severe geometric deformation or plastic flow. This is indicative of the preliminary conditioning of the liner material, along the lateral surfaces of the liner, before it reaches the collision zone. Other evidence involving examination of the deflected liners prior to their entry into the collision zone indicates that grain refinement also occurs during the convergence process. For the larger charges,

one can find very large internal areas displaying the reflectivity change and the grain refinement (Fig.11). Converging flow lines become more extensive in the longitudinal sections in the center of the plastically deformed regions and the severity of the shock processing on the rearmost grains becomes quite dramatic (see Fig.15).

There is also additional study and analysis required to provide an interpretation of the significance of the radial and circumferential structures (e.g. as seen in Fig.14) which are generated early in the collapse process, and an evaluation of how they may affect the particulation process.

Further computational analysis of the flow process in the partially collapsed copper liners has been carried out by employing the LaGrangean tracer particle technique (Ref. 13) to track the strain and the strain rates in those specific regions of the liner apex which undergo severe flow and deformation during the early stages of the collapse process. These preliminary results indicate very large axial gradients in the strain and the strain rates, as one moves from the inner apex into the liner, toward the outer apex, for those interior regions along the axial direction where the liner material is separating into the jet and the slug. These are also the locations at which the metallurgical observations indicated severe flow and grain deformation. The local strain rates were found to attain surprisingly high levels, e.g. as large as 4.7 x 10 /sec, even in those liners which were only slightly partially collapsed with a small 7.5 gram charge of explosive. This analysis is now being reviewed. The data will be displayed at the poster session and will be the subject of a separate future paper.

ACKNOWLEDGMENT

The work reported in this paper was supported under Contract N60921-89-C-0172 with funds provided by the U. S. Army (BRL), U. S. Navy (NSWC [WOL]) and DARPA. The computational work at the Los Alamos National Laboratory (X-3) was supported under the joint DOD/DOE Munitions Technology Development Program.

The sectioning of the metallurgical specimens and their optical examination was carried out by Paul Jacoy at the California Institute of Technology-NASA-Jet Propulsion Laboratory in Pasadena, California. The authors are indebted to Paul for his outstanding photographic work and for the extensive coverage of the photomicrographs.

LIST OF REFERENCES

1. P.C.Chou and J. Carleone, "The Stability of Shaped Charge Jets", J.Appl.Phys.Vol. 48 4187-4195 (1977).

2. P.C.Chou, J. Carleone, W.J.Flis, R.D.Cicarelli and E.P.Hirsch, "Propellants, Explosives and Pyrotechnics", Vol.8, 175 (1983).

3. J.M.Walsh, "Plastic Instability and Pa..iculation in Stretching Metal Jets",J.Appl.Phys,Vol.56 (7) Oct. 1984.

4. J.P.Curtis, "Axisymmetric Instability Model for Shaped-Charge Jets", J.Appl.Phys.Vol 61 (11) June 1987.

5. D.C.Pack, J.Appl.Phys.Vol 63, 1864 (1988).

6a L.A.Romero, "Instability of Rapidly Stretching Metal Jets", J.Appl.Phys.Vol.65(8) April 1989.

6b L.A.Romero, "The Stability of Stretching and Accelerating Plastic Sheets", J.Appl.Phys.Vol.69 (11) June 1991.

7. J.Brown, J.P.Curtis and D.D.Cook, "The Formation of Jets from Shaped-Charges in the presence of Asymmetry", J.Appl.Phys.Vol.72 (6) Sept.1992.

8. L.Zernow and L.E.Lowry, "High Strain Rate Deformation of Copper in Shaped Charge Jets", International Conference on High Strain Rate-Phenomena in Materials (EXPLOMET '90), San Diego, CA Aug. 1990.

9. R.G.Johnson and W.H.Cook, "A Constitutive Model and Data for Metals Subjected to Large Strains, High Strain Rates and High Temperatures", Proceedings of the Seventh International Symposium on Ballistics, The Hague, The Netherlands, April 1983.

10. L.Zernow, "Metallurgical, X-Ray Diffraction and SEM Studies of Indiv. Shaped Charge Jet Particles Captured by Soft Recovery-II,International Conference on Ballistics, Nanjing,PRC (1988).

11. Current work in progress under Contract DAAH01-92-C-R044.

12. A.H.Chokshi and M.A.Meyers, "The Prospects for Superplasticity at High Strain Rates: Preliminary Considerations and an Example", Scripta.Metall.-Vol. 24, 605, 1990.

13. L.Zernow, E.J.Chapyak, K.Meyer and R.H.Zernow, "The Origins of Liner Material in a Shaped Charge Jet Particle", Paper presented at the 13th International Symposium on Ballistics, Stockholm, Sweden, June 1- 3, 1992.

14. Sheila K. Schiferl, "Texture and Textural Evolution in Explosively Formed Jets", J.Appl.Phys Vol. 66 (6) 15 Sept. 1989.

15. L.Zernow, S.Kronman, "Experiments Generating Partially Collapsed Copper Shaped Charge Liners" 1950 (BRL-Unpublished).

16. W.P.Walters, J.A.Zukas, "Fundamentals of Shaped Charges", John Wiley & Sons, 1989

17. E.M.Pugh, R.J.Eichelberger and N.Rostoker, "Theory of Jet Formation by Charges with Lined Conical Cavities," J.Appl.Phys.,Vol.23,May 1952,Page 532.

18. L.Zernow, "New Results from the Examination of Jet Particles Captured by Soft Recovery", 11th International Symposium on Ballistics, Brussels, Belgium (1989).

19. D.E.Grady and J.R.Asay, "Calculation of Thermal Trapping in Shock Deformation of Aluminum", J.Appl.Phys. Vol.53 (11) 1982.

20. F.Jamet and G.Thomer C.R.Acad. Sci., Ser.B 279 (1974) 50.

21. F.Jamet, "Mesure de la densite d'un jet de charge creuse en cuivre par radiographie-eclair" - R101/76 - Institute St. Louis, 1976.

22. R.R.Karpp, "Direct Dynamic Measurement of the Material Density Within a Shaped Charge Jet", Proceedings of 37th Annual Bomb and Warhead Meeting, Charleston, South Caroline, May 1987.

23. Current work in progress under Contract N60921-89-C-0172.

24. J.Bolstad and David Mandell, "Calculation of a Shaped Charge Jet using MESA-2D and MESA-3D Hydrodynamic Computer Codes", LA Report 12274, UC-000, Feb.1992.

1992 HVIS Symposium • List of Attendees

Adams, Dr. Thomas F.	Los Alamos National Laboratory
Alder, Francis	Polymer Corp.
Alexander, Carl	BATTELLE Memorial Institute
Alme, Dr. Marv L.	Alme and Associates
Altmayer, Claude	DAT/ETBS
Amdahl, David	
Anderson, Scot	Martin Marietta
Anderson, Jr., Dr. Charles E.	Southwest Research Institute
Andricopoulos, Evan	U.S. Army ARDEC
Ang, Dr. Jim	Sandia National Laboratories
Angel, Y.C.	Rice University
Ari, Nasit	Kaman Sciences Corporation
Asay, Dr. James R.	Sandia National Laboratories
Atkinson, Dale	POD Associates, Inc.
Attaway, Dr. Steve	Sandia National Laboratories
Aussourd, Christian	CEL-V
Babcock, Dr. Susan M.	Titan Corporation/CRT
Backofen, Joseph	Brigs Co.
Bailey, John W.	Wright Laboratory
Baker, Louis	Dagonet Software
Barber, John	IAP Research, Inc.
Barker, Lynn	VALYN International
Bauer, Ernst	ERNO Raumfahrttechnik GmbH
Baum, Dennis	Lawrence Livermore National Laboratory
Bell, Lanny	AEDC/Calspan
Bender, Fred	Nichols Research Corporation
Bermudez, Marcelo	Kaman Sciences Corporation
Bernhard, Ron	Lockheed Engineering & Sciences Co., Inc.
Berry, Don	Institute for Advanced Technology
Biele, Dr. Joachim K.	WTD 91
Bilyk, Stephan	U. S. Army Research Laboratory
Birnbaum, Naury	Century Dynamics, Inc.
Blaylock, Neil	Southwest Research Institute
Bless, Stephan	Institute for Advanced Technology
Bloom, Bernard	
Blouin, Bruno	SNC, Inc.
Boezer, Gordon L.	Institute for Defense Analysis
Bol, Johannes	Battelle-Institut E.V.
Boslough, Mark B.	Sandia National Laboratories
Bozier, Jean Claude	Centre D' Etudes
Brooks, Alan L.	Lawrence Livermore National Laboratory
Budge, Kent	Sandia National Laboratories
Bulmash, Gerald	U. S. Army Research Labatory
Burke, Wayne	General Dynamics Land Systems, Inc.
Candland, Dr. Calvin T.	Alliant Techsystems
Carlyle, John	General Research Corporation
Carson, Dr. W.A.J.	Defense Research Agency
Chabai, Al	Sandia National Laboratories
Chapyak, E.J.	Los Alamos National Laboratory
Charest, Dr. Jacques	Dynasen, Inc.
Chau, Henry	Lawrence Livermore National Laboratory
Chavez, David	Lockheed Engineering & Sciences Co., Inc.
Chhabildas, Lalit C.	Sandia National Laboratories
Choi, Joon-Hong	A.D.D. Advanced Technology Research Center
Choo, Young-il	Lockheed Missiles and Space Co., Inc.
Christiansen, Eric	NASA-Johnson Space Center

Clark, Steven	MEVATEC Corporation
Cohen, Larry	Science Applications International Corp.
Collins, John	Wright Laboratory
Colton, Jim	SRI International
Cook, Dr. William	Wright Laboratory
Cooper, Thomas	SRI International
Cour-Palais, Burton	McDonnell Douglas Space Systems
Courter, Dr. Robert	Louisiana State University
Crawford, David	Brown University
Crews, Ms. Jeanne	NASA-Johnson Space Center
Cunningham, Bruce	Lawrence Livermore National Laboratory
Cunningham, Timothy M.	General Research Corporation
Cunningham, Timothy W.	Wright Laboratory
Curtis, Dr. John P.	EDS-Scicon Defence Ltd.
Dahl, Kim	McDonnell Douglas Space Systems
Darrigade, Alain	GIAT Industries
David, Patrick	CISI Ingenierie
Davidson, Rich	Los Alamos National Laboratory
Davidson, Thomas E.	U.S. Army ARDEC
Davies, Frank	K-Tech Corporation
deRosset, Dr. William	U.S. Army Research Laboratory
Destefanis, Roberto	Alenia Spazio
Dickinson, David	Naval Surface Warfare Center
Diehl, Steve R.	Kaman Sciences Corporation
Dike, Jay	Sandia National Laboratories
Dingus, Ronald	Strategic Defense Initiative Organization
Driga, Dr. Mircea	Institute for Advanced Technology
Dunham, Stanley	Kaman Sciences Corporation
Dunn, Dr. William P.	U.S. Army ARDEC
Ehrgott, John	USAE-WES/SL
Eibl, Stephan	Technical University Munchen
Elia, Eric	CEA
Enblom, Royne	Bofors Weapon Systems
Fahrenthold, Eric P.	The University of Texas at Austin
Fair, Dr. Harry	Institute for Advanced Technology
Fang, H. Eliot	Sandia National Laboratories
Finnegan, Stephen	Naval Air Warfare Center
Fletcher, Robert	NASA-Johnson Space Center
Fortov, Dr. Vladimir	Russia Academy of Sciences
Frank, Konrad	U.S. Army Research Lab
Franzen, Roland	Titan Corporation
Frederickson, Alma	Defense Nuclear Agency
Frischkorn, John	DOE
Fry, Mark	Science Applications International Corp.
Furnish, Dr. Michael	Sandia National Laboratories
Geille, M.	CEA/CESTA/ESD
German, Michael T.	Ministry of Defence
Gilath, Dr. Irith	SOREQ Nuclear Research Center
Glenn, Dr. Lewis A.	Lawrence Livermore National Laboratory
Godbold, Robert	British Embassy
Goddard, Stanley	BATTELLE Memorial Institute
Godwin, Robert	Los Alamos National Laboratory
Gooch, William	U.S. Army Research Laboratory
Gora, Dr. Thaddeus	U.S. Army ARDEC

Grace, Dr. Fred	U.S. Army Research Laboratory
Grady, Dr. Dennis	Sandia National Laboratories
Graf, Al J.	U.S. Army ARDEC
Greene, Ronald	Sandia National Laboratories
Groenenboom, Dr. Paul	Engineering Systems International
Grosch, Don	Southwest Research Institute
Haffenden, D.	Defence Research Agency
Haugstad, Dr. Bjarne	Norwegian Defence Research Establishment
Hawke, Ronald S.	Lawrence Livermore National Laboratory
Hawkins, A.J.	DRA (Military Division)
Hayami, R.A.	The University of Alabama in Huntsville
Held, Dr. Manfred	MBB-VAGT
Hellberg, Lennart	Bofors Weapon Systems
Henninger, Rudolph	Los Alamos National Laboratory
Herrmann, Walter	Sandia National Laboratory
Hertel, Eugene	Sandia National Laboratories
Hogan, Billy	Los Alamos National Laboratory
Hogg, David M.	Wright Laboratory
Hohler, Dr. V.	Ernst Mach Institut
Holmberg, Lars	National Defense Research Establishment
Holsapple, K.A.	University of Washington
Holt, William	Naval Surface Warfare Center
Horz, Friedrich	NASA-Johnson Space Center
House, Joel W.	University of Kentucky
Housen, Kevin	The Boeing Company
Hunt, Ronald D.	Wright Laboratory
Isbell, William	ATA Associates
Jackson, George	LORAL Vought Systems Corporation
Jerome, David M.	Wright Laboratory
Johnson, Ronald H.	DOE
Johnson, Gordon R.	Alliant Techsystems
Johnson, J.D.	Los Alamos National Laboratory
Johnson, Michael	McDonnell Douglas Space Systems
Joinson, Roger	U.S. Army ARDEC
Jolly, William	Kaman Sciences Corporation
Jones, Dennis	Kaman Sciences Corporation
Jones, Norman	The University of Liverpool
Jordan, Timothy	CAS, Inc.
Katayama, Masahide	CRC Research Institute, Inc.
Kemmey, Peter	DARPA
Kerr, Justin	NASA-Johnson Space Center
Kerrisk, Jerry F.	Los Alamos National Laboratory
Kiehne, Thomas M.	Institute for Advanced Technology
Kipp, Marlin	Sandia National Laboratories
Kiser, Laura	Carnahan and Associates
Kitchens, Jr., Clarence W.	U.S. Army Research Laboratory
Kneff, Dennis	Rockwell International Corporation
Knutelsky, Bruce	U.S. Army ARDEC
Kohlberg, Ira	Institute for Defense Analysis
Kosel, Frank	Hadland Photonics, Inc.
Lacomme,	CEA
Lambert, Michel	European Space Agency
Lambert, David	Wright Laboratory

Lantz, Robert	U.S. Army ARDEC
Larriva, Rene	Interfermetrics, Inc.
Lawrence, Jeffery	Sandia National Laboratories
Lee, Thomas W.	Utah Valley Community College
Lee, Ronald	Lawrence Livermore National Laboratory
Lehr, Dr. Hartmuth F.	Institute Saint Louis
Leyrat, Jean-Pierre	Centre d'Etudes deVaujours-Moronvilliers
Liquornik, Dave	The University of Alabama in Huntsville
Littlefield, Dr. David L.	Southwest Research Institute
Louie, Nikolai	McDonnell Douglas Corporation
Loupias, Christian	Centre D'Etudes de Gramat
Lundberg, Patrik	FOA 25
Lundberg, MAJ Randy	U.S. Army ARDEC
Lyles, Gayland	U.S. Government/CIA
Lynch, N.	Defence Research Agency
Maclay, Timothy	University of Colorado
Mandell, Dr. David	Los Alamos National Laboratory
Marchand, Alain	Thomson Brandt Armements
Marte, Lorenzo	Physics International Company
Martin, Lt Col Charles	Strategic Defense Initiative Organization
Mattsson, Arne	Scandiflash AB
McDonald, Dr. Robert A.	Baylor University
McGlaun, Dr. J. Michael	Sandia National Laboratories
McKeown, Reid	Naval Surface Warfare Center
Meier, John	Los Alamos National Laboratory
Menna, Thomas L.	General Research Corporation
Metcher, Graeme	Defense Research Agency
Miller, L.D.	Army FSTC
Moon, Sung-Ki	A.D.D. Advanced Technology Research Center
Moore, Timothy	Naval Surface Warfare Center
Morrison, Walter F.	U.S. Army Ballistic Research Laboratory
Mullin, Scott A.	Southwest Research Institute
Murphy, Michael	Lawrence Livermore National Laboratory
Nellis, William J.	Lawrence Livermore Naitonal Laboratory
Normandia, Dr. Michael J.	Kaman Sciences Corporation
Oldroyd, Buddy	Naval Air Warfare Center
Olsen, Gregory D.	NASA-Marshall Space Flight Center
Orphal, Dennis L.	California Research & Technology, Inc.
Ortega, Javier	Lockheed Engineering & Sciences Co., Inc.
Overley, Richard	U.S. Army White Sands Missile Range
Pace, Christopher D.	General Research Corporation
Partom, Yehuda	Institute for Advanced Technology
Patterson, Bruce C.	Wright Laboratory
Peery, J.	Sandia National Laboratories
Perea, Aaron	Phillips Laboratory
Perez, Vivian	Alliant Techsystems
Persson, Ake	Dynamec Research AB
Peterson, Rob	
Peterson, Brian D.	Wright Laboratory
Peterson, Dennis	Institute for Advanced Technology
Piekutowski, Andrew J.	The University of Dayton
Pinedo, John	Lockheed Engineering & Sciences Co., Inc.
Plenge, Benjamin T.	Wright Laboratory

Pomykal, Glenn W.	Lawrence Livermore National Laboratory
Poormon, Kevin L.	University of Dayton Research Institute
Raftenberg, Dr. Martin N.	U.S. Army Research Laboratory
Rapacki, Jr., Edward	U.S. Army Research Lab
Reaugh, Jack	Lawrence Livermore National Laboratory
Reeder, Douglas	General Research Corporation
Rego, Jr., Jack	Lawrence Livermore National Laboratory
Reimerdes, Dr. Hans	Institut fur Leichtbau
Reinecke, William	Institute for Advanced Technology
Reitsma, H. J.	PML-TNO
Reschauer, Winfried	LRT/TUM
Riegel, John P.	Southwest Research Institute
Ronn, Torsten	Bofors Weapons Systems
Ross, C. Allen	University of Florida
Roth, George J.	University of Dayton Research Institute
Saravane, Isaac	Potomac Research, Inc.
Sarjeant, Dr. W.J.	State University of New York at Buffalo
Schildknecht, Dr. Manfred	DIEHL GmbH & Co.
Schmidt, Martin J.	Wright Laboratory
Schmidt, Robert M.	The Boeing Company
Schmidt, E. M.	U.S. Army Laboratory Command
Schneidewind, Philip N.	Titan Corporation
Schonberg, Dr. William P.	University of Alabama - Huntsville
Schroder, Dr. Gustav-Adolf	Ernst Mach Institut
Schultz, Peter H.	Brown University
Sedgwick, Robert T.	Maxwell Labs
Senf, Hermann	Ernst Mach Institut
Shafer, Barry	Los Alamos National Laboratory
Shephard, Gillian	Lockheed Engineering & Sciences Co., Inc.
Sheridan, Dr. Jim	Defence Research Agency
Simon, Dr. Charles	Institute for Space Science
Simonson, III, Dr. S. Christian	Lawrence Livermore National Laboratory
Sinclair, John	DOE
Skaggs, Dr. S. Robert	Los Alamos National Laboratory
Smith, Vernon	Kaman Sciences Corporation
Smith, Mark	AEDC/Calspan
Sommers, Bill	Nichols Research Corporation
Sparks, Dr. Warren	Los Alamos National Laboratory
Speyer, Brian	Hadland Photonics
Stanton, P.L.	Sandia National Laboratories
Steinmann, Fritz	DIEHL CmbH & Co.
Stellingwerf, R.	Los Alamos National Laboratory
Stevenson, Donald	Rockwell International Corporation
Stilp, Dr. A. J.	Ernst Mach Institut
Stradling, Gary L.	Los Alamos National Laboratory
Strobel, Eric	W.J. Schafer Associates, Inc.
Subramanian, Ravi	Institute for Advanced Technology
Swift, Hallock F.	Titan Corporation
Tanner, Jr., William G.	Baylor University
Taylor, Robert	LORAL Vought Systems Corporation
Tedeschi, Dr. William	Sandia National Laboratories
Thurmond, Leo	FMC Corporation
Tipton, John	U.S. Army Corps of Engineers
Touze, Patrick	Centre d'Etudes de Gramat
Tower, Dr. Michael	LORAL Vought Systems Corporation

Vallee, Daniel	GIAT Industries
Vaught, Wade H.	Wright Laboratory
Voelker, Eugene	Sandia National Laboratories
Waggener, Sam	Naval Surface Warfare Center
Walker, James D.	Southwest Research Institute
Walton, John	CIA
Watts, Alan J.	POD Associates, Inc.
Weber, Karl	Ernst Mach Institut
Weickert, Dr. Chris	Defence Research Establishment
Weir, Sally	U.S. Army Corps of Engineers
Weirick, Lawrence J.	Sandia National Laboratories
West, Michael	McDonnell Douglas Corporation
White, Everett	Olin Corporation
Whitney, James	Lockheed Engineering & Sciences Co., Inc.
Wightman, Mark	Defence Research Agency
Wilbeck, James	Kaman Sciences Corporation
Williams, Andrew	Naval Research Laboratory
Williamsen, Joel	NASA-Marshall Space Flight Center
Wilson, Dennis	Institute for Advanced Technology
Winfield, Darrell	Calspan
Wingate, Charles A.	Los Alamos National Laboratory
Wong, M.	Sandia National Laboratories
Yatteau, Jerome	Applied Research Associates, Inc.
Yaziv, Dan	RAFAEL
Yew, C. H.	The University of Texas at Austin
Zakraysek, Alan	Naval Research Laboratory
Zernow, Dr. Louis	Zernow Technical Services, Inc.

Author Index

Alexander, W. M. 509, 729
Anderson, Jr., C. E. 1, 85, 551
Ang, J. A. 13, 95
Angel, Y. C. 25
Ari, N. 37
Atkinson, D. 49

Babcock, S. M. 695
Bahk, S. 61
Baker, J. R. 73
Bar-Noy, T. 279
Bareiss, L. 479
Bernhard, R. P. 347
Bless, S. J. 85
Blossom, A. A. Hopkins 719
Boslough, M. B. 95
Budge, K. G. 107
Burkett, M. W. 819

Chapyak, E. J. 863
Charvet, E. 467
Chau, H. 451
Chavez, D. 61
Chhabildas, L. C. 95, 121, 133
Christiansen, E. L. 95, 145, 157, 169
Cintala, M. J. 347
Collopy, M. T. 719
Colton, J. D. 597
Cook, W. H. 373
Cooper, T. 181
Cour-Palais, B. G. 95, 193
Crawford, D. A. 205
Crews, J. L. 95
Culp, R. D. 479
Curling, Jr., H. L. 719, 775
Curtis, J. P. 217
Cykowski, E. 157

Dahl, K. V. 193
Davidson, R. F. 819
Dickinson, D. L. 831
Dunn, J. E. 121

Eliezer, S. 279
Emery, B. 61
Englman, R. 279

Fahrenthold, E. P. 229
Finnegan, S. A. 241
Franzen, R. R. 551
Frey, J. D. 255
Fuerstenau, S. 719
Furnish, M. D. 267

Gallagher, P. J. 809
Garaud, X. 255
Gerassimenko, M. 451
Gilath, I. 279
Gillespie, T. G. 479
Gillis, P. P. 503
Gilman, J. J. 291
Gosling, S. M. 13
Grace, F. I. 303
Grady, D. E. 427, 851
Gratz, A. J. 531
Griffiths, D. J. 751
Groenenboom P. 255
Grosch, D. J. 315, 763

Hall, C.A. 95
Hansche, B. D. 13
Hatfield, S. L. 503
Hatt, D. J. 785
Heimdahl, O. E. R. 241
Helba, M. J. 519
Held, B. J. 619
Henninger, R. 491
Hertel, E. S. 133
Hickman, R. J. 13
Hill, S. A. 133
Hohler, V. 325, 797
Holsapple, K. A. 335
Hörz, F. 347
House, J. W. 407, 503
Humphrey, J. W. 695

Idzorek, G. C. 719, 775
Igenbergs, E. 587
Isbell, W. M. 359

Jaeger, Z. 279
Janicot, F. 255
Johnson, G. R. 373, 385
Johnson, M. S. 739
Jolly, W. H. 395
Jones, S. E. 407

Kerr, J. H. 169
Kerrisk, J. F. 417
Kipp, M. E. 427
Konrad, C. H. 13
Kustas, F. M. 479

Lambert, M. 255
Lawrence, R. J. 439, 851
Lee, T.-S. 325
Lee, R. 451
Levadou, F. 631
Leyrat, J. P. 467
Lindfors, A. J. 241
Littlefield, D. L. 1

Maag, C. R. 729
Maclay, T. D. 479
Majerus, M. E. 551
Mandell, D. A. 491
Marlow, R. B. 407
Mayes, J. L. 503
McDonald, R. A. 509, 729
Meier, J. K. 417
Miller, J. M. 121
Mog, R. A. 519
Mullin, S. A. 763

Nahme, H. 325
Nellis, W. J. 531
Nolen, A. M. 541

Olsen, G. D. 541
Orphal, D. L. 551
Ortega, J. 157
Osher, J. 451

Peery, J. S. 107
Persechino, M. A. 73, 561
Petersen, E. H. 385
Piekutowski, A. J. 193, 573
Pomykal, G. 451
Poormon, K. L. 193
Pringle, J. K. 241
Pujols, H. C. 467

Reinhart, W. D. 95, 121
Reschauer, W. 587
Riegel, J. P. 315, 843
Robinson, J. H. 519
Rott, M. 631

Sanai, M. 597
Saravane, I. 607
Savick, D. S. 619
Scheer, S. A. 671
Schmidt, E. M. 619
Schneider, E. 631
Schneidewind, P. N. 551
Schonberg, W. P. 637, 647
Schultz, P. H. 205, 659
Schulz, J. C. 241
Schwehm, G. 631
See, T. H. 347
Shafer, B. P. 719, 775
Shephard, G. L. Y. 671
Simon, C. G. 683
Smith, J. P. 25
Sobota, T. H. 695
Speer, R. 451
Stellingwerf, R. F. 707, 819
Stilp, A. J. 325, 631, 797
Stoltzfus, J. 61
Stradling, G. L. 719, 775
Stryk, R. A. 385
Sweatt, W. C. 13
Swegle, J. W. 427

Tanner, Jr., W. G. 509, 729
Tedeschi, W. J. 359
Tham, R. 325
Thompson, L. E. 739
Trott, W. M. 439
Tsou, P. 751

Walker, J. D. 1, 551, 763
Walsh, J. M. 775
Wang, J.-P. 325
Waschl, J. A. 785
Watts, A. 49
Weber, K. 325, 797
Weickert, C. A. 809
Wilbeck, J. S. 37
Williams, A. E. 561, 607
Williamsen, J. E. 395
Wilson, B. 61
Wilson, L. L. 407
Wingate, C. A. 707, 819

Yang, F. 647
Yatteau, J. D. 831
Yaziv, D. 843
Yeh, Y.-K. 325
Yew, C. H. 851

Zernow, L. 863

Subject Index

ablation pressure, 279
absorption coefficient, 439
acceleration, 121, 315
accelerator
  electric gun, 451
  energy deposition--laser, 279
  exploding bridge foil, 785
  scram accelerator, 695
advection, 107
aerodynamics
  free-flight, 619
aerogel, 683
aluminum
  see projectile, target
aluminum oxide
  see target
aluminum oxide film, 61
angular impulse, 561
angular momentum, 561
Arbitrary Lagrange-Euler, 107, 255
atmospheric erosion, 763
atmospheric interactions, 659

backsplash, 451, 797
ballistic limit, 25, 73, 145, 169, 395, 637, 647
blow off, 439, 451
bonding energy, 291
bulging, 279
bumper shield, 25, 37, 95, 133, 145, 157, 229, 255, 395, 479, 519, 541, 573, 637, 647, 671, 707, 851
bumper shield
  areal density, 739
  dual wall, 395
  mesh double bumper, 95, 145, 169, 479
  multi-shock, 95, 145, 193, 229, 255, 479, 519, 541, 739
  optimization, 479
  projectile shape, 95
  shield design, 145, 169, 193, 541, 647
  thickness effect, 395
  wall spacing, 519
BUSSL, 729

cadmium, 335
carbon fiber/epoxy, 279
ceramic
  aluminum oxide, 85, 181, 491
  aluminum oxide film, 61
  boron carbide, 491
  silicon carbide, 491
  titanium diboride, 491
ceramic cloth
  see target
ceramics
  see target
chemical bonding, 291
compressibility, 1
concrete, 385
copper
  see projectile, target
coupling efficiency, 439
covalent bonding, 291
cracking, 49
crater damage, 157
crater diameter, 73, 347, 819
crater shape, 1, 157
crater volume, 587, 607
cratering, 49, 205, 255, 325, 347, 587, 659, 719, 729, 775, 819
cratering
  atmospheric effects, 659
  crater growth, 659
  critical angle, 157
  diameter, 325, 551
  LDEF, 157
  lunar, 157
  magnetism, 205
  oblique impact, 157
  penetration, 325
  scaling, 719, 775
  velocity dependence, 551
  volume, 325
crystalline olivine, 683
cylindrical convergence, 181

damage, 279, 503
damage
  brittle materials, 279
  ductile materials, 279
damage class, 169, 671
DDT, 241
debris
  charge, 587
  expansion velocity, 427
  mixed phase, 707
  particle size, 427
  residual velocity, 427
debris bubble, 241
debris cloud, 13, 25, 37, 95, 133, 229, 255, 395, 427, 479, 607, 671, 739, 797, 851
debris cloud
  debris velocity, 95
  dispersion, 607, 831
  dynamics, 573
  expansion, 325, 607
  expansion velocity, 325, 573, 797, 851
  formation, 573
  fragment distribution, 37
  fragment number, 37
  fragmentation, 607
  geometry, 325
  impact velocity effects, 573
  mass distribution, 37

modeling, 647
plate thickness effects, 573
radial velocity, 851
spray angle, 37
debris clouds, 573
debris formation, 133
debris generation, 359
debris morphology, 683
debris particle
trajectory distribution, 831
velocity distribution, 831
decomposition energy, 439
defect formation, 279
depleted uranium
see projectile
detector
capture cell, 49, 683, 729
charge, 587
holography, 13
impact, 587
impact flash, 315, 587, 683
plasma velocity, 683
PVDF thin film, 683
VISAR, 267
diagnostic systems, 359
dislocation motion, 291
dolomite, 205
DOP test, 85
dual-wall
see bumper shield
ductility, 291, 863

EFP, 809
electron delocalization, 291
emission line spectra, 751
energetic materials, 241
energy deposition, 439
energy partitioning, 1
epoxy, 719
equation of state, 267, 451, 531
exothermic reaction, 241
expansion velocity, 427, 851
exploding bridge foil, 785
explosive launcher, 181, 467, 763
explosive simulation, 597
explosive volcanism, 531
explosively formed projectile, 809

failure, 279
fast shock tube, 417
fluence, 439
flyer plate, 181, 785
flyer plate
acceleration, 439
fracture, 255, 279, 385, 417, 427, 491, 707, 851
fragment distribution, 37
fragment launcher
fast shock tube, 417
flyer plate, 121
shaped charge, 763
fragment mass, 607
fragment number, 37, 607
fragment simulator, 597
fragmentation, 13, 37, 49, 157, 229, 255, 325, 427, 573, 607, 707, 831, 851
free Lagrange, 181
fullerenes, 531

geologic materials, 267
geologic materials
see target
glass
see projectile, target
glide activation energy, 291
gold
see target
grain structure, 863
granite, 531
graphite epoxy, 607
gun dynamics, 315, 619
Gurney theory, 439

hole formation, 597
hole growth, 509
hole size, 73, 347, 509, 587, 631, 637, 671, 739, 797, 831
holography, 13
Hugoniot, 267, 451, 531

ignition, 61
ignition temperature, 61
image analysis, 13
image reconstruction, 13
image reconstruction
resolution limits, 13
impact flash, 315, 587, 797
impulse
angular, 561
impulse gain, 451
impulse generation, 439
impulse loading, 831
inhibited shaped charge, 763
intact capture, 683, 751
intact recovery
see soft recovery
ionization, 205, 587
iron
see projectile
isentropic compression, 121

jet incoherence, 763

kapton
see projectile

L/D effects, 551
laser interaction, 439
launch dynamics, 121, 315, 417, 619
launcher, 359
launcher
  exploding bridge foil, 785
  explosive cylinder, 467
  modified two-stage, 121
  plasmadynamic, 587
  scram accelerator, 695
  two-stage light-gas gun, 315
  Van de Graaff, 719
LDEF, 49, 157, 347, 631, 729
light-gas gun, 315
luminescence, 587
lunar craters, 157

magnetic fields, 205
magnetism, 205
magnetohydrodynamics, 205
material synthesis, 531
melting, 451, 707
melting
  see phase transformation
metastable phases, 531
micrometeoroids, 359
microparticle
  see projectile
microstructure, 531
mixture theory, 229
modeling
  BRDF, 49
modeling
  brittle material response, 49
  bulging, 279
  Cour-Palais, 49
  cracking, 49
  damage, 279, 417, 503
  debris clouds, 851
  debris environment, 49
  electrical Gurney, 785
  explosive launch, 181
  fragment simulator, 597
  fragmentation, 37, 427, 851
  Grady-Kipp, 37
  Gurney, 439
  impulse gain, 451
  Johnson spall, 417
  Johnson-Cook damage, 417
  Johnson-Holmquist model, 491
  Kessler model, 49
  laser interaction, 439
  late stage equivalence, 719, 819
  magnetohydrodynamics, 205
  mixture theory, 229
  momentum enhancement, 451
  optical scatter, 49
  optimization, 315, 467
  see penetration modeling
  PCLGGP, 315
  RASCAL, 619
  shock pressure decay, 279
  Steinberg ceramic model, 491
  strength, 775, 819
  stress wave propagation, 279
  TIS, 49
molecular dynamics, 509
momentum enhancement, 451
multi-bumper, 519
multi-particle penetration, 831
multi-shock shield
  see bumper shield
muzzle blast, 619

numerical simulation
  advection, 107
  ALE, 107, 255
  bumper shield, 479, 707
  CALE, 763, 819
  CEL, 467
  code linking, 229
  constitutive response, 385, 707
  cratering, 157, 325, 551, 809
  CSQ, 551
  CSQIII, 241
  CTH, 1, 133, 157, 229, 303, 427, 479, 509, 551, 729
  debris cloud, 37, 133
  DYNA2D, 229
  EFHYD, 255
  EFP, 809
  EPIC, 373, 385, 763, 819
  fracture, 385, 427
  fragmentation, 427
  free Lagrange, 181
  hole formation, 597
  hole size, 509
  HULL, 37
  JOY, 451
  L2D, 181, 597
  long-rod penetration, 1
  LS-DYNA2D, 325
  MESA, 417, 491, 819, 863
  mesh sensitivity, 491
  mixture theory, 229
  molecular dynamics, 509
  oblique impact, 37, 157, 373, 707
  penetration, 1
  PLEXUS, 467
  projectile shape, 133
  RHALE, 107
  Riemann shock problem, 707
  short L/D, 551

SMERF, 241
SPH, 385, 707, 819
SPHINX, 707
tensile fracture, 491
void, 229
yawed impact, 373
ZeuS, 61, 157, 809
nylon
see projectile

oblique impact, 37, 73, 157, 373, 395, 561, 637, 647, 671, 707
optical scatter, 49
optimization, 479, 519
orbital debris, 359

particle shape, 531
particle size, 531
particle size distribution, 427
penetration, 145, 169, 809
L/D effect, 551
long-rod, 1, 217
primary, 1
residual, 1
secondary, 1
shaped charge, 217
steady-state, 1
unsteady, 1
velocity dependence, 1, 551
velocity effect, 1, 325, 551
velocity history, 1, 551
penetration efficiency, 85, 217, 551
penetration modeling, 647
angular momentum, 561
area removal, 831
Baker, 561
crater diameter, 73
cratering, 729
critical impact velocity, 303
debris cloud, 25, 647
debris cloud damage, 831
debris cloud loading, 647
debris dispersion, 831
empirical fit, 157
FATEPEN, 831
finite-thickness effects, 843
hole size, 73, 831
hydrodynamic, 217
hydrodynamic limit, 1
hydrodynamic theory, 1
impulse, 561
impulse loading, 831
Jones-Gillis-Foster, 407
KAPP code, 597
long-rods, 303
see modeling
MITI, 843
multi-bumper, 519
nonsteady, 303
obliquity, 73
off-axis velocity, 217
one-dimensional, 407
optimization, 519
phases of impact, 1
plate damage, 831
radial velocity, 217
regression analysis, 519
residual length, 561
rotation rate, 561
shear strength, 561
shield design, 25, 145, 169, 193, 395, 647
short L/D, 551
statistical approach, 217
steady-state, 1, 85, 843
strain, 407
target resistance, 1, 85
Tate, 1, 85
Tate resistance, 1, 85
thermal softening, 843
thickness effects, 25, 73, 145, 169, 395, 541, 647
thin films, 729
trajectory distribution, 831
tumbling, 561
unsteady penetration, 407
velocity distribution, 831
Wilkinson Predictor, 519
witness plate damage, 831, 1, 303
perforation, 25, 145, 157, 169, 325, 347, 373, 395, 561, 587, 637, 647, 831
perforation
thickness effects, 347, 519, 587, 607, 637
petalling, 637
phase change,
vaporization, 587
phase transformation, 95, 133, 193, 205, 255, 291, 335, 451, 479, 531, 573, 683, 729, 739, 797
phase transformation
vaporization, 819
plasma, 205
plastic
see projectile
plasticity, 291, 503, 863
plate deflection, 25, 647
porosity, 751
pressure distribution, 407
pressure wall, 637
primary penetration, 1
projectile
acceleration, 417
projectile

aluminum, 25, 49, 95, 107, 121, 145, 169, 205, 229, 255, 479, 509, 519, 541, 607, 631, 637, 647, 659, 729, 751, 763, 797
aluminum oxide, 49
aluminum rod, 385
aluminum--2017, 73
aluminum--2017-T4, 157, 193, 573
aluminum--2017-T3, 671
aluminum--2024-T3, 407
aluminum--2024-T86, 561
aluminum--6061-T6, 133
aluminum-2024, 467
Armco iron, 809
chunky, 37, 597
compact fragment, 831
copper, 13, 467, 503, 819, 863
copper disc, 851
copper rod, 385
crystalline olivine, 683
cylinder, 169, 325
disk, 707
DU, 85, 373, 843
EFP, 809
fin stabilized, 619
flare stabilized, 619
flat plate, 95, 417
flyer plate, 121
fragmentation, 417
glass 145, 587, 631, 683
graphite epoxy, 607
integrity, 417
iron, 519, 631, 719, 729, 775, 819
kapton, 785
kapton membrane, 451
L/D effects, 551
long-rod, 85, 107, 619
low L/D, 407
magnesium, 95, 121
microparticle, 61, 315, 347, 587, 683, 719, 775, 819
microparticles, 49, 631, 729
mushrooming, 407
nylon, 169, 671
ogive, 241
orbital debris, 359
plastic, 145
plate, 133
polyetheline, 659
residual length, 561
rod, 707
rods, 561
shape, 809
shape effects, 133
short cylinder, 607
short L/D, 325, 551
short rods, 407
soda-lime glass, 347
sphere, 133, 157, 169, 241, 395, 573, 597, 637, 671, 707, 797, 831
stabilize, 619
steel, 13, 145, 169, 241, 303, 385, 831
steel--4340, 407, 561
steel--9SMn28, 325
steel--C1015, 407
steel--E51200, 427
thin flyer, 451
titanium, 121
tungsten, 1, 37, 85, 303, 407, 491, 551, 597, 843
projectile rotation, 561
projectile tumbling, 561
pulsed laser, 279
pyrolization, 751
pyrolytic graphite, 719

radiation
gray body, 751
recovery experiments, 531
release, 267
release temperature, 451, 797
residual penetration, 1
residual projectile
length, 561, 843
rotation, 561
velocity, 561, 843
Riemann shock problem, 707
rocket motor, 241

sabot, 315, 619, 695
discard, 619
scaling, 335, 607, 719, 775, 819
SDT, 241
secondary debris, 671
secondary penetration, 1
semiconductors, 291
shaped charge, 467, 763, 863
atmospheric erosion, 763
coherence, 763
collapse, 863
fragment launcher, 763
inhibited, 763
jet tip, 763
jet tip velocity, 763
off-axis velocity, 217
shear strength, 561
shield design, 395
TMB, 479
shock heating, 751
shock initiation, 241
shock recovery, 531
shock tube, 417
shock wave
wave shaping, 181
shock wave damage, 279

similarity, 335
smooth particle hydrodynamics, 385, 707
soda-lime glass, 347
soft recovery, 863
soft recovery
  see intact recovery
spaced targets, 373
spallation, 279, 587, 637
spectroscopy, 751
steady-state penetration, 1
steel
  see projectile
strain, 863
  metallization, 291
  mushroom, 407
strain-rate effects, 775, 819, 863
strength, 85, 267, 279, 385, 707, 775, 819
superconductivity, 531
surrogate material, 335

target
  aerogel, 683
  aluminum, 25, 37, 49, 61, 95, 107, 229, 255, 279, 335, 385, 395, 451, 509, 519, 587, 637, 647, 719, 729, 763, 775, 797, 819, 831, 851
  aluminum foils, 683
  aluminum oxide, 85, 491
  aluminum oxide film, 61
  aluminum--1100, 347
  aluminum--1100-0, 407, 573
  aluminum--1100-F, 607
  aluminum--2014, 73
  aluminum--2024, 73
  aluminum--2024-T3, 573, 607
  aluminum--2024-T86, 561
  aluminum--2219, 671
  aluminum--6061, 73
  aluminum--6061-T6, 133, 157, 193, 541, 573, 671
  aluminum--7039, 809
  Astroquartz, 739
  bonded adhesive joint, 279
  boron carbide, 491
  bumper shield 25, 37, 95, 133, 145, 157, 169, 193, 255, 395, 479, 519, 541, 607, 637, 671, 739
  cadmium, 335
  carbon fiber/epoxy, 279
  ceramic cloth, 145, 169, 193, 739
  ceramics, 85
  concrete, 385
  copper, 13, 279, 503, 531, 719, 775, 797, 809, 819
  dielectric ceramic, 49
  dolomite, 205
  dual-wall, 637
  energetic materials, 241
  epoxy, 719
  fullerenes, 531
  geologic materials, 267
  glass, 49
  gold, 719, 775, 797
  granite, 531
  grout, 267
  heat shield, 597
  iron, 279
  Kevlar, 95, 169
  lead, 797
  limestone, 267
  mesh, 145, 169
  microspheres, 659
  molybdenum, 797
  mylar foil, 719
  Nextel, 95, 145, 169, 193, 739
  nickel foil, 719
  particulates, 659
  perforation, 157, 325, 373, 561
  plate thickness effects, 561
  plexiglas, 13
  PMMA, 427
  polymer foams, 751
  pressure wall, 637
  propellant, 241
  pumice, 659
  PVDF foils, 683
  quartz, 531, 719
  RHA, 85, 303, 407, 809, 843
  rock, 267
  sand, 659
  semi-infinite, 1, 157, 303, 325, 407, 551, 809, 843
  semiconductor, 291
  silica phenolic/aluminum, 597
  silicon carbide, 491, 531
  silver, 797
  spaced plates, 373
  Spectra, 169
  steel, 13, 385, 831
  steel (hard), 373
  steel--4340, 1, 407, 551, 561
  steel--C45, 325
  steel--mild, 809
  Teflon foil, 631
  teflon, 347
  thickness effects, 25, 73, 157, 347, 395, 541, 561, 573, 587, 607, 797, 831
  thin film, 729
  tin, 797
  titanium, 519
  titanium diboride, 491
  TMB, 479
  transition metals, 291
  tuff, 267

zinc, 335
zinc, 797
target obliquity, 157
target resistance, 1, 85
Tate resistance, 1, 85
thermal softening, 843
thin films, 509, 531
titanium, 121
transformation strain, 291
transition metals, 291
transition pressure, 291
tungsten
see projectile

unsteady penetration, 1

vaporization, 707
see phase transformation
velocity scaling, 335, 551
void growth, 503
void size, 503

wave shaping, 181
Whipple shield
see bumper shield
witness panel, 607
witness panels, 671
witness plate
damage, 325, 831
hole diameters, 325
hole size, 831
standoff, 831
witness plates, 797
witness plates
crater ring, 797

XDT, 241

yawed impact, 373
yield stress, 291